AD_____

AWARD NUMBER: DAMD17-03-2-0021

TITLE: Molecular Genetic and Gene Therapy Studies of the Musculoskeletal System

PRINCIPAL INVESTIGATOR: Subburaman Mohan, Ph.D.

CONTRACTING ORGANIZATION: Loma Linda Veterans Association for Research and Education
Redlands, CA 92374

REPORT DATE: September 2009

TYPE OF REPORT: Final

PREPARED FOR: U.S. Army Medical Research and Materiel Command
Fort Detrick, Maryland 21702-5012

DISTRIBUTION STATEMENT: Approved for Public Release;
Distribution Unlimited

REPORT DOCUMENTATION PAGE

Form Approved
OMB No. 0704-0188

1. REPORT DATE	2. REPORT TYPE	3. DATES COVERED
1 September 2009	Final	9 Sep 2003 – 31 Aug 2009

4. TITLE AND SUBTITLE

Molecular Genetic and Gene Therapy Studies of the Musculoskeletal System

5a. CONTRACT NUMBER

5b. GRANT NUMBER
DAMD17-03-2-0021

5c. PROGRAM ELEMENT NUMBER

6. AUTHOR(S)

Subburaman Mohan, Ph.D.

E-Mail: subburaman.mohan@va.gov

5d. PROJECT NUMBER

5e. TASK NUMBER

5f. WORK UNIT NUMBER

7. PERFORMING ORGANIZATION NAME(S) AND ADDRESS(ES)

Loma Linda Veterans Association for Research and Education
Redlands, CA 921374

8. PERFORMING ORGANIZATION REPORT NUMBER

9. SPONSORING / MONITORING AGENCY NAME(S) AND ADDRESS(ES)
U.S. Army Medical Research and Materiel Command
Fort Detrick, Maryland 21702-5012

10. SPONSOR/MONITOR'S ACRONYM(S)

11. SPONSOR/MONITOR'S REPORT NUMBER(S)

12. DISTRIBUTION / AVAILABILITY STATEMENT
Approved for Public Release; Distribution Unlimited

13. SUPPLEMENTARY NOTES

14. ABSTRACT

The proposed research projects focuses on bone health, including relevance to the musculoskeletal system in battlefield performance and in battlefield injury. We have utilized state-of-the-art molecular genetic and gene therapy technologies to address fundamental questions in bone biology with particularly emphasis on attempting to clarify gene function for those genes that are involved in digit tip regeneration, bone size, skeletal repair and anabolic response to mechanical loading. The molecular genetic approaches have utilized various knockout mouse models and whole genome microarray analysis for evaluation of gene functions. The gene therapy approaches have utilized various viral and non-viral vectors to transfer gene of interest to treat localized and systemic skeletal deficits. We have successfully accomplished nearly all of the objectives proposed in the grant. The four core facilities funded by this project have contributed enormously to the success of our research activities. Our research activities during the past funding period have lead to 14 publications and 14 abstracts. Our studies have led to the identification of key genes and their pathways that are involved in skeletal regeneration and repair. Furthermore, we have developed successful gene therapy application to promote healing of skeletal injuries and increase bone formation throughout the skeleton.

15. SUBJECT TERMS
Mechanical strain, quantitative trait loci analysis, microarray analysis, osteoblasts, Signaling pathways, bone formation

16. SECURITY CLASSIFICATION OF:			17. LIMITATION OF ABSTRACT	18. NUMBER OF PAGES	19a. NAME OF RESPONSIBLE PERSON
a. REPORT	b. ABSTRACT	c. THIS PAGE			19b. TELEPHONE NUMBER *(include area code)*
U	U	U	UU	547	USAMRMC

Standard Form 298 (Rev. 8-98)
Prescribed by ANSI Std. Z39.18

Table of Contents

GENERAL INTRODUCTION

This proposal is divided into three sections: A) Molecular Genetic Projects, of which there are four projects. B) Gene Therapy Projects, of which there are three projects; and C) support Service Facilities, of which there are four projects. Each of the above projects has an introduction.

We have successfully accomplished nearly all of the technical objectives proposed in the grant. Additionally, the four core facilities funded by this project have contributed enormously to the success of our research activities as well as to our progress which are described below. The progress report for each project is organized according to the outline provided by the office of the U.S. Army Medical Research and Materiel Command.

A. MOLECULAR GENETICS PROJECTS

Project 1. Studies on Genetic Regulation of Digit Tip Regeneration

INTRODUCTION

Experiments with amphibian limbs, first undertaken in the 18th century, demonstrate that limb regeneration in vertebrates is possible. In amphibians, the first stages of regeneration are initial wound healing by formation of an epidermal layer over the wound, followed by dedifferentiation of cells that cluster under this epidermal layer. These dedifferentiated cells (blastema cells), similar to stem cells, redifferentiate into other cell types including bone, cartilage and epithelial cells. The genes and genetic pathways that determine how the cells dedifferentiate and redifferentiate into other cell types are not completely understood.

Higher mammals also have marginal abilities to regenerate. For example, children and newborn mice will replace digit tips when they are amputated distal to the last interphalangeal joint. Another example of regeneration in mammals is the healing of ear holes in rabbits without scarring. Recently, we and others have demonstrated that the MRL inbred strain of mouse shows greater regeneration and healing of earhole punches as opposed to several other inbred strains of mice. Among inbred mouse strains, the MRL mouse was found to completely heal earhole punches, the DBA strain was found to be an intermediate regenerator, and the B6 strain found to be a poor regenerator of earhole punches. Other studies have found that the MRL mouse is also capable of cardiac muscle regeneration. Thus, the MRL mouse is a unique model to study the genetic mechanisms that regulate wound healing and tissue regeneration.

BODY

1. Studies Related to Regeneration Differences in Different Mouse Strains

a. Animal Maintenance and Surgery

Our initial goal was to compare digit regeneration in four to six inbred strains of mice (MRL, DBA, SJL, C57BL/6J, C3H and 129/Sv). We obtained four-week old MRL, SJL, C3H, 129, B6 and DBA mice from The Jackson Laboratories (Bar Harbor, ME). The mice were housed at the Veterinary Medical Unit (VMU), JL Pettis VA Medical Center, Loma Linda, CA, under the standard conditions of 14 hours light, 10 hours darkness, ambient temperature of 20^0C,

and relative humidity of 30-60%. For each strain three female and one male were housed in one cage. When female mice were found to be pregnant they were caged separately. The day that mouse pups were born surgery was conducted on the pup's digit tips. The neonatal mice were anesthetized with 5% Halothane mixed with O_2 5L/min. The right front 3rd and 4th digit tips were amputated, with the left side as uncut controls. The amputation level was set up at the bottom of nail level under the microscope. The amputated tissues were collected into RNAlater (Ambion), and the tissues from the pups of one litter were pooled. Both left (uncut) and right (cut) paws X-ray images were taken at 0, 7, 14, 21, and 28 days post surgery with a Faxtron. Also, at four days post surgery, mice were euthanized and regenerating digit tips were collected by surgery and the tissue was pooled in RNA later and stored at –80C for later RNA extraction. One problem we experienced was with mother pups abandoning or cannibalizing pups following surgery. This was particularly a problem for the SJL mouse strain. No pups in the SJL strain survived more than 1-day following surgery. For this reason we compared the MRL to the DBA strain in the microarray expression studies rather than the SJL strain.

b. Growth Rate Measurements

Faxitron x-ray images were measured using the ruler feature of Photoshop (Adobe) (**Figures 1, 2**). Four growth amounts were determined. 1) the amount of dissected tissue; 2) the length of first phalanx of 3rd and 4th digits of front two paws; 3) the length from the bottom of 2nd phlanx to the tissue edge; and 4) the length from the top of 2nd phalanx to the tissue edge. Measurements were made of both left uncut and right cut digits. The growth was determined for 7, 14, 21 and 28 days post surgery.

Figure 1. Measurement of Amounts of Dissected Tissues in Newborn Mouse Pups. The digit tip dissections were carried out on the 3rd and 4th tips of the right paw. The left paw digit tips were not dissected and used as uncut controls to correct for inbred mouse strain size differences. Mice were x-rayed before and after digit tip dissection. Amounts of tissue dissected were calculated by subtracting the after dissection values from the before dissection values of the top of the second phalanx to the digit tip edge (Table 1).

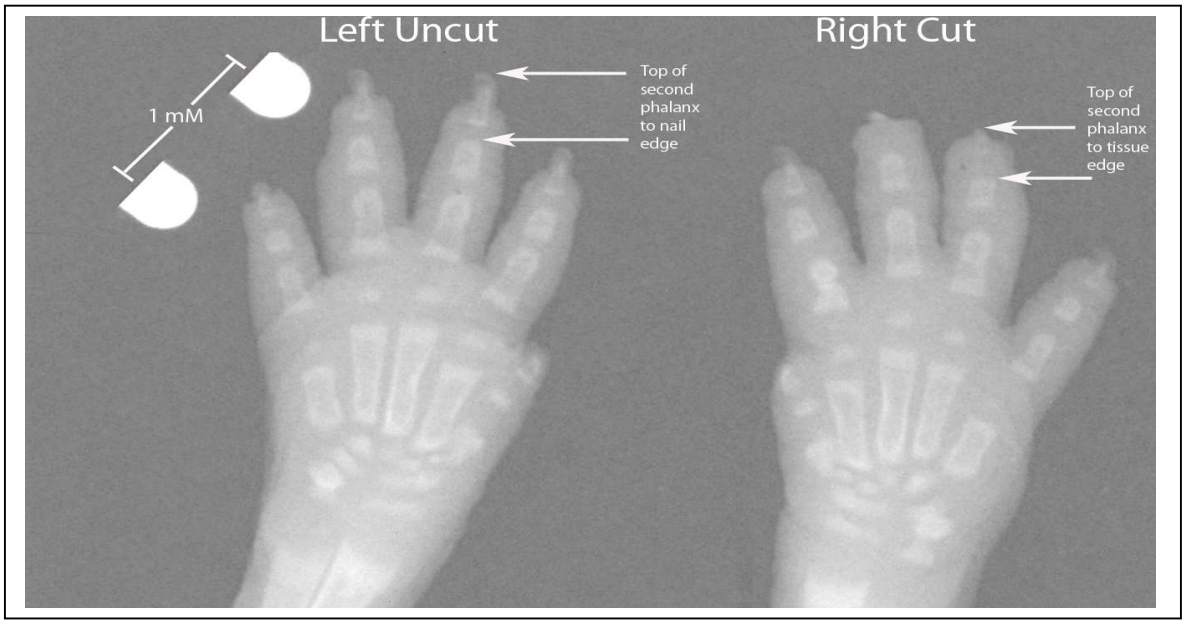

Table 1. Amount of digit tip tissue dissected in mice. The mean amount of tissue dissected in MRL mice was slightly greater (0.14 mM) than in other mouse strains.

Digit	Strain	N	Mean Tissue Dissected (mM)	SD
3rd Right Digit	MRL	20	0.14	0.04
	C3H	4	0.09	0.04
	DBA	24	0.12	0.05
	B6	26	0.12	0.05
	129	4	0.11	0.04
	Total	78	0.14	0.09
4th Right Digit	MRL	20	0.14	0.06
	C3H	4	0.16	0.07
	DBA	24	0.11	0.05
	B6	26	0.11	0.05
	129	4	0.12	0.05
	Total	78	0.13	0.11
Mean of 3rd and 4th Digits	MRL	20	0.14	0.04
	C3H	4	0.13	0.05
	DBA	24	0.12	0.05
	B6	26	0.11	0.05
	129	4	0.12	0.04
	Total	78	0.13	0.10

Figure 2. Measurement of Digit Tip Regrowth. Mice were x-rayed at days 7, 14, 21 and 28 post digit tip dissection. Growth was calculated as follows:

The length of first phalanx of 3rd and 4th digits of both front paws (C to D below);
The length from the bottom of 2nd phalanx to the tissue edge (C to A below)
The length from the top of 2nd phalanx to the tissue edge (B to A below).

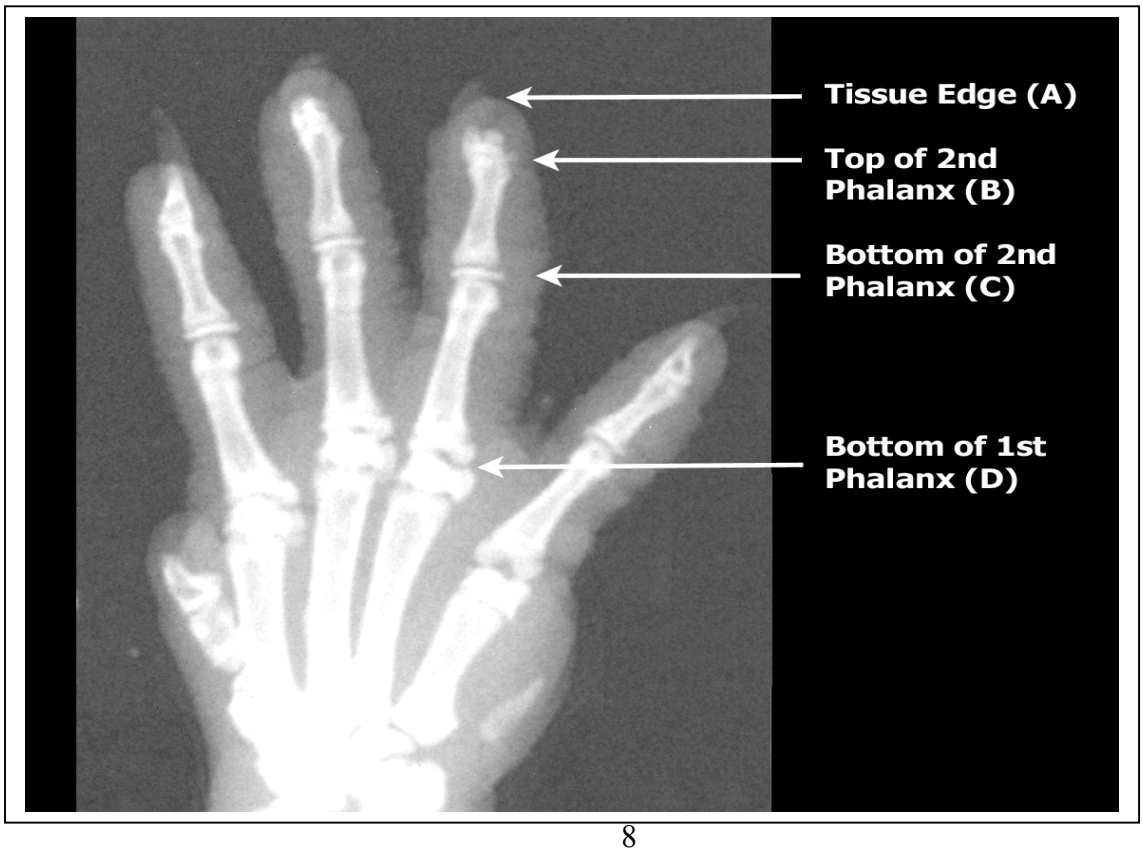

Regeneration Results

In order to insure that regeneration results were not influenced by differences in strain size, the data was normalized by dividing right cut growth measurements by left uncut growth measurements. We first tested the validity of this normalization by dividing the right first phalanx measurements by the left first phalanx measurements (**Figure 3**). As shown below, these ratios do not show significant differences among the mouse strains and the growth ratios all cluster around 1.00. Since the first phalanges were not dissected, this indicates that normalizing for strain size by calculating a growth ratio is a valid method of correcting for strain size.

Figure 3. Normalization for Strain Size. Division of first phalanx right measurements by left measurements gives expected ratios of ~1.00. Also, no significant difference between strains is seen in normalized data for the first phalange growth ratios.

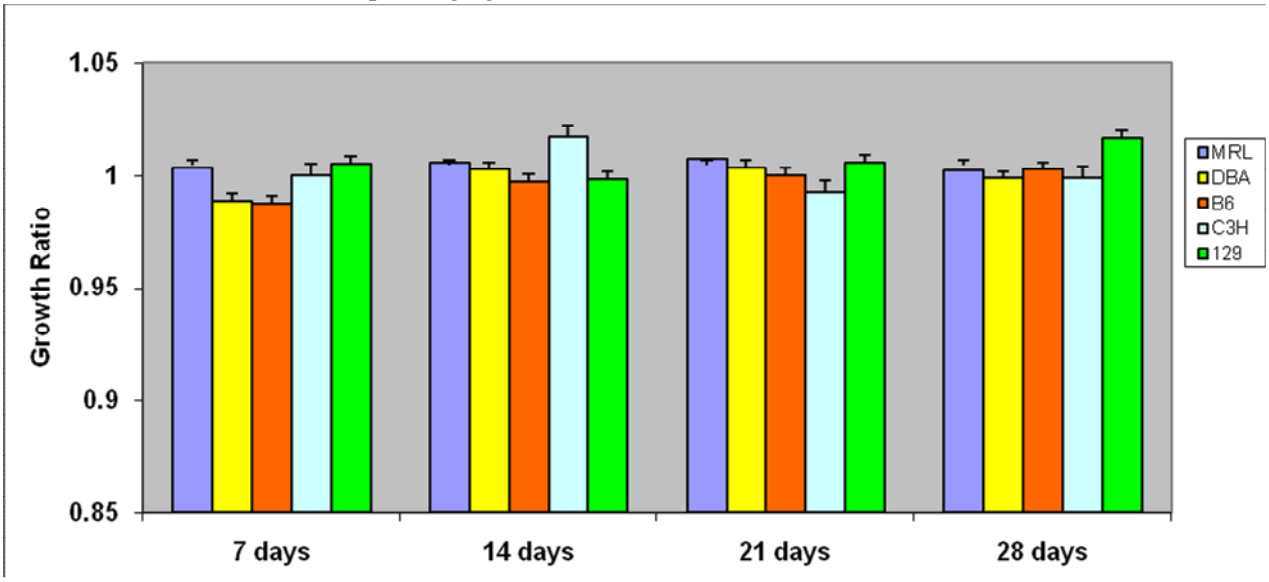

Next we examined the normalized regeneration ratios for dissected digit tips in the mice. As expected, the regeneration ratios are less than one, indicating growth of dissected digit tips is less than undissected digit tips (**Figure 4**). However, the MRL mouse regenerates digit tips significantly greater than the other mouse strains ($p < 0.05$). This is seen particularly at times when mice are in their primary growth phase (days 0 to 21).

Figure 4. Normalized Growth Ratio Regeneration of MRL, DBA, B6, C3H and 129 Digit Tips. Growth ratios measured from the bottom of 2nd phalanx to the tissue edge (C to A in Figure 2) for 14 and 21 days post dissection, show that MRL mice regenerate digit tips greater than other strains of mice ($p < 0.05$, marked by * in plot).

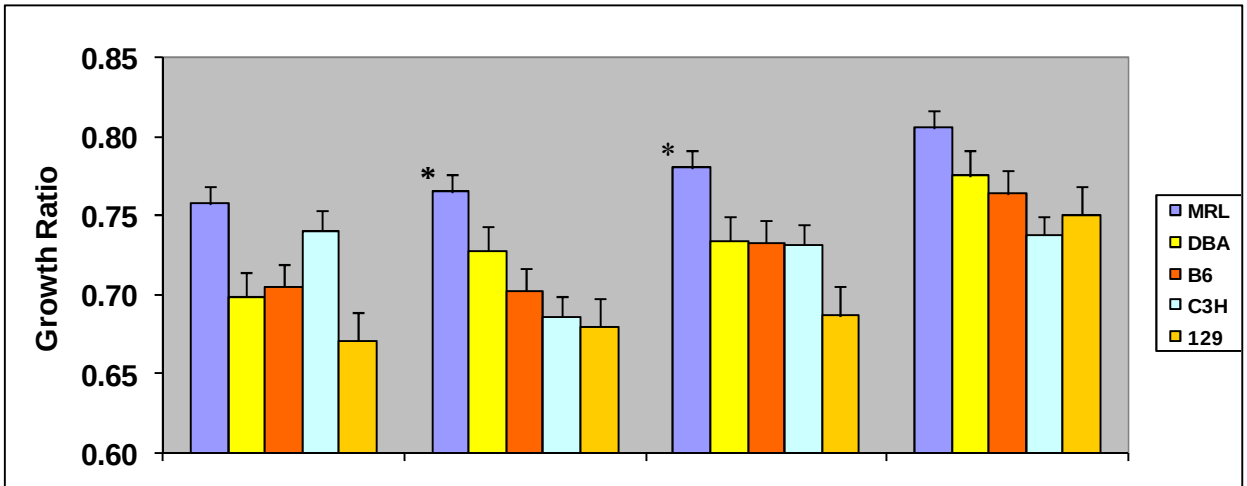

Table 2. Statistical Analysis for Growth among MRL, DBA, B6, C3H and 129 mice. Statistical analysis of the regeneration data was undertaken by 1-way ANOVA using SPSS software. Differences that are statistically significant ($p < 0.05$) are highlighted. Note that for normalized growth ratios of the first phalanges there is no significant difference between the strains. Since no surgery was done on the first phalanges this demonstrates that the growth ratio method of comparison is valid. However, in regenerating digit tips there are significant differences among the mouse strains, particularly when the mice are in their primary growth phase (days 0 to 21).

Time and Phalanx		SS	df	Mean Square	F	Sig.
7 days 1st phalanx	**Between Groups**	0.01	4.00	0.00	1.06	0.38
	Within Groups	0.20	73.00	0.00		
	Total	0.21	77.00			
14 days 1st phalanx	**Between Groups**	0.00	4.00	0.00	0.26	0.90
	Within Groups	0.13	73.00	0.00		
	Total	0.13	77.00			
21 days 1st phalanx	**Between Groups**	0.00	4.00	0.00	0.34	0.85
	Within Groups	0.06	73.00	0.00		
	Total	0.06	77.00			
28 days 1st phalanx	**Between Groups**	0.00	4.00	0.00	0.33	0.86
	Within Groups	0.06	73.00	0.00		
	Total	0.06	77.00			
7 days digit tip	**Between Groups**	0.06	4.00	0.01	2.37	0.06
	Within Groups	0.42	73.00	0.01		
	Total	0.48	77.00			
14 days digit tip	**Between Groups**	0.06	4.00	0.01	2.93	0.03
	Within Groups	0.37	73.00	0.01		
	Total	0.43	77.00			
21 days digit tip	**Between Groups**	0.05	4.00	0.01	2.73	0.04
	Within Groups	0.31	73.00	0.00		
	Total	0.35	77.00			
28 days digit tip	**Between Groups**	0.03	4.00	0.01	1.82	0.13
	Within Groups	0.30	73.00	0.00		
	Total	0.33	77.00			

We also examined the degree of nail regeneration seen in the mice. Mice were sacrificed at day 28 and examined to determine if digits had completely or partially regenerated nails, or if no nail regrowth was seen. As shown in Table 4, partial and full regeneration of nails in MRL mice approached but did not reach statistical significance. This may be due to slightly greater amounts of tissue being initially dissected from the MRL mice (Table 1).

Table 3. Nail Regrowth in 129, B6, C3H, DBA and MRL Mouse Strains.

Mouse Strain	No Regrowth	Partial Regrowth	Full Regrowth	Total
129	1	7	0	8
B6	18	28	8	54
C3H	2	5	1	8
DBA	13	25	10	48
MRL	4	29	7	40
Total	38	94	26	158

Chi-Square Tests

	Value	df	Asymp. Sig. (2-sided)		
Pearson Chi-Square	11.1	8	0.20		
Likelihood Ratio	13.0	8	0.11	N of Valid Cases	158

Next we examined DBA, B6, MRL, C3H and 129 in-bred strains for blastema formation by sacrificing the mice at 1-day post digit tip dissection. No SJL pups survived after surgery since all were abandoned or cannibalized by the SJL mother mice. For the five other strains at 1-day post surgery two pups were sacrificed and paws were dissected. The dissected tissues were stored in 10% formalin until processing. The MDC Phenotype Core facility fixed the tissues in paraffin and mounted and stained five micron tissue sections from each of the strains. Following hematoxylin and eosin (H&E) staining, the tissues were examined under a microscope.

In amphibians, the first stages prior to regeneration are initial wound healing by formation of an epidermal layer over the wound, followed by dedifferentiation (a loss of specialized cellular characteristics and a return to a less specialized cellular structure). These dedifferentiated cells cluster under the epidermal layer of the dissected tip and are termed a blastema. The blastema then rediffentiates into other cell types including bone, cartilage and epithelial cells. This involves pattern formation genes and pathways that are thought to direct the fate of the blastema cells. In the five mouse strains examined, we see the formation of an epidermal layer over the wound only in the MRL and DBA mouse strains at 1 day post dissection. No epidermal layer is seen at 1-day in the C3H, B6 and SJL strains (Figure 5).

Figure 5. Histology Images of Digit Tip Regeneration at Day 1 Post Surgery. In MRL and DBA mice an epidermal layer has formed after 1-day post surgery. In 129/Sv, B6 and C3H mice little or no epidermal growth has formed to close over the wound.

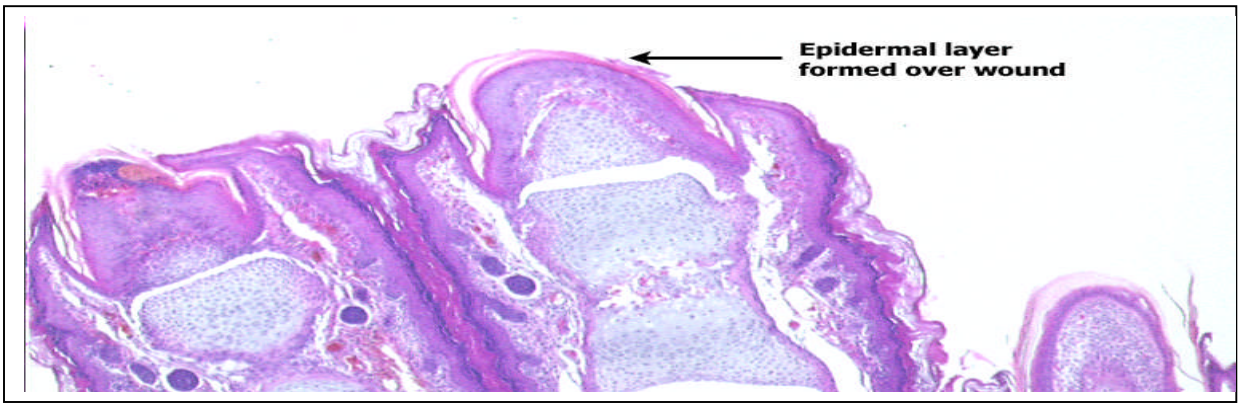

MRL 1-day post surgery

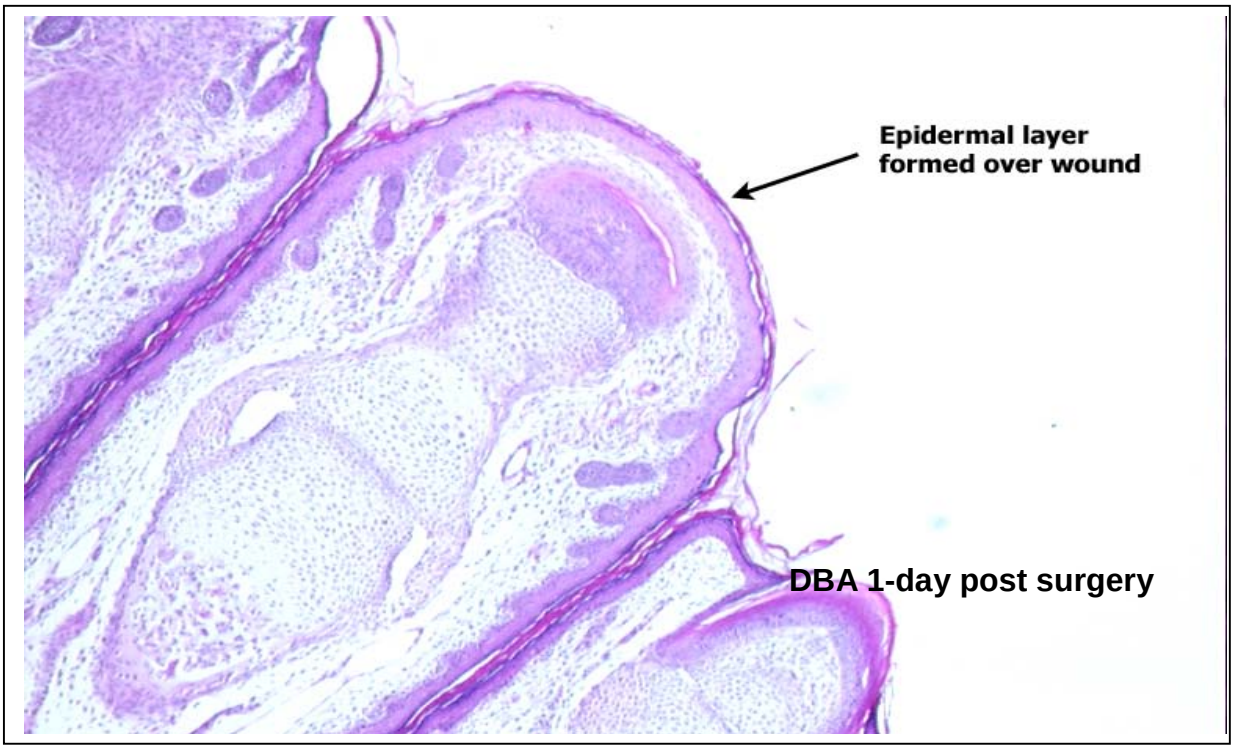

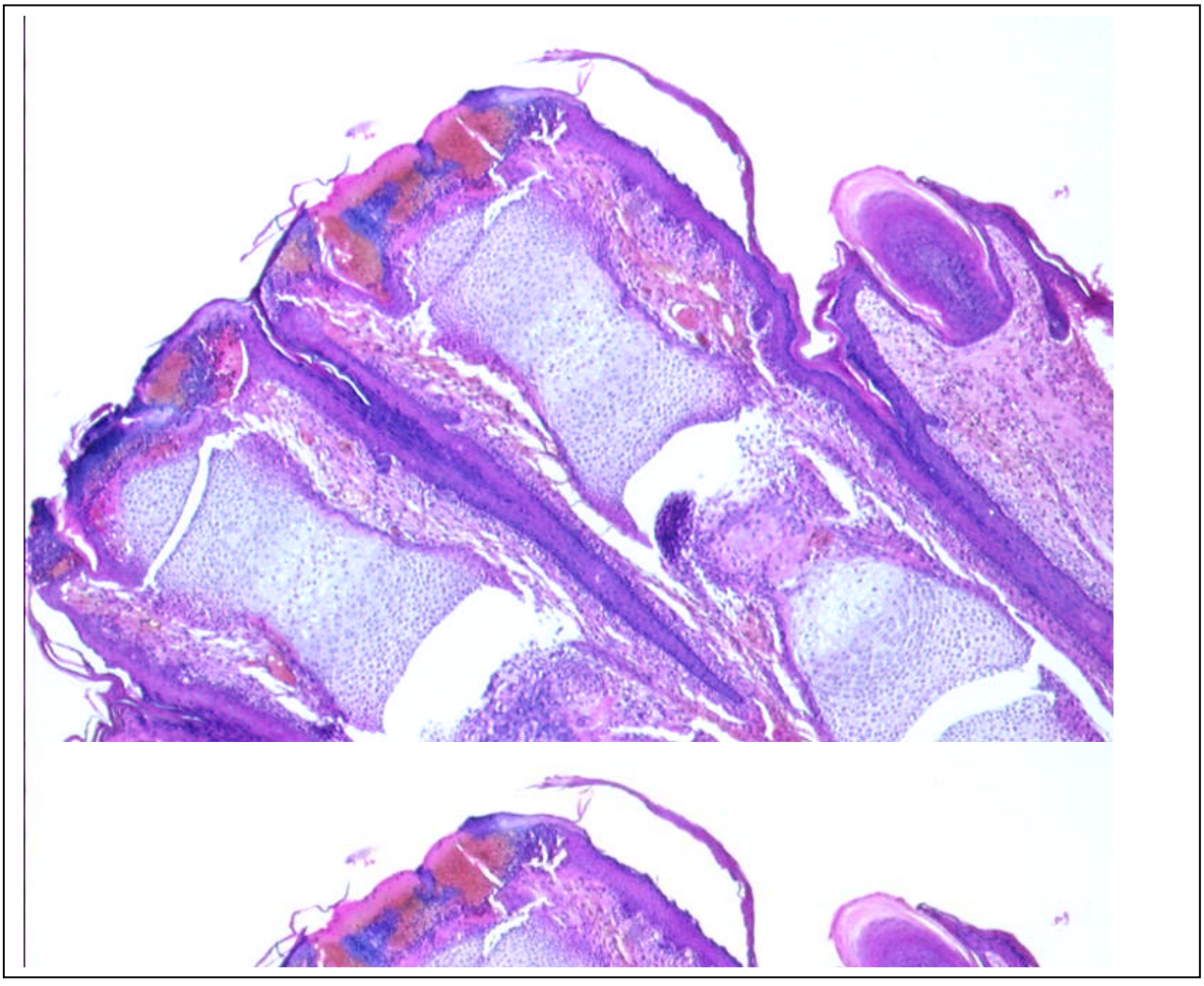

129 1-day post surgery

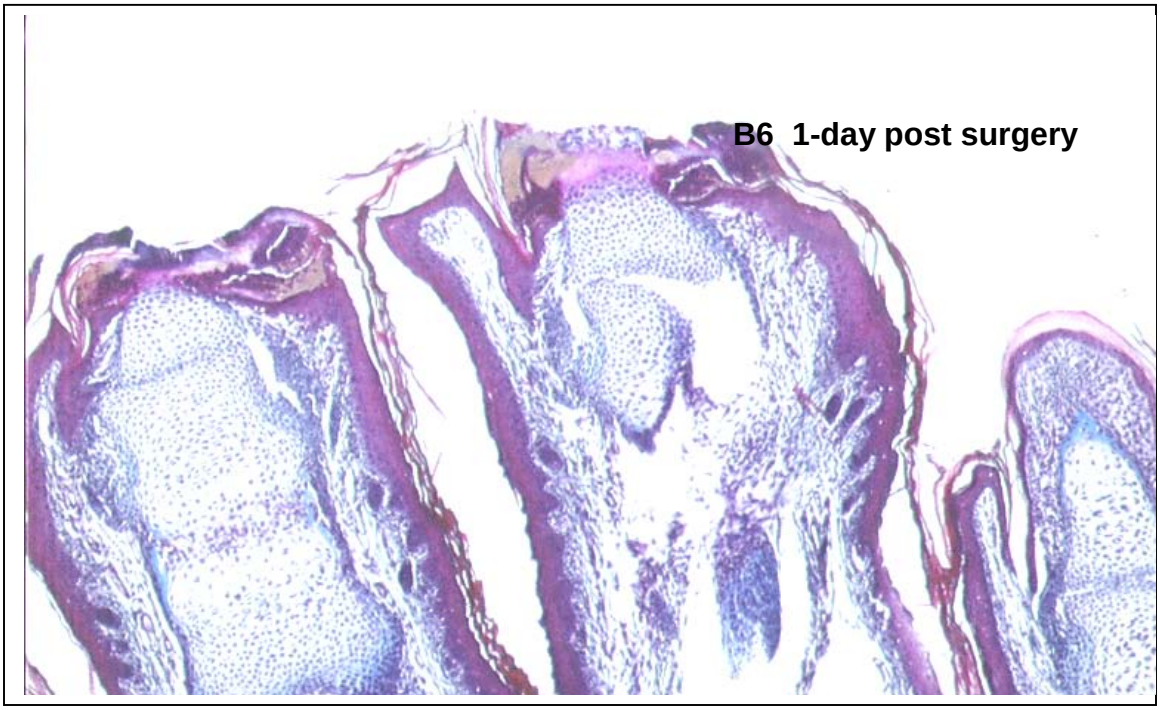
B6 1-day post surgery

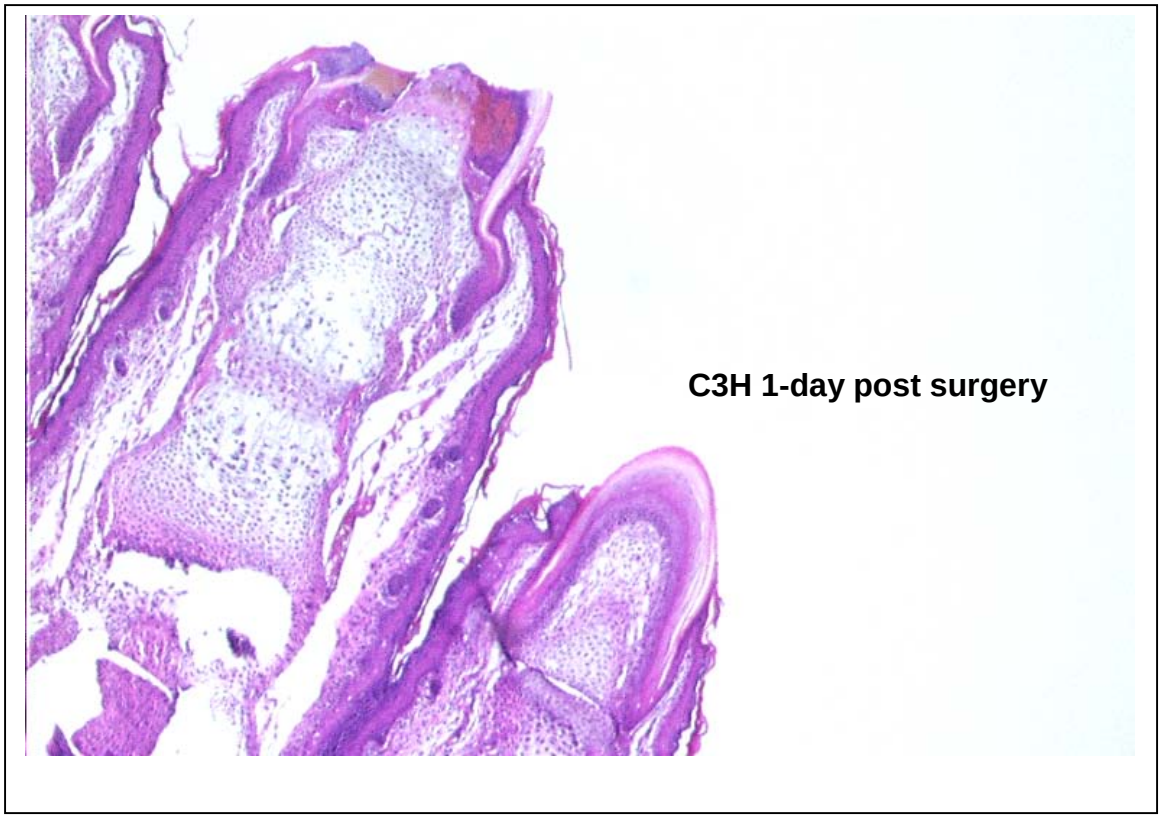
C3H 1-day post surgery

The histology results indicate that the 1-day time point is too early for a blastema to form since only an epidermal wound layer is seen in the MRL and DBA mice.

Next we initiated microarray expression profiling of the digit tip healing tissue at one and four days post amputation in the MRL mouse and the SJL mouse. Control tissue was also obtained from both strains of mice.

C. Gene Expression Studies

1) RNA Extraction for Expression Analysis

Total RNA was isolated from dissected tissues at day 0 and day 4 day using the Agilent Total RNA Isolation Kit (Agilent Technologies). Tissues were lysed using a Polytron Generator (Kinemalica AG, Switzerland), and then processed following the manufacturer's protocol (Agilent). The total RNA concentration was determined by NanoDrop spectrophotometer and RNA quality was determined by 18S/28S ribosomal peak intensity on an Agilent Bioanalyzer. For microarray expression profiling and real-time PCR, RNA samples were used only if they showed little to no degradation.

2). Microarray Hybridization

Custom cDNA slides were spotted in duplicate with ~15,000 cDNA clones obtained from the National Institute on Aging (NIA). A Q-Array2 robot (Genetix) was used for spotting. The arrays were also spotted with Amersham Lucidea Universal Scorecard controls to insure correct gene expression values were obtained from each array. These spotting and spike-in controls contain 10 calibration RNAs of increasing gene copy number with 1:1 Cy3:Cy5 ratios, 8 ratio controls of 1:3 low, 3:1 low, 1:3 high, 3:1 high, 1:10 low, 10:1 low, 1:10 high, 10:1 high Cy3:Cy5 ratios and two negative hybridization controls (Amersham). Controls were spotted in duplicate in the first and last PCR plates to insure proper data tracking. A total 250 ng RNA was used to synthesize double stranded cDNA using the Low RNA Input Fluorescent Linear Application Kit (Agilent). First strand cDNA synthesis was primed with T7-(dT24) promoter primer. From the purified cDNA, cRNA was synthesized using transcription master mix and purified. 250 ng of purified cRNA was used to reverse transcribe to fluorescent cDNA. Cyanine-3-dCTP and cyanine-5-dCTP were used to label experimental samples (day 4) and control samples (day 0). Dye swaps were also conducted to eliminate potential dye bias effects. Samples were hybridized at 60°C for 17 hours. The slides were then washed with Solution I (6X SSC, 0.005% Triton X-102) for 10 min. in the dark and then with Solution II (0.1X SSC, 0.005% Triton X-102) for 5 min. in the dark. The slides were dried with pressurized nitrogen and immediately scanned using a GSI Lumonics ScanArray 4000 scanner. The signal intensity of all microarray images was determined using Imagene 5.6 software.

3). Normalization and Analysis of Microarray Data

Expression analysis of microarray experiments was performed with GeneSpring 6.1 (Silicon Genetics) using the raw intensity data generated by the ImaGene software. Local

background-subtracted median signal intensities were used as intensity measures, and the data was normalized using per spot and per chip LOWESS normalization. The transcripts that passed with flag values present or marginal were targeted for further analyses. The transcripts were then further analyzed by utilizing a one-sample Student's t-test to test whether the mean normalized expression level for the gene is statistically different from 1.0. Genes greater than 1.5 fold up and downregulated at day 4 vs day 0 were determined for both the MRL and DBA strains.

4). Microarray Expression Results

Over 500 genes out of 15,000 on the microarrays were significantly differentially expressed ($p < 0.05$) in MRL and DBA mice at day four in comparison to control tissue at day zero. Of these, 170 genes were upregulated and 280 were downregulated in both mouse strains. About 50% of these genes represent ESTs and unknown genes. Pathway analysis of the known genes reveals that genes in the BMP/TGF pathway are differentially expressed in both mouse strains (BMP-1, Actr2, Smad 4, TGFb1i4, Fstl3, Twsg1, TSC22), thus implicating the BMP/TGF signaling pathway in regulation of digit tip regeneration ($p < 0.05$). Shown in Table 4, is a summary of genes with known functions that are differentially expressed in regenerating digits in both MRL and DBA strains at day 4 in comparison to control tissue at day 0.

Table 4. Genes Differentially Expressed in Both MRL and DBA at Day 4 Post Digit Tip Dissection. Over 500 genes out of 15,000 were significantly differentially expressed ($p < 0.05$) in MRL and DBA mice at day four in comparison to control tissue at day zero. Of these, 170 genes were upregulated and 280 were downregulated in both mouse strains. About 50% of these genes represent ESTs and unknown genes. Pathway analysis of the known genes reveals that genes in the BMP/TGF pathway are differentially expressed in both mouse strains (BMP-1, Actr2, Smad 4, TGFb1i4, Fstl3, Twsg1, TSC22), thus implicating the BMP/TGF signaling pathway in regulation of digit tip regeneration. In the following table, only genes whose functions are known are listed, not ESTs of unknown function. Genes involved in the BMP/TGF signaling pathway are in bold.

Clone Name	Gene Name	Gene Ontology Function
H3031B07	**Twsg1**	**GO:0001503 ossification**
H3005D09	**Fstl3**	**GO:0030514 negative regulation of BMP signaling pathway**
H3098E10	Mor1	GO:0006099 tricarboxylic acid cycle
H3052A04	Mor2	GO:0006099 tricarboxylic acid cycle
H3138A12	4632428N09Rik	GO:0006118 electron transport
H3156A07	Nme6	GO:0006228 UTP biosynthesis
H3031E10	Ahcy	GO:0006306 DNA methylation
H3051D06	2700078H01Rik	GO:0006350 transcription
H3004A11	Tceb3	GO:0006350 transcription
H3097C06	**TGFB1I4 (TSC-22)**	**GO:0006355 regulation of transcription**
H3087E04	Cnot7	GO:0006355 regulation of transcription
H3016G05	Ewsh	GO:0006355 regulation of transcription
H3113H06	Fem1b	GO:0006355 regulation of transcription
H3123B05	Hdac2	GO:0006355 regulation of transcription
H3055B11	Nrf1	GO:0006355 regulation of transcription
H3058C01	Rora	GO:0006355 regulation of transcription

H3016H10	Sp1	GO:0006355 regulation of transcription
H3017H05	Wbp4	GO:0006355 regulation of transcription
H3089B10	Zfp398	GO:0006355 regulation of transcription
H3076G09	9430065L19Rik	GO:0006397 mRNA processing
H3107B08	Upf2	GO:0006397 mRNA processing
H3045D06	Psmd7	GO:0006413 translational initiation
H3023F07	Cct5	GO:0006457 protein folding
H3023D07	D630041K24Rik	GO:0006464 protein modification
H3066E06	C430014H23Rik	GO:0006468 protein amino acid phosphorylation
H3057F01	Csnk1e	GO:0006468 protein amino acid phosphorylation
H3063A08	Lgmn	GO:0006508 proteolysis and peptidolysis
H3048C09	Fbxl12	GO:0006511 ubiquitin-dependent protein catabolism
H3113D07	Psma3	GO:0006511 ubiquitin-dependent protein catabolism
H3013F01	Alad	GO:0006779 porphyrin biosynthesis
H3089A11	Abcf2	GO:0006810 transport
H3054H04	Kcnn4	GO:0006811 ion transport
H3109D12	2210017A09Rik	GO:0006813 potassium ion transport
H3030E02	Gabarapl2	GO:0006886 intracellular protein transport
H3040F06	Mpv17	GO:0006886 intracellular protein transport
H3028C06	Sec13r	GO:0006886 intracellular protein transport
H3076G10	Tomm22	GO:0006886 intracellular protein transport
H3085H07	Vps26	GO:0006886 intracellular protein transport
H3153D07	Ngfrap1	GO:0006917 induction of apoptosis
H3002C02	Actr2	GO:0006928 cell motility
H3006C11	Rps18	GO:0007046 ribosome biogenesis
H3125H12	Rps6	GO:0007046 ribosome biogenesis
H3147D06	Cdk4	GO:0007049 cell cycle
H3054A03	D5Ertd249e	GO:0007049 cell cycle
H3098A09	Epdm2-pending	GO:0007160 cell-matrix adhesion
H3066H10	Mapk8	GO:0007165 signal transduction
H3007D07	Pwp2h	GO:0007165 signal transduction
H3133D05	Rock1	GO:0007165 signal transduction
H3002D10	**Madh4**	**GO:0007184 SMAD protein nuclear translocation**
H3091D08	Gna14	GO:0007186 G-PCR protein signaling pathway
H3018D02	Gnai2	GO:0007186 G-PCR protein signaling pathway
H3001E05	Homer2	GO:0007186 G-PCR protein signaling pathway
H3154B03	Frap1	GO:0007281 germ-cell development
H3065C08	Ppp3cb	GO:0007507 heart development
H3040F05	Smyd1	GO:0007507 heart development
H3022F08	Tpm3	GO:0007517 muscle development
H3054D06	Ovgp1	GO:0008152 metabolism
H3082B04	Pfkfb3	GO:0008152 metabolism
H3048G06	Srm	GO:0008295 spermidine biosynthesis
H3069G01	9930118K05Rik	GO:0008654 phospholipid biosynthesis
H3115C03	**Bmp1**	**GO:0009887 organogenesis**
H3029F09	Atp6v1e1	GO:0015986 ATP synthesis coupled proton transport
H3002B06	Ehd1	GO:0016197 endosome transport
H3001H10	Tmsb10	GO:0030036 actin cytoskeleton organization and biogenesis

H3043B04	**Strap**	**GO:0030512 regulation of TGFB receptor signaling pathway**
H3020F08	Was	GO:0042110 T-cell activation
H3114B04	Rdx	GO:0045176 apical protein localization

Microarray Expression Results. 400 genes out of 15,000 on the microarrays were significantly differentially expressed ($p < 0.05$) in MRL, DBA and B6 mice at day four in comparison to control tissue at day zero. Of these, 207 genes were upregulated and 193 were downregulated. About 50% of these genes represent ESTs and unknown genes. The biological process gene ontology functional classes that are significantly overrepresented in all the strains regenerating digit tips are shown in the supplementary data table. Pathway analysis of these known genes reveals that genes in the IGF and BMP/TGF pathway are differentially expressed in all mouse strains (IGF2, IGF2BP3, IGFBP4, BMP-1, TGFb1i4), thus implicating the IGF and BMP/TGF signaling pathways in regulation of digit tip regrowth. The BMP family of genes has previously been implicated in digit regeneration [8]. Also, several genes involved in cell cycle and growth were found to be differentially expressed in all the strains, including CALM2, NFKB, and Annexin A2. Transcription factors that were found to be differentially expressed in all strains include MYST3, ATRX, SOX13, TCFL4, ANKIB1, TSC22D4, 6030490I01RIK, ZFP110, GATA3, GTF2H3, PHF7, ICSBP1, TRPV2, KLF4, MLL3, ANKRD10, IKBKG, CNOT2, FOXM1, ASH2L, HNRPR, NFE2L1, and ZFP113.

Table 5. Genes Differentially Expressed in Only MRL Mice at Day 4 Post Digit Tip Dissection. The NIA15K library was created from developing mouse embryos and represents 15,264 unique genes (78% novel and 22% known). Many of these genes are expressed primarily in development and the clones are a unique source for studies of regeneration. Genes that are differentially expressed only in MRL include multiple transcription factors suggesting increased cellular replication in regenerating digit tips. Additional genes are implicated in gastrulation and pattern formation (Mesp2, Shrm). Also, genes differentially expressed are highly expressed in nerve cells (Fmn2, Net1). These genes are particularly intriguing since previous studies have shown that signals from nerves are required to induce formation of blastemas. These results suggest that many genes and unknown ESTs are involved in digit regeneration.

Clone ID	Gene ID	Expression Ratio	Description	Gene Ontology Biological Process
H3046D02B		6.3	UNKNOWN	
H3094C11	A630020C 16Rik	5.5	UNKNOWN	ubiquitin-dependent protein catabolism(GO:0006511)
H3069B02	1810037G0 4Rik	4.1	EST similar to Bola-like transcription factor	
H3072F08		3.8	UNKNOWN	
H3001G12		3.4	UNKNOWN	
H3139B07	Hnrpu	3.2	Mus musculus heterogeneous nuclear ribonucleoprotein U (Hnrpu), mRNA	
H3139F02	Tcea1	3.2	UNKNOWN: Similar to Mouse transcription factor S-II, clone PSII-2	regulation of transcription, DNA-dependent(GO:0006355)

H3118G08A	G7e-pending	3.1	Mus musculus G7e protein (G7e-pending), mRNA	
H3139G05	EST Mm.270291	3.0	UNKNOWN: Similar to Mus musculus similar to zinc finger protein 97 [Mus musculus] (LOC233168), mRNA	
H3043F11		2.9	UNKNOWN	
H3074G12	Mesp2	2.8	Mus musculus mesoderm posterior 2 (Mesp2), mRNA	gastrulation (GO:0048276)
H3133G07	Daf1	2.8	UNKNOWN	complement activation, classical pathway(GO:0006958)
H3076F01	Pdzk2	2.7	Mus musculus natrium-phosphate cotransporter IIa C-terminal-associated protein 2 (AF334612), mRNA	intracellular signaling cascade(GO:0007242)
H3138A06		2.6	UNKNOWN	
H3115F01	2610027O18Rik	2.6	Mus musculus RIKEN cDNA 2610027O18 gene (2610027O18Rik), mRNA	
H3137F08	G630041M05Rik	2.5	UNKNOWN: Similar to Homo sapiens chromosome 1 clone RP11-397P13, complete sequence	
H3072D07		2.2	UNKNOWN	
H3004A01	Gjb3	2.2	Mus musculus gap junction membrane channel protein beta 3 (Gjb3), mRNA	cell communication(GO:0007154);cell-cell signaling(GO:0007267)
H3138F07		2.2	UNKNOWN	
H3082B03	Mylk	2.2	Mus musculus myosin, light polypeptide kinase (Mylk), mRNA	cytoskeleton organization and biogenesis(GO:0007010)
H3155G11	1810024J12Rik	2.2	UNKNOWN: Similar to Mus musculus LOC244336 (LOC244336), mRNA	
H3098E07A	Calb1	2.2	Mus musculus calbindin-28K (Calb1), mRNA	
H3126F07		2.1	UNKNOWN	
H3024A05	Sparc	2.1	Mus musculus secreted acidic cysteine rich glycoprotein (Sparc), mRNA	
H3130D01	4933421G18Rik	2.1	UNKNOWN: Similar to Homo sapiens, Similar to IDN3 protein, clone IMAGE:5496103, mRNA	

H3028F04	Ctsl	2.0	Mus musculus cathepsin L (Ctsl), mRNA	proteolysis and peptidolysis(GO:0006508)
H3019H05		2.0	UNKNOWN	
H3029B05		2.0	Mus musculus brachyury (T), mRNA	regulation of transcription, DNA-dependent(GO:0006355);development(GO:0007275)
H3046F02A		2.0	UNKNOWN	
H3026H02	Nrd1	1.9	Mus musculus hypothetical protein MGC25477 (MGC25477), mRNA	proteolysis and peptidolysis(GO:0006508)
H3089C10	8430436C05Rik	1.9	Mus musculus 16 days embryo lung cDNA, RIKEN full-length enriched library, clone:8430436C05:unclassifiable transcript, full insert sequence	
H3077A05		1.9	UNKNOWN	
H3031F01	Uqcrc1	1.9	Mus musculus ubiquinol-cytochrome c reductase core protein 1 (Uqcrc1), mRNA	electron transport(GO:0006118);proteolysis and peptidolysis(GO:0006508)
H3048F06		1.9	UNKNOWN	
H3021A04		1.9	UNKNOWN	
H3078D11	shrm	1.9	Mus musculus, clone IMAGE:3484373, mRNA, partial cds	pattern specification(GO:0007389);intracellular signaling cascade(GO:0007242)
H3083B07		1.8	UNKNOWN	
H3099H03		1.8	UNKNOWN	
H3022C07		1.8	UNKNOWN	
H3101C02		1.8	UNKNOWN	
H3149D01	2810450M21Rik	1.8	Mus musculus similar to Rad50-interacting protein 1; hypothetical protein FLJ11785 [Homo sapiens] (LOC231040), mRNA	
H3043C06		1.8	UNKNOWN	
H3148C11		1.7	UNKNOWN	
H3015C11	Arcp-pending	1.7	Mus musculus, RIKEN cDNA 2310016N05 gene, clone MGC:29418 IMAGE:5043872, mRNA, complete cds	biological_process unknown(GO:0000004)
H3011B08	2310061B02Rik	1.7	Mus musculus, clone IMAGE:3584936, mRNA	
H3050B08		1.7	UNKNOWN	

H3062H03		1.7	UNKNOWN	
H3086H09	Net1	1.7	Mus musculus mRNA for Rho guanine nucleotide-exchange factor, splice variant NET1A	
H3083E03	Raly	1.7	Mus musculus hnRNP-associated with lethal yellow (Raly), mRNA	
H3080H11	Plat	1.7	Mus musculus plasminogen activator, tissue (Plat), mRNA	proteolysis and peptidolysis(GO:0006508)
H3119C09		1.7	UNKNOWN	
H3073G03		1.7	Mus musculus histone binding protein NASP (Nasp) gene, complete cds, alternatively spliced	
H3015F12	1110056N09Rik	0.47	UNKNOWN: Similar to Mus musculus RIKEN cDNA 1110056N09 gene (1110056N09Rik), mRNA	
H3094E02	A230106A15Rik	0.46	UNKNOWN	
H3001E07		0.45	UNKNOWN	
H3057F01	Csnk1e	0.44	Mus musculus casein kinase 1, epsilon (Csnk1e), mRNA	circadian rhythm(GO:0007623);protein amino acid phosphorylation(GO:0006468)
H3023G09	Ddx5	0.44	Mus musculus DEAD (aspartate-glutamate-alanine-aspartate) box polypeptide 5 (Ddx5), mRNA	
H3030D06	Dctn5	0.43	Mus musculus, dynactin 4, clone MGC:19347 IMAGE:4235312, mRNA, complete cds	
H3070F07	9430020K16Rik	0.42	UNKNOWN	
H3113H06	Fem1b	0.42	Mus musculus LOC213060 (LOC213060), mRNA	regulation of transcription, DNA-dependent(GO:0006355)
H3061A09C		0.41	UNKNOWN	
H3115D09	9630025B04Rik	0.38	UNKNOWN	

H3016H10	Sp1	0.35	Mus musculus trans-acting transcription factor 1 (Sp1), mRNA	regulation of transcription, DNA-dependent(GO:0006355)
H3156A07	Nme6	0.35	Mus musculus expressed in non-metastatic cells 6, protein (nucleoside diphosphate kinase) (Nme6), mRNA	GTP biosynthesis(GO:0006183);UTP biosynthesis(GO:0006228);CTP biosynthesis(GO:0006241)
H3109A10		0.33	UNKNOWN	
H3040F03		0.30	UNKNOWN	
H3059A01		0.28	UNKNOWN	
H3050D11	D2Ertd391e	0.27	Mus musculus similar to Hypothetical protein KIAA0652 (LOC228360), mRNA	
H3052A04	Mor2	0.26	Mus musculus malate dehydrogenase, soluble (Mor2), mRNA	tricarboxylic acid cycle(GO:0006099)
H3133H08	1110067M05Rik	0.16	Mus musculus 18 days embryo whole body cDNA, RIKEN full-length enriched library, clone:1110067M05:unclassifiable transcript, full insert sequence	
H3031E07	Myg1-pending	0.13	Mus musculus melanocyte prolifeating gene 1 (Myg1-pending), mRNA	
H3085D12		0.12	Mus musculus NIMA-related kinase Nek9 (Nek9), mRNA	
H3143D05C	4930562C03Rik	0.12	UNKNOWN: Similar to Mus musculus RIKEN cDNA 4930562C03 gene (4930562C03Rik), mRNA	
H3007D07	Pwp2h	0.12	Mus musculus RIKEN cDNA 6530411D08 gene (6530411D08Rik), mRNA	signal transduction(GO:0007165)
H3045D06	Psmd7	0.11	Mus musculus proteasome (prosome, macropain) 26S subunit, non-ATPase, 7 (Psmd7), mRNA	translational initiation(GO:0006413)
H3037A08		0.09	UNKNOWN	
H3089A11	Abcf2	0.07	Mus musculus similar to ATP-binding cassette, sub-family F, member 2 [Homo sapiens] (LOC214267), mRNA	transport(GO:0006810)

H3138A12	4632428N09Rik	0.07	Mus musculus RIKEN cDNA 1810019E15 gene (1810019E15Rik), mRNA	electron transport(GO:0006118)
H3094C04		0.05	UNKNOWN	
H3043F09	Grcc8	0.01	UNKNOWN: Similar to Mus musculus, gene rich cluster, C8 gene, clone MGC:5778 IMAGE:3592108, mRNA, complete cds	
H3055B11	Nrf1	0.01	UNKNOWN	regulation of transcription, DNA-dependent(GO:0006355);carbohydrate metabolism(GO:0005975);mitochondrion organization and biogenesis(GO:0007005)
H3040F05	Smyd1	0.01	Mus musculus t-BOP (Bop) mRNA, complete cds	heart development(GO:0007507);chromatin modeling(GO:0006338);negative regulation of transcription(GO:0016481)
H3114D02		0.01	UNKNOWN	
H3084G12	C630029K18Rik	0.01	UNKNOWN	
H3134E08		0.01	UNKNOWN	

Seventy five genes and ESTs were significantly differentially expressed only in MRL mice in comparison to DBA and B6 mice . Of genes with known function, LRP6, a WNT co-receptor which functions in limb morphogenesis and pattern formation, was found to be differentially expressed. Also FMN2, which functions in cytoskeletal organization and meiosis, is differentially expressed in MRL regenerating digit tips. Transcription factors that were found to be differentially expressed only in MRL regenerating digit tips include SS18L1, NFE2L1, ZFP251, RXRIP110, and TAF5l. Many of the differentially expressed genes are expressed sequence tags (ESTs). This suggests that there are many currently unknown genes and genetic pathways involved in digit tip regrowth.

Confirmation of Microarray Results by Real Time PCR

Reverse transcription of 200ng of total RNA (Day 4 and Day 0) was carried out in a final volume of 20ul using Invitrogen's reverse transcriptase kit according to the manufacturer's instructions. To prevent 3' bias of the real-time PCR reactions random decamers (Ambion) were used for priming rather than oligo-dT. Real-time PCR was done using the SYBR Green PCR Core Reagents Kit (Applied Biosystems). Five microliters of cDNA at a concentration of 10ng/ul, and 0.1 uM of each primer in a final volume of 25 ul was used. For statistical significance, each RT-PCR had six replicates. Once the master mix was made, the 25ul aliqots were transferred into a MicroAmp optical 96-well reaction plate (Applied Biosystems). vortexed, and sealed with an optical adhesive cover (Applied Biosystems). Cycling and signal detection were done using the ABI-7900HT Sequence Detection System with the following cycling conditions: initial activation at 95^0C for 10 minutes, then 40 cycles at 95^0C for 15 seconds and 60^0C for 1 minute.

Product specificity was checked by including a dissociation stage according to the manufacturer's instructions (Applied Biosystems). The gene expression level was normalized by housekeeping gene Beta-Actin expression level.

Figure 6. Confirmation of MRL Microarray Results by Real-time PCR. Plotted below are the fold change values of RNA expression in MRL mice at day 4 in comparison to day 0 control RNA. Real-time PCR fold changes are normalized to beta-actin. Most genes determined to be differentially expressed by microarray also show differential expression by real-time PCR. Differences in Smad4, MMP9 and Maged are likely due to cross hybridization of genes with high sequence similarity or polymorphic sequence mismatches in real-time PCR primers.

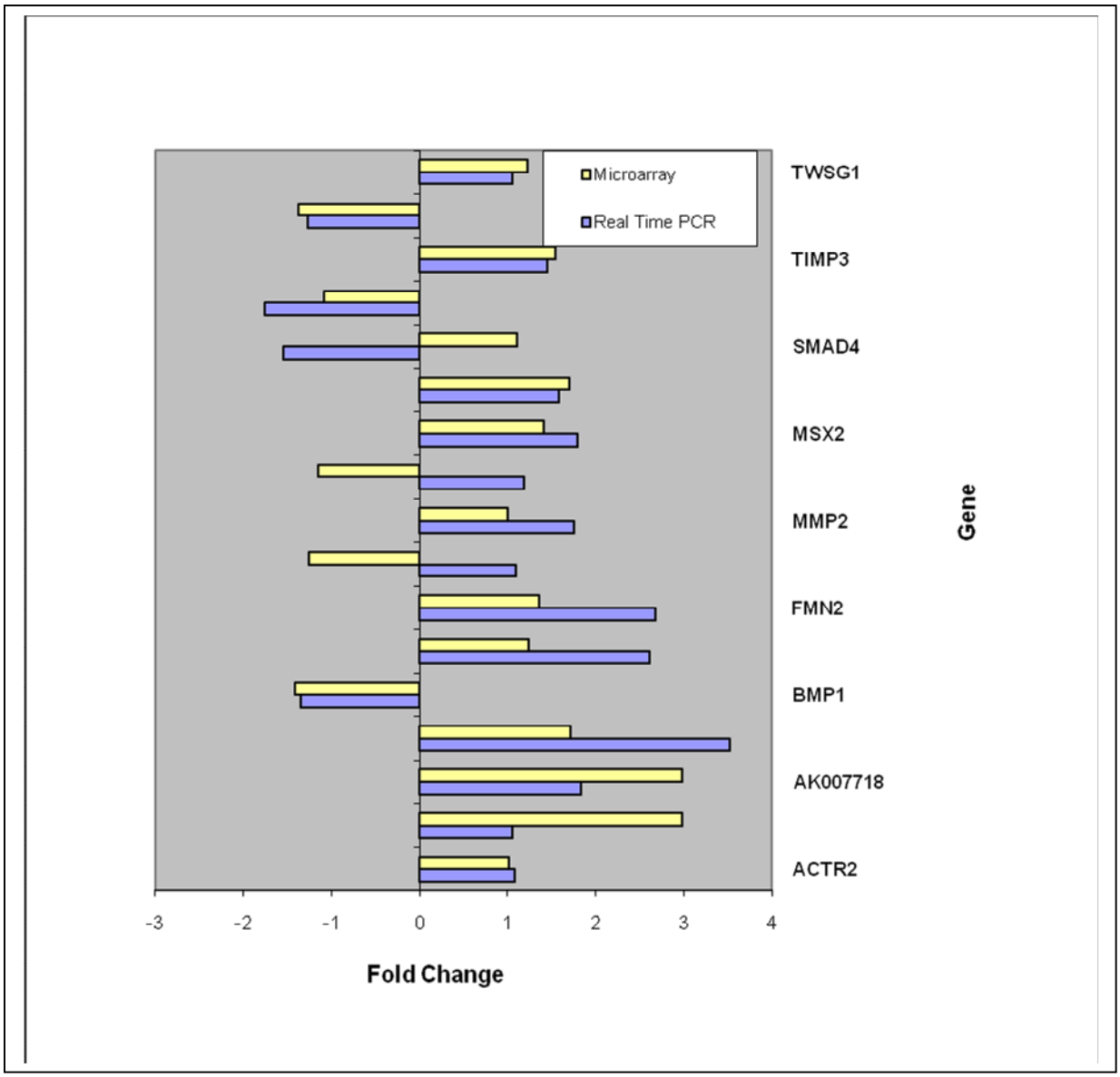

Figure 7. Confirmation of DBA Microarray Results by Real-time PCR. Plotted below are the fold change values of RNA expression of digit tips in DBA mice at day 4 in comparison to day 0 control RNA. Most genes determined to be differentially expressed by microarray also show differential expression by real-time PCR. Differences in BMP2 are likely due to cross hybridization of genes with high sequence similarity or polymorphic sequence mismatches in real-time PCR primers.

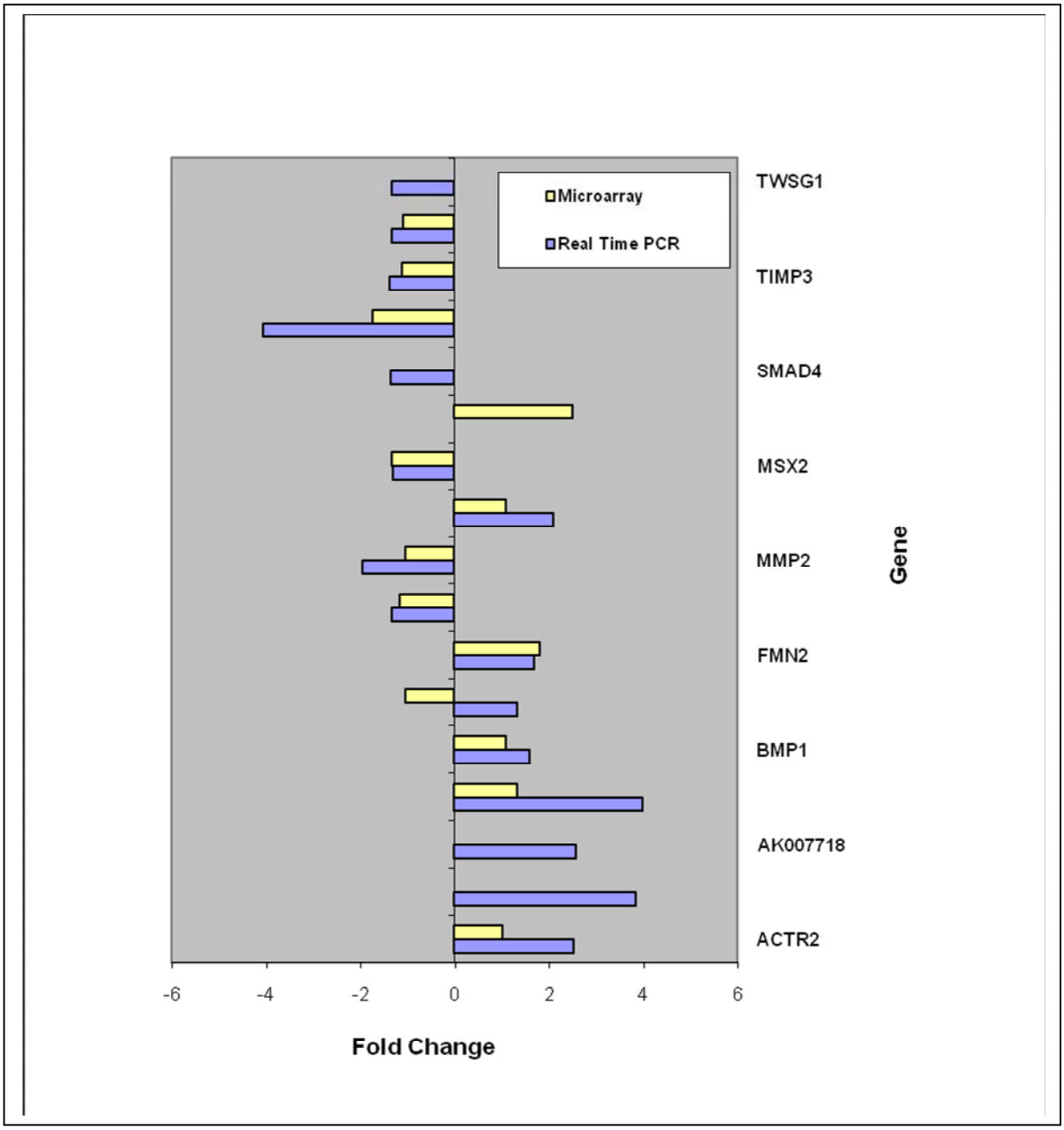

Confirmation of microarray results was done by real-time PCR of 17 genes (TWSG1, TSC22, TIMP3, TGFBLi4, SMAD4, NET1, MSX2, MMP9, MMP2, MAGED1, FMN2, BMP2, BMP1, B2M, AK007718, AI987944, ACTR2). RT-PCR results for these genes were consistent with the microarray results and gave correlation coefficients of 0.62, 0.91 and 0.40 for MRL, DBA and B6 expression results respectively.

We also undertook additional microarray and real-time PCR expression studies at the above times points to determine the genes and genetic pathways involved in the digit tip regeneration at each time point.

Microarray Expression Analysis. Total RNA was isolated from dissected tissues at days 4, 7, 14, 21 and 28 days post surgery using the Agilent Total RNA Isolation Kit (Agilent Technologies). For control RNA samples, tissue was collected from uncut paw tissue at these same time points. Tissues were lysed using a Polytron Generator (Kinemalica AG), and then processed following the manufacturer's protocol (Agilent). The total RNA concentration was determined by NanoDrop spectrophotometer and RNA quality was determined by 18S/28S ribosomal peak intensity on an Agilent Bioanalyzer. For microarray expression profiling and real-time PCR, RNA samples were used only if they showed little to no degradation. Oligonucleotides were spotted on to slides using a Q-Array2 robot (Genetix). A total of 250 ng RNA was used to synthesize double stranded cDNA using the Low RNA Input Fluorescent Linear Application Kit (Agilent). First strand cDNA synthesis was primed with T7-(dT24) promoter primer. From the purified cDNA, cRNA was synthesized using transcription master mix and purified. 250 ng of purified cRNA was used to reverse transcribe to fluorescent cDNA. Cyanine-3-dCTP and cyanine-5-dCTP were used to label experimental samples and control samples. Samples were hybridized at 60°C for 17 hours. The slides were then washed with Solution I (6X SSC, 0.005% Triton X-102) for 10 min. in the dark and then with Solution II (0.1X SSC, 0.005% Triton X-102) for 5 min. in the dark. The slides were dried with pressurized nitrogen and immediately scanned using an Axon Genepix 4200 scanner. The signal intensity of all microarray images was determined using Imagene 6.0 software. Expression analysis of microarray experiments was performed with GeneSpring 7.2 (Silicon Genetics) using the raw intensity data generated by the ImaGene software. Local background-subtracted median signal intensities were used as intensity measures, and the data was normalized using per spot and per chip LOWESS normalization. The transcripts were then further analyzed by utilizing a one-sample Student's t-test to test whether the mean normalized expression level for the gene is statistically different from 1.0.

Microarray Expression Results. A particularly interesting gene was found to be differentially expressed in MRL mice in comparison to DBA and B6 mice at 4 days post dissection (**Figure 2**). Formin 2 (FMN 2) is related to Formin 1 which is differentially expressed in the mouse embryo and is required for normal expression of fibroblast growth factor 4 (FGF-4) and sonic hedgehog (SHH) in the limb bud (12, 13). Thus, we focused on the FMN2 gene for further investigations. Confirmation of microarray results was done by real-time PCR of 20 genes. RT-PCR results for these genes were consistent with the microarray results and gave correlation coefficients of 0.62, 0.91 and 0.40 for MRL, DBA and B6 expression results. Additionally, FMN2 was found to be expressed in osteoblast cell line MC3T3 by RT-PCR. FMN2 was also found to be increased 2 fold in expression in WNT3A treated MC3T3 cell lines in comparison to control MC3T3 cell lines by realtime PCR ($p = 0.01$).

Time points at 7, 14, 21 and 28 days were also examined by microarray expression analysis. Analysis finds that at the 7 day time point, FMN2 is differentially expressed in only MRL digit tips. Later time points do not show differential expression of FMN2, suggesting that it is important in the initial regenerative response. Table 6 shows a list of genes differentially expressed only in MRL mice.

Table 6. Genes significantly differentially expressed in MRL mouse regenerating digit tips but not DBA and B6 mice. Many of these genes are ESTs of unknown function.

Name	Ratio	p-value	Ratio	Ratio	Name	Description	Biological Process
H3001C06	0.40	0.04	0.74 *	0.87	5730436H21Rik	UNKNOWN: Similar to clone MGC:37386 IMAGE:4977054	
H3002E06	1.91	0.01	0.95	absent	Dbt	Dihydrolipoamide branched chain transacylase (Dbt)	metabolism(GO:0008152)
H3002G06	1.80	0.04	0.91	1.22	AA410130	UNKNOWN	
H3002H12	1.96	0.01	0.90	absent			
H3003A01	2.23	0.04	0.83	absent		Mus musculus similar to LOC264166 mRNA	
H3004G07	1.71	0.04	0.77	0.91	Tmod3	Tropomodulin 3 (Tmod3), mRNA	actin filament organization(GO:0007015)
H3005D06	1.65	0.04	1.24	0.96			
H3008E02	0.63	0.03	0.90	1.21		UNKNOWN	
H3010G07	3.77	0.01	2.81	1.29	Ak4	Adenylate kinase 4 (Ak4), mRNA	
H3011G06	1.88	0.02	1.23	0.59		Ferritin light chain 1 (Ftl1), mRNA	
H3017B10	0.68	0.04	1.01	1.01			
H3019B02	1.70	0.05	1.01	1.06	Nfat5	UNKNOWN	transcription, DNA-dependent(GO:0006351);regulation of transcription
H3024A05	1.73	0.01	0.87	1.09	Sparc	Secreted acidic cysteine rich glycoprotein (Sparc), mRNA	
H3028F03	1.96	0.00	0.96	1.12	Ctsl	Cathepsin L (Ctsl), mRNA	proteolysis and peptidolysis(GO:0006508)
H3028F04	1.98	0.00	1.34	1.01	Ctsl	Cathepsin L (Ctsl), mRNA	proteolysis and peptidolysis(GO:0006508)
H3029B01	1.69	0.02	1.04	absent	Slc11a2	Natural resistance macrophage protein-2 (Nramp2) mRNA	transport(GO:0006810);iron ion transport(GO:0006826)
H3031D07	1.59	0.04	0.68	absent	Psmd1	Proteasome, non-ATPase, 1 (Psmd1), mRNA	
H3034F02	1.63	0.01	1.04	0.97	Hel308-pending	UNKNOWN	DNA metabolism(GO:0006259)
H3037C05	1.52	0.02	0.80	0.89		UNKNOWN	
H3037D01	0.64	0.04	0.99	0.90		UNKNOWN	
H3037D07	1.99	0.04	1.05	1.12		UNKNOWN	
H3038C05	1.52	0.04	0.62	0.39 *		UNKNOWN	
H3039A12	1.53	0.02	1.08	absent		UNKNOWN	
H3041F03	1.53	0.05	0.86 *	1.01		UNKNOWN	
H3042B01	1.57	0.01	1.15	0.95		UNKNOWN	
H3042F06	1.53	0.02	1.38	absent		UNKNOWN	
H3050A02	2.25	0.04	1.08	absent		UNKNOWN	
H3051D04	1.54	0.03	0.81	1.07	Mdm2	Double minute 2 (Mdm2) gene, 3' untranslated region	cell growth and/or maintenance(GO:0008151)
H3053D05	1.54	0.01	0.89	0.91		UNKNOWN	
H3054F02	1.81	0.04	0.93	1.09		UNKNOWN	
H3054G08	1.71	0.04	0.94	absent		UNKNOWN	
H3056C01	1.53	0.01	1.42 *	0.94	Fmn2	Formin 2 (Fmn2)	development(GO:0007275)
H3060H01	1.59	0.04	0.98	0.98		UNKNOWN	
H3061D03	1.68	0.00	1.02	absent	Pcsk5	Clone MGC:18501 IMAGE:4036159, mRNA	electron transport(GO:0006118);proteolysis and peptidolysis(GO:0006508)
H3062G12	1.68	0.03	1.03	0.95		UNKNOWN	
H3065B10	1.63	0.02	1.07	0.78		UNKNOWN	
H3065D02	1.58	0.04	1.10	0.96		UNKNOWN	
H3065F05	0.65	0.02	0.97	1.04		UNKNOWN	
H3067C07	1.55	0.05	0.88	absent		UNKNOWN	
H3067E04	0.70	0.03	1.00	1.14		UNKNOWN	
H3069H05	0.69	0.04	1.02	0.95	2310015A05Rik	RIKEN cDNA 2310015A05 gene (2310015A05Rik), mRNA	
H3070E09	1.77	0.00	1.06	1.00		UNKNOWN	
H3071H07	1.85	0.04	0.96	absent		UNKNOWN	
H3072D01	1.50	0.03	0.92	1.29		UNKNOWN	
H3075D02	1.51	0.01	0.98	absent		UNKNOWN	
H3079B08	1.80	0.02	1.08	1.33	6030466N05Rik	dCMP deaminase, IMAGE:3672932, mRNA	pyrimidine nucleotide metabolism(GO:0006220);nucleotide biosynthesis(GO:0009165)
H3081F06	1.51	0.01	0.76	0.82		UNKNOWN	
H3083B04	1.66	0.04	0.85	1.03		UNKNOWN	
H3084F04	1.55	0.02	0.87	1.26		UNKNOWN	
H3087A08	1.59	0.03	0.94	0.98		UNKNOWN	
H3097G06	1.54	0.04	0.96	1.03	5730530J16Rik	UNKNOWN	
H3097H10	0.70	0.05	1.03	1.00		UNKNOWN	
H3098G02	1.82	0.04	0.73	absent		UNKNOWN	
H3104G06	1.57	0.05	0.71 *	0.53 *		UNKNOWN	
H3106A02	1.71	0.02	1.29	absent	2210409E12Rik	RIKEN cDNA 2210409E12 gene (2210409E12Rik), mRNA	
H3114A12	1.58	0.04	0.87	absent	3010021M21Rik	UNKNOWN	ubiquitin cycle(GO:0006512);protein modification(GO:0006464)
H3119H03	1.94	0.03	1.10	1.12	Col1a1	Collagen alpha 1(I) chain precursor (LOC217123), mRNA	cell adhesion(GO:0007155)
H3121E06	2.29	0.04	0.96	0.99	2900057D21Rik	RIKEN cDNA 2900057D21 gene (2900057D21Rik), mRNA	intracellular signaling cascade(GO:0007242)
H3123G08	0.64	0.04	1.07	0.99		UNKNOWN	
H3124H10	2.42	0.00	1.48	1.44	Col3a1	Procollagen, type III, alpha 1 (Col3a1), mRNA	cell adhesion(GO:0007155)
H3128B02	0.69	0.01	0.94	0.80		UNKNOWN	
H3134H07	1.55	0.00	0.96	1.49	Birc6	Inhibitor of apoptosis mRNA (LOC210168)	apoptosis(GO:0006915)
H3143F07	1.55	0.03	0.95	0.92		UNKNOWN	
H3144F02	2.00	0.05	1.27	0.88	A230053O16Rik	Similar to hypothetical protein FLJ12547	
H3146G03	1.92	0.04	0.91	2.05		UNKNOWN	
H3146H05	0.69	0.01	1.08	0.92		UNKNOWN	
H3150H02	1.53	0.00	0.17	absent		UNKNOWN	
H3152F07	1.54	0.03	0.47	1.10		UNKNOWN	
H3156C06	1.61	0.02	1.17	absent		UNKNOWN	
H3159A06	0.70	0.02	1.00	0.97		UNKNOWN	
H3159B04	0.49	0.05	0.80	1.00		UNKNOWN	

5). Blastemas Evaluation

Since blastemas were not seen to form at 1 day post digit tip dissection, we have begun examining other times points. We believe that we have seen the beginning of blastema formation by 4 days post dissection in B6 mice. As shown in Figure 8, a mass of dedifferentiated cells is seen below the epithelial layer in a B6 mouse pup at 4 days post surgery. These results and extending the histology studies to additional times point and the other mouse strains.

Figure 8. Blastema Formation in B6 Regenerating Digit Tip at Four Days Post Surgery.

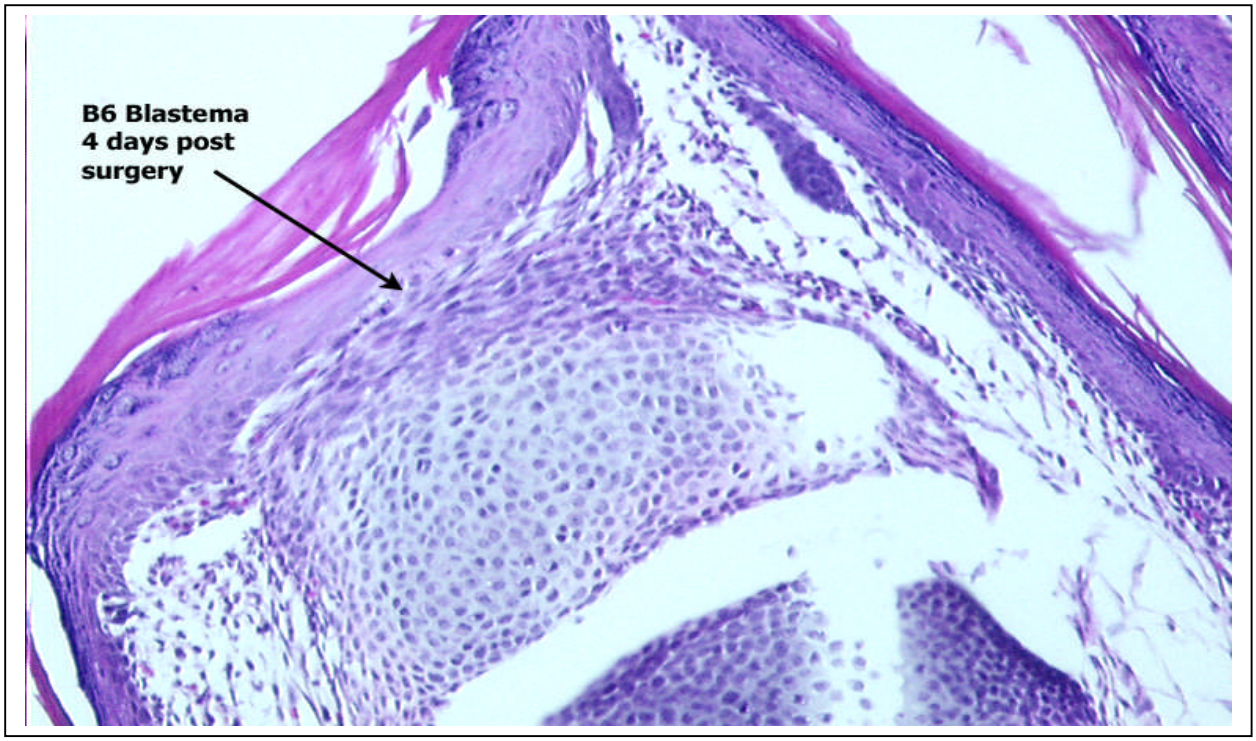

Studies undertaken in the first year of subproject 1 only examined a single time point, namely at day 1 post dissection, for determination of blastema formation in MRL, DBA, B6, C3H and 129Sv inbred mice. These studies found that day 1 was too early for a blastema to form. In the last year, we examined mice for blastema formation at additional time points by euthanizing mice at 1, 4, 14 and 21 and 28 days post digit tip dissection. Dissected paw tissues were stored in 10% formalin until processing. The tissues were fixed in paraffin and five micron tissue sections were mounted on to microscope slides. Following hematoxylin and eosin (H&E) staining, the tissues were examined under a microscope. In these studies, our histology studies found that the early stages of digit tip regeneration are partially similar to that of axolotls (Figure 1). Within one day of digit tip amputation epithelial cells have formed over the wound in MRL mice. At four days, epithelial cells have completely covered the wound and undifferentiated cells beneath the wound epithelium begin to proliferate. At 7-days osteoblasts are present and have begun to form bone. At 14-days post dissection the cells beneath the wound epithelium are not as de-differentiated and the bone marrow cavity has begun forming above the third phalange's joint. By 21-days post dissection, the cells have

redifferentiated, the nail has begun reforming and the digit tip has almost completely regenerated. It is interesting that when de- and re- differentiation of cells beneath the wound epithelium is occurring is also when the MRL mouse shows the greatest regenerative capacity. This suggests possible links between the enhanced healing and regeneration capabilities of MRL mice and the molecular causes of de- and re-differentiation of cells.

Figure 9. Regeneration Histology. At 1-day post dissection a wound epithelial layer has begun to form. By 4-days post dissection the wound epithelial layer has completely covered the tip and beneath this dedifferentiated and proliferating cells are present. At 7-days post dissection, bone has begun to form and by day 14 the marrow cavity is forming above the 3rd phalange's joint. By 21 days, the digit has nearly completed regenerated and the nail has begun reforming. In Figure 9 the left imagesa are at 4X, the right images are 10X or 20X.

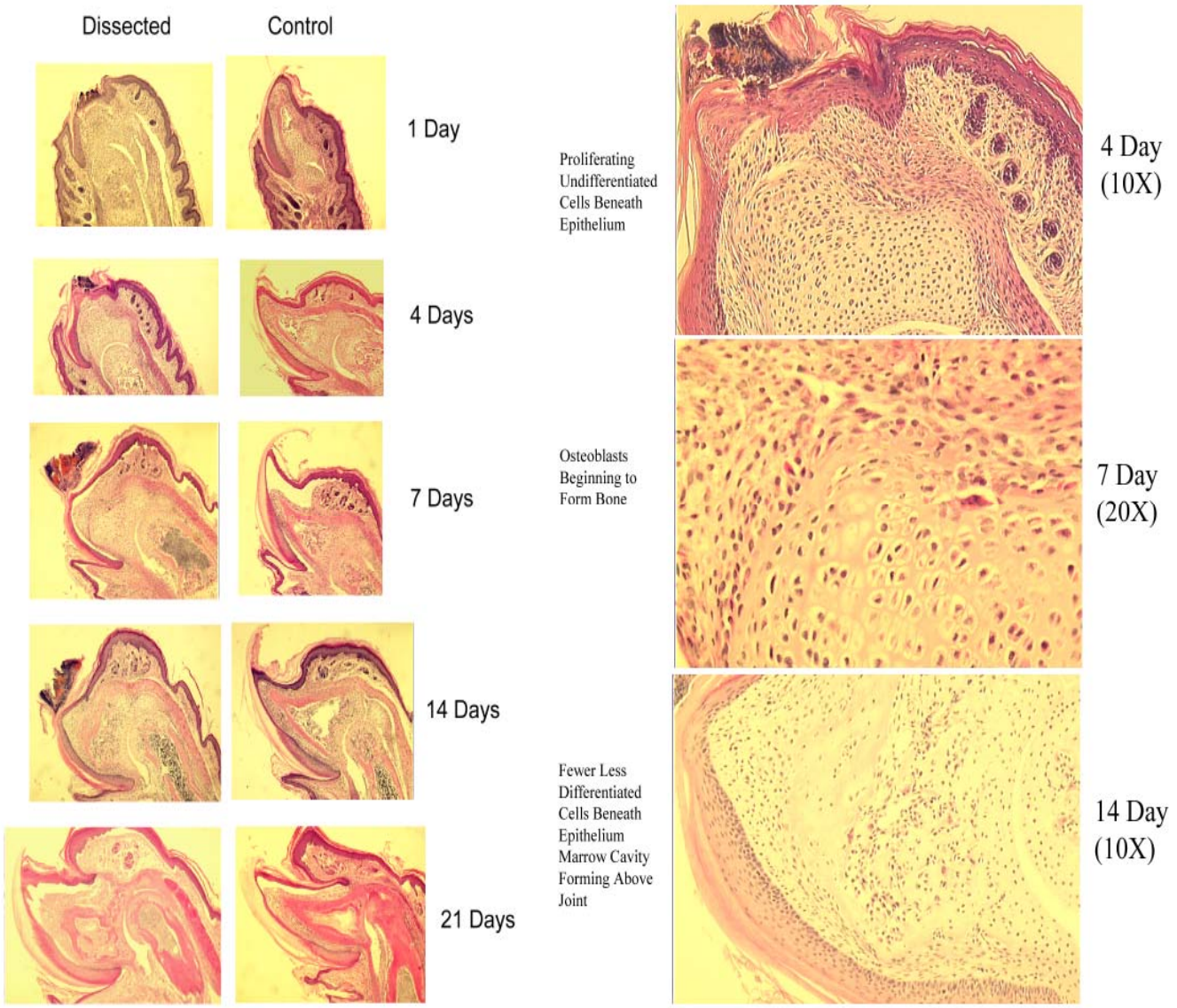

2. FMN2 Mouse Studies

a. Introduction

Since the formin-2 (FMN2) was uniquely expressed in regenerating mouse digit tips. we undertook studies to evaluate bone formation and remodeling in the Formin-2 (FMN2) knockout mouse. The formin protein family functions in activating signaling pathways and interacting with actin filaments in the cytoskeleton. These formin/actin interactions are required for cellular cytokinesis and morphogenesis. Additionally, the actin cytoskeleton has been implicated in responses of osteocytes to mechanical loading induced signal transduction and subsequent increases in bone formation. The formin-1 gene (FMN1) is required for proper skeletogenesis in mice. Mice homozygous for mutations in FMN1 display multiple limb abnormalities such as fusion of the long bones (ulna/radius, tibia/fibula) and syndactyly (fusion of digits). This phenotype is first manifested during formation of the limb bud as a failure of proper apical ectodermal ridge development and a reduction in the width of the posterior limb axis.

b. FMN2 Expression and Function

In order to determine the cell types and cellular locations of FMN2 expression in bone we investigated the distribution of FMN2 using immunohistochemistry (IHC). 4-day old MRL mice were sacrificed and dissected paw tissues were stored in 10% formalin until processing. Five micron paraffin sections were mounted on poly-L-lysine coated slides. Antigen retrieval was done using pH 6.0 Citrate buffer followed by incubation at 80°C and 70°C for ten minutes at each temperature. The sections were blocked in 20% Horse serum at 37°C for 1 hour. Primary antibodies were diluted at both 1:50 and 1:200 and incubated for 60' at 37°C (Santa Cruz Biotechnology). The sections were rinsed extensively and incubated with the secondary anti-goat antibody for 12 minutes at 37°C. The sections were reacted with diaminobenzidine and hydrogen peroxide, counter-stained with Methyl Green and cover-slipped.

FMN2 protein was found to be expressed in both osteoblasts and osteoclasts but to a lesser extent in osteoclasts than osteoblasts (**Figure 10**).

Figure 10. Immunohistochemistry of Formin-2 expression. FMN2 protein is expressed in osteoblasts. Note that osteoblasts expressing FMN2 are present at both the endosteum (lower arrow) and periosteum (upper arrow). However osteoblasts at the endosteum are larger suggesting they are more active than those at the periosteum.

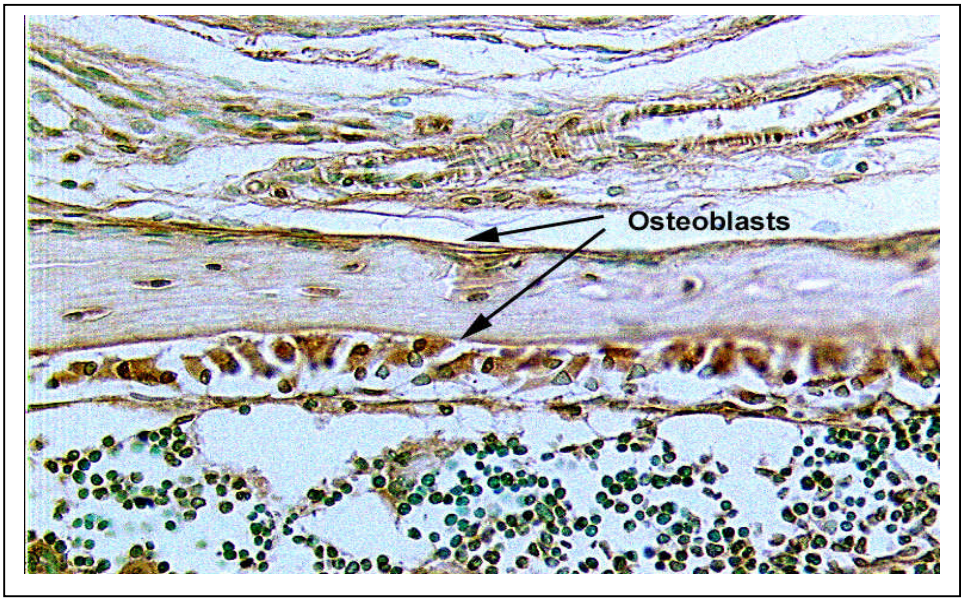

c. Generation of FMN2 Knockout Mice. FMN2 knockout mice were obtained from Dr. Philip Leder (Department of Human Genetics, Harvard Medical School, Howard Hughes Medical Institute, Boston, MA). The mice were originally generated in inbred 129Sv mice by homologous recombination of a targeting vector with 1300 bp of the FH1 domain of FMN2 deleted and replaced by 1257 bp containing the PGK-Neo gene followed by stop codons in all three reading frames (10). Two heterozygote FMN2 (+/-) male/female pairs were bred to generate wildtype (+/+), and knockout (-/-) pups for subsequent bone density, bone size and bone volume studies.

d. Regeneration Studies in FMN2 Knockout Mice. Surgery was conducted on the pup's digit tips within 1-day of birth. The neonatal mice were anesthetized with 5% Halothane mixed with O2 5L/min. The right front 3rd and 4th digit tips were amputated, with the left side as uncut controls. Since the level of amputation is very important to subsequent regrowth capabilities, all surgery was performed under a microscope and a scalpel was used to dissect the digit tips as accurately as possible at the mid-point of the third phalanges. The accuracy of digit tip surgery and amounts of tissue dissected were documented and measured by capturing images of the digits both before and after surgery. Both left (uncut) and right (cut) paw X-ray images were taken at 0, 7, 14, 21, and 28 days post surgery with a Faxitron MX-20 X-ray. In order to insure that regrowth results were not influenced by differences in mouse size, the data was normalized by dividing right cut growth measurements by left uncut growth measurements. **Figure 11** shows the results of the regeneration studies. Knockout FMN2 mice appear to have slightly appeared regeneration. However, these regrowth percentages did not reach statistical significance. This is likely due to measurement variations implicit in manual measurement methods.

Figure 11. Percent Digit Tip Regrowth in FMN2 Knockout and Wildtype Mice. FMN2 knockout mice display slightly less regeneration than wildtype mice. The difference did not reach statistical significance however.

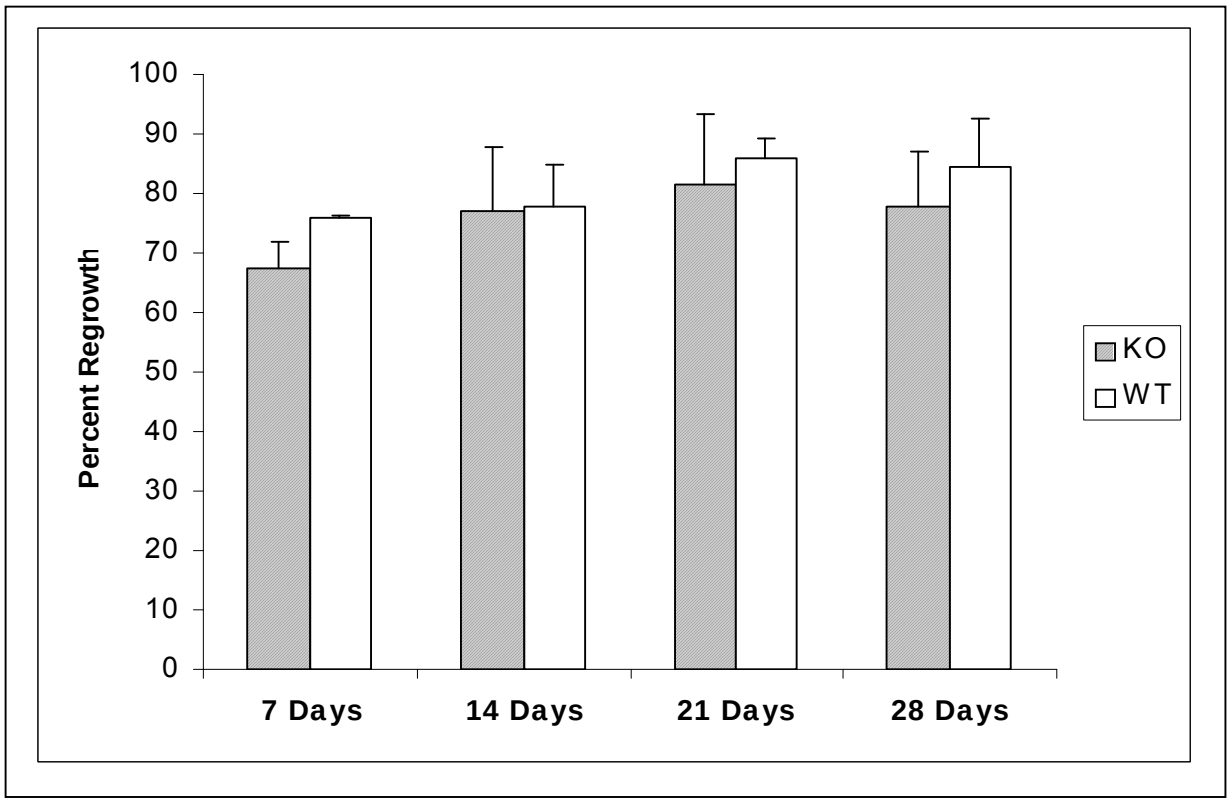

e. FMN2 Knockout and Wildtype Microarray Expression Analysis. Whole genome microarray analysis examines the expression analysis of all known genes in a single experiment. By comparing the expression levels of all genes in wildtype and mutant cells can give clues to a genes function and pathway. Thus, we undertook whole genome microarray expression analysis of FMN2 knockout and wildtype cells in order to determine the molecular functions and pathways of the FMN2 gene. Total RNA was isolated from mouse calvarial osteoblast cells and bones using Trizol followed by RNAEasy column purification (Qiagen). Custom oligonucleotide slides were spotted with ~38,000 70mer oligonucleotides that represent the mouse geneome (MEEBO set) obtained from Illumina. A Q-Array2 robot (Genetix) was used for spotting. A total of 250 ng RNA was used to synthesize double stranded cDNA using the Low RNA Input Fluorescent Linear Application Kit (Agilent). The slides were scanned using an 4200A Genepix scanner (Axon). Expression analysis of microarray experiments was performed with GeneSpring software (Agilent) using the raw intensity data generated by ImaGene software. Local background-subtracted total signal intensities were used as intensity measures, and the data was normalized using per spot and per chip LOWESS normalization. Genes that were significantly differentially expressed between wildtype and knockout FMN2 osteoblast cells were determined by utilizing a one-sample Student's t-test to test whether the mean normalized expression level for the gene is statistically different from 1.0. To characterize and classify the function of genes significantly differentially expressed in FMN2 knockout and wildtype osteoblast cells, genes were then classified according to their biological process Gene-Ontology (GO) category. Table 3 lists genes significantly downregulated in FMN2 knockout osteoblast cells and Table 4 lists genes significantly upregulated in FMN2 knockout osteoblast cells.

Table 7. Genes significantly ($p < 0.05$) downregulated in FMN2 knockout primary osteoblast cells in comparison to wildtype primary osteoblast cells.

Gene Name	Normalized ratio	P-value	Description	Gene Ontology Biological Process
Postn	0.41	0.009	Periostin, osteoblast specific factor	cell adhesion
Igfbp5	0.46	0.002	Insulin-like growth factor binding protein 5	regulation of cell growth
Lrrc15	0.47	0.001	Leucine rich repeat containing 15	
Crabp1	0.50	0.003	Retinoic acid binding protein I	transport
Ccl8	0.60	0.009	Chemokine (C-C motif) ligand 8	chemotaxis; signal transduction
Fbn1	0.61	0.004	Fibrillin 1	
Egfl6	0.62	0.009	EGF-like-domain, multiple 6	
D15Ertd781e	0.62	0.022	TBC1 domain family, member 22a	
H2-T22	0.63	0.026	Histocompatibility 2, T region locus 22	MHC class I; defense response
Kif2c	0.63	0.030	Kinesin family member 2C	microtubule-based movement
Lpl	0.64	0.000	Lipoprotein lipase	lipid catabolism; lipid metabolism
Pdzrn3	0.66	0.028	PDZ domain containing RING finger 3	intracellular signaling cascade
Plac8	0.66	0.029	Placenta-specific 8	biological process unknown
Gsta3	0.66	0.015	Glutathione S-transferase, alpha 3	
Csrp2	0.67	0.001	Cysteine and glycine-rich protein 2	cell differentiation; development

D330027H18Rik	0.67	0.005	RIKEN cDNA D330027H18 gene	
Epc2	0.67	0.019	Enhancer of polycomb homolog 2	
9530025L08Rik	0.69	0.037		
1300017K07Rik	0.69	0.040	Threonine aldolase 1	
Nvl	0.70	0.013	Nuclear VCP-like	
Dhrs6	0.70	0.036	Dehydrogenase/reductase member 6	biological process unknown
5730523P12Rik	0.71	0.002		
Evc2	0.71	0.022	Ellis van Creveld syndrome 2 homolog	
BC043944	0.71	0.035	CDNA sequence BC043944	
Slc27a3	0.72	0.013	Solute carrier family 27	fatty acid metabolism; lipid metabolism; lipid transport
A430060F13Rik	0.72	0.045	RIKEN cDNA A430060F13 gene	
H2-T10	0.72	0.039	Histocompatibility 2, T region locus 10	MHC class I; defense response
1810054O13Rik	0.73	0.026	Transmembrane protein 86A	
6720460K10Rik	0.73	0.025		
Suox	0.73	0.001	Sulfite oxidase	electron transport
Sp7	0.73	0.008	Trans-acting transcription factor 7	osteoblast differentiation; regulation of transcription from Pol II promoter
5730596B20Rik	0.73	0.022	RIKEN cDNA 5730596B20 gene	
Snapap	0.74	0.015	Synaptosomal-associated protein 25 binding protein	exocytosis; synaptic vesicle exocytosis
Bach2	0.74	0.030	BTB and CNC homology 2	regulation of transcription, DNA-dependent
Il17f	0.74	0.048	Interleukin 17F	
BC023892	0.74	0.028	cDNA sequence BC023892	
4930546E12Rik	0.74	0.039		
Phgdhl1	0.74	0.031		
IGHV1S1	0.74	0.050	Ig H-chain V-region 186-1	
BC034664	0.75	0.023	CDNA sequence BC034664	electron transport
Thbs2	0.75	0.008	Thrombospondin 2	cell adhesion
Scd2	0.75	0.008	Stearoyl-Coenzyme A desaturase 2	fatty acid biosynthesis; lipid biosynthesis
Trim59	0.75	0.012	Tripartite motif-containing 59	regulation of transcription, DNA-dependent
Hoxd8	0.75	0.003	Homeo box D8	development; organogenesis; pattern specification; regulation of transcription, DNA-dependent
1810020D17Rik	0.75	0.008	RIKEN cDNA 1810020D17 gene	
Mrgprb4	0.75	0.009	MAS-related GPR, member B4	G-protein coupled receptor protein signaling pathway
AI173486	0.75	0.033	RIKEN cDNA 1500015A07 gene	
1110013I04Rik	0.75	0.040		
A430057M04Rik	0.75	0.019	RIKEN cDNA A430057M04 gene	
Fgf3	0.75	0.025	Fibroblast growth factor 3	cell proliferation; induction of an organ; regulation of cell cycle; signal transduction
Gpr74	0.75	0.033	G protein-coupled receptor 74	G-protein coupled receptor protein signaling pathway

4930511H11Rik	0.76	0.013	RIKEN cDNA 4930511H11	
Armcx2	0.76	0.023	Armadillo repeat containing, X-linked 2	
Slc30a9	0.76	0.029	Solute carrier family 30	protein biosynthesis
Col5a1	0.76	0.048	Procollagen, type V, alpha 1	cell adhesion
Gas1	0.77	0.010	Growth arrest specific 1	cell cycle arrest; programmed cell death
2610034H20Rik	0.77	0.045	De-etiolated homolog 1 (Arabidopsis)	ubiquitin cycle
Cga	0.77	0.023	Glycoprotein hormones, alpha subunit	
2310047D07Rik	0.77	0.004	RIKEN cDNA 2310047D07 gene	
AK052220	0.77	0.011	Periostin, osteoblast specific factor	
0610009C03Rik	0.77	0.019	WD repeat domain 57	
Gars	0.78	0.001	Glycyl-tRNA synthetase	glycyl-tRNA aminoacylation; protein biosynthesis; regulated secretory pathway; tRNA aminoacylation for protein translation
Uchl3	0.78	0.049	Ubiquitin thiolesterase	protein deubiquitination; ubiquitin cycle; ubiquitin-dependent protein catabolism
1700001E16Rik	0.78	0.035	Decapping enzyme, scavenger	
D930050H05Rik	0.78	0.006	Kelch-like 20 (Drosophila)	cytoskeleton organization and biogenesis
2900046L07Rik	0.78	0.019		
Erbb3	0.79	0.012	v-erb-b2 erythroblastic leukemia viral oncogene homolog 3	cellular physiological process; heart development; peripheral nervous system development; protein amino acid phosphorylation; regulation of cell cycle
9530013L04Rik	0.79	0.025		
9030607L20Rik	0.79	0.049		
Tns	0.79	0.021		
AW125391	0.79	0.028	Radical S-adenosyl methionine domains 1	
Cnbp2	0.79	0.021	Cellular nucleic acid binding protein 2	electron transport
Amh	0.79	0.039	anti-Muellerian hormone	gonad development; gonadal mesoderm development; urogenital system development
Qscn6l1	0.79	0.005	Quiescin Q6-like 1	
Hmgn2	0.79	0.024	High mobility group nucleosomal binding domain 2	DNA packaging
1810009M01Rik	0.79	0.028	RIKEN cDNA 1810009M01 gene	
Sort1	0.79	0.016	Sortilin 1	carbohydrate metabolism; endocytosis
Tna	0.79	0.041	C-type lectin domain family 3	skeletal development
Siat8c	0.80	0.019	sialyltransferase 8C	protein amino acid glycosylation
2900073F20Rik	0.80	0.033		
BC009118	0.80	0.045	CDNA sequence BC009118	
Phf10	0.80	0.018	PHD finger protein 10	regulation of transcription,

				DNA-dependent
AI450757	0.80	0.021	Splicing factor, arginine/serine-rich 12	mRNA processing; nuclear mRNA splicing, via spliceosome

Table 8. Genes significantly ($p < 0.05$) upregulated in FMN2 knockout primary osteoblast cells in comparison to FMN2 wildtype primary osteoblast cells.

Gene Name	Normalized ratio	P-value	Description	Gene Ontology Biological Process
Cugbp2	1.20	0.020	CUG triplet repeat	mRNA processing; mRNA splice site selection; nuclear mRNA splicing, via spliceosome
Nap1l1	1.20	0.050	Nucleosome assembly protein 1-like 1	nucleosome assembly
App	1.21	0.008	Amyloid beta (A4) precursor protein	apoptosis; cell adhesion; endocytosis; extracellular matrix organization and biogenesis
C530043A13Rik	1.21	0.046	RIKEN cDNA C530043A13 gene	
Atp6v1a1	1.22	0.004	ATPase, isoform 1	ATP biosynthesis; ATP synthesis coupled proton transport; ion transport
Ccrl2	1.23	0.049	Chemokine (C-C motif) receptor-like 2	G-protein coupled receptor protein signaling pathway
Rpl10	1.23	0.049	Ribosomal protein 10	protein biosynthesis
Pgam1	1.23	0.050	Phosphoglycerate mutase 1	glycolysis; metabolism
Fkbp8	1.24	0.043	FK506 binding protein 8	cell fate specification; dorsal/ventral pattern formation; eye morphogenesis (sensu Mammalia); protein folding; smoothened signaling pathway
2010319C14Rik	1.24	0.003	Phosphatidylinositol glycan, class X	
Prrx1	1.24	0.043	Paired related homeobox 1	development; regulation of transcription, DNA-dependent
E430002N23Rik	1.24	0.037		
Ppia	1.25	0.005	Peptidylprolyl isomerase A	protein folding
Hmga1	1.25	0.000	High mobility group AT-hook 1	DNA packaging; chromosome organization and biogenesis (sensu Eukaryota); regulation of transcription, DNA-dependent; spermatogenesis
Tessp2	1.25	0.030	Testis serine protease 2	
Stc1	1.25	0.020	Stanniocalcin 1	calcium ion homeostasis; monovalent inorganic anion homeostasis; protein amino acid phosphorylation
B930082K07Rik	1.26	0.011		
Rps7	1.26	0.037	Ribosomal protein S7	protein biosynthesis; ribosome

				biogenesis
9530076L18	1.27	0.034		
NC004605	1.27	0.046	mVI036803	
4930563A19Rik	1.27	0.039		
S100a4	1.28	0.035	S100 calcium binding protein A4	
Lig4	1.28	0.001	Ligase IV, DNA, ATP-dependent	DNA recombination; DNA repair; DNA replication; cytokinesis; single strand break repair
Thbd	1.28	0.000	Thrombomodulin	blood coagulation; embryonic development; negative regulation of coagulation; pregnancy
D15Ertd621e	1.28	0.048	DNA segment, Chr 15 expressed	
Adm	1.28	0.008	Adrenomedullin	neuropeptide signaling pathway
Hspa5	1.29	0.012	Heat shock 70kD protein 5	ER-overload response; protein folding; response to unfolded protein
5930435M05Rik	1.29	0.050		
Rps26	1.30	0.032	Ribosomal protein S26	protein biosynthesis
A330102K04Rik	1.30	0.050	RIKEN cDNA A330102K04 gene	
Crim1	1.30	0.007	Cysteine-rich motor neuron 1	regulation of cell growth
AK038963	1.30	0.035	Lectin, galactose binding, soluble 8	
V1rd15	1.30	0.007	Vomeronasal 1 receptor, D15	G-protein coupled receptor protein signaling pathway
Ercc6	1.32	0.032	Excision repair cross-complementing	pyrimidine dimer repair; response to oxidative stress; transcription-coupled nucleotide-excision repair
Pafah1b1	1.32	0.034	Platelet-activating factor acetylhydrolase	acrosome formation; cell migration; cytokinesis; mitosis; neuroblast proliferation; neurogenesis; neuronal migration; retrograde axon cargo transport
AU067695	1.33	0.013	TRNA splicing endonuclease 2	mRNA processing; tRNA processing
Kcnrg	1.33	0.036	Potassium channel regulator	
Mapk9	1.33	0.049	Mitogen activated protein kinase 9	protein amino acid phosphorylation
Gababrbp	1.34	0.049	Gamma-aminobutyric acid receptor binding protein	biological_process unknown
Rnf10	1.34	0.013	Ring finger protein 10	
Rad1	1.35	0.042	RAD1 homolog (S. pombe)	DNA repair
AU021034	1.35	0.038	Expressed sequence AU021034	
Ribc2	1.36	0.041	RIB43A domain with coiled-coils 2	biological_process unknown
Mia1	1.36	0.035	Melanoma inhibitory activity 1	cell-matrix adhesion; extracellular matrix organization and biogenesis
Gnb3	1.36	0.039	Guanine nucleotide binding protein	G-protein coupled receptor protein signaling pathway; signal transduction
A930027G11Rik	1.37	0.042		

Rab22a	1.37	0.046	RAB22A, member RAS oncogene family	protein transport; small GTPase mediated signal transduction
4930519F16Rik	1.37	0.023	RIKEN cDNA 4930519F16 gene	
LOC238771	1.37	0.037	Similar to Metaxin 1	
4930515G01Rik	1.37	0.009	RIKEN cDNA 1100001D10 gene	
2010300F17Rik	1.38	0.004		
Cxcl5	1.38	0.003	Chemokine (C-X-C motif) ligand 5	chemotaxis; immune response; inflammatory response; signal transduction
Slpi	1.39	0.042	Secretory leukocyte protease inhibitor	
Serpinb2	1.39	0.049	Serine proteinase inhibitor, clade B	
4933436E23Rik	1.40	0.001		
1700061N14Rik	1.41	0.034		
Dio3	1.42	0.014	Deiodinase	
4933430F16Rik	1.42	0.041	RIKEN cDNA 4933430F16 gene	
1190002H09Rik	1.43	0.048	RIKEN cDNA 1190002H09 gene	
AK081844	1.43	0.002		
Ddx3y	1.43	0.047	DEAD (Asp-Glu-Ala-Asp) box polypeptide	
1100001I19Rik	1.43	0.004	RIKEN cDNA 1100001I19 gene	
Gm1960	1.44	0.003	Gene model 1960, (NCBI)	
Timm22	1.45	0.034	Translocase of inner mitochondrial membrane 22	intracellular protein transport
Sertad2	1.45	0.011	SERTA domain containing 2	regulation of transcription, DNA-dependent
Sprrl9	1.47	0.006	Small proline rich-like 9	
Pigt	1.48	0.026	Phosphatidylinositol glycan, class T	
Cdc42ep3	1.48	0.030	CDC42 effector protein	
Sqrdl	1.48	0.001	Sulfide quinone reductase-like (yeast)	electron transport
2900016D05Rik	1.49	0.005	RIKEN cDNA 2900016D05 gene	
Sdpr	1.51	0.008	Serum deprivation response	
Serping1	1.54	0.005	Serine peptidase inhibitor, clade G	blood coagulation; complement activation; complement activation, classical pathway
Tm4sf1	1.54	0.003	Transmembrane 4 superfamily member	
Odd1	1.57	0.029	Odd-skipped related 1	
Atp1a1	1.60	0.030	ATPase, Na+/K+ transporting, alpha 1	cation transport; metabolism; monovalent inorganic cation transport; potassium ion transport; sodium ion transport
S100a8	1.61	0.025	Calgranulin A	Chemotaxis
Akr1c18	1.61	0.004	Aldo-keto reductase family 1	progesterone metabolism
B430201A12Rik	1.65	0.006	RIKEN cDNA B430201A12 gene	
1700009P13Rik	1.67	0.036	RIKEN cDNA 1700009P13 gene	
Lcn2	1.70	0.035	Lipocalin 2	Transport
Efemp1	1.73	0.008	Epidermal growth factor-containing fibulin-like extracellular matrix protein 1	cell adhesion

Cxcl2	1.74	0.006	Chemokine (C-X-C motif) ligand 2	chemotaxis; immune response; inflammatory response; signal transduction
Psca	1.81	0.033	Prostate stem cell antigen	
2610028F08Rik	1.89	0.005	R-spondin 2 homolog	protein amino acid phosphorylation; transmembrane receptor protein tyrosine kinase signaling pathway
Esm1	2.02	0.022	Endothelial cell-specific molecule 1	regulation of cell growth
Ssxb1	2.08	0.016	Synovial sarcoma, X member B	regulation of transcription, DNA-dependent
Aqp1	2.29	0.020	Aquaporin 1	transport; water transport

f. In Vivo Skeletal Phenotype Measurements of FMN2 Knockout and Control Mice.

PIXImus scans (PIXImus, LUNAR, Madison, WI) for the determination of bone mineral density (BMD) and bone mineral content (BMC) were carried out on 3, 6, 9, and 12 week old FMN2 mutant and control mice. The PIXImus instrument is calibrated routinely and a quality assurance test is performed daily prior to scanning. Volumetric bone mineral density (vBMD) and geometric parameters of femurs were determined by peripheral quantitative computed tomography (pQCT) (Norland Medical Sytems) on isolated mouse femurs. Analysis of the pQCT scans was performed using Bone Density Software version 5.40 (Norland Medical Systems). Femur bone parameters were measured and averaged for three scans at mid-diaphysis. Trabecular bone phenotypes of femurs were also determined by micro-computed tomography (micro-CT) using a VivaCT 40 micro-CT scanner (ScanCo Medical, Switzerland) The VivaCT 40 is equipped with a micro-focus X-ray source and can achieve 10 μm resolution. Femur trabecular bone parameters were adjusted for bone length to insure that identical regions directly beneath the growth plate were measured. Micro-CT mid-shaft measurements were taken at 50 scans proximal to 50 scans distal the femur mid-shaft. Statistical analyses of bone parameters were done by Student's T-test.

Knockout (-/-) and wildtype (+/+) FMN2 mice were measured for total aBMD and BMC by DXA using PIXImus at 3, 6, 9, and 12 weeks of age. We observed the expected gender differences in growth parameters after 4 weeks of age with males being larger than females, a gender by treatment interaction was not observed. Therefore, male and female data are combined for the data analysis for the sake of clarity. Total body weight was 14% reduced ($p<0.05$) in FMN2 knockout mice at 12 weeks of age (**Figure 12**). In order to determine if lack of FMN2 influences bone accretion at different skeletal sites, we measured changes in BMC in femur, tibia and lumbar vertebra of FMN2 knockout and control mice. These results showed that disruption of FMN2 produced a greater deficit in the long bones (37% and 32.5% reduction in femur and tibia BMC respectively, $P<0.01$) compared to lumbar vertebra (12% reduction, not significant) (**Figure 13**). DXA measurements also revealed that this reduction in BMC in the FMN2 knockout mice was caused by both reduced bone density as well as reduced bone size. Accordingly, femur BMD was reduced by 14% in the FMN2 knockout mice compared to control mice.

Figure 12. FMN2 Knockout and Wildtype PIXIMus Femur, Tibia and Vertebra aBMD Phenotypes. Total body weight is 14% reduced in FMN2 knockout mice at 12 weeks of age ($p<0.05$).). Disruption of FMN2 produced a greater deficit in the long bones (37% and 32.5% reduction in femur and tibia BMC respectively, $P<0.01$) compared to lumbar vertebra (12% reduction, not significant). Femur and tibia aBMD are significantly reduced (*=$p<0.05$) at 6, 9, and 12 weeks of age in FMN2 knockout mice. Vertebra aBMD is only 1.5% reduced at 12 weeks of age and this difference is not statistically significant (n= 6 to 20 per time point group).

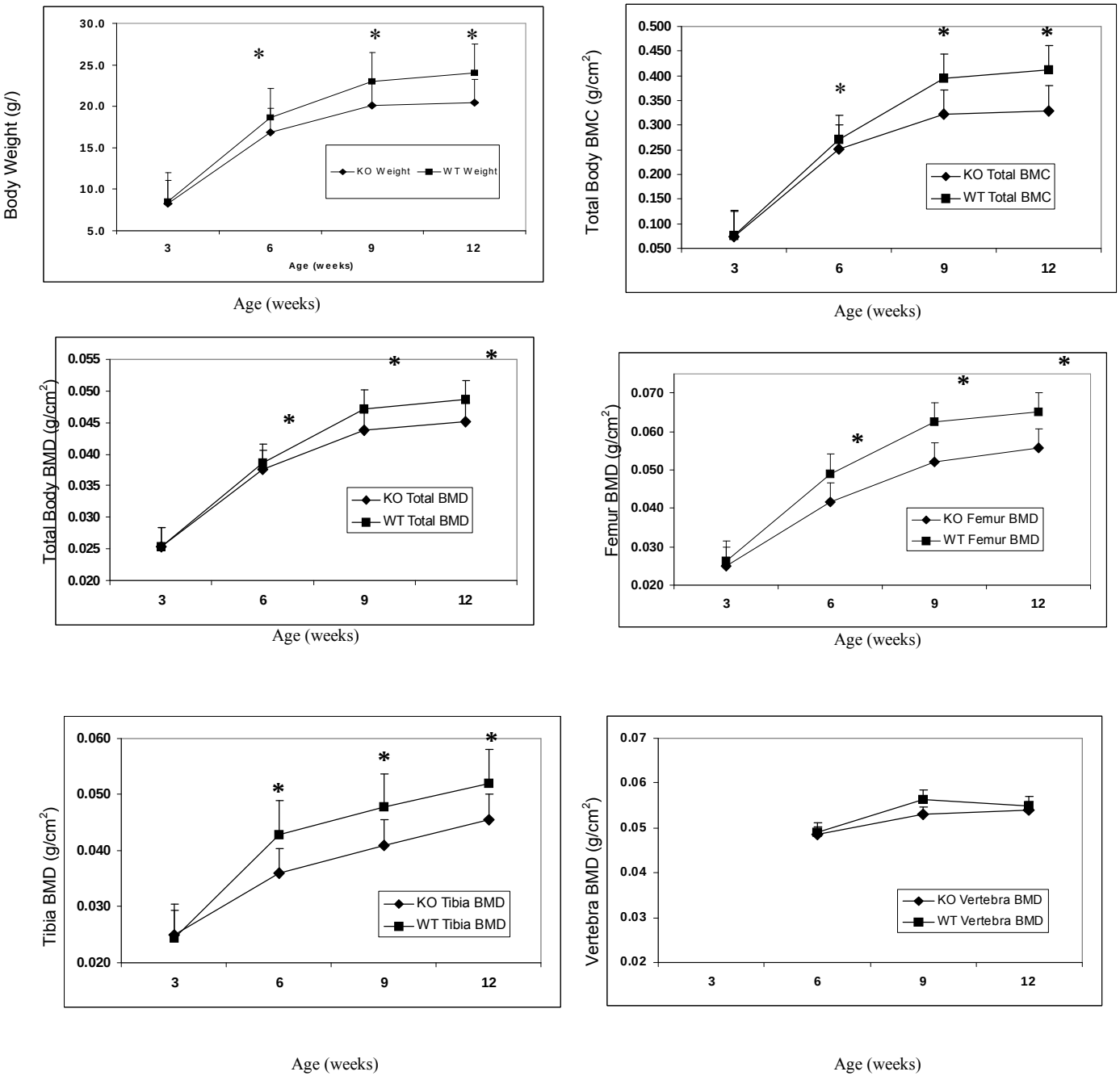

Areal BMD measurements by DXA are known to be influenced by differences in bone size. We, therefore, undertook pQCT measurements of volumetric BMD which is not influenced by differences in bone size between knockout and control mice. Femur volumetric BMD is decreased by 7% in the knockout mice (Figure 14). This reduction in volumetric BMD is apparently caused by reduced cortical thickness and cortical content. Consistent with the DEXA data, femur periosteal circumference is reduced by 5% (p=0.001), femur cortical thickness is reduced by 7.3% (p=0.004), femur total area is reduced by 9.7% (p=0.001), and femur cortical content is reduced by 12.8% (p=0.002).

Figure 13. Skeletal Deficits in FMN2 Knockout Mice. At 12 weeks of age total body BMC is 20.1% reduced (*=p<0.01), femur BMC is 36.7% reduced (*=p<0.01), tibia BMC is reduced by 32.5% *=p<0.01), and vertebra BMC is 11.7% reduced (not significant). Total body aBMD is 7.3% reduced (*=p<0.01), femur aBMD is 14.4% reduced *=p<0.01), tibia aBMD is reduced by 12.3% (*=p=0.02), and vertebra aBMD is 1.5% reduced (not significant). Total body aBMD is 7.3% reduced (*=p<0.01), femur aBMD is 14.4% reduced *=p<0.01), tibia aBMD is reduced by 12.3% (*=p=0.02), and vertebra aBMD is 1.5% reduced (not significant).

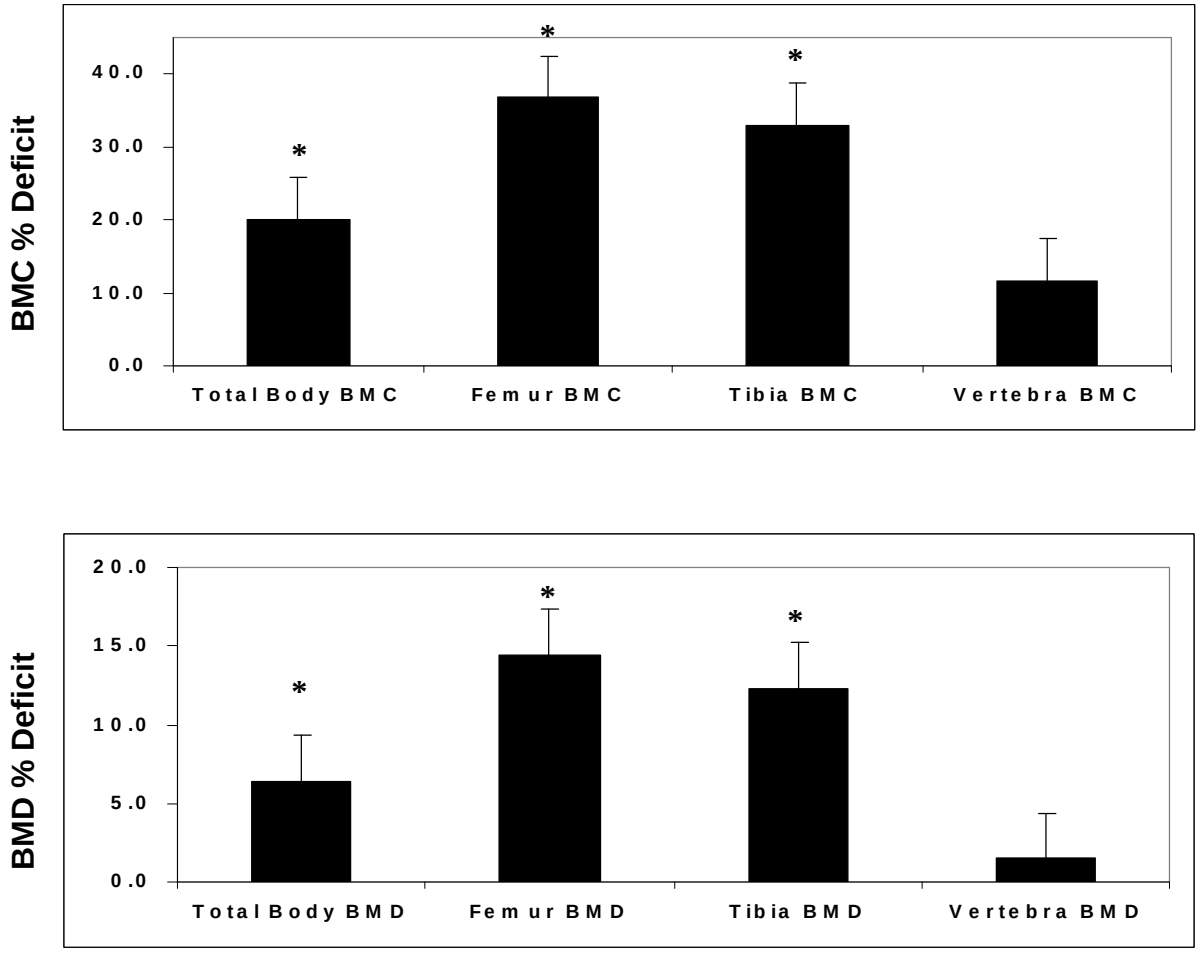

Figure 14. Percent of Skeletal Deficit KO vs WT FMN2 Femur pQCT Bone Parameters. Significantly altered pQCT parameters are plotted as percent change of knockout to wildtype femur parameters. Femur

periosteal circumference is reduced by 5% (*=p=0.001), femur cortical thickness is reduced by 7.3% (p=0.004), and femur cortical content is reduced by 12.8% (*=p=0.002).

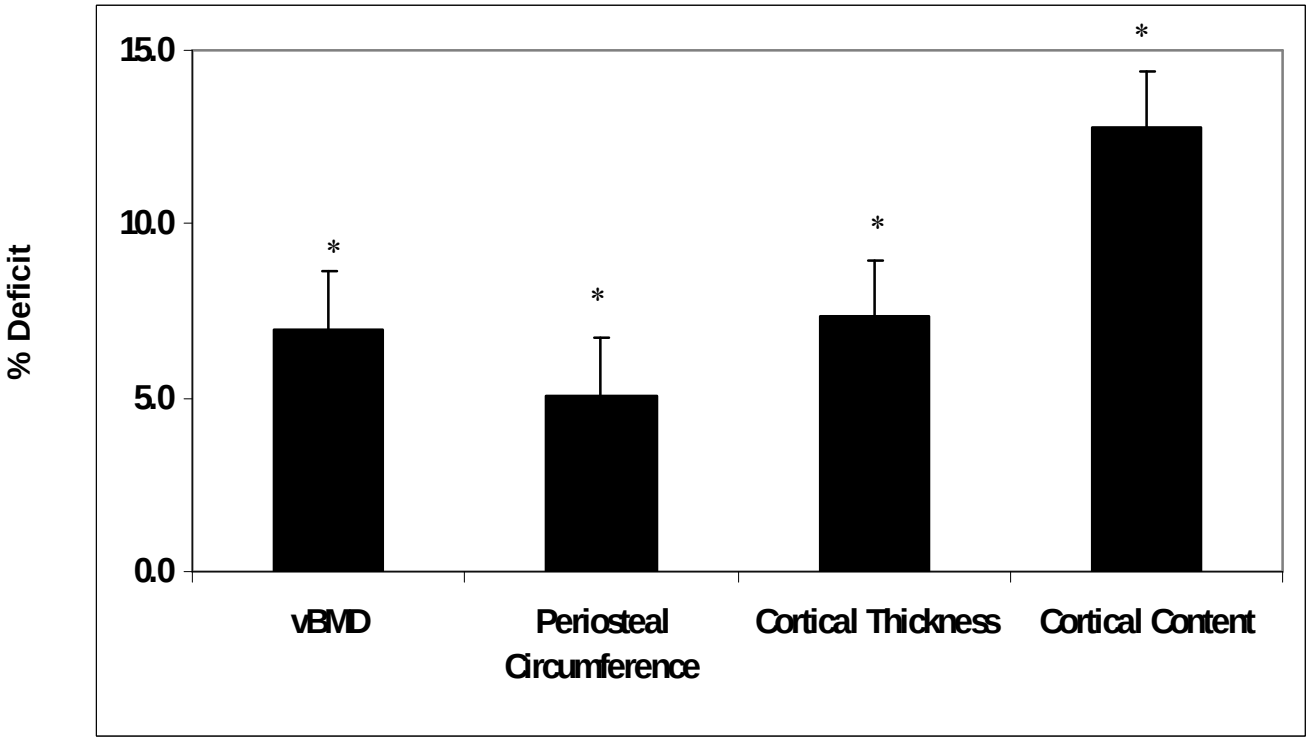

Trabecular bone phenotypes of femurs were also determined for five knockout and eight control mice by micro-computed tomography (micro-CT) using a VivaCT 40 micro-CT scanner (ScanCo Medical, Switzerland) Femur trabecular bone parameters were measured and calculated for 180 scans directly beneath the femur growth plate. The bone volume/trabecular volume (BV/TV) ratio is 30% reduced (p=0.03), trabecular number is 5% reduced and trabecular thickness is 14% decreased (p=0.06) in the FMN2 knockout femur in comparison to wildtype femur (Table 9).

Table 9. Micro-Computed Tomography. The bone volume/total volume (BV/TV) ratio is 30% reduced (p=0.03), trabecular number is 5% reduced, trabecular thickness is 14% decreased (not significant) and trabecular spacing is 5% increased (not significant) in FMN2 knockout femur in comparison to wildtype femur.

Parameter	WT (n=8)	KO (n=5)	T-Test
Bone Volume/Total Volume	0.096	0.067	0.03
Trabecular Number (1/mm)	4.03	3.84	0.35
Trabecular Thickness (mm)	0.049	0.042	0.06
Trabecular Spacing (mm)	0.249	0.260	0.21

g. Real Time PCR Expression of FMN2.

Bone marrow cells were also isolated from C57BL/6J femurs and treated with 100 ng/ml macrophage-colony stimulating factor (M-CSF) for 3 days to generate M-CSF dependent bone marrow (MDBM) cells. Both primary C57BL/6J osteoclasts and RAW264.7 undifferentiated osteoclast-like

cells were then differentiated into TRAP-positive multinucleated osteoclasts by culturing for 7 days in the presence of M-CSF and RANKL. RNA was extracted from the cells using an RNAeasy Mini Kit (Qiagen) according to the manufacturer's protocol. RNA samples were normalized to 300 ng per sample and reverse transcribed with oligo (dT) primers and Superscript II (Invitrogen). Real-time PCR was done using the SYBR Green PCR Core Reagents Kit (Applied Biosystems). The gene expression levels were normalized to housekeeping gene TBP using the comparative Ct method. RT-PCR reactions were sequenced to insure gene specificity for the reactions.

MC3T3-E1 osteoblast-like cells expressed FMN2 transcript at 5 to 20 fold higher levels than RAW264.7 osteoclast-like and primary cultures of osteoclast undifferentiated and differentiated osteoclasts. Furthermore, WNT3A treatment increased the expression of FMN2 by 2.7 fold ($P<0.01$) (Figure 15). Expression analysis of RNA isolated from primary C57BL/6J osteoclasts and RAW264.7 undifferentiated and differentiated osteoclast-like finds that FMN2 is expressed at 5 to 20 fold lower levels in both differentiated and undifferentiated osteoclasts in comparison to osteoblasts (**Figure15**).

Figure 15. Expression of FMN2 in MC3T3-E1, RAW264.7 and Primary Osteoclast Cells. MC3T3-E1 osteoblasts express FMN2 transcript at 5 to 20 higher levels than undifferentiated and differentiated RAW264 osteoclast-like and C57BL/6J primary osteoclasts (* = $p<0.01$). Also, treatment of MC3T3 osteoblast-like cells with WNT3A, a bone formation stimulator, increased the expression of FMN2 by 2.7 fold (* = $p<0.01$).

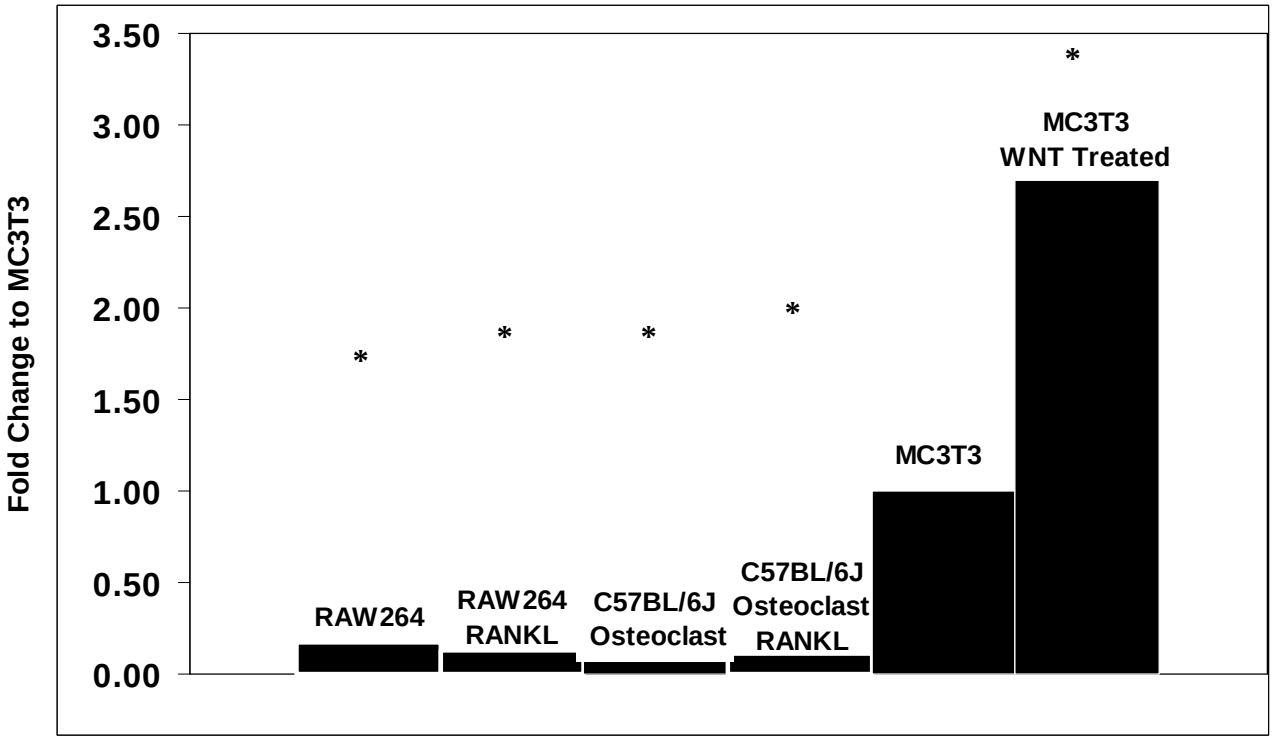

h. Cellular Proliferation and Differentiation Assays.

Calvaria and femurs from 28-day-old FMN2 knockout and control mice were digested by collagenase for isolation of osteoblasts as previously described. The cultures were expanded in α-MEM containing serum and used for proliferation and ALP differentiation assays. For proliferation assays, BrdU (Exalpha Biologicals, Inc.) was incorporated into DNA in osteoblast cell cultures for 1

hour. The amount of BrdU was quantified with a microplate spectrophotometer at a wavelength of 450 nm with reference at a wavelength of 570 nm. Monolayer cultures without BrdU incorporation were used as a negative control. For differentiation assays, calvaria cells were seeded into 96-well plates at 10,000 cells per well in 50 µl of α-MEM containing 0.1% CS and 0.1% BSA and grown to 90% confluency. Osteoblast differentiation was measured by the increase in the specific activity of ALP as described previously.

Cellular proliferation as measured by BrdU incorporation into newly synthesized DNA was reduced by 37% in osteoblasts derived from FMN2 knockout mice in comparison to wildtype control mice ($p<0.01$) (Figure16). ALP activity was found to be reduced by over 20% in knockout FMN2 calvarial osteoblasts ($p<0.01$) (**Figure 16**).

Figure 16. FMN2 Knockout Osteoblast Proliferation, ALP Activity and Bone Nodule Formation. Knockout FMN2 osteoblasts show significantly reduced proliferation (*=$p<0.01$), ALP activity (*=$p<0.01$) and bone nodule formation (*=$p<0.04$) in comparison to control osteoblasts.

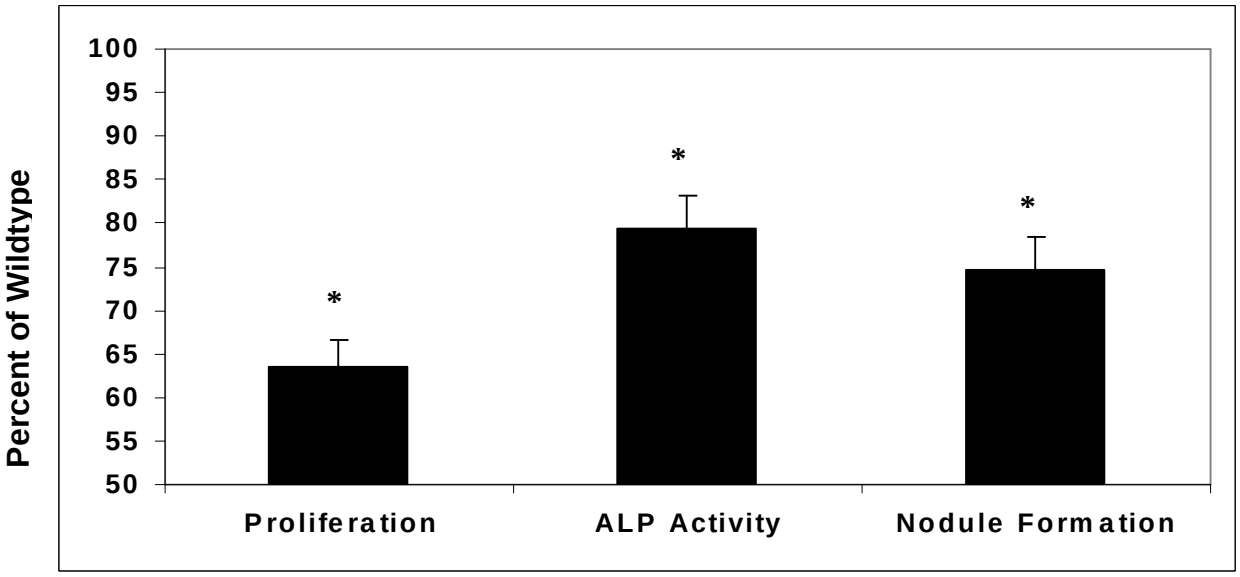

Mesenchymal Stem Cells and Mineralized Bone Nodule Formation Assay. FMN2 knockout and wildtype calvarial cells were plated at a density of 7 × 106 cells/90-mm per plastic tissue culture dish in α-MEM containing 10% calf serum, 100 U/ml penicillin, and 100 µg/ml streptomycin. Culture media were changed every 2 days for 6 days and then switched to mineralization media by adding 50 µg/ml ascorbic acid and 10 mM β-glycerophosphate. After 24 days, cultures were stained with alizarin red to assess mineralized nodules as described. The area and the number of bone nodules stained were measured with the use of computerized image analyzer software and the percent area of the plates covered with bone nodules calculated. For mesenchymal stem cell (MSC) differentiation assays, FMN2 knockout and wildtype stromal cells were flushed out of femurs and plated at a density of 7 × 106 cells/90-mm per plastic tissue culture dish in α-MEM containing 10% calf serum, 100 U/ml penicillin, and 100 µg/ml streptomycin. Culture media was changed every 2 days for 6 days and then switched to mineralization media by adding 50 µg/ml ascorbic acid and 10 mM β-glycerophosphate. Cells were cultured for 10 days and then identified and counted after staining with ALP. The number of CFU-F (mesenchymal cells) are those colonies not stained by ALP (osteoblast colonies). The number of CFU-F and CFU-OB were measured and percent CFU-OB/CFU-F calculated.

Mineralized bone nodule formation assays find that knockout FMN2 osteoblasts have 25% reduced bone nodule formation in comparison to wildtype FMN2 osteoblasts ($p = 0.04$) (Figure 7). Also, stromal cells (MSC) isolated from femur lacking FMN2 exhibit 55% reduced ALP staining in comparison to wild type FMN2 MSC ($p < 0.001$) (**Figure 17**).

Figure 17. Mesenchymal Stem Cell (MSC) Differentiation in Wildtype and Knockout FMN2 Stromal Cells. MSC lacking FMN2 exhibit 55% reduced ALP staining in comparison to wild type FMN2 MSC ($p < 0.001$).

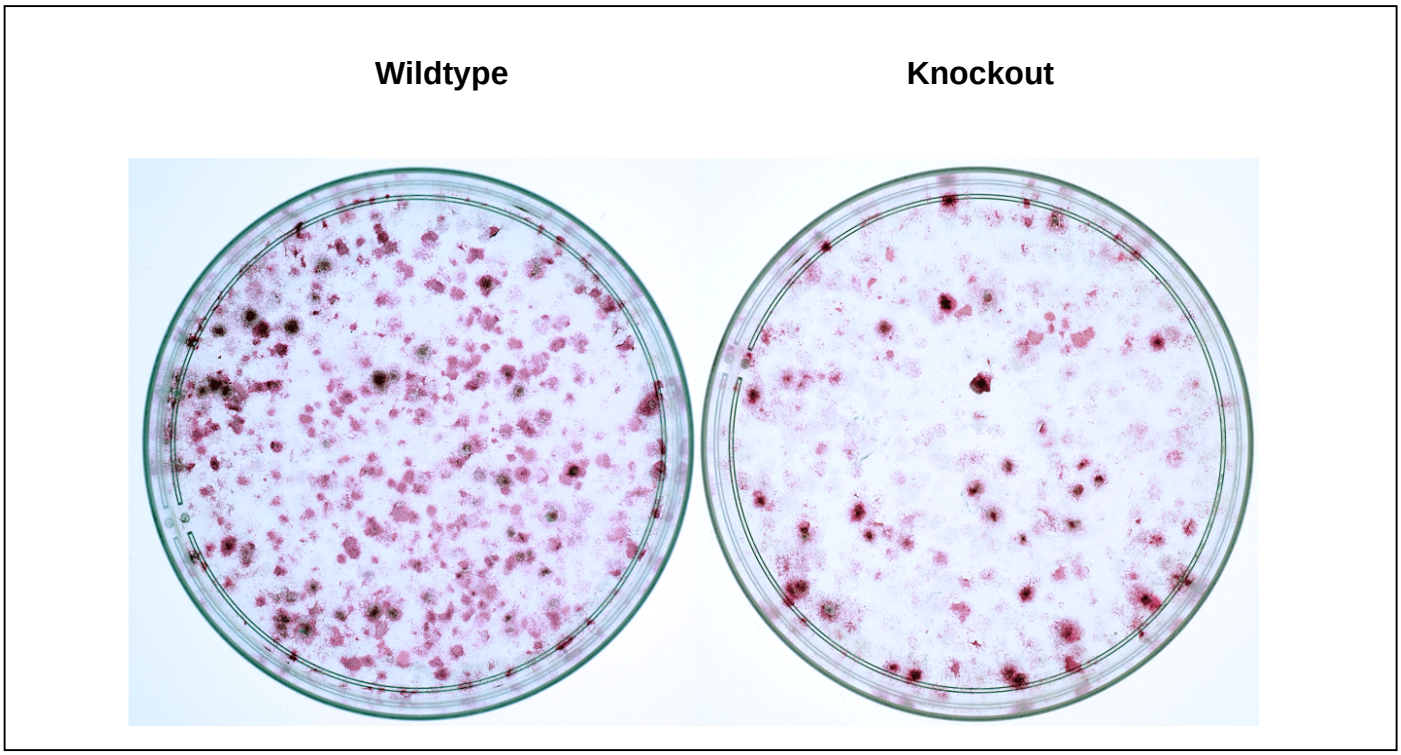

i. Western Blot Analysis of β-Catenin Protein Levels.

Cells were harvested from calvaria and were maintained in α-MEM containing 10% calf serum and antibiotics at 37°C in a humidified atmosphere consisting of 5% CO2 in air. WNT and GFP (control) conditioned media were generated using HT1080 cells that have been transduced with MLV-based vectors expressing WNT1 and GFP protein (~500ng/ml). After the transduction, conditioned media was collected. FMN2 KO and WT primary osteoblast cells were treated with the WNT or GFP control conditioned media for 4 hours, washed with phosphate-buffered saline twice, and cell lysates extracted in protein lysis buffer. Extracted proteins were separated by SDS-PAGE, transferred to PVDF membrane, and probed with mouse monoclonal anti-beta-catenin antibody and anti-beta-actin antibody (loading control) (Sigma). After washing, bound secondary antibodies were detected using chemiluminescence. The integrated density values of the β-catenin and β-actin protein bands were determined by densitometry, and the KO and WT osteoblast WNT treated and GFP control treated β-catenin integrated density values normalized (divided) by the β-actin integrated density values.

The normalized β-catenin values were found to be 47.2% reduced in WNT treated knockout osteoblasts in comparison to WNT treated wildtype osteoblasts ($p=0.02$). Additionally, WNT treatment of wildtype osteoblasts induces a 42% increase in β-catenin levels ($p<0.001$) while knockout osteoblasts do not show a significant response to WNT treatment (**Figure 18**).

Figure 18. Western Blot of β-Catenin and β-Actin. Densitometry analysis of western blot band intensity of β-catenin and β-actin proteins finds that in response to WNT treatment FMN2 wildtype osteoblasts produce 42% more β-catenin protein than wildtype osteoblasts treated with GFP control ($p<0.001$). Also, normalized β-catenin values were found to be 47.2% reduced in WNT treated knockout osteoblasts in comparison to WNT treated wildtype osteoblasts ($p=0.02$) and WNT treatment of knockout osteoblasts did not produce a significant increase of β-catenin protein.

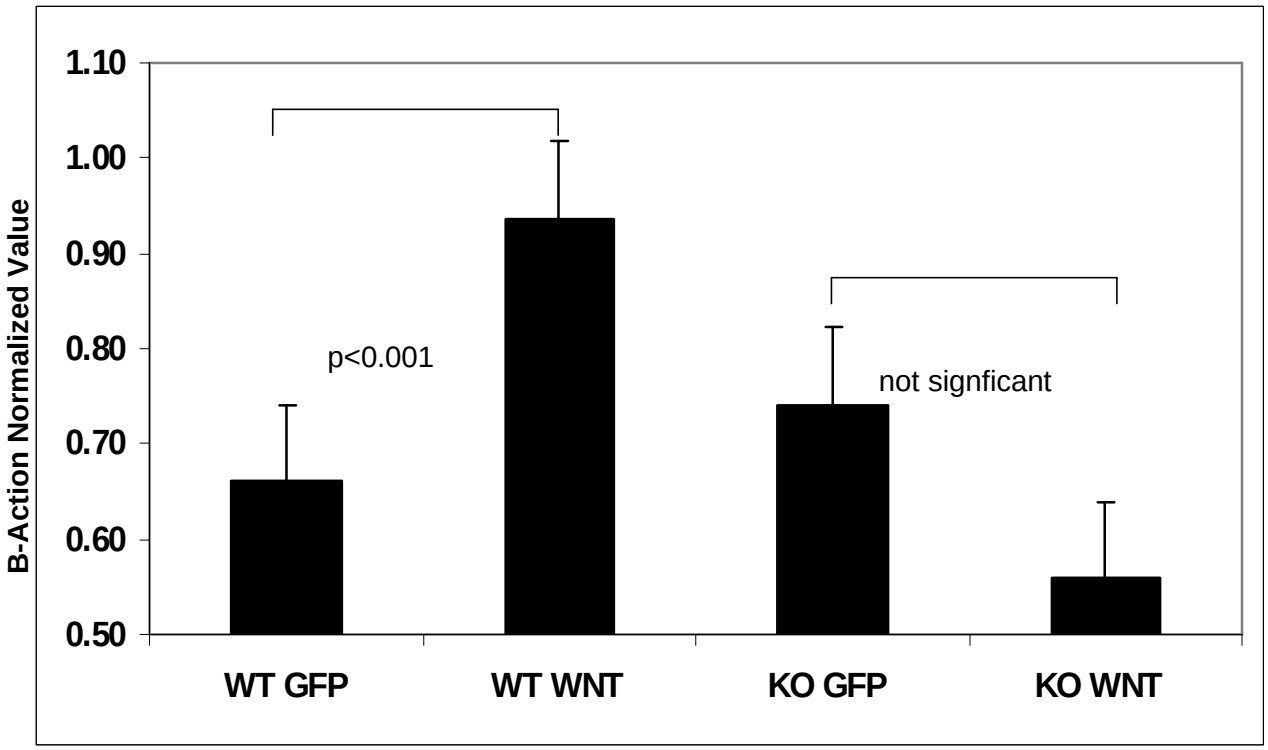

j. TCF-LEF Reporter Assays of Osteoblast WNT Treatment.

Osteoblasts were harvested from 4-week old KO and WT FMN2 mouse femur and were maintained in a-MEM containing 10% calf serum and antibiotics at 37°C in a humidified atmosphere consisting of 5% CO2 in air. After growing to 50-80% confluency, the TOPFLASH and pRL-TK renilla reporter plasmids were transfected transiently into cells using FuGene transfection reagent (Roche). WNT1, WNT10B and B-GAL (control) conditioned media were generated using HT1080 cells that have been transduced with MLV-based vectors expressing WNT1, WNT10B and B-GAL protein (~500ng/ml). All experiments were performed in triplicate. After 48 hours, the media was removed, cells washed twice with PBS and the cells trypsinized. The cells were transferred to eppendorf tubes, washed with PBS and resuspended in 130µl Lysis buffer (Promega dual luciferase assay system). After incubation at room temperature for 15-20 minutes, the cellular debris was spun down cell and the supernatant transferred to 96-well luminometer plates. The activities of the Luciferase and Renilla reporters were determined using the dual luciferase assay system of Promega and a MPL2 microplate luminometer (EG & G Berthold). Dual-Glo Stop & Glo Reagent was used to quench the luminescence from the firefly reaction and simultaneously provide a substrate for Renilla luciferase. The value obtained for the Renilla luciferase activity is a measure of the efficiency of transfection and was used to normalize the TCF-LEF firefly luciferase values by dividing the TCF-LEF luciferase values by the Renilla luciferase values.

Normalized TCF-LEF luminosity signals were found to be 20% reduced in FMN2 knockout osteoblasts in response to WNT1 treatment (p=0.045). Knockout osteoblasts also displayed a 14% reduction in response to WNT10B treatment (not significant). B-GAL treatment of knockout osteoblasts resulted in no difference in Renilla luciferase normalized TCF-LEF luminosity signals (**Figure 19**).

Figure 19. TCF-LEF Reporter Assays of FMN2 KO and WT Osteoblasts. Normalized TCF-LEF luminosity signals were found to be 20% reduced in FMN2 knockout osteoblasts in response to WNT1 treatment (*=p=0.045). Knockout osteoblasts also displayed a 14% reduction in response to WNT10B treatment (not significant). B-GAL treatment of knockout osteoblasts resulted in no difference in Renilla luciferase normalized TCF-LEF luminosity signals.

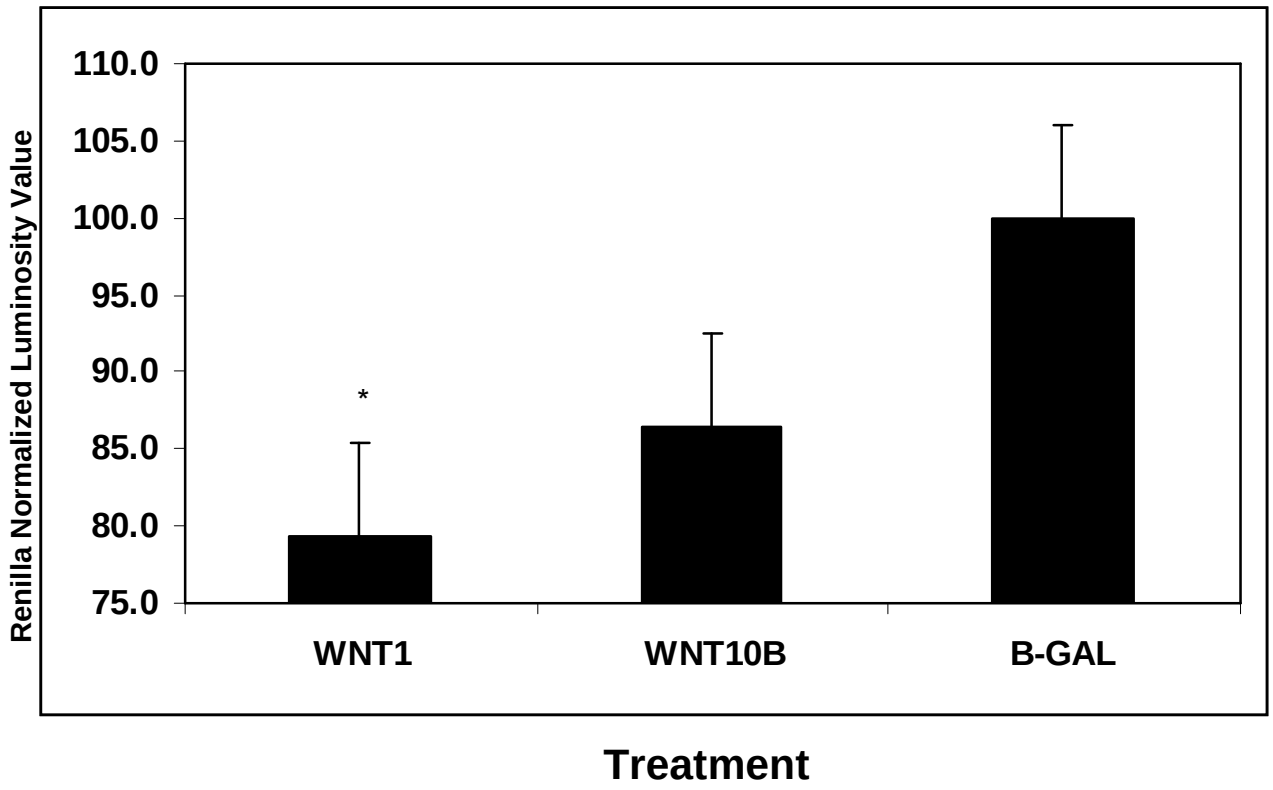

3. Ephrin-A4 Mouse Studies

a. Introduction

The EphA4 gene belongs to the ephrin receptor subfamily of the protein-tyrosine kinase family. Ephin receptors typically have a single kinase domain and an extracellular region containing a Cys-rich domain and 2 fibronectin type III repeats. The ephrin receptors are divided into 2 groups based on the similarity of their extracellular domain sequences and their affinities for their respective ligands. Accordingly, EphrinB ligands are primarily preferential ligands for EphB receptors and EphrinA ligands primarily function as ligands for EphA receptors. However, EphA4 can bind all the ephrin-A ligands as well as ephrin-B2 and ephrin-B3 ligands. The importance of Ephrin receptor/ligand interactions is shown by the multitude of cellular processes that have been implicated in ephrin signaling. These include stem cell differentiation, cell migration and skeletal formation. In calcified tissues, ephrin receptor/ligand interactions have been implicated in skeletal developmental, bone

response to mechanical laoding and osteoblast/osteoclast homeostasis. For example, mutations in mice of ephrinB1 ligands cause skeletal abnormalities. Knockout mouse phenotypes of several ephrin receptors display skeletal abnormalities including and EphA5, EphB1, EphB2 and EphB3. Knockout mice for the Ephrin-B3 and the Ephrin-A ligands primarily display neuronal and corticospinal cord defects and the ligand Ephrin-B2 knockout is embryonic lethal (http://www.informatics.jax.org/).

In humans, mutations of Ephrn-B1 cause craniofrontonasal syndrome in which females show multiple skeletal malformations, but only mild abnormalities are displayed in males. Also, Xing et al. found that in response to mechanical loading of mouse bones, the EphB2 receptor is increased in expression. Other studies have found EphrinB2 ligands and EphB4 receptors regulate the differentiation of osteoclasts and osteoblasts, resulting in suppression of bone resorption and enhancement of bone formation. These findings demonstrate that Ephrin-B receptors and their ligands are key regulators of skeletal development.

The Ephrin-A family of receptors and ligands have been shown to be important regulators of nerve formation and regeneration. Disrupting the expression of the EphA4 receptor in mice has been shown to modify neuronal connections in the brain and spinal cord. This results in an unusual hopping gait in EphA4 knockout mice. Also, knockout mice lacking EphA4 (-/-) have been reported to exhibit nerve regeneration after spinal cord injury. Due to the importance of the Ephrin-B mediated signaling pathway in bone biology homeostasis, we hypothesized that the related Ephrin-A gene family may also influence bone formation and remodeling. Thus, we undertook investigations into the bone phenotypes of EphA4 knockout mice through Piximus bone densitometry and micro computed tomography (μCT).

b. EphA4 Knockout Mice.

Two mating pairs of heterozygous EphA4 (+/-) mice were obtained from Jackson Laboratories (Bar Harbor, ME). The recessive mutation of Epha4 arose spontaneously on the C57BL/6J inbred strain at the Jackson Laboratory in 1964 and was transferred to the C3H/HeSnJ background and has been maintained by backcrossing mice homozygous for Epha4rb to C3H/HeSnJ mice, then intercrossing the progeny.

c. Skeletal Phenotype Measurements. Total body PIXImus scans (PIXImus, LUNAR, Madison, WI) for the determination of bone mineral density (BMD) and bone mineral content (BMC) were done on 3, 6, 9, and 12 week old EphA4 mutant and control mice. The PIXImus instrument is calibrated routinely and a quality assurance test is performed daily prior to scanning. Volumetric bone mineral density (vBMD) and geometric parameters of femurs were determined by micro computed tomography (μCT) using a VivaCT 40 scanner (ScanCo Medical, Switzerland) The VivaCT 40 is equipped with a micro-focus X-ray source and can achieve 10 μm resolution. Femur trabecular bone parameters were measured and calculated for 180 scans directly beneath the femur growth plate. For mid-shaft measurements 100 scans were measured at femur mid-shaft.

Total body BMD in EphA4 mutant and control mice was measured by PIXImus at week 3, 6, 9 and 12 weeks of age. EphA4 knockout mice were found to be significantly smaller in size at all time points. The reduced growth phenotype was accompanied also by significantly reduced total body BMD (Figures 20, 21). Body weight and total body BMD were reduced by 16% and 11% in female mice and 11% and 7% in male mice respectively at 12 weeks of age (**Figures 20-23**).

Figure 20. Body weight of female EphA4 mutant and wildtype mice. EphA4 female knockout mice (n=10) body weight is significantly reduced at all time points in comparison to wildtype mice (n=14) ($p < 0.05$ at all time points). At 12 weeks of age female EphA4 knockout mice are 16% reduced in weight in comparision to control mice.

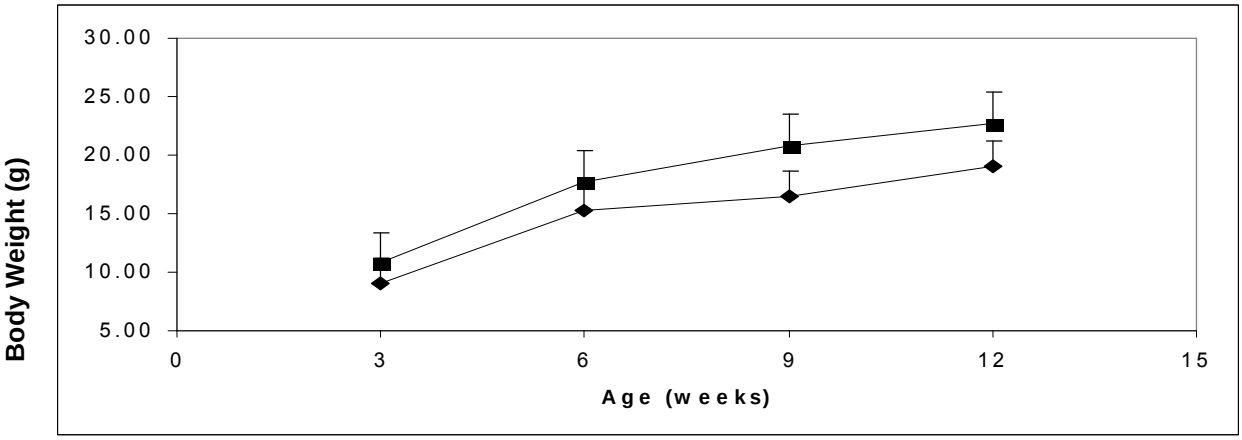

Figure 21. Bone mineral density (BMD) of female EphA4 mutant and wildtype mice. EphA4 female knockout mice (n=10) have significantly reduced BMD in comparison to wildtype mice (n=14) at 6, 9, and 12 weeks ($p < 0.05$). At 12 weeks of age female EphA4 knockout mice are 11% reduced in total BMD in comparision to control mice.

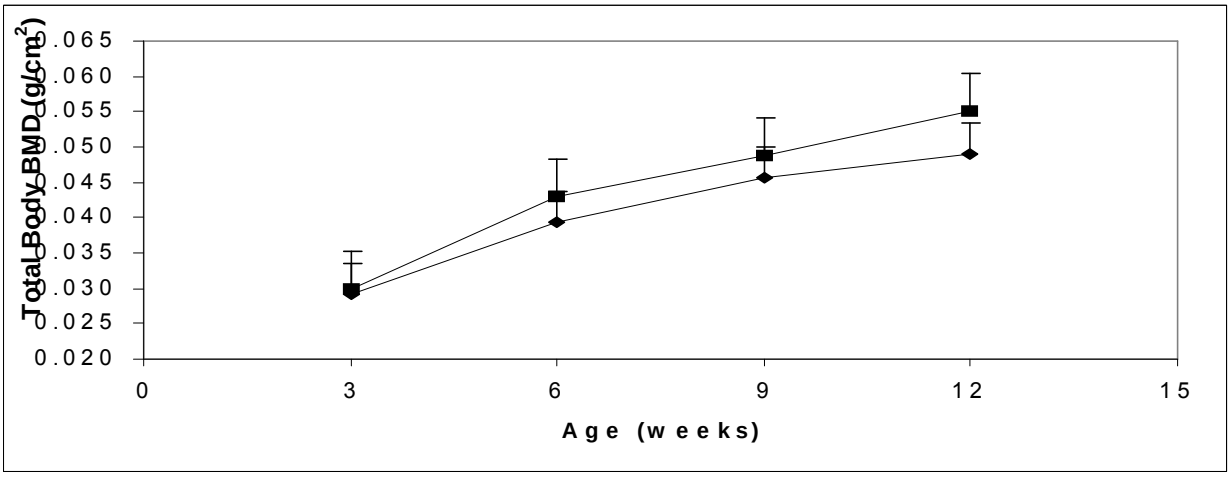

Figure 22. Body weight of male EphA4 mutant and wildtype mice. EphA4 knockout male mice (n=10) are significantly smaller at all time points in comparison to wildtype mice (n=13) ($p < 0.05$). At 12 weeks of age male EphA4 knockout mice are 11% reduced in weight in comparision to control mice.

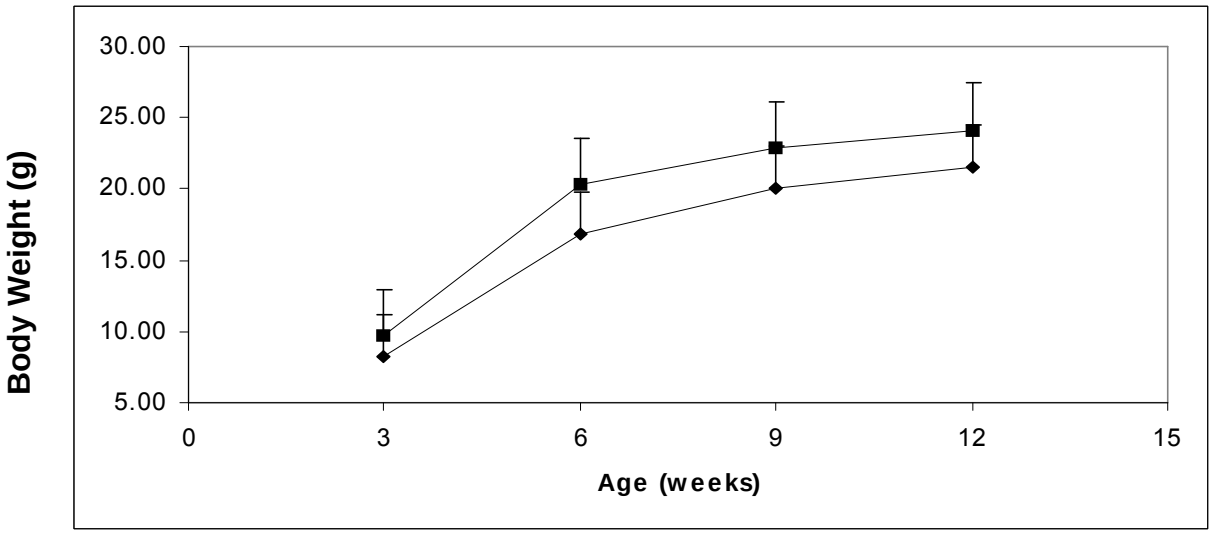

Figure 23. Bone mineral density (BMD) of male EphA4 mutant and wildtype mice. EphA4 male knockout mice (n=10) have reduced BMD in comparison to wildtype mice (n=13) at 6, 9, and 12 weeks ($p < 0.05$). At 12 weeks of age male EphA4 knockout mice are 7% reduced in total BMD in comparision to control mice.

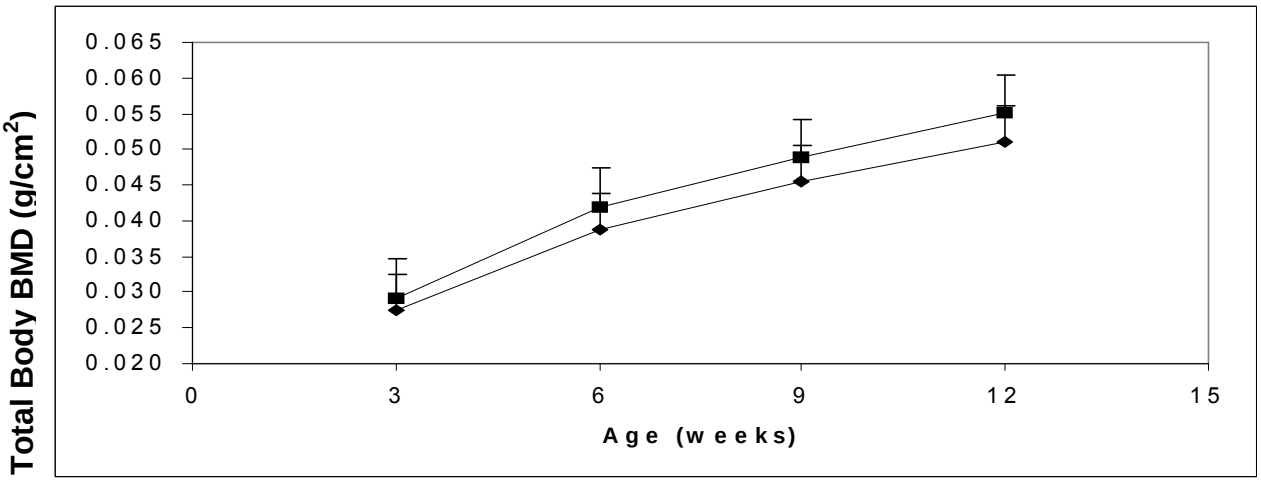

Trabecular bone phenotypes of femurs were also determined by micro-computed tomography (micro-CT) using a VivaCT 40 micro-CT scanner (ScanCo Medical, Switzerland) The VivaCT 40 is equipped with a micro-focus X-ray source and can achieve 10 μm resolution. Femur trabecular bone

parameters were adjusted for bone length to insure that identical regions directly beneath the growth plate were measured. Micro-CT mid-shaft measurements were taken at 50 scans proximal to 50 scans distal the femur mid-shaft (Table 10). Statistical analyses of bone parameters were done by Student's T-test. At 12 weeks of age, trabecular femur volume was significantly reduced in EphA4 knockout mice. The bone volume/trabecular volume (BV/TV) ratio is 29% reduced, trabecular number is 27% reduced, and trabecular spacing is 49% increased in EphA4 knockout femur in comparison to wildtype femur (all $p<0.03$). At femur mid-shaft the bone area is 23% reduced ($p=0.01$).

Table 10. Micro-Computed Tomography. The bone volume/trabecular volume (BV/TV) ratio is 29% reduced, trabecular number is 27% reduced, and trabecular spacing is 49% increased in EphA4 knockout femur in comparison to wildtype femur. At femur mid-shaft the bone area is 23% reduced ($p=0.01$).

Femur Trabecular Parameter	WT (n=6)	KO (n=6)	T-Test	% Difference
Bone Volume/Trab Volume	0.258 ± 0.026	0.185 ± 0.078	0.01	-28.5
Trabecular Number (1/mm)	4.93 ± 0.45	3.590 ± 1.03	0.02	-27.1
Trabecular Thickness (mm)	0.075 ± 0.008	0.075 ± 0.009	0.89	-0.9
Trabecular Spacing (mm)	0.204 ± 0.033	0.305 ± 0.084	0.02	+49.5
Femur Midshaft Parameter	WT (n=6)	KO (n=6)	T-Test	% Difference
Bone Area (mm^2)	1.043 ± 0.129	0.800 ± 0.125	0.01	-23.3
Total Density (mg/cm^3)	891.5 ± 46	864.8 ± 25.9	0.24	-3.00
Cortical Density (mg/cm^3)	1231.8 ± 8.4	1243.1 ± 13.7	0.11	+0.92

d. Serum IGF-1 Measurements.

Since growth is highly influenced by circulating levels of IGF-1, serum levels of IGF-1 were measured in EphA4 knockout (n=6) and wildtype mice (n=5). IGFs in serum are bound to IGFBPs and it is known that IGFBPs produce artifacts in IGF radioimmunoassays (RIA). Therefore, IGFs are separated from IGFBPs by using the Bio-Spin separation. This rapid acid gel filtration protocol has been validated previously. The IGF concentration is determined by a RIA, using recombinant human IGF-I as a tracer and standard, and rabbit polyclonal antiserum as described earlier. The intra-and interassay coefficient of variation for IGF-I assay is less than 10%. Knockout EphA4 mice were found to have a 23% reduction in serum IGF-1 levels in comparison to wildtype EphA4 mice ($p=0.05$) (Figure 24).

Figure 24. Serum circulating IGF-1 levels of EphA4 mutant and wildtype mice. EphA4 knockout mice have a 23% reduction in levels of serum IGF-1 in comparison to wildtype mice ($p = 0.05$).

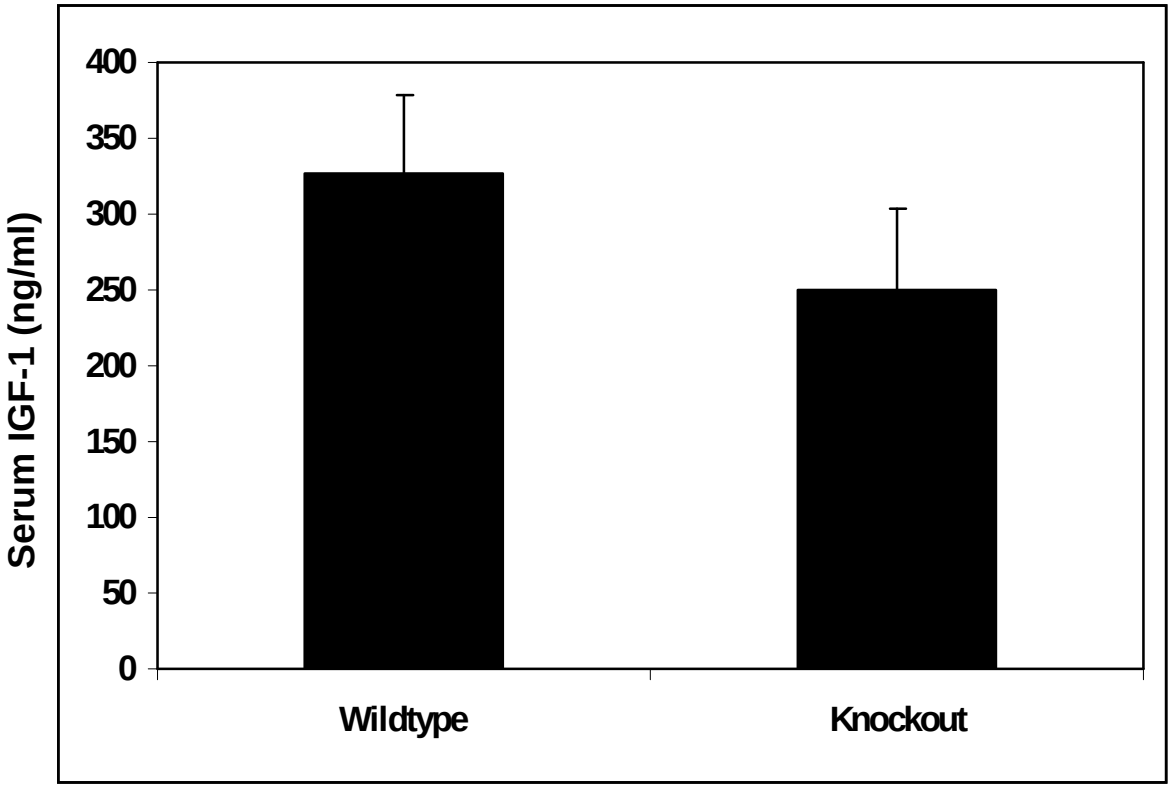

KEY RESEARCH ACCOMPLISHMENTS

- Determined that MRL mouse strains regenerate digit tips more quickly and to a greater extent than DBA, SJL, C57BL/6J, C3H and 129/Sv mouse strains.
- Found that at 1-day post surgery only the MRL and DBA strains have formed an epidermal layer over the dissected digit tip.
- Discovered evidence of blastema formation at day 4 post digit tip dissection in B6 mice.
- Undertook global microarray expression profiling in MRL and DBA regenerating digit tips in RNA isolated from day 4 regenerating digit tips in comparison to control RNA at day 0.
- Identified that the BMP/TGF-beta signaling pathway is likely involved in digit tip regeneration in the MRL and DBA mouse strains.
- Found several interesting candidate genes that are differentially expressed only in MRL regenerating digit tips (Shrm, Mesp2, Fmn2, Net1). These are known to function in embryogenesis and pattern formation and/or are highly expressed in neurons.
- Histology studies were undertaken at time points of 1, 4, 7, 14, and 21 days post dissection. These studies find that by 4-days post dissection wound epithelium has completely covered the tip and beneath this dedifferentiated and proliferating cells are

present. At 7-days post dissection, bone has begun to form and by 21 days the digit tip has nearly completely regenerated.

- Additional microarray expression experiments were undertaken at days 7, 14, 21 and 28 post dissection. These experiments (and previous 4 day experiments) find that the FMN2 gene is differentially expressed in MRL digit tips at days 4 and 7 post dissection.
- FMN2 was found to be highly expressed in the nuclei of osteoblasts by immunohistochemistry.
- FMN2 was found to be increased in RNA expression in Wnt3A treated MCT3T osteoblast cell line, suggesting that FMN2 is in the Wnt signaling pathway.
- Femur and tibia aBMD are significantly reduced ($p<0.05$) at 6, 9, and 12 weeks of age in FMN2 knockout mice.
- Disruption of FMN2 produced a greater deficit in the long bones (37% and 32.5% reduction in femur and tibia BMC respectively, $P<0.01$) compared to lumbar vertebra.
- Femur periosteal circumference is reduced by 5% ($p=0.001$), femur cortical thickness is reduced by 7.3% ($p=0.004$), and femur cortical content is reduced by 12.8% ($p=0.002$) in FMN2 knockout mice.
- Bone volume/trabecular volume (BV/TV) ratio is 30% reduced ($p=0.03$), trabecular number is 5% reduced and trabecular thickness is 14% decreased ($p=0.06$) in the FMN2 knockout femur in comparison to wildtype femur
- MC3T3-E1 osteoblast-like cells expressed FMN2 transcript at 5 to 20 fold higher levels than RAW264.7 osteoclast-like and primary cultures of osteoclast undifferentiated and differentiated osteoclasts.
- Cellular proliferation as measured by BrdU incorporation into newly synthesized DNA was reduced by 37% in osteoblasts derived from FMN2 knockout mice in comparison to wildtype control mice ($p<0.01$).
- Differentiation as measured by ALP activity was found to be reduced by over 20% in knockout FMN2 calvarial osteoblasts ($p<0.01$).
- Mineralized bone nodule formation assays find that knockout FMN2 osteoblasts have 25% reduced bone nodule formation in comparison to wildtype FMN2 osteoblasts ($p = 0.04$).
- Stromal cells (MSC) isolated from femur lacking FMN2 exhibit 55% reduced ALP staining in comparison to wild type FMN2 MSC ($p < 0.001$) .
- WNT treatment of FMN2 wildtype osteoblasts induces a 42% increase in β-catenin protein levels ($p<0.001$) while FMN2 knockout osteoblasts do not show a significant response to WNT treatment
- Normalized TCF-LEF luminosity signals were found to be 20% reduced in FMN2 knockout osteoblasts in response to WNT1 treatment ($p=0.045$).
- Body weight and total body BMD were reduced by 16% and 11% in EphA4 knockout female mice and 11% and 7% in EphA4 knockout male mice respectively at 12 weeks of age.
- At 12 weeks of age, trabecular femur volume was significantly reduced in EphA4 knockout mice. The bone volume/trabecular volume (BV/TV) ratio is 29% reduced, trabecular number is 27% reduced, and trabecular spacing is 49% increased in EphA4 knockout femur in comparison to wildtype femur (all $p<0.03$). At femur mid-shaft the bone area is 23% reduced ($p=0.01$).
- Knockout EphA4 mice were found to have a 23% reduction in serum IGF-1 levels in comparision to wildtype EphA4 mice ($p=0.05$) .

REPORTABLE OUTCOMES

1). Chadwick R.B., Bu L.M., Yu H., Sachdev R., Tan Q.W., Wergedal J.E., Mohan S., and Baylink D.J. Digit Tip Regeneration and Global Gene Expression Profiling in the MRL Super-Healer Mouse. 26th Annual Meeting American Society of Bone and Mineral Research, Seattle, Washington, October 1-5, 2004

2). Chadwick R.B., Bu L.M., Yu H., Hu Y., Sachdev R., Tan Q.W., Wergedal J.E., Mohan S., and Baylink D.J. Digit Tip Regeneration and Differential Expression Profiling in the MRL Super-Healer Mouse. Wound Healing and Regeneration, Chicago, Illinois, May 2005.

3). Chadwick RB, Bu LM, Yu H, Hu Y, Sachdev R, Wergedal JE, Mohan S, Baylink DJ. "Digit Tip Regrowth and Differential Gene Expression Profiling in the MRL Super-Healer Mouse." Wound Repair and Regeneration, Volume 15(2), pages 275-84. (2007).

4). Bu L, Hu Y, Wergedal J, Mohan S and Chadwick RB. Lack of EphA4 Causes Reduction in Body Size, Total Body Bone Mineral Density and Serum IGF-1 Levels in Mice. Journal of Bone and Mineral Metabolism, submitted (2009).

5). Chadwick RB, Bu L, Hu Y, Wergedal J, and Mohan S. Formin-2 Knockout Affects Osteoblasts and Bone Formation in Mice. AJP Endocrinology and Metabolism, submitted (2009).

CONCLUSIONS

1) MRL Regeneration Studies

The salient findings of the MRL regeneration studies are as follows: 1) It provides direct evidence that newborn MRL mice heal digit tips more quickly and regenerate nails to a greater degree than DBA and B6 mice; 2) It provides evidence that the IGF and BMP/TGF pathways are important in digit tip regrowth in all inbred strains of mice tested; 3) It indicates the improved regenerative capabilities of MRL mice may be due to genes implicated in the WNT signaling pathway and morphogenesis.

MRL mice have a unique ability to heal and regenerate multiple cell types, including ear tissue, and heart tissue. In this study, we find that all strains of mice tested have the capability to regenerate digit tips. However, MRL mice can more quickly heal and more completely reform nails of dissected digit tips. The regrowth of digit tips is more complex than simple wound healing of ear punches and cardiac lesions since it involves the regrowth of multiple cell types including bone, cartilage, nervous and epithelial cells. Similar to stem cells, regenerating digit tips require proper patterning of the regenerating cells to direct their cellular fate. Studies undertaken in axolotls have documented the stages in amphibian limb regeneration. In axolotls, the first stage after amputation involves the formation of wound epithelial cells to cover the wound [http://www.uoguelph.ca/zoology /devobio/210labsregen1.html]. After two days, beneath this epithelial layer, cells begin to dedifferentiate and form a blastema. These blastema cells redifferentiate and completely regenerate the amphibian limb within six weeks post amputation. In MRL mice, our histology studies find that the early stages of digit tip regrowth are partially similar to that of axolotls (Figure 4). Within one day of digit tip amputation epithelial cells have formed over the wound in MRL mice. At four days, epithelial cells have completely covered the wound and undifferentiated cells beneath the wound

epithelium begin to proliferate. At 7-days osteoblasts are present and have begun to form bone. At 14-days post dissection the cells beneath the wound epithelium are not as de-differentiated and the bone marrow cavity has begun forming above the third phalange's joint. By 21-days post dissection, the cells have redifferentiated, the nail has begun reforming and the digit tip has almost completely regenerated. It is interesting that when de- and re- differentiation of cells beneath the wound epithelium is occurring is also when the MRL mouse shows the greatest regenerative capacity. This suggests possible links between the enhanced healing capabilities of MRL mice and the molecular causes of de- and re-differentiation of cells.

The NIA15K cDNA library used to create the microarrays in this study was isolated from developing mouse embryos. Thus, many of these genes are expressed primarily in embryonic development and are a unique source for studies of regrowth. In all the strains examined in this study we found that genes involved in the IGF and BMP/TGF pathways are differentially expressed. This is not unexpected since the IGF and BMP/TGF pathways are known to be critical to limb formation, bone induction and fracture repair. Also, previous studies have reported that high levels of TGFB1 mRNA and/or protein are localized in developing cartilage, bone, and skin, and play a role in the growth and differentiation of these tissues. This study confirms the importance of the IGF1 and TGFB/BMP pathways in regrowth and wound healing and the importance of the BMP family of genes in regulating a regenerative response. Genes involved in cell cycle, transcription and growth were also found to be differentially expressed in all the strains (CALM2, NFKB, ANXA2, GATA3, RFPL4, KLF4, TCF14, and ZF110).

In only MRL regenerating digit tips, LRP6, SPARC, CTSL and FMN2 are particularly interesting genes that are differentially expressed. LRP6 and its co-receptor LRP5 are required for WNT/Beta-catenin mediated signal transduction. LRP6 knockout mice exhibit severe developmental abnormalities, including the truncation of the axial skeleton, reduced bone mineral density and limb defects. The Wnt signaling pathway plays important roles in bone cell function and LRP6 and LRP5 are essential for proper gastrulation in developing embryos. SPARC (osteonectin) is a bone-specific phosphoprotein that accounts for the unique properties of bone collagen to undergo calcification. The absence of SPARC in mice gives rise to alterations in the composition of the extracellular matrix that result in osteopenia, and pathological closure of dermal wounds. SPARC regulates the activity of several growth factors including platelet-derived growth factor (PDGF), fibroblast growth factor (FGF), and vascular endothelial growth factor (VEGF). This suggests links between increased expression levels of SPARC in MRL mice and growth factor regulation in regenerating digit tips. Cathepsins are cysteine proteases with essential roles in osteoclast mediated bone matrix degradation. Cathepsin L acts by integrating endothelial progenitor cells into wounds and is required for neovascularization of ischemic tissue. Also, CTSL knockout mice have impaired healing following limb ischemia. Thus, the increased levels of CTSL in MRL regenerating digit tips may lead to increased regenerative capacity by increasing vascularization of wound tissue.

In only MRL regenerating digit tips, the FMN2 gene is another intriguing gene that is differentially expressed. Mutations in a related formin gene, formin-1, lead to developmental defects in limb formation due to a reduction in the number of bony elements in the fore and hind limbs. Formin-1 is thought to act in limb bud polarization through establishment of a SHH/FGF-4 feedback loop. Also, studies in a yeast homologue of formin, forp1, have found that its mutation leads to asymmetric patterns of cell growth. This suggests that formins are critical signaling components of pattern formation and directing cellular fate. Our previous microarray studies of mouse ear punch wound healing found that formin-binding protein 21 is differentially expressed in healing ear tissue. Thus, the formin family of genes is involved in both soft tissue wound healing and digit tip regrowth. This indicates that there are common genetic mechanisms influencing soft tissue wound healing and digit tip regrowth in the MRL super-healer mouse. Members of the formin gene family have been implicated in the WNT signaling pathway. The WNT signaling pathway initiates outgrowth, controls

patterning, and regulates cell differentiation in a number of tissues. Also, bone formation has been shown to be activated by WNT signaling in osteoblast stem cells by promoting osteoblastic differentiation. FMN2 has been reported to be highly expressed in both developing and adult central nervous systems. This is intriguing since denervation of has been shown to eliminate regeneration capabilities in amphibians.

In conclusion, we find that MRL mice show greater regenerative capacities to heal digit tips in comparison to all inbred strains of mice tested. This increased regrowth is seen primarily during the times of greatest growth in mice and during the times of de-differentiation and re-differentiation of cells in the healing and regrowth process. The determination of the molecular causes of de- and re-differentiation of cells during growth and healing have important implications in stem cell research. The capability of neonatal mammals to regenerate is reduced when they reach adulthood. It is thought that this reduced regenerative capacity is due to a reduction in multipotent cells with age. Future studies will focus on determining whether MRL mice retain more of their regenerative capacity than other strains of mice. The further elucidation of the mechanisms by which genes contribute to regrowth and bone formation will likely lead to new targets and eventually treatments for wound healing, regeneration and bone diseases.

2) FMN2 Knockout Mouse Studies

Our studies using mice with disruption of FMN2 and corresponding littermate control mice reveal that lack of FMN2 interferes with development of peak bone mass as shown through DXA, pQCT and micro-CT measurements. Null FMN2 mice also display a 14% reduction in body weight and affect overall growth. However, the effect in bone is greater than body growth since lack of FMN2 produced a greater deficit in the long bones (37% and 32.5% reduction in femur and tibia BMC respectively. Thus, FMN2 has an important role in bone. FMN2 effects bone growth differently in vertebra and long bones. This is consistent with previous genetic studies which found skeletal site specific loci in QTL BMD linkage studies. Also, previous studies of the disruption of other genes in mice found skeletal site specific BMD differences. The skeletal site specific differences seen in FMN2 regulation of BMD and bone volume between long bones, trabecular bone and lumbar vertebra may be due to skeletal site specific differences in FMN2 expression. Alternatively, there may be compensation by other formin family genes in vertebra which act to a lesser extent in long bones.

It is known that peak bone mass varies in different strains of mice. Since FMN2 knockout mice were generated in a mixed background (129 X C57BL/6J), one could question that some of the differences observed between the skeletal phenotype of FMN2 knockout and control mice could be due to genetic background. Because the FMN2 knockoug mice have been backcrossed for many generations in 129 background and because we used corresponding littermate wildtype mice as controls, it is unlikely that the observed phenotypic between the knockout and control mice are due to differences in the genetic background. Formins are intracellular proteins that regulate actin assembly. Thus, it is likely that defective actin assembly in FMN2 null cells give rise to the observed bone phenotypes. The reduction in BMC and BMD shown from lack of FMN2 may be due to defective actin assembly in osteoblasts or osteoclasts leading to decreased bone formation or increased bone resorption. However, the immunohistochemistry and in vitro expression studies find much higher expression of FMN2 in osteoblast cells than in osteoclast cells. Also, the stromal cell (MSC) differentiation and osteoblast proliferation studies suggest that FMN2 acts by primarily influencing bone formation by osteoblasts.

Our in vitro studies show that knockout of FMN2 effects the WNT signaling pathway, an important pathway in bone regulation. This is not entirely surprising since previous studies have shown that other members of the formin gene family are involved in WNT signaling. For example, the formin DIA1 has been shown to directly interact with APC which is an important member of the

canonical WNT signal transduction pathway. Also, bone formation has also been shown to be activated by WNT signaling in osteoblast stem cells by promoting osteoblast differentiation. Activation of the WNT pathway results in dephosphorylation and nuclear translocation of beta-catenin, which interacts with T-cell factor lymphoid-enhancing factor (TCF-LEF) transcription factors to control the expression of downstream target genes. Beta-catenin interacts with the TCF-LEF, leading to the transcription and up-regulation of downstream target genes. One plausible explanation for the observed bone phenotypes in FMN2 null mice is that FMN2 is a downstream transcriptional target of the TCF-LEF transcription factor or a potential member of the WNT signal transduction pathway. The in vitro expression studies finding that FMN2 is increased in expression in WNT treated MC3T3-E1 osteoblast-like cells suggest that FMN2 may be a downstream transcriptional target of TCF-LEF. However, FMN2 shows high homology to the forming family member DIA1 which directly interacts with APC. Thus, FMN2 may potentially interact with APC or other WNT signal transducers. There is evidence that APC is involved in the organization of cytoskeletal networks and interacts with microtubules and accumulates at their plus ends in membrane protrusions. It has also been reported that APC is associated with the cell membrane in an actin-dependent manner. Lack of FMN2 may influence this association. Future studies are needed to verify this mechanism of FMN2 action in osteoblasts.

3) EphA4 Knockout Mouse Studies

These studies find that the absence of EphA4 influences overall body size, total body BMD, femur trabecular bone volume and serum IGF-1 levels. The EphA4 receptor is widely expressed in many cell types including bone, brain, bone marrow, thymus, heart and muscle tissues (http://www.genecards.org/cgi-bin/carddisp.plgene=EPHA4). Also, the EphA4 receptor binds the ephrin-A1, ephrin –A2, ephrin-A3, ephrin-A4, ephrin-A5, ephrin-B2, and ephrin-B3 ligands which are also widely expressed in many different tissues. Normal bone expresses ephrin receptors A1, A4 and B2. The EphrinB2 ligand which interacts with the EphA4 receptor is expressed by osteoclasts in the absence of any detectable Ephrin receptor, whereas osteoblasts express both ephrinB2 ligand and the EphB4 receptor. Due to the broad expression in multiple tissues of both the EphA4 receptor and its many ligands, it is not surprising that the lack of EphA4 effects overall growth in multiple tissues, including bone.

EphA4 mutant mice are significantly smaller in size and have reduced total BMD. Thus, EphA4 influences overall growth and that the phenotype of reduced total BMD of EphA4 mutant mice appears to be due to reduced body and bone size. However, the 29% reduction in femur trabecular bone volume indicates that EphA4 influences trabecular bone formation or remodeling. Since trabecular bone turns over more rapidly than cortical bone, lack of EphA4 appears to influence trabecular bone to a greater extent than cortical bone. Alternatively, cortical bone may have actively expressed ephrins in cortical bone that are expressed to a lesser extent in trabecular bone.

The mechanisms of reduced serum IGF1 levels in EphA4 knockout mice can only be speculated at this point. Growth requires the coordinated action of growth hormone (GH) and IGF-1. The secretion of GH from the pituitary into circulation stimulates the production of IGF-1 which in turn stimulates the proliferation of chondrocytes, formation of cartilage and subsequently ossification and bone growth. EphA4 is enriched in the developing and adult mouse hippocampus and mutations of EphA4 cause neuronal and structural alterations in the hippocampus. The pituitary gland controls the release of GH and it lies immediately beneath the hypothalamus. Thus, one could hypothesize that reduced levels of serum IGF-1 in EphA4 knockout mice may be due to alterations of pituitary and hypothalamic structures that alter the release of GH from the pituitary gland. However, further studies are needed to determine the contribution of IGF-1 in mediating the effects of EphA4 on growth and development.

REFERENCES

1. Muller TL, Ngo-Muller V, Reginelli A, Taylor G, Anderson R, Muneoka K. Regeneration in higher vertebrates: limb buds and digit tips. Semin Cell Dev Biol 1999; 10(4):405-413.
2. Brockes JP. Amphibian limb regeneration: rebuilding a complex structure. Science, 1997; 276(5309): 81-87.
3. Endo T, Bryant SV, Gardiner DM. A stepwise model system for limb regeneration. Developmental Biology 2004; 270(1): 135-45.
4. Illingworth CM. Trapped fingers and amputated finger tips in children. J Pediatr Surg. 1974;9(6):853-58.
5. Borgens RB. Mice regrow the tips of their foretoes. Science. 1982;217(4561):747-50.
6. Neufeld DA, Zhao W. Phalangeal regrowth in rodents: postamputational bone regrowth depends upon the level of amputation. Prog Clin Biol Res. 1993;383A:243-52.
7. Zhao W, Neufeld DA. Bone regrowth in young mice stimulated by nail organ. J Exp Zool. 1995; 271(2):155-9.
8. Reginelli AD, Wang YQ, Sassoon D, Muneoka K. Digit tip regeneration correlates with regions of Msx1 (Hox 7) expression in fetal and newborn mice. Development. 1995;121(4):1065-76.
9. Goss RJ, Grimes LN. Epidermal downgrowths in regenerating rabbit ear holes. J Morphol, 1975; 146(4):533-542.
10. Joseph J, Dyson M. Effect of anabolic androgens on tissue replacement in the ear of the rabbit. Nature 1966; 211(45): 193-194.
11. Li X, Gu W, Masinde G, Hamilton-Ulland M, Xu S, Mohan S, Baylink DJ. Genetic control of the rate of wound healing in mice. Heredity 2001; 86(Pt 6): 668-674.
12. Clark LD, Clark RK, Heber-Katz E. A new murine model for mammalian wound repair and regeneration. Clin Immunol Immunopathol, 1998; 88(1):35-45.
13. Leferovich JM, Bedelbaeva K, Samulewicz S, Zhang XM, Zwas D, Lankford EB, Heber-Katz E. Heart regeneration in adult MRL mice. Proc Natl Acad Sci U S A, 2001; 98(17):9830-9835.
14. Tanaka TS, Jaradat SA, Lim MK, Kargul GJ, Wang X, Grahovac MJ, Pantano S, Sano Y, Piao Y, Nagaraja R, Doi H, Wood WH 3rd, Becker KG, Ko MS. Genome-wide expression profiling of mid-gestation placenta and embryo using a 15,000 mouse developmental cDNA microarray. Proc Natl Acad Sci U S A, 2000; 97(16): 9127-9132.
15. Shih JH, Michalowska AM, Dobbin K, Ye Y, Qiu TH, Green JE. Effects of pooling mRNA in microarray class comparisons. Bioinformatics. 2004; 20(18):3318-25.
16. Draghici S, Khatri P, Bhavsar P, Shah A, Krawetz S, Tainsky MA. Onto-Tools, The toolkit of the modern biologist: Onto-Express, Onto-Compare, Onto-Design and Onto-Translate. Nucleic Acids Research 2003; 31(13):3775-81.
17. Draghici S, Khatri P, Shah A, Tainsky MA. Assessing the functional bias of commercial microarrays using the Onto-Compare database. BioTechniques, Microarrays and Cancer: Research and Applications, 2003.
18. Draghici S, Khatri P, Martins RP, Ostermeier GC, Krawetz SA. Global functional profiling of gene expression. Genomics 81(2):98-104, Feb 2003.
19. Zuniga A, Haramis AP, McMahon AP, Zeller R. Signal relay by BMP antagonism controls the SHH/FGF4 feedback loop in vertebrate limb buds. Nature. 1999 Oct 7;401(6753):598-602.

20. Cho TJ, Gerstenfeld LC, Einhorn TA. Differential temporal expression of members of the transforming growth factor beta superfamily during murine fracture healing. J Bone Miner Res. 2002 Mar;17(3):513-20.
21. Dickinson ME, Kobrin MS, Silan CM, Kingsley DM, Justice MJ, Miller DA, Ceci JD, Lock LF, Lee A, Buchberg AM, Siracusa, LD, Lyons KM, Derync R, Hogan BLM, Copeland NG, Jenkins NA. Chromosomal localization of seven members of the murine TGF-beta superfamily suggests close linkage to several morphogenetic mutant loci. Genomics. 1990 6(3):505-20.
22. Han M, Yang X, Farrington JE, Muneoka K. Digit regeneration is regulated by Msx1 and BMP4 in fetal mice. Development. 2003 Nov;130(21):5123-32.
23. Tamai K, Semenov M, Kato Y, Spokony R, Liu C, Katsuyama Y, Hess F, Saint-Jeannet JP, He X. LDL-receptor-related proteins in Wnt signal transduction. Nature 407: 530-535, 2000.
24. Pinson KI, Brennan J, Monkley S, Avery BJ, Skarnes WC. An LDL-receptor-related protein mediates Wnt signalling in mice. Nature 407: 535-538, 2000.
25. Holmen SL, Giambernardi TA, Zylstra CR, Buckner-Berghuis BD, Resau JH, Hess JF, Glatt V, Bouxsein ML, Ai M, Warman ML, Williams BO. Decreased BMD and limb deformities in mice carrying mutations in both Lrp5 and Lrp6. J Bone Miner Res. 2004;19(12):2033-40.
26. Kelly OG, Pinson KI, Skarnes WC. The Wnt co-receptors Lrp5 and Lrp6 are essential for gastrulation in mice. Development. 2004;131(12):2803-15.
27. Termine JD, Kleinman HK, Whitson SW, Conn KM, McGarvey ML, Martin GR. Osteonectin, a bone-specific protein linking mineral to collagen. Cell. 2001; 26: 99-105.
28. Puolakkainen PA, Bradshaw AD, Brekken RA, Reed MJ, Kyriakides T, Funk SE, Gooden MD, Vernon RB, Wight TN, Bornstein P, Sage EH. SPARC-thrombospondin-2-double-null Mice Exhibit Enhanced Cutaneous Wound Healing and Increased Fibrovascular Invasion of Subcutaneous Polyvinyl Alcohol Sponges. J. Histochem. Cytochem. 2005; 53(5): 571 - 581.
29. Urbich C, Heeschen C, Aicher A, Sasaki K, Bruhl T, Farhadi MR, Vajkoczy P, Hofmann WK, Peters C, Pennacchio LA, Abolmaali ND, Chavakis E, Reinheckel T, Zeiher AM, Dimmeler S. Cathepsin L is required for endothelial progenitor cell-induced neovascularization. Nature Med. 2005; 11: 206-213.
30. Zeller R, Haramis AG, Zuniga A, McGuigan C, Dono R, Davidson G, Chabanis S, Gibson T. Formin defines a large family of morphoregulatory genes and functions in establishment of the polarising region. Cell Tissue Res. 1999; 296(1):85-93.
31. Leader B, Lim H, Carabatsos MJ, Harrington A, Ecsedy J, Pellman D, Maas R, Leder P. Formin-2, polyploidy, hypofertility and positioning of the meiotic spindle in mouse oocytes. Nat Cell Biol. 2002;4(12):921-8.
32. Sawin KE. Cell polarity: following formin function. Curr Biol. 2002; 12(1):6-8.
33. Li X, Mohan S, Gu W, Baylink DJ. Analysis of gene expression in the wound repair/regeneration process. Mamm Genome. 2001; 12(1):52-9.
34. Habas R, Kato Y, He X. WNT/Frizzled activation of Rho regulates vertebrate gastrulation and requires a novel Formin homology protein Daam1. Cell. 2000; 107(7):843-54.
35. Church VL, Francis-West P. WNT signalling during limb development. Int. J. Dev. Biol. 2002; 46: 927-936.
36. Bain G, Muller T, Wang X, Papkoff, J. Activated beta-catenin induces osteoblast differentiation of C3H10T1/2 cells and participates in BMP2 mediated signal transduction. Biochem. Biophys. Res. Commun. 2003; 301: 84-91.
37. Leader B, Leder P. Formin-2, a novel formin homology protein of the cappuccino subfamily, is highly expressed in the developing and adult central nervous system. Mech Dev. 2000; 93(1-2):221-31.

38. Mullen LM, Bryant SV, Torok MA, Blumberg B, Gardiner DM. Nerve dependency of regeneration: the role of Distal-less and FGF signaling in amphibian limb regeneration. Development. 1996; 122(11):3487-97.
39. Bryant SV, Endo T, Gardiner DM. Vertebrate limb regeneration and the origin of limb stem cells. Int J Dev Biol. 2002; 46(7):887-96.
40. Evangelista M, Zigmond S, Boone C. "Formins: signaling effectors for assembly and polarization of actin filaments." J Cell Sci. 2003:116(13):2603-11.
41. Pruyne D, Evangelista M, Yang C, Bi E, Zigmond S, Bretscher A, Boone C. Role of formins in actin assembly: nucleation and barbed-end association. Science. 2002:297:612-615
42. Wallar BJ, Alberts AS. The formins: active scaffolds that remodel the cytoskeleton. Trends Cell Biol. 2003:13:435-446
43. Watanabe N, Higashida C. Formins: processive cappers of growing actin filaments. Exp. Cell Res. 2004:301:16-22
44. Sawin KE. Cell polarity: following formin function. Curr Biol. 2002:12(1):6-8
45. Zeller R, Haramis AG, Zuniga A, McGuigan C, Dono R, Davidson G, Chabanis S, Gibson T. Formin defines a large family of morphoregulatory genes and functions in establishment of the polarising region. Cell Tissue Res. 1999:296(1):85-93
46. Campbell JJ, Blain EJ, Chowdhury TT, Knight MM. "Loading alters actin dynamics and up-regulates cofilin gene expression in chondrocytes." Biochem Biophys Res Commun. 2007:361(2):329-34
47. Han Y, Cowin SC, Schaffler MB, Weinbaum S. "Mechanotransduction and strain amplification in osteocyte cell processes." Proc Natl Acad Sci U S A. 2004:101(47):16689-94
48. Lau KH, Kapur S, Kesavan C, Baylink DJ. Up-regulation of the WNT, estrogen receptor, insulin-like growth factor-I, and bone morphogenetic protein pathways in C57BL/6J osteoblasts as opposed to C3H/HeJ osteoblasts in part contributes to the differential anabolic response to fluid shear. J Biol Chem. 2006:281(14):9576-88
49. Zigmond SH. Formin-induced nucleation of actin filaments. Curr. Opin. Cell Biol. 2004:16:99-105
50. Woychik RP, Maas RL, Zeller R, Vogt TF, Leder P "'Formins:' proteins deduced from the alternative transcripts of the limb-deformity gene." Nature 1990:346: 850-853
51. Chadwick RB, Bu L, Yu H, Hu Y, Wergedal JE, Mohan S, Baylink DJ. Digit tip regrowth and differential gene expression in MRL/Mpj, DBA/2, and C57BL/6 mice. Wound Repair Regen. 2007:15(2):275-84
52. Leader B, Leder P. Formin-2, a novel formin homology protein of the cappuccino subfamily, is highly expressed in the developing and adult central nervous system. Mech. Dev. 2000:93: 221-231
53. Leader B, Lim H, Carabatsos MJ, Harrington A, Ecsedy J, Pellman D, Maas R, Leder P. Formin-2, polyploidy, hypofertility and positioning of the meiotic spindle in mouse oocytes. Nature Cell Biol. 2002:4: 921-928
54. Miyakoshi N, Richman C, Kasukawa Y, Linkhart TA, Baylink DJ, Mohan S. Evidence that IGF-binding protein-5 functions as a growth factor. J Clin Invest. 2001:107(1):73-81
55. Dimai HP, Linkhart TA, Linkhart SG, Donahue LR, Beamer WG, Rosen CJ, Farley JR, Baylink DJ. Alkaline phosphatase levels and osteoprogenitor cell numbers suggest bone formation may contribute to peak bone density differences between two inbred strains of mice. Bone. 1998:22:211–216
56. Mohan S, Kapoor A, Singgih A, Zhang Z, Taylor T, Yu H, Chadwick RB, Chung YS, Donahue LR, Rosen C, Crawford GC, Wergedal J, Baylink DJ. Spontaneous fractures in the mouse mutant sfx are caused by deletion of the gulonolactone oxidase gene, causing vitamin C deficiency. J Bone Miner Res. 2005: 20(9): 1597-610

57. Bouxsein ML, Uchiyama T, Rosen CJ, Shultz KL, Donahue LR, Turner CH, Sen S, Churchill GA, Müller R, Beamer WG. Mapping quantitative trait loci for vertebral trabecular bone volume fraction and microarchitecture in mice. J Bone Miner Res. 2004: 19(4):587-99.
58. Beamer WG, Shultz KL, Donahue LR, Churchill GA, Sen S, Wergedal JR, Baylink DJ, Rosen CJ. Quantitative trait loci for femoral and lumbar vertebral bone mineral density in C57BL/6J and C3H/HeJ inbred strains of mice. J Bone Miner Res. 2001:16(7):1195-206
59. Govoni KE, Baylink DJ, Chen J, Mohan S. Disruption of four-and-a-half LIM 2 decreases bone mineral content and bone mineral density in femur and tibia bones of female mice. Calcif Tissue Int. 2006:79(2):112-7.
60. Windahl SH, Vidal O, Andersson G, Gustafsson JA, Ohlsson C. Increased cortical bone mineral content but unchanged trabecular bone mineral density in female ERbeta(-/-) mice. J Clin Invest. 1999: 104(7):895-901.
61. Habas R, Kato Y, He X. WNT/Frizzled activation of Rho regulates vertebrate gastrulation and requires a novel Formin homology protein Daam1. Cell. 2000:107(7):843-54
62. Watanabe N, Kato T, Fujita A, Ishizaki T, Narumiya S. Cooperation between mDia1 and ROCK in Rho-induced actin reorganization. Nat. Cell Biol. 1999:1, 136-143
63. Nakano K, Takaishi K, Kodama A, Mammoto A, Shiozaki, H, Monden, M. Takai, Y. Distinct actions and cooperative roles of ROCK and mDia in Rho small G protein-induced reorganization of the actin cytoskeleton in Madin-Darby canine kidney cells. Mol. Biol. Cell 1999:10,2481 -2491
64. Akiyama T, Kawasaki Y. Wnt signalling and the actin cytoskeleton. Oncogene. 2006; 25(57):7538-44.
65. Himanen JP, Nikolov DB (2003) Eph receptors and ephrins, Int. J. Biochem. Cell Biol. 35: 130–134
66. Wang Z, Cohen K, Shao Y, Mole P, Dombkowski D, Scadden DT. Ephrin receptor, EphB4, regulates ES cell differentiation of primitive mammalian hemangioblasts, blood, cardiomyocytes, and blood vessels (2004) Blood 103:100–109
67. Batlle E, Henderson JT, Beghtel H, van den Born MM, Sancho E, Huls G, Meeldijk J, Robertson J, van de Wetering M, Pawson T, Clevers H (2002) β-catenin and TCF mediate cell positioning in the intestinal epithelium by controlling the expression of EphB/ephrinB, Cell 111: 251–263
68. Compagni A, Logan M, Klein R, Adams RH (2003) Control of skeletal patterning by ephrinB1-EphB interactions. .Dev Cell. 5(2):217-30
69. Twigg SR, Kan R, Babbs C, Bochukova EG, Robertson SP, Wall SA, Morriss-Kay GM, Wilkie AO (2004) Mutations of ephrin-B1 (EFNB1), a marker of tissue boundary formation, cause craniofrontonasal syndrome. Proc Natl Acad Sci U S A. 8;101(23):8652-7
70. Davy A, Aubin J, Soriano P (2004) Ephrin-B1 forward and reverse signaling are required during mouse development, Genes Dev. 18: 572–583
71. Xing W, Baylink D, Kesavan C, Hu Y, Kapoor S, Chadwick RB, Mohan S (2005) Global gene expression analysis in the bones reveals involvement of several novel genes and pathways in mediating an anabolic response of mechanical loading in mice. J Cell Biochem. 96(5):1049-60
72. Zhao C, Irie N, Takada Y, Shimoda K, Miyamoto T, Nishiwaki T, Suda T, Matsuo K (2006) Bidirectional ephrinB2-EphB4 signaling controls bone homeostasis. Cell Metab. 4:111–121
73. Goldshmit Y, Galea MP, Wise G, Bartlett PF, Turnley AM (2004) Axonal regeneration and lack of astrocytic gliosis in EphA4-deficient mice. J Neurosci. 24(45):10064-73
74. Mohan, S. and D.J. Baylink (1995) Development of a simple valid method for the complete removal of insulin-like growth factor (IGF)-binding proteins from IGFs in human serum and

other biological fluids: comparison with acid-ethanol treatment and C18 Sep-Pak separation. J Clin Endocrinol Metab, 80(2): p. 637-47.

75. Mohan S, Bautista CM, Herring SJ, Linkhart TA, Baylink DJ (1990) Development of valid methods to measure insulin-like growth factors-I and -II in bone cell-conditioned medium. Endocrinology 126(5): p. 2534-42.
76. Hafner C, Schmitz G, Meyer S, Bataille F, Hau P, Langmann T, Dietmaier W, Landthaler M, Vogt T. Differential gene expression of Eph receptors and ephrins in benign human tissues and cancers. Clin Chem. (2004);50(3):490-9
77. Mundy GR, Elefteriou F (2006) Boning up on Ephrin Signaling. Cell, 126(3):441-443
78. Varelias A, Koblar SA, Cowled PA, Carter CD, Clayer M (2002) Human osteosarcoma expresses specific ephrin profiles, implications for tumorigenicity and prognosis. Cancer, 95(4):862-869
79. Murai KK, Nguyen LN, Irie F, Yamaguchi Y, Pasquale EB (2003) Control of hippocampal dendritic spine morphology through ephrin-A3/EphA4 signaling. Nat Neurosci 6:153–160
80. Yue Y, Chen ZY, Gale NW, Blair-Flynn J, Hu TJ, Yue X, Cooper M, Crockett DP, Yancopoulos GD, Tessarollo L, Zhou R (2002) Mistargeting hippocampal axons by expression of a truncated Eph receptor. Proc Natl Acad Sci U S A. 99(16):10777-82
81. Dottori M, Hartley L, Galea M, Paxinos G, Polizzotto M, Kilpatrick T, Bartlett PF, Murphy M, Kontgen F, Boyd AW (1998) EphA4 (Sek1) receptor tyrosine kinase is required for the development of the corticospinal tract. Proc. Nat. Acad. Sci. 95:13248-13253
82. Gilardi-Hebenstreit P, Nieto MA, Frain M, Mattéi MG, Chestier A, Wilkinson DG, Charnay P (1992) An Eph-related receptor protein tyrosine kinase gene segmentally expressed in the developing mouse hindbrain. Oncogene 7: 2499-2506
83. Kullander K, Butt SJ, Lebret JM, Lundfald L, Restrepo CE, Rydström A, Klein R, Kiehn O (2003) Role of EphA4 and ephrinB3 in local neuronal circuits that control walking. Science 299: 1889-1892

Project 2: Sensitizer Screening to Enhance Detection of ENU-Induced Mutant Phenotypes

INTRODUCTION

The goal of the Sub Project 2 was to identify and characterize novel genes or to elucidate the function of known genes that play a key role in the musculoskeletal and soft tissues using a phenotype driven mutagenesis approach. The ultimate aim of this project was to provide a fundamental molecular foundation for future therapies and diagnostic risk assessments for the musculoskeletal system in battlefield injuries.

Osteoporosis is a systemic skeletal disease characterized by low bone mass and micro architectural deterioration of bone tissue. Quantitatively, the most important determinant of bone mass is hereditary, which is exemplified in the genetic epidemiological analyses related to recurrence risk and twin studies on bone mineral density (BMD) and bone turnover. Several studies have estimated the heritability for BMD to be as high as 80%, suggesting that the majority of variance in peak BMD values can be explained by genetic factors. These genetic predispositions can result in differences between individuals on how they attain peak BMD early in life or as differences in the rate of bone loss later in life. BMD is a polygenetic trait with multiple genes believed to be involved in regulating bone density. Genome-wide linkage screens for genes underlying BMD variability, conducted in humans and mice, have identified important regions on several chromosomes (described as QTLs) that regulate BMD and other traits. We have utilized a complementary phenotype driven N-ethyl-N-nitrosourea (ENU) mutagenesis screen to identify genes that regulate skeletal tissues. The chemical mutagen ENU was proven to be most effective in generating mutations in mice. The ENU approach has produced variants in several disease models that mimic phenotypes commonly seen in humans in the clinical setting. An added advantage of this approach is that any locus identified in the ENU study would presumably represent one gene in contrast to QTLs identified by linkage studies, which is likely to represent multiple genes at each locus.

In Sub Project 2, we proposed to employ a phenotype driven screen in mouse models in which genes that have been previously implicated to play a critical role in the development and maintenance of musculoskeletal tissues have been totally or partially disabled. By using mice with mutation in a gene known to affect musculoskeletal phenotypes, we propose to sensitize a classical ENU mutagenesis screening system, and thereby increase the recovery of mutants by discovering genes that otherwise have subtle effects on the musculoskeletal phenotype and are hard to detect. The principle for increased sensitivity of recognition is synergism between the unknown ENU mutation and the known knock out gene. This approach has been successfully demonstrated in drosophila to uncover genes in a Notch signaling pathway. For example, mutations in a Notch signaling pathway have been used to sensitize mutations in gene regulating many unknown components in bristle development in Drosophila. Application of the sensitized screen in the mouse model is promising.

One of the important requirements for the success of our approach involving a sensitizer screen to identify novel mouse mutants for musculoskeletal phenotypes relates to which knockout mouse models are selected for ENU mutagenesis screens. In this regard, it is now widely accepted that IGF-I and TGF β are two critical regulatory molecules that regulate growth and development of musculoskeletal tissues and that deficiencies in these two growth factors contribute to impaired growth and maintenance. Furthermore, IGF-I and TGF β have been

implicated in mediating the effects of many systemic and local factors that regulate the musculoskeletal system. Therefore, we identified mouse models deficient in molecules involved in these two pathways. We used these mouse models to screen for musculoskeletal phenotypes based on the hypothesis that ENU-induced mutation will exhibit a greater effect on the musculoskeletal phenotype under reduced dosage of IGF-I and TGF-β.

BODY

2.2 OVERVIEW OF SPECIFIC OBJECTIVES

The typical whole genome mutagenesis screen involves treating the male mice with ENU and breeding them to wild type females. The offspring are screened through a series of tests to identify the individual phenotypic deviant (a term used for extreme-scoring) mice, which is most likely to bear a large effect Mendelian mutation. The phenotypic deviant mouse, which is often defined as 2-3 SD units from non-mutagenized control mean, are backcrossed with wild type mice to determine whether the abnormality segregates bimodally in their offspring with the expected 1:1 or 1:3 Mendelian ratios. In the sensitized ENU screen, the ENU mutations are created in mouse strains in which genes that have been previously implicated to play a critical role in the development and maintenance of musculoskeletal tissues have been mutated or knocked-out (KO). The presence of initial (or targeted) mutation renders the screening system highly sensitive to small changes that would be too small to be detected in an otherwise wild type (WT) background. The genes identified in the 'sensitized screen' are often modifier genes; their effects are subtle and hard to detect in commonly employed genetic screens. A similar approach has been used in *Drosophila* to identify novel mutant phenotypes. For example, mutations in a Notch (a receptor for cell–cell interaction mechanism in many metazoan developing tissues) signaling pathway have been used to sensitize mutations in genes regulating many unknown components in bristle development in *Drosophila* (2-4). More recently, the sensitized screens have been applied to mouse models with successful identification of mutants with diabetes and behavioral phenotypes.

To accomplish the sensitized screen we utilized two mutant mouse models with deficiencies in the growth hormone (GH) and transforming growth factor-beta (TGF-β) pathways, (5,6) both of which are critical for the normal development and maintenance of musculoskeletal tissues. To study genes that interact with the GH pathway, we used a 'little' mouse strain that has a naturally occurring mutation in growth hormone releasing hormone receptor (*Ghrhr*). The *Ghrhr* mutant mouse is a spontaneous dwarf mouse strain with an autosomal recessive GH deficiency caused by a missense mutation (D60→G) in the extracellular domain of the *Ghrhr* that impairs the ability of the receptor to bind to *Ghrh*. Mice that are homozygous for the missense mutation ($Ghrhr^{lit/lit}$) have reduced GH secretion, impaired GH–IGF-I axis, and a severe deficiency in bone mass and size.

The second mouse model that we employed in the sensitized screen lacks mothers against decapentaplegic homolog 2 (*Smad2*), signal transducer for TGF-β ( ). The $Smad2^{-/-}$ mice are lethal, but the $Smad2^{+/-}$ mice exhibit normal growth. It is now fairly well established that TGF-β, like GH, plays a critical role in both bone development and the pathogenesis of bone loss. The biological effects of TGF-β in osteoblasts are known to be mediated by phosphorylation of

Smad2/3, which associates with *Smad4* to cause transcriptional activation of genes in osteoblasts and other cell types. Furthermore, *Smad2* has also been shown to be involved in mediating the effects of activins, which are also known to regulate osteoblasts. Thus, inactivation of *Smad2* will disrupt the actions of various forms of TGF-β and also activins.

After a mutant strain a with musculoskeletal phenotype was identified in the sensitized screen the second step was to establish that the mutation is stable and inheritable. To achieve that we proposed to backcross each phenotypic deviant with wild type B6 mice as well as $Ghrhr^{lit/+}$ or $Smad2^{+/-}$ mice. Our major interest was identifying the modifiers of GH and TGF-β signaling pathways. Thus we anticipated mutant lines to show co-inheritance of a phenotype with the disrupted *Ghrhr* or *Smad2* gene. However, our screen design also had a probability for finding mutations in wild type animals. This probability is dependent upon the penetrance of the phenotype, genetic background of the mouse strains, and the number of animals screened. The scope of this project was limited only to identifying a mutant strain and confirming them in backcross. In future studies, we proposed to perform preliminary mapping of the mutant locus, which is achieved by standard quantitative trait loci (QTL) mapping techniques. In addition, we also proposed to determine the consequences of mutation on gene product and its functions in backcrossed progeny.

Following the above overall described strategy, we proposed two Specific Objectives during the entire grant periods, the first Specific Objective involved screening of mutant mice and second Specific Objective involved confirming the mutant strains in the backcross. During grant period 2003-2005, our aims were to procure $Ghrhr^{lit/+}$ or $Smad2^{+/-}$ mice, breed them in-house and maintain live colonies, develop genotyping methods to identify gene mutations and/or copy numbers, identify various musculoskeletal phenotypes, and optimize the screening procedure to increase the feasibility of identifying mutant mice. Since C57Bl/6J (B6) strain was the background strain in both mutant types selected in this screen, we used B6 mice for wild type breeding and backcross. We utilized a systematic and detailed screening procedure described previously for identifying phenotypes related to bone mass, bone turnover, bone structural properties, and addressed issues related to reliability of screening procedures. Bone mineral density (BMD) measurement is the most common phenotypic traits used in studies evaluating heritability or polymorphic gene markers of osteoporosis because osteoporosis is defined in individual patients by low bone density. However, several other factors also contribute to bone strength and determine fracture risk, including: bone size, shape, architecture, tissue quality, age, body weight, and muscle strength. Therefore, we have used multiple skeletal, and some extra skeletal traits to assess the skeletal status of ENU mutagenized progeny.

We have compiled the final report in two sections related to the specific objectives proposed grant period 2003-2005 for Sub Project 2 and during 2005-2009 no-cost extension period. During the 2003-2005 grant periods, we screened mice, performed extensive characterization of phenotypes, and backcrossed several mutant mice. During no-cost extension periods (2006-2008) we performed extensive characterization of one of the mutant strain, mapped the chromosomal location of the mutation, identified potential candidate genes, and initiated functional study to study function of a candidate gene.

2.3 SPECIFIC OBJECTIVES FOR GRANT PERIODS 2003-2005

Our goal of this sub project was to use a novel approach, namely sensitizer screening, to increase the power of ENU mutagenesis screens such that novel phenotypes can be identified with the new approach that are not feasible with the traditional approach. To this end, we identified the mouse mutants with musculoskeletal phenotypes in the F1 progeny of ENU treated male mice mated with IGF-I deficient *lit/lit* and TGF β deficient Smad2 knockout female mice or their respective wild type female mice.

To achieve the above technical objective, we followed three Specific Objectives during the entire study period.

a) Establish breeding colonies for *lit/lit* and Smad 2 knockout mice (We currently have *lit/lit* mice. Breeding pairs of Smad2 knockout mice were obtained from our academic collaborator). Generate homozygous and heterozygous mutant mice for production of normal data for our screens for musculoskeletal phenotypes.
b) Breed knockout females with wild type ENU treated males to generate 150 F1 progeny for each *lit/lit* and Smad2 mutant. Breed wild type females with ENU treated males to produce 150 F1 control progeny.
c) Perform musculoskeletal screens at 10 weeks of age in the F1 progeny to measure bone mineral content, bone density, bone size, muscle size and fat content using PIXImus and pQCT instruments. Perform biochemical measurements of bone turnover in the serum samples.

One Specific Objective was proposed for final 12 months of this study.

d) Begin to confirm the mutant phenotypes by backcrossing the mutant mice with *lit/lit* or Smad2 knockout mice, as appropriate.

2.4 SPECIFIC OBJECTIVES FOR NO-COST EXTENSION PERIOD 2005-2009

During the no-cost extension period no additional Specific Objectives were proposed. However, during this period we continued breeding of several phenotypic deviants. The phenotypic deviants were backcrossed several generations to determine if there was any significant change in phenotype as genetic background became more and more homogeneous. We utilized the progeny produced in these backcrosses to further characterize the skeletal phenotype in mutant mice. This breeding regiman incurred significant per diem expenses during no-cost extension period. Finally, sperms from the mutant strains were cryopreserved and stored at The Jackson Laboratry, Maine.

2.5 PROGRESS FOR GRANT PERIOD 2003-2005

During the grant period 2003-2005 we acquired the $Smad2^{+/-}$ mice from our collaborator Dr. Michael Weinstein, Molecular Genetics Division, Ohio State University and bred these mice in-house to maintain a viable colony for screening. The $Ghrhr^{lit/lit}$ mice were obtained from The Jackson Laboratory, Maine and bred in-house to produce $Ghrhr^{lit/+}$ for screening purpose. The optimization of ENU injections for maximum recovery of F1 progeny and standardization of the screening procedures has been described by Srivastava et al (Bone, 2003). Our results on injection schedule, time of

recovery, breeding procedures, and screening of F1 progeny has been described by Srivastava et al (Bone, 2008).

We used two mouse models from the sensitized screen. The first model involves mice carrying a mutation in growth hormone releasing hormone receptor (*Ghrhr*$^{lit/lit}$, mutation is denoted as '*lit*' allele) resulting in GH deficiency, low IGF-I expression, and reduced growth. The second mouse model lacked *smad2*, signal transducer for TGF-beta, an important bone growth factor. The *smad2*$^{-/-}$ mice are lethal, but *smad2*$^{-/+}$ mice exhibit normal growth. Designs of these sensitized screens have been described in **Figure-1**.

We successfully completed all the technical objectives in this reporting period. The highlight of the progress was identification of a mutant mouse, ID 14104, in the *Ghrhr*$^{lit+}$ screen. The 14104 mutant phenotype was dependent on *Ghrhr* mutation status of the mice in that the magnitude of phenotype increased with dose of mutated *Ghrhr*. Consequently, this mouse strain offers a unique resource to identify the function of a gene that is an important regulator of bone size and interacts with GH pathway. Over the years we have maintained a live colony of the mutant strain (14104) in *Ghrhr*$^{lit/+}$ or *Ghrhr*$^{+/+}$ genetic backgrounds and made efforts to cryopreserve the strain. In *smad2*$^{-/+}$ genetic background screen we identified two phenotypic deviants (ID 1665 and ID 2195). Since the *Smad2*$^{-/-}$ knock out mice was not in 100% C57BL/6J genetic background, we could confirm if the mutation was independent of *Smad2* status.

Detailed descriptions of the screening procedures and generation of the mutant strains have been described in this section of report.

2.5a Progress on Specific Objective 2.3a

Breed knockout females with wild type ENU treated males to generate approximately 100 F1 progeny for each lit/lit and Smad2 mutant. Breed wild type females with ENU treated males to produce 100 F1 control progeny.

Generation of *Ghrhr*$^{lit/+}$ and *Smad2*$^{+/-}$ Mice for Breeding with ENU Injected Males. To achieve the objective of generating 200 F1 progeny from breeding ENU injected males with *Ghrhr*$^{lit/+}$ or *Smad2*$^{+/-}$ genetic background, we generated breeding pairs of *Ghrhr*$^{lit/lit}$ mice from our previous studies. We bred heterozygous *Ghrhr*$^{lit/lit}$ male mice with heterozygous *Ghrhr*$^{lit/+}$ females to produce approximately 80 *Ghrhr*$^{lit/lit}$, *Ghrhr*$^{lit/+}$, *and Ghrhr*$^{+/+}$ male and female progeny. Both *Ghrhr*$^{lit/+}$ and Smad2$^{-/+}$ progeny were identified by PCR based genotyping assays described in next section.

The little (*Ghrhr*$^{lit/lit}$) mouse has an autosomal recessive mutation in the growth hormone-releasing hormone receptor (*Ghrhr*) gene. The mutation affects only one nucleotide, an A to G mutation, at base number 112 in the *Ghrhr* gene. The PCR based genotype assay identifies this single nucleotide polymorphism (SNP) to verify the heterozygote (*Ghrhr*$^{lit/+}$) mice that have only one mutated copy of the gene.

For reporting purpose, the *Smad2*$^{+/-}$ denotes that one copy of *Smad2* gene was disabled with neomycin gene insertion whereas one copy was present as a normal *Smad2* gene. The homozygous (*Smad2*$^{-/-}$) KO mice die during embryonic development, whereas, heterozygous (*Smad2*$^{+/-}$) mice survive and live normally. We generated >100 *Smad2*$^{+/-}$ or *Smad2*$^{+/+}$ mice from

breeding heterozygous *Smad2*$^{+/-}$ male and females. To determine which mice have the mutant *Smad2* allele, we genotyped all *Smad2* progeny with a PCR based assay to detect the neomycin sequence.

Development of a SNP assay for genotyping of sensitized screen progeny generated from ENU injected B6 males and lit/lit females: The *Ghrhr*$^{lit/lit}$ mouse is a dwarf strain with an autosomal recessive mutation in the growth hormone-releasing hormone receptor (*Ghrhr*) gene. The mutation affects only one nucleotide, an A to G mutation, at base number 112 in the GHRHR gene. Since a genotype assay for this mouse has not been reported, we developed a single nucleotide polymorphism (SNP) assay to identify the 'lit' allele especially for identifying heterozygote (*Ghrhr*$^{lit/+}$) mice that have only one mutated copy of the gene and are difficult to identify by phenotype screen.

The assay used for SNP genotyping of the *lit* gene was a 5' nuclease assay (**Figure-2**). This assay uses primers that amplify the *lit* gene region and probes that are specific to the target region containing the SNP (A to G) to determine which alleles are present in each sample of DNA. Each probe has a reporter dye and a quencher attached to opposite ends of the 20 base pair sequence. The wild type probe has a different reporter dye than the probe used for *Ghrhr*$^{lit/lit}$ mice. These fluorescent dyes cannot be detected when the probe is intact because when the quencher is in close proximity, it quenches the dye by fluorescence resonance energy transfer (FRET). To identify *lit* alleles, the 5' nuclease activity of Taq Polymerase is utilized to cleave the probe and allow the reporter dye to fluoresce (see **Figure-3**).

In a sample with only the normal gene, the probe for the mutant gene will not bind to the DNA, so the Taq Polymerase will not get a chance to cleave it, thus the only signal will be from the wild type reporter dye. For the genotyping assay, the DNA was extracted from mouse tails (clips <1 cm in 2 pieces) using the DNeasy 96 kit and SNP specific region of *Ghrhr* gene was amplified using primer pair- 5'-CCT TCA GCA CTG CCA TTC AG-3'and 5'-CAG GGG AGA GAG ACC CAC TG-3.' To identify wild type alleles we used "ACC TGG GAT GGG CTG CTG TG—BHQ" probe and "ACC TGG GGT GGG CTG CTG T—BHQ" probe was used for the *Ghrhr*$^{lit/lit}$ genotype. After PCR amplification of the gene, the ABI Prism 7900 Sequence Detection System (SDS) was used to detect how much of each dye is reported in each sample and results (mutant dye vs. wild-type dye) were presented in a graph form. Three distinct groups (see **Figure-3**) could be identified. One group of points represents those that are *Ghrhr*$^{+/+}$ a second represents those that are *Ghrhr*$^{lit/+}$, and the third, those that are *Ghrhr*$^{lit/lit}$. We used three controls; a wild-type B6 mouse, the *Ghrhr*$^{lit/lit}$ mice obtained from The Jackson Lab and a non-template control (NTC).

Development of a PCR based genotype assay for screening progeny generated from ENU injected B6 males and Smad2$^{+/-}$ *females*

Smad2 is an intracellular mediator of TGF-β signaling pathway. The homozygous *Smad2*$^{-/-}$ mice die during embryonic development, whereas, heterozygous (*Smad2*$^{+/-}$) mice survive and live normally. Our sensitized screen is designed to screen ENU mutations in a *Smad2*$^{+/-}$ background. Therefore, in order to determine which mice have the *Smad2*$^{+/-}$ allele, it is necessary to genotype them. We took advantage of the fact that in *Smad2*$^{-/-}$ mice the Smad2 gene is

replaced with a neomycin reporter gene. Our assay is based on detection of the PCR product corresponding to the neomycin sequence. Primers listed in Table –1 and specific to the Smad2 gene and the neo gene were used to distinguish which mice are Smad2 heterozygous. For the genotyping assay, DNA was extracted using the DNeasy 96 kit and the Smad2 sequence was amplified using a primer pair described in **Table-1**. The PCR products were separated on 6% polyacrylamide gel, stained with ethidium bromide and visualized by Chemilmager 4400 Low Light Imaging system. Primer pair 1 amplifies a region, about 150 base pairs (BP) long, of the Smad2 gene and thus a band indicates a wild type allele. Primer pair 2 amplifies a larger region of the same gene, about 300 BP. Primers 3, 4, and 5 are all from the neo gene. Using primer pairs 1, 3 and 6, we have genotyped each mouse generated from *Smad2*$^{+/-}$ and ENU injected B6 mice. All mice will have a wild type band and mice that have a band with primer pair 6 were identified as *Smad2*$^{+/-}$.

Normative data on musculoskeletal phenotypes in lit/lit and Smad2$^{+/-}$ *knockout mice:* To obtain normative data we bred homozygous and heterozygous (*Ghrhr*$^{lit/lit}$, *Ghrhr*$^{lit/+}$, and *Smad2*$^{+/-}$) mice with wild type B6 males and females to generate *Ghrhr*$^{lit/+}$, and *Smad2*$^{+/-}$ progeny (see representative data in **Tables 2-3**). These mice were genotyped between 6-10 weeks age and screened for blood markers, DEXA, and pQCT measurements at 10 week age as described below in section-B (age varied by ±2days). The phenotype measurements were repeated at 16-weeks of age to establish reference values for the 16-week old mice. The availability of normative data is essential for identification of outlier mice based on quantitative differences.

For the genotyping assay, DNA was extracted using the DNeasy 96 kit and the Smad2 sequence was amplified using primer pairs specific for 'smad2' and 'neomycin' gene. The PCR products were separated on 6% polyacrylamide gel, stained with ethidium bromide and visualized by Chemilmager 4400 Low Light Imaging system.

2.5b Progress on Specific Objective 2.3b

Breed knockout females with wild type ENU treated males to generate 150 F1 progeny for each lit/lit and Smad2 mutant. Breed wild type females with ENU treated males to produce 150 F1 control progeny.

Production of ENU mutagenized male: We first attempted to produce mutant mice by injecting ENU to *Ghrhr*$^{lit/+}$ or *Smad2*$^{+/-}$ mice and breeding them with female *Ghrhr*$^{lit/+}$ and *Smad2*$^{+/-}$ mice. We injected 3x100 mg/kg of ENU to *Ghrhr*$^{lit/+}$ or *Smad2*$^{+/-}$ mice and bred them with *Ghrhr*$^{lit/+}$ and *Smad2*$^{+/-}$ female mice. However, breeding potential of ENU injected *Ghrhr*$^{lit/+}$ and *Smad2*$^{+/-}$ males was significantly lower as compared to ENU injected wild type B6 mice, thus, very few mice could be produced for screening. Consequently, we switched to breeding ENU injected wild type B6 mice with *Ghrhr*$^{lit/+}$ or *Smad2*$^{+/-}$ female mice. We injected three batches of 8-10 week old C57BL/6J mice with 3x100 mg/kg of ENU. Previous studies by our group have shown that B6 mice can tolerate this dose and regain fertility within 12-20 weeks post ENU injection. These batches of ENU injected males were spaced at a 3-4 months period to allow a continuous supply of ENU mutagenized B6 males for breeding. After 10-12 weeks, each ENU injected B6 male was bred with two 8-20 week old *Ghrhr*$^{lit/+}$ or *Smad2*$^{+/-}$ females. The B6 ENU injected male mice typically recovered in 14-15 weeks and produced litters with 2-6 pups/litter.

However, the fertile period was brief and lasted between 10-14 weeks. Females are checked routinely for pregnancy, and the pregnant mice were removed from mating cages and replaced by fresh females.
This second breeding strategy also generated additional animals that have the *Ghrhr*$^{+/+}$ or *Smad2*$^{+/+}$ genotype, which were not useful for our sensitized screen. Therefore, even though we produced more than 200 mice (**Table-4**) the total number of mice screened for sensitized mutations in the current reporting period was 105 mice. Total number of mice screened for dominant mutations in *Ghrhr*$^{lit/+}$, *Smad2*$^{+/-}$, *Ghrhr*$^{+/+}$, and *Smad2*$^{+/+}$ background is shown in **Table-4**, which also includes mice that had the wild type genetic background and mice that could not be genotyped.

The numbers of phenotypic deviants that we identified in our screen are described in **Table-5**. The percentage of phenotypic deviants identified as compared to the number of mice screened exceeded our expectations. Once we observed a higher number of phenotypic deviants from previous screens, we thought it was important and necessary to confirm these phenotypic deviants by backcrossing them with *Ghrhr*$^{lit/+}$ or *Smad2*$^{+/-}$ mice, which would require 300-400 additional mice. Consequently, we focused on confirming the interesting phenotypic deviants in backcross to *Ghrhr*$^{lit/+}$ and *Smad2*$^{+/-}$ mice. We produced approximately 448 F1 mice from these backcross breedings to confirm several phenotypic deviants. Out of these 448 F1 backcross mice, approximately 100 mice were produced in previous year screen but not reported earlier. Details of the backcross progeny are described below under 'Inheritance Testing' under Specific Objective 3.

2.5c <u>Progress on Specific Objective 2.3c</u>

Perform musculoskeletal screens at 10 weeks of age in the F1 progeny to measure bone mineral content, bone density, bone size, muscle size and fat content using PIXImus and pQCT instruments. Perform biochemical measurements of bone turnover in the serum samples.

<u>Musculoskeletal screening of 10 week old F1 progeny from Ghrhr$^{lit/+}$ and Smad2$^{+/-}$:</u> All sensitized screen mice and control mice were first screened for visible phenotypes at weaning when their body weights were also recorded. After weaning, mice were kept in groups of 2-3 males/cage and 3-4 females/cage until 10-week old. At 10-weeks, mice were screened for: a) visible abnormalities, b) body weight; c) total body bone density determined by DEXA instrument PIXImus (excluding skull area); d) total body bone mineral content by DEXA; e) total body bone area by DEXA; f) total body fat mass; g) lean mass; h) volumetric bone density at tibia determined by peripheral quantitative computed tomography; i) IGF-I levels in *lit*/+ mice; j) skeletal alkaline phosphatase; k) serum calcium; and l) lipid profile. An abnormality is usually recognized if a phenotype differs by 2-3 standard deviations (SD) units as compared to values obtained from age and sex matched non-mutagenized control mice. Measurements that are found to be outside the cutoff range are repeated at 16-weeks to confirm the phenotype. For this purpose, we obtained additional baseline values for age and sex matched *Ghrhr*$^{lit/+}$ and *Smad2*$^{+/-}$ mice at 16-week of age. Some phenotype measurements, such as BMC, bone area, femur BMD are size-dependent and show strong correlation with body weight. Therefore, these measurements were normalized with body weight for identifying phenotypic deviants. Those phenotypic deviants that are confirmed after repeat testing are introduced to inheritance-test (IT)

or backcross with wild type *Ghrhr*$^{lit/+}$ and *Smad2*$^{+/-}$ mice. A mutation is considered inheritable if the phenotype is recovered in backcross progeny.

Since the TGF-β pathway has been implicated in the tissue regeneration, we also screened *Smad2*$^{+/-}$ mice for 'soft-tissue regeneration' (STR). To screen mice, we punched a 2 mm hole in both ears and tissue regeneration was monitored by measuring hole size after 14-day and 21-day period using a magnifying glass (4x) with an embedded measuring scale (reading capabi*lit*y of ±0.1 mm). We observed that healing is normally slow in Smad2/+ background with mean hole size after 3-weeks of 1.8±0.2. Therefore, we anticipate hypomorphic mutation could be easier to identify.

Screening of Control Mice: We generated 193 mice from breeding of *Ghrhr*$^{lit/+}$ mice (n=80) or *Smad2*$^{+/-}$mice (n=113) with wild type B6 mice. About 40% mice carried *Ghrhr*$^{lit/+}$ or *Smad2*$^{+/-}$ genotype (**Table-4**). Out of the 193 mice generated, we screened 53 mice for generating normative data at 10-week and 16-week as described above for phenotype screening of mutant mice.

Phenotypic deviants Identified in Sensitized ENU Screening: We observed several phenotypic deviant in *Ghrhr*$^{lit/+}$ and *Smad2*$^{+/-}$ genetic backgrounds in our primary screening performed at 10-weeks and confirmed this quantitative phenotypic deviant in 16-weeks repeat testing (**Table-5**).

Detailed Phenotypic Characterization of Selective Phenotypic Deviants Identified in the Sensitized Screen

Mutant Line 14104 – The phenotypic deviant mouse 14104AM (male mouse) was identified in the *Ghrhr*$^{lit/+}$ background strain with normal appearance. The original 14104AM mouse had 18% high volumetric bone density measured by pQCT. As compared to control mice, the periosteal circumference (PC) at midshaft tibia was 17% lower but endosteal circumference was 38% lower, thus, the increased BMD was mainly due to increased bone at the endosteal surface. The cortical thickness was increased by 5%. We bred the 14104 phenotypic deviant with *Ghrhr*$^{lit/+}$ females and generated about 42 progeny in the 2003-2005 grant period. Among 42 mice, 23 were with lit/+ genotype and approximately 13 pups or about 50% appear to be affected. A representative micro-CT scan of femur midshaft shows bone size differences in **Figure-5**. Percent difference in bone size phenotype measured by in-vivo pQCT at midshaft tibia of 14104 mice and normal littermates is described in **Table-6**. An extensive breeding of 14104 mutant mice from first generation were performed with *Ghrhr*$^{lit/+}$ and wild type B6 mice generating more than >150 progeny (**Figure-6**) that were followed up for skeletal phenotype. The bone size phenotype was observed in 5-6 generations without any significant alterations in the magnitude of phenotype, which indicated that mutation was stable and inheritable. A more extensive characterization of mutant phenotype was performed during the no-cost extension period of this grant. In addition, this mutant strain was transferred to other institutionally supported projects for mapping the chromosomal location of the mutation.

Mutant Line 1665CM – The male mouse 1665CM was identified in the *Smad2*$^{+/-}$ genetic background. The phenotypic deviant had 18% high body weight and 13% higher total body bone density measured by DEXA (Dual Energy X-ray Absortiometry), as compared to control *Smad2*$^{+/-}$ mice (data shown in **Table-7** and **Figure-7**). The body weight adjusted bone density

was not significantly higher in mutant mice. The lean body mass was increased by 19%. Since TGF-b is implicated in growth, we believe the mutant mouse has a high growth phenotype. We bred the 1665CM phenotypic deviant with *Smad2*$^{+/-}$ females and generated about 120 progeny. Out of 86 mice screened, 55 mice with *Smad2*$^{+/-}$ background have been screened at 10-weeks and 37 mice screened at 16-weeks. At 16-weeks, approximately 16 pups from inheritance testing backcross or about 43% appeared to be affected.

Mutant Line 1665DF – The female 1665DF mouse was identified in the *Smad2*$^{+/-}$ genetic background. The phenotypic deviant had a 23% higher body weight and a 17% higher total body bone density measured by DEXA (Dual Energy X-ray Absortiometry), as compared to control *Smad2*$^{+/-}$ mice (data shown in **Table-8** and **Figure-8**). The body weight adjusted bone density was 4-8% higher in 16-week old 1665DF mutant mice ($p<0.05$ vs control smad2/+ mice). The lean body mass was 25% higher in 1665DF. We believe the mutant mouse has a high growth as well as high BMD phenotype. We bred the 1665DF phenotypic deviant with *Smad2*$^{+/-}$ male mice and generated about 146 progeny. Out of 107 mice screened, 65 mice with *Smad2*$^{+/-}$ background were screened at 10-week and 45 mice were screened at 16-weeks of age. At 16-week, approximately 13 pups from inheritance testing backcross or about 29% appear to be affected. The 1665DF mutant appears to be similar to 1665CM described above, however, the body weight adjusted total body BMD was 4-8% higher ($p<0.05$) in 1665DF indicating that increase in BMD was greater than that explained by increased body weight. Therefore, the 1665DF mutation also affects BMD. Both mutant lines 1665CM and 1665DF were generated from same ENU injected male and could represent the same mutation.

Mutant Lines 1617EF and 1617DF: Two mutants 1617EF and 1617DF were identified in the *Smad2*$^{+/-}$ strain of mice; both these mutants were littermates and could represent same mutation. Therefore, we have combined data from these two mutants. The phenotypic deviants 1617EF and 1617DF had 20% faster healing as compared to WT control mice (*Smad2*$^{+/-}$). The healing phenotype was measured by punching a 2 mm hole and measuring the hole size after 3-5 weeks. We bred the 1617EF and 1617DF phenotypic deviant with *Smad2*$^{+/-}$ male and generated about 31 progeny (including those mice that had *Smad2*$^{+/+}$ genotype). Out of 31 mice generated, approximately 4 pups from inheritance testing backcross appear to be affected (**Figure-9**). The mutation could not be confirmed.

Mutant Line 2195: Mutant line (ID) 2195 was identified in *Smad2*$^{+/-}$ genetic background. Backcross of mutant 2195 mice with *Smad2*$^{+/-}$ mice produced about 50 progeny, among them > 50% progeny appeared to be affected. The phenotypic deviant mice had 6% low body weight and 10–13% ($p < 0.001$) low total body bone area and bone mineral content measured by DEXA, as compared to control *Smad2*$^{+/-}$ mice. The body weight adjusted bone density was not significantly different but body weight adjusted bone area was 9–11% ($p < 0.001$) lower in 16-week old 2195 mutant mice as compared to control littermates. The 2195 mutant was also inherited in the WT genetic background with no statistically significant interaction effect of *Smad2*$^{+/-}$ genotype as shown in **Figure-10**.

2.5d Progress on Specific Objective 2.3d

Begin to confirm the mutant phenotypes by backcrossing the mutant mice with lit/lit or Smad2 knockout mice, as appropriate

Those phenotypes that are confirmed after repeat testing at 16-weeks were backcrossed with *Ghrhr*$^{lit/+}$ and *Smad2*$^{+/-}$ mice to test inheritance. A mutation is considered inheritable if the phenotype is recovered in backcross progeny (a minimum of 20 mice).

We introduced 11 phenotypic deviant mice (including mutant mice from both *Ghrhr*$^{lit/+}$ and *Smad2*$^{+/-}$ background) into inheritance testing (**Table-5**) by mating affected male and female mice with *Ghrhr*$^{lit/+}$ and *Smad2*$^{+/-}$ mice. Each phenotypic deviant is mated with 1-2 normal wild type male or female mice. Once the mating is successful, pregnant mice are placed separately to give birth to backcross littermates. If an F1-affected mouse is a female, it is reintroduced for mating to produce 3-5 litters totaling about 20-25 backcross pups. If the affected mouse is male, 3-5 female mice were mated simultaneously. The progeny produced in backcrosses were screened at 10-week and 16-weeks of age. The animals are genotyped to identify the background alleles such as *Ghrhr*$^{lit/+}$ and *Smad2*$^{+/-}$ genotype. To differentiate mutant from non-mutant genotypes, 2-3 SD cut-offs were used for separating the mutants from their unaffected littermates. To avoid potential breeding of an un-affected progeny, we bred only extreme scoring mice for generating affected progeny in subsequent breeding. All phenotypic deviant mice that were confirmed or partially confirmed after inheritance testing are listed in **Table-5**.

Three mutant lines, 14104AM, 1665DF, and 1665CM were extensively bred in several generations of backcrosses. Individual data points from these mice have been shown in **Figure-6 - 8**.

2.6 SUMMARY OF SENSITIZED ENU SCREEN

We produced >200 F1 progeny from ENU injected male mice and we screened 105 *Ghrhr*$^{lit/+}$or *Smad2*$^{+/-}$ F1 progeny for dominant mutations (**Table-4**) for various musculoskeletal and soft tissue healing phenotypes. We observed 19 phenotypic deviants in our primary screening performed at 10-weeks and confirmed 11 quantitative phenotypic deviants in 16-weeks repeat testing. The phenotypic deviant mice could be broadly classified in two main categories: 1) phenotypic deviants with high body weight, high bone density and high bone mineral content; and 2) phenotypic deviants with low body weight, low bone density and low bone mineral content. Both of these categories were anticipated because mutations in *Ghrhr* and *Smad2* genes are involved in developmental type phenotypes.

We can draw two major conclusions from our sensitized screen results. As anticipated the sensitized screen showed greater recovery of mutation as compared to our standard ENU mutagenesis screen. Results of our previous ENU screen employed in the B6 mouse strain revealed a frequency of approximately 2-3% outliers per 100 mice screened from ENU injected males (with a dose of 100 mg/kg). If we compare the frequency of a non-sensitized ENU

mutation rate with results obtained in our current sensitized screen where we observed 13 quantitative phenotypic deviants, we see approximately 4-5 fold higher rates of phenotypic deviants. However, our estimate of mutation rate for the current sensitized screen is only based on about 100 mice, which can only be considered preliminary. The second major conclusion was that the magnitude of phenotype was much larger in the sensitized screen as compared to the standard ENU mutagenesis screen. Although several mutant mice died or were unable to breed, one of the mutant mice we recovered (ID 14104) showed the largest changes in skeletal phenotype we observed in any type of ENU based phenotype screen. This was due to synergism between the ENU induced mutation and the defective genetic background where a known pathway was altered. Thus, these studies not only provided a proof of concept but also resulted in identification of a mutant resource to identify a major regulator of bone size.

2.7 Characterization of 14104 mutant line during the no Cost Extension period 2005-2009

During the no-cost extension period no additional Specific Objectives were proposed. However, during this period we continued the breeding of several phenotypic deviants. The major focus of this breeding was to generate several generations of mutant 14104 and utilized the progeny to further characterize the skeletal phenotype in mutant mice. The work on characterization of the mutant 14104 was performed with additional institutionally supported projects. The characterization of mutant 14104 is highlighted in this section to show case that sub project 2 produced a very attractive novel mutant for identification of a gene that regulates bone size.

Bone Size Phenotype of the 14104 Mutant mice

The 14104 mutation was inherited as an autosomal dominant trait and mutant phenotype is expressed in both *Ghrhr*$^{lit/+}$ and *Ghrhr*$^{+/+}$ genotypes. The body weights of the 14104 mice were 6-13% (between 3-16 week age) lower as compared to the non-affected littermates. The body weight adjusted bone size phenotype was nevertheless 30-40% lower (**Figure-11**). The bone size parameters analyzed by histomorphometric analysis of midshaft femur of 16-week old mice are described in **Table-9**. The excised tibia and femur scanned by pQCT at 9-different slices demonstrated that reduced bone size covered the entire femur length with mean PC was 22-27% lower, CSA was 39-46% lower, and endosteal perimeter was 27-37% lower (data from 6-12 week old mice). The concomitant changes in both periosteal and endosteal perimeters resulted in maintenance of cortical thickness (0.232±0.0076 mm in mutant vs 0.234±0.012 mm in control male mice, 0.218±0.0065 vs 0.222±0.0092 in female mice, n=5-6, $p>0.05$). The cortical data determined by μCT from 6-week old female mice are presented in **Table-10**. Although the bone size was significantly reduced in mutant mice the shape of the cross-sectional shape of the midshaft was remarkably similar to wild type determined by CT (Figure-1) and histological section (details not shown).

To observe the time course of bone size development in mutant mice we determined PC and cross-sectional area (CSA) between 3-day and 16-week old mice. The reduced PC (1.39±0.11 mm in mutant vs 1.73±0.23 mm in control, n=7) and total bone area (0.145±0.026 mm^2 in mutant vs 0.213±0.066 mm^2 in control, n=8) phenotypes were detectable in 3-7 day old mice as determined by histomorphometric analysis of midshaft femur. At 3-weeks age, the PC and total bone area phenotypes were clearly manifested with PC 15-17% ($p<0.001$) lower and CSA 28-

31% ($p<0.001$) lower in mutant mice (n=37-45) as compared to control mice (n=58-65). The maximum differences in PC were achieved in 6-week old mice when PC was approximately 20% decreased in both male and female mice. The CSA continues to decrease until it is approximately 40% lower in mutant mice at 16-week age (**Figure-12**).

Histomorphometrical Analysis of Trabecular bone: To study if the decreased bone size also affects trabecular bone structure, we analyzed the proximal tibia and femurs by histology and μCT. Both histological analysis and the μCT analysis (shown in **Table-11**) of the femur metaphysis showed that 14104 mutation affected the morphological properties of trabecular bone with similar extent as observed for cross-sectional area or periosteal perimeter. As shown in **Table-11**, the bone area parameters of trabecular bone were 33-52% reduced in 14104 mice as compared to control mice. These data suggest that the mutation affects both cortical and trabecular bone morphological properties.

C2d. *Mechanical Properties of Tibia Shafts*: Because the cross-sectional area of 14104 was 30-40% reduced from that of control, the mechanical properties were suspected to differ exponentially between 14104 and control bones. However, due to a greater decrease in endosteal circumference or reduced marrow area of 14104 mice, the bone volume/total volume was higher in mutant to that of control (**Table-10 & 11**).

*Bone Size Phenotype is Modulated by GH***:** Although the mutation was originally detected in the *Ghrhr*$^{lit/+}$ genotype background, subsequent breeding confirmed that the bone size phenotype is also expressed in *Ghrhr*$^{+/+}$ background. Thus, our preliminary data clearly shows that 'mutant gene' and 'lit' allele segregate independently. To measure the interaction between the mutant gene and *Ghrhr* mutation, we analyzed the cross-sectional area of midshaft tibia from 6-week old female 14104 mutant mice in presence of *Ghrhr*$^{+/+}$, *Ghrhr*$^{lit/+}$, and *Ghrhr*$^{lit/lit}$ genotypes. Although the bone size phenotype is well expressed in the *Ghrhr*$^{+/+}$ genotype, the magnitude of bone size phenotype is significantly influenced by the presence of "lit" allele as indicated by two-way ANOVA (**Figure-13**). Post-Hoc analysis by two-way ANOVA indicates that *Ghrhr*$^{lit/+}$ genotype significantly ($p<0.02$ for interaction) decreased the bone size. These data indicate that the mutant gene effect is modulated by GH. This phenomenon will be utilized in prioritizing genes for mutation detection.

Dynamic Histomorphometric Analysis to Measure Rate of Bone Formation and Bone Resorption: Bones from 14104 and control mice were dual labeled at a 10-day interval using calcein and animals were sacrificed at 12-weeks of age. The histomorphometric measurements revealed a 25% lower bone formation rate at periosteal surfaces in the 14104 mice (n=8) as compared to control (n=6) (**Figure-14,** data from male and female mice were combined). There was a small increase in the bone formation rate in the 14104 mice at the endosteal surface but it was not statistically significant. We measured TRAP stained surface at endosteum as an indicator of osteoclast number at midshaft humerus, which showed similar decrease in bone size as observed with tibia and femur (details not shown). The TRAP stained surface at endosteum were 45% lower (Mean±SD, 7.1±3.4 in mutant vs 12.8±7.4 in control mice, n=4-6, $p=0.065$), which would indicate that there is decreased number of osteoclasts at endosteum (**Figure-15**). We speculate that decreased endosteal bone resorption is a compensatory mechanism to offset the drastic decrease in bone strength because of reduced bone size at periosteum. Importantly, results of dynamic histomorphometric studies provide an important insight into the cellular

functions altered by the mutant gene. We observed that the reduced BFR at the periosteum is primarily due decreased labeled surface, which is a measure of osteoblast number and not due to mineral apposition rate (MAR) which is a measure of osteoblast activity.

Biochemical Bone Markers: Since mutation is expressed in a GH deficient environment, we measured the IGF-I levels in the serum of the 14104 mice (n=11-30) and non-affected littermates (n=13-24). The IGF-I levels were not significantly different in the 14104 mice (mean±SD, 250±93 ng/ml) as compared to control littermates (mean±SD, 236±93 ng/ml). This may indicate that the mutant gene, though acting through interaction with GH pathway, may not involve deficiency in IGF-I circulating levels. The bone formation marker osteocalcin was 20% lower ($p=0.021$) in 14104 mice (131±59 ng/ml) as compared to normal littermates (163±81 ng/ml), which indicates an overall decrease in osteoblast activity or bone formation rate.

In vitro Phenotypic Characterization of Cell Function in the 14104 Mice: We isolated osteoblast from long bones of 14104 mice and determined cell proliferation and differentiation using established procedures. To obtain quantitative differences, cells from four mutants and four control mice that were used for each experiment. Proliferation was measured by uptake of AlmarBlue dye and 3H-thymidine incorporation. The basal proliferation rate was 40-50% lower in cells from the 14104 mice as compared to normal littermates. To identify if osteoblasts from mutant mice have lower differentiation potential, the osteoblasts were grown until confluent and then treated with β-glycerophosphate and ascorbic acid. The basal differentiation rate, measured by increase in alkaline phosphatase activity, was slightly lower in osteoblasts from 14104 mice but it was not statistically significant. Thus, our preliminary in vitro cell culture data indicates that decreased bone size in 14104 mice could be attributed to a deficiency in osteoblast proliferation.

Evidence that Single Gene Mutation Contributes to Observed Bone Size Phenotype:
We believe that the bone size phenotype in the 14104 mice is caused by a single gene mutation. Typically, the ENU treatment of male mice could produce 50-100 random mutations covering the whole genome. By assuming that there may be 50-100 genes that regulate bone size in the whole genome, the likelihood of a single gene ENU mutant carrying multiple gene mutations for bone size phenotype is rather low. In addition, We have now bred the 14104 lines for five generations and mice produced from fifth generation have a phenotype similar to that observed in the original 14104 mutant mice (Z-score –5) indicating that successive breeding with WT mice has not significantly altered the phenotype and that the mutation is stable. Typically, the ENU mutations are diluted by a factor of 50% after each generation of breeding with WT mice. If multiple mutations contributed to the reduction in bone size, the magnitude of bone size are reduced in successive generations as the number of mutations becomes diluted because of the recombination. However, this was not observed in the 14104 mice.

Mapping the 14104 Mutant Locus: The first step towards identifying the mutant gene is to determine the chromosomal location of the mutation. Since the ENU mutations are randomly created in any part of the genome, we used a whole-genome scan to identify the chromosomal location of the mutant gene by determining the association between the trait values (cross-sectional area and/or periosteal circumference) and the marker genotypes in a F2 populations derived from an intercross involving the mutant mice (C57BL/6J) and DBA/J strain of mice.

Genome-Wide Scan to Identify the Mutant Locus: We have selected the DBA mouse strain because the morphology and size of their femur and tibia is similar to that of 14104 mutant mice. In addition, our preliminary studies involving C3H/HeJ and DBA/J strains of mice showed that bone size phenotype is well expressed in the DBA background (**Figure-16**) with expected 50% affected-to-normal ratio (details of intercross with C3H/HeJ mice are not shown). Therefore, we bred 14104 mutant mice (in *Ghrhr*$^{lit/+}$ genetic background) with DBA male and females to produce 28 F1 hybrids. Subsequent breeding of selected F1 mice produced 182 F2 mice. Since mutation is inherited as an autosomal dominant trait, approximately 50% of the F2 mice had mutant bone size phenotype. All F1 (n=28) and F2 mice (n=182) were screened for cross-sectional area and periosteal circumference phenotypes by in vivo pQCT at 3-week age. At 6-weeks, we sacrificed the F2 animals and collected femurs for ex vivo pQCT analysis. Each F2 femur was scanned at 9 slices covering the entire length and mean cross-sectional area and periosteal circumference of middle three slices were used for linkage analysis. We used both 3-week in vivo bone size measurements and 6-week ex vivo bone size measurements for linkage analysis of the F2 mice.

Identification of Chromosomal Location of the 14104 Mutant Gene by Selective Genotyping and Phenotype based DNA Pooling Technique: To analyze F2 DNA samples, we employed selective genotyping and a phenotypic pooling method to scan the genome, which has been well established for identifying ENU mutations in mouse model. To make pools, first frequency distribution of CSA and periosteal circumference phenotype was calculated and the lowest 20% fraction and highest 20% fraction of the F2 mice were identified for selective genotyping (**Figure-16**). Based on their CSA and periosteal circumference phenotype, we classified each F2 mice into two groups: 1) mutant; and 2) wild type. We collected tail clips from all F2 mice, isolated DNA following a method that we have previously established quantified DNA by spectrophotometry, and adjusted the DNA concentration to 100 ng/µl. We pooled equal amounts of DNA from each of the 35 F2 mice representing the lowest 20% fraction of the (representing mutant phenotype) F2 population. Similarly, a pool of about 35 F2 mice with the highest 20% fraction (representing wild type phenotype) was made. A control pool was made with equal amounts of DNA from WT B6DBA F1 and WT DBA mice. The final concentration of DNA in the pools was adjusted to 10 ng/µl. We used 4 fluorescent-labeled microsatellite markers for Chrs 1, 2 and 5, and, 3 fluorescent-labeled microsatellite markers for each of the remaining autosomes. Markers were analyzed in three replicates for fragment size and allele densities were read using ABI Model 3100 DNA Analyzer (Applied Biosystems). Our preliminary mapping data identified one distal chromosome 11 marker that showed 100% (B6): 0% DBA ratio, which was expected signal ratio for alleles of a linked marker. Once the linked marker was identified we used flanking markers to confirm the linkage (details not shown). The linkage results were similar when we used CSA and periosteal circumference as phenotype trait (details not shown). Based on these data, we concluded that the mutant locus was located in Chr 11.

Refine the 14104 Mutant Locus using Additional Genetic Markers: Once we identified the linkage on chromosome 11, we used 18 markers on chromosome 11 and individually genotyped DNA from 182 F2 mice. Because we used body weight adjusted periosteal circumference as the phenotype, we combined the male and female data for interval mapping. We genotyped all F2 mice to determine if they carried Ghrhr$^{lit/+}$ of Ghrhr$^{+/+}$ alleles. We analyzed the marker data

using Pseudomarker MAINSCAN algorithm written for MATLAB (Mathworks Inc., Natick, MA, USA) program. Threshold for permutation based genome-wide significance was set at 5% for significant linkage. Chromosomal linkage map with 18 markers, shown in **Figure-17,** localized the mutant gene to a 66-79 cM region (based on flanking markers D11mit333 and D11mit104). Presence of 'lit' allele was used as covariate, which accounted for background effects. Posterior probability density, which is a likelihood statistic that gives rise to the 95% confidence intervals (CI), shown in **Figure-17,** indicates a support interval of 109-119 Mb. The physical distance was based on markers D11Mit181 (69 cM and 109.14 Mb) and D11Mit104 (79 cM and 119.12 Mb). Based on the fine mapping data, we constructed a comparative map of QTLs from other species. The 95% CI interval for the 14104 mutant locus was syntenic with human chromosome 17q22-25. As described in the Background section, a QTL regulating femoral head width have been mapped to rat Chr 10 (39) and a QTL regulating wrist size have been mapped to human Chr 17q23 (29). Alignment of sequences derived from flanking markers of rat bone size QTLs indicated that the QTL regulating bone size in rat falls within the 95% CI of 14104 mutant locus. In addition, an important mouse QTL regulating periosteal circumference also (at peak location of 65 cM, 95% Confidence Interval not reported) overlaps with the 14104 mutant locus. These data suggest that 14104 mutant locus was precisely mapped to a region which has been consistently linked to bone size regulation in independent studies. However, overlapping the syntenic mouse, rat, and human QTLs did not improve the resolution of the 14104 support interval. Combined together, we conclude that the mutant locus on Chr 11 contains a key gene(s) that regulates bone size in multiple species.

Allele Distribution of Peak Marker Linked to Mutant Locus: At the peaks of 14104 mutant locus, the phenotypic means in F2 mice represented by the closest markers were calculated and are shown in **Figure-18**. Alleles for the peak markers on the Chr 11 interval that were inherited from the B6 parental strain contribute to approximately 20% lower ($p<0.001$) periosteal circumference than do alleles inherited from DBA/J mice. Thus, allele distribution data was consistent with the 20% decreased periosteal circumference observed in the 14104 mutant mice. Based on the one-way ANOVA, the phenotypic effect of the B6 allele best fits an additive model.

Candidate Genes in the Chromosome 11 Locus: The physical map of 95%CI of 14104 locus was identified to a region extending from 109.14 to 119.12 Mb. Using the Mouse Genome Informatics (MGI 3.51, http://www.informatics.jax.org/), we identified 131 known transcripts in this region. The potential candidate genes include those genes that regulate growth and differentiation of bone cells. Based on these criteria, potential candidate genes identified in the support interval on the Chr 11 region are listed in **Table-12**.

2.8 Summary Of Progress During The NO-Cost Extension Period

During the no-cost extension period of the grant, we extensively characterized the bone size phenotype in the 14104 mice. The work performed during no-cost extension was also supported by other institutional funds. Five generations of breeding indicated that the 14104 mutation was stable and was caused by single gene mutation. The mutation affects bone size in 3-week old mice and appears to regulate periosteal expansion and most importantly cortical thickness during 3-16-week growth period. The mutant gene is a major determinant of bone size (affecting 30-

40% cross-sectional area) in both male and female mice and appears to be modulated by GH axis. The histomorphometric evidence suggests that the mutation reduces bone formation rate at the periosteum. Our data also showed that although the bone size was decreased but the cortical bone volume is maintained or comparatively increased in mutant mice. Thus, mutant gene is also involved in determining the cortical bone mass. Our data showed that reduced BFR is caused by reduced total labeled surface, which indicates reduced osteoblast proliferation. We localized the mutation to a 10 Mb region of chromosome 11. The mutation is located in a genomic region which harbors several important QTLs that regulate bone size in mouse, rat and humans. This indicates that mutant gene is an important regulator of bone size. We identified 131 transcripts in the locus harboring the mutation; among these transcripts we have identified nine functional positional candidates for mutation detection. The functional candidates represents gene that are well expressed in osteoblasts and are known to be involved the in proliferation and/or differentiation of osteoblasts. These genes will be investigated on a priority basis for mutation detection. A grant application will be submitted to outside funding agency to continue this work.

KEY RESEARCH ACCOMPLISHMENTS

1. We maintained a breeding colony of *Ghrhr*$^{lit/+}$, *Ghrhr*$^{lit/lit}$, *Ghrhr*$^{+/+}$, and *Smad2*$^{+/-}$ mice to have a continuous supply of *Ghrhr*$^{lit/+}$ or *Smad2*$^{+/-}$ mice for breeding with ENU injected B6 males.
2. We injected 3 X 100 mg/kg ENU in three batches of B6 males and bred them with *Ghrhr*$^{lit/+}$ and *Smad2*$^{+/-}$ mice. We generated more than 200 F1 mice for dominant screen and screened 105 F1 mice with *Ghrhr*$^{lit/+}$ or *Smad2*$^{+/-}$ genetic background or sensitized mice.
3. To obtain normative data, we bred wild type B6 mice with *Ghrhr*$^{lit/+}$ and *Smad2*$^{+/-}$ mice. We have screened 53 F1 control mice with *Ghrhr*$^{lit/+}$ or *Smad2*$^{+/-}$ genetic background. Using these normative data we calculated normal variation and devised appropriate cut-off values to identify abnormal or mutant mice.
4. We have identified 19 phenotypic deviant in primary 10-week sensitized screen and confirmed 11 phenotypic deviants in 16-week repeat testing.
5. We introduced 11 phenotypic deviant mice to backcross for testing inheritance of mutant phenotypes. We generated 448 mice from backcrosses of various phenotypic deviants.
6. We confirmed three phenotypic deviants in inheritance testing. Two phenotypic deviants were in *Smad2*$^{+/-}$ background genotype and exhibit higher growth and high total body bone density phenotype. One phenotypic deviant was in *Ghrhr*$^{lit/+}$ background and showed 30% low bone area and high volumetric bone density phenotype.
7. The inheritable phenotypic deviants are single gene mutations, and therefore, provide an interesting mouse model to identify genes that are involved in the genetic regulation of growth and musculoskeletal phenotypes.
8. We maintained a small breeding colony of *Ghrhr*$^{li/-}$ mice and *Smad2*$^{-/+}$ mice for breeding with phenotypic deviants. We cryopreserved sperms from 14104 mutant strain and archived them at The Jackson Laboratory, Maine.

9. One of the mutant lines, ID 14104, was transferred to another project for further studies where we mapped the mutation to a distal region of chromosome 11.
10. We published one manuscript describing the sensitized screen design and identification of phenotypic deviants. Another manuscript has been written for publication.
11. The mutant 14104 strain provides a valuable mouse model to identify genes that are involved in the genetic regulation of bone size.

REPORTABLE OUTCOMES

Abstracts

1. **Srivastava AK**, Mohan S, Baylink DJ. A Sensitized ENU Screening System to Discover Modifier Genes by Utilizing Mouse Models Deficient in Genes Regulating Skeletal Tissues. 28th Annual Meeting of American Society for Bone and Mineral Research, 2006.
2. **Srivastava AK**, Mohan S, Baylink DJ. Identification of Mutant with a Large Decrease in Bone Size Identified in a Sensitized ENU Screen using Growth Hormone Deficient 'Little' Mouse. 28th Annual Meeting of American Society for Bone and Mineral Research, 2006.

Publication

1. Mohan, S, Baylink, DJ, Srivastava, AK. A chemical mutagenesis screen to identify modifier genes that interact with growth hormone and TGF-beta signaling pathways. Bone 42:388-95; 2008.

CONCLUSIONS

1. We utilized mouse models representing two key pathways, IGF-I growth hormone axis and TGF-β signaling, to perform a sensitized ENU screening for musculoskeletal phenotypic deviants. These strains involved mutant *Ghrhr* and *Smad2* genes.
2. We have injected three batches of C57BL/6J males with ENU dose of 3 X 100 mg/kg to generate ENU founder males. We bred the ENU injected males in a breeding scheme to generate about >200 F1 mice for dominant screening. Among those >200 mice, 105 mice were sensitized and were subsequently screened for mutation. In addition, we have generated 193 F1 mice by breeding $Ghrhr^{lit/+}$ or $Smad2^{+/-}$ mice with WT B6 mice and screened 53 mice with $Ghrhr^{lit/+}$ and 80 mice with $Smad2^{+/-}$ genotype to generate normative data for identification of mutants. We proposed to screen 150 F1 mice for sensitized mutation. Therefore, we have accomplished our main goal of the Specific Objective 1.
3. We have performed musculoskeletal screens at 10 weeks of age in the F1 progeny to measure bone mineral content, bone density, bone size, muscle size and fat content using PIXImus and pQCT instruments. We identified 19 phenotypic deviants in the 10-week screen and confirmed 11 phenotypic deviants in the repeat testing performed at 16-week age. Therefore, we have accomplished our main goal of the Specific Objective 2.

4. We bred 11 phenotypic deviants identified in backcross to test inheritability of the mutations. We generated more than 400 progeny from backcrosses and confirmed three phenotypic deviants to be inheritable. We have partially confirmed one soft tissue regeneration mutant in the backcross. The number of mice generated in backcross far exceeded those proposed in the current grant period. Therefore, we exceeded our goals for final objective Specific Objective 3.
5. The proposed work carried out over the entire no-cost extension period was above and beyond that proposed Specific Objectives and resulted in significant outcome. Through this grant we have created a mutant strain that provides a valuable tool to identify a gene that is very important regulator of bone size. We have mapped the chromosomal location of mutation and performed extensive characterization of mutant phenotype. The mutation is stable and the mutant strain has been archived so there is less probability that the mutant strain will be lost in breeding. Therefore, we far exceeded our goals for all 'Specific Objectives.'

REFERENCES

1. Srivastava AK, Mohan, S, Wergedal JE, Baylink DJ. A Genome-wide Screening of N-Ethyl-N-nitrosourea Mutagenized Mice for Musculoskeletal Phenotypes. Bone, 33, 179-191, 2003.
2. Go MJ and Tsakonas SA. A genetic screen for novel components of the Notch signaling pathway during Drosophila bristle development. Genetics 150:211-220, 1998.
3. Carrera P, Abrell S, Kerber B, Walldorf U, Preiss A, Hoch M, Jackle H. A modifier screen in the eye reveals control genes for Kuüppel activity in the Drosophila embryo. Proc. Natl. Acad. Sci. 95:10779-10784, 1998.
4. Satterthwaite AB, Willis F, Kanchanastit P, Fruman D, Cantley LC, Helgason, Humphries RK, Lowell CA, Simon M, Leitges M, Tarakhovsky A, Tedder TF, Lesche R, Wu H, and Witte ON. A sensitized genetic system for the analysis of murine B lymphocyte signal transduction pathways dependent on Bruton's tyrosine kinase. Proc. Natl. Acad. Sci. 97: 6687-6692, 2000
5. Attisano, L. and J.L. Wrana, Signal transduction by the TGF-beta superfamily. Science, 296(5573): 1646-7, 2002.
6. Donahue, L.R. and W.G. Beamer, Growth hormone deficiency in 'little' mice results in aberrant body composition, reduced insulin-like growth factor-I and insulin-like growth factor-binding protein-3 (IGFBP-3), but does not affect IGFBP-2, -1 or -4. J Endocrinol, 136(1): 91-104,1993.

TABLES

Table 1. Primers and PCR products used for genotype assay for screening Smad2 allele.

Primer Pair No	Sequence Information	Size of band (Base Pair)	Allele
1	5'—CAT GAA TAC TAC GAC GGA GG—3' 5'—GGA CCA GAC TCA CTA GTT CA—3'	150	WT
2	5'—CAT GAA TAC TAC GAC GGA GG—3' 5'—CTC CTT GAT GGA TGA ACT TC—3'	300	WT
3	5'—TGA ATG AAC TGC AGG ACG AG—3' 5'—ATA CTT TCT CGG CAG GAG CA—3'	171	Smad2
4	5'—AGA CAA TCG GCT GCT CTG AT—3' 5'—AGT GAC AAC GTC GAG CAC AG—3'	176	Smad2
5	5'— AGA CAA TCG GCT GCT CTG AT —3' 5'—CAA TAG CAG CCA GTC CCT TC—3'	203	Smad2

Table-2. Representative data on reference values of bone density and other parameters on 10-week and 16-week old control mice (n=15-20).

Phenotype	Sex	10-Week Old Mice		16-Week Old Mice	
		Mean±SD	Population Variance (CV)	Mean±SD	Population Variance (CV)
Total body BMD (g/cm^2)	F	0.0491±0.0021	4.4	0.0523±0.0027	5.1
	M	0.0483±0.0016	3.2	0.0533±0.0018	3.5
Total body BMC (g)	F	0.427±0.024	5.7	0.492±0.031	6.3
	M*	0.464±0.035	7.6	0.506±0.048	9.4
Total body Bone Area (cm^2)	F	8.8±0.34	3.9	9.2±0.49	5.3
	M*	9.5±0.45	4.8	9.7±0.68	7.1
Body Weight	F	21.5±1.2	5.6	23.8±1.6	6.9
	M*	26.0±2.2	8.4	28.6±2.8	9.7
Bone Density at Midshaft Tibia (mg/cm^3)	F	720±20	5.6	750±21	2.9
	M*	720±20	2.8	750±28	3.7
Periosteal Circumference at Tibia Midshaft (mm)	F	4.1±0.1	4.3	4.1±0.11	4.4
	M*	4.3±0.2	4.6	4.4±0.2	4.5

*Male significantly ($p<0.05$) different from female.

Table-3. Representative data on reference values of bone density and other parameters on 10-week and 16-week old *Smad2*$^{+/-}$ control mice (n=20-30).

Phenotype	Sex	10-Week Old Mice	
		Mean±SD	Population Variance (CV)
Total body BMD (g/cm^2)	F	0.0509±0.0018	3.6
	M	0.0566±0.0051	8.9
Total body BMC (g)	F	0.518±0.031	5.9
	M*	0.531±0.043	8.1
Total body Bone Area (cm^2)	F	10.0±0.5	5.4
	M*	10.7±0.4	3.7
Body Weight	F	23.8±1.8	7.6
	M*	30.6±2.9	9.5
Bone Density at Midshaft Tibia (mg/cm^3)	F	682±20	3.0
	M*	719±29	4.0
Periosteal Circumference at Tibia Midshaft (mm)	F	4.5±0.2	3.7
	M*	4.7±0.2	4.3

*Male significantly ($p<0.05$) different from female.

Table-4. Number of mice generated, mice screened for various phenotypes, and number of mice introduced to inheritance testing.

Procedure	Number of Mice with *Ghrhr*$^{lit/+}$ Genotype	Number of Mice with *Smad2*$^{+/-}$ Genotype
Control Mice Screened for Dominant Mode of Inheritance (F1)	80	113
Sensitized ENU Mice Screened for Dominant Mode of Inheritance (F1)	84*	131*
Abnormal Phenotypes Identified in Primary Screen (in *Ghrhr*$^{lit/+}$ *and Smad2*$^{+/-}$ background and excluding *Ghrhr*$^{+/+}$ *and Smad2*$^{+/+}$ background)	14	6
Abnormal Phenotypes Confirmed in Secondary Screen (in *Ghrhr*$^{lit/+}$ *and Smad2*$^{+/-}$ background and excluding *Ghrhr*$^{+/+}$ *and Smad2*$^{+/+}$ background)	9	5
Phenotypes Introduced to Progeny Testing	5	3

*Includes mice with genotypes *Ghrhr*$^{+/+}$ *and Smad2*$^{+/+}$ and mice that could not be genotyped.

Table-5. List of phenotypic deviants identified and introduced to inheritance testing.

Phenotype (Mice ID)	Description of 16-Week Repeat Phenotype	Strain	Mutation Confirmed in IT
14.9.8.EM	BMD Z-Score=3.0 BMC Z-Score=3.3 (Body weight adjusted BMC 20% High)	*Ghrhr*$^{lit/+}$	Not Confirmed
14.10.4.AM	Reduced Bone Size Z-Score=-5	*Ghrhr*$^{lit/+}$	Confirmed
15.2.3.BM	Body Weight Z-Score=3.2 BMD Z-Score=3.6 BMC Z-Score=3.8	*Ghrhr*$^{lit/+}$	Not Confirmed
15.12.7.FF	Body Weight Z-Score=-5.7 BMD Z-Score=-6.1 BMC Z-Score=-5.5	*Ghrhr*$^{lit/+}$	Not Confirmed
14.10.6.AF	Body Weight Z-Score=-2.3 BMD Z-Score=-2.6 BMC Z-Score=-2.6	*Ghrhr*$^{lit/+}$	Not Confirmed
14.10.12	High IGF-I, Z-Score=-2.3	*Ghrhr*$^{lit/+}$	Not Confirmed
16.1.7.EF	20% Higher Tissue Healing	*Smad2*$^{+/-}$	Under Testing
16.6.5.CM	Body Weight Z-Score=2.2 BMD Z-Score=3.8 BMC Z-Score=3.7	*Smad2*$^{+/-}$	Partially Confirmed
16.6.5.DF	Body Weight Z-Score=2.4 BMD Z-Score=4.9 BMC Z-Score=4.1	*Smad2*$^{+/-}$	Partially Confirmed
16.16.8.CM	Body Weight Z-Score=4.4 Lean Mass Z-Score=1.5 BMD Z-Score=3.3 BMC Z-Score=2.1	*Smad2*$^{+/-}$	Not Confirmed
21.9.5	Low BMC and Bone Area Low Body Weight	*Smad2*$^{+/-}$	Partially Confirmed

BMD= Bone Mineral Density, BMC= Bone Mineral Content, Z-Score indicates differences in a particular phenotype in terms of SD units from non-mutagenized control mice.

Table-6. Percent difference in bone size phenotype measured by in-vivo pQCT at midshaft tibia of 14104 mice and normal littermates

Age (weeks)	**Sex**	**Mutant (14104)[a]**			**Control (non-affected littermates)**		
		No. of mice	**Periosteal circumference[b] (mm)**	**Endosteal circumference[b] (mm)**	**No. of mice**	**Periosteal circumference (mm)**	**Endosteal circumference (mm)**
3	Male	$n = 45$	2.60 ± 0.16	1.32 ± 0.15	$n = 65$	3.06 ± 0.18	2.03 ± 0.18
	Female	$n = 37$	2.56 ± 0.12	1.26 ± 0.16	$n = 62$	3.08 ± 0.21	2.08 ± 0.22
6	Male	$n = 40$	3.12 ± 0.16	1.40 ± 0.14	$n = 46$	3.86 ± 0.21	2.03 ± 0.18
	Female	$n = 29$	2.97 ± 0.16	1.27 ± 0.15	$n = 41$	3.72 ± 0.22	2.13 ± 0.15
10	Male	$n = 39$	2.49 ± 0.23	1.41 ± 0.14	$n = 39$	4.38 ± 0.19	2.26 ± 0.12
	Female	$n = 32$	3.21 ± 0.20	1.22 ± 0.17	$n = 35$	4.06 ± 0.18	2.13 ± 0.14
16	Male	$n = 8$	3.68 ± 0.23	1.37 ± 0.15	$n = 8$	4.77 ± 0.26	2.35 ± 0.12
	Female	$n = 15$	3.34 ± 0.10	1.00 ± 0.18	$n = 7$	4.22 ± 0.11	2.15 ± 0.06

[a]Data includes mice with both $Ghrhr^{+/+}$ and $Ghrhr^{lit/+}$ genotypes.
[b]The p-values for differences in both periosteal and endosteal circumference as compared to control mice were $p < 0.01$ for all data points. Data are shown as mean ± SD.

Table-7. Phenotype of affected 1665CM mutant measured by total body DEXA scan expressed as percent difference from *Smad2*$^{+/-}$ control mice (n=25-30).

Mice (n=No of Affected Mice)*	Body Weight	Total Body BMD	Total Body BMC	Femur BMD
10-Wek Female (n=13)	10.3	6.6	10.2	5.8
10-Week Male (n=8)	17.3	10.6	18.1	11.0
16-Week Female (n=10)	16.2	11.4	15.8	10.7
16-Week male (n=7)	20.9	10.7	17.4	16.0

All values were statistically significant from *Smad2*$^{+/-}$ control mice ($p<0.01$)
*Total number of 1665CM *Smad2*$^{+/-}$ mice screened was 55.

Table 8. Phenotype of affected 1665DF mutant measured by total body DEXA scan expressed as percent difference from *Smad2*$^{+/-}$ control mice (n=25-30).

Mice (n=No of Affected Mice)*	Body Weight	Total Body BMD	Total Body BMC	Femur BMD
10-Wek Female (n=10)	21.5	11.7	20.3	15.2
10-Week Male (n=7)	20.1	12.2	20.8	12.8
16-Week Female (n=9)	22.1	14.0	24.3	15.7
16-Week male (n=7)	24.6	12.7	20.2	15.2

All values were statistically significant from smad2/+ control mice ($p<0.01$)
*Total number of 1665DF *Smad2*$^{+/-}$ mice screened was 65.

Table-9. *Ex vivo* measurement of femur midshaft bone size phenotypes by histology.

Phenotype	Sex	14104 (n=4-5) (Mean±SD)	Control (n=4-5) (Mean±SD)	% Diff
Total Bone Area (mm^2)	Male	1.088±0.120*	1.893±0.062	-43
	Female	1.052±0.039*	1.710±0.062	-38
Endosteal Circumference (mm)	Male	2.663±0.138*	3.813±0.098	-30
	Female	2.706±0.156*	3.712±0.139	-27
Periosteal Circumference (mm)	Male	3.938±0.198*	5.078±0.076	-22
	Female	3.798±0.089*	4.788±0.132	-22
Marrow Area (mm^2)	Male	0.506±0.062*	1.095±0.046	-54
	Female	0.485±0.044*	1.028±0.050	-53

*$p<0.001$ vs control

Table-10. *Ex vivo* measurement of femur midshaft bone size phenotypes by μCT.

Phenotype	14104 (n=3) (Mean±SD)	Control (n=3) (Mean±SD)	% Diff
Total Volume (TV)	1.048±0.031***	1.776±0.021	-41
Bone Volume (BV)	0.470±0.034**	0.680±0.052	-31
BV/TV	0.448±0.023*	0.383±0.027	17
TV-BV	0.578±0.021**	1.095±0.046	-47

***p<0.001, **p<0.01, *p<0.05 vs control

Table-11. Trabecular bone measurement of femur metaphysis by histology and μCT.

Method	Phenotype	14104 (n=3-4) (Mean±SD)	Control (n=3-4) (Mean±SD)	% Diff
Histology	Total Tissue Area (TV)	0.679±0.122*	1.015±0.195	-33
	Bone Area (BV)	0.071±0.016**	0.146±0.028	-52
μCT	Trabecular Number	1.89±0.33	2.27±0.51	-17
	Trabecular Thickness	0.049±0.0023	0.0579±0.0072	-15

**p<0.01, *p<0.05

Table-12. Functional positional candidate genes identified in the 14104 mutant locus.

Symbol, Name	Known Molecular or Cellular Function	Skeletal Phenotype of Targeted Disruption
Axin2, Axin 2	Negatively regulates expansion of osteoprogenitors and maturation of osteoblasts	Skeletal defects, craniosynostosis
Map2k6, mitogen activated protein kinase 6	Activation of MAPK activity	Not Characterized
Sox9, SRY-box containing gene 9	Transcriptional regulation of osteoblast	Skeletal dysplasias
Rab37, member of RAS oncogene family	Small GTPase mediated signal transduction	Not Characterized
Grb2, growth factor receptor bound protein 2	Intracellular signaling cascade, Negative regulator of osteoclastogenesis and osteoblast differentiation	Enhanced Bone Volume, Craniofacial
Itgb4, Integrin beta 4	cell adhesion and cell survival	Not Characterized
Cbx2, chromobox homolog 2 (Drosophila Pc class)	chromatin assembly or disassembly	Mutations cause malformations of the axial skeletal
Socs3, Suppressor of cytokine signaling	Involved in GH signaling (JAK2)(STA5) in osteoblasts	Not Characterized
Timp2, tissue inhibitor of metalloproteinase 2	negative regulation of cell proliferation, regulation of cAMP metabolism	Not Characterized

FIGURES

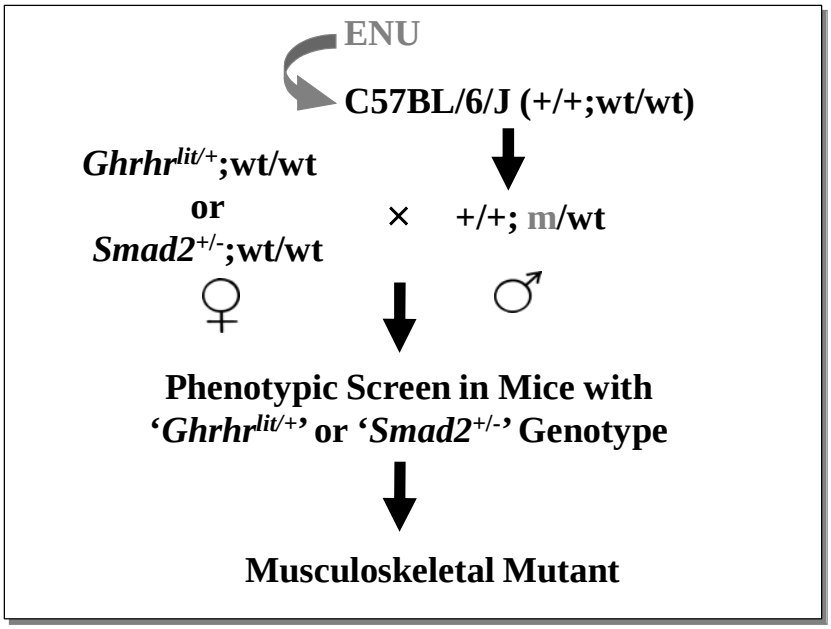

Figure – 1. Design of the ENU screen to identify modifier mutations that interact with the GH and TGF-β signaling pathways. To identify modifiers, we used a growth hormone releasing hormone receptor (*Ghrhr*) mutant mice (mutation denoted by 'lit' allele) and mothers against decapentaplegic homolog 2 (*Smad2*) knock out heterozygous mice (denoted by $Smad2^{+/-}$ allele). The ENU injected wild type C57BL/6J males were bred with $Ghrhr^{lit/+}$ and $Smad2^{+/-}$ females. The F1 progeny with $Ghrhr^{lit/+}$ and $Smad2^{+/-}$ genotypes were candidate for modifier mutations. For clarity, the wild type alleles are denoted as two separate symbols '+' and 'wt' for *Ghrhr* or *Smad2* locus and ENU mutation is denoted as 'm' locus, respectively.

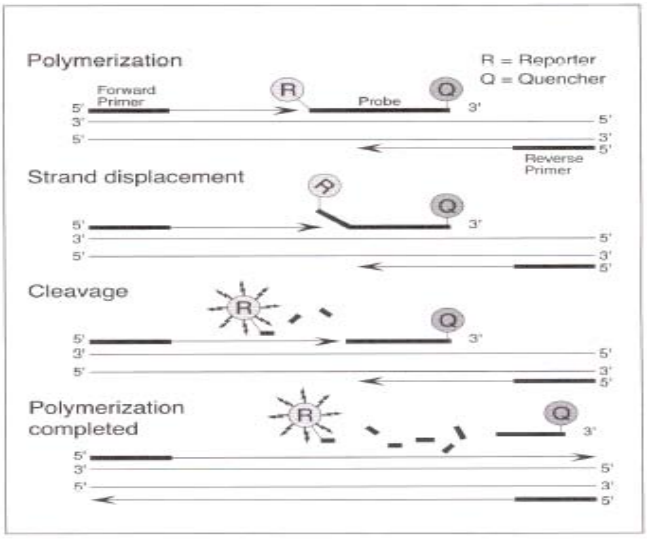

Figure – 2. PCR Amplification and detection with fluorrogenic probes in the 5' nuclease assay.

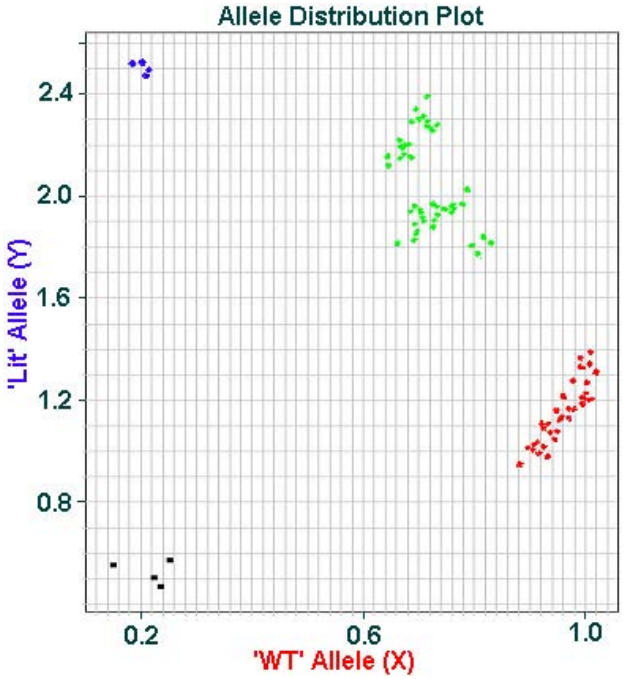

Figure – 3. Allele X is the wild type allele (shown in red), and Allele Y is the Mutant allele (*lit*) (shown in blue). The wild type probe has a different reporter dye than the mutant probe. The heterozygotes (green) have both reactions taking place in the well. Black dots indicate non-template controls.

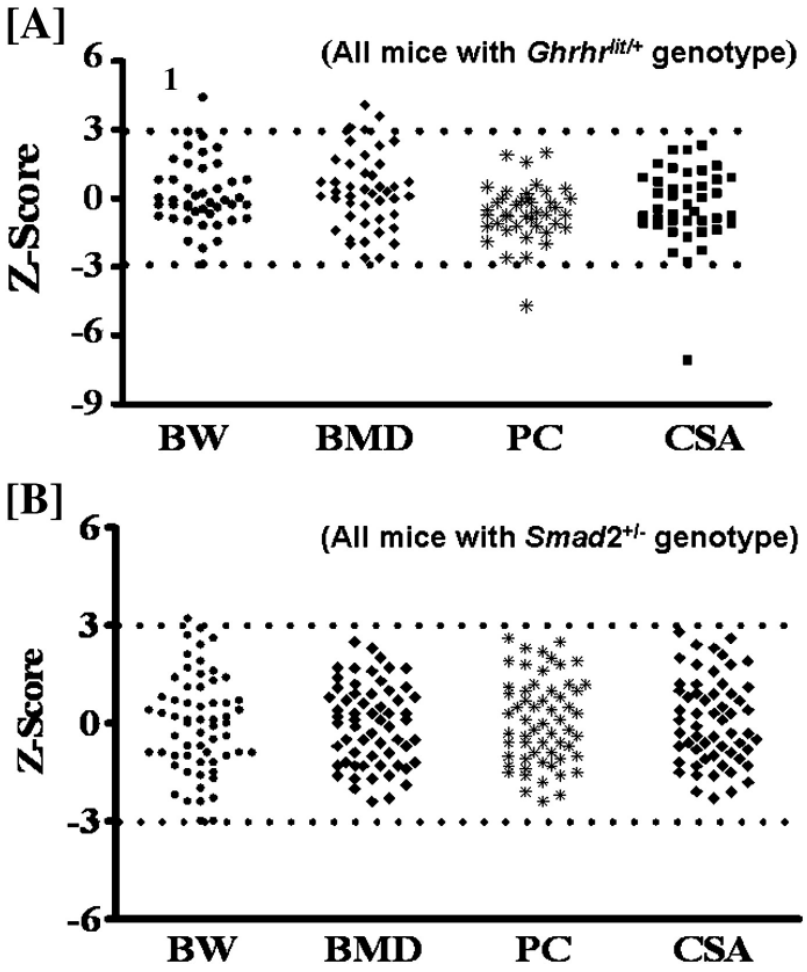

Figure – 4. Representative phenotype data for the sensitized screen in *Ghrhr*$^{lit/+}$ and *Smad2*$^{+/-}$ background. Bone density and bone size phenotypes are shown as *Z*-score, which indicate differences in a phenotype in terms of SD units as compared to control mice (in this case, *Ghrhr*$^{lit/+}$ and *Smad2*$^{+/-}$ mice). The broken horizontal lines indicate our cut-off levels for identifying outlier mice. Data points outside 3 SD units potentially represent potential phenotypic deviants. Several phenotypic deviants were backcrossed with control mice for confirmation of inheritable mutation. BW = Body weight, BMD = Total body bone mineral density, PC = Periosteal circumference, CSA = Cross-sectional area, EC = Endosteal circumference.

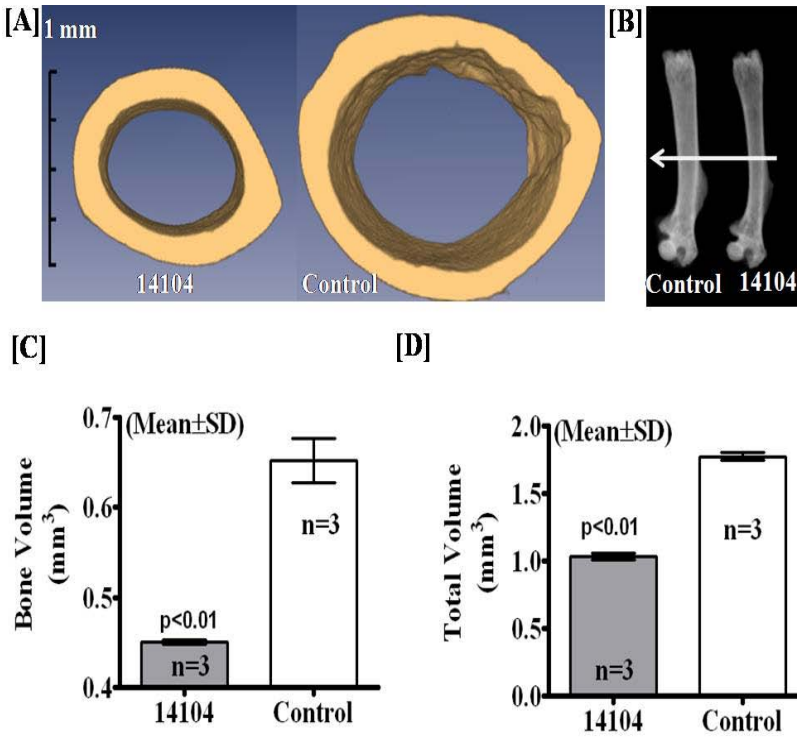

Figure-5. Cortical bone parameters computed from μCT measurements at midshaft femurs from mutant (14104) and control mice. A. Mutant mice have about 30% lower bone size as compared to normal littermates. B. The X-ray image of femur from mutant and control mice shows significantly slender bones with 17-23% lower periosteal circumference ($p<0.001$) C-D. The total volume and bone volume measured by μCT were 42% and 31% lower, respectively, as compared to control.

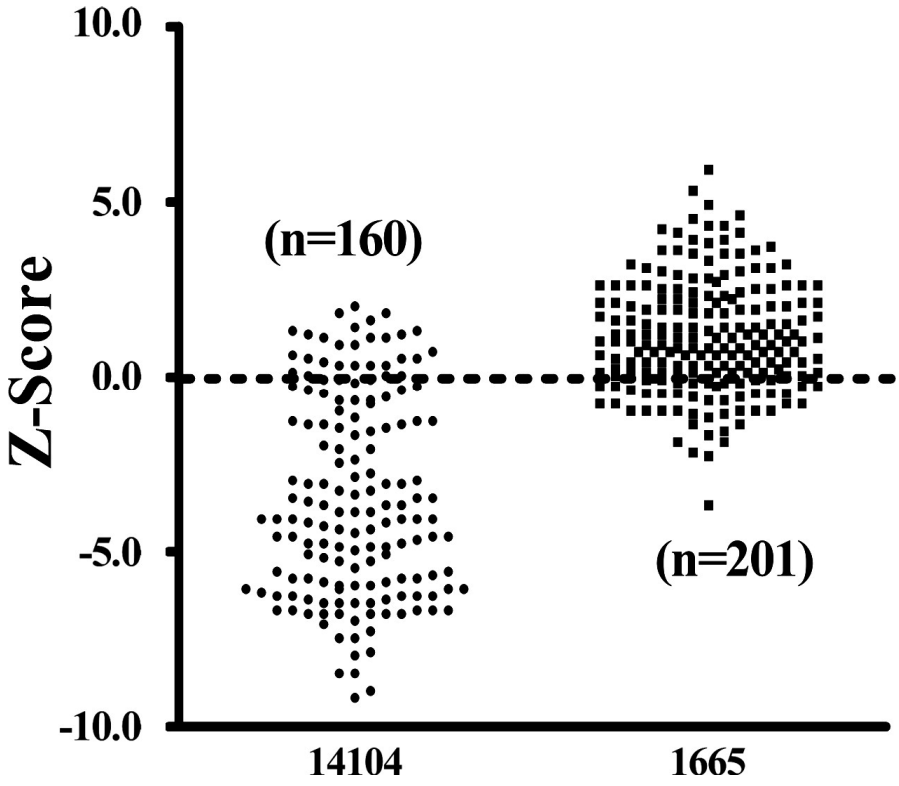

Figure – 6. Phenotype data for two backcrossed mutant lines. The *x*-axis shows the ID of the two lines that were successfully backcrossed to produce several litters. The *y*-axis shows phenotype data converted to Z-score. Line 14104 was produced in GH deficient background and cross-sectional area of midshaft tibia is shown as mutant phenotype. Line 1665 was produced in *Smad2*$^{+/-}$ background and total body bone density phenotype was shown as Z-score. Each data point represents one backcross mouse. All mice produced in the backcross, including non-affected littermates (> 50%), are shown for each line.

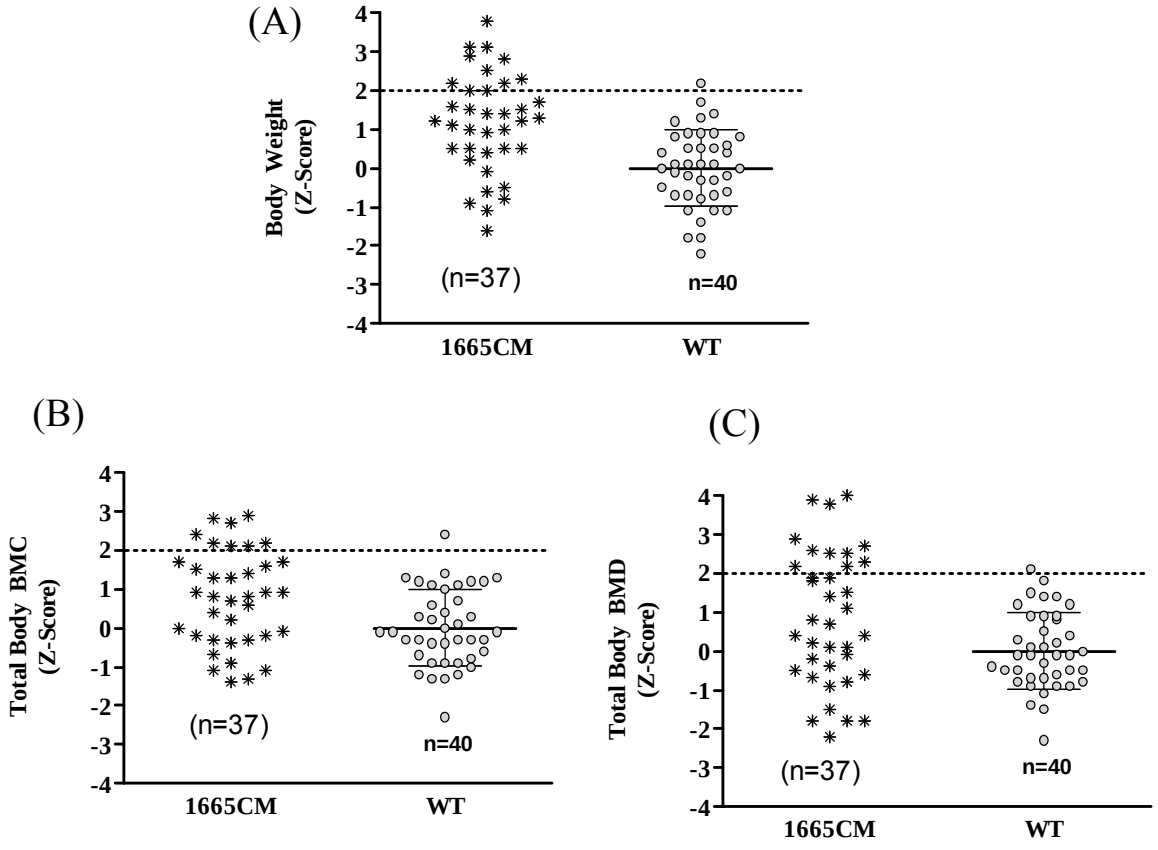

Figure – 7. Phenotype data from 16-week old mutant progeny generated from backcross of a mutant mouse, 1665CM, identified in sensitized screening in *Smad2*$^{+/-}$ background. The progeny from 1665CM mutant shows 10-17% higher body weight (A) phenotype. In addition to body weight, the mutant progeny has 10-18% higher total body BMC (B) and 7-10% higher total body BMD (C). Each data point represents one mouse and both affected and non-affected littermates are shown under 1665CM progeny. The horizontal line indicates 2SD cut-off for identifying mutant mice from non-affected littermates. WT=Wild Type (*Smad2*$^{+/-}$) (data shown as Mean±SD).

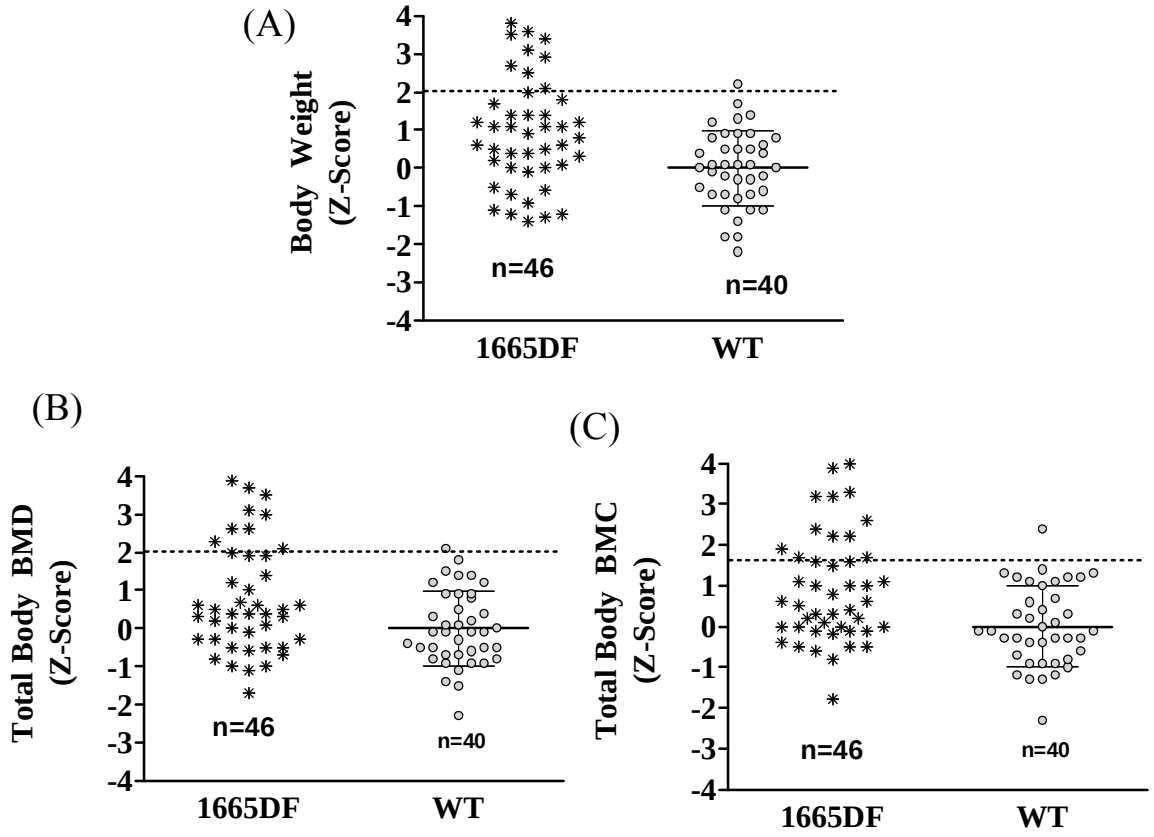

Figure – 8. Phenotype data from 16-week old mutant progeny generated from backcross of a mutant mouse, 1665DF, identified in sensitized screening in *Smad2*$^{+/-}$ background. The progeny from 1665CM mutant shows 20% high body weight (A) phenotype. In addition to body weight, the mutant progeny have 15-16% higher total body BMD (B) and 20-25% higher total body BMC (C). Each data point represents one mouse and both affected and non-affected littermates are shown under 1665DF progeny. The horizontal line indicates 2SD cut-off for identifying mutant mice from non-affected littermates. WT=Wild Type (*Smad2*$^{+/-}$) (data shown as Mean±SD).

(A)

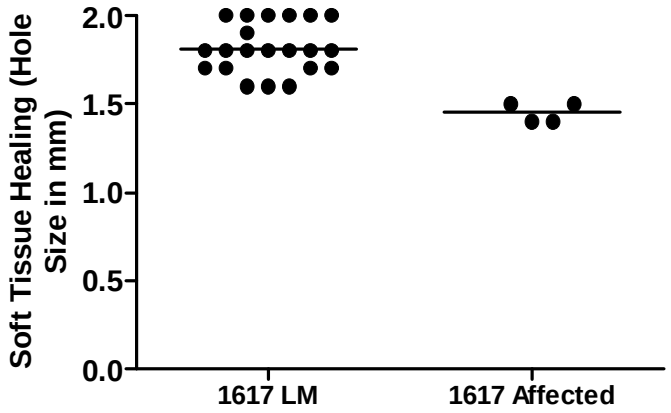

(B)

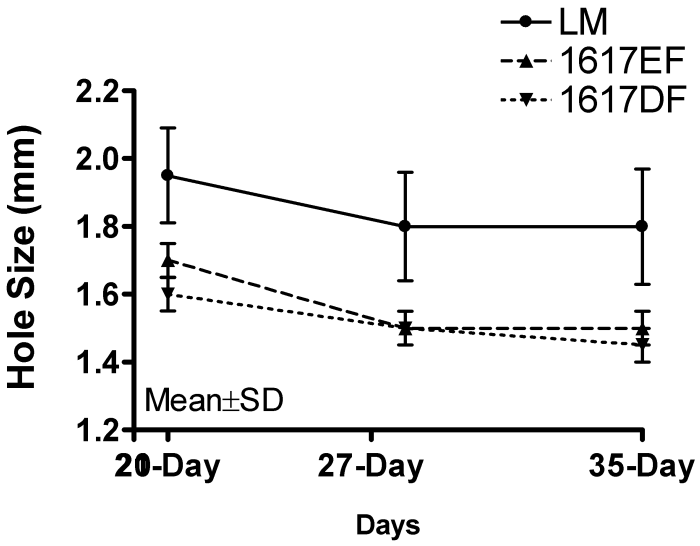

Figure – 9. Soft tissue regeneration phenotype data from 6-week-old mutant progeny (A) generated from backcross of mutant mice identified in sensitized screening in *Smad2*$^{+/-}$ background. The bottom figure shows the tissue healing capacity of mutant mice measured at 3-, 4-, and 5-weeks after a 2 mm hole punched in ear lobe (B). The affected mice have approximately 20% more healing as compared to non-affected littermates (LM) or WT control (data not shown).

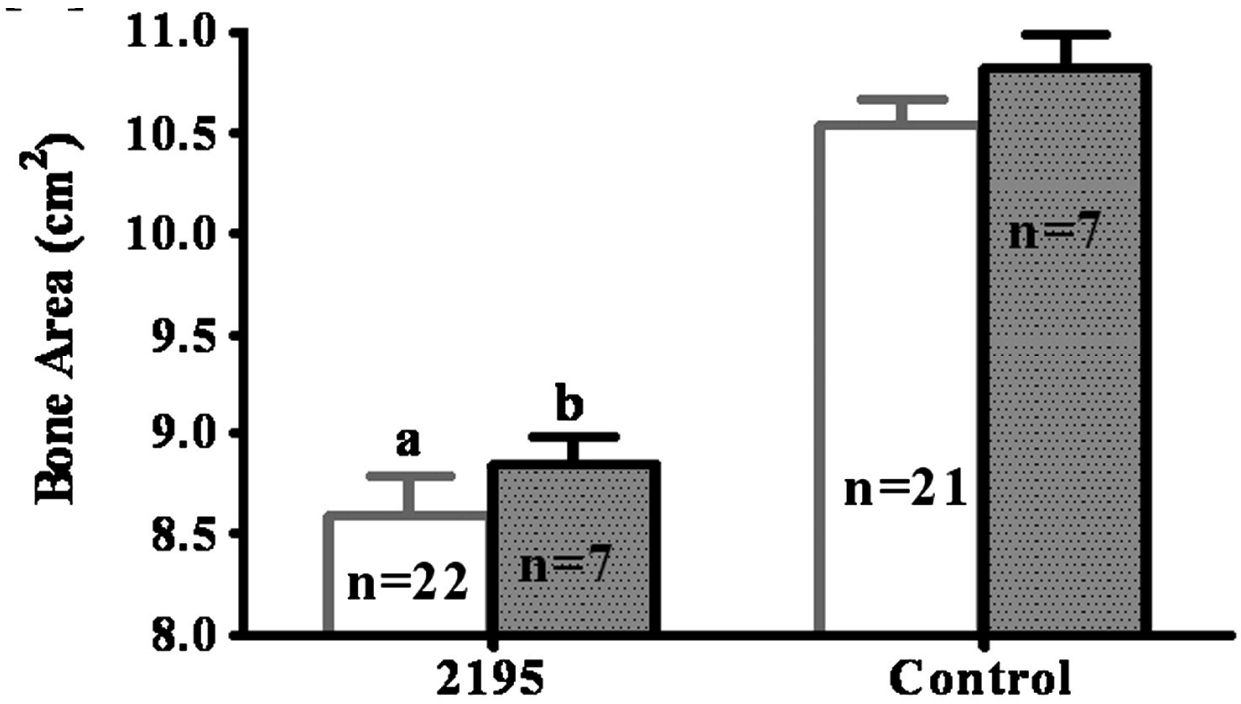

Figure-10. A dominant mutation identified in *Smad2*$^{+/-}$ background with decreased total body area (ID 2195). The mutant phenotype is expressed in both *Smad2*$^{+/+}$ and *Smad2*$^{+/-}$ genetic backgrounds. The mutant phenotype was not significantly influenced by the loss of *Smad2* allele as indicated by Post-Hoc analysis using two-way ANOVA (p = NS for interaction). a = $p < 0.001$ vs control, b = $p < 0.001$ vs control and $p > 0.05$ vs 2195 mice with *Smad2*$^{+/-}$ genotype.

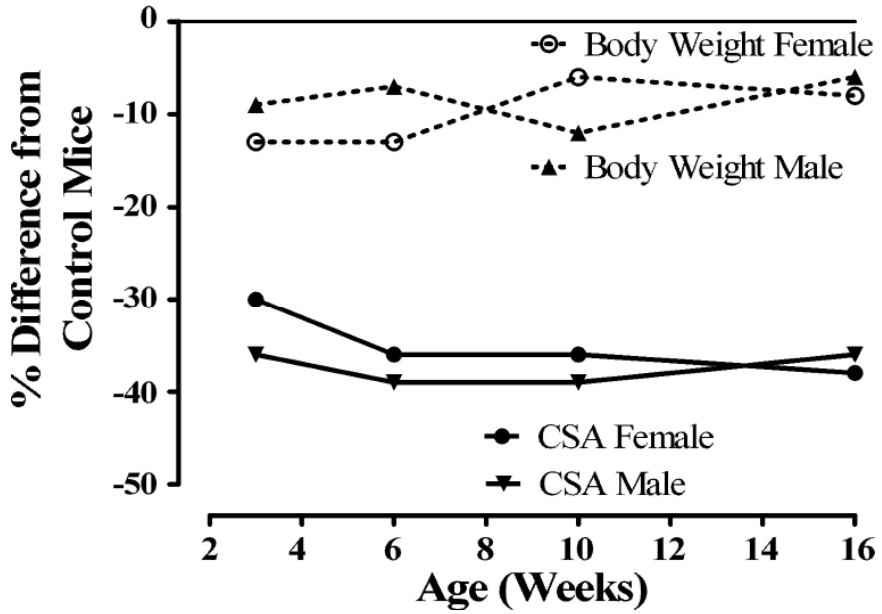

Figure – 11. Longitudinal analysis of body weight and bone size phenotypes in mice from mutant Line 14104. The data on *x*-axis shows age of the progeny generated from the 14104 mutant mice and data on *y*-axis shows percent difference in phenotypes as compared to non-affected littermates at same age. The body weight of mutant mice was 6–13% lower as compared to non-affected littermates, whereas, the cross-sectional area (CSA) was 30–40% decreased ($p < 0.001$) in mutant mice. These data show that changes in bone size were significantly larger than those in body weight (number of mice for various groups were 6–22). To simplify the figure, data from mice with genotype *Ghrhr*$^{lit/+}$ were used even though mice with *Ghrhr*$^{+/+}$ genotypes were also affected.

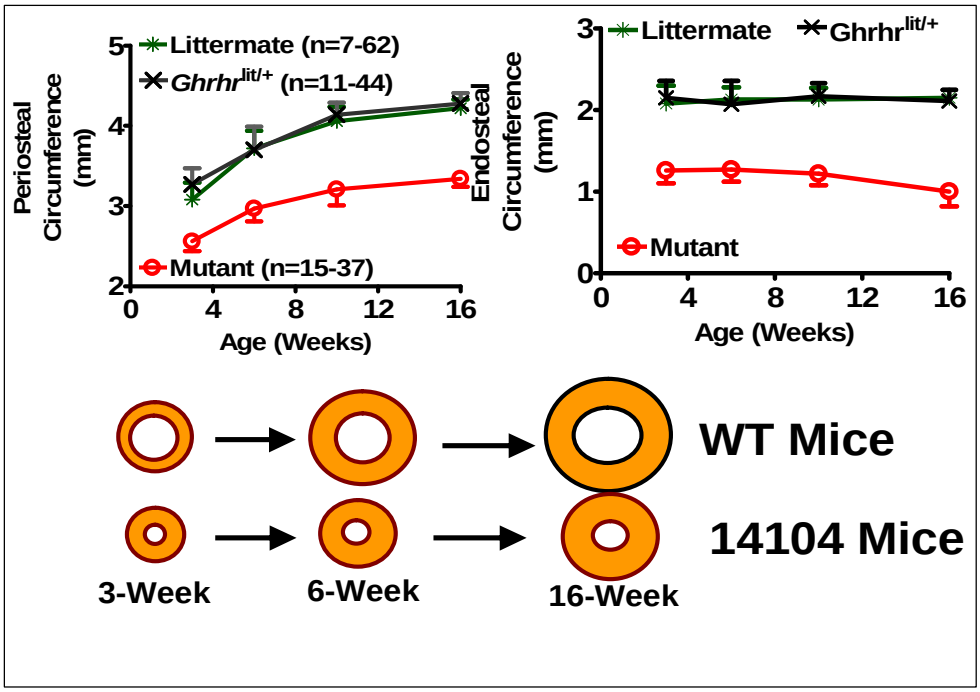

Figure-12. Periosteal (PC) and endosteal circumference (EC) at midshaft tibia of female 14104M mutant mice as compared to the unaffected littermates and non-mutagenized Ghrhr$^{lit/+}$ mice. The bottom illustration shows how these differences in PC (-20%) & EC (-45%) decreases the cross-sectional area but increased cortical thickness relative to bone size. Mean±SD

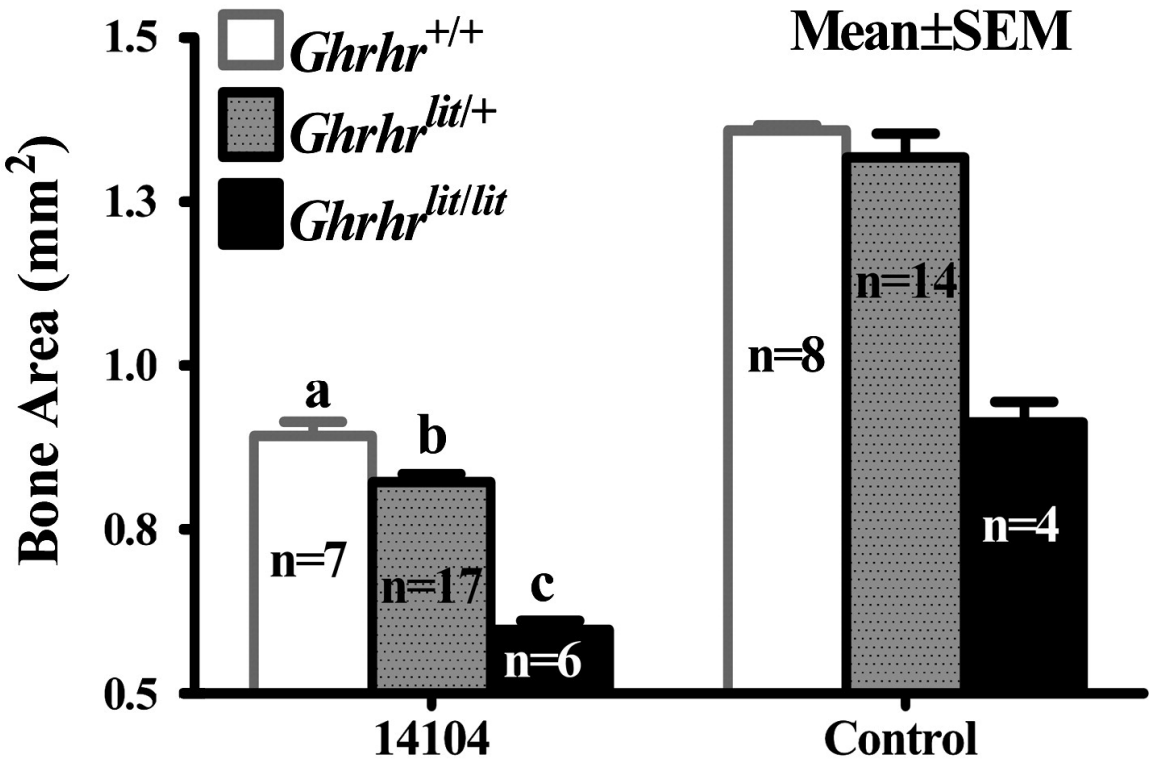

Figure-13. Amplification of the magnitude of the mutant phenotype in the presence of one copy of disrupted *Ghrhr* gene (*Ghrhr*$^{lit/+}$). The cross-sectional area of midshaft tibia from 6-week old female 14104 mutant mice is shown in the presence of *Ghrhr*$^{+/+}$ or *Ghrhr*$^{lit/+}$ genotypes. Although the bone size phenotype is also expressed in *Ghrhr*$^{+/+}$ genotype, the magnitude of bone size phenotype is significantly influenced by the presence of "lit" allele as indicated by two-way ANOVA. Post-Hoc analysis by two-way ANOVA indicates that *Ghrhr*$^{lit/+}$ genotype significantly ($p < 0.02$ for interaction) decreased the bone size. The differences in CSA between *Ghrhr*$^{+/+}$ and *Ghrhr*$^{lit/+}$ in control mice were not statistically significant. a = $p < 0.001$ vs *Ghrhr*$^{+/+}$ and *Ghrhr*$^{lit/+}$ control and $p < 0.05$ vs 14104 *Ghrhr*$^{lit/+}$ and *Ghrhr*$^{lit/lit}$ 14104 mice, b = $p < 0.001$ vs all control mice, c = $p < 0.001$ vs all other groups.

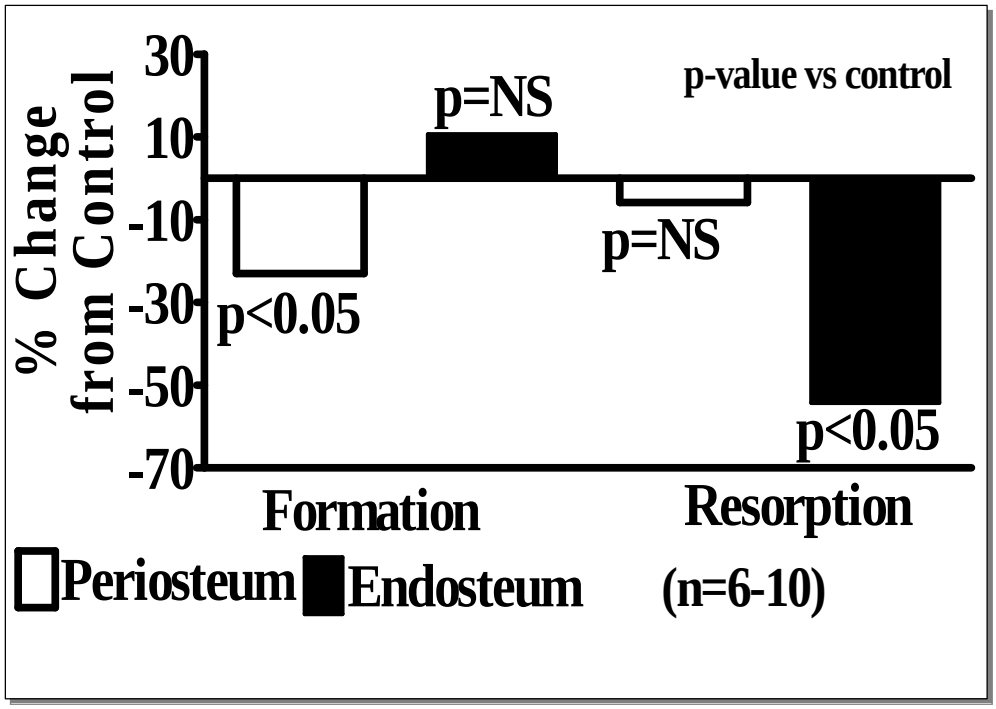

Figure-14. Bone formation rate (BFR) at femur midshaft measured by dual labeling and bone resorption (BR) measured by TRAP stained surface (at midshaft humerus). The decreased periosteal perimeter is due to significantly reduced bone formation rate per bone surface. However, the decreased endosteal perimeter appears to be mainly due to decreased bone resorption. (Control-Non Affected Littermates of 14104 mutant mice).

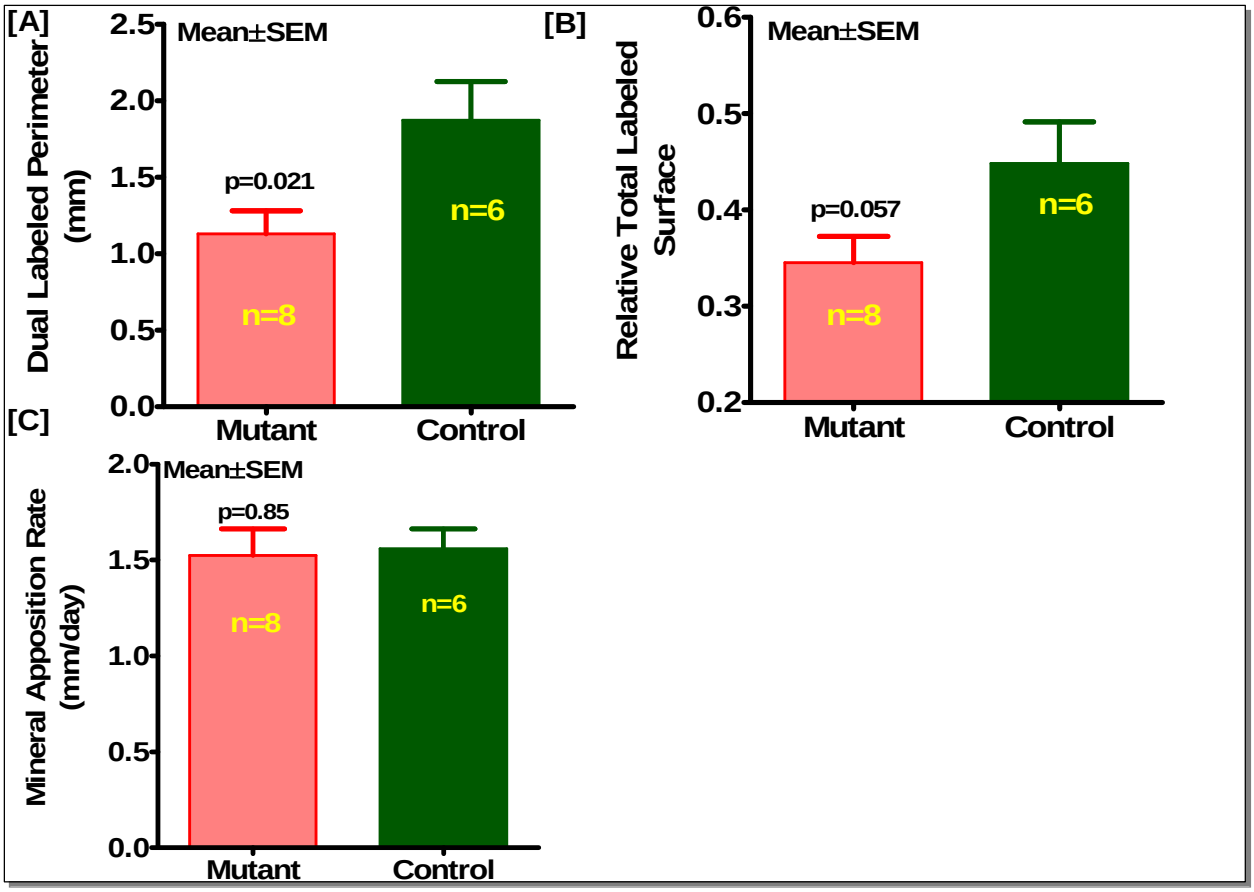

Figure-15. Histomorphometric assessment of reduced bone formation rate at the periosteal surface. Dynamic labeling was performed in 10-12 week old mice and data from male female mice were combined. The total labeled surface (A) and labeled surface relative to total bone surface (RTLS) (B) were lower in the mutant mice as compared to control. Whereas, the mineral apposition rate was not significantly altered in mutant mice as compared to the control (C).

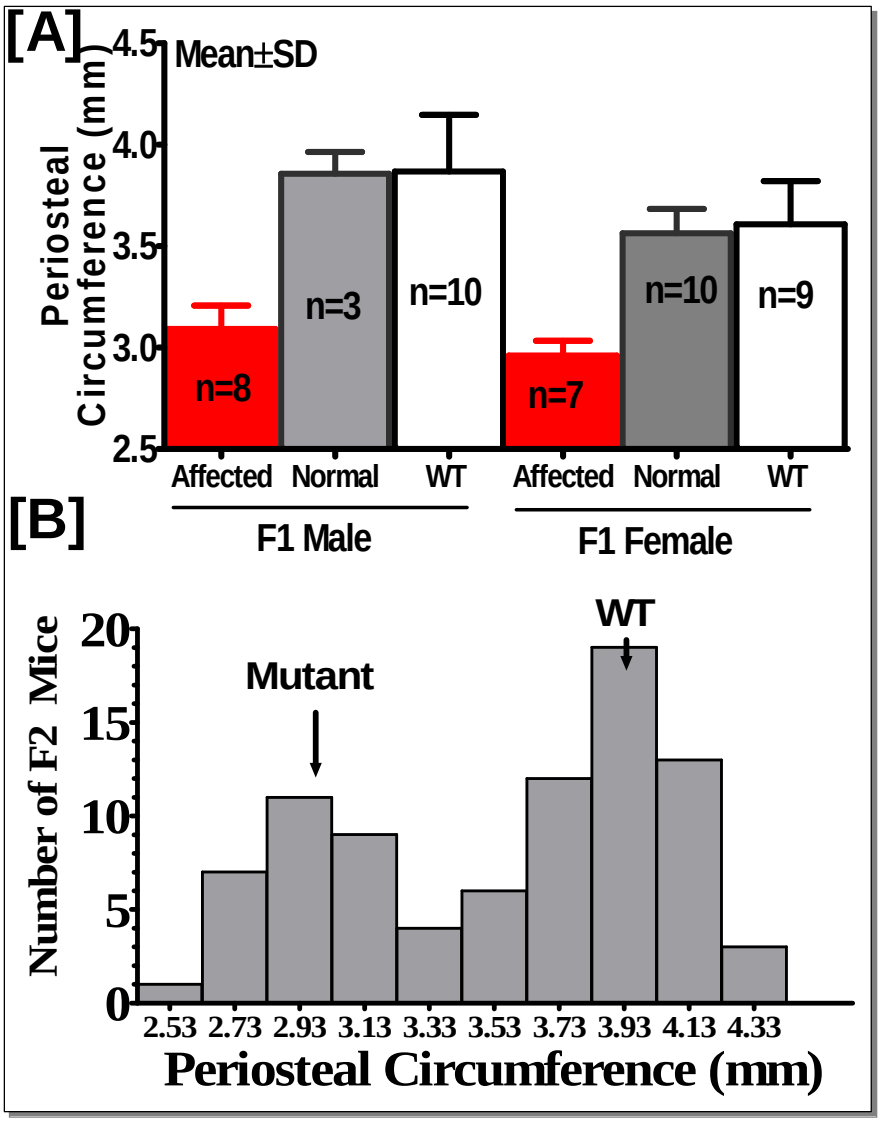

Figure-16. [A] Periosteal circumference (PC) of 6-week old F1 mice produced from breeding the 14104 mutant mice (B6) with DBA/2J strain of mice. The F1 mice had 15-20% lower PC as compared to the normal littermates and wild type B6/DBA F1 mice. These data show that mutant phenotype is well expressed in B6(14104)DBA F1 mice. [B] Frequency histogram of periosteal circumference measured in 6-week old 14104(B6)DBA female F2 mice. The phenotype distribution shows two populations with mutant and WT allele, which enabled us to identify mutant mice for pooled DNA analysis for mapping.

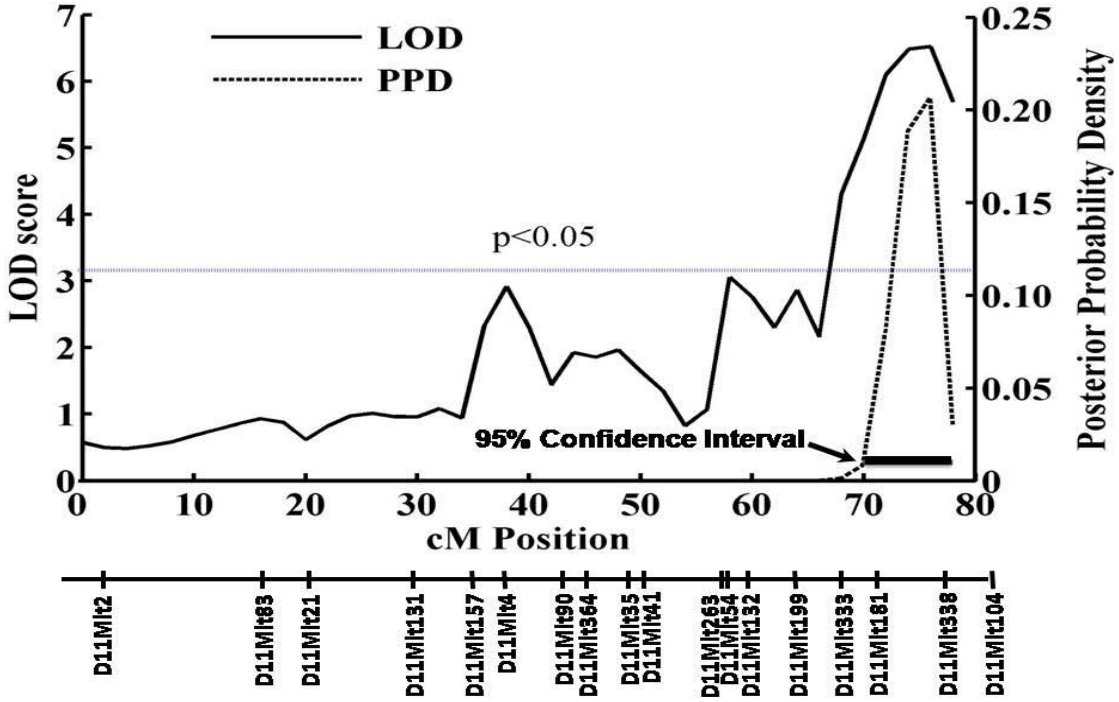

Figure-17. LOD score and posterior probability density plots (which is a likelihood statistic that gives rise to the 95% confidence intervals) for the chromosome 11 locus that influences the periosteal circumference at midshaft femur of 6-week old (B6×DBA)F2 mice. Locations of the markers are shown on the x-axis. The peak was flanked by markers D11Mit333 (66 cM) and D11Mit104 (79 cM). However, the posterior probability density plots showed the 95% confidence interval as 70-79 cM (indicated by thick black horizontal bar).

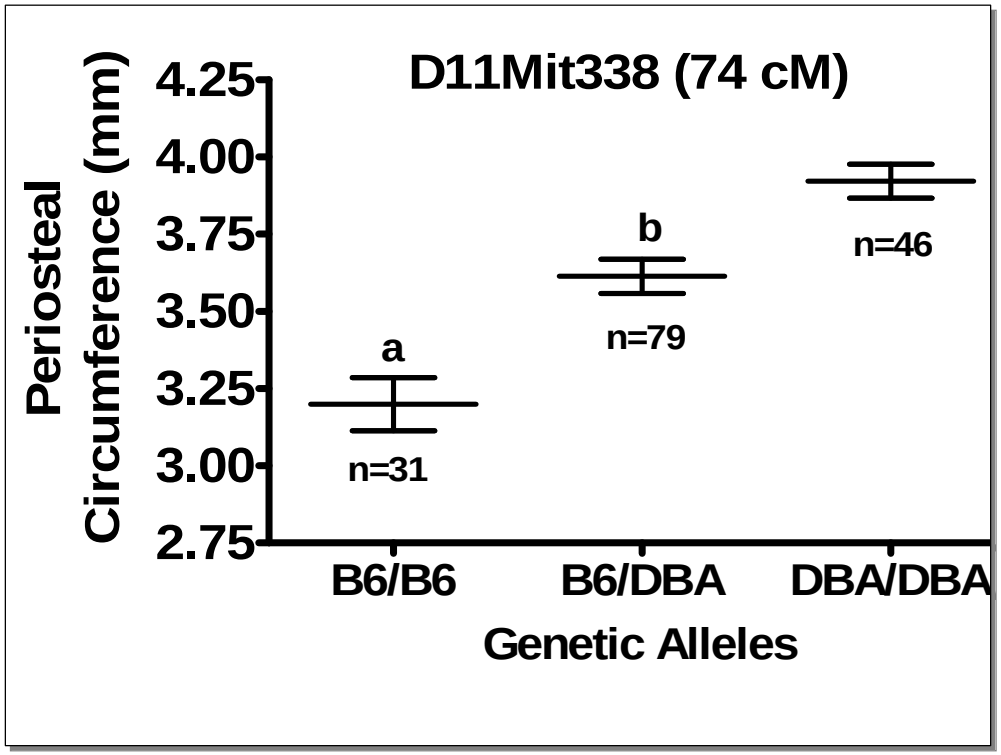

Figure-18. Allelic contribution of the closest marker located near the peak on chromosome 11 locus harboring mutant gene. B6/B6 represents homozygosity for B6 alleles (mutant strain), B6/DBA represents homozygosity for B6 alleles, and heterozygosity at the locus is represented by B6/DBA. Error bars represent SEM. a=$p<0.001$ vs DBA/DBA, b=$p<0.05$ vs both B6/B6 and DBA/DBA (by ANOVA) cM, centimorgan.

Project 3. Development of Transgenic Approaches Using BAC Clones to Identify Candidate Genes for Musculoskeletal Phenotypes

INTRODUCTION

The primary goal of our studies is to localize chromosomal regions and subsequently identify genes responsible for various musculoskeletal phenotypes including bone density, fracture repair and soft tissue regeneration, and evaluate the molecular function of these genes. We have been using two main strategies to identify these genes for musculoskeletal system. They are: 1) Ethylnitrosourea (ENU) chemical mutagenesis to induce mutant mice with significant musculoskeletal alteration and 2) Genetic linkage analysis to discover genetic components of quantitaive trait loci (QTL) that contribute to phenotypic changes. In our previous studies, we have made significant progress with both ENU and QTL approaches, and identified several mutant mouse strains and genetic loci that are associated with phenotypes of small bone size, high bone density and soft tissue regeneration. However, these regions contain dozens of intact genes with a large piece of genomic DNA in several overlapping bacterial artificial chromosomes (BACs) and need to be further tested for their functions. The aim of this project is to develop a gene transfer systems of BAC or plasmid to deliver a testing gene as large as 150-kb into bone cells to "rule out" or "rule in" a genetic component contributing to the phenotype of interest. To achieve our objective of developing an optimal protocol for efficient transfer of BAC clones or testing gene into mouse cells in vitro for functional evaluation, we proposed to use an improved infectious BAC (iBAC) technology mediated by the herpes simplex virus type 1 (HSV-1) amplicon to deliver a genomic locus containing intact BMP-2 gene into MC3T3-E1 cells (12). We modified our retrofitting strategies to make a construct more useful by utilizing a vector containing multiple marker genes. We believe that the iBAC offers a rapid and simple method of BAC DNA transfer for functional genomic studies. We also undertook studies to clone the complete coding sequence of candidate genes into the HSV amplicon-based expression vector and package them into infectious viral particles to deliver the transgene into bone cells (5, 12). We established this gene transfer approach for the following reasons. 1) Some of our test genes may contain large introns (>100 kb) such that the size of intact gene including introns and exons could be beyond limitation of HSV packaging capacity (e.g. >150 kb). 2) The BAC clone containing candidate gene may be not available in the mouse genome databases. 3) The BAC clone may encode multiple alternatively spliced variants with diverse functions from a single gene. In addition, we also developed an optimal protocol of non-viral transfection technique by utilizing a modified form of "Nucleoporation" to make the delivery system safer and more feasible (7). We believe that either viral transduction or non-viral transfection of the complete coding sequence of candidate genes offers a rapid, simple alternative method of gene transfer for functional studies.

BODY

a) **Specific Objective 1:** To develop an optimal protocol for efficient transfer of BAC clones into mouse bone cells in vitro for functional evaluation using a known test gene.

In order to identify the BMP-2 gene, we modified our strategy by searching databases instead of screening a BAC clone library that we originally proposed. This is because BAC and P1 artificial chromosomes (PAC) libraries have been generated for sequencing the human and mouse genomes, and are commercially available for most genes. In addition, the commercial BAC or PAC clones contain one wild type loxp site built-in in the library vectors (e.g. pbeloBAC11, PBACe3.6, PCYPAC2, PPAC4), which allow us to retrofit any DNA sequence without further DNA manipulations. We searched the GenBank database and identified a mouse BAC library clone (clone, RP23-302H4) containing a complete 8.7-kb BMP-2 genomic DNA locus driven by a 20.5-kb native promoter within a 128.5-kb insert. We chose this clone because it contains a single BMP-2 gene with most, if not all, of the regulatory elements in the

promoter, introns and 3' non-coding regions that may regulate a physiological gene expression (1, 6). The length of the BAC clone is also within the size limits that the HSV-1 vector can efficiently package into an iBAC (9).

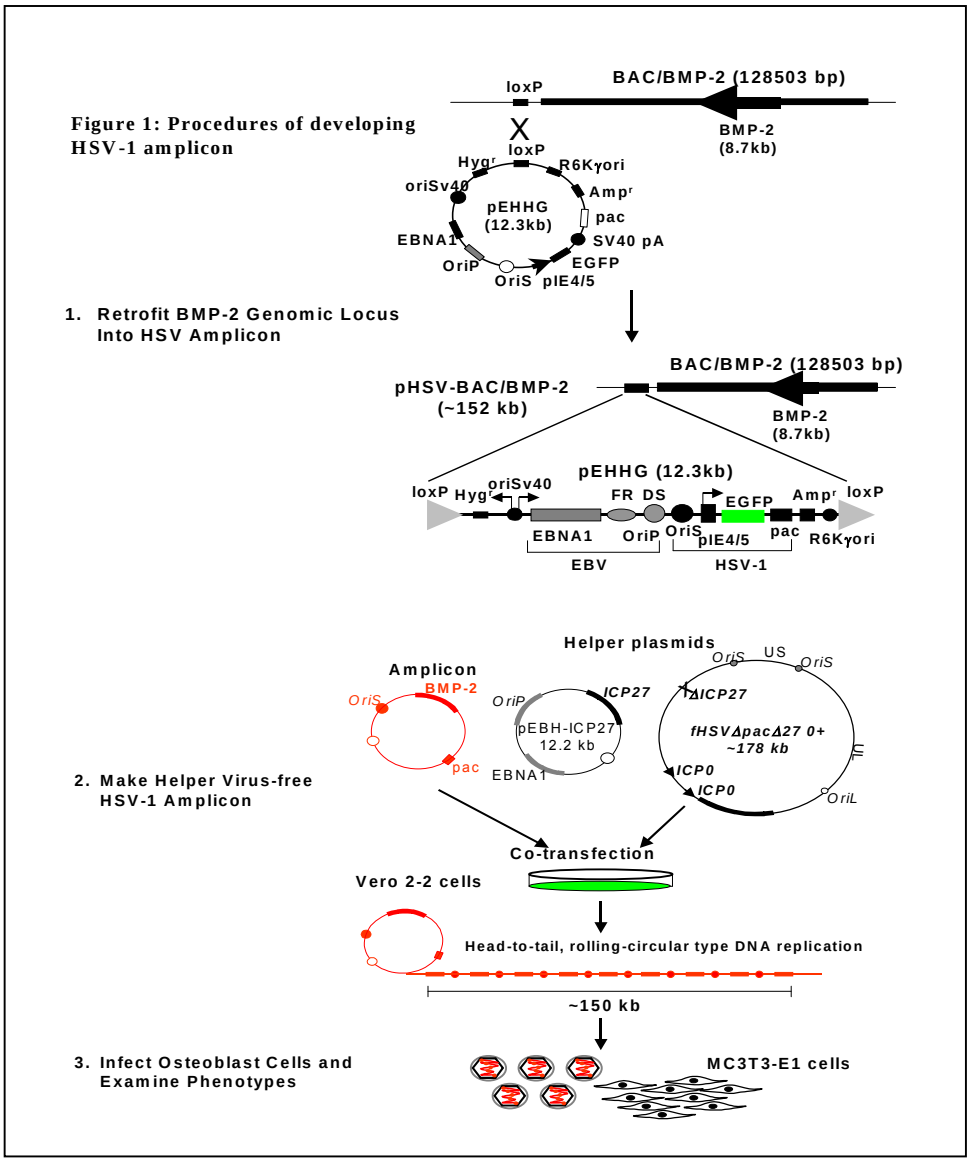

We chose pEHHG that consists of HSV-1 amplicon elements, enhanced green fluorescent protein (GFP), hygromycin resistance gene, Epstein-Barr virus (EBV) episome retention cassette, R6K bacterial replication origin, and a *loxP* site as a retrofitting vector for several reasons: 1) the GFP marker facilitates evaluation of the transfection or transduction efficiency in living cells, and GFP-positive cell sorting by Flow cytometry, if necessary, without drug-selection; 2) the hygromycin resistance gene allows us to select antibiotic resistant cells (e.g. stable cell line containing BAC transgenes) when chemical transfection is applied; 3) the EBNA-1 episomal cassette from the Epstein Barr virus allows long-term retention and high level of position-independent expression of BAC transgenes as mini-chromosomes in the host cells (9, 13).

A detailed protocol of our study was illustrated in **Figure 1**. Briefly, an aliquot of 35 µl electro-competent cells containing BAC/BMP-2 (RP23-302H4) was mixed with 10 ng each of pEHHG and pCTP-T plasmid DNA, and the mixture was transferred into 0.1-cm gap width electroporation cuvette. After 5 minutes incubation on ice, the cells were electroporated with 25 µF at 1800 V using a Gene Pulser, and then transferred into a 15-ml conical tube containing 500 µl SOC with 20 µg chlortetracycline, and incubated at 30 ^{o}C with rigorous shaking for 1 hour. An aliquot of 100 µl of the bacterial culture was transferred into a new 15-ml tube containing 20 µg/ml chlortetracycline, 100 µg/ml ampicillin, and 20 µg/ml chloramphenicol in 900 µl SOC, and incubated at 30 ^{o}C with shaking for another 3 hours. Subsequently, 50-100 µl of the bacterial culture was plated on LB plates containing 100 µg/ml ampicillin and 20 µg/ml chloramphenicol, and incubated overnight at 43 ^{o}C. We used a Cre/loxP-based retrofitting method to convert the BAC/BMP-2 with the pEHHG to generate a 152-kb construct of pHSV-BAC/BMP-2 (**Figure 2A**) (9**, 13**). DNA of individual clones was purified, and verified by PCR using specific primers to BMP-2 and GFP to confirm the presence

of two genes within a single pHSV-BAC/BMP-2 construct (**Figure 2B**). Thus the retrofitted BAC can be either transfected into osteoblast cells or packed into iBAC for functional testing.

We then packaged HSV amplicon into infectious virion as described in the diagram (**Figure 1**). We plated Vero 2-2 cells (10^6) in a 60-mm dish. After 18 hours, the cells were co-transfected with 2.0 μg pHSV-BAC/BMP-2 or pEHHG, 0.2 μg pEBHICP27, and 2 μg fHSVΔ-pac, Δ-27, 0+ using LipofectAMINE Plus for 4 hours. The cells were scraped into the supernatant 60 hours post infection, frozen and thawed once, sonicated for 1 minute and centrifuged at 3,500 r.p.m. for 15 minutes. The supernatant was then concentrated through a 25% sucrose by ultracentrifuging, and the amplicon pellet was resuspended in Hank's buffered salt solution. The purified HSV-1 amplicon was tittered in Vero 2-2 cells by counting the number of GFP positive cells after 24 hours infection. Typically, the titration of HSV-1 amplicon stocks was around 5 x 10^6 to 10^7 GFP transducing units/ml. After 24 hours, the cells were infected at a multiplicity of infection (MOI) of 5 with HSV-1 amplicon. After 6 hours infection, the medium was removed, and fresh medium was added to the cells. Twenty-four hours after infection, the GFP reporter gene was expressed in most of MC3T3-E1 cells transduced with either an HSV-1 mock (**Figure 3C**) or an HSV-BAC/BMP-2 amplicon (**Figure 3D**). Flow cytometry analyses revealed that 84% of the osteoblast cells transduced with HSV-1 mock amplicon expressed GFP (**Figure 3E**) and 77% of the cells infected with HSV-BAC/BMP-2 virion showed GFP-positive (**Figure 3F**). To compare the efficiencies of transduction and transfection, we also transfected MC3T3-E1 cells with pEHHG and pHSV-BAC/BMP-2 (**Figure 2A**) using Lipofectamine-Plus. Only less than 5% of MC3T3-E1 cells transfected with pHSV-BAC/BMP-2 expressed GFP (**Figure 3A**) whereas approximately 10% of the cells transfected with pEHHG control vector turned green (**Figure 3A**). Obviously, the efficiency of transduction of BAC-based amplicon was at least 15-fold higher than that of lipid-based transfection (**Figure 3**).

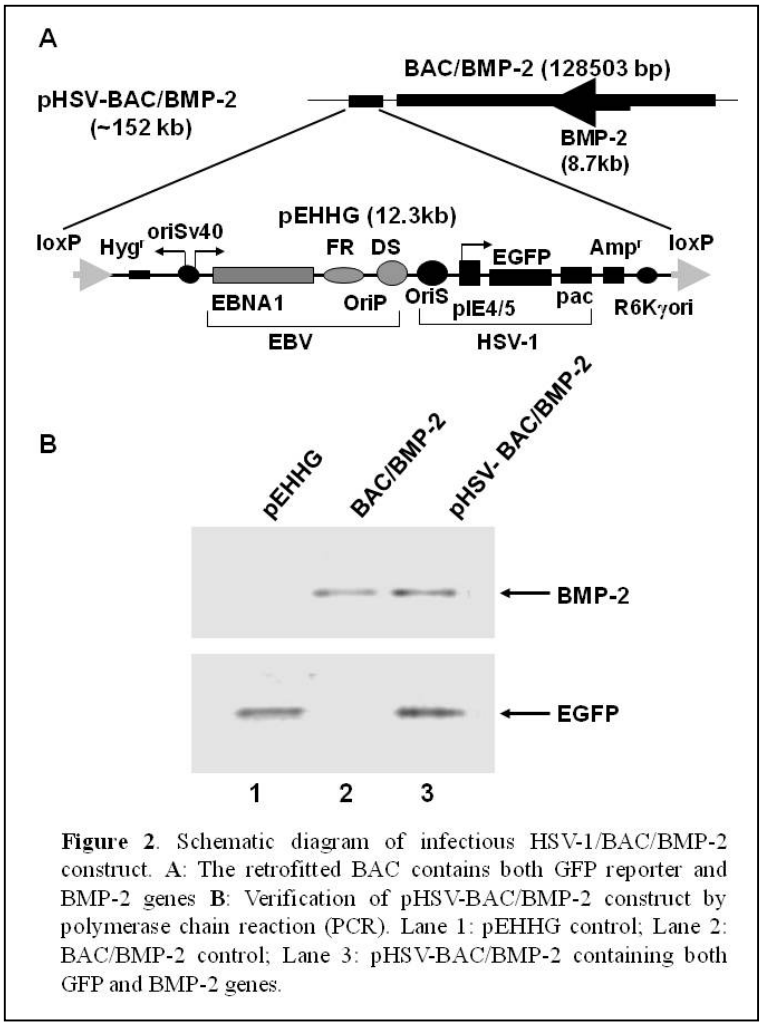

Figure 2. Schematic diagram of infectious HSV-1/BAC/BMP-2 construct. A: The retrofitted BAC contains both GFP reporter and BMP-2 genes B: Verification of pHSV-BAC/BMP-2 construct by polymerase chain reaction (PCR). Lane 1: pEHHG control; Lane 2: BAC/BMP-2 control; Lane 3: pHSV-BAC/BMP-2 containing both GFP and BMP-2 genes.

The expression of the transgene was examined by utilizing Western blot with specific antibodies against BMP-2 and GFP, and by real-time PCR with specific primers to BMP-2 and GFP genes (Figure 4). The cells infected by iBAC containing BMP-2 gene trasncripted approximately 99-fold higher of BMP-2 mRNA than the cells transduced control BAC only containing GFPgene. The amount of BMP-2 protein was estimated to be 10 ng per 10^6 cells based on Western blot analysis (**Figure 4**). However, we failed to detect BMP-2 expression in the same number of either native MC3T3-E1 cells or the cells transfected with pHSV-BAC/BMP-2 (Figure 4). To assess osteoblast phenotype in the cells expressing BMP-2 transgene, we carried out an ALP staining 9 days after transduction (**Figure 5**). Like the cells treated with 200 ng/ml recombinant human BMP-2, about 20% of the osteoblast cells were differentiated and exhibited positive ALP-staining (**Figure 5B and 5D**). No ALP-positive cells were seen in the control cells infected with

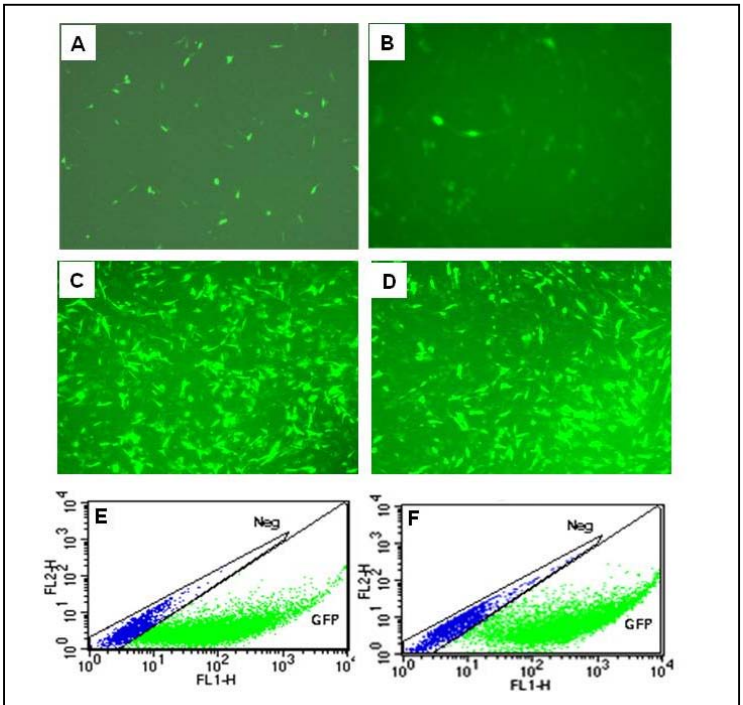

Figure 3. GFP expression in MC3T3-E1 cells transfected and transduced with HSV-1 amplicon for 24 hours A & B: the cells transfected with pEHHG and pHSV-BAC/BMP-2, respectively using optimized lipofectamine; C: the cells transduced with infections HSV-1 mock amplicon; D: the cells transduced with infections HSV-

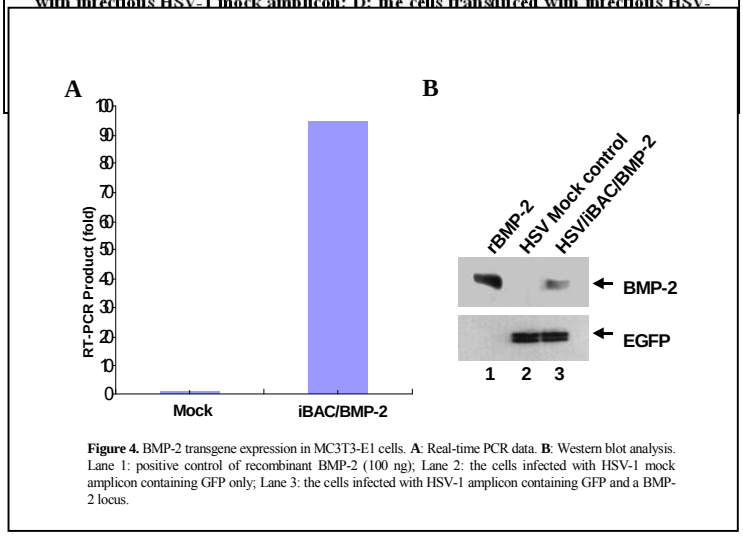

Figure 4. BMP-2 transgene expression in MC3T3-E1 cells. **A**: Real-time PCR data. **B**: Western blot analysis. Lane 1: positive control of recombinant BMP-2 (100 ng); Lane 2: the cells infected with HSV-1 mock amplicon containing GFP only; Lane 3: the cells infected with HSV-1 amplicon containing GFP and a BMP-2 locus.

HSV-1 mock amplicon without BMP-2 genomic locus (**Figure 3A**) or the cells treated with vehicle alone (**Figure 5C**).

We have observed that the HSV-1 amplicon can efficiently transfer a large piece of genomic locus, and retain it as episomes in proliferating cells. The GFP gene is consistently active and visible for at least 2 weeks, although the intensity becomes weaker. The functional BMP-2 protein in the infected cells was detectable 72 hours and even longer after infection, and mediated cell differentiation. In addition, viral infection yields more than 75% efficiency without antibiotics selection. Therefore, we believe that making a stable cell lines is not necessary.

In addition to the HSV amplicon-based viral gene transfer, we also developed a non-viral gene transfer system to express the coding sequence of test genes in the bone cells. We established this gene transfer strategy for the following reasons: 1) Some of our test genes may contain large introns (>100 kb), such that the size of the intact gene, including introns and exons, could be beyond the limitation of the HSV packaging capacity (e.g. >150 kb); 2) The bacterial artificial chromosome (BAC) clone containing the entire candidate gene may not be available in the mouse genome databases; and 3) The BAC clone may encode multiple, alternatively-spliced variants with diverse functions from a single gene. To validate the non-viral gene transfer system, we modified the construct of pHGCX containing a CMV promoter in front of multiple cloning sites (MCS) by inserting a small CMV intron from pmaxGFP (Amaxa Inc., Gaithersburg, MD) into the corresponding sites of SnaB1 and NheI sites of pHGCX to generate a new expression vector driven by CMV promoter/intron (**Figure 1**). We amplified the complete coding sequence of osterix (Osx) from a mouse bone cDNA library by polymerase chain reaction (PCR) using specific primers with an overhang of Flag sequence at the 5' end of the forward primer. The PCR product of Flag-Osx was cloned into pCR2.1 to generate pCR2.1/Flag-Osx using a TA cloning kit (Invitrogen, Carlsbad, CA). The Flag/Osx fusion gene was then released from pCR2.1/Flag-Osx, and subcloned into the BamH1 and XhoI sites of modified pHGCX to generate pHGCX/Flag-Osx that also contains a green fluorescence protein (GFP) (Figure 6).

We believe that unlike BAC clone, plasmid DNA can be transferred into bone cells by chemical transfection or electroporation. Therefore, we optimized a protocol of "Nucleoporation" technique to deliver the transgenes into nuclei of MC3T3-E1 cells, by utilizing a commercial "Nucleofection buffer" (Amaxa Inc) and "Gene Pulser" (Biorad). Briefly, 10^6 MC3T3-E1 cells were resuspended in 100 µl of nucleofector buffer T containing 5 µg of pHGCX/Osx/flag plasmid DNA. The cells were then transferred into a 2-mm

gap width electroporation cuvette, and electroporated at 160 V for 20 milliseconds, using a Gene Pulser. After electroporation, the cells were transferred into prewarmed αMEM medium containing 10 % fetal bovine serum, 2 mM L-glutamine, 100 units/ml penicillin and 100 μg/ml streptomycin in 6-well plate, and cultured in a humidified 37 ^{0}C incubator with 5% CO_2. Twenty four hours after transfection, the cells were lysed in a lysis buffer containing 50 mM Tris-HCl (pH8.0), 150 mM NaCl, 0.1% SDS, 1% Triton X-100, 1 x Phosphatase Inhibitor, and 1 x Protease Inhibitor cocktail (Sigma, ST. Louis, MO) 24 hours after transfection. An aliquot of 30 μg cellular protein was separated on a 10% SDS-polyacrylamide gel and transferred to nitrocellulose. The membrane was incubated at 4 ^{0}C overnight in a buffer containing 5% dry skim milk, 150 mM NaCl, 50 mM Tris-HCl (pH 8.0), and 0.05% Tween-20. Immunoblotting was performed in the same buffer containing 0.2 μg/ml antibody against Flag (Sigma) or GFP (Santa Cruz, CA) at room temperature for 1 hour. Specific proteins were detected using appropriate secondary antibodies and Enhanced Chemiluminescence's Plus Western blotting detection system (Amersham Pharmacia Biotech UK Limited, Buckinghamshire, England). The cells in a parallel plate were trypsinized 24 hours post transfection and analyzed by fluorescence-activated cell sorter (FACS) (BD Biosciences, San Lose, CA) to assess the transfection efficiency. Another 6-well plate of cells was fixed in 0.05% glutaraldehyde for alkaline phosphatase (ALP) staining 3 days after transfection (14).

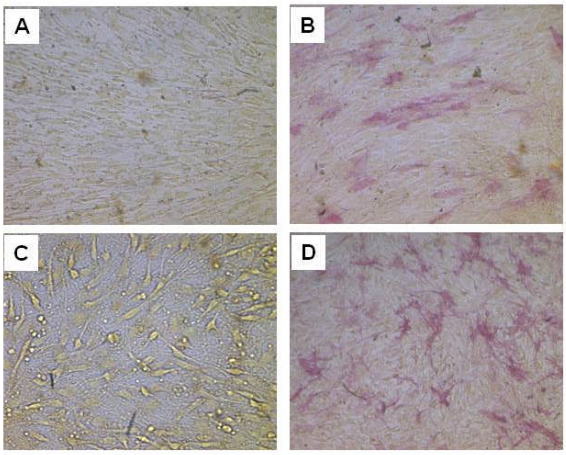

Figure 5: Alkaline phosphatase (ALP) staining of differentiated MC3T3-E1 cells (x 40 images). The cells are differentiated for 9 days and subjected for ALP staining. A: the cells infected with HSV-1 mock amplicon; B: the cells infected with HSV-1 amplicon containing a BMP-2 locus; C: The cells treated with vehicle; D: The cells treated with recombinant BMP-2 (200 ng/ml).

Our studies demonstrated that twenty-four hours after electroporation, the GFP reporter gene was expressed in most of MC3T3-E1 cells transfected with either pHGCX (**Figure 2A**) or pHGCX/Flag-Osx (**Figure 7B**). Flow cytometry analyses revealed more than 94% of the osteoblast cells transfected with the pHGCX or the pGHCX/Fla-Osx plasmid expressed GFP (**Figure 7C & D**). We have repeated the experiments and found that the efficiency of nucleoporation is reliable. The variation in transfection efficiency was less than 1%, and the viability of electroporated cells were more than 90%. In comparison with our previous data, the efficiency of gene transfer by nucleoporation was approximately 10% higher than that of a viral delivery system mediated by a HSV-amplicon in mouse preosteoblast cells (15). The transgene expression of GFP and Flag-Osx was easily detected in the cells transfected with pHGCX/Flag-Osx by utilizing Western blot with specific antibodies against Flag and GFP (**Figure 7E**). The pHGCX/Flag-Osx transfected cells expressed high levels of Flag-Osx fusion protein. As expected, the Flag-Osx fusion protein was undetectable while the expression of GFP was present in the cells transfected with pHGCX (**Figure 7E**). To assess osteoblast differentiation in the cells expressing the Osx transgene, we carried out an ALP staining 3 days after transfection (Figure 3). Approximately 20% of

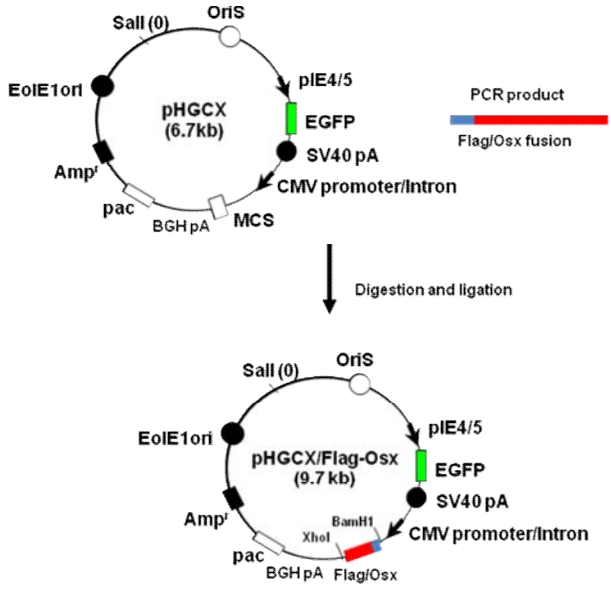

Figure 6. A schematic diagram of pHGCX/Flag-Osx construction. The PCR product of mouse osterix (Osx) coding sequence tagged with Flag is inserted into the BamH1 and XhoI sites downstream of the CMV promoter/intron of pHGCX plasmid to generate an expression vector of pHGCX/Flag-Osx.

the osteoblast cells overexpressing Osx were differentiated and exhibited positive ALP-staining (**Figure 3A**). In contrast, less than 1% ALP-positive cells were seen in the control cells overexpressing GFP only (**Figure 8B**).

Our studies indicated that non-viral gene transfer of nucleoporation can efficiently deliver plasmid DNA directly into the nuclei of preosteoblast cells. The transgene is consistently active and visible for more than 5 days, although the intensity of the GFP reporter becomes weaker with the culture time. A high level of transgene expression of GFP and Osx in the transfected cells was visual as early as 4 hours after electroporation and mediated cell differentiation, validating the application of nucleoporation technology for functional studies of candidate genes. Although the protocol provided in this study is specific to MC3T3-E1 cells, the system can be applied to other types of cells by modifying pulse time, voltage, and nucleofection buffer. In general, an electroporation with a low-voltage and prolonged pulse time can be applied to primary cells while a high-voltage and short pulse time should be considered for immortalized cell lines. Large cells require a low-voltage pulse.

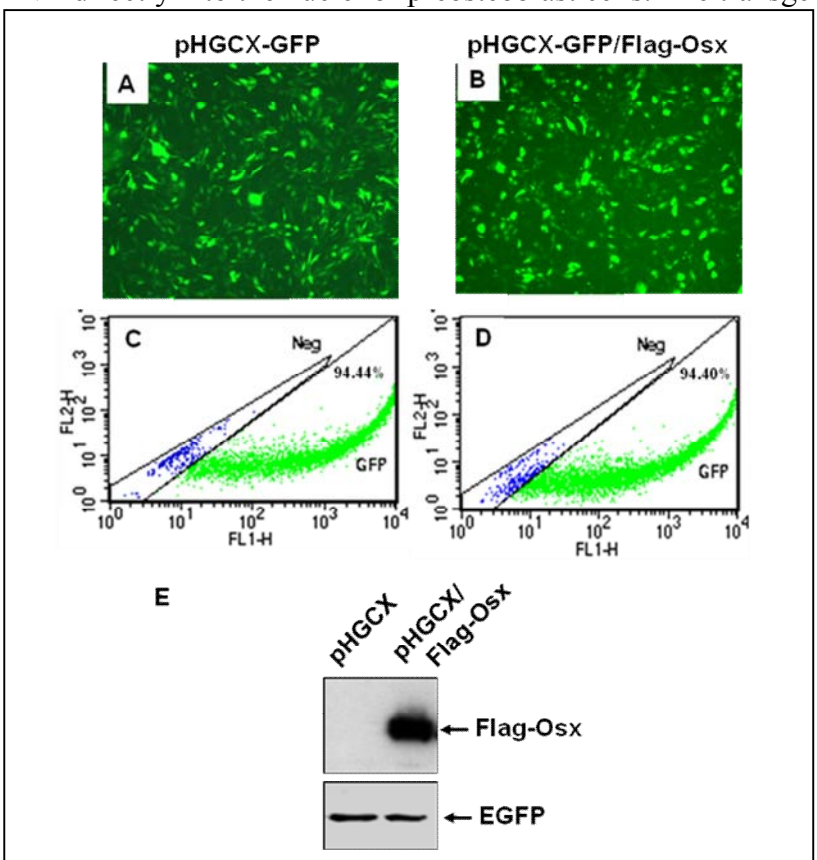

Figure 7. **Transgene expression in MC3T3-E1 cells transfected by nucleoporation. A & B: GPF expression in MC3T3-E1 cells transfected with pHGCX and pHGCX/Flag-Osx, respectively; C & D: Representative data of flow cytometric analysis in the cells transfected with pHGCX and pHGCX/Flag-Osx, respectively; E: Flag-Osx and GFP protein expression in MC3T3-E1 cells transfected with pHGCX and pHGCX/Flag-Osx, respectively, detected by Western blot.**

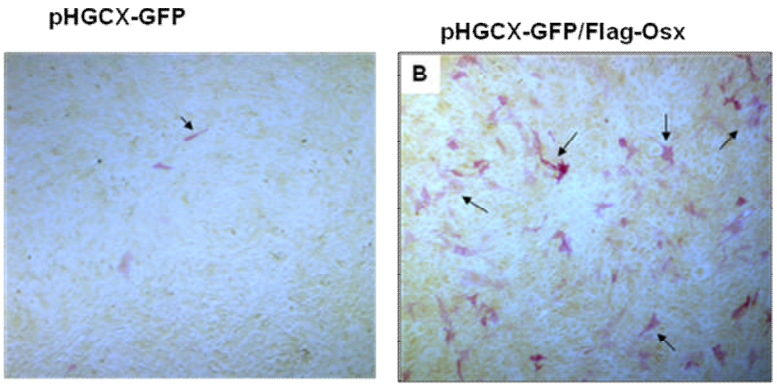

Figure 8. Alkaline phosphatase (ALP) staining of differentiated MC3T3-E1 cells (x 40 images). MC3T3-E1 cells are subjected for ALP staining 72 hours after transfection. **A**: the cells transfected with pHGCX control plasmid; **B**: the cells transfected with pHGCX/Flag-Osx. Arrows indicate the ALP-positive cells.

In vivo testing of candidate genes in a transgenic mouse is time-consuming and expensive, requiring the injection of a DNA fragment into fertilized eggs and the examination of mouse phenotypes. Therefore, it would be more efficient to use *in vitro* cell models via viral or non-viral gene transfer approaches to test candidate gene function before initiating *in vivo* transgenic studies. Although infectious viral transduction medicated by a HSV amplicon provides an alternative approach, the intensive work of purifying viral particles and potential contamination of viral particles limits its wide use. The studies provided here demonstrate that cloning the cDNA of an unknown gene into the pHGCX expression vector can be accomplished within a week. By utilizing this approach, a candidate gene search in a QTL region is cheaper, safer, and faster once an appropriate cell model and end points for candidate gene function are determined. Our data also indicates that it

is feasible to use the Gene Pulser for nucleofection once the conditions of pulse voltage and time are optimized. In addition, nucleoporation overcomes the limitation of infectious BAC (iBAC) technology to allow testing of the genes that iBAC cannot apply (5, 7, 12). In this regard, our data demonstrate that nucleoporation in MC3T3-E1 cells can be used as another gene transfer system for high throughput screening to identify genes important for osteoblast cell differentiation.

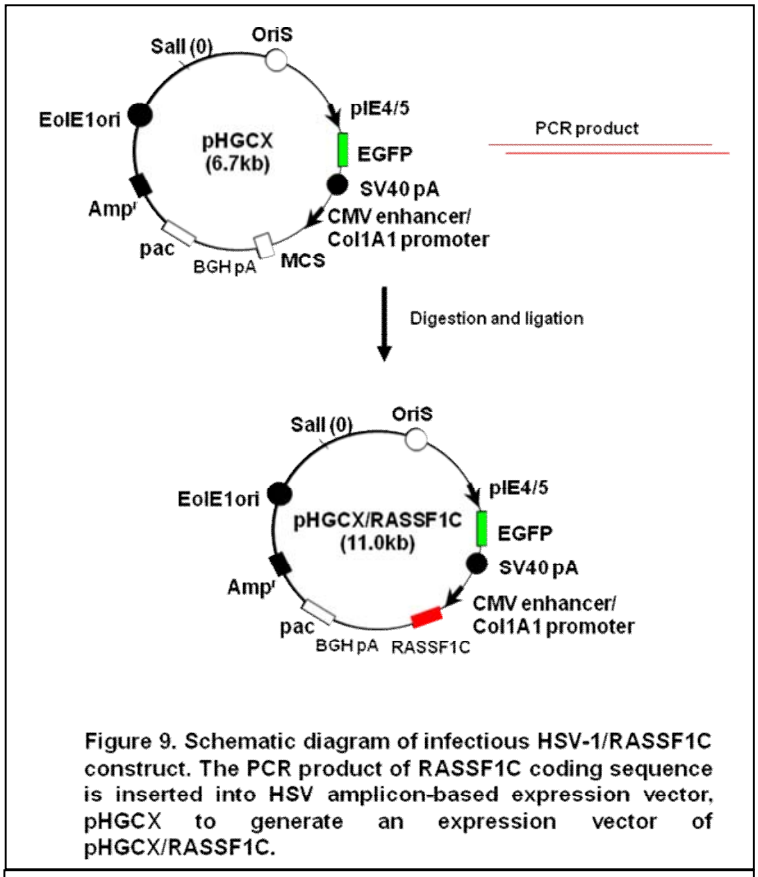

Figure 9. Schematic diagram of infectious HSV-1/RASSF1C construct. The PCR product of RASSF1C coding sequence is inserted into HSV amplicon-based expression vector, pHGCX to generate an expression vector of pHGCX/RASSF1C.

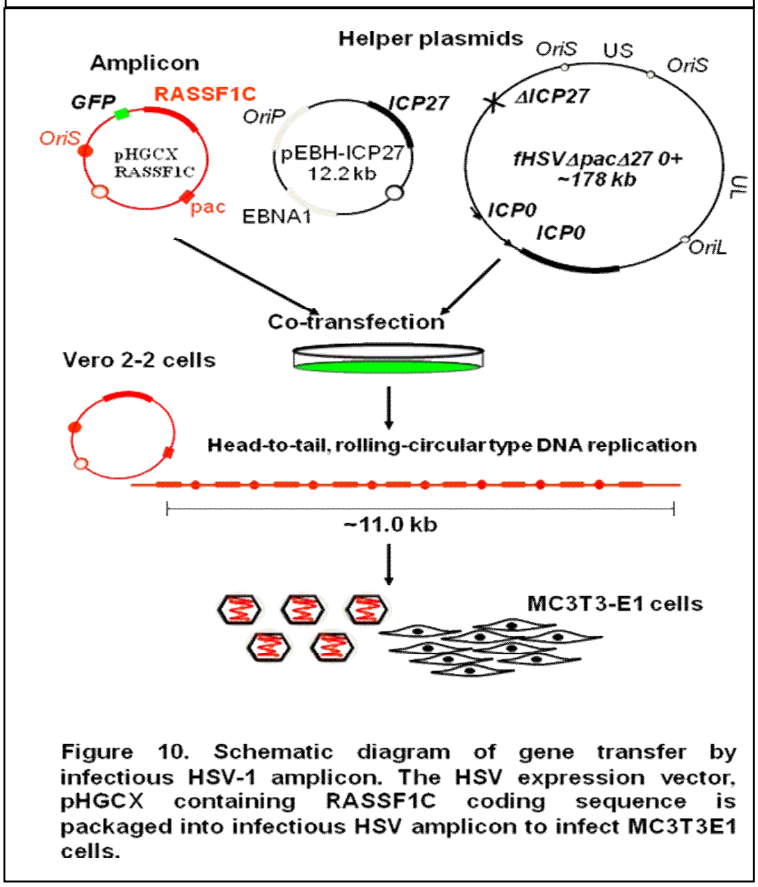

Figure 10. Schematic diagram of gene transfer by infectious HSV-1 amplicon. The HSV expression vector, pHGCX containing RASSF1C coding sequence is packaged into infectious HSV amplicon to infect MC3T3E1 cells.

One of the test genes that we selected for evaluation using HSV based amplicon system is an alternatively spliced form of ras-association domain family 1 protein, RASSF1C. There are four variants encoded from the same gene in mouse, and the RASSF1C is believed to be involved in regulating osteoblast cell number (3). In order to test the RASSF1C's function, we amplified the coding sequence from c-DNA libraries by PCR with specific primers to RASSF1C, tagged it with Flag synthetic sequence and cloned Flag/RASSF1C into pHGCX expression vector that contains CMV enhancer/collagen 1A1/rabbit beta-globin intron heterogeneous promoter, HSV amplicon and GFP reporter gene (**Figure 9**). We then carried out co-transfection, and packaged pHGCX/RASSF1C into HSV viral particles to transduct MC3T3-E1 cells (**Figure 10**). We modified our expression vector, and inserted a 2.3 kb Collagen 1A1 to drive transgenes to boost the expression level specifically in osteoblast cells. Our experiments revealed that the transduction efficiency of HSV-based amplicon bearing coding sequence of RASSF1C variant was approximately 85% in MC3T3-E1 cells (Figure 11A & B). The high level expression of transgene, Flag-RASSF1C, driven by CMV enhancer/Collagen 1A1 promoter was detected by Western blot with antibody against Flag 24 hours after transduction (**Figure 11C**). Experiments are in progress to evaluate the consequence of RASSF1C overexpression on osteoblast cell function.

We also have begun to test the function of a novel expressed sequence tag (EST) named as P37nb with leucine-rich repeats (LRR), a known functional domain present in a number of proteins with diverse functions and cellular locations (11). In our

previous studies, we have demonstrated that the expression of P37nb gene in bone was significantly induced by mechanical loading in mice. The high level expression of P37nb was consistent with the robust anabolic response, increased bone size and bone mineral density. In addition, one recent study found evidence that one of the LRR proteins, CMF608, a mechanical strain-induced bone-specific protein, is involved in promoting osteochondroprogenitor proliferation (10). Based on these data, we believe that further studies are needed to evaluate whether the expressed sequence of P37nb with an important functional domain is involved in regulating osteoblast cell proliferation leading to bone formation. Since the BAC clone containing P37nb is not available, we amplified the complete coding sequence by PCR, and inserted the transgene into pHGCX expression vector with Flag tag at its amino terminus. Therefore, the fusion protein of Flag/P37nb driven by CMV promoter in pHGCX vector can be expressed in osteoblast or bone marrow stromal cells for functional testing (**Figure 12**).

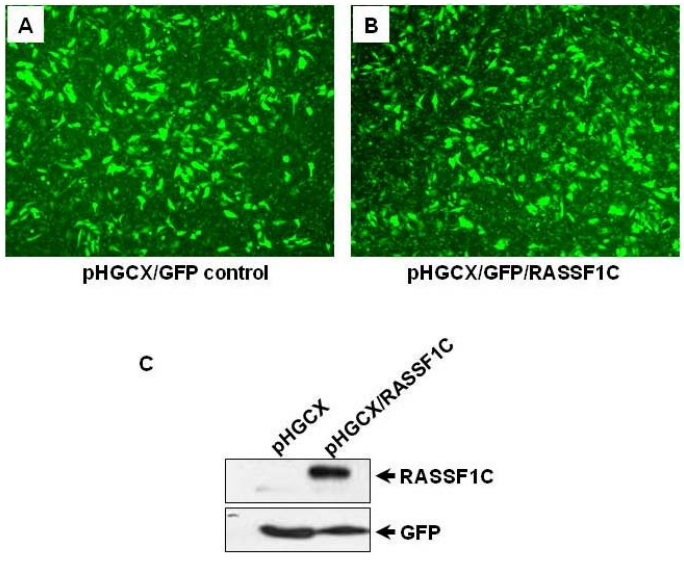

Figure 11. Transgene expression in HSV amplicon infected MC3T3-E1 cells. A: GFP expression in MC3T3-E1 cells transducted with pHGCX/GFP control amplicon. B: GFP expression in MC3T3-E1 cells transducted with pHGCX/GFP/RASSF1C amplicon. C: RASSF1C and GFP protein expression in MC3T3-E1 cells detected by Western blots.

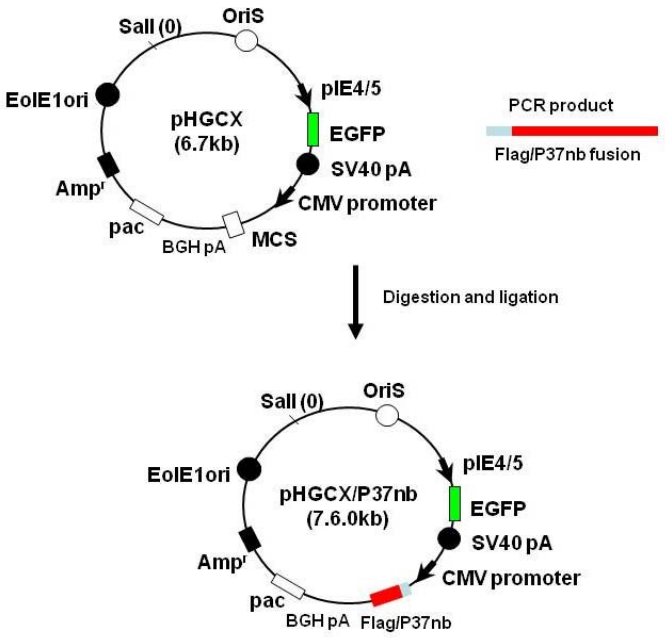

Figure 12. Schematic diagram of infectious HSV-1/P37nb construct. The PCR product of P37nb coding sequence is inserted into HSV amplicon-based expression vector, pHGCX to generate an expression vector of pHGCX/P37nb.

In addition to the two genes mentioned above, we have started functional testing of a signaling molecule, Ephrin B2 receptor (EphB2). It has been previously established that the EphB2 is localized within the QTL region of mouse chromosome 4 which is believed to contain mechanosensitive gene(s) (8). The Eph receptor and its membrane-anchored ephrin ligands (Eprin B1, B2 and B3) direct both reverse and forward signaling by cell-cell interactions regulating cell proliferaction, differentiation and migration (2). Targeted disruption of the Eph receptor ligand ephrinB1 in mice has also been reported to cause abnormal cartilage segmentation and the formation of additional skeletal elements, suggesting that ephrinB1 signaling is required for normal morphogenesis of skeletal elements (4). Our previous study provided evidence that mechanical loading increased Eph receptor B2 expression in bone cells, and established the groundwork for further examination of the Eph receptor signaling pathway's role in regulating bone formation. To test the function of EphB2, we searched the BAC clones from the mouse genome databases, and found that the EphB2 gene contains 16 introns, two of which are greater than 50 kb. The size of intact gene in a single BAC clone is greater than 200 kb, which is far beyond

the limitation of HSV amplicon packaging system. Thus, we engineered the complete coding sequence of EphB2 into pHGCX expression vector as describle in Figure 4. The 3.0 kb length of the coding sequence of EphB2 gene driven by CMV promoter in pHGCX can be either packaged into infectious HSV viron to deliver the transgene into osteoblast cells or directly transfected into bone cells by utilizing non-viral transfection technique.

We also established a non-viral gene transfer system for the constructs less than 12 kb in length. We believe that unlike BAC clone, plasmid DNA can be transferred into bone cells by chemical transfection or electroporation. Therefore, we optimized a protocol of "Nucleoporation" technique to deliver the transgenes into nuclei of MC3T3-E1 cells, by utilizing a commercial "Nucleofection buffer" (Amaxa Inc) and "Gene Pulser" (Biorad). Briefly, 10^6 MC3T3-E1 cells were resuspended in 100 µl of nucleofector buffer T containing 5 µg of pHGCX/EphB2 plasmid DNA. The cells were then transferred into a 2-mm gap width electroporation cuvette, and electroporated at 160 V for 20 milliseconds, using a Gene Pulser. After electroporation, the cells were transferred into prewarmed αMEM medium containing 10 % fetal bovine serum, 2 mM L-glutamine, 100 units/ml penicillin and 100 µg/ml streptomycin in 6-well plate, and cultured in a humidified 37 ^{0}C incubator with 5% CO_2. Twenty-four hours after transfection, the green fluorescent protein (GFP) reporter gene was expressed in most of MC3T3-E1 cells transfected with either control plasmid pHGCX or pHGCX/EphB2 (**Figure 13A & B**). Flow cytometry analyses revealed that 94.44% of the cells transduced with pHGCX and 94.42% of the cells transfected with pHGCX/EphB2 were GFP-positive (Figure 13C & D). We have repeated this experiment, and found that the efficiency of Nucleoporation was reliable. The transgene expression of EphB2 was easily detected by Western blot using specific antibody against mouse EphB2 (**Figure 13E**) 24 hours after transfection. The green fluorescent protein exprssed in transfected cells was visible 5 days after transfection.

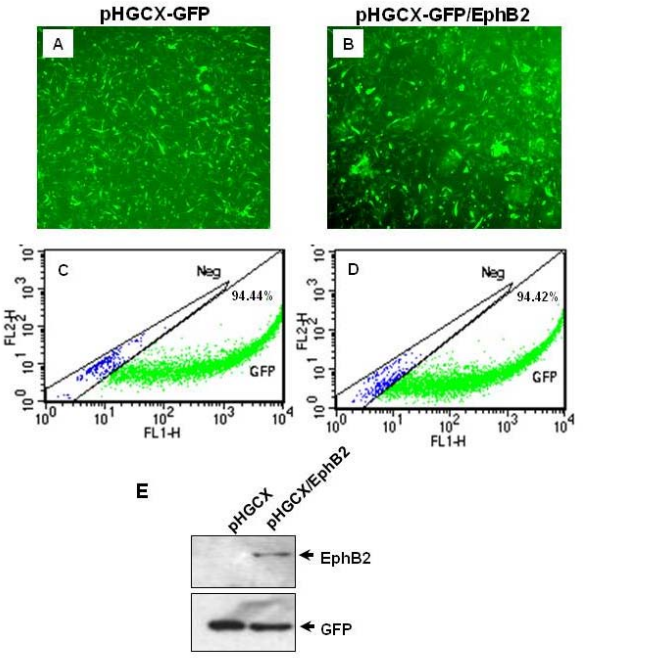

Figure 13. Transgene expression in MC3T3-E1 cells transfected. A & B: GPF expression in MC3T3-E1 cells transfected with pHGCX and pHGCX/EphB2 by Nucleoporation; C: Representive data of flow cytometric analysis in the cells transfected with pHGCX; D: Representive data of flow cytometric analysis in the cells transfected with pHGCX/EphB2; E: EphB2 and GFP expression in transfected cells, detected by Western blot.

In conclusion, we have successfully established another non-viral gene transfer system for functional testing of candidate genes in our QTL regions. We believe that the approaches of viral and non-viral transgene delivery are useful for our future studies.

b) Specific Objective 2: To isolate periosteal cells from mutant mice and transfect with one or more BAC clones.

In a previous study funded by the Department of Defense (DAMD17-99-1-9571), we identified a bone size mutant mouse strain, the B6. This B6 mouse mutant displayed a total body bone area that was 10-13% lower and periosteal circumference 5-8% lower at the femur and tibia midshaft compared to wild type B6 mice. Interval mapping in B6C3H F2 males (n=69) indicated two major loci affecting bone size on Chr 1 at 45 cM (LOD 4.9) and Chr 4 at 10.5 cM (LOD 7.9, genome wide $p<0.01$). Interval mapping using body weight as covariate revealed only one significant interval at Chr 4 (LOD 6.8). Alleles of the Chr 4 interval

inherited from the B6 mutant strain contribute to a significantly lower bone size than those inherited from C3H.

Interval mapping using additional markers for Chromosome 4 revealed an ENU mutant locus located between 7.5-36 cM. Thus, we developed a BAC contig for this region using RP23 clones. This contig is shown in Table 1 below.

Table 1.

id	name	acc	start	stop	length	weight	orient_end1	orient_end2	overlap
1	RP23-115F19		9832065	10039368	207303	Highest	+	-	#VALUE!
2	RP23-444O1		10000160	10163727	163567	Highest	+	-	39208
3	RP23-455B8	AL805930	10116748	10291395	174647	Medium	+	-	46979
5	RP23-429I15		10215570	10427388	211818	Highest	+	-	75825
8	RP23-438A13		10395367	10536785	141418	Highest	+	-	32021
10	RP23-240F1		10437823	10614357	176534	Highest	+	-	98962
11	RP23-354G12		10531758	10719885	188127	Highest	+	-	82599
12	RP23-144K18	AL671880	10614403	10806382	191979	Highest	+	-	105482
16	RP23-480O3		10773401	10961298	187897	Highest	+	-	32981
18	RP23-464D11		10910403	11087548	177145	Highest	+	-	50895
23	RP23-25E12		11058315	11266413	208098	Highest	+	-	29233
26	RP23-322G9	AL772170	11219514	11442995	223481	Highest	+	-	46899
27	RP23-295B7		11282889	11503029	220140	Highest	+	-	160106
28	RP23-244J11		11489317	11707550	218233	Highest	+	-	13712
30	RP23-417N13		11590964	11828972	238008	Highest	+	-	116586
33	RP23-295L9		11796064	11976935	180871	Highest	+	-	32908
35	RP23-203A12	AL772167	11821926	12026956	205030	Highest	+	-	155009
36	RP23-301C4		11969851	12122812	152961	Highest	+	-	57105
37	RP23-107F24		12185639	12382896	197257	Highest	+	-	-62827
38	RP23-271J14		12210164	12418212	208048	Highest	+	-	172732
39	RP23-119J18		12441690	12627439	185749	Highest	+	-	-23478
40	RP23-59O21		12581371	12767705	186334	Highest	+	-	46068
41	RP23-219E6		12630106	12831827	201721	Highest	+	-	137599
42	RP23-122G12		12814760	12994496	179736	Highest	+	-	17067
45	RP23-56F9		12869355	13125165	255810	Highest	+	-	125141
48	RP23-34L17		13071447	13290840	219393	Highest	+	-	53718
54	RP23-456G17		13270110	13432510	162400	Highest	+	-	20730
59	RP23-306G24		13407005	13642549	235544	Medium	+	-	25505
62	RP23-291L14		13619670	13773556	153886	Medium	+	-	22879
65	RP23-472I19		13691231	13883435	192204	Highest	+	-	82325
67	RP23-134H12	AL807804	13769980	13976684	206704	Medium	+	-	113455
69	RP23-287O8	AL808118	13946512	14138756	192244	Highest	+	-	30172
71	RP23-384E7		14097032	14270979	173947	Highest	+	-	41724
72	RP23-458M15		14132437	14302944	170507	Highest	+	-	138542
73	RP23-194M5		14285852	14492095	206243	Highest	+	-	17092
77	RP23-138B7		14448706	14676988	228282	Highest	+	-	43389
80	RP23-129D22		14550220	14776118	225898	Highest	+	-	126768
82	RP23-379L17	AL831792	14726182	14895882	169700	Highest	+	-	49936
87	RP23-153A15		14841308	15028457	187149	Highest	+	-	54574
89	RP23-356M11		14955220	15139976	184756	Highest	+	-	73237
90	RP23-113G17		15027414	15213099	185685	Highest	+	-	112562
91	RP23-193N22		15208207	15413927	205720	Highest	+	-	4892
94	RP23-396L22		15363948	15563390	199442	Medium	+	-	49979

95	RP23-233N14		15486676	15721025	234349	Highest	+	-	76714
97	RP23-298B17		15670284	15846237	175953	Highest	+	-	50741
99	RP23-384F21		15822641	16030052	207411	Highest	+	-	23596
103	RP23-267K10		15962449	16132815	170366	Highest	+	-	67603
104	RP23-300F16		16328336	16512721	184385	Highest	+	-	-195521
105	RP23-360O17	AL929447	16566011	16751208	185197	Highest	+	-	-53290
106	RP23-358M21	AL772196	16644062	16882025	237963	Highest	+	-	107146
107	RP23-227B13		16928466	17116541	188075	Highest	+	-	-46441
109	RP23-222P6		16999309	17226274	226965	Highest	+	-	117232
111	RP23-477N19		17200316	17393629	193313	Highest	+	-	25958
112	RP23-297F22		17350546	17536575	186029	Medium	+	-	43083
113	RP23-290G13		17551730	17751307	199577	Highest	+	-	-15155
114	RP23-293O10		17678222	17868125	189903	Highest	+	-	73085
116	RP23-259P7	AL805957	17839699	18072289	232590	Highest	+	-	28426
117	RP23-191I13		17903818	18111672	207854	Highest	+	-	168471
118	RP23-99G22		18070478	18268431	197953	Highest	+	-	41194
120	RP23-276F7	AL732623	18159272	18338972	179700	Highest	+	-	109159
121	RP23-382A14		18390689	18592081	201392	Highest	+	-	-51717
124	RP23-421D17	AL929519	18556811	18762392	205581	Highest	+	-	35270
125	RP23-377M4		18678056	18844880	166824	Highest	+	-	84336
126	RP23-13I21		18763159	18995336	232177	Medium	+	-	81721
127	RP23-309E23		19047584	19228869	181285	Highest	+	-	-52248
128	RP23-199B9	BX001053	19133772	19345874	212102	Medium	+	-	95097
131	RP23-138O20	AL772281	19288747	19504225	215478	Highest	+	-	57127
134	RP23-106F23		19437061	19651682	214621	Highest	+	-	67164
135	RP23-408P4		19537851	19744683	206832	Highest	+	-	113831
138	RP23-334P1		19708115	19926937	218822	Highest	+	-	36568
141	RP23-89A4		19812399	20062499	250100	Highest	+	-	114538
142	RP23-311D6		19991668	20186163	194495	Highest	+	-	70831
146	RP23-305O17		20142441	20319129	176688	Highest	+	-	43722
147	RP23-319K20		20181514	20369784	188270	Highest	+	-	137615
150	RP23-382D19		20345282	20534268	188986	Highest	+	-	24502
152	RP23-393P6		20501299	20697883	196584	Highest	+	-	32969
154	RP23-137M6		20624964	20823185	198221	Highest	+	-	72919
155	RP23-234B18		20693535	20884688	191153	Highest	+	-	129650
157	RP23-437K10		20854327	21035838	181511	Medium	+	-	30361
160	RP23-431N12		20969446	21126427	156981	Highest	+	-	66392
161	RP23-55D6		21590786	21840569	249783	Highest	+	-	-464359
163	RP23-365O14		21724003	21934485	210482	Highest	+	-	116566
166	RP23-433G4		21875138	22094897	219759	Highest	+	-	59347
170	RP23-237K13	AL683854	22071102	22305715	234613	Medium	+	-	23795
173	RP23-402G3		22238022	22416760	178738	Highest	+	-	67693
175	RP23-28C12		22345389	22570432	225043	Highest	+	-	71371
176	RP23-456B13		22650776	22826521	175745	Highest	+	-	-80344
177	RP23-447O9		22729576	22893250	163674	Highest	+	-	96945
178	RP23-242O10		23003571	23180326	176755	Highest	+	-	-110321
179	RP23-310N9		23200512	23428113	227601	Highest	+	-	-20186
182	RP23-210D12		23384254	23612212	227958	Highest	+	-	43859
183	RP23-338P7		23479510	23655179	175669	Highest	+	-	132702
184	RP23-370B12		23665380	23842338	176958	Highest	+	-	-10201
185	RP23-140J12	AL671868	23665394	23851178	185784	Highest	+	-	176944

186	RP23-239J20		23917008	24135881	218873	Highest	+	-	-65830
187	RP23-202E18		23956913	24141953	185040	Highest	+	-	178968
188	RP23-26N2		24336305	24564681	228376	Highest	+	-	-194352
192	RP23-367L15		24542438	24704925	162487	Highest	+	-	22243
194	RP23-24I19		24589598	24809622	220024	Highest	+	-	115327
195	RP23-434I23		24687651	24889841	202190	Highest	+	-	121971
196	RP23-19M3		24789836	24965497	175661	Highest	+	-	100005
197	RP23-333P3		24952684	25152670	199986	Highest	+	-	12813
200	RP23-111M14		25070275	25291808	221533	Highest	+	-	82395
202	RP23-145B24		25233506	25449652	216146	Highest	+	-	58302
207	RP23-299E10		25419408	25596627	177219	Medium	+	-	30244
208	RP23-389G9		25882666	26077969	195303	Medium	+	-	-286039
210	RP23-69N21		25952322	26160118	207796	Highest	+	-	125647
211	RP23-117E19	AC101374	26137965	26358054	220089	Highest	+	-	22153
212	RP23-476K17		26343507	26512139	168632	Highest	+	-	14547
214	RP23-336M1		26362829	26577759	214930	Highest	+	-	149310
215	RP23-177K20		26537554	26741391	203837	Highest	+	-	40205
219	RP23-274H7		26681842	26900864	219022	Highest	+	-	59549
220	RP23-313C1		26908311	27120120	211809	Highest	+	-	-7447
221	RP23-402O20		27138118	27337835	199717	Highest	+	-	-17998
222	RP23-205F9		27276337	27481451	205114	Highest	+	-	61498
223	RP23-203B4		27458396	27670845	212449	Highest	+	-	23055
224	RP23-24H13		27569105	27739866	170761	Highest	+	-	101740
225	RP23-353L18		27654752	27869296	214544	Highest	+	-	85114
227	RP23-94C13		27811937	28054445	242508	Highest	+	-	57359
231	RP23-151N17	AL671872	27944773	28133102	188329	Highest	+	-	109672
233	RP23-408N9		28110865	28417496	306631	Highest	+	-	22237
236	RP23-87N9	AL929397	28389920	28571993	182073	Highest	+	-	27576
237	RP23-59L20		28440521	28698812	258291	Highest	+	-	131472
238	RP23-223D8		28615364	28794277	178913	Highest	+	-	83448
240	RP23-105F14		28755808	28958098	202290	Medium	+	-	38469
241	RP23-358I18	BX323546	28900904	29108984	208080	Highest	+	-	57194
243	RP23-134E11		29047944	29255584	207640	Highest	+	-	61040
245	RP23-425N3		29190830	29382804	191974	Highest	+	-	64754
247	RP23-451B19		29339048	29511833	172785	Highest	+	-	43756
250	RP23-439A9		29400053	29607504	207451	Highest	+	-	111780
251	RP23-440K16		29550507	29765460	214953	Medium	+	-	56997
252	RP23-334M6	BX530076	29625830	29828304	202474	Highest	+	-	139630
253	RP23-215H7		29828360	30038027	209667	Highest	+	-	-56
255	RP23-192D22	AC101535	29923607	30149686	226079	Highest	+	-	114420
256	RP23-446K23		30054226	30235797	181571	Highest	+	-	95460
257	RP23-325J14		30149726	30334334	184608	Highest	+	-	86071
258	RP23-145H16		30316201	30492178	175977	Highest	+	-	18133
261	RP23-192E7		30451258	30631164	179906	Highest	+	-	40920
263	RP23-296F5	BX255966	30606622	30795237	188615	Highest	+	-	24542
265	RP23-456B2	AL929408	30715673	30912535	196862	Highest	+	-	79564
266	RP23-165G10	AC073702	30794337	30986486	192149	Highest	+	-	118198
267	RP23-77O12	AC100998	30912584	31153806	241222	Highest	+	-	73902
269	RP23-221I2		31133464	31350304	216840	Highest	+	-	20342
274	RP23-76B2		31280927	31522928	242001	Highest	+	-	69377
276	RP23-351L1		31493636	31718430	224794	Highest	+	-	29292

280	RP23-84I16	AC101029	31694096	31900515	206419	Highest	+	-	24334
283	RP23-31M8		31743192	31947761	204569	Highest	+	-	157323
284	RP23-120K20		31898012	32114942	216930	Highest	+	-	49749
288	RP23-142K3		32078095	32287725	209630	Highest	+	-	36847
292	RP23-358N13	BX323545	32254690	32433770	179080	Highest	+	-	33035
294	RP23-24E11	AL732547	32399866	32606572	206706	Highest	+	-	33904
304	RP23-308C15		32580304	32800453	220149	Highest	+	-	26268
312	RP23-117E21		32763885	32973196	209311	Highest	+	-	36568
318	RP23-248A9		32939929	33184079	244150	Highest	+	-	33267
320	RP23-360H6	AL772288	33147084	33352181	205097	Medium	+	-	36995
321	RP23-122L3		33230371	33473325	242954	Highest	+	-	121810
324	RP23-369I8	AL772272	33354189	33608475	254286	Highest	+	-	119136
325	RP23-225I6		33629777	33834477	204700	Highest	+	-	-21302
329	RP23-224K19		33731735	33966913	235178	Highest	+	-	102742
331	RP23-437A5		33923544	34143144	219600	Highest	+	-	43369
334	RP23-16I2		34056626	34223923	167297	Medium	+	-	86518
335	RP23-286P4		34505704	34671808	166104	Highest	+	-	-281781
336	RP23-209A17		34613329	34795928	182599	Highest	+	-	58479
339	RP23-29M7		34718098	34951116	233018	Medium	+	-	77830
341	RP23-320J8		34903072	35144150	241078	Highest	+	-	48044
342	RP23-232A6		34961509	35174689	213180	Medium	+	-	182641
343	RP23-434N2		35195819	35396676	200857	Highest	+	-	-21130
346	RP23-192E23		35302782	35465120	162338	Highest	+	-	93894
347	RP23-140F12		35394632	35583670	189038	Highest	+	-	70488
348	RP23-12K18		35641708	35857978	216270	Highest	+	-	-58038
350	RP23-429H11		35741492	35952060	210568	Highest	+	-	116486
352	RP23-39F22	AL844199	35888045	36093575	205530	Highest	+	-	64015
354	RP23-415O10		36012374	36213105	200731	Highest	+	-	81201
355	RP23-118A20	AL831712	36096748	36307595	210847	Highest	+	-	116357
356	RP23-293H21		36307690	36506338	198648	Highest	+	-	-95
360	RP23-19I8		36475537	36670011	194474	Highest	+	-	30801
363	RP23-287B11	AL833783	36647227	36876019	228792	Highest	+	-	22784
366	RP23-34B14		36835176	37086325	251149	Highest	+	-	40843
368	RP23-341A3		37026179	37229381	203202	Highest	+	-	60146
369	RP23-15N22		37203732	37414430	210698	Highest	+	-	25649
376	RP23-30J14		37387965	37617485	229520	Highest	+	-	26465
377	RP23-65A23		37606191	37747717	141526	Highest	+	-	11294
380	RP23-211C18		37674193	37878686	204493	Highest	+	-	73524
381	RP23-323B18		37857355	38069363	212008	Highest	+	-	21331
386	RP23-336H21		38000593	38208014	207421	Highest	+	-	68770
388	RP23-86I14		38163074	38375993	212919	Highest	+	-	44940
389	RP23-63K11		38562343	38772354	210011	Highest	+	-	-186350
390	RP23-202J15		38718728	38912474	193746	Highest	+	-	53626
394	RP23-330D5		38862393	39103890	241497	Highest	+	-	50081
396	RP23-90G18		39033975	39253238	219263	Highest	+	-	69915
397	RP23-290N7		39166443	39370973	204530	Medium	+	-	86795
398	RP23-138K24		39258295	39457676	199381	Highest	+	-	112678
401	RP23-296O13		39437174	39595457	158283	Highest	+	-	20502
402	RP23-374J24		39499874	39707613	207739	Medium	+	-	95583
403	RP23-101C9		39609108	39804310	195202	Highest	+	-	98505
406	RP23-263N5		39754170	39967831	213661	Highest	+	-	50140

408	RP23-403C16		39927626	40126248	198622	Highest	+	-	40205
410	RP23-259I21		40100354	40267760	167406	Highest	+	-	25894
411	RP23-9F23	AL831793	40224573	40460999	236426	Highest	+	-	43187
417	RP23-102N20		40402937	40616929	213992	Highest	+	-	58062
418	RP23-284I1		40569227	40773814	204587	Highest	+	-	47702
421	RP23-218M7		40702111	40931461	229350	Highest	+	-	71703
425	RP23-236N23		40901357	41090246	188889	Highest	+	-	30104
428	RP23-404A21		41043467	41251856	208389	Highest	+	-	46779
432	RP23-65E3		41212067	41470453	258386	Highest	+	-	39789
436	RP23-368G11		41411067	41596920	185853	Highest	+	-	59386
439	RP23-100C7	AL831723	41565407	41796051	230644	Highest	+	-	31513
441	RP23-311O23		41704592	41903060	198468	Highest	+	-	91459
442	RP23-80L18		41890078	42095507	205429	Highest	+	-	12982
446	RP23-111G9		42073923	42286654	212731	Highest	+	-	21584
452	RP23-77L9		42241273	42491944	250671	Highest	+	-	45381
458	RP23-173O17		42459169	42683683	224514	Highest	+	-	32775
464	RP23-207P5		42632959	42870507	237548	Highest	+	-	50724
470	RP23-86E14		42794041	42988555	194514	Highest	+	-	76466
471	RP23-321C13		42906622	43113645	207023	Highest	+	-	81933
472	RP23-9F18	AL773539	42988635	43170791	182156	Highest	+	-	125010
473	RP23-107K17		43139726	43345065	205339	Highest	+	-	31065
480	RP23-140C14		43287091	43501348	214257	Highest	+	-	57974
484	RP23-140K8		43456332	43675550	219218	Highest	+	-	45016
489	RP23-46K20		43613859	43836653	222794	Highest	+	-	61691
494	RP23-125D9		43796363	44021380	225017	Highest	+	-	40290
496	RP23-159N16	AL805914	43877463	44055236	177773	Highest	+	-	143917
498	RP23-346F11		44028258	44241108	212850	Highest	+	-	26978
504	RP23-405L15		44133053	44328987	195934	Highest	+	-	108055
507	RP23-238D21		44292056	44462804	170748	Highest	+	-	36931
510	RP23-348H14		44428069	44643717	215648	Highest	+	-	34735
514	RP23-30F6	AL772376	44599936	44837186	237250	Highest	+	-	43781
518	RP23-12C18		44703454	44947686	244232	Highest	+	-	133732
520	RP23-139E24		44916535	45143642	227107	Medium	+	-	31151
528	RP23-421O11		45062725	45275851	213126	Highest	+	-	80917
529	RP23-102E20		45184060	45438063	254003	Highest	+	-	91791
533	RP23-91P12		45408725	45623429	214704	Highest	+	-	29338
535	RP23-97L12		45593269	45843711	250442	Highest	+	-	30160
540	RP23-161K7	AL772350	45785434	45998179	212745	Highest	+	-	58277
542	RP23-339F2		45833973	46033037	199064	Highest	+	-	164206
543	RP23-246L2		46137134	46374964	237830	Highest	+	-	-104097
545	RP23-350C18		46228496	46477456	248960	Highest	+	-	146468
548	RP23-206K1		46380555	46590964	210409	Highest	+	-	96901
551	RP23-351M21		46522259	46723947	201688	Highest	+	-	68705
553	RP23-217M8		46608104	46792158	184054	Highest	+	-	115843
558	RP23-22N16		46758120	46993352	235232	Highest	+	-	34038
560	RP23-311J14		46948048	47103489	155441	Highest	+	-	45304
562	RP23-144L20	AL732553	47072595	47273481	200886	Highest	+	-	30894
568	RP23-22D16		47250356	47486727	236371	Highest	+	-	23125
574	RP23-383M4		47441938	47657650	215712	Highest	+	-	44789
577	RP23-302J16		47596320	47770389	174069	Highest	+	-	61330
580	RP23-298H2		47733929	47920374	186445	Highest	+	-	36460

583	RP23-141C15	AL807771	47873771	48106817	233046	Highest	+	-	46603
589	RP23-357A7		48083637	48310354	226717	Highest	+	-	23180
592	RP23-187F9		48287386	48491862	204476	Highest	+	-	22968
595	RP23-135G14		48454555	48659621	205066	Highest	+	-	37307
596	RP23-34B24	AL772310	48657081	48868928	211847	Highest	+	-	2540
603	RP23-111F13		48806068	49024179	218111	Highest	+	-	62860
607	RP23-193M14		48999110	49214549	215439	Highest	+	-	25069
609	RP23-325E1		49166355	49390361	224006	Highest	+	-	48194
610	RP23-332L19	AL928574	49301702	49498899	197197	Highest	+	-	88659
611	RP23-361M6		49703801	49847911	144110	Highest	+	-	-204902
613	RP23-408J1		49791206	49992745	201539	Highest	+	-	56705
614	RP23-67K2		49925519	50114187	188668	Medium	+	-	67226
617	RP23-368A8		50058554	50247450	188896	Highest	+	-	55633
618	RP23-208P1		50331804	50513622	181818	Highest	+	-	-84354
619	RP23-215O19	AL732569	50486275	50663530	177255	Highest	+	-	27347
620	RP23-37H21		50694375	50881242	186867	Highest	+	-	-30845
623	RP23-32J7		50809393	51016890	207497	Highest	+	-	71849
625	RP23-123E1	AL732520	50974368	51182095	207727	Medium	+	-	42522
629	RP23-73L2		51161652	51385712	224060	Medium	+	-	20443
630	RP23-82G13		51323256	51457573	134317	Highest	+	-	62456
631	RP23-343C10		51486182	51690120	203938	Highest	+	-	-28609
634	RP23-187K5		51592274	51822435	230161	Highest	+	-	97846
636	RP23-113N2		51767148	51959992	192844	Highest	+	-	55287
640	RP23-148K17		51857184	52061970	204786	Highest	+	-	102808
641	RP23-115G24		52099283	52306878	207595	Medium	+	-	-37313
646	RP23-25D17	AL807243	52244978	52440813	195835	Highest	+	-	61900
648	RP23-300B24		52338512	52531242	192730	Highest	+	-	102301
650	RP23-204P1	AL773567	52492665	52682574	189909	Highest	+	-	38577
655	RP23-399G23		52562649	52782525	219876	Highest	+	-	119925
656	RP23-324N5		52670061	52905255	235194	Highest	+	-	112464
659	RP23-46H3		52879888	53042813	162925	Highest	+	-	25367
660	RP23-356K15		52888111	53079637	191526	Highest	+	-	154702
661	RP23-92G18		53053003	53257216	204213	Highest	+	-	26634
666	RP23-436E9		53204887	53402600	197713	Highest	+	-	52329
670	RP23-125G19		53312069	53543866	231797	Medium	+	-	90531
672	RP23-265E5		53410662	53592287	181625	Highest	+	-	133204
673	RP23-351I4		53579263	53789951	210688	Highest	+	-	13024
675	RP23-466A17	AL772349	53625815	53822051	196236	Highest	+	-	164136
676	RP23-390I8	AL772353	53817819	54006164	188345	Highest	+	-	4232
682	RP23-115N23		53932903	54149508	216605	Highest	+	-	73261
687	RP23-68C16		54104555	54295369	190814	Highest	+	-	44953
692	RP23-331C13		54272257	54490073	217816	Highest	+	-	23112
698	RP23-86N13		54426634	54638162	211528	Highest	+	-	63439
702	RP23-111D19		54615839	54841457	225618	Highest	+	-	22323
706	RP23-308I5		54783200	55036177	252977	Highest	+	-	58257
709	RP23-142K12		54956167	55183932	227765	Highest	+	-	80010
710	RP23-434J11		55123124	55309454	186330	Highest	+	-	60808
714	RP23-82K8	AL929491	55251304	55450933	199629	Highest	+	-	58150
715	RP23-160J6		55524154	55740356	216202	Highest	+	-	-73221
718	RP23-37N10		55615842	55797129	181287	Highest	+	-	124514
721	RP23-148O2		55769983	55982546	212563	Highest	+	-	27146

726	RP23-155E17		55932774	56150984	218210	Highest	+	-	49772
728	RP23-303I1		56047142	56229919	182777	Highest	+	-	103842
729	RP23-337I1		56151055	56392018	240963	Highest	+	-	78864
732	RP23-11H12		56286285	56495043	208758	Highest	+	-	105733
734	RP23-424G21		56461870	56638395	176525	Highest	+	-	33173
737	RP23-434P11		56489604	56709398	219794	Highest	+	-	148791
739	RP23-178E9		56638475	56860792	222317	Highest	+	-	70923
743	RP23-301E13		56787106	57007247	220141	Highest	+	-	73686
744	RP23-85M8		56990023	57216682	226659	Highest	+	-	17224
746	RP23-448N14		57158401	57341365	182964	Highest	+	-	58281
750	RP23-284I12		57297237	57534183	236946	Highest	+	-	44128
752	RP23-181I22		57509495	57718850	209355	Highest	+	-	24688
757	RP23-317N18		57693285	57911784	218499	Highest	+	-	25565
762	RP23-228M22		57882790	58047953	165163	Highest	+	-	28994
764	RP23-57J9		57964737	58165878	201141	Highest	+	-	83216
769	RP23-67A22		58140096	58421829	281733	Highest	+	-	25782
773	RP23-57N22	AL808112	58383829	58619927	236098	Highest	+	-	38000
775	RP23-351O5		58588398	58795271	206873	Highest	+	-	31529
780	RP23-6E12	BX005031	58737676	58953140	215464	Highest	+	-	57595
789	RP23-443B13		58922558	59130769	208211	Highest	+	-	30582
791	RP23-235L20		59105133	59257642	152509	Highest	+	-	25636
794	RP23-452J18		59112150	59296107	183957	Highest	+	-	145492
795	RP23-67O19		59799125	60123861	324736	Medium	+	-	-503018
796	RP23-61I16		59936348	60174849	238501	Medium	+	-	187513
797	RP23-57A6		60414343	60638749	224406	Medium	+	-	-239494
802	RP23-107D12		60567103	60757537	190434	Medium	+	-	71646
805	RP23-429G9		60692732	60898779	206047	Medium	+	-	64805
808	RP23-39D14		60851886	61108846	256960	Highest	+	-	46893
812	RP23-103G7		60992900	61213298	220398	Highest	+	-	115946
815	RP23-139I19		61162879	61380834	217955	Highest	+	-	50419
817	RP23-24J18	AL928565	61307378	61513589	206211	Highest	+	-	73456
819	RP23-324B9		61490683	61719836	229153	Highest	+	-	22906
825	RP23-341G1		61613928	61828236	214308	Highest	+	-	105908
826	RP23-454E10	AL928624	61744755	61920212	175457	Highest	+	-	83481
829	RP23-101D6		61869262	62062865	193603	Highest	+	-	50950
832	RP23-345F15		62021866	62236689	214823	Highest	+	-	40999
838	RP23-456C2		62200467	62398759	198292	Highest	+	-	36222
840	RP23-344I2		62295715	62511272	215557	Highest	+	-	103044
841	RP23-76N22		62427953	62653074	225121	Highest	+	-	83319
842	RP23-396A15		62532140	62745664	213524	Highest	+	-	120934
844	RP23-381O16		62724135	62929698	205563	Highest	+	-	21529
847	RP23-132F4	BX649255	62904300	63098916	194616	Highest	+	-	25398
849	RP23-4E22		62984839	63222739	237900	Highest	+	-	114077
853	RP23-173C3	AL691481	63173943	63404018	230075	Highest	+	-	48796
856	RP23-452N7		63242552	63431485	188933	Highest	+	-	161466
857	RP23-206A1		63426630	63613965	187335	Highest	+	-	4855
862	RP23-142L5		63585413	63791477	206064	Highest	+	-	28552
866	RP23-357C7		63755339	63949482	194143	Highest	+	-	36138
869	RP23-74M12		63884985	64122791	237806	Highest	+	-	64497
873	RP23-36A3		64085961	64294558	208597	Highest	+	-	36830
879	RP23-291O18		64271609	64466397	194788	Highest	+	-	22949

883	RP23-240I15		64425121	64639814	214693	Highest	+	-	41276
887	RP23-321H19		64615184	64811219	196035	Medium	+	-	24630
892	RP23-323E15		64782893	64982482	199589	Highest	+	-	28326
894	RP23-153P14	BX571882	64851844	65044106	192262	Highest	+	-	130638
895	RP23-15K21		64978652	65189770	211118	Highest	+	-	65454
898	RP23-348N14		65150003	65331989	181986	Highest	+	-	39767
901	RP23-27M9		65253677	65476329	222652	Highest	+	-	78312
904	RP23-30E14		65425388	65594375	168987	Highest	+	-	50941
905	RP23-87K16		65476130	65679905	203775	Highest	+	-	118245
906	RP23-206P23	BX322649	65627979	65825370	197391	Highest	+	-	51926
907	RP23-195E16	BX571887	65825447	66029840	204393	Highest	+	-	-77
910	RP23-118N17		65999067	66205006	205939	Highest	+	-	30773
911	RP23-94O16	BX936372	66205043	66383927	178884	Highest	+	-	-37
912	RP23-402A22		66723550	66920315	196765	Highest	+	-	-339623
913	RP23-61I15		66864062	67115743	251681	Highest	+	-	56253
917	RP23-399C17		67081840	67280191	198351	Highest	+	-	33903
920	RP23-333J24		67223351	67436826	213475	Highest	+	-	56840
924	RP23-164F9		67388341	67589047	200706	Highest	+	-	48485
925	RP23-294N12		67632247	67808324	176077	Highest	+	-	-43200
926	RP23-284H21		67750284	67983192	232908	Highest	+	-	58040
927	RP23-380M15		67920070	68087259	167189	Highest	+	-	63122
928	RP23-356I15		68087505	68288965	201460	Highest	+	-	-246
929	RP23-432L24		68109485	68317318	207833	Highest	+	-	179480
930	RP23-233I19		68335067	68526095	191028	Highest	+	-	-17749
934	RP23-159F17		68439028	68644485	205457	Highest	+	-	87067
939	RP23-435J11		68599625	68810278	210653	Highest	+	-	44860
941	RP23-38N8	AL845171	68774027	69003527	229500	Highest	+	-	36251
943	RP23-432P15		68957947	69172090	214143	Highest	+	-	45580
945	RP23-95M20	AL929442	69101339	69311758	210419	Highest	+	-	70751
946	RP23-380I15		69317645	69499131	181486	Highest	+	-	-5887
949	RP23-458G19		69343723	69515289	171566	Highest	+	-	155408
950	RP23-420C7		69515436	69709344	193908	Highest	+	-	-147
951	RP23-358A23		69545558	69728433	182875	Highest	+	-	163786
952	RP23-29G22		70017793	70270141	252348	Highest	+	-	-289360
955	RP23-161B14		70195530	70395928	200398	Highest	+	-	74611
958	RP23-420G13		70356077	70559607	203530	Highest	+	-	39851
959	RP23-347D6		70410010	70579554	169544	Highest	+	-	149597
960	RP23-309C6		70547278	70699596	152318	Highest	+	-	32276
961	RP23-439M13		70573929	70757382	183453	Highest	+	-	125667
962	RP23-379O23	BX640496	70955452	71127752	172300	Medium	+	-	-198070
964	RP23-222P16		71084834	71303436	218602	Highest	+	-	42918
966	RP23-342C12		71270077	71506148	236071	Highest	+	-	33359
967	RP23-180O12		71385786	71599301	213515	Medium	+	-	120362
968	RP23-313M22		71678040	71875731	197691	Medium	+	-	-78739
969	RP23-357O16		71859807	72026378	166571	Highest	+	-	15924
970	RP23-32H24		72026461	72217073	190612	Highest	+	-	-83
971	RP23-438B17		72286282	72453868	167586	Highest	+	-	-69209
972	RP23-476C7		72395139	72587746	192607	Highest	+	-	58729
974	RP23-115P24		72475717	72677349	201632	Highest	+	-	112029
976	RP23-268I2		72648058	72844666	196608	Highest	+	-	29291
979	RP23-101H20		72781739	72984142	202403	Highest	+	-	62927

980	RP23-92G15		73131844	73281564	149720	Highest	+	-	-147702
982	RP23-302J8		73176066	73412450	236384	Highest	+	-	105498
985	RP23-141O2	CR396588	73365424	73558131	192707	Highest	+	-	47026
989	RP23-147F16		73537874	73725026	187152	Highest	+	-	20257
991	RP23-87H14		73696384	73919630	223246	Highest	+	-	28642
996	RP23-431G10		73859033	74057005	197972	Highest	+	-	60597
998	RP23-290N18		73976029	74135358	159329	Highest	+	-	80976
999	RP23-451G1		74127733	74292762	165029	Medium	+	-	7625
1001	RP23-325D14		74151599	74339799	188200	Medium	+	-	141163
1002	RP23-42K13		74273912	74533139	259227	Medium	+	-	65887
1011	RP23-247N5	AL844848	74462714	74664550	201836	Highest	+	-	70425
1012	RP23-310L11	BX296523	74610670	74841754	231084	Highest	+	-	53880
1017	RP23-467N14		74787304	74977155	189851	Highest	+	-	54450
1021	RP23-15P19		74948199	75178164	229965	Highest	+	-	28956
1023	RP23-180H11		75049598	75244731	195133	Highest	+	-	128566
1024	RP23-391A4		75161880	75348597	186717	Highest	+	-	82851
1025	RP23-14G7		75349227	75553228	204001	Highest	+	-	-630
1026	RP23-245E19	AL845333	75434470	75620603	186133	Highest	+	-	118758
1028	RP23-303H3		75566191	75766219	200028	Highest	+	-	54412
1033	RP23-342O7		75716202	75949676	233474	Highest	+	-	50017
1036	RP23-416J19		75838768	76031604	192836	Highest	+	-	110908
1040	RP23-415E9		76007998	76229284	221286	Highest	+	-	23606
1045	RP23-232K22		76178165	76368591	190426	Highest	+	-	51119
1046	RP23-405M24	AL954189	76327020	76544942	217922	Medium	+	-	41571
1047	RP23-117O5		76479718	76655408	175690	Highest	+	-	65224
1048	RP23-147D24		76585946	76800250	214304	Medium	+	-	69462
1049	RP23-426O2		76970319	77151403	181084	Highest	+	-	-170069
1050	RP23-101C7		77139405	77362207	222802	Medium	+	-	11998
1052	RP23-79D4		77265388	77476558	211170	Highest	+	-	96819
1053	RP23-128L7		77617526	77808655	191129	Highest	+	-	-140968
1054	RP23-183M11		77795700	77984914	189214	Highest	+	-	12955
1055	RP23-444K7		77811412	77997705	186293	Highest	+	-	173502
1056	RP23-34E12		78014156	78246085	231929	Highest	+	-	-16451
1059	RP23-120A3		78141881	78351641	209760	Highest	+	-	104204
1063	RP23-235B22		78293459	78480525	187066	Highest	+	-	58182
1064	RP23-149B22		78453914	78637585	183671	Highest	+	-	26611
1065	RP23-419H18	BX640502	78542802	78754537	211735	Medium	+	-	94783
1066	RP23-416O14		78750536	78916089	165553	Medium	+	-	4001
1068	RP23-205K24		78872174	79087361	215187	Highest	+	-	43915
1074	RP23-212J5		79042646	79258811	216165	Highest	+	-	44715
1078	RP23-325F19		79210496	79401074	190578	Highest	+	-	48315
1079	RP23-338C16		79358158	79562037	203879	Highest	+	-	42916
1081	RP23-233O19		79483226	79665146	181920	Highest	+	-	78811
1083	RP23-390K8		79590541	79788603	198062	Highest	+	-	74605
1086	RP23-125N5	BX682542	79750484	79957669	207185	Highest	+	-	38119
1087	RP23-475N10		79773937	79966759	192822	Highest	+	-	183732
1088	RP23-293L20		80102236	80297982	195746	Highest	+	-	-135477
1093	RP23-454C1		80277637	80475958	198321	Highest	+	-	20345
1095	RP23-458C21		80424659	80598877	174218	Highest	+	-	51299
1097	RP23-181G21		80546632	80760188	213556	Medium	+	-	52245
1102	RP23-56D19		80684936	80958115	273179	Highest	+	-	75252

1104	RP23-117M16		80916458	81131980	215522	Highest	+	-	41657
1110	RP23-109N19		81099549	81323059	223510	Highest	+	-	32431
1112	RP23-152G9		81288850	81498577	209727	Highest	+	-	34209
1117	RP23-354A4		81460078	81660380	200302	Medium	+	-	38499
1122	RP23-138G14		81608565	81791763	183198	Highest	+	-	51815
1129	RP23-228O1		81769935	81963942	194007	Highest	+	-	21828
1134	RP23-22O4		81934131	82141082	206951	Highest	+	-	29811
1136	RP23-381B20		82105700	82293773	188073	Highest	+	-	35382
1142	RP23-471O23	AL807790	82250232	82429805	179573	Highest	+	-	43541
1146	RP23-78O19		82364226	82619636	255410	Highest	+	-	65579
1150	RP23-292P23		82541931	82750906	208975	Highest	+	-	77705
1155	RP23-395M3	AL805919	82727249	82926267	199018	Medium	+	-	23657
1162	RP23-148E3		82852383	83075683	223300	Highest	+	-	73884
1166	RP23-146L3		83020700	83236502	215802	Highest	+	-	54983
1167	RP23-79O16		83166991	83410055	243064	Highest	+	-	69511
1172	RP23-203M7		83374319	83595928	221609	Medium	+	-	35736
1174	RP23-459J19	AL929430	83497008	83697592	200584	Highest	+	-	98920
1177	RP23-9G18		83643134	83869752	226618	Highest	+	-	54458
1181	RP23-15H18		83809822	84004283	194461	Highest	+	-	59930
1182	RP23-433E8		83937670	84147428	209758	Highest	+	-	66613
1187	RP23-313G2	AL929448	84097770	84301884	204114	Highest	+	-	49658
1188	RP23-26E20		84190175	84402249	212074	Highest	+	-	111709
1192	RP23-152G19	AL807242	84370394	84584033	213639	Medium	+	-	31855
1200	RP23-190E17		84563912	84762092	198180	Highest	+	-	20121
1204	RP23-95O1	AL824707	84724583	84949479	224896	Medium	+	-	37509
1207	RP23-85A2		84860314	85104771	244457	Highest	+	-	89165
1210	RP23-110F8	AL773553	85081655	85304723	223068	Highest	+	-	23116
1213	RP23-367C18		85276168	85471942	195774	Highest	+	-	28555
1215	RP23-222F14		85356041	85579188	223147	Highest	+	-	115901
1216	RP23-325L22	AL953839	85463601	85654762	191161	Medium	+	-	115587
1217	RP23-298K4		85654771	85842305	187534	Highest	+	-	-9
1221	RP23-212O24	BX284642	85806126	86006582	200456	Highest	+	-	36179
1227	RP23-263N20		85959042	86148944	189902	Highest	+	-	47540
1230	RP23-222G21		86112676	86317952	205276	Highest	+	-	36268
1236	RP23-402B13		86264324	86473699	209375	Medium	+	-	53628
1240	RP23-83N3		86419634	86625190	205556	Highest	+	-	54065
1242	RP23-11A16		86587657	86795373	207716	Highest	+	-	37533
1244	RP23-64G11		86674327	86871124	196797	Highest	+	-	121046
1245	RP23-67C1	AL772394	86777925	86916608	138683	Highest	+	-	93199
1246	RP23-213G4		86987500	87239681	252181	Highest	+	-	-70892
1250	RP23-357D3		87199228	87419867	220639	Highest	+	-	40453
1254	RP23-139P5		87388260	87584747	196487	Highest	+	-	31607
1255	RP23-95P16		87412520	87613876	201356	Highest	+	-	172227
1256	RP23-445E3	BX649611	87695879	87877749	181870	Highest	+	-	-82003
1262	RP23-357N14		87787908	87980897	192989	Highest	+	-	89841
1263	RP23-12N4		87860970	88101732	240762	Highest	+	-	119927
1264	RP23-266G24		88084755	88282686	197931	Highest	+	-	16977
1266	RP23-359B13		88239390	88424184	184794	Highest	+	-	43296
1267	RP23-21I15		88333674	88571603	237929	Highest	+	-	90510
1268	RP23-462D2		88499893	88679888	179995	Medium	+	-	71710
1269	RP23-236O21	AL671925	88702697	88921064	218367	Medium	+	-	-22809

1270	RP23-183P20		88775544	88966654	191110	Highest	+	-	145520
1271	RP23-118I21		88909335	89128079	218744	Highest	+	-	57319
1273	RP23-326H20		89085282	89274074	188792	Highest	+	-	42797
1274	RP23-137B11		89327668	89535374	207706	Medium	+	-	-53594
1279	RP23-173M22		89450949	89678246	227297	Highest	+	-	84425
1285	RP23-240F2		89637929	89815335	177406	Highest	+	-	40317
1287	RP23-190K9	BX537306	89740758	89925194	184436	Highest	+	-	74577
1289	RP23-2O10	AC099413	89888398	90096939	208541	Highest	+	-	36796
1291	RP23-256D21		90075496	90220319	144823	Highest	+	-	21443
1294	RP23-282K2		90153849	90321451	167602	Highest	+	-	66470
1296	RP23-129H4		90236370	90419080	182710	Highest	+	-	85081
1297	RP23-24G6		90384214	90533741	149527	Highest	+	-	34866
1298	RP23-132L3		90499853	90693444	193591	Highest	+	-	33888
1300	RP23-127K21		90554929	90768757	213828	Highest	+	-	138515
1302	RP23-145B12		90716064	90927887	211823	Highest	+	-	52693
1303	RP23-288P14		90920592	91132922	212330	Highest	+	-	7295
1305	RP23-12K12		91074255	91275743	201488	Highest	+	-	58667
1308	RP23-322F24		91211628	91425841	214213	Medium	+	-	64115
1311	RP23-328I9		91381855	91569779	187924	Medium	+	-	43986
1315	RP23-442C1		91541902	91731622	189720	Highest	+	-	27877
1317	RP23-103J13		91694849	91896838	201989	Highest	+	-	36773
1319	RP23-301A10		91727542	91935523	207981	Highest	+	-	169296
1320	RP23-138N13	BX664632	91934344	92175787	241443	Highest	+	-	1179
1323	RP23-337H15		92136269	92366716	230447	Highest	+	-	39518
1326	RP23-356F18		92343111	92533626	190515	Highest	+	-	23605
1330	RP23-432K21		92485473	92698369	212896	Highest	+	-	48153
1333	RP23-82L24		92621775	92826407	204632	Highest	+	-	76594
1336	RP23-173G7		92796792	93001533	204741	Highest	+	-	29615
1337	RP23-82J4		92891589	93138388	246799	Highest	+	-	109944
1339	RP23-225D6		93067908	93308115	240207	Highest	+	-	70480

To further test the candidate genes in bone cells in vitro, we have isolated periosteal cells from mutant mice. Briefly, 10 weeks-old 16137M mutant B6 mice were sacrificed, and the femur and tibias were removed. The bones were dissected free of soft tissue, and digested with 1 mg/ml collagenase in DMEM for 90 minutes at 37°C to isolate periosteal osteoblasts. The cells were then plated at a density of 10^5 per well in 6-well-plates and cultured in DMEM supplemented with 10% fetal bovine serum (FBS), 100 units/ml penicillin and 100 μg/ml streptomycin in a humidified 37 ^{0}C incubator with 5% CO_2. The control cells were isolated in identical manner from age-and sex-matched wild-type B6 mice. The cells were confirmed as osteoblasts by alkaline phosphatase (ALP) staining after vitamin D-induced differentiation. The periosteal osteoblasts at passages 2-3 were used for cell proliferation, differentiation, and apoptosis assays

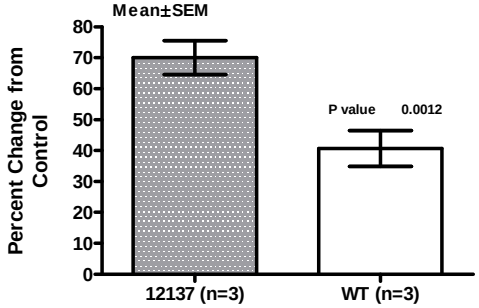

Figure 14. Proliferation rate determined by uptake of Almar Blue dye in periosteal osteoblasts isolated from femur and tibia of 10-week 12137 mutant and WT mice. Equal number of cells was seeded at a density of 2000 cells/well in a 96 well plate and grown in presence of 10%FCS for 48 hours. Each column represents mean of 9 replicates including three from each animal. The differences between groups were analyzed by TTEST.

In our initial studies, we used Alamar Blue assay to examine the cell proliferation and viability. Briefly, 2 x 10^3 osteoblast cells per well in 96-well plates were incubated in DMEM supplemented with 10% calf serum (CS), 100 units/ml penicillin and 100 μg/ml streptomycin for 24 hours, followed by starvation in serum-free media for another 24 hours. The same number of

cells in two paired wells were then cultured in the media supplemented with 10% CS and in serum-free media respectively for 48 hours at 37 ^{0}C. The cells were washed once in phosphate buffered saline (PBS), followed by 2-4 hours incubation at 37 ^{0}C in fresh culture media containing 10% alamar blue. The plates were read on a fluorescent plate reader with excitation at 544 nm and emission at 590 nm. The proliferation rate was evaluated by comparing the uptake of alamar blue in the cells grown in the presence of 10% CS to the cells cultured in serum free media. Our experiments demonstrated that the proliferation of periosteal osteoblasts from mutant mice with high bone density was increased by 70% in the presence of serum whereas the proliferation of osteoblasts from wild-type mice was stimulated by 40% in the same culture conditions (P=0.0012) (**Figure 14**). In addtion to Alamar Blue assay, we are currently comparing the cell proliferation in these two lines of mice by using [^{3}H] thymidine incorporation assay.

We have also compared apoptosis rate of the osteoblasts from mutant and wild-type mice by utilizing Homogeneous Caspase Assay. We quantified the activity of caspases 2, 3, 6, 7, 8, 9 and 10 to cleave fluorogenic tetrapeptide in isolated bone cells in vitro. Briefly, 2 x 10^3 osteoblast cells per well in 96-well plates were incubated in DMEM supplemented with 10% calf serum (CS), 100 units/ml penicillin and 100 μg/ml streptomycin for 24 hours. The cells were then washed once, and starved in serum-free media for 48 hours. The starved osteoblasts were then incubated in the culture media supplemented with 100 μl fluorogenic tetrapeptide for 1-24 hours at 37 ^{0}C. The fluorescence of the released Rhodamine was measured with an excitation filter 470-500 and emission filter 500-560. Our experiments have found that caspase activity in periosteal osteoblasts from mutant mice was significantly higher than the cells from wild-type mice (Figure 15). Our data indicate that increased osteoblast proliferation may contribute to the high bone density in mutant mice.

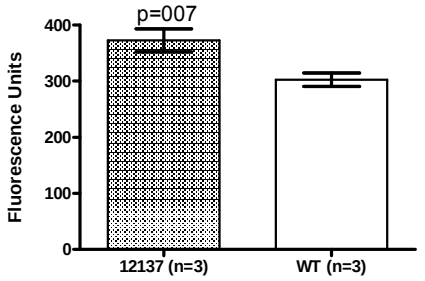

Figure-15 Caspase activity in periosteal osteoblasts isolated from 12137 and wild type mice. Equal number of cells was seeded at a density of 2000 cells/well in a 96 well plate and grown under serum-depleted conditions for 48 hours. Each column represents mean of 9 replicates including three from each animal. The differences between groups were analyzed by TTEST. WT=wild type

In conclusion, we have successfully isolated periosteal osteoblasts from mutant mice, and expended them in vitro for cell proliferation, differentiation and apoptosis studies. We believe that the approaches of isolating periosteal cells, cell proliferation and apoptosis are useful for testing candidate genes in our future functional studies.

c) **Specific Objective 3:** To begin to evaluate the phenotypic change (cell proliferation/ differentiation/ apoptosis) in cells transfected with one or more BAC clones.

We have constructed three pHGCX-based cDNA expression vectors, and demonstrated that test genes were expressed in bone cells after viral or non-viral gene transfer. Since the endogenous EphB2 expression was undetectable in MC3T3-E1 cells by Western blot, we have transfected the cells with pHGCX/EphB2, treated the cells with recombinant Ephrin B2 (0, 0.01, 0.1, 1 and 2 μg/ml), and examined the effect of EphB2 forward signaling on alkaline phosphotase (ALP) activity and cell proliferation (thymidine incorporation assay). In addition, we have over expressed Ephrin B2 ligand and treated cells with EphB2 soluble receptor to examine the role of reverse signaling in bone cells.

KEY RESEARCH ACCOMPLISHMENTS

- Have successfully developed an approach using an HSV-1 amplicon system for efficient transfer of BAC genomic locus into bone cells, and established that the candidate gene is expressed at high level and is functional.
- Have begun to test candidate genes on cell proliferation, differentiation, migration and apoptosis in bone cells using viral and non-viral deliver approaches, and established that the expression of coding sequences of candidate gene can compensate for the limitation of infectious BAC gene transfer.
- Have established in vitro functional assay using periosteal cells from mutant mice for in vitro testing of candidate genes.

REPORTABLE OUTCOMES

1.Xing W, Baylink D, Kesavan C and Mohan S. HSV-1 Amplicon-Mediated Transfer of 128-kb BMP-2 Genomic Locus Stimulates Osteoblast Differentiation *in vitro* Biochem Biophys Res Commun 319(3): 781-6, 2004

2.Xing W, Baylink D, Kesavan C and Mohan S. Transfer of 128-kb BMP-2 Genomic Locus by HSV-Based Infectious BAC Stimulates Osteoblast Differentiation: A Platform for Functional Genomic Studies. *ASBMR-2004, 19 suppl 1: S150, 2004*

3.Xing W, Baylink D, Kappor A and Mohan S. A platform of high-efficiency non-viral gene transfer in mouse osteoblast cells in vitro. Molecular Biotechnology 34(1):29-35, 2006

CONCLUSIONS

- We have successfully transferred 128-kb 1.BMP-2 genomic locus into osteoblast cells with high efficiency by utilizing HSV amplicon system.
- The transgene was retained in osteoblast cells as minichromosomes for a long period of time.
- The infected cells with transgene express functional protein, and induced cell differentiation.
- The BAC gene transfer provides a rapid and efficient approach for functional testing of candidate genes within the QTL region *in vitro.*
- We have successfully cloned the complete coding sequence of candidate genes into pHGCX expression vector, and deliver the transgenes into osteoblast cells with high efficiency by utilizing either viral HSV amplicon system or non-viral "Nucleoporation" approach.
- The osteoblast cells containing transgenes express high level of proteins for functional studies.
- Transfer of the coding sequence of candidate genes into bone cells provides an alternative approach for functional studies when the infectious BAC technique is not applicable.
- We have successfully isolated periosteal cells from mutant mice, and established the cell proliferation and apoptosis methods for future studies.

REFERENCE

1. **Abrams, K. L., Xu, J., Nativelle-Serpentini, C., Dabirshahsahebi, S., and Rogers, M. B. An** evolutionary **and molecular analysis of BMP2 expression. J Biol Chem; 2004.**
2. **Adams, R. H., Diella, F., Hennig, S., Helmbacher, F., Deutsch, U., and Klein, R. The cytoplasmic** domain **of the ligand ephrinB2 is required for vascular morphogenesis but not cranial neural crest migration. Cell 104:57-69; 2001.**
3. **Amaar, Y. G., Baylink, D. J., and** Mohan**, S. Ras-Association Domain Family 1 Protein, RASSF1C, Is an IGFBP-5 Binding Partner and a Potential Regulator of Osteoblast Cell Proliferation. J Bone Miner Res 20:1430-9; 2005.**
4. **Compagni, A., Logan, M., Klein, R., and Adams, R. H. Control of skeletal patterning by ephrinB1-EphB interactions. Dev Cell 5:217-30; 2003.**
5. **Cortes, M. L., Bakkenist, C. J., Di Maria, M. V., Kastan, M. B., and Breakefield, X. O. HSV-1 amplicon vector-mediated expression of ATM cDNA and correction of the ataxia-telangiectasia cellular phenotype. Gene Ther 10:1321-7; 2003.**
6. **Helvering, L. M., Sharp, R. L., Ou, X., and Geiser, A. G. Regulation of the promoters for the human bone morphogenetic protein 2 and 4 genes. Gene 256:123-38; 2000.**
7. **Lenz, P., Bacot, S. M., Frazier-Jessen, M. R., and Feldman, G. M. Nucleoporation of dendritic cells: efficient gene transfer by electroporation into human monocyte-derived dendritic cells. FEBS Lett 538:149-54; 2003.**
8. **Robling, A. G., Li, J., Shultz, K. L., Beamer, W. G., and Turner, C. H. Evidence for a skeletal mechanosensitivity gene on mouse chromosome 4. Faseb J 17:324-6; 2003.**
9. **Saeki, Y., Breakefield, X. O., and Chiocca, E. A. Improved HSV-1 amplicon packaging system using ICP27-deleted, oversized HSV-1 BAC DNA. Methods Mol Med 76:51-60; 2003.**
10. **Segev, O., Samach, A., Faerman, A., Kalinski, H., Beiman, M., Gelfand, A., Turam, H., Boguslavsky, S., Moshayov, A., Gottlieb, H., Kazanov, E., Nevo, Z., Robinson, D., Skaliter, R., Einat, P., Binderman, I., and Feinstein, E. CMF608-a novel mechanical strain-induced bone-specific protein expressed in early osteochondroprogenitor cells. Bone 34:246-60; 2004.**
11. **Strausberg, R. L., Feingold, E. A., Grouse, L. H., Derge, J. G., Klausner, R. D., Collins, F. S., Wagner, L., Shenmen, C. M., Schuler, G. D., Altschul, S. F., Zeeberg, B., Buetow, K. H., Schaefer, C. F., Bhat, N. K., Hopkins, R. F., Jordan, H., Moore, T., Max, S. I., Wang, J., Hsieh, F., Diatchenko, L., Marusina, K., Farmer, A. A., Rubin, G. M., Hong, L., Stapleton, M., Soares, M. B., Bonaldo, M. F., Casavant, T. L., Scheetz, T. E., Brownstein, M. J., Usdin, T. B., Toshiyuki, S., Carninci, P., Prange, C., Raha, S. S., Loquellano, N. A., Peters, G. J., Abramson, R. D., Mullahy, S. J., Bosak, S. A., McEwan, P. J., McKernan, K. J., Malek, J. A., Gunaratne, P. H., Richards, S., Worley, K. C., Hale, S., Garcia, A. M., Gay, L. J., Hulyk, S. W., Villalon, D. K., Muzny, D. M., Sodergren, E. J., Lu, X., Gibbs, R. A., Fahey, J., Helton, E., Ketteman, M., Madan, A., Rodrigues, S., Sanchez, A., Whiting, M., Young, A. C., Shevchenko, Y., Bouffard, G. G., Blakesley, R. W., Touchman, J. W., Green, E. D., Dickson, M. C., Rodriguez, A. C., Grimwood, J., Schmutz, J., Myers, R. M., Butterfield, Y. S., Krzywinski, M. I., Skalska, U., Smailus, D. E., Schnerch, A., Schein, J. E., Jones, S. J., and Marra, M. A. Generation and initial analysis of more than 15,000 full-length human and mouse cDNA sequences. Proc Natl Acad Sci U S A 99:16899-903; 2002.**
12. **Wade-Martins, R., Saeki, Y., and Antonio Chiocca, E. Infectious delivery of a 135-kb LDLR genomic locus leads to regulated complementation of low-density lipoprotein receptor deficiency in human cells. Mol Ther 7:604-12; 2003.**

13. **Wade-Martins, R., Smith, E. R., Tyminski, E., Chiocca, E. A., and Saeki, Y. An infectious transfer and expression system for genomic DNA loci in human and mouse cells. Nat Biotechnol 19*:*1067-70; 2001.**
14. **Wergedal, J. E., and Baylink, D. J. Characterization of cells isolated and cultured from human bone. Proc Soc Exp Biol Med 176*:*60-9; 1984.**
15. **Xing, W., Baylink, D., Kesavan, C., and Mohan, S. HSV-1 amplicon-mediated transfer of 128-kb BMP-2 genomic locus stimulates osteoblast differentiation in vitro. Biochem Biophys Res Commun 319*:*781-6; 2004.**

Project 4: The Application of Transgenic Mice to Assess Gene Function in Mechanical Loading and in Bone Fracture Healing Models

Introduction

Bone formation in response to exercise or injury requires the coordinated interactions of a number of molecular pathways of gene expression. Observational studies have provided valuable information on the contributions of these molecular pathways to bone repair. However, a more complete understanding of gene expression in bone formation and fracture repair requires definitive proof of the functional significance of the genes participating in the pathways. In this regard, the analysis of mice engineered to be deficient in the expression of a particular gene-of-interest (i.e., knockout, KO, mice) is especially critical. The study of knockout mice provides conclusive evidence of the functional significance of a particular gene in the development and repair of a tissue. With respect to bone, not only will the examination of bone formation and repair characterize the effects of the knockout gene in each case, but subsequent examination of the expression of other genes in knockout mouse bone will help to further define the regulatory networks that modulate the observed knockout phenotype. These studies will elucidate the regulation of gene expression in bone formation and repair, and suggest therapeutic strategies to augment or accelerate bone formation and repair.

We have utilized commercially available knockout mice to determine the effect that the absence of a particular gene has on bone in response to mechanical loading (Technical Objective 1) and in fracture repair (Technical Objective 2). Three strains of mouse were chosen because their phenotype suggested functional importance of their respective genes in tissue formation and wound healing that might also be involved in bone formation and fracture repair. These knockout mouse strains are described in Table 1.

Knockout Mice

Table 1. Knockout (KO) Mice with Phenotypes for Mechanical Loading and Fracture Studies

Gene	JAX[A] Stock #	Genotype[B]	Phenotype
Leptin	0632	B6-*Lep* ^{ob}	NIDDM, obese, delayed wound healing
Bax	2994	B6.129X1-*bax* ^{tm1Sjk}	delayed apoptosis, organ defects (gonads)
Serpine	2507	B6.129S2-Serpine1^{tm1Mlg}/J	enhanced wound healing, fibrinolysis

A: JAX, The Jackson Labs
B: The wild-type control strain for all knockout mouse strains is C57BL/6JJ (B6, JAX Stock #664).

a) Leptin Knockout (Obese) Mice:

Leptin, a 16 kDa protein, expressed predominantly in adipose tissue, functions as a hormone that keeps the brain apprised of the amount of body fat and regulates carbohydrate metabolism (1). This mouse is also a model for non-insulin dependent (NIDDM, Type 2) diabetes. Other

functions related to bone formation include stimulating osteoblastic differentiation and mineralization of bone matrix (2), stimulating the development of the periosteal envelope in growing bone (3), as well as both systemic versus local effects of leptin on the fat and bone cell lineages that are only partially characterized (4,5).

The homozygous leptin knockout phenotype becomes obvious after weaning, when a dramatic increase in body fat occurs. The heterozygous *ob/ob* knockout breeder mice were purchased from the Jackson Labs and bred in our animal facility. Because of the character of recessive inheritance, only ¼ of pups were expected to be homozygous. The homozygous mice were identified by both the obese phenotype and PCR-based genotyping for the *ob* mutation.

b) Bax Knockout Mice:

Bax, the Bcl-2-associated X protein and a member of the Bcl-2 protein family, binds to Bcl-2 to form a heterodimeric complex. It functions to oppose Bcl-2 and promote apoptosis (6). The Bax/Bcl-2 ratio controls the apoptosis frequency in each cell. Both genes are expressed in cartilage and bone cells in the rat (7). Apoptosis has a major impact on skeletal development and remodeling, and is essential for the elimination of osteoblasts during skeletal development (reviewed in 8). The frequency of osteoblast apoptosis controls osteoblast lifespan and bone formation during the postnatal life (reviewed in 9).

The homozygous Bax KO mouse phenotype presents as altered hematopoiesis under infectious challenge, suggesting that challenge by injury might identify an otherwise subtle phenotype in bone formation and repair. Heterozygous breeder mice were purchased from the Jackson Labs and inbred in our animal facility. Only ¼ of all pups were expected to be homozygous mice, but we often observed only a 15% frequency of homozygous knockouts. All mice were identified by PCR-based genotyping for the Bax gene deletion.

c) Serpine Knockout Mice:

The fibrinolytic system has been claimed to play a very important role in a variety of biological phenomena, such as maintenaince of vascular patency, inflammation, embryogenesis, angiogenesis and tissue remodeling processes. Activation of plasminogen by tissue-type plasminogen activator (t-PA) is believed to be required for these functions. However, specific plasminogen activator inhibitor (PAI-1; Protease Nexin-1, PN-1) appears to be the primary physiological inhibitor for this fibrinolytic system. Theoretically, the removal of PAI-1 should result in more or faster plasminogen activation and enhance the process of fibrin-specific clot lysis, promoting healing after fracture or other tissue injury (reviewed in 10).

The serpine-1 mouse is viable and breeds well as a homozygote. The homozygous mutants have a mild hyperfibrinolytic state but normal hemostasis with no obvious knocknout phenotype without challenge through tissue injury. Homozygous breeder mice (PAI-1 deficiency), in which the serpine-1 gene is disrupted (11), were purchased from the Jackson Labs and bred in our animal facility. The genotype of all breeders and pups was identified by PCR-based genotyping for the serpine-1 gene deletion.

The homozygous *Npr3* "Longjohn" (Natriuretic peptide receptor-3, B2;B6-Npr3 $^{lgj\text{-}2J}$ JAX Stock #3507) knockout mouse (12) was originally intended to be one of the knockout mouse strains for studies on bone formation and repair (13), and breeder pairs were purchased from the Jackson Labs. This mouse strain was chosen for its skeletal overgrowth phenotype (hence the nickname "Longjohn") that suggested an important function for the *Npr3* gene in bone formation

and repair. Because the "Longjohn" mice breeders were guaranteed by the supplier to be homozygous, and the pups were assumed to be homozygous, surgery and fracture were performed as soon as they became available and the bones were collected for X-ray, pQCT and RNA extraction. We assumed that the difficulty in genotyping this strain was a technical difficulty, and we proceeded with the studies while we attempted to resolve the genotyping problems. The pups bred in our animal facility failed to show the described phenotype when mature, and we suspected that the genotype of the supplied breeder pairs had been misidentified. Additionally, there was no significant difference in phenotype observed between these knockout mice and wild-type mice by gross examination, X-ray and pQCT examination. Sequence analysis failed to identify the *Npr3* point mutation and confirmed that the genotype of the mice acquired from the Jackson Labs was in fact a wild-type DBA strain, and not the knockout "Longjohn" strain. The Jackson Labs was notified, initiated an investigation and concluded that the genotype of this strain was in fact not "Longjohn". Unfortunately, considerable effort had been expended to establish this colony and begin the studies during the first year of this project before our suspicions were confirmed. We therefore acquired the serpine-1 (Plasminogen Activator Inhibitor-1, *PAI-1* or Protease Nexin-1, *PN-1*) mouse strain as the third knockout mouse strain for the proposed studies.

Body

Technical Objectives

Our Technical Objectives were as follows:

Technical Objective 1: The functional significance of a gene of interest on bone formation will be identified by characterizing the skeletal phenotype in mice deficient in that gene (i.e., knockout, KO, mice) in response to mechanical loading of the bone by exercise.

Our Specific Objectives during the study were as follows:

1. adapt a mechanical loading model for mouse bones that approximates an exercise routine.
2. identify differences in bone formation between knockout and wild-type mice, through measurements of mechanically loaded bone by peripheral quantitative computed tomography (pQCT) and conventional molecular markers of bone formation in the loaded bones of the one strain of knockout mice that exhibited the greatest phenotypic differences in bone response to mechanical load.
3. apply microarray technology to study gene expression in the bones of the one strain of knockout mice that exhibited the greatest phenotypic differences in response to mechanical loading.

Technical Objective 2: The functional significance of a gene of interest on bone formation in response to injury will be identified by characterizing the skeletal phenotype in mice deficient in that gene (i.e., knockout mice) during fracture healing.

Our Specific Objectives for fracture repair during the study were as follows:

1. develop a model for femur fracture in mice.
2. identify the phenotypic differences between 3 strains of knockout mice and wild-type control mice by X-ray examination, pQCT and micro-CT measurements, histological examination of the fracture callus and molecular bone marker analysis of the fracture tissues.

3. apply microarray technology to study gene expression in the fracture tissues of the one strain of knockout mice that exhibited the greatest phenotypic differences in fracture healing.

Additional specific objectives were proposed for a continuation period for these studies.

Our Specific Objectives for the continuation period were as follows:

1. characterize the skeletal phenotype of mice lacking Ephrin-B1 specifically in osteoblasts using PIXImus, pQCT and histology.
2. evaluate the effects of four point bending in Ephrin-B1 conditional knockout mice.

Progress on Technical Objectives

Technical Objective 1:

Specific Objective 1: Adapt a mechanical loading model for mouse bones that approximates an exercise routine.

Mechanical loading determines both the mechanical density and the architecture of bone. Previous studies have established changes in bone mineral content and bone mineral density in response to exercise among boys (14), and our own studies have demonstrated that mechanical loading by exercise increased bone formation in mice (15). In this study, we used knockout mice to identify and characterize the functional effects of exercise-induced bone formation in mice deficient for a gene-of-interest previously implicated in bone growth or development (Table 1, "Leptin", "Bax" and "Serpine" knockout mice). The phenotypic response to mechanical loading in the particular strain of knockout mouse was correlated to X-ray and molecular measurements of bone formation.

Findings

A mechanical loading procedure that approximates exercise was developed. It consisted of a 12-day four-point bending routine of a 9 Newton (N) force applied at 2 Hertz (Hz) and 36 cycles to the right tibia. This routine was developed from a load response trial that tested bone formation in response to loads of 6N through 9N, with the 9N load established as producing the optimal bone response, as measured by pQCT analysis and the expression of molecular markers of bone formation.

The loaded and unloaded contralateral tibias were analyzed for bone formation by pQCT following the final loading. The bone parameters examined in knockout and C57BL/6J wildtype control mice were total bone mineral content, total bone area, periosteal circumference, endosteal circumference, total bone mineral density, cortical bone mineral content and cortical bone mineral density. This wildtype data was compared with that of the knockout strains of mice when they became available through the breeding program and is presented with those strains below.

A mechanical loading routine was performed on the right tibia of leptin KO mice at 10 weeks of age. A 9 Newton (N) load was applied at 2 Hertz (Hz) for 36 cycles for 12 consecutive days. pQCT measurements on both tibias were performed after the final loading and the data were collected and analyzed.

Findings from the four-point mechanical loading test:

There were apparently no statistically significant differences in the response of any of the bone parameters to the 9N mechanical loading routine in the leptin KO mice as compared to the wild-type control mice. Although it would appear that the leptin mouse response was no different than the control mouse response, the leptin mouse is much larger than the control mouse. Because the amount of loading on a bone varies according to its size and geometry, it becomes very necessary to compare the differences in bone parameters using loads normalized to the mechanical strain produced by a particular load on the bone. The mechanical loading approach was modified to account for bone size differences by performing strain gauge tests to normalize the actual strain produced by a force on bones of different sizes.

Leptin Knockout Mice

A four-point bending mechanical loading procedure that approximates exercise was developed. It consisted of a 12-day four-point bending routine of a 9 Newton (N) force applied at 2 Hertz (Hz) and 36 cycles to the right tibia. This routine was developed from a load response trial that tested bone formation in response to loads of 6N through 9N, with the 9N load established as producing the optimal bone response, as measured by pQCT analysis and the expression of molecular markers of bone formation.

For an accurate comparison of bone response after loading between two strains of mice, the larger tibias encountered in the leptin mice must be normalized to their wild-type control bones through force-induced strain. Thus, we measured the tibial Moment of Inertia (MOI) and periosteal circumference (PC) by pQCT and calculated the strains by different loading forces using the formula: Strain = F x L x C/(2 x I x E), I = moment of inertia, C = bone radius, E = 38 Gpa, a coefficient, L = a distance between loading parts. We established the theoretical linear relationship of loading force and strain in B6 and leptin mice (**Figure 1**). To demonstrate the accuracy of theoretical calculation curve, actual strain was measured using strain gauges for several different loading forces in male, female B6 and leptin KO mice.

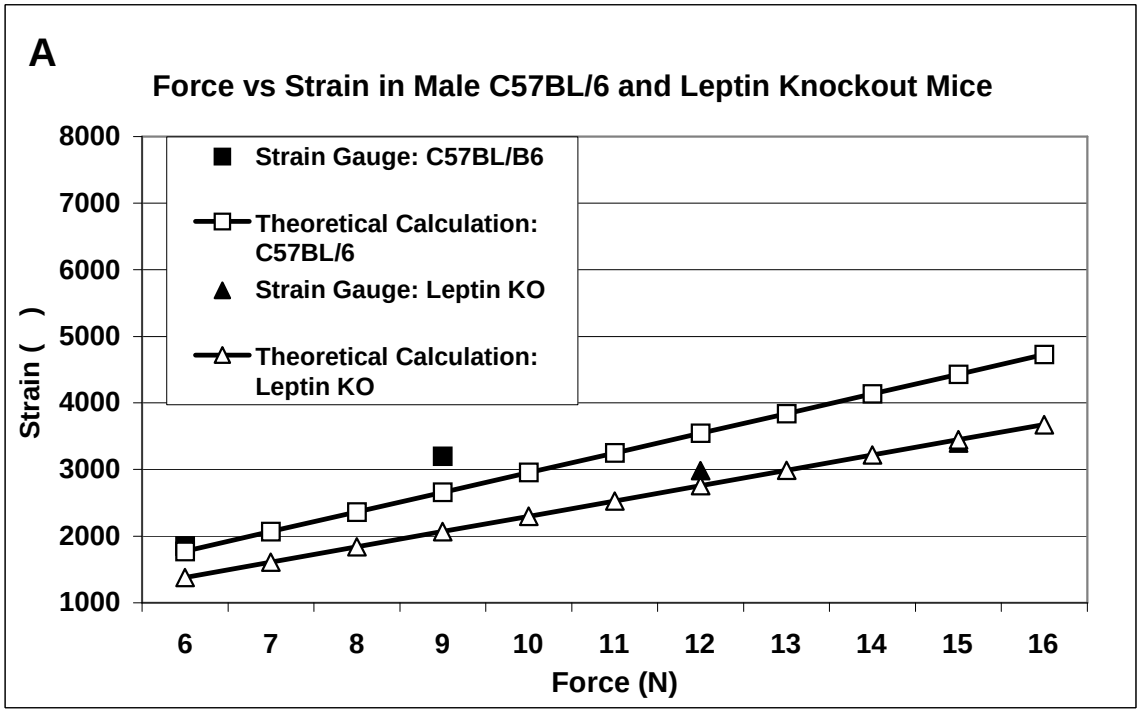

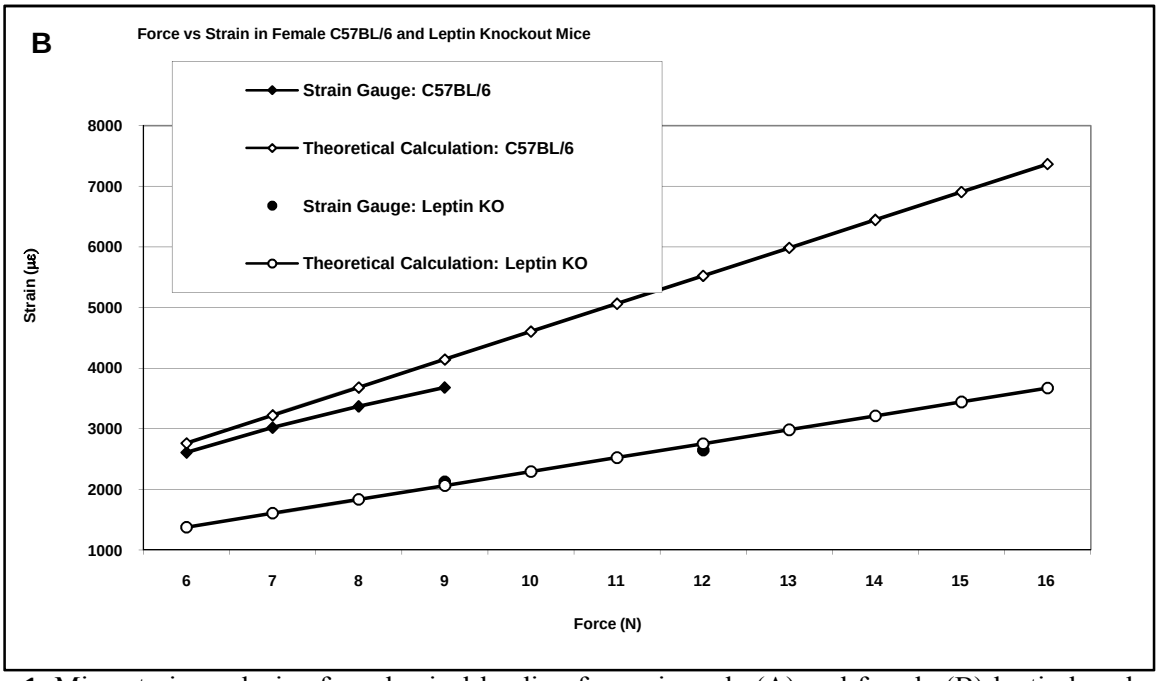

Figure 1. Microstrain analysis of mechanical loading forces in male (A) and female (B) leptin knockout (KO) and C57BL/6J wild-type control mice. Theoretical calculations of strain were compared with strain gauge measurements at different forces. Strain gauge measurements in (A) at 6N in the C57BL/6J mice and 12N in the leptin KO mice are so close to theoretical calculations that the data points are barely visible under the theoretical data points at these forces. This is also true of the 9N and 12N strain gauge measurements of the leptin KO female mice in (B).

Findings from the development of the microstrain gauge approach:

1. From our theoretical calculation curve, leptin KO male and female mice have a same force-strain relationship curve, as they share the same bone periosteal circumference (PC) and (polar) Moment of Inertia (MOI). However, the strain is much higher in female C57BL/6J than in male C57BL/6J mice under a same loading force. This is because female mice have a smaller PC than male mice, resulting in a higher loading force/area unit. The strain in leptin male and female knockout mice is lower than that in female and male C57BL/6J mice under the same loading force. For example, at a force of 9N, we observe a strain 4145 με in female C57BL/6J, 2659 με in male C57BL/6J, and 2067 με in male and female leptin KO mice.
2. From the strain gauge test results (Figure 1), we found that the leptin KO mice displayed a much lower microstrain (2129) in response to 9N load, as we expected, than the control C57BL/6J mice displayed for the same 9N load (3600 microstrain). In both cases, several of the parameters measured in the loaded bone displayed significant changes ($p<0.05$) as compared to the unloaded bone.
3. C57BL/6J mice were then tested for their mechanical response at a load of 6N, a load found to produce a microstrain of 2500, close to the 9N, 2129 microstrain produced by the bone size differences in the leptin KO mice (Figure 1).

Specific Objective 2: identify differences in bone formation between knockout and wild-type mice, through measurements of mechanically loaded bone by peripheral quantitative computed tomography (pQCT) and conventional molecular markers of bone formation in the loaded bones

of the one strain of knockout mice that exhibited the greatest phenotypic differences in bone response to mechanical load.

Findings

Breeding colonies were established for the knockout strains that were expected to exhibit altered bone formation or wound healing due to their particular gene deficiency. We selected three prospective knockout mice (Table 1), which have good viability and fertility, and are commercially available from the Jackson Labs: the Leptin KO, Bax KO and the Serpine KO mice. Because each of these strains had been developed on the C57BL/6J genotype background, the wildtype control mice for comparison in these procedures were purchased as needed from The Jackson Labs.

Polymerase Chain Reaction (PCR)-based procedures were developed to identify heterozygotes for further breeding and homozygous knockouts for experimental procedures. PCR primer design resolved the point mutation that produced the leptin KO, or the gene segments engineered into the Bax KO and serpine-1 KO genomes to interrupt the expression of their respective genes. The leptin KO mice were also identified through their phenotype, as fat accumulation started soon after weaning and well before the 10 to 12 week deadlines for the proposed procedures. The Bax KO pups exhibited a light coat color and eye color phenotype that facilitated the identification of their particular genotype. The serpine-1 KO mouse strain produced only heterozygous KO pups. These factors helped to confirm the genotpye of the respective knockout pups and minimize errors in knockout identification.

The leptin mouse strain bred well and homozygous knockouts were obtained in the expected frequencies, although The Bax mouse mechanical loading study has suffered from reduced homozygous knockout frequencies. Initially, this knockout strain displayed unexpected litter mortality, with a high proportion of pups either neglected or cannibalized. However, with more experienced mothers, litter survival improved substatially. The serpine-1 mouse bred very well, and despite being a homozygote, the genotype of individual pups was confirmed by PCR, largely due to the delays caused by the misidentified genotype of a knockout mouse strain parents originally intended for this study. *Because of the difficulty in obtaining and breeding sufficient numbers of mice quickly enough for these studies, the progress on this Technical Objective was delayed but eventually completed.*

Leptin KO Mice

The mechanical loading routine was repeated in the leptin KO and control mice under loads expected to impart a similar strain to each type of mouse. The load response curve that established the 9N load as best for our leptin KO mouse in preliminary mechanical loading experiments had also determined the microstrain (ms) applied by each load from 6N to 9N. Microstrain measurements on leptin KO mice established that the 2500 ms produced by 9N was produced by a 6N load in a smaller wildtype mouse. Loads in the loading routine were then modified to 6N (wildtype mice) or 9N (leptin KO mice) to apply similar microstrain to bones of different sizes, and the measurements repeated. A microstrain gauge was attached to the bone following loading to confirm the microstrain produced by loading at forces of 9N on leptin KO (Table 2) and C57BL/6J control (Table 3) mice, as compared to 6N on C57BL/6J control mice (Table 4).

Table 2. Strain gauge and mechanical loading results on 10-week female leptin knockout (KO) mice for a **9N load** (2129 ms).

N=4

Raw Data	**10-week female Leptin KO mice** Mean ± SD		
Bone parameters	Unloaded	Loaded	P-value
Total content mg/mm	1.24 ± 0.07	1.41 ± 0.02	0.01
Total Area mm^2	2.43 ± 0.24	2.71 ± 0.16	0.11
Periosteal circumference mm	5.51 ± 0.26	5.81 ± 0.16	0.1
Endosteal circumference mm	4.54 ± 0.28	4.76 ± 0.18	0.23
Total Density mg/ccm	585.26 ± 25.67	631.81 ± 25.35	0.04
Cortical Density mg/ccm	1004.06 ± 18.21	1026.55 ± 10.06	0.07

Table 3. Strain gauge and mechanical loading results on 10-week female C57BL/6J (B6) control mice for a **9N load** (3600 ms).

N=4

Raw Data	**10-week female B6** Mean ± SD		
Bone parameters	Unloaded	Loaded	P-value
Total content mg/mm	0.89 ± 0.02	1.08 ± 0.02	0.00004
Total Area mm^2	1.48 ± 0.04	1.74 ± 0.04	0.0001
Periosteal circumference mm	4.31 ± 0.06	4.67 ± 0.05	0.0002
Endosteal circumference mm	3.26 ± 0.06	3.45 ± 0.08	0.01
Total Density mg/ccm	635.26 ± 19.81	673.17 ± 16.58	0.02
Cortical Density mg/ccm	1078.1 ± 39.50	1115.40 ± 34.70	0.005

Table 4. Strain gauge and mechanical loading results on 10-week female C57BL/6J (B6) control mice for a **6N load** (2500 ms).

N=6

Raw Data	**10-week female B6 mice** Mean ± SD		
Bone parameters	Unloaded	Loaded	P-value
Total content mg/mm	0.88 ± 0.09	0.92 ± 0.10	0.42
Total Area mm^2	1.40 ± 0.35	1.51 ± 0.42	0.59
Periosteal circumference mm	4.18 ± 0.53	4.32 ± 0.61	0.63
Endosteal circumference mm	3.1 ± 0.54	3.19 ± 0.63	0.76
Total Density mg/ccm	701.75 ± 111	689.25 ± 121	0.83

Findings from the microstrain gauge test:

1. From strain gauge test results, we found the leptin KO mice displayed a much lower microstrain (2129, Table 2) in response to 9N load, as we expected, than the control C57BL/6J mice displayed for the same 9N load (3600 microstrain, Table 3). In both cases,

several of the parameters measured in the loaded bone displayed significant changes ($p<0.05$) as compared to the unloaded bone.

2. C57BL/6J mice were then tested for their mechanical response at a load of 6N, a load found to give a 2500 microstrain (Table 4) close to the 9N, 2129 microstrain that produced the bone parameter differences in the leptin KO mice. Based on our strain gauge data in control mice tibia at 2500 ms, we did not find any significant change ($p<0.05$) in the bone parameters in the loaded bone as compared to the unloaded bone. This observation at 6N loading contrasts with the 9N loading routine, and confirms that microstrain normalization is important to accurately measure differences in bone of different sizes.

These results confirm that, when the loading routine is normalized for bone size, the absence of leptin expression does indeed affect the cortical and total bone mineral content and bone mineral density in response to mechanical loading (Table 2).

This mechanical loading routine was then performed on the right tibia of 6 female and 6 male leptin KO mice and 12 female and 9 male B6 control mice at 10 weeks of age. For the desired equivalent microstrain, a 9N load was applied at 2 Hertz (Hz) for 36 cycles for 12 consecutive days to the leptin KO mice, and compared with an identical approach using 6N for the B6 mice. pQCT measurements on both tibias were performed after the final loading on the 12th day and the data were collected and analyzed. The pQCT thresholds were 180-730, designed to detect the low-density bone that might be produced by mechanical loading by this time. Statistical analysis was performed by t-test and the results were deemed significant at $P<0.05$.

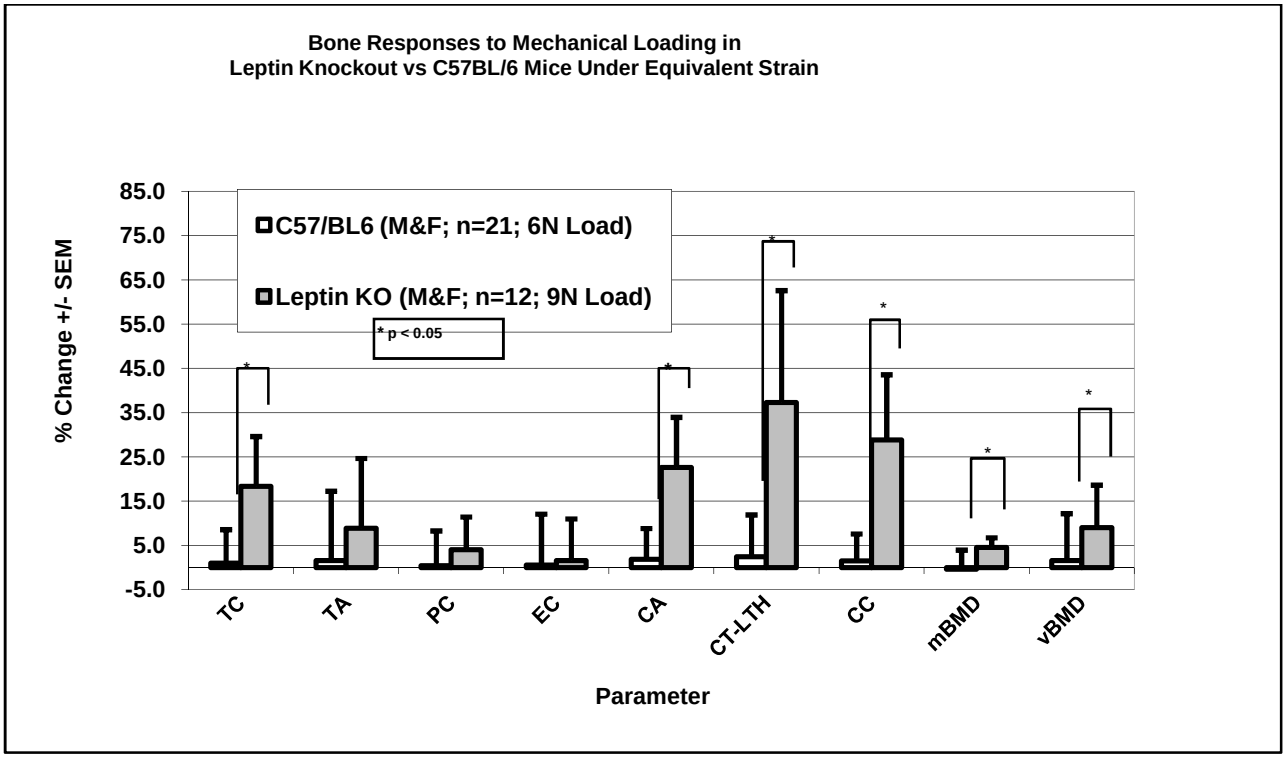

Figure 2. Bone responses to mechanical loading in leptin knockout (KO) and C57BL/6J wild-type control mice under forces providing equivalent strain. The loaded and unloaded contralateral tibias were compared for bone formation by pQCT following the final loading. Males and females were combined for

analysis. The bone parameters examined in knockout and C57BL/6J wild-type control mice were total bone mineral content (TC), total bone area (TA), periosteal circumference (PC), endosteal circumference (EC), cortical area (CA), lower pQCT threshold cortical thickness (CT-LTH), cortical ontent (CC), total bone mineral density (mBMD) and volumetric bone mineral density (vBMD).

Findings from the four-point mechanical loading test in the leptin KO mice:

There were statistically significant differences in the response of the bone parameters to the 9N mechanical loading routine in the leptin KO mice as compared to the wild-type control mice applied to 6N loading. By measures of trabecular bone mineral content, cortical area, cortical thickness, cortical bone mineral content, total and volumetric bone mineral density, leptin KO mice show more sensitivity of loading response than C57BL/6J mice at an equivalent microstrain (Figure 2).

These results confirm that, when the loading routine is normalized for bone size, the absence of leptin expression does indeed affect the cortical and total bone mineral content and bone mineral density in response to mechanical loading. These differences were too subtle to be observed by an examination of the bone histology. Measurements by histomorphometry were therefore not pursued. Micro-CT measurements were also not attempted because of the very successful pQCT measurements (Figure 2). The increase in these parameters must reflect leptin effects on bone formation and deserves further study in this regard, in addition to the obvious involvement of obesity in skeletal loading.

Bax Knockout Mice

The mechanical loading routine was then performed on the right tibias of 5 Bax KO mice and 7 male C57BL/6J control mice at 10 weeks of age. Because the bone sizes of these strains were very similar, both received a 6N load applied at 2 Hertz (Hz) for 36 cycles for 12 consecutive days. pQCT measurements on both tibias were performed after the final loading on the 12^{th} day and the data were collected and analyzed. Statistical analysis was performed by t-test and the results were deemed significant at $P<0.05$.

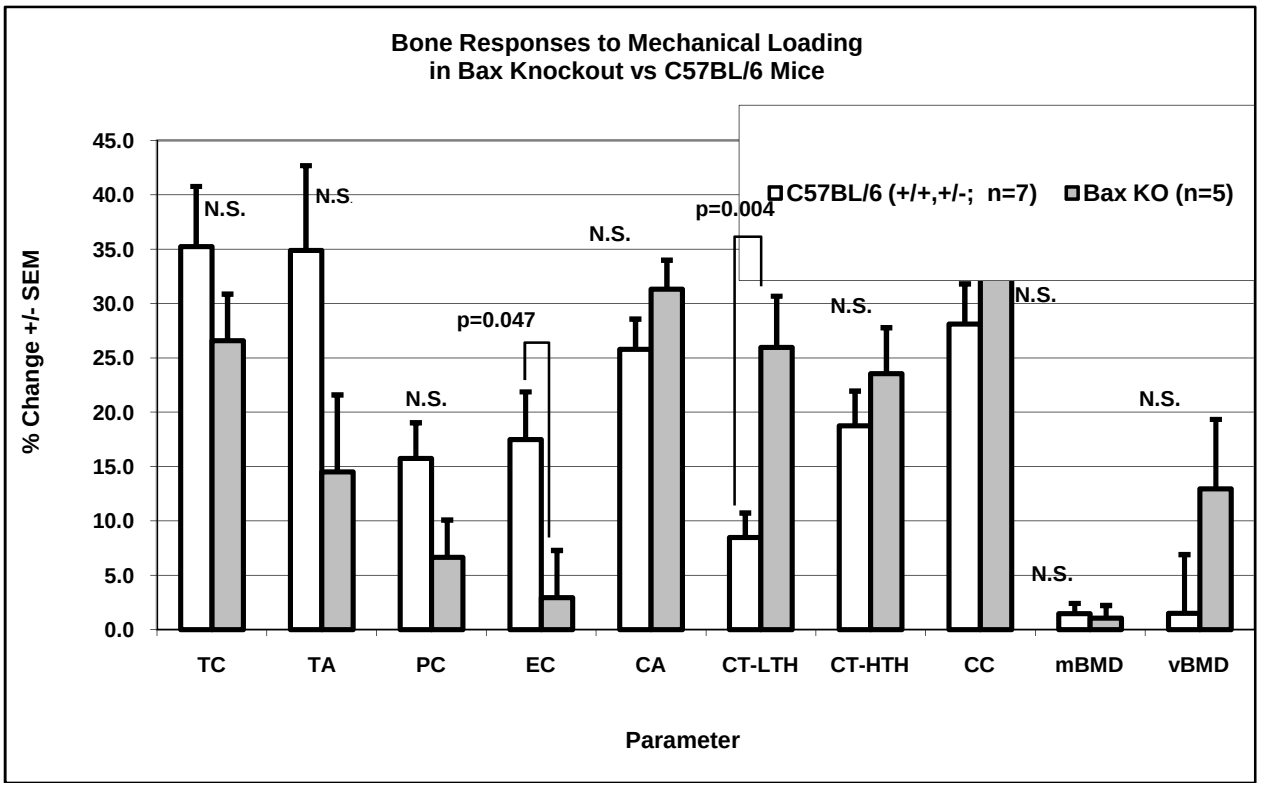

Figure 3. Bone responses to mechanical loading in Bax knockout (KO) and C57BL/6J wild-type control mice under equivalent force (6N). The loaded and unloaded contralateral tibias were analyzed for bone formation by pQCT following the final loading. Only male mice were examined. A comparison of Bax heterozygous littermates (+/-) revealed no significant differences from the C57BL/6J wild-type (+/+); they were combined for the analysis. The bone parameters examined in knockout and C57BL/6J wild-type control mice were total bone mineral content (TC), total bone area (TA), periosteal circumference (PC), endosteal circumference (EC), cortical area (CA), lower pQCT threshold cortical thickness (CT-LTH), higher pQCT threshold cortical thickness (CT-LTH), cortical content (CC), total bone mineral density (mBMD) and volumetric bone mineral density (vBMD).

There were statistically significant differences in the response of only very few of the bone parameters in the Bax KO mice as compared to the wild-type control mice applied at 6N loading (Figure 3). Bax KO mice did display significant differences in the responses of the endosteal circumference and the cortical thickness, when the latter was measured at a lower threshold (Figure 3, CT-LTH) to identify lower density cortical bone. These differences were subtle in effect and could not be observed in an examination of the bone histology, so measurements by histomorphometry were not possible. Determination of the expression of two molecular markers of bone formation from the RNA repertoire of Bax KO and control mice was undertaken; real-time PCR analysis of osteocalcin and collagen-1 gene expression with gene-specific primers also revealed no significant differences in Bax KO bone response to mechanical loading (Figure 4). The latter result suggested that the molecular marker approach for identifying bone formation from mechanical loading was inadequate, and it was discontinued at this point. Micro-CT measurements were not attempted, both because of the success of the pQCT measurements and the availability of the micro-CT instrument, which was undergoing repair. By pQCT measurements, however, the leptin KO mice produced a more dramatic response to mechanical

loading and were at this point the choice for microarray analysis of gene expression induced by mechanical loading.

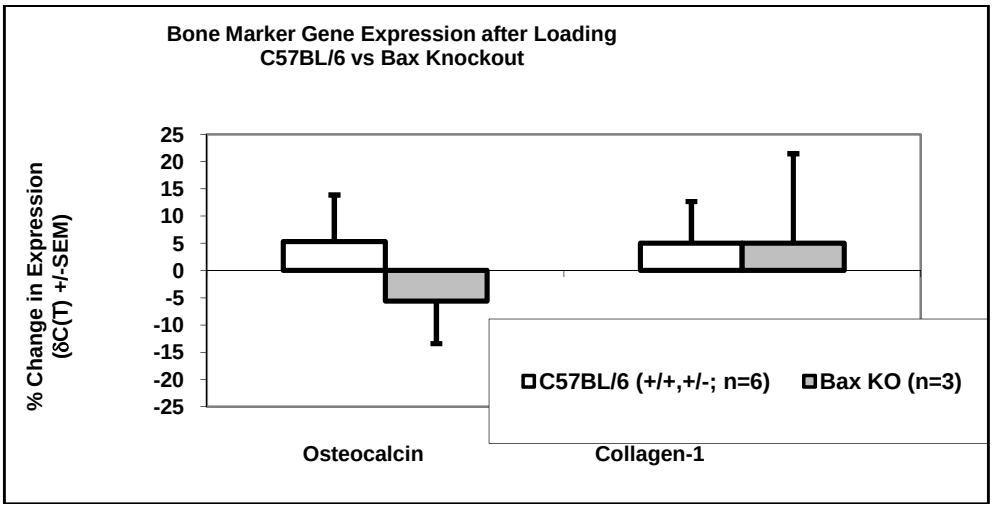

Figure 4. Real-time PCR determination in C57BL/6J wild-type control and Bax knockout (KO) bones after mechanical loading. Six control mice (homozygotes and heterozygotes) were compared with 3 Bax KO mice. Expression was determined through the change in PCR cycle number on osteocalcin and collagen-1 gene expression in total RNA isolated from tibias subjected to mechanical loading. No significant changes in gene expression were observed.

There were statistically significant differences in the response of only very few of the bone parameters in the Bax KO mice as compared to the wild-type control mice applied at 6N loading and described in the previous reporting period. By pQCT measurements, however, the leptin KO mice produced a more dramatic response to mechanical loading and were chosen for microarray analysis of gene expression induced by mechanical loading.

Serpine Knockout Mice

Because the Specific Objectives of the mechanical loading study in Technical Objective 1 had already been completed with respect to the leptin KO and Bax KO strains by the time the serpine-1 KO strain became available, the mechanical loading study of this strain was ommitted in favor of a detailed phenotypic characterization of the serpine-1 KO strain femurs prior to the fracture repair study, and is reported below.

Ephrin B-1 Knockout Mice

d) LoxP-Ephrin B-1 (Conditional) Knockout Mice:

In our continuation studies, we chose to identify the role of a new gene, Ephrin B-1, in fracture repair and mechanical loading. We have chosen Ephrin B-1 since this gene is differentially expressed in bone in response to four-point bending, and since Eph-ephrin signaling has been implicated in the regulation of many critical events during development in a number of tissues including bone (16). Specifically, disruption of Ephrin-B1 resulted in perinatal lethality associated with a range of skeletal phenotypes including abnormal skeletal patterning (17). We propose to conditionally disrupt Ephrin B-1 in osteoblasts and evaluate its role in bone

formation in response to mechanical loading. Such conditional knockouts are generated when the LoxP-Ephrin B-1 gene is established in an animal and bred to an animal with a combination of a promoter from a gene of interest (in our case a bone-specific collagen, type I collagen) and Cre, an endonuclease that excises sequences between Loxp sites. In this way the activation of the collagen promoter in bone expresses Cre and results in the tissue-specific excision of Ephrin B-1 gene with LoxP. This conditional knockout technique is well refined and produces tissue (i.e., bone)-specific knockouts, yet avoids the pre-, peri- and post-natal mortality and morbidity that often accompany more conventional, global gene knockout approaches.

The Ephrin B-1 knockout mouse strain was examined to characterize its skeletal phenotype during the 12-month continuation period, when the Specific Objectives were:

1) To obtain breeding pairs of loxp Ephrin-B1 mice from our collaborator, Dr. Philippe Soriano at Fred Hutchinson Cancer Center, Seattle and establish a colony.
2) Breed loxp Ephrin-B1 mice with type I collagen cre mice to generate cre positive loxp homozygous experimental and cre negative loxp homozygous control mice.
3) To characterize the skeletal phenotype of mice lacking Ephrin-B1 specifically in osteoblasts using PIXImus, pQCT and histology.

The Ephrin B-1 knockout mouse strain was also examined during the final 3-month continuation period, when the third Specific Objective of that period was:

1) To evaluate the effects of four-point bending (i.e., mechanical loading) in Ephrin-B1 conditional knockout mice.

Ephrin B-1 KO mice proved very difficult to breed in sufficient numbers. Additionally, the defect produced a perinatal lethality that confounded attempts to examine mature individuals for mechanical loading studies (or fracture studies). *This problem did not allow us to complete the Specific Objective described for this mouse strain.* A detailed phenotypic analysis of this knockout mouse strain was completed and reported below.

Specific Objective 3: apply microarray technology to study gene expression in the bones of the one strain of knockout mice that exhibited the greatest phenotypic differences in response to mechanical loading.

Microarray analysis provides a powerful tool for the characterization of global gene expression. This study used whole genome microarray gene analysis to identify the genes expressed in fracture repair of the leptin KO mouse tibia at after a mechanical loading routine, when the pQCT data indicated that those bones displayed altered bone formation as compared to the wild-type C57BL/6J wild-type control. The repertoire of expressed genes regulating leptin KO bone formation would be expected to differ greatly from controls at this time.

Total RNA was compared by microarray analysis of “mechanically loaded” tibias from 5 individual male leptin KO mice and 5 individual C57BL/6J wild-type control mice (Table 5). The individual pairs of RNA samples obtained from the fracture calluses were hybridized and analyzed separately, with analysis performed using (Agilent) Genespring software. Changes in expression between the Bax KO fracture callus and the C57BL/6J callus deemed significant at $p<0.05$.

Table 5. Gene Counts: Leptin KO Loading Microarray Dye Swap						
Dyes	**Total Genes**					
	All			2-fold difference		
	Up	Down	Total	Up	Down	Total
Cy5	1013	128	1141	141	55	196
Cy3 Swap	497	312	810	105	65	170
Dyes	**Known Genes**					
	All			2-fold difference		
	Up	Down	Total	Up	Down	Total
Cy5	905	82	987	98	29	127
Cy3 Swap	443	275	719	74	47	121
Dyes	**Unknown Genes**					
	All			2-fold difference		
	Up	Down	Total	Up	Down	Total
Cy5	108	46	154	43	26	69
Cy3 Swap	54	37	91	31	18	49
N=5, 3 females, 2 males						

Up to approximately 1000 known and unknown genes displayed changes in gene expression in response to mechanical loading. In this regard, the unknown genes are of particular interest, as they comprised approximately 10% of the total number of genes with expression changes and suggest a complex regulation of bone formation. The accuracy of the measurement was checked using the "dye swap" approach and seems to provide similar data in each case, but especially for the genes with greater than 2-fold changes in expression. The Cy3 analysis did seem to be less sensitive, however.

The interpretation of gene expression is complicated by the diabetes that accompanies such weight gain. The phenotypic analysis of the leptin KO mouse strain provided valuable information. The phenotypic analysis of the mechanical loading data revealed sex-related differences in bone size that were pursued in a study that was recently concluded and reported below. The microarray data in the male and female mouse tibias that underwent mechanical loading will be examined separately to attempt to identify sex-specific molecular markers of bone formation in this bone.

Technical Objective 2:

During the first twelve months of the study, the functional significance of a knockout gene of interest in bone formation induced by fracture repair was established by a comparison of the skeletal phenotypes in knockout mice deficient in that gene with wild-type control mice. The standardized tibia fracture was abandoned early in this study due to the procedural difficulties with consistent fracture stabilization; the tibia, although easy to experimentally fracture, varies enough in curvature and diameter along its length that any variations in stabilization affect the healing to an unacceptable degree. Thus, we developed a new experimental fracture model in the femur, a bone with more consistent dimensions less susceptible to variations in stabilization,

although more difficult to surgically fracture. Two strains of wild-type mice, C57BL/6J and DBA, were used to develop the femoral fracture model and generate wild-type control mouse data for comparison to knockout mouse data.

The three knockout mouse strains used in the exercise study (Technical Objective 1) were also used in this study (Table 1, "Leptin", "Bax" and "Serpine" KO mice). Bone formation was measured following healing intervals that have been determined to provide characteristic landmarks of fracture callus maturation in our pilot experiments in wild-type mice. The phenotypic response to fracture healing in the particular strain of knockout mouse was compared to X-ray and molecular measurements of bone formation and histologic examination of the fracture tissues. These measurements were used to determine whether the knockout gene-of-interest was functionally significant in fracture healing, and what fracture tissues were affected by the absence of its expression.

Specific Objective 1: Develop the femur fracture model of bone repair in mice.

Findings

Preliminary experiments indicated that the tibia fracture model was inadequate for this fracture healing study. The tibia fracture and subsequent healing were inconsistent and produced unacceptable statistical variations due to variations in the tibial dimensions and curvature. Although its size and proximity to the torso made the femur fracture surgery more difficult, we successfully developed the femur fracture model in wild-type mice (18). Briefly, an intramedullary pin is surgically implanted in the femur prior to fracture and the incisions closed. The mechanical testing device used in Technical Objective 1 is used to produce a fracture by the three-point bending technique. The procedure produced fractures that were more consistently transverse and midshaft (Figure 5), and expected to provide an excellent basis for the comparison of the differences in fracture healing between wild-type and knockout mice.

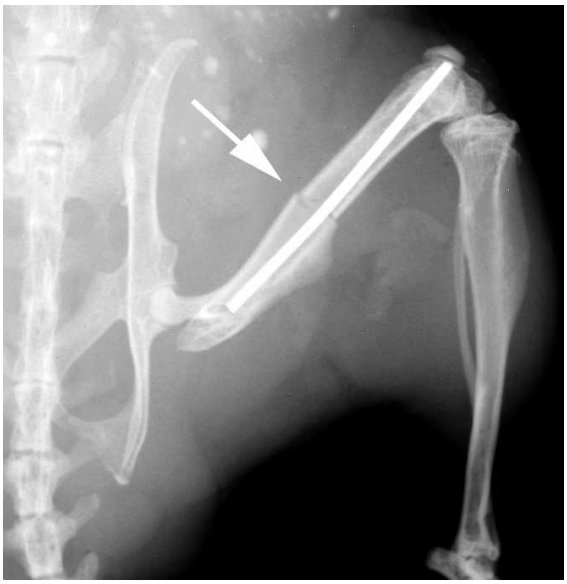

Figure 5. Femur fracture model. An X-ray photograph was obtained immediately after femoral fracture surgery in a C57BL/6J mouse. The arrow indicates the fracture site. The stabilizing pin is easily visible.

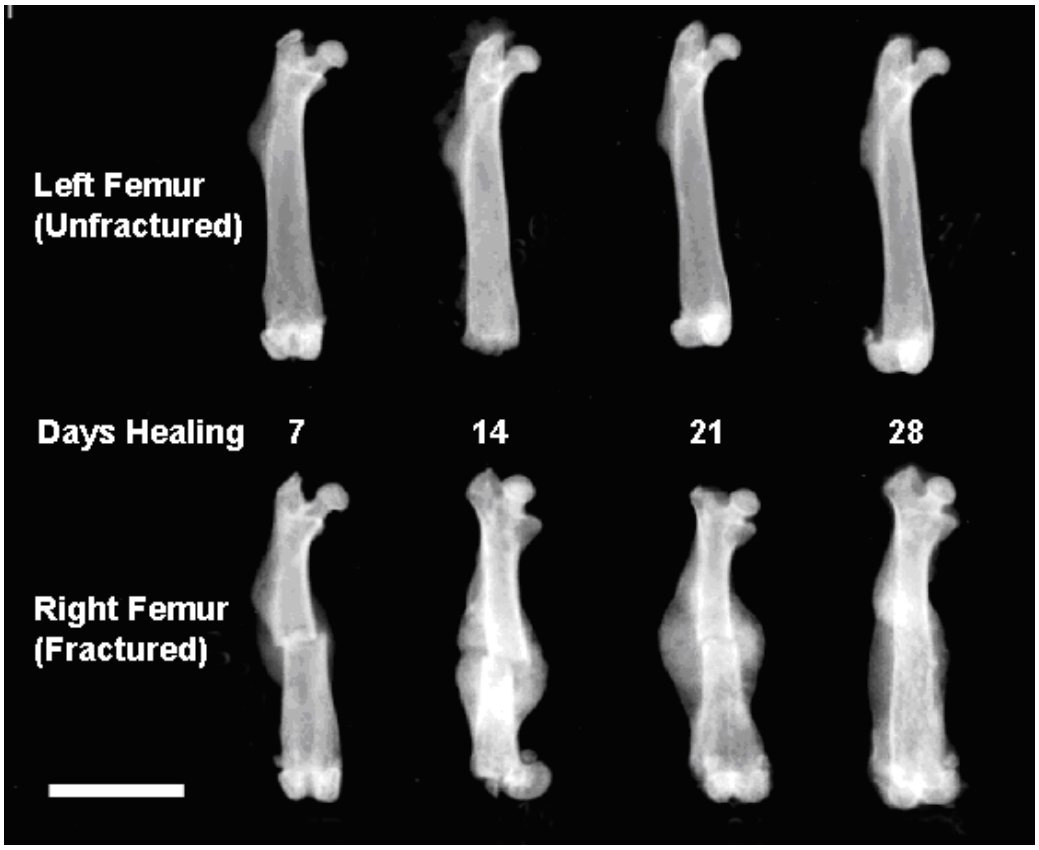

Figure 6. X-ray photograph of healing mouse fractured right femurs compared with unfractured left femurs at 7, 14, 21 and 28 days post-fracture. The development of the mineralized (i.e., hard) callus can be monitored from its early stages, at 7 days, through its maximum, at 14 to 21 days, and into remodeling to cortical bone, at 28 days. Each stage has characteristic features for comparison to impaired fracture repair. Healing is defined as that point when the bony tissue of the hard callus bridges the fracture gap, usually after 28 days in the mouse; remodeling to cortical bone continues after this time, eventually resolving the fracture callus. Scale bar = 5 mm.

Because the C57BL/6J is the background strain on which all of the knockout mouse strains have been developed, the same C57BL/6J mice served as controls for the X-ray and pQCT analysis of all 3 knockout mouse strains. Fractures were produced in several C57BL/6J mice (wild-type control) mice. X-rays of individual fractured femurs were obtained at days 7, 14, 21 and 28 after facture were (Figure 6). The expected progession of callus development was easily visible by X-ray.

pQCT data for each of the 4 post-fracture healing times was collected in C57BL/6J mice (Figure 7). For analysis of callus development during healing, it was necessary to adapt the pQCT analysis to quantify soft and hard tissues of the maturing fracture callus. We therefore adjusted the thresholds of the pQCT analysis and measured the bone mineral content at 1 mm intervals, or "slices", along the length of the fracture callus so that only the lower density (noncortical) bone was detected. The values at each interval were added together to quantify the bone mineral content of the entire fracture callus. As expected, the bone mineral content (BMC) of this low-density callus bone peaked at 14 and 21 days, and then declined upon remodeling later in healing (Figure 7). An additional analysis further adjusted the pQCT thresholds and

measured the cross-sectional area at 1 mm slices along the length of the fracture callus, detecting the combined soft callus tissues and lower density (noncortical) bone of the hard callus (i.e., the callus cross-sectional area per slice). The cross-sectional area values at each 1 mm interval were added together to quantify the cross-sectional area of all callus tissues of the entire fracture callus (data not shown). These cross-sectional areas therefore represent a measure of the size of the fracture callus that can be compared with the bone mineral content measurements. It was possible to resolve the total callus area from the lower density bone area simply by adjusting the thresholds of the analysis. For all parameters, statistical analysis was performed by least significant analysis test, and deemed significant at $p<0.05$. In this way we used pQCT data to analyze the development of the soft and hard callus and identify differences between wild-type (normal) and the three strains of knockout mice.

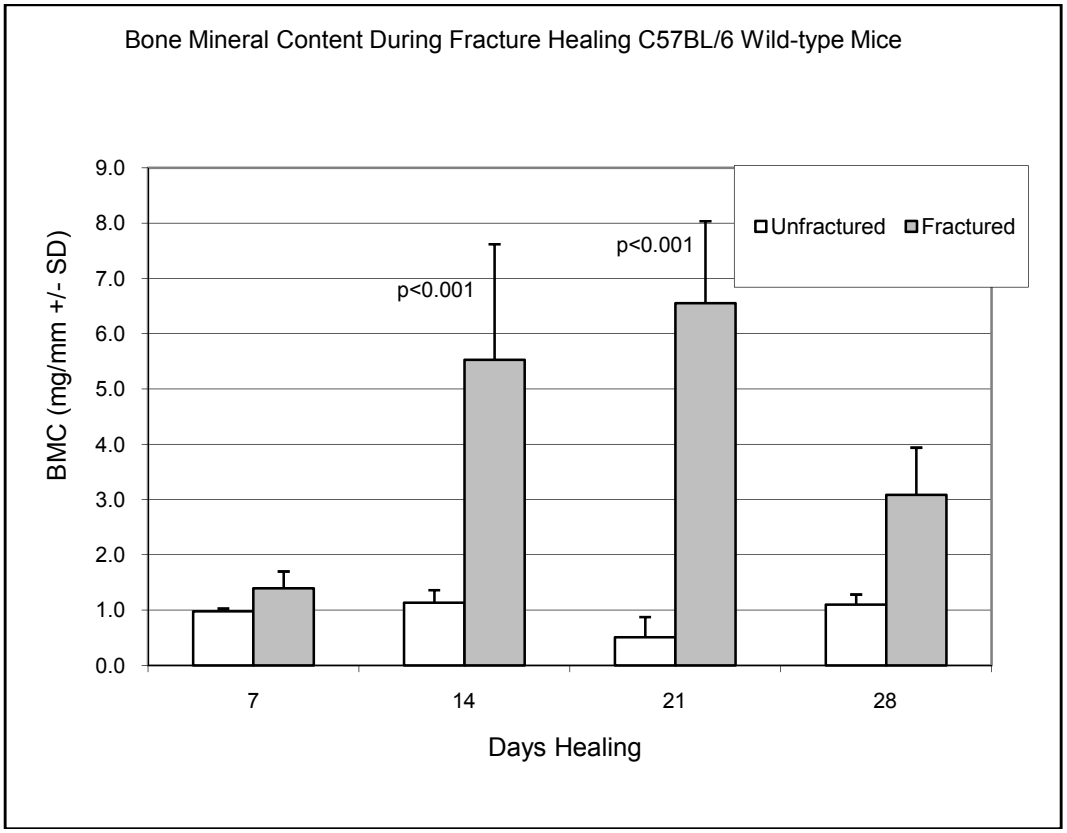

Figure 7. Bone mineral content after femoral fracture in C57BL/6J wildtype control mice. Results represent fractures produced in the (right) femurs of 4 mice at each healing time as compared to the unfractured (left) contralateral bone in each mouse. pQCT parameters are adjusted to exclude the bone mineral content of the cortical bone and measure only the lower density bone of the hard callus or the intramedullary trabecular bone (the values observed in the unfractured left bones, above). This profile of the bone mineral content during healing is typical; it quantifies the visual interpretation of the X-rays (Figure 6) and serves as a basis of comparison for the knockout mouse fracture analysis at different stages of healing.

Histological analysis of the C57BL/6J wildtype control mice fractures throughout healing confirmed that fracture repair was progressing normally. The histology at the 7, 14, 21 and 28 day post-fracture time points was highly characteristic of the usual development of the fracture

callus (**Figure 8**, below). The histology of the knockout mouse fractures was also compared against this profile to elucidate the functions of the knockout gene in fracture repair. Histological analysis of fracture healing in the different knockout strains of mice employed different staing approaches, including hematoxylin-eosin staining for general examination, Safranin-Orange (Safranin-O) staining for cartilage, and tartrate resistant acid phosphatase (TRAP) staining for osteoclasts, a measure of resorption.

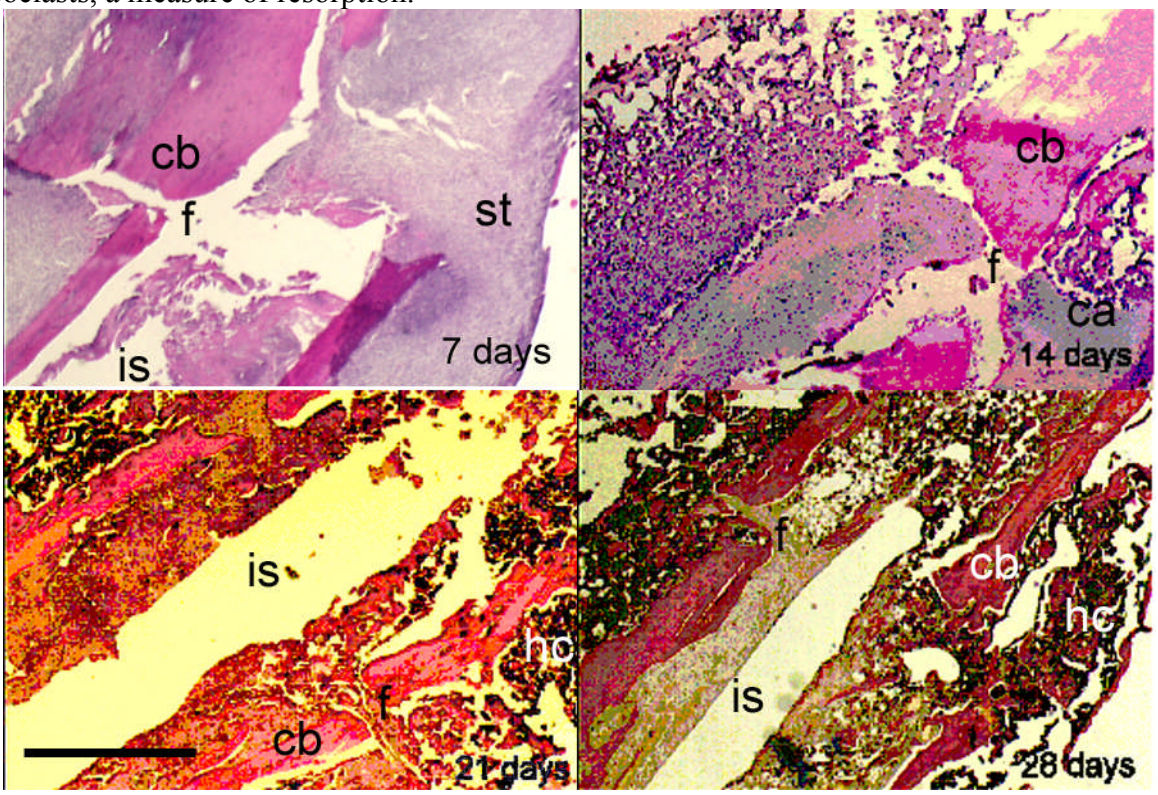

Figure 8. Hematoxylin and eosin stains of histological sections for each post-fracture healing time point show fracture healing at 7 days (upper left), 14 days (upper right), 21 days (lower left) and 28 days (lower right). The cortical bone (cb) and fracture (f) are visible in each panel, and the intramedullary space (is) where the marrow has been ablated by the stabilizing pin is visible in three pictures. The soft tissue (st) at 7 days healing matures to cartilage (ca) the noncortical bone that comprises the hard callus (hc) at 14 days, which eventually bridges the fracture at approximately 28 days healing. The hard callus that is measured for bone mineral content by pQCT under our parameters that exclude the cortical bone, and all tissues except the cortical bone are measured in the cross-sectional area. Scale bar = 0.50 mm.

Specific Objective 2: identify the phenotypic differences between 3 strains of knockout mice and wild-type control mice by X-ray examination, pQCT and micro-CT measurements, histological examination of the fracture callus and molecular bone marker analysis of the fracture tissues.

Findings

This Specific Objective with respect to fracture repair studies (Technical Objective 2) was undertaken at the same time as the mechanical loading studies (Technical Objective 1). The same problems were encountered with respect to litter survival and, above all, misidentification of the

originally proposed “Longjohn” strain breeders. As with mechanical loading, the serpine-1 KO strain was substituted and the respective knockout mouse colonies were eventually developed to sufficient numbers to procede with the fracture studies in Specific Objective 3 (below), although delayed.

The femur fracture model was developed in the first year of this study and was applied to all 3 knockout mouse strains and the C57BL/6 wild-type control strain. Briefly, an intramedullary pin was surgically implanted in the femur prior to fracture and the skin incision closed. A diaphyseal fracture was produced by the three-point bending technique (15). This procedure produced fractures that were consistently transverse and midshaft (Figure 5, above), and provided a uniform basis for the comparison of the differences in fracture healing between wild-type and knockout mice. The development of the knockout fracture calluses during healing was examined by X-ray (**Figure 9**), pQCT and histology (Figure 10). X-ray analysis revealed the expected development of the soft and hard fracture callus, and bony union of the hard callus at 3 to 4 weeks post-fracture (Figure 9). A qualitative examination of the X-rays suggested that there were differences in the dimensions of the fracture callus at different post-fracture intervals that might be related to the (knockout) gene-of-interest. Histologic staining revealed the fracture callus tissues expected during healing (14 days post-fracture in **Figure 10**). These analysis techniques were therefore well-suited to the analysis of knockout fracture repair.

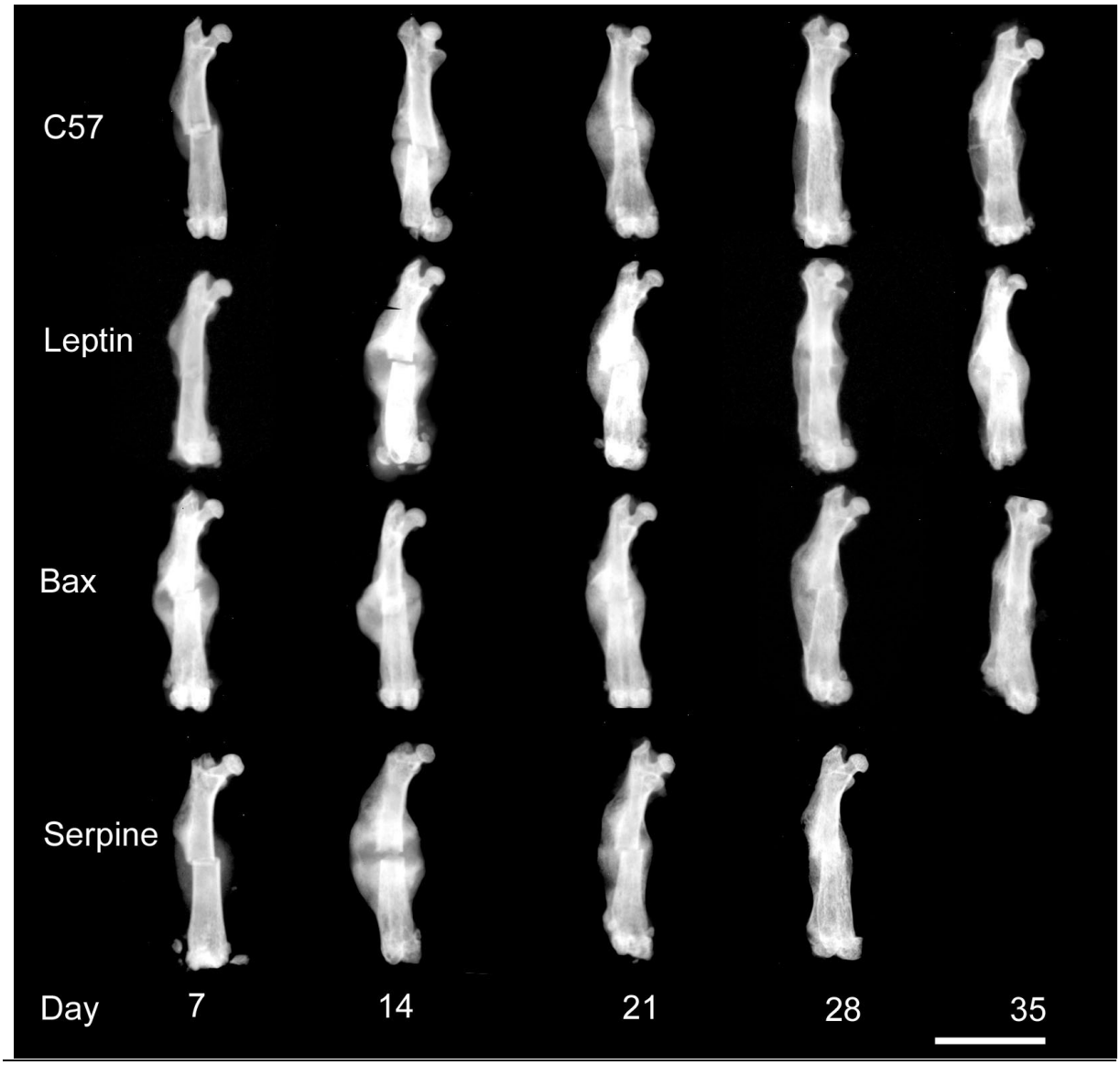

Figure 9. X-ray photograph of healing mouse fractured right femurs in C57BL/6J femurs, compared at weekly intervals throughout fracture healing to fractured right femurs in the three knockout (KO) mouse strains: Leptin KO, Bax KO and Serpine KO. The X-ray contains representative femur fractures from each strain. Healing, as defined by bony union of the fracture callus tissues, normally occurs between three and four weeks post-fracture, as seen here. Scale bar = 5 mm.

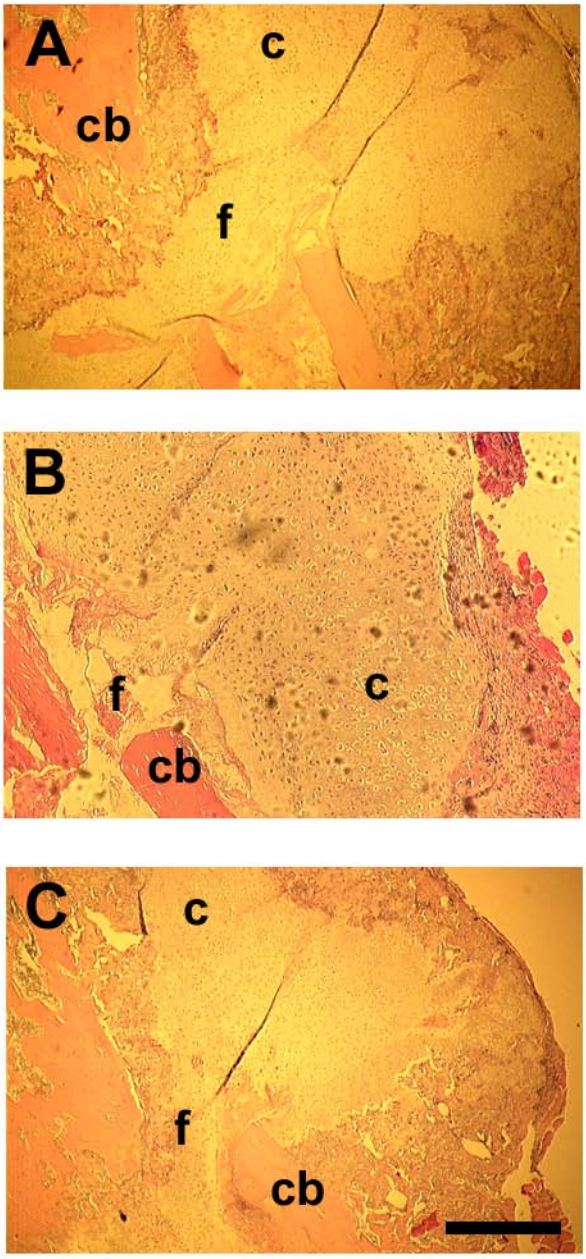

Figure 10. Hematoxylin and eosin stains of fracture callus sections at 14 days healing. (A) C57BL/6J wild-type control mouse, (B) leptin KO mouse, (C) Bax knockout mouse. The cortical bone (cb), cartilage (c) and the fracture (f) are visible in each panel. Healing is typical of normal fracture repair in the mouse. The gap will eventually bridge by 28 days healing. Scale bar = 0.50 mm.

During the first twelve months of the study, the functional significance of a knockout gene of interest in fracture repair was begun by a comparison of femur fracture healing in knockout mice deficient in that gene with wild-type control mice. Subsequently, the three knockout mouse strains used in the exercise study (Technical Objective 1) were also used in this study (Table 1, "Leptin", "Bax" and "Serpine" KO mice). The description of each knockout mouse and the

relevance of the phenotype to bone formation in mechanical loading and fracture repair are provided in Table 1.

Bone formation in the healing fracture was measured following weekly healing intervals that have been determined to provide characteristic landmarks of fracture callus maturation in our pilot experiments in wild-type mice. The phenotypic response to fracture healing in the particular strain of knockout mouse was correlated to X-ray, pQCT, histology and molecular measurements of bone formation and histologic examination of the fracture tissues. These measurements were used to determine whether the knockout gene-of-interest was functionally significant in fracture healing, and which fracture tissues were affected by the absence of its expression.

For the analysis of callus development, it was necessary to adapt the pQCT analysis to quantify soft and hard tissues of the maturing fracture callus. We therefore scanned the bone at high resolution 1 mm intervals along the length of the fracture callus. The thresholds of the pQCT analysis were adjusted so that only the lower density (noncortical) bone or soft tissue was measured. The values at each 1 mm scan interval were added together to quantify the bone mineral content of the entire fracture callus. In this way we used pQCT data to analyze the development of the soft and hard callus and identify differences between wild-type (normal) and knockout (altered) healing in mice. The pQCT parameters and their threshold settings used to quantify the fracture callus were the:

1) bone mineral content (BMC) of the lower density fracture callus and intramedullary bone, at threshold 214-570, a measurement of the bone in the fracture callus, excluding the cortical bone.
2) cross-sectional area of the lower density fracture callus and intramedullary bone, at threshold 214-570, a measurement of the cross-sectional area of the bony fracture callus, excluding the cortical bone (i.e., the trabecular area).
3) cross-sectional area of the soft tissue and lower density fracture callus and intramedullary bone, at threshold 0-570, a measurement of the cross-sectional area of all bony and soft tissue of the fracture callus, excluding the cortical bone (i.e., the total area, excluding cortical bone).

Because the C57BL/6J is the background strain on which all 3 knockout mouse strains have been developed, the same C57BL/6J mice served as controls for the X-ray and pQCT analysis of all 3 knockout mouse strains. Statistical analysis was performed by least significant analysis test, and deemed significant at $p<0.05$.

Findings

Leptin Knockout Mice

A preliminary examination of the fracture calluses by X-rays revealed that the healing was very similar in leptin KO and control mice throughout healing (**Figure 9**). Because differences were difficult to quantify visually (Figure 9), pQCT measurements of the fracture bone mineral content, bony cross-sectional area and total callus hard and soft tissue area were undertaken for all samples (Figures 11, 12, 13).

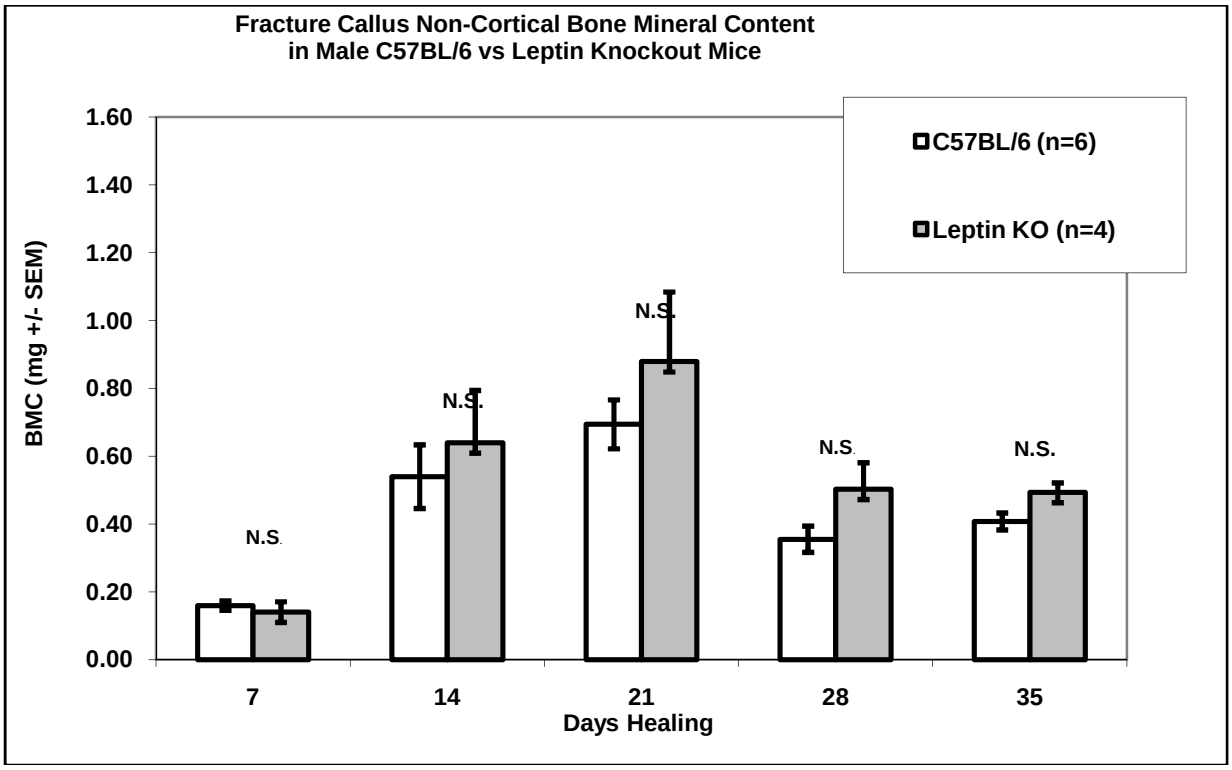

Figure 11. Bone mineral content after femoral fracture in male leptin knockout (KO) and C57BL/6J wildtype control mice. This profile of the bone mineral content during healing is typical of normal fracture healing.

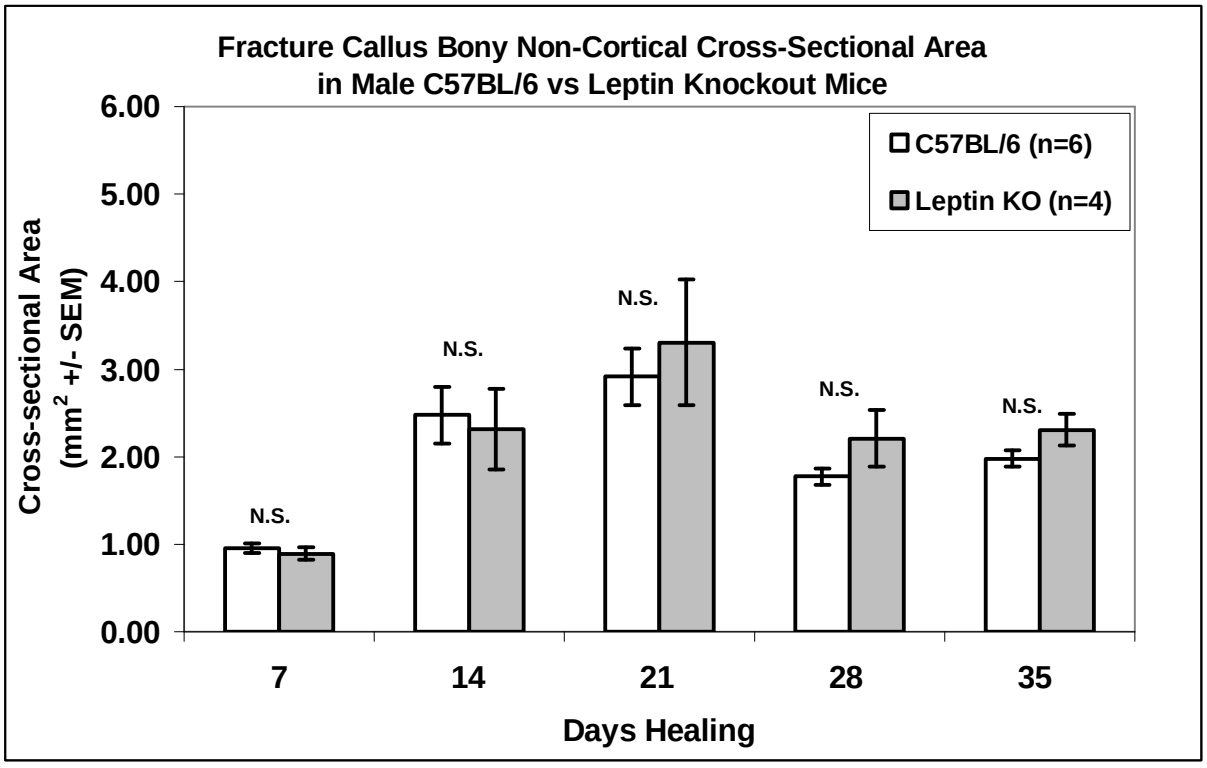

Figure 12. Cross-sectional area of the bony fracture callus after femoral fracture in male leptin knockout (KO) and C57BL/6J wildtype control mice. This profile of this area during healing is typical of normal fracture healing.

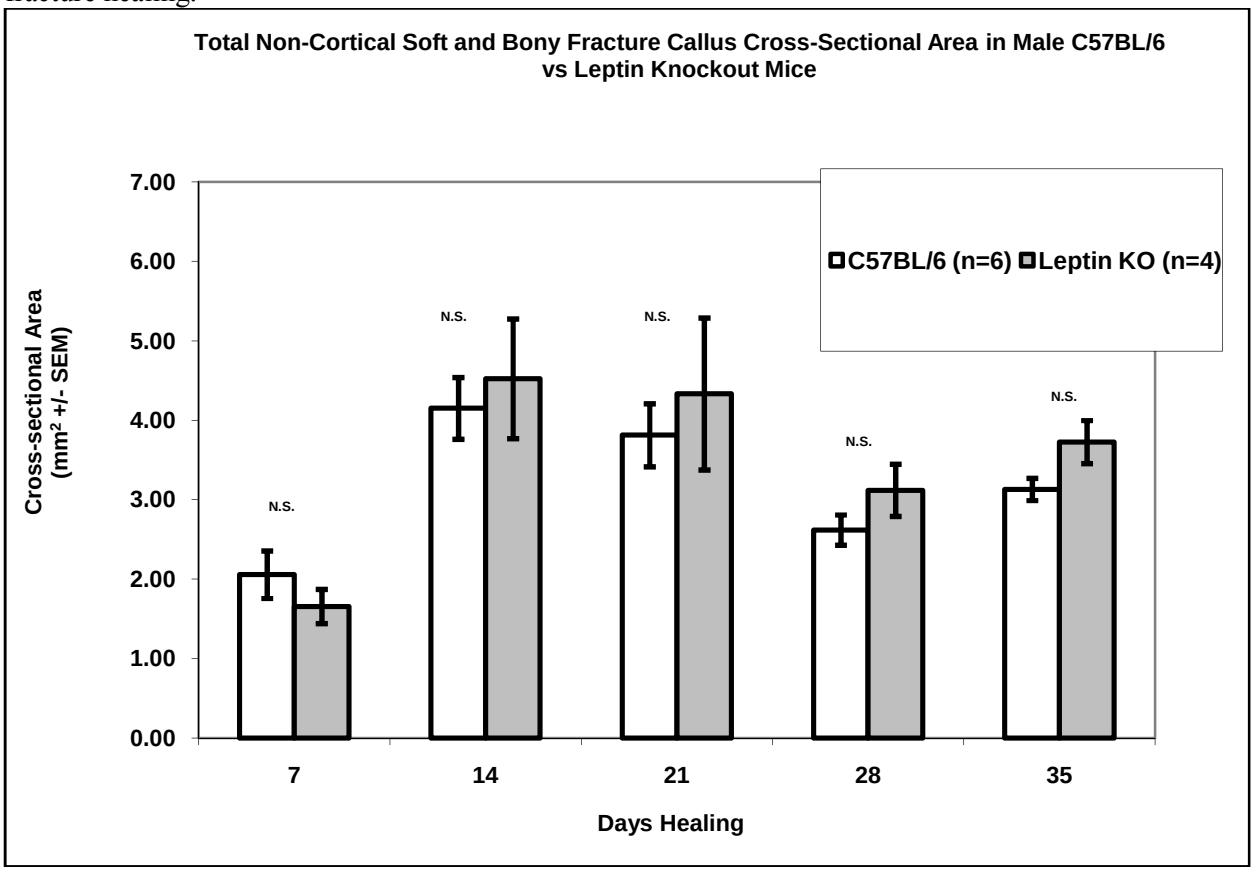

Figure 13. Cross-sectional area of the total fracture callus (soft and bony tissue) area after femoral fracture in male leptin knockout (KO) and C57BL/6J wildtype control mice. This profile of this area during healing is again typical of normal fracture healing.

The pQCT data for each of the 5 post-fracture healing times was collected in the leptin KO and and C57BL/6J mice. As observed in the X-ray, the bone mineral content of this low-density callus bone peaked at 14 and 21 days, and then declined upon remodeling later in healing (**Figure 11**). This pattern was also reflected in the callus bony cross-sectional area (Figure 12) and the total callus cross-sectional area (**Figure 13**). By pQCT measurement, at no time during healing did the leptin KO mice display any significant changes in the bone content or cross-sectional area of the bony tissue or total tissue. The different phases of callus development that are manifested in these callus parameters were therefore normal during fracture healing in this knockout mouse strain. The leptin KO mice probably had additional physiologic complications, such as diabetes, that confounded their normal fracture healing. When micro-CT analysis became available, leptin KO fracture calluses were examined to obtain a higher resolution measurement of healing.

As stated above in Specific Objective 2, breeding sufficient numbers of this mouse proved to be difficult due to litter mortality. Unfortunately, there was also a higher than expected mortality after surgery, and more than 50% died due to difficulties following injectable surgical anesthesia. *Though slightly delayed, with the application of the micro-CT analysis Specific Objective 3 was successfully completed for the leptin KO mouse strain.*

Micro-CT Analysis of Leptin KO Fracture Healing

As described above, at no time during fracture healing did the leptin KO mice display any significant changes in the bone content or cross-sectional area of the bony tissue or total tissue by pQCT. *The micro-CT portion of the Technical Objective was recently achieved with the acquisition of micro-CT instrumentation and the implementation of micro-CT studies of fracture healing.* Leptin knockout fracture calluses were harvested at 14 days post-fracture and examined by micro-CT to obtain a higher resolution measurement of healing. These results were also examined with respect to the sex-specific differences in unfractured femur size observed in these mice, another study that was pursued and is discussed immediately below.

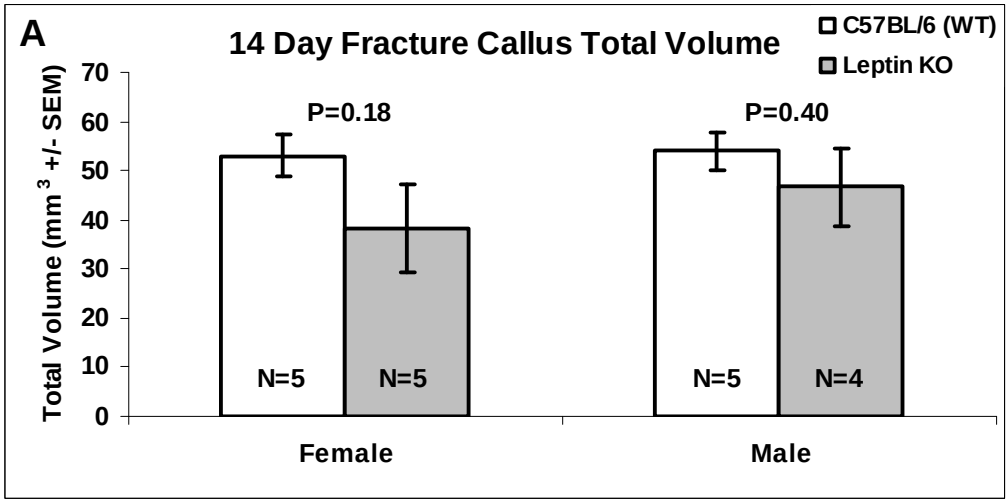

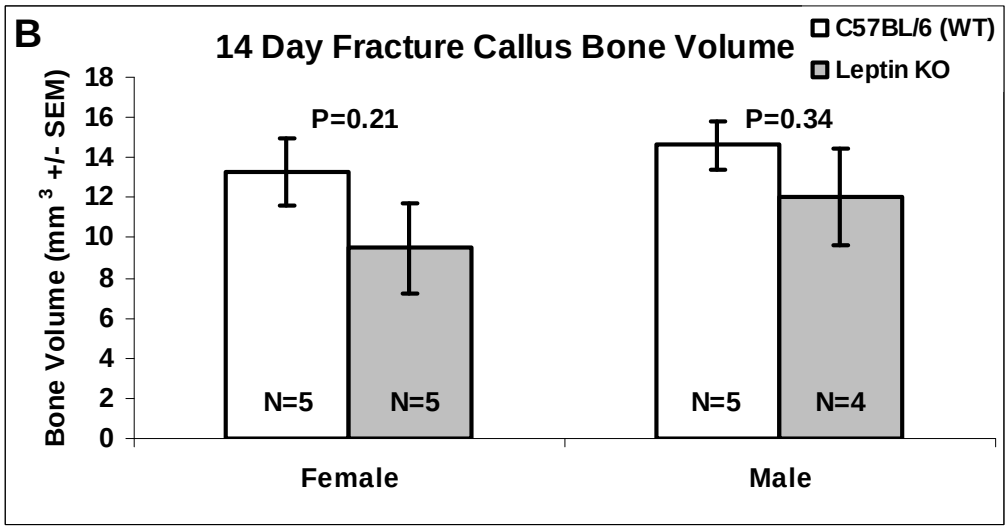

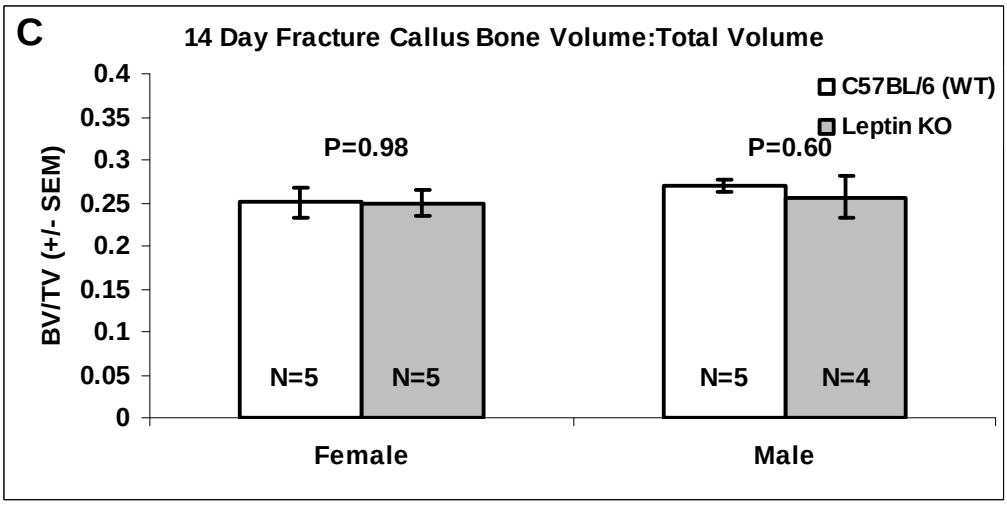

Figure 14. Micro-CT analysis of fracture callus size through bone and tissue volume parameters in male and female C67BL/6 wild-type control mice and leptin KO mice. Group sizes are indicated. Statistics were performed by t-Test.

A) Total volume of all fracture callus tissues.
B) Volume of mineralized fracture callus tissues.
C) The ratio of bone volume to tissue volume of the fracture callus.

It was found that the routine measurements of fracture callus size, the total volume, bone volume and bone volume:total volume (bone volume fracture) were no different between leptin KO and C57BL/6J wild-type control mice at 14 days post-fracture, confirming the pQCT assessment of the fracture callus dimensions (Figure 12).

However, the improved sensitivity of the micro-CT identified significant increases in the trabecular number and decreases in the trabecular spacing of male leptin KO fracture calluses as compared to male C57BL/6J wild-type fracture calluses (**Figure 15B** and **15D**, respectively). The female fracture calluses trended in the same directions as the males for each of these parameters, and might also reach significance if more individuals were examined. These two observations suggest a higher density of trabeculae in the maturing leptin KO fracture callus at 14 days post-fracture, when fracture callus size is at its maximum, and might compensate for a reduced bone quality in the leptin KO mouse. None of the other callus parameters normally reported in micro-CT analysis of fracture repair (bone and tissues volumes, connectivity density and trabecular thickness) were significantly different between these two mouse strains (**Figure 15**).

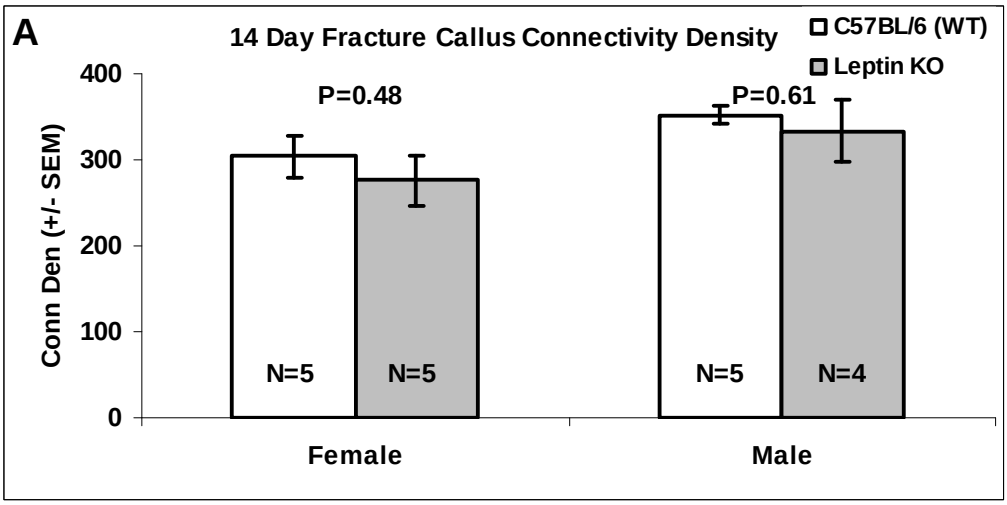
A
14 Day Fracture Callus Connectivity Density
C57BL/6 (WT)
Leptin KO
Conn Den (+/- SEM)
400
300
200
100
0
P=0.48
P=0.61
N=5
N=5
N=5
N=4
Female
Male

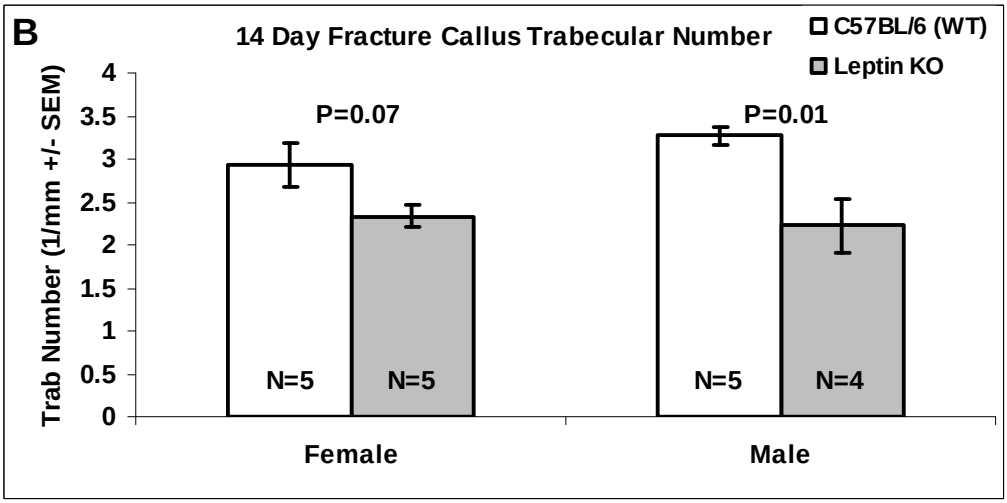
B
14 Day Fracture Callus Trabecular Number
C57BL/6 (WT)
Leptin KO
Trab Number (1/mm +/- SEM)
4
3.5
3
2.5
2
1.5
1
0.5
0
P=0.07
P=0.01
N=5
N=5
N=5
N=4
Female
Male

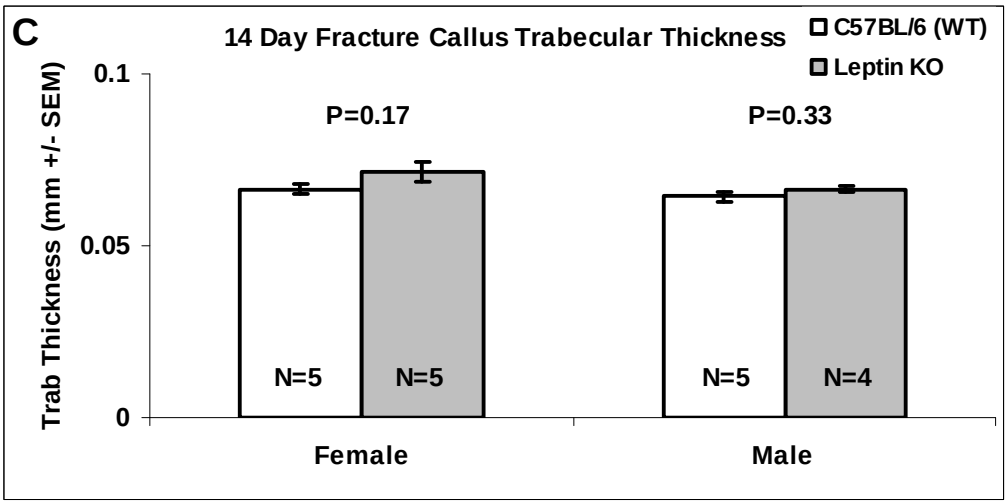
C
14 Day Fracture Callus Trabecular Thickness
C57BL/6 (WT)
Leptin KO
Trab Thickness (mm +/- SEM)
0.1
0.05
0
P=0.17
P=0.33
N=5
N=5
N=5
N=4
Female
Male

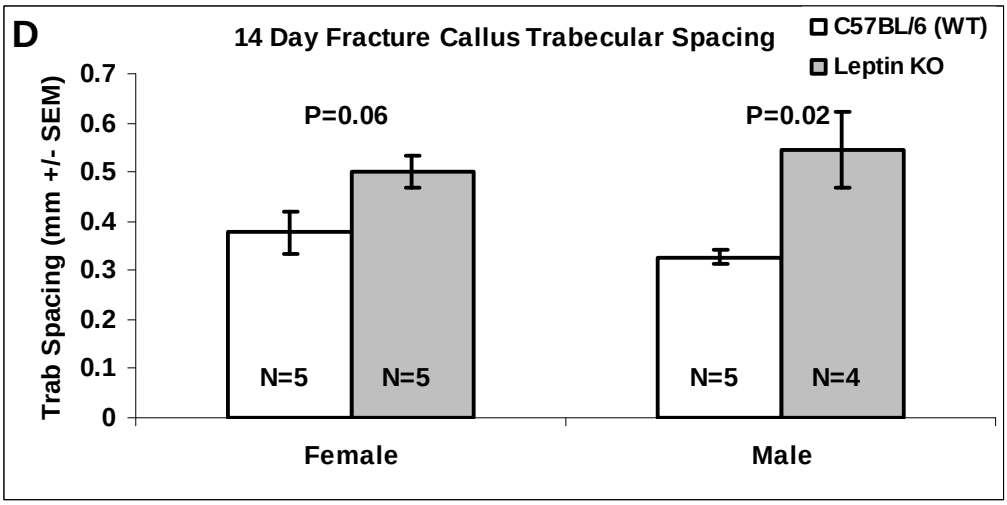

Figure 15. Micro-CT analysis of fracture callus trabecular parameters in male and female C57BL/6 wild-type control mice and leptin KO mice. Group sizes are indicated. Statistics were performed by t-Test.
A) Connectivity density
B) Trabecular number
C) Trabecular thickness
D) Trabecular spacing

The apparently greater effect in the male mice suggests that there might be sex differences in bone repair, although several metabolic issues might complicate this interpretation in the leptin KO mouse. The leptin KO mouse does exhibit sex-related differences in bone size that are reported in a study of additional findings in leptin KO mice bone formation below.

Additional Findings in the Leptin Knockout Mice

As initially considered in the mechanical loading studies conducted on the tibias, measurement of the unfractured contralateral bones of male leptin KO mice in the fracture study revealed surprising changes in femur size relative to male wild-type mice and female leptin KO and wild-type mice. We pursued this investigation. To determine whether leptin differentially affects bone formation in males and females, we compared body characteristics and several parameters of bone size in male and female knockout mice with male and female mice of its wild-type C57BL/6J background strain. *This entire study represents an important description of sex-specific differences in bone size and is in addition to that described in the original Technical Objective.*

1. The initial phenotypic comparison of body weight, total body fat and total lean body mass (**Figures 16, 17** and **18**, respectively) was performed on male and female mice at 10 weeks of age. Each study group contained at least 12 animals.
2. Bone parameters in male and female mice were then compared at 12 weeks of age. Femur length was measured (**Figure 19**). The midpoint of the femoral diaphysis was analyzed by peripheral quantitative computerized tomography (pQCT). The periosteal circumference (PC, **Figure 20**), endosteal circumference (EC, **Figure 21**), trabecular area (TA, **Figure 22**), total bone mineral content (BMC, **Figure 23**) and total bone mineral density (BMD, **Figure 24**) using an analysis threshold of 630-630. pQCT measurements of the trabecular bone area used an analysis threshold of 570-214. Each study group contained more than 11 animals.

3. Gender-specific differences in bone mass and size also implicate the sex steroid hormones in bone metabolism (19). To determine whether a reduction in androgen levels might explain the effect of leptin deficiency on bone size, the circulatory levels of androgen and estrogen in male and female leptin KO mice were also assessed (**Figure 25**). Each study group contained more than 18 animals.

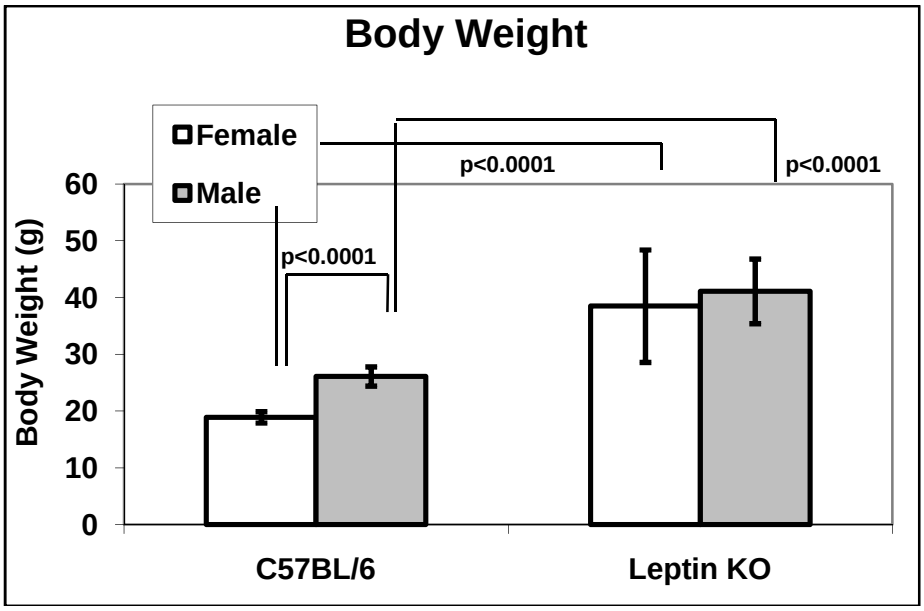

Figure 16. Phenotypic comparison of body characteristics in male and female leptin knockout (KO) and C57BL/6J wild-type mice: body weight. Values are expressed as mean +/- Standard Error of the Mean (SEM). Statistical analysis was performed by two-way ANOVA with a post-hoc Newman-Kuels Test. Differences were deemed significant at $p<0.05$.

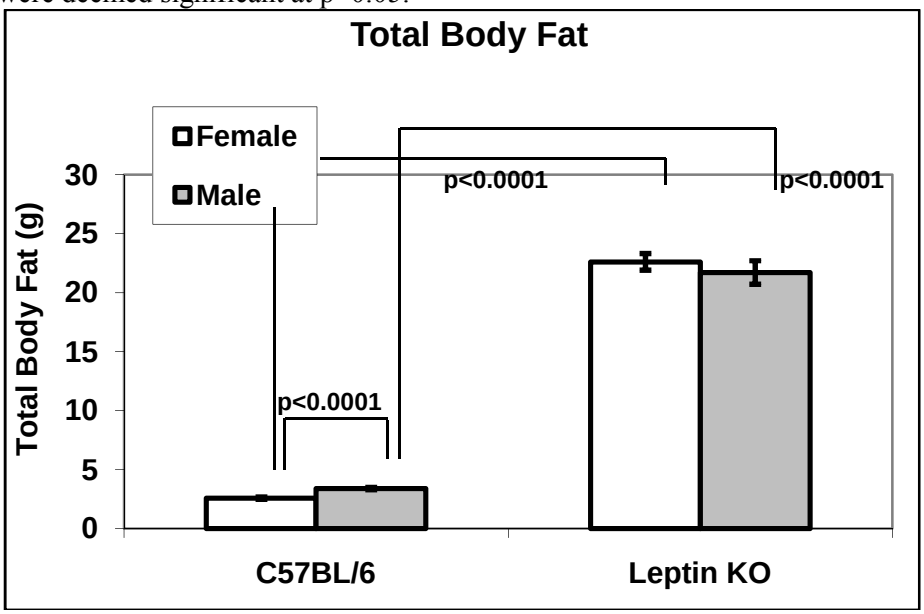

Figure 17. Phenotypic comparison of body characteristics in male and female leptin knockout (KO) and C57BL/6J wild-type mice: total body fat. Values are expressed as mean +/- Standard Error of the Mean (SEM). Statistical analysis was performed by two-way ANOVA with a post-hoc Newman-Kuels Test. Differences were deemed significant at $p<0.05$.

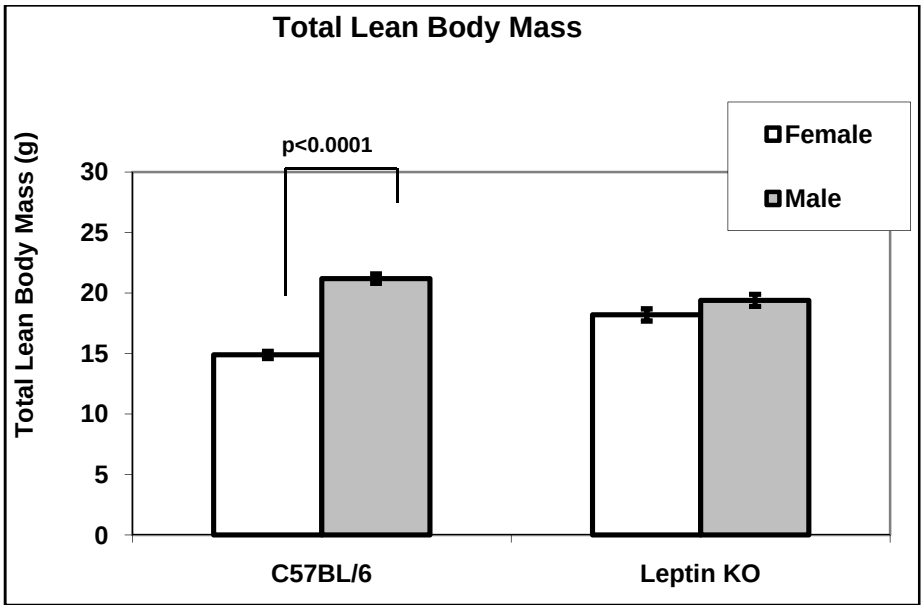

Figure 18. Phenotypic comparison of body characteristics in male and female leptin knockout (KO) and C57BL/6J wild-type mice: total lean body mass. Values are expressed as mean +/- Standard Error of the Mean (SEM). Statistical analysis was performed by two-way ANOVA with a post-hoc Newman-Kuels Test. Differences were deemed significant at $p<0.05$.

The results from (**Figures 16, 17** and **18**) indicate that the expected significant differences in the body weight, total body fat and total lean body mass between male and female C57BL/6J mice were not observed between male and female leptin KO mice. Sex-specific body characteristics were therefore lost in the obese male mouse, and leptin deficiency interfered with androgen-related effects on bone formation in male leptin KO mice. This effect reduced male characteristics of lean body mass and body fat to those of female mice. The femurs of leptin KO male and female mice were then compared with those of C57BL/6J male and female mice to further characterize sex-specific differences that might contribute to bone formation or repair. Several femoral parameters were examined by pQCT measurements at the femoral midshaft. Statistical analysis was performed by two-way ANOVA with a post-hoc Newman-Kuels Test. Differences were deemed significant at $p<0.05$.

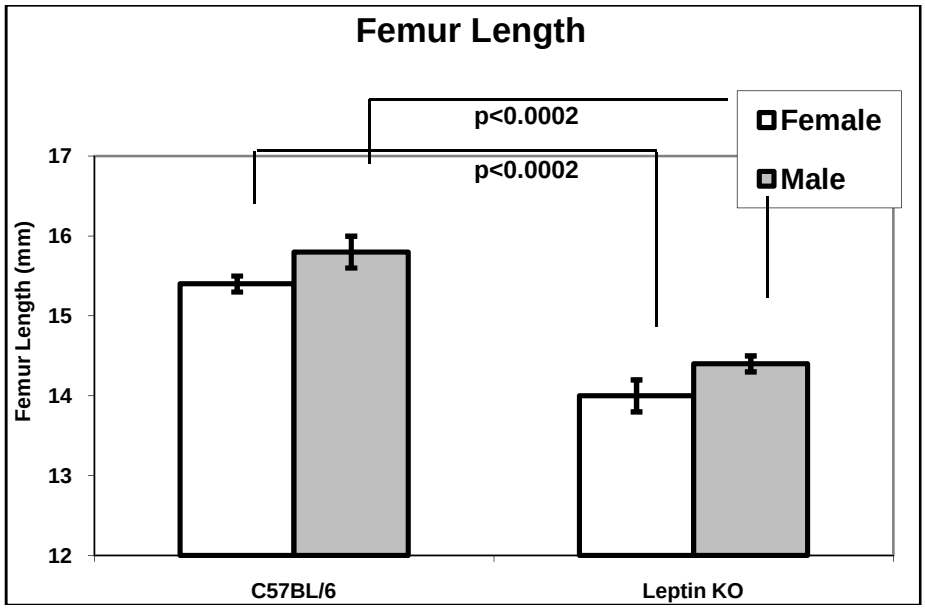

Figure 19. Phenotypic comparison of bone size in male and female leptin knockout (KO) and C57BL/6J wild-type mice: femur length. Values are expressed as mean +/- Standard Error of the Mean (SEM).

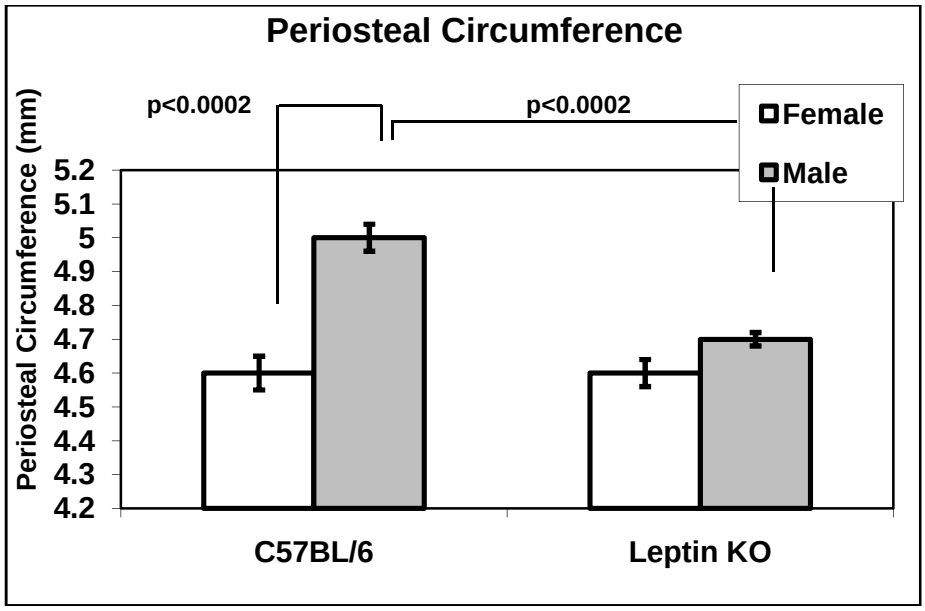

Figure 20. Phenotypic comparison of bone size in male and female leptin knockout (KO) and C57BL/6J wild-type mice: femoral periosteal circumference. Values are expressed as mean +/- Standard Error of the Mean (SEM).

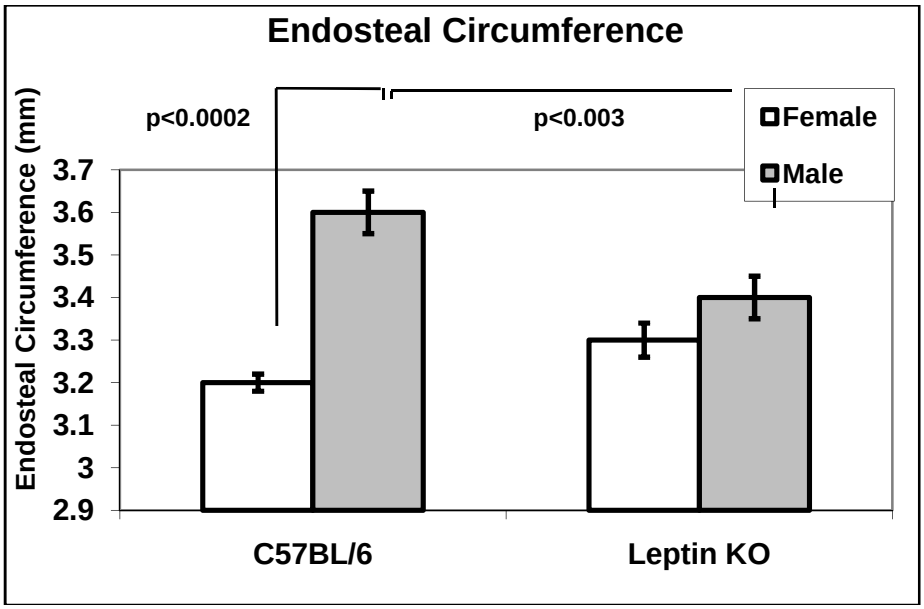

Figure 21. Phenotypic comparison of bone size in male and female leptin knockout (KO) and C57BL/6J wild-type mice: femoral endosteal circumference. Values are expressed as mean +/- Standard Error of the Mean (SEM).

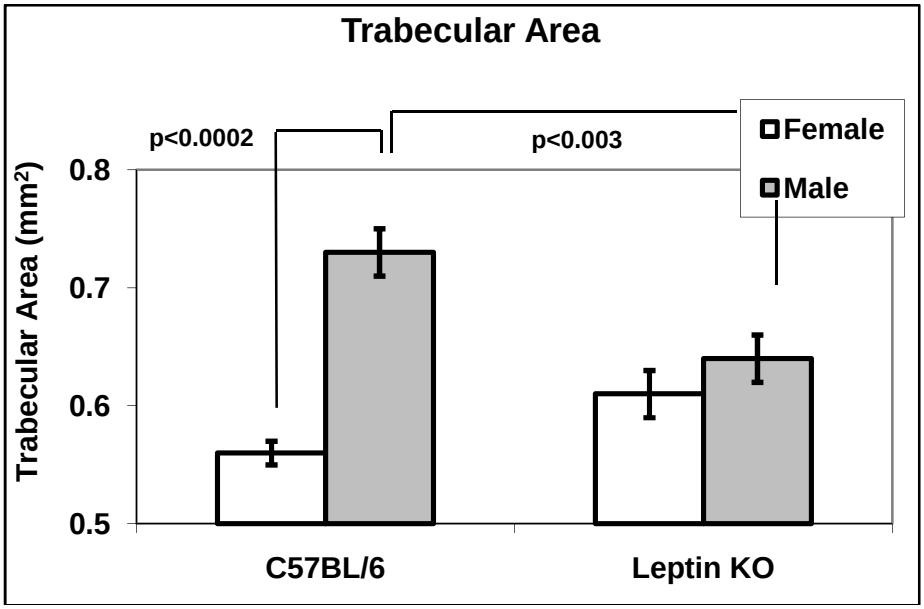

Figure 22. Phenotypic comparison of bone size in male and female leptin knockout (KO) and C57BL/6J wild-type mice: femoral cross-sectional trabecular area. Values are expressed as mean +/- Standard Error of the Mean (SEM).

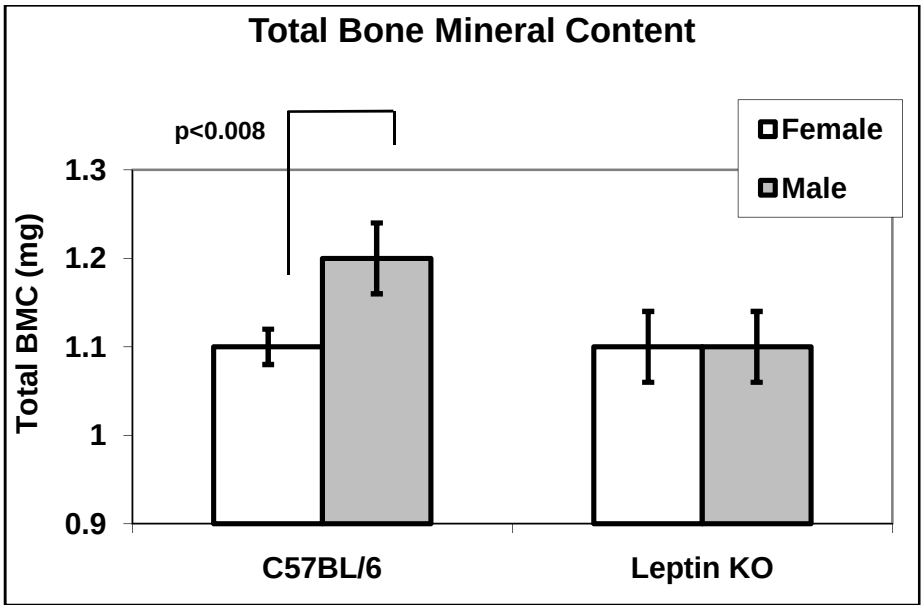

Figure 23. Phenotypic comparison of bone size in male and female leptin knockout (KO) and C57BL/6J wild-type mice: total femoral bone mineral content. Values are expressed as mean +/- Standard Error of the Mean (SEM).

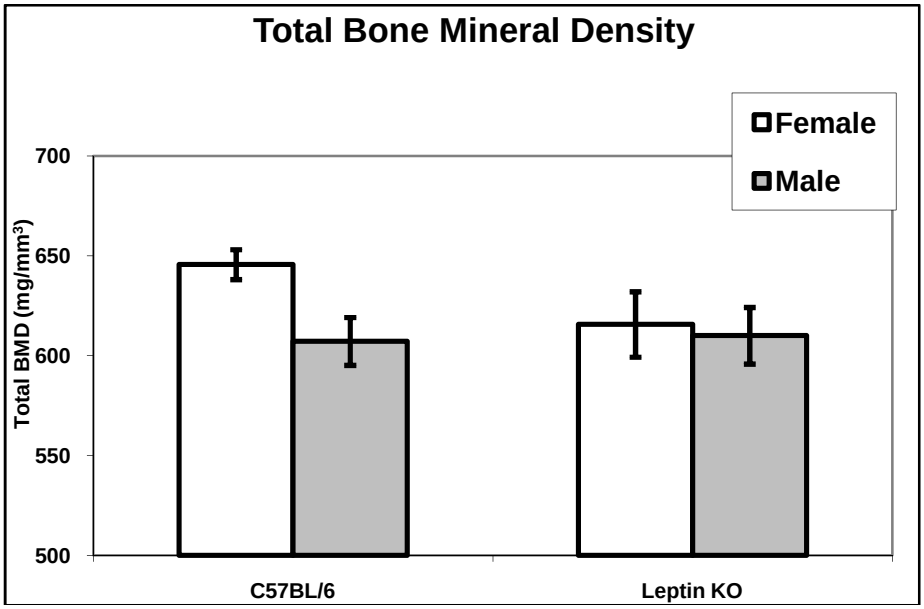

Figure 24. Phenotypic comparison of bone size in male and female leptin knockout (KO) and C57BL/6J wild-type mice: total femoral bone mineral density. Values are expressed as mean +/- Standard Error of the Mean (SEM).

A comparison of the femoral measurements between mouse strains and genders established that several parameters of the femur were also altered in male leptin KO mice (**Figures 19** to **24**). Significant differences in the periosteal circumference, endosteal circumference and trabecular bone area between male and female C57BL/6J mice were not observed between male and female leptin KO mice (**Figures 19** to **21**). The total bone mineral content was also significantly reduced in male leptin KO mice (**Figure 23**). There was no significant difference in the total bone

mineral densities between male and female leptin KO mice (**Figure 24**); because the total bone mineral content of each was reduced in males, this observation suggested a coordinated reduction of several parameters of bone formation in male leptin KO mice. The exception was the femur lengths, which were the not significantly different between males and females of either strain (**Figure 19**). We conclude that leptin deficiency in the male mouse resulted in a loss of several sex-specific differences in bone size that might be attributable to androgen effects on bone formation. Although leptin deficiency has been shown to affect the limbs and spine differently (20), we did not determine whether the sex-dependent leptin effects extended to skeletal structures beyond the femur.

Gender-specific differences in bone mass and size are suggestive of sex steroid hormone functions in bone metabolism (19). To determine whether a reduction in androgen levels might explain the effect of leptin deficiency on bone size, the circulatory levels of androgen and estrogen in male and female leptin KO mice were more rigorously examined than in the previous report. In this case, each study group contained more than 18 animals and both testosterone and estradiol were measured in both males and females. Mouse sera were collected from the retro-orbital venous plexus under general anesthesia, and serum testosterone and estradiol were determined using the respective ^{125}Iodine radioimmunoassay (RIA) kits (**Figure 25**).

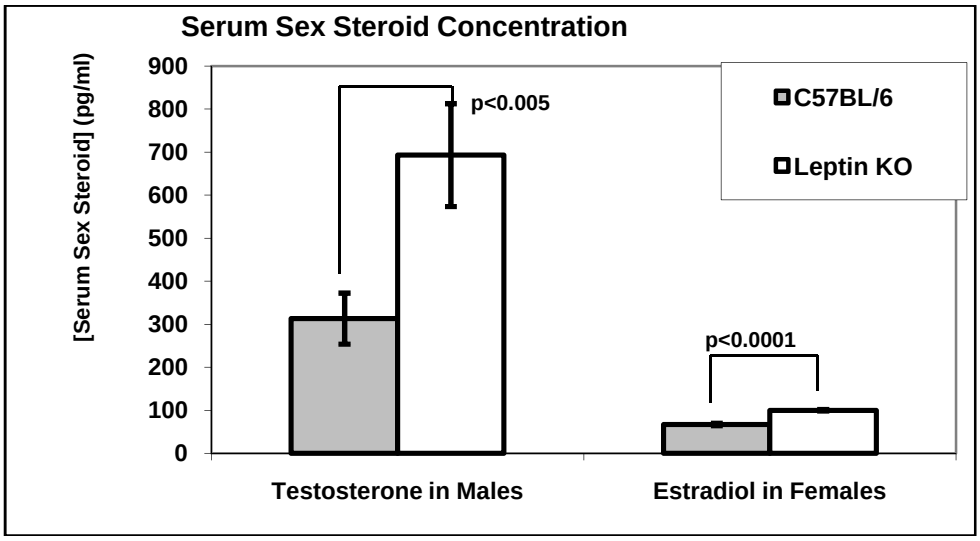

Figure 25. Comparison of serum sex hormone levels in leptin knockout (KO) and C57BL/6J wild-type male and female mice. Values are expressed as mean +/- Standard Error of the Mean (SEM). Statistical analysis was performed by two-way ANOVA with a post-hoc Newman-Kuels Test. Differences were deemed significant at $p<0.05$.

The serum testosterone levels in male leptin KO mice were compared to C57BL/6J wild-type mice and indicated that the loss of sex-specific characteristics in the body phenotype and bone parameters could not be attributed to a reduction in testosterone levels (**Figure 25**, above), but possibly to a defect in testosterone signaling. Estradiol levels were significantly higher in leptin KO female mice, but the similarities in the body characteristics and femoral bone parameters between the C57BL/6J and leptin KO female mice suggest that the effects observed in males were not estrogen-related. The increased androgen levels in the leptin KO mice suggest a signaling defect that induces feedback regulation to increase androgen levels and overcome the defect.

We then examined androgen receptor expression in the leptin KO mouse to determine whether androgen signaling is defective in the absence of leptin. As measured by real-time RT-PCR, we could find no significant differences in androgen receptor expression between male leptin KO mice and male C57BL/6J wild-type mouse periosteal cells in response to testosterone stimulation in vitro. This observation remained the same, despite examining several different genes linked to testosterone function that would be expected to display altered expression levels in response to defective androgen signaling. A list of the testosterone genes examined is presented in Table 6.

Table 6. Androgen-responsive gene expression examined in response to testosterone stimulation of male leptin KO and wild-type periosteal cells in vitro

Androgen-Responsive Gene		
TFAM-A	CAMKKB	XORF43
RAB-7	NCL	SARG
NKX-3.1	SynSTK	SYTL4
HMG-20B	SIAH-BP	NGFRAP1
EAR-2	KIAA0830	Clusterin
BTG-1	BCOR	

Additional Findings in Leptin Knockout Mice:

The MOI is an important addition to these measurements, as it estimates the adaptive bone formation around the axis of the bone that might be expected in an obese subject such as the leptin KO mouse (21). Because the polar moment of inertia was not significantly different in the leptin KO mice and the female wild-type mice (data not shown), we conclude that the sex-specific differences in bone formation were not caused by a response to the increased load in the obese subjects. In summary, male leptin KO mice displayed reductions in several parameters of bone size; the exception was the femur lengths, which were the not significantly different between males and females of either strain. Leptin deficiency appeared to cause a sex-specific reduction in bone size.

To more conclusively demonstrate that the differences in bone size in leptin KO mice sex-related, pre-pubertal male and female leptin KO mice were compared to pre-pubertal wild-type mice to determine whether these effects could be observed in the absence of the sex hormones. The reductions in the bone size in adult male leptin KO mice would not be expected in immature mice prior to the onset of puberty and sex hormone function. In this case, the pQCT parameters were adjusted to 150-300 to detect the less mineralized bone of such young animals. At least 6 male and female weanlings (3 weeks of age) were compared for the leptin KO and C57BL/6J genotypes. Between 6 and 15 individuals were examined. As can be seen in (**Figure 26** below), the body weight (Figure 26A) and total lean body mass (**Figure 26C**) were not significantly different in leptin KO mice versus their wild-type counterparts, though the body fat (**Figure 26 B**) was increased in both genders of the leptin KO mice, even at this early time.

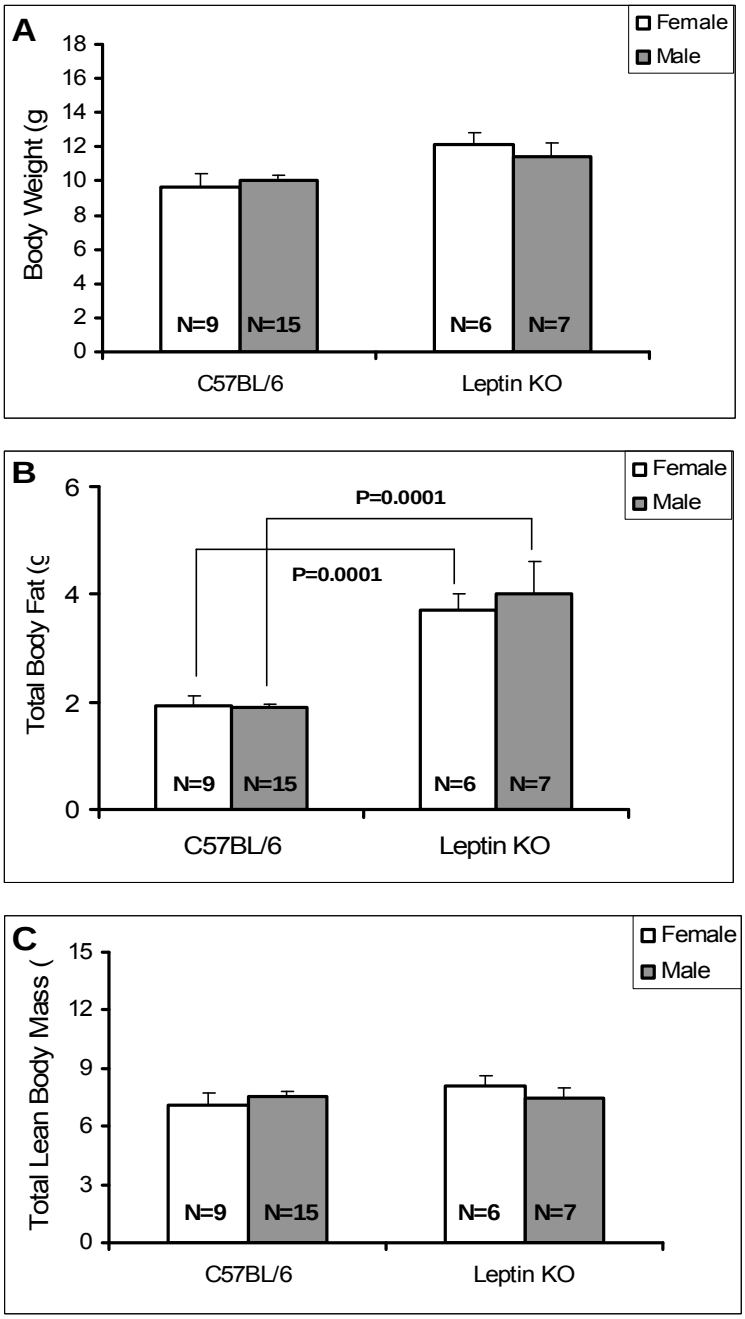

Figure 26. Comparison of leptin KO and C57BL/6J phenotypes in pre-pubertal mice. Male and female mice were compared at 3 weeks of age. Numbers of individuals are provided. Values are presented as Mean +/- Standard Error of the Mean (SEM). Statistical analysis was performed by Student's t-Test. (A) Body weight (B) Body fat (C) Total lean body mass.

An examination of the bone parameters in the pre-pubertal mice revealed no significant differences in any of the bone size parameters examined in the leptin KO and wild-type males or females prior to sexual maturity (data not shown). This observation indicates that the observed reductions in the femur size in the adult male leptin KO mice were indeed influenced by sex hormone function.

We conclude that leptin deficiency in the male mouse resulted in a loss of several sex-specific differences in bone size that might be attributable to androgen effects on bone formation. These results contrast with previous studies that have established that leptin affects on bone formation, but have not evaluated sex differences (1, 21). However, the molecular pathway remains difficult to elucidate, probably because of cross-talk between the components of the various intracellular signaling pathways, including the sex hormone and leptin pathways. Because of obvious implications for the interactions of bone size, obesity and sex hormone effects, we will continue to investigate this phenomenon in leptin KO mice, especially with respect to androgen signal transduction.

Androgen action is primarily anabolic, while the estrogens act mainly through the suppression of resorption. The sex hormones are also influenced by body fat accumulation and distribution (reviewed in 20), which suggests interactions with regulators of body fat, such as leptin. The significantly higher serum testosterone levels in male leptin KO mice as compared to C57BL/6J wild-type mice indicate that the loss of sex-specific characteristics in the body phenotype and bone parameters could not be attributed to a reduction in testosterone levels, but possibly to a defect in testosterone signaling. Estradiol levels were significantly higher in leptin KO female mice, but the similarities in the body characteristics and femoral bone parameters between the C57BL/6J and leptin KO female mice suggest that the effects observed in males were not estrogen-related. We are currently examining androgen receptor expression and function in the leptin KO mouse to test the hypothesis that androgen signaling is defective in the absence of leptin. Because of obvious implications for the interactions of bone size, obesity and sex hormone effects, as well as the differences in fracture healing detected through micro-CT examination, we will continue to investigate this phenomenon in leptin KO mice.

Bax Knockout Mice

The Bax KO mouse fracture project was successfully completed when sufficient number of Bax KO became available. Initially, this knockout strain displayed litter mortality similar to the leptin KO mouse, with a high proportion of pups either neglected or cannibalized. As with the leptin KO strain, surgical mortality was also a problem, but was overcome with experience.

From the pQCT results, Bax KO mice display a BMC (**Figure 27**) and lower density (trabecular-type) bony callus area (**Figure 28**) that is increased at both 14 and 28 days of healing relative the the wild-type control mice. This observation suggests normal soft callus formation, but reduced apoptosis in early healing (14 days) that prolongs osteoblast function and increases bone formation, and slower remodeling later in healing (28 days) that reduces the removal of hard callus bone. This observation is visible in the X-ray of the slightly more mineralized Bax KO callus at 14 and 28 days post-fracture (**Figure 9**, above). As of now, this conclusion is consistent with our hypothesis that the absence of Bax gene expression might reduce apoptosis and both increase bone formation and reduce bone remodeling, and might be explained by an inhibition of Bax-mediated apoptosis.

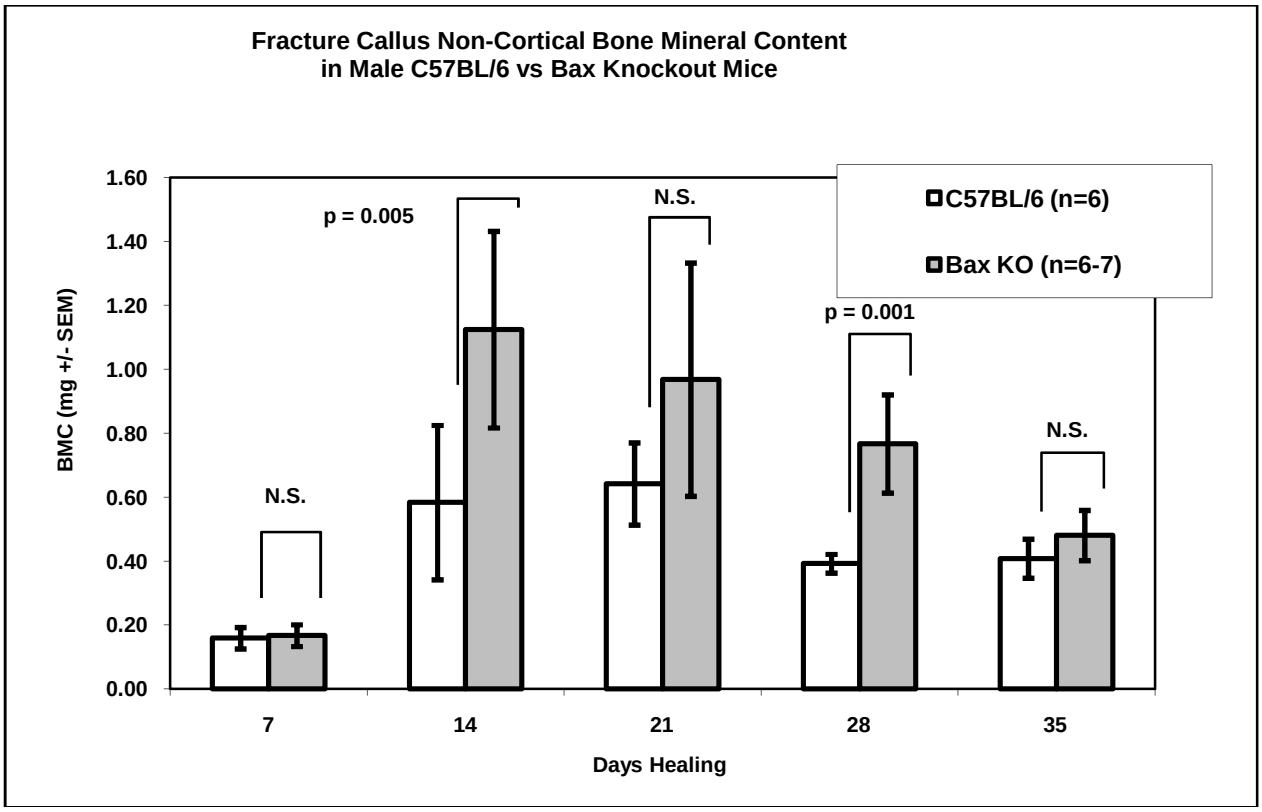

Figure 27. Bone mineral content after femoral fracture in male Bax knockout (KO) and C57BL/6J wild-type control mice. The bone mineral content of the fracture callus was significantly different at 14 and 28 days healing.

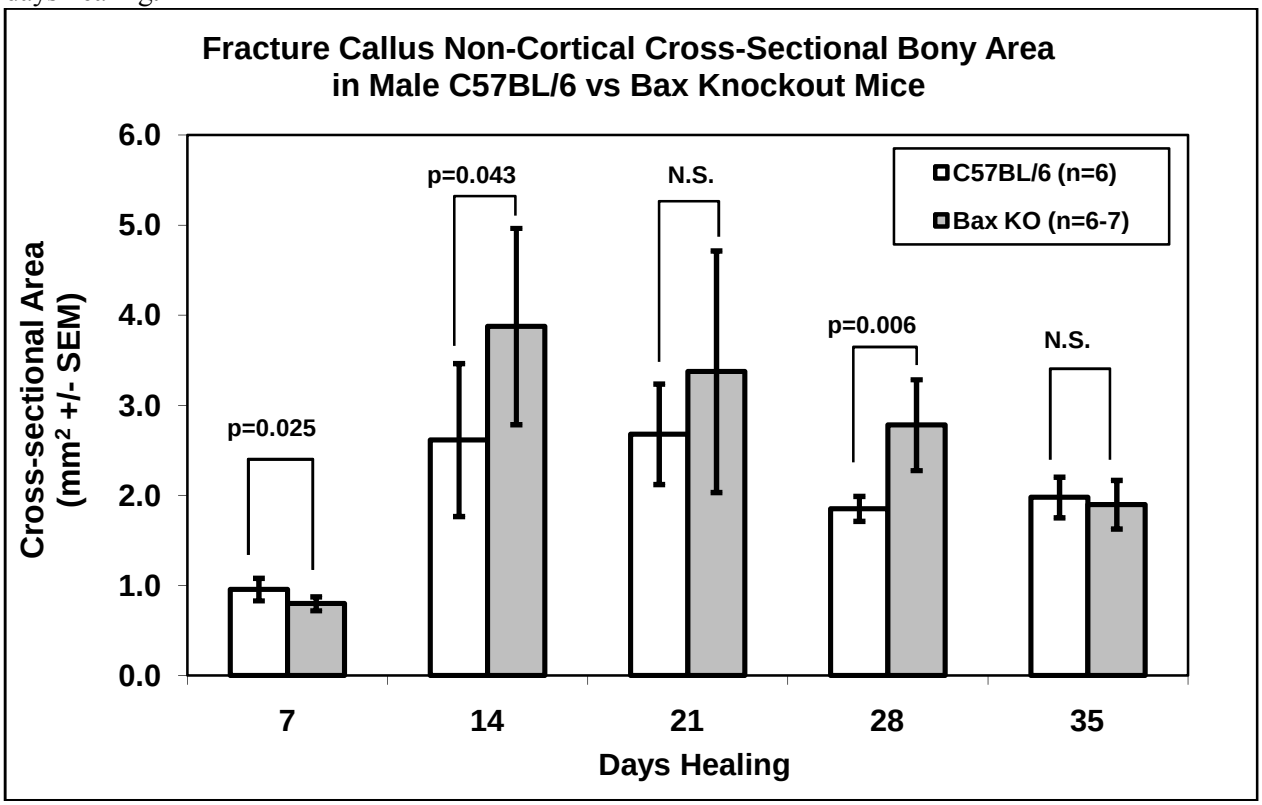

Figure 28. Cross-sectional area of the bony fracture callus after femoral fracture in male Bax knockout (KO) and C57BL/6J wildtype control mice. As with the bone mineral content, the cross-sectional area of bony tissue was significantly different at 14 and 28 days healing. However, it was also significantly different during early fracture healing, at 7 days.

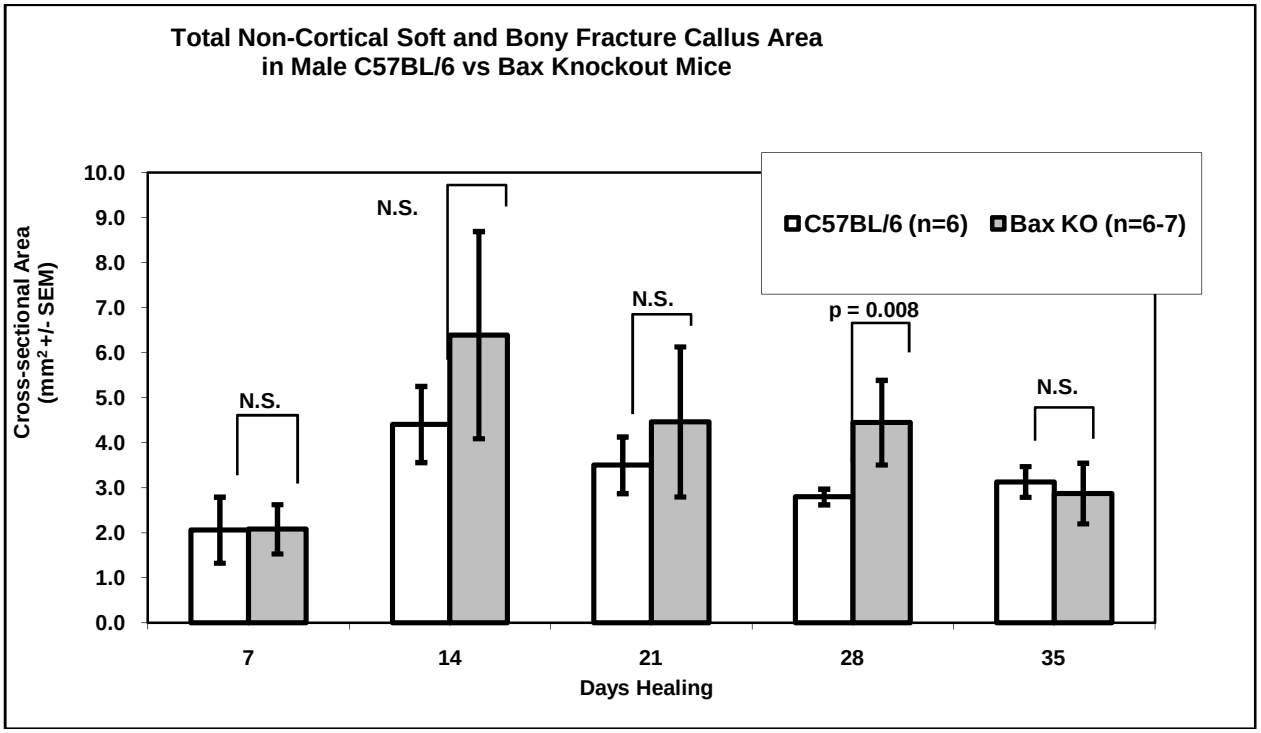

Figure 29. Cross-sectional area of the total fracture callus (soft and bony tissue) area after femoral fracture in male leptin knockout (KO) and C57BL/6J wildtype control mice. In contrast to the hard callus measurements of Figures 27 and 28, the total callus area was significantly different only at 28 days healing, indicating a persistence of soft tissue in the fracture callus of the Bax KO mice.

From the pQCT results of (**Figures 27** and **28**), it is evident that the Bax KO mice develop hard callus areas with significant differences during early (7 and 14 days) and later (28 days) fracture healing. A close examination of the Bax KO mice fracture results revealed changes in fracture bone mineral content (BMC), trabecular-type bony area produced significant increases in each parameter at both the 14 and 28 day post-fracture intervals, while the total non-cortical callus (hard and soft tissue) area was different only at 28 days (**Figure 29**). This observation suggested normal soft callus formation with reduced apoptosis in early healing (14 days) prolongs osteoblast function and increases bone formation, but slower remodeling later in healing (28 days) reduces the removal of hard callus bone. The conclusion remained consistent with our hypothesis that the absence of Bax gene expression might reduce apoptosis and both increase bone formation and reduce bone remodeling. We further investigated this hypothesis using additional histologic and molecular approaches.

Initially, we attempted to visualize the apoptotic phenotype of the Bax cells in the fracture callus histology. This study was undertaken to determine whether Bax-mediated apoptosis was operative in the fracture. Figure 30 shows the results of TUNEL staining of the fracture callus at 14 days post-fracture, when the greatest effects Bax gene deficiency were observed in fracture healing by pQCT. Because the original description of this model determined apoptosis to occur

primarily in the bone marrow, we examined intramedullary bone marrow cells in the fracture callus, as well as fracture cartilage, where apoptosis would be expected to be important. There were no significant differences in apoptotic cells of fractured femurs between Bax KO and B6 control mice.

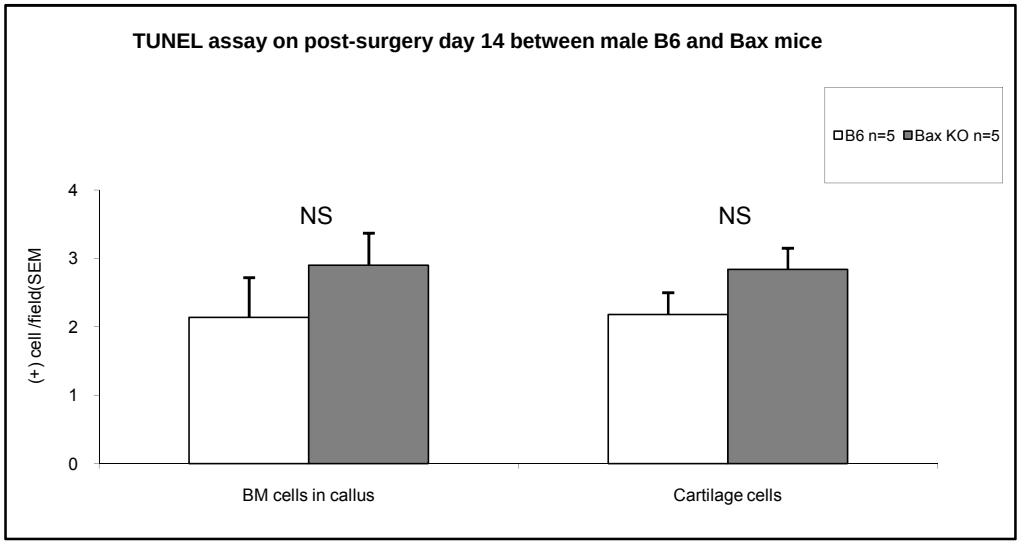

Figure 30. TUNEL assay for apoptosis on sections of fractured femurs in Bax KO mice and B6 control mice at 14 days post-fracture. Five fractures were analyzed from Bax and wild-type mice. Multiple sections were examined for each fracture. Callus intramedullary bone marrow (BM) cells and callus cartilage cells were examined. Data is presented as mean number of TUNEL-positive cells per field +/- standard error of the mean. Statistics were performed by t-Test. NS, no significant difference.

The results of the TUNEL Assay comparison in Bax KO and wild-type fractures at 14 days post-fracture indicate that there are very few apoptotic cells per field and the frequency of apoptosis is very low (**Figure 30**). This result was somewhat surprising. The original description of these mice required a challenge to elicit a measurable apoptotic response in the bone marrow, so it is possible that Bax-mediated apoptosis does not affect fracture repair; rather Bax might act directly on the fracture callus at 14 and 28 days through proliferative effects. Because the original description of this model determined apoptosis to occur primarily in the bone marrow, we examined intramedullary bone marrow cells in the fracture callus, as well as fracture cartilage, where apoptosis would be expected to be important. There were also no significant differences in apoptotic cells of fractured femurs between Bax KO and C57BL/6J wild-type control mice. Moreover, the frequency of apoptotic cells was generally very low, and seemed insufficient to explain such dramatic changes in fracture healing.

To explain the larger callus and more BMC in Bax KO mice, we examined the cartilage area change in both fractured femur from healing day 7 to 28 by Safranin-O stain and histomorphometric quantification. Histomorphometry was used to evaluate the Safranin-Orange-stained cartilage. In (**Figure 31**), it can be seen that the cartilage area was significantly greater in Bax KO mice at 7 (approximately 3-fold) and 14 days post-fracture (approximately 2-fold), and almost negligible at 21 and 28 days. The observation that Bax expression produces a larger fracture callus early in fracture healing (14 days), and late in fracture healing (28 days) but not at the time between these two post-fracture times suggests that Bax might have different functions during early and later fracture repair. The absence of observable apoptosis given such differences in the fracture callus bone and cartilage is difficult to interpret, however.

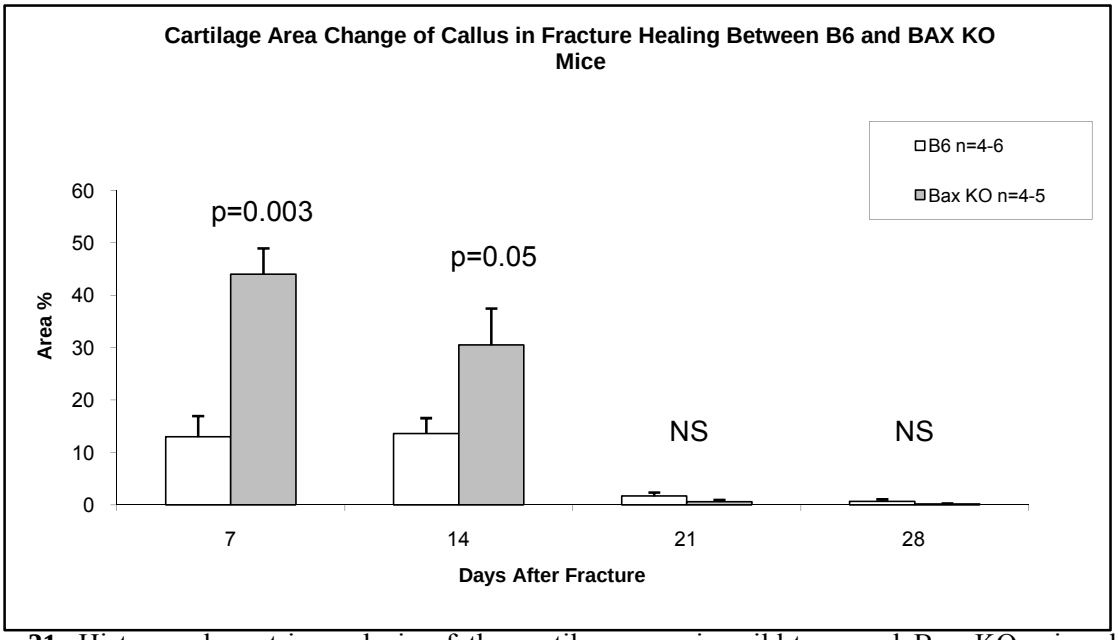

Figure 31. Histomorphometric analysis of the cartilage area in wild-type and Bax KO mice during fracture healing. Between 4 and 6 different fractures were measured for each mouse strain, and duplicate sections were counted; each of the duplicates was taken from a different plane of the callus and the measurements are representative of different areas of the callus. Data is presented as mean +/- standard error of the mean. Statistics were performed by Student's t-Test.

The numbers of osteoclasts were counted from TRAP-stained sections from Bax KO and wild-type fractures (Figure 32) at weekly intervals during healing, from 7 through 28 days. In (**Figure 33)**, it can be seen that the osteoclast numbers were significantly greater in Bax KO fractures than the wild-type fractures at both 21 days (approximately 20 per mm versus 15 per mm) and at 28 days (approximately 15 per mm versus 10 per mm). The increased number of osteoclasts at these later healing times is consistent with an increased resorption of the callus that might be required to remove much of the larger callus from 14 days healing. This might explain the larger callus at 28 days healing, but not at 14 days healing.

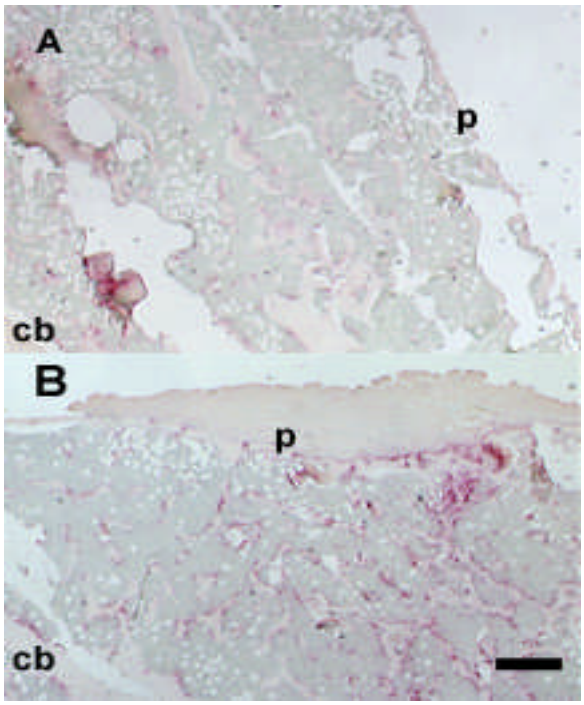

Figure 32. TRAP stain of fracture callus sections at 14 days healing. (A) C57BL/6J wild-type control mouse, (B) Bax KO mouse. The cortical bone (cb) and periosteum (p) are visible in each panel, and the fracture site is outside the lower left of each panel. More osteoclasts are visible in panel, and the fracture site is outside the lower left of each panel. More osteoclasts are visible in Bax KO fracture. Scale bar = 0.50 mm.

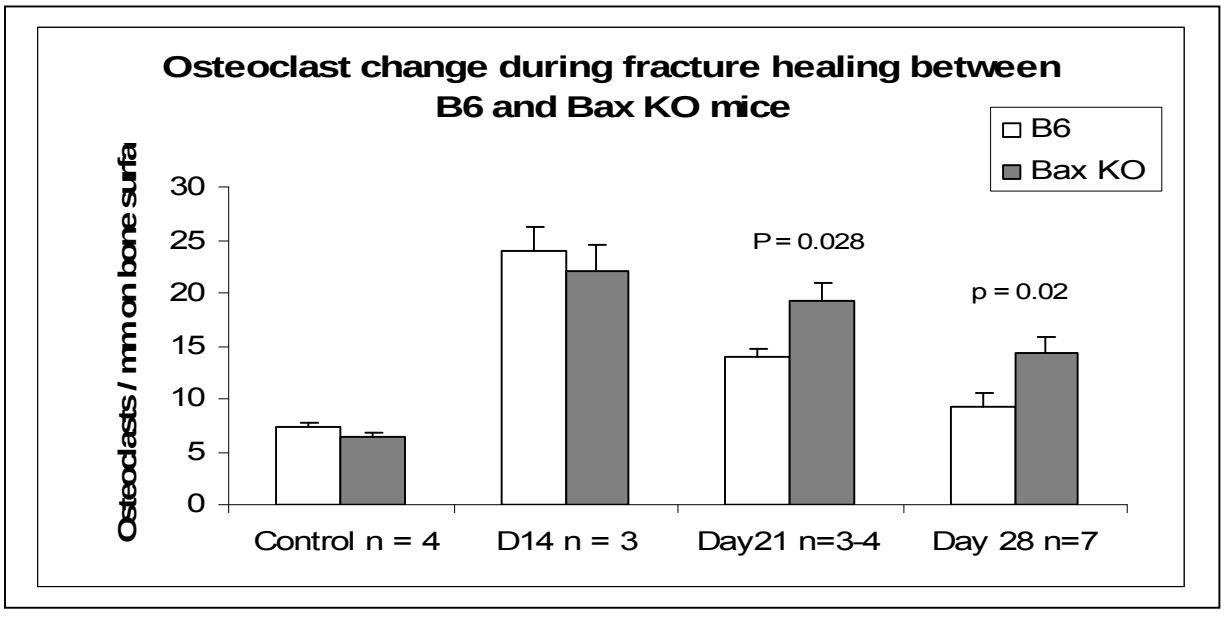

Figure 33. Histologic determination of the numbers of fracture callus osteoclasts in wild-type and Bax KO mice during healing. Between 3 and 7 different fractures were measured for each mouse strain, and multiple sections were counted; each of the duplicates was taken from a different plane of the callus and the measurements are representative of different areas of the callus. Data is presented as mean +/- standard error of the mean. Statistics were performed by t-Test.

To further attempt to relate Bax gene regulation of fracture histology, especially during the earlier times of fracture callus development, we more closely quantified the cellular components of the fracture cartilage. Histomorphometry had identified significantly greater cartilage area in Bax KO mice at 7 and 14 days post-fracture (described above). Although cartilage cell density measurements (the number of cells/area) were found not to be significantly different between the two strains, when the total number of chondrocytes was calculated from these densities and the increased cartilage area/callus area of the Bax KO fractures, differences were observed between Bax KO and wild-type control fractures at both 7 and 14 days healing. The ratio of pre-hypertrophic to hypertrophic chondrocytes were not different at either time (**Figure 34**), but the total numbers of chondrocytes were greater at both times, and much more so at 7 days healing (Figure 35). This observation suggests that the larger cartilage area is caused by an increase in cell proliferation in Bax KO fractures, but that the hypertrophic maturation of chondrocytes remains the same as in wild-type fractures. This observation is consistent with the collagen marker gene expression stuies at 7 and 14 days post-fracture (**Figures 36** and **37**, respectively). The observation that Bax expression produces a larger fracture callus early in fracture healing (14 days), and late in fracture healing (28 days) suggests that Bax might have proliferative functions during early fracture repair and resorptive functions in later fracture repair. The latter was observed by the higher osteoclast content in resorbing Bax fractures (previously reported). The lack of observable changes of apoptosis in the fracture callus by TUNEL assay does not discount apoptotic regulation, but the very limited numbers of apoptotic cells in either Bax KO or wild-type control fracture calluses suggest that Bax-mediated apoptosis cannot account for the dramatic increase in Bax fracture callus cartilage, and the proposed proliferation function must be significant in Bax-related regulation of fracture healing. We conclude that Bax must negatively regulate fracture callus proliferation and its absence in Bax KO mice produces the large fracture callus.

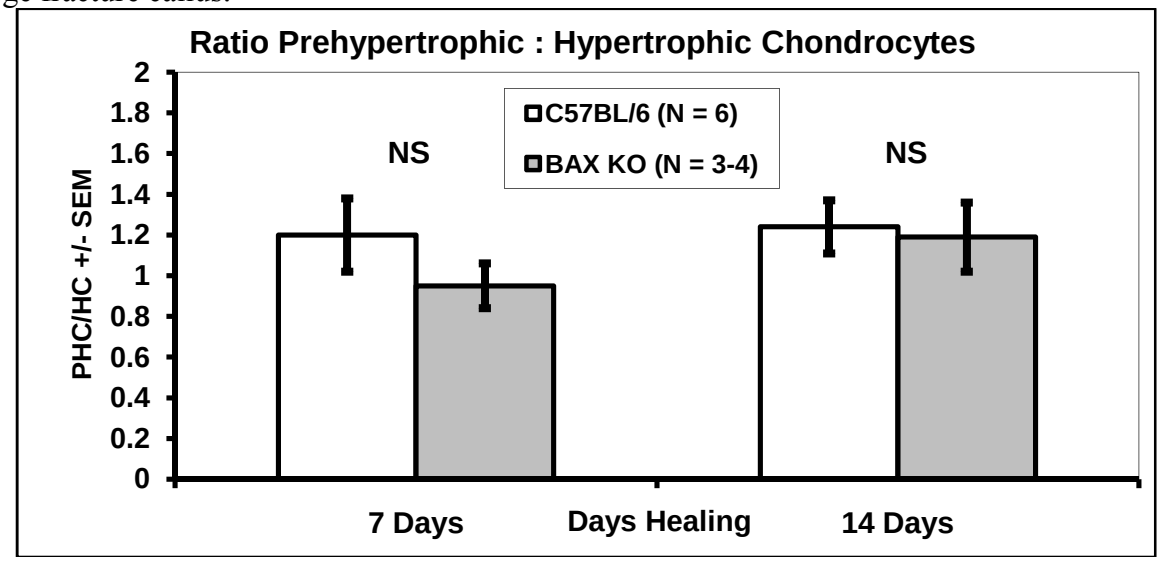

Figure 34. The ratio of prehypertrophic to hypertrophic chondrocytes in fracture healing. The ratio was calculated from multiple counts chondrocyte density in the fracture cartilage in Bax KO and C57BL/6J wild-type control mice at 7 and 14 days post-fracture. The number of each type of chondrocytes in the cartilage was calculated from the area counted for each type of chondrocyte relative to the total cartilage area/callus area The total cartilage area per callus measured by histomorphometric measurements of Safranin-Orange staining of the callus and presented in the previous progress report (which was described

and illustrated in the previous progress report). Results are presented as mean +/- standard error of the mean (SEM). Statistics were performed by ANOVA.

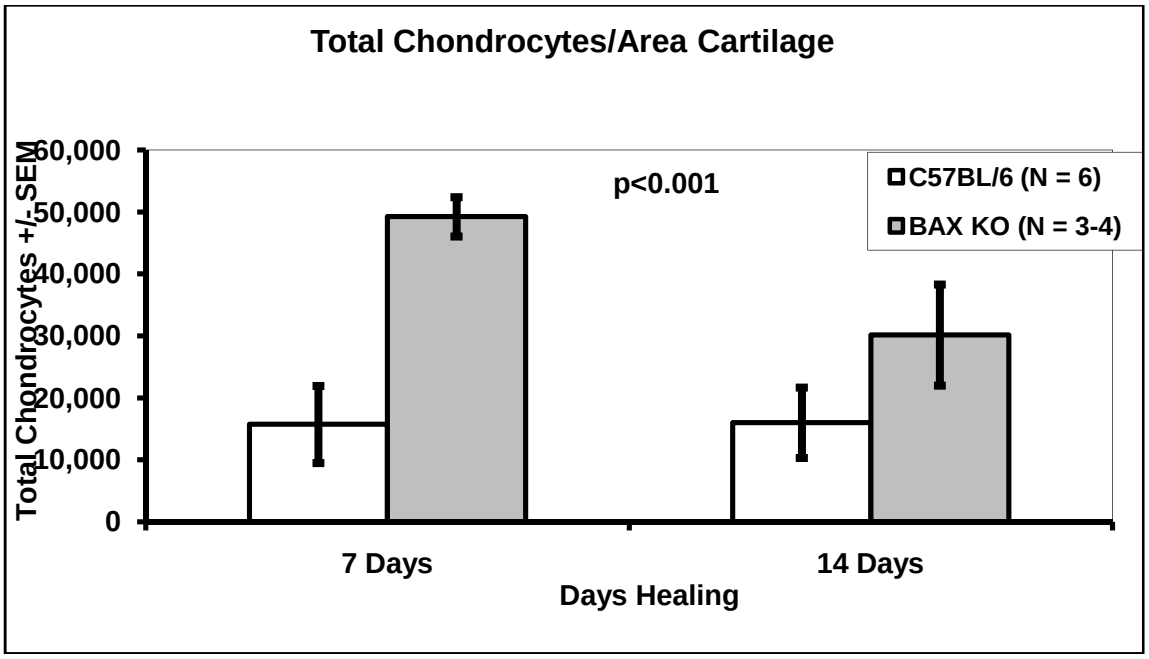

Figure 35. Total chondrocytes per area cartilage in fracture healing. The total number of chondrocytes was calculated from multiple counts chondrocyte density in the fracture cartilage in Bax KO and C57BL/7 wild-type control mice at 7 and 14 days post-fracture. The number of chondrocytes in the cartilage was calculated from the area of the section counted relative to the total cartilage area. The total cartilage area per callus measured by histomorphometric measurements of Safranin-Orange staining of the callus and presented in the previous progress report. Results are presented as mean +/- standard error of the mean (SEM). Statistics were performed by ANOVA.

A molecular approach was also undertaken to attempt to identify the molecular characteristics of the Bax KO fracture callus that might suggest a mechanism for the enlarged fracture cartilage. Real-time RT-PCR measurements compared Bax KO mouse fracture gene expression to C57BL/6J (wild-type) mouse fracture gene expression. Cartilage-related gene expression was examined during early chondrogenesis at 7 days (**Figure 36**), and at 14 days (**Figure 37**), during later chondrogenesis, when the differences in Bax gene healing were observed by pQCT and histology. Total RNA was compared from fracture calluses obtained from at least 3 individuals from each genotype at 7 days and 14 days post-fracture. The collagen genes Col2α1, a marker for prehypertrophic chondrocytes, Col9α1, a marker for all chondrocytes, and Col10α1, a marker for hypertrophic chondrocytes were examined to determine the degree of chondrocyte proliferation versus chondrocyte maturation. The 7 day and 14 day analysis was also extended to include the early chondrocyte regulatory genes Sox-6 and Sox-9 that displayed slight but significant differences in expression in the microarray analysis of Bax KO fracture healing at 14 days (below, Specific Objective 2). However, only Sox-9 displayed significant changes in expression by real-time PCR, and then only at 7 days post-fracture (**Figure 36**).

It was found that Col2α1 and Col9α1 gene expression was up-regulated in the Bax fracture callus at 7 days healing; increases in Col2α1 and Col9α1 expression are consistent with increased prehypertrophic chondrocytes in Bax KO fractures, as is the absence of change in the expression of Col10α1, which suggests that there was no change in the hypertrophic chondrocytes in Bax KO fractures. The early regulator of chondrocyte development, Sox-9, was also up-regulated at 7 days post-fracture, consistent with augmented early fracture chondrogenesis (**Figure 36**). By 14 days post-fracture, none of these cartilage–specific genes displayed any changes in expression in Bax KO fractures (**Figure 37**). These results are consistent with the histology observations (above) which identified an accumulation of prehypertrophic chondrocytes in early chondrogenesis in the Bax KO; these chondrocytes mature to hypertrophy at the same rate as the wild-type chondrocytes in later chondrogenesis.

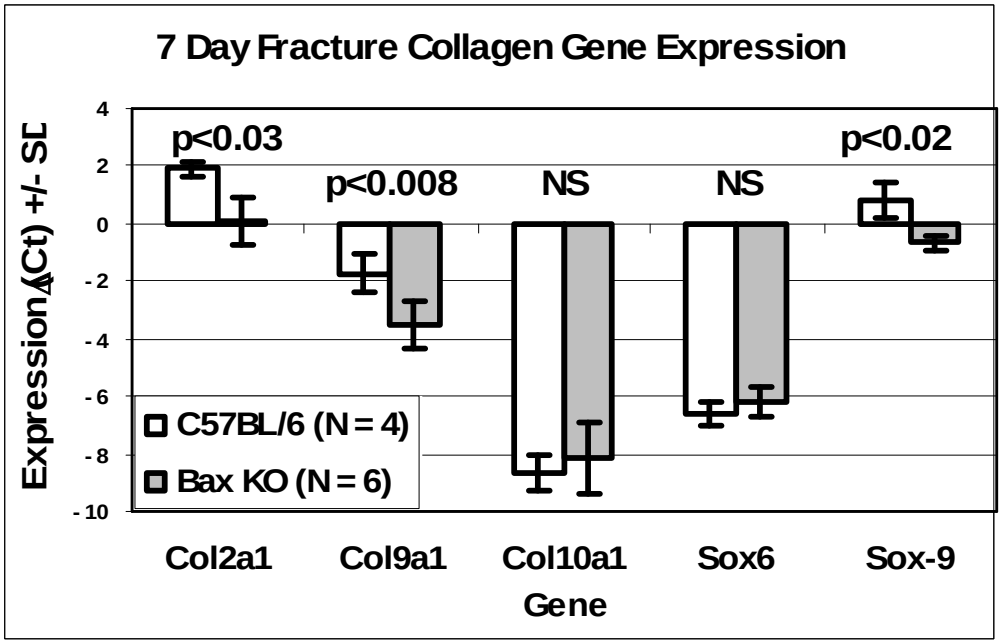

Figure 36. Real-time PCR analysis of cartilage gene expression in wild-type and Bax KO mice at 7 days post-fracture. RNA from 4-6 different fractures was measured for each mouse strain. Data is presented as mean +/- standard deviation. Greater gene expression is identified as a greater negative difference in cycle number (□Ct) relative to the cyclophilin housekeeping gene, defined as zero □Ct. Results are presented as mean +/- standard deviation (SD). Statistics were performed by t-Test. NS, no significant difference.

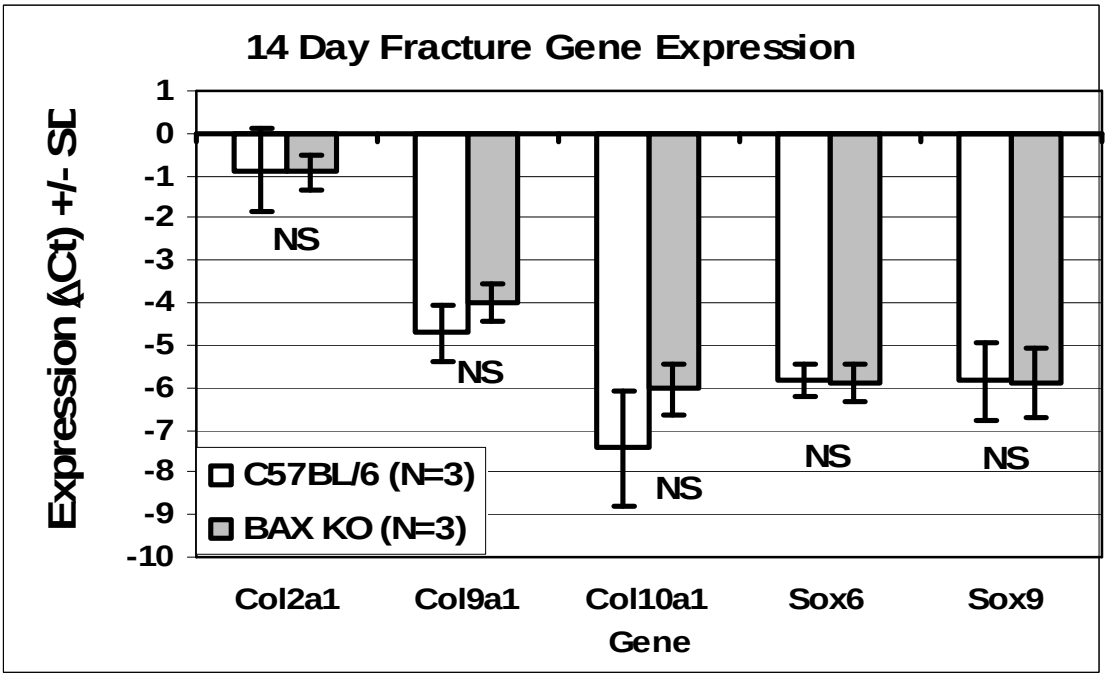

Figure 37. Real-time PCR analysis of cartilage gene expression in wild-type and Bax KO mice at 14 days post-fracture. RNA from 3 different fractures was measured for each mouse strain. Data is presented as mean +/- standard deviation. Greater gene expression is identified as a greater negative difference in cycle number (□Ct) relative to the cyclophilin housekeeping gene, defined as zero □Ct. Results are presented as mean +/- standard deviation (SD). Statistics were performed by t-Test. NS, no significant difference.

Based upon the histologic and molecular characterization of the Bax KO fracture cartilage, we then sought to determine the contributions of cell proliferation to the Bax fracture cartilage by measuring the numbers of proliferative cells in Bax KO fracture healing. Bax KO and heterozygous and homozygous littermate controls are injected *in vivo* with the DNA base analog bromodeoxyuridine (BrdU). BrdU is incorporated into the DNA of actively proliferating cells. It is expected that Bax KO calluses will have a greater number of proliferating cells. This test is illustrated in Figure 38; the brown precipitate localizes BrdU incorporation to the nucleus of cells that are entering the prehypertrophic phase of chondrocyte development.

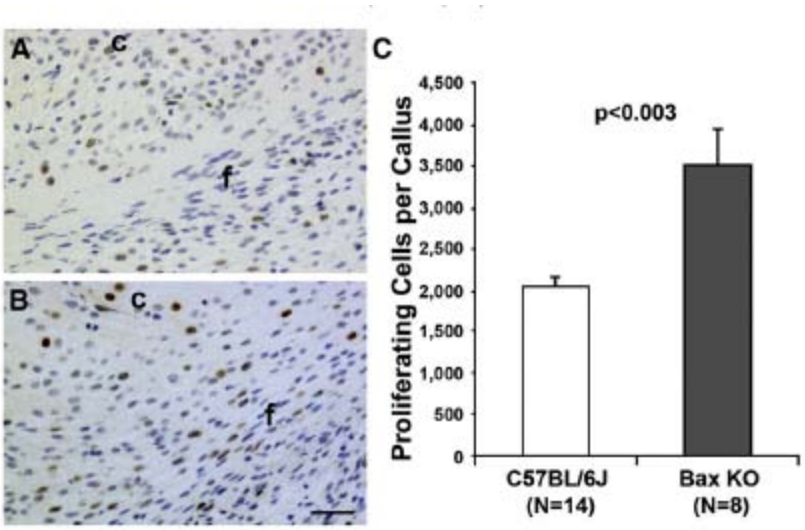

Figure 38. Bromodeoxyuridine (BrdU) immunohistochemistry for proliferating cells of (A) C57BL/6J wild-type control mice and (B) Bax KO mice at 7 days post-fracture. Mice were injected intraperiotoneally with 50 mg/kg BrdU and 10 mg/kg fluorodeoxyuridine at 7 days post-fracture and sacrificed 2 hours afterward. Demineralized fracture callus sections were stained with anti-BrdU (the brown precipitate) to detect cells in S-phase of mitosis that had incorporated these DNA base analogs. The fracture is just beyond the upper right-hand corner of each panel. The counterstain is methyl green. c, cartilage; p, periosteum. Scale bar = 100 um. (C) counts of S-phase cells in the fracture calluses of C57BL/6J wild-type and Bax KO mice at 7 days post-fracture. Results are presented as meand +/- standard error of the mean (SEM). Statistical analysis was performed by Student's t-Test.

In summary, Bax fracture healing therefore produced a larger fracture callus that probably indicates Bax expression regulates different steps of fracture healing. The additional cartilage area in the Bax KO mouse callus might be due to augmented prehypertrophic cell proliferation and prehypertrophic cell number per callus, but not increased cell density. Bax might negatively regulate fracture callus proliferation. There were more osteoclasts on the callus trabecular-type bone surface in the callus of Bax KO mice at a later healing stage, consistent with enhanced remodeling. No significant difference in apoptotic cells was found between Bax KO and B6 control mice as had been expected. These observations are quite interesting, and imply that Bax gene expression is redundant or that Bax might have other functions in wound healing.

With the exception of the micro-CT analysis, we completed the Specific Objective for the analysis of fracture healing in the Bax KO mice. Additionally, we have extended the histologic analysis of Bax KO fracture repair to cartilage characterizations that have yielded additional information, which is in addition to the originally described Specific Objective.

Serpine Knockout Mice:

The serpine-1 KO mouse fracture study has initially suffered from delayed acquisition and breeding, but phenotypic characterization and fracture studies were successfully completed when sufficient numbers of animals were obtained. Because the Specific Objectives of the mechanical loading study in Technical Objective 1 had already been completed with respect to the leptin KO and Bax KO strains, a detailed phenotypic characterization of the serpine-1 KO strain femurs prior to the fracture repair study was substituted for the mechanical loading study, and is reported below.

The analysis of the phenotype of the serpine-1 KO skeleton was performed through a pQCT comparison the femurs with wild-type femurs. In each case male mice were examined. This approach was adopted instead of the PIXImus and histology examinations because we have extensive experience with femur measurements with respect in the leptin KO mouse, and data can be most easily used to interpret the phenotype in the fracture repair model. Analysis was performed at the midshaft fracture scan (pQCT slice 5 by our appraoch) under thresholds that rigorously identify the cortical bone (630-630). *The results of the serpine-1 KO bone phenotype analysis that completed this Specific Objective are presented below.*

An examination of several parameters of the femoral cortical bone revealed significant differences in the size of serpine-1 KO mice versus wild-type mice. Specifically, the periosteal and endosteal circumferences were smaller in the serpine-1 KO mice (Figure 39). The length of the bone was also less in the serpine-1 KO mice (Figure 39), which is consistent with an overall size reduction and not merely a reduction in circumference in a femur of the same length as the wild-type femur.

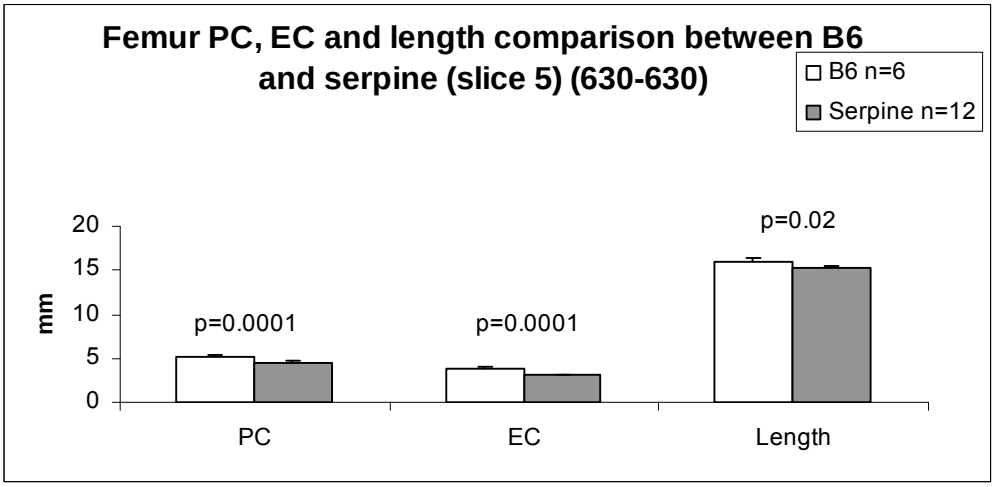

Figure 39. Comparison of femur dimensions in male serpine-1 KO and wild-type mice. Cortical bone pQCT thresholds (630-630) were compared at a mishaft scan (slice 5). Periosteal circumference (PC), endosteal circumference (EC) and femur length were compared in 12 serpine-1 KO and 6 wild-type mice. Data is presented as the mean +/- standard error of the mean. Statistics were performed by t-Test.

An examination of the bone mineral content and the area also revealed significant reductions in the serpine-1 KO femur (**Figure 40**). These results indicate that the mineral content and the area it occupies are lower in serpine-1 KO femurs and consistent with a smaller bone as suggested by the bone circumference measurements in Figure 39.

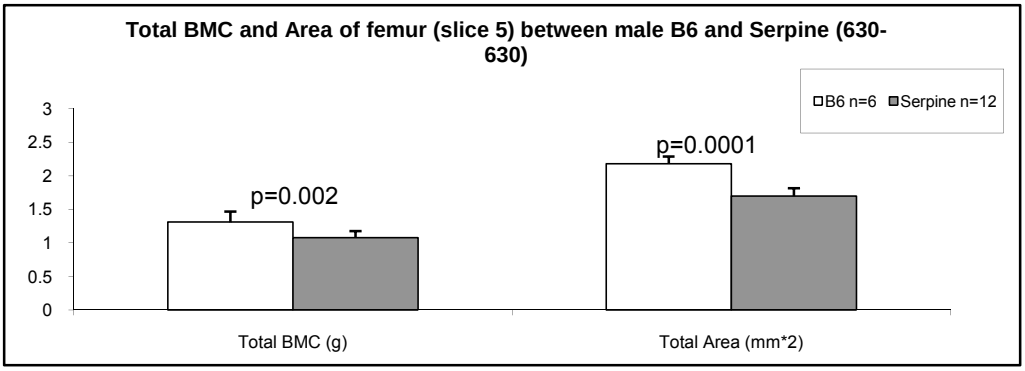

Figure 40. Comparison of femur cortical bone mineral content (BMC) and cortical area in male serpine-1 KO and wild-type mice. Cortical bone pQCT thresholds (630-630) were compared at a mishaft scan (slice 5). BMC and area were compared in 12 serpine-1 KO and 6 wild-type mice. Data is presented as the mean +/- standard error of the mean. Statistics were performed by t-Test.

An examination of the bone mineral density under these same pQCT thresholds revealed no significant difference between the serpine-1 KO and wild-type mice (Figure 41). The bone mineral density measurement is consistent the bone mineral content of the serpine-1 KO mice (**Figure 40**) in a smaller bone, as first suggested in the serpine-1 KO femur circumference measurements (**Figure 39**).

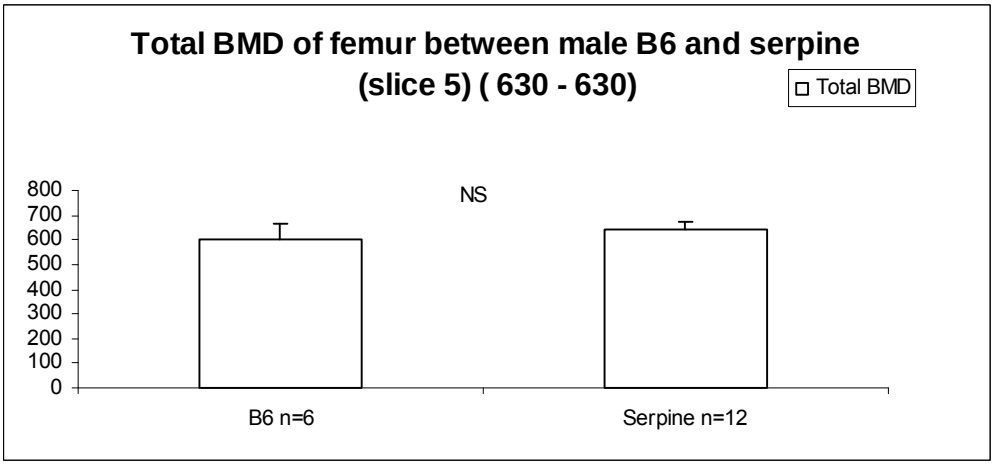

Figure 41. Comparison of femur cortical bone mineral density (BMD) in male serpine-1 KO and wild-type mice. Cortical bone pQCT thresholds (630-630) were compared at a mishaft scan (slice 5). BMD was compared in 12 serpine-1 KO and 6 wild-type mice. Data is presented as the mean +/- standard error of the mean. NS, no significant difference.

An examination of the cortical polar moment of inertia a measure of the mineralized cortical bone around the bone axis and an indicator of the torsional strength of the femur (**Figure 42**) confirms that the serpine-1 mice have a smaller femur that might affect interpretations of native bone strength, as well as fracture healing. This is a critical observation, as this gene is important in extracellular matrix aspects of wound healing.

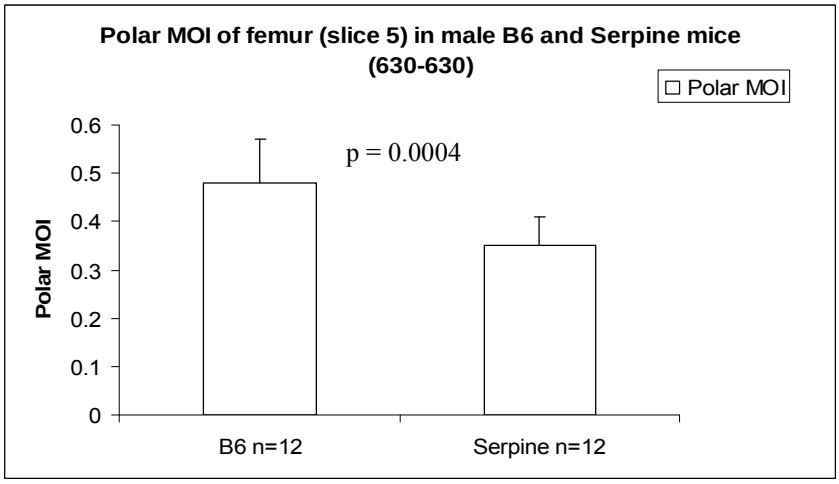

Figure 42. Comparison of femur cortical bone polar moment of inertia (MOI) in male serpine-1 KO and wild-type mice. Cortical bone pQCT thresholds (630-630) were compared at a mishaft scan (slice 5). Polar MOI was compared in 12 serpine-1 KO and 6 wild-type mice. Data is presented as the mean +/- standard error of the mean. Statistics were performed by Student's t-Test.

The femur fracture model that was developed in the first year of this study was again applied to the serpine-1 KO mouse strain and the C57BL/6J wild-type control strain. As described previously, an intramedullary pin was surgically implanted in the femur prior to fracture and the skin incision closed. The fracture callus was examined by pQCT as described for the leptin KO and Bax KO strains, above, with the lower density (trabecular-type) fracture callus BMC, area and the total non-cortical (trabecular-type bone and soft tissue) area. Groups of 6 animals were examined for each strain at each post-fracture healing interval.

Interestingly, the serpine-1 KO mice displayed a significant increase in fracture callus bone mineral content at 14 and 28 days healing, but not at the intervening 21 days healing time (**Figure 43**). These results suggest that the influence on fracture healing by serpine-1 (PAI-1) is complex and might involve different regulatory processes.

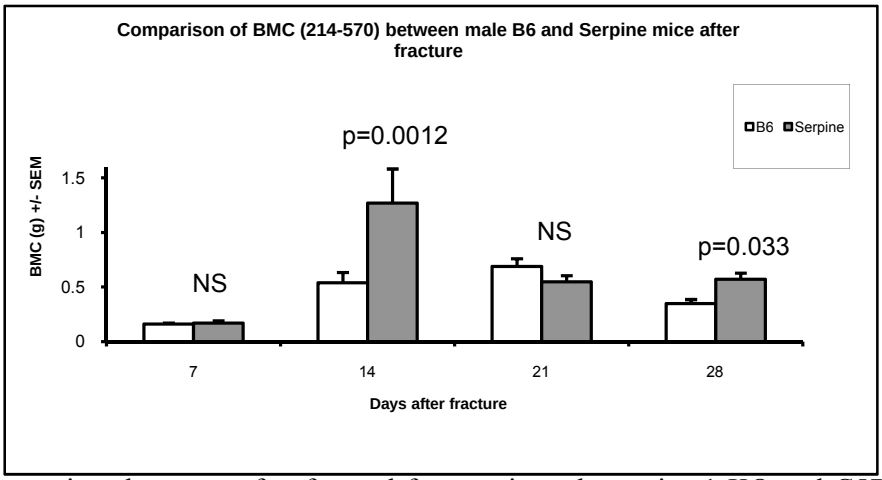

Figure 43. Bone mineral content after femoral fracture in male serpine-1 KO and C57BL/6J wild-type control mice. The bone mineral content of the fracture callus was significantly different at 14 and 21 days healing. Six mice from each strain were examined at each time. Data is presented as mean +/- SEM. Statistics were performed by t-Test. NS, no significant difference.

Measurements of the area of the lower density trabecular-type bone confirm the bone mineral content measurements, in that the area of callus bone is significantly greater only at 14 and 28 days healing (**Figure 44**). These results indicate that the bony component of the fracture callus is significantly larger at these times, but, as the bone mineral content (**Figure 43**) and the callus bone area have both increased, the bone mineral density has not. We have confirmed this observation using pQCT measurements of the fracture callus bone mineral density, which is not significantly different between mouse strains (data not shown).

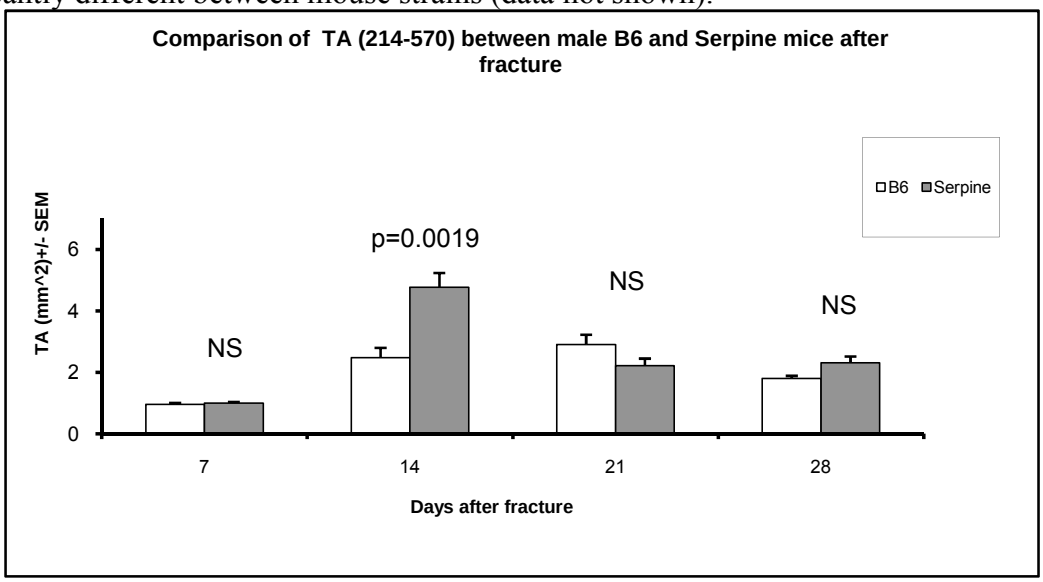

Figure 44. Area of trabecular-type bone (TA) after femoral fracture in male serpine-1 KO and C57BL/6J wild-type control mice. The bone mineral content of the fracture callus was significantly different at 14 and 21 days healing. Six mice from each strain were examined at each time. Data is presented as mean +/- SEM. Statistics were performed by t-Test. NS, no significant difference.

To determine whether serpine-1 gene expression affects the total callus size (i.e., the bony callus and the soft callus components) the fracture callus was examined by pQCT using measurement thresholds that exclude the cortical bone. These results are shown in **Figure 45**, and demonstrate that the size of the serpine-1 KO fracture callus was greater at 14 and 28 days healing; the greater difference at 14 days was no doubt due to a much greater quantity of soft callus tissue than that normally observed at this time. Most of the soft tissue has been replaced by bony callus at 28 days, when the difference between mouse strains in much smaller and barely significant.

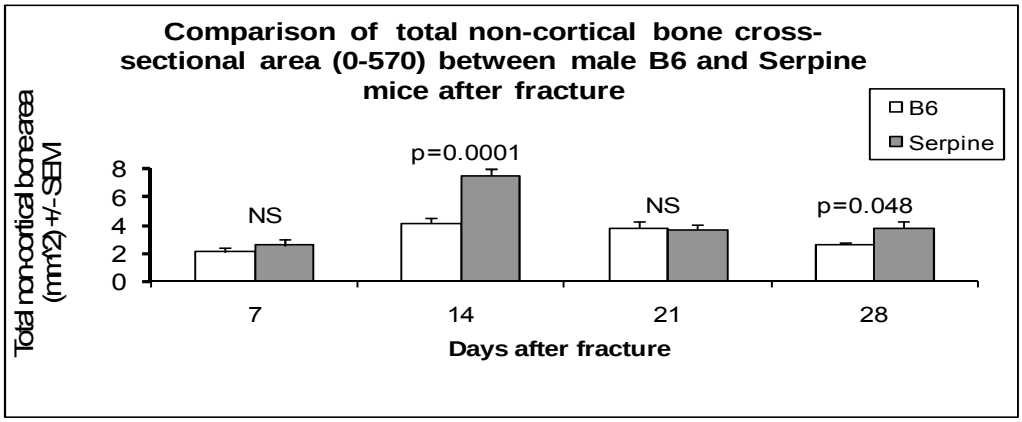

Figure 45. Area of soft tissue and trabecular-type bone (i.e., all non-cortical callus components) after femoral fracture in male serpine-1 KO and C57BL/6J wild-type control mice. Six mice from each strain were examined at each time. Data is presented as mean +/- SEM. Statistics were performed by t-Test. NS, no significant difference.

The effects of impaired serpine-1 expression that were manifested at 2 different post-fracture healing times confirm the qualitative X-ray observations from the previous report, and we have pursued an analysis of the 14 day interval because the difference is quite large and expected to produce observable results by other histology techniques. An examination of the fracture callus cartilage at this time has also revealed large changes in the fracture callus at this time. **Figure 46** shows a view of the fracture cartilage for the entire callus at 14 days post-fracture, and qualitatively demonstrates that the fracture cartilage appears to make a large contribution to the serpine-1 callus (**Figure 46 B**) at this time.

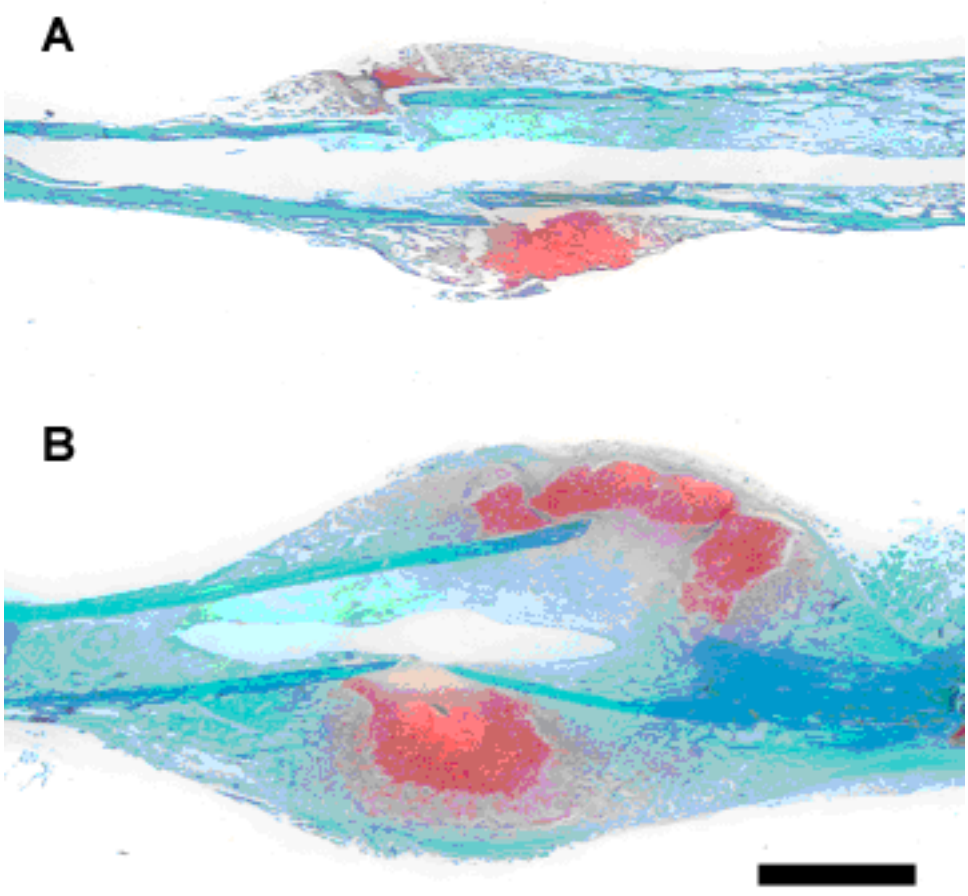

Figure 46. Global view of the fracture callus comparing cartilage formation at 14 days in (A) wild-type and (B) serpine-1 KO mice. The cartilage stains red by Safranin-Orange, and the non-cartilage components stain with the methyl green counterstain. Scale bar = 2 mm.

Quantification of the cartilage by histomorphometric analysis of Safranin-Orange stains (**Figure 47**) was performed to confirm the qualitative observations in **Figure 46**. In this case, duplicate sections were collected from more than 3 fracture calluses from each strain of mouse and measured at 7, 14 and 21 days. The duplicate sections were not adjacent to one another and therefore more representative as they are derived from different areas of the fracture callus. It was found that the serpine-1 KO fracture calluses had significantly more cartilage than their wild-type counterparts at 14 days (and close to significance at the other times), and that this difference was quite large. These results suggest that serpine-1 gene expression is an important regulator of fracture chondrogenesis at 14 days healing.

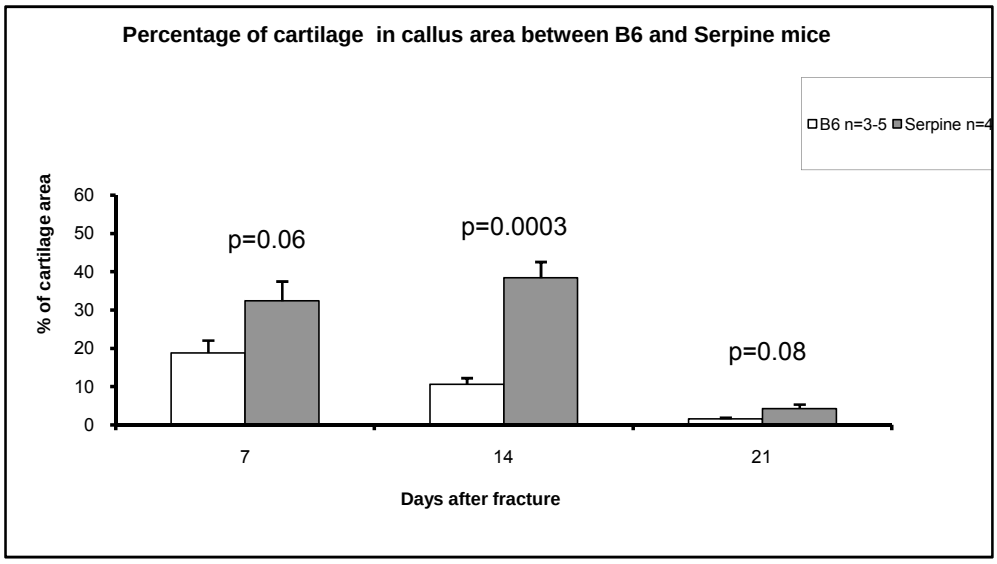

Figure 47. Histomorphometric analysis of the cartilage area in wild-type and serpine-1 KO mice during fracture healing. More than 3 different fractures were measured for each mouse strain, and duplicate sections were counted; each of the duplicates was taken from a different plane of the callus and the measurements are representative of different areas of the callus. Data is presented as mean +/- standard error of the mean. Statistics were performed by Student's t-Test.

Quantification of the cartilage by histomorphometric analysis of Safranin-Orange stains established that the serpine-1 KO fracture calluses had significantly more cartilage than their wild-type counterparts at 14 days (and close to significance at the other times), and that this difference was quite large. These results suggest that serpine-1 gene expression is an important regulator of fracture chondrogenesis at 14 days healing. Macroscopically, the fracture cartilage appeared normal in PAI-1 knockout mice compared to C57BL/6J wild-type mice at 14 days post-fracture. However, a higher magnification examination of the serpine-1 KO fracture histology at 14 days post-fracture using a conventional stain revealed that serpine-1 KO fractures also exhibit a layer of bone immediately under the periosteum that is not typical of the normal pattern of

callus cartilage conversion to bone that eventually produces the normal bony union of healing observed in wild-type mice (Figure 48). In this case, cartilage conversion to bone appeared to proceed from the periphery of the callus to the interior (arrow in Figure 48B), a pattern unlike the usual callus bony union, in which the opposing bony callus on either sides of the fracture gap eventually joins over the fracture (arrows in **Figure 48A**). It is highly suggestive of some molecular pathway that more efficiently mineralizes the cartilage at the perimeter of the fracture callus. It is probable that the absence of the serpine-1 (PAI-1) inhibition of the plasminogen activators has accelerated cartilage replacement with bone at the perimeter, and the mechanism of this action certainly warrants further investigation. We have no data to support an explanation for this observation at this time, but we intend to investigate this aspect of serpine-1 KO fracture healing further.

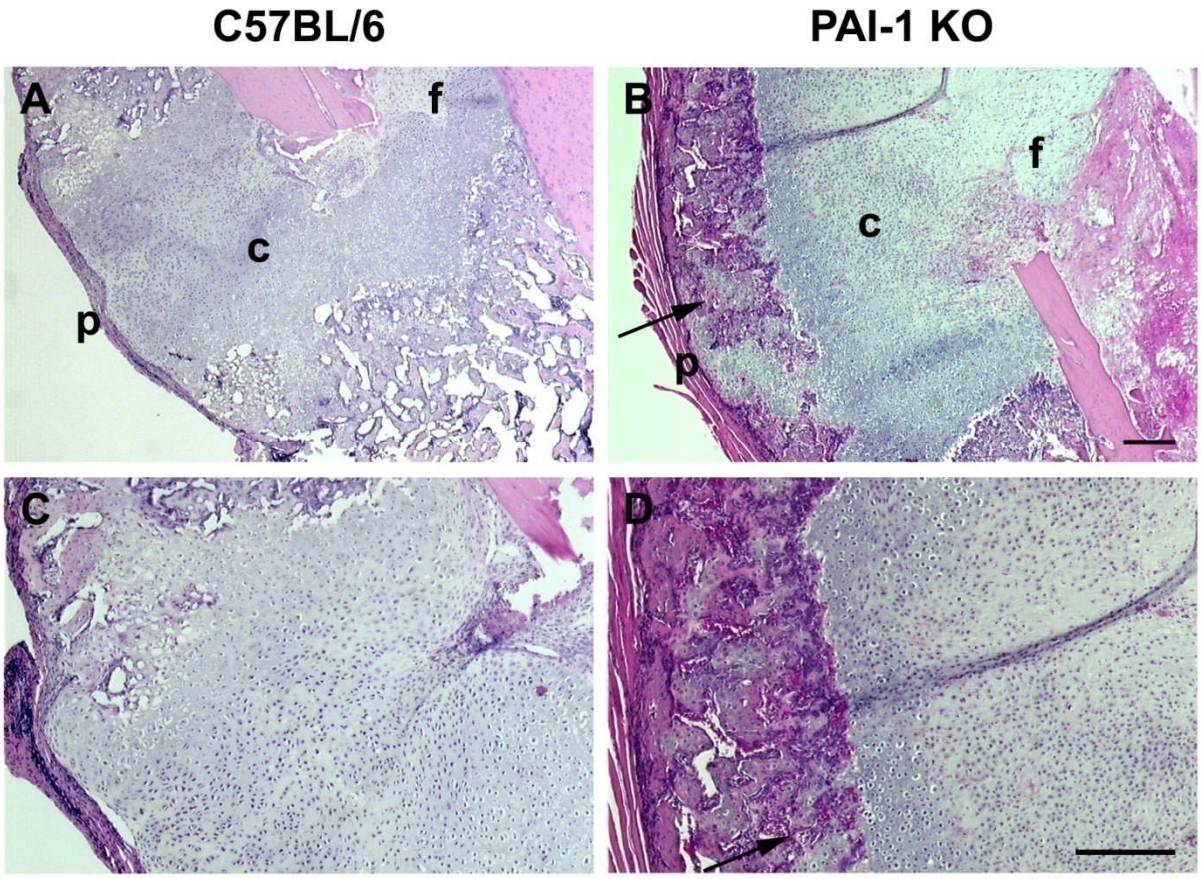

Figure 48. Fracture callus histology at 14 days post-fracture. Hematoxylin-Eosin staining for cartilage compared fracture cartilage in C57BL/6J wild-type mice (A), and PAI-1 knockout mice (B). (C) and (D) are higher magnification images of (A) and (B), respectively. c, cartilage f, fracture; p, periosteum. Scale bar = 0.5 mm.

The pattern of fracture healing that produces bone around the perimeter of the fracture callus cartilage was suggestive of enhanced callus strength. We therefore examined the strength of the serpine-1 fracture callus at 14 days post-fracture by torsional mechanical testing. An analysis of fracture strength in comparison to wild-type mice reveals that the serpine-1 KO calluses displayed a higher ultimate force to failure than their wild-type counterparts (**Figure 49**). In this

case, the ultimate force from each fracture was normalized to that obtained from torsional testing of the unfractured contralateral femur from each animal, and presented as the percentage fractured force versus unfractured force for each animal. This approach accounted for the smaller size of the serpine-1 KO femurs observed in the Specific Objective. Therefore, not only does serpine-1 gene expression regulate the type of the fracture callus tissues, it also regulates the normal pattern of callus development might produce a stronger fracture callus even at 14 days post-fracture, a very early time in bony callus tissue development. It is probable that the absence of the serpine-1 (PAI-1) inhibition of the plasminogen activators has promoted plasmin production from the plasminogens and accelerated cartilage replacement with bone at the perimeter, although PAI-1 overexpression has also previously been demonstrated to result in increases in uninjured bone strength (22). The mechanism of this action certainly warrants further investigation. *This mechanical testing study was performed to pursue the serpine-1 KO fracture analysis in addition to the original description of the Specific Objective.*

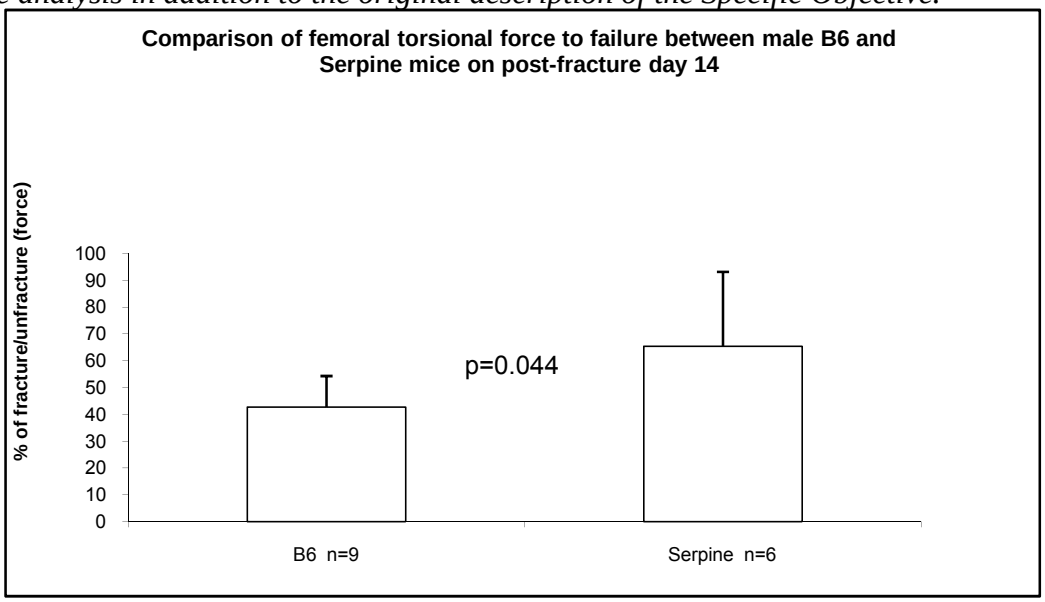

Figure 49. Torsional mechanical testing of male serpine-1 KO and wild-type mice at 14 days post-fracture. Nine wild-type and 6 serpine-1 KO mice were examined. Data is presented as mean +/- SEM. Statistics were performed by Student's t-Test.

Because of the success of the pQCT approach with respect to serpine-1 KO fracture examination, the torsional mechanical testing study and especially the histologic investigation of fracture healing in these mice, the micro-CT analysis was not undertaken; histology in particular had already provided information on serpine-1 KO fracture repair attainable through micro-CT. Additionally, the histology approach was able to examine earlier fracture calluses at 7 days post-fracture, when there is little hard callus, and no soft callus, detectable through micro-CT examination.

In summary, the serpine-1 KO fracture healing analysis has yielded interesting results that might have significant implications for fracture therapy. We intend to follow these studies with additional investigations on the plasminogen system of extracellular mediators.

Specific Objective 3: apply microarray technology to study gene expression in the fracture tissues of the one strain of knockout mice that exhibited the greatest phenotypic differences in fracture healing.

Microarray analysis provides a powerful tool for the characterization of global gene expression in fracture repair (23). This study used whole genome microarray gene analysis to identify the genes expressed in fracture repair of the Bax KO mouse femur at 14 days healing, when the pQCT data indicated, and subsequent histology data confirmed, that the Bax KO fracture callus displays altered healing as compared to the wild-type C57BL/6J wild-type control. This study used whole genome microarray gene analysis to identify the genes expressed in fracture repair of the Bax KO mouse femur at 14 days healing, when the pQCT data indicated that the Bax KO fracture callus contained more lower-density (non-cortical) bone in the fracture callus than the wild-type C57BL/6J wild-type control. This observation suggested that the midpoint of fracture healing displayed higher bone formation as a result of the reduced apoptosis produced by the Bax deficiency. This healing time in this knockout mouse presented the greatest differences bone formation in fracture healing relative to the control mice fractures, as well as a time prior to other potential differences Bax callus remodeling after 21 days healing. Additionally, this stage was prior to the 21 day to 28 day period of healing when the Bax fracture callus again displayed more lower-density bone than the wild-type control mice, and suggested that reduced apoptosis from Bax deficiency slowed remodeling of the fracture callus. The repertoire of expressed genes regulating these two processes would be expected to differ greatly from controls at this time, so the Bax KO 14 day fracture callus was chosen for an analysis of global gene expression in fracture repair.

Total RNA was compared by microarray analysis of 14 day fracture calluses from 5 individual male Bax KO mice and 5 individual C57BL/6J knockout mice. The individual pairs of samples were hybridized and analyzed separately. The RNA from each fracture callus was labeled with Cy3 or Cy5 dye and hybridized to our in-house mouse gene chip that contained approximately 28,000 unique mouse gene targets. Analysis was performed using (Agilent) Genespring software and changes in expression between the Bax KO fracture callus and the C57BL/6J callus deemed significant at $p<0.05$.

We have confirmed the expression of several gene candidates by real-time PCR, to confirm the previous X-ray and current histology observations of Bax KO fracture cartilage development and to elucidate the regulatory pathways of Bax KO fracture healing. For these purposes, real-time PCR analysis of gene expression was compared in RNA preparations from healing Bax KO and wild-type fractures at 14 days post-fracture, as well as at 7 days post-fracture, prior to the observed histology but when the genes that regulate the pathways that produce the observed effects should be expressed.

Findings:

An examination of the differences in global gene expression in the 14 day fracture calluses revealed that 5,458 genes displayed significant changes in expression (Table 7). Approximately 15% were unknown genes or expressed sequence tags (ESTs), indicating that a large portion of the molecular regulation of fracture repair remains to be elucidated. Surprisingly, in contrast to other fracture microarray studies, where most genes are up-regulated, approximately equal numbers of known and unknown genes were up-regulated and down-regulated. This difference might be caused by Bax-related apoptotic interactions with other pathways of fracture repair.

Table 7. Summary of Bax Knockout Fracture Microarray Gene Expression Changes			
14 Days Healing			
Expression Change (P<0.05)	**Known Genes**	**Unknown Genes**	**Total**
Up-regulated in Bax Knockout	**2234**	**409**	**2643**
Down-regulated in Bax Knockout	**2459**	**356**	**2815**
Total	**4693**	**765**	**5458**

An examination of the Bax-related genes revealed that several of the gene products that Bax interacts with displayed significant changes in gene expression (Table 8). These genes included several Bcl genes, including Bcl-2. Bax binds and inhibits Bcl-2, thereby promoting apoptosis (reviewed in 24). Bcl-2 up-regulation in the absence of Bax inhibition would be expected to inhibit apoptosis. Bad, a close relative of Bax and one that binds Bcl-XL and which might be expected to compensate for Bax deficiency through an up-regulation in expression, was in fact down-regulated almost two-fold in Bax KO fractures. Transcriptional compensation by closely related Bax-related proteins in the fracture was not easily explained, and the lack of an effect on apoptosis by Bax deficiency in fracture repair remained unknown.

As we found no changes in the numbers of apoptotic cells in the fracture calluses of Bax KO mice, we undertook an evaluation of mitochondrial-related gene expression by real-time PCR to identify any changes in the expression of other Bax-related genes at 7 and 14 days post-fracture that might account for the apparent lack of change in apoptosis. Real-time RT-PCR confirmations of the microarray expression data were extended to 7 and 14 days post-fracture healing times (when the Bax KO effect on fracture healing was observed), as well as to confirm additional genes of interest at these critical times. Most surprisingly, the confirmations of Bax-related gene expression from the microarray data were successful, yet they failed to define changes in the mitochondrial apoptotic pathway that would compensate for Bax gene deficiency and produce the observed effects on fracture healing when the expected reduction in apoptosis was not observed. As expected, Bax gene expression was not detected in the knockout fractures. This study also examined the Bcl-2 and Bcl-X_L ratios that might be expected to be altered in response to Bax deficiency and restore the balance in apoptosis. Such compensation might be expected if, as previously reported, there were no differences in the apoptotic cell frequencies between Bax KO and wild-type control fractures. The expression of several other mediators of mitochondrial apoptosis, among them Bad, Bak, Bok, was also expanded to 7 days but there were no significant differences in the expression of any of these genes that might explain the apparent lack of Bax deficiency on fracture apoptosis (Table 8). This observation indicates that there was no transcriptional compensation for Bax deficiency, at least from these genes. The lone exception was the up-regulated expression of Biklik (Bik-like, Table 8), a (BH-3-only domain) mitochondrial apoptotic regulator that binds and inhibits both Bcl-2 and Bcl-X_L (25); Biklik expression initially observed in the microarray analysis with relatively uncommon Bax-related genes (Table 9) and was susequently confirmed by real-time RT-PCR to be up-regulated approximately 2-fold, suggesting that its expression compensated for the absence of Bax in promoting apoptosis and reduced the severity of the Bax KO phenotype and its effect on fracture healing. Our real-time RT-PCR confirmations of the microarray analysis of gene expression

validated our approach, although the effects of Bax deficiency on fracture healing remained difficult to define.

Table 8. Real-time RT-PCR analysis of mitochondrial apoptosis gene expression in Bax KO fracture tissues.

Gene	7 Days Post-fracture*	14 Days Post-fracture *
Bax	ND	ND
Bcl-2	NS	NS
Bcl-X_L	NS	NS
Bak	NS	NS
Bid	NS	NS
Bok	NS	NS
Bik-lik	NS	2.3- fold up ($p<0.05$)

ND, not detected; NS, not significant.
*Expression in Bax KO fracture tissues was compared to C57BL/6J wild-type fracture tissue expression at 7 days (N = 2-4) and 14 days (N = 2) post-fracture. Statistics were performed by t-Test.

The examination of the gene expression in the 14 day microarray analysis was extended to several other categories of genes that might be expected to affect (1) fracture chondrogenesis at 7 days (Figure 50) 14 days (Figure 51), where the major effect of Bax deficiency was observed on fracture cartilage development. These studies attempted to identify changes in gene expression between early fracture chondrogenesis (7 days) and later chondrogenesis (14 days, also identified by the microarray) and elucidate possible interactions that balance cartilage proliferation, maturation and apoptosis between these two times. They included genes that might regulate p53 control pathways of proliferation and apoptosis (p53, p21, Inhibitor of Apoptosis-2, IAP-2; 27), Hypoxia-Inducible Factor-1α (HIF-1α; 28) and Growth Arrest DNA Damage-45 (GADD-45, observed in the microarray analysis).

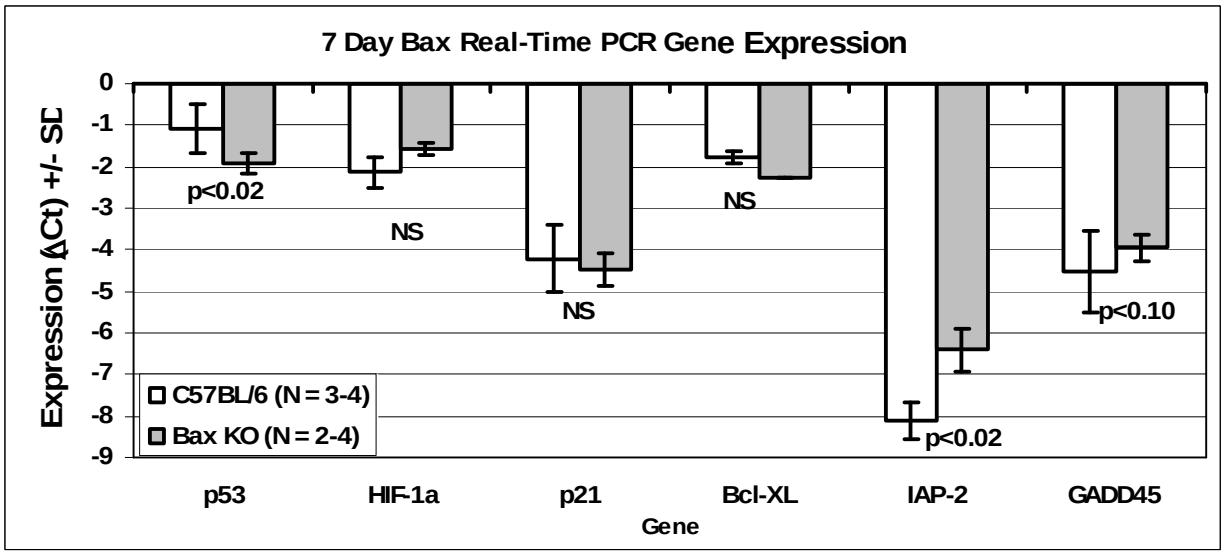

Figure 50. Real-time RT-PCR analysis of cartilage gene expression in wild-type and Bax KO mice at 7 days post-fracture. RNA from between 4 or 6 different fractures were measured for each mouse strain. Data is presented as mean +/- standard deviation. Greater gene expression is identified as a greater negative difference in cycle number (□Ct) relative to the cyclophilin housekeeping gene, defined as zero □Ct. Results are presented as mean +/- standard deviation (SD). Statistics were performed by t-Test. HIF-1□, hypoxia-inducible factor; IAP-2, inducible apoptosis promoter; GADD45, growth arrest DNA damage 45; NS, no significant difference.

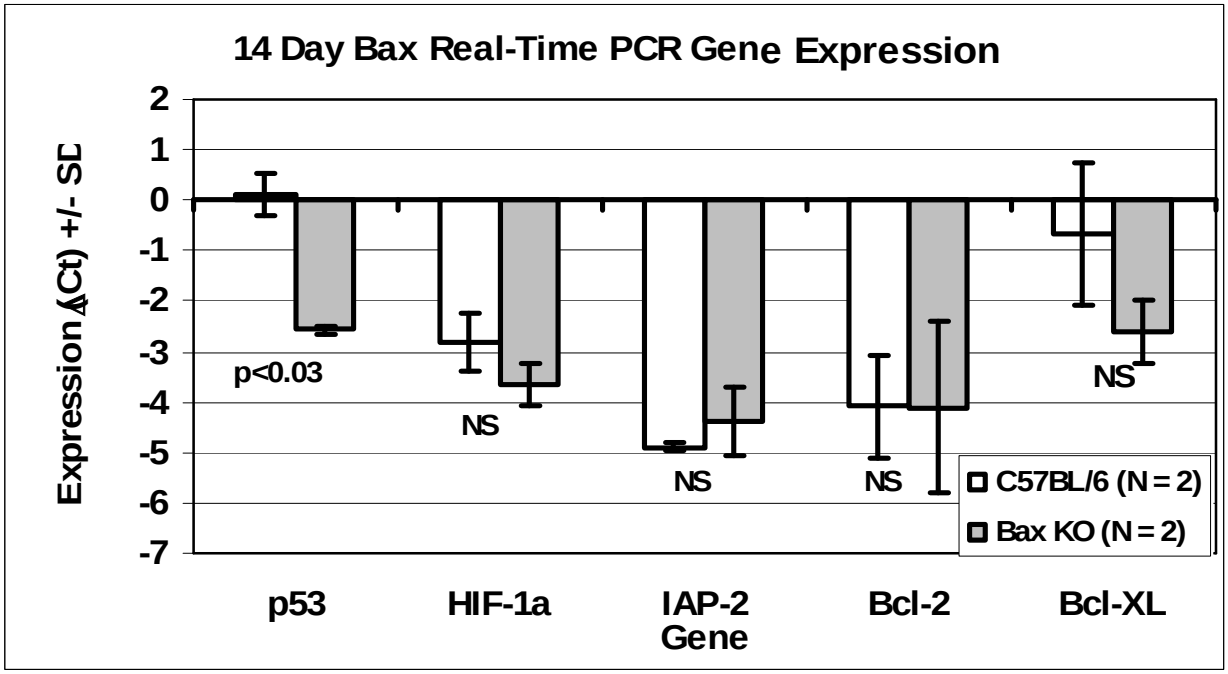

Figure 51. Real-time RT-PCR analysis of cartilage gene expression in wild-type and Bax KO mice at 14 days post-fracture. RNA from 2 different fractures was measured for each mouse strain. Data is presented as mean +/- standard deviation. Greater gene expression is identified as a greater negative difference in cycle number (□Ct) relative to the cyclophilin housekeeping gene, defined as zero □Ct. Results are presented as mean +/- standard deviation (SD). Statistics were performed by t-Test. NS, no significant difference.

In **Figure 50** (7 days post-fracture) and **Figure 51** (14 days post-fracture), it can be seen that with the notable exception of p53, few of the genes that might be expected to affect cell proliferation or apoptosis display significant differences in expression. p53 expression was up-regulated at both times, suggesting that it might regulate a balance between the cell proliferation and apoptotic regulatory pathways; it is best known as an anti-proliferative agent and a decrease in expression in Bax KO fractures is consistent with increased proliferation. None of the other markers at this time show significant differences in expression between Bax KO and wild-type fractures at 7 days, with the exception of the apoptosis inhibitor IAP-2 (**Figure 50**). Its decrease in expression at 7 days healing would increase apoptosis, which is not what we have observed, and its function remained poorly defined in this study, although it might function like Bax (or through Bax) in fracture callus development. By 14 days post-fracture, HIF-1α, a component of the apoptotic regulatory pathway, displays increased expression in the Bax KO mice (**Figure 51**), suggesting that hypoxia-induced apoptosis might regulate Bax KO cartilage development and help to resolve the fracture callus and balance the initial bias towards a cartilage increase at 7 days post-fracture.

One final study of additional Bax-related regulatory genes was attempted to more thoroughly characterize gene expression and resolve the observed effects on Bax KO fracture repair. Additional chondrocyte regulatory genes identified with slight differences in expression in the microarray analysis at 14 days were examined and compared at 7 days post-fracture to the chondrocyte markers of differentiation (**Figure 52**). These genes included Sox-6, Frizzled (Fzd) and Max binding inhibition transcription factor (Mitf). The 14 day post-fracture gene expression data revealed no significant differences between mouse strains in the expression of these genes (data not shown). It appears that by this later time that some regulatory event has compensated for the uncoupled early chondrogenesis and hypertrophy.

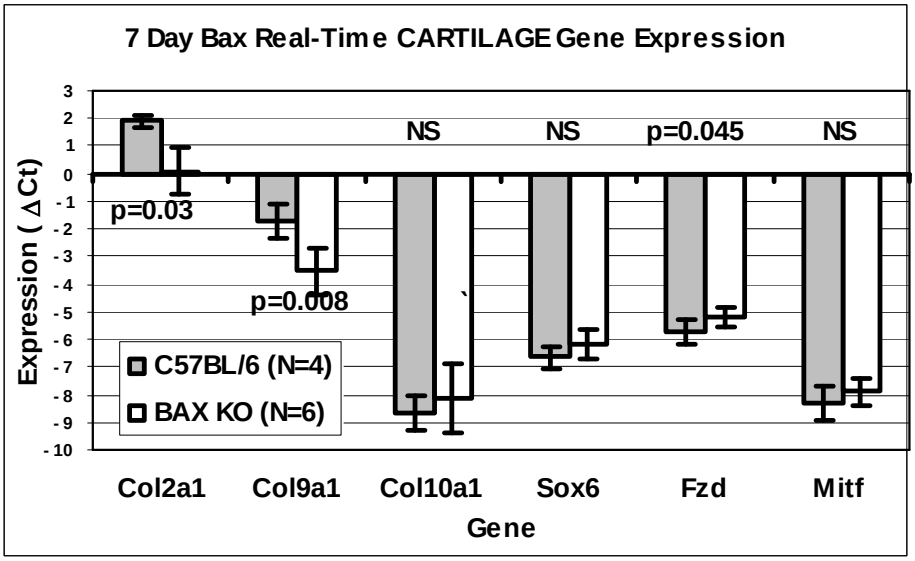

Figure 52. Real-time PCR analysis of cartilage gene expression in wild-type and Bax KO mice at 7 days post-fracture. RNA from between 4 or 6 different fractures were measured for each mouse strain. Data is presented as mean +/- standard deviation. Greater gene expression is identified as a greater negative difference in cycle number (□Ct) relative to the cyclophilin housekeeping gene, defined as zero □Ct. Statistics were performed by t-Test. The collagen structural genes are Col2□1, Col9□1 and Col10□1.

The collagen regulatory genes are Sox-6, Frizzled (Fzd) and Max binding inhibition transcription factor (Mitf). NS, no significant difference.

Microarray analysis of the Bax KO fracture callus at 14 days post-fracture provided some insights to the larger fracture callus observed during healing in these mice, but the gene expression pathways appear to be quite complex and very difficult to define, despite considerable effort. *Nevertheless, considerable information on mitochondrial apoptotic regulation fracture repair was generated by the microarray analysis of the Bax KO mouse, and this Specuific objective was accomplished.*

LoxP-Ephrin B-1 (Conditional) Knockout Mice:
Our specific objectives during this continuation period were as follows:

1) To obtain breeding pairs of loxp Ephrin-B1 mice (B6.loxp Ephrin-B1) from our collaborator, Dr. Philippe Soriano at Fred Hutchinson Cancer Center, Seattle and establish a colony.
2) Breed loxp Ephrin-B1 mice with type I collagen cre mice to generate cre positive loxp homozygous experimental and cre negative loxp homozygous control mice.
3) To characterize the skeletal phenotype of mice lacking Ephrin-B1 specifically in osteoblasts using PIXImus, pQCT and histology. To evaluate the effects of four-point bending in Ephrin-B1 conditional knockout mice, we will perform four-point bending in efnb1 conditional knockout mice once we have sufficient numbers of mice (10 weeks old, females and males).

We have chosen to identify the role a new genes, Ephrin B-1, in fracture repair and mechanical loading. We have chosen Ephrin B-1 since this gene is differentially expressed in bone in response to four-point bending, and since Eph-ephrin signaling has been implicated in the regulation of many critical events during development in a number of tissues including bone (16). Specifically, disruption of Ephrin-B1 resulted in perinatal lethality associated with a range of skeletal phenotypes including abnormal skeletal patterning (17). We proposed to conditionally disrupt Ephrin B-1 in osteoblasts and evaluate its role in bone formation in response to mechanical loading. Such conditional knockouts are generated when the Loxp-Ephrin B-1 gene is established in an animal and bred to an animal with a combination of a promoter from a gene of interest (in our case a bone-specific collagen) and Cre, an endonuclease that excises sequences between Loxp sites. In this way the activation of the collagen promoter in bone expresses Cre and results in the tissue-specific excision of Ephrin B-1 gene with Loxp. This conditional knockout technique is well refined and produces tissue (i.e., bone)-specific knockouts, yet avoids the pre-, peri- and post-natal mortality and morbidity that often accompany more conventional, global gene knockout approaches.

We received a breeding pair of EphrinB-1 loxp mice whose exons 2-5 of the EphrinB-1 gene were flanked by loxp sites from Dr. Philippe Soriano at Fred Hutchinson Cancer Center, Seattle (16) and expanded the breeding of this transgenic loxp mouse line. To generate osteoblast-specific conditional knockout mice, we first crossed homozygous EphrinB-1/loxp females with B6 males that express Cre recombinase under the control of type 1-alpha-2 collagen promoter to generate Cre positive EphrinB-1/loxp hemizygous males. We then bred the homozygous loxp females with Cre positive loxp hemizygous males to generate Cre positive homozygous/hemizygous loxp mice and Cre negative homozygous/hemizygous loxp mice for our experiments. The Cre positive loxp mice were used as experimental mice for bone fracture

and mechanical loading and the Cre-negative loxp mice from the same litter will be set up as control mice.

Mice carrying the conditional allele of EphrinB-1 were genotyped by PCR on tail DNA using the following primers: 5'-tggccttacacccgcttaag-3, 5'-agcagtggggtagtgactacc-3'. The PCR product of loxp was 500 base pairs, and the PCR product of wild-type allele of EphrinB-1 is 250 base pairs. We expected to generate Cre positive loxp homozygous females (25%), Cre negative loxp homozygous females (25%), Cre positive loxp hemizygous males (25%) and Cre negative loxp hemizygous males (25%) from the above breeding scheme.

Unfortunately, our preliminary data of breeding showed that less than 5% of pups were Cre-positive loxp homozygous females. We hypothesized that some of the Cre positive homozygous females may die prior to birth because of X chromosome-linked mutation of EphrinB-1 gene. We will examine this possibility in future studies. *This breeding problem has prevented the completion of the Specific Objective.*

We had expected to generate Cre positive loxp homozygous females (25%), Cre negative loxp homozygous females (25%), Cre positive loxp hemizygous males (25%) and Cre negative loxp hemizygous males (25%) from the above breeding scheme. Though approximately 1/3 of efnb1$^{flox/flox}$;Col1α2-Cre mutant mice died before or shortly after birth, reducing the size of the litters (Figure 53), we obtained adequate number of Cre+ pups that are loxp homozygous (female) or hemizygous (males) for phenotypic characterization.

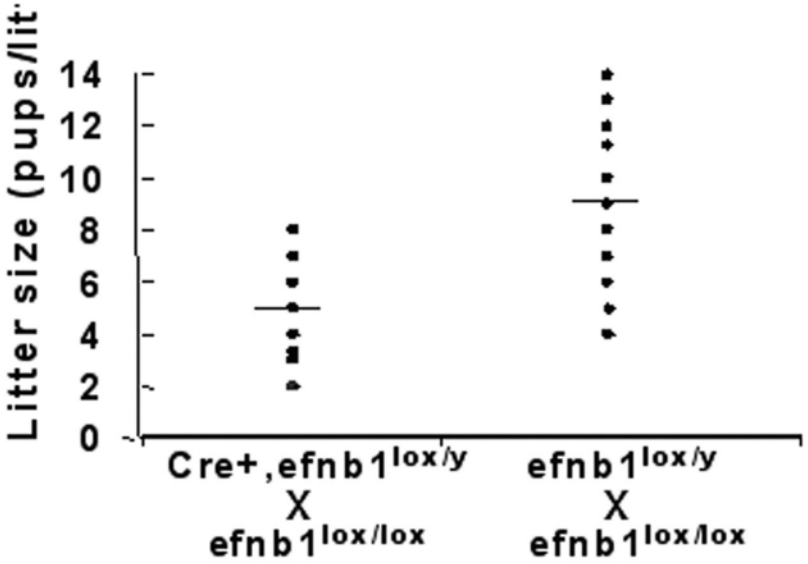

Figure 53. Reduced litter size in ephrin B1 conditional KO mice

We compared the litter size for pups that were generated using Cre positive versus Cre negative males for breeding with efnb1$^{lox/lox}$ homozygous females. As shown in Figure 53, the average litter size was approximately 5 live pups for Cre+, efnb1$^{lox/y}$ males versus 9 live pups for Cre-, efnb1$^{lox/y}$ males.

Among all live pups from the cross of efnb1 loxp homozygous mice with Cre+ loxp hemizygous mice, 60% of pups were males, and 40% were females. There was only 12% of

Cre+, efnb1$^{lox/lox}$ females. The rate of Cre+ hemizygous males was near normal. These data suggest that some mutant females carrying Cre allele might die either prior to birth or immediately after birth (Figure 54). The percentage of Cre negative mice may be an overestimate because of loss of nearly 50% Cre positive females embryonically.

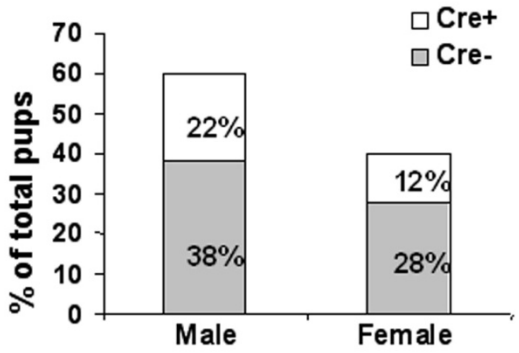

Figure 54. Distribution of live pups from breeding of efnb1$^{lox/lox}$ with Cre+, efnb1$^{lox/y}$ (N=64)

As previously reported, our preliminary breeding showed that less than 5% of pups were Cre-positive loxp homozygous females. We hypothesized that some of the Cre positive homozygous females died prior to birth because of X chromosome-linked mutation of EphrinB-1 gene. Because of this lethality, we have had difficulty getting sufficient numbers of female loxp homozygous Cre positive mice.

Consistent with this hypothesis, ephrin B-1 deficiency caused skull defects. To obtain both of experimental and control littermates, we bred efnb1$^{lox/y}$ hemizygous males carrying Col1α2-Cre allele with efnb1$^{lox/lox}$ homozygous females. Because of a significant reduction in the litter size from the cross of loxp homozygous mice with Cre+ male, we decided to examine whether the loss of ephrin B-1 in OBs is associated with embryonic lethality. We dissected the pregnant mice with 19 days of gestation (E19), and removed the embryos from the mother. We found that the ephrin B-1-deficient fetuses were recovered at the expected Mendelian ratio at E19. However, more than half (4/25) of Cre+ females that were efnb1 loxp homozygous had severe defects of the skull, and exencephaly (**Figure 55A**). The size of skull was reduced and was not big enough to accommodate the growing brain. Skeletal preparations revealed that the basal aspect of the skull and jaw were intact. However, the frontal, parietal and interparietal bones were missing in efnb1$^{lox/lox}$ mutant females. The mandible and maxilla were smaller (**Figure 55B** & **55C**). The overall size of the skull of the efnb1$^{lox/lox}$ mutant females was about 35% smaller than those of the wild-type corresponding littermates. As a result of defects of calvaria bones, the basal elements of the skull became visible when viewed from above (**Figure 55B**). Besides the calvarial defects, the Cre+ females were much smaller that the corresponding WT and bone mineralization were reduced too. So far, we have not seen similar skull defects in the Cre+ male fetus. However, the skeletal size of efnb1 mutant males was also smaller, and the bones were less mineralized compared to the corresponding littermate controls (**Figure 55D**). These data strongly support our hypothesis in this grant that ephrin B-1 is a critical regulator of bone development and bone mineralization.

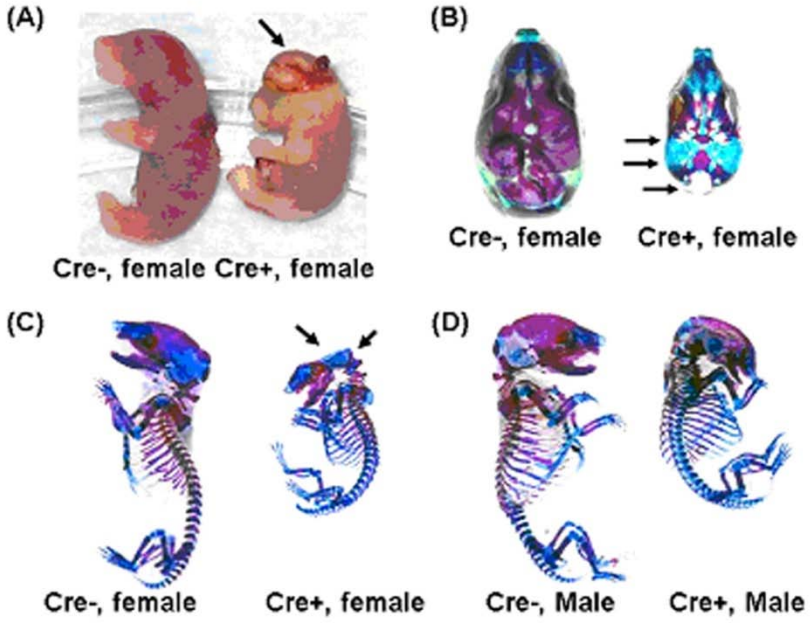

Figure 55. Defects of the skull in efnb1$^{lox/lox}$; Col1α2-Cre mutant. (A) Embryos, arrowhead indicates the exposed brain. (B) Skulls, Arrowheads indicate bone defects. (C, D) Skeletal preparations of females and males, arrowheads indicate calvaria bone defects.

Once sufficient numbers of experimental knockout mice and corresponding control mice were obtained, we characterized the skeletal phenotypes by using PIXImus, pQCT and histology. Targeted disruption of efnb1 in osteoblasts reduced bone size and bone density. As shown in **Figure 56**, the body length of sex-mixed efnb1 mutants was reduced by 15% and 10% compared to the corresponding littermates at 3 weeks and 8 weeks of age respectively (**Figure 56A** & **56B**). Femur length was reduced by 14% and 13% in Cre+ males and Cre+ females respectively at 8 week of age (**Figure 56C** & **56D**). The reduced skeletal deficit at 8 weeks compared to 3 weeks suggests that there may be compensation by other mechanisms during pubertal growth.

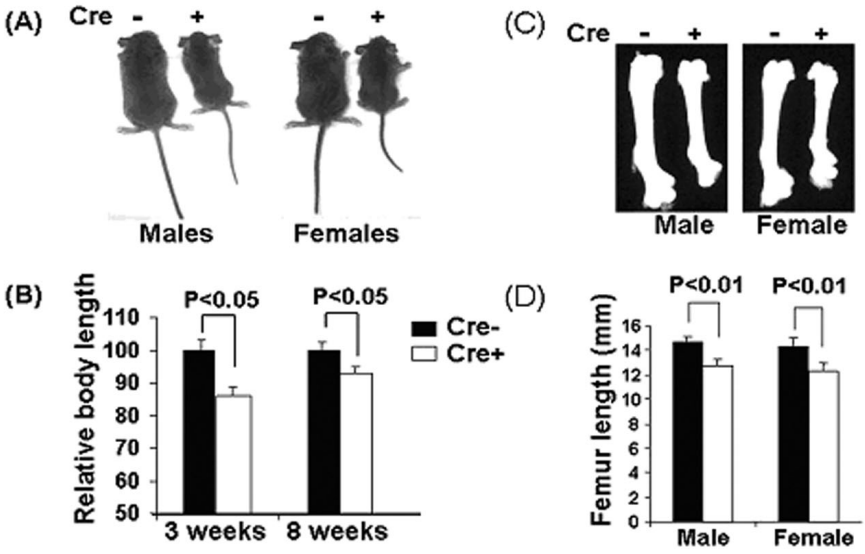

Figure 56. Reduced body length and bone size of efnb1 mutants
(A) 3 week-old of WT and mutant mice. (B) body length of WT and mutant mice at 3 and 8 weeks of age. (C) femurs of WT and mutant mice at 8 weeks of age. (D) femur length of mice at 8 weeks of age.

To determine if the targeted disruption of efnb1 in osteoblasts impairs bone density, we performed PIXImus measurement (**Figure 57**). We found that total body BMC was reduced by 30% and 23% at 3 and 8 weeks of age respectively. Total body area BMD was reduced by 10% at both time points, while total body bone area was reduced by 25 and 15% at 3 and 8 weeks of age respectively.

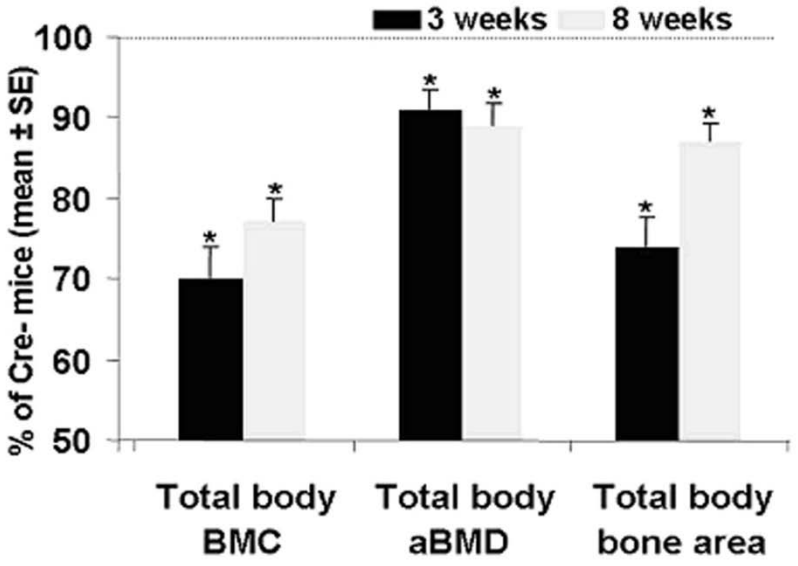

Figure 57. PIXImus measurements showed reduced total body BMC, area BMD and bone area in efnb1 mutant mice. An asterisk indicates a significant difference between Cre+ and Cre- mice (Star: $P < 0.05$).

Studies on the function of ephrin B-1 in osteoblast-specific (conditional) ephrin B-1 conditional knockout mice demonstrated that targeted disruption of ephrin B-1 gene in osteoblasts results in decreased bone size, BMD and trabecular bone volume. Resorption was no different in ephrin B-1 knockout mice, suggesting that ephrin B-1 had no effect on osteoclasts. We conclude that ephrin B-1 produced by osteoblasts is an important regulator of osteoblast activity, bone formation and peak bone mass.

We undertook an investigation of a possible mechanism by which ephrin B-1 gene deficiency in osteoblasts (Obs) might cause impaired bone formation (BF) and osterix expression that result in the severe calvarial defects observed in the ephrin B-1 knockout mouse.

Ephrin B ligands can transmit signals by activating both ephrin B receptor (EphB)-mediated forward signaling and ligand-mediated reverse signaling through its PDZ binding motif at its c-terminus. Because mutation of the PDZ binding motif exhibited the same severe skeletal phenotypes as ephrin B-1 knockout (KO) mice, we undertook studies to characterize the reverse signaling by identifying the proteins that interacted with the PDZ binding motif of ephrin B-1. We focused on Ob produced NHERF1 because it contains PDZ domains which can bind to both membrane proteins and TAZ, a transcriptional coactivator of Runx2. Accordingly, immunoprecipitation of TAZ complex with TAZ specific antibody revealed a protein complex formation containing ephrinB1, NHERF1 and TAZ in bone marrow stromal (BMS) cells. Furthermore, activation of ephrin B-1 reverse signaling with soluble clustered EphB2-Fc receptors led to a time-dependent increase in the phosphorylation of ephrin B-1 (15.4-fold at 30 min), and the dephosphorylation of TAZ (3.3-fold at 120 min). By using BMS cells derived from ephrin B-1 wild type (WT) mice, we determined that TAZ is primarily localized in the cytoplasm and that activation of ephrin B-1 reverse signaling with soluble clustered EphB2-Fc receptors led to shuttling of TAZ from cytoplasm to nucleus. To determine if the release of TAZ from ephrin B-1/NHERF1/TAZ complex is involved in ephrin B-1 reverse signaling-induced increase in osterix expression, we evaluated the consequence of blockade of TAZ expression on osterix expression. Treatment of BMS cells with exogenous addition of soluble EphB2-Fc resulted in a 4-fold increase in osterix expression as determined by Western blot in BMS cells-derived from WT but not KO mice. Disruption of TAZ expression using specific lentivirus shRNA decreased TAZ mRNA by 80% and ephrin B-1 reverse signaling-mediated increases in osterix mRNA by 75% ($P<0.01$).

We conclude that locally produced ephrin B-1 mediates its effects on Ob differentiation by a novel molecular mechanism in which activation of reverse signaling leads to phosphorylation of ephrin B-1 and subsequent release of TAZ from ephrin B-1/NHERF1/TAZ complex to translocate to nucleus for induction of expression of osterix and perhaps other Ob differentiation marker genes.

At this time this breeding problem has prevented the completion of the four-point bending studies of this Specific Objective. However, this mouse line has provided much valuable information on the developmental role of ephrin B-1 during bone formation.

KEY RESEARCH ACCOMPLISHMENTS

1) A total of four knockout mouse strains (leptin KO, Bax KO, serpine-1 KO, and Ephrin B-1 conditional KO) were obtained, bred and their genotypes identified for skeletal studies.
2) The mechanical loading model of exercise and the femoral fracture model of repair have been developed and adapted to knockout mouse studies and this allowed the analysis of the functional significance of genes of interest for bone formation in each case.
3) Two knockout mice strains (leptin KO and Bax KO) have been phenotypically characterized for their bone response to mechanical loading. One of those strains (leptin KO) underwent a microarray analysis for the repertoire of genes expressed in response to mechanical loading.
4) Three knockout mice strains (leptin KO, Bax KO and serpine-1 KO) have been phenotypically characterized for their repair reponse to bone injury. One strain (Bax KO) underwent a microarray analysis for the repertoire of genes expressed in the repair response to bone injury. The third of those knockout mouse strains (serpine-1 KO) also underwent a detailed femoral phenotypic characterization.
5) One of the knockout mouse strains (leptin KO) underwent an additional study that described its sex-related differences in bone size.
6) The fourth knockout mouse strain (Ephrin B-1 conditional KO) underwent a phenotypic characterization.

REPORTABLE OUTCOMES

Publications:

1. Wang, X., C.H. Rundle, J.E. Wergedal, A.K. Srivastava, S. Mohan and K.-H.W. Lau (2007) Loss of sex-specific difference in femoral bone parameters in male leptin knockout mice. Calcif. Tissue Int. 80: 374-382.
2. Rundle, C.H., X. Wang, M.H-C. Sheng, J.E. Wergedal, K-H.W. Lau and S. Mohan (2008) Bax deficiency in mice increases cartilage production during facture repair through a mechanism involving increased chondrocyte proliferation without changes in apoptosis. Bone 43: 880-888.
3. Rundle, C.H., X. Wang, J.E. Wergedal, S. Mohan and K-H.W. Lau (2008) Fracture healing in mice deficient in plasminogen activator inhibitor-1. Calcif. Tissue Int. 83: 276-284.
4. Xing, W., J. Kim, J.E. Wergedal, S-T. Chen and S. Mohan (2009) Ephrin B1 Regulates Bone Stromal Cell Differentiation and Bone Formation by Influencing TAZ Transactivation via Complex Formation whith NHERF1 Mol Cell Biol (in revision).

Abstracts:

1. Wang, X., C.H. Rundle, A. Srivastava, J. Tesfai, E.I. Davis, J.E. Wergedal, K.H-W. Lau, S. Mohan and D.J. Baylink (2005). Loss of sex-specific difference in bone size in leptin knockout mice. Poster presentation at the 27th Annual Meeting of the American Society for Bone and Mineral Research, Nashville, TN.
2. Rundle, C.H., X. Wang, J.E. Wergedal, A. Srivastava, E.I. Davis, K.H-W. Lau, S. Mohan and D.J. Baylink (2006). Loss of sex-specific difference in bone size in leptin-deficient (ob/ob) mice. Oral presentation at the 52nd Annual Meeting of the Orthopaedic Research Society, Chicago, IL.
3. Xing, W., J. Kim, S-T.Chen and S. Mohan (2007) Ephrin B1 Reverse Signaling Regulates Osteoblast Differentiation by a Novel Mechanism That Involves Release of Membrane Bound TAZ from EphrinB1/NHERF1/TAZ Complex for Subsequent Nuclear Localization and Induction of Osterix Gene Transcription. Oral presentation at the 29th Annual Meeting of the American Society for Bone and Mineral Research, Honolulu, HI.
4. Rundle, C.H., X. Wang, R.M. Porte, J.E. Wergedal, S. Mohan and K-H.W. Lau (2007) Plasminogen activator inhibitor (PAI-1) deficiency enhances fracture callus size but reduces cartilage remodeling during fracture repair. Poster presentation at the 29th Annual Meeting of the American Society for Bone and Mineral Research, Honolulu, HI.
5. Rundle, C.H., X. Wang, J.E. Wergedal, M.H-C. Sheng, R.M. Porte, K-H.W. Lau and S. Mohan (2007) Bax-deficient mice exhibit marked increase in callus size and cartilage during endochondral repair of femur fractures. Oral presentation at the 29th Annual Meeting of the American Society for Bone and Mineral Research, Honolulu, HI.
6. Xing, W., J. Kim, J.E. Wergedal and S. Mohan (2008) Ephrin B1 Reverse Signaling Regulates Bone Formation via Influencing Osteoblast Activity in Mice. Oral presentation at the 30th Annual Meeting of the American Society for Bone and Mineral Research, Montreal, QB, Canada
7. Xing, W., J. Kim, S-T. Chen and S. Mohan (2009) Ephrin B1 Reverse Signaling Regulates Osteoblast Differentiation by a Novel Mechanism That Involves Release of Membrane Bound TAZ from EphrinB1/NHERF1/TAZ Complex for Subsequent Nuclear Localization

and Induction of Osterix Gene Transcription Oral presentation at the 31st Annual Meeting of the American Society for Bone and Mineral Research, Denver, CO.

CONCLUSIONS

1) Leptin Knockout

X-ray and pQCT analysis suggests that leptin expression affects different parameters of the tibia and influences bone formation in mechanical loading. Microarray data suggest that the molecular regulation of bone formation in mechanical loading is complex.

Leptin expression reduced the lower density trabecular-type bone in the fracture callus during bone repair when examined with micro-CT, suggesting that regulated fracture callus bone formation. pQCT analysis and serum sex steroid analysis suggests that leptin also influences sex-specific differences in bone size in males through sex hormone-related effects.

2) Bax Knockout

X-ray and pQCT analysis suggests that Bax expression regulates the cortical parameters of bone formation in mechanical loading.

X-ray, pQCT and histological analysis of fracture healing suggest that Bax expression influences fracture callus cartilage development through increased proliferation of the tissues, a function not previously attributed to Bax gene regulation. Microarray analysis of fracture healing at 14 days post-fracture suggests that Bax regulation of fracture chondrogenesis is complex and not directly affected by Bax regulation of mitochondrial apoptosis, and although mitochondrial apoptotic gene compensation is possible, interacting pathways of proliferation and differentiation might ultimately produce the observed effects in Bax KO fractures.

3) Serpine-1 Knockout

A phenotypic analysis of the normal serpine-1 KO femur indicated that serpine-1 positively regulates different parameters of bone size. X-ray, pQCT and histological analysis of fracture healing suggests that serpine-1 (plasminogen activator inhibitor, PAI-1) regulates cartilage development during fracture repair, although the mechanism by which it does so remains elusive.

4) Ephrin B-1 Conditional Knockout

A phenotypic characterization of ephrin B-1 knockout mice identified several aspects of body and bone size that it regulated, the most severe of which was in the skull. A novel mechanism was proposed for these activities of Ephrin B-1.

REFERENCES

1. Ducy P., Amling M., Takeda S., et al. (2000). Leptin inhibits bone formation through a hypothalamic relay: A central control of bone mass. Cell 100:197-207.
2. Steppan CM., Crawford DT., Chidsey-Frink KL., et al. (2002). Leptin is a potent stimulator of bone growth in ob/ob mice. Regulatory Peptides 92:73-78.
3. Matkovic V., Ilich JZ., Skugor M., et al. (1997). Leptin is inversely related to age at menarche in human females. J. Clin. Endocrinol. Metab. 82:3239-3245.
4. Takeda S., Elefteriou F., Levasseur R., et al. (2002). Leptin regulates bone formation via the sympathetic nervous system. Cell 111:305-317.
5. Lee, Y-J., Park, J-H., Ju, S-K., et al. (2002). Leptin receptor isoform expression in rat osteoblasts and their functional analysis. FEBS Letters 528:43-47.
6. Knudson CM., Tung KSK., Tourtellotte WG., et al. (1995). Bax-deficient mice with lymphoid hyperplasia and male germ cell death. Science 270:96-98.
7. Mocetti P., Silvestrini G., Ballanti P., et al. (2001). Bcl-2 and Bax expression in cartilage and bone cells after high-dose corticosterone treatment in rats. Tissue & Cell 33:1-7.
8. Hock, JM., Krishnan, V., Onyia, JE., et al. (2001). Osteoblast apoptosis and bone turnover. J. Bone Miner. Res. 16:975-984.
9. Xing, L. and Boyce, BF. (2005). Regulation of apoptosis in osteoclasts and osteoblastic cells. Biochem. Biophys. Res. Commun. 328:709-720.
10. Collen, D. and Lijnen, HR. (1991). Basic and clinical aspects of fibrinolysis and thrombolysis. Blood 78:3114-3124.
11. Carmeliet, P., Kiekens, L., Schoonjans, L., et al. (1993). Plasminogen activator inhibitor-1 gene-deficient mice. I. Generation by homologous recombination and characterization. J. Clin. Invest. 92:2746-2755.
12. Suda, M., Ogawa Y, Tanaka K., et. al. (1998). Skeletal overgrowth in transgenic mice that overexpress brain natriuretic peptide. Proc. Natl. Acad. Sci USA 95:2337-2342.
13. Yasoda A., Ogawa Y., Suda M et al. (1998). Natriuretic peptide regulation of endochondral ossification. J. Biol. Chem. 273, 11695-11700.
14. Mackelvie KJ. McKay HA., Petit MA., et al. (2002). Bone mineral response to a 7-month randomized controlled, school-based jumping intervention in 121 pre-pubertal boys: Associations with ethnicity and body mass index. J. Bone Miner. Res 17:834-844.
15. Kodama Y., Dimai HP., Wergedal J., et al. (2000). Exercise and mechanical loading increase periosteal bone formation and whole bone strength in C57BL/6J mice but not in C3H/Hej mice. Calcif. Tissue Int. 66:298-306.
16. Davy, A., Aubin, J. and Soriano, P. (2004) Ephrin-B1 forward and reverse signaling are required during mouse development. Genes Dev. 18:572-583.
17. Coulthard, MG., Duffy, S., Down, M., et al (2002) The role of Eph-ephrin signaling system in the regulation of developmental patterning. Int. J. Dev. Biol. 46:375-384.
18. Bonnarens, F. and Einhorn, TA. (1984). Production of a standard closed fracture in laboratory animal bone. J. Orthop. Res. 2:97-101.
19. Nelson, DA., Simpson, PM., Johnson, CC., et al. (1997). The accumulation of whole body skeletal mass in third- and fourth-grade children: Effects of age, gender, ethnicity and body composition. Bone 20:73-78.
20. Hamrick MW., Pennington C., Newton D., et al. (2004) Leptin deficiency produces contrasting phenotypes in bones of the limb and spine. Bone 34:376-383.

21. Thomas, T. and Burguera, B. (2002). Is leptin the link between fat and bone mass? J. Bone Miner. Res. 9;1563-1569.
22. Nordstrom, S.M., Carleton, S.M., Carson, W.L., et al. (2007) Transgenic overexpression of plasminogen activator inhibitor-1 results in age-dependent and gender-specific increases in bone strength and mineralization. Bone 41:995-1004.
23. Hadjiargyrou, M., Lombardo, F., Zhao, S., et al. (2002). Transcriptional profiling of bone regeneration: Insight into the molecular complexity of wound repair. J. Biol. Chem. 277:30177-30182.
24. Willis, S., Day, CL., Hinds, MG., et al. (2003). The Bcl-2-regulated apoptotic pathway. J. Cell Science 116:4053-4056.
25. Coultas, L., Bouillet, P., Stanley, EG., et al. (2004). Proapoptotic BH-3-only Bcl-2 family member Bik/Blk/Nbk is expressed in hematopoietic and endothelial cells but is redundant for their programmed death. Mol. Cell. Biol. 24:1570-1581.
26. Deschamps, J. and van Nes, J. (2005). Developmental regulation of the Hox genes during axial morphogenesis in the mouse. Development 132:2931-2942.
27. Basu, A. and Haldar, S. (1998) The relationship between Bcl2, Bax and p53: consequences for cell cycle progression and cell death. Mol. Hum. Reprod. 4:1099-1109.
28. Greijer, AE. and van der Wall, E. (2004) The role of hypoxia inducible factor 1 (HIF-1) in hypoxia induced apoptosis. J. Clin. Pathol. 57:1009-1014.

B. GENE THERAPY PROJECTS

Project 6: Systemic Gene Therapy For The Skeleton

INTRODUCTION

For this project, we propose to develop and test the efficacy of a mouse model for systemic gene therapy for massive skeletal tissue damage by means of hematopoietic stem cells (HSC) transplant. For this model, we will determine the skeletal marrow tissue and non-skeletal sites of engraftment, the quantity of short-term and long-term bone formation achieved, and the effect of the age of the recipient mice on the bone formation response. To our knowledge, our studies will be the first to use transplantation of transduced HSCs to deliver gene therapy to induce bone formation. These studies will focus on the induction of bone formation for massive skeletal injury. However, there is evidence that HSCs have the plasticity to regenerate other tissue types. Therefore, a successful HSCs-delivered gene therapy strategy for bone injury could be adapted to treat other damaged tissues, such as skin and muscle that are likely to be sustained along with massive skeletal injury, by the insertion of tissue-specific promoters to drive the therapeutic gene

BODY

Technical Objectives: To develop and test the efficacy of a mouse model for systemic gene therapy for massive skeletal tissue damage by means of hematopoietic stem cell (HSC) transplant. For this model, we will determine the skeletal marrow tissue and non-skeletal sites of engraftment, the quantity of short-term and long-term bone formation achieved, and the effect of the age of the recipient mice on the bone formation response.

Our specific objectives for this grant period were as follows:

Specific Objective 1: To initiate studies to determine the skeletal marrow and non-skeletal sites of engraftment in recipient mice after transplant with donor HSCs.

a. Transplant GFP-expressing HSCs derived from transgenic mice into myelosuppressed recipient mice and assess the short-term (8 weeks), mid-term (6 months) and long-term (1 year) engraftment in the skeletal marrow and non-skeletal sites. Engraftment efficiencies will be quantitated by measuring the percentage of GFP-expressing cells in the peripheral blood and bone marrow of the recipient mice using flow cytometry.

b. Assess the pluripotent ability of the engrafted donor cells to produce mature hematopoietic lineages (T-cell, B-cell, neutophil/granulocyte/monocyte and erythroid) by using lineage-specific immunostaining and FACs analysis of the recipients' peripheral blood.

c. Detection of donor cells in non-skeletal tissues will be accomplished by frozen sectioning of the heart, lungs, liver and spleen of the recipients and fluorescent microscopic observation.

Specific Objective 2: To initiate studies to assess and quantitate the short-term and long-term bone formation achieved in mice following transplantation with HSCs transduced to express a growth factor gene.

a. Transduce HSC-enriched cells with an HIV-based vector expressing the BMP 2/4 gene under the control of the CMV promoter. Transgene expression will be assessed using immunohistochemical staining of the transduced cell cultures and Western blot analysis of the conditioned media

b. Transplant transduced donor cells via tail vein into myelosuppressed recipient mice and evaluate bone formation after 8 weeks, 6 months and 1 year. Bone formation will be evaluated by measuring serum

osteocalcin and alkaline phosphatase. Bone density and cortical thickness in the host animals will also be assessed by faxitron X-ray and pQCT analysis.

Specific Objective 3: To initiate studies to determine the effect of recipient age on engraftment and the bone formation response in mice transplanted with HSCs transduced to express a growth factor gene.

a. Transplant transduced donor cells expressing the BMP-2/4 gene into myelosuppressed recipient mice of 2 ages (8 weeks old vs. greater than 1 year old).

b. Compare the engraftment and bone formation response in young vs. old recipient mice by measuring serum osteocalcin and ALP, 12 weeks and 6 months post-transplant. We will also perform faxitron X-ray and pQCT analysis to evaluate the effects of transgene expression on bone density and cortical thickness in the recipient animal.

NOTE: Technical Objective 3 revision was approved in June, 2005.
Revised Technical Objective 3: To explore the possible mechanism(s) for why transplantation of HSC-enriched cells transduced to express BMP4 did not induce bone formation as expected.

a. To determine if silencing of the BMP2/4 transgene occurs we will, Transplant donor Sca-1^+ cells transduced to express BMP 2/4 (or marker control gene) into myelosuppressed recipient mice and evaluate transgene expression at 8 weeks and 6 months post transplant. Transgene expression will be evaluated by real time RT-PCR in RNA extracts and PCR in DNA extracts

b. To determine if BMP2/4 interferes with engraftment of Sca-1^+ cells we will: transduce Sca-1^+ cells transduced to express BMP 2/4 (or marker control gene) and transplant at 4 cell doses (500, 5000, 50,000 or 500,000 cells/recipient) into myelosuppressed recipient mice and evaluate engraftment at 4, 6, 8, 10 and 16 weeks.

c. To determine if BMP2/4 induces Sca-1^+ cell differentiation into hematopoietic lineages. Transduce Sca-1^+ cells transduced to express BMP 2/4 (or marker control gene) and transplant at 4 cell doses (500, 5000, 50,000 or 500,000 cells/recipient) into myelosuppressed recipient mice and evaluate the percentage of various hematopoietic lineages (T-lymphocytes, B-lymphocytes, monocytic and erythroid) at 4, 6, 8, 10 and 16 weeks. Hematopoietic lineage will be assessed by immunostaining and FACs analysis.

Progress on Technical Objectives
Objective 1a: To transplant GFP-expressing HSCs derived from transgenic mice into myelosuppressed recipient mice and assess the short-term (8 weeks), mid-term (6 months) and long-term (1 year) engraftment in the skeletal marrow and non-skeletal sites.

The Sca-1 molecule has been implicated as a marker for hematopoietic stem cell (HSCs). Sca-1^+ cells isolated from TgN-GFP donor mice were transplanted into recipient mice, and skeletal marrow and non-skeletal sites were analyzed for engraftment at various time points post-transplant. The donor TgN mouse is a transgenic strain transduced to produce the eGFP marker gene. Use of this donor strain allows for the tracking of donor cells *in vivo* after transplantation. For these studies, whole bone marrow cells were harvested by flushing tibiae and femurs with PBS using a 26g needle and syringe. Erythrocytes were removed by osmotic lysis using a solution of 155 mM NH_4Cl, 10mM $KHCO_3$ and 110μM Na_2EDTA, followed by rinsing with PBS. The cell preparation was then incubated with Sca-1 specific antibody-magnetic microbead conjugates and applied to an automated magnetic separation column (AutoMacs™) according to manufacturer instructions. Viable cell yields at each stage of enrichment were determined by manual cell count using a hemocytometer and trypan blue dye exclusion assay. To assess enrichment efficiency at each stage of preparation, aliquots were incubated

with either PE conjugated Sca-1 specific or rat isotype control antibody and assessed by FACs analysis. Figure 1 shows the FACs analysis of cell preparations after each preparation step for the Sca-1^+ specific antibody. Table 1 is a summary of enrichment data from several experiments and includes total % Sca-1^+ cells (derived by adding the upper right FACs quadrant (Sca-1^+/GFP$^-$) plus the upper left FACs quadrant (Sca-1^+/GFP$^+$)). Comparison of the % total Sca-1^+ cells in the WBM (5.8%) and the final Sca-1^+-enriched preparations (74.3%).indicates that the average increase in Sca-1^+ cells achieved with our enrichment method is approximately 12-fold.

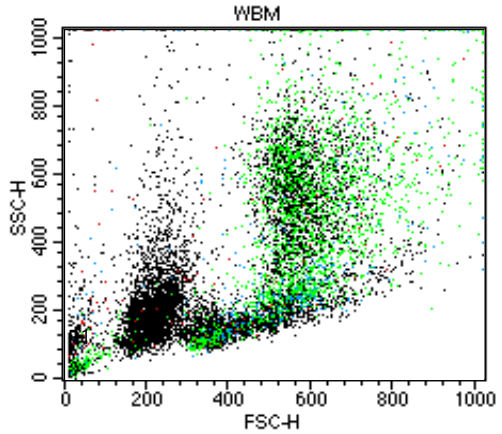

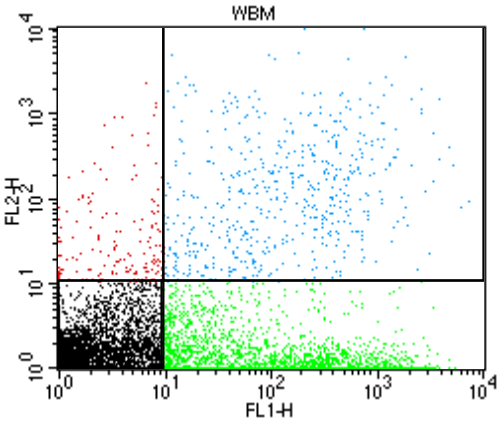

Sca-1^+/GFP$^-$ 1%	Sca-1^+/ GFP$^+$ 4%
Sca-1^-/GFP$^-$ 69%	Sca-1^-/GFP$^+$ 26%

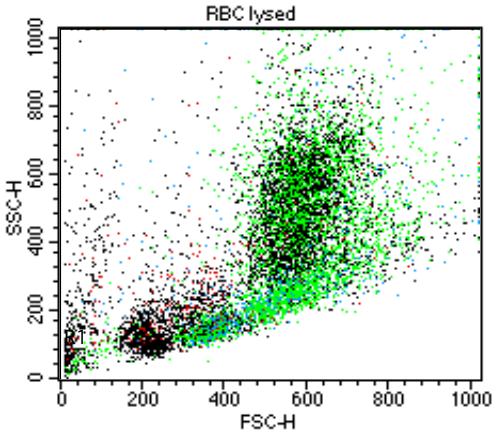

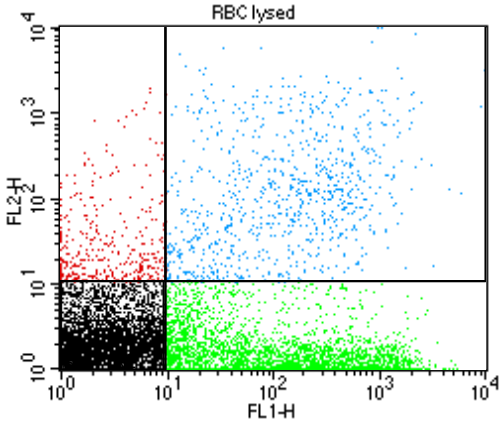

Sca-1^+/GFP$^-$ 5%	Sca-1^+/ GFP$^+$ 7%
Sca-1^-/GFP$^-$ 47%	Sca-1^-/GFP$^+$ 39%

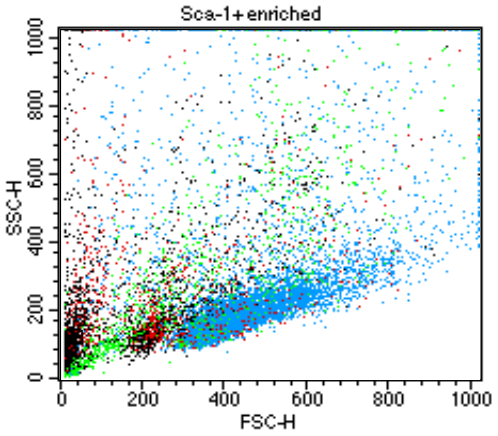

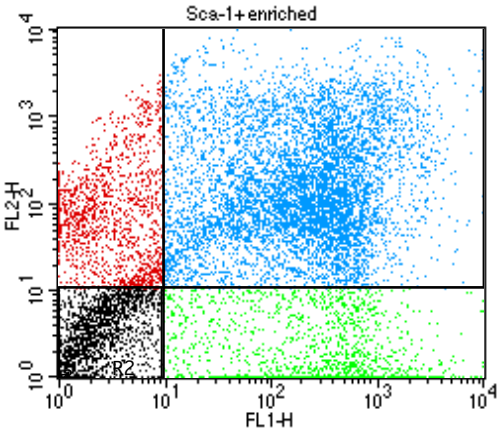

Sca-1^+/GFP$^-$ 10%	Sca-1^+/ GFP$^+$ 60%
Sca-1^-/GFP$^-$ 9%	Sca-1^-/GFP$^+$ 21%

Figure 1: Flow cytometeric analysis of cell preparations at each step of the enrichment process. Cell preparations were incubated with PE-conjugated antibodies specific for Sca-1. Upper 3 panels show data for whole bone marrow (WBM), middle 3 panels for cells after osmotic lysis of erythrocytes and lower 3 panels for Sca-1^+-enriched cells after magnetic microbead selection.

Cell counts	Total cells per donor mouse Mean (st. dev.) X 10^6	% Sca-1^+ and GFP$^-$	% Sca-1^+ and GFP$^+$	% Total Sca-1^+
Whole bone marrow	116.0 (15.5)	1.2 (0.4)	4.7 (0.5)	5.8 (0.7)
RBC-lysed	43.9 (8.5)	2.8 (0.8)	8.0 (1.7)	10.7 (0.9)
Sca-1-enriched	3.0 (0.7)	16.6 (5.1)	57.7 (9.9)	74.3 (5.3)

Table 1: Cell yields and % Sca-$1^+$and/or GFP$^+$ cells at each step of the enrichment

Subsequent to these initial studies, due to a nationwide unavailability of Sca-1 specific antibody-magnetic microbead conjugates from the manufacturer (Miltenyi Biotech), we tested a new method of Sca-1 cell isolation (secondary antibody method) in parallel with the original method (primary antibody method). Figure 2 is a diagram of the Sca-1 enrichment scheme describing the primary and secondary antibody enrichment methods.

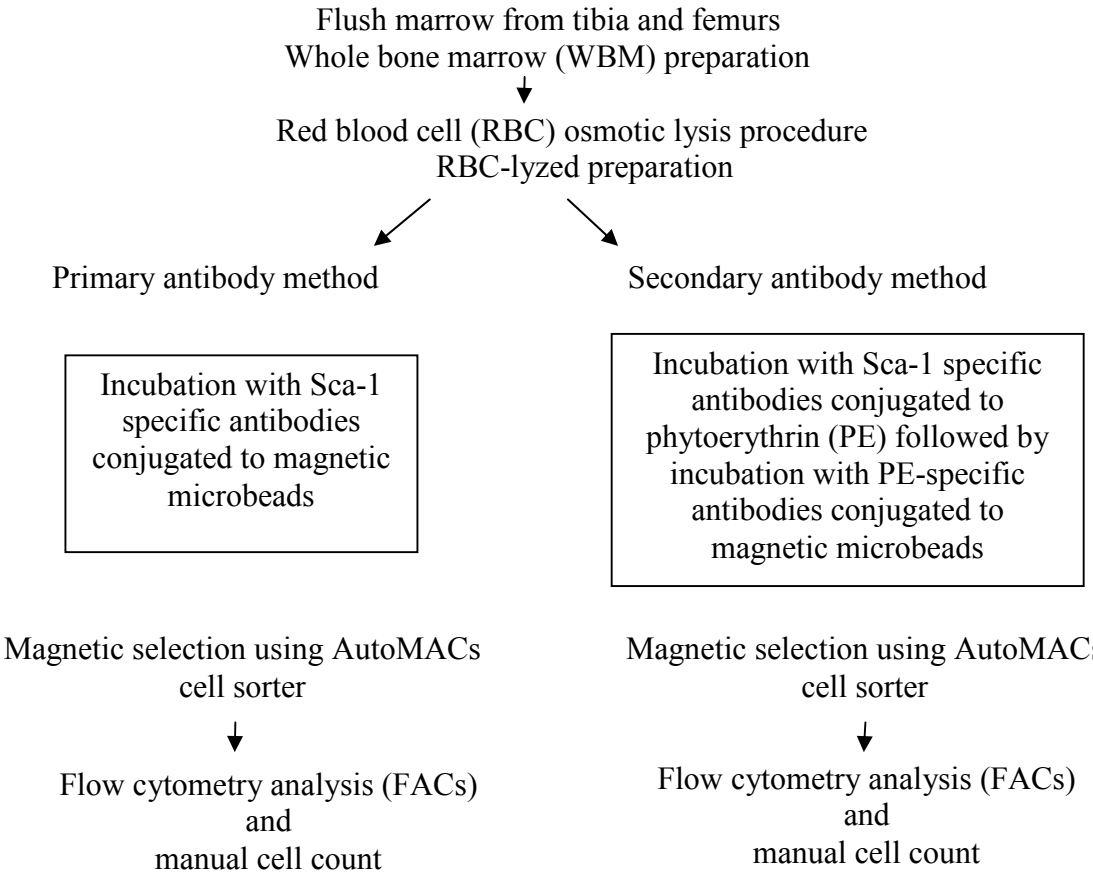

FIGURE 2: Comparison of Sca-1 Enrichment Schemes

Briefly, whole bone marrow cells were harvested and erythrocytes removed as described above. After osmotic depletion of erythrocytes (RBC-lyzed), the cell preparation was divided in half. One half was enriched for Sca-1 cells by the primary antibody method by incubating the cells with Sca-1 specific antibody-magnetic microbead conjugates. The other aliquot of RBC-lyzed cells was enriched using the secondary antibody method by incubating the cells with Sca-1 antibodies conjugated to phycoerythrin (PE) fluorochrome, followed by incubation with a secondary anti-PE antibody conjugated to a magnetic microbead. In separate runs, the mixtures were applied to an automated magnetic separation column (AutoMacs™) according to manufacturer instructions. Figure 3 shows the FACs analysis of cell preparations after each preparation step. Additionally, cell yields of aliquots of the WBM, erythrocyte-lysed, and Sca-1^+ cell-enriched preparations were measured by manual cell count of viable cells as determined by trypan dye exclusion. Table 2 is a summary of enrichment and viability data of the two cell preparations. Recovery was calculated by dividing the total number of cells counted after RBC-lysis and after Sca-1^+ enrichment methods by the total number of WBM cells. Total % Sca-1^+ cells was derived by adding the upper right FACs quadrant (Sca-1^+/GFP^+) plus the upper left FACs quadrant (Sca-1^+/GFP^+) from each panel in Figure 3 after adjustment for non-specific binding using a PE conjugated rat isotype control antibody. The fold-increase Sca-1 enrichment was calculated by dividing the percentage of total Sca-1^+ cells at each preparation step by that of the WBM preparation. Recovery of cells was similar between the primary and secondary antibody methods (1.5 vs. 1.9%, respectively). As seen in the far right column of Table 2, the Sca-1 enrichment by the two methods was also similar. The primary antibody method increased the percentage of Sca-1^+ by 19-fold and the secondary antibody method by 14-fold. Furthermore, calculation of the actual number of Sca-1 cells yielded from one donor mouse by multiplying the total cells per donor mouse by % total Sca-1^+ were similar between the primary antibody and secondary antibody methods (1.3 and 1.2 million Sca-1^+ cells, respectively). These data suggest that cell enrichment and viability are comparable between the two methods of enrichment.

We next assessed the ability of cells prepared by each enrichment method to engraft in recipient mice. The Sca-1^+ cells prepared by each method were transplanted (500,000 cells in 25uL normal saline) via retro orbital injection into 14 W41/W41 recipient mice (N = 7 per group). This mouse stain has a c-kit mutation that results in a deficiency in hematopoietic stem cells. Use of this strain as recipients in our model has allowed us to achieve high engraftment efficiencies with a sub lethal preconditioning regimen. To provide optimal engraftment, prior to transplantation, the recipient mice were sublethally irradiated by single dose (500cGY) total body irradiation. At 6 and 10 weeks post transplantation, peripheral blood was collected from each recipient by tail vein bleed. Engraftment was evaluated by FACs analysis of the percentage of GFP-expression (donor) cells in the peripheral blood samples after red blood cell lysis. A high transplantation success rate was observed with both cell preparations, with all 14 mice showing high engraftment (> 80% donor cells). Figure 4 is a bar graph showing the engraftment expressed as % GFP+ cells in recipient peripheral blood at the two time points. At 6 weeks, high engraftment was observed in both the primary and secondary antibody method (87.5 ± 2.3% and 84.7 ± 1.8%, respectively). This high engraftment was also observed at 10 weeks (90.3 ± 1.4% for the primary antibody method and 91.9 ± 1.2% for the secondary antibody method).

These results indicate that the two methods of Sca-1+ cell isolation are comparable in cell recovery rates, enrichment and engraftment efficiencies. For the remainder of experiments we used the secondary antibody method and were able to achieve consistent recovery rates (2.6%), enrichment (12-fold increase in Sca-1+ cells) and engraftment efficiencies (70-95%) donor cells in peripheral blood of recipients.

Whole bone marrow

Panel A

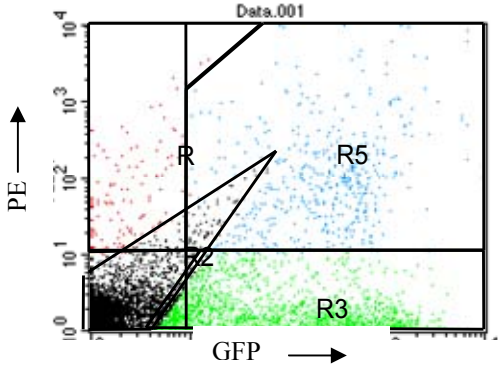

Sca-1$^+$/GFP$^-$ 1.2%	Sca-1$^+$/GFP$^-$ 4.6%
Sca-1$^-$/GFP$^-$ 67.1%	Sca-1$^-$/GFP$^+$ 26.9%

RBC-lyzed

Panel B

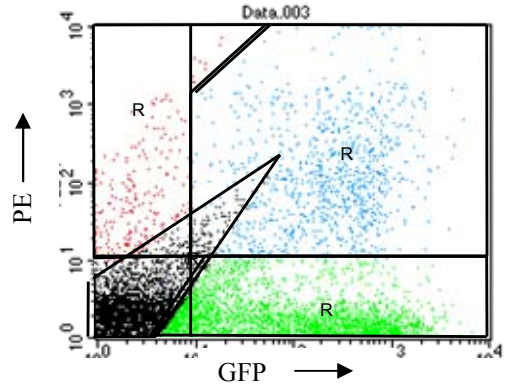

Sca-1$^+$/GFP$^-$ 2.3%	Sca-1$^+$/GFP$^-$ 9.1%
Sca-1$^-$/GFP$^-$ 40.1%	Sca-1$^-$/GFP$^+$ 48.1%

Sca-1 enriched – Primary antibody method

Panel C

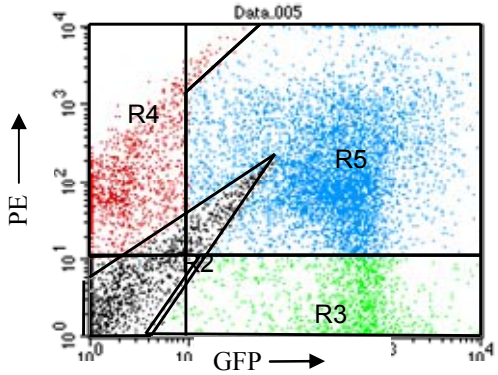

Sca-1$^+$/GFP$^-$ 11.0%	Sca-1$^+$/GFP$^-$ 60.0%
Sca-1$^-$/GFP$^-$ 13.7%	Sca-1$^-$/GFP$^+$ 14.9%

Sca-1 enriched –Secondary antibody method

Panel D

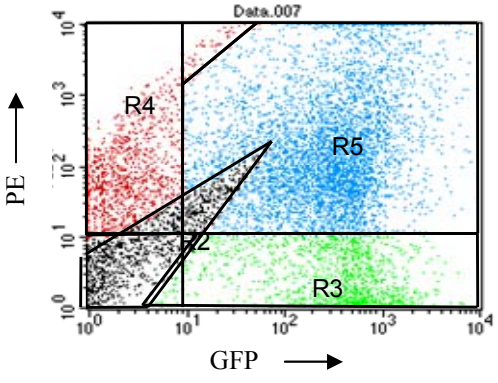

Sca-1$^+$/GFP$^-$ 11.5%	Sca-1$^+$/GFP$^-$ 49.6%
Sca-1$^-$/GFP$^-$ 13.8%	Sca-1$^-$/GFP$^+$ 24.4%

Figure 3: Flow cytometeric (FACs) analysis of cell preparations at each enrichment step. Aliquots of whole bone marrow cells from GFP-transgenic mice before (Panel A) and after (Panel B) RBC-lysis were incubated with PE-conjugated antibodies specific for Sca-1. Half of the RBC-lyzed cell preparation was enriched for Sca-1+ cells by the original method (primary antibody method) and half was enriched by an alternative method (secondary antibody method). Details of the methods are described in the text. Panels C and D show FACs analysis of the primary antibody method and secondary antibody method, respectively. Percentages of cells in each quadrant are displayed in the tables to the right of the FACs analysis graphs in each panel.

Cell counts	Total cells per donor mouse # cells x 10^6	Recovery (%)	% Sca-1^+ and GFP$^-$	% Sca-1^+ and GFP$^+$	% Total Sca-1^+	Fold-increase Sca-1 Enrichement
Whole bone marrow	131	-	0.29	3.30	3.59	-
RBC-lysed	47	36	1.38	7.75	9.13	3
Sca-1-enriched (primary antibody method)	1.9	1.5	10.33	58.14	68.47	19
Sca-1-enriched (secondary antibody method)	2.5	1.9	8.63	40.6	49.23	14

Table 2: Summary of enrichment and viability data of the 2 cell preparation methods (primary antibody and secondary antibody)

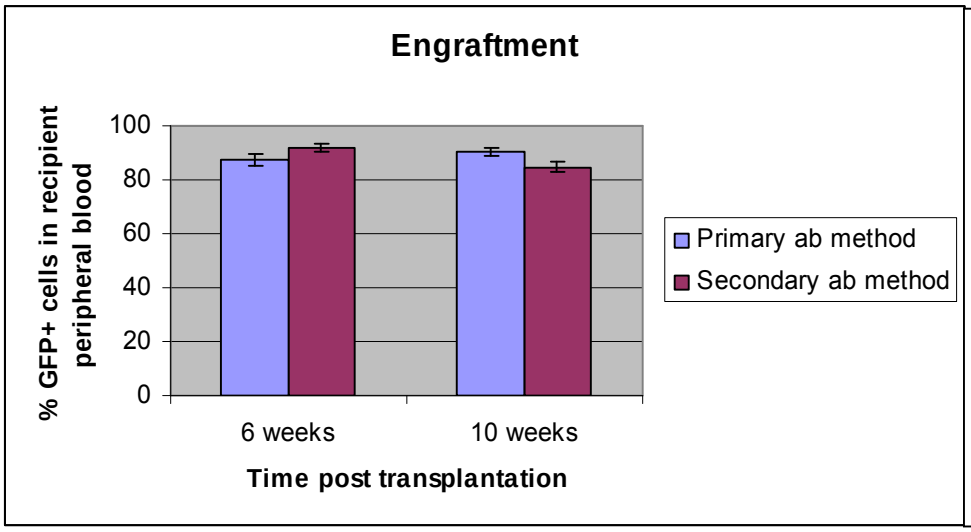

Figure 4: Engraftment expressed as % GFP+ cells in mononuclear cells in the peripheral blood of pre-conditioned recipient mice at 6 weeks and 10 weeks after transplantation. GFP expression was determined by FACs analysis after erythrocytes were removed by osmotic lysis.

To assess engraftment of GFP-expressing HSCs derived from transgenic mice into myelosuppressed recipient mice and assess the short-term (8 weeks), mid-term (6 months) and long-term (1 year) engraftment in the skeletal marrow and non-skeletal sites, we injected 12 pre-conditioned (500cGY irradiation) W41/W41 mice via retroorbital injection with 500,000 Sca-1+ cells isolated from GFP-expressing transgenic donor mice. Peripheral blood from the recipient mice was collected at 12, 24, 36 and 52 weeks post-transplant via tail vein bleed and assayed by FACs for the presence of GFP^+ donor cells. As the site of hematopoietic regeneration, peripheral blood was used to assess donor cell engraftment in the skeletal marrow. Results of this experiment are displayed in Figure 5. All 12 mice were engrafted (100% success) at a high level of chimerism (range 88.8 – 98.5% donor cells at 12 weeks). This high level of engraftment was also observed at all later time points. These data show that with our transplant model, we are able to achieve high, stable engraftment for up to 52 weeks.

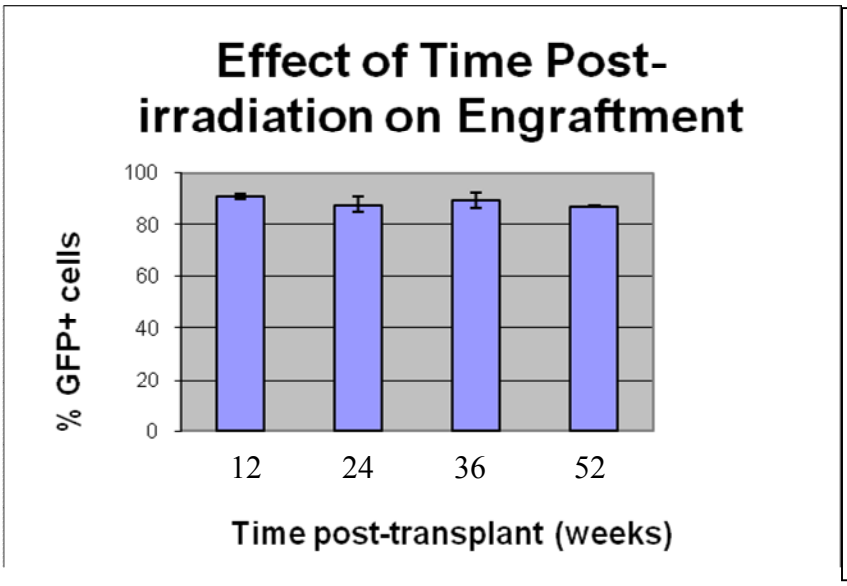

Figure 5: Mean % GFP-positive cells in host mice peripheral blood. Recipient mice were preconditioned by sub lethal irradiation prior to transplantation with 1 x 10^6 Sca-1^+ cells from TgN-GFP donors. At the indicated time points, 12, 24, 36 and 52 weeks post transplantation peripheral blood was collected and assayed for % GFP cells by flow cytometry.

Objective 1b: Assess the pluripotent ability of the engrafted donor cells to produce mature hematopoietic lineages (T-cell, B-cell, neutrophil/granulocyte/monocyte and erythroid) by using lineage-specific immunostaining and FACs analysis of the recipients' peripheral blood. To assess the pluripotent ability of the engrafted donor cells to produce mature hematopoietic lineages we performed experiments using lineage-specific immunostaining and FACs analysis of the recipients' peripheral blood. For these experiments, whole bone marrow cells from TgN (GFP+) mice were harvested by flushing tibiae and femurs with PBS using a 26g needle and syringe. Erythrocytes were removed by osmotic lysis using a solution of 155 mM NH_4Cl, 10mM $KHCO_3$ and 110μM Na_2EDTA, followed by rinsing with PBS. After osmotic depletion of erythrocytes (RBC-lyzed), the cell preparation was enriched for Sca-1 cells by incubating the cells with Sca-1 specific antibody-magnetic microbead conjugates. The mixture was then applied to an automated magnetic separation column (AutoMacs™) according to manufacturer instructions. This procedure resulted in 19-fold enrichment in Sca-1+ cells. The enriched cells were transplanted into sublethally irradiated recipient W41/W41 mice. At 5 months post transplantation, recipient peripheral blood was collected and erythrocytes were removed by osmotic lysis. The mononuclear fraction was assessed by immunostaining for expression of hematopoietic lineage surface markers and measured by FACs analysis. For this analysis, PE-fluorochrome conjugated antibodies specific for hematopoietic lineage were incubated for 30 minutes in separate tubes with the mononuclear cell fraction from each recipient mice. For T-lymphocytes (T-cells) lineage, a mixture of CD3-, CD4e-, and CD8a-specific antibodies was used. For granulocytes/monocytes/macrophages, a mixture of Mac-1- and Gr-1-specific

antibodies was used. For B-lymphocytes (B-cells), a B220-specific antibody was use and for erythroid lineage cells, a Ter-119-specific antibody was used. After incubation the cells were rinsed once and resuspended in PBS and % PE positive cells were assessed by FACs analysis. Parallel tubes were processed using PE-conjugated isotype non-specific antibodies and FACs results were adjusted to account for non-specific binding. In addition, the total engraftment (%GFP positive cells) was assessed. Table 3 shows the mean ± SD for each cell lineage type in mice transplanted with Sca-1+ cells 5 months after transplantation. Cells that were PE+ and GFP+ were of donor origin, while cells that were PE+ but GFP– were considered of recipient host origin. No significant difference in contribution of T-lymphocyte lineage was observed between host (14.7%) and donor (11.8%) origin. In contrast, donor cells contributed a larger percentage than host cells to the macrophage-monocyte-neutrophil lineage (22.9 vs. 6.9%; $p < 0.001$) and B lymphocytes (22.9 vs. 6.9%; $p < 0.01$). The erythroid hematopoietic compartment was made up exclusively of cells of donor origin. These results are comparable with the relative distribution of cells of hematopoietic lineage in peripheral blood of control mice reported by Morel et al. (Hematologic recovery in mice transplanted with bone marrow stem cells expressing anti-human immunodeficiency virus genes. (1) Morel reported for control mice: Gr1+ (granulocytes) ~17% , Mac1+ (macrophages) ~26%,B220 (b-cells) ~ 55% and CD3+ (t-cells ~22%) Thus, the results indicate that our Sca-1+ cell transplantation strategy leads to multilineage hematopoietic cell engraftment.

TABLE 3

	Total % PE^+ mean (st.dev.)	% PE^+ & GFP^- mean (st. dev.)	% PE^+ & GFP^+ mean (st.dev.)
T-cells	19.4 (5.8)	14.7 (3.0)	11.8 (4.4) ^{ns}
Mac/Mono/Gr	32.2 (25.7)	6.9 (3.5)	22.9 (5.8) **
B-cells	21.4 (6.7)	11.6 (5.2)	22.9 (7.2) *
Erythroid	4.8 (3.8)	Non-detectable	5.4 (2.8)

Independent t-test comparisons of % PE^+ & GFP^- (host) vs. % PE^+ & GFP^+ (donor): NS = non-significant, * $p< 0.01$, ** $p<0.001$

Table 3: Independent t-test comparisons of % PE^+ & GFP^- (host) vs. % PE^+ & GFP^+ (donor): NS = non-significant, * $p< 0.01$, ** $p<0.001$, St. Dev. = Standard Deviation of Mean. Results are shown as mean ± SD. For this analysis, W41/W41 mice were transplanted with GFP-expressing Sca-1 cells isolated from TgN-GFP mice. Five months after transplantation, erythrocyte-lyzed cells from recipient mice were incubated with PE-conjugated antibodies specific to various hematopoietic lineages: T lymphocytes (T-cells), macrophages, monocytes and granulocytes (Mac/Mono/Gr), B lymphocytes (B-cells) and erythroid lineage cells. The percentage of each hematopoietic cell lineage in peripheral cells was determined with a FACSCalibur System. Cells positive for PE but negative for GFP were considered of recipient host origin, while cells positive for PE and positive for GFP were considered of donor.

Objective 1c: Detection of donor cells in non-skeletal tissues will be accomplished by frozen sectioning of the heart, lungs, liver and spleen of the recipients and fluorescent microscopic observation. The engraftment of donor Sca-1^+ cells in the skeletal marrow and in non-skeletal tissues was assessed by histological examination of tissues in control mice and mice transplanted with GFP-expressing Sca-1^+ cells. Six months and 24 months after transplantation, mice (N = 6 at each time point) were euthanized and their peripheral blood (mononuclear cells (MNCs), femurs, spleens, hearts, livers and lungs were removed. Several 8-μm thick longitudinal frozen sections of each organ were prepared by cryostat and visualized by fluorescent microscopy. The figures below (Figures 6 – 12) show representative frozen sections under bright field (left

panels) and fluorescent (right panels) microscopy for peripheral blood, bone, spleen, liver, heart, lungs and kidney, respectively. GFP-positive cells were observed in the peripheral blood and in the marrow space of the femurs of mice transplanted with the GFP-expressing cells, as numerous small, bright, GFP-expressing cells were observed under the fluorescent filter. No such cells were observed in the blood or femurs of control mice. In most of the non-skeletal tissues (liver, lungs, kidneys) few or no GFP-expressing cells were observed. In the rare cases that GFP-expressing cells were observed in the non-skeletal tissues of GFP-transplanted mice, the green donor cells were observed to be part of the hematological tissue compartment rather than the parenchymal cardiac tissue.

Frozen sectioning of bone tissue revealed severe autofluorscence from the surface of the bony tissues in both control and GFP-transplanted mice. Due to this technical difficulty valid comparisons could not be made. Therefore, FACs analysis of the bone marrow of the GFP-transplanted mice was performed. At the 6 month and 24 month endpoints, 30-50% of the bone marrow cells in the recipients were GFP+, indicating that Sca-1+ cells of donor origin had homed and established long term (24 months) engraftment in the bone marrow cavity of the recipients. Similarly, increased GFP fluorescence was observed in the spleens of GFP+ cell transplanted recipients compared to non-transplanted control mice. These data suggest that intravenously injected donor cells home and engraft within the spleen and represent a potential for unwanted side effects. However, recent studies have demonstrated that the degree of spleen engraftment after transplantation can be vastly lowered by infusing cells from donors of an age different than that of the recipient (2). Nevertheless, our results indicate that future studies evaluating the safety of hematopoietic stem cell-delivered gene therapies will require the assessment of effects on the spleen as well as the targeted tissues.

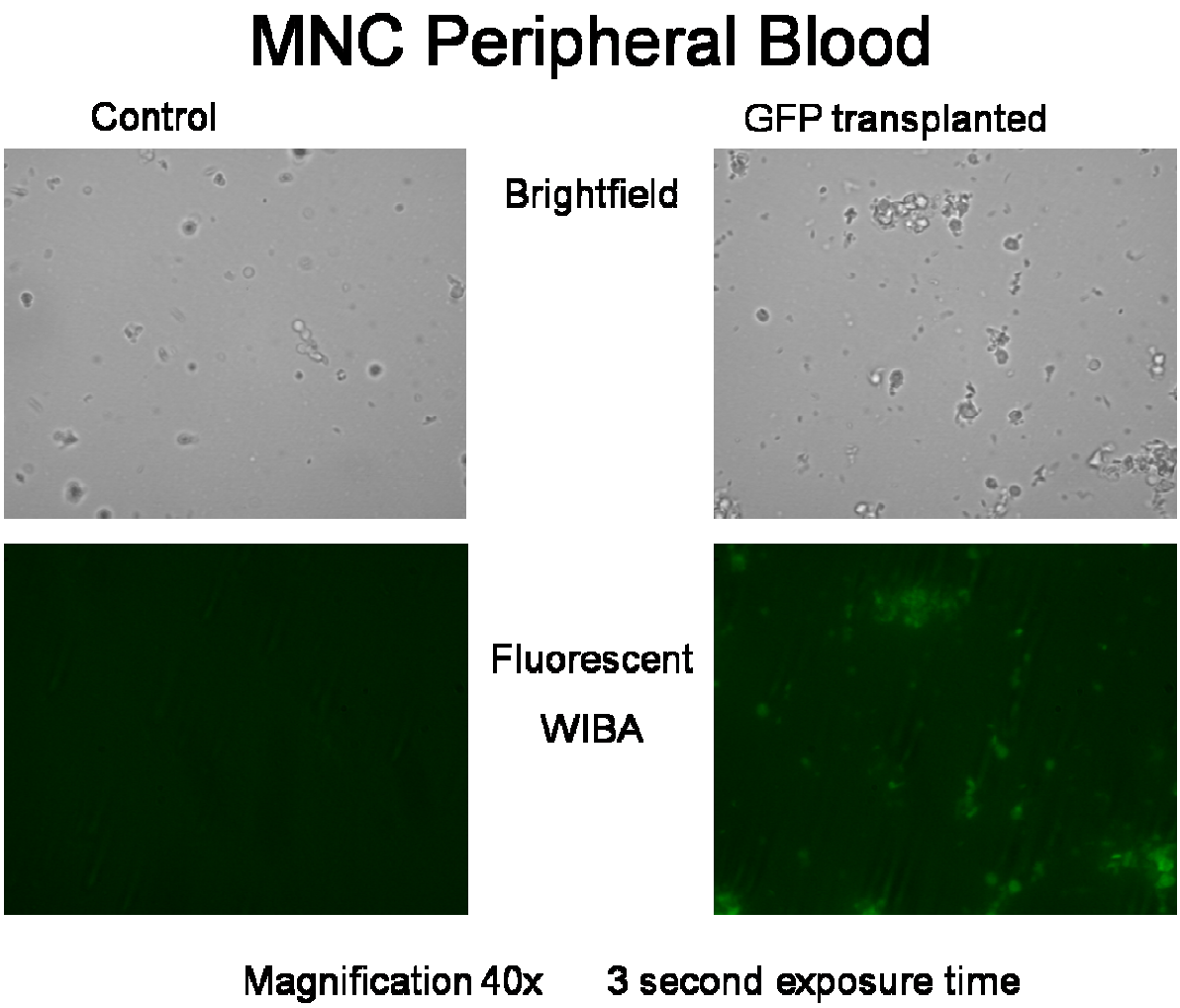

Figure 6: Representative frozen sections under bright field (upper panels) and fluorescent (lower panels) microscopy of mononuclear cells (MNC) in the peripheral blood of control mice (left panels) and recipient mice transplanted with GFP-expressing cells (right panels).

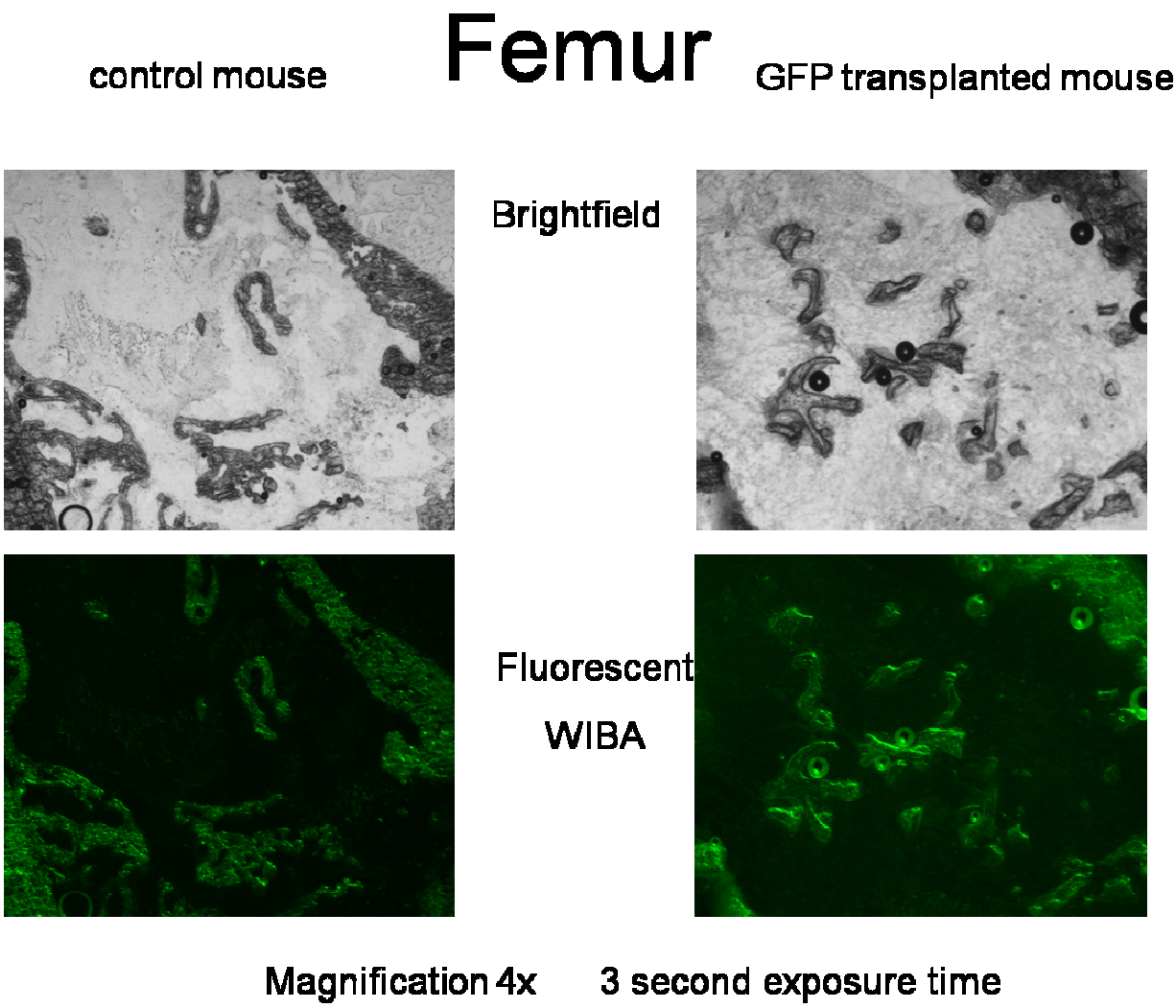

Figure 7: Representative frozen sections under bright field (upper panels) and fluorescent (lower panels) microscopy of femurs of control mice (left panels) and recipient mice transplanted with GFP-expressing cells (right panels).

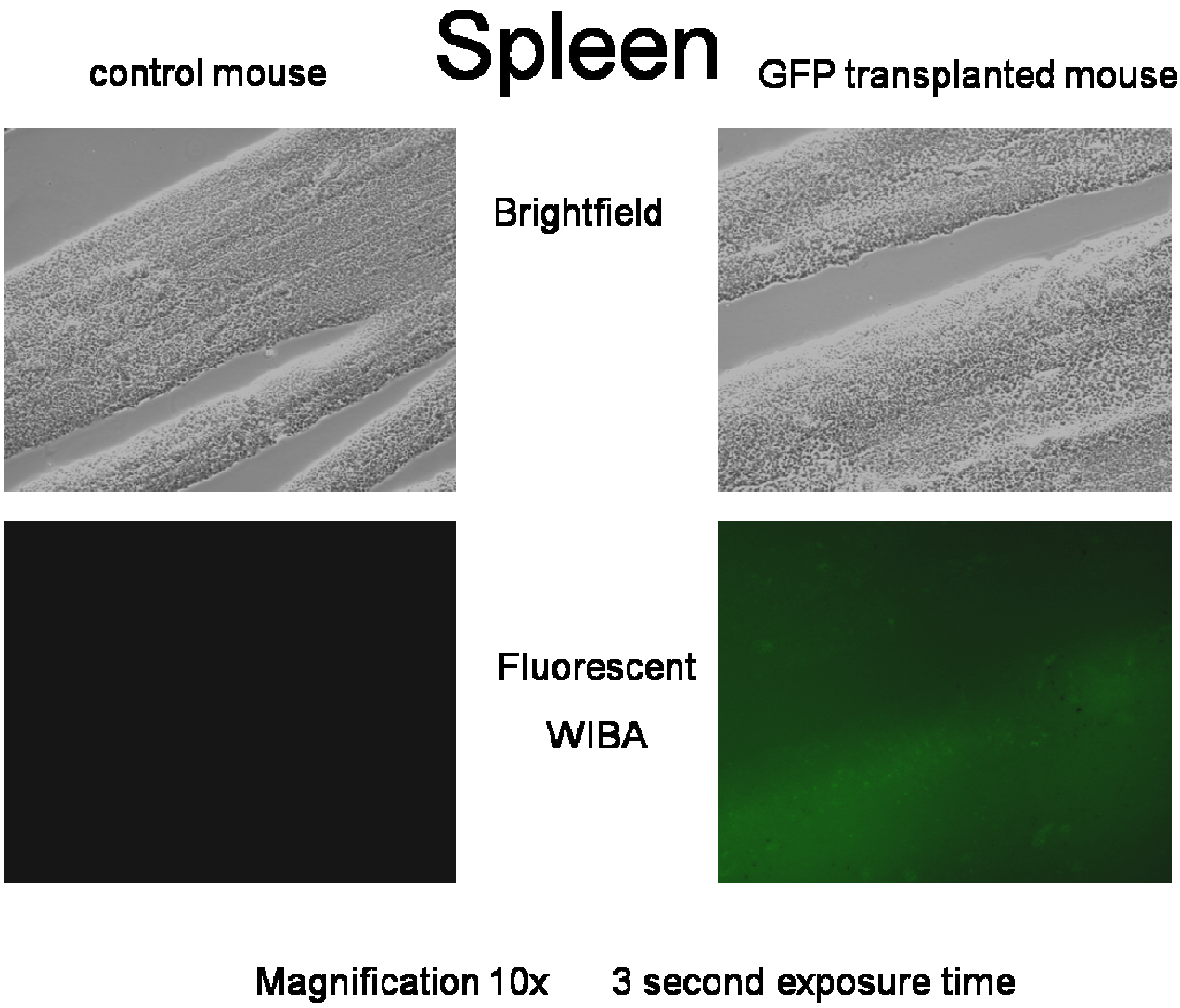

Figure 8: Representative frozen sections under bright field (upper panels) and fluorescent (lower panels) microscopy of the spleens of control mice (left panels) and recipient mice transplanted with GFP-expressing cells (right panels).

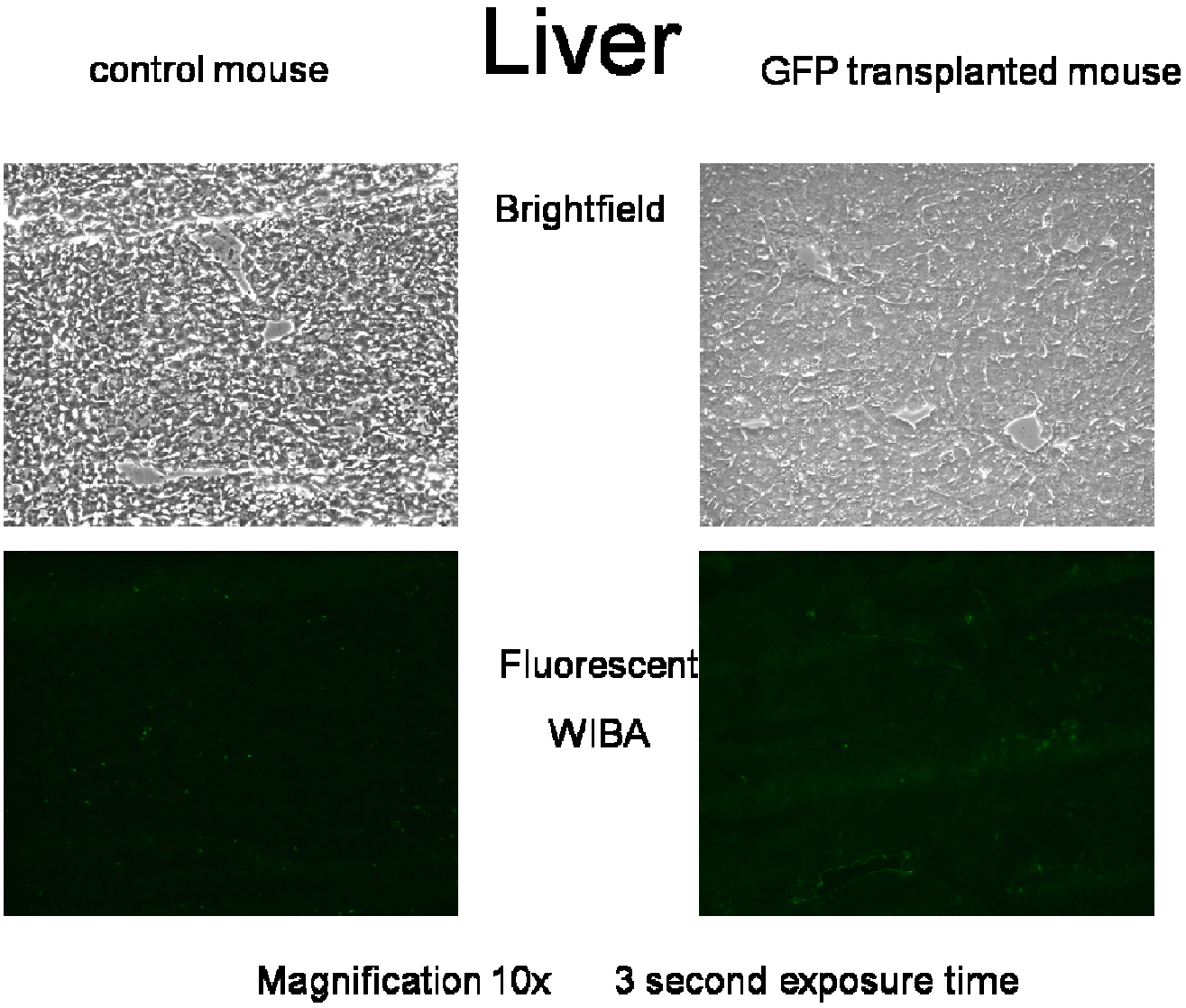

Figure 9: Representative frozen sections under bright field (upper panels) and fluorescent (lower panels) microscopy of the livers of control mice (left panels) and recipient mice transplanted with GFP-expressing cells (right panels).

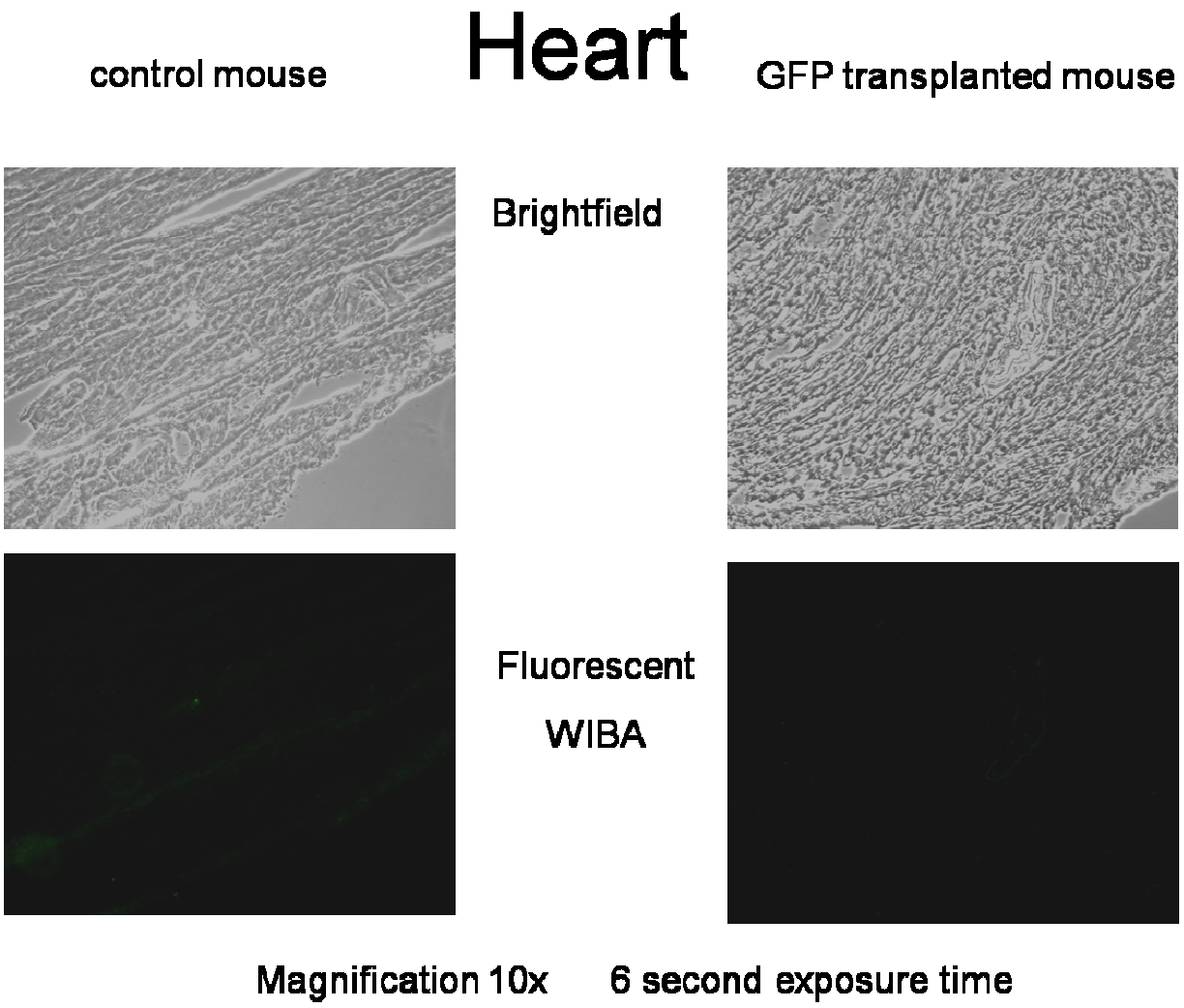

Figure 10: Representative frozen sections under bright field (upper panels) and fluorescent (lower panels) microscopy of the hearts of control mice (left panels) and recipient mice transplanted with GFP-expressing cells (right panels).

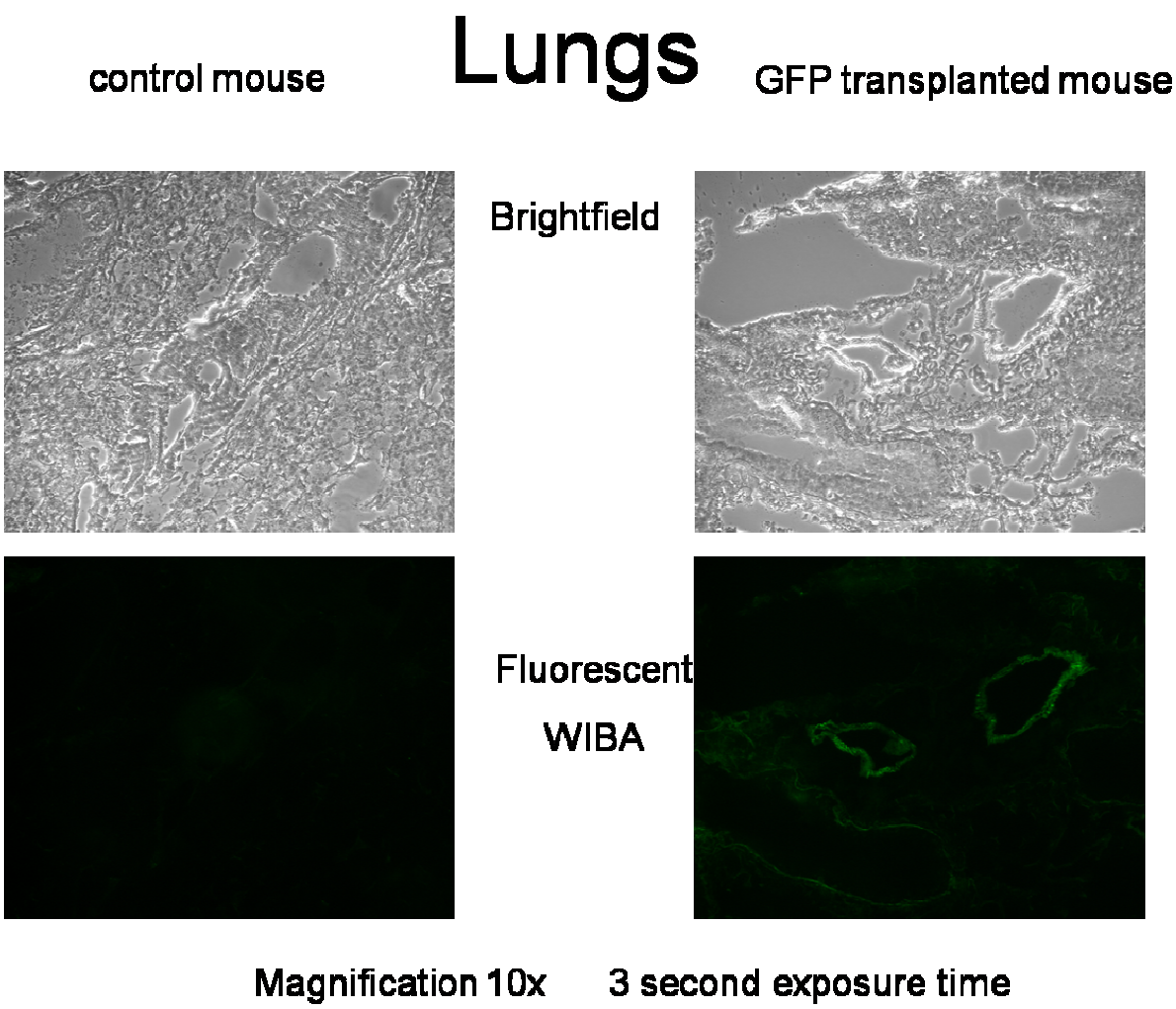

Figure 11: Representative frozen sections under bright field (upper panels) and fluorescent (lower panels) microscopy of the lungs of control mice (left panels) and recipient mice transplanted with GFP-expressing cells (right panels).

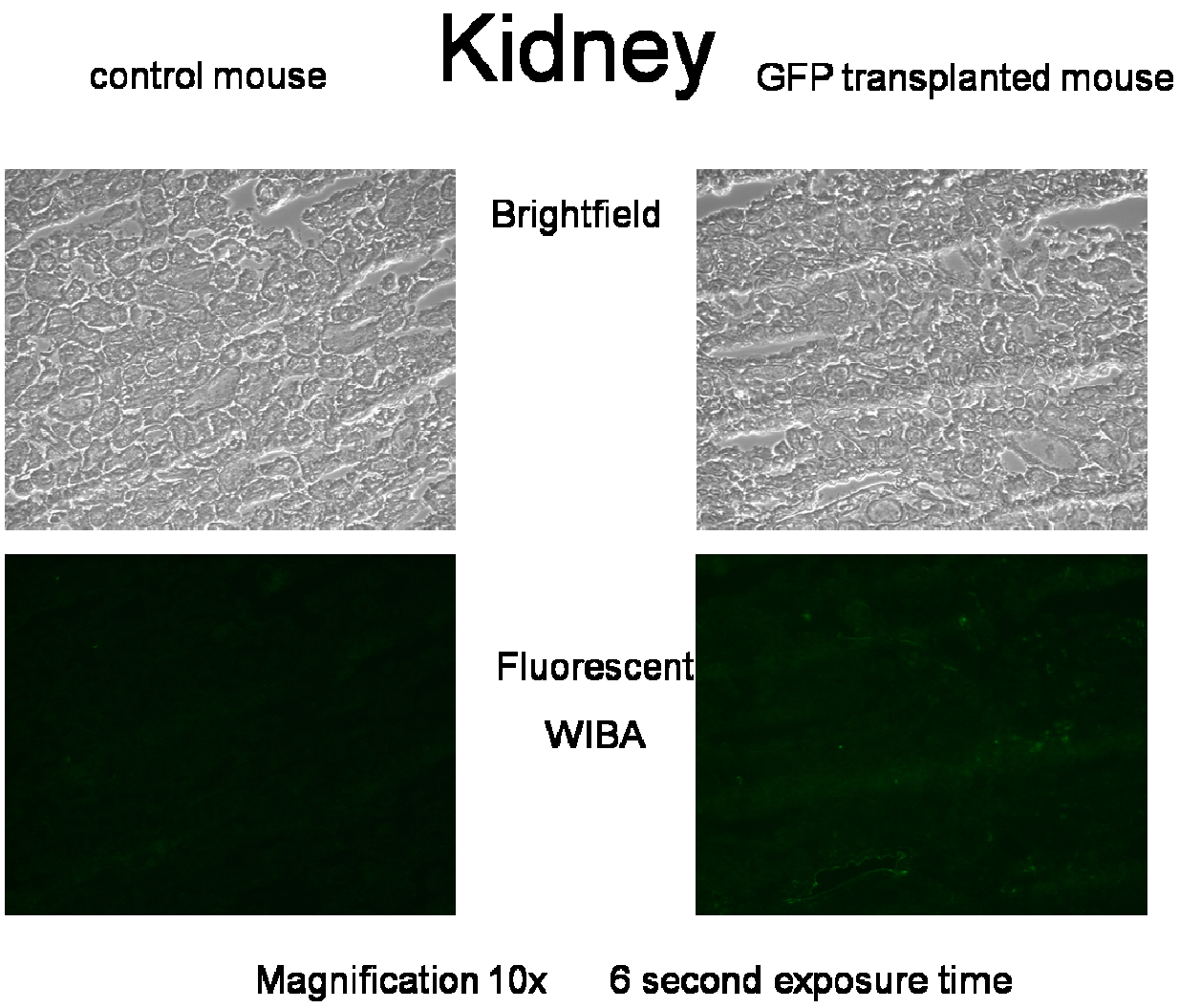

Figure 12: Representative frozen sections under bright field (upper panels) and fluorescent (lower panels) microscopy of the kidneys of control mice (left panels) and recipient mice transplanted with GFP-expressing cells (right panels).

<u>Technical Objective 2</u>: To assess and quantitate the short-term and long-term bone formation achieved in mice following transplantation with HSCs transduced to express a growth factor gene.
Objective 2a: To transduce HSC-enriched cells with an HIV-based vector expressing the BMP 2/4 gene under the control of the CMV promoter. Transgene expression will be assessed using immunohistochemical staining of the transduced cell cultures and Western blot analysis of the conditioned media.
To assess and quantitate the short-term and long-term bone formation achieved in mice following transplantation with HSCs transduced to express a growth factor gene, we performed *in vivo* transplantation studies using Sca-1+ cells transduced to overexpress an anabolic bone agent. We selected a protein known to stimulate bone formation, human bone morphogenetic protein 4. For these studies, the overexpression of BMP4 was accomplished using a BMP2/4 hybrid gene, in which the large portion of the BMP4 signal sequence was replaced with the complete BMP2 signal sequence to enhance secretion of mature BMP4 protein (3) Briefly,

Whole bone marrow cells were harvested from wild type C57BL6 mice and enriched for HSCs by selection of Sca-1^+ cells. The cells were transduced with an HIV-based viral vector expressing either the GFP marker gene or a modified human BMP4 therapeutic gene. The modified BMP vector (BMP2/4) was created by replacing the propeptide of the BMP4 gene with the BMP2 propeptide. As a result of this substitution, high expression levels of BMP4 (0.5 to 1μg/10^6cells/24 hours) are obtained. For the transduction procedure, the cells were cultured in 6-well retronectin-coated plates at a density of 4 million cells/well in IMDM media containing fetal bovine serum, human Flt-3 ligand, murine stem cell factor, murine IL-6, murine IL-1α and murine IL-3 and 100uM additional dNTPs. After 24 hours, unconcentrated viral stocks (MOI = 15) were applied to the cells. After 8 hours and 16 hours, fresh media, cytokines and viral stocks were reapplied. Five days after transduction, aliquots of 500,000 cells were extracted and assayed for BMP4 by SDS-PAGE and Western blot analysis. Blots were probed using a primary anti-BMP4: monoclonal antibody (host mouse) at a 1:1000 dilution and a secondary anti-Mouse IgG-HRP antibody (host goat) at a 1:10,000 dilution. Figures 13 and 14 are photographs of the blots of the GFP- transduced and BMP2/4-transduced cell preparations, respectively. In Figure 14 (right panel), a distinct band corresponding to BMP4 (24kD) is evident in Lane 1 (BMP-transduced cells), while no such band is observed in the GFP-transduced control cells (Figure 13, Lane 3) (left panel).

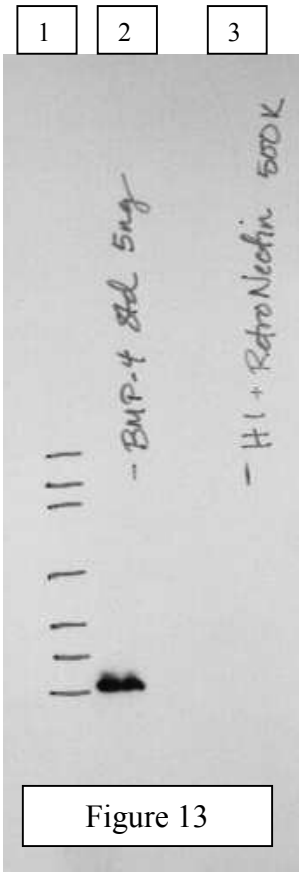

Figure 13

Figure13: (Left) Western blot for BMP4 protein in extracts of control (GFP-transduced) cells. Sca-1^+ cells were transduced with an HIV-based viral vector expressing GFP. Blots were probed using a primary anti-BMP-4: monoclonal antibody and a secondary anti-Mouse IgG-HRP antibody.
Lane 1: Molecular weight standard,
Lane 2: BMP4 protein standard (5ug)
Lane 3: 500,000 Sca-1^+ cells transduced with the GFP-expression HIV-based vector

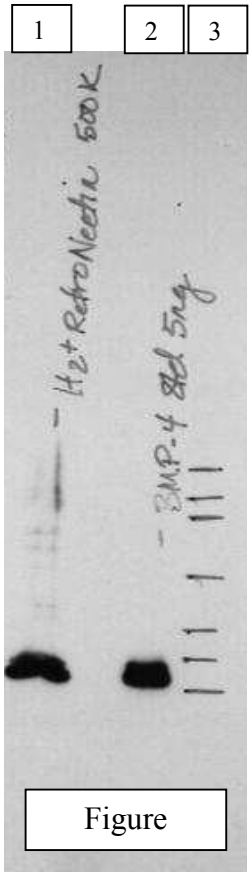

Figure

Figure 14: Western blot for BMP4 protein in extracts of BMP4-transduced) cells. Sca-1^+ cells were transduced with an HIV-based viral vector expressing BMP4. Blots were probed using a primary anti-BMP-4: monoclonal antibody and a secondary anti-Mouse IgG-HRP antibody
Lane 1: Molecular weight standard,
Lane 2: BMP4 protein standard (5ug)
Lane 3: 500,000 Sca-1-positive cells transduced with the BMP-expression HIV-based vector

To further examine BMP2/4 transgene expression, we attempted to develop a BMP2/4 immunohistochemical staining method using a two-antibody system. Bone marrow cells were collected from a mouse transplanted with Sca-1 cells transduced with the HIV-based BMP2/4 viral vector and from a control (non-transplanted) mouse. The bone marrow samples were fixed with formalin, rinsed 3 times with PBS and then smeared on microscope slides. The slides were baked for 45 minutes in a dry oven and stored overnight at 4°C. The cells were then incubated with a primary anti-BMP-4 antibody (monoclonal, 1:200 dilution) for 45 minutes. After washing, the slides were incubated with a biotinylated anti-mouse IgG antibody (1:100 dilution) for 30 minutes.

After additional washing, the slides were incubated with Strept-avidin-HRP (1:200 dilution) for 15 minutes, washed and incubated with DAB-H_2O_2 for 5 minutes. The slides were counterstained with hematoxylin for 1 minute, dehydrated with ethanol and cleared with 3 changes of xylene. Microscopic visualization of the control mouse and the transplanted mouse showed similar results (data not shown). Numerous brown stained cells were visible on both slides indicating an unacceptable degree of background staining. This background staining is likely due to endogenous production of BMP4 and cross-reactivity with the human BMP4 antibody. From this data we concluded that immunohistochemical staining would not be an appropriate means to assess expression of the BMP2/4 transgene.

As a result of the difficulty we experienced in developing an immunohistochemical assay for BMP4 detection, we adapted an immunostaining protocol developed in a related project as an alternative method. Preliminary studies were performed using D1 cells. The D1 cell line is a bone marrow-derived mesenchymal stem cell line that has been shown to localize to bone marrow after intravenous injections. These cells have been generously provided to us by Dr. Gary Balian's laboratory and are relatively easy to maintain in culture. D1 cells were transduced with the hybrid BMP2/4 vector. Cells were cultured in the standard media and plated in 6-well dishes at a density of 4 million cells per well. The cells were transduced by 2 exposures to the viral preparation at a multiplicity of infection (MOI) of 20. Intracellular staining for BMP4 was performed using reagents and antibodies purchased from Santa Cruz Biotechnologies, Inc. ™ BMP2/4 transduced and non-transduced (control) D1 cells were fixed and then rendered permeable. The cells were then blocked with 2% normal donkeys serum and incubated for 30 minutes in either a 1:400 or 1:800 dilution of the primary antibody (anti-BMP4 goat polyclonal IgG). After washing, the cells were incubated for 30 minutes in one of two concentrations (1:800 or 1:1600) of the PE-conjugated secondary antibody (donkey anti-goat IgG $F(ab')_2$). Table 4 shows the results of flow cytometry for PE-positive cells. These results suggest that the best results occurred using either dilution of primary antibody dilution followed by incubation with the secondary antibody 1:1600 dilution.

[primary ab]	[secondary ab]	control cells	BMP4 transduced
1:400	1:800	8	40
1:800	1:800	47	30
1:400	1:1600	5	58
1:800	1:1600	5	54

Table 4: FACs analysis of PE positive BMP4 transduced D1 cells after immunostaining using a 2 antibody system (PE-conjugated).

Objective 2b: To transplant transduced donor cells via tail vein into myelosuppressed recipient mice and evaluate bone formation after 8 weeks, 6 months and 1 year. Bone formation will be evaluated by measuring serum osteocalcin and alkaline phosphatase. Bone density and cortical thickness in the host animals will also be assessed by faxitron X-ray and pQCT analysis

To determine if transplantation of BMP2/4-transduced donor cells into myelosuppressed recipient mice would induce bone formation, we performed in vivo transplantation studies. For these studies, Sca-1^+ cells were isolated and transduced with either the lentiviral-based viral vectors expressing either the GFP or BMP2/4 transgene using the protocol described above. Forty eight hours after transduction, aliquots of 500,000 cells of the cell preparations were injected via tail vein into 24 sub lethally irradiated W^{41}/W^{41} recipient mice (N =12 per group). Additional aliquots of the cells were stained with propridium iodide for measurement of cell survival and GFP expression. Both HIV-virus-transduced cells preparations showed a large % of cell death (81% and 80% for GFP- and BMP4-transduced cells, respectively). Parallel cultures of GFP-transduced cells were assayed by FACs for transduction efficiency two and five days after transduction. Approximately half (51% at 2 days and 49% at 5 days (Figure 15) post-transduction (a) were expressing the GFP transgene. At

various time points (5, 9 and 22 weeks) post transplantation peripheral blood was collected from the two groups (GFP-transduced transplants and BMP2/4-transduced transplants) of recipient mice and engraftment was assessed by measurement of % GFP positive (donor) cells by FACs analysis. In the GFP-transplanted group, 5 mice showed significant engraftment. Figure 15 (b) shows the FACs analysis of one representative mouse transplanted with GFP-transduced cells 9 weeks after transplantation. To confirm engraftment of donor cells

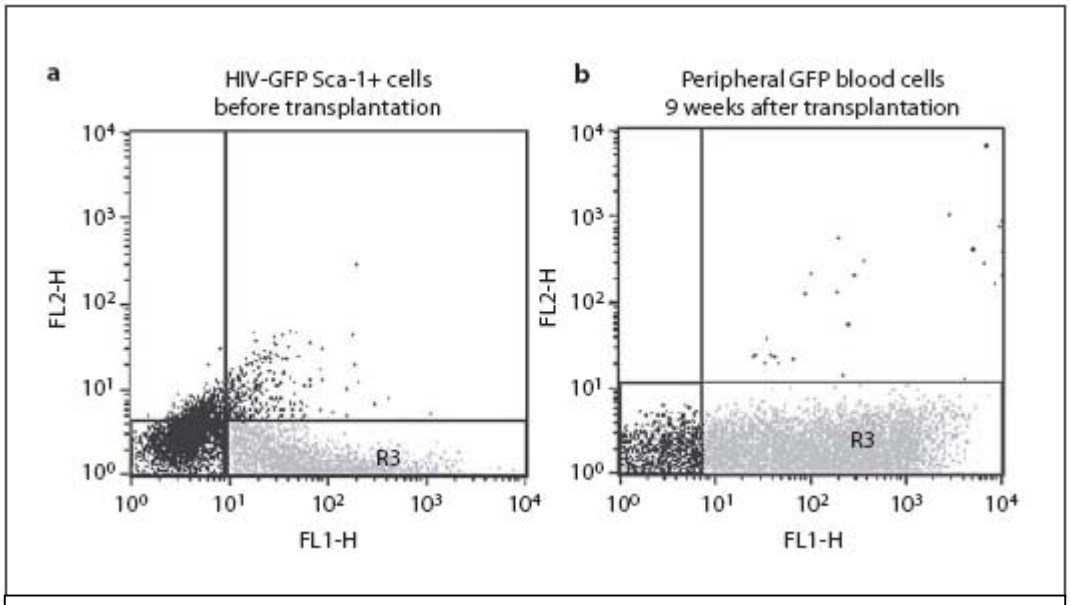

Figure 15. Percentage of GFP-expressing donor cells in C57BL/6J Sca-1+ cells transduced with an HIV-based vector expressing the GFP marker gene 5 days after transduction (a) and in peripheral blood of a representative recipient mouse 9 weeks after transplantation (b). The percentage of GFP+ cells was analyzed by FACS.

overexpressing the transgenes, we measured transgene mRNA expression in mononuclear cells of the blood of recipient mice transplanted with Sca-1+ cells transduced with GFP or BMP2/4 vectors in the blood samples collected at the 9-week post transplantation time point. RNA was isolated from the mononuclear cell fraction and transgene expression was evaluated by real time RT- PCR using primers specific for the two transgenes (GFP and BMP2/4). In addition, GAPDH expression (murine housekeeping gene) was measured as a reference gene. Quantitation was made using standardization with external reference DNA. In the recipient mice receiving GPF-transduced cells, the same 5 mice shown to be engrafted by FACs analysis showed detectable GFP expression (mean GFP:GAPDH ratio 91.9 ± 54.3). No GFP^+ cells were observed in the other GFP-treated mice or in the BMP2/4-treated mice. Results for BMP2/4 expression showed 5 of the 12 mice transplanted with the BMP2/4-transduced cells had significant BMP expression (mean BM2/4:GAPDH ratio 11.5 ± 9.4). These results demonstrated an 8-fold difference in transgene expression between the GFP-positive and BMP-positive results and confirmed that donor cells had been transduced with the transgene, had engrafted and persisted for at least 9 weeks.

Engraftment levels of the recipient mice over time, as assessed by the percentage of GFP+ cells in the peripheral blood of the in the 5 GFP-positive recipient mice, is shown in Figure 16. A slow decline in % GFP positive cells was observed in the mean % GFP^+ cells. Individual analysis of the engrafted mice revealed that this observed declined occurred in all mice except for mouse 7 which showed relatively consistent 80% engraftment at all three time points (data not shown). This decline is possibly the result of transplanting $Sca\text{-}1^+$ cells, a relatively heterogeneous stem cell population. At early engraftment time points, progeny cells from GFP-positive hematopoietic progenitor cells and from GFP-positive hematopoietic stem cells are present.

However, at later time points, as donor progenitor cells differentiate, only the progeny from donor stem cells are evident. Alternatively, this decline could be due to changes in transgene expression over time. These data suggested that of the total 12 mice transplanted with BMP2/4-transduced cells, 5 mice demonstrated transgene expression (as assessed by RT-PCR) at 9 weeks post transplantation. To assess if bone formation was increased, the serum samples collected from tail vein bleedings at 5, 9, 17 and 22 weeks post transplantation was assayed for alkaline phosphatase (AP). AP activities were determined in 0.15M CO_3 buffer (pH 9.3)

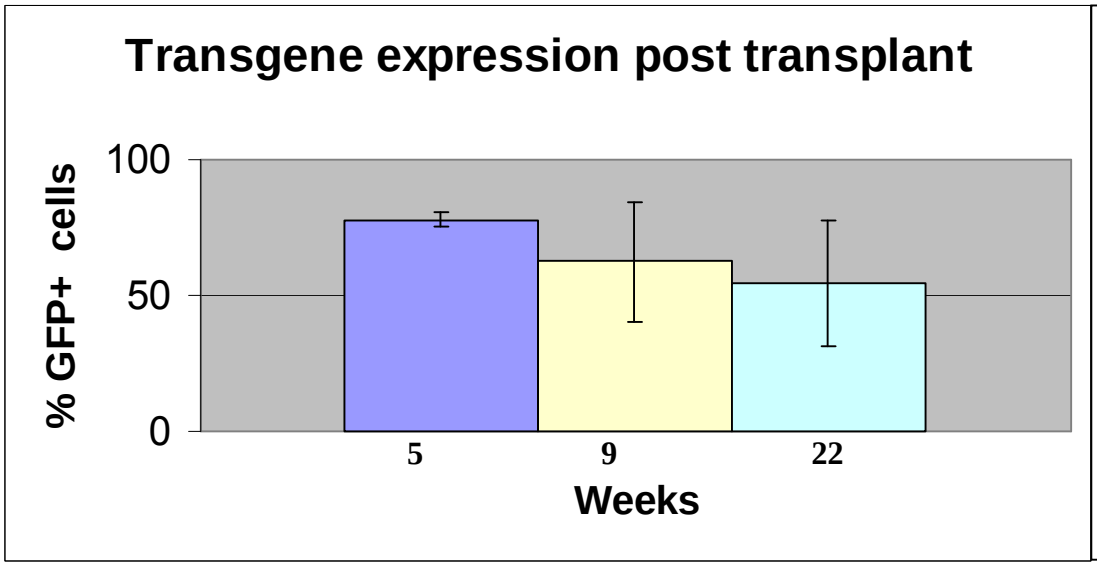

Figure 16: % GFP positive cells determined by flow cytometry at 5, 9 and 22 weeks post transplant in the 5 recipient mice that were successfully transplanted with HIV-GFP transduced Sca-1^+ donor cells.

containing 1mM $MgCl_2$, 10mM p-nitrophenylphosphate (PNPP) and 10mM L-phenylalanine in 96-well microtiter plates and were calculated from the time-dependent increase in absorbance at 410 nm measured with an automatic recording microtiter plate spectrophotometer. Comparisons using Students t-test for independent variables were made between the 5 successfully GFP-engrafted mice (as determined by FACs and confirmed by real time RT-PCR) and the 5 successfully BMP2/4 engrafted mice (as determined by real time RT-PCR). As seen in Table 5, no significant difference in AP activity was observed at any of the time points. Serum osteocalcin was also measured in the 17-week serum samples using a modified mouse osteocalcin ELISA assay. No significant difference in osteocalcin was observed (data not shown).

Treatment	Mean AP (st. dev) 5 weeks	Mean AP (st. dev) 9 weeks	Mean AP (st. dev) 17 weeks
GFP-transduced donor cells	77.1 (12.9)	73.4 (29.6)	65.9 (6.0)
BMP2/4 transduced donor cells	76.5 (8.2)	85.5 (14.8)	72.7 (16.7)

Table 5: Serum alkaline phosphatase (AP) U/L. Values reported are means ± standard deviation of the 5 successfully engrafted mice from each treatment group (mice transplanted with GFP-tranduced donor cells vs. mice transplanted with BMP2/4 transduced donor cells).

At 22 weeks post transplant, the mice were euthanized and femurs and tibiae were dissected out. The femurs were assayed for total bone density (BMD) and cortical BMD by pQCT. BMD was calculated by averaging the two femurs of each mouse from the 5 successfully transplanted mice from each treatment group. No significant difference was detected in mean total BMD between mice engrafted with GFP-transduced donor cells vs. mice engrafted with BMP2/4-transduced donor cells (766.5 ± 31.3 vs. 786.8 ± 44.1, respectively). Similarly, no

significant difference in cortical thickness was observed between the two groups (0.330 ± 0.013 vs. .341 ± 0.022, respectively). Faxitron analysis of the bones was not attempted. No differences were detected using pQCT (a sensitive quantitative analysis), therefore, it is unlikely that differences would be observed using the less sensitive, non-qualitative Faxitron analysis.

Skeletal AP was extracted from the dissected tibiae by incubation in a solution of 0.1% triton x-100 (250uL). AP activity was determined as described above and normalized to total protein using a bicinchonicinic acid colorimetric assay. No significant difference in AP activity/mg protein was observed between the two treatment groups (data not shown). These results suggested that transplantation with BMP2/4-transduced Sca-1^+ cells did not result in significant bone formation.

One possible explanation for the lack of bone formation in treated mice is that engraftment of BMP4-expressing cells may have been low. To examine this possibility, we conducted a similar experiment using donor cells from a transgenically marked mouse. For this experiment, Sca-1^+ cells were isolated from the bone marrow of TgN donor mice. The TgN mouse strain is a transgenic strain that expresses the GFP marker gene. Use of this strain provided an endogenous marker by which we could track engraftment. The GFP-expressing Sca-1^+ cells were transduced with our HIV-based BMP2/4 viral vector as described above. Half of the cells were mock transduced (cultured in parallel but not exposed to viral vector) to serve as controls. Two days after transduction, the two cell preparations were injected via tail vein into 36 sub-lethally irradiated W^{41}/W^{41} recipients (N=18 per treatment group). Engraftment was assessed by FACs analysis for GFP-positive cells at 8, 24, 33, 37 and 40 weeks. As in the previous experiment, not all mice were successfully engrafted. At 8 weeks, only 8 of 18 mice transplanted with mock-transduced cells had evidence of engraftment. Of these 8 mice, 1 mouse showed moderate engraftment (37.4% GFP^+ cells), whereas the remaining 7 showed high engraftment (range 71.9 – 90.7% GFP^+ cells). One of the highly engrafted mice from this group unexpectedly died at 9

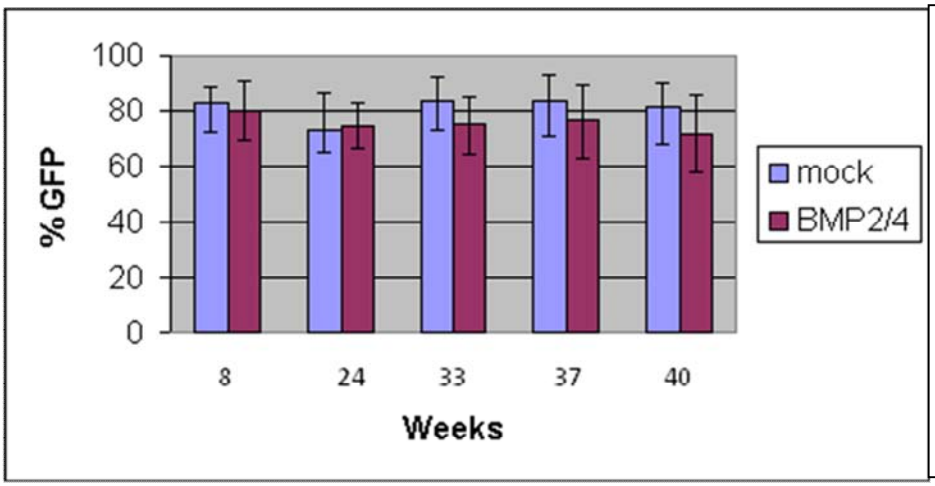

Figure 17: % GFP positive cells as determined by flow cytometry at 8, 24, 33, 37 and 40 weeks post transplant in recipient mice that were transplanted with GFP-expressing Sca-1^+ cells that were either mock – transduced or BMP2/4 transduced.

weeks of unknown causes. At the same time point, in the group transplanted with BMP2/4-transduced cells, only 9 of 18 mice were engrafted with donor cells. Two of these mice showed low engraftment (17.7, 15.6% GFP^+ cells) while the remaining 7 were highly engrafted (63.5 – 90.4% GFP^+ cells). Only the 13 highly engrafted mice (6 from the mock group and 7 from the BMP2/4 group) are included in the subsequent analysis for this report. As seen in Figure 17, stable engraftment was achieved for up to 40 weeks after transplantation. No significant difference was noted between the mock-transduced and BMP2/4-transduced groups at any time point.

The 13 successfully engrafted mice (6 mock-transduced and 7 BMP2/4-transduced) were analyzed for bone formation by measurement of serum AP at 10 weeks, 26 weeks and 40 weeks post transplant. AP activities were assayed as described above and the results are listed in Table 6. As in the previous experiment, no significant difference was observed in serum AP activities between mice transplanted with mock-transduced cells and mice transplanted with BMP2/4-transduced cells.

Treatment	Mean AP (st. dev) 10 weeks	Mean AP (st. dev) 26 weeks
Mock-transduced donor cells	92.7 (22.0)	69.3 (30.7)
BMP2/4 transduced donor cells	73.3 (30.7)	55.7 (8.7)

Table 6: Serum alkaline phosphatase (AP) U/L. Values reported are means ± standard deviation of the successfully engrafted mice from each treatment group (mice transplanted with mock-tranduced cells vs. mice transplanted with BMP2/4 transduced cells).

At 40 weeks post transplant, the mice were euthanized and femurs and tibiae were dissected out. The right femurs were assayed for total, trabecular and cortical BMD by pQCT. BMD was calculated by averaging values from the successfully transplanted mice from each treatment group. As before, no significant difference was observed in mean total BMD between control mice and mice transplanted with BMP2/4-transduced (770.3 ± 33.8 vs. 783.4 ± 47.0 respectively). Similarly, no significant difference in cortical BMD was observed between the two groups (0.323 ± 0.022 vs. 0.337 ± 0.024, respectively). AP activity in triton extracts of the left tibiae and 2 tibiae was assayed as described above. No significant difference in AP activity/mg bone weight was observed between the two treatment groups (data not shown). These results, and those of the previous transplant experiment, indicate that transplantation with BMP2/4-transduced Sca-1^+ cells does not result in significant bone formation.

There are several potential explanations for why cells transduced with BMP2/4 did not elicit the expected bone formation response. It is possible that silencing of the transgene occurred over time after engraftment. This is supported by the data presented in Figure 16, where a decrease in cells expressing the transgene GFP marker was observed. Studies conducted to explore this possibility are described below under Revised Technical Objective (below) It is also possible that the transgene product (BMP4) is exerting an autocrine effect on HSC biology. For example, BMP4 may cause HSCs to undergo differentiation and release into the blood, resulting in a reduction in the number of high expressing transduced cells in the marrow cavity. Alternatively, BMP4 may be toxic to HSCs, causing a reduction in cell number of the high BMP4-expressing cells.

Analyses from this experiment and the previous experiment suggested that we were able to achieve good engraftment efficiencies (60-90%) with our transplant methodology. However, results from both experiments, indicate sub-optimal transplant success (40-50%) with engraftment efficiencies ranging from 5% to 70%. We believe this low engraftment success is due to the use of the tail vein method. Because a lower number of mice achieved engraftment, the statistical power to detect a possible BMP4 effect was reduced. Therefore, we sought to improve our technical protocol in order to improve our transplantation success rate. An alternative method of donor cell administration to recipient mice is by retroorbital injection. Retroorbital delivery is less technically demanding and the results are less variable than in the tail vein injection approach. Previous direct comparison between tail vein injection and retroorbital injection showed no differences in organ distribution or blood concentration of injected material (4), suggesting that retroorbital injection could be a reliable delivery method of donor cells. In our studies, retroorbital injection resulted in greatly enhanced engraftment success (from an original rate of 37% to nearly 100%), higher engraftment levels, and a significant reduction in variation compared with the tail vein method. The retroorbital injection method also led to engraftment in every injected mouse and a 3- to 4-fold reduction in intra-assay variations compared with the tail vein method (5).(Since the power of an experiment is directly proportional to sample size and magnitude of the difference to be detected and inversely proportional to the inherent variability of the observations (6), the reduction in intra-assay variability with retroorbital injection generates an increase in experimental power and the ability to detect small differences and/or decreased sample size required. The retroorbital injection method is relatively safe to the host, as none of the mice injected by retroorbital injection have suffered adverse effects to their eyes and, in most experiments, no animal was lost due to anesthesia or other complication. Thus, after these first initial studies, we began using retroorbital injections for all transplantations.

Using the improved transplantation protocol (i.e. use of the retroorbital injection method), we repeated previous experiments. Sca-1^+ cells from TgN donor mice were transduced with either the b-galactosidase marker gene (control) or the BMP2/4 gene. At week 11 post transplant, the mean engraftment (%GFP^+ donor cells in peripheral mononuclear blood cells) was 77.9 ± 7.4 in the β-gal group and 75.2 ± 11.0 in the BMP2/4 group. No significant difference by between the two groups was observed. Blood samples at various time points (6, 8, 10, 14, 20, 22 and 24 weeks post-transplantation) were collected and analyzed for serum bone formation markers. As seen in Figure 18, no significant differences in engraftment levels between the groups was observed at any time point.

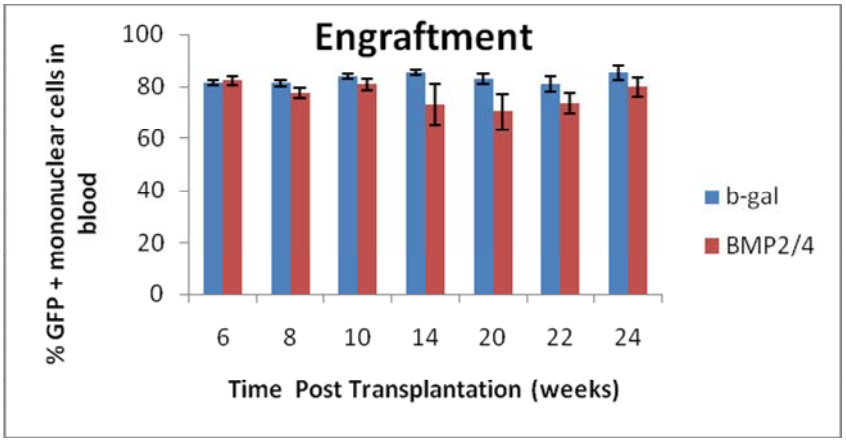

Figure 18. Engraftment of Sca-1+ cells transduced with lentiviral-based vectors (b-gal or BMP2/4) in W^{41}/W^{41} recipient mice preconditioned by sublethal irradiation. Engraftment was reflected by the percentage of GFP-positive mononuclear cells in peripheral blood at the indicated time points post-transplantation. Results are shown as the mean ± SEM with n = 6. No significant difference was observed between the two groups at any time point

To assess for bone formation, serum skeletal alkaline phosphatase (AP), a bone formation biochemical indicator was measured using a Hitachi 912 Clinical Chemistry analyzer. Serum AP levels were significantly elevated in the BMP2/4-treated group (53.7 ± 4.4 U/ml) compared to the control group (46.2 ± 7.4 U/ml) ($p < 0.05$). At 26 weeks, post transplantation, the recipient mice were euthanized and femurs were harvested. Bone formation parameters (total bone mineral density (BMD), trabecular BMD, cortical BMD, cortical thickness, endosteal circumference or periosteal circumference) of femurs from the mice were also determined (Table7).

	total BMD	trabecular BMD	Cortical BMD	Cortical thickness	Periosteal Circumference	Endosteal Circumference
b-gal	784.3 (16.7)	256.8 (15.2)	1093.7 (26.6)	0.344 (0.007)	5.59 (0.106)	3.44 (0.076)
BMP	807.0 (19.0)	324.0 (93.1)	1114.3 (44.2)	0.321 (0.12)	5.38 (0.213)	3.36 (0.170)
p-value	0.67	0.60	0.68	0.39	0.56	0.90

Table 7: pQCT measurements of bone mineral density (BMD) and bone size parameters of recipient mice transplanted with HIV-BMP2/4-transduced Sca-1+ cells compared to those of recipient mice transplanted with HIV-β-gal-transduced Sca-1+ cells at 26-weeks post-transplantation. Values reported as mean (standard error of mean).

Although total BMD, trabecular BMD and cortical BMD values were increased in the BMP2/4-tranplanted mice, the differences did not reach statistical significance. These data confirmed our previous work and therefore, we concluded that transplantation of Sca-1+ cells transduced to express BMP4 protein did not induce significant bone formation as had been expected.

Since transplantation of BMP4 overexpressing Sca-1+ cells did not increase bone formation as expected, we next examined an alternate bone-forming agent, human growth hormone (hGH) in our model. For these studies, we transduced Sca-1+ cells from TgN (GFP-expressing) donor mice with lentiviral-based vectors overexpressing either the b-gal (marker gene), hGH or BMP2/4 transgene. Forty-eight hours after transduction, aliquots of 500,000 cells of each preparation were transplanted via retro orbital injection into sublethally irradiated W^{41}/W^{41} recipient mice (N =8 per group). Peripheral blood was collected from the recipient mice at 6, 8, 11, 14, 16 and 24 weeks post transplantation. Mononuclear cells were isolated by osmotic lysis and the % of GFP+ cells was determined by FACs analysis. Statistical analysis by one-way ANOVA, showed no significant differences in % GFP+ cells between the groups at any time point (Figure 19).

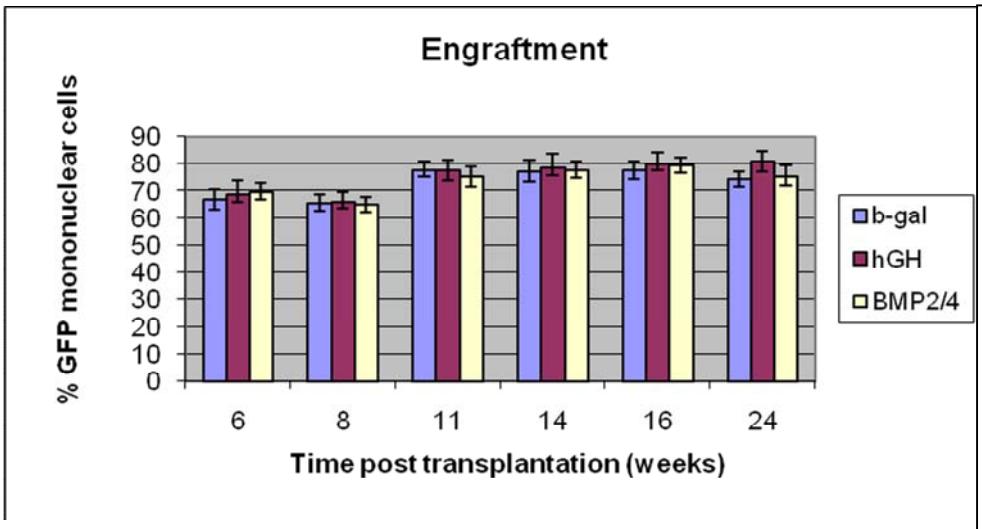

Figure 19. Engraftment of Sca-1+ cells transduced with lentiviral-based vectors (b-gal, hGH or BMP2/4) in W_{41}/W_{41} recipient mice preconditioned by sublethal irradiation. Engraftment was reflected by the percentage of GFP-positive mononuclear cells in peripheral blood at the indicated time points post-transplantation. Results are shown as the mean ± SEM with n = 6. Analysis by two-factor ANOVA revealed no significant differences (N.S.; $p>0.05$) between the treatment groups at any of the time points.

We next evaluated bone formation of the recipient mice. Mice not surviving the transplantation (N=2) or showing low engraftment (N=4, less than 50% GFP+ cells in peripheral blood) were eliminated from the analysis. At 16 weeks post transplantation, recipient peripheral blood was collected via tail vein bleed and serum was isolated using microtainer specimen tubes. Serum was analyzed for expression of insulin-like growth factor-1 (IGF-1), a surrogate marker for hGH expression and skeletal alkaline phosphatase (AP), a bone formation biochemical indicator. Results (mean ± standard deviation) are presented in Table 8. Serum IGF-1 levels in mice transplanted with cells overexpressing hGH (N=5) were significantly higher than those of control mice (N=6) and BMP2/4-transplanted mice (N=7) ($p < 0.01$). There were no significant differences in serum IGF-1 levels in BMP2/4-transplanted mice compared to controls. The increased levels of IGF-1 indicate that we successfully transduced donor cells with the hGH transgene, and achieved transgene expression after transplantation.

Serum AP levels were elevated in the BMP2/4-treated group compared to the control group, but this difference did not reach statistical significance. Surprisingly, as seen in Table 8, serum AP levels in the hGH-treated mice were significantly lower than those of BMP2/4 ($p < 0.05$).

Treatment	Serum IGF-1 (ng/ml)	Serum AP (U/L)
b-gal (control)	382 (42)	29 (4)
hGH	545 (71) *†	25 (4) †
BMP	417 (36)	32 (3)

Table 8: Serum biochemical indices of mice transplanted with cells overexpressing b-gal (control), hGH or BMP2/4. Mean ± (standard deviation). * p-value < 0.01 vs., b-gal controls, † p-value < 0.05 compared to BMP2/4 treatment group.

Bone formation parameters (total bone mineral density (BMD), trabecular BMD, cortical BMD, cortical thickness, endosteal circumference or periosteal circumference) of femurs from the 3 groups of mice were determined (Table 9). ANOVA analysis indicated significant differences in 3 parameters: total BMD, trabecular BMD and endosteal circumference. Post hoc analysis using the Tukey HSD test showed that total BMD was significantly lower in mice transplanted with cells overexpressing hGH compared to controls ($p < 0.05$) and to the BMP2/4 group ($p < 0.01$). In contrast, no significant differences were observed in total BMD between the BMP2/4-transplanted mice and controls. Trabecular BMD was elevated in mice in the BMP2/4 treatment group compared to control mice ($p < 0.05$) and hGH treated mice ($p = 0.01$). However, comparison of hGH-treated mice and controls showed no significant difference between the two groups. Endosteal circumference was largest in the hGH group, followed by values for the control mice. Mice transplanted with

cells expressing hGH had the highest endosteal circumference and were significantly increased compared to the BMP2/4-treated mice ($p < 0.01$). No difference was observed in endosteal circumference in control mice and those transplanted with cells overexpressing either BMP2/4 or hGH.

Taken together, these data suggest that overexpression of the hGH transgene results in a decrease in bone formation. Parameters in the hGH-transplanted mice showing significant differences from controls (decreased serum AP, decreased total BMD and increased endosteal circumference) indicate a negative effect on bone formation. Congruent with these results, trabecular BMD in the hGH group was lower than that of controls,

	Total BMD	Trabecular BMD	Endosteal circumference
b-gal (control)	0.770 (0.03)	0.266 (0.03)	3.61 (0.25)
hGH	0.687 (0.08)* †	0.234 (0.02)	3.90 (0.05) †
BMP2/4	0.790 (0.04)	0.312 (0.03)* ‡	3.45 (0.24)
ANOVA p-value	0.01	0.0009	0.015

Table 9: pQCT analysis of mice transplanted with cells overexpressing b-gal (control), hGH or BMP2/4. Mean ± (standard deviation). * p-value = 0.05 vs., b-gal controls, † p-value = 0.01 compared to BMP2/4 treatment group, ‡ p-value = 0.01 compared to hGH treatment group.

although statistical significance was not achieved. In contrast, parameters for the BMP2/4 group suggest a positive effect on bone formation. Trabecular BMD was significantly increased in the BMP2/4-transplanted mice compared to controls, and although not statistically significant, the BMP2/4 mice had higher serum AP, total BMD and smaller endosteal circumference.

These results confirmed our initial work that transplantation of BMP2/4-transduced Sca-1+ cells did not result in significant increases in bone formation. **As a result of these findings, in February, 2005 we submitted new technical objectives (Revised Technical Objectives 3) that proposed to explore mechanisms that may interfere with bone formation induction with overexpression of BMP4. In June 2005, we received approval to proceed with the revised Technical Objectives.**

Recently our facility purchased high resolution μCt equipment (VivaCT40, Scanco Medical) which is able to perform highly sensitive quantitative 3-dimensional analysis of calcified tissue. Since this equipment is much more sensitive than pQCT, we re-assessed the femurs from the recipient mice from our previous experiments to determine if small changes in bone formation had occurred after transplantation of BMP2/4-transduced cells. The trabecular bone architecture of the distal femoral metaphysic region of recipient mice was assessed using high resolution μCT (10 μm voxel size) A threshold of 200 was used and 180 slices (10.5 μM) transverse CT Measurements were done in the region 360 μM proximal to the growth plate and extended 1800 μM proximally slices. Parameters measured were bone volume fraction (BV/TV, %), trabecular thickness, trabecular number, trabecular separation, connectivity density and structure model index. Three-dimensional analyses of bone parameters of these same femurs by μCT (Table 10, below) confirmed the results from the pQCT, in that no significant differences in any of the measured μCT parameters between the HIV-BMP2/4 and the HIV-β-gal groups of recipient mice.

Table 10. μCT measurements of femurs of recipient mice transplanted with HIV-BMP2/4-transduced Sca-1^+ cells compared to those of recipient mice transplanted with HIV-β-gal-transduced Sca-1^+ cells 26-weeks post-transplantation (mean±SEM).

group	TV (mm^3)	BV (mm^3)	% BV/TV	Conn-Dens. (mm^3)	TRI-SMI (unit)	DT-Tb.N	DT-Tb.Th (mm)	DT-Tb.Sp (mm)
HIV-β-gal (n=6)	2.93±0.09	0.212±0.010	7.24±0.35	58.1±7.3	2.82±0.07	3.48±0.09	0.046±0.001	0.28±0.01
HIV-BMP2/4 (n=7)	2.86±0.08	0.182±0.020	6.38±0.63	48.6±6.7	2.85±0.10	3.25±0.10	0.046±0.001	0.31±0.01
p**	N.S.	N.S.	N.S.	N.S.	N.S.	N.S.	N.S.	N.S.

TV = total volume, BV = bone voume, % BV/TV = relative bone volume percent, Conn-Dens = connectivity density normed by TV, TRI-SMI = structural model (0 for parallel plates, 3 for cylindrical rods), DT-Tb.N = trabecular number, DT-Tb.Th = trabecular thickness, DT-Tb.Sp = trabecular separation.
**Statistical significance was determined by two-tailed Student's t-test. N.S. = not significant (i.e., $p>0.05$).

ORIGINAL

Technical Objectives 3a & 3b: To determine the effect of recipient age on engraftment and the bone formation response in mice transplanted with HSCs transduced to express a growth factor gene.

a. Transplant transduced donor cells expressing the BMP-2/4 gene into myelosuppressed recipient mice of 2 ages (8 weeks old vs. greater than 1 year old).
b. Compare the engraftment and bone formation response in young vs. old recipient mice by measuring serum osteocalcin and ALP, 12 weeks and 6 months post-transplant. We will also perform faxitron X-ray and pQCT analysis to evaluate the effects of transgene expression on bone density and cortical thickness in the recipient animal.

REVISED Technical Objective 3a & 3b: To explore the possible mechanism(s) for why transplantation of HSC-enriched cells transduced to express BMP4 did not induce bone formation as expected.

a. To determine if silencing of the BMP2/4 transgene occurs we will, transplant donor Sca-1^+ cells transduced to express BMP 2/4 (or marker control gene) into myelosuppressed recipient mice and evaluate transgene expression at 8 weeks and 6 months post transplant. Transgene expression will be evaluated by real time RT-PCR in RNA extracts and PCR in DNA extracts.
b. To determine if BMP2/4 interferes with engraftment of Sca-1^+ cells we will: transduce Sca-1^+ cells transduced to express BMP 2/4 (or marker control gene) and transplant at 4 cell doses (500, 5000, 50,000 or 500,000 cells/recipient) into myelosuppressed recipient mice and evaluate engraftment at 4, 6, 8, 10 and 16 weeks.

The lack of a large bone formation effect with the BMP4-based strategy is interesting; but it is also somewhat surprising, given the facts that 1) in the rat fracture model, intramedullary delivery of MLVBMP2/4 vector to the femur was shown to significantly enhance bone formation at the fracture site (7) and 2) there is recent evidence that HSC-derived BMP2 and BMP6 have regulatory roles in the HSC-mediated induction of mesenchymal stromal cells into osteoblasts within the HSC niche at the endosteum in response to stresses (8).

One possible reason for why no changes in bone formation changes were noted in these studies with transplantation of BMP2/4-transduced Sca-1+ cells is that the transgene integration into donor cell DNA and/or

gene expression levels in the recipient mice may be widely variable and/or at a dose too low to elicit statistically significant measurable differences. To explore these possibilities, we revised our technical objectives and conducted experiments to determine transgene transduction levels (DNA incorporation), engraftment of transduced cells and expression levels (RNA) of the transgene in cells samples from the recipient mice using real time PCR and RT-PCR assays.

In the first set of studies, Sca-1^+ cells from TgN donor mice were isolated and transduced with a lentiviral-based vector overexpressing either a control gene (pYb-gal) or BMP2/4 (pYBMP) transgene. Forty eight hours after transduction, aliquots of 500,000 cells of each preparation were transplanted via retro orbital injection into sublethally irradiated W^{41}/W^{41} recipient mice (N =8 per group). At 8 weeks and 24 weeks post-transplant, engraftment was assessed in the two groups. Peripheral blood was collected from the recipient mice, mononuclear cells were isolated by osmotic lysis and the % of GFP+ cells was determined by FACs analysis. Statistical analysis by independent t-test showed no significant differences in engraftment (% GFP+ cells) between the BMP2/4-transplanted and control mice at any either point (Figure 20).

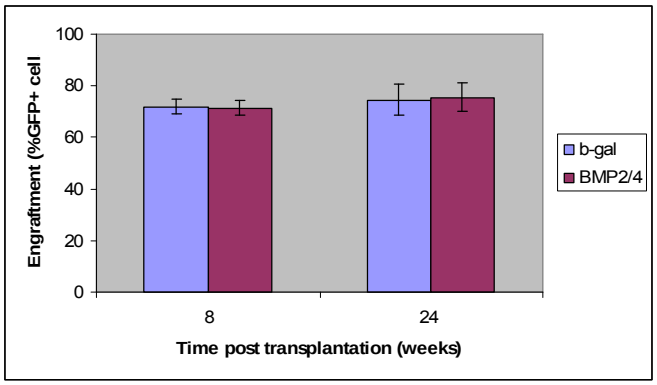

Figure 20: Sca-1^+ cells transduced to overexpress b-gal (control) or BMP2/4 protein were transplanted via retro orbital injection into sublethally irradiated recipient mice. Peripheral blood was evaluated by FACs analysis for percentage of GFP-expression (donor) cells after red blood lysis. Mean ± SEM.

We next evaluated transduction efficiency by assessing levels of transgene DNA and transgene mRNA in bone marrow extracts of recipient mice at experimental endpoint (26 weeks post transplantation). Two mice (one in each transplantation group, were found to have relatively low engraftment levels (39.2% and 42.7% GFP chimerism), were determined to be outliers by Grubbs test and were excluded from further analysis. Bone marrow harvested from the long bones of recipient mice was split into 2 aliquots and DNA and RNA was separately extracted using DNeasy Blood and Tissue Kit (Qiagen) and RNeasy Mini Kit (Qiagen) according to manufacturer's protocols. Real time PCR and RT-PCR was assessed. Primer sets used were as follows: b-gal: forward 5-CGG CAA GCC GTT GCT GAT TC-3, reverse 5-CAC ATA CAG GCC GTA GCG-3, human BMP2/4 forward 5-AAT GCA AGC AGG TGG GAA AGT-3, reverse 5'-CTG AAG TCC ACA TAG AGC GAG-3', and mouse/rat/human cyclophilin A forward 5'-GCA TAC AGG TCC TGG CAT CT-3' and reverse 5'-TGC TGG TCT TGC CAT TC-3'. Relative abundances of DNA (Table 11) or mRNA (Table 12) were quantified as Ct (cycle threshold value) relative to the Ct of cyclophilin A, a housekeeping gene and reported as average ΔCt ± SEM from pooled of 7-8 recipient mice, with lower ΔCt values indicating higher levels of nucleic acid. Expression levels are also displayed as fold increase in transgene nucleic acid levels as compared to control group and calculated by the $2^{-\Delta\Delta Ct}$ method (9).

Consistent with previous studies, large intra-treatment variations in DNA and mRNA levels were observed. As seen in Table 11, the relative level of BMP2/4 DNA in the blood and bone marrow extracts was significantly increased over that of control mice (527-fold and 1100-fold, respectively), indicating not only successful transduction of donor cells by the pYBMP2/4 vector, but also that the BMP2/4 transduced cells had engrafted in the bone marrow of recipient mice. Furthermore, the engraftment persisted for at least 26 weeks (experimental endpoint).

	BMP2/4 blood DNA 8 weeks		BMP 2/4 BM DNA 26 weeks	
Recipient group	ΔCt Mean ± SEM	Fold Increase	ΔCt Mean ± SEM	Fold Increase
b-gal	15.2 ± 0.9		16.6 ± 0.6	
BMP2/4	6.1 ± 0.4 *	527	6.5 ± 0.4 *	1100

Table 11: Relative BMP2/4 transgene DNA levels in recipient mice peripheral blood at 8 weeks and bone marrow at 27 weeks after transplantation of cells overexpressing either b-gal (control) or BMP2/4. Values are normalized to cyclophilin housekeeping gene.

Consistent with the increases in DNA levels, expression levels of BMP2/4 were also significantly elevated in the blood and bone marrow cell extracts of the BMP2/4-transplanted mice compared to control mice (Table 12), indicating long term engraftment and BMP2/4 transgene expression was established in the recipient mice. Furthermore, these results suggest that gene silencing may not be a significant cause for the lack of bone effects observed with the BMP2/4 ex vivo gene therapy.

	BMP2/4 blood mRNA 8 weeks		BMP 2/4 BM mRNA 26 weeks	
Recipient group	ΔCt Mean ± SEM	Fold Increase	ΔCt Mean ± SEM	Fold Increase
b-gal	10.8 ± 0.2		12.1 ± 0.3	
BMP2/4	-0.4 ± 0.5 *	2336	1.2 ± 1.2 *	1876

Table 12: Relative BMP2/4 transgene mRNA levels in recipient mice peripheral blood at 8 weeks and bone marrow at 27 weeks after transplantation of cells overexpressing either b-gal (control) or BMP2/4. Values are normalized to cyclophilin housekeeping gene

In the second set of studies, preconditioned W41/W41 recipient mice were each injected with 350,000 Sca-1+ cells from GFP+ donor mice that were transduced to express either the b-gal marker (control) gene, modified bone morphogenetic protein (BMP2/4) gene or the human growth hormone (hGH) gene. At 8 weeks post transplantation, peripheral blood was collected from the recipient mice and DNA and RNA was extracted from the mononuclear cells fractions. Real time PCR (reflecting successful insertion of the transgene into the donor cells and successful engraftment of donor cells) and real time RT-PCR (reflecting transgene expression) was performed on the DNA and RNA isolates, respectively and results of these analyses are displayed in Tables 13 and 14. As seen in Table 13, as expected, hGH DNA was detected in the peripheral mononuclear blood cells of mice transplanted with Sca-1+ cells expressing this transgene but not of mice in the b-gal and BM2/4 groups and BMP4 protein was only detected in mice transplanted with cells transduced to express the BMP4 gene, suggesting that donor cells were successfully transduced and successfully engrafted recipient mice. Comparison of the amount of DNA relative to the housekeeping gene (cyclophilin) suggests that cells transduced with the hGH vector were more efficient in transduction and/or engraftment than donor cells transduced with the BMP2/4 vector.

Measurements of RNA expression levels as reported in Table 14 are consistent with the DNA data, as reflected by higher relative levels of hGH mRNA compared to BMP4. At this time the cause for the differential DNA and RNA levels observed between different transgenes are unclear.

mean DNA ratio (st. dev)		
cells transplanted	**hGH /cyclophillin**	**BMP4 /cyclophillin**
b-gal-transduced	**0.00 (0)**	**0.00 (0)**
hGH-transduced	**1.16 (0.44) ***	**0.00 (0)**
BMP2/4-transduced	**0.00 (0)**	**0.02 (0.01) ***

Table 13: Real time PCR analysis of mononuclear blood cells 8 weeks post transplantation from recipient mice transplanted with Sca-1+ cells transduced to express b-galactosidase (b-gal-transduced), human growth hormone (hGH-transduced) or bone morphogenic 2/4 (BMP2/4-transduced) genes. DNA quantities (pg) were determined for hGH and BMP4 transgenes and cyclophillin housekeeping gene using specific primers and standard curves. Ratios were calculated by quantity of DNA of specific gene divided by quantity of cyclophillin DNA. ANOVA * p-value < 0.0001

mean RNA ratio (st. dev)		
cells transplanted	**hGH /cyclophillin**	**BMP4 /cyclophillin**
b-gal-transduced	**0.00 (0)**	**0.00 (0)**
hGH-transduced	**4.15 (3.32) ***	**0.00 (0)**
BMP2/4-transduced	**0.00 (0)**	**0.05 (0.03) ** **

Table 14: Real time RT-PCR analysis of mononuclear blood cells 8 weeks post transplantation from recipient mice transplanted with Sca-1+ cells transduced to express b-galactosidase (b-gal-transduced), human growth hormone (hGH-transduced) or bone morphogenic 2/4 (BMP2/4-transduced) genes. DNA quantities (pg) were determined for hGH and BMP4 transgenes and cyclophillin housekeeping gene using specific primers and standard curves. Ratios were calculated by quantity of DNA of specific gene divided by quantity of cyclophillin DNA. ANOVA * p-value < 0.002, ** p-value < 0.0002

<u>Revised Technical Objective 3b</u>: Sca-1$^+$ cells transduced to express BMP 2/4 (or marker control gene) and transplant at 4 cell doses (500, 5000, 50,000 or 500,000 cells/recipient) into myelosuppressed recipient mice and evaluate the percentage of various hematopoietic lineages (T-lymphocytes, B-lymphocytes, monocytic and erythroid) at 4, 6, 8, 10 and 16 weeks. Hematopoietic lineage will be assessed by immunostaining and FACs analysis.

To determine if BMP2/4 interferes with engraftment of donor HSCs, Sca-1$^+$ cells from GFP+ transgenic donor mice were transduced with either the pYb-gal or pY-BMP2/4 vector and transplanted in preconditioned myelosuppressed recipient mice. For these studies, whole bone marrow cells were harvested by flushing tibiae and femurs with PBS using a 26g needle and syringe. Erythrocytes were removed by osmotic lysis using a solution of 155 mM NH_4Cl, 10mM $KHCO_3$ and 110μM Na_2EDTA, followed by rinsing with PBS. After osmotic depletion of erythrocytes, the preparation was enriched for Sca-1 cells by incubation with a Sca-1 specific antibody-magnetic microbead conjugate and applied to an automated magnetic separation column (AutoMacs™) according to manufacturer instructions. Next, the Sca-1+ cells were plated in 6-well plates

coated with at a density of 4 $\times 10^6$ cells/well in IMDM medium containing 20% fetal bovine serum, 50 ng/ml of human flt-3L, 50 ng/ml of murine stem cell factor, 50 ng/ml of interleukin-6, 10 ng/ml of murine interleukin-3, 0.1 ng/ml murine interleukin- 1α, 100mol/l of deoxyribonucleotide triphosphate. After overnight incubation, 40 µl of concentrated viral stock (pY-b-gal or pY-BMP2/4 at 5 × 105 transforming units/µl) was applied to the cells. The medium was removed 8 hours later, and the transduction was repeated. Cell yields were measured by manual count of viable cells as determined by trypan dye exclusion, and transduced cells were transplanted into recipient mice 24 hours after transduction. To reduce the risk of infection associated with pre-conditioning, two weeks before and two weeks after transplantation, recipient mice were provided sterile food and autoclaved, acidified water (pH 2.0–2.5) containing 50 mg/l neomycin sulfate and 13 mg/l polymixin B sulfate. On the day of transplantation, the recipient mice were preconditioned by total body irradiation from a 60Co source delivering a single dose of 5 Gy (80 cGy/minute). After 4 hours, 8 randomly assigned groups of anesthetized mice (N=5) were intravenously injected with 1 of 4 doses of (500, 5000, 50,000 or 500,000 cells in 30 µl sterile saline/recipient) of either b-gal or BMP2/4 transduced Sca-1+ cells and engraftment at 4, 6, 8 and 10 weeks post transplantation was evaluated. Chimeric levels were assessed as the percentage of GFP-expressing cells as determined by analysis of mononuclear cells in recipient PB or BM with a FACSCalibur System. Two mice transplanted with b-gal-transduced cells (1 in the 500 cell dose group and 1 in the 500,000 cell dose

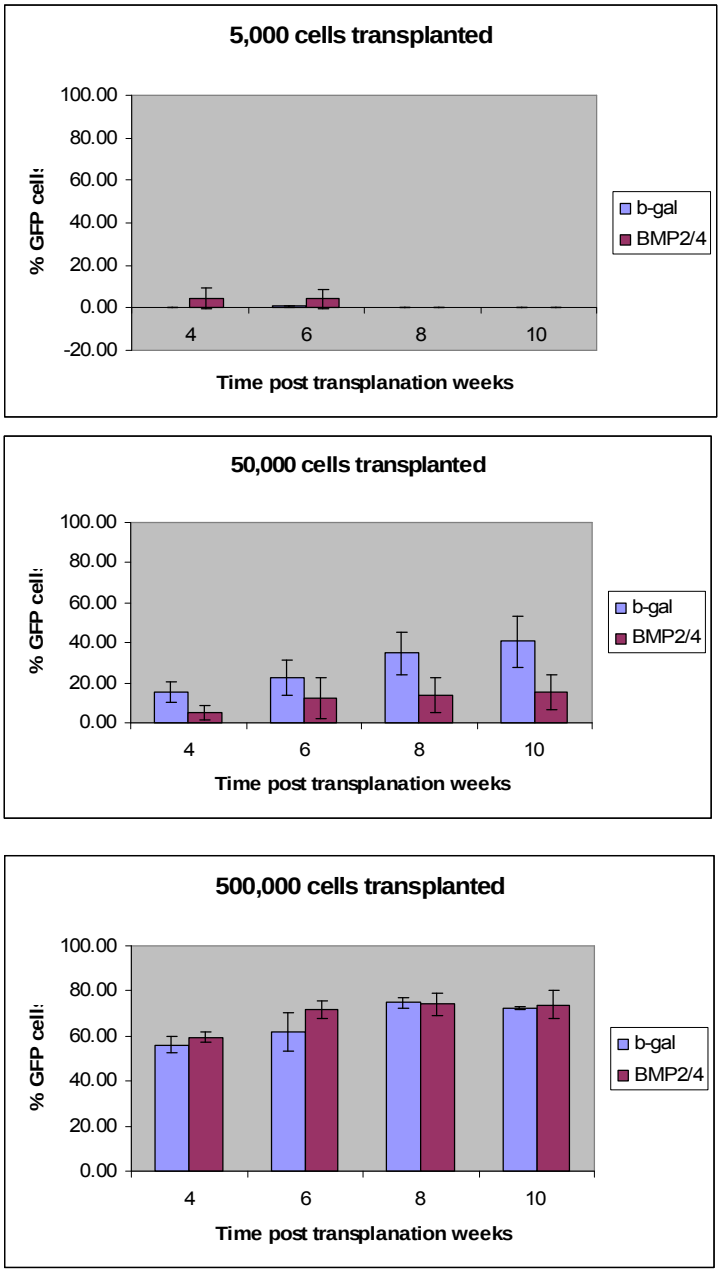

Figure 21: Levels of engraftment over time and number of donor cells transplanted. Sca-1$^+$ cells transduced to overexpress b-gal (blue bars) or BMP2/4 (red bars) protein were transplanted at various doses: 5,000 (upper), 50,000 (middle panel) or 500,000 lower panel) into sublethally irradiated recipient mice. Peripheral blood was evaluated by FACs analysis for percentage of GFP-expression (donor) cells after red blood lysis. Mean ± SEM.

group) died within days of the transplant. Therefore, the sample size was reduced to 4 for these groups. Due to large variation within the data, statistical analysis was performed using the Mann-Whitney non-parametric test for independent samples. In mice transplanted with the lowest number of cells (500), the % of GFP+ cells in peripheral blood (representing engraftment) at or below levels observed in non-transplanted control, indicating no engraftment occurred at this cell dose (data not shown). As seen in Figure 21 upper panel, minimal engraftment was observed in recipient mice that were transplanted with 5,000 donor cells regardless of type of transgene. In contrast, at cell doses of 50,000 (middle panel) and 500,000 (lower panel) significant engraftment, which increased over time, was observed in both the b-gal and BMP2/4-transplanted mice. At 50,000, average engraftment in the BMP2/4 group was lower than that of control mice at all 4 time points, however this difference did not reach statistical significance. At the cell dose of 500,000, average engraftment in the b-gal and BMP2/4 group were almost identical. The trend in engraftment data in the mice transplanted with 50,000 cells suggests that BMP2/4 overexpression may hinder donor cell engraftment. However, caution must be used in the interpretation of these results due to the wide variation in measurement of chimerism and the small sample size (N = 5). Variation in the chimeric levels in the b-gal and BMP2/4 groups of mice at the 50,000 cell dosage was particularly high, with the coefficients of variation (CV) over the 4 time points ranging from 74 to 181. In contrast, at the cell dosage of 500,000, the range of CVs was greatly reduced (4 to 27). Next, analysis of mean engraftment levels within each treatment group was performed, comparing mice receiving 50,000 donor cells with those receiving 500,000 donor cells (e.g. b-gal mice at 50,000 cells vs. b-gal mice at 500,000 cells). Transplantation of 500,000 cells resulted in significantly higher chimeric levels at all time points and for both treatment groups ($p = 0.04$ or less). These data indicate that transplantation of 500,000 donor cells is superior to lower cell doses as evidenced by higher mean engraftment and reduced variation in engraftment levels.

To determine if BMP2/4 induces Sca-1$^+$ cell differentiation into hematopoietic lineages we transplanted Sca-1$^+$ cells from GFP+ transgenic donor mice that had been transduced to overexpress either b-gal or BMP2/4 into preconditioned myelosuppressed recipient mice at 4 cell doses (500, 5000, 50,000 or 500,000 cells/recipient). At various time points post transplantation the percentage of various hematopoietic lineages (T- lymphocytes, B-lymphocytes, myeloid and erythroid) were assessed by immunostaining and FACs analysis.

For these studies, Sca-1 cells were isolated, transduced and transplanted as described above in Technical Objective 3b. At four weeks after transplantation, peripheral blood from the recipient mice was collected via tail vein bleeding and erythrocytes were removed by osmotic lysis. The mononuclear fraction was assessed for expression of hematopoietic lineage surface markers by immunostaining and measured by FACs analysis. For this analysis, PE-fluorochrome conjugated antibodies specific for hematopoietic lineage were incubated for 30 minutes in separate tubes with the mononuclear cell fraction from each recipient mice. Specific antibodies used were as follows: for T-lymphocytes (T-cells) a mixture of CD3-, CD4e-, and CD8a-specific antibodies was used; for myeloid cells (granulocytes/monocytes/macrophages) a mixture of Mac-1- and Gr-1-specific antibodies was used; for B-lymphocytes (B-cells) a B220-specific antibody was used and for erythroid lineage cells a Ter-119-specific antibody was used. After incubation the cells were rinsed once and resuspended in PBS and % PE positive cells were assessed by FACs analysis. Parallel tubes were processed using a PE-conjugated isotype non-specific antibodies and FACs results were adjusted to account for non-specific binding. In addition, the total engraftment (%GFP positive cells) was assessed. Based on our results from studies conducted for Technical Objective 3b indicating that transplantation with 500,000 donor cells yields higher and more reproducible engraftment, we limited our analysis to mice receiving this high donor cell injection. Data was first analyzed for % of each hematopoietic lineage (T-cell, myeloid, B-cell and erythroid) within the total mononuclear cell sample. The total mononuclear cell sample includes cells of donor-origin (GFP+) and host-origin (GFP-). As seen in Figures 22a-e, there was no significant difference in the percentage of cells

Figure 22a-e: Percentages of various hematopoietic cell lineages within the total mononuclear cell sample from the blood of mice transplanted with Sca-1+ cells transduced to overexpress either the b-gal (blue bars) or BMP2/4 (red bars) transgenes at 4 weeks (a), 6 weeks (b), 8 weeks (c), 10 weeks (d) and 16 weeks (d) post transplantation. Mean ± St. dev. Gr/m/M denotes Granulocytes/monocytes, macrophages.

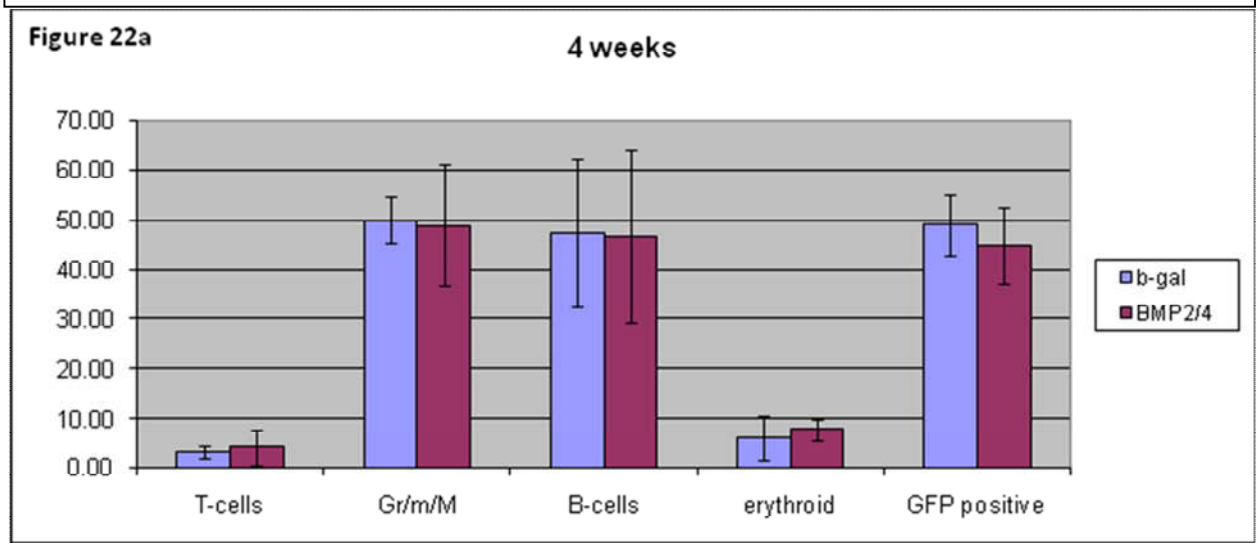

Figure 22b

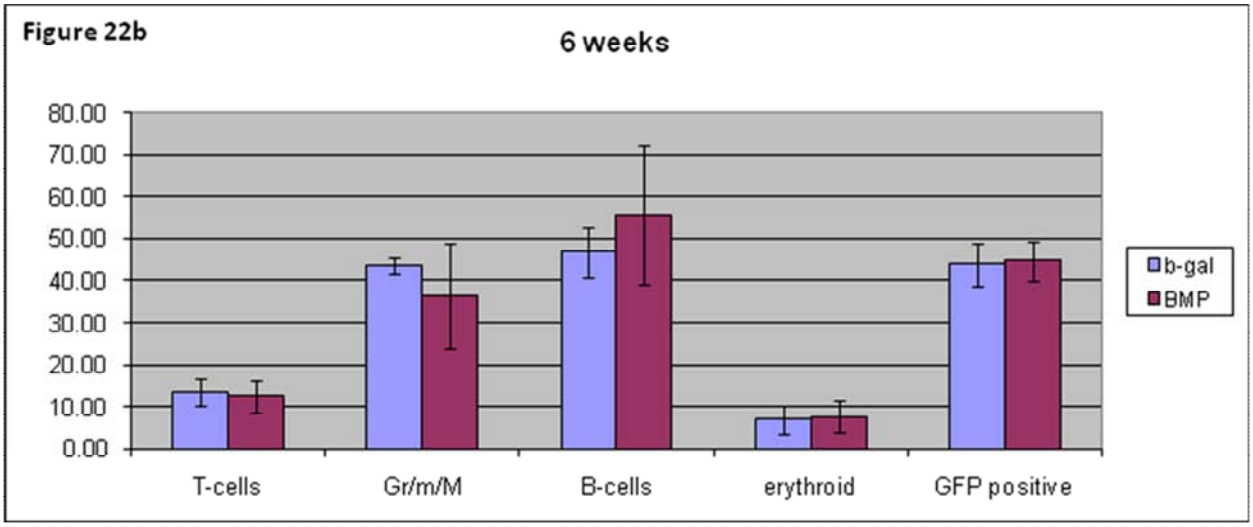

Figure 22c

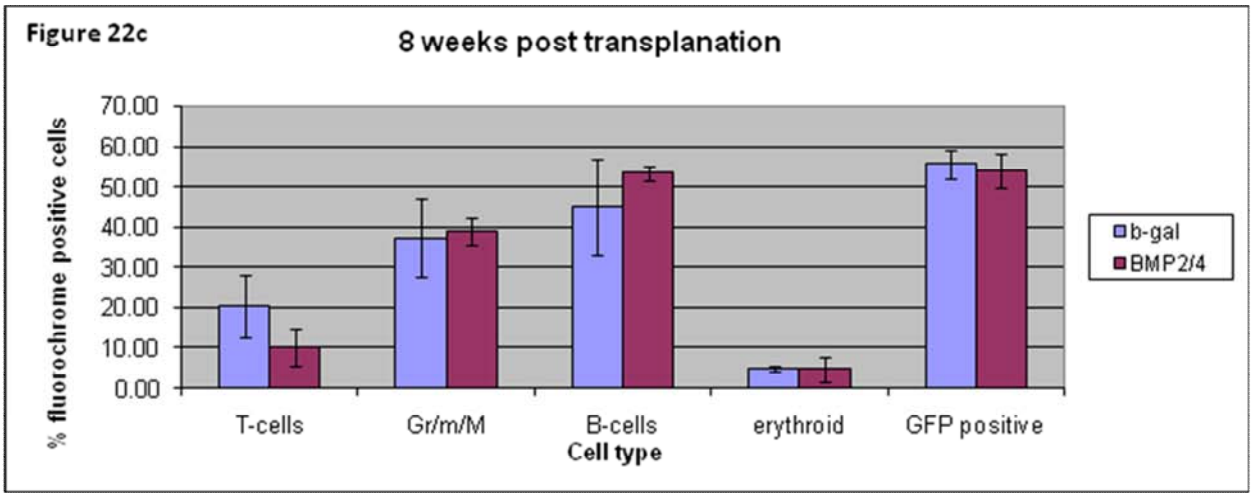

Figure 22d

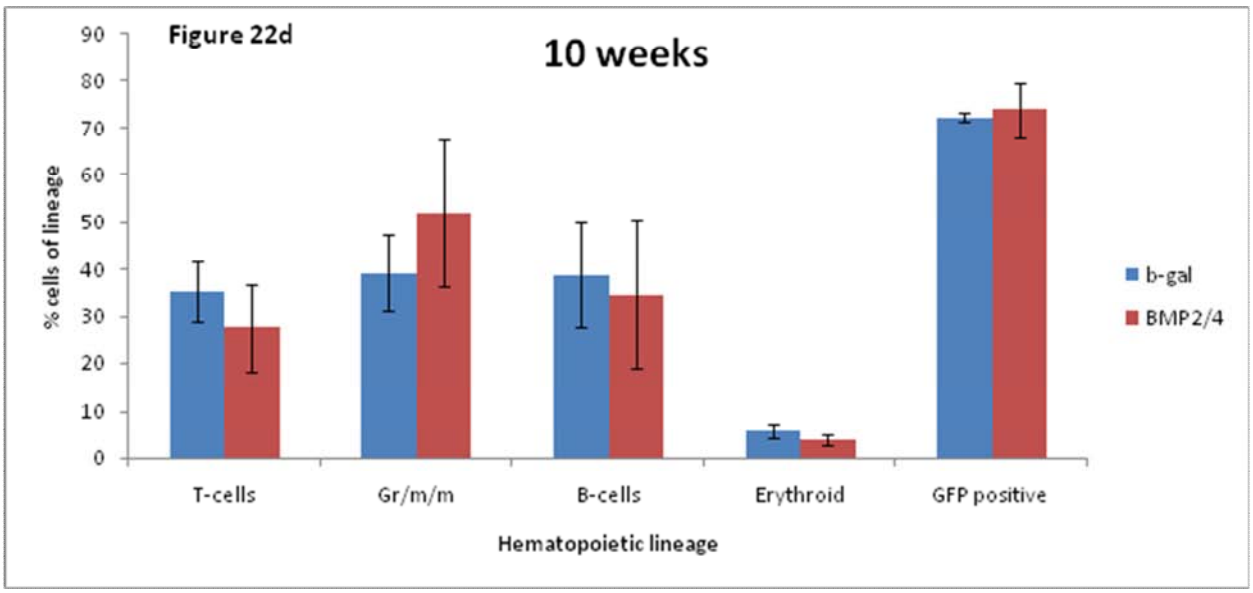

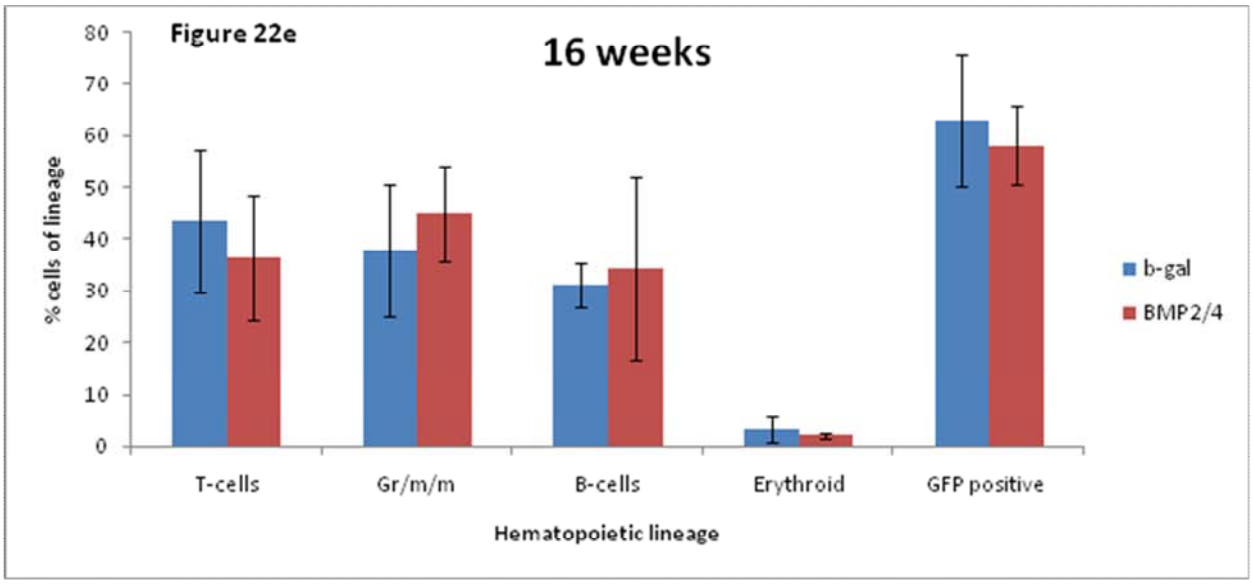

expressing each lineage-specific surface marker between mice in the b-gal and BMP2/4 groups in any of the four hematopoietic lineages. These data suggest that overexpression of the BMP2/4 transgene does not affect the overall hematopoietic lineage balance.

A second analysis was performed on the data derived from FACs analysis of the mononuclear cells samples obtained from recipient mice at 4 weeks. For this analysis, the % of each hematopoietic lineage was calculated separately for cells of donor origin (GFP+) and for cells of host origin (GFP-). Two-way ANOVA was performed using a 2 by 2 table with blocks of GFP phenotype (GFP+ and GFP-) and treatment groups (b-gal and BMP2/4). The results of this analysis are displayed in Figure 23. Consistent with our previous conclusion

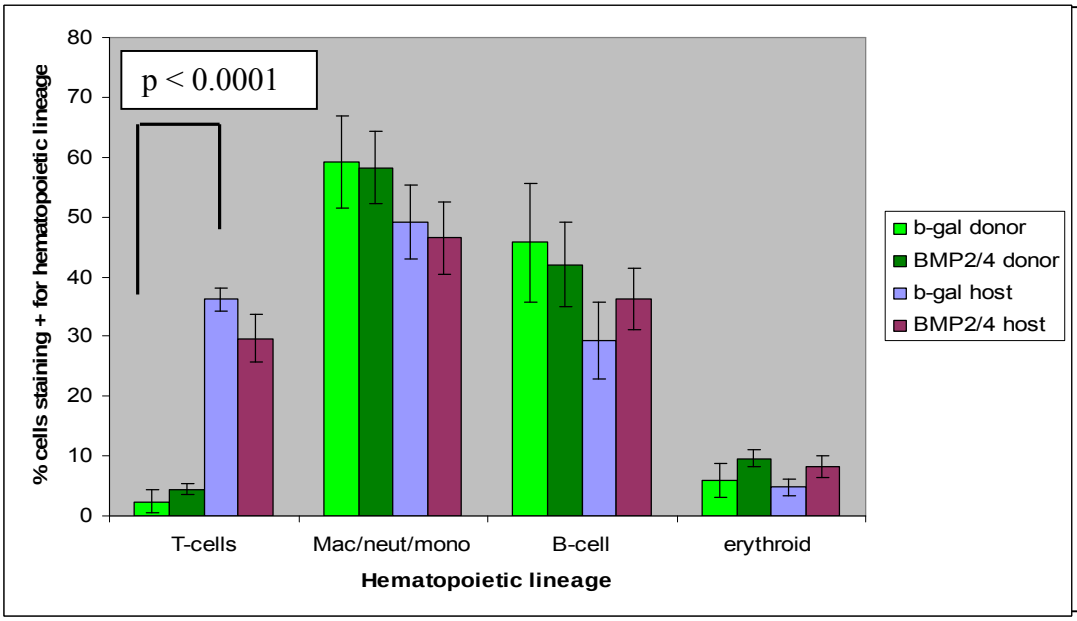

Figure 23: Percentage of various hematopoietic cell lineages within the GFP+ or GFP- subpopulations from the peripheral blood of recipient mice transplanted with Sca-1+ cells transduced to overexpress either the b-gal (blue bars) or BMP2/4 (red bars) transgenes at four weeks post transplantation. Mean ± SEM

that BMP2/4 overexpression does not affect the hematopoietic lineage balance, no significant differences in the percentage of T-cell, myeloid, B-cell or erythroid cell lineages in the peripheral blood of mice in the BMP2/4

group and controls. However, the percentage of cells expressing T-cell surface markers was significant decreased in the donor-origin fraction of cells (GFP+) compared to the host-origin cell fraction ($p < 0.0001$). The two-analysis indicated that the difference observed was due to GFP phenotype rather than by treatment group and no synergistic effect between these variables was observed. In the GFP+ cell fraction, the mean ± SEM values for T-cells were 2.4 ± 1.9% for b-gal treated mice and 4.5 ± 0.8% for BMP2/4-treated mice. In contrast, T-cell values in the host-origin (GFP-) subpopulation for the b-gal and BMP2/4 groups were 36.2 ± 1.9% and 29.7 ± 7.0 %, respectively. There are several potential mechanisms which could explain this apparent decrease in T-cells in the GFP+ population. First, it is possible that the GFP protein interferes with the development of cells of the T-cell lineage, resulting in lower T-cell production. It is also possible that T-cell progenitor cells in the Sca-1+ GFP+ subpopulation have inefficient homing ability or they lag in expansion abilities once engrafted compared with other GFP+ hematopoietic progenitor cells.

An additional set of experiments was performed to ascertain if the lack of a robust enhancing effects on endosteal bone formation in recipient mice of BMP4-expressing Sca-1+ cells was due the release of biologically inactive BMP4 protein by the transduced donor cells. For these studies, we assayed the biological activity of the BMP4 protein in the conditioned media (CM) using the mouse C2C12 myoblastic cell-based bioassay. This bioassay is frequently used to determine the biological activity of BMPs and is based on the principal that primitive C2C12 myoblastic cells are induced by BMPs to differentiate along the osteogenic linage as evidenced by production of AP (10,11,12). The biological activity of secreted recombinant BMP4 was assessed by measuring the ability of conditioned media (CM) from cell cultures of HIV-BMP2/4-transduced Sca-1+cells to stimulate AP activity in murine C2C12 myoblastic cells, using a protocol adapted for Sca-1+ cells. Briefly, Sca-1+ cells were isolated, plated and transduced with either the HIV-BMP2/4 or HIV-GFP vector as described above. After 4 days of culture, CM was collected from the Sca-1+ cell cultures and an aliquot (100 µl) of serially diluted CM samples in triplicate were applied to C2C12 cells, which been seeded 48 hours previously at a density of 250 cells/mm^2 in 96-well plates. After incubation for 72 hrs, the C2C12 cells were collected, and the cell extracts were prepared in 0.05% Triton X-100. The specific enzymatic activity of AP in the C2C12 cell extracts was determined by measuring production of pnitrophenolate from p-nitrophenylphosphate using the Sigma Diagnostics AP kit, and is reported as mU/mg cellular protein; where 1 U was defined as 1µmole of product formed/min at room temperature,

As seen in Figure 24, the CM from the cultures of Sca-1+ cells transduced with the HIV-BMP2/4 vector, in

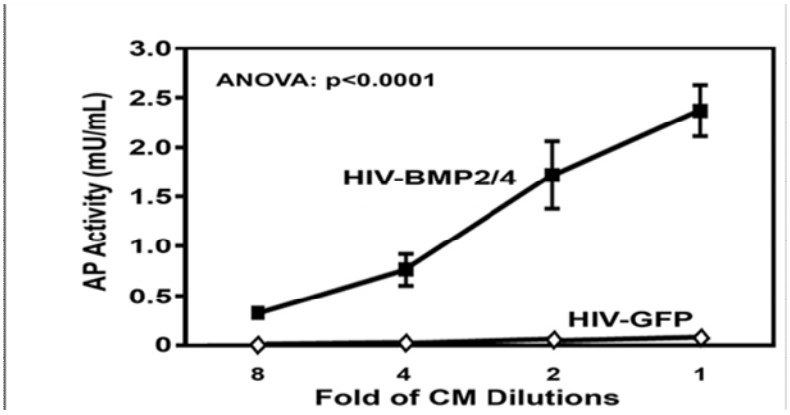

Figure 24: Conditional media (CM) from cell cultures of Sca-1+ cells transduced with either the HIV-BMP2/4 vector or HIV-GFP control vector was collected and the respective serially-diluted CM was added to six replicate wells of C2C12 myogenic cells. The cellular AP activity in each C2C12 cell culture was measured 72 hours laterand the results are shown as mean ± SEM. Statistical significance of the difference between the HIVBMP2/4 group and the HIV-GFP control group was assessed by ANOVA.

contrast to the CM of HIV-GFP-transduced cells, showed a dose-dependent stimulation of cellular AP activity in the C2C12 cells. These findings suggest that Sca-1+ cells transduced with a retroviral vector expressing BMP2/4 were capable of producing and secreting substantial amounts of biologically active BMP4 protein.

KEY RESEARCH ACCOMPLISHMENTS

- Successfully initiated and maintained a breeding colony of c-kit mutation mice (not commercially available) to produce progeny to serve as recipients in our transplantation experiments.
- Achieved consistently high enrichment (74%) and good cell yields (3 million cells/donor mouse) of Sca-1^+ donor cell subpopulation. Results were confirmed indicating that consistent, high enrichment of Sca-1^+ cells is achieved with our strategy. This is in spite of a change in technique that was necessary due to difficulty in obtaining reagents from the manufacturer.
- Demonstrated consistently high, stable engraftment of Sca-1^+ cells (70-90%) in the skeletal tissues of recipient mice for up to 52 weeks.
- Determined that the bone marrow cavity and the spleen are the primary sites of engraftment of the Sca-1+ donor cells after transplantations. In contrast, the liver, heart, kidneys and lungs tissues of recipient mice demonstrated insignificant engraftment of Sca-1^+ cells.
- Improved the transplantation method by using retroorbital injection to administer donor Sca-1+ cells resulting in greatly enhanced engraftment success (from an original average rate of 37% to nearly 100%), higher engraftment levels, and a significant reduction (3- to 4-fold) in variation compared with the tail vein method. We confirmed these engraftment experiments indicating we can consistently achieve high transplantation success (85-100%) and high, stable engraftment of Sca-$^{1+}$ cells (70-90%) in the skeletal tissues of recipient mice for up to 52 weeks using the retro orbital injection method.
- Successfully transduced Sca-1^+ cells using a retroviral-based vectors overexpressing GFP, b-galactosidase, and BMP2/4 achieving up to 50% transduction efficiency. In addition, we repeated transduction experiments using the BMP2/ transgene and confirmed that we can successfully transduced Sca-1^+ cells using a retroviral-based vector.
- Demonstrated the ability to transduce cells using a retroviral-based vector that overexpresses an alternative transgene, the human growth hormone (hGH), as evidenced by elevated expression of a surrogate protein (IGF-1) observed in the serum of recipient mice transplanted with hGH-transduced cells.
- Achieved relatively stable chimeras with transplanted retrovirally transduced Sca-1 cells. Results were confirmed in repeat studies.
- Results from several transplantation studies using the BMP2/4 transgene suggest that overexpression of BMP2/4 results in little or no increase in bone formation.
- Demonstrated that while BMP2/4 transduced cells successfully engraft, the level of BMP4 DNA and RNA present in the recipient mice is much lower than observed with other transgenes such as hGH, suggesting that one mechanism contributing to the lack of effect on bone formation observed with BMP2/4 in previous studies is likely insufficient therapeutic levels of the transgene after engraftment.
- Results from transplantation studies demonstrated that Sca-1^+ cells retrovirally transduced to express hGH result in decreased bone formation in recipient mice
- Demonstrated that transplanted Sca-1^+ cells are able to reconstitute all four hematopoietic lineages (T-lymphocyte, macrophage/monocyte/neutrophils, B-lymphocyte and erythroid).

REPORTABLE OUTCOMES

Publications

1. Hall SL, Chen ST, Gysin R, Gridley DS, Mohan S, Lau H-K W. Stem cell antigen-1^+ cell-based bone morphogenetic protein-4 gene transfer strategy in mice failed to promote endosteal bone formation. J Gene Med 2009; 11:877-888.

2. Hall SL, Lau H-K W, Chen ST, Wergedal JE, Srivastava A, Klamut H, Sheng MH, Gridley DS, Mohan S, Baylink DJ. Sca-1+ Hematopoietic Cell-Based Gene Therapy with a Modified FGF-2 Increased Endosteal/Trabecular Bone Formation in Mice. Molecular Therapy 2007 Oct;15(10):1881-9.

3. Hall SL, Lau H-K W, Chen ST, Felt, JC, Gridley DS, Yee KJ, and Baylink DJ. An Improved Mouse Sca-1$^+$ Cell-Based Bone Marrow Transplantation Model For Use In Gene- And Cell-Based Therapeutic Studies. Acta Haematol 2006;117:24-33.

Abstracts

1. Hall SL, Chen ST, Mohan S, Wergedal JE, Strong DD, Lau KHW. Stem Cell Antigen Positive (Sca-1$^+$) Hematopoietic Cell-based Human Growth Hormone (hGH) Gene Therapy Enhanced Endosteal Bone Resorption in Mice. Submitted for presentation to the annual meeting of the American Society for Bone and Mineral Research, September 12, 2008, Montreal, Canada.

2. Hall SL, Lau HK, Chen ST, Sheng MH, Gysin R, Wergedal JE, Srivastava AK, Mohan S, Baylink DJ. Sca-1$^+$ Cell-Based Gene Therapy with Fibroblast Growth Factor-2 Gene (but not BMP-4) Dramatically Increased Endosteal Bone Formation in Mice, Oral Presentation at the annual meeting of the American Society for Bone and Mineral Research, September 17, 2006, Philadelphia

CONCLUSIONS

In our systemic gene therapy subproject, we can achieve consistently high yields of highly-enriched hematopoietic progenitor cells from donor mice. Transplantation of these cells into preconditioned recipient mice results in consistently high, stable engraftment in the skeletal and splenic tissues, with minimal engraftment in non-skeletal tissues (lung, liver, kidneys, heart) of the recipient animal. We have successfully transduced the hematopoietic progenitor cells using retroviral-based vectors which overexpress BMP2/4 or hGH. Transplantation with donor cells retrovirally transduced to express BMP4 or hGH did not produce large increases in bone formation in recipient mice as expected.

The mechanistic reason(s) for the apparent lack of endosteal bone formation response in recipient mice of BMP4-expressing Sca-1+ cells is unclear. It was not likely the result of inefficient viral transduction, engraftment of donor cells, production on biologically inactive protein or BMP4-mediated effects on engraftment or on hematopoiesis.

REFERENCES

1. Morel et al Human Gene Ther. 10:2779-2787, 1999).
2. Liang, et. al., Effects of aging on the homing and engraftment of murine hematopoietic stem and progenitor cells**, Blood** 2005, Vol. 106, No. 4, pp. 1479-1487).
3. Peng H, Chen S-T, Wergedal JE, *et al.* Development of an MFG-based retroviral vector system for high secretion of functionally active human BMP-4. **Mol Therapy** 2001; 4: 95-104).
4. Price JE, Barth RF, Johnson CW, Staubus AE, Injection of cells and monoclonal antibodies into mice: comparison of tail vein and retroorbital routes. **Proc Soc Exp Biol Med** 1984; 177: 347–353).
5. Hall SL, Lau K-HW, Chen S-T, *et al.* An improved mouse Sca-1+ cell-based bone marrow transplantation model for use in gene- and cell-based therapeutic studies. **Acta Haematol** 2007; 117: 24-33).
6. Samuals M: **Statistics for the Life Sciences. San Francisco,** Dellen Publishing Company, 1989.
7. Rundle CH, Chen S-T, Porte R, *et al.* Retroviral-based BMP-4 *in vivo* gene transfer strategy with intramedullary viral delivery optimizes transgene expression in rat femur fractures. **The Open Tissue Eng Regener Med J** 2008; 1: 14-22**.**
8. Jung Y, Song J, Shiozawa Y, *et al.* Hematopoietic stem cells regulate mesenchymal stromal cell induction into osteoblasts thereby participating in the formation of the stem cell niche. **Stem Cells** 2008; 26: 2042-2051.
9. Livak KJ, Schmittgen TD. Analysis of relative gene expression data using real-time quantitative PCR and the 2 –delta delta CT method. **Methods** 2001; 25: 402-408.
10. Franceschi RT, Wang D, Krebsbach PH, *et al.* Gene therapy for bone formation: in vitro and in vivo osteogenic activity of an adenovirus expressing BMP7. **J Cell Biochem** 2000; 78: 476–486,

11. Nishimura R, Kato Y, Chen D, *et al.* Smad5 and DPC4 are key molecules in mediating BMP-2-induced osteoblastic differentiation of the pluripotent mesenchymal precursor cell line C2C12. **J Biol Chem** 1998; 273: 1872–1879.
12. Katagiri T, Yamaguchi A, Komaki M, *et al.* Bone morphogenetic protein-2 converts the differentiation pathway of C2C12 myoblasts into the osteoblast lineage. **J Cell Biol** 1994; 127: 1755–1766.

Project 7: Study Of Synergistic Growth Factors In Skeletal Gene Therapy

INTRODUCTION

Skeletal gene therapy strategies utilizing a single osteogenic growth factor can be an effective means to stimulate bone regeneration and enhance healing of skeletal injuries and defects [1]. Recent studies have strongly suggested that the effect of a single growth factor on the healing of skeletal injuries can be considerably enhanced by combination with a second growth factor [2]. Accordingly, synergistic gene therapies, would not only provide significantly greater osteogenic effects, but would also allow the use of significantly lower dosages of the growth factor genes. The use of lower dosages would reduce the costs of the therapy and could also potentially reduce undesirable side effects due to high doses of growth factors. Thus, there is a strong rationale for the need of development of combination growth factor therapies that employ two or more therapeutic anabolic genes that act synergistically to promote more rapid and complete healing of skeletal injuries. Consequently, the long-term goal of this project is to develop safe and effective combination therapies for skeletal injuries that involve *ex vivo* gene transfer of two or more osteogenic genes to primary bone marrow stromal cell cultures, followed by transplantation of transgenically engineered cells expressing high levels of two or more osteogenic genes at appropriate concentrations to the skeletal injury site to promote healing of bone defects.

The immediate objectives were: 1) to assess the feasibility of a combination *ex vivo* skeletal gene therapy strategy to locally express two osteogenic genes in bone to act synergistically to promote healing of a large skeletal defect, 2) to identify an appropriate combination pair of osteogenic growth factor genes that would produce synergistic enhancement of bone formation, and 3) to determine the optimal conditions for the synergistic combination gene therapy. Our original objective was to evaluate the therapeutic potential of primary bone marrow-derived stromal cells overexpressing two osteogenic genes [cyclooxygenase-2 (Cox-2) and vascular endothelial growth factor (VEGF)] in a mouse calvarial critical-sized defect model. However, our initial work in this project (summarized below) has shown that Cox-2 and VEGF did not synergistically interact with each other to promote healing of the critical-sized calvarial defect. Thus, we have subsequently changed our objectives (with approval from the granting agency) to investigate the potential interaction between BMP-4 and VEGF and between BMP-4 and Cox-2. In addition, we have also initiated work to test other osteogenic growth factors, such as FGF-2 and growth hormone (see below for detailed reports).

BODY

Technical Objectives:

1. To prepare MLV-based retroviral vectors expressing the Cox-1 and VEGF genes, and to characterize transgene expression levels following transduction of primary bone marrow derived stromal cell cultures (MSCs) *in vitro*.
2. To evaluate the impact of transplantation of MSCs expressing Cox-1 and VEGF on the rate and quality of healing of critical-sized mouse calvarial defects *in vivo*.

3. To optimize the dose and time of growth factor combinations with regard to bone formation time and bone quality.
4. To evaluate the impact of alternative MSC-based *ex vivo* combination strategies (i.e., BMP-4 and VEGF-A or BMP-4 and Cox-2) to synergistically promote healing of critical-sized calvarial defects.
5. To initiate studies aimed at determining the molecular mechanism of bone formation by osteogenic growth factors.

The first three objectives were the original technical objectives of the project. However, while working on the first two technical objectives, we have obtained evidence that Cox-2 and VEGF did not synergistically interact with each other to promote healing of the critical-sized calvarial defect (see below). Thus, with the permission from the funding agency, we have subsequently shifted our focus and investigated the potential interaction between BMP-4 and VEGF and between BMP-4 and Cox-2. Specifically, we added the fourth Technical Objective to initiate investigations in determining interactions between BMP-4 and VEGF and between BMP-4 and Cox-2, as well as other osteogenic factors, such as FGF-2 and growth hormone in the healing of a mouse critical-sized calvarial defect model.

Progress on Technical Objectives:

1. Technical Objective 1*: *To prepare MLV-based retroviral vectors expressing the Cox-1 and VEGF genes, and to characterize transgene expression levels following transduction of primary bone marrow-derived stromal cell cultures (MSCs) in vitro.

The *ex vivo* gene transfer strategy would require relatively large number of vehicle cells for transduction and transplantation. Our approach was to use a cell type that has been previously used successfully as donor cells to promote bone growth in *ex vivo* gene transfer-based therapies. Of the three cell types (skin fibroblasts, skeletal muscle-derived myoblasts, and bone marrow-derived stromal cells) that have been used successfully as donor cells in *ex vivo* skeletal gene therapy applications, we chose bone marrow-derived stromal cells (MSCs) for these experiments because of our previous success in healing critical-sized bone defects in a rat calvarial model using an *ex vivo* gene therapy strategy that employed MSCs. However, we found that mouse MSCs do not grow well (with relatively long population doubling time and allowing limited number of passages) under cell culture conditions that support the growth of rat MSCs [i.e., DMEM + 10% fetal bovine serum (FBS)]. We decided to first optimize the cell culture conditions for mouse MSCs. We found that mouse MSCs grow well in α-MEM supplemented with 15% fetal bovine serum. Under these culture conditions, mouse MSCs exhibit a reasonable cell population doubling time of 24 to 48 h. The cultured cells can also be continuously passaged in a weekly basis for at least 8 –12 weeks without significant loss of proliferative capacity (Figure 1). We believed that this culturing condition should produce sufficient number of cells for our subsequent *ex vivo* gene therapy applications. Therefore, this cell culture condition was adopted for use in this study. Very briefly, MSCs were isolated from long bones of C57BL/6J mice of 7 to 8 weeks of age (obtained from The Jackson Laboratories, Bar Harbor, ME). Femora and tibiae were dissected, and bone marrow cells were collected by flushing the cavity with α-MEM. The isolated cells were cultured in α-MEM supplemented with 15% FBS at 37°C for 2 days. The non-adherent cells were discarded and the adherent MSCs cultured in α-MEM with

15% of FBS until confluent. Cells from the first passage of multiple preparations were pooled and kept frozen in liquid nitrogen until use.

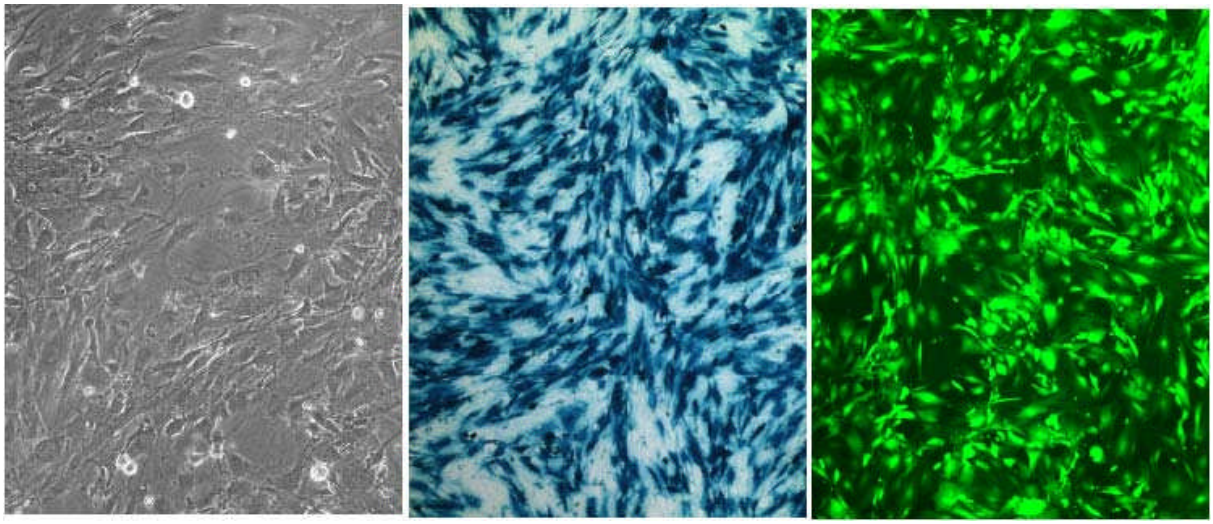

Figure 1. Culture of Mouse Bone Marrow-Derived Stromal Cells (MSCs) *in vitro* and transduction with reporter genes. Marrow stromal cell cultures were prepared by flushing out the marrow of tibiae and femurs, rinsing the cells 3 times in phosphate-buffered saline (PBS), and placing them in standard plastic culture dishes in α-MEM, containing 15% FBS and antibiotics. Half the medium was changed on days 2, 3, and 4. Cells had attached and started to divide by then, and the medium was changed every 3-4 days until cells reached confluency, usually after 8 – 12 days. Cultures were then passaged weekly. The left panel shows a phase contrast image of a confluent MSC culture. MLV reporter gene preparations [β-galactosidase (β-gal), enhanced green fluorescent protein (eGFP)] were used to transduce cells. The center panel shows cells stained for β-gal after transduction with MLV-β-gal. The right panel shows a fluorescent image of cells transduced with MLV-eGFP.

For the bone growth factor transgenes, we initially chose VEGF-A and Cox-2 genes for testing because 1) these two genes have been shown to have osteogenic and angiogenic effects in bone, and 2) both angiogenic action and osteogenic action are necessary for complete bone regeneration and complete healing. There are at least five forms of VEGF (VEGF-A, B, C, D, and placental growth factor, PlGF). We selected human VEGF-A for investigation, because 1) VEGF-A is the major and the most studied form, 2) VEGF-A has been shown to stimulate bone formation [3], and 3) VEGF-A is the isoform that is most strongly associated with angiogenesis. There are nine major VEGF-A isoforms [VEGF-A_{121}, -A_{145}, -A_{148}, -A_{162}, -A_{165}, -A_{165b} (an endogenous inhibitory isoforms that binds to VEGFR2 with similar affinity to VEGF-A_{165} but does not activate it), -A_{183}, -A_{189}, and -A_{206}]. Because VEGF-A_{165} has been shown to synergize with BMP-4 to promote bone formation [2], we chose VEGF-A_{165} for this work. MLV-based vectors were used because we have extensive experience with these vectors [4] and because these vectors have been shown to effectively transduce proliferating rat and human MSCs.

For construction of the MLV-VEGF vector, an expression plasmid containing the 165 amino acid form of human VEGF-A_{165} [5] was kindly provided by Dr. D. Losordo of the Tufts University, Boston MA [6]. The human VEGF-A_{165} cDNA was cloned downstream of a constitutively active CMV promoter in an MLV-based retroviral expression plasmid backbone. For construction of the MLV-Cox-2 vector, an expression plasmid containing the human Cox-2 gene was prepared by Dr. D. Strong at the Musculoskeletal Disease Center (MDC) of the Jerry

L. Pettis Memorial VA Medical Center [7]. Cox-2 is an inducible gene and its mRNA is highly unstable because, like most inducible genes, the Cox-2 mRNA contains numerous AU-rich elements (AREs) in its 3' untranslated region (3'-UTR); AREs have been shown to be responsible for mRNA instability and degradation [8]. The half-life of unmodified Cox-2 mRNA is therefore extremely short, which would limit production of the Cox-2 protein. Thus, the human Cox-2 transgene was modified to improve mRNA stability and protein translation by a) removing the large majority of the ARE-containing 3'-UTR and b) replacing the native Kozak sequence of human Cox-2 gene with an optimized Kozak sequence [9]. An MLV-based vector expressing the modified human Cox-2 gene was constructed as described previously [7]. The 72-kDa Cox-2 gene product catalyzes the first step in the biosynthesis of prostaglandins: the conversion of arachidonic acid to prostaglandin H_2. The biological activity of recombinant Cox-2 has been verified in the rat femoral fracture model [7]. An MLV retroviral vector expressing human bone morphogenetic protein 4 (BMP-4) was also prepared as a positive control to which the therapeutic efficacy of VEGF and Cox-2, either alone or in combination, can be compared. In this construct (designated BMP2/4), the signal sequence of the BMP-4 gene is replaced by a signal sequence from the BMP-2 gene. The MLV retroviral vector expressing BMP2/4 has been described previously [4] and has been shown to completely heal critical-sized calvarial defects in a rat model [10]. Similarly, MLV-based vectors expressing FGF-2, and β-gal and eGFP control genes in the same viral backbone were also produced and used as control and as alternative osteogenic genes for comparison. In each of these MLV vectors, expression of the trangene is under control of a constitutively active, potent CMV promoter. All MLV retroviral vectors used in this study were produced by the Vector Support Service at the MDC as described previously [4].

Mouse bone marrow-derived MSCs were transduced with MLV-based retroviral vectors using a "3-hit" protocol (i.e., three repeat retroviral transductions) established by the Vector Support Service Facility. Briefly, primary murine BMCs were transduced with the MLV-based vectors expressing BMP2/4, Cox-2, VEGF-A, or a reporter gene (β-gal or GFP) using an established protocol [4,7,10,11,12]. Briefly, MSCs were plated in 6-well dishes, grown to 50-70% confluence, and were transduced three times (for 12 hrs each) with the respective MLV vector at a concentration corresponding to 10 – 20 transforming units/cell in α-MEM, 15% FBS, and 8 μg/ml of polybrene over a span of 36 hrs. After the transduction, the virus-containing medium was replaced with fresh α-MEM supplemented with 15% FBS. Transduced cells were allowed to recover for two days in α-MEM + 15% FBS before being passaged. The transduced MSCs were expanded for 3–6 weekly passages prior to use. This protocol ensures that cells are actively proliferating and undergo at least one cell division in the presence of the retroviral vector, which is necessary for stable integration of the retroviral genome (carrying the growth factor transgene) into cellular DNA. As shown in Figure 1, transduction efficiencies of mouse MSCs [using these MLV vectors expressing the reporter genes β-galactosidase (β-gal) or enhanced green fluorescent protein (eGFP)] exceeded 90%. Accordingly, untransduced MSCs did not express β-gal or GFP (left panel). In contrast, >90% of the MLV-β-gal-transduced MSCs showed strong β-gal activity (middle panel) and >90% of the MLV-eGFP-transduced MSCs showed strong GFP levels (right panel) 14 days after transduction, confirming that primary murine MSCs can be effectively transduced with the MLV vectors.

To ascertain that murine MSCs transduced with the MLV-BMP2/4- or MLV-Cox-2 vector expressed substantial amounts of mature BMP4 and Cox-2 protein, respectively, the relative

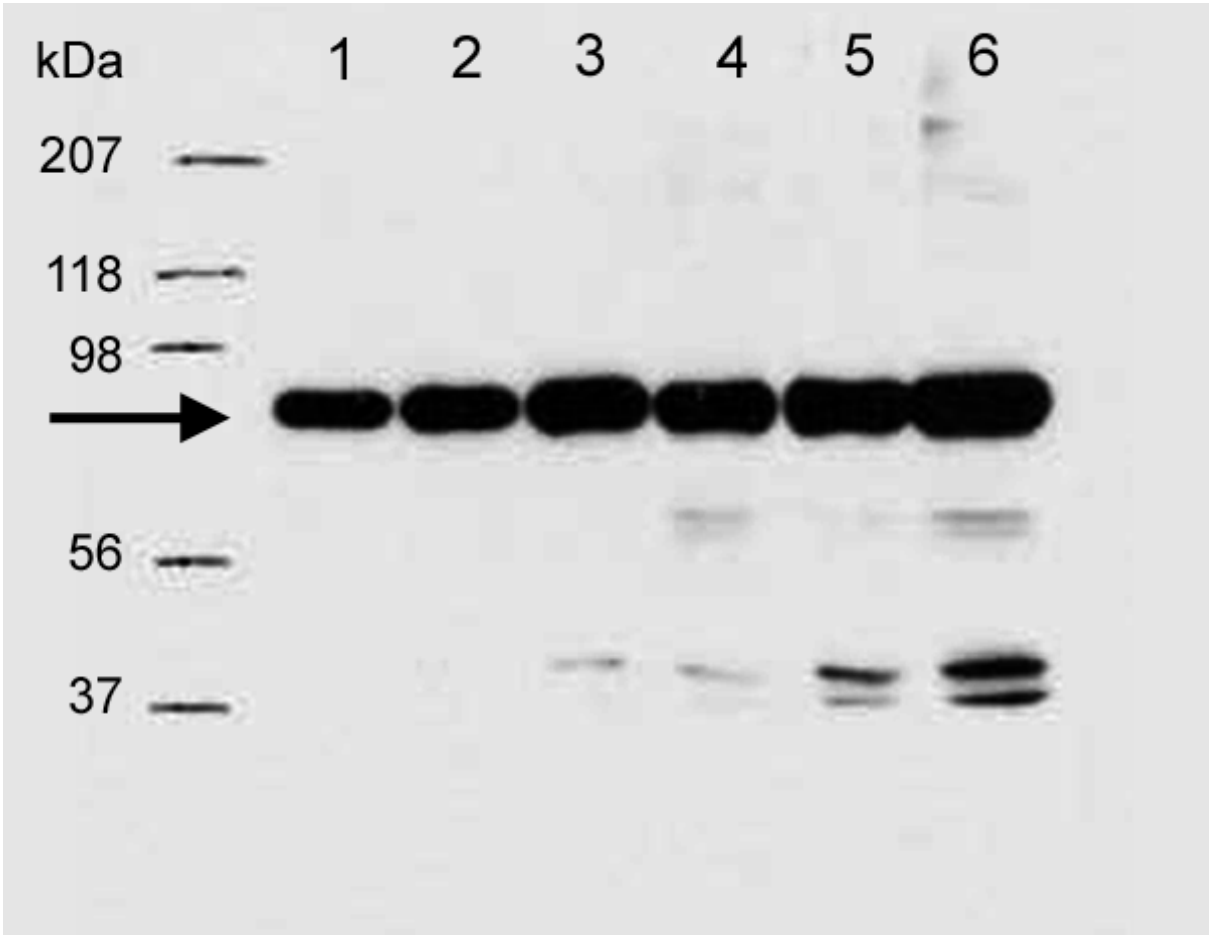

Figure 2: Western Immunoblot of Cox-2-Transduced Bone Marrow-Derived Stromal Cells (MSCs). Mouse MSCs were harvested 10 days after transduction with MLV containing the gene for human Cox-2. After lysis in gel treatment buffer containing SDS and 2-mercaptoethanol, the equivalent of 2.5 x 10^4, 5 x 10^4, and 1 x 10^5 cells were loaded in lanes 4, 5, and 6, respectively. Ovine Cox-2 standard (Cayman Chemical) was loaded in lanes 1 (25 ng), 2 (50 ng), and 3 (100 ng). After separation on an 8% polyacrylamide gel, the proteins were transferred to a nylon membrane and then incubated with monoclonal Cox-2 (raised against a 19-amino acid peptide homologous to human Cox-2, Cayman Chemical). The membrane was incubated with HRP-conjugated secondary antibody and reacted proteins visualized using a chemiluminescence kit (Super Signal West Pico, Pierce). The position of marker proteins is indicated on the left. Transduced cells display a strong band at 72-kDa (arrow), co-migrating with the standard.

cellular levels of mature human Cox-2 or BMP4 in respective transduced MSC populations were measured by Western immunoblot assays 7 days post-transduction (Figures 2 and 3, respectively). Untransduced mouse MSCs did not express detectable levels of human BMP4 or Cox-2 protein (data not shown), but cell extracts of MSCs transduced with MLV-BMP2/or MLV-Cox-2 contained substantial amounts of mature human BMP-4 protein or Cox-2 protein, respectively. Densitometric analysis of relative band intensities on Western blots from several experiments that contained multiple sample and standard concentrations demonstrated that recombinant Cox-2 levels reach 1,500 – 3,000 ng/10^6 cells, whereas recombinant BMP2/4 is expressed at levels of 100 – 200 ng/10^6 cells 7 days after transduction. Unlike Cox-2, which is an intracellular protein, BMP-4 is a secretory protein. Although we did not measure the amounts of mature human BMP4 protein secreted by the transduced cells in this experiment, we have previously shown that rat MSCs transduced with the same MLV-BMP2/4 construct secreted up

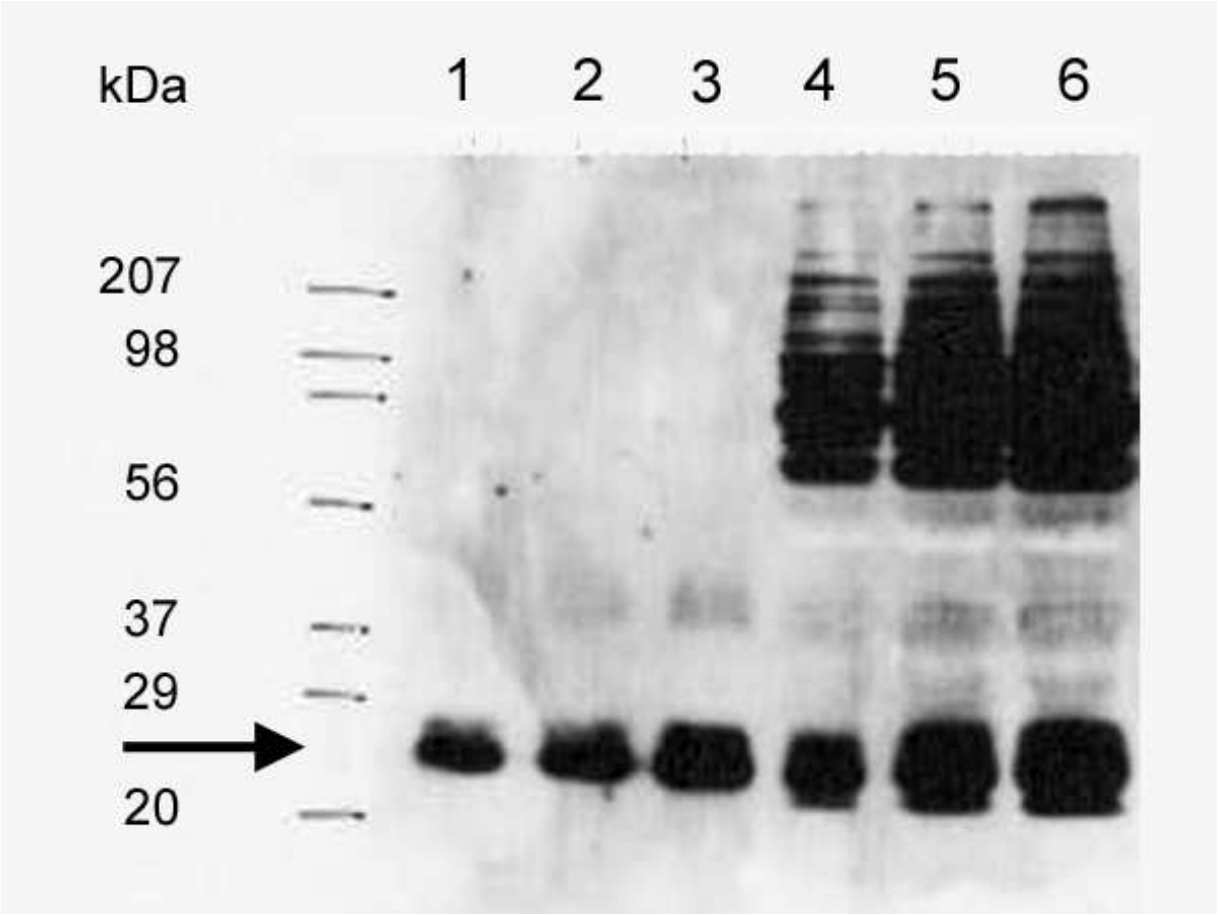

Figure 3: Western Immunoblot of BMP4-producing mouse MSCs. Mouse bone marrow-derived MSCs were harvested 2 weeks after transduction with MLV containing the gene for human BMP-2/4. The lysed cells were loaded in lane 1 (5×10^4), lane 2 (1×10^5), and lane 3 (1.5×10^5 cells). Lanes 1, 2, and 3 contain 1.5 ng, 2.5 ng, and 5 ng of recombinant human BMP-4 standard, respectively. Electrophoresis separation was performed on a on a 10% polyacrylamide gel. After blotting to a nylon membrane, the separated proteins were incubated with monoclonal anti-human BMP-4 antibody (R&D Systems), and visualized as in Figure 2. The position of marker proteins (Bio Rad) is indicated on the left. Transduced cells display a strong band at 24-kDa (arrow), co-migrating with the standard.

to 1 μg/10^6 cells/24 hrs [4]. Because the transduction efficiency of this MLV vector and relative biosynthesis rate of mature BMP-4 were very similar between rat MSCs and mouse MSCs (data not shown), the MLV-BMP2/4-transduced mouse MSCs would most likely also secrete similar high levels of mature human BMP4 protein. The expression levels of recombinant VEGF-A in mouse MSCs transduced with MLV-VEGF-A were measured by ELISA (R&D Systems) in conditioned medium. Recombinant VEGF-A was found to be secreted at a rate of 250 to 500 ng/10^6 cells in 24 hrs 7 days after transduction. The biological functional activity of VEGF-A was subsequently confirmed by increased angiogenesis *in vivo* and that of Cox-2 was confirmed by increased PGE_2 formation in transduced cells *in vitro* (see below).

It is interesting and also important to note that, although recombinant bone growth factor expression was maintained for several weeks after MLV transduction, the growth factor production levels were found to decrease at different rates for each of the three recombinant proteins. Over a 4-week period, Cox-2 and BMP-4 levels declined to 10% of their initial values, whereas VEGF-A production decreased by only 40%. Interestingly, β-gal and eGFP expression

was reduced by only 20% over this period of time. Subsequent studies (see below) suggest that this decline may be caused by gene silencing.

In summary, we have made substantial progress and successfully completed all of the original proposed work in Technical Objective #1 of this project.

2. Technical Objective 2: To evaluate the impact of transplantation of MSCs expressing Cox-1 and VEGF on the rate and quality of healing of critical-sized mouse calvarial defects in vivo. This Technical objective may be divided into two goals: 1) development of the mouse critical-sized calvarial defect model, and 2) evaluation of the effects of transplantation of Cox-2- and/or VEGF-A_{165}-expressing mouse MSCs on healing of the critical-sized mouse calvarial defects *in vivo*. The following describes our progress toward each of these two goals.

1. Adaptation of the rat critical-sized calvarial defect model in mice. A prerequisite for an assessment of feasibility of the combination gene therapy strategies to promote bone regeneration is a reliable bone regeneration model. A widely used bone regeneration model in small laboratory animal is the rodent critical-sized calvarial defect model, which involves the creation of a circular defect in the center of the parietal bone. We chose the critical-sized calvarial defect model, primarily because we have good experience with the rat calvarial defect model and because we have used the rat calvarial defect model to demonstrate the bone healing effects of BMP-4 in the past [10]. A bone defect is defined to be of critical size, when healing does not occur spontaneously over an extended period of time. In this regard, our rodent critical-sized calvarial defects do not heal over a period of up to 12 weeks without treatment [13]. However, treatment with an appropriate growth promoting modality can effect complete healing within 3-4 weeks [10]. Thus, critical-sized calvarial defects are ideal for testing bone regeneration activities of novel therapeutic modalities such as *ex vivo* growth factor-based gene therapy. The critical-sized calvarial defect model has an important advantage over critical-sized bony defects involving limbs or the spinal column. Unlike defects involving limbs or the spinal column that require stabilization, the calvarial model does not require surgical stabilization of the defects as the calvarial defect site does not bear significant load. An additional advantage is that test substances can easily be inserted into the defect and are held tightly in place after suturing of the skin. We elected to use the mouse model rather than the rat model, because we wish to take advantage of the availability of a large number of transgenic and knockout mouse strains in which we can use these transgenic mouse strains to investigate the impact of bone growth factor gene therapy on molecular mechanisms governing bone regeneration. However, while we have extensive experience in the rat calvarial defect model, we did not have much experience in the mouse calvarial defect model when we started the investigation. Consequently, our initial work toward this Technical Objective was to adapt the rat critical-sized calvarial defect model in mice to produce a mouse critical-sized calvarial defect model for the proposed work.

Our mouse critical-sized calvarial defect model is as follows. Briefly, male C57BL/6J mice of 7-8 weeks of age were maintained in the Veterinary Medical Unit of the Jerry Pettis VA Medical Center for 7–14 days prior to surgery. Mice were anesthetized by intraperitoneal injection of ketamine and xylazine. The surgical site at the top of the skull was prepared by shaving and cleaning with disinfectant. A 3-cm incision was made over the calvariae and the skin held open by retractors. The periosteum was pushed to the side bilaterally and a 5-mm diameter

critical-sized defect in the calvariae was created with a diamond-based dental burr. The calvarial disk was removed by severing the remaining connections with a blunt surgical probe. Careful handling of the instrument was required to avoid damaging the highly vascularized dura mater, which could cause excessive blood loss and death of the animal.

For implantation of MSCs, gelatin-based sponges (Gelfoam; Pharmacia and Upjohn, Kalamazoo, MI, USA) were cut to the size of the defect and placed in six-well plates. The transduced murine MSCs (indicated number in a volume of 200 µl) were added slowly onto the Gelfoam disk and left to settle for 15 min. After an hour of incubation at 37^{o}C, 5 ml of α-MEM supplemented with 15% FCS was added and the transduced mouse MSCs were allowed to attach to the Gelfoam matrix overnight. The MSCs impregnated Gelfoam disk was inserted into each defect to completely fill in the hole. The skin was then closed using 4-0 silk sutures. The animals were monitored closely until they were fully recovered from the anesthesia. New bone formation within the bony defect was detected by X-ray and quantitated with DEXA. X-ray imaging and DEXA densitometry measurements were done as follows: at the endpoint of each experiment, mice were euthanized and calvariae dissected out for analysis. Bone regeneration was assessed with soft X-ray using an MX20 X-ray specimen radiography system (Faxitron X-ray Corporation, Wheeling, IL, USA). Bone mineral density (BMD) was measured by dual-energy X-ray absorptiometry (DEXA) using a PIXImus soft-X-ray densitometer (Lunar, Madison, WI, USA) and the analysis software (version 1.45) provided by the manufacturer. A rectangular area encompassing the defect was defined as the total area of measurement. The 5-mm circular defect area was determined and the peripheral area outside the defect (containing the original intact bone) was also determined for comparison. The bone density results were also confirmed with bone histology.

2. Evaluation of the impact of transplantation of mouse MSCs expressing Cox-2 and VEGF-A_{165} on the rate and quality of healing of critical-sized mouse calvarial defects *in vivo*. To evaluate the impact of transplantation of mouse MSCs expressing Cox-2 and VEGF-A on the healing of the critical-sized calvarial defect in syngeneic C57BL/6J mice, a gelatin matrix scaffold (Gel-foam) cut to fit the calvarial defect was impregnated with 1 x 10^6 each of transduced MSCs expressing Cox-2, VEGF-A, BMP-4 (positive control), VEGF-A + Cox-2 (1:4 ratio), or GFP control gene alone overnight. The Gel-foam impregnated with transduced cells was then transplanted to the critical-sized calvarial defect. Recipient mice receiving Gel-foam without cells were also included as an untreated negative control. New bone formation (assessed by X-ray and DEXA) was measured 14 days post-tranplantation to assess the efficacy of bone regeneration of the transgene. During the initial phase of healing of calvarial defects, osteoblasts (or precursors) at the margin of the defect proliferate and differentiate rapidly, migrate towards the center of the wound and establish formation and mineralization of the bone matrix along the wound periphery until the entire defect is filled up with newly formed bone. This bone regenerating activity is thought to be stimulated by growth and differentiation factors that are released locally in response to the injury. Failure to close the critical-sized defect is believed to result from a deficiency in the level or persistence of local bone growth factor production [14]. Accordingly, it is anticipated that transplantation of MSCs (which contain osteoblast precursors) expressing a suitable osteogenic factor in the defect would promote repair of the defect. In this regard, we have clearly demonstrated that transplantation of BMP4 expressing MSCs in the rat critical-sized calvarial defect promoted complete healing of the defect [10].

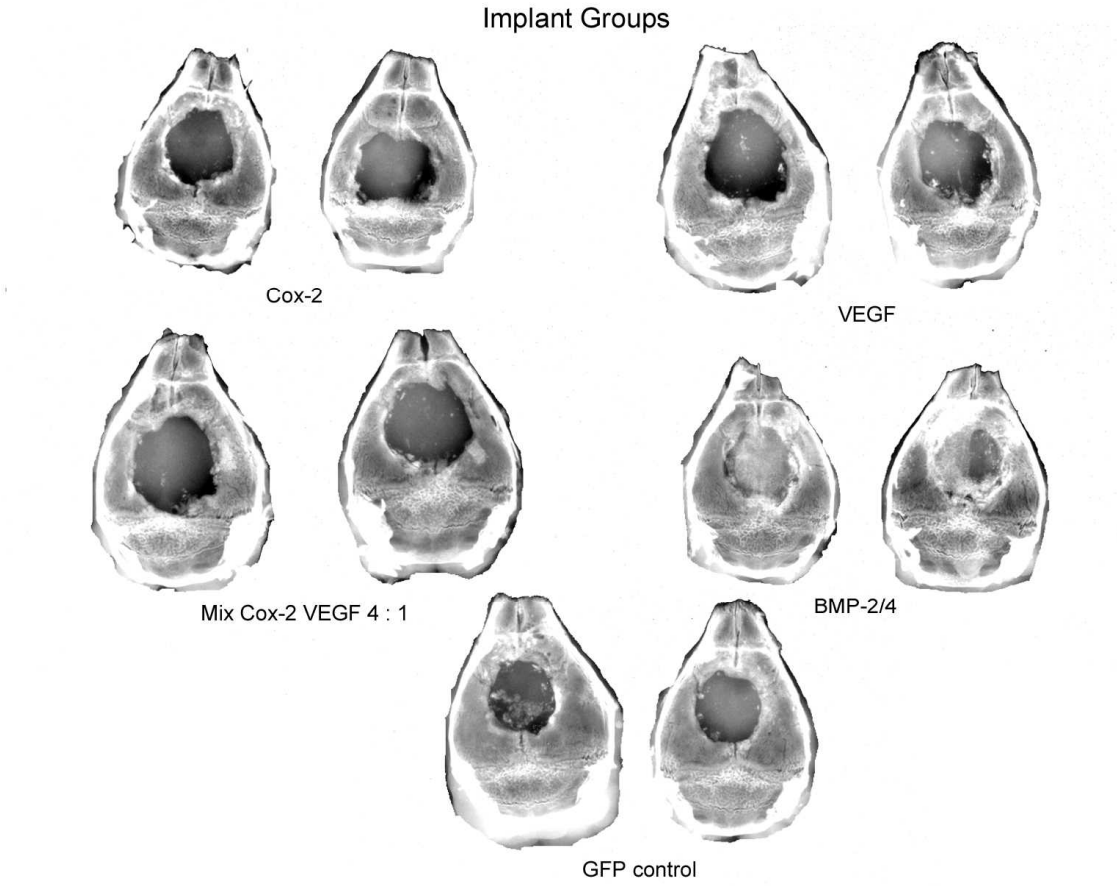

Figure 4. Analyses of new bone formation within the calvarial critical-sized defect receiving mouse MSCs expressing Cox-2 and/or VEGF-A after 14 days of healing. Digital soft X-ray image of healing calvarial defects of two representative mice per group after two weeks of healing are shown. Each defect was implanted with a Gelfoam implant containing a total of 1 x 10^6 MSCs: Cox-2 group received 1 x 10^6 MLV-Cox-2-transduced MSCs; VEGF group received 1 x 10^6 MLV-VEGF-A-transduced MSCs; Cox-2 + VEGF group received 8 x 10^5 MLV-Cox-2-transduced MSCs and 2 x 10^5 MLV-VEGF-A-transduced control cells; BMP-2/4 group received 1 x 10^6 MLV-BMP2/4-transduced MSCs, and the GFP control group received 1 x 10^6 MLV-eGFP-transduced MSCs.

As predicted, there was no evidence for new bone formation in the defects receiving untreated Gel-foam or those transplanted with control cells expressing the GFP control gene after 4 weeks (Figure 4). There was also no new bone formation in control defects transplanted with untransduced marrow stromal cells. Conversely, as in the rat critical-sized defect model, transplantation of mouse marrow stromal cells expressing BMP-4 yielded a complete regeneration of the defect after 14 days. Surprisingly and intriguingly, there was also no clear evidence for significant new bone formation in defects receiving cells expressing Cox-2 or VEGF-A_{165} alone or in combination compared to the GFP control group (Figure 4). However, there was strong evidence for a massive increase in blood vessel formation in the defects receiving cells expressing VEGF-A_{165} (data not shown), indicating that there were sufficient amounts of functional VEGF-A produced within the treated defects over the course of treatment. Thus, the lack of bone formation effects of the VEGF-A in this model was not due to insufficient

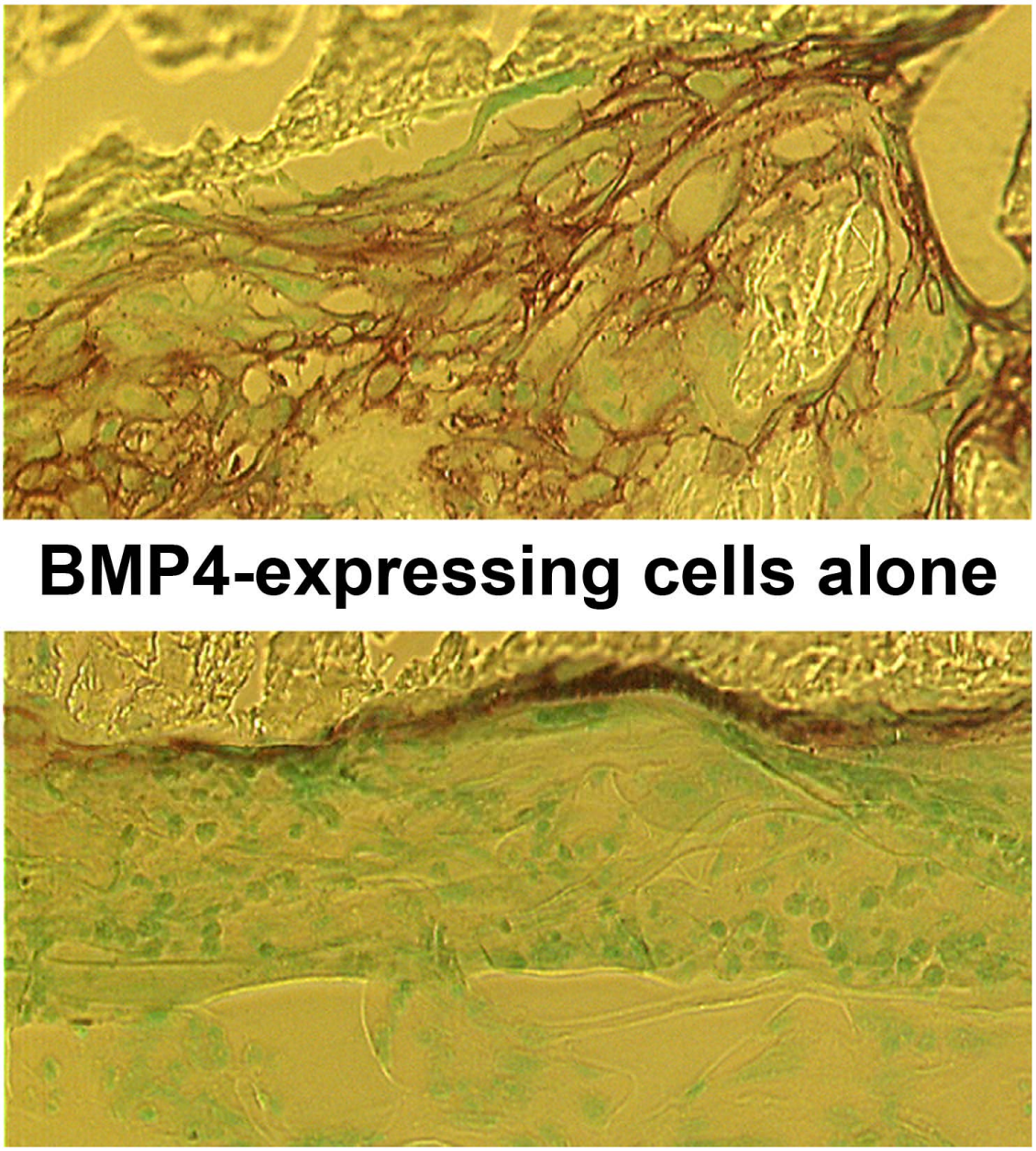

Figure 5. Histology of calvarial defect area after two weeks of healing. Top panel shows a representative section of the healing defect treated with BMP4-expressing MSCs after two weeks. Strong ALP activity (stained in reddish brown) was found throughout the entire defect. Bottom panel shows a representative section of the healing defect treated with Cox-2-expressing cells after two weeks. Only weak ALP staining was found along the original intact bone and at the edge of the defects.

expression of VEGF-A and/or production of inactive VEGF-A protein. No increase in angiogenesis was evident in animals treated with Cox-2 expressing cells (data not shown).

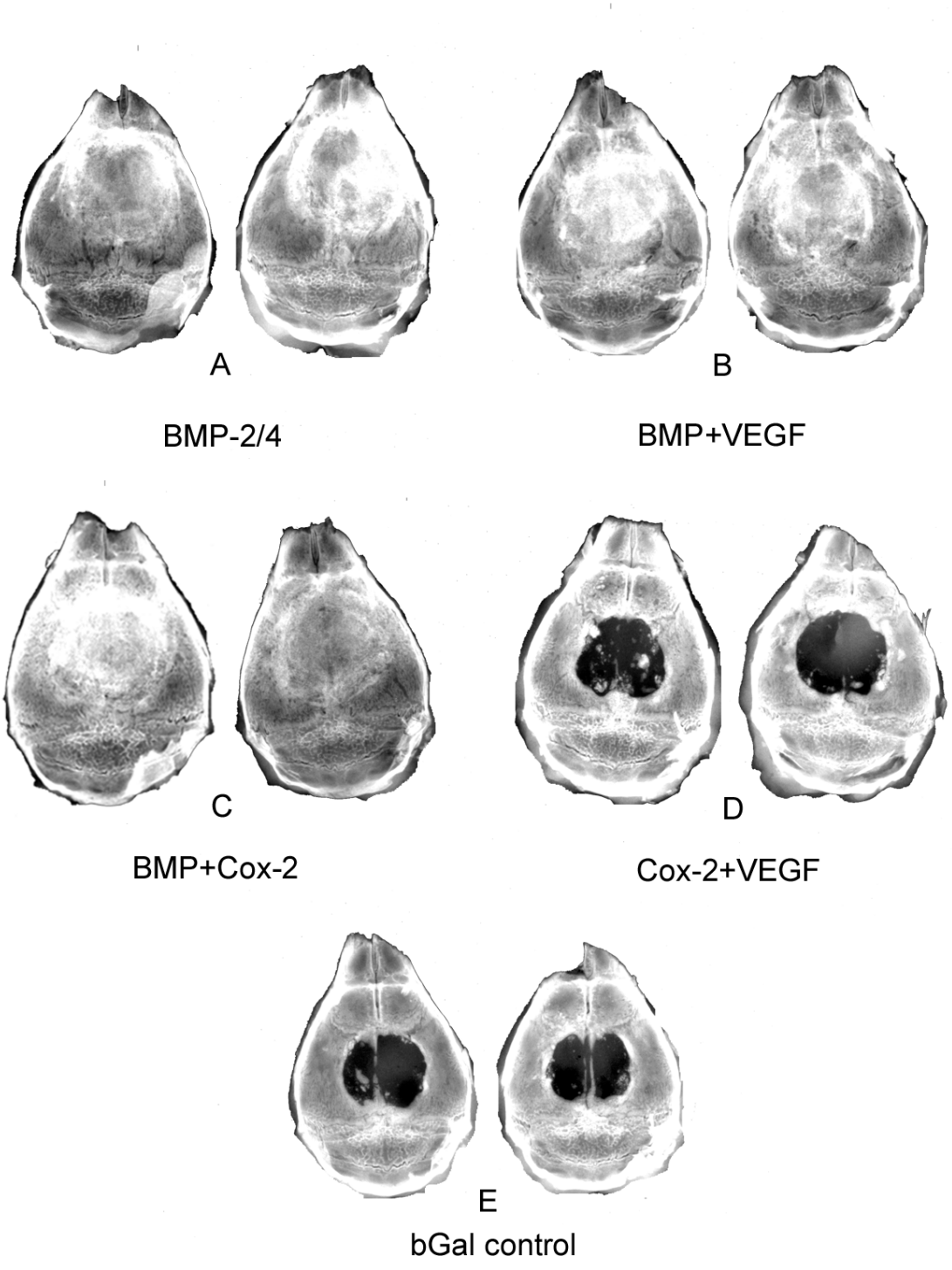

Figure 6. Digital Soft X-Ray Images of Calvarial Defect Model. Shown are 2 representative examples from implant groups that obtained a total of 1 x 10^6 gene-modified mouse bone MSCs. Group A was implanted with BMP4-expressing cells alone, and group E with β-gal-expressing control cells only. Mixtures in a 4:1 ratio were implanted in groups B-D, namely BMP4-expressing MSCs (8 x 10^5) + VEGF-A-expressing MSCs (2 x 10^5) in B, BMP4-expressing MSCs (8 x 10^5) plus Cox-2-expressing MSCs (2 x 10^5) in C, and Cox-2-expressing MSCs (8 x 10^5) plus VEGF-A-expressing MSCs (2 x 10^5) in D.

The lack of bone regeneration in detects treated with transplantation of VEGF-A-expressing and/or Cox-2-expressing MSCs was confirmed by histological analysis. For example, histology staining for ALP-expressing osteoblastic cells within the defects after 2 weeks of healing (Fig. 5) shows that strong staining was seen throughout the entire defect of animals receiving BMP2/4-expressing cells (top panel). Defects of the Cox-2 alone group (bottom panel) and the β-gal control group displayed only weak ALP staining along the original intact bone and also at the edge of the defects. These findings are consistent with the lack of *de novo* bone formation in defects implanted with Cox-2-expressing MSCs. Consistent with alkaline phosphatase staining, von Kossa staining for calcium deposits showed increased mineralization in BMP2/4 treated animals. No mineralization was evident in any of the other experimental groups. Interestingly, in addition to increased blood vessel formation, critical defects treated with VEGF-A expressing cells also contained more soft tissue in the area of the defect (data not shown). This was not observed in defects treated with Cox-2-expressing or GFP-expressing control cells.

The absence of a bone formation response with VEGF-A therapy alone was not entirely surprising as a previous study showed that transplantation of MSCs expressing VEGF-A alone in a segmental defect model not only did not enhance bone formation, but actually slightly inhibited bone formation, although the VEGF-A and BMP-4 combination markedly enhanced the bone formation response of BMP4 [2]. What was surprising is that the Cox-2 treatment did not produce a bone formation response in this calvarial defect model, given the fact that the same MLV-Cox-2 vector markedly enhanced bone formation and fracture repair in the femoral fracture model [7] and that Cox-2 and PGE_2 treatments have been shown to promote bone formation in a number of *in vivo* and *in vitro* models [15-20]. However, experiments utilizing Cox-2 as a therapeutic gene in a femur fracture model have shown that significant increases in bone formation do not occur until 14 to 21 days post-treatment [7].

In summary, we were surprised that the MSC-based Cox-2 *ex vivo* gene transfer strategy did not promote healing of the mouse critical sized defects. More surprisingly, we noted no significant synergy between the Cox-2 strategy and the VEGF-A strategy in promoting bone regeneration in the mouse critical sized defect model. Further work is needed to determine the mechanistic causes for the lack of synergistic interaction between Cox-2 and VEGF-A on promoting bone regeneration. Accordingly, our studies have clearly indicated that Cox-2 and VEGF did not synergistically interact with each other to promote healing of the critical-sized calvarial defect. Regardless of the reason for the lack of a bone formation response for the VEGF-A or Cox-2 therapy in our model, this study clearly indicates that the combination gene therapy of VEGF-A and Cox-2 would not produce synergistic response in repairing calvarial defects in mice. Therefore, we have decided (with permission from the grant agency) to revise our technical objectives to investigate the potential interaction between BMP-4 and VEGF and between BMP-4 and Cox-2 (Technical Objective #4).

3. Technical Objective # 3: Optimize the dose and time of growth factor combinations with regard to bone formation time and bone quality.

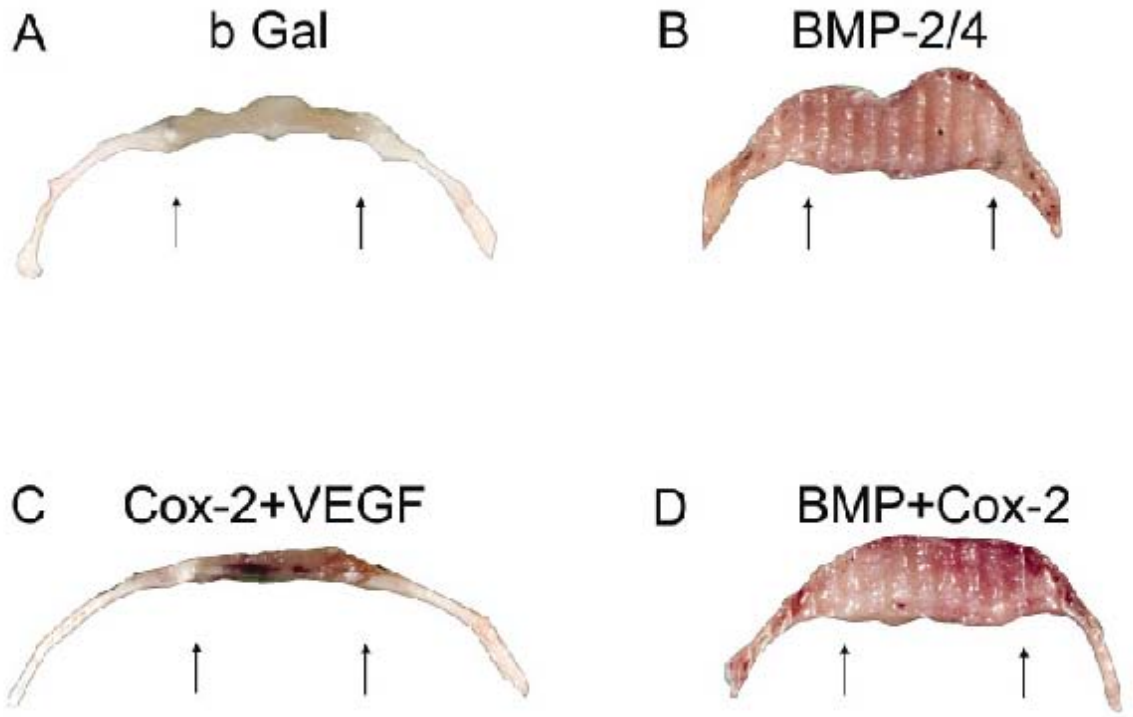

Figure 7. Cross-Section of Calvarial Defect 4 weeks after Implant. Calvariae were dissected after 4 weeks and photographed after coronal sectioning. Arrows mark the edges of the 5-mm defects that were implanted with 1 x 10^6 cells. Shown are representative examples of implant groups that obtained βGal control cells (A) and BMP-4 producing cells (B). Implants containing 4:1 mixture of Cox-2 and VEGF transduced cells (C) and 4:1 mixture of BMP and Cox-2 cells (D) are also shown

Previous experiments utilizing Cox-2 as the therapeutic gene in a rat femur fracture model have shown that significant Cox-2-mediated increases in bone formation did not occur until 14 to 21 days post-treatment [7]. To determine if calvarial healing is also delayed following Cox-2 treatment, we have performed a second experiment to assess bone formation response after 4 weeks of implantation. In this experiment, Gelfoam scaffold disk impregnated with a total of 1 x 10^6 mouse MSCs cells transduced with the MLV-BMP2/4 (BMP2/4 group, positive control), MLV-β-gal control vector (β-gal group, negative control), MLV-BMP2/4 + MLV-VEGF-A (4:1 mixture), MLV-BMP2/4 + MLV-Cox-2 (4:1 mixture), or MLV-Cox-2 + MLV-VEGF-A (4:1 mixture), was implanted into the critical-sized defect of a group of five mice each. Animals were sacrificed 4 weeks post-transplantation and calvariae were again analyzed for bone formation by X-ray and DEXA densitometry (Figure 6). Similar to the results seen after 2 weeks of treatment, substantial bone formation was seen in defects treated with MSCs expressing BMP2/4 alone. The extent of bone formation was much more pronounced at this later time point, as evidenced by the calvarial cross sections shown in Figure 7. Defects implanted with BMP2/4 expressing cells (Figure 7, panels B and D) exceeded the thickness of the original bone several fold. Soft X-ray imaging (Figure 6, panels A, B, and C) indicated that each of the defects treated with cells expressing BMP-4 had completely healed by 4 weeks post-transplantation. On the other hand, no significant increase in bone formation was evident in defects treated with cells expressing Cox-2 and VEGF-A cells in combination (4:1 ratio) (Figure 6, panel D, and Figure 7, panel C) relative to negative control animals treated with cells expressing β-gal (Figure 6, panel E, and Figure 7, panel A). Consequently, these findings indicate that the lack of synergistic interaction

between Cox-2 and VEGF-A was not due to insufficient treatment duration. These results also confirmed our conclusion that Cox-2 *ex vivo* gene transfer strategy does not synergize with the VEGF-A *ex vivo* strategy in promoting healing of critical sized calvarial defects. Because of these findings, we have abandoned the originally proposed additional optimization studies of the Cox-2-VEGF-A combination strategy and started to examine alternative combination strategies. Our findings of this alternative approach are summarized below in the following Technical Objective #4.

4. Technical Objective #4: Evaluation of the impact of alternative MSC-based ex vivo combination strategies (i.e., BMP-4 and VEGF-A or BMP-4 and Cox-2) to synergistically promote healing of critical-sized calvarial defects.

a) Interaction between VEGF-A and BMP-4 *ex vivo* gene therapy strategy on healing of critical sized calvarial defects. Since our overall objective is to develop a synergistic gene transfer-based therapeutic strategy for enhancing bone healing and repair, we next revised our Technical Objectives to identify a more suitable pair of synergistic osteogenic growth factor genes for evaluation. In this regard, we sought to test the possibility that either Cox-2 or VEGF-A might synergize with and enhances the bone formation effect of BMP4 in the mouse critical-sized calvarial defect model. We first examined the potential synergistic effects between BMP4 and VEGF-A, since it has previously been reported that VEGF-A when given in the ratio of 1:5 with BMP4 produced a synergistic enhancement of bone formation in a rat segmental defect model compared to BMP4 ex vivo gene therapy alone [4,21].

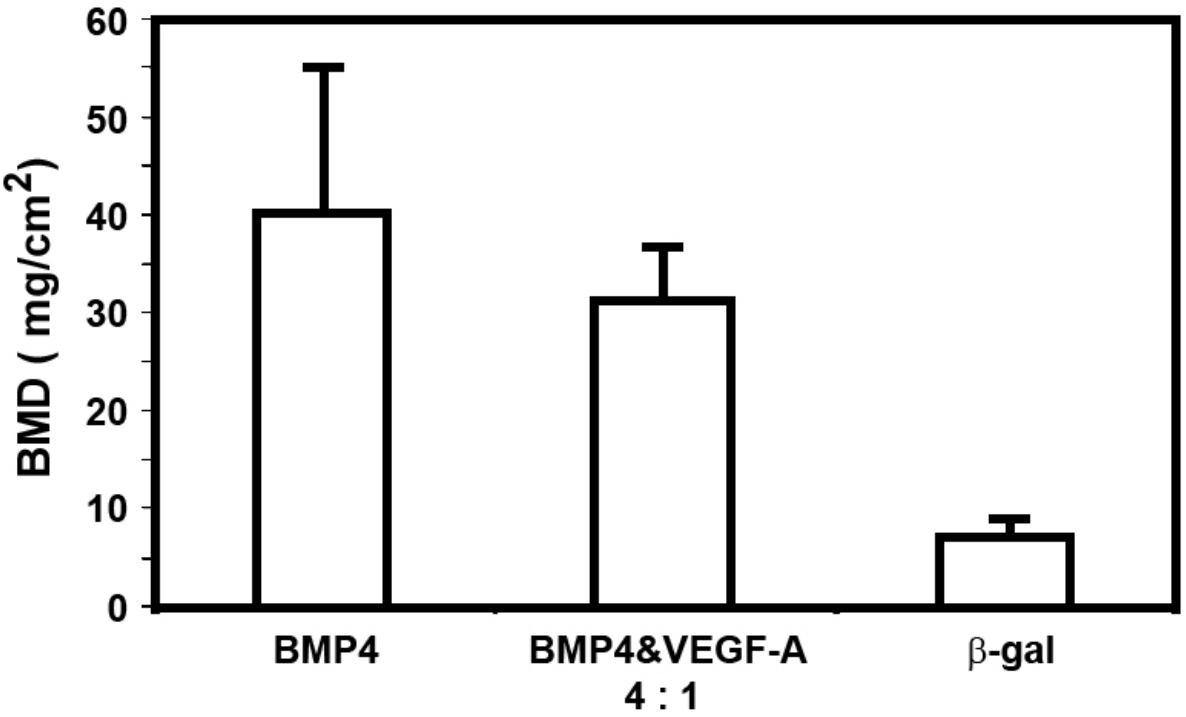

Figure 8: Bone Density in Calvarial Defects after Implanting with MSCs expressing BMP4 and/or VEGF-A. Calvariae were dissected 4 weeks after implant of cells as described in the text. Bone mineral density (BMD) was measured by dual-energy X-ray absorptiometry (DEXA) using a PIXImus soft-X-ray densitometer (Lunar, Madison WI) and analysis software version 1.46 provided by the manufacturer. Values are average (± SD) from 4 animals for each group.

To test whether VEGF-A would synergize with BMP4, defects transplanted were with 4 x 10^5 cells of BMP4 expressing mouse marrow stromal cells, 1 x 10^5 cells of VEGF-A expressing cells, alone or in combination (BMP-4:VEGF-A in 1:4 ratio). As expected, BMP4 treatment produced a significant increase in bone formation (Figures 6 and 8), while VEGF-A treatment had no significant bone formation effect compared to control defects with no cells or transplanted with GFP expressing control cells (159±57% of GFP controls). However, contrary to what was reported for the rat segmental defect model, the BMP4 and VEGF-A combination regiment did not produce a large synergistic enhancement in new bone formation (Figures 6 and 8). On the contrary, quantitative bone mineral density (BMD) measurements by DEXA revealed that the combination therapy produced a significant 20% reduction in BMD compared to BMP4 treatment alone 4 weeks after transplantation (123±57% of GFP controls vs. 159±57% of GFP controls) (Figure 8). Aside from consistent increased bone formation in BMP-4-treated defects, the only other consistent change seen in this study was an increase in vascular tissue mass in animals treated with cells expressing VEGF-A. Nevertheless, these findings indicate that VEGF-A not only does not have bone regenerative actions, but also does not synergize or enhance the bone regeneration effects of BMP-4. Thus, the BMP-4 and VEGF-A combination strategy would not be an effective strategy to promote bone regeneration in the calvarial defect model.

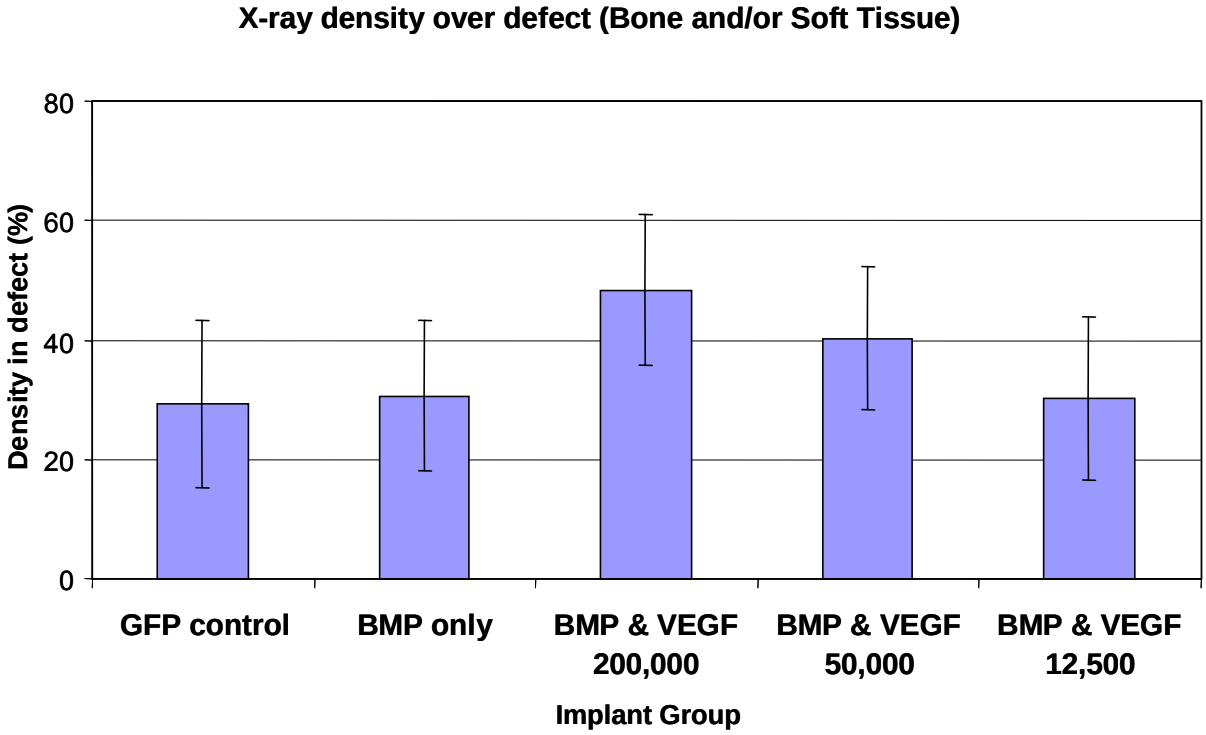

Figure 9. Tissue Density in Calvarial Defects after 4 weeks with transplantation of BMP-4- and/or VEGF-A-expressing MSCs. Calvariae were implanted with 3 x 10^5 modified MSCss and dissected after 4 weeks. X-ray images of the calvariae were taken with a Faxitron MX20 system using Cronex 10T medical X-ray film. Density over the defect area was determined from the film on a low light imaging system (Alpha Innotech) and analyzed with Chemi-Imager 4400 software. Values are average (± SD) from 4 animals for each group, which received (from left to right): 3 x 10^5 GFP control cells; 1 x 10^5 BMP4 + 2 x 10^5 GFP cells; 1 x 10^5 BMP4 + 2 x 10^5 VEGF-A cells; 1 x 10^5 BMP4 + 5 x 10^4 VEGF-A + 1.5 x 10^5 GFP cells; 1 x 10^5 BMP4 + 5 x 10^4 VEGF-A + 1.5 x 10^5 GFP cells; and 1 x 10^5 BMP4 + 1.25 x 10^4 VEGF-A + 1.875 x 10^5 GFP cells.

We have also performed dose-response experiments of VEGF-A (from 5 x 10^5 to 1 x 10^6 VEGF-A-expressing MSCs) with or without 1 x 10^5 BMP-4-expressing MSCs and measured soft and bony tissues within the defects after 4 weeks. While we found that in the absence of BMP-4-expressing cells the implanted VEGF-A-expressing MSCs increased vascularization in an apparent dose-dependent manner, but not soft tissue or bone formation, addition of 2 x 10^5 or 5 x 10^4 VEGF-A cells increased the amount of soft tissue formed after 4 weeks in the presence of 1 x 10^5 BMP cells (Figure 9). The increase in soft tissue density was dose-dependent at the higher VEGF-A cell concentration, and had reached background levels with the lowest amount of VEGF-A cells implanted in this experiment (1.25 x 10^4 cells). While there was no increased formation of mineralized bone in this combination of BMP-4 and VEGF-A cells, the increase in soft tissue formation was only seen with the combination of BMP-4 and VEGF-A cells, and not with VEGF-A cells alone (Figure 9). Accordingly, the VEGF-A treatment led to a massive increase in highly vascularized, soft tissue. When the total material density of both hard and soft tissues over the defect were measured by X-ray and the Alpha Innotech light imaging system, quantified by the Chemi-Imager 4400 software, the BMP4/VEGF-A combination therapy produced a dose-dependent (with respect to the number of VEGF-A expressing cells) decrease compared to BMP4 treatment alone. Our results are very different from that of Peng et al. (5), which reported synergistic enhancement of bone formation and healing of segmental defects in the long bones by muscle stem cell-expressed VEGF-A and BMP-4. Potential explanations for the differences seen in our studies and their study include, but are not limited to, the use of different bony defect model (calvarial defect model vs. long bone segmental defect), the different vehicle (MSCs vs. muscle stem cells), or the cell dosages. Regardless of the reasons, our data confirm that the *ex vivo* BMP4 gene therapy can effectively repair the mouse critical-sized calvarial defect. However, the presence of VEGF expressing cells did not synergistically enhance the bone formation response of BMP4 in this model. Thus, our findings clearly do not support a synergistic enhancement between BMP2/4 and VEGF in bone formation at the test doses.

We should emphasize that VEGF-A is known to play an important role in bone repair by promoting angiogenesis as well as the recruitment and survival of chondrocytes, osteoblasts, and osteoclasts at the site of injury. VEGF-A is particularly important for hypertrophic cartilage remodeling and ossification during endochondral bone formation. More recently, VEGF has been shown to be an early mediator of intramembranous bone formation in response to mechanical force (distraction osteogenesis) [22]. Therefore, we cannot rule out the possibility that the absence of a significant increase in bone regeneration in the presence of both BMP-4- and VEGF-A-expressing could be due to the fact that the ratio of BMP-4 and VEGF-A expression has not been optimized in our studies.

b) Bone regeneration effects of MSC-based *ex vivo* MLV-BMP2/4 and MLV-Cox-2 gene transfer strategies, alone or in combination, in the mouse critical-sized calvarial defect model. We next determined the relative potency of the MLV-BMP2/4- or MLV-Cox-2-based *ex vivo* gene transfer combination strategy in promoting healing of critical-sized calvarial defects in syngeneic C57BL/6J mice. In this experiment, Gelfoam scaffold disk impregnated with a total of 1 x 10^6 mouse MSCs cells transduced with the MLV-BMP2/4, MLV-Cox-2, or MLV-β-gal control vector, was implanted into the critical-sized defect of a group of five mice each. To evaluate bone regeneration effect of the BMP2/4 and Cox-2 combination strategy, an additional group of five mice were implanted with Gelfoam scaffold disks, impregnated with 8 x 10^5 MLV-

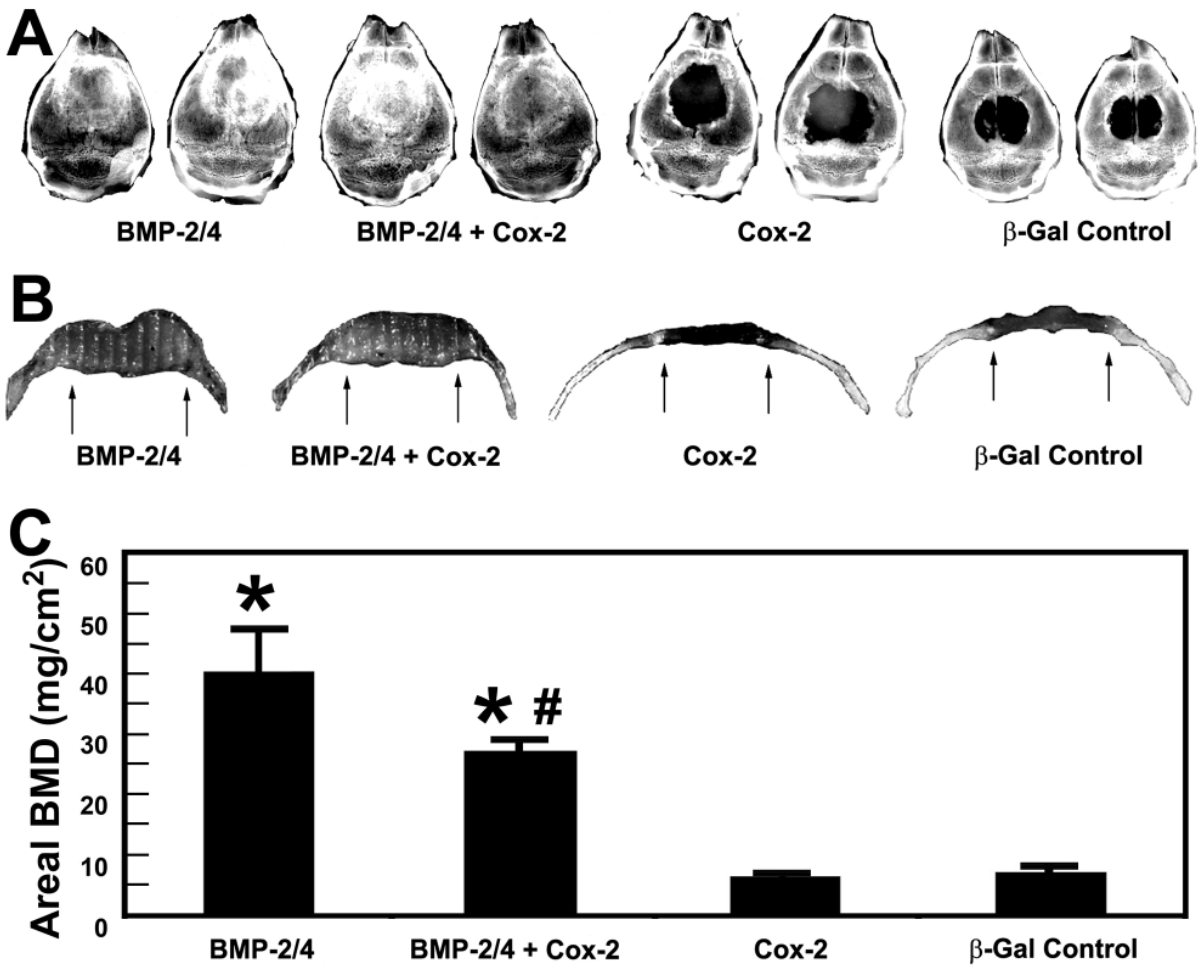

Figure 10. Comparison of bone regeneration effects of BMP4 *ex vivo* gene transfer strategy and Cox-2 *ex vivo* gene transfer strategy each alone or in combination in the mouse critical-sized calvarial defect model. A: digital soft X-ray image of healing calvariae of two representative mice per group after two weeks of healing. Each defect was implanted with a Gelfoam implant containing a total of 1 x 10^6 MSCs: BMP-2/4 group received 1 x 10^6 MLV-BMP2/4-transduced MSCs; BMP-2/4 + Cox-2 group received 8 x 10^5 MLV-BMP2/4-transduced MSCs along with 2 x 10^5 MLV-Cox-2-transduced MSCs; Cox-2 group received 2 x 10^5 MLV-Cox-2-transduced MSCs and 8 x 10^5 MLV-β-gal-transduced control cells; and the control group received 1 x 10^6 MLV-β-gal-transduced control MSCs only. B: Cross-sectional images of calvarial defect of a representative mouse of each treatment group after four weeks of healing. Old lamellar bone was stained with Goldner's stain. Arrows mark the edges of the 5-mm defects. C: The areal BMD (by PIXImus DEXA) over the healing calvarial defects after 4 weeks of healing. Results are shown as mean ± SD from 4 mice per treatment group. *$p<0.05$, compared to the control group, and $^{\#}p<0.05$, compared with the BMP-2/4 alone group.

BMP2/4-transduced MSCs and 2 x 10^5 MLV-Cox-2-transduced MSCs. Assessment of bone regeneration over the defect by soft X-ray at 2 weeks (Figure 10A) revealed that calvarial defects implanted with MSCs expressing BMP4 with or without Cox-2 were completely healed. As reported earlier, the bone regeneration ability of BMP4 was so potent that the regenerated bone overfilled the defect as the thickness of the regenerated bone exceeded that of the surrounding original intact bone (Figure 10B). In contrast, no X-ray evidence for bone formation was seen in defects implanted with Cox-2-expressing cells (Figure 10A). The Cox-2-treated and control defects were filled mostly with soft tissues (data not shown).

Previous experiments utilizing Cox-2 as the therapeutic gene in a rat femur fracture model have shown that significant Cox-2-mediated increases in bone formation did not occur until 14 to 21 days post-treatment [7]. To evaluate if the Cox-2-mediated calvarial healing is also delayed, we extended the healing time to 4 weeks in a repeat experiment. Fig. 10C shows that the areal BMD over the defect area of mice implanted with BMP4 cells alone reached 159±57% of the area BMD of surrounding intact bone (i.e., 40.1±7.5 mg/cm^2 vs. 25.3±1.2 mg/cm^2, $p<0.01$). No significant bone regeneration occurred in defects receiving only Cox-2-expressing cells even after 4 weeks, as the areal BMD within the defect of the Cox-2 alone group was not different significantly from that of the β-gal negative control group (i.e., 6.5±0.5 mg/cm^2 vs. 7.4±0.9 mg/cm^2, p=N.S.). Implants with combination of BMP4- and Cox-2-expressing cells resulted slightly but significantly lower in areal BMD (i.e., 27.0±2.3 mg/cm^2 vs. 25.3±1.2 mg/cm^2, $p<0.05$) than that with BMP-4-expressing cells alone, suggesting that the Cox-2 strategy might have even suppressed the bone regeneration action of BMP4 in this calvarial defect model.

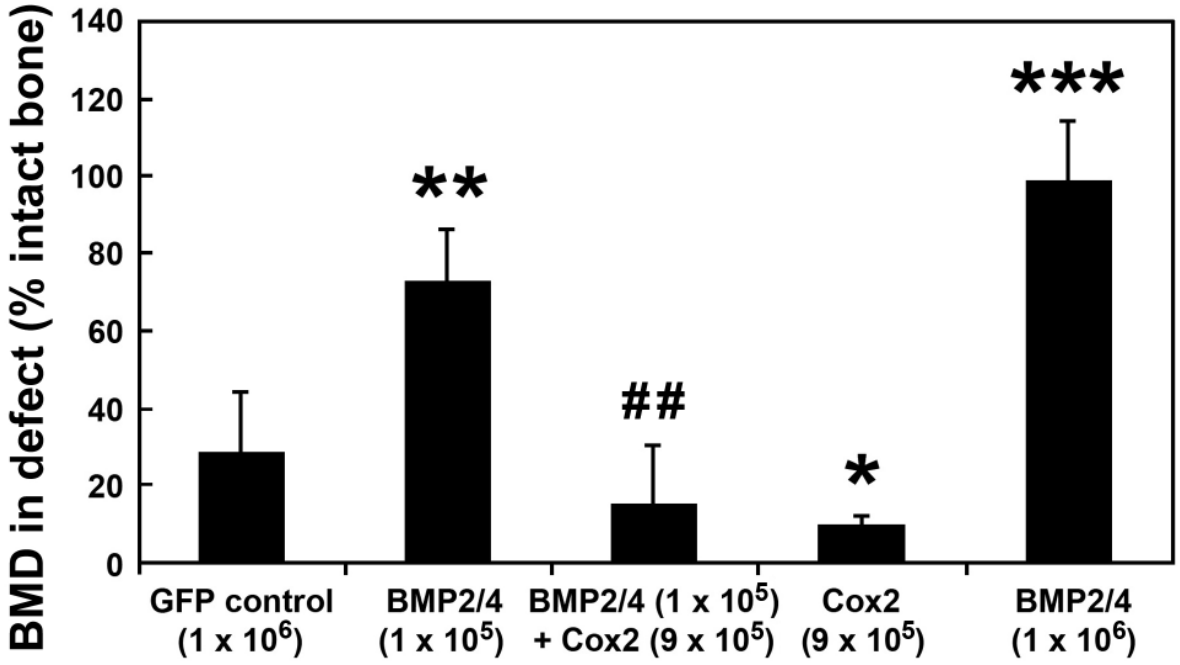

Figure 11. Bone regeneration in mouse critical-sized calvarial defects after 4 weeks with BMP-4 and Cox-2 *ex vivo* gene-transfer strategy each alone or in combination. Mouse critical-sized calvarial defects were implanted with Gelfoam impregnated with 1 x 10^6 GFP expressing primary mouse marrow stromal cells alone (Control Cells), 1 x 10^5 BMP4 expressing cells plus 9 x 10^5 GFP control cells (BMP4 Cells), 9 x 10^5 Cox-2 expressing cells plus 1 x 10^5 BMP expressing cells (BMP4 Cells + Cox-2 Cells), or 9 x 10^5 Cox-2 expressing cells plus 1 x 10^5 GFP expressing control cells (Cox-2 Cells). Areal BMD was determined as described in Methods after 4 weeks. Results are shown as relative percentage of the surrounding original intact bone. Values are shown as average ± S.D. from 4 animals per test group. *$p<0.05$; and **$p<0.01$ compared with Control cells group, $^{\#\#}p<0.01$ compared with BMP4 cells group.

The total number of BMP4-expressing cells in the absence of Cox-2-expressing cells in this particular experiment was 20% more than that in the BMP4 and Cox-2 combination group (1 x 10^6 cells vs. 8 x 10^5 cells). Thus, to rule the possibility that the reduced bone regeneration effects could have been due to the 20% less BMP4-expressing cells in the combination group, we

repeated the experiment with two modifications: 1) the number of BMP4-expressing MSCs in Gelfoam scaffolds was kept at 1 x 10^5 cells per implant, and 2) the number of Cox-2-expressing cells was increased to 9 x 10^5 cells per implant to enhance the chance of detecting suppressive effects of the Cox-2 strategy. Appropriate numbers of GFP-expressing control MSCs were added to each Gelfoam implant to maintain the number of total MSCs in the scaffold at 1 x 10^6 cells. There were five test groups with four mice each: 1) negative control group, which received an implant containing 1 x 10^6 GFP-expressing MSCs; 2) the BMP4 alone group, which received 1 x 10^5 BMP4-expressing MSCs and 9 x 10^5 GFP-expressing control cells; 3) the BMP4-Cox-2 combination group, which received 1 x 10^5 BMP4-expressing MSCs and 9 x 10^5 Cox-2-expressing cells; 4) the Cox-2 alone group, which received 9 x 10^5 Cox-2-expressing cells and 1 x 10^5 GFP-expressing control cells; and 5) a positive control group, which received 1 x 10^6 BMP-4-expressing cells. Figure 11 shows that defects treated with this dosage of BMP4-expressing cells alone significantly increased areal BMD over the defect area to ~70% of that of surrounding original calvarial bone. Defects receiving Cox-2 expressing cells alone not only did not increase but slightly reduced the areal BMD over the defect area, when compared to control defects that received only the GFP-expressing cells. The most striking observation was the complete suppression of the bone regeneration response to the BMP4-expressing cells when they were combined with 9-fold excess of Cox-2-expressing cells. This experiment has been repeated three times with different ratios of BMP4-expressing cells to Cox-2-expressing cells (i.e., 1:1, 1:3, and 1:9), and each yielded significant suppressive effects of the Cox-2 strategy on the bone regeneration action of BMP4 in healing of the critical-sized calvarial defects. However, because of the differences in viral titers, transduction efficiencies, growth rate of transduced mouse marrow stromal cells, etc., the amounts of BMP4 and/or Cox-2 protein produced by the same number of transduced cells could vary in different experiments. Thus, the absolute values of changes in mineral density varied from experiment to experiment. However, the suppression of the BMP4 bone formation response in this defect model was reproducible and seen in every repeat experiment. The suppression of bone formation response of BMP4 by Cox-2 was confirmed with histology (data not shown). In short, our findings not only did not support a synergistic enhancement between BMP4 and Cox-2 gene therapy, at least at the test dose, in bone formation with the mouse calvarial defect model. These observations are intriguing but also very puzzling, as we anticipated that even if Cox-2 had no bone formation effect or enhancing effect in bone formation, Cox-2 should not abrogate the bone formation effects of BMP2/4. Because the finding that Cox-2 blocked BMP2/4 in stimulating bone formation could be relevant to the molecular mechanism of Cox-2 in the regulation of bone formation. Consequently, our work in Technical Objective #5 has focused on the mechanistic reasons for the lack of bone regeneration effects of the Cox-2 *ex vivo* gene transfer strategy and its apparent suppressive effects on the bone regeneration actions of BMP-4 in healing of the critical sized calvarial defects in the mouse.

5. Technical Objective #5. Initiation of studies in determining the molecular mechanism of bone formation by osteogenic growth factors. Two key findings of this project are surprising and also very intriguing. First, despite the large body of *in vitro* and *in vivo* evidence that Cox-2 and its biological product, PGE_2, are potent osteogenic factors [19,23], there is complete lack of X-ray, densitometric, and/or histological evidence for an osteogenic response to the MSC-based Cox-2 *ex vivo* gene transfer strategy in the healing of the mouse critical-sized calvarial defect in this study. The apparent lack of bone regeneration response to the MSC-based Cox-2 *ex vivo*

gene transfer strategy was not due to inefficient retroviral transduction of primary mouse MSCs, since the transduction efficiency of our MLV vectors in these cells was ~90%. *In vitro* characterization of the MLV-Cox-2-transduced MSCs revealed that the transduced MSCs produced up to 3,000 ng of mature human Cox-2 protein per million cells per 24 hrs. This amount of human Cox-2 protein was similar to that of mature human BMP4 protein produced and secreted by MLV-BMP2/4-transduced MSCs [4], which induced massive bone formation when implanted in the mouse calvarial defect model in this study. Thus, the lack of bone regeneration response to the Cox-2 strategy was probably not due to ineffective Cox-2 production by the transduced MSCs. Similarly, the lack of bone regeneration response was also not due to production of inactive Cox-2 protein, since our previous studies have demonstrated that the human Cox-2 protein produced by rat MSCs with our MLV-based vectors was able to induce PGE_2 biosynthesis, promote osteoblastic differentiation of MSCs *in vitro*, and enhance fracture healing *in vivo* [7].

To assess the potential mechanistic reasons for the lack of osteogenic actions of Cox-2, we first sought to confirm the synergistic interaction between Cox-2 and/or its bioactive product PGE_2 and BMP4 *in vitro*. To test our assumption that Cox-2 (or PGE_2) would produce synergistic interaction with BMP4 on osteoblastic differentiation of MSCs *in vitro*, we treated mouse MSCs with 200 ng/ml recombinant BMP4 protein, 10 μM PGE_2, or both. To monitor osteoblastic differentiation, we measured cellular ALP activity (a well-accepted marker of osteoblast differentiation [36]) in extracts of treated MSCs after 3 and 7 days. Figure 12A shows that treatment with BMP4 alone for 7 days led to ~8-fold increase in ALP activity, and treatment with PGE_2 alone for 7 days also yielded ~2-fold increase. The combination treatment with PGE_2 and BMP4 yielded a significantly bigger increase ($p < 0.05$, ANOVA) compared to BMP-4 or PGE_2 alone. Same results were also seen after 3 days of treatment (data not shown). These results were highly reproducible and were obtained in two repeat experiments.

To test if Cox-2 would also act synergistically with BMP4 on osteoblastic differentiation of MSCs *in vitro*, we assessed the effects of co-culture of Cox-2-expressing MSCs with BMP4-expressing cells on cellular ALP activity compared to that in the BMP4 or Cox-2 alone group at three different cell densities (i.e., 50,000 cells, 25,000 cells, or 10,000 cells of each transduced cell type) of BMP4- and Cox-2-expressing MSCs (each in 1:1 ratio). As expected, BMP4-expressing cells showed significant increases in ALP activity after 7 days in culture compared to GFP-expressing control cells, and the extent of the increase was proportional to the number of BMP4-expressing cells plated (Figure 12B). When Cox-2-expressing cells were co-cultured with BMP4-expressing cells, the increase in ALP activity was significantly ($p<0.05$, ANOVA) greater than that in BMP4-expressing cells alone, suggesting a synergistic stimulation by Cox-2-expressing cells. The synergistic interaction was seen in all test cell densities, and was also observed after 3 days (data not shown).

The mechanism(s) responsible for the surprisingly lack of bone regeneration response to the *ex vivo* Cox-2 strategy is unclear. There are several potential mechanistic explanations. First, most of past studies that demonstrated bone regeneration effects of Cox-2 and PGE_2 were performed with long bones [7,15,18,23,24], which utilize both endochondral and intramembranous bone formation for bone regeneration and repair [25]. In contrast, the healing of calvarial defects involves only intramembranous bone formation [26]. Thus, it may be

possible that Cox-2 (and/or PGE_2) stimulates only endochondral, but not intramembranous, bone formation. However, we do not favor this possibility, since mice deficient in Cox-2 expression exhibited impaired intramembranous as well as endochondral bone formation [15].

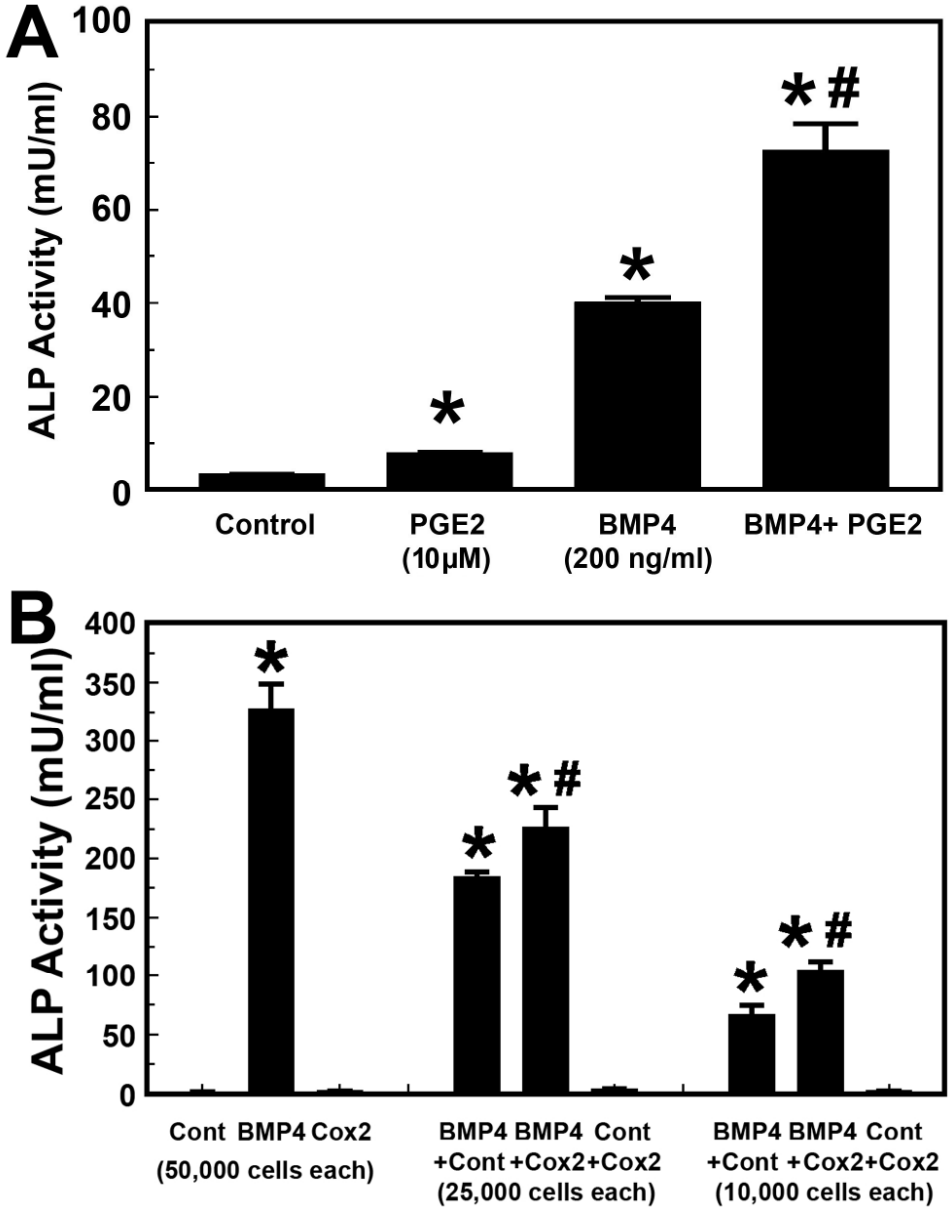

Figure 12. Synergistic stimulation of ALP expression in primary mouse MSCs by PGE_2 (A) or Cox-2 expression (B) and BMP4 *in vitro*. A: Primary mouse MSCs were treated with PGE_2 (10 μM), recombinant human BMP4 (200 ng/ml), each alone or in combination as described in the Materials and Methods. The ALP activity in each extract is shown as mean ± S.D. *$p<0.05$, compared to the vehicle control, and $^{\#}p<0.05$, compared with BMP4 alone. ANOVA indicates a significant ($p<0.05$) interaction between PGE_2 and BMP4 treatment. B: Cellular ALP activity in 7 days cultures with various numbers (i.e., 50,000, 25,000, or 10,000) of BMP4-expressing mouse MSCs, Cox-2-expressing MSCs, or GFP-expressing control MSCs is shown as mean ± S. D. (n = 6 per group). *$p<0.05$, compared to GFP-expressing control cells; and #$p<0.05$, compared to each corresponding BMP4-expressing cell group. ANOVA indicates a significant ($p<0.05$) interaction between Cox-2 and BMP4 treatment.

The second possibility relates to the fact that the Cox-2-expressing cells were placed at the center of the Gelfoam disk, which was then inserted into a relatively large (5 mm, i.d.) calvarial defect. Accordingly, the Cox-2-expressing cells were located some distance away from the edge of the defect, where bone regeneration would take place. Cox-2 is an intracellular enzyme and its anabolic actions are mediated primarily by PGE_2. It is presumed that the secreted PGE_2 will permeate towards the edge of the defect to promote bone regeneration. In order for a significant bone regeneration response, the impregnated Cox-2-expressing MSCs within the Gelfoam scaffold must be able to produce sufficient amounts of PGE_2 that would permeate to the edge of the healing defect. However, our recent findings indicate that MLV-Cox-2-transduced rat MSCs produced several-fold less PGE_2 than MLV-Cox-2-transduced rat osteoblasts *in vitro* [7], raising the possibility that MSCs may have significantly lower capacity for PGE_2 production compared with osteoblasts. Thus, it is possible that the MLV-Cox-2-transduced mouse MSCs may not produce sufficient PGE_2 gradient needed to elicit a bone regeneration response in this calvarial defect model. Quantitative analysis of the concentration gradient of PGE_2 within the healing defect would provide helpful clues about the validity of this possibility. However, we did not measure the PGE_2 production within the Gelfoam scaffold in this study, because reliable determinations of the PGE_2 gradient within Gelfoam scaffolds are technically difficult. On the other hand, our findings that increasing the cell dosage of Cox-2-expressing cells from 1×10^5 cells to 9×10^5 cells per scaffold not only did not enhance, but even suppressed, the basal bone formation response when compared to the GFP-expressing control MSCs would argue against this possibility.

Recent evidence has suggested that Cox-2 has a suppressing effect on the proliferation of osteoblasts [27]. Thus, the third possibility is that the lack of bone regeneration response of the Cox-2 strategy is due in part to the suppressive effect of Cox-2 on the proliferation of osteoblastic cells at the defect site. However, although we did not measure the effects of Cox-2-expression on the proliferation of murine MSCs, we did not note large differences in the cell population doubling time between the MLV-Cox-2-transduced MSCs and the MLV-β-gal-transduced control MSCs as well as the untransduced murine MSCs. On the other hand, we cannot completely dismiss this interesting possibility.

A recent study showed that MSCs and calvarial osteoblasts of Cox-2-deficient mice exhibited an enhanced response to the PTH-induced osteoblast differentiation and bone nodule mineralization *in vitro* and that the Cox-2 specific inhibitor (NS-398) also synergistically enhanced the osteogenic effects of PTH in MSCs and calvarial osteoblasts of wild-type mice [28]. This would suggest that Cox-2 may have potential suppressive effects on the osteogenic action of PTH *in vivo*. Although the mechanism by which Cox-2 suppresses the osteogenic action of PTH has not been defined, it is suggested that Cox-2 and/or PGE_2 reduce the osteogenic action of PTH by either inhibiting the suppressive action of PTH on the expression of sclerostin, a key inhibitor of the Wnt signaling [29], or directly increasing the expression of sclerostin in osteoblastic cells [28]. The potential inhibitory effect of Cox-2 (and/or PGE_2) on the osteogenic action of PTH could be pertinent to the potential mechanism for the lack of bone regeneration response in intramembranous bone formation to the Cox-2 *ex vivo* gene transfer strategy, since PTHrp (and perhaps also PTH) has been reported to be required for normal intramembranous bone development [30]. Unfortunately, our original experimental design did

not include measurements of the expression levels of sclerostin in the healing defects. The concept that Cox-2 could have suppressive effects on the osteogenic actions of other bone growth factors through regulation of secretion of sclerostin is very interesting and will be pursued in our future studies.

The second and more puzzling observation of this study is that the Cox-2 *ex vivo* gene transfer strategy when used in combination with the BMP2/4 strategy not only did not synergistically enhance, but actually suppressed, the bone regeneration action of the BMP4 strategy in this critical-sized calvarial defect model. The suppressive action of Cox-2-expressing cells on the BMP4-mediated bone regeneration appeared to be dose-dependent, as the inhibition was greater in the presence of more Cox-2-expressing cells (i.e., 9:1 ratio of Cox-2-expressing cells to BMP4-expressing cells) than in the presence of less Cox-2-expressing MSCs (i.e., 1:4 ratio of Cox-2-expressing cells to BMP4-expressing cells), suggesting that the suppressive effects were mediated through Cox-2 expression in the transduced cells.

The mechanism(s) contributing to the suppressive effects of Cox-2 expression on the bone regeneration actions of the nearby BMP4-expressing MSCs in healing critical-sized calvarial defects *in vivo* can only be speculated. In this regard, the recent findings that Cox-2 and/or PGE_2 suppress the osteogenic action of PTH through an increase in expression of sclerostin [28] and that sclerostin is a potent inhibitor of the osteogenic actions of BMPs [31], raise the interesting possibility that the increased sclerostin expression in osteoblastic MSCs mediated by the Cox-2 *ex vivo* gene transfer strategy may suppress the bone regeneration action of the BMP4 strategy. On the other hand, our *in vivo* studies have clearly demonstrated that Cox-2 and/or PGE_2 not only did not suppress, but synergistically enhance, the BMP4-induced osteoblastic differentiation of the transduced MSCs do not support an direct inhibitory effect of Cox-2 and/or PGE_2 on the osteogenic actions of BMP4 (Figure 12). However, our *in vitro* findings did not preclude the possibility that the *in vivo* inhibitory effects of Cox-2 and/or PGE_2 may be mediated through indirect actions of Cox-2 and/or PGE_2 on the expression of inhibitory proteins, such as sclerostin, in other cell types, such as osteocytes. In addition, although it is generally assumed that the biological actions of Cox-2 are mediated primarily through PGE_2, Cox-2 also produces other eicosanoids, including other prostaglandins, prostacyclin, leukotrienes, and thromboxanes. There is also the remote possibility that the suppressive action of Cox-2 on BMP4-induced bone regeneration may be mediated through these eicosanoids.

It may be possible that co-culturing of Cox-2-expressing MSCs with BMP4-expressing MSCs in Gelfoam scaffolds together might suppress BMP4 expression in BMP4-expressing MSCs through Cox-2 or PGE2-mediated gene silencing. To test if the suppressive action of the Cox-2 strategy on the bone regeneration effect of the BMP4 strategy was in part mediated by Cox-2-dependent inhibition of BMP4 expression in Gelfoam scaffolds, we measured the relative levels of human BMP4 mRNA transcript in Gelfoam impregnated with 1×10^5 BMP-4 expressing MSCs in the absence or presence of low (1×10^5 cells per scaffold) and high (9×10^5 cells per scaffold) numbers of Cox-2-expressing MSCs after incubation in culture medium for 1 day or 4 days *in vitro*. To ensure that there were sufficient numbers of cells to cover the entire scaffold that would yield more optimal recovery of total RNA isolation, the total number of transduced MSCs in each scaffold was increased to 2×10^6 cells by supplementing them with GFP-expressing MSCs. The relative level of human BMP4 mRNA was normalized against

mouse GAPDH mRNA transcript to adjust for variations in the cell number. There was a time-dependent decrease in the human BMP4 mRNA transcript, normalized against the endogenous mouse GAPDH mRNA transcript level in Gelfoam scaffolds (Figure 13). Because there were no significant time-dependent changes in the GAPDH mRNA levels (data not shown), the reduction of BMP4 mRNA transcript may be due to gene silencing of the human BMP4 transgene in the transduced MSCs, which is not unexpected because time-dependent silencing of the transgene expression is known to occur with MLV-based vectors [32]. However, the time-dependent decrease in the human BMP4 mRNA transcript was significantly enhanced ($p<0.05$, ANOVA) by the presence of Cox-2-expressing MSCs (Figure 13). Again, because the presence of Cox-2-expressing MSCs also did not alter the GAPDH mRNA level, it appears that Cox-2 overexpressing cells further augmented the silencing of BMP4 transgene expression in MLV-BMP4-transduced MSCs.

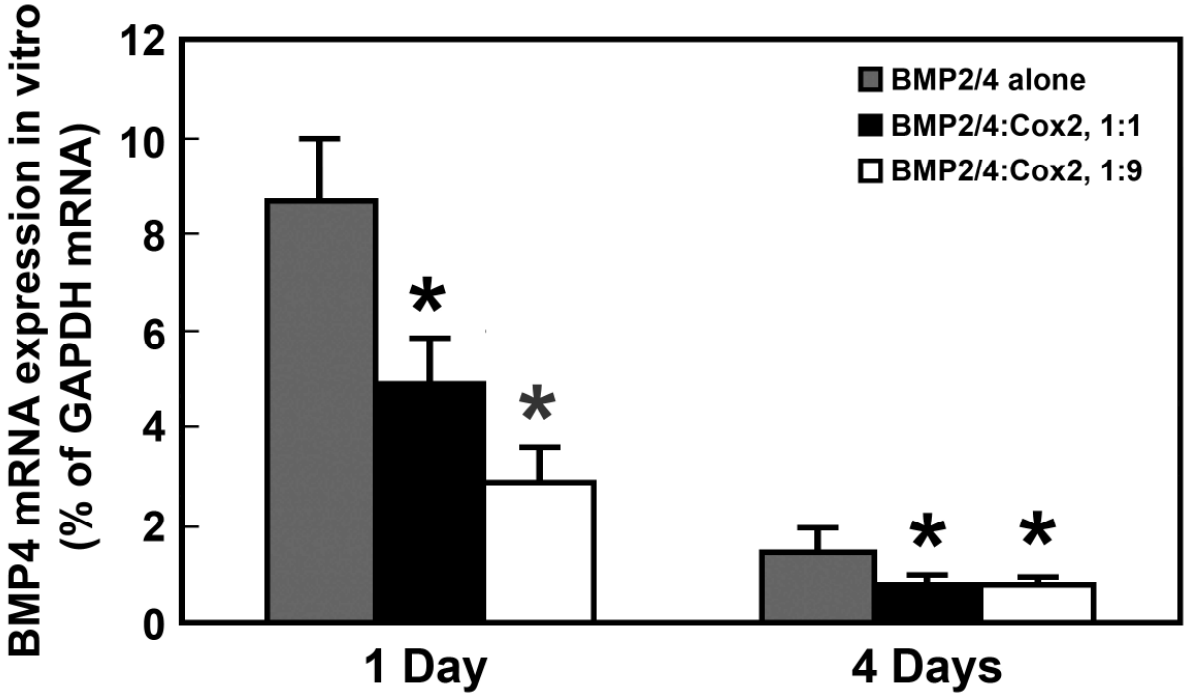

Figure 13. Effects of Cox-2 expression on BMP4 transgene expression in MLV-BMP2/4-transduced mouse MSCs *in vitro*. Gelfoam disks (5 x 10 mm) were impregnated with 2 x 10^5 BMP4-expressing MSCs in combination with Cox-2-expressing MSCs (or GFP-expression cells) in 1:1 or 1:9 ratios. The total number of transduced cells in each Gelfoam scaffold was 2 x 10^6 cells. After 1 day or 4 days in culture, the disks were washed briefly with phosphate-buffered saline, cut in half, and the total RNA was isolated and reverse-transcribed to cDNA. The relative levels of human BMP4 transgene transcript was determined by real-time RT-PCR assay using a primer set specific for human BMP4. The relative human BMP4 transcript levels (as percentage of endogenous GAPDH transcript level) are shown as average ± SD from three scaffolds per group. Each was done in triplicate. *$p<0.05$ compared to the BMP2/4 alone.

Our finding that co-culturing of Cox-2-expressing MSCs with BMP4-expressing MSCs in Gelfoam scaffolds *in vitro* significantly reduced the total BMP4 mRNA transcript level raised yet another potential mechanism. This observation can be interpreted as that co-culturing of BMP4-expressing cells with Cox-2-expressing cells in the context of Gelfoams could lead to gene silencing of the BMP4 transgene expression in BMP4-expressing cells. Alternatively, it

may also be interpreted as that the presence of Cox-2-expressing cells somehow induced death (apoptosis) of BMP4-expressing cells. While our experimental design did not allow us to distinguish the two alternative interpretations, our data that co-culture of BMP4-expressing cells and Cox-2-expressing cells in the Gelfoam matrix did not yield similar decrease in the mRNA transcript level of the housekeeping gene, GAPDH, is consistent with a mechanism that involves Cox-2-dependent silencing of BMP4 gene expression. In this regard, transcription from retrovirus long terminal repeats (LTR) is known to be silenced in stem cells [32,33]. Both methylase-dependent and -independent mechanisms have been shown to be involved in silencing of LTR promoter [34]. Future studies are needed to identify if Cox-2-induced silencing of LTR promoter occurs *in vivo* and contributes to reduced BMP4 expression and suppression of bone formation at the calvarial defect site.

There may be potential regulatory effects of PGE_2 on bone cell production of BMPs, as it has been reported that PGE_2 treatments increased bone formation and BMP7 mRNA and protein levels *in vivo* and *in vitro*, but the effects of PGE_2 on the increases in BMP7 mRNA and protein levels were mediated through post-transcriptional mechanisms [35]. Thus, we cannot completely dismiss the remote possibility that PGE_2 produced by Cox-2-expressing MSCs, while enhances BMP7 mRNA stability, may decrease the stability of BMP4 mRNA through post-transcriptional mechanisms. This possibility, if confirmed, would provide an alternative mechanism that could explain the significant reduction in the total BMP4 mRNA transcript level, when BMP4-expressing MSCs were co-cultured with Cox-2-expressing MSCs. However, the issue of whether PGE_2 produced by Cox-2 transduced cells would have any effect on the BMP4 mRNA stability remains to be determined.

Healing of the bony defect not only involves the proliferation and activation of osteoblastic cells, but also involves recruitment and migration of osteoblastic cells to the wound site. Accordingly, another possible explanation for the suppressive effects of Cox-2 on the bone healing response of BMP4 may involve a suppression of migration of osteoblastic cells to the center of the wound to establish formation and mineralization of the bone matrix along the wound periphery until the entire defect is filled up with newly bone. Consequently, as a preliminary testing of this interesting possibility, we measured the effect of expression of BMP4 or Cox-2 on cell migration using an in vitro cell migration assay. In this assay, 1 x 10^6 untreated or each test transduced cells were plated in the bottom of the transwell. The number of cells migrated to the membrane from day 3 to day 14 were then measured. Table 1 summarizes the results of this preliminary experiment.

Table 1. Effect of BMP4 or Cox-2 expression on migration of the transduced mouse marrow stromal cells. Results are shown as average ± S.D. (n = 3 per group).

Cells	Cells Migrated to the membrane (x 10^5 cells)	P value*
Untreated cells	4.17 ± 0.10	n.s.
GFP-expressing cells	3.68 ± 0.48	---
BMP4-expressing cells	5.89 ± 0.47	<0.05
Cox-2-expressing cells	4.37 ± 0.55	n.s.

* P values are comparison between the test group and the GFP-expressing control cells.

This preliminary experiment suggests that expression of BMP4 significantly increased the migration of transduced marrow stromal cells. In contrast, expression of Cox-2 also appeared to also slightly (but did not reach statistically significant level due to the small sample size) increased the migration of mouse marrow stromal cells compared to GFP-expressing cells. These findings support the contention that each of these two effects also possesses cell migration promoting activity. This preliminary experiment did not address the issue whether Cox-2 expression would suppress the BMP4-mediated cell migration, which will be done in our future experiment. However, since both agents appeared to promote cell migration, we do not believe the possibility that Cox-2 suppressed BMP4-induced cell migration is a very likely explanation for the suppression effect of Cox-2 on BMP4-induced bone healing.

In addition to stimulating bone formation, Cox-2 induces a number of physiologically important biological actions. Among the various biological actions of Cox-2, Cox-2 is a well-known, potent pro-inflammatory agent. Several pro-inflammatory cytokines, such as TNFα, IL-1 and IL-6, can inhibit bone formation. Therefore, the possibility that the suppressive effects of Cox-2 might suppress the bone formation response of BMP4 in part through its pro-inflammatory cytokine pathways cannot be ruled out. Our future work will attempt to address this possibility. Finally, there is strong evidence that many of Cox-2 biological actions are of biphasic nature. We also cannot rule out the possibility that the suppressive effect might be a result of too high of a dosage of Cox-2-expressing cells. Consequently, we may re-examine if there is potential synergy with reduced dosages of Cox-2-expressing cells in our future work.

In summary, this study discloses two surprising discoveries of the MLV-based Cox-2 *ex vivo* gene transfer strategy in that the Cox-2 *ex vivo* gene transfer strategy, not only completely lacks bone regeneration effects, but also markedly suppresses the bone regeneration action of the BMP4 *ex vivo* gene transfer strategy in healing of mouse calvarial defects in a dose-dependent manner. Our *in vitro* studies have suggested several possible explanations for the lack of an osteogenic action of the Cox-2 strategy and to the suppressive effects of the Cox-2 strategy on the BMP4-induced bone formation at the calvaria defect, but more sophisticated studies will be needed to definitively define the mechanisms.

KEY RESEARCH ACCOMPLISHMENTS

1) Cell culture conditions for the growth of mouse bone marrow derived mesenchymal stem cells (MSCs) have been optimized.
2) MLV-based retroviral vectors expressing recombinant Cox-2 and VEGF-A have been constructed.
3) Mouse MSCs have been shown to be efficiently transduced by MLV-based retroviral vectors, and recombinant Cox-2 and VEGF-A expression has been verified and quantitated *in vitro* over a 4 week period.
4) Surgical techniques needed to produce consistent mouse calvarial critical defects have been established.
5) Transplantation of mouse MSCs expressing human BMP-4 alone was shown to result in complete healing of critical sized mouse calvarial defects by 4 weeks post-treatment.
6) Transplantation of mouse MSCs expressing human Cox-2 alone did not promote regeneration of critical sized mouse calvarial defects at either 2 or 4 weeks post-treatment.

7) Transplantation of mouse MSCs expressing human VEGF-A alone increased blood vessel formation at 2 and 4 weeks post-treatment, but did not promote bone formation at either time point.
8) Cox-2 and VEGF-A combination gene therapy produced no synergistic or enhancing effects on bone regeneration in the mouse calvarial defect model.
9) Transplantation of mixtures of mouse MSCs expressing human BMP-4 and VEGF-A, BMP-4 and Cox-2, and Cox-2 and VEGF-A did not produce a significant increase in bone formation at 4 weeks post-treatment relative to the impact that each of these growth factors had alone.
10) Cox-2-expressing MSCs in high concentration reduced the amount of soft tissue formation in the defect, and in combination with suboptimal concentrations of BMP cells, completely abolish the bone formation response.
11) Very surprisingly, Cox-2 not only did not synergize with BMP-4, but also completely suppressed the bone formation effect of BMP-4 in this mouse calvarial defect healing model. The inhibitory effect of Cox-2 was dose-dependent.
12) *In vitro* studies suggested that Cox-2 or PGE_2 did not appear to have an inhibitory effect on BMP-4 gene expression or the survival of the transduced marrow stromal cells.
13) BMP-4 enhanced alkaline phosphatase expression in marrow stromal cells, Cox-2 or PGE2, a product of Cox-2, not only did not inhibit, but significantly enhanced, the stimulatory effects of BMP-4 on alkaline phosphatase expression in these cells *in vitro*.
14) Cox-2-expressing cells in implant matrix incubated *in vitro*, reduce the production of BMP-4 mRNA from BMP-4-expressing cells. This observation suggests that Cox-2 or PGE2 might induce gene silencing of the BMP4 transgene in BMP4-expressing mouse MSCs, which could explain the suppressive actions of Cox-2 strategy on BMP4 strategy in healing of mouse critical sized calvarial defects.

REPORTABLE OUTCOMES

1. Lau K-HW, Gysin R, Chen S-T, Wergedal JE, Baylink DJ, and Mohan S (2009) Marrow stromal cell-based cyclooxygenase 2 *ex vivo* gene transfer strategy surprisingly lacks bone regeneration effects and suppresses the bone regeneration action of bone morphogenetic protein 4 in a mouse critical-sized calvarial defect model. ***Calcif Tissue Int*** in press. [DOI: 10.1007/s00223-009-9282-2].

CONCLUSIONS

1. The MSC-based VEGF-A and Cox-2 combination *ex vivo* gene transfer strategy did not produce synergistic enhancement in healing of mouse critical sized calvarial defects.
2. Surprisingly, the Cox-2 strategy not only did not promote bone regeneration in the mouse critical sized calvarial defects, but also markedly suppressed the bone regeneration actions of BMP-4 in this bone regeneration model.
3. The findings that Cox-2 and/or PGE_2 significantly and synergistically enhanced the osteogenic effects of BMP4 in mouse mesenchymal cells raise the interesting possibility that Cox-2 and BMP4 interact with each other differently *in vivo* and *in vitro* in stimulating bone regeneration.
4. Cox-2 and/or PGE_2 may induce gene silencing of the human BMP4 transgene in BMP4-expressing mouse MSCs. This may in part be responsible for the unexpected suppression of

the bone regeneration action of the BMP4 *ex vivo* gene transfer strategy to promote healing of critical sized calvarial defects in the mouse.

REFERENCES

1. Klamut HJ, Chen S-T, Lau K-HW, Baylink DJ (2004) Progress toward skeletal gene therapy. Crit. Rev. Eukaryot. Gene Expr. 14:89-136.
2. Peng H, Wright V, Usas A, Gearhart B, Shen H-C, Cummins J, Huard J (2002) Synergistic enhancement of bone formation and healing by stem cell-expressed VEGF and bone morphogenetic protein-4. J. Clin. Inv. 110:751-759.
3. Tarkka T, Sipola A, Jämsä T, Soin Y, Ylä-Herttuala S, Tuukkanen J, Hautala T (2003) Adenoviral VEGF-A gene transfer induces angiogenesis and promotes bone formation in healing osseous tissues. J. Gene Med. 5:560-566.
4. Peng H, Chen S-T, Wergedal JE, Polo JM, Yee J-K, Lau K-HW, and Baylink DJ (2001) Development of an MFG-based retroviral vector system for high secretion of functionally active human BMP-4. Mol. Therapy 4:95-104.
5. Tischer E, Mitchell R, Hartman T, Silva M, Gospodarowicz D, Fiddes JC, Abraham JA (1991) The human gene for vascular endothelial growth factor: Multiple protein forms are encoded through alternative exon splicing. J. Biol. Chem. 266:11947-11954.
6. Simovic D, Isner JM, Ropper AH, Pieczek A, Weinberg DH (2001) Improvement in chronic ischemic neuropathy after intramuscular phVEGF165 gene transfer in patients with critical limb ischemia. Arch. Neurol. 58:761-768.
7. Rundle CH, Strong DD, Chen S-T, Linkhart TA, Sheng M-HC, Wergedal JE, Lau K-HW, Baylink DJ (2008) Retroviral-based gene therapy with cyclooxygenase-2 promotes the union of bony callus tissues and accelerates fracture healing in the rat. J. Gene Med. 10:229-241.
8. Cok SJ, and Morrison AR (2001) The 3'-untranslated region of murine cyclooxygenase-2 contains multiple regulatory elements that alter message stability and translational efficiency. J. Biol. Chem. 276:23179-23185.
9. Lida Y and Masuda T (1995) Quantification analysis of translation initiation signal sequences in vertebrate mRNAs. Nucleic Acids Symp. Ser. (34)**:**103-104.
10. Gysin R, Wergedal JE, Sheng MH-C, Kasukawa Y, Miyakoshi N, Chen S-T, Peng H, Lau K-HW, Mohan S, Baylink DJ. (2002) *Ex vivo* gene therapy with stromal cells transduced with a retroviral vector containing the BMP4 gene completely heals critical size calvarial defect in rats. Gene Therapy 9:991-999.
11. Rundle CH, Miyakoshi N, Kasukawa Y, Chen S-T, Sheng MH-C, Wergedal JE, Lau KHW, and Baylink DJ (2003) *In vivo* bone formation in fracture repair induced by direct retroviral-based gene therapy with BMP-4. Bone 32:591-601.
12. Zhang XS, Linkhart TA, Chen S-T, Peng H, Wergedal JE, Guttierez GG, Sheng MH-C, Lau K-HW, and Baylink DJ (2004) Local *ex vivo* gene therapy with bone marrow stromal cells expressing human BMP4 promotes endosteal bone formation in mice. J. Gene Med. 6:4-15.
13. Krebsbach PH, Mankani MH, Satomura K, Kuznetsov SA, Gehron Robey P (1998) Repair of craniotomy defects using bone marrow stromal cells. Transplantation 66:1272-1278.
14. Blum JS, Barry MA, Mikos AG, Jansen JA (2003) *In vivo* evaluation of gene therapy vectors in *ex vivo*-derived marrow stromal cells for bone regeneration in a rat critical-size calvarial defect model. Human Gene Therapy 14:1689-1701.

15. Zhang X, Schwarz EM, Young DA, Puzas JE, Rosier RN, O'Keefe RJ (2002) Cyclooxygenase-2 regulates mesenchymal stem cell differentiation into the osteoblast lineage and is critically involved in bone repair. J. Clin. Invest. 110:1405-1415.
16. Arikawa T, Omura K, Morita I (2004) Regulation of bone morphogenetic protein –2 expression by endogenous prostaglandin E_2 in human mesenchymal stem cells. J. Cell Physiol. 200:400-406.
17. Chikazu D, Li X, Kawaguchi H, Sakuma Y, Voznesensky OS, Adams DJM, Hoshio K, Katavic V, Herschman HR, Raisz LG, Pilbeam CC (2002) Bone morphogenetic protein 2 induces cyclo-oxygenase 2 in osteoblasts via a Cbfa1 binding site: Role in effexts of bone morphogenetic protein 2 *in vitro* and *in vivo*. J. Bone Miner. Res. 17:1430-1440.
18. Simon AM, Manigrasso MB, O'Connor JP (2002) Cyclo-oxygenase 2 function is essential for bone fracture healing. J. Bone Miner. Res. 17:963–976.
19. Kawaguchi H, Pilbeam CC, Harrison JR, Raisz LG (1995) The role of prostaglandins in the regulation of bone metabolism. Clin. Orthop. 313:36–46.
20. Klenke FM, Gebhard MM, Ewerbecj V, Abdollahi A, Huber PE, Sckell A (2006) The selective Cox-2 inhibitor Celecoxib suppresses angiogenesis and growth of secondary bone tumors: an intravital microscopy study in mice. BMC Cancer 6:9.
21. Peng H, Usas A, Olshanski A, Ho AM, Gearhart B, Cooper GM, Huard J (2005) VEGF improves, whereas sFlt1 inhibits, BMP2-induced bone formation and bone healing through modulation of angiogenesis. J Bone Miner Res 20:2017-2027.Hla T, Neilson K (1992) Human cyclooxygenase-2 cDNA. Proc. Natl. Acad. Sci. USA 89:7384-7388.
22. Carvalho RS, Einhorn TA, Lehmann W, Edgar C, Al-Yamani A, Apazidis A, Pacicca D, Clemens TL, Gerstenfeld, LC. (2004) The role of angiogenesis in a murine tibial model of distraction osteogenesis. Bone 34:849-861.
23. Keila S, Kelner A, Weinreb M (2001) Systemic prostaglandin E_2 increases cancellous bone formation and mass in aging rats and stimulates their bone marrow osteogenic capacity in vivo and *in vitro*. J. Endocrinol. 168:131–139.
24. Keller J (1996) Effects of indomethacin and local prostaglandin E_2 on fracture healing in rabbits. Dan. Med. Bull. 43:317–329.
25. Bolander ME (1992) Regulation of fracture repair by growth factors. Proc. Soc. Exp. Biol. Med. 200:165-170.
26. Komuro Y, akizuki T, Kurakata M, Ohmori K (1999) Histological examination of regenerated bone through craniofacial bone distraction in clinical studies. J. Craniofac. Surg. 10:308-311.
27. Xu Z, Choudhary S, Voznesensky O, Mehrotra M, Woodard M, Hansen M, Herschman H, Pilbeam C (2006) Overexpression of Cox-2 in human osteosarcoma cells decreases proliferation and increases apoptosis. Cancer Res. 66:6657-6664.
28. Choudhary S, Huang H, Raisz L, Philbeam C (2008) Anabolic effects of PTH in cyclooxygenase-2 knockout osteoblasts *in vitro*. Biochem. Biophys. Res. Commun. 372:536-541.
29. Li X, Zhang Y, Kang H, Liu W, Liu P, Zhang J, Harris SE, Wu D (2005) Sclerostin binds to LRP5/6 and antagonizes canonical Wnt signaling. J. Biol. Chem. 280:19883-19887.
30. Suda N, Baba O, Udagawa N, Terashima T, Kitahara Y, Takano Y, Kuroda T, Senior PV, Beck F, Hammond VE (2001) Parathyroid hormone-related protein is required for normal intramembranous bone development. J. Bone Miner. Res. 16:2182-2191.
31. ten Dijke P, Krause C, de Gorter DJ, Löwik CW, van Bezooijen RL (2008) Osteocyte-derived sclerostin inhibits bone formation: its role in bone morphogenetic protein and Wnt signaling. J. Bone. Joint Surg. Am. 90 (Suppl 1):31-35.
32. Pannell D, Ellis J (2001) Silencing of gene expression: implications for design of retrovirus vectors. Rev. Med. Virol. 11:205-217.

33. Gram GJ, Nielsen SD, Hansen JE (1998) Spontaneous silencing of humanized green fluorescent protein (hGFP) gene expression from a retroviral vector by DNA methylation. J. Hematother. 7:333-341.
34. Swindle CS, Kim HG, Klug CA (2004) Mutation of CpGs in the murine stem cell virus retrovial vector long terminal repeat represses silencing in embryonic stem cells. J. Biol. Chem. 279:34-41.
35. Paralkar VM, Grasser WA, Mansolf AL, Baumann AP, Own TA, Smock SL, Martinovic S, Borovecki F, Vukicevic S, Ke HZ, Thompson DD (2002) Regulation of BMP-7 expression by retinoic acid and prostaglandin E_2. J Cell Physiol 190:207-217.

Project 8: Nuclear Targeting of Transposon-Based Plasmid Vectors For Gene Therapy

Introduction

Our primary research objective was to develop improved nonviral plasmid vectors for *in vivo* applications in hard and soft tissues by incorporating into a single vector a nuclear entry sequence to increase transfection efficiency and a transposon to increase long term transgene expression. Plasmid vectors will provide a safer, less expensive and more easily manufactured reagents for gene delivery compared to viral vectors, but have not been widely used for *in vivo* applications because of several different cellular barriers to *in vivo* transfection and transgene expression. These barriers include plasmid entry into the cell, subsequent entry into the nucleus, and for long term expression, stable transgene integration into genomic DNA. After entering cells, traditional plasmids enter the nucleus during mitosis, so transfection efficiency is dependent on active cell proliferation. We and others have identified nuclear entry DNA sequences, such as the virally derived SV40 DTS, that enhance nuclear entry of plasmid DNA and increase *in vivo* transfection efficiency and transgene expression levels even in non- proliferating cells (**Figure. 1** upper panel) (2-13).

Traditional plasmid DNA integrates into genomic DNA randomly and with low efficiently. To improve efficiency of integration, we have developed a single plasmid vector named Prince Charming that expresses the transposase, *Sleeping Beauty* and incorporates the gene of interest but not the transposase coding region within a transposon. The transposase facilitates transposon and transgene integration into AT-rich regions of genomic DNA, resulting in high levels of long term expression (**Figure. 1** Lower panel) (15-23). No single plasmid vector has been developed that incorporates a nuclear entry sequence, transposon with gene of interest, and transposase coding region. We proposed that our plasmid expression vectors with these components would significantly increase nonvi ral transfection efficiency and transgene integration, resulting in higher levels of long term therapeutic gene expression *in vivo* than are possible with existing nonviral gene therapy vectors.

TECHNICAL OBJECTIVE.

Develop and test a novel nonviral protein expression vector for use in gene therapy. The plasmid will contain DNA sequences to a) increase movement of the plasmid DNA into the nucleus and thus increase transfection efficiency and expression levels; and b) produce a transposase to increase stable vector DNA integration into genomic DNA, thus increasing long term transgene expression.

Specific objectives:

1. insert the nuclear entry sequence from the SV40 DNA virus (SV40 DTS) into different positions of an optimized plasmid vector that can express the sleeping beauty transposase (SBT) and a marker gene, Red Fluorescent Protein (RFP).
2. compare expression levels and longevity of marker genes *in vitro* in rat bone marrow stromal cells (MSCs), and osteoblasts transfected with the SBT/SV40DTS plasmid vectors or transduced with a MLV retroviral reporter gene vector.

3. prepare SBT/SV40DTS plasmid and MLV retroviral vectors that express human BMP-4, and test BMP-4 short term expression levels in transfected/ transduced rat MSC cultures.
4. Initiate studies to compare effectiveness of SV40DTS/SBT BMP-4 plasmid and MLV BMP-2/4 viral vector in stimulating osteoblast differentiation in cultured rat MSCs and osteoblasts. Differentiation will be assessed by expression of osteoblast specific marker genes and by development of mineralized nodules.
5. Initiate studies to compare bone formation induced by rat MSCs transduced *in vitro* with SV40DTS/SBT-BMP-2/4 plasmid or MLV BMP-2/4 viral vectors *in vivo* in a rat subcutaneous implant model.

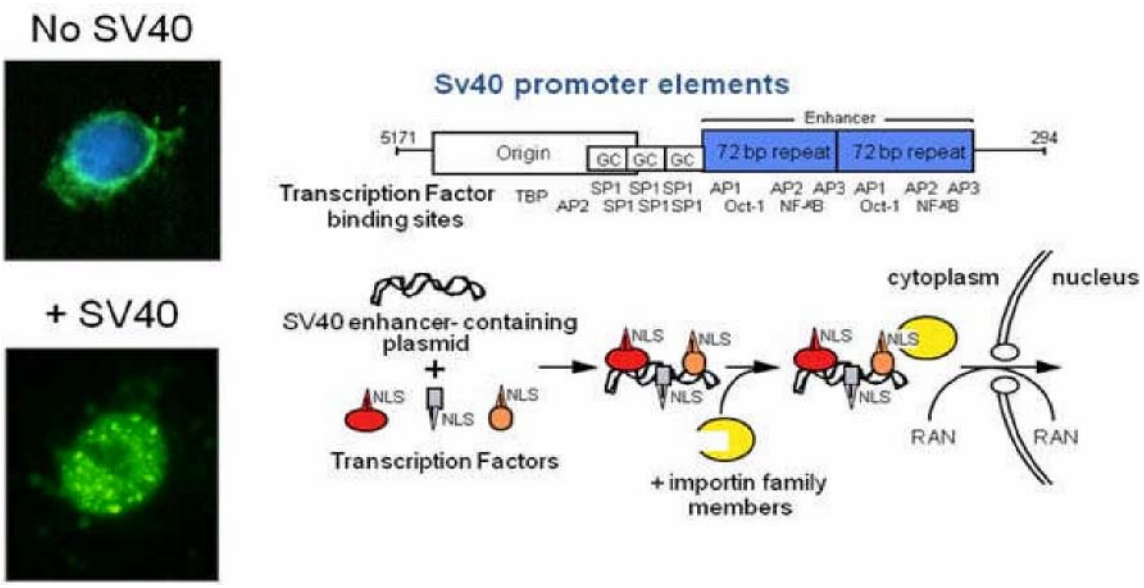

Figure 1. **Merging a DNA nuclear targeting activity with the *Sleeping Beauty* transposon into a single nonviral vector**. The upper panel illustrates the region in the SV40 early promoter that has nuclear targeting activity. Transcription factors with nuclear localization sequences (NLSs) bind to the DNA targeting sequence (DTS) and in conjunction with Importin family proteins facilitate movement of plasmid DNA into the nucleus without cell division. The lower panel illustrates that a transposon with transposase can cut and paste a plasmid segment into the genome. Short inverted repeats (green arrows) that are recognized by the Transposase mark the DNA sequence that is inserted into the genome at TA rich sites. We propose to combine in a single plasmid vector sequence with DTS activity, a transposon with a gene of interest and a transposase expression cassette. Theoretically the resulting vectors should transfect primary cells *in vitro* and *in vivo* with higher efficiencies and the transgenes within the transposon should integrate into the genome to stabilize expression of the gene of interest.

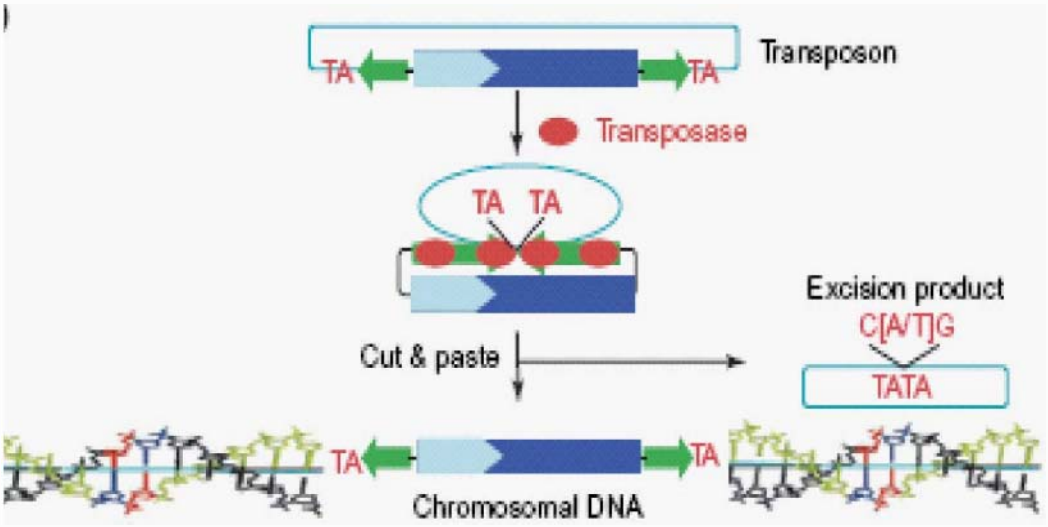

Our studies proposed to prepare novel plasmid vectors with nuclear entry activity, Sleeping Beauty transposase activity, and a transposon with a marker gene or the BMP-2/4 therapeutic gene. We also proposed to show that cells expressing the BMP-2/4 nonviral vector produced BMP-2/4 levels corresponding to levels produced by the retroviral vector MLV-BMP-2/4 (1).

BODY

2.a. **Development of nonviral vectors with a transposon containing a gene of interest (marker gene and BMP-2/4 gene), separate *Sleeping Beauty* Transposase expression cassette and SV40 DNA nuclear targeting sequence.** Vector development was a multistep process conducted by modifying the Prince Charming Vector (pPC) developed by our laboratory (14). This multistep process included removal of the Neomycin cassette from the pPC vector, replacement of the Red Fluorescent Protein (RFP) coding region with a Bone Morphogenetic Protein (BMP)-2/4 coding region also constructed in our laboratory for retroviral gene therapy (1) and addition of a DNA Targeting Sequence (DTS) derived from the SV40 early promoter to facilitate nuclear entry of the plasmid DNA (3). Plasmid or nonviral vectors containing these elements, theoretically should efficiently transfect nondividing cells *in vivo* and be expressed in these cells for longer durations than plasmid vectors now available.

2.a.1. Development of modified pPC based-RFP vectors that contain the *SB* transposon/transposase: The Prince Charming (pPC) vector, which expresses Red Fluorescent Protein that accumulates in the nucleus was reduced in size by 2 kb by PCR by removing the Neomycin expression cassette (**Figure. 2**) to form the A1-50b plasmid vector. This size reduction, should increase transfection efficiency, increase production in *E.Coli* and allow for larger genes

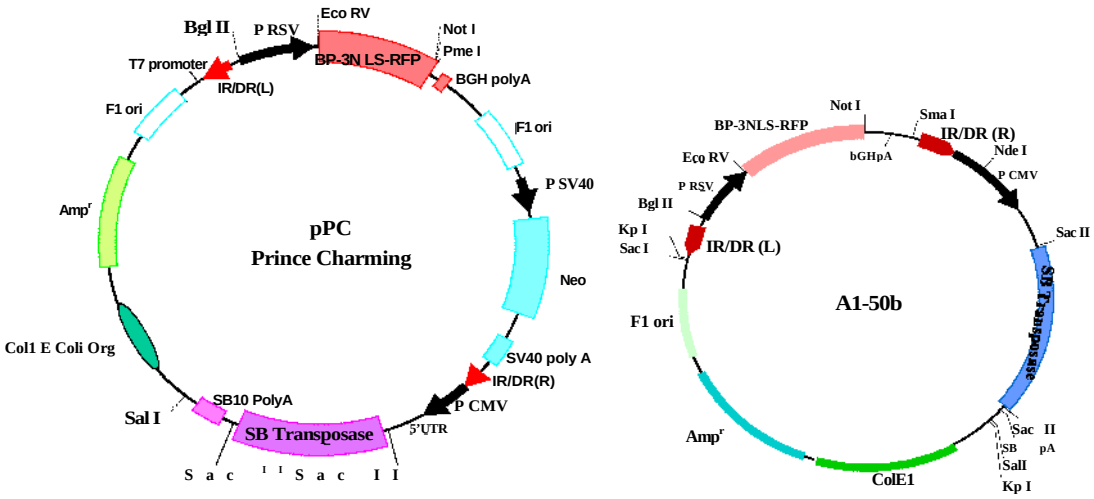

Figure 2. **pPC and A1-50b vector constructs**. The Prince Charming (pPC) and A1-50b plasmid vector derived by PCR from pPC contain the *Sleeping Beauty* (SB) Transposon with red fluorescent protein (RFP) with a nuclear localization sequence on the amino terminal of RFP flanked by the IR/DR elements required for genome integration, and the Sleeping Beauty transposase. When RFP is expressed from this vector it is localized in the nucleus. The RSV promoter (PRSV) drives RFP expression and the CMV promoter (PCMV) drives SB transposase production. The pPC and A150b vectors express an Amp resistance gene. The non-essential Neomycin resistance gene expression cassette was removed from pPC by PCR to produce A1-50b. A1-50b is 2 kb smaller than pPC and smaller plasmid vectors transfect cells with higher efficiency. This size reduction will also allow for the introduction of larger transgenes. Plasmids larger than 10 kb do not efficiently transfect cells.

of interest to be inserted for gene delivery.

The A1 50b vector contains the *SB* Transposase expression cassette which was driven by the strong CMV promoter. It has been reported that high levels of *SB* transposase expression can inhibit the very transposition events that we wanted the vector to facilitate (24). To test this in osteoblasts, we replaced the strong CMV promoter with a minimal TK promoter to reduce SB Transposase production and further reduce the size of the A1 -50b vector.

2.a.2. Development of pPC-based vectors with a SV40DTS-based nuclear entry sequence. A 72 bp segment from the early SV40 promoter (**Figure. 1a**) was found to provide robust nuclear entry activity when inserted in plasmid vectors in a number of cell types *in vitro* and *in vivo* (2).

A synthetic 87 bp double-stranded SV40 DTS (ATGCTTTGCATACTTCTGCCTGCTGGGGAGCCTGGGGACTTTCCACACCCTAACTGACA CACATTCCACAGCTGGTTGGTACCTGCA) was prepared by annealing two single-stranded oligonucleotides. Blunt end ligation of the small SV40 DTS fragments into the pPC-based plasmid vectors as originally proposed did not work and we subsequently changed to sticky-end ligation by adding restriction enzyme sites to the DTS fragment. The SV40DTS was engineered with Sal I or Bgl II overhangs and subcloned into $_{pGL3Basic}$ and peGFP (Clontech) vectors. Large quantities of the SV40DTS with either Bgl II or Sal I 5' and 3' ends could be generated from the purified plasmid vectors or as PCR products from these plasmid templates.

After many attempts, we found that we were unable to subclone the blunt or the sticky-

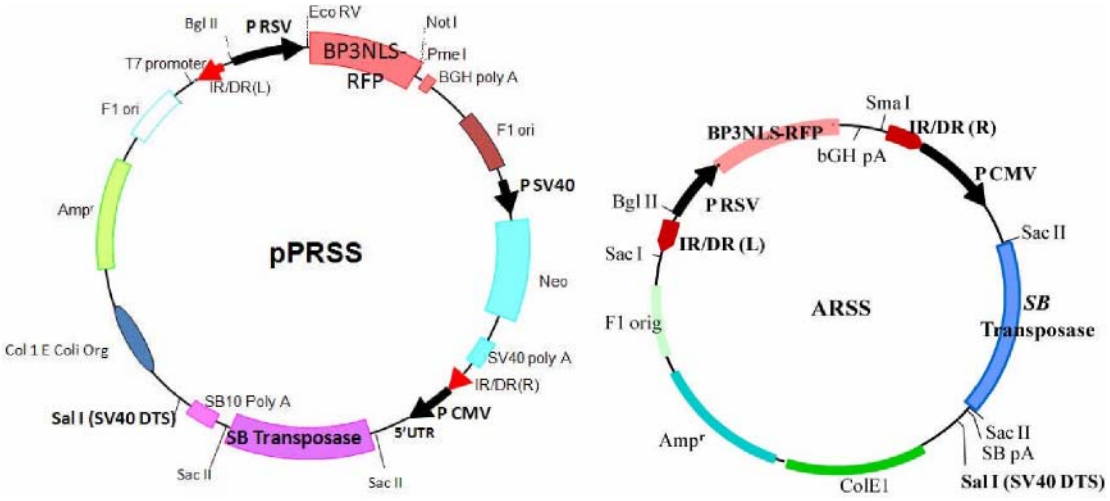

Figure 3. **Structure of the Sleeping Beauty transposon/nuclear entry based plasmid vectors pRRSS and pARSS plasmid vectors developed for expression testing**. The plasmid vectors for gene delivery contain the *Sleeping Beauty (SB)* Transposon with a gene of interest, the *SB* transposase and the DNA nuclear targeting sequence (DTS) from the SV40 early viral promoter. pPRSS and pARSS contain a red fluorescent protein (RFP) marker protein that accumulates in the nucleus.

ended small SV40DTS fragments directly into the A1-50b vector. We were also unable to sequence the A1-50b vector without devising new sequencing strategies (longer primers at distance from the transposon and higher temperatures) suggesting that the vector had significant secondary structure. Because of this problem, the SV40 DTS fragments prepared by PCR or from $_{pGL3Basic-SV40DTS}$ templates were first subcloned into a pPC-based vector, which readily accepted the sticky-end DNA fragments, in single or multiple copies. pPC-based vectors that expressed Red Fluorescent protein (RFP), contained the *Sleeping Beauty (SB)*

Transposon, the *Sleeping Beauty (SB)* Transposase and the SV40DTS in single or multiple copies were named pPRSS. We subsequently removed the Neo Cassette by PCR with Fusion DNA Polymerase (New England Biolabs) and recreated the A1 -50b vector with the SV40 DTS.These were named pARSS. Thus we have both the pPC and A1-50b-based constructs with the SV40 DTS. The SV40 DTS was placed into the SalI site in the pPC vector as one, two or three copies. This vector was reduced in size by PCR to make A1-50b-SalI-SV40DTS (1-3). These vectors are described in Table I.

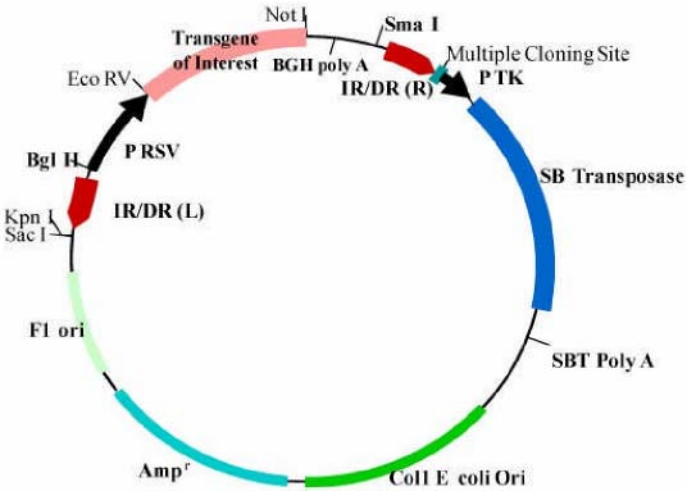

Figure 4. **Structure of the A1-50b-TK-SB vector**. The 6.38 kb modified pPC vector contains the BMP-2/4 expression cassette within the *SB Transposon* defined by the inverted repeats (IR/DRs). Low levels of constitutively expressed *SB* Transposase is driven by the TK promoter. An enhancer to increase expression can be placed in the multiple cloning site using the unique Nhe I or other sites. An optimized Kosak sequence was added to the *SB* Transposase to increase protein production.

Placement of the SV40DTS in the Bgl II sited within the transposon did not significantly alter the plasmid vector characteristics when compared to placement in the Sal I site. Because construction of each of the vectors required so many manipulations, we focused on preparing a full set of vectors with the SV40DTS in the Sal I site.

2.a.3. Development of pPC-based vectors with adjustible *SB* Transposase production. A recent publication (24) indicated that some promoters used to drive SB transposase expression do not function well in liver tissue to provide long term transgene expression. It was found that the relative strength of different promoters expressed in mouse liver did not correlate with the amount of stable transgene expression. Peak levels of long term gene expression were obtained with promoters 30-40 fold less active than the CMV promoter. By correlating the relative strength of the promoter driving transposase production with levels of short term and stable transgene expression, a narrow window of optimal transposase expression could be defined. The investigators concluded that successful *in vivo* transposition may depend primarily on a narrow window of SB transposase concentration obtained shortly after plasmid injection, and that overproduction of transposase can cause inhibition of long term transgene expression (24).

The pPC vector was originally constructed with the CMV promoter to drive SB transposase activity (14) and thus might not be optimal for *in vivo* gene delivery in liver

and other tissues. Our original grant was written without knowledge of this information and we proposed to use the CMV promoter and the EF1a promoter to drive *SB* transposase activity.

Because of this publication, we modified our aim to use a promoter that is not expressed as strongly as the CMV promoter so that inhibitory levels of the SB Transposase would not be produced in cells after plasmid vector delivery. We did not want to be limited to a single plasmid regarding expression of SB Transposase after plasmid delivery *in vivo*. We wanted to choose a promoter system that we could easily manipulate to alter SB transposase expression levels to be optimum in each cell types and provide for cell specific transgene production in the future. We anticipated that by developing the weakly expressed minimal Thymidine Kinase (TK) promoter together with a tissue specific enhancer, we could both modulate the level of transposase expression and also provide for tissue specific expression by using different tissue specific enhancers. Tissue specific expression would also increase the safety of the plasmid vectors developed for clinical use. Thus we have modified our vector design to include the TK promoter in the *SB* transposase expression cassette and have created another set of pPC and A1-50b plasmids (Table 2).

Additionally we found that the SV40DTS only in a forward orientation relative to the transgene expression cassette increased transfection efficiency while the reverse orientation of the SV40DTS suppressed transgene expression (data not shown).

Table 1. Plasmid vectors expressing the nuclear localizing Red Fluorescent Protein (RFP) transgene.

Vector Name	Description of Components	Comments
pPrince Charming (pPC)	RSV promoter driving transgene, SB transposase driven by the CMV promoter, Neo cassette for selection with G418	Harris, et al., 2001
pPRSS	RSV promoter driving transgene, SB transposase driven by the CMV promoter, 1 or 3 copies of the SV40 DTS in the Sal I site, Neo cassette for selection with G41 8	The SV40 DTS is in a forward orientation relative to the transgene expression cassette.
pA1 -50b	RSV promoter driving transgene, SB transposase driven by the CMV promoter	Shortened pPC by PCR to remove neomycin expression cassette
pARSS	RSV promoter driving transgene, SB transposase driven by the CMV promoter	Shortened pPRSS by PCR

2.a.4. Development of pPC-based plasmid vectors that express BMP-2/4: A robustly produced BMP-2/4 from an MFG-based retroviral vector was prepared from human BMP-2 and BMP-4 coding sequences. The BMP-2 N-terminal facilitated processing to and secretion of BMP-4 in osteoblasts and mature BMP-4 readily stimulated alkaline phosphatase (ALP) activity in osteoblasts, signaling differentiation. The plasmid vector with a *SB* Transposon, *SB*

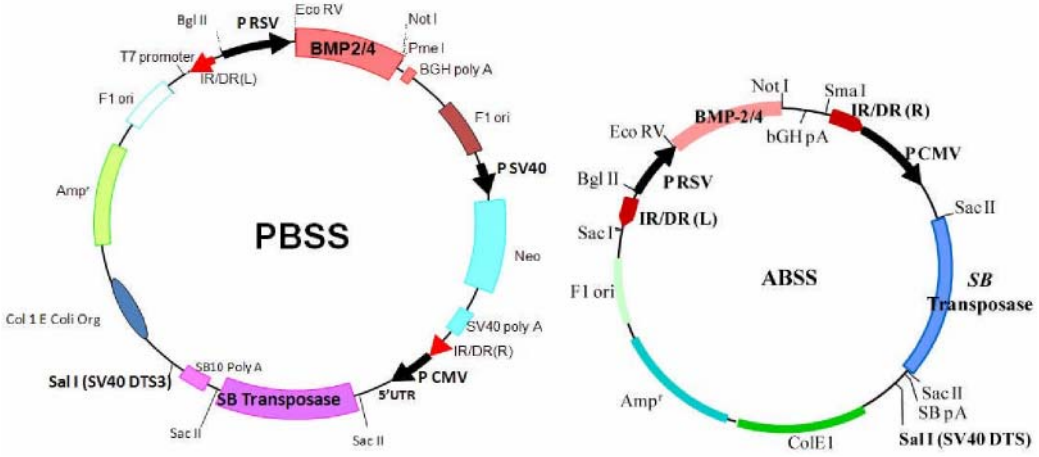

Figure 5. **Structure of the SB Transpson/SV40DTS based BMP-2/4 plasmid expression vectors**. The human BMP-2/4 cDNA was removed from an MFG-based retroviral vector (1) and subcloned into the pPRSS vector. The pPBSS vector created was reduced in size by PCR to form the pABSS vector. From one to three copies of the SV40 DTS were placed in tandem in the Sal I site. Vectors with one or three copies of the SV40DTS outperformed other pPC-based vectors in transfection and transdifferentiation studies.

Transposase and SV40DTS nuclear targeting sequence and the BMP-2/4 expression cassette driven by the RSV promoter was prepared by removing and replacing the BP3-NLS-RFP coding region with the BMP-2/4 coding region in the pPRSS plasmid vector. The 1.3 kb BMP-2/4 coding region was released with Sal I and Bgl II from a retroviral vector (1), the fragment blunted with Klenow Polymerase and subcloned by blunt end ligation into the pPSS vector (BP3-NLSRFP removed). After removal of BP3-NLS-RFP coding region from the pPRSS vector with EcoRV and Not I, the Not I ends were filled in with Klenow. Blunt end ligation was used to incorporate the human BMP-2/4 coding region in place of BP3-NLS-RFP to form the pPBSS vector. The pABSS vector was prepared by PCR with the pPBSS templace to remove the Neomycin cassette.

Table 2 summarizes the pPC-based constructs that are available to test BMP-4 expression in osteoblasts, MSCs or other types of cells. The pABSS and A1-50b-BMP-SalISV40DTS-TK-SB vectors will be used for in vivo gene delivery in future studies.

Table 2. Plasmid vectors expressing the BMP-2/4 transgene.

Vector Name	Description of Components	Comments
pPC-BMP-2/4	RSV promoter driven transgene, SB transposase driven by the CMV promoter, Neo selection expression cassette	
PBSS	RSV promoter driven transgene, SB transposase driven by the CMV promoter, 1 copy of the SV40 DTS in the Sal I site, neo selection expression cassette	Effective transfecting reagent
pPC-BMP-Sal I-SV40 DTS2	RSV promoter driven transgene, SB transposase driven by the CMV promoter, 2 tandem copies of the SV40 DTS in the Sal I site, neo selection expression cassette	Least effective transfecting reagent
pPC-BMP-Sal I-SV40 DTS3	RSV promoter driven transgene, SB transposase driven by the CMV promoter, 3 copies of the SV40 DTS in the Sal I site, neo selection expression cassette	Effective transfecting reagent
ABSS	RSV promoter driven transgene, SB transposase driven by the CMV promoter, 1 copy of the SV40 DTS in the Sal I site	Smaller effective transfecting reagent.Derived from PBSS. Should be tested in vivo.
pPC-BM P-SalI-SV40 DTS-TK-SB	RSV promoter driven transgene, SB transposase driven by the TK minimal promoter, 1 copy of the SV40 DTS in the Sal I site, neo selection expression cassette	
A1 -50b-BMP-Sal I-S V40 DTS-TK-SB	RSV promoter driven transgene, SB transposase driven by the TK minimal promoter, 1 copy of the SV40 DTS	Smallest effective transfecting reagent, should be tested *in vivo*

2. b.**Testing the transfection efficiency and expression patterns of the modified pPC-based plasmid vectors**.

2.b.1. Optimizing *in vitro* transfection with pPC-based plasmid vectors in cell lines and primary cells. 2.b.1 .a. **Effectene**: The optimum dose of pPC-based plasmid vector was determined in ROS 17/2.8 cells (widely used rodent osteoblast cell model) with Effectene (Qiagen). Several other lipid-base transfection agents were tested but failed to reach the transfection efficiencies of Effectene (30-60% in ROS 17/2.8 cells). Cells were plated at 70,000 cells per well in a 6 well plate and from 0.25-1.5 .tg of purified (Qiagen Chromatography) plasmid DNA was added to each well with 5 µl of Effectene, Enhancer and EC Buffer overnight at 37 C in 1 ml of DMEM/10% CS. DNA was removed and media was changed to DMEM/10% CS and 48 hours after transfection, transfection efficiency was analyzed by FACS. The optimal dose of pPC-based vectors was obtained ~1 .tg. The pPC vector transfection efficiency was more dependent on DNA concentration than the smaller pARSS vector.

Transfections of rat marrow stromal cells (rMSCs) and primary rat osteoblasts (rCobs) were conducted under the same conditions to visualize fluorescent products but transfection efficiencies were low (1-5%). This result prompted us to test additional reagents.

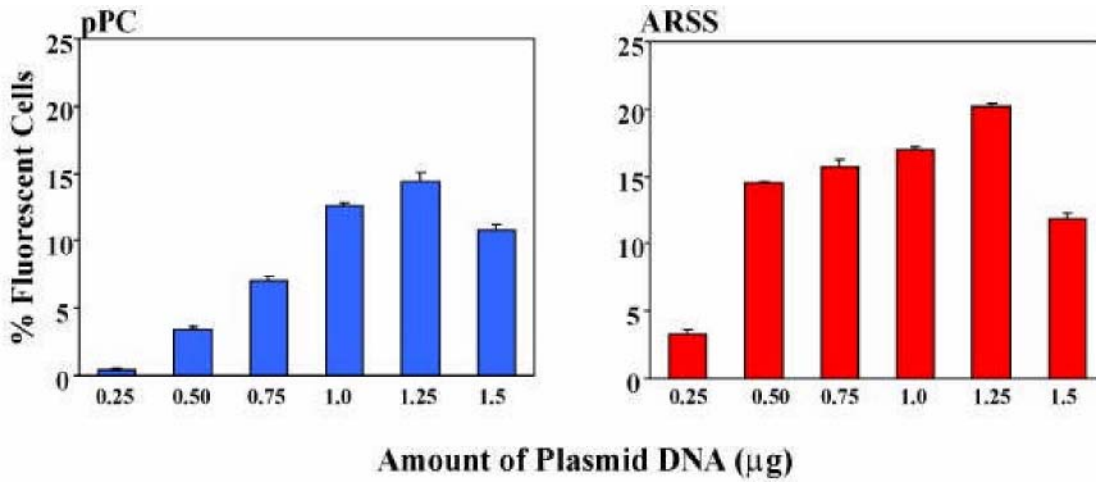

Figure 6. **Comparison of pPC and pARSS vector transfection efficiency in rat osteoblasts.** ROS 17/2.8 cells were transiently transfected with increasing amounts of plasmid DNA (0.25 .tg to 1.5 .tg) and fluorescent cell number was evaluated after 48 hours by FACS analysis. Optimal doses for transfection were achieved at 1-1.25 .tg of DNA. pPC does not have the SV40DTS while the ARSS vector does. Both vectors have the SB transposon. In replicate experiments with different lots of Effectene, from 5-20% of ROS 17/2.8 cells were optimally transfected with either vector. The pPC vector is more dependent on DNA concentration than the smaller ARSS vector.

2.b.1 .b. **Nucleofector reagents:** It is well recognized that nontransformed cells are difficult to transfect at high efficiency with the widely used lipid-based and Starburst Dendrite- based transfection agents such as Effectene and others. Amaxa has developed hundreds of cell specific reagents, a special plasmid vector (p*Max*GFP) that can be used with electroporation to increase transfection efficiency in almost any cell type including

nontransformed cells. We tested two of their kits that worked well with mouse cells. The Kit T which was shown by our group to transfect mouse MC3T3 cells with high efficiency (80-90%). While Amaxa's fibroblast kit transfected early passage mouse marrow stromal cells at 80% efficiency. We tested the ability of Amaxa's T Kit with the p*Max*GFP vector to transfect rMSCs. Early passage rMSCs (500,000) were transfected with 2 µg of p*Max*GFP vector using the T Kit,

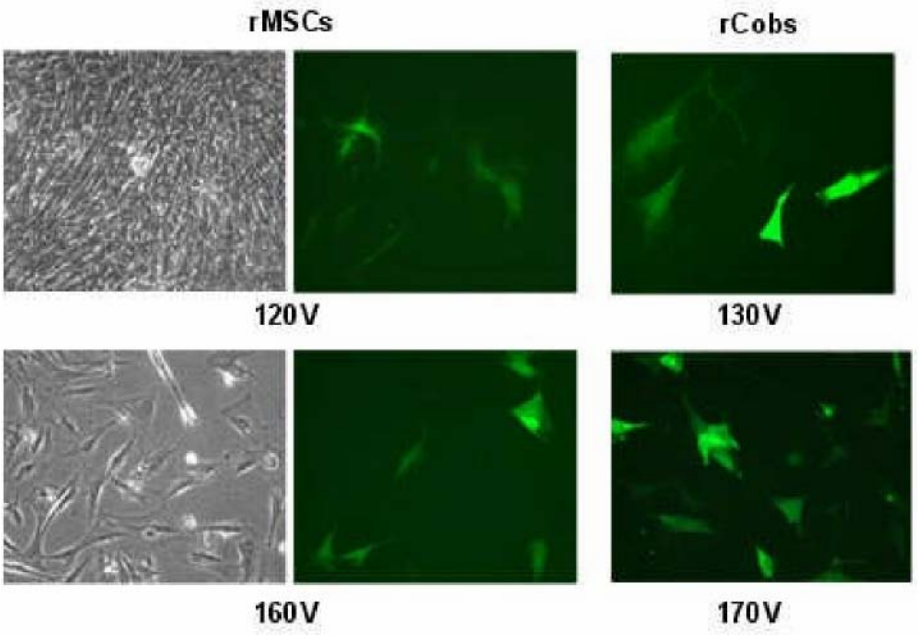

Figure 7. **Electroporation of rMSCs and rCobs with Nucleofector (Amaxa) reagents**. rMSCs were electroporated with 2 .tg of p*Max*GFP at 160V (15 ms) in the Nucleofector T kit reagent and plated in DMEM/10%FBS. Cells expressed GFP at 24 hours after electroporation and at 48 hours 20% of the cells (by FACS analysis) expressed GFP. At 160V about 50% of the cells were not viable. At lower voltages there was less cell death but only 5-15% transfection efficiency. rCobs were transfected as describe above except with a 20ms pulse with the fibroblast kit. Cells were transfected with 21-34% efficiency.

a 20 ms single square wave pulse at 120V, 130V, 140V or 160V. Cells expressing fluorescence were monitored by fluorescent microscopy at 24 hours and by FACS analysis at 48 hours. It was found that over 20% of rMSCs expressed GFP when electroporated at 1 60V (15 ms), however more than 50% of the cells were killed. 1 20V transfections provided 30% cell survival with a transfection efficiency of 15% while cells transfected at 170V resulted in 15-20% cells survival with a 21% transfection efficiency. rCobs (500,000) were transfected under the same conditions and did not transfect with high efficiency with the T-kit at any voltage conditions tried.

Early passage rCobs (500,000) were transfected with 2 µg of p*Max*GFP vector using the fibroblast kit as recommended by Amaxa. A 20ms pulse between 130-1 70 volts was applied. 50-70% of the cells survived and transfection efficiencies ranged from 21-34%. 1 70V optimally delivered plasmid DNA into rCobs with the fibroblast kit with 50% survival (Figure. 7). The fibroblast kit did not deliver DNA into rMSCs using the same conditions (data not shown).

After identifying Nucleofector reagents that transfected at least 20% of each cell type with the p*Max*GFP vector, transfections were conducted with pARSS, a larger (7.4 kb) vector with the SV40DTS and the *SB* transposon/transposase. A dose response experiment was conducted with 2,4,6 µg pARSS plasmid vector with the fibroblasts kit at 1 70V, 20 ms pulse in rCobs with the fibroflast kit. 4 - 6 µg of pARSS resulted in the highest transfection efficiency. Expression was monitored for up to 3 weeks. Transfection efficiencies ranged from 1-5 % but expression was observed for longer than 3 weeks. While transfection efficiencies up to 34% could be obtained with the 3.8 kb p*Max*GFP vector provided by the manufacturer, efficiencies with our 7.4 kb pARSS vector was much lower. Expression from the pMaxGFP vector disappeared from cells after 5-7 days. Transfection of the pARSS vector into rMSCs with the T kit was less than 1% using conditions optimal for transfections with p*Max*GFP (data not shown).

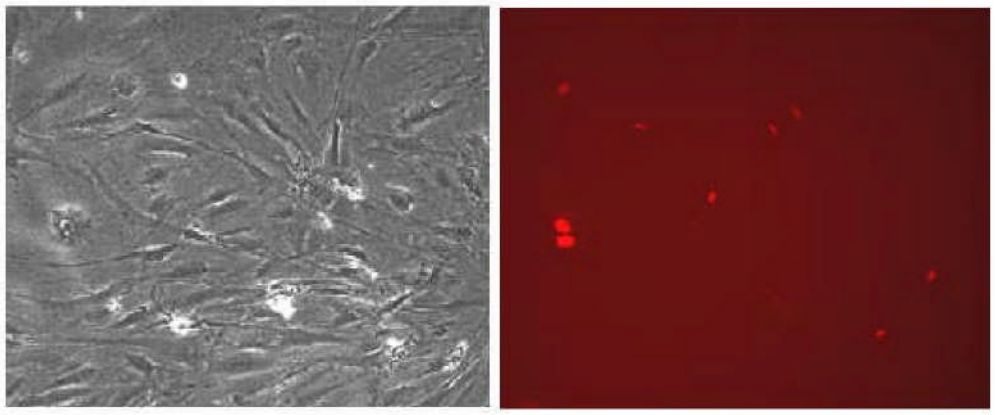

Figure 8. **Evaluation of the transfection efficiency of pARSS in rCobs**. 500,000 rCobs were transfected with the Amaxa fibroblast kit, 5 µg pARSS at 170V with a 20 ms pulse in a 2 mm cuvette. Cells were cultured for three weeks and RFP expression in the nucleus was assessed by fluorescent microscopy

2.b.1 .c.**siPORT**: We tested siPort transfection reagents and developed electroporation protocols that delivered the pABSS vector into rMSCs without killing the cells. rMSCs cells were seeded in a 6 well plate at a cell density of 200,000 cells per well, and incubated for 24 hours at 37°C,5%CO2. Cells were were trypsinized and resuspended in siPORT siRNA electroporation buffer (Ambion, Austin, TX) at a density of 1X 10^7cells/ ml. 3 X 10^6cells were transfected by electroporation in 2 ml of Serum Free Opti-Mem I (Gibco-Invitrogen, Carlsbad, CA) with 1.tg of pARSS at 160V (one 15 ms pulse) using the Gene PulserXcell Eukaryotic System (Bio Rad, Hercules, CA). Epifluorescent microscopy was used to visualize RFP production in cells after 24 hours (Figure. 9). 1-10% of rMSCs were transfected under these conditions and expression was persistent for more than three weeks.

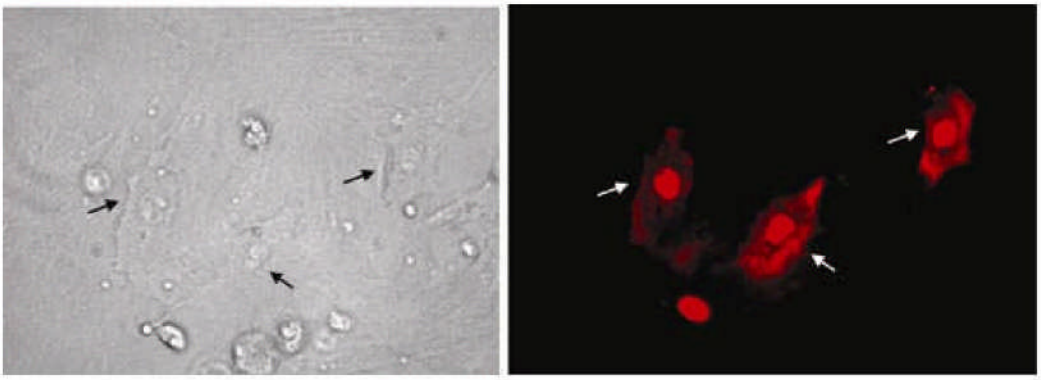

Figure 9. **Evaluation of transfection efficiency of rMSCs with Ambion electroporation reagents.** 400,000 cells were electroporated in a 2 mm pathlength cuvette with 1 .tg of pARSS in siPort electroporation buffer (Ambion) with one pulse of 160 Volts of 15 ms duration using the Square Wave Gene Pulse X cell instrument (BioRad). 5-10% of the cells were transfected and produced RFP within 48 hours. Cells in this picture were grown 1 week. RFP expression was persistent for over three weeks.

While the results regarding the longevity of expression were encourgaging, the results regarding transfection efficiency were disappointing. Our results suggest that cultured rat cells were very sensitive to transfection conditions with different plasmid vectors, and that larger plasmids were much more difficult to transfect into rat cells than smaller plasmids. These results were not observed in mouse cells. Because of these problems, we considered testing our plasmid vectors directly in animals and to optimize conditions *in vivo* rather than pursuing additional experiments *in vitro* in rat cells. We also considered using a mouse model rather than a rat model for future experiments because our electroporation studies suggested that rat cells were much more resistant to transfection by electroporation than mouse cells. We submitted and obtained funding in 2009 from Loma Linda University (National Medical Testbed) for a grant entitled "Development of plasmid vectors with nuclear While the results regarding the longevity of expression were encouraging, the results While

transfection efficiency were disappointing. Our results suggest that cultured rat cells were very sensitive to transfection conditions with different plasmid vectors, and that larger plasmids were much more difficult to transfect into rat cells than smaller plasmids. These results were not observed in mouse cells. Because of these problems, we considered testing our plasmid vectors directly in animals and to optimize conditions *in vivo* rather than pursuing additional experiments *in vitro* in rat cells. We also considered using a mouse model rather than a rat model for future experiments because our electroporation studies suggested that rat cells were much more resistant to transfection by electroporation than mouse cells. We submitted and obtained funding in 2009 from Loma Linda University (National Medical Testbed) for a grant entitled "Development of plasmid vectors with nuclear import sequences for improved skeletal gene therapy" proposing to use a mouse model to test our pPC-based plasmid vectors.

2.c. **Further comparison of expression from pPC-based plasmids in osteoblast cell lines.** We transfected rat osteoblast line cells with pPC-based plasmids that contained or did not contain the SV40DTS. Transient transfection was conducted with Effectene (Qiagen) and1 μg of DNA. We found that RFP expression was maintained in cultured cells for up to three weeks. ROS 17/2.8 cells transfected with peGFP vectors (Clontech) that do not contain the SB Transposon or the SV40DTS were expressed in cells for only 48 hr (data not shown).

2.c.1. Transfection of cell lines. ROS 17/2.8 and C2C12 cells were transfected with Effectene as described above with the prepared pPC-based plasmid vectors (Table 1). Transfection efficiency and longevity of expression were further studied. In our studies with a number of transfection agents, we found that RFP expression was maintained for more than 3 weeks. This is in agreement were earlier studies with the pPC vector (14).

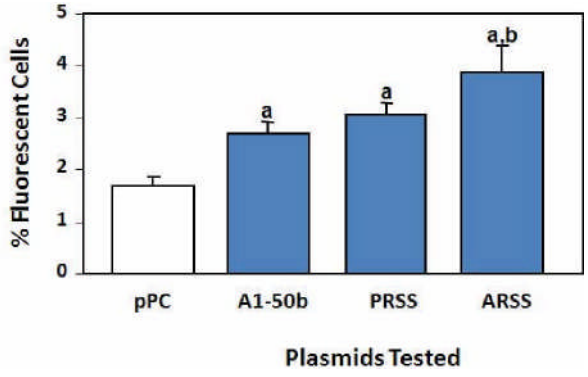

Figure 10. **Comparison of transfection efficiency in osteoblasts with pPC-based plasmid expression vectors**. ROS17/2.8 cells were transiently transfected 1 μg of each plasmid. After 24 hours FACS analysis was performed to determine transfection efficiency. Two plasmids did not contain the SV40DTS (pPC, A1-50b) and two plasmids contained one copy of the SV40DTS (pPRSS, pARSS). a, $P<0.05$ vs pPC, b, $P<0.05$ vs pPC and A1-50b. Values are the mean fluorescent cell number out of 10,000 cells counted + S.E.M. Significantly higher transfection efficiencies were obtained with the pPRSS and pARSS vectors than with the pPC vectors that had no SV40DTS.The smallest vector pARSS vector with the SV40DTS transfected cells with higher efficiency than the larger pPRSS vector.

We compared transfection efficiencies of the pPC vector with our vectors that contained the SV40DTS. When the SV40DTS was placed in the Sal I site (outside the transposon), this placement did not interfere with the expression of the transgene. Smaller plasmids (A150b and pARSS) transfected cells more efficiently than the larger plasmids (pPC, pPRSS). Plasmids that contained the SV40DTS and were smaller (ARSS), transfected cells the most efficiently.

2.c.2. Assessment of SV40DTS copy number on transfection efficiency. ROS 17/2.8 cells were transiently transfected with Effectene and the BMP expressing CM V-based SBtranspoase vectors and ALP activity was assessed after three days. The vectors contained either one, two or three copies of the SV40 DTS in the Sal I site. All of the plasmid vectors tested significantly increased ALP activity (Figures. 11,12). The SV40 DTS significantly increased the amount of ALP activity produced by osteoblasts. One and three copies of the SV40 DTS increased ALP activity transfected cells with higher efficiency. Vectors with one or three copies of the SV40DTS will be used for *in vivo* studies based on this work.

2.c.3. Assessment of TK promoter driving SB transposase**.** The CMV promoter and long 5'UTR were removed from the PBSS vector and the TK-SB transposase cassette with an optimized Kozak sequence (gccgccatgg) was substituted. This reduced the size of the pPBSS vector by 600 bp. The PBSS-TK-SB vector was subsequently reduced in size by PCR to prepare ABSS-TK-SB. The ability of the pPC, A1 -50b, PBSS, ABSS, PBSS-TK-SB and ABSSTK-SB vectors to stimulate osteoblast differentiation was assessed in ROS 17/2.8 cells. **Figure 12**

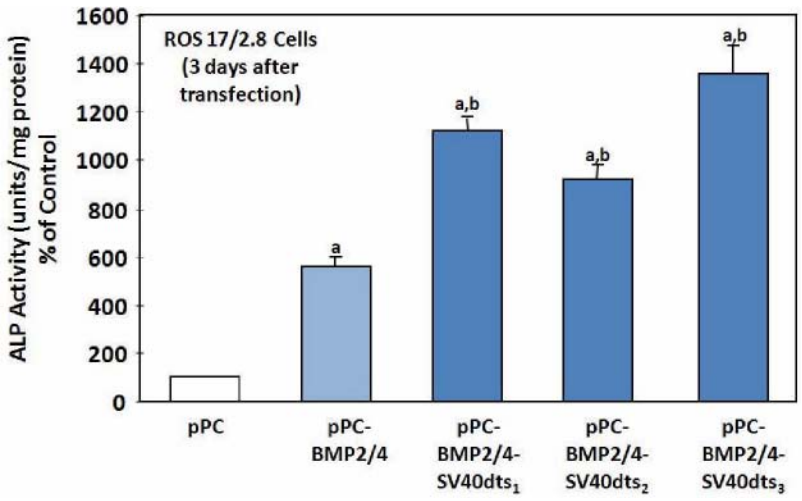

Figure 11. **Expression of BMP-2/4 stimulates ALP activity in rat osteoblasts** (ROS 17/2.8). ALP activity was evaluated 3 days (72 hours) after transfection with Effectene and 1 .tg of each plasmid DNA. Each value is the mean + S.E.M. of six replicates. a, P<0.05 vs pPC control; b, P<0.05 vs pPC-BMP-2/4.

illustrates this assessment. The PBSS, ABSS, PBSS-TK-SB and ABSS-TK-SB vectors were found to be superior to the pPC and A1-50b RFP containing vectors. The PBSS, ABSS, PBSSTK-SB and ABSS-TK-SB vectors that expressed BMP-2/4 all stimulated ALP activity. Vectors

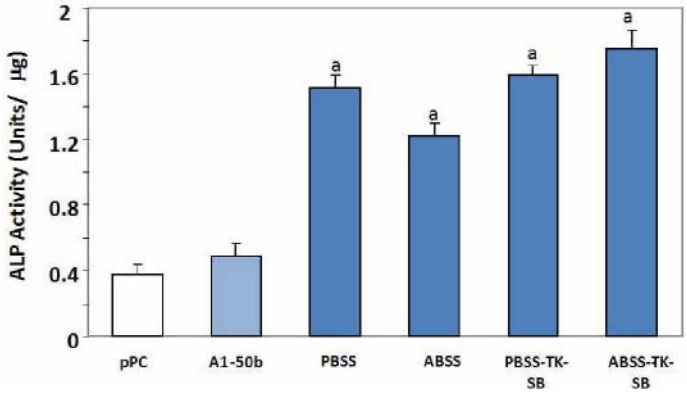

Figure 12. **Effect of pPC and A1-50b vectors with the TK promoter driving the SB transposase on ALP activity in osteoblasts**. ROS 17/2.8 cells were transiently transfected with 1 .tg of each plasmid vector with Effectene. After 48 hours ALP activity was assessed. Both the pPC and A1-50b vectors with either version of the SB Transposase cassette stimulated ALP activity *in vitro*. The SV40 DTS significantly increased ALP activity. Values are the mean + S.E.M of six replicates, a, P<0.05 vs pPC control.

with the CMV and TK promoter will be tested in vivo in future studies to determine if one is superior.

2.c.4. Assessment of ability of pPC-based BMP-2/4 vectors to transdifferentiate C2C12 cells. BMPs are known to transdifferentiate nondifferentiated cells. We used immature C2C12 myoblast cells as a model for transdifferentiation based on their sensitivity to BMPs to increase ALP activity (25).

C2C1 2 cells were transfected and cultured for 5 days in order to allow development of the osteoblast phenotype. The pPC-BMP2/4 vector did not significantly change ALP activity in C2C1 2 cells but this vector containing either 1 or 3 copies of the SV40dts (PBSS) increased ALP activity (1.6 and 2 fold) and the osteoblast phenotype. Transfection efficiency in C2C12 cells was 1-2% vs ROS 17/2.8 cells which transfected at 10-20% efficiency. This difference in transfection efficiency may explain the small increase in ALP activity compared to the increase seen in ROS cells. Transfection of C2C12 cells with pABSS stimulated the cells to produce ALP activity (data not shown).

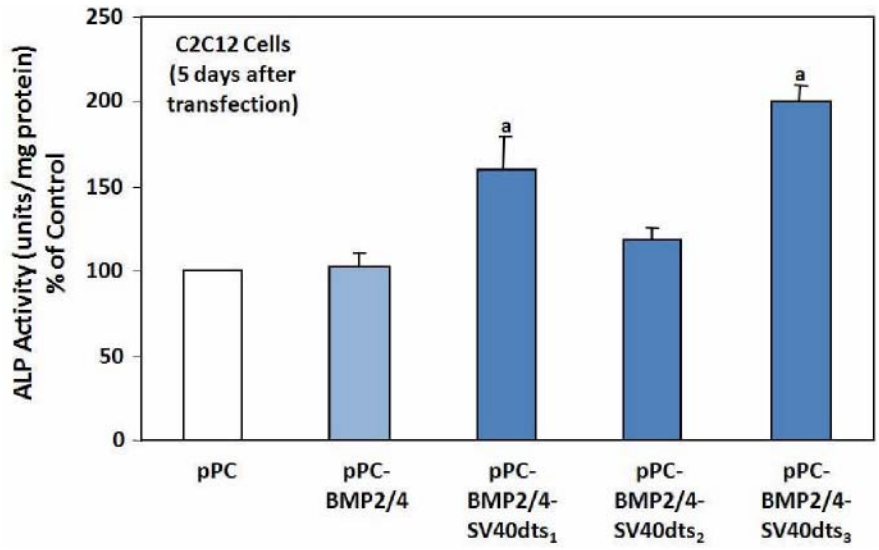

Figure 13 . **Assessment of transdifferentiation activity of pPC-based BMP-2/4 expressing vectors.** ALP activity was evaluated five days (120 hours) after transfection with Effectene and 1 .tg of DNA. Values are the mean + S.E.M. of 6 replicate samples. a, P <0.05 vs pPC control. Only vectors containing one or three copies of the SV40 DTS expressed enough BMP-2/4 to stimulate C2C12 cell transdifferentiation.

2.d. **Compare retroviral and plasmid vector expression in cells on three dimensional (3D) scaffolds**. These experiments were approached as a step by step process in the development of 3D models for cell growth that could be used to evaluate our pPC-based plasmid vectors. Completion of these studies would require 1) transduction of rMSCs and osteoblasts with retroviral vectors that express a marker gene and BMP-2/4, 2) preparation of the pPC-based plasmid vector with the SV40DTS and BMP-2/4 coding sequence in the transposon (pABSS), 3) development of plasmid vector transfection methods that will transfect >30% of cells with pARSS or pABSS, and 4) identification of a scaffold material that would support rMSC or osteoblast growth for *in vitro* and *in vivo* studies.

2.d.1. Prepare stable rMSC and osteoblasts that produce Green Fluorescent Protein (GFP) and/or BMP- 2/4 for use as a positive control in scaffolds for implant studies. We have , the Viral Vector Core Facility has transduced them retrovirus (MLV-MBMP-2/4) and we have determined that the cells stably express the GFP marker gene or BMP-2/4 protein when cultured for several weeks (up to passage 10) as monolayers.

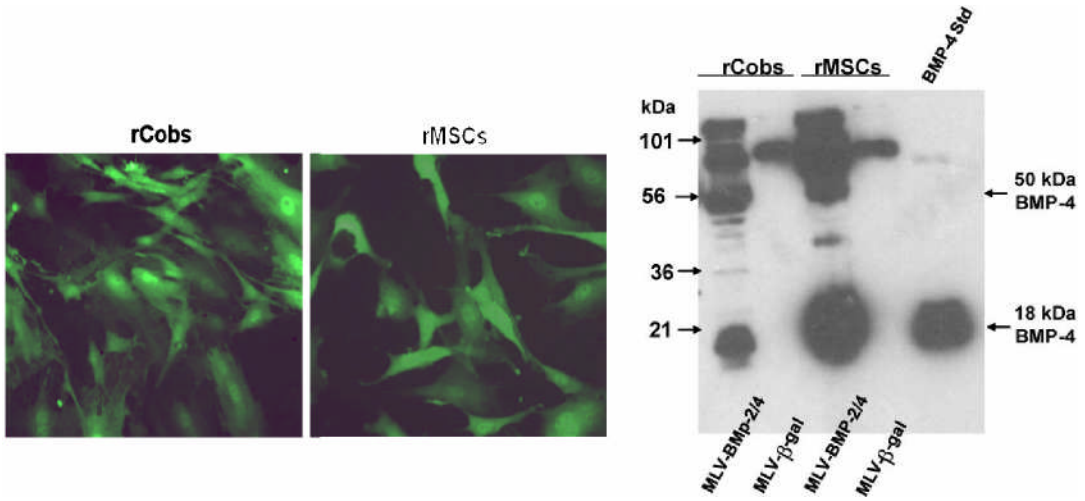

Figure 14. **Synthesis of GFP and BMP-2/4 from normal rat MSCs and Cobs after transduction with GFP or BMP-2/4 retrovirus.** *Left Panel*. rCobs and rMSCs were **transduced** (M.O.I. 20-40) with MLV-GFP**, plated and cultured for 72** hrs. GFP was visualized by **epifluorescent microscopy.** 80-**90% of cells were transduced.** Frozen cells could be passaged **over 10 times** and these cells continued to produce GFP. ***Right Panel.*** Cells transduced with BMP-**2/4 were plated and grown for 72 hrs. Cell lysates were analyzed fr**om cells that had been passed 3-**5 times post**-transduction and frozen. BMP-**2/4 was produced by both types of cells. The rhBMP4 monomer is ~18 kDa and the monomer of proBMP2/4 runs as a ~50 kDa protein.**

rRMCs and rCobs were transduced with MLV-BMP-2/4 or MLV-3-gal as described and frozen (1). Frozen stocks of cells were thawed and cultured for several additional passages. Expression of hBMP-4 produced by BMP-2/4 transduced cells was monitored by western blot analysis. Cells were grown to confluence, washed and protein was extracted with reporter lysis buffer. 10 tg samples of cell extract were added to gel loading buffer with reducing agent and run on a 10% separating/ 4.5% acrylamide stacking gel. Protein was transferred to a 0.2 micron PVDF Immunoblot (Biorad) and incubated with monoclonal anti BMP4 antibody (R & D systems, Cat. # MAB757) diluted 1:1,000. A secondary antibody (goat, anti mouse IgG-HRP, Pierce, Cat.#31430 was diluted 1:10,000. 100ng of BMP-4 standard from R & D Systems (Cat # 355- BEC) was run concurrently on the gel with cell extracts. BMP 4 was not detectable in

unconcentrated media from either rMSC or rCob transduced cells (data not shown), however, both the mature 18 kDa BMP-4 and the 50 kDa proBMP-2/4 protein was present in cell extracts from the cultured cells grown from frozen stocks. These experiments demonstrate that frozen stocks of cells transduced with MVL-GFP or MLV-BMP-4 can be used to test the ability of the Extracel matrix to support the growth of cells expressing GFP or BMP-4 *in vitro* or *in vivo*.

2.d.2. Development of premade scaffolds (OPLA, ceramic or collagen) as implant materials. It was originally anticipated that work with plasmid vectors would be conducted as an *ex vivo*-cell based therapy once transfection conditions were optimized. The rationale for using ceramic, collagen or OPLA scaffolds in our studies was that bone marrow stromal or osteoblast cells could be maintained in a confined space for up to one month and bone formation or marker gene expression could be easily evaluated by histology and qRT-PCR after the scaffolds were removed from the animal. The model was to act as a surrogate for other more complex procedures involving transduction of cell in vivo (intrafemoral injection model). Krebsbach (26)

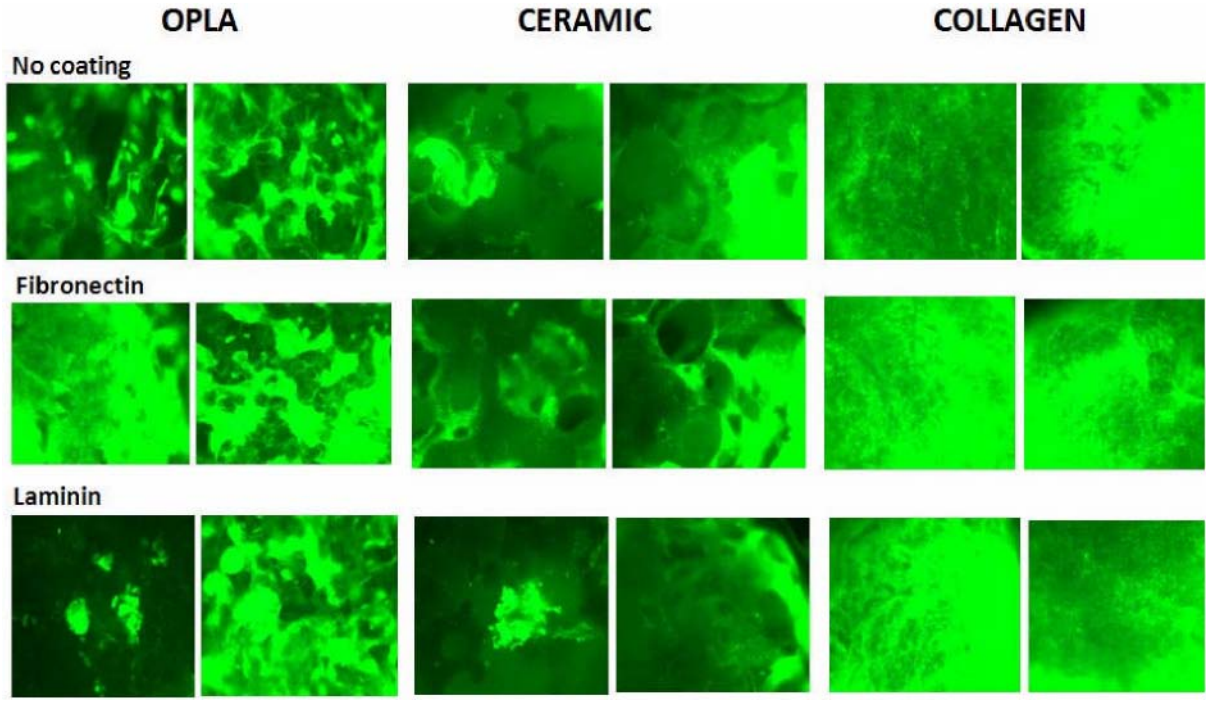

Figure 15 . **GFP-rMSC growth on OPLA, collagen and ceramic scaffolds**. rMSCs (10^4-10^5cells) were seeded on the scaffolds coated with nothing, fibronectin or laminin and cells were observed for 14 days. Fibronectin coated scaffords supported the growth of more cells than laminin while the collagen scaffold supported the growth of more cells than the OPLA or ceramic scaffolds.

reported that blood vessels and marrow elements invaded gelfoam (collagen) scaffolds loaded with marrow stromal cells. The entrance of fibrous connective tissue and blood vessels into the collagen scaffolds in our studies suggested that immune cells and other cells may have been attracted to the implants and that an inflammatory/immune reactions was induced by the collagen implant or the cells. These findings prompted us to test different

scaffold materials so that materials that did not induce an inflammatory response could be identified.

A variety of 3D biodegradable scaffolds provide an adhesive substrate that can be used as artificial substitute for the Extra Cellular Matrix (ECM). These scaffolds are prepared from
natural molecules and/or synthetic polymers. BD Biosciences sells a number of three dimensional (3D) supports that have been used for *in vivo* tissue regeneration as well as *in vitro* cell culture. We initially tested premade OPLA scaffolds (synthesized from D,D-L, L polylactic acid), calcium phosphate (ceramic) scaffolds, and collagen composite scaffolds (prepared from a mixture of type I and II collagens derived from bovine hide).

The 3D supports were pre-coated with PBS, fibronectin or laminin by adding 100 µl of a 100 µg/ml solution to each dry scaffold in wells of a 24 well plate. The scaffold absorbed this solution completely. The scaffolds were incubated 1 hour before adding cells. Cells were trypsinized and filtered through a 40 tM nylon sieve (BD Bioscience) counted and added to each well as 400,000 cells in 1 ml. This number of cells just covered the scaffold. After 3 hours, 1 ml more media was added and the cultures were incubated with media changes for 7-21 days. Scaffolds were moved to new 6 well plates when cells began to populate the bottom of the tissue culture dish. Scaffolds prepared in this manner could be followed long term in culture or could be implanted after 7-14 days. Before implanting, the scaffolds were examined by epifluorescence microscopy and GFP cells were observed on the surface of the scaffold (Figure 15).

We cultured cells (rMSC, rCobs) on the matrices. Virally transduced cells expressing GFP were viable on the surface of each of the scaffolds and continued to express GFP for up to 2-3 weeks in culture. The Collagen matrix when coated with fibronectin supported the growth of more rMSCs than OPLA or Ceramic supports (**Figure.15**).

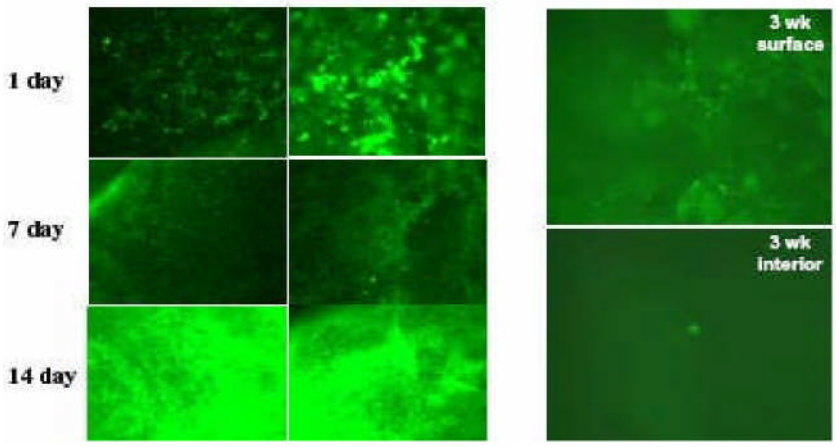

Figure 16. **GFP-rMSC growth on collagen scaffolds *in vitro***. Left panel: rMSCs were seeded on scaffolds ond grown for 1-14 days in vitro. More cells were visible on the cell surface at day 14 compared to day 1 and 7. Right panel: rMSCs remaining on the exterior and interior of the collagen scaffold after 21 days in culture.

GFP cells were cultured on the scaffolds for up to 3 weeks. After that time we noted that the intensity of the green on the scaffold surface was reduced. We determined if the cells died or moved to the interior of the scaffold. We found that very few cells were found at one, two or three weeks on the inside of any of the matrices. Figures 16, 17 show representative examples of GFP on the cellular interior and exterior of collagen and ceramic scaffolds. These experiments led us to consider the use of other matrix materials that would support the growth of cells on the scaffold's interior so that more therapeutic agents could be delivered in *ex vivo* therapeutic implants. Prior to initiating studies with other materials, we assessed if the collage scaffolds stimulated osteoblast differentiation in rMSCs. We also assessed the ability of the three types of scaffold materials and surface cells to withstand *in vivo* conditions.

2.d.3. <u>RNA isolation and preparation of cDNA from rat cells on scaffolds.</u> RNA was isolated from rMSCs populating a single 3 mm^3 OPLA, collagen or ceramic support using the Versagene Kit from Gentra. From 350-500 ng of total RNA was isolated from the OPLA, Ceramic or collagen chips. More RNA was recovered with this kit than with the "Absolutely RNA" kit. cDNA from three separate reactions was prepared and mixed with 20 ng of total RNA/reaction, 1 µl(5 tM) oligo dt 20 mer primer mix (IDT) and 1 µl of dNTP (10 mM) master

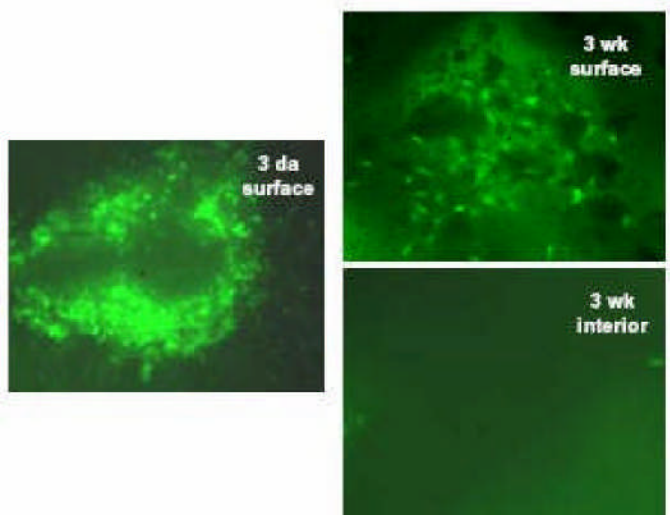

Figure 17. **Growth of GFP-rMSC on ceramic scaffolds *in vitro***. rMSCs expressing GFP were seeded on scaffolds and grown for 3-21 days *in vitro*. GFP expressing cells on the surface and interior were inspected after 3 and 21 days.

mix. RNA was heated to 65 C for 5 minutes and at 4 C for 1 minute before adding 1 µl(200 units) of Superscript III (Invitrogen) reverse transcriptase, 4 µl 5 X first strand buffer mix (250 mM Tris HCl (pH 8.3 at RT), 375 mM KCl, 15 mM MgCl2), 1 µl of 0.1 M DTT and 1 µl of RNAse Out, recombinant RNAse inhibitor (Invitrogen) to a 20 µl total reaction volume. After mixing the

Table 3. Primer sets developed for Real Time PCR analysis of rat mRNA levels of osteoblast marker genes.

Gene	Accession #	Primer Sequence	Size of Product	Tm Amplification (^{0}C)
cycloph il in	BC059 141	Gcatacaggtcctggcatct gctctcctgagctacagaag	281	56.4
Type Ia2 procollagen	AF121217	gtgtcagcggaggaggctat	344	56.4
Osteopontin	M14656	Gaagaccagccatgagtcaag cttgtcctcatggctgtgtgaa	243	56.4
Alkaline Phosphatase	Y00714.1	Ggattcctgctgccgttgtt gagggactggctgtgactat	223	48
Osteocalci n 123-338	N M_0 13414.1	cagcgactctgagtctgacaa gtgtccatagatgcgcttgta	215	48

solution was incubated at 50 C for 30 minutes and at 70 C for 15 minutes to inactivate the enzyme. After incubating the samples at 4 C for 2 minutes, 1 µl of RNAse H was added and incubation was continued for 20 min at 37 C. cDNA was made in a Minicycler from MJ Research. Samples were removed and stored at –20 C until use.

2.d.4. Real-Time PCR assay for osteoblast marker genes**.** We and others have shown that rMSCs that are attached to scaffolds undergo differentiation into mature osteoblasts that produce bone (27). To analyze bone formation from cells attached to the scaffolds or in implants recovered from animals, the mRNA levels of a number of osteoblast marker genes were analyzed. The osteoblast marker genes will be divided into categories that reflect several stages of differentiation. One gene expressed early in the differentiation process is type I

Support Material	ΔC_T Collagen	ΔC_T Osteopontin
Collagen premade cube	-2.3	2.1
Collagen cube coated with fibronectin	-2.6	3.1

Collagen cube coated with laminin	-4.0	2.0

procollagen when preosteoblasts are in the proliferative stage. ALP is expressed at the onset of

Table 4. Assessment of osteoblast differentiation gene expression of cells on scaffolds.

C_T (cycle threshold) values for collagen and osteopontin were determined in quadruplicate and normalized to C_T values for cyclophinin (a housekeeping gene) also determined in quadruplicate. The normalized values are expressed at ΔC_Ts. Negative ΔC_Ts values indicate that expression of collagen mRNA was higher than cyclophilin mRNA expression. Osteopontin mRNA was not expressed at levels higher than cyclophilin.

mineralization, while genes expressed during the later mineralization stage include osteocalcin, and osteopontin. We tested and validated four osteoblast marker genes for in vitro and *in vivo* testing (Table 3). Table 4 provides preliminarydata from quantitative (q)RT-PCR analysis of RNA from scaffolds. These results indicate that the collagen scaffold findings support differentiation of rMSCs to osteoblast lineage cells. Cycle thresholds of quadruplicate samples were determined from PCR products generated from 1 ng of cDNA prepared from total RAN from cells on a single support chip. Cyclophilin thresholds were determined and the cyclophilin CT values were subtracted from CTs from either type I collagen or osteopontin to normalize for differenced in cDNA starting material amounts. Collagen and osteopontin mRNAs were expressed at high levels in the cells on the supports, however, cells from the collagen support coated with fibronectin made higher levels of osteopontin than the uncoated or laminin coated support. If osteopontin expression is more indicative of obsteoblast mineralization, and collagen more indicative of cells in a less mature proliferating phenotype, then this result suggests that the collagen support coated with fibronectin might be better to use for the implant model to increase mineralization *in vivo.* Table 4 indicates that GFP-rMSCs express type I procollagen and osteopontin, markers of osteoblast differentiation.

2.d.5. Preparation and analysis of rMSC populated scaffolds in vivo. Because cells grew well on the exterior of the matrices (OPLA, collagen, ceramic) for 2-3 weeks, we conducted preliminary implant surgeries to determine if GFP-expressing cells could survive in the inbred Fischer 344 rat model.

2.d.5.a Rat skin implant surgery. Fischer 344 rats, 13 weeks old, were anesthetized with ketamine and xylazine and four 0.8-1.2 cm incisions were made on the shaved back skin. Blunt dissection with a small hemostat was used to create a small pocket to the lateral side of each incision, then one scaffold (containing rMSC-GFP cells) was inserted into the pocket. The

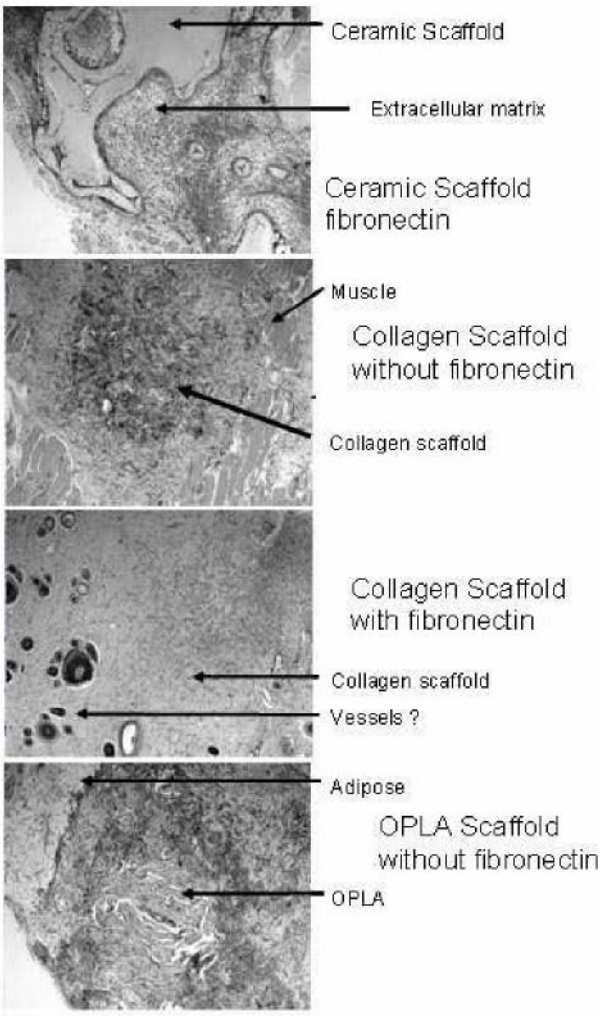

Figure 18. **Analysis of the rMSC-GFP-collagen scaffolds after 14 days *in vivo* in the implant model.** Scaffolds were removed and residual GFP positive cells visualized by microscopy. The implants were fixed, sectioned and stained with H&E. GFP positive were found on the surface and inside the collagen matrix. The scaffold was filled with cells and vessels were found to penetrate the material. Not all of the cells in the scaffold expressed GFP. This could result from transgene silencing or in rMSC cell death.

incisions were closed with 3 stitches (3-0 non-resorbable) and the rats were allowed to recover in plastic cages on a warm pad before return to normal housing. Rats were monitored hourly until normal feeding patterns returned.

2.d.5b. Analysis of implanted scaffolds**.** rMSCs expressing GFP from MLV-GFP vector were grown for one week in culture and then implanted on the back of Fischer rats as described above. Initial implant experiments to assess whether the scaffolds and attached cells would induce a significant inflammatory reaction in the host rat tissues were negative. Because syngenic cells were used, a cell rejection reaction was not anticipated, but we did not know what effect the scaffold materials (OPLA, ceramic or collagen), the fibronectin or the fetal bovine serum (from the cultures) would have on the rat tissues. The experiment was designed so that one scaffold was implanted per site, with duplicate scaffolds (one with and one without fibronectin) per rat.

After 7-16 days, the rats were euthanized with CO2 and the implants were dissected out and placed in PBS on ice. There was no indication of an inflammatory reaction in the implant sites. The implants were fixed in 10% buffered formalin overnight, then processed for paraffin sectioning. Other implants were frozen in the cryostat and sections were made to examine GFP expression in the microscope.

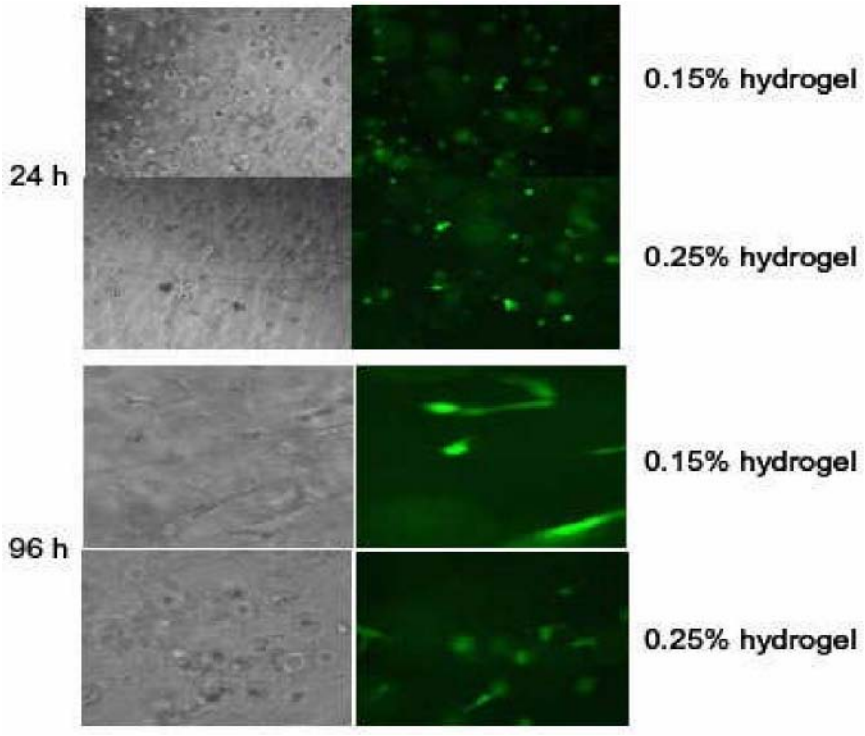

Figure 19. **MLV-GFP rMSC survival in hydrogel prepared by the drop method**. rMSCs were grown for 24 hrs in DMEM/10%FBS and media was replaced with media containing either 0.15%, or 0.25% PuraMatrix that was dropped onto adherent cells. Cells were grown in culture for 24-96 hrs and GFP was monitored by fluorescence microscopy.

The collagen and OPLA scaffolds were reduced in size after 16 days (30% of original) suggesting significant resorption of the scaffold material occurred. The OPLA and collagen scaffolds were also tightly incorporated into the overlying skin dermis layer and had some blood vessel growth. Krebsbach's group (27) reported that blood vessels and marrow elements invaded gelfoam scaffolds (collagen based) that were loaded with mouse

MSCs. The collagen scaffolds were not eroded in the immunocompromised mouse model that this group used for their experiments. In our experiments, a few GFP positive cells were found on the scaffold surface and inside the scaffold after 14-21 days.

We found that very few GFP-expressing cells were visible in or on the matrices after 7 days. GFP expressing cells could not be identified in the surrounding tissues. After fluorescent microscopy, the implants were fixed in 10% buffered formalin overnight and then were sectioned to assess the cellular content of the matrix. Each of the matrix materials were populated with cells (Figure. 18). Because these cells did not express GFP, we concluded that the cells had invaded from surrounding tissues. Blood vessels appeared to infiltrate the collagen matrix but not the other matrices. Additional experiments were conducted and collagen scaffolds were removed at 2 days. Again very few GFP-expressing rMSCs were found on the exterior or interior of the scaffold. GFP-rMSCs as well as rCobs formed a layer on the scaffold surface material and did not penetrate into the scaffold interior. Similar results have been reported by others. Mineralization measured and quantitated by tCT only occurred on the surface of collagen disks implanted with mouse myoblasts expressing osteoinductive trangenes *in vitro* (28,29). This result and the results of others ((30,31) prompted us to consider the use of immunocompromised mice for future implant studies and using a different, more readily populated matrix material to support growth of rMSCs or rCObs in three dimensional matrices (3D).

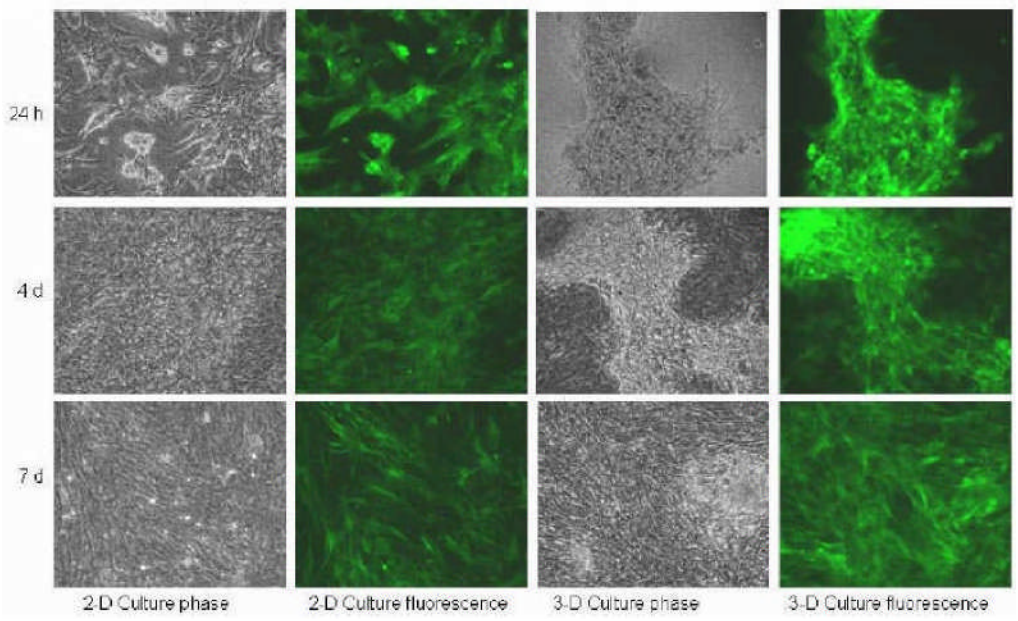

Figure 20. **Survival of MLV-GFP transduced rMSCs in PuraMatrix-hydrogel.** Cells were plated and grown in 2D culture or were suspended in PuraMatrix by encapsulation methods in wells of a 6 well plat for 24h, 4 days or 7 days. 100,000 cells were encapusulated in 0.15% hydrogel/sucrose and dropped into the culture well. 2 ml of DMEM/10% FBS was added to the well for cell growth assessment. Fluorescent microscopy was used to evaluate cell growth from 1-7 days.

2.d.6. Testing additional scaffold materials. Our studies with collagen, OPLA and ceramic scaffolds suggested that cell viability was limited when implanted on premade scaffolds and that extensive erosion of the collagen and OPLA scaffolds occurred in inbred rats. These findings led us to test other scaffold materials that would support the growth of three dimensional cultures and that would also support the viability and expansion of rMSCs and rObs *in vitro* an *in vivo.* Successful use of hydrogel matrices found in the literature (30-33) prompted our test of these materials.

2.d.6.a. **PuraMatrix-hydrogel:** BD Biosciences produces a liquid hydrogel product for better dispersion and growth of cells throughout a 3D matrix. Because the preformed scaffolds did not readily support cell growth throughout the matrix and the cells on the surface were rapidly lost from the scaffold *in vivo*, we initiated experiments with PuraMatrix hydrogel-based materials based on successful studies by others (30,31).

We conducted *in vitro* experiments with BD™ PuraMatrix™ Peptide Hydrogel matrix (BD Biosciences). PuraMatrix Hydrogel is a synthetic matrix that is used to create defined three- dimensional (3D) microenvironments for a variety of cell culture experiments. This material is composed of a synthetic peptide containing four repeats of Arg-Ala-Asp-Ala and was recently reported to support differentiation and mineralization of mouse embryonic fibroblasts. Under physiological conditions, the peptide component self-assembles into a 3D hydrogel that exhibits a nanometer scale fibrous structure that promotes cell attachment, but does not activate RGDdependent integrin signaling. The gel is biocompatible and devoid of animal-derived material and pathogens and can be used in implant studies. The material can be dropped onto growing cells (drop method) or cells can be suspended with the hydrogel (encapsulation method) and placed in a culture dish. We cultured rMSCs with different concentrations of hydrogel under both conditions. Figure 19 illustrates growth of GFP-rMSC cultures 1, 4 and 7 days after drop culturing and Figure 20 illustrates growth in hydrogel after encapsulation of cells. MLV-GFP expressing rMSCs were grown in parallel cultures for comparison. rMSCs (70,000 cells/well in 6-well plate) were seeded in culture dishes in DMEM/10%FBS and then covered with 0.15% PuraMatrix (drop method). GFP-rMSCs did not establish three dimensional cultures. rMSCs (70,000 cells/well) were encapsulated in 0.15% PuraMatrix with 10% sucrose and then were placed in plastic culture wells containing DMEM/10%FBS for up to 7 days. GFP-rMSCs attached to the bottom of the well and expressed GFP. The cells did not remain in the hydrogel.

The cells did not grow well using the drop method and did not form three dimensional cultures. Cells did not grow in the 3D encapsulation experiments but the cells that were encapsulated continued to express GFP. These results led us to continue our search of 3D matrices and other hydrogels.

2.d.6.b. **Extracel-LG hydrogel-based matrix:** While preliminary experiments looked promising regarding use of the PuraMatrix hydrogel (BD Biosciences, Bedford, MA) for growth of genetically engineered rMSCs and rCobs, the matrix was not amenable for use as a cell laden, injectable scaffold for *ex vivo* delivery. As found with the preformed scaffolds, cells survived and grew only on the matrix surface. We believe that this occurred because PuraMatrix forms a hydrogel with a low-pH step to maintain the hydrogel as a liquid for injection; it is possible that the low pH killed all of the cells in the interior when cells and hydrogel were mixed. Cells on the surface were in contact with the buffered culture media for a longer period and survived.

This result prompted our search for and identification of alternative injectable scaffold materials to deliver genetically engineered cells. Extracel™, Extracel-X™, and Extracel-LG™ hydrogel kits from Glycosan Systems (Salt Lake City, UT) were studied as a potential scaffold to use in the skin implant model. The Extracel™, and Extracel-LG™ hydrogel kits contain Glycosil™ (thiol-modified hyaluronan, HA), Gelin-S™ (a thiol-modified gelatin or collagen) and Extralink ™ (a thiol-reactive crosslinking agent). Cells are encapsulated during crosslinking where they are proposed to grow within the hydrogel matrix. Cells can also be plated on top of the hydrogel for pseudo 3-D growth. Glycosil can also be used in conjunction with ECM proteins such as laminin, collagen, or fibronectin as well as Gelin-S for most 3-D cell culture and tissue-engineering applications. For our studies, we were interested in the fact that reconstituted Glycosil remains liquid at 15 to 37°C. If Extralink™ is used to crosslink the Glycosil, the gelation time is about twenty minutes with no low-temperature or low-pH steps. Diluting Glycosil with phosphate-buffered saline (PBS) or cell-culture medium can increase its gelation time. These features of Glycosil were tested in our , and other laboratories (32, 33) to evaluate the usefulness of this 3-D matrix system to deliver rMSCs or rCobs in our rat inplant model.

We found that $>10^6$ cells could be collected by centrifugation and resuspended in liquid Glycosil at neutral pH in PBS at 4 C. The liquid/cell mixture can then be transported to the Animal Research Facility. Without Extralink treatment, the cells/Glycosil would be injuectable for up to 24 hours. This would allow time to set up animal injections without worrying about the injectability of the Glycosil. Within 15 minutes of injection under the skin in a 37 C environment, Extralink™ would be added so that cell pellets would be imbedded in the 3D matrix.

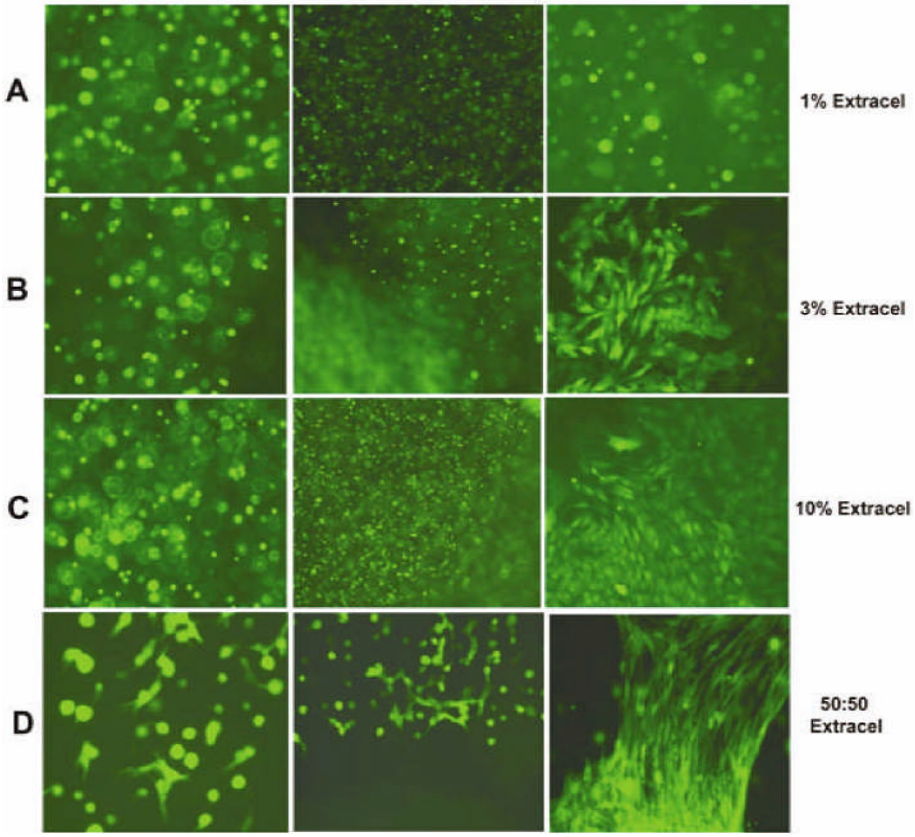

Figure 21 . **Use of Extracel hydrogels as scaffolds to sustain cell growth. MLV**-GFP-rMSCs (0.5-1 x 10^6 cells in 100 .t**l of Extracel) were cultured for 8-21 days in Extracel scaffolds formed from** 1% (A), 3% (B), 10% **(C) and 50% (D)Gelin-S. The left panels illustrate cells taken with a 20**-30X **optical objective. Cells in 1%, 3% and 10% extracel were distributed throughout the matrix. Cells in the 50:50 cell matrix were not found in lower levels of matrix (center panel). Many cells in the 50:50 matrix were found on the plastic cell surface. The cells in the center and right panels were taken with the 10X optical objective. The center panel illustrates cells in the floating discs of Extracel** matrix with the cells attach**ed to the culture surface below. Cells in the right panel are on the surface of plastic culture dish with cells in extracel matrix floating overhead. Cells were not as readily found on the plastic culture dish surface when 1% gels were used.**

2.d.6.b.1 Extracel Hydrogel Matrix Preparation. To make the materials for Extracel matrix formation, Glycosil, Gelin-S and ExtraLink stock vials are resuspended in nanopure water and rocked at 37 C for up to 20 minutes until the solids are dissolved and sterile filtered. The materials are used immediately or can be frozen in aliquots and thawed one time within one month of reconstitution.

In a typical experiment, rMSCs or rCobs transduced with a MLV-GFP expression vector are harvested with trypsin and the cell pellets were suspended in a small volume of complete media to make 10^7cells/ml. 100 tl of cells are mixed per ml of Glycosil/Gelin-S mix. Extralink solution is mixed with the matrix at a ratio of 1 volume of Extralink per 4 volumes of matrix/cell suspension. Within 10 minutes the suspension is added to a Teflon/silicone 3 mm diameter cylindrical mold. The plates with gel are placed at 37 in a CO2 incubator and crosslinking is allowed to continue for 1 hour. Gels were extruded from the mold using a glass rod and were placed in complete culture media in a 6 well plate.

We tested several different hydrogel compositions using the cylindrical mold to prepare matrix samples to float in tissue culture media, to determined if 1) the hydrogels could be manipulated, 2) the hydrogels supported cell viability and growth throughout multiple layers so that more than 10^6 cells could be injected, and 3) transgene expression continued in cells embedded in the scaffold for up to three weeks. We reasoned that if these conditions were met, our chances of delivering an effective gene therapy with BMP 2/4 by injection of cells with pA-BMP-2/4 or MLV-BMP-2/4 directly under the skin would be increased.

3-D cell culture scaffolds were prepared from Glycosil (a thiol-modified hyaluronic acid) - and different percentages of Gelin S (gelatin), to produce 1%, 3%, 10% and 50:50 Extracel hydrogels. The gels are arranged in order of the amount of Gelin S added to the Glycosil which increasingly produced progressively stiffer hydrogel scaffolds when crosslinked with ExtraLink.

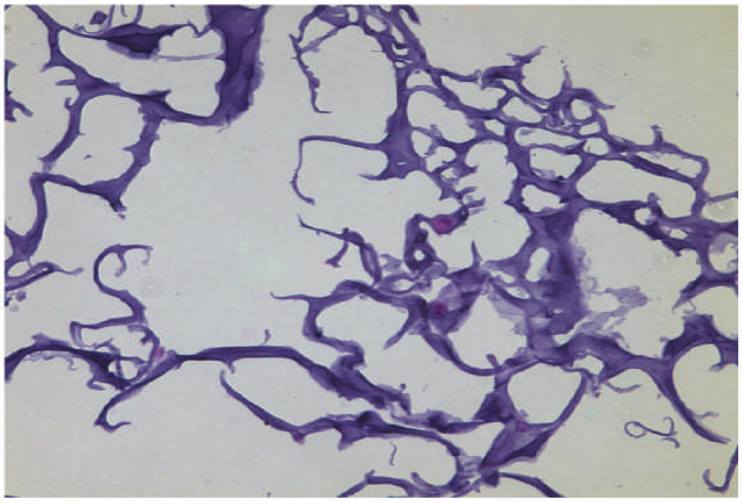

Figure 22. Cell viability in Extracel scaffolds. MLV-GFP transduced rMSCs (0.5 x 10^6) were cultured in 50:50 Extracel matrix for 3 days as floating scaffolds in 10% FBS/ctMEM. Cells were fixed, cut as a frozen sections and stained with H & E. GFP producing cells remained viable inside the Extracel matrix formed elongated structures within the 3D-matrix. Cells did not, however, expand and fill the Extracel matrix. This suggests that cells survive but do not proliferate in the extracel matrix and form a *in vivo* more tissue like structure. To do studies and deliver a therapeutic dose of BMP-2/4 transgene, the cell number must be increased to fill the matrix.

2.d.6.b.2. Assessment of cell growth in Extracel. To test Extracel hydrogels, we incorporated 0.5-1 X 10^6 MLV-GFP cells in 100 tl of matrix. We found that Extracel could be mixed directly with pelleted cells or with cells resuspended in PBS. In either case or we could pellet cells and mix the cells in the Extracel components prior to the addition of Extralink. The use of cell pellets will allow us to encapsulate up to 10^7 or more cells in 100 tl of liquid matrix material in PBS. We also found that cells were more easily distributed in 3% and 10% Extracel and that the gels could be manipulated with forceps.

In this comparison study with varying Gelin-S amounts, it was found that cell dispersion in the matrix appeared to be greater in the 1-10% Extracel matrices compared to the 50% Gelin-S matrix (Figure 21). These experiments demonstrated that cells were suspended throughout the matrix and that cells were viable and expressed GFP for up to three weeks. The cells retained spherical shapes in the 1-10% Genlin-S matrices, however, cells morphology was more like that in a solid tissue in the 50% matrix as illustrated in the H & E stained cells in Figure 22. In all of the matrices, cells continued to express GFP for up to three weeks or longer. From these experiments, we propose to do continuation studies in Extracel based hydrogel matrices with 1- 10X 10^7cells/100 tl expressing either RFP or BMP-2/4. The durability and injectability of the Extracel matrix will direct which % gel we use for *in vivo* studies.

2.d.6.b.3. Extracel-based scaffolds are injectable: We tested the ability to inject the 3 and 10% hydrogel matrices with 23 and 26 gauge needles. Extralink was added to each Extracel matrix suspension and we were able to inject the material over a 15-20 minute period at room temperature. We found that after 15 minutes both the 3 and the 10% gel could not be injected with either the 23 or 26 gauge needle for 20 minutes. Addition of cells to the mixture did not alter the ability to inject the matrix.

These studies provided a usable protocol for in *vivo* implant studies. Based on these studies, the following procedure is proposed: 10^7 rMSCs or rCobs will be pelleted in PBS and maintained on ice. PBS will be removed from the cells after centrifugation and Glycosil and Gelin-S (0.5-1 ml total) will be added to the cell pellet. The cells will be resuspended in the Extracel and placed on ice. The cells in the liquid matrix will be taken to the Animal Research Facility. The matrix and cells will be mixed with Extralink just prior to each injection. After Extralink is added, 100 tl injections (1-2 X 10^6 cells) with a 26 gauge needle will be placed under the skin on the back.

Key Research Accomplishments

- We found that our pPC-based vectors (especially pABSS) when delivered to cultured cells expressed adequate levels of BMP-2/4 to stimulate ALP activity in osteoblasts and transdifferentiated myoblasts.
- We found that manipulation of the SB transposase expression with an alternate minimal promoter increased ALP activity as well as, or better than, plasmids with the CMV promoter. The multiple cloning site adjacent to the minimal promoter could be used for enhancer addition to manipulate expression to optimize gene delivery or to provide vectors with tissue specific SB transposase expression.
- Electroporation rMSCs with siPort and pPC-based vectors led to persistent expression of transgenes.
- We found that Extracel, a novel synthethic nanofiber scaffold supported the growth of encapsulated MLV-GFP transduced rat marrow stromal cells and osteoblasts for up to three weeks in culture.
- Extracel matrices with viable cells expressing transgenes can be injected for up to 15 minutes. This would allow gel/cell mixtures to be injected into animals. The matrix/cells would solidify *in vivo* and the encapsulated cells would express transgene.

Reportable Outcomes

- U.S. Patent Application No. 11/503,365 "Methods for Accelerating Bone Repair" was filed 8/10/06 by the Technology Transfer Program, Dept Veterans Affairs, 103 South Gay St. Fifth Floor, Baltimore, MD 21202. This patent describes the use of the BMP-2/4 expressing, SV40DTS/SB based vectors to stimulate bone formation and fracture repair.
- We have prepared and tested a number of novel plasmid vectors based on the use of the SV40DTS and the *Sleeping Beauty (SB*) transposon/transposase that can be used for *in vivo* gene delivery and expression. Table 1 and Table 2 list and describe these plasmid vectors.
- We have received funding for a grant entitled "Development of plasmid vectors with nuclear import sequences for improved skeletal Gene Therapy" (July1, 2009-June 30, 2010). This grant is funded by Loma Linda University/National Medical Testbed to test the nonviral vectors pPC vectors that were prepared *in vivo* by direct injection/electroporation or by introduction of transfected cells in extracel scaffolds. A mouse model will be used.
- The *in vivo* data gained with the Loma Linda University/NMTB funding will be combined with the data described in this report to prepare manuscripts.

Conclusions

- We have developed several pPC-based nonviral vectors that express BMP-2/4 at levels that can differentiate osteoblasts and transdifferentiate myoblasts *in vitro*.

- Cultured cells on scaffolds do not survive *in vivo* in Fisher 344 rats. Therefore immunocompromised animals (SCID mice model) should be substituted for Fisher 344 rats in implant models in order to test our plasmids.

- Rat MSCs and Osteoblasts are difficult to transfect with the same reagents that transfect mouse cells with high efficiency. Success of our studies depend on reproducibility of transfecting cells with >30% efficiency. A better model to test our plasmid vectors might be provided in a mouse model. Nucleofector reagents that produce transfection efficiencies of 70-90% in mouse osteoblast and marrow stromal cells result in transfection efficiencies of 1-20% in cultured rat osteoblast and marrow stromal cells with a small plasmid. The larger pPC-based vectors are transfected with 1-5% efficiency.siPort transfection reagents transfect rat and mouse cells to the same degree as nucleofector reagents. siPort reagents are less expensive than Nucleofector reagents. However the transfection efficiency with either of these reagents is not adequate for comparison of plasmid transfected and virally transduced cultures which can be transduced at 80-90% efficiency. Again there is a need to switch to a mouse model.

- Because we have identified a scaffold (Extracel) that can be injected and maintains cellviability and transgene expression for several weeks *in vitro*, we can now test the engineered cell-laden matrices in mice *in vivo.* The focus of these new LLU/NMTB funded studies will be to test the pPC-based vectors and others by direct injection into tissues.

References

1). Peng H, Chen S T, Wergedal J E, Polo J M, Yee J K, Lau K H, Baylink DJ 2001 Development of an MFG-based retroviral vector system for secretion of high levels of functionally active human BMP4. Mol Ther 4(2):95-104.

2). Li S, MacLaughlin F C, Fewell J G, Gondo M, Wang J, Nicol F, Dean D A, Smith L C 2001 Muscle- specific enhancement of gene expression by incorporation of SV40 enhancer in the expression plasmid. Gene Ther 8(6):494-7.

3). Dean D A 1997 Import of plasmid DNA into the nucleus is sequence specific. Exp Cell Res 230(2) :293-302.

4). Dean D A, Byrd J N, Jr., Dean B S 1999 Nuclear targeting of plasmid DNA in human corneal cells. Curr Eye Res 19(1):66-75.

5). Wilson G L, Dean B S, Wang G, Dean D A 1999 Nuclear import of plasmid DNA in digitonin- permeabilized cells requires both cytoplasmic factors and specific DNA sequences. J Biol Chem 274(31):22025-32.

6) Vacik J, Dean B S, Zimmer W E, Dean D A 1999 Cell-specific nuclear import of plasmid DNA. Gene Therapy 6(6):1006-14.

7). Dean D A, Dean B S, Muller S, Smith L C 1999 Sequence requirements for plasmid nuclear import. Exp Cell Res 253(2):713-22.

8). Young J L, Benoit J N, Dean D A 2003 Effect of a DNA nuclear targeting sequence on gene transfer and expression of plasmids in the intact vasculature. Gene Ther 10(17):1465-70.

9). Munkonge F M, Dean D A, Hillery E, Griesenbach U, Alton E W 2003 Emerging significance of plasmid DNA nuclear import in gene therapy. Adv Drug Deliv Rev 55(6):749-60.

10). Gasiorowski J Z, Dean D A 2003 Mechanisms of nuclear transport and interventions. Adv Drug Deliv Rev 55(6):703-16.

11). Dean K A, von Ahsen O, Gorlich D, Fried H M 2001 Signal recognition particle protein 19 is imported into the nucleus by importin 8 (RanBP8) and transportin. J Cell Sci 114(Pt 19):3479-85.

12). Dean D A, Strong D D, Zimmer W E 2005 Nuclear entry of nonviral vectors. Gene Ther 12(11) :881-90.

13.) Prasad T K, Rao N M 2005 The role of plasmid constructs containing the SV40 DNA nuclear-targeting sequence in cationic lipid-mediated DNA delivery. Cell Mol Biol Lett 10(2):203-15.

14). Harris J W, Strong D D, Amoui M, Baylink D J, Lau K H 2002 Construction of a Tc1-like transposon Sleeping Beauty-based gene transfer plasmid vector for generation of stable transgenic mammalian cell clones. Anal Biochem 310(1) :15-26.

15). Izsvak Z, Ivics Z 2004 Sleeping beauty transposition: biology and applications for molecular therapy. Mol Ther 9(2):147-56.

16). Ivics Z, Hackett P B, Plasterk R H, Izsvak Z 1997 Molecular reconstruction of Sleeping Beauty, a Tc1-like transposon from fish, and its transposition in human cells. Cell 91(4):501-10.

17). Ivics Z, Kaufman C D, Zayed H, Miskey C, Walisko O, Izsvak Z 2004 The Sleeping Beauty transposable element: evolution, regulation and genetic applications. Curr Issues Mol Biol 6(1):43-55.

18). Ivics Z, Izsvak Z 2005 A whole lotta jumpin' goin' on: new transposon tools for vertebrate functional genomics. Trends Genet 21(1) :8-11.

19). Ivics Z, Izsvak Z 2006 Transposons for gene therapy! Curr Gene Ther 6(5):593-607.

20). Hackett P B, Ekker S C, Largaespada D A, McIvor R S 2005 Sleeping beauty transposon-mediated gene therapy for prolonged expression. Adv Genet 54:189-232.

21). Liu G, Geurts A M, Yae K, Srinivasan A R, Fahrenkrug S C, Largaespada D A, Takeda J, Horie K, Olson W K, Hackett P B 2005 Target-site preferences of Sleeping Beauty transposons. J Mol Biol 346(1):161-73.

22). Liu H, Visner G A 2007 Applications of Sleeping Beauty transposons for nonviral gene therapy. IUBMB Life 59(6):374-9.

23). Score P R, Belur L R, Frandsen J L, Geurts J L, Yamaguchi T, Somia N V, Hackett P B, Largaespada D A, McIvor R S 2006 Sleeping Beauty-mediated transposition and long-term expression in vivo: use of the LoxP/Cre recombinase system to distinguish transposition-specific expression. Mol Ther 13(3):617-

24). Mikkelsen J G, Yant S R, Meuse L, Huang Z, Xu H, Kay M A 2003 Helper-Independent Sleeping Beauty transposon-transposase vectors for efficient nonviral gene delivery and persistent gene expression in vivo. Mol Ther 8(4):654-65.

25). Rauch C, Brunet A C, Deleule J, Farge E 2002 C2C12 myoblast/osteoblast transdifferentiation steps enhanced by epigenetic inhibition of BMP2 endocytosis. Am J Physiol Cell Physiol 283(1):C235-43.

26). Krebsbach P H, Zhang K, Malik A K, Kurachi K 2003 Bone marrow stromal cells as a genetic platform for systemic delivery of therapeutic proteins in vivo: human factor IX model. J Gene Med 5(1):11-7.

27). Lennon D P, Haynesworth S E, Young R G, Dennis J E, Caplan A I 1995 A chemically defined medium supports in vitro proliferation and maintains the osteochondral potential of rat marrow-derived mesenchymal stem cells. Exp Cell Res 219(1):211-22.

28). Gersbach CA, Guldberg R E, Garcia A J 2007 In vitro and in vivo osteoblastic differentiation of BMP-2- and Runx2-engineered skeletal myoblasts. J Cell Biochem 100(5):1324-36.

29). Gersbach C A, Byers B A, Pavlath G K, Guldberg R E, Garcia A J 2004 Runx2/Cbfa1-genetically engineered skeletal myoblasts mineralize collagen scaffolds in vitro. Biotechnol Bioeng 88(3):369-78.

30). Zhang, S. et al., 1995 Self-complementary oligopeptide matrices support mammalian cell attachment. Biomaterials 16:1385-91.

31). Semino CE et al. 2004Entrapment of migrating hippocampal neural cells in 3D peptide nanofiber scaffold. Tissue Engineering 10:643-57.

32). Behravesh E, Zygourakis K, Mikos A G 2003 Adhesion and migration of marrow-derived osteoblasts on injectable in situ crosslinkable poly(propylene fumarate-co-ethylene glycol)-based hydrogels with a covalently linked RGDS peptide. J Biomed Mater Res A 65(2):260-70.

33).TemenoffJ S, Park H, Jabbari E, Sheffield T L, LeBaron R G, Ambrose C G, Mikos AG 2004 In vitro osteogenic differentiation of marrow stromal cells encapsulated in biodegradable hydrogels. J Biomed Mater Res A 70(2):235-44.

C. SUPPORT SERVICE FACILITIES

Project 9

Progress Report – Administrative Support Service Facility

INTRODUCTION

The research proposed in this application was performed within the Musculoskeletal Disease Center (MDC), which is a large, multi-disciplinary research center consisting of more than 70 scientific and technical staff members, including 15 senior investigators with diverse expertise and research training. Of the 70 staff members, 43, including 13 senior investigators, are currently working on the Army projects. Strong administrative support is needed for organizing, coordinating, facilitating, and monitoring the research supported by the Army projects and is absolutely essential for the success of such a large, dynamic, and expanding research program. Consequently, the primary responsibility of this Administrative Support Service Facility was to support the administrative needs of the investigators supported by this Army grant. Moreover, synergistic interactions and collaborations between the investigators of the Army grant and other investigators of the MDC, as well as other investigators at local academic institutions and research organizations, such as Loma Linda University (LLU), Loma Linda Veterans Association for Research and Education (LLVARE), Loma Linda VA Medical Center, the University of California at Riverside, and the City of Hope, would enhance the productivity of the Army projects. Accordingly, the secondary objective of this Administrative Support Service Facility was to provide and stimulate interdepartmental, interdisciplinary, and inter-institutional dialogue and to improve the existing interactions and productivity between various investigators of the local institutions and organizations in musculoskeletal research

Technical Objective 1:

To continue to provide a stimulating and supportive environment for Investigators supported by the Army grant that is conducive to focusing on bench research work so that administrative responsibilities are reduced.

Our Administrative Support Staff work with the investigators on these awards to keep them apprised of ongoing budgetary issues; to facilitate supply and equipment purchasing decisions; to order supplies and equipment; to prepare manuscripts for publication; to prepare paperwork for submission to oversight committees; to organize meetings; to help with staff recruitment; and to help facilitate the preparation of progress reports. Maintaining a strong administrative support team has been critical to the success of our scientists. During the this grant period, our scientists have published **5** articles and **1** abstracts. The total number of Army project related publications for our group since 2000 is **60** plus **39** abstracts.

Regular weekly or bi-weekly meetings are convened at which our senior investigators (Drs. Mohan, Lau, Wergedal) discuss scientific issues related to the fulfillment of the specific objectives of all of our Army funded projects. In order to insure that all of the scientific work of our current Army awards remains on track and progress toward meeting the specific objectives

of each of our awards is being met, these regular meetings are essential. Our current awards include: DAMD17-01-1-0744 and DAMD17-03-2-0021.

Technical Objectives 2:

To continue to serve as the necessary and essential Support Service in order to stimulate interdepartmental, interdisciplinary, and inter-institutional dialogue and enhance the existing interactions and productivity between various investigators of LLU, Loma Linda University Medical Center, and LLVARE in musculoskeletal research.

Weekly staff meetings are held for all Musculoskeletal Disease Center (MDC) staff. When scientific issues are presented at the MDC staff meetings, these meetings are open to other investigators from Loma Linda University (LLU) as well as other VA and LLVARE investigators. Senior Investigators give talks on new technologies and areas relevant to the Army funded projects. Likewise, MDC investigators are invited to meetings of various research groups at LLU, the City of Hope and, periodically, the University California Riverside (UCR). We invite expert scientists from other institutions to give talks on issues relevant to our Army funded research. This sharing of ideas with investigators from other institutions has proven to be very important.

Technical Objective 3:

The Core Facility "user" committee" will continue to evaluate the service rendered by each of the support service facilities. This information will then be provided in written form to the director of the corresponding support services facilities.

The end users evaluate the performance of our Informatics/Microarray, Vector, and Phenotype Core facilities on an ongoing basis and report to the Principal Investigator if any problems in service are found. Suggestions for improvement are discussed with the individual leaders of the Support Facilities as well as at general Staff Meetings. No major problems have been reported with any of the Core Facilities during the grant period.

Project 10: Phenotype Support Services.

INTRODUCTION

The phenotype support service facility is essential for efficient progress in all of the specific projects in this proposal as well as other projects in the molecular genetics and gene therapy divisions of the Musculoskeletal Disease Center (MDC). The assays performed in the phenotype support service facility include: 1) total bone density in rodents by pQCT; 2) total skeletal bone density in rodents by dual energy x-ray densitometry (PIXI); 3) bone strength analysis and performance of very precise femoral fracture using the Instron mechanical tester; 4) X-ray imaging by the Faxitron; 5) histological analysis, including quantitative morphology, immunocytochemistry, and fluorescence microscopy; 6) serum and urine chemical assays, including bone markers and IGF assays; and 7) statistical support. It would be difficult for the principal investigator of each of the separate projects to set-up the facilities to perform this large array of routine phenotypic measurements without considerable duplication of effort. Consequently, this phenotypic vector support facility is highly efficient and cost effective for the specific projects in this grant. The emphasis in this support service facility is to perform highly reliable, precise measurements of the phenotype requested. The director of this support facility keeps abreast of new technologies and transfers this information to those principal investigators potentially interested in the corresponding new technology. The director of this support facility will also provide training courses in the various phenotypic measurements made in this support service facility. It is essential for the investigators to have a fundamental understanding of the measurements being made so that they will be aware of the pitfalls and advantages of the application of these techniques. Study design and statistical support will also be provided when requested. As part of the Phenotype Core, bone and tissue samples from several of the subprojects have been processed, sectioned and stained for histomorphological and cytochemical evaluation. Modifications have been made to existing methods where necessary in order to meet project objectives.

BODY

Technical Objectives

The major technical objective for this phenotype support service facility is to receive samples, perform the appropriate measurements on these samples, and then transfer all the data electronically to the corresponding investigator. Specific objectives include:

1. To assist investigators in the design of studies involving given phenotypes.

2. To perform measurements as requested by the investigators on the samples provided.

3. To follow the development of emerging technologies in the literature and at conferences and make recommendations to investigators regarding the possibility of adopting some of these new technologies in the phenotype support service facility.

Progress for Specific Objectives

Specific Objective 1: To assist investigators in the design of studies involving given phenotypes.

Project 1: Studies on Genetic Regulation of Digit Tip Regeneration

This project required the establishment of new protocols to carry out histological examination of regenerating mouse digit tips. Several embedding techniques were tested to determine optimum methods of histology of mouse digits. Embedding in glycol methacrylate without demineralization allows good enzyme staining (alkaline phosphatase and acid phosphatase), which is useful for the identification of osteoblasts and osteoclasts at the site of regeneration. However, cracking of the mineralized bone occurs, leading to some loss of bone pieces during staining. Demineralization of specimens followed by embedding in paraffin gave better preservation of intact specimens. In addition, paraffin embedding allows for better control over specimen orientation during embedding. Furthermore, paraffin sections are more suitable for immunostaining protocols to identify the presence of key molecules. It was also shown that penetration of the digits by the embedding medium was improved if the skin is at least partially removed before tissue processing. Paraffin embedding has been selected as the method of choice for routine processing of the samples.

Selection of the appropriate sampling site is always an important aspect of bone histology. The digits are composed of three phalanxes, with the third phalanx being the digit tip that is covered by the nail. To keep the digits in a consistent orientation during embedding, the digits were left attached to the rest of the paw. The initial objective was to be able to see all three phalanxes from each digit in order to compare the regeneration in the cut digit with uncut controls. Longitudinal sections through the middle of the phalanx potentially provided this view. One difficulty with obtaining a consistent sampling site was that the digits are normally slightly flexed. This was particularly true of phalanx 3, the main site of regeneration. Flexure was greater in the older animals than in the young ones. Maintaining pressure on the paws to orient the digits parallel to the bottom of the mold during embedding minimized the effect of flexure. However, it was still necessary to examine multiple sections in order to see all phalanxes and multiple digits. It also appeared that placing the upper or extensor surface of the paw down on the bottom of the mold gave the best orientation.

Several stains have been identified as informative for studying the regeneration process. The standard cell stain is an hematoxylin and eosin. This works well for paraffin sectioning to identify cell types and has proven useful in identification the regenerating epithelium and the blastema.

Further work on the appropriate orientation of the specimen during embedding suggested an alternative may be better. Our studies have continued to improve the sampling site selection for the digit wound healing study. Our previous work had used latero-medial sectioning which allowed several digits including cut and uncut digits to be seen on one section. However, it became apparent that the view of the wound-healing site varied with depth of the sectioning. Therefore, optimum depth required different sections for different digits. Consequently, we considered antero-posterior sectioning (perpendicular to the nail). It was apparent from test sections on normal digits that this orientation of the specimens gave a better view of the bone in the third phalanx and was less sensitive to depth of the section. These advantages offset the disadvantages that only one digit could be viewed at a time and maintaining a consistent orientation was more difficult. With more experience with the new technique, the sampling orientation became more consistent. It was also found that maintaining the paw intact helped to keep the orientation constant. However, partial cutting and removal of the skin proximal to the third phalanx improved the infiltration of fixatives and paraffin.

This modified sampling method was used to process samples for the time study of wound healing with multiple inbred strains of mice. The investigators were assisted in interpreting the morphology and cell staining in the wound-healing site. The cell morphology, Hematoxylin-eosin staining and Masson trichrome (collagen) staining helped to identify a sub dermal site with some characteristics of a blastema. These characteristics included mitotic figures, indicating increased cell proliferation, and cells with mesenchymal cell morphology.

The investigators were also assisted in testing immunostaining for products of several genes. The protocols, basic staining reagent, the expertise and equipment needed were provided. Digit tip regeneration samples were prepared for immunostaining and evaluation of blastema formation.

The disruption and regeneration of the basement membrane may be an important part of limb regeneration. Therefore good methods for the demonstration of basement membranes at the regeneration site will be important. We further developed a laminum immunostaining method for identification of basement membrane under the epidermal cell layer. Previously we have tested several methods for determining basement membranes including immunostaining for type IV collagen, and silver staining for reticulin fibers. These methods gave variable staining for the basement membranes under the epidermal cell layer of the skin. Laminum is one of the components of the basement membrane. We have previously established that laminum immunostaining as an excellent way to outline muscle fiber bundles. Staining in digit tip samples with a 1:50 dilution of stock anti laminum antibodies (a concentration that works well with

skeletal muscle samples) resulted in highly overstained digit tip samples. Further testing of lower concentrations of antibody showed that dilution of the antibody 1:600, still resulted in staining of the epithelial membrane while minimizing staining of other structures.

Formin 2 has been identified by microarray analysis as playing a role in digit tip regeneration. We examined digit tip samples with immunohistochemistry to identify formin 2 protein expression levels in sections of digit tips. The immunostaining identified the chondroblast in the regenerating digit tip as showing the highest level of formin 2 expression while osteoblasts and osteoclast showed low levels of expression.

Because the closely related gene, formin 1, has been shown to affect bone phenotypes, the expression of formin 1 was also examined by immunostaining of digit tip samples. A range of antibody dilutions were tested. Again the highest expression level of the Formin 1 appeared in cartilage cells with low levels expressed in osteoblasts and osteoclasts. The distribution of high formin 1 expression extended into the hypertrophic cartilage cells and thus, it appeared to be more widely expressed as fomin 2.

Project 2: Sensitizer Screening to Enhance Detection of ENU-Induced Mutant Phenotypes

Bone samples from mutant mice developed in project 2 have been processed for evaluation of bone structures, and parameters of bone formation and bone resorption.

pQCT examination of one of the ENU mutants showed a strain with low bone density. The density was low even when corrected for body weight. The histomorphological examination of animals injected with the fluorescent label calcein (which labels newly formed bone) showed a decreased rate of bone formation. In vitro studies suggested the low formation rate was due to decreased osteoblastic proliferation. To determine if osteoblastic proliferation was decreased in vivo, the technique of injecting bromouridine into the mice and determining its incorporation into proliferating cells was tested. Sections of femur from bromouridine injected animals were prepared by demineralization and paraffin embedding. The bromouridine incorporated into DNA is detected by immunostaining by antibodies against the bromouridine. The antibodies against bromouridine proved to be relatively sensitive, so that staining artifacts were evident at high levels of bromouridine even though controls without primary antibody treatment were negative. The artifacts were evident as staining in osteocytes and in hypertrophic cartilage cells. These cell types are not proliferating and should not be incorporating bromouridine. Further dilutions of the primary antibody yielded cleaner staining. However, some adjustment of antibody concentration was necessary between sample sets as optimum staining varied significantly.

Project 4. The Application of Transgenic Mice to Assess Gene Function in Mechanical Loading and in Bone Fracture Healing Models.

Transgenic mice with Leptin or Bax gene knockouts are being studied to determine the influence of these genes on mechanical testing and bonefracture repair. Evaluation of fracture healing is being done by pQCT densitometry and Faxitron X-ray analysis using the phenotype core facilities. Because fracture healing involves the addition of a cancellous bone bridge on the periosteal surface, the thresholding parameters in the pQCT analysis need to be adjusted. Parameters that work well with normal bone structure do not distinguish the new bone on the periosteal surface. Furthermore, lowering of the outer threshold value allows determination of the total hard and soft callus. These parameters have now been established and are being used to assess fracture healing in the transgenic mice.

Bone samples from healing fractures in Leptin, Bax or Serpine knockout mice were processed for histological evaluations. Bone samples were demineralized in EDTA and embedded in paraffin. Longitudinal sections through the fracture site were prepared and stained with H&E, Van Geisen Trichrome stain, or Mason's trichrome stain. Cartilage is determined by Safranin-O staining.

Bax knockout mice have increased cartilage amounts in the callus as shown by increased unmineralized callus by pQCT analysis. To determine if this could be increased cartilage sections of paraffin embedded femurs were stained for cartilage by Saffronin O. The histological examination showed increased cartilage in the fracture callus site.

Project 6. Systemic Gene Therapy for the Skelton

Green fluorescent protein (GFP) is a fluorescent marker used to label the hematopoietic stem cells in the gene therapy study. GFP labeled hematopoietic stem cells infused into mice appear in bone marrow and can be detected by GFP fluorescence. The FACS analysis is a sensitive way to detect GFP fluorescence in cell suspensions. Generation of GFP labeled hematopoietic cells in the blood stream or in marrow cell suspensions can be readily detected by FACS analysis. Histological detection of GFP labeled cells appears to be less sensitive. Fluorescence microscopy of bone sections readily detects strongly labeled cells. However, weakly labeled cells are difficult to distinguish from background autofluorescence. Frozen sections are the optimum platform for viewing fluorescence because autofluoresence is minimized. However, frozen sections do not attach well to the slide. In addition, staining procedures designed to identify the nature of the labeled cells commonly result in distortion and loss of tissue. An alternative approach is to use antibodies to detect GFP. Good antibodies are available for GFP. The methodological details are being adjusted to increase the sensitivity of the immunostaining procedure. To compare methodologies, we have devised three approaches for the detection and identification of GFP labeled cells in bone: 1) fluorescence in frozen sections followed by staining for cell identification, 2) Fluorescence in plastic embedded section (with revised protocol to improve preservation of fluorescence) followed by staining for cell identification, and 3) GFP immunostaining followed by staining for cell identification. These procedures were

compared using samples with a known range of GFP labeled cells. Preliminary results show advantages and disadvantages of each of the three approaches.

Progress continued on developing methods suitable for identifying osteoblasts expressing green fluorescent protein GFP. One of the needed methodologies is to be able to examine GFP expression and osteoblast markers in the same section. This is needed to confirm that GFP labeled cells that have been introduced in to the animal can develop into osteoblasts. While GFP expressing cells can be identified by immunostaining in paraffin sections, alkaline phosphatase, the most commonly used osteoblast marker, is inactivated by this protocol. We have tested an alternative approach that employs frozen sectioning. The technical difficulty with frozen sections is that they do not attach well to the slides. Attachment needs to be good enough in order to maintain the osteoblasts on the surface of the bone during staining. We have found that mineralized bone matrix does not attach well to the slides and the matrix will move or be lost during staining. Demineralized bone matrix attaches better but still not well enough to have good retention of the samples. Demineralization does decrease alkaline phosphatase activity in the frozen sections, but the activity is still sufficient for osteoblast identification.

In order to improve attachment, we have tested a new cryostat attachment that is a tape transfer system. A transfer tape is placed over the block before the sections are cut. The tape is used to transfer the section to special slides that are coated with unpolymerized plastic. The slide is then flashed with UV light to polymerize the plastic binding the intact section to the slide. Attachment is still variable so that multiple sections must be prepared to find ones that are satisfactory. Attachment to the slide is better with demineralized sections than with mineralized sections.

Another difficulty is balancing the ALP staining with the antibody horseradish peroxidase staining. Neither staining should be too strong or the presence of the second stain will be obscured; and selection of the appropriate color of dye affects the detection of dual staining. An alternate substrate for the DAB used in horseradish peroxidase labeled antibodies (AEC) was tested. The AEC yielded a reddish orange color that lacked the intensity necessary for the dual staining. The brownish color of the product of DAB substrate was better. However, some brown deposits in the normal marrow caused some confusion in the interpretation of the stained sections. These brown deposits were shown to be homosiderine by staining them for iron. The Prussian blue iron stain converted the brown to blue so that it could be distinguished from the brown DAB staining. Thus the combination of red staining (ASTR substrate) for ALP and brown staining (DAB substrate) for GFP antibodies with blue blocking of iron deposits and blue hemetoxylin counterstaining appears to provide the best combination for osteoblast identification.

Endogenous peroxidase activity in bone is readily blocked in paraffin sections of bone by hydrogen peroxide pretreatment. Endogenous peroxidase activity is much stronger in frozen sections and less sensitive to inactivation by hydrogen peroxide pretreatment. While osteoblasts

do not have much endogenous peroxidase, some of the marrow cells have strong peroxidase activity. This activity gives strong marrow cell staining in control sections and complicates the interpretation of staining patterns. Alternative blocking methods for endogenous peroxidase activity are being sought.

We have explored and reported on a number of technical approaches to identifying bone cells that express the green fluorescent protein (GFP) as well as osteoblastic markers such as alkaline phosphatase. These approaches have identified cells with these properties but have not been satisfactory for quantitation. A new method for identifying the osteoblastic marker, alkaline phosphatase activity has recently been introduced. This is a fluorescent method. It has the advantage that the GFP and alkaline phosphatase could both be determined fluorescently. The alkaline phosphatase substrate is ELF97. It is a naptholic phosphate ester that becomes fluorescent and insoluble when the phosphate is hydrolyzed off. Determination of phosphatase is straightforward. The ELF97 is dissolved in an alkaline buffer and the resulting substrate solution applied to the slide. In bone sections with preserved alkaline phosphatase activity, activity is evident within minutes. If monitored under a fluorescent microscope, the incubation time can be optimized. The reaction is terminated by rinsing off the slide. The optimum microscope filter set required for viewing the fluorescence is different for the two agents. Comparison between GFP and alkaline phosphatase can be done by flipping between filter sets. This fluorescent method has been found to be an effective method for the identification of both acid and alkaline phosphatases.

A major part of the study was to examine bone tissue sections from mice infused with FGF producing cells. We have advised the investigators throughtout the grant period on the most appropriate histomorphometry methods to use for the studies. Therefore sections were prepared for histocytological and histomorphological evaluation.

Sub-Project 7: Study of Synergistic Growth Factors in Skeletal Gene Therapy

Sections were prepared from calvaria of animals with critical size calvarial defect and treated by gene therapy.

Specific Objective 2: To perform measurements as requested by the investigators on the samples provided.

Project 1. Studies on the Genetic Regulation of Digit Tip Regeneration.

Samples of paws from several mouse strains and several time points have been processed. Paraffin sections have been prepared and stored for future work. These sections have been used for the development of immunostaining protocols and other staining techniques.

Microarray studies and histological immunostaining studies suggested that Formin 2 has a role in digit Tip regeneration. To examine its role in bone, Formin 2 knockout animals were obtained for study. The bone density and bone geometry of the knockout mice were examined by pQCT. These studies showed a significant decrease in bone density in the Formin 2 knockout mice.

Project 2: Sensitizer Screening to Enhance Detection of ENU-Induced Mutant Phenotypes

Bone samples from mutant lines identified in the ENU screening project have been processed for bone histology and bone histomorphometery. The samples were from animals injected with fluorescent tetracycline or calcein labels so that bone formation measurements could be done. Thick cross sections of undemineralized femurs were prepared from methyl methacrylate embedded samples. Measurement of fluorescent label lengths and separation were made. Bone formation rates at the endosteum and periosteum were calculated using standard histomorphological calculations.

To further evaluate the mutant lines, femoral bone samples from bromouridine injected mice were examined for incorporation of bromouridine into proliferating bone cells. Examination of sections immunostained for bromouridine showed incorporation of bromouridine (nuclear labeling) into proliferating cells. Labeling rates in the marrow were relatively high as expected and confirming that the labeling method worked. Epiphyseal cartilage also showed significant labeling in the proliferating zone. However, incorporation of the label into periosteal bone cells was low (1-2%) making it difficult to find enough cells for statistical evaluation of labeling differences. Alternative methods were sought to increase periosteal cell labeling. A triple injection of bromouridine was tested but incorporation rates failed to rise sufficiently for quantitation of periosteal osteoblast proliferation rates. Other investigators have used infusion pumps to allow exposure of the mice to Bromouridine over a longer period but this approach was not tested.

Project 4. The Application of Transgenic Mice of Assess Gene Function in Mechanical Loading and in Bone Fracture Healing Models.

Methods were established for the confirmation of bone healing effects using histomorphological evaluation. Fractured and control bones are demineralized in neutralized ethylendiaminetetraacetic acid. Samples are embedded in paraffin and cut longitudinally. Sections are stained for H&E, Mason's trichrome, Van Geisens, and Saffranin O.

Bone Sections from Leptin and Bax knockout mice have been prepared and stained. Samples include fractured and unfractured bones at various times after fracture. Samples were

demineralizedin EDTA, processed in a tissue processor, embedded in paraffin and sectioned. Sections are stained for H&E, Mason's trichrome, Van Geisens, and Saffranin O. The Saffranin O stained sections were used to follow the development and loss of cartilage during fracture repair. Samples were also evaluated for bone resorption by staining for tartrate-resistant acid phosphatase an osteoclast marker. Tunnel staining is being used to evaluate apoptosis in BAX knockout mice.

Bone density and bone geometry measurements have been made by pQCT and Faxitron X-Ray analysis to establish basal values and to follow fracture healing. The instrument threshold settings must be done carefully because of the deposition of low density "woven bone" at the fracture repair site.

Project 6. Systemic Gene Therapy for the Skelton

Bone samples for this study have been processed for histological evaluation in the Phenotyping laboratory. This project involves the use of green fluorescent protein as a cell tag. Histological processing techniques tend to quench the fluorescence of the green fluorescent protein and increase the autofluorescence. Frozen sections are desirable because this technique requires less processing. A procedure for the preparation of frozen sections was established and initial samples have been examined. Bone is a difficult material from which to obtain good frozen sections.. Therefore, the frozen section methodology is still undergoing optimization.

Bone samples from mice treated with GFP labeled hematopoietic stem cells are being processed for histological evaluation in the phenotyping laboratory. Histological processing includes both frozen and paraffin embedded sections of bone and soft tissues.

Bones were also evaluated for bone formation by analysis of density and geometry by pQCT analysis.

Bone samples from mice treated with GFP labeled hematopoietic stem cells are being processed for histological evaluation in the phenotyping core laboratory. Histological processing includes both frozen and paraffin embedded sections of bone and soft tissues.

Specific Objective 3: To follow the development of emerging technologies in the literature and at conferences and make recommendations to investigators regarding the possibility of adopting some of these new technologies in the phenotype support service facility.

Project 1. Studies on the Genetic Regulation of Digit Tip Regeneration.

The study of the wound regeneration process will be facilitated by the establishment of additional histological methods based on literature and meeting presentations. Wounding or cutting the digit tip interrupts the basement membrane below the epithelium. The restoration of this basement membrane may act to regulate the extent of the regeneration. Several different immunhistochemical or cytochemical stains for basement membranes have been investigated. Laminum and type IV collagen are two components of basement membranes that have been investigated immunohistologically. Two cytochemical stains based on the high carbohydrate content of the basement membrane, methenamine silver (GOYA) and the PAS stain, are under investigation. Collagen structure of the dermal tissues is being examined by Mason's Trichrome stain. The normal structure of the dermal layer includes a dense collagen layer just under the epidermal basement membrane and looser, more randomly oriented fibers in the lower dermal layer. Restoration of this collagen organization is part of the regeneration process.
We continue to review the literature and attend presentations related to wound healing. As noted previously we have looked at methods for evaluating basement membrane development in healing fractures. Both the methamine silver (GOYA) method and PAS staining techniques show basement membranes but also stain other membranes. Thus, they are not specific but do give information about the structure. As described above we have added a method to identify the basement membrane under epithelial cells using immunostaining for laminin. This method identifies the basement membrane more clearly. The concentration of the antibody is critical and must be optimized for each batch of enzyme.

Project 2: Sensitizer Screening to Enhance Detection of ENU-Induced Mutant Phenotypes

The study requires some determination of osteoblast proliferation in vivo to confirm findings in vitro. Initial findings using bromouridine labeling to identify proliferating osteoblasts on bone tissue sections, have shown low proliferation rates in the periosteum of the femur. The literature has been reviewed to determine how other investigators have addressed this problem. Although the standard technique uses a single peritoneal injection of bromouridine, other investigators have used multiple injections or infusions to lengthen the labeling time and increase cell labeling rates.

Development of New Technologies

During the course of the study we have been evaluating new technologies including literature review and attending lectures. An evaluation of current methodologies has been presented annually at the workshop for "non-invasive Assessment of Trabecular Bone Microarchitecture Working Group" given at the American Society of Bone and Mineral Research meetings. The technology has been steadily advancing.

1. General. MicroCT and microMRI are two relatively new techniques that have great potential for phenotyping bones. The resolution obtainable with these techniques has been steadily improving with technological advances. Both of these techniques have potential use for phenotyping in live animals as well as *in vitro* bone analysis. An advantage of these two

techniques is that they are non-destructive. Members of Dr. Obenause's Laboratory at Loma Linda University have visited our laboratory to assess the usefulness of these instruments for their ongoing studies funded by the Department of Defense.

2. Summary of microCT. The microCT instrument at Loma Linda University is an ImTec Microcat II for *in vivo* scanning. Aluminum filters have been added to harden the beam and increase the discrimination for bone. From the pictures and monitor views it is evident that the resolution is in the neighborhood of 40 microns. The instrument can also be used for *in vitro* scanning. However, microCT instruments specifically designed for *in vitro* scanning can have better resolution on the order of 10-20 microns. Multiple bone samples could be scanned at the same time to reduce scanning time.

For *in vivo* scanning, the animals must be anesthetized so there is no movement during scanning. Dr. Obenause uses an isofluorane anesthetic system set up. This works very well for rats that can go 2-3 hours under anesthesia without any problems. Mice can also be anesthetized with this setup except that if the mice are sick there may be some mortality. The same anesthesia setup was used with MRI.

Dr. Obenause uses a proprietary software system for analyzing the scans. The same software package is used for MRI, PET and microCT. Analysis could be done off site once scans were done. One difficulty is that there is no section specifically on bone analysis in the operation manual. Therefore, a protocol for using the software for bone analysis would have to be developed. Other microCT systems such as the Scanco system have built-in software specifically designed for bone. The system is flexible in that if the threshold is set low during scanning, the software can adjust the threshold during analysis to extract structures of different density. While the analysis can separate structures of different densities, it does not provide readouts of the actual mineral density. The latest ScanCo microCt software can give density values.

Test samples of mouse bone demonstrate that the ImTek instrument successfully scans mouse femurs and can generate trabecular bone parameters. Moreover, the literature and the ASBMR workshop on non-invasive methods indicate that trabecular parameters generated by microCT, even low resolution microCT, are highly correlated with histologically generated parameters. Thus, the instrument still should be able to examine and identify differences in trabecular structures. Further work with the instrument and analysis may be able to improve on the resolution. Although the resolution of the Imtek is not sufficient to give precise resolution of the woven bone that develops following fractures, this resolution is still better than that obtained with the current pQCT. Thus scanning with this instrument would have an advantage over our current methodology.

3. Summary of microMRI. Dr. Obenaus has two instruments with field strengths differing by five fold. They have a small coil designed for scanning rat brains that would work for bones. The

scans are done in five different modes: "T", etc. The instruments have some versatility in that different modes of scanning can emphasize different structures. One of the modes is useful for blood flow and vascularity (*in vivo*) and might be useful for looking at the role of vascularity in bone fracture healing. The resolution is 40 microns so this would be a limitation (probably not good enough for digit tip studies). MRI is used at Loma Linda University for measuring volumes of different brain structures or tumors. Based on the views of the brain with micro MRI, it should be possible to identify structures including bone. The instruments are setup to do primarily *in vivo* studies but *in vitro* scanning of bone specimens can be readily done.

The microMRI setup used the same anesthesia system and analysis system as the microCT. Further analysis of actual bone specimens are needed to fully evaluate the utility of this technique.

4. Further developments of MicroCT. We are continuing to monitor the development of MicroCT equipment. New developments include the addition of bone density determination to the Scanco MicroCT instrument. This is the first instrument to include density measurement to the area measurements. It involves standardizing the beam with phantom standards. Other companies are adding this feature.

Analytical methods for generating trabecular bone parameters from microCT scans are continuing to evolve. Analytic approaches can sharpen the images obtained and reduce the scan time. This is important for in vivo scanning where radiation exposure is a limiting factor for longitudinal studies. However equipment costs remain high.

We are continuing to monitor the development of MicroCT equipment. As previously reported, the Scanco instrument includes the determination of bone density. A Scanco instrument for *in vivo* studies is available and has been used effectively by other investigators.

5. Finite lement Analyses methods for estimating trabecular bone strength from structural parameters have been developed. This increases the usefulness of the instrument. The FEA methods for estimating trabecular bone strength from microCT measurements have been largely validated by mechanical testing. However, analytical methods with different approaches are continuing to evolve. This evolution is aimed at improving the fracture risk assessment. So far the use of microarchitecture determination has not greatly improved fracture risk assessments. Work is continuing on developing better methods of evaluating bone strength from non-invasive approaches. However, this type of strength analysis should be useful for fracture healing assessment in rodent studies.

6. MRI. The resolution of microMRI continues to improve and instruments specifically designed for small animals are becoming available. Improvements in the instrumentation for micro-MRI on small animals are continuing. These do require greater capital investment in higher field strength instruments. Clinical instruments are also improving and a few clinical studies are

underway with this non-invasive technology. Attempts are also being made to get better standardization among manufacturers so that data obtained on different instruments can be compared.

Improvements in the instrumentation for micro-MRI on small animals and on human studies are continuing. Clinical instruments are improving with higher field strengths to increase resolution and standardization.

7. pQCT The instruments for peripheral quantitative computed technology (pQCT) has been improved for clinical use. Changes in beam parameters have allowed greater resolution. The "extremeCT" instrument from Scanco has improved the resolution or voxel size from 170 microns down to 70 microns and is comparable to the resolution obtained in small animal studies. A number of clinical studies have been reported to use this instrument.

Project 11. Microarray & Informatics Support Services

INTRODUCTION

As a result of the sequencing of the human and mouse genomes there has been a tremendous increase in discovery of novel genes with unknown functions. It is important to next interpret and determine the function and genetic pathways of the large amounts of sequence information now available. One powerful method of determining unknown gene function and genetic pathways is by microarray expression profiling. Microarrays (also called DNA chips) are glass or plastic substrates on to which known sequences of DNA have been synthesized or spotted. Fluorescently labeled RNA from different biological samples are hybridized to their complementary sequences on the microarrays. The resulting fluorescent intensities are quantified and data analysis performed to determine expression levels of RNA transcripts. Thus, microarrays allow for the experimental analysis of many genes in a single experiment, and one can compare expression levels of genes over several timepoints and different biological or disease conditions. Comparing these expression levels gives clues to gene function and is a very powerful method of discovery. Project 11 of this grant had the goal to upgrade and improve the microarray and informatics support services in the Musculoskeletal Disease Center. Following are the technical objectives:

BODY

B. Technical Objectives:

Following are the specific objectives during the second year of the grant period:

Technical Objective 1: **To provide technical service.**

Technical Objective 2: **To provide education.**

Technical Objective 3: **To update on recent advances.**

To achieve the above technical objectives, the following Specific Objectives were proposed during years 1 and 2 of this proposal:

1) To provide technical service, microarray and informatics support service will:

i) Prepare cDNA probes for genes related to musculoskeletal tissues
ii) Spot cDNA probes on the slides
iii) Perform labeling of cDNA, hybridization and detection of labeled probes
iv) Develop the informative infrastructure to produce, analyze, interpret and house the information derived from microarray experiments
v) Mining of functional and expression data for genes spotted in the slides
vi) Identify SNPs for genes involved in the IGF regulatory system using various SNP databases

vii) Build maps of genetic loci for ENU mutant and QTL studies and identify overlapping BAC clones for functional testing

2) To provide education, microarray and informatics support service will:

i) Train investigators in the preparation of good quality RNA
ii) Train investigators in the use of appropriate statistical methods for data analysis

3) To update on recent advances, microarray and informatics support service will:

i) Improve spotting and labeling techniques by incorporating latest technology developments in these areas
ii) Incorporate new advances in data management and analysis

We have accomplished all of the above specific objectives. Our progress in each of the Specific Objectives is given below.

C. Progress on Technical Objectives

1. Specific Objective 1: To provide technical service

Our goal was to create a nearly complete representation of the genes in the mouse genome for spotting on to microarrays. For this purpose, we obtained a copy of a mouse clone library that consists of approximately 15,000 genes that was developed by researchers at the National Institute on Aging, a center of the National Institutes of Health. In the first year of this grant, we received a copy of this clone set and processed the clones for microarray spotting. The clone set has the following characteristics:

- Approximately 15,000 unique cDNA clones were obtained from expressed sequence tags (ESTs) from developing mouse embryos (E12.5).
- Up to 50% are derived from novel genes.
- The clones have approximately 1.5 kb average insert size.
- All the clones were sequenced from 5' and 3' termini to verify the clone's sequence and to insure that unique clones are represented in the library.

Processing of the clones involved first replicating the library by growing all 15,000 clone cultures and then purifying plasmid DNA from the clone cultures. The cloned inserts in the plasmid DNAs were then amplified by PCR and purified. The remainder of the plasmid DNAs was then archived at –20C. Following is the protocol used for processing the 15,000 clone cultures into plasmid DNA and then PCR products to make them suitable for microarray spotting:

b. Preparation of NIA 15K Clone Set

1) Growing the Plasmid Clones

Make stock 2XYT Medium (for 1L)	
Tryptone	16g
Yeast Extract	10g
NaCl	5g
0.1 Sodium Citrate	17mL
1M KH_2PO_4	36mL
1M KH_2PO_4	13.2mL
80% Glycerol	55mL

Adjust the pH to 7.0 with HCl acid and sterilize media by autoclaving.

1. Take plasmids to be grown out of the –80 °C freezer and set on ice to thaw.
2. Preparing to grow the plasmids. Flame the caps and openings of the flasks used before and after transfer of medium. Add the following to the amount of 2XYT medium to be used:

1.0 $MgSO_4$	0.4uL per 1mL of 2XYT medium
2.0M $(NH_4)_2SO_4$	3.4uL per 1mL of 2XYT medium
100mg/mL Ampicillin	1.0uL per 1mL of 2XYT medium

3. Transfer 1.5mL per well of the 2XYT medium to a 96-deep well plate.
4. Add 1uL of the stock plasmid into each well using a 96-pin replicator. Dip the pins into the well, swirl gently to scrape up a few cells and insert into deep well plate with medium. Grow the plasmids with the 96-pin replicator as the lid.
5. Incubate at 37 °C, and shake at 120 rpms overnight. Make sure plate is secured on the base of the shaker. The lid should be loose to allow air flow.

2) Plasmid DNA Purification

For Plasmid DNA purification we use the Millipore Montage 96-well plate purification kit. Following is the protocol used to purify the 15,000 plasmid cultures:

1. Pellet the cells in the 96 well plate using a swinging bucket centrifuge. Spin at 1500xg for 10 minutes. For rotor GH-3.8, that is about 2000rpms for 10 minutes.
2. Discard the medium from the pellet by slowly inverting the plate. The solid cell mass will remain at the bottom of the plate. DON'T tap the plate-- this may dislodge the pellet. Leave the plate upside down on paper towels to drain the remainder of the medium (about 5 min).
3. Resuspend the cells by adding 100uL of Solution 1 to each well. Resuspend pellet by pipetting up and down. All cells must be suspended for best yields. If the samples cannot be taken to the next step immediately, keep at 4°C until ready to move on to the next step.
4. Lyse the cells by adding 100uL of Solution 2. Shake plate vigorously for 1 minute. Allow to sit at room temperature for 2 minutes, but not to exceed 5 minutes.
5. Neutralize the lysed cells by adding 100uL of Solution 3. Mix by shaking vigorously for 2 minute.

6. Place the Plasmid 96 well plate in the vacuum manifold. Place the Clearing plate on top of the manifold. The vacuum manifold needs to be connected to a flow through flask for waste solution to collect. The flow through should be disposed regularly. The waste in neutralized and can be dumped down the sink.
7. Transfer the full volume into the 96 well Clearing plate (300uL maximum volume). Vacuum at a maximum pressure of 8 inches of Hg until all the volume is has passed though the filter. Don't move the manifold during this time, it may cause cross contamination in the transfer from the clearing plate to the plasmid plate.
8. Discard the dry clearing plate. Move the plasmid plate to the top of the manifold.
9. Vacuum at a maximum pressure of 24 inches of Hg until the wells are dry.
10. Wash the plasmid DNA by adding 200uL of Solution 4. Vacuum until the wells are dry. Dab the bottom of the plate with a towel to remove excess wash.
11. Resuspend the plasmids by adding 50uL of Solution 5. Shake the plate for 10 minutes on a plate shaker. Transfer the plasmid into a 96 well plate.
12. Use 2uL to run on an agarose gel to check the quality.
13. Store the stock plasmids at –20 °C.

3) PCR Amplification of Clone Inserts

PCR amplications are done using the following protocol:

PCR Primers: NIA15K-For 5'-CCAGTCACGACGTTGTAAAACGAC-3'

NIA15K-Rev 5'-GTGTGGAATTGTGAGCGGATAACAA-3'

1. Dilute an aliquot of the stock plasmids. Take 1ul of stock plasmid DNA into 99ul of DNA water in a 96 well plate.

2. PCR Reaction Master Mixes:

	100ul rxn	96 well plate
10X Qiagen PCR buffer	10ul	980ul
10mM dNTPs	2ul	196ul
10mM primer Forward	1ul	98ul
10mM primer Reverse	1ul	98ul
Sterile deionized water	84.8ul	8310.4ul
5U/uL HotStarTaq (5U/ul)	0.3ul	29.4 ul
		add 99 ul per well
1:100 plasmid DNA	1ul	1ul

3. PCR Cycling Parameters

Step 1	95°C for 14 minutes
Step 2	95°C for 1 minute
Step 3	56°C for 1 minute
Step 4	72°C for 1:30 minutes
Step 5	Go to Step 2 for 39 more times
Step 6	72°C for 10 minutes
Step 7	10°C hold

4. PCR success and quality is determined by running 4ul of the PCR product on a 1% agarose gel. Some samples that don't amplify with the diluted plasmid DNA will be seen. Re-amplification of failed PCRs should use 1ul of stock plasmid DNA to amplify and the above reaction mixes.
5. Store the PCR product at –20°C until ready for purification

4) Purification of PCR Products.

Purification of PCR products was done using Millipore Multiscreen kits. Following is the protocol:

1. Thaw the PCR products and transfer the full volume into the MultiScreen filtration plate and place the filter plate on the vacuum manifold. The filters have a maximum volume capacity of 300uL but for best results, no more than 200uL should be loaded.
2. Vacuum the plate at about 24psi until dry; it will take 5 to 10 minutes.
3. Remove dry plate from manifold and dab the bottom to absorb excess flow though.
4. To resuspend the DNA, add 40uL DNA water into each filter well. Shake the plate on a plate shaker for 10 to 15 minutes.
5. Collect the samples and transfer into a 96 well plates.
6. Store purified PCR plates at -20°C.

Using the above protocols, over 90% of the 15,000 NIA clones gave a single PCR amplification product. The purified PCR products were then re-arrayed into 384 well plates in 25% DMSO. Microarrays were created using these PCR products using a Genetix Q-Array2 robotic arrayer.

C. Creation of Microarrays Using the Genetix Q-Array2

Following amplification, the purified PCR products were re-arrayed into forty-four 384-well plates in 25% DMSO spotting buffer. For re-arraying 96-well plates to 384-well plates the Robbins Scientific Hydra-96 robotic liquid handler was used. Microarrays were then created using Corning UltraGaps II glass slides. The PCR products were spotted using a Genetix Q-Array2 robotic arrayer. After extension optimization, the following parameters were used to create microarrays with 30,000 features (the 15,000 clones spotted in duplicate).

Head:	48-Pin Microarraying Head (65 micron split tungsten pins)	
Source:	Plate holder:	Stacker source plate holder

Plate type:	Genetix plate 38X7022		
Plate number:	44		
Source order:	Column		
Slide Design:	3X1" Slide (48 pins/ 1 field)		
Arraying by:	Spotting position		
Array pattern:	Spot view, Estimated spot size:	65 microns	
Row count:	27 Row pitch:	160	
Column count:	27 Column pitch:	160	
Replicate type:	Cyclic		
Replicate count:	2		
Number of blot:	12		
Blot set / over spot:	6		
Blot pitch:	800		
Blot change:	Yes		
Max stamps per ink:	800		
Number of stamp per spot:	1		
Stamp time:	0		
Ink time: (ms)	1000		
Print adjustment:	0		
Wash:	Wash	Dry	Wait
Water:	5000		
Water:	5000		
Water:	5000		
80% EtOH:	5000	6000	2000
Export date:	yes		
File name:	NIA 15K database		
File format:	GSI		
Plate sequencing:	See Data tracking NIA 15K		
Barcodes:	Manual		
Spotting Position:	From 1- 352 (Each Plate has 8 position)		

Using the above parameters we have created to date over 100 microarray slides with over 30,000 features. Following spotting the slides were processed to fix the DNA to the slides and to denature the DNA to single stranded DNA. Below are the parameters developed to fix the slides:

1. Cross link the slides at 60 milliJoules using the Stratagene UV Crosslinker (600 setting). Place the slides on glass trays horizontally without overlapping.
2. Bake the slides for 3 hrs at 80°C in the hybridization oven. Place the slides on glass trays horizontally without overlapping.
3. Transfer slides to a slide histology rack. Allow one space between slides so they do not touch. Denature the DNA in 98°C water bath for 2 min.
4. Store the slides in a sealed slide holder in the dark at room temperature. The slides should be good for at least six months.

In the past year, we have investigated new methods of RNA isolation to improve the yields and quality of total RNA obtained from various tissues. Since the initial isolation of the

total RNA is the most labor intensive step this has led to an increase in output in experimental data productivity. One method of RNA isolation has been found to increase the amounts of total RNA that we obtain from soft tissues. The method uses a polytron to quickly lyse cells rather than manually lysing cells with a mortar and pestle. The polytron processes tissue more quickly thus allowing for rapid RNA isolation and high quality RNA preparations. Following is the protocol we use for isolation of RNA from soft tissues:

D. Total RNA Isolation Protocol with Polytron

1. Wash the Polytron probe with RNase away at half speed (15/30) for 1 minute. Rinse the probe with DEPC water twice at the same speed and time; use DEPC water at full speed 30 seconds, repeat twice. Use 100 percent ethanol at full speed to wash the probe 25 seconds, repeat twice. Air dry until use.
2. Prepare tissue homogenate in appropriate amount or lysis solution/beta-mecaptoethanaol mixture (20ul/mg).
3. Polytron the tissue in lysis solution for 20-40 seconds. Wash the probe with a small amount of lysis solution to insure that all cellular debris is removed from the probe.
4. Centrifuge up to 600ul of homogenate through the mini prefiltration column, for 3 minutes at 13000 rpm, collect the filtrate.
5. Add an equal volume of 70% ethanol to the filtrate, mixing very well, and place on ice at least 5 minutes.
6. Add up to 700ul ethanol/lysis mixture to the mini isolation column then centrifuge 30 seconds at 13000 rpm. Discard the flow through, and place the RNA-loaded column into the same collection tube.
7. Add 500ul wash solution to the mini isolation column, then centrifuge 30 seconds at 13000 rpm. Discard flow through, replace the mini isolation column in the collection tube.
8. Repeat step 5 one more time.
9. Spin the mini isolation column for 2 minutes at 13000rpm.
10. Elute the purified RNA by addition of 10-50ul of nuclease-free water, wait 1 minute, then centrifuge 1 minute at 13000rpm.

Using the above protocol we have obtained very high quality RNA from small amounts of tissue (50 milligrams and less). An example of RNA isolated from mouse DBA strain digit tips by the protocol is shown in **Figure 1**.

Figure 1. High Quality RNA Sample Isolated By Modified Protocol. RNA quality is determined by running the samples on the Agilent Bioanalyzer. The RNA sample in the upper panel indicates high quality RNA since the 28S ribosomal RNA peak (at ~47 seconds) is greater intensity than the 18S ribosomal RNA peak (at ~ 41 seconds). Quantification of the RNAs is calculated by comparing the fluorescent intensity of the marker peak that migrates at a time of approximately 23 seconds to the intensity of the ribosomal RNA bands.

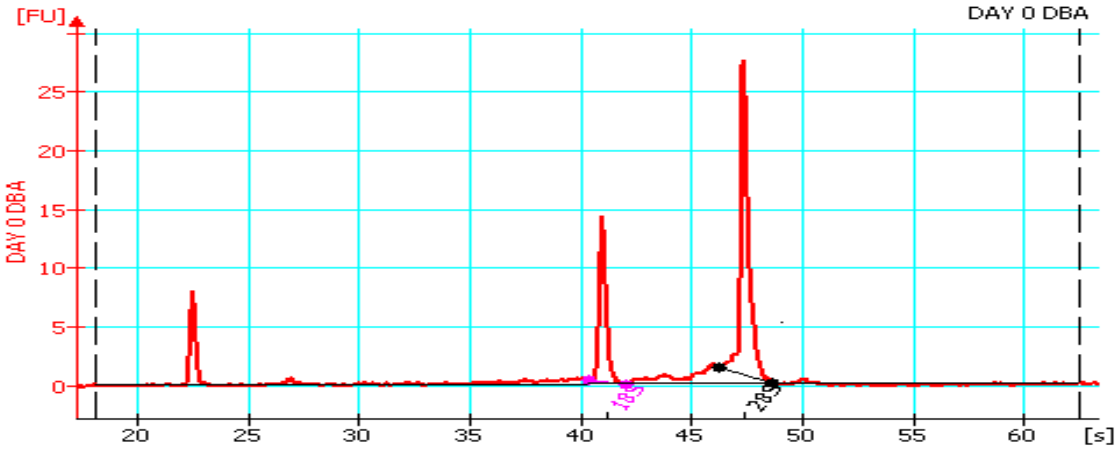

The microarray support laboratory has investigated new methods of RNA labeling and hybridization that require less amounts of initial total RNA. This is significant and important since in the past it has been difficult to obtain sufficient amounts of total RNA from limited amounts of cells that are obtained from bone and other tissues. The previous labeling methods used in the microarray laboratory required 2 to 10 micrograms of total RNA for each hybridization. In the past year, we have investigated new methods of RNA labeling and hybridization and have successfully reduced the amounts of initial RNA needed to 50 to 250 nanograms (a 40 to 200 fold reduction). The method that we have begun using is the Low RNA Input Fluorescent Linear Amplification Kit for cDNA Microarray Hybridization (Agilent). Following is the protocol:

E. cDNA Synthesis From total RNA

1. Add 200-400ng of total RNA in a volume of 9.3ul or less.
2. Add 1.0ul of Test Spikes (Amersham Lucidea controls) into the Experiment Sample or
3. Add 1.0ul of Reference Spikes into Control Sample.
4. Add 1.2ul of T7 Promoter Primer
5. Bring volume up to 11.5ul with nuclease-free water
6. Denature the primer and the template by incubating the reaction at 65°C in a heating block for 10 minutes.
7. Place the reactions on ice and incubate for 5 minutes
8. Prepare the cDNA Master Mix per reaction:

5X First Strand Buffer*	4.0ul (Pre-warm at 65°C, 3-4 min)
0.1 M DTT	2.0ul
10mM dNTP mix	1.0ul
RNaseOUT	0.5ul
MMLV RT	1.0ul
Total Volume	8.5ul

9. To each sample add 8.5ul cDNA Master Mix.
10. Incubate samples at 40°C for 2 hours, 65°C for 15 min, on ice 5 min.

F. cRNA Amplification

1. Prepare the Transcription Master Mix:

Nuclease-free water	12.1ul
4X Transcription Buffer	20.0ul
0.1 M DTT	6.0ul
NTP Mix	8.0ul
CTP	5.6ul
50% PEG	6.4ul(Pre-warm it at 40°C for 1min)
RNAseOUT	0.5ul
Inorganic Pyrophospatase	0.6ul
T7 RNA Polymerase*	0.8ul
Total Volume	60.0ul

2. Add 60.0ul of Transcription Master Mix.
3. Incubate samples at 40°C for 2 hours.

G. Purification of Amplified cRNA

1. Use the Qiagen's RNeasy mini spin columns.
2. 80ul cRNA sample
3. Add 20ul of DEPC water.
4. Add 350ul of Buffer RLT .
5. Add 250ul of ethanol (200 proof)
6. Transfer 700ul of mix to an RNeasy mini column in a 2mL collection tube. Centrifuge the sample at 13,000rpm for 30 seconds
7. Wash the column with 500ul of buffer RPE , Centrifuge the sample at 13,00rpm for 30 seconds.
8. Wash the column with 500ul of buffer RPE, Centrifuge the sample at 13,00rpm for 60 seconds.
9. Elute the cleaned cRNA sample. Add 35ul RNase-free water directly onto the RNeasy filter membrane. Wait 60 seconds before centrifuging for 30 seconds at 13,000 rpm. SAVE THE FLOW THROUGH and the collection tube. Store at -80°C until needed.

H. Quantitating cRNA Products

1. Use 1.5ul on nuclease free water to blank the NanoDrop instrument. Then use 1.5ul of amplified cRNA for analysis. Calculate the concentration of cRNA by using the formula:
    a. 1 OD260 = (10) x 40ug/ml RNA.

I. Fluorescent cDNA Synthesis from Amplified cRNA

1. Add 500ng-2ug cRNA and bring the total volume to 13.25ul with nuclease free water.
2. Add 1ul of Random Hexamers.
3. Incubate the sample at 65°C for 10 minutes, on ice for 5 min.
4. Add 1.25ul of either Cyanine 3-dCTP or Cyanine 5-dCTP(500uM)
5. Prepare cDNA master mix:

5X FS Buffer	5.0ul
0.1M DTT	2.5ul
dNTP	1.0ul
MMLV RT	1.0ul
Total	9.5ul

6. Aliquot 9.5ul of cDNA master mix to each sample
7. Incubate cDNA synthesis reaction at 40°C for 60 min, 65°C for 10 min, on ice for 5 minutes.

J. Purifying Labeled cDNA

1. Combine Cy3 and Cy5 cDNA reaction.
2. Add 5 volume of Buffer PB.
3. Apply the sample to the QIAquick Column and centrifuge at 13,000rpm for 30 sec.
4. Wash the column with 400ul of Buffer PE . Centrifuge the column at 13,000rpm at 30 seconds.
5. Wash the column with 400ul of Buffer PE. Centrifuge the column at 13,000rpm at 60 seconds.
6. Elute the sample, add 30ul of buffer EB, Wait 60 seconds before centrifuging for 30 seconds at 13,000 rpm.
7. Repeat the eluted step.
8. Dry the sample (Option).

K. Hybridization

1. Bring volume up to 250ul with sterile ddH20.
2. Denature at 98°C for 3 minutes.
3. Add 250ul 2X Hybridization buffer to the sample then mix it.
4. Add mix to the Hybridization Chamber.
5. Hybridize in oven at 60°C for 17 hours. Attach the chamber to the rotating rack securely.

L. Washing the Slides

1. Wash with Solution I (6X SSC, 0.005% Triton X-102) for 10 min. in dark.
2. Wash with Solution II (0.1X SSC, 0.005% Triton X-102) for 5 min. in dark.
3. Dry the slide with the nitrogen-filled air gun.
4. Slides are ready for scanning.

For scanning the laboratory uses a GSI Lumonics ScanArray 4000 scanner. This scanner is several years old but is still usable with our new microarrays. The arrays are scanned at a resolution of 10 microns which corresponds to ~15 pixels in diameter of each of the ~30,000 spots and a spacing of ~5 microns between the spots. The signal intensity of all microarray images is determined using Imagene 5.1 software. This software uses a patented image processing technology to provide quantification of microarray images of high density. Quality control measures include automated flagging of good, marginal and absent spots so that these can be filtered in the expression analysis.

Figure 2. Scanned Image of NIA15K Microarray. Shown below is a small region of a microarray manufactured and hybridized in the Microarray Laboratory in the Musculoskeletal Disease Center. Note that most spots are circular and well defined.

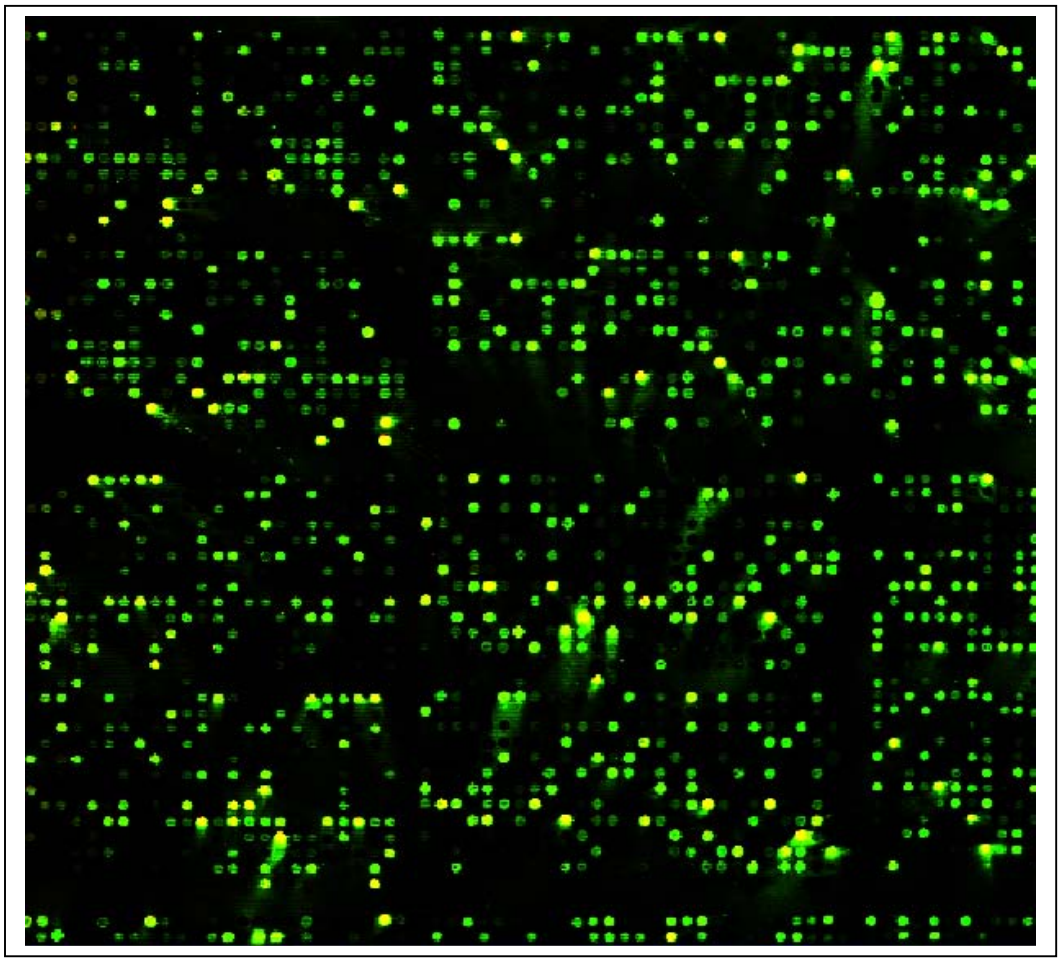

2. Specifi c Objective 2: To Provide Informatics Support and Microarray Data Analysis

a) Evaluation of data quality and analysis.

Microarray data is analyzed with GeneSpring software (Silicon Genetics, Redwood City, CA). The purpose of the analysis is to obtain a list of differentially expressed genes. These are the candidate genes that play an important role in a microarray study, for example in bone fracture in rat, one of our ongoing studies.

Before the formal analysis, we use the Scatter plot and the Condition tree features of GeneSpring to evaluate the chips to determine if they are suitable to be included in the analysis. The Scatter plot shows the data skewness between the Cy3 and Cy5 dyes (i.e. the treatment vs. control) for a particular chip. If there are too many genes that are highly expressed in one color, but not in the other, this might indicate that there are problems with the labeling process. Take the following image of scatter plot of Cy3 versus Cy5 intensities as an example. It can be seen that most genes are expressed nearly equally in both samples. This is usually the case in a well – designed expression experiment, since out of 15,000 genes most are not expected to show differential expression.

Figure 3. GeneSpring Analysis of Microarray Data. Shown above is a scatter plot of fluorescent intensities of 15000 genes from MRL mouse RNA. The normalized Cy3 (day 4) labeled cDNA is plotted versus the normalized Cy5 (day 0) labeled cDNA. The data is normalized to correct for differences in labeling or detection efficiencies between the fluorescent dyes used or for slightly unequal quantities of starting RNA. The center line of the three lines shown corresponds to a slope of one and samples that lie along this line show no differences in expression for that respective gene. Greater than 2-fold differences in expression are indicated by dots that fall outside the two outer lines.

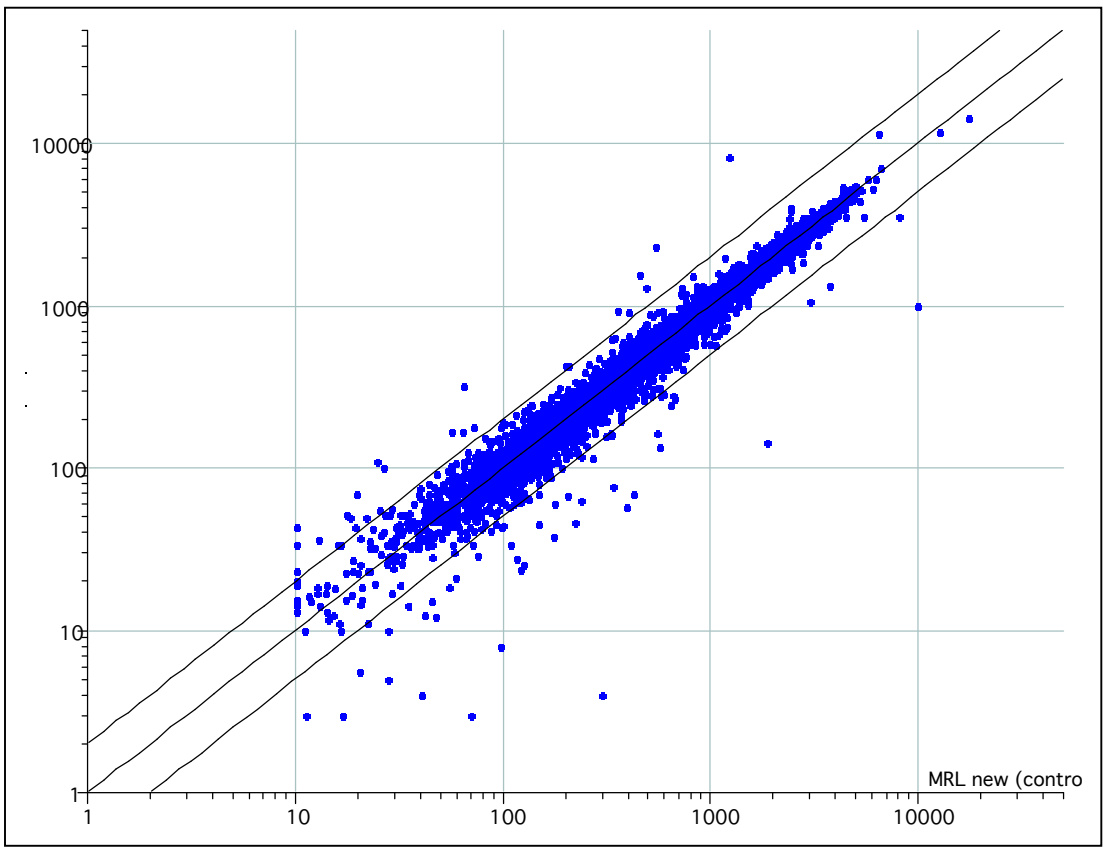

Another way to determine data quality is to examine the condition tree of the individual slides in a microarray experiment. For example in the following image of condition tree analysis, the expression pattern for RNA samples and control RNAs cluster together. The experiment is of digit tip RNA from two inbred strains of mice (MRL and DBA). The condition tree analysis shows that the DBA and MRL run samples are more different between each other than the replicate microarrays for that respective species. Also, the analysis shows that individual microarrays run of the respective specie's day 4 experimental RNA and day 0 control RNA are more like itself than another microarray. This indicates that for determination of differential expression of genes between the day 4 and day 0 RNA samples, the individual microarrays must first be normalized and expression ratios determined. Once these differential expression ratios are determined, the replicate microarrays can be combined for statistical analysis of significance.

Figure 4. GeneSpring Condition Tree Analysis of Microarray Data. RNA samples from MRL and DBA in-bred strains of mice cluster separately from each other. Since RNA from different strains should be more different from each other, this indicates that the microarray data is high quality.

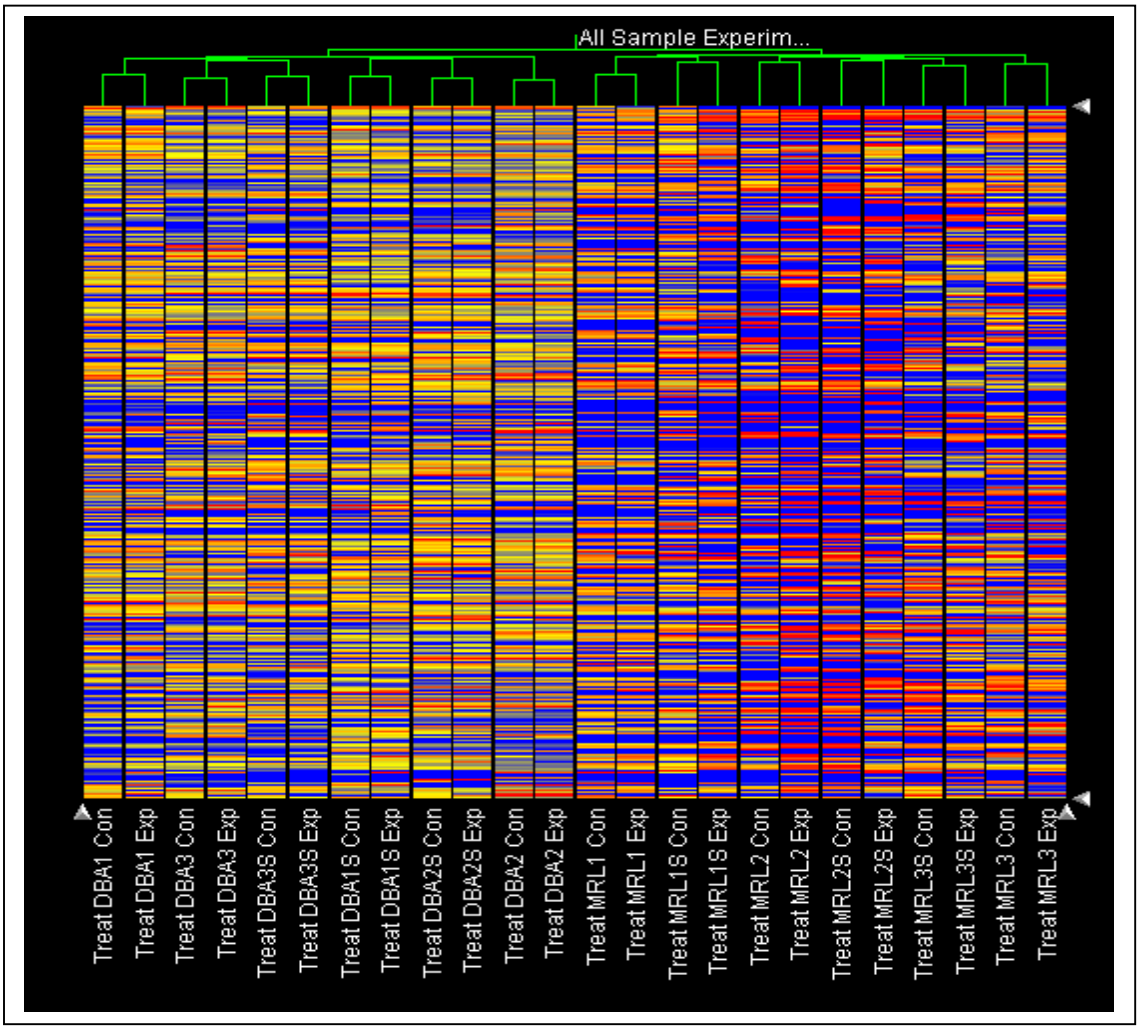

For two color (i.e. treatment vs. control) expression experiments, we do paired analysis and using the Per Spot and Per Chip: Intensity dependent (Lowess) normalization. We are using P of 0.05 and 0.01 as critical values to determine whether a gene is differentially expressed.

After we obtain the list of differentially expressed genes, we cluster these genes. We use the K-Mean clustering feature of the GeneSpring. This clustering will identify the major gene clusters or modules that are differentially expressed in the experiments (i.e. between experiment and control, or the time series). In this analysis, the transcription factors, regulatory elements, DNA biding motifs and signal proteins will be taken into the consideration. It is highly likely that a particular module of differentially expressed genes is under the same regulation of a common transcription factor, or has the same set of DNA binding motifs. Understanding the transcription regulation of the gene modules in a microarray study holds the key to understanding the gene networks.

B. Master Gene Annotation of NIA15K Microarrays. For the in-house manufactured microarrays, we have also generated an annotated master gene table for use with GeneSpring software. This table is loaded into GeneSpring and investigator can display the annotation information for his/her list of differentially expressed genes.

In order to create this master gene table for our in-house microarray (NIA Mouse 15k Clone Set Data), information is downloaded from the NIA (National Institute of Aging) website (http://lgsun.grc.nia.nih.gov/download.html). A local database is then created using MySql software. A program is written in PHP computer language to create this table. This database is updated each time that the database in the NIA website is updated. The current annotation of the NIA15K microarrays is too large to include in this report. It is over 700 pages describing each gene's function and the molecular, functional and cellular location description. Approximately half of the 15,000 genes are unknown expressed sequence tags (ESTs) of unknown function, however.

C. Pathway Analysis Using Gene Ontology. Further understanding the role of the differentially expressed genes in the pathways is critical in microarray studies. For this purpose, we use Gene Ontology to classify genes, to identify the pathways involved in each microarrya study. Gene Ontologies are structured, controlled vocabularies that describe gene products in terms of their associated biological processes, cellular components and molecular functions in a species-independent manner. The current annotation of the NIA15K microarrays is too large to include in this report. It is over 700 pages describing each gene's function and gene ontology. Approximately half of the 15,000 genes are unknown expressed sequence tags (ESTs) of unknown function and ontology, however.

The whole Gene Ontology (GO) database was downloaded from the website of the Gene Ontology Consortium (http://www.godatabase.org/dev/database/archive/latest/) into a local MySql database. A program is written in PHP computer language to classify the differentially expressed genes into GO categories. The following table lists the GO classifications (ontology of biological process only) of an example set of differentially expressed genes. For each category,

the GO accession number, full name, and the number of genes are shown. Below each category are the gene identification number, gene symbol, and the full name of the gene.

```
_____________________________________________________________________
GO:0030198(extracellular matrix organization and biogenesis) (1)
1     DCN   Mouse Decorin (DCN)
GO:0006412(protein biosynthesis) (6)
3     Rpl7a Ribosomal Protein L7a(Rpl7a)
8     Erf1  Mouse ETS-Related Transcription Factor(Erf1)
27    Arbp  Mouse Acidic Ribosomal Phosphoprotein
28    Rps18 Mouse Ribosomal Protein S18(Rps18)
29    Rps9  Mouse Similar to Ribosomal Protein S9(Rps9)
35    Rps7a Mouse Ribosomal Protein L7a(Rps7a)
GO:0045103(intermediate filament-based process) (1)
4     Vim   Mouse Vimentin (Vim)
GO:0006259(DNA metabolism) (3)
7     NACA  Mouse Nascent Polypeptide
30    Naca  Mouse Nascent Polypeptide-Associated
31    Recql5      Mouse RecQ Protein-Like 5(Recql5)
GO:0006265(DNA topological change) (2)
7     NACA  Mouse Nascent Polypeptide
30    Naca  Mouse Nascent Polypeptide-Associated
GO:0006415(translational termination) (1)
8     Erf1  Mouse ETS-Related Transcription Factor(Erf1)
GO:0006444(nascent polypeptide association) (1)
8     Erf1  Mouse ETS-Related Transcription Factor(Erf1)
GO:0009873(ethylene mediated signaling pathway) (1)
8     Erf1  Mouse ETS-Related Transcription Factor(Erf1)
GO:0042829(defense response to pathogen) (1)
8     Erf1  Mouse ETS-Related Transcription Factor(Erf1)
GO:0006118(electron transport) (2)
9     Cox5a Mouse Cytochrome C oxidase (Cox)
34    cox5  Mouse Cytochrome C oxidase
GO:0009060(aerobic respiration) (1)
9     Cox5a Mouse Cytochrome C oxidase (Cox)
GO:0006355(regulation of transcription, DNA-dependent) (1)
14    EF1   Elongation Factor 1-Alpha 1 (EF1-alpha1)
GO:0007010(cytoskeleton organization and biogenesis) (1)
19    Krt1-14     Mouse Keratin Complex 1
GO:0008544(epidermal differentiation) (1)
19    Krt1-14     Mouse Keratin Complex 1
GO:0000902(cellular morphogenesis) (1)
19    Krt1-14     Mouse Keratin Complex 1
GO:0006122(mitochondrial electron transport, ubiquinol to cytochrome c) (1)
21    cytb  Cytochrome B (cytb)
GO:0008152(metabolism) (1)
25    Sptlc1      Mouse Serine Palmitoyltransferase(Sptlc)
GO:0009058(biosynthesis) (1)
25    Sptlc1      Mouse Serine Palmitoyltransferase(Sptlc)
GO:0006414(translational elongation) (1)
27    Arbp  Mouse Acidic Ribosomal Phosphoprotein
GO:0006413(translational initiation) (1)
28    Rps18 Mouse Ribosomal Protein S18(Rps18)
GO:0007046(ribosome biogenesis) (1)
28    Rps18 Mouse Ribosomal Protein S18(Rps18)
GO:0006281(DNA repair) (1)
```

```
31    Recql5      Mouse RecQ Protein-Like 5(Recql5)
GO:0006091(energy pathways) (1)
34    cox5  Mouse Cytochrome C oxidase
GO:0007391(dorsal closure) (1)
36    SAC1  mutations(SAC1 gene)
GO:0030384(phosphoinositide metabolism) (1)
36    SAC1  mutations(SAC1 gene)
GO:0016311(dephosphorylation) (1)
36    SAC1  mutations(SAC1 gene)
GO:0006378(mRNA polyadenylation) (1)
37    Pabpn1      Mouse Poly A Binding Protein
```

We further increased the number and density of genes on our microarrays. To accomplish this, we obtained the MEEBO (Mouse Exonic Evidence Based Oligonucleotide) set from Illumina. The set contains a collection of oligo probes, derived from constitutively expressed exons, allowing interrogation of almost 25,000 mouse genes. The set was designed to enable study of mouse transcription patterns and, as broadly as possible, alternative splicing of genes. An exon-centric design was selected to allow the differentiation of constitutively expressed versus alternatively expressed exons. In addition to the exon-centric probes, the set contains an extensive assortment of controls that facilitate accurate evaluation of expression results. The MEEBO Set contains 38,467 70mer oligonucleotide probes with an amino modification on the 5' end. The amino modification enhances binding efficiency to microarray glass slides. The probes in the MEEBO set are at a final yield of 200pmol each, and delivered in 101 384-well microarray plates. The probes are normalized to have an average melting temperature of 80C, and are designed to minimize cross-hybridization and secondary structure. The set contains a total of 35,302 probes targeting mouse genes. Probes are categorized as follows:

1. Constitutive Exonic Probes (30,125 probes): A probe that will recognize all known transcripts of a gene.
2. Alternatively Spliced / Skipped Exonic Probes (4,201 probes): Probes that will recognize exons that are present in some, but not all, transcripts of a gene.
3. Non Coding RNA Probes (196 probes): Probes recognizing non-protein coding transcripts (ribosomal RNAs, miRNAs).
4. BCR / TCR Genic / Regional Probes (372 probes): Probes recognizing transcripts from genes that undergo somatic rearrangement.
5. Mitochondrial Probes (13 probes): Probes recognizing mouse mitochondrial derived DNA sequences.
6. Transgenic / Cassette Probes (37 probes): Probes recognizing elements commonly used for transgenic constructs (e.g. GFP, YFP).
7. Murine Viral Probes (358 probes): Probes recognizing mouse viral pathogen sequences.
8. Controls. The set contains a total of 3,482 controls. The controls fall into the following categories:
    a) Negative Controls (317 empty wells and 97 probes). Empty wells and 97 random sequences are positioned throughout the set to assist in determining background.
    b) Positive Controls (1,152 probes): Probes recognizing a small subset of mouse transcripts.

c) Doped (Spike-in) Controls (1,916 probes): Probes recognizing non-mouse sequences that can be spiked into RNA samples.

Mouse Sequence Selection and Probe Design. A systematic methodology was applied to identify the exons, generate all possible 70mer candidate probes, and select the optimal probe from the candidates. The pipeline for sequence selection and probe design included three steps:

1) Collect and curate exon sequences. Supplement as needed with transcript sequences.
2) Design the candidate 70mer probes for exon or transcript sequences. Using ArrayOligoSelector, an open source tool for selecting 70mer oligo probes from a defined set of sequence data, was used to generate a list of candidate probes for each exon or transcript sequence. Multiple filters including uniqueness, self-binding, complexity, GC, content, and user defined parameters were used to narrow and rank the list of candidate probes.
3) Pick the best probe from the list of candidate probes. Several criteria were used to identify the optimal probe from the list of candidate probes:
    a. Uniqueness: Probes that had binding energies of > -35 kcal / mol for other sequences were preferred.
    b. 3' Proximity: Probes that were less than 1,000 bases from the 3' end of the transcript were preferred.
    c. Constitutive: Probe should be present in all transcripts.

If the above three criteria could not be met, more than one probe would be selected for the exon or transcript sequence.

D. Gene Annotation of MEEBO Microarrays

The new MEEBO microarrays have many additional genes of known and unknown function. Thus, in order to assist researchers in analyzing their microarray data, we have updated the genetic information for each gene and probe spotted on to the microarrays. The following are the Annotation Details for the MEEBO microarrays.

Probe annotation information contains the following data elements:

1. Plate_Name: Contains the name that will appear on the plate label. MCC plates contain mouse probes; non-MCC plates contain controls.
2. Plate_Number: Contains the plate number used to identify which packing box a plate is located.
3. Row: Oligo plate row position.
4. Column: Oligo plate column position.
5. Probe_Name: Contains the oligo name. The following codes can assist with interpreting the oligo name:
6. Rockefeller MouSDB3 constitutive exons / islands (oligo names start with 'scl' followed by a number >0)
7. LocusLink constitutive exons / islands (oligo names start with 'scl0' followed by a number >0)
8. mRNA derived 70mers which may span intron/exon boundaries (oligo names start with 'scl00' followed by a number >0)
9. A collection of alternative spliced / skipped exons generated through extensive curation of published datasets (oligo names start with 'scl000' followed by a number >0)
10. Syntenic orthologs of human loci exhibiting cis-antisense transcription (1).

Table 3. Annotation information from a small portion of the MEEBO set. Only 12 probes out of 35,302 are shown due to space limitations.

Plate_Name	Plate_Num	Row	Column	Oligo_ID	Probe_Name	LocusLink_ID	Gid	Accession	Symbol	Probe_Sequence	Sequence_ID	Tm	GC	Product
003-MCC	3	A	1	mMC000769	scl44253.13.1_34	218030	GI_27923922	NM_175006	Pou6f2	CCGAGATTGCTGAGAAGCTAAACTACGA CCGGGAAGTAGTTAGAGTTTGGTTCTGC AATAAGAGACAAGC	mSQ000769	76.5	46%	POU domain, class 6, transcription factor 2
003-MCC	3	A	2	mMC000770	scl40603.7.49_6	13494	GI_6681224	NM_007879	Drg1	AGGTGCCTCACTGTGTACCCATCTCTGCT CATCACCGCTGGAATTTTGATGACCTTTT GGAGAAAATCTG	mSQ000770	77.1	47%	developmentally regulated GTP binding prote
003-MCC	3	A	3	mMC000771	scl18378.11.1_20	11486	GI_31982514	NM_007398	Ada	AAGCTTCCTCCCAGAGGAAGAGAAGAAG GAACTTCTGGAACGGCTCTACAGAGAATA CCAATAGCCACCA	mSQ000771	77.7	49%	adenosine deaminase
003-MCC	3	A	4	mMC000772	scl41070.6_518	22344	GI_26024204	NM_016686	Vezf1	GTATTAGATAATCTTCAAATCTGACATCCA GCCTGTTATGCTTGCTCTAGGGCTCGCT GCTTGGCCTGCA	mSQ000772	77.1	47%	vascular endothelial zinc finger 1
003-MCC	3	A	5	mMC000773	scl53823.22.1_4	170722	GI_30794231	NM_130888	Nxf7	ATACTCCAACTTCAAGCTTGTCCTTTCTC AAGAGCAGCAAAGAATGGTGCAGGCTTT CTCCACCCAGTCG	mSQ000773	77.7	49%	nuclear RNA export factor 7
003-MCC	3	A	6	mMC000774	scl32668.4.1_181	13170	GI_8393239	NM_016974	Dbp	CCATGGCCAGTGGTCTGGCCAGCTAGGT GCCCGAAGAACGTCATGATGCAGACAAA TACATTTATATTTT	mSQ000774	77.1	47%	D site albumin promoter binding protein
003-MCC	3	A	7	mMC000775	scl40952.3_414	68127	GI_51766405	XM_484073	B230217C12Rik	GGTCACAGTCATTTAAGCGCTACAGCTCT AGTTTATTCCCAGACTGGAAAAGATTTCC TATCTCTTCCCA	mSQ000775	75.3	43%	RIKEN cDNA B230217C12 gene
003-MCC	3	A	8	mMC000776	scl34898.4.1_27	80857	GI_13447395	NM_030610	Fgf20	CTTTTTACCAAGACCAGTAGACCCAGAAA GAGTTCCAGAATTATACAAAGACCTACTG ATGTACACTTGA	mSQ000776	73.6	39%	fibroblast growth factor 20
003-MCC	3	A	9	mMC000777	scl24377.3_47	230119	GI_34328403	NM_173399	Zbtb5	CACAGGGATTCTAACGGGGACTGGGGAC CTGACTTTTGACTTTTAGCCTTAATTCTAG CCCGGCATAATC	mSQ000777	77.7	49%	zinc finger and BTB domain containing 5
003-MCC	3	A	10	mMC000778	scl33120.2.1_47	68992	GI_51763176	XM_133134	Zfp580	GCCACCTGTCGCGGCACCGCGCCACCCA CCGTGCGCGCGCTGGTCCACCTCACACC TGCCCGCTCTGTCC	mSQ000778	88.8	76%	zinc finger protein 580

E. Genetix Q-Array 2 for Improved Microarray Manufacture

In order to improve the technical service of the microarray support service, we upgraded our Genetix Q-Array-2 robotic spotting pins to 50 micron silicon pins. These pins have highly precise volumetric uptakes of as little as 25 nanoliters. The pins also have the ability to print completely to dryness. Both of these advantages have greatly reduced waste of our expensive oligo spotting libraries. The use of these pins has also greatly improved the quality of our manufactured arrays. The pins make arrays with very uniform spots and with little to no bleeding through from one spot to another. Figure 5A demonstrates an actual microarray RNA hybridization of a chip with over 38,000 spots manufactured using these new pins. Figure 5B is a magnified image of one of the 48 fields spotted by one of the 48 silicon pins.

Figure 5A. →
Microarray image of over 38,000 spotted oligos using 48 silicon pins (50 micron tip size) from Parallel Synthesis Technologies. Note the uniform printing shown in all 48 printing fields.

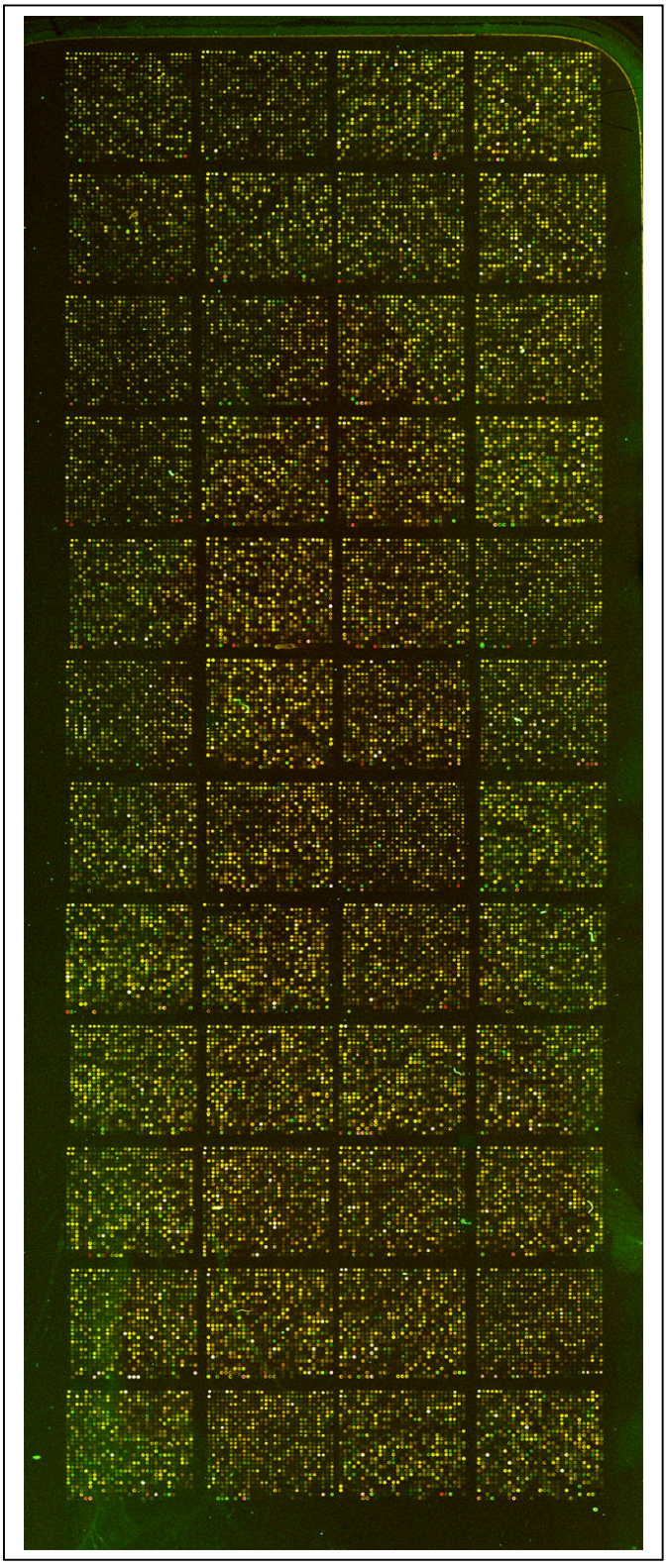

Figure 5B. ↓
Close up image of a single printing field. The printed oligos show uniform size and good circular morphology. The data is from an actual labeled RNA hybridization sample and the variation in intensity corresponds to normal variation in RNA expression.

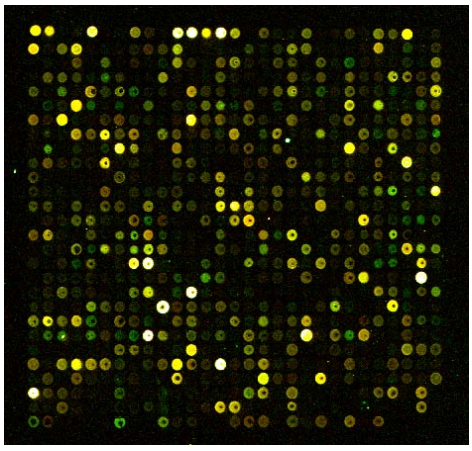

F. Microarray Quality Control Improvements.

We also developed new methods of validating microarray manufacture and quality control. Since our new oligo microarrays are single stranded DNA, this necessitated developing new methods to determine the proper quantity of DNA to spot as well as to determine the size, quality and distance between each spot on the microarrays. In order to optimize these parameters, we have begun QCing manufactured slides using fluorescently labeled random nanomer oligonucleotides. These "panomer" oligodeoxynucleotides are random primers that are labeled at the 5' end with either Cy3 or Cy5 dyes. These labeled controls are very useful for assessing microarray spot morphology, hybridization efficiency and channel bleed-through on oligo microarrays. Each lot of microarrays we manufacture is now QCed using these labeled nanomers. Figure 1 shows images of a microarray that was hybridized with the panomer controls. In the microarray shown, the highest density of genes that could be spotted on to a 1" x 3" glass slide was determined. From this experiment, we determined we could spot a maximum of 40,638 spots.

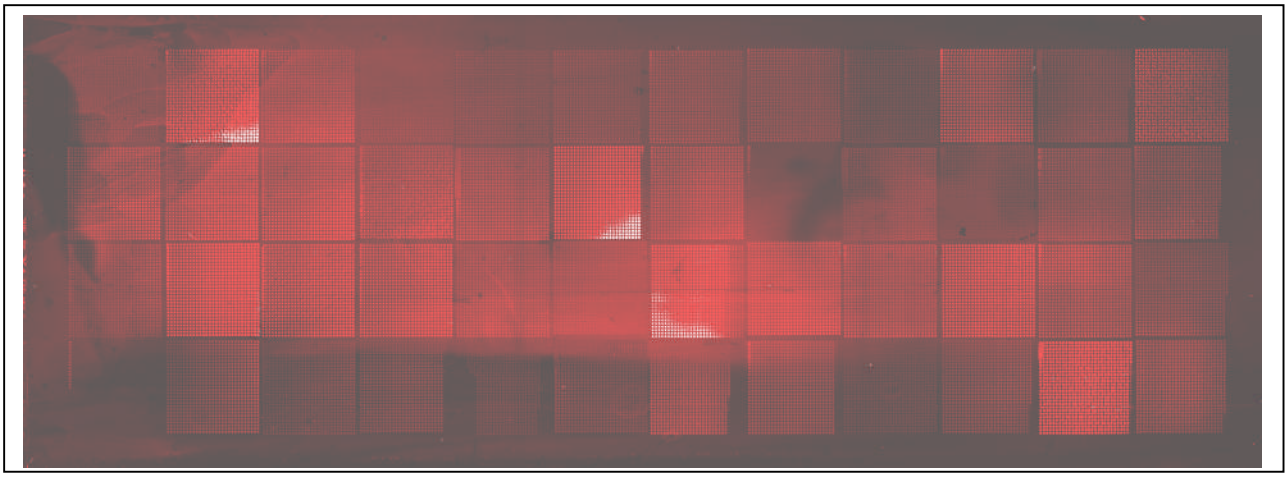

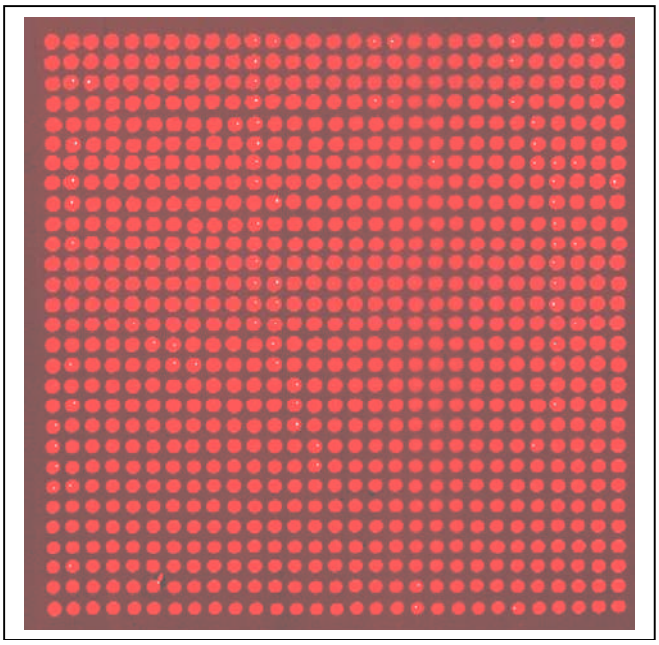

↑ 40,638 oligonucleotide spots printed on to a Corning UltraGap glass slide (above image). There are 48 grids of 841 spots in each grid.

← 841 oligonucleotide spots in a 29 x 29 grid (left image). The spot size of each spot is approximately 100 microns and the distance between each spot is about 25 microns.

spots in each grid. 48 grids x 841 spots = 40, 638 spots).

Figure 6. Hybridization of Cy5 Labeled Random Nanomers for Microarray Manufacture Quality Control. In the images below 48 tungsten pins were used to stamp oligonucleotides on to a Corning UltraGap glass slide. This corresponds to a total of 40,368 spots on the microarray (29 x 29 grid = 841 spots

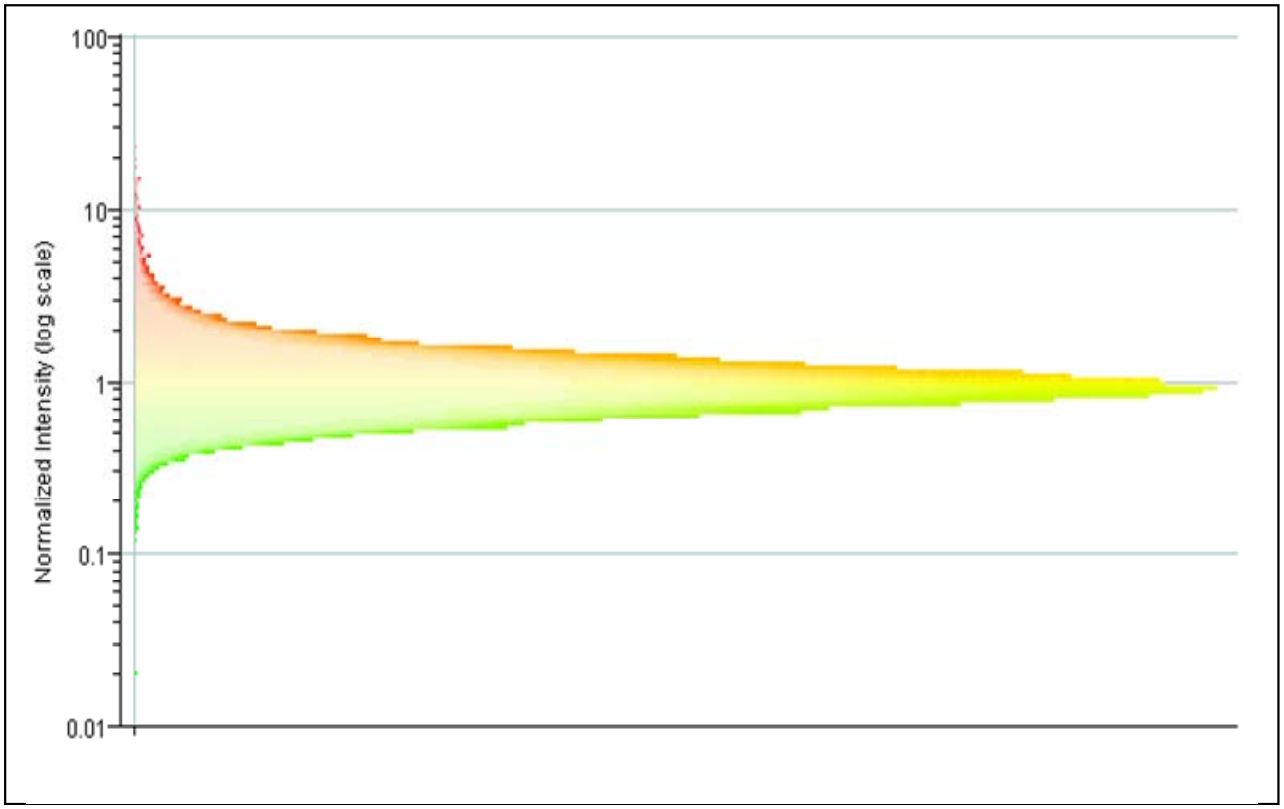

Figure 7. A combined normal plot of 11 microarrays with 38,467 probes each. This corresponds to 423,137 expression values for the 11 microarrays. Note that the data is highly normal and shows little to no skewness, indicating that the data follows Gaussian statistics.

Microarray Controls. The Microarray Facility has also three types of controls on to our microarrays; negative controls, positive controls and spike-in controls. The negative controls consist of empty spots which are spotted only with 25% DMSO buffer. The positive controls consist of housekeeping genes that are constitutively expressed in nearly all tissues. The spike-in controls are obtained from Ambion, Inc. and consist of E. coli genes that show no sequence similarity to mammalian genomes. These have been tested experimentally to insure that they do not cross-hybridize to each other or to human and mouse RNA.

Through the use of the spike-in controls, gene expression data can be evaluated by relating experimental data to that obtained from our spike-in control genes of known concentration and ratio. This allows us to evaluate the microarray data quality of each slide. If the spike-in controls give the expected concentrations and expression ratios, this is a good indication that the experimental RNA samples have been labeled and normalized correctly and that correct expression values are being obtained. Figure 8 shows experimental results obtained from the spike-in controls. Table 4 shows the expected ratio values of the spike-in controls.

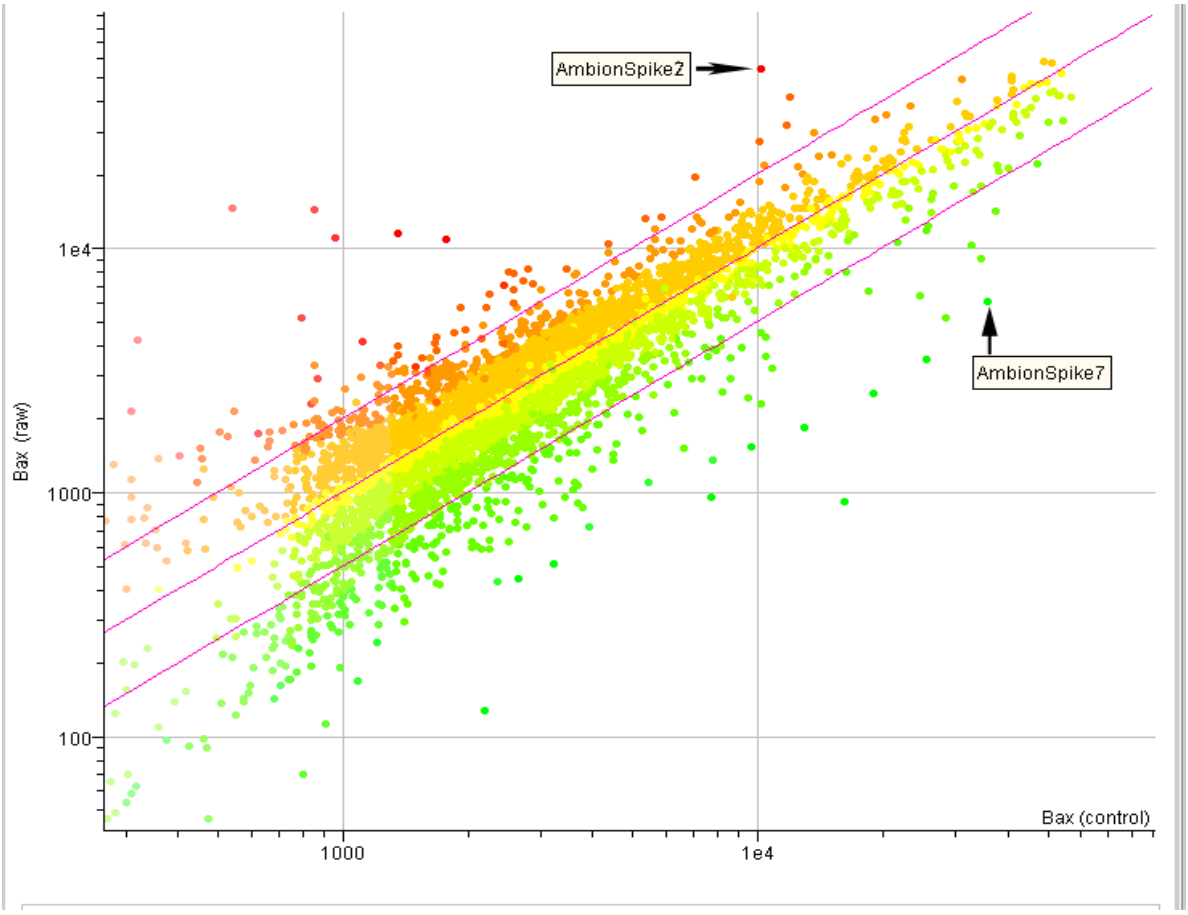

Figure 8. A scatter plot of 11 microarray experiments combined for analysis. The Ambion Spike in controls 2 and 7 are highlighted. Note that they flank the expression data and give approximately the correct expression ratios (10 and 0.1 respectively).

Table 4. The input ratios of the Ambion RNA spikes in the experiment and control samples

	Ambion spike 1	Ambion spike 2	Ambion spike 3	Ambion spike 4	Ambion spike 5	Ambion spike 6	Ambion spike 7	Ambion spike 8
Cy3 channel	2.5	5	0.125	5	0.25	5	1	1
Cy5 channel	2.5	0.5	0.25	1	10	2	10	1
Ratio (Cy3/Cy5)	1	10	0.5	5	0.25	2.5	0.1	1

3. Technical Objective 3: To update on recent advances.

A. Conferences and Continuing Education. The methods described are advancements developed as a result of learning of new methods and technologies from networking and scientific conferences attended by scientists in the MDC. Following is a list of conferences attended and talks given by scientists in the MDC. These conferences led to improvement and incorporations of state of the art technologies in the Microarray Laboratory and Informatics Support Services:

Latest Technologies and Development Conferences attended by Dr. Subburuman Mohan:

- The Endocrine Society, 88th Annual Meeting, June 24-27, 2006, Boston, MA
- American Society for Bone and Mineral Research, 28th Annual Meeting, Sept 15-19, 2006, Philadelphia, PA
- International Congress Of Growth Hormone And Insulin-Like Growth Factor Research Societies, 3rd International Meeting, Nov 11-15, 2006, Kobe, Japan.

Latest Technologies and Development Conferences attended by Dr. Robert Chadwick:

- American Society for Bone and Mineral Research, 28th Annual Meeting, Sept 15-19, 2006, Philadelphia, PA

American Association for Cancer Research, 96th Annual Meeting, April 16-20, 2005, Anaheim, CA Latest Technologies and Development Conferences attended by Dr. Robert Chadwick:

- American Association for Cancer Research, 96th Annual Meeting, April 16-20, 2005, Anaheim, CA

Latest Technologies and Development Talks given by Dr. Robert Chadwick:

- Update on genetics and new technologies, a report for the 96th Annual Meeting of The American Association for Cancer Research, May 18, 2005, MDC staff meeting.

Latest Technologies and Development Conferences attended by Dr. Liming Bu and Yan Hu:

- Agilent Technologies Microarray Workshop, University of California, San Diego, October 24-26, 2004, San Diego, CA

Also, the microarray and informatics support services have trained and assisted multiple investigators in the MDC with their microarray experiments and data analysis.

B. Additional Progress

Scientific collaborations were undertaken investigating isolation of RNA from archival tissue specimens. Since these specimens yield RNA that is of lower quality than flash frozen tissue samples, we are working on developing improved RNA isolation and labeling methods from degraded RNA. If the methods can be optimized to give consistent and reliable expression results from archival tissue, this will be of great use in proposed future clinical studies.

For isolation of RNA from paraffin embedded tissue we found that the Epicentre MasterPure Nucleic Acid isolation kit gives high yields of RNA. Following is the protocol we currently use:

RNA Isolation from Paraffin Embedded Tissue

1. Cut 10 micron sections from the paraffin embedded tissue.and place the tissue in a 1.5 ml microtube.
2. Deparaffinize the tissue through successive washes of citrosolve (1 ml for 5 min each time), 96% ethanol (1 ml twice for 5 min each time), and 70% ethanol (1 ml once for 5 min).
3. Dilute 2ul of Proteinase K into 300ul of Tissue and Cell Lysis solution for each sample. Resuspend the cell pellet with this Lysis solution and mix thoroughly.
4. Incubate at 65°C for 45min, and vortex every 15min.
5. Place the sample on ice for 5min.
6. Add 150ul of MPC protein Precipitation Reagent to 300ul of lysed sample and vortex the mixture for 10sec.
7. Spin for 10min 4°C at max speed in a microcentrifuge. Transfer the supernant to a clean tube.
8. Add 50ul of MPC protein Precipitation Reagent and repeat above step.
9. Add 500ul isopropanol to the recovered supernatant, invert the tube 30-40 times.
10. Pellet the RNA by centrifugation at 4°C for 10min in a microcentrifuge.
11. Carefully pour off the isopropanol without dislodging the RNA pellet. Remove all of the residual isopropanol with a pipet.
12. Air dry 10-15min.
13. Quantify and determine the quality of the RNA by Agilent Bioanalyzer and Nanodrop UV260 analysis.

If the tissue is frozen, steps one and two of the above protocol are omitted. Frozen tissue RNA gives very high quality RNA as well as high yields. The initial experiments on RNA isolation from paraffin embedded tissue show that the RNA is highly degraded (Figure 9). However, high yields of RNA have been obtained from paraffin embedded tissue.

Using the RNA samples shown in Figure 4, microarray expression profiling was attempted. The frozen RNA sample gave high yields of Cy3 and Cy5 labeled RNA. However, the paraffin

RNA sample did not give usable yields of labeled RNA. We believe that this is due to the highly fragmented nature of the paraffin RNA. Microarray labeling protocols use oligo dT for priming and the short fragments of paraffin RNA do not hybridize oligo dT and label efficiently.

Thus, we undertook experiments using realtime PCR expression profiling and initial cDNA synthesis by random decamer priming. We found that expression profiling of paraffin RNA by realtime PCR works well, as long as the RT-PCRs are short (~100 bp).

KEY RESEARCH ACCOMPLISHMENTS

- Increased the quality of manufactured arrays through the use of 50 micron silicon printing pins.
- Increased oligo library life through the reduction of waste from print blotting and printing to complete dryness with the silicon pins.
- Improved microarray analysis results by the use of Ambion spotting and spike-in controls. These controls have known RNA concentrations and Cy3/Cy5 ratios and their use gives confidence that correct expression results are obtained.
- Improved quality control of microarray manufacture through the use of Cy3 and Cy5 labeled random nanomers (panomer). These controls allow for the determination of optimal DNA concentration for spotting and grid parameter determination for maximum gene density.
- Investigated new methods for isolation of RNA from archival specimens (paraffin embedded tissue).
- Improved microarray analysis results by the use of GeneSpring GX Version 7.3.1 expression analysis software.
- Trained multiple investigators in informatics and microarray data analysis.
- Attended research conferences to learn of latest advances in microarray manufacture and analysis.

CONCLUSIONS

1) The technical objectives (1) To provide technical service; (2) To provide education; and (3) To update on recent advances have been achieved.
2) The microarray and informatics support services have increased throughput and improved microarray expression results in the Musculoskeletal Disease Center.

3) The improvements made to the microarray and informatics support services will expedite and advance research into gene discovery, function and genetic pathway analysis in the MDC.

REFERENCES

1. Yelin R, Dahary D, Sorek R, Levanon EY, Goldstein O, Shoshan A, Diber A, Biton S, Tamir Y, Khosravi R, Nemzer S, Pinner E, Walach S, Bernstein J, Savitsky K, and Rotman G. "Widespread occurrence of antisense transcription in the human genome." Nature Biotechnology Volume 21(4):379-86 (2003).
2. Tanaka T.S. et al., Genome-wide expression profiling of mid-gestation placenta and embryo using a 15,000 mouse developmental cDNA microarray. Proc Natl Acad Sci U S A, 2000. 97(16), p. 9127-9132.

PROJECT 12: VECTOR SUPPORT SERVICE

INTRODUCTION

Several sub-projects of this grant involve investigations of gene function and gene therapy, both of which require gene transfer technology. Investigators working on these sub-projects of this Army grant need to use gene transfer technology. Gene transfer uses vectors that carry a gene-of-interest and deliver it to target cells. Development and design of appropriate vectors requires technical expertise. It is more efficient and cost-effective to have a centralized Support Service Facility within the Musculoskeletal Disease Center to serve these investigators by providing service in vector design and production, education, training, and technical advice in gene transfer technology. The Vector Support Service Facility serves as a dynamic resource for investigators working on projects funded by the Army. As a result, the emphasis of this Support Service is on development and production of viral vectors, especially retroviral vectors that are based on Moloney murine leukemia virus (MLV) and human immunodeficiency virus (HIV), and non-viral plasmid vectors for gene transfer and to provide training and assistance to investigators with respect to vector development and production.

There were three specific objectives for this subproject:

1. To serve as a dynamic resource to construct and provide vectors for delivery and expression of appropriate genes for investigators supported by the Army grant.
2. To serve as an educational resource, providing technical assistance and training to investigators in the use of viral and non-viral vector gene delivery and gene expression.
3. To improve and expand vector systems available to investigators as gene transfer technologies advance.

BODY

- **Progress on Specific Objective 1: To serve as a dynamic resource to construct and provide vectors for delivery and expression of appropriate genes for investigators supported by the Army grant**

Since the beginning of the grant period, the vector support service produced numerous VSV-G pseudotyped MLV vectors and HIV-based vectors for various investigators working on projects supported by the Army. Specifically, 1) in collaboration with Dr. Rundle (sub-project 4), the facility generated various batches of concentrated VSV-G pseudotyped MLV vectors expressing different growth factor or control genes that have been used successfully in animal experiments. These growth factor or control genes included β–galactosidase (β-gal), enhances green fluorescent protein (EGFP), basic fibroblast growth factors (FGF-2) and its derivatives, bone morphogenetic protein-4 and its derivatives (BMP-4), growth hormone (GH), and inducible cyclooxygenase (Cox-2). 2) In collaboration with Dr. Gysin (sub-project 7), the facility produced different batches of concentrated MLV-based vectors, expressing β–gal, BMP2/4, and Cox-2 genes, respectively. These viral vectors were used in Dr. Gysin's experiments testing a potential synergistic interaction between BMP2/4 and Cox-2 in promoting bone formation in the critical sized calvarial bone defect model. 3) In collaboration with Dr. Strong (sub-project 8), the facility produced several batches of concentrated VSV-G pseudotyped MLV vectors, expressing β–gal, LMP-HA, and IGFBP6 gene with or without secretion signal, for animal experiments.

Additionally, we also produced MLV-based vectors with different truncations of Cox-2 genes for Dr. Strong's experiments. In our original Cox-2 vector, pY-Cox-2, the 3' un-translated region (UTR) was removed to ensure the expression of Cox-2 gene in primary cells. We also included Kozak sequences at the 5'end of the gene to ensure efficient translation. However, these hypotheses have not been tested with the proper control Cox-2 gene. Dr. Strong has constructed three different Cox-2 genes. These new Cox-2 genes are Cox2-1963, Cox2-2532 and Cox2-2080. The Cox2-1963 gene doesn't contain Kozak sequences at the 5'of the gene. The Cox2-2080 gene contains partial 3'UTR sequence and the Cox2-2532 contains the complete 3' UTR sequence. After production of the MLV-based vectors with these genes, we transduced a primary rat calvarial cell line, RCOB and a transform cells line, HT1080 with these vectors. The experiments to verify the level of Cox-2 expression have been performed in Dr. Strong's laboratory.4) In support of sub-project 6, the facility generated a number of different batches of HIV-based vectors for use in the study of systemic gene therapy of musculoskeletal diseases. These HIV-based vectors included those expressing β-gal, EGFP, BMP2/4, FGF-2 and GH genes.

- **Progress on Specific objective 2: To serve as an educational resource, providing technical assistance and training to investigators in the use of viral and non-viral vector gene delivery and gene expression**

To fulfill the specific objective 2, the core director has updated investigators at staff meetings regarding new technologies and vectors that are available in the Vector Support Service Facility. Dr. Chen (the director of the vector support facility) gave several lectures to the J.L.Pettis VAMC, Musculoskeletal Diseases Center staff during the grant period. These lectures were designed to educate and tutor investigators in viral gene transfer technology. Dr. Chen also gave lectures addressing the safety issues concerning the use of viral vectors in gene therapy and in research of musculoskeletal disease gene therapy. Additionally, Dr. Chen lectured to animal research facility personnel of J. L. Pettis VAMC on the safe handling of animals treated with HIV-based and other viral vectors on an annual basis.

The Vector Support Service also provided essential technical assistance to various investigators. For example, the Service assisted Dr. Rundle (sub-project 4) in the design and development of several new HIV-based vectors for expression of therapeutic genes for the use of fracture repair in the rat tibial fracture model. In the past, ubiquitously expressed viral promoters (e.g., CMV or LTR) were used to drive expression of BMP2/4 in the viral vectors. While these promoters are powerful, they also lack tissue specificity. The lack of tissue specificity has been a potential safety risk with respect to BMP gene therapy, since BMPs are known to convert muscle into bone. As a result, the use of ubiquitous promoters could represent a substantial safety risk of ectopic bone formation. A potential approach to minimize ectopic bone formation is to use an osteoblast specific promoter to drive the expression of the BMP gene. The use of an osteoblast-specific promoter should restrict the expression of the transgene in bone. HIV-based viral vectors are particularly suited for this application. Unlike vectors based on murine leukemia virus, HIV-based vectors are compatible with tissue-specific promoters and also can transduce non-dividing cells. HIV-based vectors have a much lower propensity for a strong immune response, which could lead to relatively long-term expression of the therapeutic gene. Consequently, The Vector Support Service assisted Dr. Rundle in the design and production of several HIV-based viral vectors with different tissue-specific promoters in the pHIV-9 construct. The pHIV-9 construct is the third generation HIV-based vector with extra cPPT and wPRE sequences to ensure the high level of viral titer and gene expression. To evaluate these pHIV-9 vector constructs, we

inserted 5 different promoters to drive a reporter gene, GFP. These promoters include: a strong viral promoter, cytomegalovirus immediate early promoter (CMV), a strong house-keeping promoter, human elongation factor 1-α (EF1−α), a 2.3 KB fragment of the promoter sequence from rat collagen 1α1 (Col2.3), a 310bp of promoter sequence from human α 1 type 1 procollagen (ColA2) and a 351bp of promoter sequence from human Cbfa1 promoter (Cbfa1). The efficiency of these HIV-based vectors with a tissue-specific promoter to drive expression of GFP was then determined and compared in osteoblastic (human SaSO-2 cells, rat ROS osteosarcoma cells, and mouse MC3T3-E1 cells) and non-osteoblastic cells (HT1080 human sarcoma fibroblastic cells, rat skin fibroblasts). We also included primary rat primary osteoblasts (RPO) in this study. The MLV-based vector was used as a control for comparison.

Each of cell types was plated in six-well plates and was transduced with 1-50 μl of each viral stock. Forty-eight hours after viral transduction, the GFP expression was evaluated by flow cytometry. The GFP positive cells were identified and the level of GFP expression was calculated with the software provided by the manufacturer of the flow cytometer, B D Biosciences. The results are summarized in Table 1.

Promoters	HT1080	SaOS-2	RSF	ROS	RPO	MC3T3-E1
CMV	1173	371	388	175	189	23
EF1-α	248	585	458	292	386	296
ColA2	24	51	46	ND	73	21
Col2.3	30	58	11	61	123	37
Cbfa1	37	92	18	52	117	37
MLV-LTR	255	216	504	149	619	61

Table 1: Mean GFP expression of HIV-based vectors in different types of cells. All the promoters are in HIV-based vector except for MLV-LTR. Cells lines were transduced with viral vectors and the level of GFP expression *****The level of GFP expression is presented as arbitrary units determined by flow cytometry. ND: Not detectable.

The viral promoters (CMV and MLV-LTR) and housekeeping promoter (EF1-α) were most potent in driving the expression of the GFP gene in each test cell type, including osteoblasts. However, the viral promoters were more potent than EF1-α in non-osteoblastic cells, the EF1-α promoter in general appeared to be better than CMV and MLV-LTR in osteoblastic cells. As expected, the osteoblastic promoters were more effective in osteoblastic cells than non-osteoblastic cells. However, the potency of osteoblastic promoters was significantly lower than that of viral promoter or that of EF1-α. The differential preference of these test promoters in osteoblastic vs. non-osteoblastic cell types appeared to be species-independent. The lentiviral-based vector with the EF1-α promoter provides the optimal expression of the transgene in the bone cells. The relatively weak potency of the test osteoblastic promoter was somewhat surprising and disappointing. A much stronger osteoblastic-specific promoter is desirable for use

in gene therapy. Consequently, we are currently working with other investigators to identify more potent osteoblastic promoter sequences for testing.

- **Progress on Specific Objective 3: To improve and expand vector systems available to investigators as gene transfer technologies advance**

A. Development of small interfering RNA retroviral vectors for studying of bone biology

Small interfering RNA (siRNA) has recently emerged as a new and powerful tool to knockdown the expression of endogenous genes. The high specificity and efficacy of siRNA to silence gene expression has opened up a new approach to study gene function *in vitro* and *in vivo*. The siRNA can be in the form of oligonucleotide RNA or expressed as a hairpin RNA from plasmid or viral vectors. The Vector Support Service has developed a siRNA retroviral vector system that can be used by other investigators to suppress endogenous gene expression. Since the expression of siRNA requires a polIII promoter, we used the pSuppressor Retro vector (pSR) (from Imgenex Corporation) for siRNA vector development. With the pSR vector backbone, we have generated VSV-G pseudotyped MLV-based vectors in our viral facility. The viral titer was between $1X10^5$ to $1X10^6$ tfu/ml.

To test the efficacy of our siRNA vector system, we collaborated with Dr. Rundle to test the efficiency of our GFP siRNA vector in the suppression of GFP expression in cells transduced with our MLV-GFP vector. To prepare the GFP siRNA vector, we inserted a pair of synthesized DNA oligonucleotides corresponding to a unique sequence of the GFP gene into the pSR vector to generated pSR-GFP. The pSR-GFP vector contains a short hairpin sequence, which is specific to GFP gene under the control of U6 promoter. To produce GFP expressing cells, we generated three HT1080 cell populations each containing a single copy of GFP gene using our MLV-based vector. Because the integration sites for MLV vectors are random, the use of three separate transduced cell population could minimize site-specific effects. We reasoned that the integration site would have a significant effect on the expression level of GFP. Accordingly, to ensure that the integration site of GFP in the transduced cells was different, we chose three different preparations with different GFP expression level. After the establishment of each of the three HT1080 GFP cell lines, we transduced each line with the pSR-GFP retroviral vectors. Since the pSR-GFP vector also contains a neo gene, the siRNA transduced cells could be selected by G418. After two weeks of selection, the G418 resistant colonies were pooled and the GFP expression level of each cell pool was analyzed by flow cytometry (Table 2).

	GFP Level Before siRNA	GFP Level After siRNA	% Reduction of GFP Expression
HT1080 GFP-1*	**1392**	**58**	**96**
HT1080 GFP-2	**699**	**35**	**95**
HT1080 GFP-3	**95**	**12**	**91**
HT1080 Control	**4**	**ND**[#]	**ND**

Table 2: Mean GFP expression before and after siRNA transduction. *HT1080 GFP-1 to 3 represent three GFP transduced clones expressed different levels of GFP. [#]ND: Not done.

The results in Table 2 clearly demonstrate that our GFP siRNA construct effectively suppressed the GFP expression more than 90%. The GFP siRNA construct was equally effective in each of the test cell pools of GFP transduced cells with varying degrees of GFP expression. Consequently, we conclude that our siRNA construct was highly effective and was also integration-independent. We also worked with Dr. Rundle and have designed and prepared six

MLV-based vectors with siRNA that target different domains of FGF receptor. These vectors were used in his proposed studies to test the role of FGF receptor in fracture healing.

B. Development of magnetic retroviral vectors for bone disease gene therapy.

Gene therapy for fracture repair requires accurate delivery of therapeutic genes to fracture sites. We recently showed that direct injection of an MLV-based vector expressing BMP4 to the rat femoral fracture callus enhanced bone formation. A major technical difficulty was associated with miss-injection of the viral vector, resulting in extra-periosteal bone formation. We sought to develop a magnetic retroviral vector (MRV) targeting system for site-specific delivery of viral vector to fracture callus to improve the safety and efficiency of the therapy. We believe that the magnetofection (transfection assisted by outside magnetic field) approach would allow the use of a magnet to target direct delivery of viral vectors to a fracture site. Moreover, magnetofection could significantly enhance viral transduction efficiency. To produce MRV, we collaborated with a research team in Taiwan, who fabricated magnetic nanoparticles of γ-Fe_2O_3 by a high-yield reduction-oxidation lyothermal method at high temperature under argon gas. Iron pentacarbonyl precursors were then reduced to form iron nanoparticles and oxidized by trimethylamine. High-resolution transmission electron microscopy (HRTEM) analysis revealed a narrow distribution of particle size of 4±0.8 nm. The resulting ferric nanoparticles were coated with polycationic, polyethyleneimine (PEI) by sonication. PEI is a cationic polymer capable of binding retroviral vectors. The average size of the PEI-coated magnetic nanoparticles was 100-200 nm, determined by HRTEM (**Figure 1**). We then synthesized the MRV complex by mixing the PEI-coated particles with various concentrations of our MLV vectors.

SEM Picture of PEI Coated Magnetic Nanoparticles

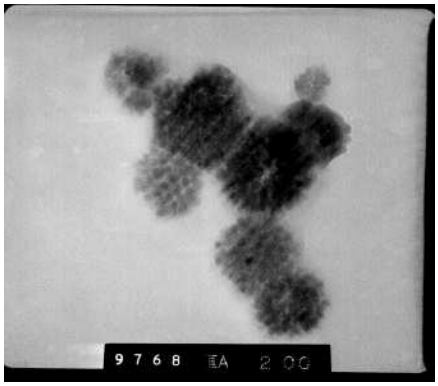

Figure 1: High-resolution transmission electron microscopic image of PEI Coated Magnetic nanoparticles.

We first evaluated the transduction efficiency of our MRV system expressing green fluorescent protein in HT-1080 cells. In **Figure 2** we show that by applying a magnetic field created by a small magnet, the transduction efficiency of the MRV carrying the GFP was markedly increased by 3- to 5-fold ($p<0.001$) with an MOI between 0.1 to 1.

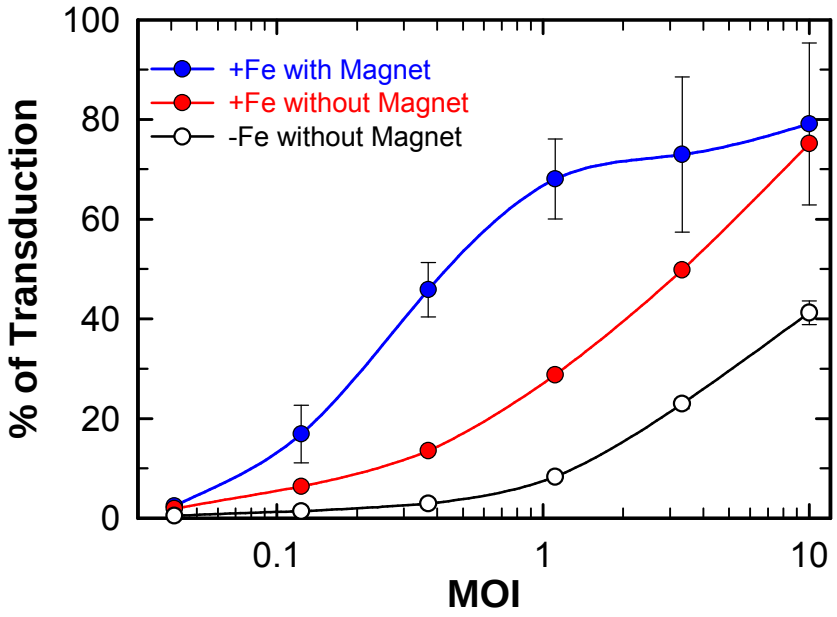

Figure 2: Magnetotransduction efficiency with respect to increasing multiplicity of infection (MOI). HT1080 cells (1.3 x 10^4 cells) in a 48-well plate were treated with various MOI of EGFP-MRV. A magnetic field was then applied for 20 min, and expression of GFP was measured by flow cytometry with the FACSCalibur. The transduction efficiency was assessed by measuring the percentage of transduced cells expressing GFP.

This confirms the effectiveness of the MRV to transduce mammalian cells. To test the ability to target delivery of the MRV to a fracture site, we collaborated with Dr. Rundle in assessing the effectiveness of the MRV to produce targeted transduction at the fracture site in the rat femur model. In this experiment, we first inserted a metal rod in a rat femoral cavity, then used the rod as the guide to insert a catheter. The MRV (50µl of concentrated MLV-based vector with β-gal gene and 50µl of magnetic nanoparticles mixed *in vitro*) was injected into the marrow space through the catheter. After the injection, two Nd-Fe-B permanent magnets were placed outside of the injection site for 15 min when animals were under anesthesia. Seven days after injection, the animals were sacrificed and the femora were harvested. The femora were then spliced longitudinally and stained x-gal overnight for β-gal activity. As shown in **Figure 3**, the femur with MRV has more x-gal staining than the control femur, particularly around the site where the magnets were placed.

A. Regular β-gal viral vectors

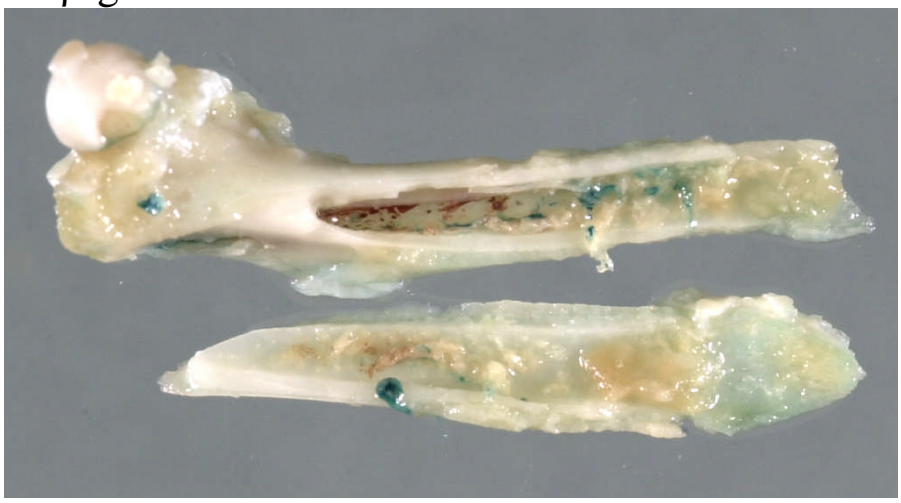

B. β-gal MRVs with magnets

Figure 3: The MRV system enhanced targeted transduction in the femoral fracture model. The rat femur was stabilized with a pin then a catheter inserted. Sixteen hours after the insertion, the β-gal-MRV was injected into the marrow cavity through the catheter. A pair of magnets was placed outside of the injection site for 15 min (bottom femoral). Seven days after the delivery of the MRVs, the animal was sacrificed and the tissue from injection site was harvested for histological staining of β-gal. The top bone was injected with regular β-gal-MLV and without the magnet treatment.

In summary, these preliminary studies demonstrate that: 1) the magnetic nanoparticles are not cytotoxic; and 2) with the β-gal reporter gene, the transduction of MRV was markedly enhanced with the direct injection into marrow cavity with the application of the magnetic field, particularly at the site where the magnets were applied. Therefore, the MRV system could be a very useful tool to deliver and enhance the transduction efficiency of viral vectors at targeted sites.

C. Development of inducible MLV-based vectors for bone disease gene therapy.

Bone disease gene therapy depends on the expression of growth factors, which can stimulate bone formation, at target sites at the appropriate time. The expression of the growth factor should be turned off when it is no longer needed. Accordingly, the ubiquitous and unregulated expression of growth factor genes could be a major safety concern. For example, over expression of BMP2/4 or FGF-2, two potent growth factors for bone formation, could cause serious side effects if their expression is unregulated. Consequently, the Vector Support Service has initiated work on the development of regulatable MLV-based vectors using ligand-inducible promoter. Our initial effort focused on the tetracycline-regulated systems. There are two general types of tetracycline-regulatable systems: 1) Tet-On system in which the expression of the transgene is enhanced by tetracycline or analogs; and 2) Tet-Off in which the transgene expression is inhibited by tetracyclines.

In 1995, Gossen et. al. [1], reported the first Tet-On inducible system, rtTA. The gene contains four amino acid exchanges from the parental Tet-Off gene, tTA. The rtTA gene exhibits a reverse phenotype, namely, it can turn on the gene expression in the presence of ligand (Tet-On). For a kinetic reason, the Tet-On system is often preferable over the Tet-Off system. However, rtTA system also comes with its own problems. First, it requires a very high concentration of ligand (1-2 μg/ml of doxycycline) and this is very difficult to achieve *in vivo*. Second, it exhibits some residual affinity to tetO promoter in absence of ligand, which is recognized as high intrinsic background activity. Therefore, the rtTA system is leaky. Third, the rtTA still contains the VP16 as the transcription activator. In many occasions, it is impossible to generate stable mouse lines that would produce a sufficient amount of rtTA in certain cell types. This may be due to the reduced stability of rtTA and toxicity of VP16. To overcome these problems, in 2000, Urlinger et. al.[2], reported a second generation of Tet-On system, rtTA-S2. In this system, the VP16 was replaced with 3 copies of F domain (F domain contains 12 amino acids domain from VP16). In addition, the new system contains four new amino acid exchanged from tTA. Interestingly, there was no overlap in amino acid changes between rtTA and rtTA-S2. The rtTA-S2 is significantly improved from rtTA. It is not as toxic or as leaky as the rtTA. Furthermore, in 2004, Das et. al.[3], improved the rtTA-S2 by additional amino acid changes. They found three additional mutations at amino acid position 12 (serine to glycine), 84 (phenylalanine to tyrosine) and 209 (alanine to threonine) would further improve the ligand sensitivity and promoter activity of new rtTA-S2. They named the new tet-on system, rtTA-YT (for two mutations at F86Y and A209T from rtTA-S2) and rtTA-GYT (for three mutations at S12G, F86Y and A209T from rtTA-S2) In collaboration with Dr. Das at the University of Amsterdam we obtained these two doxycycline induced transcriptional factors.

To prepare the TET-ON MLV-based vectors, we used PCR techniques to generate the rtTA-GYT, transcriptional factor genes and subcloned into our pY-based vector (MLV with MFG-like backbone and CMV promoter in the 5' end). Furthermore, we put the reporter gene (EGFP) under the control the tetracycline promoter (tetO) in the same vectors. In Figure 4 we show the diagrams of these vectors.

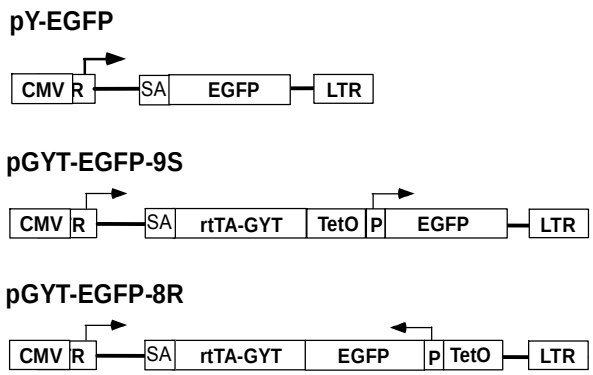

Figure 4: Schematic illustration of TET-OFF and TET-ON MLV-based vectors. The pGYT-EGFP is the new TET-ON system. The arrows indicate the direction of the transcription. The only difference between 9S and 8R is the direction of the tetracycline controlled expression unit.

To demonstrate the function of rtTA-GYT, we transduced the vectors to three different cell lines, 293T, rat marrow stromal cells and rat skin fibroblast. We measured the expression of marker gene (EGFP) expression under suppressed condition (regular medium) or inducible condition (regular medium plus 1μg/ml of doxycycline). The results are summarized in Table 3.

	Types of Media	Mean Intensity	Fold Induction*
In 293T cells			
pY-EGFP	Regular	43.1	1.0
	+Doxy	45.6	1.2
pGYT-EGFP-9S	Regular	41.2	1.0
	+Doxy	428.2	**14.9**
pGYT-EGFP-8R	Regular	21.7	1.0
	+Doxy	121.4	**14.1**
In Rat marrow stromal cells			
pY-EGFP	Regular	237.9	1.0
	+Doxy	240.5	1.1
pGYT-EGFP-9S	Regular	66.82	1.0
	+Doxy	1371.7	**20.3**
pGYT-EGFP-8R	Regular	25.7	1.0
	+Doxy	127.2	**26.5**
In Rat skin fibroblasts			
pY-EGFP	Regular	283.9	1.0
	+Doxy	281.6	1.1
pGYT-EGFP-9S	Regular	70.6	1.0
	+Doxy	1532.6	**31.3**
pGYT-EGFP-8R	Regular	47.4	1.0
	+Doxy	179.6	**26.5**

Table 3:*Expression levels of EGIP in the absence or presence of doxycycline. Fold induction is calculated by comparing the value of mean intensity multiplied by the percentage of the positive cells. We selected the value from regular medium as 1.

We observed 14-31 fold induction in these cell lines under the inducible condition (1μg/ml of doxycycline). The level of GFP expression of pGYT-EGFP is consistently stronger than the pY-

EGFP vector. The results indicate that the promoter activity of tetO under inducible condition is stronger than MLV-LTR promoter. Based on these data, we chose the new Tet-On system (pGYT-EGFP) as our inducible system and introduced the growth factor genes in this vector.
Previously, we have shown the human FGF-2 gene can be expressed and secreted by adding a BMP2/4 secretion peptide at the 5'end and replacing the second and third cysteines of FGF-2 with serine and asparagines, respectively. Using this gene, we demonstrated the FGF can significantly increase the proliferation of the implanted cells *in vivo*. In addition, we also demonstrated mice Sca1 positive cells transduced with FGF-2 can greatly increase bone formation in the marrow cavity after transplanted into a recipient mouse. These data all suggest that FGF-2 can be a good candidate gene for bone gene therapy. However, the un-controllable FGF-2 expression may also have adverse effects. For example, transplantation of FGF-2 transduced hematopoietic stem cells (Sca1+ cells) may reduce the marrow space for blood cells and subsequently have a detrimental effect on the hematopoietic system. We may solve this problem by a controllable expression of FGF-2. Toward this goal, we constructed a doxycycline inducible FGF-2 vector based on our construct, pGYT-EGFP. We show the diagram of this vector in **Figure 5**.

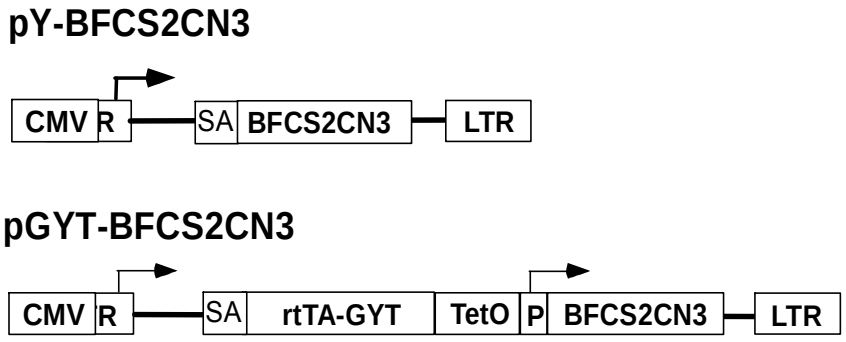

Figure 5: Schematic illustration of Tet-On MLV-based vectors. The pY-BFCS2CN3 is our original FGF vector. The expression of the FGF is originated from MLV-LTR promoter after transduction. The pGYT-BFCS2CN3 is the new inducible MLV-based vector. The expression of the FGF gene is from TetO promoter and it is controlled by doxycycline. The arrows indicate the direction of the transcription.

After the construction of the vectors, we picked two clones of the pGYT-BFCS2CN3 and named them as pGYT-BFCS2CN3-18S and pGYT-BFCS2CN3-22S. Based on these two clones, we generated VSV-G pseudotyped MLV-based vectors by transient transfection in 293T cells. We transduced HT1080 cells either in the induction media (+Dox for pGYT-BFCS2CN3 vectors) or suppression medium (regular medium without doxycycline). Forty-eight hours after transduction, the supernatants were harvested. The amount of FGF in the conditional media was determined by ELISA. The results are summarized in the Table 4.

	pY-BFCS2CN3	pGYT-BFCS2CN3-18S	pGYT-BFCS2CN3-22S
Doxycycline (1μg/ml)	**40**	**68**	**84**
Regular	**48**	**2.0**	**4.2**
Fold Induction	**0.8**	**34**	**20**

Table 4: One hundred μl of viral stocks were used to transduce duplicate sets of HT10080 cells in a 6 well plate containing 2E5 cells per well. After transduction, 1 μg/ml of Doxycycline was added to one set of the wells. Forty-eight hours after transduction, the supernatants were harvested. The amount of FGF in the conditional media was determined by ELISA and presented as ng/ml.

These results are consistent with our previous results in marker gene expression. We can observe 20 and 34 fold induction in FGF expression under the inducible condition (1μg/ml of doxycycline) in HT1080. The level of FGF expression of pGYT-BFCS2CN3 is consistently higher than the pY-BFCS2CN3 vector. This result is in line with the marker gene expression in pGYT-EGFP. We conclude that the promoter activity of tetO under inducible condition is stronger than MLV-LTR promoter in HT1080 cells.

One application for the inducible vector is to use it in musculoskeletal cells. Therefore, we tested the expression of the inducible retroviral vector, pGYT-EGFP in human bone cells (HBC), mouse osteoblast cells (MC3T3), Rat marrow stromal cells (RMSC), mouse macrophage cell line (Raw) and mouse muscle stem cell line (C_2C_{12}). We plated the cells in 6 well plates with 1 $X10^5$ cells per well. After overnight incubation, 200μl of pGYT-EGFP vectors (viral titer around 1 X 10^7 tfu/ml, MOI around 10) were added to the cells in duplicated wells. After another overnight incubation, the medium of one of the wells was replaced with doxycycline containing medium (1μg/ml). After an additional 48 hr of incubation, the cells were harvested and analyzed by flow cytometery (Table 5).

Cell Types	Types of Media	% GFP(+) Cells	Mean Intensity	Fold Induction*
HBC	Regular	52.7	1294	1.0
	+Doxy	83.3	5465	**6.7**
MC3T3	Regular	49.8	295	1.0
	+Doxy	72.3	3975	**19.6**
RMSC	Regular	41.6	464	1.0
	+Doxy	38.0	4063	**8.0**
Raw	Regular	71.2	601	1.0
	+Doxy	99.8	5076	**11.8**
C_2C_{12}	Regular	38.7	607	1.0
	+Doxy	93.3	3259	**12.9**

Table 5:*Fold induction is calculated by comparing the value of mean intensity multiplied by the percentage of the positive cells. We selected the value from regular medium as 1.

From these results we conclude the new Tet-On system can be used in all the cells checked. The inductions range from 6.7 to 19.6 fold. Since the MIO used in this experiment in rather high

(MOI~10), we expect expression is saturated in some cells. Therefore, the fold induction may be underestimated.

In collaboration with Drs. Lau and Hall in the MDC, we have demonstrated $Sca1^+$ cells based transplantation strategy with modified FGF-2 gene can induce endosteal trabecular bone formation. However, we also found several adverse effects with high FGF-2 expression. These problems include depletion of serum calcium levels, high levels of serum PTH and incomplete mineralization of trabecular bone. We hypothesize that the use of an inducible promoter to regulate FGF-2 expression in the engrafted cells would optimize the bone formation and minimize the adverse side effects. We tested the pGYT-EGFP vector in HT1080 cell and $Sca1^+$ cells under a range of doxycycline concentration. We transduced $Sca1^+$ cells with an inducible vector (pGYT-EGFP) or a regular vector (pY-EGFP) with MOI around 6. We also transduced HT1080 cells with the same vectors with MOI around 1.5. After the transduction, the cells were exposed to a range of doxycycline (1-2000ng/ml). Seventy-two hours after transduction, the cells were analyzed by flow cytometery. The results are summarized in **Figure 6**.

(A) (B)

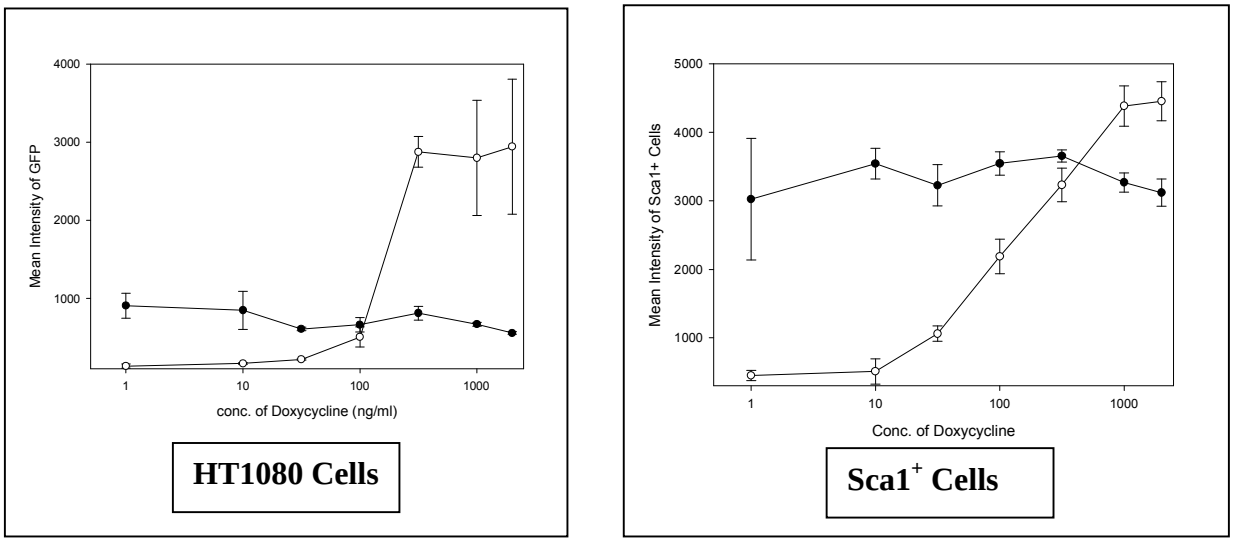

Figure 6: (A) HT1080 cells were transduced with MLV-based vectors containing the GFP gene under the control of either a constitutively expressing promoter (solid dots) or doxycycline inducible promoter (open dots). Cells were cultured in different concentrations of doxycycline (1-2000ng/ml). Seventy-two hours after incubation, the cells were assayed for GFP by flow cytometery. (B) is the same as part (A) except the $Sca1^+$ cells were used.

The expression of GFP in the doxycycline inducible promoter can reach the full induction under 1000ng/ml of doxycycline. The level of expression of inducible promoter is stronger than the MLV-LTR viral promoter in both HT1080 cells and mouse $Sc1^+$ cells. We also tested a similar construct with modified FGF-2 gene. We found FGF-2 level in the conditioned medium of $Sca1^+$ cells transduced with the modified FGF-2 gene under the control of the doxycycline inducible promoter was 10-fold higher in the presence of 1000ng/ml doxycycline (48.3 ± 2.6pg/ml vs. 467.5 ± 71.6 pg/ml).

The major problem for the Tet-On inducible is the induction requires a high concentration of doxycycline (1000 ng/ml). The high level of doxycycline is hard to achieve in animals and may limit its application *in vivo*. Lately, the same group has reported [4] new versions of Tet-On transcriptional factors that can further enhance the transcriptional activity and doxycycline-

sensitivity. Based on the transcriptional factor, rtTA-YT, they found the optimized transcriptional factors contains one or more mutations at amino acid position 9 (val to Ile), 67 (phe to ser), 138 (gly to asp), 157 (glu to lys) and 171(arg to lys). They reported triple mutants V14 (V9I, F67S, G138D), V15 (V9I, F67S, E157K) and V16 (V9I, F67S, R171K), are the most active and most doxycycline sensitive rtTA in their system. According to their results, these new rtTA transcriptional factors are 7 fold more active than the wild-type rtTA and 2.8 fold more active then the rtTA-YT with high doxycycline concentration (1000ng/ml). More importantly, they also observed 100-fold more sensitive to doxycycline when compared with wild-type rtTA and 30-fold more sensitive to doxycycline when compared with the rtTA-YT.
This new generation of Tet-On transcriptional factors has significantly improved the conditional expression of gene-of-interest and would be very useful for our conditional expression of FGF gene in animals. In 2007, we used our MLV-based vector. pGYT-EGFP and pYT-EGFP, as templates and incorporated these mutation into our vectors to generate a more efficient Tet-On MLV-based vectors. To incorporate the mutations into our clones, we employed a method developed by Stratagene to create mutations at multiple sites simultaneously. First, we synthesized six oligonucleotides that have covered all the mutations we would like to change. The sequences of these six oligonucleotides are shown in Table 6.

GYT-V9I (G to A)
TCTAGACTGAAGAGCAAA**A**TCATAAACGGAGCTC
YT-V9I (G to A)
TCTAGACTGAAGAGCAAA**A**TCATAAACTCAGCTC
YT- F76S (T to C)
GCATCATACCCACT**C**CTGCCCCCTGGAAG
YT- G138D (G to A)
TCTGTCCGCCGTGG**A**CCACTTTACACTGG
YT-E157K (G to A)
GCATCAAGTAGCAAAAGAG**A**AAAGAGAGACACCTACCAC
YT-R171K (G to A)
TTCTATGCCCCCACTTCTGA**A**ACAAGCAATTGAGC

Table 6: The table shows the oligonucleotide sequences used for mutagenesis. The underlined sequences represent the codons that will be changed. The nucleotide sequences with the bold phase represent the nucleotide changes for each primer. Since the V9I primer will cover the number 12 codon (S12G), we used two separated primers. The rest of primers were shared by pYT-EGFP and pGYT-EGFP for mutagenesis.

Using the QuikChange Multi Site-directed mutagenesis kit from Stratagene, we are able to generate seven constructs from pYT-EGFP and pGYT-EGFP based on the combination of oligonucleotides described in table 1. After we obtained the colonies, the mutated sequences were confirmed by DNA sequencing. We found more than half of the clones contain the desirable mutations. Therefore, this method is a very efficient and accurate method to generate

mutants. The amino acids changes of these seven clones in the rtTA gene are summarized in Table 7.

(Amino Acid Position)	**9**	**12**	**67**	**86**	**138**	**157**	**171**	**209**
New rtTA Constructs								
Original rtTA-S2	Val	Ser	Phe	Phe	Gly	Arg	Arg	Ala
GYT-rtTA	Val	**Gly**	Phe	**Tyr**	Gly	Arg	Arg	**Thr**
V15-rtTA	**Ile**	Ser	**Ser**	**Tyr**	Gly	**Lys**	Arg	**Thr**
V16-rtTA	**Ile**	Ser	**Ser**	**Tyr**	Gly	Arg	**Lys**	**Thr**
GV14-rtTA	**Ile**	**Gly**	**Ser**	**Tyr**	**Asp**	Arg	Arg	**Thr**
GV15-rtTA	**Ile**	**Gly**	**Ser**	**Tyr**	Gly	**Lys**	Arg	**Thr**
GV16-rtTA	**Ile**	**Gly**	**Ser**	**Tyr**	Gly	Arg	**Lys**	**Thr**
GS-rtTA	**Ile**	**Gly**	**Ser**	**Tyr**	**Asp**	**Lys**	**Lys**	**Thr**
GV1415-rtTA	**Ile**	**Gly**	**Ser**	**Tyr**	**Asp**	**Lys**	Arg	**Thr**

Table 7: The table shows all the amino acids that have been changed through mutagenesis from the original rtTA-S2. The amino acid position is presented from the rtTA-S2 amino acid sequence. The amino acids representing the mutated amino acids from each new construct are underlined and in bold.

Based on these constructs, we prepared MLV-based vectors with our standard transient transfection in 293T cells. We then transduced HT1080 cells with 5µl of viral stock in 6-well plates in quadrupeds. In these four wells, we used four different concentrations of doxycycline (1000, 100, 10 and 0 ng/ml). Thirty-six hours after the transduction, we harvested the cells and determined the mean intensity of the GFP gene expression through a flow cytometer. The results are summarized in Table 8.

Table 8

Constructs	Doxycycline (ng/ml)	GFP Mean Intensity	Fold Induction*
pGYT-EGFP	0	56.23	1
	10	89.84	1.60
	100	138.31	2.46
	1000	254.30	4.52
pGV-14-EGFP	0	42.88	1

	10	144.99	3.38
	100	296.28	6.91
	1000	308.19	7.19
pGV-15-EGFP	0	55.15	1
	10	177.00	3.21
	100	437.81	7.94
	1000	717.74	13.01
pGV-16-EGFP	0	51.63	1
	10	181.69	3.52
	100	321.54	6.23
	1000	425.87	8.25
pV-15-EGFP	0	45.03	1
	10	105.62	2.35
	100	268.58	5.96
	1000	485.82	10.79
pV-16-EGFP	0	49.81	1
	10	123.71	2.48
	100	331.20	6.65
	1000	516.16	10.36
pGS-EGFP	0	42.46	1
	10	133.73	3.15
	100	337.40	7.95
	1000	457.80	10.78
pGC1514-EGFP	0	44.89	1
	10	113.10	2.52
	100	287.88	6.41
	1000	483.27	10.77

Table 8:*Expression levels in the absence or presence of doxycycline, Fold induction is calculated by comparing the value of mean intensity multiplied by the percentage of the positive cells. We selected the value from regular medium as 1.

Based on these FACS results, we found three interesting phenomena. First, the background expression (no doxycycline in the medium) is very similar between these clones (mean intensity between 44-56) and they are still significantly higher than the background (mean intensity less than 10). Second, under the full induction (1000ng/ml of doxycycline), the mean intensity of new constructs is almost two times higher than the parental construct (pGYT-EGFP). Third, under conditions of medium induction (10-100ng/ml of doxycycline), the new constructs have more induction than the parental constructs.

Since this experiment was conducted with a single well for each concentration of doxycycline, we repeated the experiment with triplicate samples in different concentrations of doxycycline. We chose constructs, pGV-15-EGFP and pGS-EGFP for further studies and we also included pGYT-EGFP as control. We used 2μl of viral stocks for each samples, and the doxycycline concentrations were ranged from 1 ng/ml to 4000 ng/ml with 7 different intervals between 1-4000 ng/ml. Sixty hours after transduction, the cells were harvested and analyzed with flow cytometery. The results are shown in **Figure 7**.

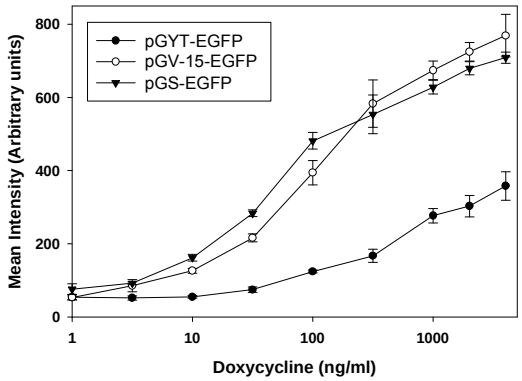

Figure 7: The figure shows the induction of three Tet-on vectors under different concentrations of doxycycline. The GFP activities (mean intensity) are shown as arbitrary unites set by the flow cytometer.

As shown, the two new constructs are significantly better than the parental construct, pGYT-EGFP. The GFP expression (mean intensity of the GFP positive cells) is more than two fold than the original construct under the full induction. In general, the MLV-LRT promoter is a very strong promoter and can express the GFP gene to mean intensity 350-400. However, we found the new constructs can achieve more than two fold in GFP expression. More importantly, these constructs only require 100ng/ml of doxycycline to achieve the expression level of MLV-LTR promoter. This is very important since it is very difficult to achieve high doxycycline concentration *in vivo*. To compare the expression pattern between pGV-15-EGFP and pGS-EGFP, we found the difference is insignificant and requires further analysis. Therefore we repeated the experiment with these two constructs. We used the same conditions as described except that we harvested the cells 36 hours after transduction. The results are shown in Figure 8.

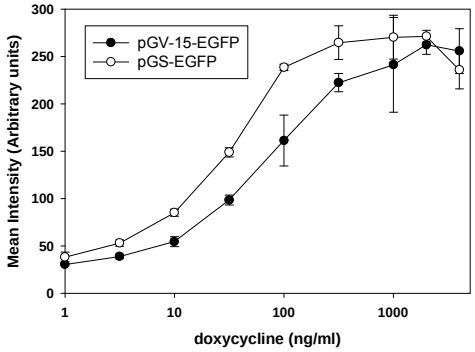

Figure 8: The figure shows the induction of two Tet-on vectors under different concentrations of doxycycline. The GFP activities (mean intensity) are shown as arbitrary units set by the flow cytometer.

Both constructs have a similar level of expression under the full induction (doxycycline level more than 1000ng/ml). However, construct, pGS-EGFP is more sensitive to the doxycycline than the construct pGV-15-EGFP. This is particularly obvious when the doxycycline concentrations are between 3 to 100 ng/ml. This advantage is very significant for our animal experiments since high concentration of doxycycline is very difficult to achieve *in vivo*. Therefore, we believe our new rtTA transcription factor is superior for *in vivo* experiments as compared to the rtTA transcription factors (V15 and V16) reported in the latest publication [4]. We referred the new tetracycline inducible promoter as the Tet-GS promoter. In HT1080 cells, pGS-EGFP is most sensitive to the doxycycline induction and can be induced to the highest level. Since this vector is designed to express FGF protein in Sca1+ cells in mouse, we would

like to test the induction of pGS-EGFP in Sca1+ cells. In collaboration with Dr. Hall in the MDC, we tested the expression of EGFP gene from pGS-EGFP vector in $Sca1^+$ cells under different concentrations of doxycycline. We first transduced $Sca1^+$ cells with pGS-EGFP or a regular vector (pY-EGFP) with MOI around 3.5. Twelve hours after transduction the cells were divided into different wells and were exposed to a range of doxycycline (0-1000ng/ml). After an additional seventy-two hours of incubation, the cells were analyzed by flow cytometery. The results are summarized in Table 9.

Table 9

pY-EGFP (GFP is expressed by MLV-LTR promoter)		
Dox. (ng/ml)	% of GFP(+) cells	Mean Intensity of GFP
0.00	19.73 ± 1.10	790.66 ± 20.09
1000.00	18.26 ± 0.88	889.54 ± 32.12
pGS-EGFP (GFP is expressed by Tet-GS promoter)		
0.00	17.64 ± 0.47	107.10 ± 1.52
0.32	17.78 ± 0.16	233.30 ± 14.93
1.00	18.89 ± 0.06	738.73 ± 6.97
3.16	19.80 ± 0.21	1727.59 ± 127.97
10.00	21.26 ± 0.74	2833.76 ± 163.96
31.62	22.98 ± 0.54	3524.96 ± 31.60
100.00	22.93 ± 0.76	3876.51 ± 7.06
316.23	22.72 ± 0.52	4210.40 ± 125.6
1000.00	21.45 ± 0.98	4237.72 ± 133.92

Table 9: The table shows the results of pGS-EGFP induction under different concentrations of doxycycline. We also included our regular MLV-based vector, pY-EGFP, as control to compare the GFP expression.

Therefore, the new Tet-GS promoter worked very well in Sca1+ cells. We can observe 40 fold increase of expression under full induction (compare mean intensity of 107.10 *vs.* 4237.72). More importantly, it requires less than 10 ng/ml of doxycycline to achieve half of the full induction. Even under this level (10 ng/ml), the GFP expression is two times stronger than the GFP expressed by MLV-LTR promoter. Previously, we have tested the original Tet-GYT promoter in Sca1+ cells. Using these data and data from previous experiments, we were able to compare these two tet-inducible promoters. In **Figure 9**, we show the difference in the doxycycline induction in these two tet-inducible promoters.

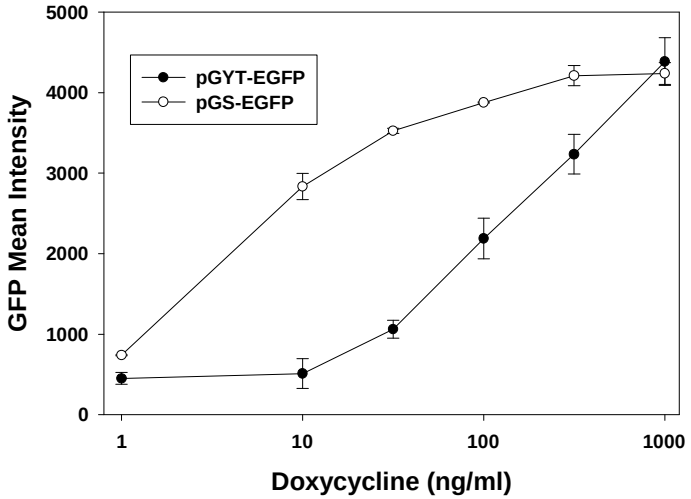

Figure 9: The Sca1+ cells were transduction with MLV-based vectors either with Tet-GYT promoter (pGYT-EGFP) or with Tet-GS promoter (pGS-EGFP). Cells were cultured in different concentrations of doxycycline (1-1000ng/ml). Seventy-two hours after incubation, we assayed the GFP expression through flow cytometery. The GFP intensity of cells transduction under un-inducible condition (no doxycycline) are 422.11$\pm$ 44.55 for pGYT-EGFP transduced cells and 107.10 $\pm$ 1.52 for pGS-EGFP transduced cells.

The expression of GFP in the Tet-GS promoter is much better than the Tet-GYT promoter in Sca1+ cells. The Tet-GS promoter offers the following advantages when compared with the Tet-GYT promoter. First, under the un-induced condition, the Tet-GS promoter is not as leaky as the Tet-GYT promoter (comparing the mean intensity of 107.10 *vs*. 422.11). Second, to achieve half of the full induction, the Tet-GYT requires 100 ng/ml of doxycycline. However, Tet-GS requires less than 10 ng/ml of doxycycline to achieve half of the full induction. Therefore, we may conclude the Tet-GS promoter is 10 times more sensitive to the doxycycline induction than the Tet-GYT promoter. This is critical since it is very difficult to achieve high concentration of doxycycline *in vivo*. Third, under full induction, the Tet-GS and Tet-GYT have similar GFP mean intensity. This is a surprise for us; in HT1080 cells the Tet-GS promoter is 80-100% stronger than the Tet-GYT promoter. Since the two experiments were carried out at two different times, we may have to repeat this experiment to further investigate this discrepancy. More importantly, we will test the function of Tet-GS promoter in Sca1+ cells in vivo.

D. Develop inducible HIV based vectors for expression of therapeutic genes for bone formation and bone repair

Previously, we constructed tetracycline inducible MLV-based and HIV-based vectors. We found tetracycline inducible MLV-based vectors can conditionally express the gene-of-interest. Under inducible conditions, the expression level is higher than then regular MLV LTR promoter and the expression level is more than 10-fold higher than in the un-inducible condition in the most of cell lines tested. However, under the similar scheme, the gene expression level in HIV-based vectors is much lower and we only can achieve 2-3 fold induction. Therefore we designed a new HIV-based inducible vector for conditional expression gene-of-interest, through a different configuration. In our original Tet-on HIV-based vector, pHIV-GYT-EGFP, transcriptional factor, GYT and the inducible expression cassette are in the same vector. The functional arrangement of this vector is shown in Figure 10. In this vector, CMV promoter drives the transcriptional factor, GYT and it is near to the tetO promoter. This arrangement can

have two potential problems. First, the strong enhancer activity of CMV promoter may interfere with TetO promoter and subsequently increase the background expression of the gene-of-interest under suppression conditions. Second, the strong transcription of CMV promoter may interfere with TetO promoter under inducible condition, since these two transcripts are in the same orientation. The arrangement of the vector doesn't have a transcription stop signal between these two transcripts. Therefore, the strong transcription of CMV may suppress the expression of TetO promoter under inducible condition. To test this hypothesis, we separated these two transcripts into two separate vectors. As shown in **Figure 10**, we constructed pHIV-TetO-EGFP containing the tet-on transcriptional unit with the marker gene, EGFP. Additionally, we constructed two viral vectors, pHIV-GYT and pMLV-GYT to express the tet-on transcriptional factor, rtTA-GYT either from a HIV-based vector or a MLV-based vector. After construction of these viral vectors in plasmids, we prepared the VSV-G pseudotyped HIV-based and MLV-based vectors with our standard transient transfection method in 293T cells. The diagrams of these HIV-based and MLV-based vectors are shown in Figure 10.

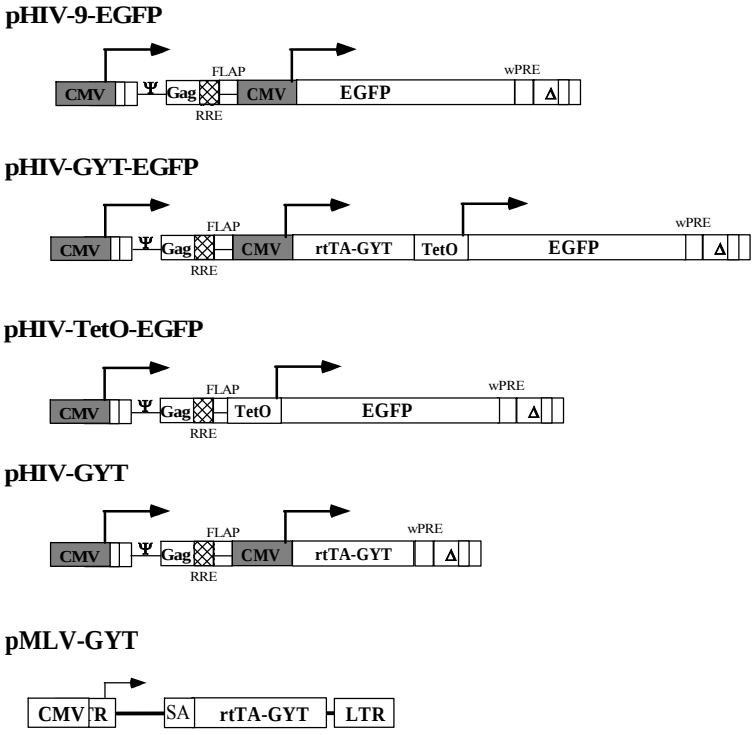

Figure 10: The diagram shows the HIV-based and MLV-based vectors used in this quarter. The pHIV-9-EGFP is the standard HIV-based vector and the EGFP gene is driven by CMV promoter. The pHIV-GYT-EGFP is the original inducible HIV-based vectors, and the EGFP gene is driven by the TetO promoter. The pHIV-TetO-EGFP is derived from pHIV-GYT-EGFP by deleting the CMV promoter and part of rtTA-GYT gene. The pHIV-GYT is the HIV-based vector with rtTA-GYT gene and the pMLV-GYT is the MLV-based vectors with rtTA-GYT. In pHIV-GYT the expression of rtTA-GYT is from CMV promoter and in pMLV-GYT, the expression of rtTA-GYT is from MLV LTR promoter.

Using HT1080 cells, we checked the induction of doxycycline with different combinations of these vectors. We first mixed the designated viral vectors and transduced HT1080 cells either in the induction medium (+Dox, 1 μg/ml) or suppression medium (regular medium without doxycycline). Then the viral mixture was added to HT1080 cells in 6-well plates. Forty-eight

hours after transduction, the cells were detached and the fluorescent activities were determined by FACS techniques. The results are summarized in Table 10.

Viral Vectors	Types of Media	% of GFP positive cells	Mean Intensity	Fold Induction*
pHIV-9-EGFP 10 μl	Regular	39.46	1694	
	+Doxy	ND**	ND	ND
pHIV-GYT-EGFP 10 μl	Regular	3.08	614	
	+Doxy	5.06	905	2.42
pHIV-tetO-EGFP 10 μl & pHIV-GYT 100 μl	Regular	1.30	188	
	+Doxy	1.54	1926	12.10
pHIV-tetO-EGFP 10 μl & pMLV-GYT 100 μl	Regular	1.94	96	
	+Doxy	30.8	2353	38.73

Table 10: *Fold induction is calculated by comparing the value of mean intensity multiple by the percentage of the positive cells. We selected the value from regular medium as 1. **ND: Not determined

From these results we found the doxycycline induction is significantly improved in the two vectors system and induction was increased from 2.42 fold to 12.10 fold (GYT-rtTA expressed by HIV-based vector) and 38.73 fold (GYT-rtTA express by MLV-based vector). To confirm these results, we repeated the experiment with higher amount of the EGFP vectors. The results are summarized in Table 11.

Table 11

Viral Vectors	Types of Media	% of GFP positive cells	Mean Intensity	Fold Induction*
pHIV-GYT-EGFP 100 μl	Regular	40.52	277	
	+Doxy	56.74	870	4.40
pHIV-tetO-EGFP 100 μl	Regular	13.38	63	
	+Doxy	15.35	65	1.19
pHIV-tetO-EGFP 100 μl & pHIV-GYT 100 μl	Regular	12.76	75	
	+Doxy	22.26	2159	49.59
pHIV-tetO-EGFP 100 μl & pMLV-GYT 100 μl	Regular	14.67	70	
	+Doxy	33.96	2708	88.37

Table 11: *Fold induction is calculated by comparing the value of mean intensity multiple by the percentage of the positive cells.

The conclusion from these two experiments is, indeed, the two vector systems significantly improved the induction system. The system has several advantages. First, the background expression is low (compares mean intensity 63 vs. 277). Second, the expression level is higher under the induction (comparing mean intensity 2159 or 2708 vs. 870). Therefore the fold induction is increased from 4.40 to 49.59 or 88.37 in this experiment. One thing worth noticing; the expression level of EGFP in the new vector under inducible conditions is stronger than the expression level of CMV driven EGFP in pHIV-9-EGFP (1926 or 2353 vs. 1694). This is very unusual since the CMV promoter in HT1080 cells is very strong. Therefore, our new doxycycline inducible HIV-based vector not only can regulate by ligand, doxycycline, but also can express the gene-of-interest very efficiently under inducible conditions. Our next goal will be studying the inducibility of these vectors in our animal models.

e) Develop methods for production of high titer retroviral vectors for bone formation and bone repair.

Concentration of retroviral vectors is one of major challenges for retroviral vector production. Previously, we used ultracentrifugation to pellet the VSV-G pseudotyped viral particles and then resuspended in a smaller volume of the buffer. This approach is very simple and easy to scale up. However, it also comes with problems. First, the viral particles may be damaged during the high speed centrifugation, subsequently lowering the yield of the recovery. Second, there are many unwanted materials that may also be concentrated during the procedures. The desired method for viral particle concentration must preserve its native biological activity upon reconstitution of the precipitate. Since a retroviral vector is an envelope virus, the precipitation must not denature the protein nor disrupt the lipid bilayer. In addition, the procedure must not add any material that would not be compatible with future applications of viral vectors *in vitro* or *in vivo*. Therefore we tested a new method to concentrate viral vectors.

One of the other methods for virus purification is polyethylene glycol (PEG) precipitation. PEG is a hydrophilic nonionic polymer which has been used for phase–separation of large molecules out of aqueous solutions. The PEG would not denature proteins at ambient temperature and requires a relatively low amount (5-10%) for precipitation. Additionally, a small amount of residual PEG is concentrated in the pellet since most of the PEG is retained in the supernatant. Based on this, we tested the method of concentrating viral vectors with PEG. First, we prepared 72 ml of viral vectors with marker gene, EGFP. Then, we mixed 36ml of viral vectors with 12ml of PEG solution (40% PEG8000 in PBS) to bring the final concentration of PEG to 10%. After overnight incubation at 4^{o}C, the mixtures were centrifuged at 3000rpm for 30 minutes. A well defined pellet can be seen after the centrifugation. The pellet was resuspended in 1.2ml of 4% lactose in PBS. For the rest of 36ml of viral stock, we precipitated with standard ultra-centrifugation method and also resuspended the pellet in 1 ml of 4%lactose in PBS. The viral titers of viral stocks and concentration viral stocks were determined by end-point dilution in HT1080 cells through flow cytometery. The results are summarized in Table 12.

Table 12

Experiment One	Viral titer before concentration	Viral titer after concentration	% of yield
PEG method	3.57 X10^{7}	1.09X10^{9}	84.8%
Ultra-Ce. Method	3.57 X10^{7}	7.31X10^{8}	56.9%
Experiment Two			
PEG method	7.22 X10^{6}	6.37 X10^{8}	43.0%
Ultra-Ce. Method	7.22 X10^{6}	7.02 X10^{8}	47.4%

Table 12: We compare two methods of concentration in two independent experiments.

Based on these results, we found the PEG method can concentrate the VSV-G pseudotyped MLV-based vectors as efficiently as the ultra-centrifugation method.

KEY RESEARCH ACCOMPLISHMENTS

- Prepared MLV and HIV-based vectors for other sub-projects (sub-projects 4, 6. 7 and 8)
- Designed tissue specific HIV-based vectors for sub-project 4.
- Developed magnetic retroviral vectors for bone diseases gene therapy
- Developed siRNA retroviral vectors to study the function of genes in bone repair
- Developed a new method to concentrate VSV-G pseudotyped retroviral vectors.
- Developed and characterized TET-ON inducible MLV-based and HIV-based retroviral vectors for bone diseases gene therapy and gene transfer.

CONCLUSIONS

In collaboration with investigators of other sub-projects of this Army grant, we have generated and provided with the investigators several different batches of MLV and HIV-based vectors for use in their approved projects.

We developed tissue specific HIV-based vector for delivering of growth factors to the bone repairing sites.

We developed siRNA retroviral vectors, which can specifically inhibit any target genes. This vector should be very useful for investigations into gene function during bone repair.

We developed a magnetic retroviral vector system that provides efficient site-specific targeted delivery of viral vectors to specific bone sites. This magnetic retroviral vector system should be useful in site-specific targeting and delivery of viral vectors for skeletal gene therapy.

We developed a new method for concentrating VSV-G pseudotyped MLV-based and HIV-based vectors.

We developed and characterized new inducible Tet-On regulatory retroviral vector systems. The gene expression of this vector can be modulated by doxycycline either in MLV-based or HIV-based vectors. The new Tet-On system is more sensitive to the doxycycline induction and can express the genes-of-interest to higher level. We can use the vector to study function of genes-of-interest during bone repair.

REFERENCES

1. Gossen M, Freundlieb S, Bender G, Muller G, Hillen W, Bujard H. Transcriptional activation by tetracyclines in mammalian cells. *Science* 1995; **268**: 1766–1769.
2. Urlinger S, Baron U, Thellmann M, Hasan MT, Bujard H, Hillen W. Exploring the sequence space for tetracycline-dependent transcriptional activators: novel mutations yield expanded range and sensitivity. *Proc Natl Acad Sci USA* 2000; **97**: 7963–7968.
3. Das AT, Zhou X, Vink M, Klaver B, Verhoef K, Marzio G *et al*. Viral evolution as a tool to improve the tetracycline-regulated gene expression system. *J Biol Chem* 2004; **279**: 18776–18782.
4. Zhou, X., M. Vink, B. Klaver, B. Berkhout and AT. Das Optimization of the Tet-On system for regulated gene expression through viral evolution *Gene Ther.* 2006 Oct;13(19):1382-90.

APPENDICES:

Molecular Genetic and Gene Therapy Studies of the Musculoskeletal System
DAMD17-03-2-0021

REPORTABLE OUTCOMES:

Subproject 1

Abstracts

Chadwick R.B., Bu L.M., Yu H., Sachdev R., Tan Q.W., Wergedal J.E., Mohan S., and Baylink D.J. Digit Tip Regeneration and Global Gene Expression Profiling in the MRL Super-Healer Mouse. 26th Annual Meeting American Society of Bone and Mineral Research, Seattle, Washington, October 1-5, 2004.

Chadwick R.B., Bu L.M., Yu H., Hu Y., Sachdev R., Tan Q.W., Wergedal J.E., Mohan S., and Baylink D.J. Digit Tip Regeneration and Differential Expression Profiling in the MRL Super-Healer Mouse. Wound Healing and Regeneration, Chicago, Illinois, May 2005.

Publications

Chadwick RB, Bu LM, Yu H, Hu Y, Sachdev R, Wergedal JE, Mohan S, Baylink DJ. Digit Tip Regrowth and Differential Gene Expression Profiling in the MRL Super-Healer Mouse. Wound Repair and Regeneration, Volume 15(2), pages 275-84, 2007.

Bu L, Hu Y, Wergedal J, Mohan S and Chadwick RB. Lack of EphA4 Causes Reduction in Body Size, Total Body Bone Mineral Density and Serum IGF-1 Levels in Mice. Journal of Bone and Mineral Metabolism, submitted, 2009.

Chadwick RB, Bu L, Hu Y, Wergedal J, and Mohan S. Formin-2 Knockout Affects Osteoblasts and Bone Formation in Mice. AJP Endocrinology and Metabolism, submitted (2009).

Subproject 2

Abstracts

Srivastava AK, Mohan S, Baylink DJ. A Sensitized ENU Screening System to Discover Modifier Genes by Utilizing Mouse Models Deficient in Genes Regulating Skeletal Tissues. 28th Annual Meeting of American Society for Bone and Mineral Research, 2006.

Srivastava AK, Mohan S, Baylink DJ. Identification of Mutant with a Large Decrease in Bone Size Identified in a Sensitized ENU Screen using Growth Hormone Deficient 'Little' Mouse. 28th Annual Meeting of American Society for Bone and Mineral Research, 2006.

Publications

Mohan, S, Baylink, DJ, Srivastava, AK. A chemical mutagenesis screen to identify modifier genes that interact with growth hormone and TGF-beta signaling pathways. Bone 42:388-95; 2008.

Subproject 3

Abstract

Xing W, Baylink D, Kesavan C and Mohan S. Transfer of 128-kb BMP-2 Genomic Locus by HSV-Based Infectious BAC Stimulates Osteoblast Differentiation

Publications

Xing W, Baylink D, Kesavan C and Mohan S. HSV-1 Amplicon-Mediated Transfer of 128-kb BMP-2 Genomic Locus Stimulates Osteoblast Differentiation *in vitro* Biochem Biophys Res Commun 319(3): 781-6, 2004

Xing W, Baylink D, Kappor A and Mohan S. A platform of high-efficiency non-viral gene transfer in mouse osteoblast cells in vitro. Molecular Biotechnology 34(1):29-35, 2006

Subproject 4

Abstracts

Wang, X., C.H. Rundle, A. Srivastava, J. Tesfai, E.I. Davis, J.E. Wergedal, K.H-W. Lau, S. Mohan and D.J. Baylink (2005). Loss of sex-specific difference in bone size in leptin knockout mice. Poster presentation at the 27th Annual Meeting of the American Society for Bone and Mineral Research, Nashville, TN.

Rundle, C.H., X. Wang, J.E. Wergedal, A. Srivastava, E.I. Davis, K.H-W. Lau, S. Mohan and D.J. Baylink (2006). Loss of sex-specific difference in bone size in leptin-deficient (ob/ob) mice. Oral presentation at the 52nd Annual Meeting of the Orthopaedic Research Society, Chicago, IL.

Xing, W., J. Kim, S-T.Chen and S. Mohan (2007) Ephrin B1 Reverse Signaling Regulates Osteoblast Differentiation by a Novel Mechanism That Involves Release of Membrane Bound TAZ from EphrinB1/NHERF1/TAZ Complex for Subsequent Nuclear Localization and Induction of Osterix Gene Transcription. Oral presentation at the 29th Annual Meeting of the American Society for Bone and Mineral Research, Honolulu, HI.

Rundle, C.H., X. Wang, R.M. Porte, J.E. Wergedal, S. Mohan and K-H.W. Lau (2007) Plasminogen activator inhibitor (PAI-1) deficiency enhances fracture callus size but reduces cartilage remodeling during fracture repair. Poster presentation at the 29th Annual Meeting of the American Society for Bone and Mineral Research, Honolulu, HI.

Rundle, C.H., X. Wang, J.E. Wergedal, M.H-C. Sheng, R.M. Porte, K-H.W. Lau and S. Mohan (2007) Bax-deficient mice exhibit marked increase in callus size and cartilage during

endochondral repair of femur fractures. Oral presentation at the 29th Annual Meeting of the American Society for Bone and Mineral Research, Honolulu, HI.

Xing, W., J. Kim, J.E. Wergedal and S. Mohan (2008) Ephrin B1 Reverse Signaling Regulates Bone Formation via Influencing Osteoblast Activity in Mice. Oral presentation at the 30th Annual Meeting of the American Society for Bone and Mineral Research, Montreal, QB, Canada

Xing, W., J. Kim, S-T. Chen and S. Mohan (2009) Ephrin B1 Reverse Signaling Regulates Osteoblast Differentiation by a Novel Mechanism That Involves Release of Membrane Bound TAZ from EphrinB1/NHERF1/TAZ Complex for Subsequent Nuclear Localization and Induction of Osterix Gene Transcription Oral presentation at the 31st Annual Meeting of the American Society for Bone and Mineral Research, Denver, CO.

Publications

Wang, X., C.H. Rundle, J.E. Wergedal, A.K. Srivastava, S. Mohan and K.-H.W. Lau Loss of sex-specific difference in femoral bone parameters in male leptin knockout mice. Calcif. Tissue Int. 80: 374-382, 2007.

Rundle, C.H., X. Wang, J.E. Wergedal, S. Mohan and K-H.W. Lau Fracture healing in mice deficient in plasminogen activator inhibitor-1. Calcif. Tissue Int. 83: 276-284, 2008.

Rundle, C.H., X. Wang, M.H-C. Sheng, J.E. Wergedal, K-H.W. Lau and S. Mohan Bax deficiency in mice increases cartilage production during facture repair through a mechanism involving increased chondrocyte proliferation without changes in apoptosis. Bone 43: 880-888, 2008.

Xing, W., J. Kim, J.E. Wergedal, S-T. Chen and S. Mohan (2009) Ephrin B1 Regulates Bone Stromal Cell Differentiation and Bone Formation by Influencing TAZ Transactivation via Complex Formation whith NHERF1 Mol Cell Biol (in revision).

Subproject 6

Abstracts

Hall SL, Lau HK, Chen ST, Sheng MH, Gysin R, Wergedal JE, Srivastava AK, Mohan S, Baylink DJ. Sca-1^+ Cell-Based Gene Therapy with Fibroblast Growth Factor-2 Gene (but not BMP-4) Dramatically Increased Endosteal Bone Formation in Mice, Oral Presentation at the annual meeting of the American Society for Bone and Mineral Research, September 17, 2006, Philadelphia

Hall SL, Chen ST, Mohan S, Wergedal JE, Strong DD, Lau KHW. Stem Cell Antigen Positive (Sca-1^+) Hematopoietic Cell-based Human Growth Hormone (hGH) Gene Therapy Enhanced

Endosteal Bone Resorption in Mice. Submitted for presentation to the annual meeting of the American Society for Bone and Mineral Research, September 12, 2008, Montreal, Canada.

Publications:

Hall SL, Lau H-K W, Chen ST, Felt, JC, Gridley DS, Yee KJ, and Baylink DJ. An Improved Mouse Sca-1^{+} Cell-Based Bone Marrow Transplantation Model For Use In Gene- And Cell-Based Therapeutic Studies. Acta Haematol;117:24-33, 2006.

Hall SL, Lau H-K W, Chen ST, Wergedal JE, Srivastava A, Klamut H, Sheng MH, Gridley DS, Mohan S, Baylink DJ. Sca-1+ Hematopoietic Cell-Based Gene Therapy with a Modified FGF-2 Increased Endosteal/Trabecular Bone Formation in Mice. Molecular Therapy Oct;15(10):1881-9, 2007.

Hall S, Chen ST, Gysin R, Gridley D, Mohan S**,** Lau K-HW. Stem Cell Antigen-1+ Cell-Based Bone Morphogenetic Protein-4 Gene Transfer Strategy in Mice Failed to Promote Endosteal Bone Formation. J Gene Med 2009; 11:877-888.

Subproject 7

Lau K-HW, Gysin R, Chen S-T, Wergedal JE, Baylink DJ, and Mohan S. Marrow stromal cell-based cyclooxygenase 2 *ex vivo* gene transfer strategy surprisingly lacks bone regeneration effects and suppresses the bone regeneration action of bone morphogenetic protein 4 in a mouse critical-sized calvarial defect model. ***Calcif Tissue Int*** in press. [DOI: 10.1007/s00223-009-9282-2]. 2009.

List of Personnel:

Mohan, Subburaman	Principal Investigator
Alva, E	Admin
Baez, I	Res. Tech
Baggett, L	Admin
Belcher,	Admin
Blanco, T	Admin
Chadwick, R	Investigator
Chen, ST	Investigator
Felt, J	Res. Tech
Gysin, R.	Investigator
Hall, S	Investigator
Hargrave, C	Res. Tech
Hu, Y	Res. Tech
Kadmiel, M.	Res Tech
Kapoor, A	Res. Tech
Klamut, H.	Investigator

Lau, W	Investigator
Levtzow, S	Admin
Lowen, N	Res. Tech
MacMurray, A	Administrative Officer
Porte, R	Res. Tech
Rundle, C	Investigator
Sheng, M	Res. Scientist
Smallwood, J	Res. Tech
Srivastava, A	Investigator
Stivers, C	Res. Tech
Sumagaysay, J	Res. Tech
Tan, Q	Res. Tech
Strong, Donna D	Investigator
Wang, X	Post Doc
Wergedal, Jon	Investigator
Weston, W	Res. Tech
Xing, W	Investigator
Zhu, Y	Res. Tech
Yu, H	Research Scientist

ORIGINAL RESEARCH ARTICLE – REGENERATION SCIENCE

Digit tip regrowth and differential gene expression in MRL/Mpj, DBA/2, and C57BL/6 mice

Robert B. Chadwick, PhD; Liming Bu, PhD; Hongrun Yu, PhD; Yan Hu, BS; Jon E. Wergedal, PhD; Subburaman Mohan, PhD; David J. Baylink, MD

Musculoskeletal Disease Center, JL Pettis VA Medical Center, Molecular Genetics Division, Loma Linda, California

Reprint requests:
Robert B. Chadwick, Musculoskeletal Disease Center, JL Pettis VA Medical Center, Molecular Genetics Division, 11201 Benton Street (151), Loma Linda, CA 92357.
Tel: +909 825 7084 ext. 1582;
Fax: +909 796 1680;
Email: robert.chadwick@med.va.gov

Manuscript received: February 10, 2006
Accepted in final form: December 13, 2006

DOI:10.1111/j.1524-475X.2007.00216.x

ABSTRACT

MRL/Mpj mice are the only known strain of mouse that can regenerate cardiac lesions and completely heal ear punches without scarring. This study was undertaken to determine if MRL mice also have greater regrowth capabilities in amputated digit tips. Right paw digit tips of neonatal MRL mice were dissected, with the left front paws as uncut controls. Controls used for regrowth comparison were the DBA/2 and C57BL/6 inbred mouse strains. Consecutive x-ray images were captured of front paws at 0, 7, 14, 21, and 28 days postamputation. MRL mouse digit tips were found to distally regrow more quickly and reform nails partially and completely to a greater degree in comparison with DBA and B6 mice ($p < 0.05$). We next undertook microarray expression analysis to identify the genes involved in digit tip regrowth. Four hundred genes out of 15,000 were significantly differentially expressed ($p < 0.05$) in MRL, DBA, and B6 mice at day 4 in comparison with day 0 control tissue. Multiple differences between MRL, DBA, and B6 strains were found in genes that are implicated in the WNT signaling pathway and transcription. We conclude that MRL mice regrow digits distally more rapidly and partially and completely regrow nails to a greater degree than B6 and DBA strains. This enhanced regrowth is likely due to strain-specific increased expression of genes involved in growth and development.

Experiments with amphibian limbs, first undertaken in the 18th century, demonstrate that limb regeneration in vertebrates is possible.[1,2] In amphibians, the first stages of regeneration are initial wound healing by formation of an epidermal layer over the wound, followed by dedifferentiation of cells that cluster under this epidermal layer.[3] These dedifferentiated cells (blastema cells), similar to stem cells, redifferentiate into other cell types including bone, cartilage, and epithelial cells. The genes and genetic pathways that determine how the cells dedifferentiate and redifferentiate into other cell types are not completely understood.

Higher mammals also have marginal abilities to regenerate.[4–8] For example, children and newborn mice will replace digit tips when they are amputated distal to the last interphalangeal joint.[4,5] Another example of regeneration in mammals is the healing of ear holes in rabbits without scarring.[9,10] Recently, we and others have demonstrated that the MRL inbred strain of mouse shows greater regeneration and healing of earhole punches as opposed to several other inbred strains of mice.[11,12] Among inbred mouse strains, the MRL mouse was found to completely heal earhole punches, the DBA strain was found to be an intermediate regenerator, and the B6 strain found to be a poor regenerator of earhole punches.[11] Other studies have found that the MRL mouse is also capable of cardiac muscle regeneration.[13] Thus, the MRL mouse is a unique model to study the genetic mechanisms that regulate wound healing and tissue regeneration. However, to date, the MRL mouse has not been investigated extensively for its abilities to regrow more complex biological structures, such as digit tips. This study examined digit tip regrowth in the MRL, DBA, and B6 inbred strains of mice in order to determine if these mouse strains have similar regenerative capabilities of digit tips as in earhole punches. We also undertook global RNA expression profiling in those strains to identify the genes and genetic pathways responsible for wound healing and digit tip regrowth.

MATERIALS AND METHODS

Mouse surgery

Four-week-old MRL, B6, and DBA mice were obtained from The Jackson Laboratories. The studies were performed with the approval of the animal ethics committee of the Jerry L Pettis Memorial VA Medical Center (Loma Linda, CA). Surgery was conducted on the pup's digit tips within 1 day of birth. The neonatal mice were anesthetized with 5% halothane mixed with O_2 5 L/min. The right front third and fourth digit tips were amputated, with the left side as uncut controls. As the level of amputation is very important to subsequent regrowth capabilities, all surgery was performed under a microscope, and a scalpel was used to dissect the digit tips as accurately as possible at the midpoint of the third phalanges.[6,7] The accuracy of digit tip surgery and amounts of tissue dissected were documented and measured by capturing images of the digits both before and after surgery.

The amputated tissues were collected into RNAlater (Ambion, Austin, TX), and the tissues from the pups of 1 litter were pooled. Both left (uncut) and right (cut) paw x-ray images were taken at 0, 7, 14, 21, and 28 days postsurgery with a Faxitron MX-20 x-ray (Faxitron, Wheeling, IL). Also, at 4 days postsurgery, mice were sacrificed, regenerating digit tips were collected by surgery, and the tissue was pooled in RNAlater and stored at –80 °C for later RNA extraction.

Growth rate measurements

Faxitron x-ray images were measured using the ruler feature of Adobe Photoshop. Three growth parameters were determined: (1) the amount of dissected tissue (A–B in Figure 1); (2) the length of first phalanx of third and fourth fingers of front two paws (C–D in Figure 1); and (3) the length from the bottom of second phalanx to the regenerating tissue edge (C–A in Figure 1). Measurements were made of both left uncut and right cut digits. All measurements were done in duplicate by two different individuals who were blinded to mouse strain. Estimates of errors in measurement were made by capturing 10 consecutive images of the same mouse's digit tips. These error estimates were determined by repositioning a mouse between each image capture to estimate the error in successive weekly image captures. Also, 10 consecutive images were captured with a mouse not repositioned between each image capture to estimate errors in measurements at a particular time point. In order to minimize disruption of mice and mother abandonment of newborn pups, the growth was determined only for 7, 14, 21, and 28 days postsurgery.

Microarray expression analysis

Total RNA was isolated from dissected tissues at days 0 and 4 using the Agilent Total RNA Isolation Kit (Agilent Technologies, Palo Alto, CA). For day 0 RNA isolations, digit tip tissue from 30 MRL, 26 DBA, and 30 B6 mice were, respectively, pooled before processing. For day 4 RNA isolations, digit tip tissue from 15 mice of each respective strain were, respectively, pooled. Tissues were lysed using a Polytron Generator (Kinemalica AG, Lucerne, Switzerland), and then processed following the manufacturer's protocol (Agilent Technologies). The total RNA concentration was determined by NanoDrop spectrophotometer and RNA quality was determined by 18S/28S ribosomal peak intensity on an Agilent Bioanalyzer. For microarray expression profiling and real-time PCR, RNA samples were used only if they showed little to no degradation. Custom cDNA slides were spotted in duplicate with ~15,000 cDNA clones obtained from the National Institute on Aging (NIA).[14] A Q-Array2 robot (Genetix, Boston, MA) was used for spotting. The arrays were also spotted with Amersham Lucidea Universal Scorecard controls to insure correct gene expression values were obtained from each array. Controls were spotted in duplicate in the first and last PCR plates to insure proper data tracking. Replicate microarrays were run for each RNA sample (10 microarrays each for MRL and DBA, and three microarrays for B6). This number of replicate microarrays is calculated to give 95% power to detect a twofold change in expression between the days 4 and 0 RNA samples and also between MRL and DBA pooled RNA samples at the 0.001 significance level.[15] A total of 250 ng RNA was used to synthesize double-stranded cDNA using the Low RNA Input Fluorescent Linear Application Kit (Agilent Technologies). First-strand cDNA synthesis was primed with T7-(dT24) promoter primer. From the purified cDNA, cRNA was synthesized using transcription master mix and purified. Two hundred and fifty nanograms of purified cRNA was used to reverse transcribe to fluorescent cDNA. Cyanine-3-dCTP and cyanine-5-dCTP were used to label experimental samples (day 4) and control samples (day 0). Dye swaps were also conducted to eliminate potential dye bias effects. Samples were hybridized at 60 °C for 17 hours. The slides were then washed with Solution I (6× SSC, 0.005% Triton X-102) for 10 minutes in the dark and then with Solution II (0.1× SSC, 0.005% Triton X-102) for 5 minutes in the dark. The slides were dried with pressurized nitrogen and immediately scanned using a GSI Lumonics ScanArray 4000 scanner. The signal intensity of all microarray images was determined using ImaGene 5.6 software. Expression analysis of microarray experiments was performed with GeneSpring 7.1 (Silicon Genetics, Palo Alto, CA) using the raw intensity data generated by the ImaGene software. Local background-subtracted median signal intensities were used as intensity measures, and the data were normalized using per spot and per chip LOWESS normalization. The transcripts that passed with flag values present or marginal were targeted for further analyses. The transcripts were then further analyzed by utilizing a one-sample Student's *t*-test to test whether the mean normalized expression level for the gene is statistically different from 1.0. To characterize and classify the function of genes differentially expressed in regenerating digit tip tissue, we used Onto-Express (Wayne State Univ., Detroit, MI; http://vortex.cs.wayne.edu/projects.htm#Onto-Express) to classify genes according to their biological process Gene-Ontology (GO) category.

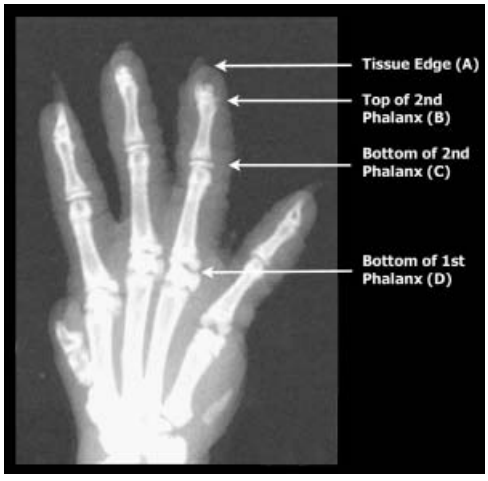

Figure 1. Measurements of digit growth in mice. X-rays were taken at days 0, 7, 14, 21, and 28 postdigit tip dissection. Surgery was performed under a microscope at the middle of the third phalanx (midpoint of A–B). Phalanx and digit tip measurements were determined by the length of first phalanx of third and fourth fingers of both front paws (C–D, measurements used in Figure 2); the length from the bottom of second phalanx to the tissue edge (C–A, measurements used in Figure 3).

The number of genes corresponding to GO category among the differentially expressed genes was tallied and compared with the number of genes expected for each GO category based on their representation in the NIA 15K set. Significant differences from the expected were calculated with a two-sided binomial distribution.[16–18]

Confirmation of microarray results by quantitative real time PCR

Reverse transcription of 200 ng of total RNA (days 4 and 0) was carried out in a final volume of 20 μL using a Superscript reverse transcriptase kit according to the manufacturer's instructions (Invitrogen, Carlsbad, CA). To prevent 3′ bias of the real-time PCR reactions random decamers (Ambion) were used for priming rather than oligo-dT. Real-time PCR was done using the SYBR Green PCR Core Reagents Kit (Applied Biosystems, Foster City, CA). Five microliters of cDNA at a concentration of 10 ng/μL and 0.1 μM of each primer in a final volume of 25 μL was used. For statistical significance, each RT-PCR had six replicates. Once the master mix was made, the 25 μL aliquots were transferred into a MicroAmp optical 96-well reaction plate (Applied Biosystems), vortexed, and sealed with an optical adhesive cover (Applied Biosystems). Cycling and signal detection were done using the ABI-7900HT Sequence Detection System with the following cycling conditions: initial activation at 95 °C for 10 minutes, 40 cycles at 95 °C for 15 seconds, and 60 °C for 1 minute. The gene expression level was normalized to housekeeping genes β-actin and TBP5. Subsets of all RT-PCR reactions were sequenced to insure gene specificity for the reactions.

Histology

We examined MRL inbred strains for blastema formation by sacrificing the mice at 1, 4, 7, 14, and 21 days postdigit tip dissection. Dissected paw tissues were stored in 10% formalin until processing. The tissues were fixed in paraffin and 5 μm tissue sections were mounted on to microscope slides. Following hematoxylin and eosin (H&E) staining, the tissues were examined under a microscope.

RESULTS

Amount of dissected tissues in newborn mouse pups

Digit tip dissections were carried out using a scalpel under a microscope on the third and fourth tips of the right paw. The left paw digit tips were not dissected and used as uncut controls. Mice were x-rayed before and after digit tip dissection. The amounts of tissue dissected were calculated by subtracting the after-dissection values from the before-dissection values of the top of the second phalanx to the digit tip edge (Figure 1). The mean amount of tissue dissected in MRL mice was slightly greater (0.14 ± 0.03 mm) than the DBA and B6 mouse strains (0.12 ± 0.02 and 0.11 ± 0.02 mm), though not significantly.

Regrowth results

The strains tested vary in size among each other; thus, it would be expected that normal growth differences among the strains would be found. In order to insure that regrowth results were not influenced by differences in strain size, the data were normalized by dividing right cut growth measurements by left uncut growth measurements. We tested the validity of this normalization by dividing the right first phalanx measurements by the left first phalanx measurements (Figure 2). These growth ratios do not show significant differences among the mouse strains and give growth ratios of approximately 1.00. As the first phalanges were not dissected, normalizing for strain size by calculating a strain-specific growth ratio is a valid method of correcting for strain growth. This normalization method was utilized for subsequent analysis of regrowth data. Measurement error estimates of 10 x-ray images found that repositioning the mouse between successive measurements give a mean third phalanx length of 1.38 ± 0.10 mm in 3-week-old mice. Ten successive measurements made without mouse repositioning give a mean third phalanx length of 1.34 ± 0.05 mm. As the growth ratio measurements were captured at the same time and did not require repositioning the mice, these measurements should also have lower measurement errors than growth rate measurements captured from successive weeks.

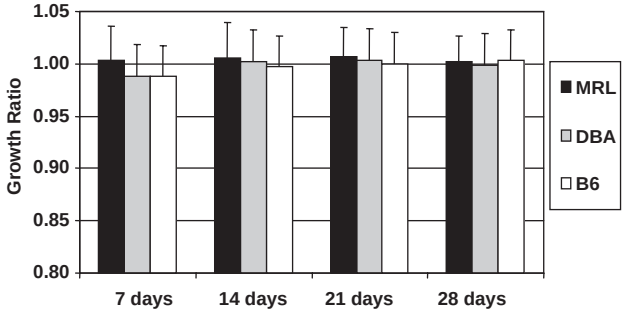

Figure 2. Normalization for strain size. Division of first phalanx right measurements by left measurements gives expected ratios of ~ 1.00 (mean $\pm$ SE). No statistically significant differences between strains are seen in normalized data for the first phalanx growth ratios.

Next, we examined the normalized regrowth ratios for dissected digit tips in the mice. As expected, the regrowth ratios are less than 1.0, indicating that growth of dissected digit tips is less than undissected digit tips (Figure 3). However, the MRL mouse regenerates digit tips more quickly than the other mouse strains at days 7, 14, and 21 postdissection. Mice exhibit most of their growth in the first 21 days after birth and this is also when digit tip regrowth in MRL mice is healed more quickly in comparison with the other inbred strains of mice. The degree of regrowth by day 28 was determined by examining mice for the degree of nail regeneration (Table 1). In MRL mice, 90% of mice completely or partially regenerated the nail. In DBA mice and B6, 72.9 and 66.7%, respectively, partially or completely regenerate nails. This difference is significant by chi-squared analysis ($p \leq 0.01$).

Microarray expression results

Four hundred genes out of 15,000 on the microarrays were significantly differentially expressed ($p < 0.05$) in MRL,

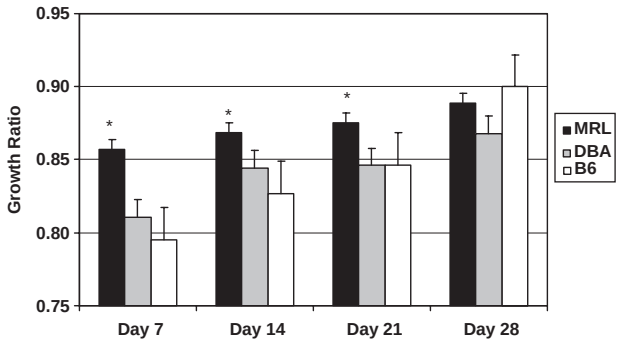

Figure 3. Normalized regrowth of MRL, DBA, and B6 digit tips. Growth ratios of digit tips for 7, 14, 21, and 28 days postdissection (mean ± SE) show that MRL mice regenerate digit tips greater than other strains of mice ($p < 0.05$, marked by * in plot). At day 14, MRL mice regrowth ratios were significant in comparison with B6 mice and approached significance in comparison with DBA mice ($p = 0.089$).

DBA, and B6 mice at day 4 in comparison with control tissue at day 0 (supplementary table). Of these, 207 genes were up-regulated and 193 were down-regulated. About 50% of these genes represent expressed sequence tags (ESTs) and unknown genes. The biological process gene ontology functional classes that are significantly overrepresented in all the strains regenerating digit tips are shown in the supplementary data table. Pathway analysis of these known genes reveals that genes in the IGF and BMP/TGF-β pathway are differentially expressed in all mouse strains (IGF2, IGF2BP3, IGFBP4, BMP-1, TGFb1i4), thus implicating the IGF and BMP/TGF-β signaling pathways in regulation of digit tip regrowth. The BMP family of genes has previously been implicated in digit regeneration.[22] Also, several genes involved in cell cycle and growth were found to be differentially expressed in all the strains, including CALM2, NFKB, and Annexin A2. Transcription factors that were found to be differentially expressed in all strains include MYST3, ATRX, SOX13, TCFL4, ANKIB1, TSC22D4, 6030490I01RIK, ZFP110, GATA3, GTF2H3, PHF7, ICSBP1, TRPV2, KLF4, MLL3, ANKRD10, IKBKG, CNOT2, FOXM1, ASH2L, HNRPR, NFE2L1, and ZFP113.

Seventy-five genes and ESTs were significantly differentially expressed only in MRL mice in comparison with DBA and B6 mice (Table 2). Of genes with known function, LRP6, a WNT co-receptor that functions in limb morphogenesis and pattern formation, was found to be differentially expressed. Also FMN2, which functions in cytoskeletal organization and meiosis, is differentially expressed in MRL regenerating digit tips. Transcription factors that were found to be differentially expressed only in MRL regenerating digit tips include SS18L1, NFE2L1, ZFP251, RXRIP110, and TAF5l. Many of the differentially expressed genes are ESTs. This suggests that there are many currently unknown genes and genetic pathways involved in digit tip regrowth.

Confirmation of microarray results was done by real-time PCR of 17 genes (TWSG1, TSC22, TIMP3, TGFBLi4, SMAD4, NET1, MSX2, MMP9, MMP2, MAGED1, FMN2, BMP2, BMP1, B2 M, AK007718, AI987944, ACTR2). RT-PCR results for these genes were consistent with the microarray results and gave correlation coefficients of 0.62, 0.91, and 0.40 for MRL, DBA, and B6 expression results, respectively (Supplementary Figure).

Histology

We examined the histology of regenerating digit tips by sacrificing MRL mice at 1, 4, 7, 14, and 21 days postdigit tip dissection. The formation of an epidermal layer over the wound is seen at 1 day postdissection. At 4 days postdissection, evidence of dedifferentiation of cells and increased proliferation can be seen underneath the wound epithelium (Figure 4A and B). At 7 days postdissection, cartilage has begun to hypertrophy and osteoblasts and osteoclasts begin bone formation and remodeling; by 14 days postdissection, there are fewer undifferentiated cells present underneath the epithelium and the marrow cavity has begun forming (Figure 4B). By 21 days, bone growth continues, the digit tip has nearly completely regrown, and the nail has begun reforming.

DISCUSSION

The salient features of this study are as follows: (1) it provides direct evidence that newborn MRL mice heal digit tips more quickly and regenerate nails to a greater degree than DBA and B6 mice; (2) it provides evidence that the IGF and BMP/TGF-β pathways are important for digit tip regrowth in all inbred strains of mice tested; (3) it indicates that the improved regenerative capabilities of MRL mice may be due to the genes implicated in the WNT signaling pathway and morphogenesis.

MRL mice have a unique ability to heal and regenerate multiple cell types, including ear tissue and heart tissue. In

Table 1. Nail regrowth in MRL, DBA, and B6 mouse strains by 28 days postdissection. Ninety percent of MRL mice regrow nails either partially or completely, in comparison with only about 70% in DBA and B6 mice ($p < 0.01$)

Strain	*N*	None (%)	Partial (%)	Complete (%)	Strain total (%)
MRL	40	10.0	72.5	17.5	100.0
DBA	48	27.1	52.1	20.8	100.0
B6	54	33.3	51.9	14.8	100.0

$\chi^2 = 18.20$.
$p \leq 0.01$.

Table 2. Genes significantly differentially expressed in MRL mouse regenerating digit tips but not in DBA and B6 mice. The LRP6 and FMN2 genes were found to be differentially expressed in MRL mice in comparison with DBA and B6 mice

Gene-Ontology (GO) ID	Gene ontology biological process	# of genes with GO ID differentially expressed in MRL	# of genes with GO ID in NIA15K set	*p*-Value	Accession number	Gene name
GO:0006515	Cell organization and biogenesis	1	4	0.001	AF218940	Fmn2
GO:0006220	Embryonic hindlimb morphogenesis	1	1	0.001	BC056479	Lrp6
GO:0007089	Embryonic forelimb morphogenesis	1	1	0.001	BC056479	Lrp6
GO:0042733	Embryonic digit morphogenesis	1	2	0.001	BC056479	Lrp6
GO:0016043	WNT receptor signaling pathway	1	31	0.028	BC056479	Lrp6
GO:0006826	Anterior/posterior pattern formation	1	15	0.007	BC056479	Lrp6
GO:0006897	Endocytosis	1	58	0.087	BC056479	Lrp6
GO:0016358	Gastrulation	1	11	0.004	BC056479	Lrp6
GO:0010003	Development	2	151	0.138	AF218940; BC056479	Fmn2; Lrp6
GO:0030032	Lamellipodium biogenesis	1	5	0.001	AK083469	Nckap1
GO:0009952	Dendrite morphogenesis	1	7	0.001	BC053087	Ss18l1
GO:0006824	Misfolded protein catabolism	1	2	0.001	AK004024	Clpp
GO:0030163	Protein catabolism	1	21	0.014	BC050902	Mdm2
GO:0015031	Actin filament organization	1	16	0.008	AK078918	Tmod3
GO:0051016	Barbed-end actin filament capping	1	7	0.001	AK078918	Tmod3
GO:0042981	Regulation of apoptosis	1	32	0.030	AK032060	Ank2
GO:0006915	Apoptosis	1	147	0.356	AK032060	Ank2
GO:0035116	Nucleotide biosynthesis	1	9	0.002	AK039066	Dctd
GO:0006260	DNA replication	1	70	0.119	AK051621	Orc4l
GO:0006810	Pyrimidine nucleotide metabolism	1	1	0.001	AK039066	Dctd
GO:0035115	Start control point of mitotic cell cycle	1	7	0.001	BC050902	Mdm2
GO:0007275	Cobalt ion transport	1	3	0.001	AK083478	Slc11a2
GO:0006355	Iron ion homeostasis	1	12	0.004	AK011244	Ftl1

Table 2. Continued.

Gene-Ontology (GO) ID	Gene ontology biological process	# of genes with GO ID differentially expressed in MRL	# of genes with GO ID in NIA15K set	*p*-Value	Accession number	Gene name
GO:0016055	Iron ion transport	2	15	0.001	AK011244; AK083478	Ftl1; Slc11a2
GO:0006350	Transport	2	635	0.088	AK083478; AK018343	Slc11a2; Syt11
GO:0008283	Calcium ion homeostasis	1	13	0.005	BC008997	Anxa7
GO:0006874	Cell proliferation	1	53	0.075	BC008997	Anxa7
GO:0009165	Intracellular signaling cascade	1	164	0.408	AK049307	2900057D21Rik
GO:0007049	Cell cycle	1	223	0.432	AK049307	2900057D21Rik
GO:0016567	Protein transport	1	255	0.358	BC053504	Tloc1
GO:0006508	Proteolysis and peptidolysis	2	142	0.120	AK004024; AK011589	Clpp; Ctsl
GO:0007015	Protein ubiquitination	1	102	0.215	BC050902	Mdm2
GO:0006512	Ubiquitin cycle	1	237	0.398	BC050902	Mdm2
GO:0008152	Metabolism	1	161	0.399	AK075831	Dbt
GO:0006879	Transcription	3	535	0.328	AK080514; AK087271; AK033477	Zfp251; Rxrip110; Taf5l
GO:0007242	Regulation of transcription	6	709	0.436	BC053087; BC022152; AK080514; AK087271; AK033477	Ss18l1; Nfe2l1; Zfp251; Rxrip110; Taf5l
					AK049010; AK008869;	1700041C02Rik;
					AK075950; AK075950;	2210409E12Rik;
					AK041714; AK014286;	Spbc24; Dhrs4;
					AF104414; AK077025;	Sparc; AW208599;
					AK080723; AK089793;	Slc16a9;
					AK041555; AK034422;	9130404D08Rik;
					BC051459; AK084556;	LOC237749;
					AK122209; AK029139;	C330046E03;
					AK087947; AK086670;	Srrm2;

None	Unknown process	34	AK009347; AK077521;	D13Wsu64e;
			AK077773; AK050612;	2010000I03Rik;
			AK026964; AK027483;	AK122209;
			AL832193; AK082477;	Sec24a;
			AK036620; AJ272268;	4930438O05Rik;
			AK037650; AK025061;	9430097H08Rik;
			AK085135; AK082946;	2310015A05Rik;
			AK085877; AK044885;	5730436H21Rik;
			AK016563; BC001136	LOC435957; BC057593

These genes have been implicated in the WNT signaling pathway, development, and morphogenesis.[22–25,29,30]

this study, we find that all strains of mice tested have the capability of regenerating digit tips. However, MRL mice can heal more quickly and reform nails of dissected digit tips more completely. The regrowth of digit tips is more complex than simple wound healing of ear punches and cardiac lesions as it involves the regrowth of multiple cell types including bone, cartilage, nervous, and epithelial cells. Similar to stem cells, regenerating digit tips require proper patterning of the regenerating cells to direct their cellular fate. Studies undertaken in axolotls have documented the stages in amphibian limb regeneration.[3] In axolotls, the first stage after amputation involves the formation of wound epithelial cells to cover the wound (http://www.uoguelph.ca/zoology/devobio/210labs/regen1.html). After 2 days, beneath this epithelial layer, cells begin to dedifferentiate and form a blastema. These blastema cells redifferentiate and completely regenerate the amphibian limb within 6 weeks postamputation. In MRL mice, our histology studies found that the early stages of digit tip regrowth are partially similar to that of axolotls (Figure 4). Within 1 day of digit tip amputation epithelial cells have formed over the wound in MRL mice. At 4 days, epithelial cells have completely covered the wound and undifferentiated cells beneath the wound epithelium begin to proliferate. At 7 days osteoblasts are present and have begun to form bone. At 14 days postdissection the cells beneath the wound epithelium are not as dedifferentiated and the bone marrow cavity has begun forming above the third phalange's joint. By 21 days postdissection, the cells have redifferentiated, the nail has begun reforming, and the digit tip has almost completely regenerated. It is interesting that when de- and redifferentiation of cells beneath the wound epithelium is occurring is also when the MRL mouse shows the greatest regenerative capacity. This suggests possible links between the enhanced healing capabilities of MRL mice and the molecular causes of de- and redifferentiation of cells.

The NIA15K cDNA library used to create the microarrays in this study was isolated from developing mouse embryos. Thus, many of these genes are expressed primarily in embryonic development and are a unique source for studies of regrowth. In all the strains examined in this study we found that genes involved in the IGF and BMP/TGF-β pathways are differentially expressed. This is not unexpected as the IGF and BMP/TGF-β pathways are known to be critical to limb formation, bone induction, and fracture repair.[19–22] Also, previous studies have reported that high levels of TGF-β1 mRNA and/or protein are localized in developing cartilage, bone, and skin, and play a role in the growth and differentiation of these tissues.[21] This study confirms the importance of the IGF1 and BMP/TGF-β pathways in regrowth and wound healing and the importance of the BMP family of genes in regulating a regenerative response.[22] Genes involved in cell cycle, transcription, and growth were also found to be differentially expressed in all the strains (CALM2, NFKB, ANXA2, GATA3, RFPL4, KLF4, TCF14, and ZF110).

In only MRL regenerating digit tips, LRP6, SPARC, CTSL, and FMN2 are particularly interesting genes that are differentially expressed. LRP6 and its co-receptor LRP5 are required for WNT/β-catenin–mediated signal transduction.[23] LRP6 knockout mice exhibit severe developmental abnormalities, including the truncation of the axial skeleton, reduced bone mineral density, and limb defects.[24,25] The WNT signaling pathway plays important roles in bone cell function, and LRP6 and LRP5 are essential for proper gastrulation in developing embryos.[25,26] SPARC (osteonectin) is a bone-specific phosphoprotein that accounts for the unique properties of bone collagen to undergo calcification.[27] The absence of SPARC in mice gives rise to alterations in the composition of the extracellular matrix that result in osteopenia and pathological closure of dermal wounds.[28] SPARC regulates the activity of several growth factors including platelet-derived growth

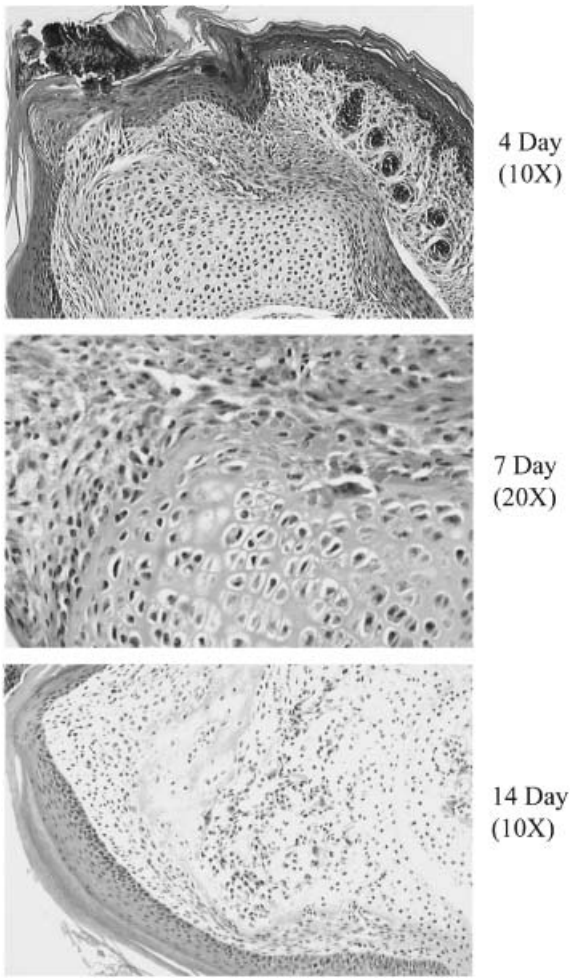

Figure 4. Regeneration histology. At 1 day postdissection a wound epithelial layer has begun to form. By 4 days postdissection the wound epithelial layer has completely covered the tip and beneath this dedifferentiated and proliferating cells are present. At 7 days postdissection bone has begun to form, and by day 14 the marrow cavity is forming above the third phalange's joint. By 21 days, the digit has nearly completed regenerating and the nail has begun reforming. In Figure 4A all images are at ×4, in Figure 4B images are ×10 or ×20.

factor (PDGF), fibroblast growth factor (FGF), and vascular endothelial growth factor (VEGF). This suggests links between increased expression levels of SPARC in MRL mice and growth factor regulation in regenerating digit tips. Cathepsins are cysteine proteases with essential roles in osteoclast-mediated bone matrix degradation. Cathepsin L acts by integrating endothelial progenitor cells into wounds and is required for neovascularization of ischemic tissue.[29] Also, CTSL knockout mice have impaired healing following limb ischemia.[29] Thus, the increased levels of CTSL in MRL regenerating digit tips may lead to increased regenerative capacity by increasing vascularization of wound tissue.

In only MRL regenerating digit tips, the FMN2 gene is another intriguing gene that is differentially expressed. Mutations in a related formin gene, formin-1, lead to developmental defects in limb formation due to a reduction in the number of bony elements in the fore and hind limbs.[30,31] Formin-1 is thought to act in limb bud polarization through establishment of a SHH/FGF-4 feedback loop.[30] Also, studies in a yeast homologue of formin, forp1, have found that its mutation leads to asymmetric patterns of cell growth.[32] This suggests that formins are critical signaling components of pattern formation and directing cellular fate. Our previous microarray studies of mouse ear punch wound healing found that formin-binding protein 21 is differentially expressed in healing ear tissue.[33] Thus, the formin family of genes is involved in both soft tissue wound healing and digit tip regrowth. This indicates that there are common genetic mechanisms influencing soft tissue wound healing and digit tip regrowth in the MRL super-healer mouse. Members of the formin gene family have been implicated in the WNT signaling pathway.[34] The WNT signaling pathway initiates outgrowth, controls patterning, and regulates cell differentiation in a number of tissues.[35] Also, bone formation has been shown to be activated by WNT signaling in osteoblast stem cells by promoting osteoblastic differentiation.[36] FMN2 has been reported to be highly expressed in both developing and adult central nervous systems.[37] This is intriguing as denervation has been shown to eliminate regeneration capabilities in amphibians.[38] Recently, we have undertaken studies of knockout FMN2 mice and preliminary data indicate that FMN2 (−/−) mice have significantly reduced femur cortical thickness (unpublished results).

In conclusion, we find that MRL mice show greater regenerative capacities to heal digit tips in comparison with other inbred strains of mice tested. This increased regrowth is seen primarily during the times of greatest growth in mice and during the times of dedifferentiation and redifferentiation of cells in the healing and regrowth process. The determination of the molecular causes of de- and redifferentiation of cells during growth and healing has important implications in stem cell research. The capability of neonatal mammals to regenerate is reduced when they reach adulthood.[39] It is thought that this reduced regenerative capacity is due to a reduction in multipotent cells with age.[39] Future studies will focus on determining whether MRL mice retain more of their regenerative capacity than other strains of mice. The further elucidation of the mechanisms by which genes contribute to regrowth and bone formation will likely lead to new targets and eventually treatments for wound healing, regeneration, and bone diseases.

ACKNOWLEDGMENT

This work was supported by US Army Grant DAMD17-02-1-0685.

Supplementary material

The following supplementary material for this article is available online:

Table S1. Genes Differentially Expressed in MRL, DBA and B6 Mice at Day 4 Post Digit Tip Dissection. About

50% of these genes represent ESTs and unknown genes. Pathway analysis of the known genes reveals that genes in the IGF and BMP/TGF pathway are differentially expressed in all mouse strains (IGF2, IGF2BP3, IGFBP4, BMP-1, TGFb1i4). Also, genes involved in cell cycle regulation and growth (CALM2, NFKB) and transcription (GATA3, RFPL4, KLF4, TCF14, ZF110) are differentially expressed in all strains.

Figure S1. Confirmation of Microarray Expression Results by Real-time PCR. Confirmation of microarray results was done by real-time PCR of 17 genes (TWSG1, TSC22, TIMP3, TGFBLi4, SMAD4, NET1, MSX2, MMP9, MMP2, MAGED1, FMN2, BMP2, BMP1, B2M, AK007718, AI987944, ACTR2). RT-PCR results for these genes were consistent with the microarray results and gave correlation coefficients of 0.62, 0.91, and 0.40 for MRL, DBA, and B6 expression results, respectively.

This material is available as part of the online article from: http://www.blackwell-synergy.com/doi/abs/10.1111/j.1742-4658.2006.00500.x (This link will take you to the article abstract).

Please note: Blackwell Publishing is not responsible for the content or functionality of any supplementary materials supplied by the authors. Any queries (other than missing material) should be directed to the corresponding author for the article.

REFERENCES

1. Muller TL, Ngo-Muller V, Reginelli A, Taylor G, Anderson R, Muneoka K. Regeneration in higher vertebrates: limb buds and digit tips. *Semin Cell Dev Biol* 1999; 10: 405–13.
2. Brockes JP. Amphibian limb regeneration: rebuilding a complex structure. *Science* 1997; 276: 81–7.
3. Endo T, Bryant SV, Gardiner DM. A stepwise model system for limb regeneration. *Dev Biol* 2004; 270: 135–45.
4. Illingworth CM. Trapped fingers and amputated finger tips in children. *J Pediatr Surg* 1974; 9: 853–8.
5. Borgens RB. Mice regrow the tips of their foretoes. *Science* 1982; 217: 747–50.
6. Neufeld DA, Zhao W. Phalangeal regrowth in rodents: post-amputational bone regrowth depends upon the level of amputation. *Prog Clin Biol Res* 1993; 383A: 243–52.
7. Zhao W, Neufeld DA. Bone regrowth in young mice stimulated by nail organ. *J Exp Zool* 1995; 271: 155–9.
8. Reginelli AD, Wang YQ, Sassoon D, Muneoka K. Digit tip regeneration correlates with regions of Msx1 (Hox 7) expression in fetal and newborn mice. *Development* 1995; 121: 1065–76.
9. Goss RJ, Grimes LN. Epidermal downgrowths in regenerating rabbit ear holes. *J Morphol* 1975; 146: 533–42.
10. Joseph J, Dyson M. Effect of anabolic androgens on tissue replacement in the ear of the rabbit. *Nature* 1966; 211: 193–4.
11. Li X, Gu W, Masinde G, Hamilton-Ulland M, Xu S, Mohan S, Baylink DJ. Genetic control of the rate of wound healing in mice. *Heredity* 2001; 86 (Part 6): 668–74.
12. Clark LD, Clark RK, Heber-Katz E. A new murine model for mammalian wound repair and regeneration. *Clin Immunol Immunopathol* 1998; 88: 35–45.
13. Leferovich JM, Bedelbaeva K, Samulewicz S, Zhang XM, Zwas D, Lankford EB, Heber-Katz E. Heart regeneration in adult MRL mice. *Proc Natl Acad Sci USA* 2001; 98: 9830–5.
14. Tanaka TS, Jaradat SA, Lim MK, Kargul GJ, Wang X, Grahovac MJ, Pantano S, Sano Y, Piao Y, Nagaraja R, Doi H, Wood WH III, Becker KG, Ko MS. Genome-wide expression profiling of mid-gestation placenta and embryo using a 15,000 mouse developmental cDNA microarray. *Proc Natl Acad Sci USA* 2000; 97: 9127–32.
15. Shih JH, Michalowska AM, Dobbin K, Ye Y, Qiu TH, Green JE. Effects of pooling mRNA in microarray class comparisons. *Bioinformatics* 2004; 20: 3318–25.
16. Draghici S, Khatri P, Bhavsar P, Shah A, Krawetz S, Tainsky MA. Onto-Tools, the toolkit of the modern biologist: Onto-Express, Onto-Compare, Onto-Design and Onto-Translate. *Nucleic Acids Res* 2003; 31: 3775–81.
17. Draghici S, Khatri P, Shah A, Tainsky MA. Assessing the functional bias of commercial microarrays using the Onto-Compare database. *BioTech Microarrays Cancer Res Appl* 2003; 34: 55–61.
18. Draghici S, Khatri P, Martins RP, Ostermeier GC, Krawetz SA. Global functional profiling of gene expression. *Genomics* 2003; 81: 98–104.
19. Zuniga A, Haramis AP, McMahon AP, Zeller R. Signal relay by BMP antagonism controls the SHH/FGF4 feedback loop in vertebrate limb buds. *Nature* 1999; 401: 598–602.
20. Cho TJ, Gerstenfeld LC, Einhorn TA. Differential temporal expression of members of the transforming growth factor beta superfamily during murine fracture healing. *J Bone Miner Res* 2002; 17: 513–20.
21. Dickinson ME, Kobrin MS, Silan CM, Kingsley DM, Justice MJ, Miller DA, Ceci JD, Lock LF, Lee A, Buchberg AM, Siracusa LD, Lyons KM, Derync R, Hogan BLM, Copeland NG, Jenkins NA. Chromosomal localization of seven members of the murine TGF-beta superfamily suggests close linkage to several morphogenetic mutant loci. *Genomics* 1990; 6: 505–20.
22. Han M, Yang X, Farrington JE, Muneoka K. Digit regeneration is regulated by Msx1 and BMP4 in fetal mice. *Development* 2003; 130: 5123–32.
23. Tamai K, Semenov M, Kato Y, Spokony R, Liu C, Katsuyama Y, Hess F, Saint-Jeannet JP, He X. LDL-receptor-related proteins in Wnt signal transduction. *Nature* 2000; 407: 530–5.
24. Pinson KI, Brennan J, Monkley S, Avery BJ, Skarnes WC. An LDL-receptor-related protein mediates Wnt signalling in mice. *Nature* 2000; 407: 535–8.
25. Holmen SL, Giambernardi TA, Zylstra CR, Buckner-Berghuis BD, Resau JH, Hess JF, Glatt V, Bouxsein ML, Ai M, Warman ML, Williams BO. Decreased BMD and limb deformities in mice carrying mutations in both Lrp5 and Lrp6. *J Bone Miner Res* 2004; 19: 2033–40.
26. Kelly OG, Pinson KI, Skarnes WC. The Wnt co-receptors Lrp5 and Lrp6 are essential for gastrulation in mice. *Development* 2004; 131: 2803–15.
27. Termine JD, Kleinman HK, Whitson SW, Conn KM, McGarvey ML, Martin GR. Osteonectin, a bone-specific protein linking mineral to collagen. *Cell* 2001; 26: 99–105.
28. Puolakkainen PA, Bradshaw AD, Brekken RA, Reed MJ, Kyriakides T, Funk SE, Gooden MD, Vernon RB, Wight TN, Bornstein P, Sage EH. SPARC-thrombospondin-2-double-null mice exhibit enhanced cutaneous wound healing and increased fibrovascular invasion of subcutaneous

polyvinyl alcohol sponges. *J Histochem Cytochem* 2005; 53: 571 –81.
29. Urbich C, Heeschen C, Aicher A, Sasaki K, Bruhl T, Farhadi MR, Vajkoczy P, Hofmann WK, Peters C, Pennacchio LA, Abolmaali ND, Chavakis E, Reinheckel T, Zeiher AM, Dimmeler S. Cathepsin L is required for endothelial progenitor cell-induced neovascularization. *Nat Med* 2005; 11: 206–13.
30. Zeller R, Haramis AG, Zuniga A, McGuigan C, Dono R, Davidson G, Chabanis S, Gibson T. Formin defines a large family of morphoregulatory genes and functions in establishment of the polarising region. *Cell Tissue Res* 1999; 296: 85–93.
31. Leader B, Lim H, Carabatsos MJ, Harrington A, Ecsedy J, Pellman D, Maas R, Leder P. Formin-2, polyploidy, hypofertility and positioning of the meiotic spindle in mouse oocytes. *Nat Cell Biol* 2002; 4: 921–8.
32. Sawin KE. Cell polarity: following formin function. *Curr Biol* 2002; 12: 6–8.
33. Li X, Mohan S, Gu W, Baylink DJ. Analysis of gene expression in the wound repair/regeneration process. *Mamm Genome* 2001; 12: 52–9.
34. Habas R, Kato Y, He X. WNT/Frizzled activation of Rho regulates vertebrate gastrulation and requires a novel Formin homology protein Daam1. *Cell* 2000; 107: 843–54.
35. Church VL, Francis-West P. WNT signalling during limb development. *Int J Dev Biol* 2002; 46: 927–36.
36. Bain G, Muller T, Wang X, Papkoff J. Activated beta-catenin induces osteoblast differentiation of C3H10T1/2 cells and participates in BMP2 mediated signal transduction. *Biochem Biophys Res Commun* 2003; 301: 84–91.
37. Leader B, Leder P. Formin-2, a novel formin homology protein of the cappuccino subfamily, is highly expressed in the developing and adult central nervous system. *Mech Dev* 2000; 93: 221–31.
38. Mullen LM, Bryant SV, Torok MA, Blumberg B, Gardiner DM. Nerve dependency of regeneration: the role of Distalless and FGF signaling in amphibian limb regeneration. *Development* 1996; 122: 3487–97.
39. Bryant SV, Endo T, Gardiner DM. Vertebrate limb regeneration and the origin of limb stem cells. *Int J Dev Biol* 2002; 46: 887–96.

Lack of EphA4 Causes Reduction in Total Body Bone Mineral Density and Femur Trabecular Bone Volume in Mice

Liming Bu, Yan Hu, Jon E. Wergedal, Subburaman Mohan, and Robert B. Chadwick*,

Molecular Genetics Division, Musculoskeletal Disease Center, JL Pettis VA Medical Center 11201 Benton Street (151), Loma Linda, CA, 92357.

*Corresponding author Telephone (909) 825-7084 ext. 1582 Fax (909) 796-1680

Email robert.chadwick@med.va.gov

ABSTRACT

The Eph receptor tyrosine kinases and their ligands are tyrosine kinase signal transduction proteins that play an important role in development and growth. Ephrin signaling is important in controlling homeostasis between bone formation by osteoblasts and bone remodeling by osteoclasts. Also, several ephrin receptors display skeletal abnormalities in knockout mice including EphA5, EphB1 and EphB2. However, little is known of the function of EphA4 in skeletal development and skeletal phenotypes have not yet been investigated in EphA4 deficient mice. Due to the importance of other ephrins in osteoclast/osteoblast homeostasis, we proposed the hypothesis that EphA4 may also play a role in the regulation of bone formation and bone resorption. To test this hypothesis, we compared the skeletal phenotypes EphA4 (-/-) and corresponding wild type (+/+) control mice by piximus densitometry and micro computed tomography (μCT). At 12 weeks of age, female EphA4 knockout mice display a 16% reduction in body weight and male EphA4 knockout mice an 11% reduction in body weight. Also total body bone mineral density is reduced by 11% in female EphA4 mutant mice and 7% in male EphA4 mutant mice. Micro CT analysis of EphA4 mutant femurs finds that trabecular bone volume is 29% reduced, trabecular number is 27% reduced and trabecular bone spacing is 49% increased ($p = 0.02$). At femur mid-shaft bone volume is 23% decreased ($p=0.01$). Furthermore, EphA4 knockout mice were found to have a 23% reduction in serum IGF-1 levels in comparision to wildtype EphA4 mice ($p=0.05$). These data suggest that EphA4 is involved in regulating growth of bone and other tissues in mice.

INTRODUCTION

The EphA4 gene belongs to the ephrin receptor subfamily of the protein-tyrosine kinase family. Ephin receptors typically have a single kinase domain and an extracellular region containing a Cys-rich domain and 2 fibronectin type III repeats. The ephrin receptors are divided into 2 groups based on the similarity of their extracellular domain sequences and their affinities for their respective ligands. Accordingly, EphrinB ligands are primarily preferential ligands for EphB receptors and EphrinA ligands primarily function as ligands for EphA receptors [1]. However, EphA4 can bind all the ephrin-A ligands as well as ephrin-B2 and ephrin-B3 ligands. The importance of Ephrin receptor/ligand interactions is shown by the multitude of cellular processes that have been implicated in ephrin signaling. These include stem cell differentiation, cell migration and skeletal formation [2, 3, 4, 5, 6]. In calcified tissues, ephrin receptor/ligand interactions have been implicated in skeletal developmental, bone response to mechanical laoding and osteoblast/osteoclast homeostasis. For example, mutations in mice of ephrinB1 ligands cause skeletal abnormalities [4]. Knockout mouse phenotypes of several ephrin receptors display skeletal abnormalities including and EphA5, EphB1, EphB2 and EphB3 [5]. Knockout mice for the Ephrin-B3 and the Ephrin-A ligands primarily display neuronal and corticospinal cord defects and the ligand Ephrin-B2 knockout is embryonic lethal (http://www.informatics.jax.org/).

In humans, mutations of Ephrn-B1 cause craniofrontonasal syndrome in which females show multiple skeletal malformations, but only mild abnormalities are displayed in males [5]. Also, Xing et al. found that in response to mechanical loading of mouse bones, the EphB2 receptor is increased in expression [7]. Other studies have found EphrinB2 ligands and EphB4 receptors regulate the differentiation of osteoclasts and osteoblasts, resulting in suppression of bone resorption and enhancement of bone formation [8]. These findings demonstrate that Ephrin-B receptors and their ligands are key regulators of skeletal development.

The Ephrin-A family of receptors and ligands have been shown to be important regulators of nerve formation and regeneration. Disrupting the expression of the EphA4 receptor in mice has been shown to modify neuronal connections in the brain and spinal cord. This results in an unusual hopping gait in EphA4 knockout mice. Also, knockout mice lacking EphA4 (-/-) have been reported to exhibit nerve regeneration after spinal cord injury [9]. Due to the importance of the Ephrin-B mediated signaling pathway in bone biology homeostasis, we hypothesized that the related Ephrin-A gene family may also influence bone formation and remodeling. Thus, we undertook investigations into the bone phenotypes of EphA4 knockout mice through Piximus bone densitometry and micro computed tomography (μCT).

MATERIALS AND METHODS

EphA4 Knockout Mice. Two mating pairs of heterozygous EphA4 (+/-) mice were obtained from Jackson Laboratories (Bar Harbor, ME). The recessive mutation of Epha4 arose spontaneously on the C57BL/6J inbred strain at the Jackson Laboratory in 1964 and was transferred to the C3H/HeSnJ background and has been maintained by

backcrossing mice homozygous for Epha4rb to C3H/HeSnJ mice, then intercrossing the progeny.

Bone Measurements. Total body PIXImus scans (PIXImus, LUNAR, Madison, WI) for the determination of bone mineral density (BMD) and bone mineral content (BMC) were done on 3, 6, 9, and 12 week old EphA4 mutant and control mice. The PIXImus instrument is calibrated routinely and a quality assurance test is performed daily prior to scanning. Volumetric bone mineral density (vBMD) and geometric parameters of femurs were determined by micro computed tomography (μCT) using a VivaCT 40 scanner (ScanCo Medical, Switzerland) The VivaCT 40 is equipped with a micro-focus X-ray source and can achieve 10 μm resolution. Femur trabecular bone parameters were measured and calculated for 180 scans directly beneath the femur growth plate. For mid-shaft measurements 100 scans were measured at femur mid-shaft.

Serum IGF-1 Measurements. IGFs in serum are bound to IGFBPs and it is known that IGFBPs produce artifacts in IGF radioimmunoassays (RIA). Therefore, IGFs are separated from IGFBPs by using the Bio-Spin separation. This rapid acid gel filtration protocol has been validated previously. The IGF concentration is determined by a RIA, using recombinant human IGF-I as a tracer and standard, and rabbit polyclonal antiserum as described earlier [10, 11]. The intra-and interassay coefficient of variation for IGF-I assay is less than 10% [11].

Statistical Analysis. Statistical analyses of bone parameters were done using Statistica software (Statsoft Inc). Data values are expressed as mean ± standard deviation (SD) differences between knockout and control. Statistical analysis of the data were analyzed by ANOVA or Student's t-test as appropriate.

RESULTS

EphA4 Mutant Mice. Total body BMD in EphA4 mutant and control mice was measured by PIXImus at week 3, 6, 9 and 12 weeks of age. EphA4 knockout mice were found to be significantly smaller in size at all time points. The reduced growth phenotype was accompanied also by significantly reduced total body BMD (Figures 1 and 2). Body weight and total body BMD were reduced by 16% and 11% in female mice and 11% and 7% in male mice respectively at 12 weeks of age.

At 12 weeks of age, trabecular femur volume was significantly reduced in EphA4 knockout mice. The bone volume/trabecular volume (BV/TV) ratio is 29% reduced, trabecular number is 27% reduced, and trabecular spacing is 49% increased in EphA4 knockout femur in comparison to wildtype femur (all $p < 0.03$). At femur mid-shaft the bone area is 23% reduced ($p = 0.01$).

Since growth is highly influenced by circulating levels of IGF-1, serum levels of IGF-1 were measured in EphA4 knockout ($n = 6$) and wildtype mice ($n = 5$). Knockout EphA4 mice were found to have a 23% reduction in serum IGF-1 levels in comparision to wildtype EphA4 mice ($p = 0.05$) (Figure 3).

DISCUSSION

These studies find that the absence of EphA4 influences overall body size, total body BMD, femur trabecular bone volume and serum IGF-1 levels. The EphA4 receptor is widely expressed in many cell types including bone, brain, bone marrow, thymus, heart and muscle tissues (http://www.genecards.org/cgi-bin/carddisp.plgene=EPHA4). Also, the EphA4 receptor binds the ephrin-A1, ephrin –A2, ephrin-A3, ephrin-A4, ephrin-A5, ephrin-B2, and ephrin-B3 ligands which are also

widely expressed in many different tissues [12, 13]. Normal bone expresses ephrin receptors A1, A4 and B2 [14]. The EphrinB2 ligand which interacts with the EphA4 receptor is expressed by osteoclasts in the absence of any detectable Ephrin receptor, whereas osteoblasts express both ephrinB2 ligand and the EphB4 receptor [13]. Due to the broad expression in multiple tissues of both the EphA4 receptor and its many ligands, it is not surprising that the lack of EphA4 effects overall growth in multiple tissues, including bone.

EphA4 mutant mice are significantly smaller in size and have reduced total BMD. Thus, EphA4 influences overall growth and that the phenotype of reduced total BMD of EphA4 mutant mice appears to be due to reduced body and bone size. However, the 29% reduction in femur trabecular bone volume indicates that EphA4 significantly influences trabecular bone formation or remodeling.

The mechanisms of reduced serum IGF1 levels in EphA4 knockout mice can only be speculated at this point. Growth requires the coordinated action of growth hormone (GH) and IGF-1. The secretion of GH from the pituitary into circulation stimulates the production of IGF-1 which in turn stimulates the proliferation of chondrocytes, formation of cartilage and subsequently ossification and bone growth. EphA4 is enriched in the developing and adult mouse hippocampus and mutations of EphA4 cause neuronal and structural alterations in the hippocampus [15, 16, 17, 18, 19]. The pituitary gland controls the release of GH and it lies immediately beneath the hypothalamus. Thus, one could hypothesize that reduced levels of serum IGF-1 in EphA4 knockout mice may be due to alterations of pituitary and hypothalamic structures that alter the release of GH

from the pituitary gland. However, further studies are needed to determine the contribution of IGF-1 in mediating the effects of EphA4 on growth and development.

Acknowledgments

This work was supported by the U.S. Army Medical Research Acquisition Activity Assistance (DAMD17-03-2-0021). The US Army Medical Research Acquisition Activity, 820 Chandler Street, Fort Detrick, MD 21702-5014, is the awarding and administering acquisition office. The information contained in this publication does not necessarily reflect the position or the policy of the government, and no official endorsement should be inferred. All the work was performed in facilities provided by the Department of Veteran Affairs.

REFERENCES

1. Himanen JP, Nikolov DB (2003) Eph receptors and ephrins, Int. J. Biochem. Cell Biol. 35: 130–134
2. Wang Z, Cohen K, Shao Y, Mole P, Dombkowski D, Scadden DT. Ephrin receptor, EphB4, regulates ES cell differentiation of primitive mammalian hemangioblasts, blood, cardiomyocytes, and blood vessels (2004) Blood 103:100–109
3. Batlle E, Henderson JT, Beghtel H, van den Born MM, Sancho E, Huls G, Meeldijk J, Robertson J, van de Wetering M, Pawson T, Clevers H (2002) β-catenin and TCF mediate cell positioning in the intestinal epithelium by controlling the expression of EphB/ephrinB, Cell 111: 251–263
4. Compagni A, Logan M, Klein R, Adams RH (2003) Control of skeletal patterning by ephrinB1-EphB interactions. .Dev Cell. 5(2):217-30
5. Twigg SR, Kan R, Babbs C, Bochukova EG, Robertson SP, Wall SA, Morriss-Kay GM, Wilkie AO (2004) Mutations of ephrin-B1 (EFNB1), a marker of tissue boundary formation, cause craniofrontonasal syndrome. Proc Natl Acad Sci U S A. 8;101(23):8652-7
6. Davy A, Aubin J, Soriano P (2004) Ephrin-B1 forward and reverse signaling are required during mouse development, Genes Dev. 18: 572–583
7. Xing W, Baylink D, Kesavan C, Hu Y, Kapoor S, Chadwick RB, Mohan S (2005) Global gene expression analysis in the bones reveals involvement of several novel genes and pathways in mediating an anabolic response of mechanical loading in mice. J Cell Biochem. 96(5):1049-60
8. Zhao C, Irie N, Takada Y, Shimoda K, Miyamoto T, Nishiwaki T, Suda T, Matsuo K (2006) Bidirectional ephrinB2-EphB4 signaling controls bone homeostasis. Cell Metab. 4:111–121
9. Goldshmit Y, Galea MP, Wise G, Bartlett PF, Turnley AM (2004) Axonal regeneration and lack of astrocytic gliosis in EphA4-deficient mice. J Neurosci. 24(45):10064-73
10. Mohan, S. and D.J. Baylink (1995) Development of a simple valid method for the complete removal of insulin-like growth factor (IGF)-binding proteins from IGFs in human serum and other biological fluids: comparison with acid-ethanol

treatment and C18 Sep-Pak separation. J Clin Endocrinol Metab, 80(2): p. 637-47.

11. Mohan S, Bautista CM, Herring SJ, Linkhart TA, Baylink DJ (1990) Development of valid methods to measure insulin-like growth factors-I and -II in bone cell-conditioned medium. Endocrinology 126(5): p. 2534-42.
12. Hafner C, Schmitz G, Meyer S, Bataille F, Hau P, Langmann T, Dietmaier W, Landthaler M, Vogt T. Differential gene expression of Eph receptors and ephrins in benign human tissues and cancers. Clin Chem. (2004);50(3):490-9
13. Mundy GR, Elefteriou F (2006) Boning up on Ephrin Signaling. Cell, 126(3):441-443
14. Varelias A, Koblar SA, Cowled PA, Carter CD, Clayer M (2002) Human osteosarcoma expresses specific ephrin profiles, implications for tumorigenicity and prognosis. Cancer, 95(4):862-869
15. Murai KK, Nguyen LN, Irie F, Yamaguchi Y, Pasquale EB (2003) Control of hippocampal dendritic spine morphology through ephrin-A3/EphA4 signaling. Nat Neurosci 6:153–160
16. Yue Y, Chen ZY, Gale NW, Blair-Flynn J, Hu TJ, Yue X, Cooper M, Crockett DP, Yancopoulos GD, Tessarollo L, Zhou R (2002) Mistargeting hippocampal axons by expression of a truncated Eph receptor. Proc Natl Acad Sci U S A. 99(16):10777-82
17. Dottori M, Hartley L, Galea M, Paxinos G, Polizzotto M, Kilpatrick T, Bartlett PF, Murphy M, Kontgen F, Boyd AW (1998) EphA4 (Sek1) receptor tyrosine kinase is required for the development of the corticospinal tract. Proc. Nat. Acad. Sci. 95:13248-13253
18. Gilardi-Hebenstreit P, Nieto MA, Frain M, Mattéi MG, Chestier A, Wilkinson DG, Charnay P (1992) An Eph-related receptor protein tyrosine kinase gene segmentally expressed in the developing mouse hindbrain. Oncogene 7: 2499-2506
19. Kullander K, Butt SJ, Lebret JM, Lundfald L, Restrepo CE, Rydström A, Klein R, Kiehn O (2003) Role of EphA4 and ephrinB3 in local neuronal circuits that control walking. Science 299: 1889-1892

Figure 1A. Body weight of female EphA4 mutant and wildtype mice. EphA4 female knockout mice (n=10) body weight is significantly reduced at all time points in comparison to wildtype mice (n=14) ($p < 0.05$ at all time points). At 12 weeks of age female EphA4 knockout mice are 16% reduced in weight in comparision to control mice.

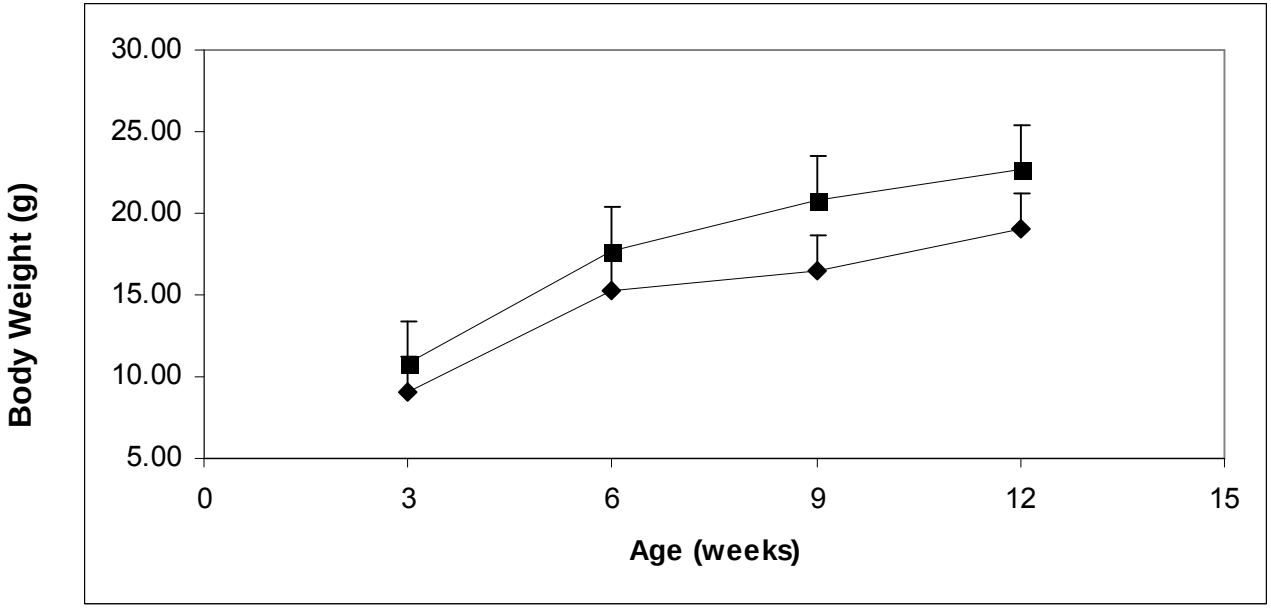

Figure 1B. Bone mineral density (BMD) of female EphA4 mutant and wildtype mice. EphA4 female knockout mice (n=10) have significantly reduced BMD in comparison to wildtype mice (n=14) at 6, 9, and 12 weeks ($p < 0.05$). At 12 weeks of age female EphA4 knockout mice are 11% reduced in total BMD in comparision to control mice.

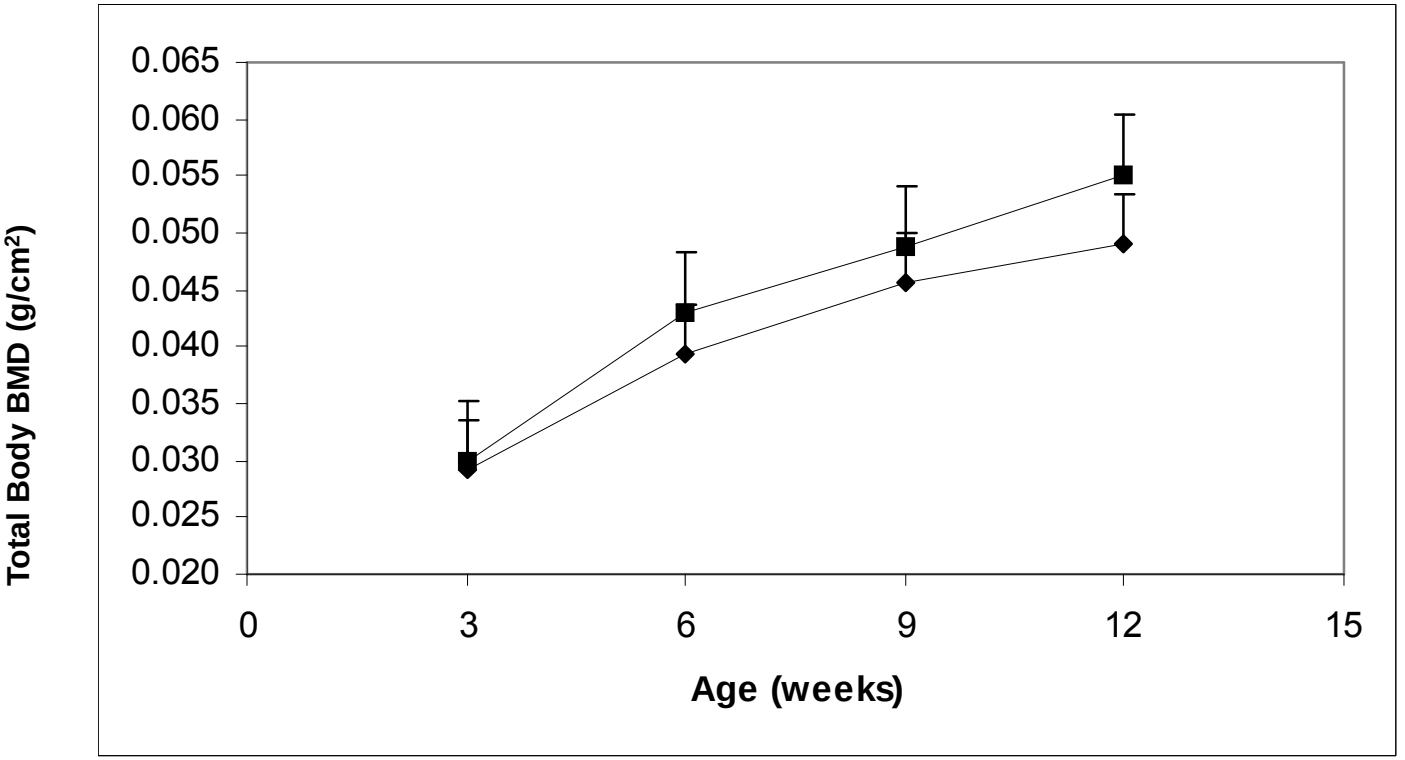

Figure 2A. Body weight of male EphA4 mutant and wildtype mice. EphA4 knockout male mice (n=10) are significantly smaller at all time points in comparison to wildtype mice (n=13) ($p < 0.05$). At 12 weeks of age male EphA4 knockout mice are 11% reduced in weight in comparision to control mice.

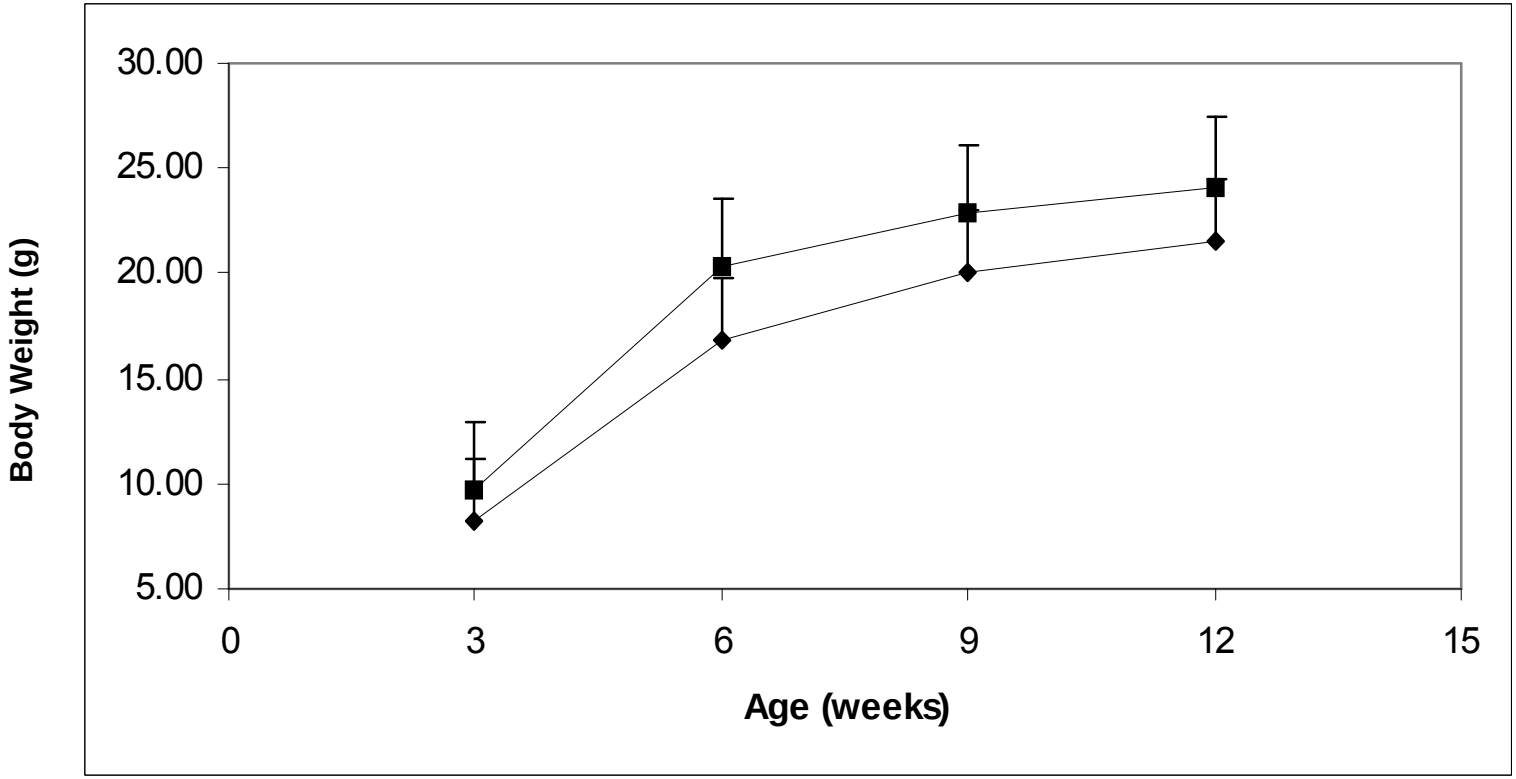

Figure 2B. Bone mineral density (BMD) of male EphA4 mutant and wildtype mice. EphA4 male knockout mice (n=10) have reduced BMD in comparison to wildtype mice (n=13) at 6, 9, and 12 weeks ($p < 0.05$). At 12 weeks of age male EphA4 knockout mice are 7% reduced in total BMD in comparision to control mice.

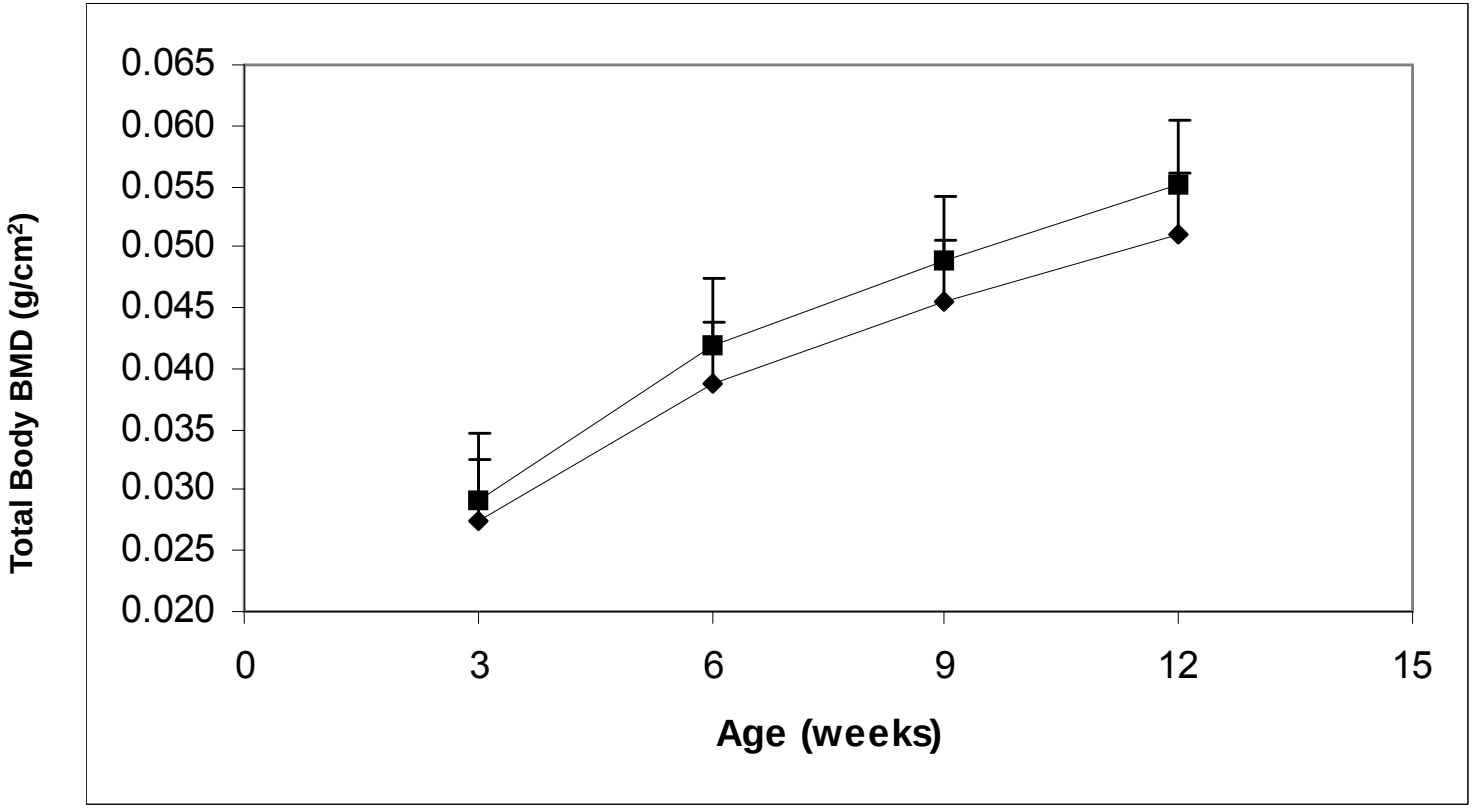

Figure 3. Serum circulating IGF-1 levels of EphA4 mutant and wildtype mice. EphA4 knockout mice have a 23% reduction in levels of serum IGF-1 in comparison to wildtype mice ($p = 0.05$).

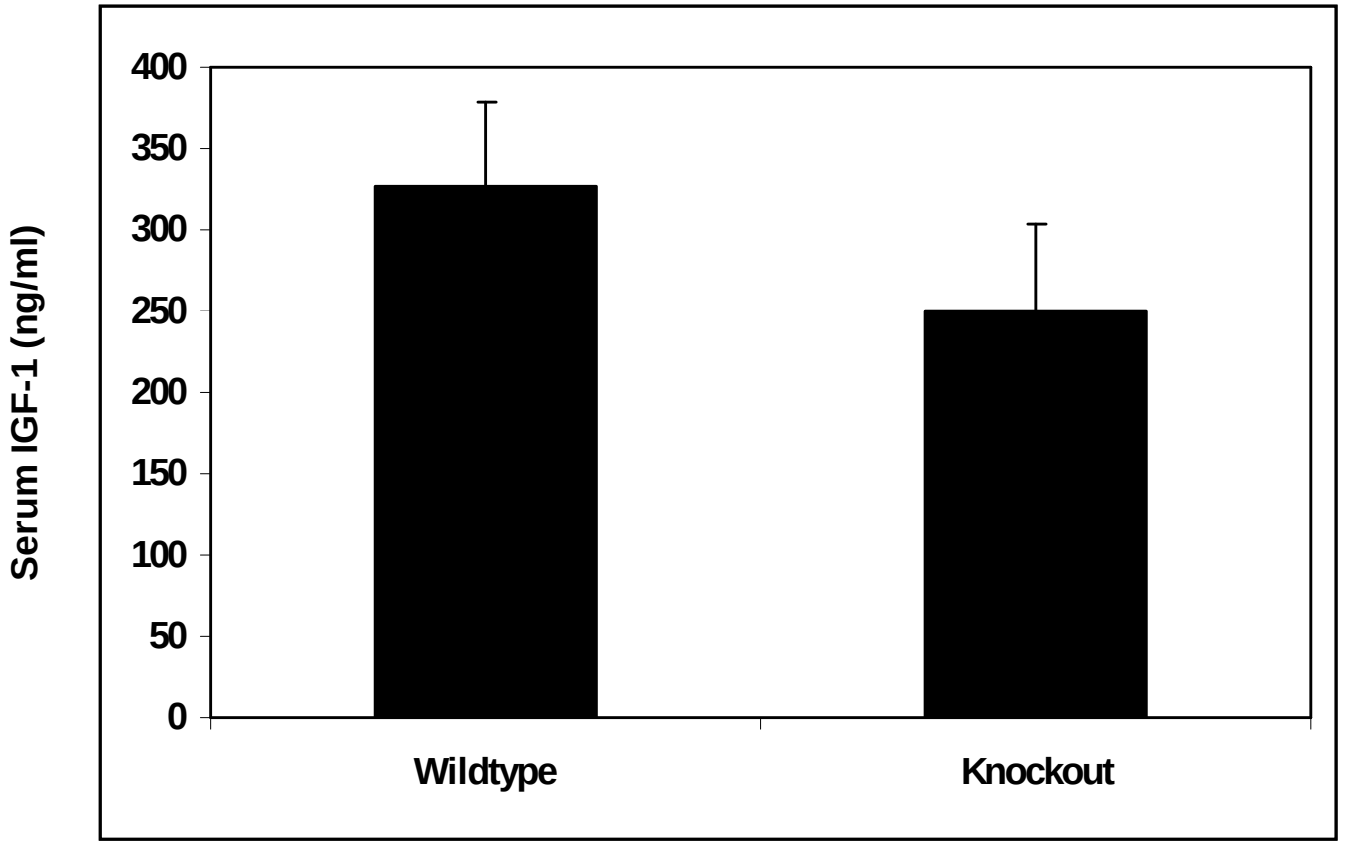

Table 1. Micro-Computed Tomography. The bone volume/trabecular volume (BV/TV) ratio is 29% reduced, trabecular number is 27% reduced, and trabecular spacing is 49% increased in EphA4 knockout femur in comparison to wildtype femur. At femur mid-shaft the bone area is 23% reduced (p=0.01).

Femur Trabecular Parameter	WT (n=6)	KO (n=6)	T-Test	% Difference
Bone Volume/Trab Volume	0.258 ± 0.026	0.185 ± 0.078	0.01	-28.5
Trabecular Number (1/mm)	4.93 ± 0.45	3.590 ± 1.03	0.02	-27.1
Trabecular Thickness (mm)	0.075 ± 0.008	0.075 ± 0.009	0.89	-0.9
Trabecular Spacing (mm)	0.204 ± 0.033	0.305 ± 0.084	0.02	+49.5
Femur Midshaft Parameter	WT (n=6)	KO (n=6)	T-Test	% Difference
VOX-Bone Area (mm^2)	1.043 ± 0.129	0.800 ± 0.125	0.01	-23.3
Total Density (mm^2)	891.5 ± 46	864.8 ± 25.9	0.24	-3.00
Cortical Density (mm^2)	1231.8 ± 8.4	1243.1 ± 13.7	0.11	0.92

Wildtype Trabecular Bone **Knockout Trabecular Bone**

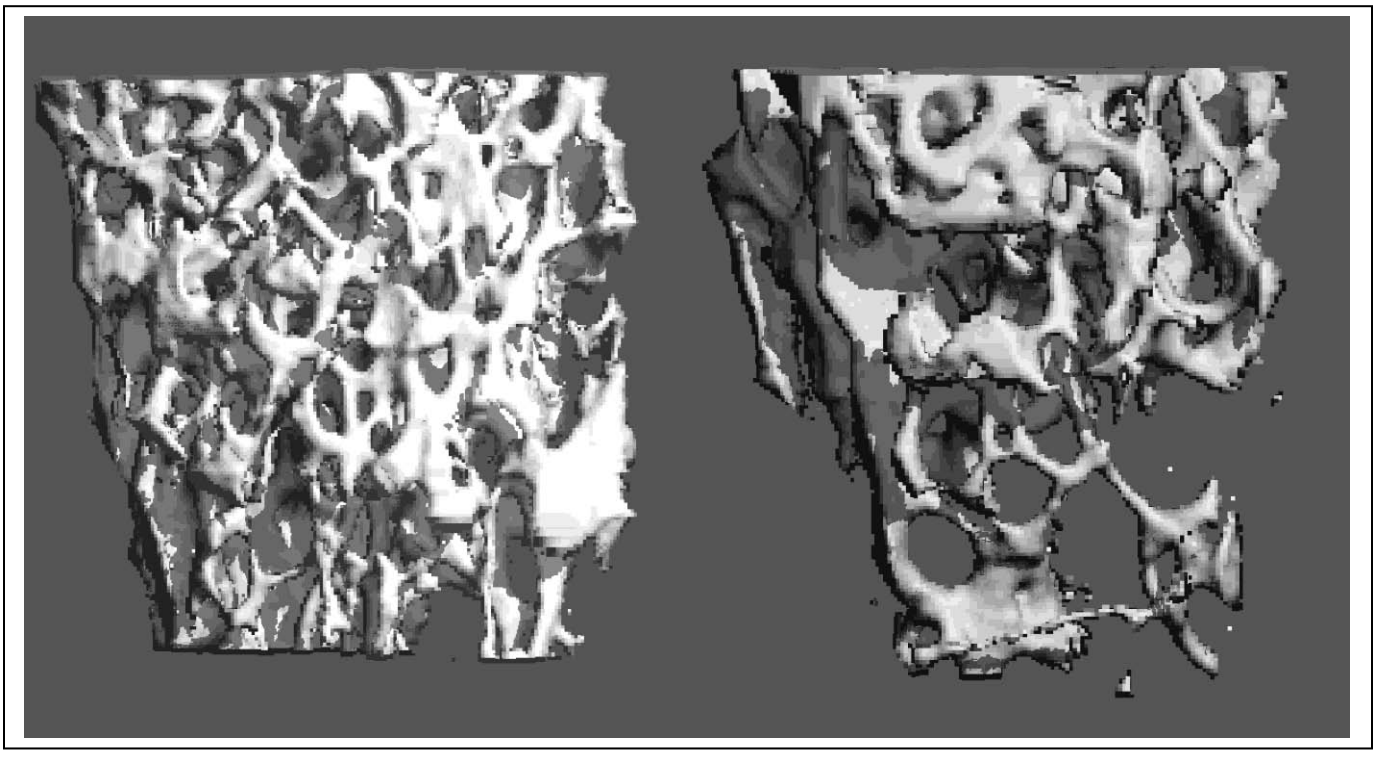

Formin-2 Gene Knockout Affects Osteoblasts and Bone Formation in Mice

Robert B. Chadwick, Hongrun Yu, Liming Bu, Yan Hu,

Jon E. Wergedal, Weirong Xing, David J. Baylink, and Subburaman Mohan*.

Molecular Genetics Division, Musculoskeletal Disease Center, JL Pettis VA Medical Center

11201 Benton Street (151), Loma Linda, CA, 92357.

*Corresponding author Telephone (909) 825-7084 ext. 2932 Fax (909) 796-1680

Email Subburaman.Mohan@va.gov

ABSTRACT

Formins are a family of proteins that are involved in the polymerization of filamentous actin. Actin filaments are known to contribute to many eukaryotic cellular processes. Mutations in the formin-1 gene result in the reduction and fusion of mouse limb bones. Based on this information and our recent finding that the expression of formin-2 gene, FMN2, was increased in the regenerating mouse digit tips, we proposed the hypothesis that FMN2 plays an important role in the regulation of bone metabolism. To test this hypothesis, we compared the skeletal phenotypes and osteoblast cells of the FMN2 knockout (KO) and the wild-type (WT) littermate control mice. As measured by body weight, the FMN2 KO mice were 14% smaller than the WT mice. This was mainly caused by the 21% reduction in total lean body mass, which was still significant after being adjusted for body weight. While DXA-based BMD measurements for total body, femur and tibia were decreased in KO compared to WT, the differences were not significant after the body weight adjustment. pQCT analysis of the femur showed a 5% reduction in the periosteal circumference and a 12% reduction in the total mineral content for the KO mice. Bone volume (BV/TV) of femur trabeculae as measured by μCT was reduced 30% in KO. This could partially be attributed to a 14% reduction in the trabecular thickness (Tb.Th). Evaluation of proliferation, differentiation and bone nodule formation by calvarial and bone marrow - derived osteoblasts in vitro revealed that FMN2 significantly affected osteoblast commitment and bone formation. Based on these data, we conclude that FMN2 regulates the growth and differentiation of osteoblasts and other cell types, and modulates overall somatic growth via these cellular functions.

Key words: Formin-2, FMN2, Osteoblasts, Bone, Mice,

INTRODUCTION

Formins are a family of proteins containing formin homology (FM) domains that are involved in the polymerization of filamentous actin through nucleation and progressive elongation at the fast growing 'barbed' end of actin filaments (1,2). Actin filaments are known to contribute to many cellular processes such as polarization, protrusion, contraction, nuclear segregation and cytokinesis in eukaryotic cells (1). In chondrocytes and osteocytes, the actin cytoskeleton has been implicated in mechanical loading - induced signal transduction, which is a key component and characteristics of bone signaling (3,4). Data from formin-1, the founding member of the formin protein family, has demonstrated an important role in skeletogenesis of mice. Mice homozygous for mutations in the formin-1 gene (FMN1) display multiple limb abnormalities characterized by synostosis of the zeugopod in combination with oligo- and syndactyly of metacarpal bones and digits, and were caused by alterations of transcriptions in both FMN1 and the down-stream gremlin gene (GREM1) (5,6). This phenotype is first manifested during the formation of limb bud as a failure of proper apical ectodermal ridge development and a reduction in the width of the posterior limb axis (7).

Knockout data show that formin-2, another member of the formin family, is required for the progression through metaphase of meiosis I in mouse oocytes, since oocytes null of the formin-2 gene (FMN2) cannot correctly position the metaphase spindle during meiosis I, and fertilization of these oocytes results in polyploid embryo formation, recurrent pregnancy loss and sub-fertility in homozygous female mice (8). Formin-2 is further shown to be involved in the

spindle migration or relocation in mouse oocytes by nucleating a continuously reorganizing cytoplasmic actin network (9,10). However, no studies to date have examined the influence of FMN2 on bone biology. In a recent published study using two inbred strains of mice that exhibit extreme differences in the healing tissues of amputated digit tips, we found that FMN2 was significantly differentially expressed (11). Based on these data and the known importance of FMN1 in proper limb formation, we hypothesized that FMN2 may be important in bone biology. To evaluate the role of FMN2 in the skeleton, we characterized the skeletal phenotype of mice with targeted disruption of FMN2 and the corresponding control mice of different ages. We found that bone parameters were significantly affected by FMN2, with reduced bone formation in the knockout mice. The reduction of bone formation was also confirmed by the in vitro assays using the osteoblast cells.

MATERIALS AND METHODS

FMN2 Knockout Mice. FMN2 knockout mice were obtained from Dr. Philip Leder at Department of Human Genetics, Harvard Medical School, Howard Hughes Medical Institute, Boston, MA. The mouse line was originally generated in the inbred 129/Sv mice via homologous recombination, where the gene was disrupted by replacement of the proline-rich exon with a neomycin resistance cassette, introducing stop codons in all 3 reading frames. The deleted region encoded 433 amino acids and contained the FH1 domain, which serves to recruit and interact with profilin in order to accelerate the rate of actin filament elongation, and is essential for FMN2's functions. The wild-type gene product in the homozygous mutants was confirmed absent by the Northern blot analysis, and the neomycin cassette was observed present in the transcript by sequencing. Two heterozygote FMN2 (+/-) male/female pairs were bred in our laboratories to

obtain homozygous knockout (-/-) and wild-type (+/+) pups for subsequent skeletal phenotype measurements. The mice have been maintained in the same 129/Sv genetic background since their generation in the year 2000 to avoid mixed background effects.

Measurements of Bone Parameters. Bone parameters were determined in three ways: in vivo dual energy X-ray absorptiometry (DXA) scans using a PIXImus densitometer (LUNAR Corporation, Madison, WI), in vitro peripheral quantitative computed tomography (pQCT) scans using a Stratec XCT 960 M machine (Norland Medical Systems, Ft. Atkinson, WI), and in vitro micro-computed tomography (μCT) scans using a VivaCT 40 μCT scanner (SCANCO USA, Southeastern, PA). In vivo DXA scans were carried out on 3, 6, 9 and 12 week old homozygous FMN2 knockout mice and the wild-type littermate control mice. The PIXImus instrument was calibrated routinely and a quality assurance test was performed daily prior to each scanning. In vitro pQCT scans were carried out to determine the geometric parameters of the isolated femurs from 12 weeks old knockout and control mice. Analysis of the pQCT scans was performed using the Bone Density Software version 5.40 (Norland Medical Systems, Ft. Atkinson, WI). Femur bone parameters were measured and averaged for three scans spaced evenly at mid-diaphysis. In vitro μCT scans were carried out to determine the trabecular bone paramers of the isolated femurs. The μCT scanner was equipped with a micro-focus X-ray source and could achieve 10 μm resolution. Femur trabecular bone parameters were adjusted for bone length to ensure that identical regions directly below the growth plate were measured.

Immunohistochemistry of FMN2 Protein Expression. Since our previous microarray study showed that FMN2 was differentially expressed in the MRL/MpJ mouse regenerating digit tips (11), we used the paw tissues of the 4-day old MRL/MpJ mice for the expression analysis. The mice were sacrificed, and the paw tissues were dissected and stored in 10% formalin until

processing. Five micron paraffin sections were mounted on poly-L-lysine coated slides. Antigen retrieval was done using pH 6.0 Citrate buffer, followed by incubation at 80°C and 70°C for ten minutes at each temperature. The sections were blocked in 20% horse serum at 37°C for 1 hour. Formin-2 primary antibodies (Santa Cruz Biotechnology, Santa Cruz, CA) were diluted at both 1:50 and 1:200, and the sections were incubated for 60 min. at 37°C. The sections were rinsed extensively and incubated with the secondary anti-goat antibody (Santa Cruz Biotechnology, Santa Cruz, CA) for 12 min. at 37°C. The sections were reacted with diaminobenzidine and hydrogen peroxide, counter-stained with Methyl Green and cover-slipped.

In Vitro Proliferation, Differentiation and Nodulation Assays. Calvaria from 28-day-old homozygous FMN2 knockout and wild-type littermate control mice were digested by collagenase for isolation of osteoblasts as previously described (12). The osteoblast cultures were expanded in α-MEM containing serum and used for proliferation, differentiation and nodulation assays. For proliferation assays, incorporation of BrdU (Exalpha Biologicals, Shirley, MA) into DNA of osteoblasts was carried out during the final 1 hour of serum - free cell culture. The amount of BrdU was quantified with a microplate spectrophotometer at a wavelength of 450 nm with reference at a wavelength of 570 nm. Monolayer cultures without BrdU incorporation were used as a negative control. For differentiation assays, calvaria cells were seeded into 96-well plates at 10,000 cells per well with 50 µl of α-MEM containing 0.1% calf serum (CS) and 0.1% bovine serum albumin (BSA), and grown overnight. Osteoblast differentiation was measured by the increase in the specific activity of alkaline phosphatase (ALP) as described previously (12,13).

For nodule assays, calvarial cells were plated at a density of 7×10^6 cells/90-mm per plastic tissue culture dish in α-MEM containing 10% CS, 100 U/ml penicillin and 100 µg/ml streptomycin. Culture media were changed every 2 days for 6 days, and then switched to

mineralization media by adding 50 μg/ml ascorbic acid and 10 mM β-glycerophosphate. After 24 days, cultures were stained with alizarin red to assess nodule formation as described previously (14). The areas stained as bone nodules were measured and determined with the use of computerized image analyzer software, and the percent areas covered with bone nodules in the plates were calculated.

We also conducted differentiation assays using the mesenchymal stem cell (MSC). FMN2 knockout and wild-type stromal cells were flushed out of femurs, and plated at a density of 7×10^6 cells/90-mm per plastic tissue culture dish in α-MEM containing 10% CS, 100 U/ml penicillin and 100 μg/ml streptomycin. Culture media was changed every 2 days for 6 days, and then switched to mineralization media by adding 50 μg/ml ascorbic acid and 10 mM β-glycerophosphate. Cells were cultured for 10 more days, and stained with ALP. The numbers of osteoblastic colony-forming units (CFU-OB) and fibroblastic colony-forming units (CFU-F) were then identified and counted. CFU-OB were colonies stained with ALP, and contained osteoblast cells, while CFU-F were not stained by ALP, and presumably contained mesenchymal cells. Finally, the percent CFU-OB/CFU-F was calculated.

Microarray Based Expression Analysis. Total RNA was isolated from mouse osteoblast cell cultures of 6 FMN2 homozygous knockout mice and 6 wild-type littermate control mice using Trizol followed by RNAEasy column purification (Qiagen, Valencia, CA). Custom oligonucleotide slides were spotted with 70mer oligonucleotides of 38,039 probes that represent the Mouse Exonic Evidence Based Oligonucleotide (MEEBO) set obtained from Illumina (San Diego, CA). A Q-Array2 robot (Genetix, Boston, MA) was used for spotting. A total of 250 ng RNA was used to synthesize double stranded cDNA using the Low RNA Input Fluorescent Linear

Application Kit (Agilent, Santa Clara CA). The slides were scanned using an Axon 4200A Genepix scanner (Molecular Devices, Sunnyvale, CA).

Statistical Analysis. We used the Statistica program (StatSoft, Inc., Tulsa, OK) for data analysis. Values, either raw or as percentage of the control, are expressed as means + standard deviation. Significance of the bone parameters were tested by Student's T-test. Expression analysis of microarray experiments was performed with GeneSpring software (Agilent, Santa Clara CA) using the raw intensity data generated by ImaGene software (BioDiscovery, El Segundo, CA). Local background-subtracted total signal intensities were used as intensity measures, and the data was normalized using per spot and per chip LOWESS normalization. Genes that were significantly differentially expressed between knockout FMN2 and wild-type osteoblast cells were determined by utilizing a one-sample Student's t-test to determine whether the mean normalized expression level for the gene is statistically different from 1.0.

RESULTS

FMN2 Knockout Mice Exhibit Reduced Body Weight and Bone Volume. In vivo body and bone parameters of the FMN2 homozygous knockout (-/-) and the wild-type littermate control (+/+) mice were measured by DXA at 3, 6, 9 and 12 weeks of age. We observed the expected gender differences in growth parameters after 4 weeks of age with males being larger than females. However, a gender by treatment interaction was not observed. Therefore, male and female data are combined for data analysis for the sake of clarity. The FMN2 knockout mice were smaller than the wild-type control mice. The significant difference started at 9 weeks of age (**Figure 1a**), and at 12 weeks, the body weight of the knockout mice was 86% of the control mice, which represented a significant reduction (**Figure 2a**). There was also a significant reduction in

total lean body mass starting at 6 weeks of age in the knockout mice (**Figure 1b**). At 12 weeks, the total lean body mass in the knockout mice reduced 21% compared to that in the control mice (**Figure 2a**).

The DXA measurements also showed that disruption of FMN2 in the KO mice produced a significant deficit in the total body bone mineral density (BMD) that began at 9 weeks of age (**Figure 1c**), and reached 9% at 12 weeks (**Figure 2a**), and an even higher deficit in femur and tibia BMD that began at 6 weeks of age (**Figure 1d,e**), and reached 16% and 14%, respectively, at 12 weeks (**Figure 2a**). However, there was no significant difference in lumbar vertebra BMD between the knockout mice and control mice (**Figure 1f, Figure 2a**). Areal bone density measurements by DXA discussed above are known to be influenced by differences in body size. Because FMN2 KO mice were smaller, we have adjusted areal BMD measurements by body weight, and found no significant differences in BMD parameters for any of the skeletal site tested between KO and control (**Figure 2b**). However, there was still a significant difference in lean body mass, which was 8% lower in the KO mice than the control mice.

Measurements of femur bone parameters of 12 week old mice were undertaken by pQCT. There were a 5% reduction in periosteal circumference and a 12% reduction in total mineral content for the KO mice, both of which were statistically significant (**Figure 3**). However, there were no significant differences in endosteal circumference and total vBMD between the KO femur and the WT control femur. Cortical thickness and cortical mineral content were reduced significantly at 7% and 12%, respectively. However, there was no change in cortical BMD.

Trabecular bone parameters of the femurs from the 12 week old mice were determined by μCT, and calculated from 180 scans directly below the growth plate. The trabecular bone volume indicated as BV/TV in the knockout was significantly reduced at 30% (**Table 1, Figure 4**). This

decrease of trabecular bone was caused mainly by a 14% reduction in trabecular thickness (Tb.Th) (P = 0.06), and a combination of non-significant changes in trabecular number (Tb.N) and trabecular spacing (Tb.S).

FMN2 Expressed in Bone. In order to determine the cell types and cellular locations of FMN2 expression in bone, we used the MRL/MpJ mice, which showed differential expression of FMN2 in the regenerating digit tips in our previous microarray study (11) and the immunohistochemistry (IHC) method, to investigate the distribution of the FMN2 protein. FMN2 was found to be expressed in both osteoblasts and osteoclasts, but to a lesser extent in osteoclasts than osteoblasts (**Figure 5**). Osteoblasts expressing FMN2 were present at both endosteum and periosteum of the dissected paw.

FMN2 Knockout Reduces Cellular Proliferation, Differentiation and Bone Nodule Formation in Vitro. In order to clarify the mechanisms through which FMN2 functions, especially in osteoblasts, we determined in vitro cellular proliferation, differentiation and bone formation for the FMN2 KO and WT control mice using primary cell cultures from calvarial osteoblasts. Cellular proliferation as measured by BrdU incorporation into newly synthesized DNA of the osteoblasts of the KO mice showed a significant 37% reduction compared to that of the WT control mice (**Figure 6**). The alkaline phosphatase (ALP) activity, a measure of cellular differentiation and bone formation, was also significantly reduced by over 20%. Similarly, mineralized bone nodule formation assays found that the KO calvarial osteoblasts had 25% less bone nodules in the culture compared to the WT osteoblasts. Consistent with these data, mesenchymal stem cells (MSC) isolated from femur's bone marrow of the KO mice exhibited a 55% reduction in ALP staining compared to the MSC of the WT mice (**Figure 7**).

FMN2 Knockout Changed Expression of Important Bone Genes in Osteoblasts. Out of 38,039 probes in the microarray, 613 probes were significantly differentially expressed between KO and WT in the calvarial osteoblasts based on t-Test of 6 slides ($P < 0.05$). Among these probes, 52 had a 1.5 fold change of either direction, with 14 down-regulated and 38 up-regulated. It is worthy to note that the most down regulated of the 14 genes (**Table 2**) was POSTN, a gene for the osteoblast specific factor 2. POSTN was identified in the mouse osteoblasts, and was proposed as a homophilic adhesion molecule in bone formation (15). The expression level of POSTN was almost six times higher than the average gene expression of the entire chip (**Table 2**). IGFBP5, with two probes, was another significant gene. The involvement of the insulin-like growth factor (IGF) and IGF binding proteins such as IGFBP5 in osteoblast differentiation and bone formation are well known (16). Other significant genes such as CRABP1, CCL8, TGFBI and EGFL6 are all signaling genes, and may also be involved in signaling during the osteoblast differentiation and bone formation. Genes encoding structural proteins among the significant genes included LRRC15, COL18A1, FBN1 and LUM, which may participate in the actin filament organization of the osteoblast cells. Finally, the expression changes for the selected genes observed by the whole genome microarray were also confirmed by real time RT-PCR.

DISCUSSION

Our findings demonstrate for the first time that knockout of FMN2 gene reduced overall body growth, which was caused in part by significant reductions in lean body mass and total body BMD but not fat content. DXA measurements revealed a significant reduction in areal (a)BMD of total body as well as femur and tibia but not vertebra. Since aBMD measurements by DXA are influenced by body size, we adjusted BMD by body weight, and found that the BMD differences

in the KO mice were lost after the adjustment. Consistent with the smaller body size, periosteal circumference of femur mid-diaphysis was also decreased significantly in the KO mice compared to the WT control mice. Furthermore, neither total volumetric (v)BMD nor cortical vBMD, measured by pQCT, was significantly different in the KO mice at this site. These data suggest that the decreased bone mass in the KO mice is primarily due to reduced skeletal size. In order to determine if disruption of FMN2 gene influences microarchitecture of trabecular bone, uCT analyses were performed at the femur directly beneath the growth plate. The data revealed significant reductions in trabecular bone volume as a consequence of decreased trabecular thickness in the KO mice.

As indicated, aBMD of lumbar vertebra which is rich in trabecular bone was not significantly different in the FMN2 KO mice. Consistent with our findings that disruption of FMN2 gene function induces site specific bone loss are the findings from quantitative trait loci (QTL) studies which demonstrate that genetic loci that regulate peak BMD are skeletal site dependent (17,18). Accordingly, the site specific differences in skeletal deficit have also been reported in published studies involving targeted disruption of genes in mice. For example, we found that mice with deletion of gulonolactone oxidase, an enzyme involved in vitamin C synthesis, exhibited similar severe reductions in BMD of femur and tibia but not vertebra (14) . In contrast, disruption of estrogen receptor beta increased cortical bone mineral content without influencing trabecular bone (19). In terms of mechanisms for site specific effects of FMN2 and other genes, it is possible that compensation by related family members of genes may be different in different skeletal sites. Alternatively, mechanisms that regulate peak bone development may vary, depending on skeletal site. Future studies are needed to understand why loss of FMN2 influenced trabecular bone loss in the femur but not in the vertebra.

Our findings on temporal changes in the skeletal parameters in the FMN2 KO versus control mice revealed that the aBMD of total body, femur and tibia were nearly identical for the two genotypes at 3 weeks of age, the end of prepubertal growth period. However, aBMD of femur and tibia of FMN2 KO mice were significantly lower compared to corresponding control mice at 6 weeks of age. These data suggested that FMN2 may be interacting with signaling pathways that are activated during prepubertal growth period to regulate peak bone mass. One of the important signaling pathways that is activated during pubertal growth period is GH/IGF pathway which has been shown be critical for bone mass accrual during this period. It remains to be determined whether FMN2 is involved in interacting with one or more components of GH/IGF signaling pathway to regulate peak bone mass.

The decreased bone size as reflected by smaller periosteal circumference in the FMN2 KO could be due to decreased periosteal bone formation and/or increased bone resorption. Our in vitro findings that osteoblasts derived from FMN2 KO mice exhibited decreased proliferation and differentiation potential compared to control mice are consistent with the idea that osteoblasts are the target cells of FMN2 action. Furthermore, our findings from uCT analyses of trabecular bone revealed a significant decrease in trabecular thickness which is a reflection of diminished osteoblast activity in the knockout mice. Consistent with the idea that osteoblasts are the major target cells of FMN2 action are the immunohistochemistry studies that showed higher FMN2 expression in cells of osteoblastic and chondrocytic lineage compared to osteoclasts (**Figure 6**) and real time RT-PCR studies using RNA extracted from in vitro cultures of osteoblasts and osteoclasts that revealed several-fold higher mRNA levels in osteoblasts compared to osteoclasts (data not shown). To confirm that the reduced bone formation is the primary cause for decreased

bone mass in FMN2 knockout mice, future histomorphometric studies need to be performed during the time window when the skeletal differences appear to manifest.

In terms of molecular mechanism for FMN2 action on osteoblasts, the well established function of FMN2 is to regulate actin assembly. Formins assemble non-branched actin filaments and modulate microtubule dynamics during cell division. Consistent with an important role for formin family members in cell proliferation, mammalian Diaphanous-related (mDia) formin levels were increased from G1 to S phase, remained elevated into mitosis, and forced expression of activated mDia yielded binucleated cells due to failed cytokinesis (20). Thus, our in vitro findings of decreased proliferation of osteoblasts derived from FMN2 KO mice could be explained on the basis of actin disassembly. Besides, cytoskeletal elements are critical for cell morphology and signal transduction, and are involved in may cellular processes including cell migration, differentiation and intracellular transport. Consistent with our in vitro data that osteoblasts derived from FMN2 KO exhibit impaired differentiation potential, it has been shown that dynamic cytoskeletal changes constitute an important intracellular signal that control cell differentiation. Two recent findings support our assumption that formin-induced actin assembly could play a role in regulating osteoblast differentiation. First, Higuchi et al. (21) have shown that treatment of MC3T3-E1 osteoblasts with cytochalasin-D, an actin polymerization interfering agent, modulated parameters of osteoblast differentiation. Second, treatment of osteoblasts with lysophosphatidic acid induced actin stress fiber accrual to promote 1, 25-dihyroxyvitamin D3-induced osteoblast maturation (22). Thus, formin-induced cytoskeletal organization could influence growth of the skeleton as well as other tissues by regulating a variety of cellular processes.

In order to identify the FMN2 downstream target genes that are affected by lack of FMN2, we performed a whole genome microarray analyses using RNA extracted from calvarial

osteoblasts of FMN2 KO and WT control mice. These studies revealed that the expression of a number of signaling genes (PSTN, IGFBP5, CRABP1, CCL8, TGFB1, EGFL6) and structural genes (LRRC15, COL18A1, FBN1 and LUM) were reduced in the skeletal tissues of FMN2 KO mice compared to control mice. Of interest are the POSTN, TGFB1 and IGFBP5, which are known to be involved in regulating bone formation. In addition, the expression levels of Cxcl2 and Cxcl12, members of chemokine family, known to be involved in regulating osteoclast functions are elevated in the KO osteoblasts. Furthermore, expression level of Smurf2, a SMAD specific E3 ubiquitin protein ligase 2, is also increased. Since Smurf2 is known to target SMAD, a key mediator of BMP signaling pathway, to ubiquitin mediated proteolytic degradation pathway, the increased levels of Smurf2 would impair BMP action and thereby reduce osteoblast differentiation. In terms of the mechanism by which FMN2 could regulate expression of genes, formins are recognized as being involved in activation of serum response factor (SRF), tying formins to transcriptional regulation (22). In this regard, mDia1 is known to regulate MyoD expression via SRF-dependent pathway (23). In our study, we found that the expression level of serum/glucocorticoid regulated kinase (Sgk) was increased significantly in the calvarial osteoblasts of FMN2 KO mice. The issue of increased Sgk expression is due to loss of SRF activity remains to be determined. Another mechanism for FMN2 regulation of gene expression is via signals generated by dynamic cytoskeletal changes caused by formin binding to cytoskeletal elements. Future studies to elucidate the signaling pathway for FMN2 action in bone cells are necessary to understand the mechanism for reduced bone accretion in the FMN2 KO mice.

Acknowledgments

We thank Dr. Philip Leder of Harvard Medical School Boston, MA for the breeding stock of FMN2 mice. This work was supported by the U.S. Army Medical Research Acquisition Activity

Assistance (DAMD17-03-2-0021). The US Army Medical Research Acquisition Activity, 820 Chandler Street, Fort Detrick, MD 21702-5014, is the awarding and administering acquisition office. The information contained in this publication does not necessarily reflect the position or the policy of the government, and no official endorsement should be inferred. All the work was performed in facilities provided by the Department of Veteran Affairs.

Legends:

Figure 1. Changes of bone and body parameters of the FMN2 knockout mice vs. the wild-type mice during development. Body weight (**a**), lean body mass (**b**), total body BMD (**c**), femur BMD (**d**), tibia BMD (**e**) and lumbar vertebra BMD (**f**) were determined by DXA at 3, 6, 9 and 12 weeks of age. N = 6 to 20 per group per time point. Significant differences at $P < 0.05$ as denoted by * between the knockout and wild-type at each time point were determined by t-Test.

Figure 2. Comparison of bone and body parameters of the FMN2 knockout mice to the wild-type mice at 12 weeks of age. Parameters were determined by DXA at 12 weeks of age. N = 6 to 20 per group for both knockout and wild-type control. Parameters (expressed as % of the WT control mice) were either unadjusted (**a**) or adjusted by body weight (**b**). Significant reductions at $P < 0.05$ as denoted by * between the knockout and the wild-type were determined by t-Test.

Figure 3. Comparison of femur bone parameters of the FMN2 knockout mice to the wild-type mice at 12 weeks of age. Parameters (expressed as % reduction compared to the WT control mice) were determined by pQCT for the femur at 12 weeks of age. N = 5 knockout, and N = 8 for wild-type. Significant reductions at $P < 0.05$ as denoted by * between the knockout and the wild-type were determined by t-Test.

Figure 4. Comparison of femur's trabecular structure bone of the FMN2 knockout mice to the wild-type mice at 12 weeks of age. The image was produced using Micro-Computed Tomography (μCT). For the detailed number of each trabecular bone parameter, please see **Table 1**.

Figure 5. Immunohistochemistry (IHC) analysis of the formin-2 expression in the dissected paw tissues of the MRL/MpJ mouse. FMN2 protein is strongly expressed in osteoblasts. Note that osteoblasts expressing FMN2 are present at both the periosteum (upper arrow) and the endosteum (lower arrow).

Figure 6. Osteoblast proliferation, ALP activity and bone nodule formation of the FMN2 knockout mice vs. the wild-type mice. Calvaria of 28-day old mice were used to obtain the osteoblasts. Significant differences at $P < 0.05$ as denoted by * between the knockout and the wild-type were determined by t-Test.

Figure 7. Mesenchymal stem cell (MSC) differentiation determined by ALP staining for the FMN2 knockout mice vs. the wild-type mice. MSC were obtained from bone marrow of the femur. MSC lacking the FMN2 wild-type allele from the knockout exhibited 55% less ALP staining compared to the wild-type ($P < 0.001$).

Reference:

1. Evangelista M, Zigmond S, Boone C 2003 Formins: signaling effectors for assembly and polarization of actin filaments. J Cell Sci **116**(Pt 13)**:**2603-11.
2. Peng J, Kitchen SM, West RA, Sigler R, Eisenmann KM, Alberts AS 2007 Myeloproliferative defects following targeting of the Drf1 gene encoding the mammalian diaphanous related formin mDia1. Cancer Res **67**(16)**:**7565-71.
3. Campbell JJ, Blain EJ, Chowdhury TT, Knight MM 2007 Loading alters actin dynamics and up-regulates cofilin gene expression in chondrocytes. Biochem Biophys Res Commun **361**(2)**:**329-34.
4. Han Y, Cowin SC, Schaffler MB, Weinbaum S 2004 Mechanotransduction and strain amplification in osteocyte cell processes. Proc Natl Acad Sci U S A **101**(47)**:**16689-94.
5. Zhou F, Leder P, Zuniga A, Dettenhofer M 2009 Formin1 disruption confers oligodactylism and alters Bmp signaling. Hum Mol Genet.
6. Zuniga A, Michos O, Spitz F, Haramis AP, Panman L, Galli A, Vintersten K, Klasen C, Mansfield W, Kuc S, Duboule D, Dono R, Zeller R 2004 Mouse limb deformity mutations disrupt a global control region within the large regulatory landscape required for Gremlin expression. Genes Dev **18**(13)**:**1553-64.
7. Woychik RP, Maas RL, Zeller R, Vogt TF, Leder P 1990 'Formins': proteins deduced from the alternative transcripts of the limb deformity gene. Nature **346**(6287)**:**850-3.
8. Leader B, Lim H, Carabatsos MJ, Harrington A, Ecsedy J, Pellman D, Maas R, Leder P 2002 Formin-2, polyploidy, hypofertility and positioning of the meiotic spindle in mouse oocytes. Nat Cell Biol **4**(12)**:**921-8.
9. Dumont J, Million K, Sunderland K, Rassinier P, Lim H, Leader B, Verlhac MH 2007 Formin-2 is required for spindle migration and for the late steps of cytokinesis in mouse oocytes. Dev Biol **301**(1)**:**254-65.
10. Schuh M, Ellenberg J 2008 A new model for asymmetric spindle positioning in mouse oocytes. Curr Biol **18**(24)**:**1986-92.
11. Chadwick RB, Bu L, Yu H, Hu Y, Wergedal JE, Mohan S, Baylink DJ 2007 Digit tip regrowth and differential gene expression in MRL/Mpj, DBA/2, and C57BL/6 mice. Wound Repair Regen **15**(2)**:**275-84.
12. Miyakoshi N, Richman C, Kasukawa Y, Linkhart TA, Baylink DJ, Mohan S 2001 Evidence that IGF-binding protein-5 functions as a growth factor. J Clin Invest **107**(1)**:**73-81.
13. Dimai HP, Linkhart TA, Linkhart SG, Donahue LR, Beamer WG, Rosen CJ, Farley JR, Baylink DJ 1998 Alkaline phosphatase levels and osteoprogenitor cell numbers suggest bone formation may contribute to peak bone density differences between two inbred strains of mice. Bone **22**(3)**:**211-6.

14. Mohan S, Kapoor A, Singgih A, Zhang Z, Taylor T, Yu H, Chadwick RB, Chung YS, Donahue LR, Rosen C, Crawford GC, Wergedal J, Baylink DJ 2005 Spontaneous fractures in the mouse mutant sfx are caused by deletion of the gulonolactone oxidase gene, causing vitamin C deficiency. J Bone Miner Res **20**(9)**:**1597-610.
15. Takeshita S, Kikuno R, Tezuka K, Amann E 1993 Osteoblast-specific factor 2: cloning of a putative bone adhesion protein with homology with the insect protein fasciclin I. Biochem J **294 (Pt 1):**271-8.
16. Mukherjee A, Rotwein P 2009 Akt promotes BMP2-mediated osteoblast differentiation and bone development. J Cell Sci **122**(Pt 5)**:**716-26.
17. Beamer WG, Shultz KL, Donahue LR, Churchill GA, Sen S, Wergedal JR, Baylink DJ, Rosen CJ 2001 Quantitative trait loci for femoral and lumbar vertebral bone mineral density in C57BL/6J and C3H/HeJ inbred strains of mice. J Bone Miner Res **16**(7)**:**1195-206.
18. Bouxsein ML, Uchiyama T, Rosen CJ, Shultz KL, Donahue LR, Turner CH, Sen S, Churchill GA, Muller R, Beamer WG 2004 Mapping quantitative trait loci for vertebral trabecular bone volume fraction and microarchitecture in mice. J Bone Miner Res **19**(4)**:**587-99.
19. Windahl SH, Vidal O, Andersson G, Gustafsson JA, Ohlsson C 1999 Increased cortical bone mineral content but unchanged trabecular bone mineral density in female ERbeta(-/-) mice. J Clin Invest **104**(7)**:**895-901.
20. Deward AD, Alberts AS 2009 Ubiquitin-Mediated Degradation of the Formin mDia2 upon Completion of Cell Division. J Biol Chem.
21. Higuchi C, Nakamura N, Yoshikawa H, Itoh K 2009 Transient dynamic actin cytoskeletal change stimulates the osteoblastic differentiation. J Bone Miner Metab **27**(2)**:**158-67.
22. Mansell JP, Farrar D, Jones S, Nowghani M 2009 Cytoskeletal reorganisation, 1alpha,25-dihydroxy vitamin D3 and human MG63 osteoblast maturation. Mol Cell Endocrinol **305**(1-2)**:**38-46.
23. Gopinath SD, Narumiya S, Dhawan J 2007 The RhoA effector mDiaphanous regulates MyoD expression and cell cycle progression via SRF-dependent and SRF-independent pathways. J Cell Sci **120**(Pt 17):3086-98.

ELSEVIER

Bone 42 (2008) 388–395

BONE

www.elsevier.com/locate/bone

A chemical mutagenesis screen to identify modifier genes that interact with growth hormone and TGF-β signaling pathways

Subburaman Mohan [a,b], David J. Baylink [b], Apurva K. Srivastava [a,b,*]

[a] *Musculoskeletal Disease Center, Loma Linda VA Health Care Systems, Loma Linda, CA 92357, USA*
[b] *Department of Medicine, Loma Linda University, Loma Linda, CA 92354, USA*

Received 9 May 2007; revised 1 October 2007; accepted 12 October 2007
Available online 28 October 2007

Abstract

We describe a phenotype-driven mutagenesis screen in which mice carrying a targeted mutation are bred with ENU-treated males in order to provide a sensitized system for detecting dominant modifier mutations. The presence of initial mutation renders the screening system more responsive to subtle changes in modifier genes that would not be penetrant in an otherwise wild type background. We utilized two mutant mouse models: 1) mice carrying a mutation in growth hormone releasing hormone receptor (*Ghrhr*) (denoted 'lit' allele, $Ghrhr^{lit}$), which results in GH deficiency; and 2) mice lacking *Smad2* gene, a signal transducer for TGF-β, an important bone growth factor. The $Smad2^{-/-}$ mice are lethal and $Ghrhr^{lit/lit}$ mice are dwarf, but both $Smad2^{+/-}$ and $Ghrhr^{lit/+}$ mice exhibit normal growth. We injected 6–7 weeks old C57BL/6J male mice with ENU (100 mg/kg dose) and bred them with $Ghrhr^{lit/+}$ and $Smad2^{+/-}$ mice. The F1 mice with $Ghrhr^{lit/+}$ or $Smad2^{+/-}$ genotype were screened for growth and skeletal phenotypes. An outlier was identified as >3 SD units different from wild type control (n=20–30). We screened about 100 F1 mice with $Ghrhr^{lit/+}$ and $Smad2^{+/-}$ genotypes and identified nine outliers. A backcross established heritability of three mutant lines in multiple generations. Among the phenotypic deviants, we have identified a mutant mouse with 30–40% reduced bone size. The magnitude of the bone size phenotype was amplified by the presence of one copy of the disrupted *Ghrhr* gene as determined by the 2-way ANOVA ($p<0.02$ for interaction). Thus, a new mouse model has been established to identify a gene that interacts with GH signaling to regulate bone size. In addition, the sensitized screen also demonstrated higher recovery of skeletal phenotypes as compared to that obtained in the classical ENU screen in wild type mice. The discovery of mutants in a selected pathway will provide a valuable tool to not only to discover novel genes involved in a particular process but will also prove useful for the elucidation of the biology of that process.

Keywords: *N*-ethyl-*N*-nitrosourea; Modifier genetic screen; *Ghrhr*; *Smad2*; Bone size

Introduction

Phenotype-driven *N*-ethyl-*N*-nitrosourea (ENU) mutagenesis has been used as a powerful tool for the establishment of mutant mouse lines that model diseases and for the elucidation of protein function [1–3]. Several recent studies have demonstrated usefulness of this phenotype-driven approach to identify genes that affect important disease phenotypes [4–10]. Earlier, we demonstrated the feasibility of a phenotype-driven *N*-ethylnitrosourea (ENU) mutagenesis approach to isolate mutations affecting skeletal tissues for gene function studies [9]. This approach produced bone size and bone density mutants that were mapped to novel loci [8]. In this study, we describe a new approach, namely sensitized ENU screen, to identify modifier genes. In this approach the ENU mutations are created in mouse strains in which genes that have been previously implicated to play a critical role in the development and maintenance of musculoskeletal tissues have been mutated or knocked-out (KO). The presence of initial (or targeted) mutation renders the screening system highly sensitive to small changes that would be too small to be detected in an otherwise wild type (WT) background. The genes identified in the 'sensitized screen' are often modifier genes; their effects are subtle and hard to detect in commonly employed genetic screens. A similar approach has been used in *Drosophila* to

* Corresponding author. Musculoskeletal Disease Center (151), Loma Linda VA Healthcare Systems, 11201 Benton Street, Loma Linda, CA 92357, USA. Fax: +1 909 796 1680.
E-mail address: apurva.srivastava@med.va.gov (A.K. Srivastava).

8756-3282/$ - see front matter © 2007 Elsevier Inc. All rights reserved.
doi:10.1016/j.bone.2007.10.014

identify novel mutant phenotypes [11–13]. For example, mutations in a Notch (a receptor for cell–cell interaction mechanism in many metazoan developing tissues) signaling pathway have been used to sensitize mutations in genes regulating many unknown components in bristle development in *Drosophila* [11]. More recently, the sensitized screens have been applied to mouse models with successful identification of mutants with diabetes and behavioral phenotypes [14–19].

To accomplish the sensitized screen we utilized two mutant mouse models with deficiencies in the growth hormone (GH) [20] and transforming growth factor-beta (TGF-β) pathway [21], both of which are critical for the normal development and maintenance of musculoskeletal tissues. To study genes that interact with the GH pathway, we used a 'little' mouse strain that has a naturally occurring mutation in growth hormone releasing hormone receptor (*Ghrhr*) [20,22,23]. The *Ghrhr* mutant mouse is a spontaneous dwarf mouse strain with an autosomal recessive GH deficiency caused by a missense mutation (D60→G) in the extracellular domain of the *Ghrhr* that impairs the ability of the receptor to bind to *Ghrh* [23]. Mice that are homozygous for missense mutation ($Ghrhr^{lit/lit}$) have reduced GH secretion, impaired GH–IGF-I axis, and a severe deficiency in bone mass and size [20].

The second mouse model that we employed in the sensitized screen lacks mothers against decapentaplegic homolog 2 (*Smad2*), signal transducer for TGF-β [24–26]. The $Smad2^{-/-}$ mice are lethal [27], but the $Smad2^{+/-}$ mice exhibit normal growth. It is now fairly well established that TGF-β, like GH, plays a critical role in both bone development and the pathogenesis of bone loss [25,26]. The biological effects of TGF-β in osteoblasts are known to be mediated by phosphorylation of *Smad2/3*, which associates with *Smad4* to cause transcriptional activation of genes in osteoblasts and other cell types [21]. Furthermore, *Smad2* has also been shown to be involved in mediating the effects of activins, which are also known to regulate osteoblasts. Thus, inactivation of *Smad2* will disrupt the actions of various forms of TGF-β and also activins [25]. In this study, we describe our findings from the sensitized mutagenesis screen using mice deficient in GH and TGF-β actions.

Materials and methods

ENU mutagenesis

All animal protocols used in this study had prior approval of the Animal Studies Sub-committee of this research institution. Male (5–6 weeks old) C57BL/6J (B6) and *Ghrhr* mutant ($Ghrhr^{lit/lit}$ and $Ghrhr^{lit/+}$) mice were purchased from The Jackson Laboratory (Bar Harbor, ME). The $Ghrhr^{lit/lit}$ and $Ghrhr^{lit/+}$ are in 100% C57BL/6J genetic background. The heterozygous $Smad2^{+/-}$ knock out mice were a generous gift from our collaborator [27]. The $Smad2^{+/-}$ mice were generated in a mixed genetic background of 129/Svev and NIH Black Swiss mice and subsequently backcrossed to C57BL/6J strain of mice. All mice were housed on a 12-hour light/dark cycle, fed a standard rodent diet and water and allowed to acclimatize for two weeks prior to any manipulation. The mice were bred in our facility to produce additional pups for this study. Male B6 mice were injected with 3×100 mg/kg dose of ENU as described previously [9] and subsequently bred with $Ghrhr^{lit/+}$ and $Smad2^{+/-}$ heterozygous females. Each of the ENU-treated B6 males was mated with 2–3 8–10 weeks old females to obtain F1 progeny.

Generation of F1 mice for sensitized screen and phenotype screening

The F1 offspring were screened at 10 weeks through a series of tests, including total body areal bone density (BMD) measurements using PIXImus (Lunar Corporation, Madison, WI) and volumetric BMD pQCT (xCT Research M, Norland Medical System, Fort Atkinson, WI). Geometrical parameters such as periosteal perimeter, endosteal circumference, and bone cross-sectional area were measured by in-vivo pQCT as described previously [8,9]. Bone size parameters were normalized with body weight [9]. Phenotypic variants were defined as F1 animals showing at least one parameter differing three standard deviations from the mean of control mice, *i.e.*, showing a *Z*-score of $>+3$ or <-3. To identify phenotypic variants, we collected normative data from several batches of control mice ($n=30$–40). If a phenotypic deviant was identified in the 10-week screening, measurements were repeated to confirm the phenotype when mice are 16 weeks old. Once a phenotype was confirmed in the 16-week repeat testing, it was bred with $Ghrhr^{lit/+}$ or $Smad2^{+/-}$ heterozygous male/female mice to determine whether their abnormality is inheritable.

PCR based genotyping of F1 mice for Ghrhr and Smad2 mutation

DNA from the F1 progeny was analyzed for $Ghrhr^{lit/+}$ and $Smad2^{+/-}$ genotypes by PCR based assays. To identify the mutation in $Ghrhr^{lit/+}$ mice, we developed a single nucleotide polymorphism (SNP) assay using primers that amplify a region of *Ghrhr* gene that harbors A→G mutation at base number 112. The DNA was extracted from mouse tails, the *Ghrhr* gene was amplified using a primer pair — 5′-CCT TCA GCA CTG CCA TTC AG-3′ and 5′-CAG GGG AGA GAG ACC CAC TG-3. Two probes, one for $Ghrhr^{+/+}$ (ACC TGG GAT GGG CTG CTG TG-BHQ) and one for $Ghrhr^{lit/lit}$ mice (ACC TGG GGT GGG CTG CTG T-BHQ) were used for 5′-nuclease assay. The ABI Prism 7900 Sequence Detection System (SDS) was used to detect how much of each dye is reporting in each sample and results (mutant dye vs wild type dye) were presented in a graph form. DNA from the WT B6 and $Ghrhr^{lit/lit}$ mice, and a non-template control (NTC) were used as controls for each genotyping assay.

To genotype $Smad2^{+/-}$ mice we used two primer pairs (5′-CAT GAA TAC TAC GAC GGA GG-3′ 5′-GGA CCA GAC TCA CTA GTT CA-3′ 150 bp, and 5′-CAT GAA TAC TAC GAC GGA GG-3′ 5′-CTC CTT GAT GGA TGA ACT TC-3′ 300 bp) to amplify WT copy of the *Smad2* gene and one primer pair (5′-AGA CAA TCG GCT GCT CTG AT-3′ and 5′-CAA TAG CAG CCA GTC CCT TC-3′ 203 bp) to amplify the neomycin cassette inserted in place of *Smad2* gene (a 2.5-kb deletion removed three exons in the 3-terminus of the gene). The WT copy of *Smad2* gene was used as control. The PCR products were separated on 6% polyacrylamide gel, stained with ethidium bromide and visualized by Chemilmager 4400 Low Light Imaging system.

Baseline data on control animals

We used population based reference values for skeletal phenotypes to identify outlier mutant mice. Male and female WT B6, $Ghrhr^{lit/+}$, $Ghrhr^{lit/lit}$, and $Smad2^{+/-}$ mice were bred to generate the control mice. All progeny produced from such breeding were genotyped for the presence of $Ghrhr^{lit/+}$ or $Smad2^{+/-}$ alleles. Blood collection, DEXA, and pQCT were performed when animals are 10 weeks and 16 weeks of age (age varied by ±2 days).

Backcross of selected phenotypic deviants to confirm heritable mutations

Selected mice were backcrossed with 3–4 $Ghrhr^{lit/+}$ or $Smad2^{+/-}$ mice. The mutant phenotypes were assessed in a minimum of 20 backcross progeny. If the mutant phenotype was inherited in a dominant fashion, then 50% of the mice heterozygous for the sensitizing mutation were expected to express the abnormal phenotype.

Statistical analyses

The total body bone areas obtained from DEXA were normalized for body weight as described earlier [9]. The *Z*-scores were calculated using the formula (with bone area as an example): *Z*-score=(Bone area of mutant mice−Mean bone area of control mice)/SD of bone area of control mice ($n=40$). The

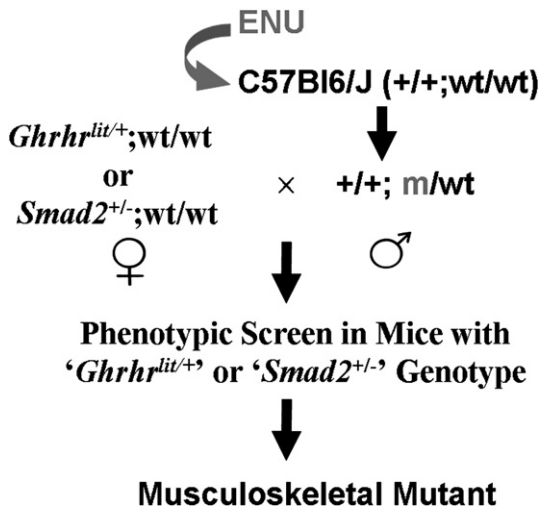

Fig. 1. Design of the ENU screen to identify modifier mutations that interact with the GH and TGF-β signaling pathways. To identify modifiers, we used a growth hormone releasing hormone receptor (*Ghrhr*) mutant mice (mutation denoted by 'lit' allele) and mothers against decapentaplegic homolog 2 (*Smad2*) knock out heterozygous mice (denoted by $Smad2^{+/-}$ allele). The ENU injected wild type C57BL/6J males were bred with $Ghrhr^{lit/+}$ and $Smad2^{+/-}$ females. The F1 progeny with $Ghrhr^{lit/+}$ and $Smad2^{+/-}$ genotypes were candidate for modifier mutations. For clarity, the wild type alleles are denoted as two separate symbols '+' and 'wt' for *Ghrhr* or *Smad2* locus and ENU mutation is denoted as 'm' locus, respectively.

statistical significance of the differences between groups was determined by unpaired TTEST or by 1-way ANOVA as appropriate. The interaction between phenotype and genotype variables was calculated using a 2-way ANOVA, using phenotype and genotype as variables, to indicate that the genetic background allele had significant effects on ENU mutant phenotype. A p-value of <0.05 was considered for significant interactions.

Results

Mice generated and screened

The design of the sensitized or modifier screen is shown in Fig. 1. We generated 228 mice by breeding the ENU injected males with $Ghrhr^{lit/+}$ and $Smad2^{+/-}$ female mice. Out of the 228 F1 mice, 44 mice carried $Ghrhr^{lit/+}$ genotype and 61 carried $Smad2^{+/-}$ genotype. Table 1 shows the number of mice generated, screened for various phenotypes, abnormal phenotypes, and mice introduced into inheritance testing. Selected screen results are shown in Fig. 2, which also includes nine outlier mice that were confirmed in 16-week repeat testing of the F1 mice (details of the 16-week data not shown). Six phenotypic

Table 1
Number of mice screened for musculoskeletal and growth related phenotypes in the sensitized ENU screen

Procedure	Number of $Ghrhr^{lit/+}$ mice	Number of $Smad2^{+/-}$ mice
Sensitized ENU mice screened for dominant mode of inheritance (F1)	44 [a]	61 [a]
Abnormal phenotypes identified	6	3
Phenotypes introduced into backcross	6	3
Mutant phenotypes confirmed in backcross	1	2

[a] The total number of mice produced in the screen was 228 including mice with $Ghrhr^{+/+}$ and $Smad2^{+/+}$ genotypes. In addition, several mice died before the screen.

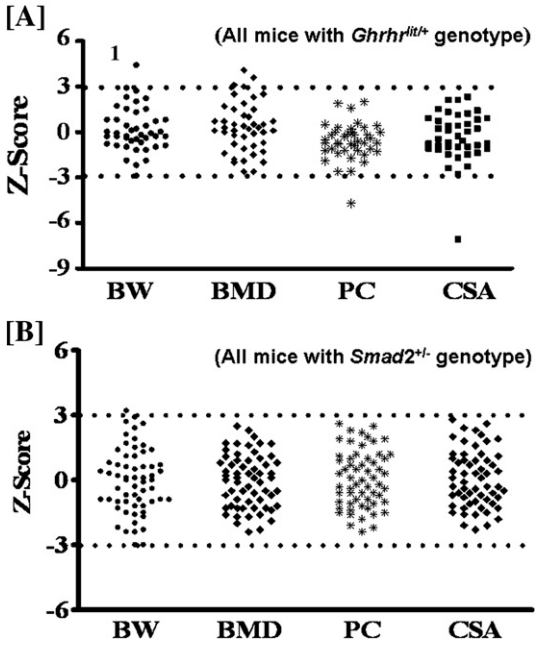

Fig. 2. Representative phenotype data for the sensitized screen in $Ghrhr^{lit/+}$ and $Smad2^{+/-}$ background. Bone density and bone size phenotypes are shown as *Z*-score, which indicate differences in a phenotype in terms of SD units as compared to control mice (in this case, $Ghrhr^{lit/+}$ and $Smad2^{+/-}$ mice). The broken horizontal lines indicate our cut-off levels for identifying outlier mice. Data points outside 3 SD units potentially represent potential phenotypic deviants. Several phenotypic deviants were backcrossed with control mice for confirmation of inheritable mutation. BW = Body weight, BMD = Total body bone mineral density, PC = Periosteal circumference, CSA = Cross-sectional area, EC = Endosteal circumference.

deviants were in $Ghrhr^{lit/+}$ genetic background and three phenotypic deviants were in $Smad2^{+/-}$ genetic background. The phenotypes of these mice ranged from high body weight and high total body BMD (*Z*-score +3 to +5) to low body weight and low total BMD (*Z*-score −3 to −5). Although low body

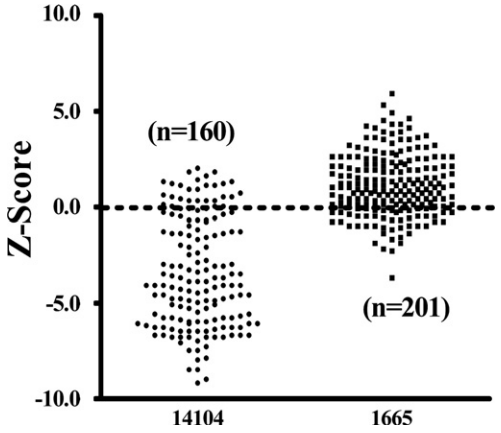

Fig. 3. Phenotype data for two backcrossed mutant lines. The *x*-axis shows the ID of the two lines that were successfully backcrossed to produce several litters. The *y*-axis shows phenotype data converted to *Z*-score. Line 14104 was produced in GH deficient background and cross-sectional area of midshaft tibia is shown as mutant phenotype. Line 1665 was produced in $Smad2^{+/-}$ background and total body bone density phenotype was shown as *Z*-score. Each data point represents one backcross mouse. All mice produced in the backcross, including non-affected littermates (>50%), are shown for each line.

weight and BMD were anticipated because both GH and TGF-β pathways are involved in development and ENU mutagenesis creates mostly hypomorphic mutations, high body weight and BMD was unexpected and it represents hypermorphic mutation.

Backcross of phenotypic deviants

Nine F1 deviants were backcrossed for testing the co-inheritance of the phenotype with the disrupted gene. Six phenotypic deviants were backcrossed to *Ghrhr*$^{lit/+}$ mice and three deviants were backcrossed to *Smad2*$^{+/-}$ mice. We were unable to successfully generate an adequate number of N2 mice for five phenotypic deviant mice because the F1 animals were sterile or died before the screen was finished and one variant phenotype was not transmitted. Heritability of at least three mutants was confirmed in two generation of breeding with WT *Ghrhr*$^{lit/+}$ or *Smad2*$^{+/-}$ mice as shown in Fig. 3 and Table 2. The two deviants confirmed in *Smad2*$^{+/-}$ genetic background were shown to be independent of the disruption of the *Smad2* allele.

Phenotypes of backcrossed mutants

Mutant 14104

The mutant male mouse, named 14104, was identified in the *Ghrhr*$^{lit/+}$ genetic background. The original 14104 mutant mouse was bred with several *Ghrhr*$^{lit/+}$ females to produce affected progeny, which have been subsequently bred with WT B6 or *Ghrhr*$^{lit/+}$ mice for five generations and data from more than 150 mice have been analyzed. Approximately 50% of the progeny were classified as affected, which is similar to the predicted number of progeny for an autosomal dominant mutation (details not shown). The 14104 mutant mice produced after five generations of breeding with WT mice still maintained its −3 *Z*-score phenotypic difference, indicating that mutation is stable. The body weights of the 14104 mice were 6–13% lower as compared to the non-affected littermates (Fig. 4). However, the body weight adjusted bone size phenotype was 30% lower ($p<0.001$) at 16-week age. The average periosteal circumference and cross-sectional area (CSA) of midshaft tibia and femurs of the 10–12 weeks old 14104 mice ($n=34$–74) were

Table 2
Phenotypes of mutant progeny confirmed in backcross

ID	Genotype	Major phenotype	*Z*-score for main phenotype [a]	% difference from control mice
14104	*Ghrhr*$^{lit/+}$	Decreased bone cross sectional area (and increased volumetric bone density)	>−4	36–37
1665	*Smad2*$^{+/-}$	Increased total body bone density (excluding skull area)	2 to 3	12–14
2195	*Smad2*$^{+/-}$	Decreased total body bone area (and bone mineral content)	>−3	10–13

[a] Since *Smad2*$^{+/-}$ mice were from mixed genetic background phenotype comparisons were made with control littermates.

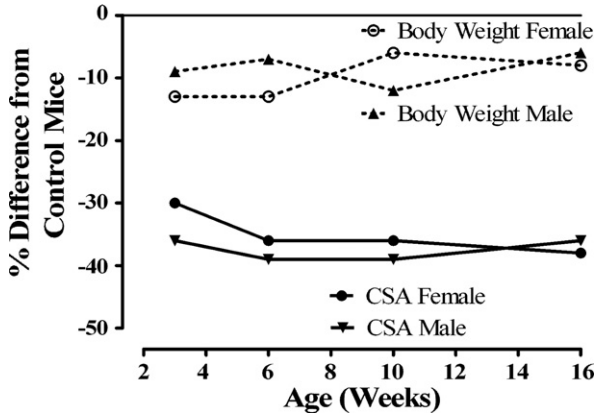

Fig. 4. Longitudinal analysis of body weight and bone size phenotypes in mice from mutant Line 14104. The data on *x*-axis shows age of the progeny generated from the 14104 mutant mice and data on *y*-axis shows percent difference in phenotypes as compared to non-affected littermates at same age. The body weight of mutant mice was 6–13% lower as compared to non-affected littermates, whereas, the cross-sectional area (CSA) was 30–40% decreased ($p<0.001$) in mutant mice. These data show that changes in bone size were significantly larger than those in body weight (number of mice for various groups were 6–22). To simplify the figure, data from mice with genotype *Ghrhr*$^{lit/+}$ were used even though mice with *Ghrhr*$^{+/+}$ genotypes were also affected.

15–20% and 30–40% lower, respectively, in affected mice as compared to control littermates (which were comparable to *Ghrhr*$^{lit/+}$ mice). The mean *Z*-score calculated for CSA for affected female 14104 mice and non-affected littermates were −5.7±0.8 and −0.2±0.9, respectively. Interestingly, femurs and tibia from the 14104 mutant mice showed 40–50% reduced endosteal circumference in both male and female mice as compared to non-affected littermates (Table 3). Due to the decrease in endosteal circumference, the cortical thickness of midshaft tibia and femur were not substantially decreased relative to bone size. Data from excised femur and tibia from the 12-week old 14104 mice and the non-affected littermate controls is shown in Fig. 5. Although the mutation was originally detected in the *Ghrhr*$^{lit/+}$ genotype, data from backcrossed progeny showed that the bone size phenotype is well expressed in WT B6 genetic background. The magnitude of bone size phenotype was significantly influenced by the presence of 'lit' allele as indicated by Post-Hoc analysis ($p<0.02$) using two-way ANOVA (Fig. 6). Since mutation was expressed in a GH deficient environment, we measured the IGF-I levels in the serum of the 14104 mice and non-affected littermates. The IGF-I levels were not significantly different in the 14104 mice (mean±SD, 250±93 ng/ml) as compared to control littermates (mean±SD, 236±93 ng/ml). This may indicate that the mutant gene, though acting through interaction with GH pathway, may not involve deficiency in IGF-I circulating levels. The bone formation marker osteocalcin was 20% lower ($p=0.021$) in 14104 mice (131±59 ng/ml) as compared to normal littermates (163±81 ng/ml), which could indicate an overall decrease in bone formation.

The 14104 mutation is inherited as autosomal dominant trait. To generate homozygous mutants, we intercrossed heterozygous (affected) male and female 14104 mice. The mean periosteal circumference in 3–4 weeks old affected mice [mean± SD, male 2.83±0.10 ($n=3$) and female 2.79±0.15 ($n=4$)] from

Table 3
Percent difference in bone size phenotype measured by in-vivo pQCT at midshaft tibia of 14104 mice and normal littermates

Age (weeks)	Sex	Mutant (14104)[a]			Control (non-affected littermates)[a]		
		No. of mice	Periosteal circumference[b] (mm)	Endosteal circumference[b] (mm)	No. of mice	Periosteal circumference (mm)	Endosteal circumference (mm)
3	Male	$n=45$	2.60±0.16	1.32±0.15	$n=65$	3.06±0.18	2.03±0.18
	Female	$n=37$	2.56±0.12	1.26±0.16	$n=62$	3.08±0.21	2.08±0.22
6	Male	$n=40$	3.12±0.16	1.40±0.14	$n=46$	3.86±0.21	2.03±0.18
	Female	$n=29$	2.97±0.16	1.27±0.15	$n=41$	3.72±0.22	2.13±0.15
10	Male	$n=39$	2.49±0.23	1.41±0.14	$n=39$	4.38±0.19	2.26±0.12
	Female	$n=32$	3.21±0.20	1.22±0.17	$n=35$	4.06±0.18	2.13±0.14
16	Male	$n=8$	3.68±0.23	1.37±0.15	$n=8$	4.77±0.26	2.35±0.12
	Female	$n=15$	3.34±0.10	1.00±0.18	$n=7$	4.22±0.11	2.15±0.06

[a] Data includes mice with both $Ghrhr^{+/+}$ and $Ghrhr^{lit/+}$ genotypes.
[b] The p-values for differences in both periosteal and endosteal circumference as compared to control mice were $p<0.01$ for all data points. Data are shown as mean±SD.

intercross was similar to the mice heterozygous for mutant locus (data shown in Table 3). However, our interpretation of the phenotypic affects of mutation in homozygous condition is provisional because of the absence of genotype information.

Mutant 1665

Mutant male mouse 1665 was identified in the $Smad2^{+/-}$ genetic background. The 1665 phenotypic deviant was backcrossed with $Smad2^{+/-}$ mice to produce 201 progeny. Since $Smad2^{+/-}$ mice had mixed genetic background (129S6/SvEv-Tac×C57BL/6J), phenotype comparisons were also made with control littermates. Although the original 1665 mouse had >3 SD difference from control mice but the backcrossed progeny showed a wide range and affected progeny was classified as those with >2 SD difference in bone density. Based on bone density phenotype, approximately 33% of the backcrossed mice were classified as phenotypic deviants. The phenotypic deviants had 18–20% ($p<0.001$) high body weight and 12–14% ($p<0.001$) higher total body bone density measured by DEXA, as compared to control $Smad2^{+/-}$ mice. The body weight adjusted bone density was 4–7% higher ($p<0.01$). The lean body mass was increased by 17% in both male and female mice. The genotyping of 1665 progeny from backcross revealed that mutation is inherited in WT genetic background with no statistically significant interaction effect of $Smad2^{+/-}$ genotype as shown in Fig. 7A. Based on overall phenotype data, the mutant mouse has a high growth phenotype with increased bone density.

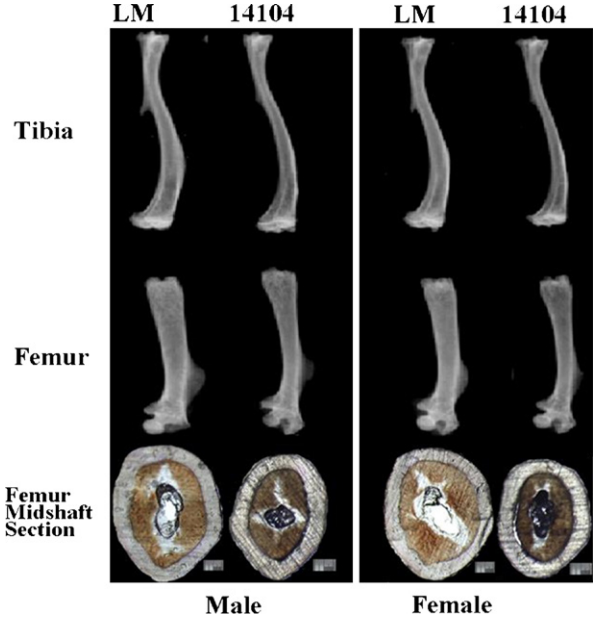

Fig. 5. Bone size phenotype of a mutant identified in sensitized screen involving GH deficient $Ghrhr^{lit}$ mice. The X-ray images of the tibia and femurs from the 10–12 weeks old 14104 mutant mice are shown along with their non-affected littermates (LM). The 14104 mice have significantly slender bones with 17–23% lower periosteal circumference and 30–40% lower cross-sectional area ($p<0.001$) as compared to the littermates. The bone length does not appear to be significantly affected by the mutation.

Mutant 2195

Backcross of mutant 2195 mice with $Smad2^{+/-}$ mice produced about 50 progeny, among them >50% progeny appeared to be affected. The phenotypic deviant mice had 6% low body weight and 10–13% ($p<0.001$) low total body bone area and bone mineral content measured by DEXA, as compared to

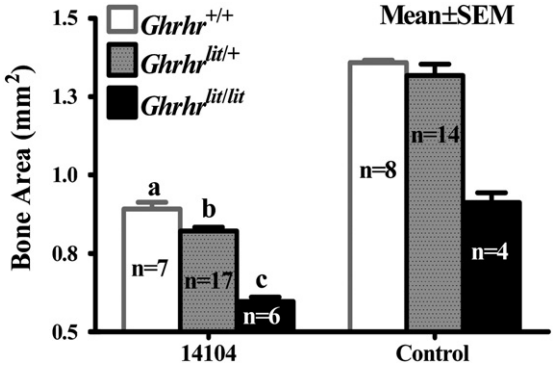

Fig. 6. Amplification of the magnitude of the mutant phenotype in the presence of one copy of disrupted *Ghrhr* gene ($Ghrhr^{lit/+}$). The cross-sectional area of midshaft tibia from 6-week old female 14104 mutant mice is shown in the presence of $Ghrhr^{+/+}$ or $Ghrhr^{lit/+}$ genotypes. Although the bone size phenotype is also expressed in $Ghrhr^{+/+}$ genotype, the magnitude of bone size phenotype is significantly influenced by the presence of "lit" allele as indicated by two-way ANOVA. Post-Hoc analysis by two-way ANOVA indicates that $Ghrhr^{lit/+}$ genotype significantly ($p<0.02$ for interaction) decreased the bone size. The differences in CSA between $Ghrhr^{+/+}$ and $Ghrhr^{lit/+}$ in control mice were not statistically significant. a = $p<0.001$ vs $Ghrhr^{+/+}$ and $Ghrhr^{lit/+}$ control and $p<0.05$ vs 14104 $Ghrhr^{lit/+}$ and $Ghrhr^{lit/lit}$ 14104 mice, b = $p<0.001$ vs all control mice, c = $p<0.001$ vs all other groups.

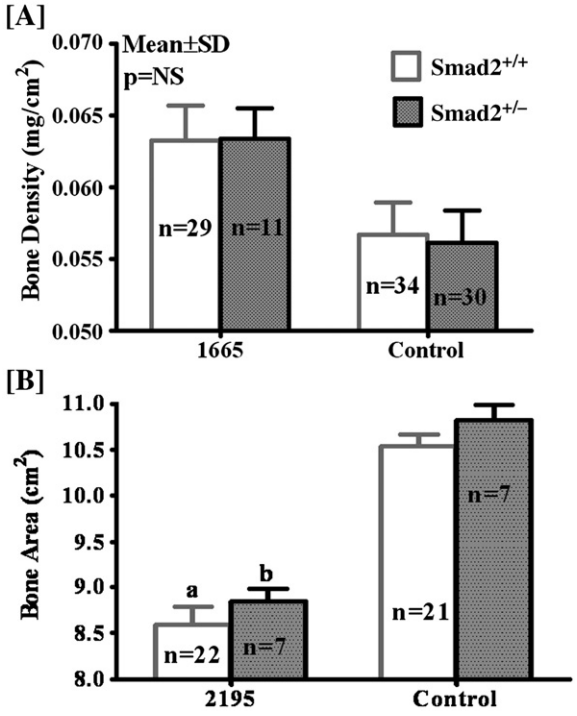

Fig. 7. Two dominant mutations where mutant phenotype was not influenced by the loss of one copy of *Smad2*$^{-/+}$ gene. (A) The total body bone density of 10-week old female mutant mice (ID 1665) is shown in the presence of WT (+/+) or '*Smad2*$^{+/-}$' alleles. (B) The total body bone area of 10-week old female mutant mice (ID 2195) is shown in the presence of *Smad2*$^{+/+}$ or *Smad2*$^{+/-}$ alleles. In both these lines, the mutant phenotype is expressed in both *Smad2*$^{+/+}$ and *Smad2*$^{+/-}$ genetic backgrounds. The mutant phenotype was not significantly influenced by the loss of *Smad2* allele as indicated by Post-Hoc analysis using two-way ANOVA (p=NS for interaction). a = $p<0.001$ vs control, b = $p<0.001$ vs control and $p>0.05$ vs 2195 mice with *Smad2*$^{+/-}$ genotype.

control *Smad2*$^{+/-}$ mice. The body weight adjusted bone density was not significantly different but body weight adjusted bone area was 9–11% ($p<0.001$) lower in 16-week old 2195 mutant mice as compared to control littermates. The 2195 mutant was also inherited in the WT genetic background with no statistically significant interaction effect of *Smad2*$^{+/-}$ genotype as shown in Fig. 7B.

Smad2 KO was produced in 129S6/SvEv and Black Swiss genetic background and then backcrossed to C57BL/6J mice. Therefore, progeny from both lines 1665 and 2195 also represent mixed genetic background.

Discussion

Modifiers of the GH and TGF-β signaling pathways need to be elucidated to explain all the biological functions and malfunctions in skeletal development. We have combined the forward and reverse genetics approaches as a way to identify either direct or indirect participants in the molecular network of these biological pathways. Our design is consistent with similar screens employed effectively in the fly and recently in the mouse models [14,15,18] except our design involved ENU mutagenesis in WT B6 males, which were subsequently bred with *Ghrhr*$^{lit/+}$ and *Smad2*$^{+/-}$ females to generate F1 animals. Previous screens employed direct mutagenesis of knock out males that are deficient in a key gene. Mutagenesis of heterozygous *Ghrhr*$^{lit/+}$ or *Smad2*$^{+/-}$ mice for the production of F1 animals was considered less efficient because of breeding deficiencies or mixed genetic background [28]. The rationale for screening the mutant in GH haploinsufficiency is based on the observation that mice carrying one copy of *Ghrhr*$^{lit/+}$ have significantly reduced IGF-I levels as compared to the WT levels of IGF-I in B6 mice [20,29–31]. This phenomenon is also evident in IGF-I knock out mice where reduced expression of IGF-I in *Igf1*$^{+/-}$ mice has a significant effect on prenatal and postnatal bone growth as compared to WT mice [20]. Thus, we anticipated that a reduced dosage of GH would be sufficient to sensitize the screening systems as compared to complete abrogation of GH levels, which causes significantly reduced fertility in *Ghrhr*$^{lit/lit}$ mice, thus, making it difficult to generate adequate number of mice for screening. Similarly, consistent with an important role for *Smad2* in mediating the effects of TGF-β family members, recent studies have shown that haploinsufficiency of *Smad2* altered TGF-β mediated tooth development [25]. The positive results of this study demonstrate that our study design was appropriate to identify dominant modifiers that affect skeletal phenotypes in the heterozygous conditions.

Our major interest towards identifying the modifiers of GH and TGF-β signaling pathways was in mutant lines that show co-inheritance of a phenotype with the disrupted *Ghrhr* or *Smad2* gene. However, our screen design also had probability for finding mutations in wild type animals. This probability is dependent upon the penetrance of the phenotype, genetic background of the mouse strains, and the number of animals screened. We observed nine phenotypic deviants in our modifier or sensitized screen. The magnitude and category (growth related) of phenotypes in these deviants indicated high probability of interacting (modifier) molecules. However, several of the phenotypic deviants identified in this study could not be confirmed because of reduced breeding performance that may be a consequence of reduced body weight, especially for mutant with disrupted *Ghrhr* gene [32]. Nevertheless, the 14104 mutant line identified and confirmed in this study showed significant (Fig. 3) interaction between bone size phenotype and the disrupted *Ghrhr* gene. This mutant line demonstrated 30–40% decrease in bone size, a considerably large effect size considering that mutation is caused by only partial disruption of a gene. The effect size of the 14104 mutation exceeds all published bone size QTL and mutations. Thus, we believe the 14104 strain represents mutation in a novel gene. Regarding interaction with GH, it is known that GH deficiency reduces periosteal bone formation and bone size [33,34]. In addition, several affecters such as androgen and estrogen can also affect periosteal circumference by GH-dependent and GH-independent mechanisms [34,35]. However, it is unclear how much these or other unknown factors regulate bone mineral acquisition independent of GH and its receptor. In this regard, identification of bone size phenotype, which is modulated by growth hormone deficiency, provides an opportunity to identify key signaling molecule in mediating GH actions on bone growth. Further analysis is required to investigate what kind of

interaction exists between the mutant gene and the GH signaling pathway.

Although two mutant lines have been confirmed in backcross using *Smad2*$^{+/-}$ mice, we have not yet found any musculoskeletal variant whose phenotype was dependent on the disruption of the *Smad2* locus. There are a number of potential explanations on why we could not detect a significant interaction between the mutant gene and the *Smad2* gene. 1. The mixed background strain used for creating the *Smad2* knock out [(129S6/SvEvTac×Swiss Black)×(C57BL/6J)] mice [27] could affect the variability in skeletal phenotypes, thus obscuring the power to detect interaction. 2. The number of mutant mice with *Smad2* genetic background were small (n=7–11) to detect interaction effects. 3. Interactors of *Smad2* were lethal because of the essential role of the *Smad2* in the embryonic development [27] or that recessive modifier screen may be required to detect variations in the skeletal phenotype. These data suggest a need to modify our protocol. To eliminate genetic background effects, lines 1665 and 2195 are being backcrossed with homogeneous B6 background to verify mutant effect.

In conclusion, we have established three mutant lines with the main focus on searching for modifiers of the GH and TGF-β signaling pathways. Of major interest is the novel mutant line (ID 14104) that might reveal new modifiers of the GH signaling pathway. Consequently, a new mouse model has been established to understand the role of GH signaling in the musculoskeletal system. The discovery of a mutant gene would prove useful for the elucidation of the biology of the processes by which GH regulates bone size and accretion of the cortical bone.

Acknowledgments

This work was supported by the Army Assistance Award No. DAMD 17-03-2-0021. The US Army Medical Research Acquisition Activity (Fort Detrick, MD) 21702-5014 is the awarding and administering acquisition office for the DAMD award. The information contained in this publication does not necessarily reflect the position or the policy of the Government, and no official endorsement should be inferred. All work was performed in facilities provided by the Department of Veterans Affairs. The authors would like to thank Dr. M. Weinstein for providing a breeding pair of *Smad2*$^{+/-}$ knock out mice and Darcie Nagel, TaMarrah Oliver, Cynthia Ganda, and Valerie Chest for their expert technical assistance.

References

[1] Nolan PM, Peters J, Vizor L, Striven M, Washbourne R, Hough T, et al. Implementation of a large-scale ENU mutagenesis program: towards increasing the mouse mutant resource. Mamm Genome 2000:500–6.
[2] O'Brien TP, Frankel WN. Moving forward with chemical mutagenesis in the mouse. J Physiol 2004:13–21.
[3] Justice MJ. Capitalizing on large-scale mouse mutagenesis screens. Nat Rev Genet 2000:109–15.
[4] Thaung C, West K, Clark BJ, McKie L, Morgan JE, Arnold K, et al. Novel ENU-induced eye mutations in the mouse: models for human eye disease. Human Molecular Genetics; 2002. p. 755–67. England.
[5] Speca DJ, Rabbee N, Chihara D, Speed TP, Peterson AS. A genetic screen for behavioral mutations that perturb dopaminergic homeostasis in mice. Genes Brain Behav 2006:19–28.
[6] Tchekneva EE, Rinchik EM, Polosukhina D, Davis LS, Kadkina V, Mohamed Y, et al. A sensitized screen of *N*-ethyl-*N*-nitrosourea-mutagenized mice identifies dominant mutants predisposed to diabetic nephropathy. J Am Soc Nephrol 2007:103–12.
[7] Ahituv N, Avraham KB. Mouse models for human deafness: current tools for new fashions. Trends Mol Med 2002;8(9):447–51.
[8] Srivastava AK, Kapur S, Mohan S, Yu H, Wergedal J, Baylink DJ. Identification of novel genetic loci for bone size and mechanosensitivity in an ENU mutant exhibiting decreased bone size. J Bone Miner Res 2005;20 (6):1041–50.
[9] Srivastava AK, Mohan S, Wergedal JE, Baylink DJ. A genomewide screening of N-ethyl-N-nitrosourea-mutagenized mice for musculoskeletal phenotypes. Bone 2003;33(2):179–91.
[10] Hoyne GF, Goodnow CC. The use of genomewide ENU mutagenesis screens to unravel complex mammalian traits: identifying genes that regulate organ-specific and systematic autoimmunity. Immunol Rev 2006;210: 27–39.
[11] Go MJ, Artavanis-Tsakonas S. A genetic screen for novel components of the notch signaling pathway during Drosophila bristle development. Genetics 1998;150(1):211–20.
[12] Carrera P, Abrell S, Kerber B, Walldorf U, Preiss A, Hoch M, et al. A modifier screen in the eye reveals control genes for Kruppel activity in the Drosophila embryo. Proc Natl Acad Sci U S A 1998;95(18):10779–84.
[13] Abrell S, Carrera P, Jackle H. A modifier screen of ectopic Kruppel activity identifies autosomal Drosophila chromosomal sites and genes required for normal eye developmant. Chromosoma 2000;109(5):334–42.
[14] Tchekneva EE, Rinchik EM, Polosukhina D, Davis LS, Kadkina V, Mohamed Y, et al. A sensitized screen of N-ethyl-N-nitrosourea-mutagenized mice identifies dominant mutants predisposed to diabetic nephropathy. J Am Soc Nephrol 2007;18(1):103–12.
[15] Rubio-Aliaga I, Soewarto D, Wagner S, Klaften M, Fuchs H, Kalaydjiev S, et al. A genetic screen for modifiers of the delta1-dependent notch signaling function in the mouse. Genetics 2007;175(3):1451–63.
[16] Howell GR, Shindo M, Murray S, Gridley T, Wilson LA, Schimenti JC. Mutation of a ubiquitously expressed mouse transmembrane protein (Tapt1) causes specific skeletal homeotic transformations. Genetics 2007;175(2):699–707.
[17] Inoue M, Sakuraba Y, Motegi H, Kubota N, Toki H, Matsui J, et al. A series of maturity onset diabetes of the young, type 2 (MODY2) mouse models moderated by a large-scale ENU mutagenesis program. Hum Mol Genet 2004;13(11):1147–57.
[18] Satterthwaite AB, Willis F, Kanchanastit P, Fruman D, Cantley LC, Helgason CD, et al. A sensitized genetic system for the analysis of murine B lymphocyte signal transduction pathways dependent on Bruton's tyrosine kinase. Proc Natl Acad Sci U S A 2000;97(12):6687–92.
[19] Godinho SI, Nolan PM. The role of mutagenesis in defining genes in behavior. Eur J Hum Genet 2006;14(6):651–9.
[20] Mohan S, Richman C, Guo R, Amaar Y, Donahue LR, Wergedal J, et al. Insulin-like growth factor regulates peak bone mineral density in mice by both growth hormone-dependent and -independent mechanisms. Endocrinology 2003;144(3):929–36.
[21] Attisano L, Wrana JL. Signal transduction by the TGF-beta superfamily. Science 2002;296(5573):1646–7.
[22] Donahue LR, Beamer WG. Growth hormone deficiency in 'little' mice results in aberrant body composition, reduced insulin-like growth factor-I and insulin-like growth factor-binding protein-3 (IGFBP-3), but does not affect IGFBP-2, -1 or -4. J Endocrinol 1993;136(1):91–104.
[23] Godfrey P, Rahal JO, Beamer WG, Copeland NG, Jenkins NA, Mayo KE. GHRH receptor of little mice contains a missense mutation in the extracellular domain that disrupts receptor function. Nat Genet 1993;4(3):227–32.
[24] Liu Y, Festing M, Thompson JC, Hester M, Rankin S, El-Hodiri HM, et al. Smad2 and Smad3 coordinately regulate craniofacial and endodermal development. Dev Biol 2004;270(2):411–26.
[25] Ferguson CA, Tucker AS, Heikinheimo K, Nomura M, Oh P, Li E, et al. The role of effectors of the activin signalling pathway, activin receptors IIA

and IIB, and SMAD2, in patterning of tooth development. Development 2001;128(22):4605–13.
[26] Zhou Y, Scolavino S, Funderburk SF, Ficociello LF, Zhang X, Klibanski A. Receptor internalization-independent activation of Smad2 in activin signaling. Mol Endocrinol 2004;18(7):1818–26.
[27] Weinstein M, Yang X, Li C, Xu X, Gotay J, Deng CX. Failure of egg cylinder elongation and mesoderm induction in mouse embryos lacking the tumor suppressor smad2. Proc Natl Acad Sci U S A 1998;95(16): 9378–83.
[28] Weber JS, Salinger A, Justice MJ. Optimal N-ethyl-N-nitrosourea (ENU) doses for inbred mouse strains. Genesis 2000;26(4):230–3.
[29] Kasukawa Y, Baylink DJ, Guo R, Mohan S. Evidence that sensitivity to growth hormone (GH) is growth period and tissue type dependent: studies in GH-deficient lit/lit mice. Endocrinology 2003;144(9):3950–7.
[30] Mohan S, Baylink DJ. Impaired skeletal growth in mice with haploinsufficiency of IGF-I: genetic evidence that differences in IGF-I expression could contribute to peak bone mineral density differences. J Endocrinol 2005:415–20.
[31] Walenkamp MJ, Karperien M, Pereira AM, Hilhorst-Hofstee Y, van Doorn J, Chen JW, et al. Homozygous and heterozygous expression of a novel insulin-like growth factor-I mutation. J Clin Endocrinol Metab 2005:2855–64.
[32] Chubb C. Biol Reprod 1987;37(3):564–9.
[33] Maheshwari HG, Bouillon R, Nijs J, Oganov VS, Bakulin AV, Baumann G. The impact of congenital, severe, untreated growth hormone (GH) deficiency on bone size and density in young adults: insights from genetic GH-releasing hormone receptor deficiency. J Clin Endocrinol Metab 2003: 2614–8.
[34] Zhang XZ, Kalu DN, Erbas B, Hopper JL, Seeman E. The effects of gonadectomy on bone size, mass, and volumetric density in growing rats are gender-, site-, and growth hormone-specific. J Bone Miner Res 1999:802–9.
[35] Lindberg MK, Vandenput L, Moverare Skrtic S, Vanderschueren D, Boonen S, Bouillon R, et al. Minerva Endocrinol 2005;30(1):15–25.

Available online at www.sciencedirect.com
SCIENCE DIRECT®
Biochemical and Biophysical Research Communications 319 (2004) 781–786
BBRC
www.elsevier.com/locate/ybbrc

HSV-1 amplicon-mediated transfer of 128-kb BMP-2 genomic locus stimulates osteoblast differentiation in vitro ☆

Weirong Xing, David Baylink, Chandrasekhar Kesavan, and Subburaman Mohan*

Musculoskeletal Disease Center, JL Pettis Memorial Veterans Administration Medical Center, Loma Linda, CA 92357, USA

Received 5 May 2004
Available online 28 May 2004

Abstract

In previous studies, we developed mouse genetic models and discovered genetic components of quantitative trait loci on mouse chromosomes that contribute to phenotypes such as bone size, bone density, and fracture healing. However, these regions contain dozens of genes in several overlapping bacterial artificial chromosomes (BACs) and are difficult to clone by physical cloning strategies. A feasible and efficient approach of identifying candidate genes is to transfer the genomic loci in BAC clones into mammalian cells for functional studies. In this study, we retrofitted a BAC construct into herpes simplex virus-1 amplicon and packaged it into an infectious BAC (iBAC) to test gene function in a cell-based system, using a 128-kb clone containing the complete bone morphogenetic protein-2 (BMP-2) gene. We transduced MC3T3-E1 cells with the iBAC bearing BMP-2 gene and examined transgene expression and function. Our results have demonstrated that an iBAC can efficiently deliver a BMP-2 genomic locus into preosteoblast cells and express functional BMP-2 protein, inducing a phenotype of cell differentiation, as indicated by an increase in alkaline phosphatase activity. Therefore, this experimental system provides a rapid, efficient cell-based model of high-throughput phenotypic screening to identify the BAC clones from physically mapped regions that are important for osteoblast differentiation. It also illustrates the potential of iBAC technology in functional testing of single nucleotide polymorphisms located in the distal promoter or/and intron regions responsible for low bone density.

Keywords: Osteoblast; HSV-1 amplicon; BMP-2; BAC; Gene transfer; Osteogenesis

Osteoporosis is a common disease characterized by an age-dependent decrease in bone mineral density (BMD) and a microarchitectural deterioration of bone tissue with a consequent increase in the risk of developing fragility fractures of the hip, spine, and other skeletal sites [1]. Although multiple environmental, nutritional, and hormonal factors influence the development of osteoporosis, it is clear that the major determinant for the disease is genetic control of BMD, particularly the achievement of peak bone mass at maturity, bone size and structure, and the subsequent rate of bone turnover [2–5]. Recently, genome-wide linkage analyses have revealed that the genetic components of quantitative trait locus (QTL) on human chromosomes 1q, 2p, 4p, 11q, and 13q are attributed to BMD [6–8], while the loci on chromosomes 17q and 19p are responsible for bone size [9]. However, none of the QTLs reported have actually met criteria for genome-wide significance for linkage, and the results are inconsistent due to the great variation between study groups and populations, as well as the possible involvement of different pathways. To localize chromosomal regions and subsequently identify the genes responsible for skeletal diseases, we have developed mouse genetic models and discovered QTLs on mouse chromosomes that contribute to phenotypes such as bone size, bone density, and fracture healing [10–12]. Subsequent analyses of the

☆ *Abbreviations:* BAC, bacterial artificial chromosomes; iBAC, infectious BAC; PAC, P1 artificial chromosomes; HSV-1, herpes simplex virus-1; ALP, alkaline phosphatase; BMP-2, bone morphogenetic protein-2; QTL, quantitative trait loci; MOI, multiplicity of infection; FACS, fluorescence-activated cell sorter; GFP, green fluorescent protein; EBV, Epstein–Barr virus; PCR, polymerase chain reaction.

* Corresponding author. Fax: 1-909-796-1680.
E-mail address: Subburaman.Mohan@med.va.gov (S. Mohan).

0006-291X/$ - see front matter © 2004 Elsevier Inc. All rights reserved.
doi:10.1016/j.bbrc.2004.05.053

congenic mice further confirmed and narrowed the genes of interest to a 3–12.5 centimorgan (cM) region in mouse chromosome 1 [13,14]. However, these regions contain dozens of genes and are still difficult to clone by time-consuming, expensive position-cloning strategies. However, a feasible and efficient approach for identifying candidate genes is to transfer the genomic loci of overlapping bacterial artificial chromosomes (BACs) or P1 artificial chromosomes (PACs) encompassing the QTL regions into bone cells in vitro for a high-throughput functional screening.

The delivery of large genomic DNA inserts of BACs or PACs into mammalian cells via chemical methods and non-viral vectors, although possible, renders a poor efficiency of gene transfer and requires the drug-selection and identification of stably integrated transformants for functional testing [15–17]. However, the recent advances in infectious BAC (iBAC) technology using the herpes simplex virus type 1 (HSV-1) amplicon in the gene therapy field have made it possible to deliver a genomic locus as large as 150-kb with a high transduction efficiency in most mammalian cells, including dividing and non-dividing cells in vitro and in vivo [18–21]. The improved delivery system of the HSV-1 amplicon also contains an EBNA-1 episomal cassette from the Epstein–Barr virus, (EBV) allowing long-term retention and high level of position-independent expression of BAC transgenes as mini-chromosomes in the host cells [20,21]. Therefore, the iBAC offers a rapid and simple method of BAC DNA transfer for functional genomic studies. This system also allows us to test the functional significance of the large number of gene-associated single nucleotide polymorphisms (SNP) located in the regions of the distal promoter or/and introns that could contribute to low bone density [22,23]. In this study, we chose a BAC clone bearing the bone morphogenetic protein-2 (BMP-2) locus and assembled the genomic DNA as an infectious virion as a model to test the genomic DNA transfer and function. Our results indicated that the iBAC could efficiently deliver a BMP-2 genomic locus and express functional protein promoting osteoblast differentiation.

Materials and methods

Vector constructs. The DNA constructs of pCTP-T, pEBHICP27, pEHHG, and fHSVΔ-pac, Δ-27, 0+ were described in detail elsewhere [20,21], and kindly provided by Dr. Yoshinaga Saeki (Massachusetts General Hospital, Harvard Medical School, MA). A BAC clone, RP23-302H4, containing a complete BMP-2 locus was purchased from Invitrogen Life Technologies (Carlsbad, CA).

Cell culture. Vero 2-2 cells (kindly provided by Dr. Rozanne Sandri-Goldin, University of California, Irvine, CA) were routinely maintained in Dulbecco's modified minimal essential medium (Invitrogen) with 10% fetal bovine serum, 100 U/ml penicillin, 100 μg/ml streptomycin, and G486 (500 μg/ml). MC3T3-E1 cells (ATCC, Manassas, VA) were propagated in alpha minimum essential medium (Invitrogen) supplemented with 10% calf serum, 100 U/ml penicillin, and 100 μg/ml streptomycin. The cells were cultured in a humidified 37 °C incubator with 5% CO_2.

Retrofitting of BAC clone. The retrofitting of BAC clone into HSV-1/EBV amplicons was carried out by Cre-mediated recombination in bacterial cells as described previously [21]. Briefly, an aliquot of 35 μl electro-competent cells containing BAC/BMP-2 (RP23-302H4) was mixed with 10 ng each of pEHHG and pCTP-T plasmid DNA, and the mixture was transferred into 0.1-cm gap width electroporation cuvette (Bio-Rad, Hercules, CA). After 5 min incubation on ice, the cells were electroporated with 25 μF at 1800 V using a Gene Pulser (Bio-Rad), then transferred into a 15-ml conical tube containing 500 μl SOC with 20 μg chlortetracycline (Sigma, St. Louis, MO), and incubated at 30 °C with rigorous shaking for 1 h. An aliquot of 100 μl of the bacterial culture was transferred into a new 15-ml tube containing 20 μg/ml chlortetracycline, 100 μg/ml ampicillin, and 20 μg/ml chloramphenicol in 900 μl SOC, and incubated at 30 °C with shaking for another 3 h. Subsequently, 50–100 μl of the bacterial culture was plated on LB plates containing 100 μg/ml ampicillin and 20 μg/ml chloramphenicol, and incubated overnight at 43 °C. DNA of individual clones was purified and verified by polymerase chain reaction (PCR) using specific primers to BMP-2 (forward: 5′-CCTTCGGAAGACGTCCTCAG and reverse: 5′-TCACTCGATTTCCCTCCAGT) and GFP (forward: 5′-TGCCACCTACGGCAAGCTGA and reverse: 5′-CCATGTGATCG CGCTTCTCG) to confirm the correct retrofitted BAC clone.

Packaging HSV-1 amplicon into virion. HSV-1 amplicon was packaged into infectious virion as described previously [21]. Briefly, Vero 2-2 cells (10^6) were plated in a 60-mm dish. After 18 h, the cells were co-transfected with 2.0 μg pHSV-BAC/BMP-2 or pEHHG, 0.2 μg pEBHICP27, and 2 μg fHSVΔ-pac, Δ-27, 0+ using LipofectAMINE Plus (Invitrogen) for 4 h. The cells were scraped into the supernatant 60 h post-infection, frozen and thawed once, sonicated for 1 min, and centrifuged at 3500 r.p.m. for 15 min. The supernatant was then concentrated through a 25% sucrose by ultracentrifuging, and the amplicon pellet was resuspended in Hanks' buffered salt solution. The purified HSV-1 amplicon was titered in Vero 2-2 cells by counting the number of GFP positive cells after 24 h infection. Typically, the titration of HSV-1 amplicon stocks was around 5×10^6–10^7 GFP transducing units/ml.

HSV-1 virion infection, Western blot and FACS analyses. MC3T3-E1 cells were plated in a 6-well plate at a density of 10^5/well. After 24 h, the cells were infected at a multiplicity of infection (MOI) of 5 with HSV-1 amplicon. After 6 h infection, the medium was removed, and fresh medium was added to the cells. The cells were lysed in a lysis buffer containing 50 mM Tris, pH 8.0, 150 mM NaCl, 0.1% SDS, 1% Triton X-100, and 1× Protease Inhibitor cocktail (Sigma) 24 h after infection. An aliquot of 60 μg cellular protein was electrophoresed on a 15% SDS–polyacrylamide gel and transferred to nitrocellulose. The membrane was incubated at 4 °C overnight in a buffer containing 5% dried skim milk, 150 mM NaCl, 50 mM Tris–HCl (pH 8.0), and 0.05% Tween 20. Immunoblotting was performed in the same buffer containing 0.2 μg/ml antibody against BMP-2 or GFP (Santa Cruz, CA) at room temperature for 1 h. Specific proteins were detected using appropriate secondary antibodies and ECL + plus Western blotting detection system (Amersham–Pharmacia Biotech UK Limited, Buckinghamshire, England). The cells in a parallel well were trypsinized 24 h post-infection and analyzed by fluorescence-activated cell sorter (FACS) (BD Biosciences, San Lose, CA) to assess the transduction efficiency [24].

Cytochemical staining for alkaline phosphatase. The cytochemical staining for alkaline phosphatase (ALP) was performed according to the protocol described previously [25]. Nine days after HSV-1 amplicon infection, the MC3T3-E1 cells were washed with PBS and fixed in 0.05% glutaraldehyde at room temperature for 5 min. The cells were then incubated at 37 °C for 30 min in a staining buffer containing 50 mM Tris–HCl, pH 8.6, 100 mM NaCl, 5 mM KCl, 1 mM $CaCl_2$, 1 mM $MgCl_2$, 0.8 mg/ml naphthol AS-TR phosphate, and 0.6 mg/ml

fast red violet LB diazonium (Sigma) in dark, followed by observation without counterstain.

Results and discussion

We searched the GenBank database and identified a mouse BAC library clone containing a complete 8.7-kb BMP-2 genomic DNA locus driven by a 20.5-kb native promoter within a 128.5-kb insert. We chose this clone because it contains a single BMP-2 gene with most, if not all, of the regulatory elements in the promoter, introns, and 3′ non-coding regions that may regulate a physiological gene expression [26,27]. The length of the BAC clone is also within the size limits that the HSV-1 vector can efficiently package into an iBAC [21]. We used a Cre/loxP-based retrofitting method to convert the BAC/BMP-2 with the pEHHG, consisting of HSV-1 amplicon elements, enhanced green fluorescent protein (GFP), EBV episome retention cassette, R6K bacterial replication origin, and a *loxP* site to generate a 152-kb construct of pHSV-BAC/BMP-2 (Fig. 1A) [20,21]. Subsequently, a PCR with specific primers to BMP-2 and GFP was performed to confirm the presence of two genes within a single pHSV-BAC/BMP-2 construct (Fig. 1B). We then packaged the pHSV-BAC/BMP-2 into the iBAC [21] and infected MC3T3-E1 cells to test the transgenes' function (Fig. 2). Twenty-four hours after infection, the GFP reporter gene was expressed in most of MC3T3-E1 cells transduced with either an HSV-1 mock (Fig. 2C) or an HSV-BAC/BMP-2 amplicon (Fig. 2D). Flow cytometry analyses revealed that 84% of the osteoblast cells transduced with HSV-1 mock amplicon expressed GFP (Fig. 2E) and 77% of the cells infected with HSV-BAC/BMP-2 virion were GFP-positive (Fig. 2F). To compare the efficiencies of transduction and transfection, we also transfected MC3T3-E1 cells with pEHHG and pHSV-BAC/BMP-2 (Fig. 1A) using Lipofectamine-Plus. Only less than 5% of MC3T3-

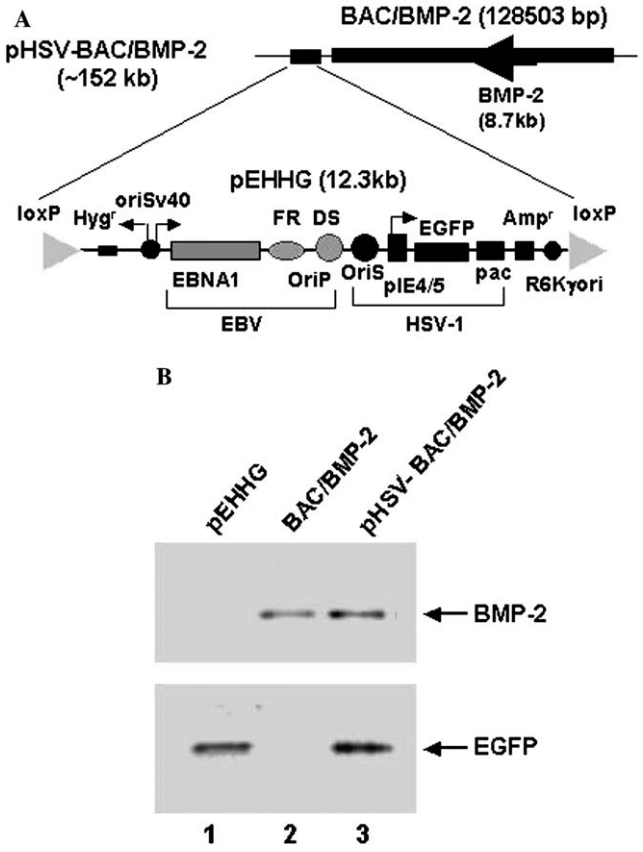

Fig. 1. Schematic diagram of infectious HSV-1/BAC/BMP-2 construct. (A) A detailed structure of retrofitted BAC clone. The retrofitting vector pEHHG containing the HSV-1 amplicon elements (*ori*$_s$ and *pac*) and GFP, the EBV episome retention cassette (*oriP*/*EBNA-1*/*hyg*^{r}), the R6K bacterial replication origin, and a *loxP* site is retrofitted into the BAC clone bearing a complete BMP-2 locus by homologous recombination. The retrofitted BAC contains both GFP reporter and BMP-2 genes. (B) Verification of pHSV-BAC/BMP-2 construct by polymerase chain reaction (PCR). Lane 1: pEHHG control; lane 2: BAC/BMP-2 control; and lane 3: pHSV-BAC/BMP-2 containing both GFP and BMP-2 genes.

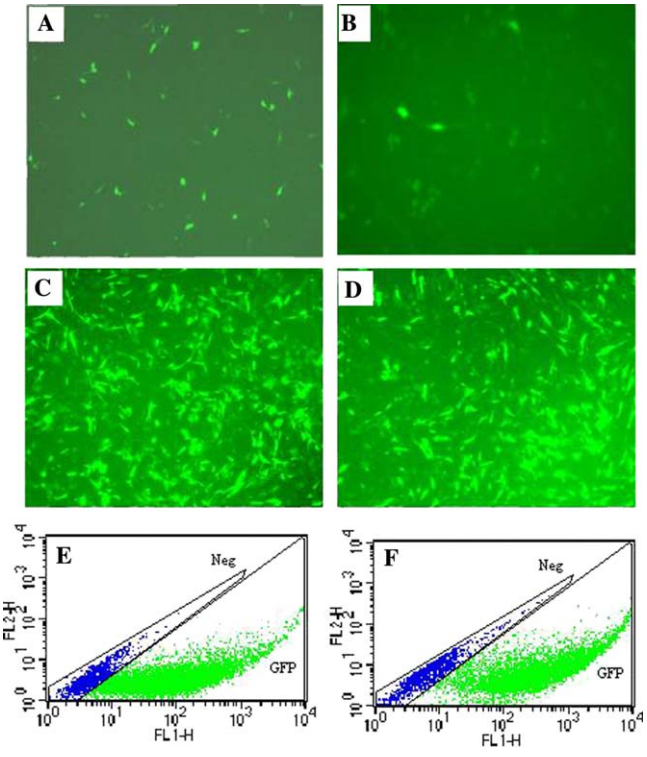

Fig. 2. GFP reporter expression in MC3T3-E1 cells transfected and transduced with HSV-1 amplicon for 24 h (40× images). (A) MC3T3-E1 cells transfected with pEHHG (4 μg) using optimized lipofectamine; (B) MC3T3-E1 cells transfected with pHSV-BAC/BMP-2 (4 μg) using optimized lipofectamine; (C) MC3T3-E1 cells transduced with infectious HSV-1 mock amplicon without BMP-2 genomic locus; (D) MC3T3-E1 cells transduced with infectious HSV-1 amplicon containing a BMP-2 genomic locus; (E) representative data of flow cytometric analysis in MC3T3-E1 cells infected with HSV-1 mock amplicon containing GFP but no BMP-2 genomic locus; and (F) representative data of flow cytometric analysis in MC3T3-E1 cells infected with HSV-1 amplicon containing GFP and a BMP-2 genomic locus.

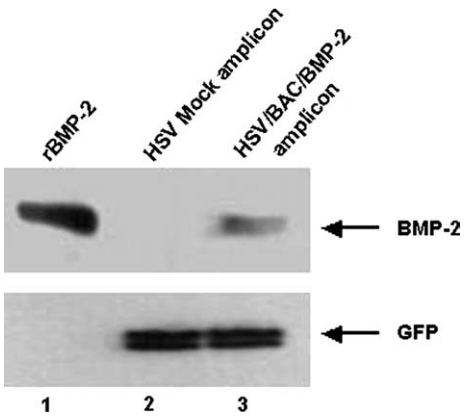

Fig. 3. Western immunoblot analyses of BMP-2 expressed in transduced MC3T3-E1 cells. MC3T3-E1 cells are infected with HSV-1 amplicon for 24 h and harvested for Western blot analysis. An aliquot (60 μg, 10^6 cells) of cellular lysate is separated on 15% SDS–PAGE, transferred to nitrocellulose membranes, and blotted using antibodies against BMP-2 and GFP, respectively. Lane 1: positive control of recombinant BMP-2 (100 ng); lane 2: the cells infected with HSV-1 mock amplicon containing GFP but no BMP-2 genomic locus; and lane 3: the cells infected with HSV-1 amplicon containing GFP and a BMP-2 genomic locus.

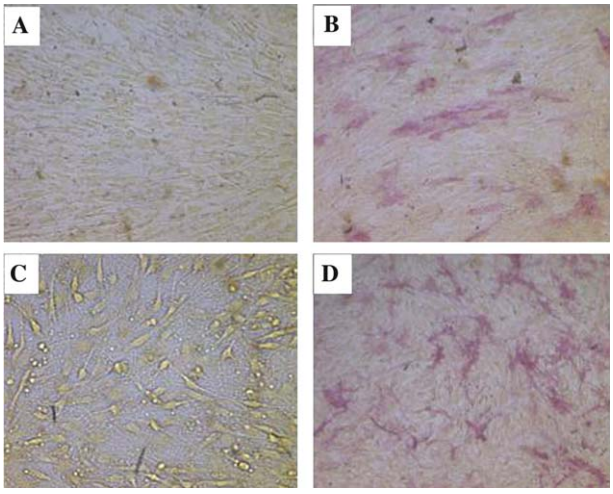

Fig. 4. Alkaline phosphatase (ALP) staining of differentiated MC3T3-E1 cells (40× images). MC3T3-E1 cells are differentiated for 9 days and subjected to ALP staining. (A) The cells infected with HSV-1 mock amplicon without a BMP-2 genomic locus; (B) the cells infected with HSV-1 amplicon containing a BMP-2 genomic locus; (C) negative control of MC3T3-E1 cells treated with vehicle; and (D) positive control of MC3T3-E1 cells treated with recombinant BMP-2 (200 ng/ml).

E1 cells transfected with pHSV-BAC/BMP-2 expressed GFP (Fig. 2A) whereas approximately 10% of the cells transfected with pEHHG turned green (Fig. 2A). Obviously, the efficiency of transduction of BAC-based amplicon was at least 15-fold higher than that of lipid-based transfection (Fig. 2).

The expression of the transgene was examined in cell extract by utilizing Western blot with specific antibodies against BMP-2 and GFP (Fig. 3). The amount of BMP-2 protein was estimated to be 10 ng/10^6 cells based on Western blot analysis (Fig. 3). However, we failed to detect BMP-2 expression in the same number of either native MC3T3-E1 cells or the cells transfected with pHSV-BAC/BMP-2 (Fig. 3 and data not shown). To assess osteoblast phenotype in the cells expressing BMP-2 transgene, we carried out an ALP staining 9 days after transduction (Fig. 4). Like the cells treated with 200 ng/ml recombinant human BMP-2, about 20% of the osteoblast cells were differentiated and exhibited positive ALP-staining (Figs. 4B and D). No ALP-positive cells were seen in the control cells infected with HSV-1 mock amplicon without BMP-2 genomic locus (Fig. 4A) or the cells treated with vehicle alone (Fig. 4C).

In this study, we have demonstrated that the HSV-1 amplicon can efficiently transfer a large piece of genomic locus (Fig. 2), and retain it as episomes in proliferating cells [18]. The GFP gene is consistently active and visible for at least 2 weeks, although the intensity becomes weaker as reported by other investigators [24]. The functional BMP-2 protein in the infected cells was detectable 24 h and even 72 h after infection (Fig. 3 and data not shown) and mediated cell differentiation (Fig. 4) [28]. However, accurate quantification of BMP-2 expression level was impossible because the secreted BMP-2 in the medium was not measured. Nevertheless, the transgene of BMP2 was active and promoted a phenotypic change of targeting cells (Fig. 3, lane 3 and Fig. 4), validating the application of iBAC technology.

In vivo testing of candidate genes in a BAC-based transgenic mouse is time-consuming and expensive, requiring the injection of BAC inserted into fertilized eggs and the examination of mouse phenotypes. Therefore, it would be more efficient to use in vitro cell models via the BAC clone approach to test candidate gene function before introducing in vivo transgenic studies. The studies provided in this manuscript demonstrate that retrofitting of the BAC clone and packaging of the HSV-1 amplicon into infectious virion can be accomplished within 1–2 weeks of work. By utilizing this approach, a candidate gene search in a QTL region is feasible once an appropriate cell model and end points for candidate gene function are determined. In this regard, our data demonstrate that MC3T3-E1 cells can be used as a model for high-throughput phenotypic screening to identify genes important for osteoblast cell differentiation. We have also used this system in C2C12 cells and proved that iBAC containing BMP-2 locus can induce premyoblast dedifferentiation and subsequently commit to osteoblast lineage (data not shown), providing another cell-based model for gene function of dedifferentiation. In addition, BAC or PAC can carry a genomic locus encompassing an intact gene(s) with all regulatory elements including enhancers, suppressors and locus control region that can direct physiological levels of tissue-specific expression for gene therapy. It can also be

manipulated to engineer a deletion, an insertion, and a site-specific mutation in *Escherichia coli* by homologous recombination to mimic natural polymorphisms to test the functional significance of SNPs located in the distal promoter or/and intron regions.

Acknowledgments

This work was supported by Assistance Award No. DAMD17-03-2-0021. The U.S. Army Medical Research Acquisition Activity, 820 Chandler Street, Fort Detrick MD 21702-5014, is the awarding and administering acquisition office. The information contained in this publication does not necessarily reflect the position or the policy of the Government, and no official endorsement should be inferred. All work was performed in facilities provided by the Department of Veterans Affairs. We are grateful to Dr. Yoshinaga Saeki (the Massachusetts General Hospital, Harvard Medical School, MA) for providing HSV-1 amplicon system and his technical assistance, and Dr. Rozanne Sandri-Goldin (the University of California, Irvine, CA) for her generous gift of a Vero 2-2 cell line. We also thank Dr. Shin-Tai Chen, Ms. Mahita Kadmiel, and Mr. Max Davis for their technical assistances of HSV-1 virion purification and FACS analyses (Musculoskeletal Disease Center, JL Pettis Memorial Veterans Medical Center, Loma Linda, CA).

References

[1] D.L. Glaser, F.S. Kaplan, Osteoporosis. Definition and clinical presentation, Spine 22 (1997) 12S–16S.
[2] C.W. Slemenda, J.C. Christian, T. Reed, T.K. Reister, C.J. Williams, C.C. Johnston Jr., Long-term bone loss in men: effects of genetic and environmental factors, Ann. Intern. Med. 117 (1992) 286–291.
[3] C.W. Slemenda, J.C. Christian, C.J. Williams, J.A. Norton, C.C. Johnston Jr., Genetic determinants of bone mass in adult women: a reevaluation of the twin model and the potential importance of gene interaction on heritability estimates, J. Bone Miner. Res. 6 (1991) 561–567.
[4] V. Nicolas, S. Mohan, Y. Honda, A. Prewett, R.D. Finkelman, D.J. Baylink, J.R. Farley, An age-related decrease in the concentration of insulin-like growth factor binding protein-5 in human cortical bone, Calcif. Tissue Int. 57 (1995) 206–212.
[5] D. Baylink, M. Stauffer, J. Wergedal, C. Rich, Formation, mineralization, and resorption of bone in vitamin D-deficient rats, J. Clin. Invest. 49 (1970) 1122–1134.
[6] M.J. Econs, D.L. Koller, S.L. Hui, T. Fishburn, P.M. Conneally, C.C. Johnston Jr., M. Peacock, T.M. Foroud, Confirmation of linkage to chromosome 1q for peak vertebral bone mineral density in premenopausal white women, Am. J. Hum. Genet. 74 (2004) 223–228.
[7] C.M. Kammerer, J.L. Schneider, S.A. Cole, J.E. Hixson, P.B. Samollow, J.R. O'Connell, R. Perez, T.D. Dyer, L. Almasy, J. Blangero, R.L. Bauer, B.D. Mitchell, Quantitative trait loci on chromosomes 2p, 4p, and 13q influence bone mineral density of the forearm and hip in Mexican Americans, J. Bone Miner. Res. 18 (2003) 2245–2252.
[8] F. Wynne, F.J. Drummond, M. Daly, M. Brown, F. Shanahan, M.G. Molloy, K.A. Quane, Suggestive linkage of 2p22-25 and 11q12-13 with low bone mineral density at the lumbar spine in the Irish population, Calcif. Tissue Int. 72 (2003) 651–658.
[9] H.W. Deng, H. Shen, F.H. Xu, H. Deng, T. Conway, Y.J. Liu, Y.Z. Liu, J.L. Li, Q.Y. Huang, K.M. Davies, R.R. Recker, Several genomic regions potentially containing QTLs for bone size variation were identified in a whole-genome linkage scan, Am. J. Med. Genet. 119A (2003) 121–131.
[10] G.L. Masinde, J. Wergedal, H. Davidson, S. Mohan, R. Li, X. Li, D.J. Baylink, Quantitative trait loci for periosteal circumference (PC): identification of single loci and epistatic effects in F2 MRL/SJL mice, Bone 32 (2003) 554–560.
[11] G.L. Masinde, X. Li, W. Gu, J. Wergedal, S. Mohan, D.J. Baylink, Quantitative trait loci for bone density in mice: the genes determining total skeletal density and femur density show little overlap in F2 mice, Calcif. Tissue Int. 71 (2002) 421–428.
[12] W.G. Beamer, C.J. Rosen, R.T. Bronson, W. Gu, L.R. Donahue, D.J. Baylink, C.C. Richardson, G.C. Crawford, J.E. Barker, Spontaneous fracture (sfx): a mouse genetic model of defective peripubertal bone formation, Bone 27 (2000) 619–626.
[13] K.L. Shultz, L.R. Donahue, M.L. Bouxsein, D.J. Baylink, C.J. Rosen, W.G. Beamer, Congenic strains of mice for verification and genetic decomposition of quantitative trait loci for femoral bone mineral density, J. Bone Miner. Res. 18 (2003) 175–185.
[14] W.K. Gu, X.M. Li, B. Edderkaoui, D.D. Strong, K.H. Lau, W.G. Beamer, L.R. Donahue, S. Mohan, D.J. Baylink, Construction of a BAC contig for a 3 cM biologically significant region of mouse chromosome 1, Genetica 114 (2002) 1–9.
[15] R.E. White, R. Wade-Martins, S.L. Hart, J. Frampton, B. Huey, A. Desai-Mehta, K.M. Cerosaletti, P. Concannon, M.R. James, Functional delivery of large genomic DNA to human cells with a peptide-lipid vector, J. Gene. Med. 5 (2003) 883–892.
[16] C. Magin-Lachmann, G. Kotzamanis, L. D'Aiuto, H. Cooke, C. Huxley, E. Wagner, In vitro and in vivo delivery of intact BAC DNA–comparison of different methods, J. Gene. Med. 6 (2004) 195–209.
[17] C. Magin-Lachmann, G. Kotzamanis, L. D'Aiuto, E. Wagner, C. Huxley, Retrofitting BACs with G418 resistance, luciferase, and oriP and EBNA-1-new vectors for in vitro and in vivo delivery, BMC Biotechnol. 3 (2003) 2.
[18] R. Wade-Martins, Y. Saeki, E. Antonio Chiocca, Infectious delivery of a 135-kb LDLR genomic locus leads to regulated complementation of low-density lipoprotein receptor deficiency in human cells, Mol. Ther. 7 (2003) 604–612.
[19] Y. Wang, C. Fraefel, F. Protasi, R.A. Moore, J.D. Fessenden, I.N. Pessah, A. DiFrancesco, X. Breakefield, P.D. Allen, HSV-1 amplicon vectors are a highly efficient gene delivery system for skeletal muscle myoblasts and myotubes, Am. J. Physiol. Cell Physiol. 278 (2000) C619–C626.
[20] R. Wade-Martins, E.R. Smith, E. Tyminski, E.A. Chiocca, Y. Saeki, An infectious transfer and expression system for genomic DNA loci in human and mouse cells, Nat. Biotechnol. 19 (2001) 1067–1070.
[21] Y. Saeki, X.O. Breakefield, E.A. Chiocca, Improved HSV-1 amplicon packaging system using ICP27-deleted, oversized HSV-1 BAC DNA, Methods Mol. Med. 76 (2003) 51–60.
[22] K. Ellnebo-Svedlund, L. Larsson, J. Jonasson, P. Magnusson, Rapid genotyping of the osteoporosis-associated polymorphic transcription factor Sp1 binding site in the COL1A1 gene by pyrosequencing, Mol. Biotechnol. 26 (2004) 87–90.
[23] S.L. Ferrari, D. Karasik, J. Liu, S. Karamohamed, A.G. Herbert, L.A. Cupples, D.P. Kiel, Interactions of interleukin-6 promoter polymorphisms with dietary and lifestyle factors and their association with bone mass in men and women from the Framingham Osteoporosis Study, J. Bone Miner. Res. 19 (2004) 552–559.
[24] R. Nunez, M. Ackermann, Y. Saeki, A. Chiocca, C. Fraefel, Flow cytometric assessment of transduction efficiency and cytotoxicity

of herpes simplex virus type 1-based amplicon vectors, Cytometry 44 (2001) 93–99.

[25] J.E. Wergedal, D.J. Baylink, Characterization of cells isolated and cultured from human bone, Proc. Soc. Exp. Biol. Med. 176 (1984) 60–69.

[26] K.L. Abrams, J. Xu, C. Nativelle-Serpentini, S. Dabirshahsahebi, M.B. Rogers, An evolutionary and molecular analysis of BMP2 expression, J. Biol. Chem. (2004).

[27] L.M. Helvering, R.L. Sharp, X. Ou, A.G. Geiser, Regulation of the promoters for the human bone morphogenetic protein 2 and 4 genes, Gene 256 (2000) 123–138.

[28] D. Noel, D. Gazit, C. Bouquet, F. Apparailly, C. Bony, P. Plence, V. Millet, G. Turgeman, M. Perricaudet, J. Sany, C. Jorgensen, Short-term BMP-2 expression is sufficient for in vivo osteochondral differentiation of mesenchymal stem cells, Stem Cells 22 (2004) 74–85.

Job: Molecular Biotechnology
Chapter: Mohan/MB06-0006
Pub Date: 2006

Operator: SV
Date: 5/06
Revision: 1st Pass

RESEARCH

A Platform of High-EfficiencyNonviral Gene Transfer in Mouse Osteoblast Cells in Vitro

Weirong Xing,[1] David Baylink,[1,2] Anil Kapoor,[1] and Subburaman Mohan[1,2,]*

AU:Please italicize any gene names in this article and leave protein names in plain type

Abstract

We have previously established mouse genetic models and identified the genetic components of quantitative trait loci (QTL) on mouse chromosomes that contribute to phenotypes such as bone size, bone density, and bone's anabolic response to mechanical loading. However, these regions contain dozens of unknown genes that are needed for functional testing. In this study, we provided a protocol of nucleoporation with high efficiency by using a commercial nucleofection buffer and Gene Pulser to deliver a test gene into bone cells for functional studies. We cloned an osteoblast differentiation-specific gene osterix (Osx) from a mouse bone cDNA library into a pHGCX expression vector and used nucleoporation to deliver pHGCX/Flag-Osx into the nuclei of MC3T3-E1 cells. We then examined the transfection efficiency, transgene expression, and function. Our results have demonstrated that nucleoporation can deliver a transgene into MC3T3-E1 osteoblast cells with approx 94% transfection efficiency, and express a functional Flag–Osx fusion protein capable of inducing cell differentiation as measured by an increase in alkaline phosphatase (ALP) activity. Therefore, this experimental system provides a rapid, safe, and efficient cell-based model of high-throughput phenotypic screening to identify candidate genes from physically mapped regions that are important for osteoblast differentiation.

Index Entries: Osteoblast; nonviral; osterix; gene transfer; electroporation; nucleofector.

1. Introduction

Osteoporosis is a common disease characterized by an age-dependent loss of bone mass and strength, and a microarchitectural deterioration of bone tissue with an increased risk of bone fractures ***(1)***. Although environmental factors, nutrition, and hormones contribute to the development of osteoporosis, it is clear that genetic factors are the primary determinants for the disease ***(2–5)***. To localize the chromosomal regions and subsequently identify the genes responsible for various musculoskeletal phenotypes, we have carried out a genome-wide linkage analyses in several inbred-strain F_2 crosses and ethylnitrosourea (ENU)-induced mutant mouse strains and discovered quantitative trait loci (QTL) on mouse chromosomes that contribute to bone phenotypes such as size, density, and the anabolic response to mechanical loading ***(6–8)***. However, these regions contain dozens of genes and are still difficult to clone by more time-consuming, expensive, positional cloning strategies. An alternate approach for identifying these disease-causing genes that is both feasible and efficient is to transfer the unknown genes from the QTL regions into the bone cells in vitro for a high-throughput functional screening.

The delivery of candidate genes into the bone cells by conventional chemical transfection or electroporation, although possible, renders a poor efficiency of gene transfer and requires

*Author to whom all correspondence and reprint requests should be addressed. [1]Musculoskeletal Disease Center, JL Pettis Memorial Veterans Administration Medical Center and [2]Department of Medicine, Loma Linda University, Loma Linda, CA 92357; E-mail: Subburaman.Mohan@med.va.gov.

 ISSN: 1073–6085/Online ISSN: 1559–0305/2006/34:X/000–000/$30.00

Job: Molecular Biotechnology
Chapter: Mohan/MB06-0006
Pub Date: 2006
Operator: SV
Date: 5/06
Revision: 1st Pass

drug selection and identification of stably integrated transformants for functional testing ***(9,10)***. We and other investigators have previously established a viral gene transfer system of a herpes simplex virus (HSV)-based amplicon to deliver a bacterial artificial chromosome (BAC) containing a genomic locus as large as 150 kb with a high transduction efficiency in most mammalian cells, including dividing and nondividing cells for functional studies ***(10–13)***. The transgene remains as minichromosomes in the host cells and expresses a protein of interest at a high level in a position-independent manner ***(13,14)***. In this study, we extended our findings and cloned the complementary DNA (cDNA) of our candidate genes into the pHGCX expression vector ***(15)***. We used this gene transfer strategy for the following reasons: (1) some of our test genes may contain large introns (>100 kb), such that the size of the intact gene, including introns and exons, could be beyond the limitation of the HSV packaging capacity (e.g., >150 kb); (2) the BAC clone containing the entire candidate gene may not be available in the mouse genome databases; and (3) the BAC clone may encode multiple, alternatively-spliced variants with diverse functions from a single gene. To overcome these limitations with the BAC clone approach, we used the strategy of using a HSV amplicon-based plasmid containing the cDNA of the test gene for nonviral transfection ***(10,15–17)***. In this regard, we developed an optimal protocol of the "nucleoporation" technique by using a commercial nucleofection buffer and Gene Pulser to make the gene transfer safer, more cost-effective, and feasible. We used the pHGCX expression vector carrying osterix (Osx) cDNA as a model system to test transfection efficiency, transgene expression, and function. Our results indicated that the nucleoporation of plasmid DNA bearing a test gene could offer a rapid, simple alternative method of gene transfer for functional studies in bone cells.

2. Materials and Methods

2.1. Vector Constructs

The DNA construct of pHGCX containing a cytomegalovirus (CMV) promoter in front of multiple cloning sites (MCS) was kindly provided by Dr. Yoshinaga Saeki (the Ohio State University Medical Center, Columbus, OH). The original construct was modified by inserting a small CMV intron from pmaxGFP (Amaxa Inc., Gaithersburg, MD) into the corresponding sites of SnaB and NheI sites of pHGCX to generate a new expression vector driven by the CMV promoter/intron (**Fig. 1**). The complete coding sequence of Osx was amplified from a mouse bone cDNA library by polymerase chain reaction (PCR) using specific primers with an overhang of Flag sequence at the 5' end of the forward primer. The PCR product of Flag–Osx was cloned into pCR2.1 to generate pCR2.1/Flag–Osx using a TA cloning kit (Invitrogen, Carlsbad, CA). The Flag–Osx fusion gene was then released from pCR2.1/Flag–Osx, and subcloned into the BamH1 and XhoI sites of pHGCX to generate pHGCX/Flag–Osx (**Fig. 1**). The sequences of the primers are: fForward: 5'-gccaccatggactacaaagacgatgacgacaaggcgtcctctct gcttgagga-3' and reverse: 5'-ttatcagatctctagca ggttgc-3'.

Fig 1

2.2. Nucleoporation

MC3T3-E1 cells (10^6) (ATCC, Manassas, VA) were resuspended in 100 µL of Cell Line Nucleofector buffer T (Amaxa, Inc.) containing 10 µg of plasmid DNA. The cells were then transferred into a 2-mm gap width electroporation cuvet, and electroporated at 160 V for 15 ms using a Gene Pulser (Bio-Rad, Hercules, CA). After electroporation, the cells were transferred into 3 mL of prewarmed minimum essential medium alpha supplemented with 10% fetal bovine serum, 2 mM l-glutamine, 100 U/mL penicillin, and 100 µg/mL streptomycin (Invitrogen) in 60-mm plates, and cultured in a humidified 37°C incubator with 5% CO_2.

2.3. Western Blot and Fluorescence-Activated Cell Sorter Analyses

MC3T3-E1 cells were lysed in a lysis buffer containing 50 m*M* Tris-HCl (pH 8.0), 150 m*M* NaCl, 0.1% SDS, 1% Triton X-100, 1 × phosphatase inhibitor, and 1 × protease inhibitor cocktail (Sigma, St. Louis, MO) 24 h after transfection.

Job: Molecular Biotechnology
Chapter: Mohan/MB06-0006
Pub Date: 2006
Operator: SV
Date: 5/06
Revision: 1st Pass

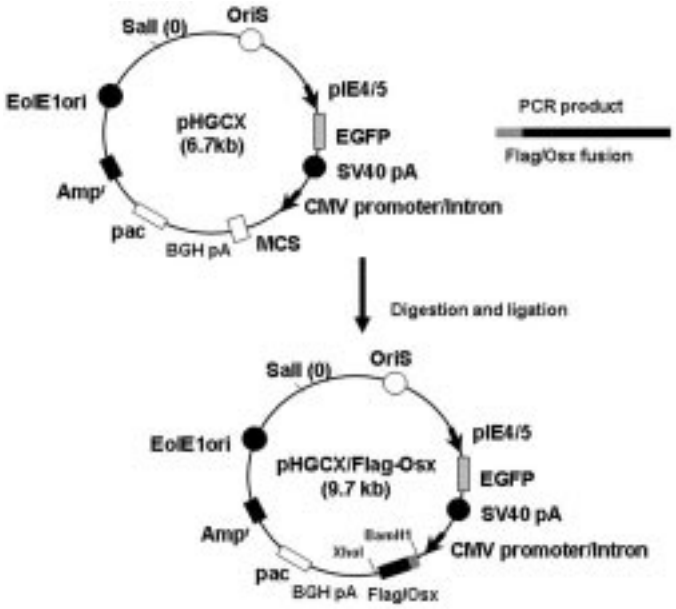

Fig. 1. A schematic diagram of pHGCX/Flag–Osx construction. The PCR product of mouse osterix (Osx) coding sequence tagged with Flag is inserted into the *Bam*HI and *Xho*I sites downstream of the CMV promoter/intron of pHGCX plasmid to generate an expression vector of pHGCX/Flag–Osx.

An aliquot of 10 to 20 µg of cellular protein was separated on a 10% SDS-polyacrylamide gel and transferred to nitrocellulose. The membrane was incubated at 4°C overnight in a buffer containing 5% dry skim milk, 150 m*M* NaCl, 50 m*M* Tris-HCl (pH 8.0), and 0.05% Tween-20. Immunoblotting was performed in the same buffer containing 0.2 µg/mL antibody against Flag (Sigma) or green fluorescent protein (GFP) (Santa Cruz, CA) at room temperature for 1 h. Specific proteins were detected using appropriate secondary antibodies and enhanced chemiluminescence's plus Western blotting detection system (Amersham Pharmacia Biotech UK Limited, Buckinghamshire, England). The cells in a parallel plate were trypsinized 24 h after transfection and analyzed by fluorescence-activated cell sorter (FACS) (BD Biosciences, San Lose, CA) to assess the transfection efficiency.

AU:GFP = green fluorescent protein?

2.4. Cytochemical Staining for Alkaline Phosphatase

The cytochemical staining for alkaline phosphatase (ALP) was performed according to the protocol described previously ***(18)***. MC3T3-E1 cells were washed with phosphate-buffered saline (PBS) and fixed in 0.05% glutaraldehyde at room temperature for 5 min, 3 d after transfection. The cells were then incubated at 37°C for 30 min in a staining buffer containing 50 m*M* Tris-HCl at pH 8.6, 100 m*M* NaCl, 5 m*M* KCl, 1 m*M* $CaCl_2$, 1 m*M* $MgCl_2$, 0.8 mg/mL naphthol AS-TR phosphate, and 0.6 mg/mL fast red violet LB diazonium (Sigma) in the dark, followed by two washings with PBS and observation without counterstain.

3. Results and Discussion

In the present study, we cloned the cDNA of candidate genes into the pHGCX expression vector ***(15)*** and established a nonviral gene transfer system for the constructs less than 12 kb in length. We chose the pHGCX as an expression system because it contains a HSV amplicon, which can be used for both viral and nonviral gene transfer, and a GFP reporter to monitor the efficiency of gene transfer. To improve the expression level, we engineered a CMV small intron at the 5' untranslated region of the Flag–Osx fusion gene.

Job: Molecular Biotechnology
Chapter: Mohan/MB06-0006
Pub Date: 2006
Operator: SV
Date: 5/06
Revision: 1st Pass

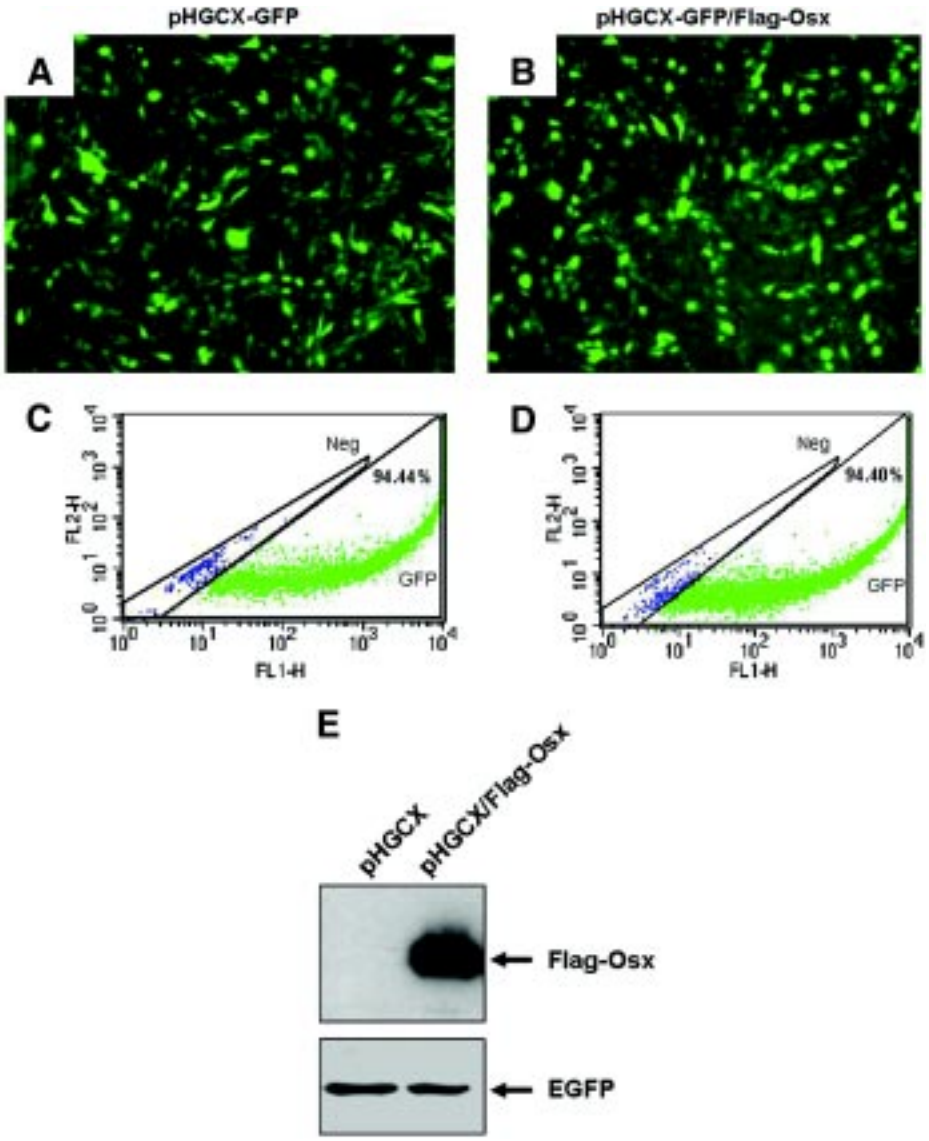

Fig. 2. Transgene expression in MC3T3-E1 cells transfected by nucleoporation. (**A and B**) GPF expression in MC3T3-E1 cells transfected with pHGCX and pHGCX/Flag–Osx, respectively. (**C and D**) Representative data of flow cytometric analysis in the cells transfected with pHGCX and pHGCX/Flag–Osx, respectively. (**E**) Flag–Osx and GFP protein expression in MC3T3-E1 cells transfected with pHGCX and pHGCX/Flag–Osx, respectively, detected by Western blot.

Therefore, the transgene was driven by a CMV promoter/intron (**Fig. 1**). We then used a commercial nucleofection buffer and Gene Pulser to deliver the plasmid DNA directly into the nuclei of the MC3T3-E1 cells. The GFP reporter gene was expressed in most of MC3T3-E1 cells transfected with either pHGCX (**Fig. 2A**) or pHGCX/Flag–Osx (**Fig. 2B**) 24 h after electroporation. Flow cytometry analyses revealed more than 94% of the osteoblast cells transfected with the pHGCX or the pGHCX/Flag–Osx plasmid expressed GFP (**Fig. 2C,D**). We have repeated the experiments and found that the efficiency of nucleoporation is reliable. The variation in transfection efficiency

Fig 2

Job: Molecular Biotechnology
Chapter: Mohan/MB06-0006
Pub Date: 2006
Operator: SV
Date: 5/06
Revision: 1st Pass

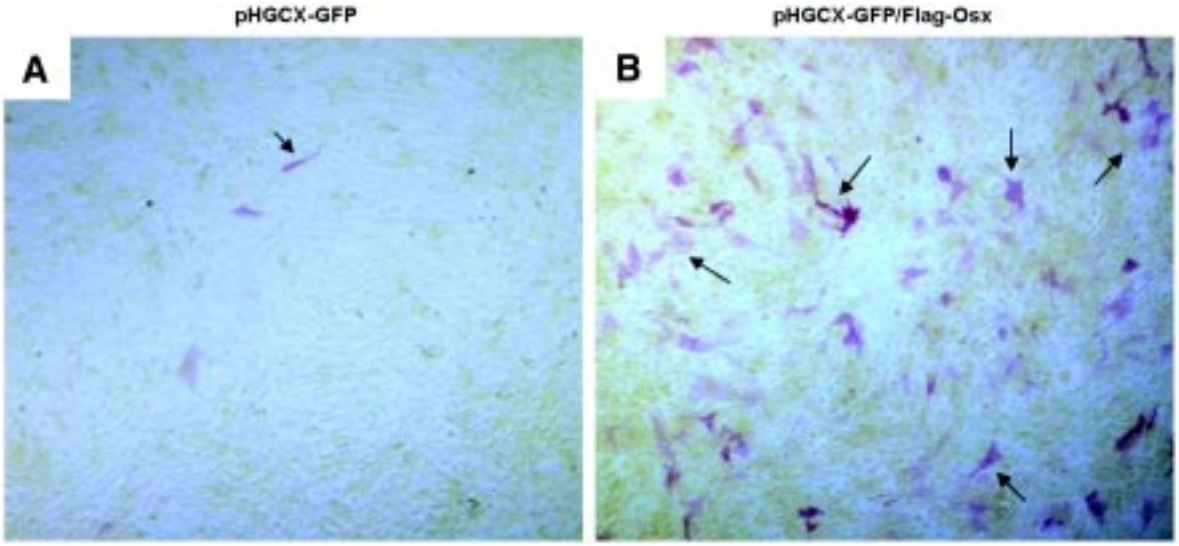

Fig. 3. Alkaline phosphatase (ALP) staining of differentiated MC3T3-E1 cells (×40 images). MC3T3-E1 cells are subjected for ALP staining 72 h after transfection. (**A)** The cells transfected with pHGCX control plasmid. (**B)** The cells transfected with pHGCX/Flag–Osx. Arrows indicate the ALP-positive cells.

was less than 1%, and the viability of electroporated cells were more than 90% (data not shown). In comparison with our previous data,/ghe efficiency of gene transfer by nucleoporation was approx 104 higher than that of a viral delivery system mediated by a HSV-amplicon in mouse preosteoblast cells ***(10)***.

The transgene expression of GFP and Flag–Osx was easily detected in the cells transfected with pHGCX/Flag–Osx by using Western blot with specific antibodies against Flag and GFP (**Fig. 2E**). The pHGCX/Flag–Osx transfected cells expressed high levels of Flag–Osx fusion protein. As expected, the Flag–Osx fusion protein was undetectable, whereas the expression of GFP was present in the cells transfected with pHGCX (**Fig. 2E**). To assess osteoblast differentiation in the cells expressing the Osx transgene, we carried out an ALP staining 3 d after transfection (**Fig. 3**). Approx 20% of the osteoblast cells overexpressing Osx were differentiated and exhibited positive ALP staining (**Fig. 3A**). In contrast, less than 1% ALP-positive cells were seen in the control cells overexpressing GFP only (**Fig. 3B**).

Fig 3

In this study, we have demonstrated that nonviral gene transfer of nucleoporation can efficiently deliver plasmid DNA directly into the nuclei of preosteoblast cells. The transgene is consistently active and visible for more than 5 d (data not shown), although the intensity of the GFP reporter becomes weaker with the culture time. A high level of transgene expression of GFP and Osx in the transfected cells was visual as early as 4 h after electroporation and mediated cell differentiation, validating the application of nucleoporation technology for functional studies of candidate genes. Although the protocol provided in this article is specific to MC3T3-E1 cells, the system can be applied to other types of cells by modifying pulse time, voltage, and nucleofection buffer. In general, an electroporation with low voltage and prolonged time can be applied to primary cells, whereas high voltage and short time should be considered for immortalized cell lines. Large cells require a low-voltage pulse. Protocols with unoptimized conditions results in either low cell viability or low transfection efficiency. In addition, a great difference in copy numbers and expres-

Job: Molecular Biotechnology
Chapter: Mohan/MB06-0006
Pub Date: 2006
Operator: SV
Date: 5/06
Revision: 1st Pass

sion levels per cell can be seen. The transfected, nonlinearized plasmid remains in the cells only for a short time for functional testing.

In vivo testing of candidate genes in a transgenic mouse is time consuming and expensive, requiring the injection of a DNA fragment into fertilized eggs and the examination of mouse phenotypes. Therefore, it would be more efficient to use in vitro cell models by viral or nonviral gene transfer approaches to test candidate gene function before initiating in vivo transgenic studies. Although infectious viral transduction mediated by a HSV amplicon provides an alternative approach, the intensive work of purifying viral particles and potential contamination of viral particles limits its wide use. The studies provided in this article demonstrate that cloning the cDNA of an unknown gene into the pHGCX expression vector can be accomplished within 1 wk. By using this approach, a candidate gene search in a QTL region is cheaper, safer, and faster once an appropriate cell model and end points for candidate gene function are determined. Our data also indicate that it is feasible to use the Gene Pulser for nucleofection once the conditions of pulse voltage and time are optimized. In addition, nucleoporation overcomes the limitation of infectious BAC (iBAC) technology to allow testing of the genes that iBAC cannot apply. In this regard, our data demonstrate that nucleoporation in MC3T3-E1 cells can be used as another gene transfer system for high throughput screening to identify genes important for osteoblast cell differentiation.

Acknowledgments

This work was supported by Assistance Award No. DAMD17-03-2-0021 and NIH grant (AG 19698). The U.S. Army Medical Research Acquisition Activity, 820 Chandler Street, Fort Detrick, MD 21702-5014, is the awarding and administering acquisition office. The information contained in this publication does not necessarily reflect the position or the policy of the government, and no official endorsement should be inferred. All work was performed in facilities provided by the Department of Veterans Affairs.

We are grateful to Dr. Yoshinaga Saeki (the Ohio State University Medical Center, Columbus, OH) for providing pHGCX plasmid, and Sean Belcher for his editorial assistance.

References

1. Glaser, D. L. and Kaplan, F. S. (1997) Osteoporosis. Definition and clinical presentation. *Spine* **22,** 12S–16S.
2. Slemenda, C. W., Christian, J. C., Reed, T., Reister, T. K., Williams, C. J., and Johnston, C. C. Jr. (1992) Long-term bone loss in men: effects of genetic and environmental factors. *Ann. Intern. Med.* **117,** 286–291.
3. Slemenda, C. W., Christian, J. C., Williams, C. J., Norton, J. A., and Johnston, C. C. Jr. (1991) Genetic determinants of bone mass in adult women: a reevaluation of the twin model and the potential importance of gene interaction on heritability estimates. *J. Bone Miner. Res.* **6,** 561–567.
4. Nicolas, V., Mohan, S., Honda, Y., et al. (1995) An age-related decrease in the concentration of insulin-like growth factor binding protein-5 in human cortical bone. *Calcif. Tissue Int.* **57,** 206–212.
5. Kesavan, C., Mohan, S., Oberholtzer, S., Wergedal, J. E., and Baylink, D. J. (2005) Mechanical loading induced gene expression and BMD changes are different in two inbred mouse strains. *J. Appl. Physiol.* **99(5),** 1951–1957.
6. Masinde, G. L., Wergedal, J., Davidson, H., et al. (2003) Quantitative trait loci for periosteal circumference (PC): identification of single loci and epistatic effects in F2 MRL/SJL mice. *Bone* **32,** 554–560.
7. Srivastava, A. K., Kapur, S., Mohan, S., Yu, H., Wergedal, J., and Baylink, D. J. (2005) Identification of novel genetic loci for bone size and mechanosensitivity in an ENU mutant exhibiting decreased bone size. *J. Bone Miner. Res.* **20,** 1041–1050.
8. Kesava, C. M., S.. Yu, H., Oberholtzer, S., Wergedal, J. E., Baylink, D. J., and Mohan, S. (2005) Novel mechanoresponsive BMD and bone size QTL identified in a genome wide linkage study involving C57BL/6J-C3H/HeJ intercross. *J. Bone Miner. Res.* **20,** S75.
9. Kofron, M. D. and Laurencin, C. T. (2005) Orthopaedic applications of gene therapy. *Curr. Gene Ther.* **5,** 37–61.
10. Xing, W., Baylink, D., Kesavan, C., and Mohan, S. (2004) HSV-1 amplicon-mediated transfer of 128-kb BMP-2 genomic locus stimulates osteoblast differentiation in vitro. *Biochem. Biophys. Res. Commun.* **319,** 781–786.
11. Wade-Martins, R., Saekim Y., and Antonio Chiocca, E. (2003) Infectious delivery of a 135-kb LDLR genomic locus leads to regulated complementation of low-density lipoprotein receptor deficiency in human cells. *Mol. Ther.* **7,** 604–612.

Ref 8: is a name missing? Kesava, C. M., ??, S.

Job: Molecular Biotechnology
Chapter: Mohan/MB06-0006
Pub Date: 2006
Operator: SV
Date: 5/06
Revision: 1st Pass

12. Wang, Y., Fraefel, C., Protasi, F., et al. (2000) HSV-1 amplicon vectors are a highly efficient gene delivery system for skeletal muscle myoblasts and myotubes. *Am. J. Physiol. Cell Physiol.* **278,** C619–C626.
13. Wade-Martins, R., Smith, E. R., Tyminski, E., Chiocca, E. A., and Saeki, Y. (2001) An infectious transfer and expression system for genomic DNA loci in human and mouse cells. *Nat. Biotechnol.* **19,** 1067–1070.
14. Saeki, Y., Breakefield, X. O., and Chiocca, E. A. (2003) Improved HSV-1 amplicon packaging system using ICP27-deleted, oversized HSV-1 BAC DNA. *Methods Mol. Med.* **76,** 51–60.
15. Cortes, M. L., Bakkenist, C. J., Di Maria, M. V., Kastan, M. B., and Breakefield, X. O. (2003) HSV-1 amplicon vector-mediated expression of ATM cDNA and correction of the ataxia-telangiectasia cellular phenotype. *Gene Ther*. **10,** 1321–1327.
16. Lenz, P., Bacot, S. M., Frazier-Jessen, M. R., and Feldman, G. M. (2003) Nucleoporation of dendritic cells: efficient gene transfer by electroporation into human monocyte-derived dendritic cells. *FEBS Lett.* **538,** 149–154.
17. Iversen, N., Birkenes, B., Torsdalen, K., and Djurovic, S. (2005) Electroporation by nucleofector is the best nonviral transfection technique in human endothelial and smooth muscle cells. *Genet. Vaccines Ther*. **3,** 2.
18. Wergedal, J. E. and Baylink, D. J. (1984) Characterization of cells isolated and cultured from human bone. *Proc. Soc. Exp. Biol. Med.* **176,** 60–69.

Calcif Tissue Int (2007) 80:374–382
DOI 10.1007/s00223-007-9026-0

Loss of Sex-Specific Difference in Femoral Bone Parameters in Male Leptin Knockout Mice

Xiaoguang Wang · Charles H. Rundle · Jon E. Wergedal · Apurva K. Srivastava · Subburaman Mohan · K.-H. William Lau

Received: 15 December 2006 / Accepted: 27 February 2007 / Published online: 23 May 2007

Abstract Sex-dependent differences were identified in the femoral bone parameters of male and female *ob/ob* (leptin knockout) mice compared with their C57BL/6 wild-type background strain. Total fat, lean weight and body weight were not different between adult male and female leptin knockout mice. However, leptin knockout males exhibited lower lean weights than C57BL/6 males. Peripheral quantitative computerized tomographic measurements at the femoral midshaft revealed that the normal differences in the periosteal circumference, endosteal circumference, total bone mineral content, and polar moment of inertia normally observed between adult male and female wild-type mice were lost between adult male and female *ob/ob* mice. Significant reductions in these bone parameters were seen in male *ob/ob* mice compared to male wild-type mice but not in female *ob/ob* mice compared to female wild-type mice. In prepubertal mice, there were no differences in phenotype and femoral bone parameters between males and females within any strain, suggesting sex hormone functions. Serum free testosterone levels were 5.6-fold higher in adult male *ob/ob* mice than in adult male C57BL/6 wild-type mice, and serum estradiol levels were 1.8- and 1.3-fold greater in adult male and female *ob/ob* mice, respectively, than in their wild-type counterparts. Androgen receptor gene expression was not different in femur-derived bone cells of male *ob/ob* mice compared with wild-type mice. The loss of sex-related differences in these bone parameters in adult male *ob/ob* mice might result from deficient signaling in the androgen signaling pathway and the fact that leptin functions are permissive for androgen effects on bone development.

Keywords Leptin · Sex-related · Femur · Androgen · Mouse

Xiaoguang Wang, Charles H. Rundle contributed equally to this work.

X. Wang · C. H. Rundle · J. E. Wergedal · A. K. Srivastava · S. Mohan · K.-H.W. Lau
Musculoskeletal Disease Center (151), J. L. Pettis Memorial Veterans Administration Medical Center, 11201 Benton Street, Loma Linda, CA 92357, USA

C. H. Rundle (✉) · J. E. Wergedal · A. K. Srivastava · S. Mohan · K.-H.W. Lau
Department of Medicine, Loma Linda University, Loma Linda, CA 92350, USA
e-mail: Charles.Rundle@med.va.gov

J. E. Wergedal · S. Mohan · K.-H.W. Lau
Department of Biochemistry, Loma Linda University, Loma Linda, CA 92350, USA

S. Mohan
Department of Physiology, Loma Linda University, Loma Linda, CA 92350, USA

Introduction

Leptin is a 16 kDa protein expressed predominantly in adipose tissue that functions as a hormone to regulate body fat [1]. Changes in the level of circulating leptin alter feeding behavior, metabolism and endocrine functions [2]. However, recent data indicate that leptin is also an important regulator of bone mass [3, 4]. Genetic variations in leptin have been associated with bone size and shape [5]. It exerts dual effects on bone formation, depending on the route of administration: when administered through the central nervous system, it produces an antiosteogenic effect, which appears to be mediated directly through hypothalamic signaling at the sympathetic nervous system

[6]; conversely, when administrated peripherally, leptin stimulates osteoblast differentiation and mineralization of bone matrix, enhancing the development of the periosteal envelope in growing bone during early life [7]. Hamrick et al. [8] showed that leptin deficiency has differential effects on bone mass in the axial and appendicular skeleton, indicating that leptin produces different local effects at different bone sites. Osteoblasts express leptin receptors, which presumably permit leptin to directly stimulate bone metabolism at different skeletal sites [9]. Thus, while it is clear that leptin has a role in regulating bone size, the mechanisms by which it regulates bone growth and development at different skeletal sites are complex and remain to be elucidated. It also remains unclear whether the osteogenic effects of leptin are mediated entirely through direct action on bone or indirectly through the systemic functions of other hormones.

Gender-specific effects on bone mass also implicate the sex steroid hormones in bone metabolism [10]; androgen action has been traditionally thought to be primarily anabolic, while estrogen acts mainly through suppression of resorption [11]. Estrogen also regulates the closure of the epiphyseal growth plate that affects bone length. The larger bone size in adult males compared to females is generally attributed to androgen activity that mediates the periosteal expansion, though aromatization and estrogen can also influence this parameter [see reviews 12, 13]. These observations suggest that the sex steroid effects on bone formation are likely to be complex.

There is also circumstantial evidence that leptin might regulate sex steroid functions, especially those of testosterone. The receptors for androgen and estrogen have been identified in bone cells [see reviews 14, 15]. Several studies have demonstrated that leptin levels are inversely correlated with testosterone [16, 17], suggesting an interaction between these hormones. However, the potential interactions between the sex hormones and leptin on the regulation of bone metabolism have not been functionally assessed, since previous studies in leptin-deficient (*ob/ob*) mice [4, 8, 18] and leptin receptor-deficient (*fa/fa*) rats [19] have examined various bone parameters in one gender or combined male and female subjects. These approaches yielded valuable information but could not resolve sex-specific differences in bone measurements produced by leptin.

The objective of this study was to evaluate whether interactions between leptin and the sex hormones affect bone formation. Accordingly, male and female leptin knockout (*ob/ob*) and wild-type control mice were examined for body and bone size to identify any sex-related effects of leptin on bone development. In this report, we show that a comparison of the femurs of male and female *ob/ob* mice with their wild-type counterparts reveals a surprising loss of sex-specific bone characteristics in the male leptin knockout mice. We conclude that leptin is an important modulator of androgen-related functions in bone growth.

Materials and Methods

Mice

Heterozygous male and female leptin knockout (*ob/ob*) mouse (B6.v-Lep^{ob}/J) breeders were obtained from Jackson Laboratories (Bar Harbor, ME) and maintained at the J. L. Pettis Memorial Veterans Administration Medical Center. Male and female mice of the wild-type background strain C57BL/6 were also obtained from Jackson Laboratories. Leptin knockout mice were bred, and the homozygous leptin-deficient genotype was confirmed by polymerase chain reaction (PCR) as previously described [20]. All animal procedures were approved by the local Institutional Animal Care and Use Committee.

Phenotypic Comparison of Body Characteristics and Bone Parameters

The body characteristic comparison was performed at 10 weeks of age in groups of 12 male and female mice. Total body fat and total lean body mass (excluding the head) of live mice were determined under general anesthesia by dual-energy X-ray absorptiometry (DXA) using a PIXIMUS system (Lunar, Madison, WI).

Bone parameters were compared in 13- to 14-week-old male and female mice following euthanasia by carbon dioxide inhalation (n = 12 each sex). Femurs were collected and fixed in 10% formalin. Femur length and midshaft diameter were manually measured with calipers. Periosteal circumference (PC), endosteal circumference (EC), polar moment of inertia (MOI, a measure of the distribution of material around a given axis), marrow area (MA), and total bone mineral content (BMC) of the midshaft of femurs were determined by peripheral quantitative computed tomography (pQCT; Stratec XCT 960M from Norland Medical Systems, Ft. Atkinson, WI) with the analysis thresholds of 630–630 for cortical bone (PC, EC, MOI) and 570–214 for cancellous bone (MA, total BMC) in adult mice.

In a separate experiment that examined bone parameters prior to the onset of sex hormone function, the femurs of 3-week-old prepubertal mice in groups of six of both sexes were also compared. The thresholds for cortical bone and cancellous bone of prepubertal mice were 300–350 and 250–300, respectively, as described by Richman et al. [21] and Taylor et al. [22].

Sex Hormone Assay

Mouse sera were separated from blood samples collected from the retro-orbital venous plexus of live animals under general anesthesia. Sera were stored frozen at –70°C until assay. Serum testosterone and estradiol levels were determined using the respective radioimmunoassay kits obtained from MPBio (Orangeburg, NY), according to the manufacturer's specifications.

Androgen Receptor Real-Time Reverse Transcription PCR

Expression of the androgen receptor gene in five leptin knockout and five wild-type male mice was analyzed by real-time PCR. Total RNA was isolated from marrow-ablated femoral diaphyses by Trizol (Invitrogen, Grand Island, NY) extraction, purified using the RNeasy mini kit (Qiagen, Valencia, CA) according to the manufacturer's specifications. RNA integrity was confirmed on the Agilent (Santa Clara, CA) Bioanalyzer and reverse-transcribed to cDNA using the SuperScript-III kit (Invitrogen) according to the manufacturer's specifications.

Androgen receptor gene expression was normalized to the expression of the cyclophilin-A housekeeping gene. Gene-specific primers were synthesized by IDT (Coralville, IA). The forward 5′-TAC TCT GCC TCC GAA GTG TG-3′ and reverse 5′-TCC GTA GTG ACA GCC AGA AG-3′ androgen receptor primers corresponded to bases 1458–1477 and 1688–1669, respectively, of the mouse androgen receptor gene (accession X53779). The forward 5′-GCA TAC AGG TCC TGG CAT CT-3′ and reverse 5′-TCT TGC TGG TCT TGC CAT TC-3′ cyclophilin-A primers corresponded to bases 351–370 and 544–525, respectively, of the mouse cyclophilin-A gene (accession XR_003025). Real-time reverse transcription (RT) PCR was performed in duplicate for each sample on an Opticon thermal cycler (Bio-Rad MJ Research, Hercules, CA) using the SYBR green-based Quantitect assay kit (Bio-Rad, Hercules, CA) according to the manufacturer's specifications. Reaction conditions providing the most efficient amplification from either set of primers were 95°C for 45 seconds, 55°C for 45 seconds, and 72°C for 30 seconds for 40 cycles. Androgen receptor gene expression was expressed as fold-activation and calculated from the cycle number difference between androgen receptor and cyclophilin-A genes.

Statistical Analysis

Statistical analysis was performed by two-way analysis of variance with a *post-hoc* Newman-Kuels test for phenotypic comparison of body and skeletal characteristics as well as serum sex hormone comparison. All data are expressed as the mean ± standard error of the mean (SEM). Differences were deemed significant at $P < 0.05$.

Results

Phenotypic Comparison of Body Characteristics in Adult Male and Female Leptin Knockout and C57BL/6 Wild-Type Mice

Homozygous leptin knockout mice are recognizable by an increased obesity that is evident by 3 weeks of age. As previously reported [21, 22], male wild-type C57BL/6 mice by the age of 10 weeks exhibit significantly higher body weight, greater body fat and greater total lean body mass than females [21, 22]. There was an approximately twofold increase in body weight (Fig. 1A), a sixfold increase in total body fat (Fig. 1B) and a significant difference in total lean body mass (Fig. 1C) in both male and female leptin knockout mice compared to male and female C57BL/6 wild-type mice. For each of these parameters, the differences between adult C57BL/6 male and female mice were not observed between male and female leptin knockout mice, indicating that the sex differences in body weight, body fat and total lean body mass were lost in leptin knockout mice.

Bone Parameter Comparison in Adult Male and Female Leptin Knockout and C57BL/6 Wild-Type Mice

Consistent with the previous report that male leptin knockout mice had a shorter femur length than male wild-type control mice [8], the femurs of 13- to 14-week-old male and female leptin knockout mice were shorter than those of C57BL/6 mice by 9% ($P < 0.0002$). There was no significant difference in femur length between males and females of either strain at this age statistically, though male femurs of both strains were slightly longer than the femurs of females (Fig. 2A).

We next evaluated various bone parameters between the leptin knockout and C57BL/6 strains for sex-related differences in femur size. The bone parameters were examined by pQCT at the midshaft of the femur. Cortical PC, EC, and polar MOI as well as MA and total BMC were examined. As previously reported [21], adult male C57BL/6 mice have a greater femoral PC than females. PC, EC and polar MOI of male C57BL/6 mice were significantly greater than those of male leptin knockout mice (Fig. 2B, C, F). These differences in PC were confirmed by caliper measurement of both the lateral-medial and anterior-posterior diameters of the femoral midshaft (data not shown). Consistent with these data, the MA and total BMC of adult

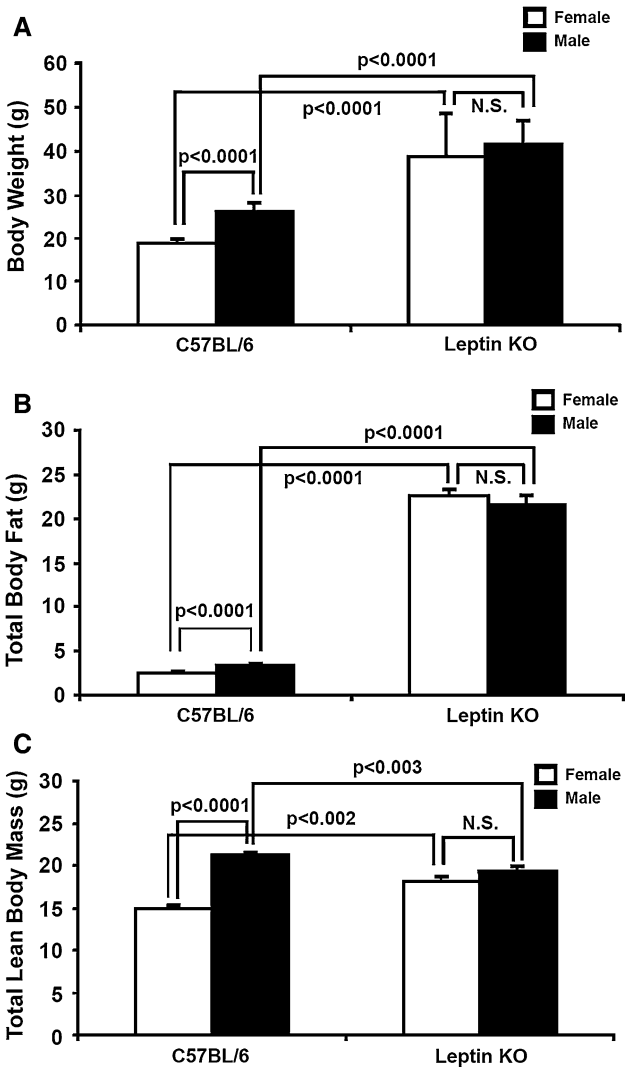

Fig. 1 Comparison of body characteristics in adult C57BL/6 and leptin knockout mice. Each group contained 12 mice at 10 weeks of age. (**A**) Body weight. (**B**) Total body fat. (**C**) Total lean body mass. Results are expressed as mean ± SEM

male C57BL/6 mice were significantly greater than values for female mice (Fig. 2D, E). The sex-related differences in these bone parameters seen in C57BL/6 mice were reduced in male *ob/ob* mice to levels similar to those of female *ob/ob* mice, so that there was no significant difference between male and female adult leptin knockout mice in any parameter of femur size (Fig. 2A–E). A closer examination of the PC and EC values for male leptin knockout mice revealed a slightly thinner cortical bone thickness in the femur compared with C57BL/6 mice (Fig. 2B, C), a result consistent with a previous study in male leptin knockout and C57BL/6 mice [8]. Also consistent with that study, male wild-type mice had a greater MA than male leptin knockout mice (Fig. 2D). There was no significant difference in any of the bone size parameters between the females of either strain. These data indicate that the male sex-related increase in bone size is completely lost in leptin knockout mice.

Phenotypic Comparison of Body Characteristics and Bone Parameters in Prepubertal Male and Female Leptin Knockout and C57BL/6 Mice

To demonstrate that the loss of sex-specific skeletal characteristics in male leptin knockout mice may relate to sex hormone biological activity, we compared the basal levels of body characteristics and bone parameters in male and female prepubertal mice at 3 weeks of age. In the phenotypic comparison, body weight, total body fat and total body lean mass did not significantly differ between male and female mice in either strain (Fig. 3A–C). These observations are consistent with previous results in C57BL/6 mice [21]. Male C57BL/6 mice have a similar body weight, total lean body mass and femur length as male leptin knockout mice. There was an approximately twofold increase in total body fat in leptin knockout mice compared to C57BL/6 mice at this age (Fig. 3B), suggesting that leptin regulation of body fat is independent of sex steroid effects.

In the comparison of the bone size parameters of these mice (Fig. 4), the length of the femurs in males and females was not significantly different in either the leptin knockout or C57BL/6 mice (Fig. 4A). From a pQCT examination of the femur at midshaft, the bone parameters PC, EC, MA, BMC and polar MOI were also not significantly different among male and female leptin knockout and C57BL/6 mice at the prepubertal age. All test bone parameters in male C57BL/6 and leptin knockout mice were similar to those of their female counterparts. Therefore, except for body fat, there were no significant differences in body characteristics and bone parameters between prepubertal leptin knockout and C57BL/6 mice or between males and females of either strain at this age.

Comparison of Serum Sex Hormone Levels in Adult Male and Female Leptin Knockout and C57BL/6 Wild-Type Mice

To assess whether the loss of the sex-related differences in leptin knockout mice was due to a deficiency in the sex steroids, we next evaluated the serum levels of free testosterone (FT) and estradiol. Male leptin knockout mice had approximately a fivefold greater serum FT than male C57BL/6 wild-type mice (Fig. 5A). The large variations in serum FT levels of male leptin knockout compared to male C57BL/6 mice reflected a greater individual difference in sex hormone levels in male leptin knockout mice. There was no detectable serum FT in either female wild-type or female leptin knockout mice.

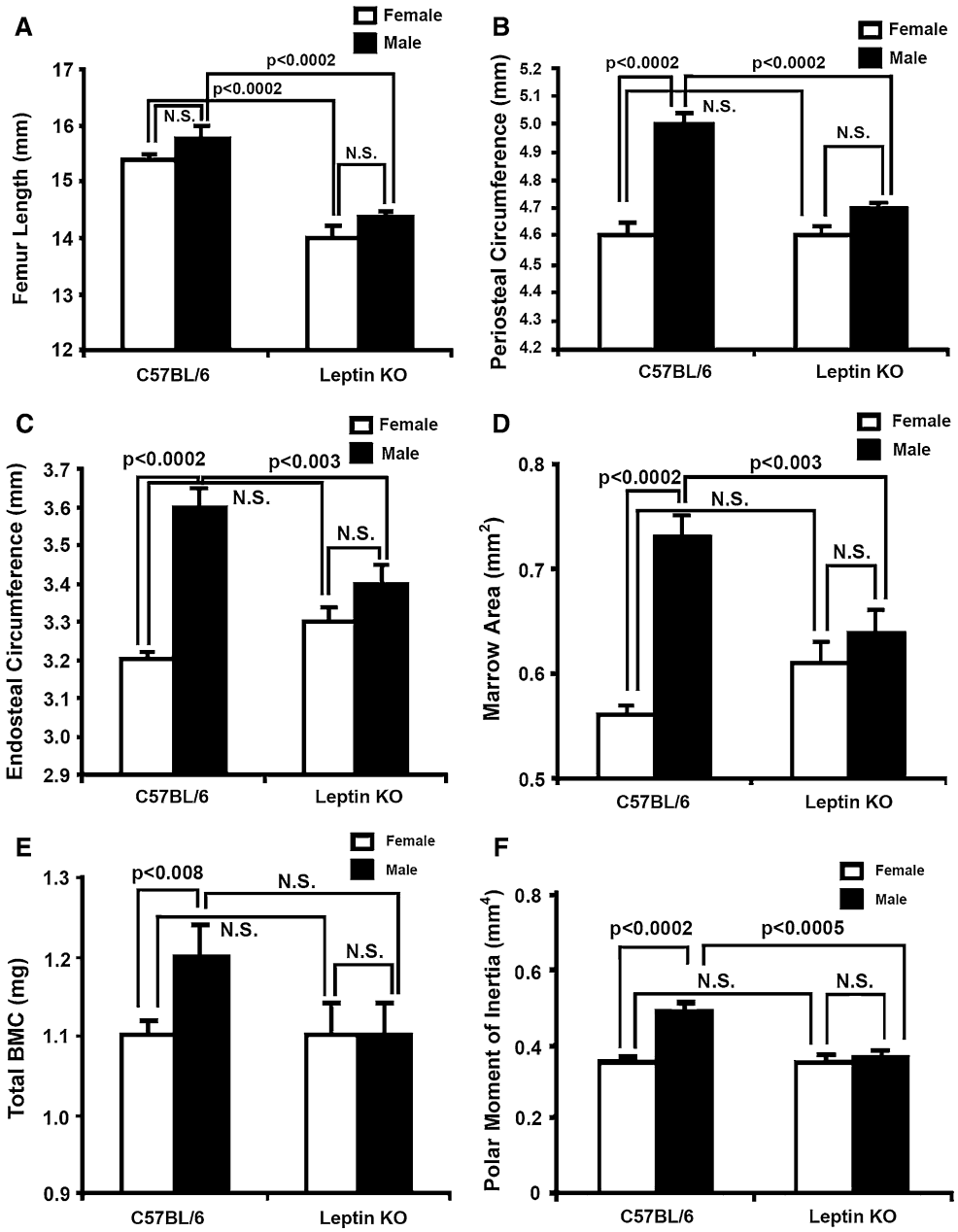

Fig. 2 Comparison of bone parameters in adult C57BL/6 and leptin knockout mice. (**A**) Femur length. (**B**) Periosteal circumference. (**C**) Endosteal circumference. (**D**) Marrow area. (**E**) Total bone mineral content. (**F**) Polar moment of inertia. Each group contained 12 mice at 13–14 weeks of age. Results are expressed as mean ± SEM

Male and female leptin knockout mice exhibited no significant differences in serum estradiol, but each was significantly more estradiol than the corresponding C57BL/6 mice (Fig. 5B). There were approximately 1.3-fold and 1.8-fold greater estradiol levels in female and male leptin knockout mice than in female and male C57BL/6 mice, respectively. These greater serum FT levels in male leptin knockout mice and estradiol levels in both sexes of leptin knockout mice imply that their concentrations should be sufficient to produce a wild-type femur size in each sex. Thus, the functional deficiency in the acquisition of normal bone size in male leptin knockout mice was not the result of insufficient levels of circulating FT. A comparison of the androgen receptor gene expression in male leptin knockout and C57BL/6 mice failed to detect any significant differences in transcript levels (data not shown).

Discussion

Leptin has pleiotropic effects, using multiple pathways to regulate bone formation and balance bone formation with fat production. Previous studies have examined various bone parameters in leptin-deficient animals [4, 8, 18, 19], but they have either examined one gender or combined males and females in the same analysis, failing to resolve

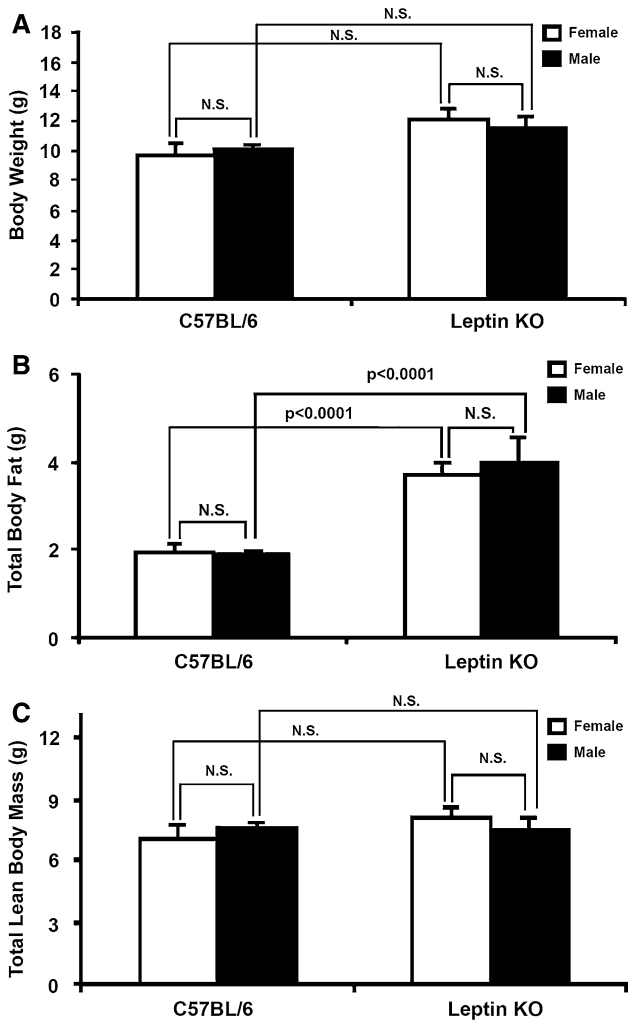

Fig. 3 Comparison of body characteristics in prepubertal C57BL/6 and leptin knockout mice. (**A**) Body weight. (**B**) Total body fat. (**C**) Total lean body mass. Each group contained six mice at 3 weeks of age. Results are expressed as mean ± SEM

sex-specific differences in bone measurements. Additionally, different components of the leptin axis have been examined in various studies, including leptin and leptin receptor models in mice and rats. Sex-specific differences in these models have not been well characterized, and to our knowledge this is the first study to identify sex-related differences in bone size in leptin knockout mice.

We compared the femoral parameters of bone size when the usual differences in lean body mass between male and female wild-type mice were not detected between male and female leptin-deficient mice, despite a doubling in the total body weight observed in adult leptin knockout mice relative to wild-type mice (Fig. 1). The reduced lean body mass in male leptin knockout mice suggested a sex hormone interaction with leptin. Because sex hormone effects are also expected to affect bone size, we examined the femur in adult mice, which has been previously established to be shorter in leptin knockout mice than in their wild-type counterparts [8] and would therefore be likely to reveal sex-related differences.

When we compared adult male and female leptin knockout mice at 13–14 weeks of age, however, several of the expected sex-related differences in bone parameters were not observed. Specifically, PC and EC as well as BMC and MA in the leptin knockout male mice were all reduced (Fig. 2A–E). Importantly, polar MOI, a major cross-sectional determinant of torsional bone strength, was not altered between female C57BL/6 and leptin knockout mice (Fig. 2F), which suggests that mechanical loading effects on bone formation did not contribute to the loss of bone size parameters.

These results contrast with the high bone mass phenotype attributed to leptin knockout mice [4]. It is possible that our results vary from previous reports because our measurements were taken at the midshaft while previous analyses examined the metaphysis. However, our results largely agree with those of Hamrick et al. [8], who found reduced femur parameters among 6-month-old male leptin knockout mice. The femurs of leptin knockout animals are significantly shorter than those of wild-type mice, an observation reported in that study. Both males and females showed this trait, suggesting that endochondral bone length, at least in the femur, is directly regulated through leptin without sex hormone-related effects. It appears that leptin is permissive for femur length, though other factors, notably estrogen regulation of growth plate chondrocyte proliferation and epiphyseal fusion, also affect femur length [23]. If androgens mediate the periosteal dimensions of the endochondral bones, the reduced femur length in leptin knockout male mice could compensate for such factors as the cortical thinning of leptin knockout mice, which might cause an unacceptable loss of bone strength in a femur of normal length.

The effect of weight of mechanical loading on the leptin knockout femur is difficult to determine because the large weight gain renders the animal relatively inactive. The lack of differences in polar MOI suggests that the increased mechanical loading expected from the greater body weight does not affect bone formation. However, the posture and gait of the animal also appear so altered by the weight mass that we cannot assume that the different elements of the skeleton will bear the increased weight in the same proportion as they would the normal weight. Hamrick et al. [8] described muscle atrophy in their male leptin knockout mice, but we did not observe differences in lean body mass between male and female leptin knockout mice, which would suggest that the muscle mass is centrally regulated by testosterone and local atrophy is less important. However, our results do agree with the femur analysis of Hamrick et al. [8], who found variations in axial and appendicular bone

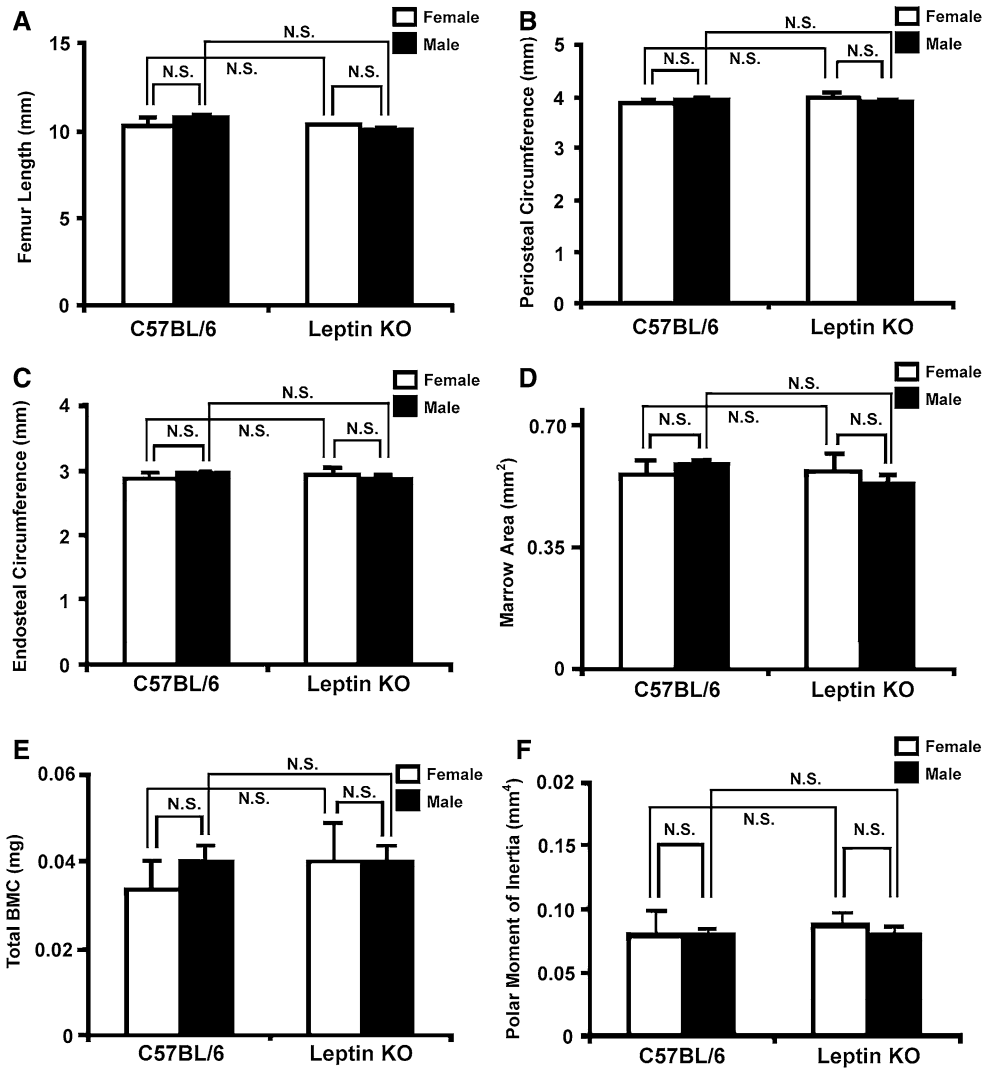

Fig. 4 Comparison of bone parameters of prepubertal C57BL/6 and leptin knockout mice. (**A**) Femur length. (**B**) Periosteal circumference. (**C**) Endosteal circumference. (**D**) Marrow area. (**E**) Total bone mineral content. (**F**) Polar moment of inertia. Each group contained six mice at 3 weeks of age. Results are expressed as mean ± SEM

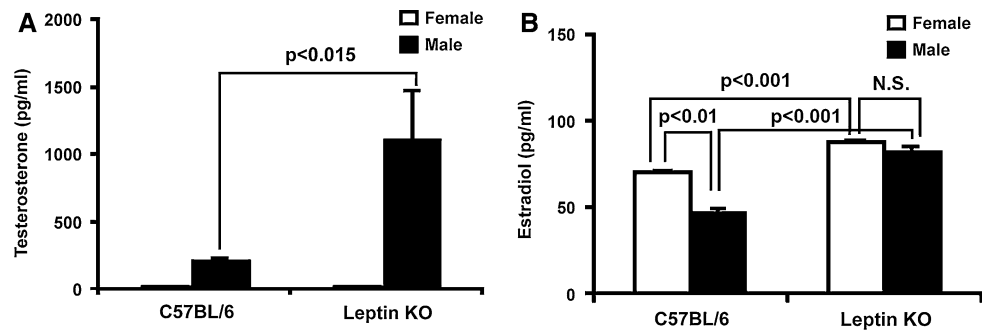

Fig. 5 Comparison of serum sex hormone levels in male and female leptin knockout and C57BL/6 wild-type mice. Each group contained 15 mice at 10 weeks of age. Results are expressed as mean ± SEM

parameters in male leptin knockout mice. The cortical thinning observed in that study was also observed in this study. These results support a peripheral role for leptin in the regulation of bone size, with leptin expression permissive for the sex hormone functions that affect bone growth. We have not examined other bones and cannot conclude that all skeletal elements of male leptin knockout mice display the loss of sex-related differences in bone size observed in the femur. We cannot discount central regulation of bone size and variable fat content within different skeletal elements that might occur in such an obese animal. To confirm that the loss of sex-related differences in leptin knockout mice was indeed due to sex hormone function, we compared the body characteristics and femur parameters in prepubertal wild-type and leptin knockout mice at 3 weeks of age. This time is prior to the sex hormone production that would be expected

to affect sex-related functions, including bone development. There were no sex-related differences in body weight, body fat or total lean body mass in prepubertal mice (Fig. 3), though both male and female leptin knockout mice exhibited an increase in body fat by this age (Fig. 3B). No differences in any femoral parameters were observed between male and female prepubertal mice of either the wild-type or leptin knockout strain (Fig. 4A–F). Taken together, these results confirmed that the loss of differences in femur size between adult male and female leptin knockout mice was related to sex hormone function.

Surprisingly, adult male leptin knockout mice expressed elevated serum levels of FT, suggesting that the increase in testosterone production may reflect a compensatory mechanism for deficient testosterone function (Fig. 5A). On the other hand, we did not measure the sex hormone binding globulin (SHBG) level in this study, because assays for murine SHBG are not commercially available. SHBG has been negatively correlated with obesity and insulin resistance [24], which suggests that it might also influence FT levels in leptin knockout male mice, although interactions with total testosterone and leptin might be complex. Accordingly, we cannot rule out the possibility that the elevated serum testosterone levels might be a consequence of a reduced circulatory SHBG. Leptin knockout males and females also exhibited elevated free serum estrogen (Fig. 5B), consistent with the aromatization of testosterone to estrogen in the males that is also observed in obese human males [25], though the response to aromatase functions could itself also be sex-specific [26]. Although we do not have evidence at this time, the elevated levels of testosterone argue against hypogonadism in leptin knockout males, and the high variation in serum FT between individuals suggests that feedback upregulation of testosterone is involved. Feedback upregulation of testosterone, such as that observed in bone cells *in vitro* [27], is consistent with a defective testosterone signaling mechanism, especially in the absence of transcriptional upregulation of the androgen receptor that we observed in male leptin knockout mouse femurs. Our future studies will address this possibility. Because testosterone affects periosteal diameter, it would be expected that androgens would mediate cross-sectional bone size through the periosteal cells. If so, this deficiency appears to reside in the testosterone receptor signaling pathway of leptin knockout cells, as real-time RT-PCR analysis of androgen receptor expression in male leptin knockout and C57BL/6 femurs failed to detect any significant differences in receptor transcript levels. Deficient testosterone signaling in the periosteum might therefore explain the reduction in cross-sectional parameters of bone size in male leptin knockout mice. We continue to investigate the testosterone signaling pathway in male leptin knockout mice.

This study also did not address the effects of obesity and leptin deficiency on diabetic hyperinsulinemia and growth hormone regulation of body composition. While the growth hormone (GH)/insulin-like growth factor (IGF) axis is affected by body fat, has been correlated with leptin levels in normal men and women, and leptin and the IGF-I system did not regulate one another [28], adipose tissue mediation of the GH/IGF system remains poorly understood. Thus, the effects of leptin deficiency on bone size are affected by multiple hormonal systems that confound interpretations of systemic regulation. Accordingly, we cannot rule out the possibility that the changes in bone size parameters that we observed might be related to peripheral leptin regulation of osteoblast and adipocyte differentiation [29].

Leptin regulation of bone size parameters would be expected to balance skeletal growth and development with body mass. The loss of sex-specific differences in femur size in the absence of leptin function suggests that leptin is permissive for androgen effects that produce the increased body mass and bone size in males. Such interactions might take place through any of the several intracellular signaling pathways that mediate leptin receptor signaling [see review 30] and androgen receptor signaling [see review 31]. We propose that in the presence of leptin, normal androgen signaling would be expected to increase bone size to accommodate the increase in body size in males. In the absence of leptin, estrogen might mediate basal bone size parameters while androgen signaling for increased size is impaired in males. Further studies will investigate the mechanism by which leptin mediates sex-specific bone parameters.

Acknowledgements This work was supported by the U.S. Army Medical Research Acquisition Activity Assistance (DAMD17-03-2-0021). The U.S. Army Medical Research Acquisition Activity, 820 Chandler Street, Fort Detrick, MD 21702-5014, is the awarding and administering acquisition office. The information contained in this publication does not necessarily reflect the position or the policy of the government, and no official endorsement should be inferred. All work was performed in facilities provided by the Department of Veterans Affairs. Preliminary results were presented at the American Society of Bone and Mineral Research, Nashville, TN, September 2005 (abstract SA508) and at the 52nd Annual Meeting of the Orthopedic Research Society, Chicago, IL, March 2006 (abstract 188). We are grateful to Mr. Emile Davis and Ms. Jann Smallwood for technical assistance.

References

1. Zhang Y, Proenca R, Maffei M, Barone M, Leopold L, Friedman JM (1994) Positional cloning of the mouse obese gene and its human homologue. Nature 372:425–432
2. Campfield LA, Smith FJ, Guisez Y, Devos R, Burn R (1995) Recombinant mouse OB protein: evidence for a peripheral signal linking adiposity and central neural networks. Science 269:546–549

3. Thomas T, Gori F, Khosla S, Jensen MD, Burguera B, Riggs BL (1999) Leptin acts on human marrow stromal cells to enhance differentiation to osteoblasts and to inhibit differentiation to adipocytes. Endocrinology 140:1630–1638
4. Ducy P, Amling M, Takeda S, Priemel M, Schilling AF, Beil FT, Shen J, Vinson C, Rueger JM, Karsenty G (2000) Leptin inhibits bone formation through a hypothalamic relay: a central control of bone mass. Cell 100:197–207
5. Livshits G, Pantsulaia I, Trofimov S, Kobyliansky E (2003) Genetic variation of circulating leptin is involved in genetic variation of hand bone size and geometry. Osteoporos Int 14:476–483
6. Takeda S, Elefteriou F, Levasseur R, Liu X, Zhao L, Parker K, Armstrong D, Ducy P, Karsenty G (2002) Leptin regulates bone formation via the sympathetic nervous system. Cell 111:305–317
7. Steppan CM, Crawford DT, Chidsey-Frink KL, Ke HZ, Swick AG (2000) Leptin is a potent stimulator of bone growth in *ob/ob* mice. Regul Pept 92:73–78
8. Hamrick MW, Pennington C, Newton D, Xie D, Isales C (2004) Leptin deficiency produces contrasting phenotypes in bones of the limb and spine. Bone 34:376–383
9. Iwamoto I, Fujino T, Douchi T (2004) The leptin receptor in human osteoblasts and the direct effect of leptin on bone metabolism. Gynecol Endocrinol 19:97–104
10. Nelson DA, Simpson PM, Johnson CC, Barondess DA, Kleerekoper M (1997) The accumulation of whole body skeletal mass in third- and fourth-grade children: effects of age, gender, ethnicity, and body composition. Bone 20:73–78
11. Sims NA, Dupont S, Krust A, Clement-Lacroix P, Minet D, Resche-Rigon M, Gaillard-Kelly M, Baron R (2002) Deletion of estrogen receptors reveals a regulatory role for estrogen receptors-beta in bone remodeling in females but not in males. Bone 30:18–25
12. Vanderschueren D, Vanderput L, Boonen S, Lindberg MK, Bouillon R, Ohlsson C (2004) Androgens and bone. Endocr Rev 25:389–425
13. Vanderschueren D, Venken K, Ophoff J, Bouillon R, Boonen S (2006) Sex steroids and the periosteum – reconsidering the roles of androgens and estrogens in periosteal expansion. J Clin Endocrinol Metab 91:378–382
14. Vanderschueren D, Bouillon R (1995) Androgens and bone. Calcif Tissue Int 56:341–346
15. Compston JE (2001) Sex steroids and bone. Physiol Rev 81:419–447
16. Luukkaa V, Pesonen U, Huhtaniemi I, Lehtonen A, Tilvis R, Tuomilehto J, Koulu M, Huupponen R (1998) Inverse correlation between serum testosterone and leptin in men. J Clin Endocrinol Metab 83:3243–3246
17. Wabitsch M, Blum WF, Muche R, Braun M, Hube F, Rascher W, Heinze E, Teller W, Hauner H (1997) Contribution of androgens to the gender difference in leptin production in obese children and adolescents. J Clin Invest 100:808–813
18. Hamrick MW, Della-Fera MA, Choi YH, Pennington C, Hartzell D, Baile CA (2005) Leptin treatment induces loss of bone marrow adipocytes and increases bone formation in leptin-deficient *ob/ob* mice. J Bone Miner Res 20:994–1001
19. Tamasi JA, Arey BJ, Bertolini DR, Feyen JH (2003) Characterization of bone structure in leptin receptor-deficient Zucker (*fa/fa*) rats. J Bone Miner Res 18:1605–1611
20. Namae M, Mori Y, Yasuda K, Kadowaki T, Kanazawa Y, Komeda K (1998) New method for genotyping the mouse Lep(ob) mutation, using a polymerase chain reaction assay. Lab Anim Sci 48:103–104
21. Richman C, Kutilek S, Miyakoshi N, Srivastava AK, Beamer WG, Donahue LR, Rosen CJ, Wergedal JE, Baylink DJ, Mohan S (2001) Postnatal and pubertal skeletal changes contribute predominantly to the differences in peak bone density between C3H/HeJ and C57BL/6J mice. J Bone Miner Res 16:386–397
22. Taylor BA, Tarantino LM, Phillips SJ (1999) Gender-influenced obesity QTLs identified in a cross involving the KK type II diabetes-prone mouse strain. Mamm Genome 10:963–968
23. Weise M, De-Levi S, Barnes KM, Gafni RI, Abad V, Baron J (2001) Effects of estrogen on growth plate senescence and epiphyseal fusion. Proc Natl Acad Sci USA 98:6871–6876
24. Osuna JA, Gomez-Perez R, Arata-Bellabarba G, Villaroel V (2006) Relationship between BMI, total testosterone, sex-hormone-binding-globulin, leptin, insulin and insulin resistance in obese men. Arch Androl 52:355–361
25. Kley HK, Deselaers T, Peerenboom H, Kruskemper HL (1980) Enhanced conversion of androstenedione to estrogens in obese males. J Clin Endocrinol Metab 51:1128–1132
26. Oz OK, Zerwekh JE, Fisher C, Graves K, Nanu L, Millsaps R, Simpson ER (2000) Bone has a sexually dimorphic response to aromatase deficiency. J Bone Miner Res 15:507–514
27. Wiren KM, Zhang X, Chang C, Keenan E, Orwoll ES (1997) Transcriptional up-regulation of the human androgen receptor by androgen in bone cells. Endocrinology 138:2291–2300
28. Gomez JM, Maravall FJ, Gomez N, Navarro MA, Casamitjana R, Soler J (2003) Interactions between serum leptin, the insulin-like growth factor-1 system, and sex, age anthropometric and body composition variables in a healthy population randomly selected. Clin Endocrinol 58:213–219
29. Martin A, de Vittoris R, David V, Moraes R, Begeot M, Lafage-Proust M-H, Alexandre C, Vico L, Thomas T (2005) Leptin modulates both resorption and formation while preventing disuse-induced bone loss in tail-suspended female rats. Endocrinology 146:3652–3659
30. Fruhbeck G (2006) Intracellular pathways activated by leptin. Biochem J 393:7–20
31. Culig Z (2004) Androgen receptor cross-talk with cell signaling pathways. Growth Factors 22:179–184

Calcif Tissue Int (2008) 83:276–284
DOI 10.1007/s00223-008-9169-7

LABORATORY INVESTIGATIONS

Fracture Healing in Mice Deficient in Plasminogen Activator Inhibitor-1

Charles H. Rundle · Xiaoguang Wang · Jon E. Wergedal · Subburaman Mohan · K.-H. William Lau

Received: 16 April 2008 / Accepted: 18 August 2008 / Published online: 27 September 2008

Abstract To evaluate the role of plasminogen activator inhibitor (PAI)-1, a key negative regulator of the plasmin system of extracellular matrix proteases in developmental bone growth and fracture repair, the bone phenotype of male adult PAI-1-deficient mice was determined and femoral fracture healing was compared with that of age- and sex-matched wild-type C57BL/6J control mice. Regarding bone phenotype, the length and size (but not cortical thickness) of the femur of male PAI-1-deficient mice were smaller than those of wild-type controls. Although the total bone mineral content of PAI-1-deficient mice was not significantly different from that of wild-type mice, the total bone area in PAI-1-deficient mice was smaller, leading to an increase in total bone mineral density. With respect to fracture healing, PAI-1-deficient mice developed fracture calluses that were larger and more mineralized than those of wild-type mice but only at 14 days postfracture. These changes were even greater given the smaller size of the normal femur in PAI-1-deficient mice. Surprisingly, the larger fracture callus remodeled rapidly to normal size and mineral content by 21 days postfracture. Examination of fracture histology revealed that these changes were associated with a dramatic increase followed by a rapid remodeling of the fracture callus cartilage. The remodeling of fracture callus cartilage in PAI-1-deficient mice also displayed an abnormal pattern. These findings demonstrate for the first time that PAI-1 (and potentially the plasminogen extracellular matrix protease system) is an important regulator of bone size during developmental growth and plays a regulatory role in the determination of fracture callus size, cartilage formation, and resorption during bone fracture repair.

Keywords Plasminogen activator inhibitor-1 · Wound healing · Cartilage · Plasmin

C. H. Rundle · X. Wang · J. E. Wergedal · S. Mohan · K.-H.W. Lau (✉)
Musculoskeletal Disease Center, Jerry L. Pettis Memorial Veterans Administration Medical Center, 11201 Benton Street, Loma Linda, CA 92357, USA
e-mail: William.Lau@med.va.gov

C. H. Rundle · J. E. Wergedal · S. Mohan · K.-H.W. Lau
Department of Medicine, Loma Linda University, Loma Linda, CA 92350, USA

J. E. Wergedal · S. Mohan · K.-H.W. Lau
Department of Biochemistry, Loma Linda University, Loma Linda, CA 92350, USA

S. Mohan
Department of Physiology, Loma Linda University, Loma Linda, CA 92350, USA

Fracture healing is mediated by multiple molecular pathways that in part regulate the proliferation and maturation of the diverse cell types of soft and bony tissues in the developing fracture callus. Timely remodeling of the damaged extracellular matrix at the fracture site is also essential for the maturation of the fracture callus. In particular, the bone formation phase of fracture repair involves chondrogenesis and angiogenesis, two processes that are dependent on cell–extracellular matrix interaction. Accordingly, extracellular matrix remodeling is expected to be one of the important elements of the fracture repair process.

The plasmin system of extracellular matrix serine proteases, which is involved in extracellular matrix remodeling during development and repair of soft tissue, is one such regulator of extracellular matrix remodeling

during bone repair. The plasmin proteases are secreted as plasminogens and activated by plasminogen activators, which include tissue plasminogen activator (tPA) and urokinase plasminogen activator (uPA). Plasminogen activator inhibitor (PAI)-1 (also known as serpine-1) is a negative regulator of these plasminogen activators. As a key mediator of the plasminogens, PAI-1 is an important regulator of tissue development and repair. The ratio of PAI to plasminogen is an important regulator of plasminogen functions [1], as well as the functions of downstream effectors of related pathways in various tissues. PAI-1 expression is induced upon injury in skin [2]. Direct evidence of its functions in wound healing is provided by studies with PAI-1 knockout (KO) mice, which showed that the rate of skin wound closure is significantly accelerated when compared to wild-type mice [2] and muscle healing is improved [3].

PAI-1 can also modulate cell adhesion and migration in a nonproteolytic fashion. PAI-1 modulates plasminogen activity through adhesion to focal contact points, notably through its receptor, vitronectin. Upon vitronectin binding, PAI-1 not only is stabilized to preserve its matrix proteolysis regulatory functions but can also reduce cellular adhesion and increase cell motility on the extracellular matrix [4] during tissue repair [5]. This not only functions in repair of the wound but also minimizes scar tissue development at the injury site. This function of PAI-1 has been associated with impaired arterial wound healing in PAI-1 KO mice [6]. Because PAI-1 regulates different aspects of development, homeostasis, and repair of a number of tissues, we postulate that PAI-1 also has similar functions in the bone repair and regeneration process.

The objective of the present study was twofold: (1) to assess the hypothesis that PAI-1 has an important regulatory role in developmental bone growth by comparing the bone phenotype of adult male PAI-1 KO mice with that of age- and sex-matched wild-type mice and (2) to evaluate if PAI-1 is involved in the fracture healing process by examining the consequences of PAI-1 deficiency on the healing of a normal femoral fracture.

Materials and Methods

Animals

All animal protocols were reviewed and approved by the Institutional Animal Care and Use Committee of the Jerry L. Pettis Memorial Veterans Administration Medical Center. Homozygous breeding pairs of PAI-1 (serpine-1)–deficient mice (B6.129S2-*Serpine1*^{tm1Mlg}/J) [7] of C57BL/6J genetic background were obtained from Jackson Labs (stock 2507; Bar Harbor, ME) and bred in the animal facility of this institution. The C57BL/6J mouse strain, recommended by Jackson Labs as wild-type control strain for comparison to PAI-1 KO mice, was also purchased from Jackson Labs (stock 664). To avoid the sex-related confounding effects on developmental bone growth and fracture repair, only male mice were used in this study. All mice were 12 weeks of age at fracture.

Characterization of Bone Phenotype in PAI-1-Deficient Mice

The bone phenotype of male PAI-1-deficient mice was determined on intact femurs by peripheral quantitative computed tomography (pQCT; Stratec XCT 960 M, Norland Medical System, Ft. Atkinson, WI) and compared with intact femurs of age- and sex-matched C57BL/6J wild-type mice. Intact femurs were obtained as the unfractured contralateral bone from mice that underwent the femur fracture procedure and were harvested with the fracture tissues at 1–4 weeks postfracture (or 13 and 16 weeks of age). pQCT scanning was performed at 70×70 voxel resolution. For examination of cortical bone–based femoral characteristics, the size, bone mineral content (BMC), and bone mineral density (BMD), measurements were obtained on a 1-mm section at the midshaft taken a set distance of 7 mm from the condyle. This site was chosen for phenotypic evaluation because the periosteal and endosteal circumferences could be accurately measured at this location. Other bone phenotypic parameters were also measured at this site for comparison. pQCT analysis was performed using contour 1 and peel 4 modes and a cortical bone threshold setting of 630–630, parameters previously validated for midshaft measurements of cortical bone by histomorphometry [8].

For examination of trabecular bone–based femoral characteristics, the area, BMC, and BMD measurements were obtained from the most distal three 1-mm sections of the femur corresponding to the condylar metaphysis. pQCT analysis was also performed using contour 1 and peel 4 modes but used a trabecular threshold setting of 570–214. Femur length was measured from the proximal tip of the greater trochanter to the lateral and medial tips of the condyle using digital calipers.

Murine Femur Fracture Healing Model

The three-point bending technique for the standard rat closed femoral fracture model [9] was adapted to the mouse femur fracture model. Briefly, a 0.56-mm-diameter stainless steel pin was surgically implanted in retrograde fashion into the intramedullary space of the femur, with the mouse under general anesthesia of 67 mg/kg ketamine and 13 mg/kg xylazine, delivered intraperitoneally. A single closed

complete fracture was then created at the midshaft of the femur by the three-point bending technique using an Instron (Norwood, MA) 8841 servohydraulic tester. Analgesia was 60 μg/kg buprenorphine provided subcutaneously and prophylactically during recovery on the day of fracture surgery, and animals were monitored for discomfort daily on the 2 days after fracture surgery. Movement of the animal was not restricted during recovery. This approach produced consistent fractures; approximately 10–20% of the fractures were excluded from analysis because of unacceptable degrees of comminution at the fracture or pin migration during healing. Healing fractures were harvested at 7, 14, 21, or 28 days postfracture, when characteristic fracture callus radiology, morphology, and histology allow accurate comparisons between normal and impaired fracture healing. Groups of six to eight animals were analyzed for fracture healing at each postfracture time. In this mouse model, union of bony callus across the gap normally begins to occur at approximately 3 weeks postfracture.

Fracture Radiology

X-ray analysis was performed at 7, 14, 21, and 28 days postfracture. Fracture callus radiology was analyzed by X-ray examination (Faxitron, Wheeling, IL) and evaluated by two observers for bridging of the fracture gap with bony callus tissues using a numerical scoring system that designated the following: 0, no callus formation; 1, callus formation without bony union; 2, callus formation with possible bony union; 3, callus present with bony union. Fracture calluses were then quantified by pQCT. Total BMC, cross-sectional area of the cancellous callus, as well as total cross-sectional area of all hard and soft callus tissues were quantified from pQCT scans for nine serial 1-mm slices along the length of the femur with the center of the fracture callus located at the center slice (i.e., slice 5). Scanning was performed at a resolution of 70 × 70 μm. Fracture callus pQCT measurements were analyzed using the same peel and contour modes as used for the native femur analysis but with trabecular threshold settings of 214–570 for total cancellous BMC and 0–570 for average cross-sectional area of cancellous bony and soft fracture callus tissues. The values of each slice were summed to determine total BMC and averaged to obtain cross-sectional areas of the bony callus and total callus tissues.

Fracture Histology

For fracture histology examination, fractured femurs were collected from each strain of mouse at the time of death and fixed in 10% formalin. Bones were decalcified in 10% EDTA (pH 7.1) for 21 days [10], then embedded in paraffin. Each sample was sectioned longitudinally at 5-μm thickness, and the center section from each callus was selected for analysis. The center sections of three to five different fractures were measured for each mouse strain at each postfracture time point. Sections were stained for cartilage with Safranin orange. Cartilage area was quantified as a proportion of the total callus area of each section using Image-Pro 4.0 analysis software (Media Cybernetics, Silver Spring, MD). Osteoclast numbers per square millimeter of callus section area were quantified by counting at least five separate fields of a fracture section from each animal that had been stained for tartrate-resistant acid phosphatase (TRAP) activity. Additional sections from these fracture calluses were stained with hematoxylin–eosin to further evaluate the fracture tissues. Photomicrographs were obtained using a BX-60 microscope (Olympus, Melville, NY) and a DXC-950P camera (Sony, New York, NY).

Statistical Analysis

Statistical analysis was performed by the *F*-test (covariate regression analysis) for femur size parameters or by two-way ANOVA for comparisons of genotype and postfracture time of healing, followed by the Scheffe post-hoc test. All values are expressed as mean ± standard deviation (SD). Differences were deemed significant at $P < 0.05$.

Results

Bone Phenotype in Adult Male PAI-1 KO Mice

Male PAI-1 KO mice displayed a 5% reduction in body weight relative to age-matched males of the C57BL/6J wild-type background strain (26.0 ± 2.6 vs. 24.7 ± 2.1 g, $P < 0.05$). A covariate regression analysis that corrected for the reduced body weight of PAI-1 KO mice established that several femur size parameters were also reduced relative to C57BL/6J control mice (Table 1). Specifically, femur length in PAI-1 KO mice was reduced by 2.4% ($P < 0.005$) compared to control mice. The periosteal circumference at midshaft was reduced by 6% ($P < 0.005$) and the endosteal circumference was reduced by 8% ($P < 0.001$) in PAI-1 KO mice compared to control mice. The slightly greater reduction in endosteal circumference produced a small but significant increase in cortical thickness at the midshaft of PAI-1 KO mice ($P < 0.05$). While the total bone area of PAI-1 KO mice was less than that of wild-type control mice (by 11%, $P < 0.005$), there was no significant difference in total BMC or cortical area. The lack of a corresponding decrease in total BMC led to a significant increase (5%, $P < 0.001$) in total BMD in PAI-1 KO mice. However, when the area, BMC, and BMD of

Table 1 Femur phenotype in C57BL/6J control and PAI-1 KO male mice

Parameter[a] (mean ± SD)	C57BL/6J ($n = 28$)	PAI 1 KO ($n = 28$)	t-test[b]	F-test[c]
Length (mm)	15.80 ± 0.48	15.42 ± 0.37	$P < 0.005$	$P < 0.005$[d]
Mid-diaphysis				
Total BMD (mg/mm^3)	599.09 ± 52.06	630.04 ± 32.05	$P < 0.005$	$P < 0.001$
Total BMC (mg)	1.22 ± 0.17	1.14 ± 0.13	NS	NS
Total area (mm^2)	2.04 ± 0.20	1.81 ± 0.17	$P < 0.001$	$P < 0.005$
Cortical BMD (mg/mm^3)	1,168.46 ± 55.07	1,168.20 ± 38.69	NS	NS
Cortical BMC (mg)	0.82 ± 0.16	0.78 ± 0.12	NS	NS
Cortical area (mm^2)	0.70 ± 0.11	0.66 ± 0.09	NS	NS
Periosteal circumference (mm)	5.05 ± 0.24	4.76 ± 0.23	$P < 0.001$	$P < 0.005$
Endosteal circumference (mm)	3.67 ± 0.20	3.38 ± 0.16	$P < 0.001$	$P < 0.001$
Cortical thickness (mm)	0.22 ± 0.02	0.22 ± 0.02	NS	$P < 0.05$
Distal diaphysis				
Trabecular BMD (mg/mm^3)	132.02 ± 30.60	138.86 ± 9.88	NS	NS
Trabecular BMC (mg)	0.08 ± 0.03	0.10 ± 0.01	$P < 0.01$	$P < 0.05$
Trabecular area (mm^2)	0.64 ± 0.20	0.72 ± 0.13	NS	NS

[a] Age 13–16 weeks

[b] Two-tailed Student's t-test without adjustment for femur length and body weight

[c] F-test covariate regression analyses with body weight and femur length as independent variables

[d] For femur length, body weight was the only independent variable

NS, not significant

cortical and trabecular bone at the midshaft and distal metaphysis, respectively, of the femur were evaluated individually and independently (Table 1), there were no significant differences between PAI-KO and C57BL/6J wild-type control mice, with the exception of trabecular BMC, which was reduced by 20% ($P < 0.05$).

Fracture Healing in PAI-1-Deficient Mice

Based upon an initial examination of the X-ray data (Fig. 1), PAI-1 KO mice appeared to have a larger fracture callus at 7 and 14 days, but not at 21 and 28 days, post-fracture compared to C57BL/6J wild-type control mice. In spite of the larger fracture callus during the early healing period, radiological grading for fracture union indicated that there were no significant differences in bony union of the fracture gap in PAI-1 KO fractures compared to wild-type fractures (Fig. 1). Thus, while PAI-1 deficiency enhances early callus formation and remodeling, it has no apparent effect on overall healing (i.e., bony bridging of the gap) of the fracture.

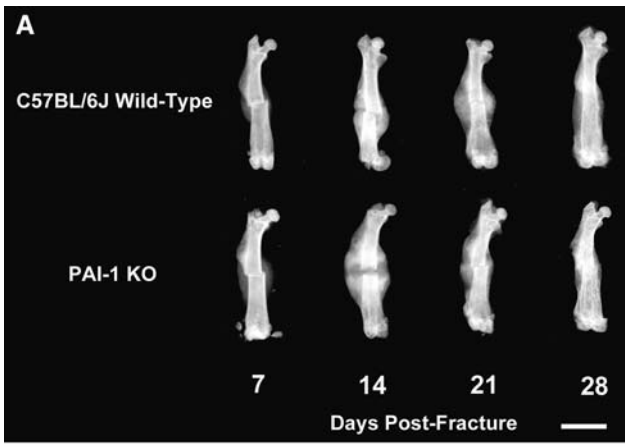

B

Fracture Union Grading	7	14	21	28
C57BL/6J Wild-Type	1.0 ± 0	1.0 ± 0.3	2.0 ± 0	3.0 ± 0
PAI-1 KO	0.4 ± 0.5	1.4 ± 0.5	2.3 ± 0.5	3.0 ± 0

Fig. 1 Fracture healing radiology. (**a**) Healing was examined by X-ray in C57BL/6J (wild-type, *top*) and PAI-1 KO (*bottom*) mice at weekly intervals postfracture. (**b**) Degree of fracture union was graded on a numerical scale of 0–3. Scale bar = 0.5 cm

pQCT Analyses of Fracture Calluses

Examination of the fracture callus with pQCT using the threshold setting that detected all cancellous bony and soft callus tissues revealed that PAI-1 KO fractures exhibited an average cross-sectional area that was approximately twofold greater than that of wild-type fractures at 14 days postfracture but returned to wild-type levels by 21 days postfracture (Fig. 2a). This confirmed the X-ray observations (Fig. 1) of the larger fracture callus in PAI-1 KO mice at 14 days postfracture but not at 7 days postfracture or

other later healing time points. When fracture calluses were assessed by pQCT using settings that detected only cancellous bony tissues, the average cross-sectional area of mineralized callus tissue (Fig. 2b) and the total callus cancellous BMC (Fig. 2c) of PAI-1 KO fractures were also increased approximately twofold compared to those of wild-type fractures. However, the increase in each case was also observed only at 14 days postfracture and not at other time points. There was no significant difference in fracture callus BMD at any time points, even at 14 days postfracture (data not shown).

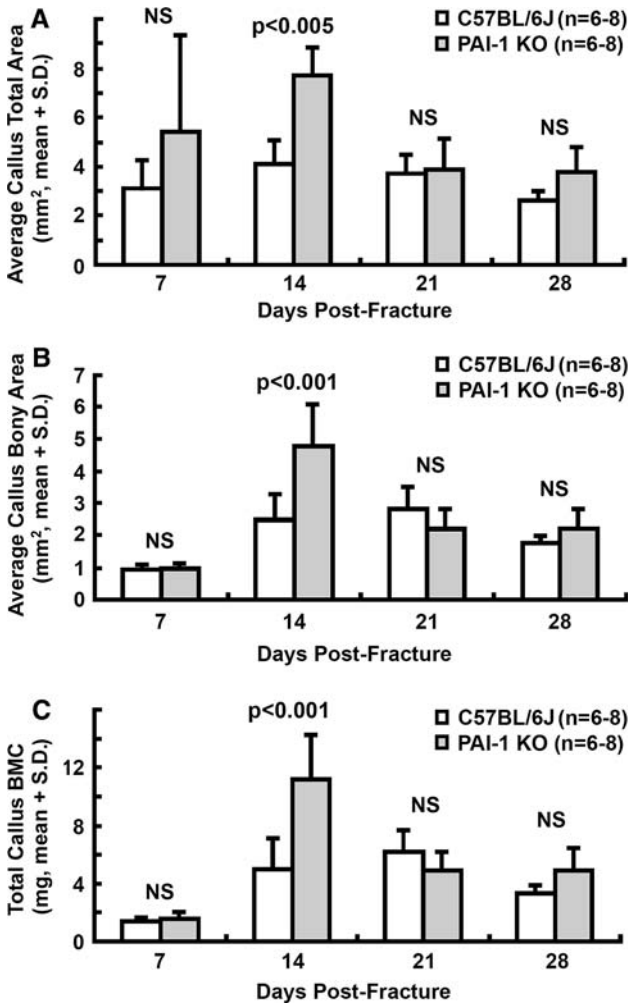

Fig. 2 Comparison of fracture callus development in C57BL/6J wild-type and PAI-1 KO mice at 7–28 days postfracture. (**a**) Average callus cancellous bone and soft tissue cross-sectional area. (**b**) Average callus cancellous bone cross-sectional area. (**c**) Total callus cancellous BMC. Values are expressed as mean ± SD. Statistical significance was analyzed by two-way ANOVA for genotype and postfracture healing time and showed $P < 0.05$ for genotype as well as interaction between genotype and healing time. Statistical significance between the two mouse strains at each time point was analyzed by the Scheffe post-hoc test and is shown in each panel

Histological Analyses of Fracture Callus

Safranin orange staining of fracture callus sections indicated that there was augmented fracture callus cartilage formation at 14 days postfracture in PAI-1 KO calluses compared to C57BL/6J control calluses (Fig. 3a). We further compared the cartilage area per callus area in fractured femurs from both strains of mice at days 7–21 postfracture, a period of time that normally includes all of fracture chondrogenesis. Quantification of the fracture callus cartilage–stained sections at 7, 14, and 21 days of healing revealed that the fracture cartilage area, when normalized to the total callus area, was approximately twofold greater at 7 days postfracture and almost threefold greater at 14 days postfracture than controls (Fig. 3b). These findings are in agreement with the measurements of bony callus cross-sectional area and BMC, where there was no significant difference in cartilage between mouse strains at 21 or 28 days postfracture (Fig. 2). However, unlike fracture callus cartilage, total callus cross-sectional area at 7 days postfracture was not significantly different between PAI-1 KO and C57BL/6J wild-type control mice.

Histology (Fig. 3) confirmed the X-ray observations (Fig. 1) that PAI-1 deficiency did not accelerate healing, for although there was increased callus cartilage and bone, there was no histological evidence for enhanced bony union at the fracture gap. However, the numbers of osteoclasts per square millimeter of callus area were approximately doubled ($P < 0.005$) in PAI-1 KO fractures compared to wild-type fractures at 21 days postfracture, suggesting that there was increased callus remodeling of this augmented fracture cartilage and bone (Fig. 4). Interestingly, histology also revealed that PAI-1 deficiency yielded an abnormal pattern of callus remodeling by 14 days healing, in which the surface of the fracture callus cartilage ossified prior to its interior, unlike wild-type fracture repair in which ossification proceeded from opposing sides of the fracture gap in the interior of the callus (Fig. 5). There were no other obvious differences between PAI-1 KO and wild-type fracture histology.

Discussion

Homozygous PAI-1-deficient mice are viable and fertile and develop normally. It was previously concluded by gross anatomical examination that adult PAI-1-deficient mice do not exhibit obvious phenotypes, with the exception of a mild hyperfibrinolytic state and greater resistance to venous thrombosis that does not impair hemostasis [11]. The more detailed examination of bone size in our study presents compelling evidence that adult male PAI-1 KO

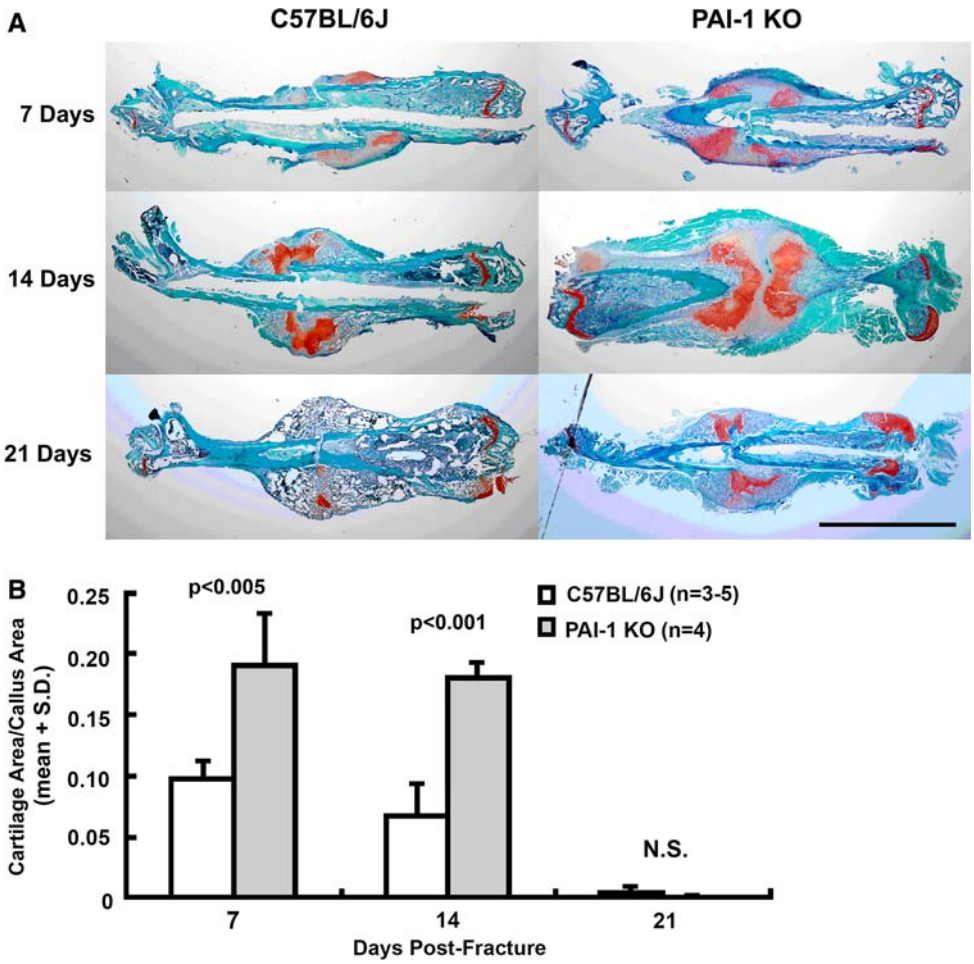

Fig. 3 Time course of cartilage area percentage change in callus of fracture healing between C57BL/6J and PAI-1 KO mice. (**a**) Longitudinal sections of representative fracture calluses of C57BL/6J and PAI-1 KO mice, respectively, at each indicated time point. Callus cartilage is stained red. (**b**) Mean cartilage area as percentage of total callus area. Values are expressed as mean ± SD. Statistical significance was analyzed by two-way ANOVA for genotype and postfracture healing time and showed $P < 0.05$ for genotype as well as interaction between genotype and healing time. Statistical significance between the two mouse strains at each time point was analyzed by the Scheffe post-hoc test and is shown

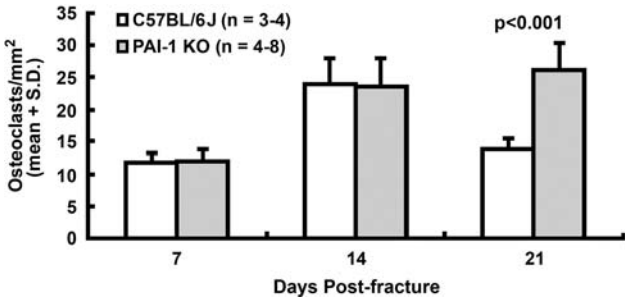

Fig. 4 Time course of fracture callus osteoclasts. Values are expressed as mean number of osteoclasts per square millimeter fracture callus section ± SD. Statistical significance was analyzed by two-way ANOVA for genotype and postfracture healing time and showed $P < 0.05$ for genotype as well as interaction between genotype and healing time. Statistical significance between the two mouse strains at each time point was analyzed by the Scheffe post-hoc test and is shown

mice exhibit reduced bone size compared to C57BL/6J control mice (Table 1).

Measurements of the femur established that the total area, periosteal circumference, and endosteal circumference at the midshaft were significantly reduced in PAI-1 KO mice. Because PAI-1 KO mice appeared to have a much lower total bony tissue area but a similar BMC, total BMD was elevated in PAI-1 KO mice (Table 1). The significance of this increase in total BMD is not clear, but it might be because PAI-1 KO mice have acquired a greater BMD to compensate for the increased mechanical strain imposed by normal loading on their smaller bones. An additional analysis of trabecular bone at the distal metaphysis, a region of the femur with much more measurable trabecular bone than the midshaft, revealed no difference in trabecular bone area and BMD between PAI-1 KO and wild-type control mice, although the trabecular BMC of PAI-1 KO mice was increased by 25% (Table 1). Because the femur length of PAI-1 KO mice was 2.4% shorter than that of C57BL/6J control mice, the site of trabecular bone measurements at the distal diaphysis of PAI-1 KO might have been slightly more distal than that of C57BL/6J mice, which might have contributed to the difference in BMC measurements between the two strains. Although our study was limited to male mice, previous studies on ovariectomized PAI-1 KO female mice suggest that PAI-1 deficiency protects against estrogen deficiency-

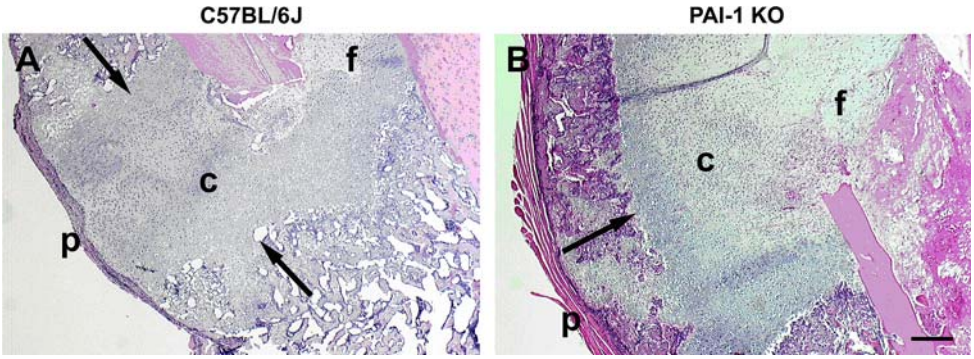

Fig. 5 Fracture callus histology at 14 days postfracture. Hematoxylin–eosin staining for cartilage compared fracture cartilage in C57BL/6J wild-type (**a**) and PAI-1 KO (**b**) mice. *Arrows* indicate the apparent direction of cartilage replacement by bone in the fracture callus. c, cartilage; f, fracture; p, periosteum. Scale bar = 0.5 mm

related trabecular, but not cortical, bone loss [12], and we cannot rule out differential effects of PAI-1 deficiency on trabecular bone in female mice.

Because the PAI-1 KO femur size was reduced proportionately in longitudinal and transverse dimensions, it can be concluded that PAI-1 deficiency produced a general developmental reduction in bone size. This change in PAI-1 KO skeletal phenotype was still significant when the reduced body weights of these mice were removed from the analysis. Congruent with our observations, Nordstrom et al. [13] recently reported that transgenic overexpression of PAI-1 in mice produced a general increase in bone size. Daci et al. [14] also reported increased bone formation in mice deficient in either uPA or tPA. Taken together, these findings indicate that PAI-1 deficiency has an adverse effect on developmental bone growth, especially with respect to bone size, supporting the premise that PAI-1 is essential for developmental bone growth.

Two general mechanisms have been postulated for PAI-1 actions on bone growth: (1) PAI-1 regulates proteolytic processing of the extracellular matrix and thereby modulates the release of active growth factors for bone formation [15–18] and remodeling, and (2) PAI-1 binds to its receptor, vitronectin, and initiates a signaling cascade that regulates the proliferation and differentiation of target cells. Since extracellular matrix proteolysis is essential for bone remodeling, it is possible that PAI-1 mediates the timely regulation of the plasminogen proteolytic system. Consistent with PAI-1 regulation of bone remodeling, osteoclasts express the PAI-1 receptor vitronectin [19]. The remodeling functions of uPA and tPA have also been demonstrated to affect the noncollagenous protein components of nonmineralized bone matrix [20]. It is interesting to note that the PAI-1 transgenic study suggests that PAI-1 modulates bone turnover through vitronectin binding, rather than proteolytic activity [13], which implies a more direct role for PAI-1 in the regulation of bone turnover.

Our interest in PAI-1 regulation of fracture repair was based upon compelling evidence that PAI-1 regulates the proteolytic activity mediating fibrinolysis and resolution of the granulation tissue that forms immediately after tissue injury [21]. The proteolytic functions of the plasmin system might also release growth factors critical for fracture repair that are sequestered in the extracellular matrix, such as transforming growth factor (TGF)-β [15] and fibroblast growth factor (FGF)-2 [16], or are bound to specific inhibitory factors, such as the insulin-like growth factors (IGFs) [17, 18]. There is also strong circumstantial evidence that plasmin processing of the extracellular matrix might facilitate fracture callus remodeling through matrix metalloproteinase functions [22].

To our surprise, examination of healing femoral fractures in PAI-1 KO mice by X-ray (Fig. 1) and histology (Fig. 3) revealed no evidence for a beneficial effect of PAI-1 deficiency on fracture healing. Specifically, we observed no X-ray evidence for accelerated bony union of the fracture gap (Fig. 1), although there was a significant increase in fracture callus size at 14 days postfracture in PAI-1 KO mice (Fig. 2). The X-ray observations were confirmed by histological analysis, which also failed to detect any improvement in bony union at the fracture site (Fig. 3). These findings suggest that the effects of PAI-1 on plasmin resolution of the granulation tissue of the initial injury are not critical for the overall fracture healing, though we cannot rule out that the robust nature of normal fracture repair in rodents might be too rapid to allow accurate assessment of any modest effects of PAI-1 deficiency. Nevertheless, these findings are not consistent with our original premise that PAI-1 regulates fracture healing.

Despite the lack of an obvious effect of PAI-1 deficiency on the union of bony callus across the gap, PAI-1 deficiency had a profound effect on the size of fracture callus (Fig. 2) as well as the formation of callus cartilage (Fig. 3). These results are consistent with an increased proliferation of soft fracture callus tissues and differentiation to bony tissues, but only during the early fracture healing phases (i.e., to 14 days postfracture). The increased cartilage at 7 days postfracture was not reflected in significant changes in the average cross-sectional area of the total callus tissues, possibly due to a reduction in the fibrous tissue in response to augmented chondrogenesis.

Inasmuch as PAI-1 deficiency increased callus size and callus cartilage formation during the early phase of the fracture healing process, the enlarged callus and cartilage area were also rapidly remodeled to the normal size observed in wild-type C57BL/6J control fractures by 21 days postfracture. The osteoclast numbers per area of PAI-1 KO callus were no different at 14 days postfracture, despite the larger fracture callus at this time, but they remained elevated relative to those of the wild-type callus at 21 days postfracture (Fig. 4), coinciding with the period of rapid remodeling of the enlarged callus and callus cartilage within PAI-1 KO fractures. This observation suggests that such rapid cartilage replacement might have been mediated by increased activity of osteoclasts and/or chondroclasts during this period of fracture repair. There is in vitro evidence that impaired PAI-1 functions do not inhibit the formation and activity of osteoclasts [19, 23, 24]. There is even circumstantial evidence that PAI-1 deficiency might improve osteoclast formation and function, as mice deficient in uPA receptor functions exhibit increases in osteoblast proliferation and differentiation and impairment of osteoclast formation and function [25]. On the other hand, since osteoclasts express vitronectin, the receptor for PAI-1 [19], we cannot rule out the possibility that PAI-1 also acts directly on osteoclasts to inhibit osteoclast activity and that the rapid remodeling of the callus and callus cartilage in PAI-1 KO mice was due to a PAI-1 deficiency–related upregulation of osteoclastic resorption during fracture repair.

Interestingly, the callus cartilage in PAI-1 KO mice appeared to undergo an unusual pattern of cartilage remodeling to bone (Fig. 5). Specifically, in the 14-day postfracture healing PAI-1 KO callus, cartilage replacement proceeded from the surface to the interior of the fracture callus as well as from the opposing ends of the fractured bone as in wild-type cartilage replacement. We speculate that this abnormal cartilage remodeling pattern in PAI-1 KO fracture calluses is related to altered proteolysis of the extracellular matrix, though we have not investigated the observation further.

Despite the increased size and rapid remodeling of the PAI-1 KO fracture callus, there was no clear evidence of improved or accelerated bony union relative to C57BL/6J control fractures. As healing, as defined by fracture union, was not altered in PAI-1 KO mice, we did not expect a significant acceleration in the return to prefracture mechanical strength, the defining characteristic of improved fracture healing, and did not conduct mechanical testing during fracture healing. Rather, our results suggest that PAI-1 is one of a number of factors that modulate fracture repair.

In summary, we demonstrate for the first time that PAI-1 KO mice exhibited a bone phenotype of reduced bone size. These findings strongly support our premise that PAI-1 has an essential role in developmental bone growth. Our studies also show that deficient PAI-1 expression, while it did not adversely affect the overall fracture healing process (i.e., bony union of the fracture gap), significantly enlarged the fracture callus. PAI-1 deficiency also accelerated the remodeling of the enlarged fracture callus and produced an abnormal pattern of cartilage replacement. Our results provide evidence that the plasmin system of extracellular matrix proteases has a regulatory role in the endochondral bone formation process in fracture repair.

Acknowledgement This work was supported by the U.S. Army Medical Research Acquisition Activity Assistance Award (DAMD17-03-2-0021). The U.S. Army Medical Research Acquisition Activity (820 Chandler Street, Fort Detrick, MD 21702-5014) is the awarding and administering acquisition office. The information contained in this publication does not necessarily reflect the position or the policy of the government, and no official endorsement should be inferred. We are grateful to Emile Davis, Nancy Lowen, Ryan Porte, and Jann Smallwood for technical assistance. All work was performed in facilities provided by the Department of Veterans Affairs.

References

1. Romer J, Lund LR, Eriksen J, Ralfkiaer E, Zeheb R, Gelehrter TD, Dano K, Kristensen P (1991) Differential expression of urokinase-type plasminogen activator and its type-1 inhibitor during healing of mouse skin wounds. J Invest Dermatol 97:803–811
2. Chan JC, Duszczyszyn DA, Castellino FJ, Ploplis VA (2001) Accelerated skin wound healing in plasminogen activator inhibitor-1-deficient mice. Am J Pathol 159:1681–1688
3. Koh TJ, Bryer SC, Pucci AM, Sisson TH (2005) Mice deficient in plasminogen activator inhibitor-1 have improved skeletal muscle regeneration. Am J Physiol Cell Physiol 289:217–223
4. Zhou A, Huntington JA, Pannu NS, Carrell RW, Read RJ (2003) How vitronectin binds to PAI-1 to modulate fibrinolysis and cell migration. Nat Struct Biol 10:541–544
5. Lazar MH, Christensen PJ, Du M, Yu B, Subbotina NM, Hanson KE, Hansen JM, White ES, Simon RH, Sisson TH (2004) Plasminogen activator inhibitor-1 impairs alveolar epithelial repair by binding to vitronectin. Am J Respir Cell Mol Biol 31:672–678
6. Carmeliet P, Moons L, Lijnen R, Janssens S, Lupu F, Collen D, Gerard RD (1997) Inhibitory role of plasminogen activator inhibitor-1 in arterial wound healing and neointima formation: a gene targeting and transfer study in mice. Circulation 96:3180–3191
7. Carmeliet P, Kieckens L, Schoonjans L, Ream B, van Nuffelen A, Prendergast G, Cole M, Bronson F, Collen D, Mulligan RC (1993) Plasminogen activator inhibitor-1 gene-deficient mice. I. Generation by homologous recombination and characterization. J Clin Invest 92:2746–2755
8. Wergedal JE, Sheng MH, Ackert-Bicknell CL, Beamer WG, Baylink DJ (2005) Genetic variation in femur extrinsic strength in 29 different inbred strains of mice is dependent on variations in femur cross-sectional geometry and bone density. Bone 36:111–122
9. Bonnarens F, Einhorn TA (1984) Production of a standard closed fracture in laboratory animal bone. J Orthop Res 2:97–101
10. Bancroft JD (2002) Enzyme histochemistry and its diagnostic applications. In: Bancroft JD, Gamble M (eds) Theory and

practice of histological techniques. Harcourt, New York, pp 593–620
11. Carmeliet P, Stassen JM, Schoonjans L, Ream B, van den Oord JJ, De Mol M, Mulligan RC, Collen D (1993) Plasminogen activator inhibitor-1 gene-deficient mice. II. Effects on hemostasis, thrombosis, and thrombolysis. J Clin Invest 92:2756–2760
12. Daci E, Verstuyf A, Moermans K, Bouillon R, Carmeliet G (2000) Mice lacking the plasminogen activator inhibitor 1 are protected from trabecular bone loss induced by estrogen deficiency. J Bone Miner Res 8:1510–1516
13. Nordstrom SM, Carleton SM, Carson WL, Eren M, Phillips CL, Vaughan DE (2007) Transgenic over-expression of plasminogen activator inhibitor-1 results in age-dependent and gender-specific increases in bone strength and mineralization. Bone 41:995–1004
14. Daci E, Everts V, Torrekens S, van Herck E, Tigchelaar-Gutterr W, Bouillon R, Carmeliet G (2003) Increased bone formation in mice lacking plasminogen activators. J Bone Miner Res 18: 1167–1176
15. Pedrozo HA, Schwartz Z, Robinson M, Gomez R, Dean DD, Bonewald LF, Boyan BD (1999) Potential mechanisms for the plasmin-mediated release and activation of latent transforming growth factor-β1 from the extracellular matrix of growth plate chondrocytes. Endocrinol 140:5806–5816
16. Saksela O, Moscatelli D, Sommer A, Rifkin DB (1988) Endothelial cell–derived heparin sulfate binds basic fibroblast growth factor and protects it from proteolytic degradation. J Cell Biol 107:743–751
17. Campbell PG, Novak JF, Yanosick TB, McMaster JH (1992) Involvement of the plasmin system in dissociation of the insulin-like growth factor-binding protein complex. Endocrinology 130:1401–1412
18. Lalou C, Silve C, Rosato R, Segovia B, Binoux M (1994) Interactions between insulin-like growth factor-I (IGF-I) and the system of plasminogen activators and their inhibitors in the control of IGF-binding protein-3 production and proteolysis in human osteosarcoma cells. Endocrinology 135:2318–2326
19. Hughes DE, Salter DM, Dedhar S, Simpson R (1993) Integrin expression in human bone. J Bone Miner Res 8:527–533
20. Daci E, Udagawa N, Martin TJ, Bouillon R, Carmeliet G (1999) The role of the plasminogen system in bone resorption in vitro. J Bone Miner Res 14:946–952
21. Weisel JW (2005) Fibrinogen and fibrin. Adv Protein Chem 70:247–299
22. Colnot C, Thompson Z, Miclau T, Werb Z, Helms JA (2003) Altered fracture repair in the absence of MMP9. Development 130:4123–4133
23. Tumber A, Papaioannou S, Breckon J, Meikle MC, Reynolds JJ, Hill PA (2003) The effects of serine protease inhibitors on bone resorption in vitro. J Endocrinol 178:437–447
24. Leloup G, Lemoine P, Carmeliet P, Vaes G (1996) Bone resorption and response to calcium-regulating hormones in the absence of tissue or urokinase plasminogen activator or of their type 1 inhibitor. J Bone Miner Res 11:1146–1157
25. Furlan F, Galbiati C, Jorgensen NR, Jensen J-EB, Mrak E, Rubinacci A, Talotta F, Verde P, Blasi F (2007) Urokinase plasminogen activator receptor affects bone homeostasis by regulating osteoblast and osteoclast function. J Bone Miner Res 22:1387–1396

Bone 43 (2008) 880–888

Contents lists available at ScienceDirect

Bone

journal homepage: www.elsevier.com/locate/bone

Bax deficiency in mice increases cartilage production during fracture repair through a mechanism involving increased chondrocyte proliferation without changes in apoptosis

Charles H. Rundle [a,b,1], Xiaoguang Wang [a,1], Matilda H.-C. Sheng [a,b], Jon E. Wergedal [a,b,c], K.-H. William Lau [a,b,c], Subburaman Mohan [a,b,c,d,*]

[a] Musculoskeletal Disease Center, Jerry L. Pettis Memorial Veterans Administration Medical Center (151), 11201 Benton Street, Loma Linda, CA 92357, USA
[b] Department of Medicine, Loma Linda University School of Medicine, Loma Linda, CA 92350, USA
[c] Department of Biochemistry, Loma Linda University School of Medicine, Loma Linda, CA 92350, USA
[d] Department of Physiology, Loma Linda University School of Medicine, Loma Linda, CA 92350, USA

ARTICLE INFO

Article history:
Received 12 June 2008
Revised 7 July 2008
Accepted 8 July 2008
Available online 29 July 2008

Edited by: Thomas Einhorn

Keywords:
Bax
Apoptosis
Fracture
Cartilage
Chondrocyte proliferation

ABSTRACT

This study sought to determine the role of the pro-apoptotic gene, Bax, in fracture healing by comparing femoral fracture healing in Bax knockout (KO) and wild-type C57BL/6J (background strain) mice. Bax KO fractures were larger, had more bone mineral content, had ~2-fold larger cartilage area per callus area in the first and second weeks of fracture healing, and showed an increased osteoclast surface area in the third and fourth weeks of fracture healing compared to C57BL/6J fractures. The increased cartilage area in the Bax KO fracture callus was due to increases in number of both pre-hypertropic and hypertropic chondrocytes. TUNEL analysis showed no significant differences in the number of either chondrocyte or non-chondrocyte apoptotic cells between Bax KO and C57BL/6J fractures at 7 or 14 days post-fracture, indicating that the increased number of chondrocytes in Bax KO fractures was not due to reduced apoptosis. Analysis of expression of apoptotic genes revealed that although the expression levels of Bcl-2 and Bcl-xL were not different between the Bax KO and C57BL/6J mice at 7 or 14 days post-fracture, the expression of BH3-domain only Bak and "Bik-like" pro-apoptotic gene increased ~1.5-fold and ~2-fold, respectively, in Bax KO fractures at 7 and 14 days post-fracture, compared to C57BL/6J fractures, suggesting that up-regulation of the Bak and Bik-like pro-apoptotic genes in Bax KO mice might compensate for the lack of Bax functions in the context of apoptosis. Analysis by *in vivo* incorporation of bromodeoxyuridine into chondrocytes within the fracture tissues indicated a highly significant increase in chondrocyte proliferation in Bax KO fractures compared to C57BL/6J fractures at day 7. The increased expression of collagen 2α1 and 9α1 gene in Bax KO fractures during early healing was consistent with an increased chondrocyte proliferation. In conclusion, this study demonstrates for the first time that Bax has an important role in the early stage of fracture healing, and that the increased callus size and cartilage area in Bax KO fractures was due to increased chondrocyte proliferation and not to reduced apoptosis or increased chondrocyte hypertrophy. The unexpected effect of Bax deficiency on chondrocyte proliferation implicates a novel regulatory function for Bax on chondrocyte proliferation during fracture repair.

Published by Elsevier Inc.

Introduction

Fracture repair involves multiple molecular regulatory pathways that coordinate the proliferation, development, as well as timely apoptosis of the diverse cells and tissues that form the fracture callus. Accordingly, apoptosis is an important regulatory mechanism of skeletal development and repair. An example of a functional role of apoptosis in bone development and repair is the chondrocyte program of cell maturation during cartilage development in the growth plate and the fracture callus [1,2]. Timely apoptosis has also been shown to be essential for the control of the life span of both osteoblasts and osteoclasts [3–5], which determines the extent of bone remodeling and regeneration during bone growth and repair.

Proliferation and apoptosis have both been characterized throughout fracture healing in the rodent model, where they were found to be associated with different stages of fracture repair. Previous knockout mouse studies have demonstrated that components of both the intrinsic pathway [6] and the receptor-mediated extrinsic pathway of

* Corresponding author. Musculoskeletal Disease Center (151), Jerry L. Pettis Memorial Veterans Administration Medical Center, 11201 Benton Street, Loma Linda, CA 92357, USA. Fax: +1 909 796 1680.
E-mail address: Subburaman.Mohan@med.va.gov (S. Mohan).
[1] These authors contributed equally to this work.

8756-3282/$ – see front matter. Published by Elsevier Inc.
doi:10.1016/j.bone.2008.07.239

apoptosis, specifically TNF-α [7,8], regulate callus chondrogenesis and resorption during fracture repair. However, although the receptor-mediated extrinsic pathway of apoptosis has been demonstrated to be an important regulator of bone repair, the role of the intrinsic mitochondrial pathway of apoptosis has not been clearly established in the context of fracture repair. Given that the intrinsic mitochondrial pathway of apoptosis is responsive to cellular stress [9] and that bone injury itself as well as the hypoxic conditions resulting from the interrupted blood supply are significant cellular stress [10], it is likely that the mitochondrial pathway of apoptosis could play an important role in bone repair, including callus development and remodeling.

Bax, the "Bcl-2-associated X" protein, is a key pro-apoptotic component of the intrinsic mitochondrial pathway of apoptosis. Like other related pro-apoptotic proteins, such as Bak, Bax promotes apoptosis when it is not complexed with the various members of the Bcl family of anti-apoptotic proteins [11–13]. In response to specific stimuli, Bax is liberated from the Bcl complex, translocates from cytosol to mitochondria, and perforates the mitochondrial outer membrane, where a process of oligomerization occurs with pore formation through which cytochrome *c* and other death molecules are released to the cytoplasm to initiate the caspase cascade, leading to cell death. Thus, the pro-death action of Bax is regulated by the interaction with the Bcl-2 family of pro-survival proteins, and the ratios of various pro-apoptotic and pro-survival mediators in a given cell determine whether it survives or undergoes apoptosis [14]. Consistent with the importance of the mitochondrial apoptosis pathway in bone formation and regeneration, recent studies have described a key role for components of the mitochondrial apoptotic system in osteoblast survival [3]. The identification of both Bax and Bcl-2 gene expression in cartilage and bone cells during fracture healing [2,15] further suggests involvement of this pathway in bone repair. Consequently, the primary goal of this investigation was to determine the functional role of Bax in the normal fracture repair process by comparing fracture healing in Bax-deficient mice with mice of their wild-type background strain, C57BL/6J.

Materials and methods

Mice

Bax knockout (KO) mice have no detectable phenotype, except in the bone marrow under infectious challenge [16] and germ cell deficiencies in males and females [16,17]. Several pairs of heterozygous breeder pairs of Bax KO mice were obtained from the Jackson Labs (Bar Harbor, Maine) and maintained at the animal research facility of the Jerry L. Pettis Memorial VA Medical Center. The genotype of Bax KO homozygous mice was confirmed by a PCR-based assay with Bax wild-type- and KO-specific primers, as described by the Jackson Labs [18]. To avoid potential sex-related differences in bone repair, only male KO mice were used in this study. The male C57BL/6J mice (also purchased from the Jackson Labs) served as the control strain for the Bax KO mice. All animal procedures were reviewed and approved by the local Institutional Animal Care and Use Committee.

Fracture surgery

The mouse femoral fracture model was adapted from the three-point bending technique described for rat femurs [19]. Fracture surgery was performed on male mice at 12 weeks of age under general anesthesia (ketamine 67 mg/kg, xylazine 13 mg/kg). A 0.56-mm diameter stainless steel intramedullary pin was surgically implanted prior to fracture to stabilize the femur. A transverse midshaft fracture was introduced by a controlled blunt impact using an Instron servohydraulic tester (Instron, Norwood, MA). This approach produces consistent fractures in rodents with minimal comminution that permit both an accurate assessment of repair and humane healing. Movement and food and water intake were not restricted after fracture. Buprenorphine (60 μg/kg) was administered as needed. Fractured femurs were harvested after euthanasia at 7, 14, 21, 28, and 35 days post-fracture for fracture callus analysis by X-ray examination, peripheral quantitative computerized tomography (pQCT, Stratec XCT 960M, Norland Medical System, FT. Atkinson, WI), gene expression, and histological examinations.

Fracture analysis

Fracture callus parameters between mouse strains were compared by X-ray and pQCT analyses. Groups of between 6 and 8 C57BL/6J and 6 and 11 Bax KO mice were evaluated at the different post-fracture healing times. Total non-cortical (i.e. cancellous) bone mineral content (BMC), average cross-sectional areas of the callus cancellous bone and total callus tissues were determined at nine serial 1-mm intervals along the length of the fracture callus by pQCT at 7, 14, 21, 28 and 35 days post-fracture. The values for all nine slices were used to calculate the total BMC and area of the entire fracture callus for each mouse strain. The pQCT threshold setting of 214 was used to resolve cancellous bone from soft tissues, and the threshold setting of 570 was used to resolve the cancellous and cortical bone.

Histological analyses

Histological analysis and comparison of fracture healing in Bax KO and C57BL/6J control mice were performed at different post-fracture times. After euthanasia, mouse femurs were collected, cleaned of adhering tissue, fixed in 10% formalin and decalcified in 14% EDTA in phosphate-buffered saline, pH 7.1, for three weeks. Bones were then embedded in paraffin wax.

Sections (5 μm in thickness) from each fracture callus at 7, 14 and 21 days of healing were stained with Safranin-Orange to examine the fracture cartilage. Duplicate sections in groups of 4 to 6 mice from each strain at each time were also stained for tartrate-resistant acid phosphatase (TRAP) activity using naphthol AS-BI as the substrate. Two longitudinal sections of 5 μm in thickness, each harvested from different regions of the fracture callus near the center of the femur, were each analyzed by counting 5 representative fields per section, and the means reported as osteoclasts per area of fracture callus. The area of stained fracture cartilage was quantified in each of two sections from groups of 4 to 6 C57BL/6J mice and 4 to 5 Bax KO mice at each post-fracture time using the Image-Pro 4.0 analysis software (Media Cybernetics, Silver Spring, MD), and reported as percentage of the total callus area. Fracture callus osteoclasts were identified as TRAP-positive, multinucleated cells and measured as the number of osteoclasts per mm^2 callus area using the OsteoMeasure software (Osteometrics, Atlanta, GA).

Terminal deoxynucleotidyl transferase-mediated diuridine triphosphate nick end labeling (TUNEL) assay

Cell apoptosis for each callus was assessed by a TUNEL assay kit (Promega, Madison, WI) on paraffin-embedded sections of 7 and 14 days healing fractures. Groups of 7 C57BL/6J and 7 Bax KO mice were evaluated at 7 and 14 days post-fracture. Briefly, thin sections were first incubated with proteinase K (20 μg/ml) for 20 min. The DNA fragments of apoptotic cells were end-labeled by biotinylated nucleotide mix through the action of the terminal deoxynucleotidyl transferase. The labeled apoptotic cells were identified by avidin-linked horseradish peroxidase-mediated oxidation of a chromogen/substrate (3,3′-diaminobenzidine/H_2O_2). The stained sections were counterstained with hematoxylin and coverslipped with Permount (Fisher Scientific, Pittsburgh, PA). Negative controls without the transferase were included in each assay. The number of apoptotic cells in six representative fields per section was counted using the

Table 1
Real-time RT-PCR primers and reaction conditions

Gene	Primers[a]
Col-IIα1	Forward 5′-CTGACCTGACCTGATGATAC-3′
	Reverse 5′-GTCTGACTCACACCAGATAG-3′
Col-IXα1	Forward 5′-CGGACAAGTGAAATCCGTAG-3′
	Reverse 5′-CCATGGACAAGGAACAAGAC-3′
Col-Xα1	Forward 5′-GCCTGTCTGACTCAATCAC-3′
	Reverse 5′-TGCCTGCCTCCATTCTATC-3′
Bax	Forward 5′-GAGCTGATCAGAACCATCATG-3′
	Reverse 5′-GTTGACCAGAGTGGCGTAGG-3′
Bcl-2	Forward 5′-TCGCAGAGATGTCCAGTCAG-3′
	Reverse 5′-ATGCCGGTTCAGGTACTCAG-3′
Bcl-xL	Forward 5′-TCGCAGAGATGTCCAGTCAG-3′
	Reverse 5′-ACTTCCGACTGAAGAGTGAG-3′
Bak	Forward 5′-ATATTAACCGGCGCTACGAC-3′
	Reverse 5′-CTGGCGATGTAATGATGCAG-3′
Bid	Forward 5′-TACACTCAGGCTCTTGCTAC-3′
	Reverse 5′-CTGTGCTCTACAACCAAGAC-3′
Bok	Forward 5′-AGACATGAGCTGGCCTCAGT-3′
	Reverse 5′-CTCTGGTTCCTGCCATGAAG-3′
Blk	Forward 5′-GAGACTTATGGCCAGAGACG-3′
	Reverse 5′-TAGGTGACAGCGAGTCTGTG-3′
Cyclophilin	Forward 5′-GCATACAGGTCCTGGCATCT-3′
	Reverse 5′-TCTTGCTGGTCTTGCCATTC-3′

[a] PCR reaction conditions for all primers were 59 °C 45 s, 55 °C 45 s, 72 °C 45 s, and 40 cycles.

Osteomeasure software (Osteometrics, Atlanta, GA). A total of at least 400 cells per field were counted in each section. The percentage of apoptotic cells in the cartilage and non-cartilage areas of the fracture callus were calculated separately. Chondrocytes were evaluated for pre-hypertrophy or hypertrophy by cell size in separate sections obtained from groups of 5 to 6 C57BL/6J and 4 to 5 Bax KO calluses at 7 or 14 days post-fracture.

Bromodeoxyuridine (BrdU) immunostaining assay

In vivo cell proliferation was quantified by *in vivo* incorporation of bromodeoxyuridine (BrdU, Sigma Chemical Co., St. Louis, MO) into the S-phase nuclei within fracture tissues. A mixture of BrdU (3 mg/ml) and fluorodeoxyuridine (FldU, 2 mg/ml, Sigma) in saline was injected intraperitoneally into groups of 14 C57BL/6J and 8 Bax KO mice at 7 days post-fracture. Fracture tissues were harvested 2 h post-injection, and decalcified, fixed, paraffin-embedded and longitudinal sections were obtained as described above. Tissues were permeabilized with trypsin, also as described above. BrdU incorporation was detected by *in situ* immunohistochemical staining using an anti-BrdU primary antibody (Zymed Laboratories, South San Francisco, CA) and a "Mouse on Mouse" horse radish peroxidase detection kit, according to the manufacturer's specifications (Chemicon International, Temecula, CA). Immunostained cells in four representative fields at the fibrocartilage junction from each section were counted using Osteomeasure software and normalized to the area of fracture callus on that section.

Gene expression analysis

Additional fractures were produced to compare gene expression by real-time reverse transcriptase-polymerase chain reaction (RT-PCR) in Bax KO and wild-type fracture tissues. Four C57BL/6J and 3 Bax KO and fractured femurs were collected each at 7 days and 14 days post-fracture, separated from the epiphyses and stored in liquid nitrogen. The frozen tissues were subsequently pulverized, total RNA isolated by the RNeasy mini kit (Qiagen, Valencia, CA) and reverse-transcribed to cDNA using the SuperScript III™ kit from (Invitrogen, Grand Island, NY). The expression of cartilage-related and mitochondrial apoptosis-related genes of interest was analyzed by real-time RT-PCR using the Qiagen "Quantitect" SybrGreen-based assay kit and Bio-Rad real-time PCR machine (Bio-Rad Laboratories — MJ Research, Hercules, CA) according to the instructions provided in the kit. The primers for real-time PCR for each gene of interest and the mouse cyclophilin A housekeeping gene were synthesized by Integrated DNA Technologies, Inc. (Coralville, IA) and are shown with their specific RT-PCR reaction conditions in Table 1. The expression levels of genes of interest in fractured and unfractured bones of male C57BL/6J and Bax KO mice were analyzed by the cycle threshold method (ΔC_T), which represented the threshold cycle difference of house keeping gene and respective gene of interest. The relative fold differences in gene expression level were determined by the $\Delta\Delta C_T$ method [20].

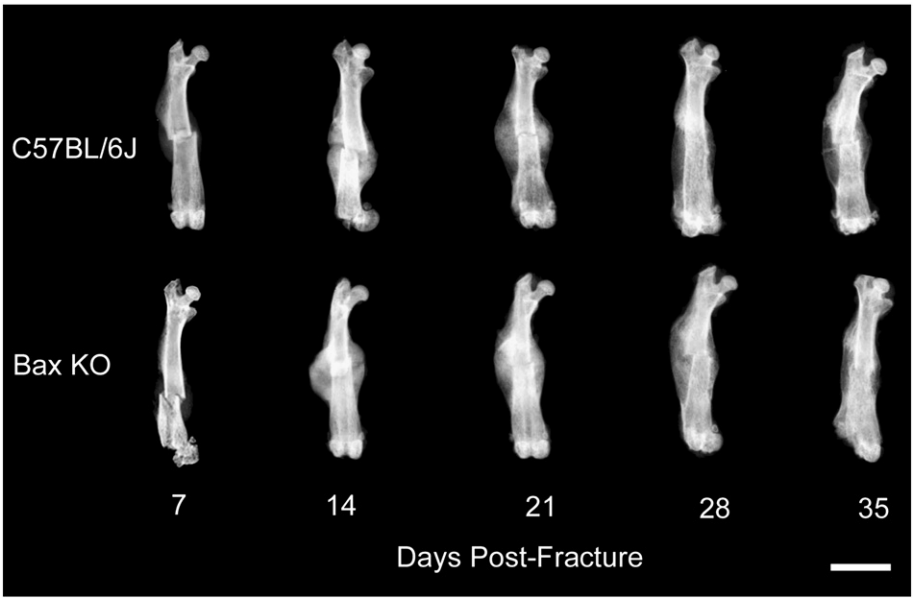

Fig. 1. X-ray comparison of fracture healing in C57BL/6J and Bax KO mice. Fractured femurs were harvested at weekly intervals during fracture healing and subjected to X-ray analysis. Scale bar=0.5 cm.

Statistical analysis

Statistical analysis was performed by two-way ANOVA followed by the LSD or Scheffe post-hoc test or by two-tailed Student's *t*-test. All data are expressed as the mean±standard error of the mean (SEM). Differences were deemed significant, when $P<0.05$.

Results

X-ray analysis of fracture healing

X-ray examination of the fracture healing up to 35 days post-fracture revealed that Bax KO mice had a larger mineralized fracture callus at 14 days post-fracture (Fig. 1). pQCT measurements of these healing fractures confirmed the X-ray analyses and showed that Bax KO fractures had significantly larger total callus (Fig. 2A) and average callus bony cross-sectional areas (Fig. 2B) compared to C57BL/6J wild-type fractures at 14 days and 28 days post-fracture. Similarly, the total BMC of the fracture calluses of Bax KO mice was also significantly greater than that of C57BL/6J fracture calluses at 14 days and 28 days (Fig. 2C). The BMC appeared ~25% greater in Bax KO fractures at 21 days, but this difference was not statistically significant. There were no differences in total cross-sectional callus area, cross-sectional callus bony area, or total BMC at 35 days of post-fracture between the two mouse strains when the remodeling of fracture calluses to cancellous bone approached completion.

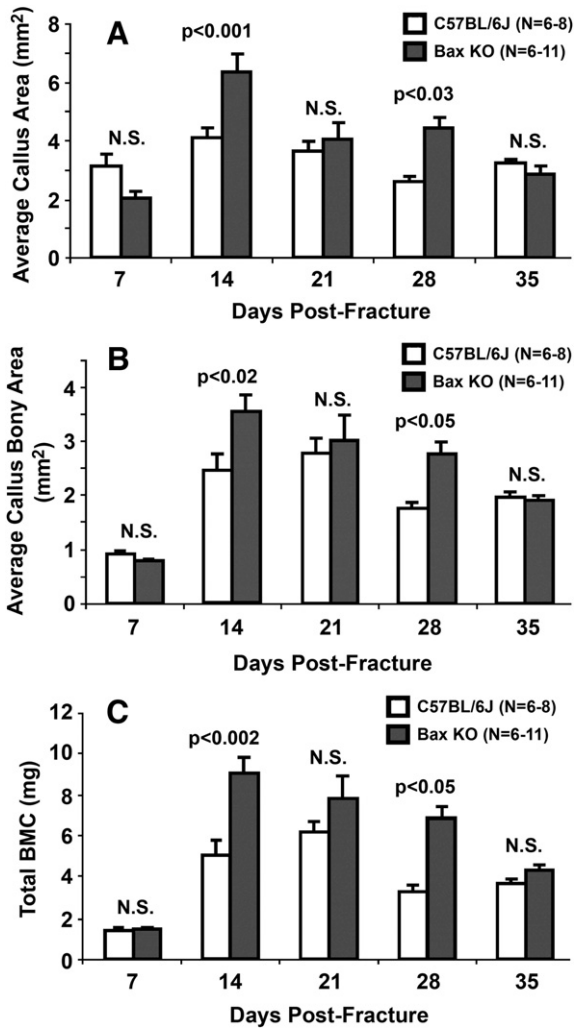

Fig. 2. Comparison of pQCT parameters of fracture calluses of C57BL/6J and Bax KO mice. (A) Average cross-sectional area of callus cancellous bone and soft tissues. (B) Average cross-sectional area of callus cancellous bone. (C) Total callus bone mineral content. Values are expressed as Mean±SEM. Statistical analyses were performed by two-way ANOVA followed by the LSD post-hoc test. N.S.=$p>0.05$. The mouse strain effect was $p<0.001$ for average callus area and total BMC and $p<0.02$ for average callus bony area.

Histological analysis

Histological examination of the cartilage sections within the calluses at 7 days post-fracture revealed that the Bax KO fracture had substantially more Safranin-Orange-stained cartilage than the C57BL/6J wild-type fracture (Figs. 3A and B). Quantification of the longitudinal cartilage area (Fig. 3C) as well as that normalized against the longitudinal callus area in each section (Fig. 3D) at 7, 14, 21, and 28 days post-fracture revealed that although the cross-sectional total callus and bony callus areas of Bax KO mice at 7 days were not different from those of C57BL/6J mice (pQCT, Fig. 2), the Bax KO fractures had >200% larger total cartilage area (Fig. 3C) as well as total cartilage area per callus area (Fig. 3D) than their C57BL/6J wild-type fracture calluses at 7 days. The total and normalized cartilage areas of Bax KO fractures at 14 days both were still greater, although not significantly, than those of C57BL/6J fractures. At 21 and 28 days, most of the callus cartilage in both Bax KO and C57BL/6J fracture calluses was remodeled to bony tissues, as almost all of the cartilage area in each mouse strain was replaced with bony tissue area, producing complete bony union of the fracture gap between 28 and 35 days (data not shown).

Remodeling of the fracture calluses is initiated and mediated by an up-regulation of osteoclast recruitment and activity. Therefore, the effect of Bax deficiency on the number of osteoclasts on bone surface within the healing fractures was also investigated. Consistent with the contention that the remodeling of bony calluses in Bax KO mice at the later phase of the fracture healing (i.e., 21 and 28 days post-fracture) was more accelerated than that in C57BL/6J mice, Figs. 4A and B show that there were more TRAP-positive osteoclasts on bone surface of the Bax KO healing calluses than on bone surface of the C57BL/6J calluses at 28 days post-fracture. Quantification of the number of TRAP-positive osteoclasts per mm^2 of callus area revealed that Bax KO fractures indeed had significantly 30–50% more osteoclasts per bone surface of fracture tissues than the C57BL/6J fractures at 21 and 28 days post-fracture, but not at earlier time points (Fig. 4C).

Callus chondrocyte analyses

To evaluate whether the greater amounts of cartilage in Bax KO fracture calluses at the earlier healing phase (i.e., 7 and 14 days post-fracture) was due to an increased number of chondrocytes and/or an enlarged size (i.e., hypertrophy) of chondrocytes, we counted and compared the total number of chondrocytes within the cartilage area of 7-day and 14-day healing calluses of each mouse strain. Consistent with the larger cartilage area to callus area (Figs. 3C and D), the number of total chondrocytes showed a >2-fold increase in Bax KO calluses compared to C57BL/6J calluses (Fig. 5A). The number of total chondrocytes in 14-day Bax KO calluses was still slightly more than that in 14-day C57BL/6J fracture calluses, but the difference was not statistically significant. We then determined the number of hypertrophic and hypertrophic chondrocytes separately in Bax KO and C57BL/6J fracture calluses at 7 and 14 days (Fig. 5B). Bax KO fractures had significantly more numbers of both pre-hypertrophic and hypertrophic chondrocytes compared to C57BL/6J calluses at 7 days post-fracture. At 14 days, the number of hypertrophic, but not pre-hypertrophic, chondrocytes in Bax KO fracture calluses was still significantly greater than that in C57BL/6J fracture calluses. These findings indicate that the greater amount of cartilage in Bax KO fractures at 7 days post-fracture was probably due to an increased

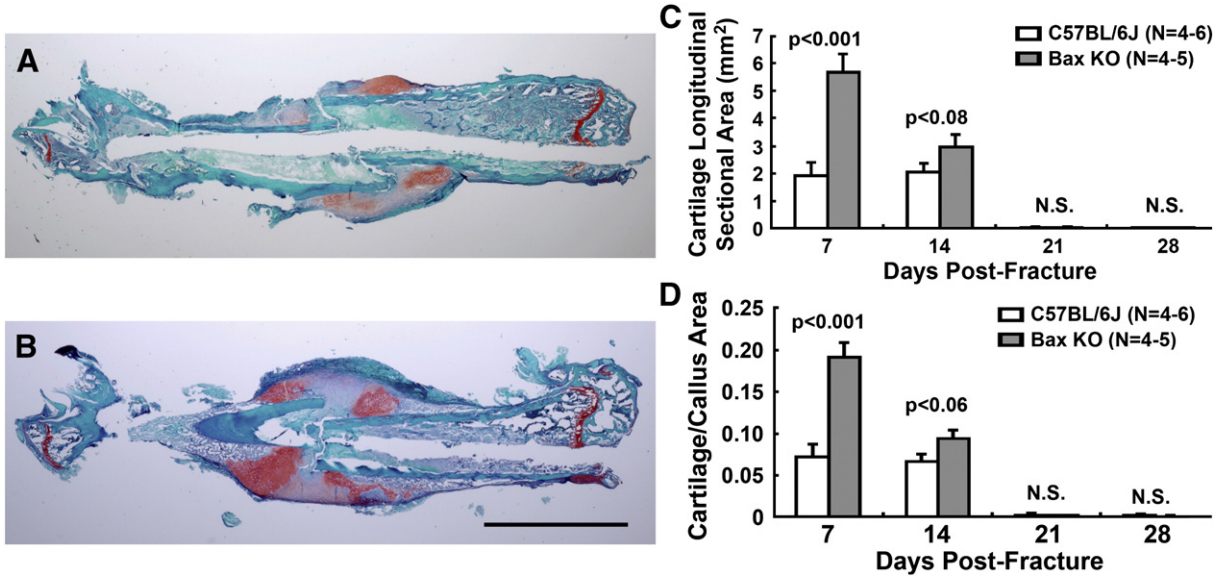

Fig. 3. Comparison of cartilage area within the healing calluses of C57BL/6J and Bax KO mice. (A) Safranin-Orange staining of cartilage within the fracture callus of a representative C57BL/6J femoral fracture at 7 days post-fracture. (B) Safranin-Orange staining cartilage within the fracture callus of a representative Bax KO femoral fracture at 7 days post-fracture. Scale bar = 1 cm. (C) Quantitative measurements of the longitudinal cross-sectional callus cartilage area in Bax KO mice and in C57BL/6J mice. (D) The normalized longitudinal cross-sectional callus cartilage as a proportion of the total callus area in Bax KO and C57BL/6J mice. Results are shown as Mean ± SEM. Statistical analysis was performed by two-way ANOVA followed by LSD post-hoc test. N.S. = $p > 0.10$. The mouse strain effect was $p < 0.05$.

number of chondrocytes and an increased hypertrophy (i.e., maturation) of chondrocytes.

To further assess the effects of Bax deficiency on the number of pre-hypertrophic and hypertrophic chondrocytes in Bax KO fractures compared to C57BL/6J fractures, we measured relative expression levels of chondrocyte-specific collagen genes by real-time PCR measurements (Table 2). The expression of collagen 2α1 was up-regulated 3.5-fold at 7 days post-fracture in Bax KO fractures relative to C57BL/6J fractures. This expression change was also reflected in the expression of collagen 9α1, which was also up-regulated 3.5-fold at 7 days post-fracture. In contrast, the expression of collagen 10α1 appeared to be reduced, but not significantly, on Bax KO fractures compared to C57BL/6J fractures at both 7 and 14 days.

Apoptosis analysis

To evaluate the possibility that the increases in the amount of cartilage and the number of chondrocytes in Bax KO fracture callus was the result of a decrease in cell apoptosis due to Bax deficiency, we measured the relative percentage of cells that were undergoing apoptosis (as indicated by the TUNEL staining) in fracture cartilage and non-cartilage tissues between Bax KO and C57BL/6J fractures at 7 days post-fracture. The relative percentage of apoptotic chondrocytes

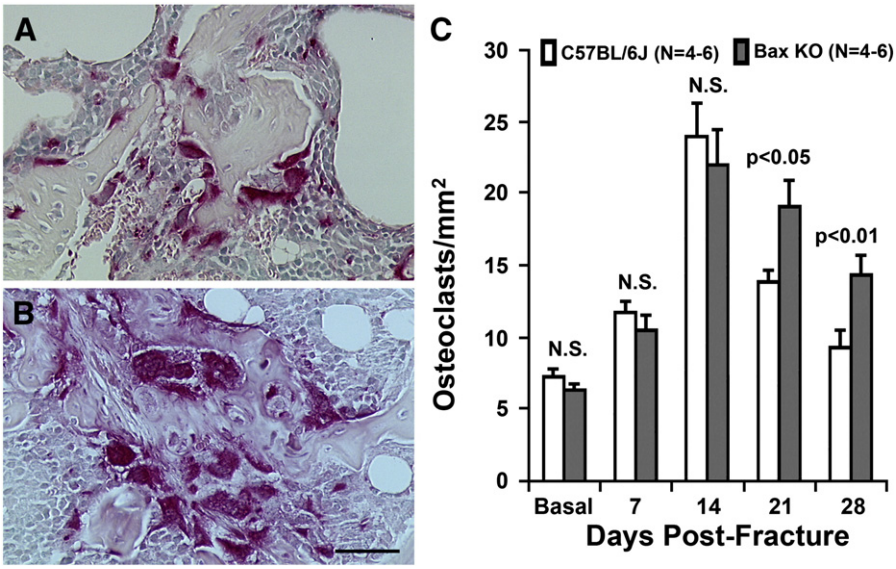

Fig. 4. Comparison of the number of active osteoclasts per callus surface of Bax KO healing fractures to that of C57BL/6J healing fractures. A and B are photomicrograph of large, TRAP-positive osteoclasts on the surface of a healing callus of a representative C57BL/6J fracture (A) and a representative Bax KO fracture at 28 days post-fracture. Scale bar = 100 μm. C shows the quantitative measurements of osteoclasts per mm^2 of callus surface area of C57BL/6J and Bax KO fractures at each indicated time points. Results are presented as mean ± SEM. Statistical analysis was performed by two-way ANOVA followed by LSD post-hoc test. N.S. = $p > 0.05$. There was a significant ($p < 0.05$) mouse strain effect.

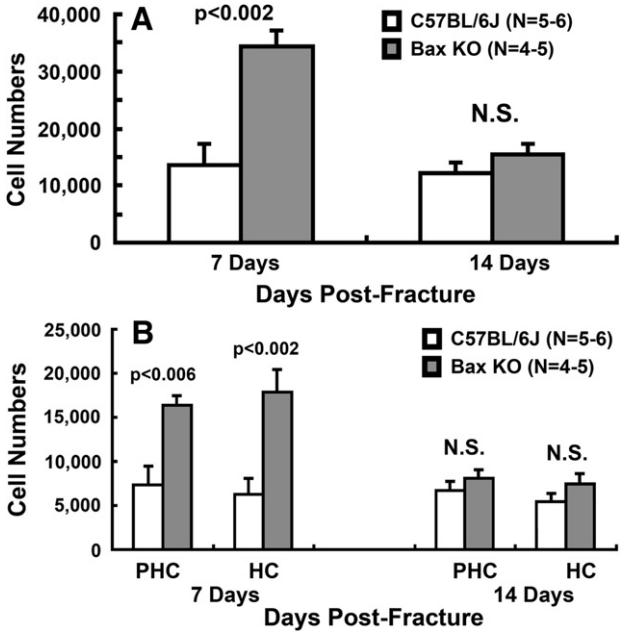

Fig. 5. Comparison of the numbers of total chondrocytes (A) as well as pre-hypertrophic and hypertrophic chondrocytes (B) within the healing calluses of C57BL/6J fractures with those within the healing calluses of Bax KO fractures at 7 days post-fracture. The results represent the number of cells inside the cross-sectional cartilage area of the fracture callus. Statistical significance was analyzed by two-way ANOVA followed by the Scheffe post-hoc test. N.S. = $p > 0.05$. There was a significant mouse strain effect ($p < 0.05$).

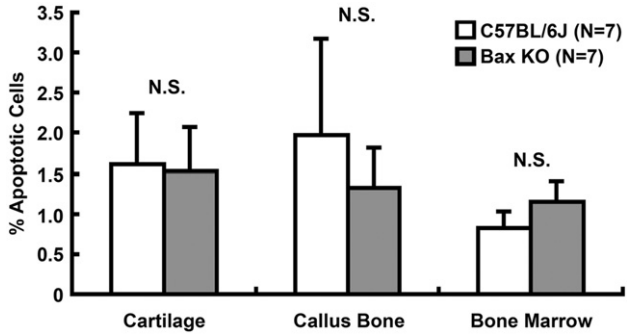

Fig. 6. Comparison of the relative percentage of apoptotic cells within the fracture calluses of C57BL/6J and Bax KO mice at 7 days post-fracture by TUNEL analysis. The relative number of labeled apoptotic cells was expressed as percentage of total cells in the cartilage, callus bone, and bone marrow within the fracture. Results are shown as mean ± SEM. Statistical analyses were performed with two-way ANOVA as well as two-tailed Student's *t*-test. N.S. = $p > 0.05$.

or non-cartilage bone and marrow cells in both Bax KO and C57BL/6J fracture calluses was low, each between 1% and 2%. More importantly, there were no significant differences in the relative percentage of apoptotic chondrocytes and other bone or marrow cells between the 7-day Bax KO and C57BL/6J fracture calluses (Fig. 6). There were also no significant differences in the number of apoptotic cells in cartilage or non-cartilage tissues within the fracture calluses area of both strains at 14 days (data not shown), indicating that Bax KO mice did not differ from C57BL/6J mice in the frequencies of cell apoptosis in cartilage or non-cartilage tissue during fracture healing, and that the increased chondrocyte number in fracture calluses of Bax KO mice was probably not the result of a reduced apoptosis frequency.

Expression level of mitochondrial apoptosis-related genes

To evaluate whether the lack of a difference in apoptosis between Bax KO and C57BL/6J fracture calluses was due to a compensatory up-regulation of the expression of one or more pro-apoptotic genes or decreases of one or more anti-apoptotic genes of the mitochondrial apoptotic pathway, the relative gene expression levels of several well known pro- and anti-apoptotic genes of the mitochondrial apoptotic pathway were measured at 7 and 14 days post-fracture by real-time RT-PCR. Table 2 indicates that although the expression levels of Bcl-2 and Bcl-xL pro-survival genes were not different between the Bax KO and C57BL/6J mice at 7 or 14 days post-fracture. The expression of BH3-domain only Bak and "Bik-like" pro-apoptotic gene, however, was increased ~1.5-fold and ~2-fold, respectively, in Bax KO fractures at 7 and 14 days, compared to C57BL/6J fractures, raising the possibility that up-regulation of the expression of Bak and Bik-like pro-apoptotic genes in Bax KO mice might compensate for the Bax deficiency in the context of apoptosis.

Table 2
Real-time RT-PCR measurements of expression of collagen and apoptosis-related genes expression at 7 days and 14 days post-fracture

Gene	Expression change: Bax KO vs. C57BL/6J fractures (relative fold relative fold changes)	
	7 days post-fracture	14 days post-fracture
Collagen genes		
Collagen 2α1	3.52 ± 0.21*	1.03 ± 0.35
Collagen 9α1	3.52 ± 0.26*	0.61 ± 0.26
Collagen 10α1	0.68 ± 0.36	0.39 ± 0.53
Apoptosis-related genes		
Bcl-2	0.93 ± 0.14	0.92 ± 0.13
Bcl-xL	0.60 ± 0.19	0.62 ± 0.16
Bak	1.47 ± 0.16*	1.46 ± 0.13*
Bik-like	1.88 ± 0.12*	2.00 ± 0.15*

Results are shown as relative fold changes between Bax KO mice and C57BL/6J mice (mean ± SEM, $N = 3$ to 4 per mouse strain per time point).
* $p < 0.05$, compared to C57BL/6J wild-type control fractures.

Fracture callus cell proliferation

To determine whether the increased cartilage production and the number of chondrocytes in Bax KO fractures was due to an increased chondrocyte proliferation, we compared the proliferation of pre-hypertrophic chondrocytes within the Bax KO fracture calluses with that of C57BL/6J fracture calluses at 7 days post-fracture by the *in vivo* BrdU incorporation assay. Fig. 7 shows that the 7-day Bax KO fracture calluses had significantly more proliferating cells at the fibroblast-chondrocyte junction of the soft tissue fracture callus, compared to the corresponding 7-day C57BL/6J fracture calluses. These findings indicate that there was an increased proliferation frequencies of pre-hypertrophic chondrocytes in Bax KO fractures compared to C57BL/6J fractures at day 7 and suggest that the increased number of chondrocytes and the amounts of cartilage in 7-day Bax KO fracture were probably due largely to an increase in the proliferation of pre-hypertrophic chondrocytes.

Discussion

The intrinsic mitochondrial pathway of apoptosis is a vital physiologic process to eliminate damaged or unwanted cells during tissue development and repair, including fracture repair [11,21,22]. Bax, a multi-domain protein belonging to the large family of BH-3 domain only Bcl-2 proteins, has a pivotal role for the initiation of intrinsic mitochondrial pathway of apoptosis. In this study, we have provided compelling *in vivo* evidence that deficiency in Bax expression in the mouse significantly affected the normal fracture repair process, especially during the early healing phase. Specifically, X-ray and pQCT evaluations of the progression of the healing of normal closed fractures in Bax KO and wild-type C57BL/6J mice (the genetic background control mouse strain) revealed that the Bax KO fracture calluses were

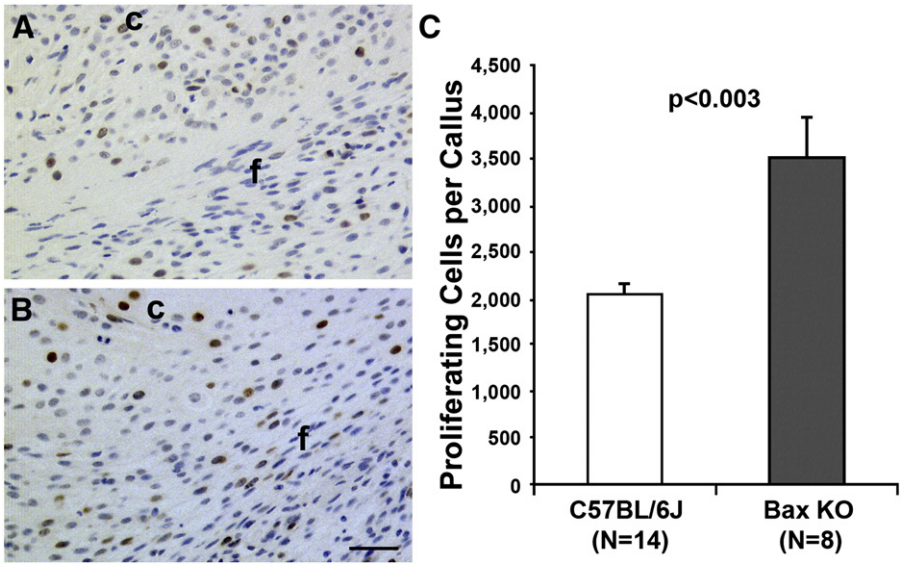

Fig. 7. Comparison of the number of proliferative pre-hypertrophic chondrocytes within Bax KO fractures to that of C57BL/6J fractures at 7 days post-fracture by the *in vivo* BrdU incorporation assay. A and B are photomicrograph of a representative C57BL/6J (A) and a representative Bax KO (B) fracture cartilage tissues at 7 days post-fracture. c, cartilage; f, fibroblasts. Scale bar = 100 μm. C shows the quantitative measurements of proliferating cells that were at the S-phase at the fibroblast-chondrocyte junction of the soft tissue fracture callus cells of C57BL/6J and Bax KO fractures at 7 days post-fracture. Results are presented as mean ± SEM. Statistical analysis was performed by two-tailed Student's *t*-test.

significantly larger and more mineralized than C57BL/6J calluses at the early healing phase (i.e., 14 days post-fracture). Taken together, these findings indicate that Bax may have an important negative regulatory role in the determination of callus size and/or remodeling of soft calluses into bony calluses during the early fracture repair process.

Three additional findings of the fracture healing process of Bax KO mice compared to that of C57BL/6J mice are noteworthy. First, although Bax is a pro-apoptotic gene, our *in vivo* TUNEL analysis did not reveal any significant differences in the relative percentage of apoptotic bone and marrow cells within the healing calluses between Bax KO and C57BL/6J mice at either 7 days or 14 days post-fracture. These findings suggest that there are compensatory mechanisms for the absence of functional Bax in Bax KO mice in the context of apoptosis. In this regard, it has been reported that the loss of Bax function with respect to apoptosis of blood cells could be compensated by Bak and Bim [23] and that Bax deficiency resulted in up-regulation of Bim_{EL} and Bak during development and after injury of tissues in the brain [24]. In this study, we found that fracture healing significantly up-regulated at least two members of the BH-3 domain only Bcl-2 family of pro-apoptotic genes, the Bak and the Bik-like gene. Although the Bik-like gene is poorly characterized, it, like Bax, is also a BH-3 domain only gene, and BH-3 only domain genes are postulated to act as modifiers of other mitochondrial pathway regulators [25]. Accordingly, our findings of up-regulation in the expression of Bak and Bik-like gene in Bax KO mice are consistent with the possibility that the lack of Bax functions, in the context of apoptosis, may be compensated by up-regulation of expression of other members of the Bcl-2 family of pro-apoptotic genes, including Bak and Bik-like genes in Bax KO mice in response to tissue injuries. On the other hand, as reported by others [7], the relative percentage of apoptotic cells in the 14-day healing fractures of both Bax KO and C57BL/6J mice as detected by the TUNEL assay was rather low (~2% in this study). We cannot completely rule out the possibility that the effects of Bax deficiency on apoptosis during fracture repair might not be readily detected due to the already low apoptotic frequency. Nonetheless, because of the already low levels of apoptosis during the early fracture healing phase, it is also unlikely that any further decreases in such low frequencies of apoptotic cells alone could account for the relatively large increases in the size and mineralization of fracture calluses during the early phase of fracture repair in Bax KO mice.

The second noteworthy observation is that, in addition to the formation of the larger and more mineralized bony fracture callus in Bax KO mice during the early healing phase, the larger Bax KO calluses also appeared to undergo a more rapid remodeling during the later healing phase than the smaller fracture callus of C57BL/6J mice. As a result, there were no significant differences in the callus size, bony callus area, and callus BMC between Bax KO mice and C57BL/6J mice beyond 28 days post-fracture. In fact, the Bax KO calluses were indistinguishable from the healing C57BL/6J calluses beyond 28 days with respect to mineral density and content, as well as bone histology. The more rapid remodeling in Bax KO fracture calluses compared to C57BL/6J calluses was probably due to an increase in osteoclastic resorption, since Bax KO fractures had 30% and 50% more osteoclasts per bone surface of fracture tissues than the C57BL/6J fractures at 21 and 28 days, respectively.

The mechanism by which Bax deficiency led to an increase in the number of active osteoclasts and the rapid callus remodeling during the later phase of fracture repair has not been determined. On the one hand, because Bax is a pro-apoptotic gene, our finding of an increased number of osteoclasts on bone surface of the remodeling callus in Bax KO mice is consistent with a reduced osteoclast apoptosis in Bax-deficient mice. On the other hand, the findings of the TUNEL analysis, which did not show any significant differences in the number of apoptotic bone and marrow cells within the healing calluses between Bax KO and C57BL/6J mice, are not consistent with the interpretation that the increased number of osteoclasts was due largely to a reduced osteoclast apoptosis in Bax KO fractures. However, because apoptosis is a major regulatory mechanism that determines the life span and number of active osteoclasts *in vivo* [26], we cannot rule out the possibility that Bax KO deficiency may have a more pronounced effect on osteoclast apoptosis than the apoptosis of other types of bone cells. Similarly, we also cannot completely overlook the possibility that Bax deficiency might directly or indirectly promote osteoclast formation and differentiation to produce the observed increase in the number of osteoclasts on the bone surface of the healing calluses. Regardless of the mechanistic reason(s) for the enhanced remodeling of fracture callus in Bax-deficient mice, this study has clearly demonstrated that deficiency of Bax expression in mice not only results in the formation of larger and more mineralized calluses, but also accelerates the remodeling of the mineralized calluses.

The third intriguing finding of this study is that there was >200% more cartilage in Bax KO fracture calluses than C57BL/6J fractures during the early healing phases (i.e., 7 days post-fracture). The greater amount of cartilage in Bax KO early fracture calluses was due to an overall increase in the number of both pre-hypertrophic and hypertrophic chondrocytes. Consistent with an increased number of chondrocytes in the early Bax KO healing fractures, the expression of collagen 2α1 (a marker for pre-hypertrophic chondrocytes) and collagen 9α1 (a pan-chondrocyte-specific marker) gene were also up-regulated 3.5-fold each at 7 days post-fracture in Bax KO fractures relative to C57BL/6J fractures. Surprisingly, the expression of collagen 10α1 (a presumed marker for hypertrophic chondrocytes) not only was not increased, but even appeared to be decreased (although not significantly) in Bax KO fractures compared to C57BL/6J control fractures at both 7 and 14 days. The significance of the reduction in collagen 10α1 expression level at 14 days post-fracture is not clear. However, although collagen 10α1 has traditionally served as a marker for chondrocyte hypertrophy, questions have recently been raised about its reliability for this purpose [27]. Nevertheless, these findings have clearly demonstrated that the Bax KO fractures produced significant amounts of callus cartilage during the early phase of fracture healing and that the increased amount of callus cartilage was due to an increase in the number and also perhaps the maturation (hypertrophy) of callus chondrocytes. Because the bony bridging of the fracture gap requires complete endochondral remodeling of callus cartilage into bone, the increased amounts of callus cartilage suggest that Bax deficiency may slow down the bony bridging of the fracture gap during the normal fracture healing. On the other hand, as indicated in above, Bax deficiency also led to a rapid remodeling of the fracture callus during later phase of the fracture repair. Thus, the large amounts of callus cartilage in Bax KO mice were also rapidly remodeled into bony tissue and as a result, there were no significant differences in the amounts of callus cartilage between Bax KO and C57BL/6J mice. Thus, despite the fact that Bax deficiency led to the formation of larger and more mineralized calluses as well as more callus cartilage during the early fracture healing phase, there were no apparent differences in overall healing, i.e., the bony bridging of the fracture gaps and/or the histology of the healed fracture bones. Consequently, the physiological relevance of the findings that Bax deficiency yielded larger, more mineralized calluses and more amounts of callus cartilage during the early healing phase is not clear.

Regardless of the physiological significance of the increased callus cartilage and greater numbers of chondrocytes during early fracture healing in Bax KO mice, our *in situ* TUNEL analysis of apoptotic cells on the healing calluses indicate that the greater number of chondrocytes in Bax KO fractures is unlikely to be due solely to a reduction in chondrocyte apoptosis. More importantly, the large increases in labeled pre-hypertrophic chondrocytes and fibroblasts of the soft callus, as well as osteoblasts of the hard callus in the *in vivo* BrdU incorporation analysis of proliferating cells, indicated that Bax deficiency also enhanced the proliferation of fracture callus cells. These surprising findings of an increased proliferation of fracture callus cells suggest that Bax not only functions as a pro-apoptotic gene, but may also have a previously unidentified novel function as an anti-proliferative gene. Consistent with the possibility that Bax and/or related members of the family of Bcl-2 proteins regulate cell proliferation, it has been reported that overexpression of Bcl-2, an anti-apoptotic gene, in mice promoted myocyte proliferation [28]. There is also circumstantial evidence that Bid, another BH-3 domain only pro-apoptotic gene, may exert anti-proliferative functions in cancer cells [29]. It has also been reported that Bax and Bak regulate T cell proliferation through control of endoplasmic reticulum Ca^{2+} homeostasis [30]. The mechanism by which Bax deficiency increases cell proliferation during fracture repair remains unknown. However, Bax gene expression is a target for the expression of p53 [31], a key regulator of the balance between the cell cycle, cell development and apoptosis. It is possible that Bax deficiency affects the regulation of p53-related pathways and reduces p53 inhibition of the cell cycle, thereby increasing proliferation [32]. Much work is needed to determine the mechanisms whereby Bax regulates cell proliferation during fracture repair. Nevertheless, our studies have demonstrated that the large increase in the number of chondrocytes and the amount of callus cartilage during the early fracture repair phase was due largely to an increase in proliferation of pre-hypertrophic chondrocytes and subsequent maturation to hypertrophic chondrocytes. More importantly, our findings have implicated a previously unknown function of Bax in the regulation of cell proliferation.

Finally, this study may have also disclosed an important difference between the functional role of the intrinsic mitochondrial pathway of apoptosis and that of the cytokine-mediated extrinsic apoptosis pathway in fracture repair. In this regard, a previous study with TNF-α receptor KO mouse femoral fracture model [7,8], which lacks the TNF-α-mediated extrinsic apoptosis pathway, has shown that there was almost a complete absence of the initial intramembranous bone formation on the periosteal surface in the TNF-α receptor KO mice, in contrast to our Bax KO mice. Importantly, although the callus tissues of TNF-α receptor KO mice were also greatly enlarged as healing progressed, there was a clear delay in hypertrophy of the chondrocytes and the resorption of cartilage tissue, which are opposite to what were observed during the healing of Bax KO fractures. Moreover, contrary to Bax KO mice, there was the absence of endochondral resorption of the callus at the later healing phase. Consequently, it is possible that there may be different functional roles for the intrinsic mitochondrial pathway of apoptosis as opposed to the cytokine-mediated extrinsic apoptotic pathway in the regulation of fracture healing.

In summary, this study has demonstrated for the first time that Bax has an important regulatory role in the early fracture healing, and that the increased callus size and cartilage area in Bax KO fractures was due largely to increased chondrocyte proliferation and not to reduced apoptosis or increased chondrocyte hypertrophy. The unexpected effect of Bax deficiency on the proliferation of pre-hypertrophic chondrocytes implicates a novel regulatory function for Bax as a negative regulator of the proliferation of chondrocytes during fracture repair.

Acknowledgments

This work was supported by the U.S. Army Medical Research Acquisition Activity Assistance Award No.DAMD17-03-2-0021. The U. S. Army Medical Research Acquisition Activity, 820 Chandler Street, Fort Detrick, MD 21702-5014, is the awarding and administering acquisition office. The information contained in this publication does not necessarily reflect the position or the policy of the government, and no official endorsement should be inferred. We are grateful to Emile Davis, Nancy Lowen, Ryan Porte and Jann Smallwood for technical assistance. All work was performed in facilities provided by the Department of Veterans Affairs.

References

[1] Aizawa T, Kon T, Einhorn TA, Gerstenfeld LC. Induction of apoptosis in chondrocytes by tumor necrosis factor-a. J Orthop Res 2001;19:785–96.
[2] Zhang X, Li R, Yang H, Gao L, Yang S. Expression of Bax protein in the cartilage cells of epiphyseal plate. Sichun Da Xue Xue Bao Yi Xue Ban 2003;34:64–6.
[3] Liang M, Russell G, Hulley PA. Bim, Bak and Bax regulate osteoblast survival. J Bone Miner Res 2008;23:610–20.
[4] Chamoux E, Houde N, L'Eriger K, Roux S. Osteoprotegerin decreases human osteoclast apoptosis by inhibiting the TRAIL pathway. J Cell Physiol 2008;216: 536–42.
[5] Yen ML, Tsai HF, Wu YY, Hwa HL, Lee BH, Hsu PN. TNF-related apoptosis-inducing ligand (TRAIL) induces osteoclast differentiation from monocyte/macrophage lineage precursor cells. Mol Immunol 2008;45:2205–13.

[6] Komatsu DE, Bosch-Marce M, Semenza GL, Hadjiargyrou M. Enhanced bone regeneration associated with decreased apoptosis in mice with partial HIF-1a deficiency. J Bone Miner Res 2007;22:366–74.
[7] Gerstenfeld LC, Cho TJ, Kon T, Aizawa T, Cruceta J, Graves BD, et al. Impaired intramembranous bone formation during bone repair in the absence of tumor necrosis factor-a signaling. Cells Tissues Organs 2001;169:285–94.
[8] Gerstenfeld LC, Cho TJ, Kon T, Aizawa T, Tsay A, Fitch J, et al. Impaired fracture healing in the absence of TNF-a signaling: the role of TNF-a in endochondral cartilage resorption. J Bone Miner Res 2003;18:1584–92.
[9] Zinkel S, Gross A, Yang E. BCL2 family in DNA damage and cell cycle control. Cell Death Diff 2006;13:1351–9.
[10] Lu C, Miclau T, Hu D, Marcucio RS. Ischemia leads to delayed union during fracture healing: a mouse model. J Orthop Res 2007;25:51–61.
[11] Reed JC. Proapoptotic multidomain Bcl-2/Bax-family proteins: mechanisms, physiological roles, and therapeutic opportunities. Cell Death Diff 2006;13:1378–86.
[12] Lalier L, Cartron PF, Juin P, Nedelkina S, Manon S, Bechinger B, et al. Bax activation and mitochondrial insertion during apoptosis. Apoptosis 2007;12:887–96.
[13] Er E, Oliver L, Cartron PF, Juin P, Manon S, Vallette FM. Mitochondria as the target of the pro-apoptotic protein Bax. Biochim Biophys Acta 2006;1757:1301–11.
[14] Korsmeyer SJ. Regulators of cell death. Trends Genet 1995;11:101–5.
[15] Mocetti P, Silvestrini G, Ballanti P, Patacchioli FR, Di Grezia R, Angelucci L, et al. Bcl-2 and Bax expression in cartilage and bone cells after high-dose corticosterone treatment in rats. Tissue Cell 2001;33:1–7.
[16] Knudson CM, Tung KSK, Tourtellotte WG, Brown GA, Korsmeyer SJ. Bax-deficient mice with lymphoid hyperplasia and male germ cell death. Science 1995;270:96–8.
[17] Perez GI, Jurisicova A, Wise L, Lipina T, Kanisek M, Bechard A, et al. Absence of the proapoptotic Bax protein extends fertility and alleviates age-related health complications in female mice. Proc Natl Acad Sci USA 2007;104:5229–34.
[18] jaxmice.jax.org/strain/002994/protocol_id=250,2004.
[19] Bonnarens F, Einhorn TA. Production of a standard closed fracture in laboratory animal bone. J Orthop Res 1984;2:97–101.
[20] Livak KJ, Schmittgen TD. Analysis of relative gene expression data using real-time quantitative PCR and the $2^{-\Delta\Delta C}{}_{T}$ method. Methods 2001;25:402–8.
[21] Darby IA, Hewitson TD. Fibroblast differentiation in wound healing and fibrosis. Int Rev Cytol 2007;257:143–79.
[22] Jun JB, Kuechle M, Harlan JM, Elkon KB. Fibroblast and endothelial apoptosis in systemic sclerosis. Curr Opin Rheumatol 2003;15:756–60.
[23] Hutcheson J, Scatizzi JC, Bickel E, Brown NJ, Bouillet P, Strasser A, et al. Combined loss of proapoptotic genes Bak or Bax with Bim synergizes to cause defects in hematopoiesis and in thymocyte apoptosis. J Exp Med 2005;201:1949–60.
[24] Gavaldà N, Pérez-Navarro E, García-Martínez JM, Marco S, Benito A, Alberch J. Bax deficiency promotes an upregulation of Bim_{EL} and Bak during striatal and cortical postnatal development, and after excitotoxic injury. Mol Cell Neurosci 2008;37:663–72.
[25] Hedge R, Srinivasula SM, Ahmad M, Fernandes-Alnemri T, Alnemri ES. Blk, a BH-3-containing mouse protein that interacts with Bcl-2 and Bcl-xL, is a potent death agonist. J Biol Chem 1998;14:7783–6.
[26] Wakeyama H, Akiyama T, Takahashi K, Amano H, Kadono Y, Nakamura M, et al. Negative feedback loop in the Bim-caspase-3 axis regulating apoptosis and activity of osteoclasts. J Bone Miner Res 2007;22:1631–9.
[27] Mwale F, Stachura D, Roughley P, Antoniou J. Limitations of using aggrecan and type X collagen as markers of chondrogenesis in mesenchymal stem cell differentiation. J Orthop Res 2006;24:1791–8.
[28] Limana F, Urbanek K, Chimenti S, Quaini F, Leri A, Kajstura J, et al. Bcl-2 overexpression promotes myocyte proliferation. Proc Natl Acad Sci USA 2002;99:6257–62.
[29] Song G, Chen GG, Chau DK, Miao J, Lai PB. Bid exhibits S phase checkpoint activation and plays a pro-apoptotic role in response to etoposide-induced DNA damage in hepatocellular carcinoma cells. Apoptosis 2008;13:693–701.
[30] Jones RG, Bui T, White C, Madesh M, Krawczyk CM, Lindsten T, et al. The proapoptotic factors Bax and Bak regulate T cell proliferation through control of endoplasmic reticulum Ca^{2+} homeostasis. Immunity 2007;27:173–8.
[31] Meulmeester E, Jochemsen AG. P53: a guide to apoptosis. Curr Cancer Drug Targets 2008;8:87–97.
[32] Eischen CM, Roussel MF, Korsmeyer SJ, Cleveland JL. Bax loss impairs myc-induced apoptosis and circumvents the selection of p53 mutations during myc-related lymphomagenesis. Mol cell Biol 2001;21:7653–62.

Ephrin B1 Regulates Bone Marrow Stromal Cell Differentiation and Bone Formation by Influencing TAZ Transactivation via Complex Formation with NHERF1

Weirong Xing[1,2], Jonghyun Kim[1], Jon Wergedal[1, 2, 3], Shin Tai Chen[1,3,4] and Subburaman Mohan[1,2,3,5]

[1]Musculoskeletal Disease Center, Jerry L Pettis VA Medical Center, Loma Linda, CA 92357, Departments of [2]Medicine, [3]Biochemistry, [4]Microbiology and [5]Physiology, Loma Linda University, Loma Linda, CA 92354

Running title: Ephrin B1 reverse signaling regulates bone formation

Corresponding author: Subburaman Mohan, Ph.D., Musculoskeletal Disease Center (151), Jerry L Pettis VA Medical Center, 11201 Benton St, Loma Linda, CA 92357

Phone: 909-825-7084, ext. 2932. Fax: 909-796-1680. Email: Subburaman.Mohan@va.gov

Keywords: Ephrin B1, ephrin receptor, molecular pathway, TAZ, NHERF1, Protein phosphotase, bone formation, conditional knockout, osteoblast.

Abstract

Mutations of ephrin B1 in humans result in craniofrontonasal syndrome. Because little is known on the role and mechanism of action of ephrin B1 in bone, we examined the function of osteoblast produced ephrin B1 *in vivo* and identified the molecular mechanism by which ephrin B1 reverse signaling regulates bone formation. Targeted deletion of ephrin B1 gene in osteoblasts resulted in severe calvarial defects, decreased bone size, bone mineral density and trabecular bone volume caused by impairment in osterix expression and osteoblast differentiation. Co-immunoprecipitation of TAZ complex with TAZ specific antibody revealed a protein complex containing ephrin B1, PTPN13, NHERF1 and TAZ in bone marrow stromal (BMS) cells. Activation of ephrin B1 reverse signaling with soluble EphB2-Fc led to a time-dependent increase in TAZ dephosphorylation and shuttling from cytoplasm to nucleus. Treatment of BMS cells with exogenous EphB2-Fc resulted in a 4-fold increase in osterix expression as determined by Western blot. Disruption of TAZ expression using specific lentivirus shRNA decreased TAZ mRNA by 80% and ephrin B1 reverse signaling-mediated increases in osterix mRNA by 75% ($P<0.01$). Knockdown of NHERF1 expression reduced basal levels of osterix expression by 90%, and abolished ephrin B1-mediated induction of osterix expression. We conclude that locally produced ephrin B1 mediates its effects on osteoblast differentiation by a novel molecular mechanism in which activation of reverse signaling leads to dephosphorylation of TAZ and subsequent release of TAZ from ephrin B1/NHERF1/TAZ complex to translocate to nucleus for induction of expression of osterix and perhaps other osteoblast differentiation genes. Our findings provide strong evidence that ephrin B1 reverse signaling in osteoblasts is critical for BMS cell differentiation and bone formation.

Abbreviations: ALP: alkaline phosphatase; shRNA: small hairpin RNA; BFR: bone formation rate; BMC: bone mineral content; BMD: bone mineral density; BMS: bone marrow stromal cells; BS: bone surface; DEXA: dual-energy X-ray absorptometry; Eph: ephrin receptor; FBS: fetal bovine serum; GFP: green fluorescent protein; KO: knockout; μ-CT: micro-computed tomography; NHEFR1/2**:** sodium-hydrogen exchanger regulatory factor 1/2; pQCT:peripheral quantitative computed tomography; PP2C: protein phosphatase 2C; PTPN13: non-receptor protein tyrosine phosphatase 13; TAZ: transcriptional coactivator with PDZ-binding motif; TRAP: tartrate-resistant acid phosphatase; MAR: mineral apposition rate; WT: wild-type.

Introduction

Osteoporosis is a common disease characterized by an age-dependent decrease in bone mineral density (BMD) and a microarchitectural deterioration of bone tissue with a consequent increase in the risk of developing fragility fractures of the hip, spine, and other skeletal sites (19). The decrease in bone mass occurs when the body fails to form enough new bone to replace the amount of old bone resorbed leading to reduced bone strength. There are two major known causes of osteoporosis; low peak BMD that is typically achieved by around age 30 and high bone loss rate that occurs particularly after menopause and during the natural process of aging. The accumulation of peak bone mass depends on bone growth during early skeletal development and the balance between osteoblastic bone formation and osteoclastic bone resorption during the postnatal growth period. Therefore, understanding the regulatory factors that govern bone development, bone size, bone mineralization and bone quality during active growth periods as well as bone homeostasis during menopause and aging is essential for development of therapeutics to prevent osteoporosis.

Ephrin ligands and their receptors have been shown to play key roles in the growth and development of multiple tissues including the skeleton (13, 49, 52). There are two types of ephrin ligands and their receptors. Ephrin As are membrane anchored proteins while ephrin Bs are transmembrane proteins. In general, ephrin As bind to ephrin A receptors (EphA) while ephrin Bs interact with ephrin B receptors (EphB), with few exceptions (28). Ephrin B1 preferentially binds to EphB2 and B3 receptors with high affinity and interacts with EphB1 and B4 receptors with low affinity (28). It has been shown that both ephrin B1/2 and their receptors (EphB2, B3, B4, B6 and A4) are expressed in bone cells (57). However, only ephrin B1/2 are expressed in osteoclasts during the osteoclast precursor differentiation while ephrin B1/2 and their receptors are consistently co-expressed during osteoblast differentiation (57). The interaction of ephrin B1/2 with their multiple receptors via cell-cell contact leads to the activation of a bidirectional signal in which both the receptor-mediated forward signal and the ligand-

mediated reverse signal activate downstream signaling cascades (12, 57). In the cells that co-express both ephrin ligands and their receptors, the ephrin ligands and receptor proteins can be segregated into distinct membrane domains from which they signal biological effects via cell surface interactions (35). Although EphB4 forward signaling and ephrin B2 reverse signaling have been implicated in regulating osteoblastic bone formation and osteoclastic bone resorption processes (57), homozygotes for targeted null mutations of ephrin B2 or EphB4 receptor exhibit severe defects in angiogenesis of both arteries and veins and embryonic lethality (15, 18, 34). In contrast, total disruption of the ephrin B1 gene in mice results in perinatal lethality and defects in skeletal patterning while mutations of ephrin B1 in humans have been found to cause craniofrontonasal syndrome (8, 12, 49, 50). Mutation of the cytoplasmic tail of ephrin B1 that allows its extracellular domain to interact with ephrin receptors exhibits the same bone phenotypes as the ephrin B1 knockout (KO) mice (12, 13). However, individual KO of EphB1, B2, B3 or A4 receptor, the major receptors for ephrin B1, showed mild phenotypes of behavior, nerve or digestive system while KO of both EphB2 and EphB3 receptors resulted in embryonic lethality (14, 23, 25, 38, 51, 57). These experimental and genetic studies strongly suggest that ephrin B1 mediated reverse signaling via its cytoplasmic tail is essential in craniofacial development and the bone formation processes.

Recent studies on the structure and function of ephrin B1 have shown that a highly conserved cytoplasmic tail of ephrin B1 contains several tyrosine residues that can be phosphorylated when the extracellular domain of ephrin B1 contacts with its multiple cognate EphB receptors (6, 12, 33). The C-terminus of ephrin B1 also contains a conserved binding motif (YYKV) to which PDZ proteins can recognize and bind (6, 32, 33, 48). Therefore, ephrin B1 functions as a receptor-like signaling molecule to transduce signals into the interior of the cell through tyrosine phosphorylation and interaction with PDZ domain-containing proteins including Pick1, GRIP, PTP-BL and Par-6 in endothelial cells and Xenopus oocytes (5, 6, 30, 32, 33, 39, 45, 48). However, whether any of these PDZ domain-containing proteins are also

involved in ephrin B1 reverse signaling to regulate mesenchymal stem cell differentiation and bone formation is unknown.

Schroeder et al. have shown that a PDZ containing protein, Na/H exchange regulatory factor 1 (NHERF1) also known as solute carrier family 9, isoform 3 regulator 1 (Slc9a3r1), is highly expressed in MC3T3-E1 osteoblasts (43). Targeted disruption of NHERF1 resulted in postnatal lethality often accompanied by bone fractures due to 25-30% reduction in BMD that is believed to be due to increased phosphate transport by Npt2a in the kidneys (44). However, the severity of skeletal phenotype in the NHERF1 KO mice cannot be explained by the sole function of NHERF1 to redistribute Npt2a because targeted disruption of Npt2a only showed mild skeletal phenotype that improved over time (3). Thus, NHERF1 may be involved in regulating other biological events besides regulating phosphate transport by Npt2a. Because NHERF2 has been shown to bind to both the membrane receptors and the transcriptional co-activator with PDZ binding motif (TAZ) via its two PDZ domains (29) and because TAZ contains a well conserved WW domain that can interact with transcription factors such as Runx2, Smad, and Pax3 (26, 27, 29), we hypothesized that ephrin B1 could also form a complex with TAZ through osteoblast produced NHERF1, a homolog of NHERF2, and transmit extracellular signals into the nuclei of bone cells to regulate bone formation. To test the hypothesis, we generated conditional KO mice with osteoblast specific disruption of ephrin B1 for evaluation of skeletal phenotypes and explored the involvement of NHERF1 and TAZ in mediating the effects of the ephrin B1 ligand on osteoblast function.

Materials and Methods

Plasmids, recombinant proteins and antibodies: The full-length cDNA of mouse EphB2 was amplified by PCR and cloned into the sites of Acc651 and XhoI of pcDNA3.1 (Invitrogen, pcDNA-EphB2). Plasmid pcDNA3-ephrin B1 was provided by Dr. Philippe Soriano (Mount Sinai School of Medicine, New York). Plasmids of pEGFP-TAZ and pEGFP-N-TAZ were generated by inserting mouse TAZ and truncated N-TAZ released from pcDNA-TAZ and pcDNA-N-TAZ (kindly provided by Dr. Cai Bin Cui at the University of North Carolina) into the corresponding sites of HindIII and XbaI of pEGFP-C1 vector (BD Bioscience) (10, 12). Retroviral vectors of pMX-ephrinB2-IRES-EGFP and pMX-EphB4-IRES-EGFP were generous gifts from Dr. Koichi Matsuo at the Keio University (57). Recombinant proteins of ephrin B1-Fc, ephrin B2-Fc, EphB2-Fc, control Fc, and antibodies against human IgG, NHERF1, histone H3 and β-actin were purchased from Sigma. Antibody specific to mouse NHERF2 was from Alpha Diagnostic International (San Antonio, TX). Antibodies against ephrin B1, ephrin B2, EphB2 and EphB4 were from R & D Systems. Anti-phospho-Tyr^{317} ephrinB was a product of PhosphoSolutions (Aurora, CO). Polyclonal Antibody specific to PTPN13 was purchased from Santa Cruz. Polyclonal antibodies to TAZ and phospho-YAP (Ser127) were from Cell Signaling Technology while monclonal antibody specific to TAZ was from BD Pharmingen. Retroviral pLKO.1-shRNA clones were purchased from Sigma and Open Biosystems. The hairpin sequences of targeting shRNA were:

Mouse TAZ: CCTGCATTTCTGTGGCAGATActcgagTATCTGCCACAGAAATGCAGG

Mouse NHERF1: GACCGAATTGTGGAGGTCAATctcgagATTGACCTCCACAATTCGGTC

EGFP: TACAACAGCCACAACGTCTATctcgagATAGACGTTGTGGCTGTTGTA

Mice: The floxed ephrin B1 mice with mixed background of C57BL/6J and 129S4 strains were kindly provided by Dr. Philippe Soriano (12). The Col1α2-iCre transgenic mice expressing improved Cre recombinase (iCre) were reported previously (17). Ephrin B1 conditional KO mice were generated by crossing efnb1$^{flox/flox}$ female with a Cre transgenic male under the control of

regulatory sequences of the col1α2 gene to generate iCre+, efnb1$^{flox/y}$ hemizygous males. The iCre+, efnb1$^{flox/y}$ hemizygous males were then bred with efnb1$^{flox/flox}$ homozygous females to generate ephrin B1 conditional KO and control wild-type (WT) mice (Figure 1A). All mice were housed at the Jerry L. Pettis Memorial VA Medical Center Veterinary Medical Unit (Loma Linda, CA) under standard approved laboratory conditions with controlled illumination (14 hours light, 10 hours dark), temperature (22^0C) and unrestricted food and water. All of the procedures were performed with the approval of the Institutional Animal Care and Use Committee (IACUC) of the Jerry L Pettis Memorial VA Medical Center. Genotyping of the ephrin B1 gene and iCre transgene were monitored by PCR using DNA extracted from tail snips as reported (12, 17). The mouse sex-determining gene sry on the Y chromosome was amplified by PCR with specific primers to determine the gender of mouse fetuses (22).

Skeleton staining: Alizarin red and alcian blue staining were performed using established methods (36). Briefly, E19.5 embryos were deskinned, eviscerated, and fixed in 95% ethanol for 5 days. The carcasses were fixed in acetone for 4 days and then stained for 3 days in a solution containing 0.1% alizarin red, 0.3% alcian blue, acetic acid, and 70% ethanol (1:1:1:17, vol/vol/vol/vol). The embryos were then transferred to a solution of 1% KOH in 20% glycerol until clear and then stored in glycerol.

Evaluation of bone phenotypes: Total bone mineral content (BMC) and bone mineral density (BMD) were measured by dual-energy X-ray absorptiometry (DEXA) as described previously (20, 21). The volumetric BMD and geometric parameters at the mid-diaphysis of the femurs isolated from 8-week old mice were determined by Peripheral Quantitative Computed Tomography (pQCT) as reported (21). Cortical and trabecular bone microarchitectures of the femurs isolated from 8-week old mice were assessed by using μ-CT (Inveon CT Module, Siemens, Malver, PA). The femurs isolated from 8-week old mice were scanned by X-ray (80 kVp volts; anode current at 250 μA) with an axial length of 1024 slides at 10 microns/slice and parallel length of 2048 slices. The voxel size was 10 microns. Reconstruction analysis was

performed with COBRA software (Exxim, Pleasanton, CA). The sections of 1 mm at the mid-diaphysis were analyzed for cortical measurements and a fixed section of 3.2 mm at the distal end for trabecular measurements by using Amira software (Mercury Computer Systems, Inc., Chelmsford, MA). The bones analyzed were adjusted for length so that the region of interest chosen for cortical and trabecular bone parameters was anatomically the same between the mutant bone and control littermates' bone.

Dynamic calcein labeling and histomorphometry: Three-week old mice were injected intraperitoneally with calcein seven days (20 mg/kg) and two days prior to the expected day of euthanization in order to label mineralizing bone surfaces. Mouse femurs were fixed in 10% formalin overnight. The bones were washed, dehydrated, embedded in methyl methacrylate resin for sectioning. Longitudinal sections of comparable anatomic position of the femurs were analyzed by fluorescence microscopy. For analysis of cortical bone formation parameters, mid diaphysis of left femurs were used as a sampling site. For evaluation of bone resorption parameters, the right femurs were partially demineralized, embedded in glycomethacrylate and cut into sections. The sections were stained for tartrate-resistant acid phosphatase (TRAP) and the TRAP covered surface was measured. All bone histomorphometric parameters were measured as previously described (2, 41). Mineral apposition rate (MAR), bone formation rate (BFR)/bone surface (BS) were calculated as described previously (40).

Serum assay: Mouse serum level of C-telopeptide was measured as described previously (46).

Primary cell culture: Bone marrow stromal (BMS) cells derived from the femurs and the tibias of ephrin B1 conditional KO and corresponding control mice were cultured as reported previously (55). The cells were cultured in α minimal essential medium (αMEM) containing 10% fetal bovine serum (FBS), penicillin (100 units/ml) and streptomycin (100 µg/ml) until 60-70% confluent prior to experiments.

Nodule assay and ALP staining: BMS cells isolated from the femurs and the tibias of ephrin B1 conditional KO and corresponding control mice were grown to 80%. The cells were then

treated with a mineralization medium containing 10 mM β-glycerophosphate, 50 μg/ml of ascorbic acid and 5% FBS for 24 days. The cells were washed, fixed and stained with 40 mM alizarin red (pH 4.2). The mineralized area was measured as described previously (54, 55). For alkaline phosphatase (ALP) staining, primary bone marrow stromal cells were grown to 70% confluence and treated with 2 μg/ml of clustered EphB2-Fc or control Fc in a differentiated medium for 6 days, followed by ALP staining and ALP activity assay (54, 55).

Transient transfection and viral transduction: Transient transfection was carried out by using LipofectAMINE Reagent according to instruction of the manufacturer (Invitrogen). Murine leukemia virus (MLV) and lentiviral productions were generated by transfection in Plat-E and 293T cells as described (37, 42). Forty eight hours after transfection, culture supernatants containing retroviral particles were collected, spun at 2,000 x g for 10 min, and filtered through a 0.45 μm filter. Titers were determined by infecting 293T cells with serial dilutions and examining GFP expression of infected cells by flow cytometry 24 hours after infection. Primary BMS cells or C3H10T1/2 cells were transduced by adding culture supernatant containing retroviral particles into the 6-well culture plates in the presence of 8 μg/ml of polybrene.

RNA extraction and quantitative PCR: RNA was extracted from primary cultures or bone marrow-free femurs and tibias of 3 week old ephrin B1 KO and corresponding WT littermates as described previously (53, 55). An aliquot of RNA (2 μg) was reverse-transcribed into cDNA in 20 μl volume of reaction by oligo$(dT)_{12\text{-}18}$ primer. Real time PCR was carried out as reported previously (53, 55). Primers for peptidyl prolyl isomerase A (PPIA) were used to normalize the expression data of test genes. Sequences of the primers were: Osterix: forward 5'-TGGCGTCCTCTCTGCTTGA; reverse 5'-TCAGTGAGGGAAGGGTGGGT. PPIA: forward 5'-CCATGGCAAATGCTGGACCA; reverse 5'-TCCTGGACCCAAAACGCTCC. ALP: forward 5'-ATGGTAACGGGCCTGGCTACA; reverse 5'-AGTTCTGCTCATGGACGCCGT. Runx2: forward 5'-TGGCCGGGAATGATGAGAACTA; reverse 5'-GGACCGTCCACTGTCACTTTAA. Msx1: forward 5'-TGCCACTCGGTGTCAAAGTGG; reverse 5'-CCGACTGAGAAATGGCCGAGA.

TAZ Nuclear translocation: C3H10T1/2 cells were co-transfected with pEGFP-TAZ or pEGFP-N-TAZ and pcDNA3-ephrin B1, and treated with soluble clustered EphB2-Fc protein (2 μg/ml) or Fc 24 hours after transfection. The transfected cells were examined under an Olympus fluorescence microscope at 4 hours after treatment. The green fluorescence images were captured by using the computer-driven Camera with Olympus MagnaFire software (v2.1; Olympus America, Melville, New York). For examination of endogenous TAZ nuclear trafficking of BMS cells, the cells were treated with soluble clustered EphB2-Fc or Fc for 4 hours. The cytoplasmic and nuclear proteins were extracted and analyzed by Western blot with specific antibodies to mouse TAZ, β-tubulin and histone H3 as described previously (55).

Immunoprecipitation and Western blot: Primary BMS cells were cultured until 70% confluent, treated with clustered EphB2-Fc protein at 37 ^{0}C for 5 minutes and cross-lined with 5 mM dithiobis (succinimidyl) propionate (Pierce) for 30 min at room temperature. The cells were lysed with lysis buffer (50 mM HEPES [pH 7.5], 100 mM NaCl, 10 mM EDTA, 10% glycerol, 1% Triton X-100, 1 mM phenylmethylsulfonyl fluoride, 1x protease inhibitor cocktail and 1x phosphatase inhibitor cocktail). Cell lysate (300 μg of total protein) was first precleared by using protein A/G-Sepharose and then incubated with 4 μg of TAZ specific monoclonal antibody or control IgG for 1 hour at 4°C with gentle shaking, followed by the addition of protein A/G-Sepharose and an additional overnight incubation at 4°C. After centrifugation, the protein A/G-Sepharose beads were washed five times with cold lysis buffer and then boiled with SDS-PAGE sample buffer to dissociate the proteins. The immunoprecipitated proteins were separated by SDS-PAGE under reducing conditions for Western Blot with polyclonal antibodies against NHERF1 and ephrin B1.

Statistical analyses: Data were analyzed by ANOVA or students T test.

Results

Characterization of osteoblast-specific conditional KO mice: Conditional KO mice with osteoblast specific disruption of ephrin B1 was generated as described in Figure 1A. To confirm loss of ephrin B1 expression in the Cre+ mice, we extracted the total cellular proteins from primary osteoblasts from 2 week-old mice for immunoblotting analyses with antibodies to ephrin B1 and Cre. As expected, the Cre recombinase was expressed in type I collagen producing osteoblasts isolated from Cre+, efnb1$^{lox/lox}$ mice, but not in Cre-, efnb1$^{lox/lox}$ mice. Accordingly, the expression of the ephrin B1 protein was absent in osteoblasts from Cre+ mice, but was detected in the cells from Cre- control mice (Figure 1B).

Ephrin B1 deficiency in osteoblasts resulted in skull defects and reductions in bone size and peak bone BMD caused by reduced bone formation and mineralization. Upon breeding efnb1$^{lox/y}$ hemizygous males carrying Col1α2-Cre allele with efnb1$^{lox/lox}$ homozygous females, the ephrin B1 conditional KO mice were not retrieved at the expected Mendelian ratio while the ratio of WT male vs. WT female offspring is almost 1:1 at 3 weeks of age. We, therefore, compared the litter size for pups generated from Cre+ versus Cre- males that were bred with efnb1$^{lox/lox}$ homozygous females. We found that the average litter size was approximately 5 and 9 live pups for Cre+, efnb1$^{lox/y}$ and Cre-, efnb1$^{lox/y}$ males, respectively. Among all live pups (n=64) from the cross of efnb1 loxp homozygous mice with Cre+ loxp hemizygous mice, 60% of pups were males, and 40% were females. Among them, 15% females and 20% males were Cre+-positive. However, the ephrin B1-deficient fetuses were recovered at the expected Mendelian ratio at E19.5. Of which, more than 40% of the Cre+ females that were efnb1 loxp homozygous and 20% of Cre+ males that were efnb1 loxp hemizygous had severe defects of the skull and exencephaly (Figure 1C). The size of the skull was reduced and was not large enough to accommodate the growing brain. Skeletal preparations revealed that the basal aspect of the skull and jaw were intact. However, the frontal, parietal and interparietal bones were missing in both KO males and females with skull defects. The mandible and maxilla were

smaller. The overall size of the skull of the ephrin B1 gene KO mice was about 35% smaller than those of the WT littermates. As a result of calvarial bone defects, the basal elements of the skull became visible when viewed from above (Figure 1D). Besides the calvarial defects, the conditional KO mice were much smaller than the WT and bone mineralization was reduced (Figure 1E).

Though nearly 30% of ephrin B1 conditional KO male and female mice died before or shortly after birth, we have obtained an adequate number of male and female mutants for phenotypic characterization. The body weights of both male and females were significantly reduced by 29 and 17% at 3 and 8 weeks of age, respectively (71 ± 13%, and 83 ± 9% of the control littermates, N=14, $P<0.05$). As shown in Figures 1F & G, the body length of ephrin B1 mutants was reduced by 15% as compared to the corresponding littermates at 3 weeks of age. Femur length was reduced by 14% and 13% in KO males and females, respectively, at 8 weeks of age (Figures 2A & B). To determine if the targeted disruption of the ephrin B1 gene in osteoblasts affects bone mass, we performed DEXA measurements. We found that total body BMC was reduced by 30% and 23%, respectively, at 3 and 8 weeks of age (Figure 2C). Total body areal BMD was reduced by 10% at both time points while total body bone area was reduced by 25% and 15% at 3 and 8 weeks of age, respectively. To further characterize the skeletal phenotypes of ephrin B1 conditional KO mice, we collected the femurs from 8 week old mice and carried out pQCT and μ-CT analyses. Our pQCT analyses demonstrated that periosteal circumference and endosteal circumference of the femurs at mid diaphysis were reduced by 12% and 16%, respectively, in ephrin B1 conditional KO mice as compared to the control littermates (Figure 2D). Consistent with the pQCT data, μ-CT analyses confirmed that both bone volume and tissue volume were reduced by 25% at the mid diaphysis of the femurs isolated from 8 weeks old KO mice as compared to the littermate controls (Figures 2E-G). The percentage of bone volume to tissue volume was not different at this site of the femur. However, trabecular bone volume adjusted for tissue volume was significantly decreased at the

metaphysis of the femur (Figures 3A-D). Three-dimensional μ-CT analyses found that trabecular numbers were reduced 50% in the distal femurs isolated from KO females. The ratio of bone volume to tissue volume was reduced by 30% as compared to WT controls.

To identify the target cell types and cellular processes that contribute to reduced bone formation and decreased peak bone mass in the ephrin B1 conditional KO mice, we performed histomorphometric studies in 3-week old KO and control mice. Figure 3E shows a decreased width of newly formed bone between two calcein labels in the KO mice as compared to control mice. Because of reduced bone size in the KO mice, we adjusted bone formation rate (BFR) for bone surface (BS). The BFR/BS was reduced by 50% at the femur mid shaft in the KO mice (Figure 3F). In order to determine if the reduced bone formation rate is caused by reduced activity of osteoblasts, we measured mineral apposition rate (MAR) and found a 43% reduction in MAR in the KO mice as compared to the WT littermates (Figure 3G).

We next determined if loss of ephrin B1 in cells of osteoblast lineage influences bone resorption. Figure 4 shows the data from tartrate-resistant acid phosphatase (TRAP) staining for periosteal and endosteal surfaces examined at the mid diaphysis of the femurs of 3 week old mice. The percentage of TRAP labeled surface at both periosteum and endosteum were not affected in the conditional KO mice as compared to the littermate controls (Figures 4A & B). In addition, the serum level of C-telopeptide, a bone resorption marker, was not changed (Figure 4C). The lack of difference in bone resorption between conditional KO and WT mice was not surprising because conditional disruption of ephrin B1 in osteoblasts did not influence expression of ephrin B1 in osteoclast precursors as shown by Western blot analyses (Figure 4D).

Interaction of Ephrin B1 and EphB2 expressed in bone cells mediates osteoblast differentiation. Our finding that conditional disruption of ephrin B1 exhibits dramatic change in skeletal phenotypes predicts that ephrin B1 produced locally in bone is important. Accordingly, we found undifferentiated BMS cells express large amount of ephrin B1 protein (Figure 5A).

However, only a trace amount of ephrin B2 protein was expressed in BMS cells when the signals of ephrin B1 and B2 were normalized with expression levels of β-actin (Figures 5B). Because ephrin B1 has been shown to preferentially bind to EphB2 and EphB3 receptors, and weakly interacts with EphB1 and EphB4, we examined the expression of these receptors in bone cells by RT real-time-PCR (28). We found that EphB2 mRNA as measured by RT real-time PCR was expressed 20 times higher than the EphB3 and EphB4 in BMS cells while EphB1 was undetectable (data shown). Because mice with disruption of EphB3 receptor only showed behavior phenotypes in the central nervous system (38), we decided to focus on the EphB2 and EphB4 receptors in this study. We therefore determined the relative expression of these two receptors at the protein level. Figures 5C & D show that EphB2 protein as determined by Western blot analyses was highly expressed while expression of EphB4 was undetectable in BMS cells. Because both ephrin B1 and its multiple receptors are expressed in BMS cells, we next examined the role of osteoblast produced ephrin B1 by using BMS cells derived from ephrin B1 conditional KO and WT mice. We found that the amount of mineralized nodule was reduced by 66% in BMS cells derived from KO mice as compared to controls after 24 days of culture in a mineralization medium (Figures 5E). To confirm the relative contribution of ephrin B mediated reverse signaling to the osteoblast differentiation, we seeded BMS cells derived from 3 week old WT and ephrin B1 conditional KO mice at low density, to minimize the cell-cell contact, and treated them with control Fc and EphB2-Fc in a differentiation medium for 6 days to activate the reverse signaling. We found that treatment of EphB2-Fc increased ALP activity by 118 % as compared to the cells treated with control Fc. In contrast, treatment of bone marrow stromal cells derived from ephrin B1 conditional KO mice with EphB2-Fc failed to stimulate ALP activity (Figure 5G).

Ephrin B1 reverse signaling regulates osterix expression. To further determine the cause for reduced osteoblastic function in the conditional ephrin B1 KO mice, we measured expression levels of transcription factors that are critical in osteoblast differentiation. Total RNA was

extracted from the marrow-free long bones of 3 week-old KO mice and corresponding littermates and used for RT real-time PCR with primers specific for ALP, osterix, Runx2, Msx1, ephrin B1, EphB2 and PPIA. As expected, the expression of ephrin B1 was reduced by 85% in the bones of conditional KO mice as compared to the WT controls. There was no change of EphB2 receptor expression between the bones isolated from WT and KO mice. The expression of ALP was decreased by 80% in the bones of conditional KO mice as compared to corresponding controls (Figure 6A). There was a significant 75% reduction in the expression of osterix in the femurs of the KO mice as compared to the WT littermates. However, the expression of Runx2 and Msx1 were not significantly altered. To further examine whether ephrin B1 mediated reverse signaling regulates osterix expression, we treated BMS cells from WT and conditional KO mice with Eph-B2-Fc soluble receptor. We predicted that soluble receptor, upon binding to ephrin B1 ligand, would activate ephrin B1 reverse signaling in WT but not KO cells. We also predicted that EphB2-Fc soluble receptor would inhibit forward signaling by competing with endogenous EphB receptor to bind to ephrin B1 ligand in WT cells. As expected, we found that treatment of WT BMS cells with 2 μg/ml EphB2-Fc for 72 hours in a mineralization medium increased osterix expression by approximately 4-fold as determined by Western blot using an osterix specific antibody. As expected, osterix protein levels were considerably lower in the ephrin B1 KO cells as compared to WT control cells. Furthermore, addition of EphB2-Fc soluble receptor did not induce osterix expression in the ephrin B1-deficient cells (Figures 6B & C). There were no changes in TAZ, NHERF1 or Runx2 expression in the BMS cells derived from KO mice as compared to the cells from WT control mice. Furthermore, treatment of BMS cells derived from bone WT and KO mice with EphB2-Fc did not stimulate the expression of TAZ, NHERF1 or Runx2.

Activation of ephrin B1 recruits PTPN13, NHERF1 and TAZ to the phosphorylated ephrin B1, and stimulates TAZ nuclear translocation. In terms of the mechanism by which ephrin B1 regulates osterix expression, it is known that the cytoplasmic tail of ephrin B1 contains a PDZ

binding motif that can interact with PDZ domain containing proteins such as PTPN13 and NHERF1/2 (33). Since NHERF1 and 2 contain two conserved PDZ domains that can potentially bind to both the membrane proteins and the transcriptional coactivator TAZ, we predicted that activation of ephrin B1 can induce a protein complex formation containing PTPN13, NHERF1/2 and TAZ. To test this prediction, we first examined whether BMS cells express NHERF1 and/or NHEFR2 protein by Western blot. We found that NHERF1 was expressed in the BMS cells at very high levels, but NHERF2 expression was undetectable with the commercial polyclonal antibody (data not shown). We then examined the interaction of ephrin B1, TAZ, NHERF1 and PTPN13 in BMS cells. The BMS cells were stimulated with clustered EphB2-Fc for 5 min, cross-linked with dithiobis (succinimidyl) propionate, and lysed for immunoprecipitation with anti-TAZ and anti-PTPN13, respectively. Because we used a strategy that involved a membrane permeable and reversible crosslinker to stabilize the protein complex, we were able to immunoprecipitate both ephrin B1 and NHERF1 with an antibody specific to TAZ, and ephrin B1 with antibody specific to PTPN13 (Figure 7A).

Because PTPN13 can dephosphorylate tyrosine residues of the clustered ephrin B1, we predicted that the formation of ephrin B1, NHERF1 and other PDZ domain containing protein phosphatases (PP) such as PTPN13 and PP2C can form a scaffold membrane-associated protein cluster, and the protein complex can dephosphorylate ephrin B1 and TAZ (24, 39). To test the prediction, we performed coimmunoprecipitation again with the antibody specific to NHERF1 to pull down NHERF1 protein complex. The co-immunoprecipitated proteins were blotted with antibodies against ephrin B1 and PTPN13, respectively. Figure 7B shows stronger interactions among ephrin B1, NHERF1 and PTPN13 30 minutes after addition of EphB2-Fc as compared to prior to EphB2-Fc treatment. As expected, the scaffold protein clustering was transient and returned to baseline by 120 minutes after EphB2-Fc stimulation. Activation of ephrin B1 reverse signaling with soluble clustered EphB2-Fc receptors also led to a time-dependent increase in the phosphorylation of ephrin B1 (7.3-, 15.4- and 9.6-fold at 5, 30, 120

minutes respectively), and the dephosphorylation of TAZ (1.5-, 2.2- and 3.3-fold at 5, 30 and 120 minutes respectively) in C3H10T1/2 cells overexpressing ephrin B1 and TAZ (Figure 7C).

To test if ephrin B1 reverse signaling-mediated TAZ dephosphorylation is concomitant with TAZ trafficking from cytoplasmic compartment to nucleus, we transfected C3H10T1/2 cells that do not express endogenous ephrin B1 with pEGFP-TAZ or pEGFP-N-TAZ with pcDNA-ephrinB1 and pEGFP alone. The cells were then stimulated with clustered EphB2-Fc or control Fc for 4 hours for examination of TAZ and N-TAZ nuclear translocation. As expected, co-transfection of C3H10T1/2 cells with N-TAZ and ephrin B1 resulted in the cytoplasmic distribution of N-TAZ whether or not cells were stimulated by EphB2-Fc because N-TAZ-GFP fusion protein lacks C-terminus that can be modified to interact with NHERF1 (Figure 7D1 & 7D4). The same cellular localization of TAZ was observed in the cells transfected with TAZ alone without overexpression of ephrin B1 (Figure 7D2 & 7D5) because C3H10T1/2 cells produce no detectable levels of ephrin B1 protein under the culture conditions used (data not shown). Co-transfection with both intact TAZ and ephrin B1 also resulted in cytoplasmic localization of TAZ without EphB2-Fc stimulation (Figure 7D3). However, EphB2-Fc treatment led to nuclear translocation of TAZ in cells cotransfected with TAZ and ephrin B1 (Figure 7D6). To rule out the possibility that the observed changes in TAZ localization in response to activation of ephrin B1 signaling is an artifact of overexpression of ephrin B1 and TAZ, we also examined endogenous TAZ nuclear translocation induced by ephrin B1 reverse signaling. Primary BMS cells isolated from WT and KO mice were cultured and treated with soluble clustered EphB2-Fc or Fc for 4 hours. The cytoplasmic and nuclear proteins were extracted, and analyzed by Western blot with specific antibodies to mouse TAZ, β-tubulin and histone H3. Consistent with the data above, we found that TAZ was predominantly localized in the cytosolic compartment in the absence of EphB2-Fc stimulation. However, activation of ephrin B1 reverse signaling by EphB2-Fc increased accumulation of TAZ in the nuclei of BMS cells, as measured by Western immunoblotting (Figure 7E). Nuclear level of TAZ was elevated 3-fold of TAZ after 4

hours treatment with clustered EphB2-Fc as compared to Fc control. In contrast, treatment of BMS cells derived from ephrin B1 KO mice with EphB2-Fc failed to induce TAZ nuclear translocation.

Knockdown of TAZ and NHERF1 expression decreases ephrin B1 reverse signaling-mediated osterix expression. To evaluate the role of TAZ in ephrin B1 reverse signaling, we first knocked down TAZ expression by lentivirus expressing shRNA, and examined the osterix expression in response to clustered EphB2-Fc stimulation in BMS cells. We found that TAZ expression was reduced by nearly 80% at the protein level and 78% at the mRNA level in the cells infected with mouse TAZ shRNA compared to the cells transduced with GFP control shRNA (Figures 8A & B). As expected, the mRNA expression of osterix was increased by 8-fold upon activation of ephrin B1 reverse signaling by EphB2-Fc in BMS cells expressing GFP control shRNA. However, EphB2-FC-induced osterix induction was reduced by 75% in the BMS cells expressing TAZ shRNA. Similarly, knockdown of NHERF1 expression significantly reduced basal level of osterix expression by 90% (data not shown), and abolished ephrin B1-mediated induction of osterix expression (Figure 8C).

Discussion

Ephrin B1 has been shown to be expressed in various types of cells and play key roles in the growth and development of multiple tissues (1, 13, 25, 30, 49, 56). Although total loss of ephrin B1 function or reverse signaling in every cell type resulted in perinatal lethality and defects in skeletal patterning in mice, little is known on the role of ephrin B1 produced locally by bone cells (12, 13). In this study, we used transgenic mice expressing an improved Cre recombinase under the control of the type-I collagen promoter to disrupt ephrin B1 in cells of osteoblastic lineage (17, 21), and examined the consequence of conditional disruption of ephrin B1 in bone cells on the skeletal phenotypes *in vivo*. With this targeting strategy, we showed that disruption of ephrin B1 in osteoblasts was almost complete, and calvarial defects in the conditional KO embryos were much more severe than PGK-Cre or Meox2-Cre mediated conditional KO mice reported previously (12, 13). Furthermore, we found that the exencephaly occurred in both mutant hemizygous males and homozygous females compared to a previous study that reported that skull defects were restricted in ephrin B1 heterozygous KO females (8). The heterozygous conditional KO mice with one efnb1 allele in the cells of osteoblastic lineage appeared normal with no obvious bone phenotypes although they were mosaic because of random X chromosome inactivation. We did not observe phenotypes of polydactyly, cleft palate or tooth defects in the ephrin B1 conditional KO or heterozygous mice. We believe that there are two main reasons for the observed differences in the magnitude of skeletal phenotype of our osteoblast-specific ephrin B1 KO versus those reported. First, the promoter used to drive Cre expression was different in the 3 studies which targeted different cell types and/or different stages of embryonic development. In our study, we used collagen1α2 promoter to express Cre recombinase in the conditional KO mice. Cre-mediated recombination could be detected in osteoblasts at the site of intramembranous bone formation at E13.5. Thus, ephrin B1 gene is deleted at later stages of embryonic development in our conditional KO mice, which apparently contributes to reduction in embryonic lethality but severe skull defects, and reduced bone size

and bone density. Second, the differences in genetic background could also in part contribute to the observed differences in the severity of the skeletal phenotype in the 3 studies.

Recent studies have demonstrated that 2.3 rat collagen 1 promoter is active in osteoclasts in a mouse transgenic model (16). In our experiments, we found that expression levels of ephrin B1 in osteoclast precursors of the KO mice were comparable to the WT littermates. In addition, our histomorphometric and serum C-telopeptide analyses demonstrated that bone resorption was not affected in the ephrin B1 osteoblast-specific conditional KO mice. Based on our data, we conclude that the reduced bone size, bone density and trabecular numbers of the conditional KO mice were due to the impaired osteoblast-mediated bone formation, but not increased osteoclast-mediated bone resorption.

All three ephrin B ligands have the same structure of a single transmembrane domain, and a well-conserved cytoplasmic domain that includes 33 amino acids with nearly 100% identity (4, 11). Among ephrin B proteins, B1 and B2 have been shown to be expressed in osteoblasts while ephrin B3 is not expressed in bone cells (12, 57). Because of the C-terminal structural similarity between ephrin B1 and B2, it raises a question as to if there is a functional compensation between these two family members. In our studies, we found that only a trace amount of ephrin B2 protein was expressed as compared to ephrin B1 in BMS cells derived from WT mice. Furthermore, loss of ephrin B1 did not cause up-regulation of ephrin B2 in BMS cells (data not shown). Accordingly, ephrin B1 deficient BMS cells exhibit impaired formation of mineralized nodules *in vitro*. Our *in vitro* data together with *in vivo* data showing severe bone phenotypes in ephrin B1 conditional KO mice strongly support the prediction that the amount of ephrin B2 protein in osteoblasts can not compensate for the loss of ephrin B1 on the skeletal phenotype in the ephrin B1 conditional KO mice.

It should be noted that BMS cells express both ephrin B1 and its cognate EphB2 receptor. Thus, both forward and reverse signals are feasible upon cell to cell contact. In this regard, Zhao et al. suggested that ephrin B2 produced by osteoclasts might interact with EphB4

receptor in osteoblasts to induce forward signaling and osteoblast differentiation based on the findings that exogenous addition of clustered ephrin B2-Fc stimulated ALP activity of calvarial osteoblasts, and over-expression of EphB4 in transgenic mice increased bone formation (57). While these studies provided evidence that EphB4 mediated forward signaling might be involved in osteoblast differentiation, the relative contribution of forward and reverse signaling in mediating ephrin B1 effects on skull development and bone formation needs to be further evaluated *in vivo* by appropriate genetic rescue experiments. In our studies, we used low density cell cultures to minimize reverse signaling via the interaction between endogenously produced EphB2 receptor from one cell with ephrin B1 ligand of neighboring cell. We found that exogenous addition of soluble EphB2-Fc receptor capable of binding to ephrin B1 caused an increase in osterix expression and ALP activity in BMS cells expressing ephrin B1. KO of EphB2 or EphB3 only showed mild phenotypes of digestive or nervous system while KO of both EphB2 and EphB3 receptors capable of activating ephrin B1 reverse signaling resulted in the embryonic lethality (14, 23, 25, 38, 51, 57). These data, supported by previous genetic studies that a single amino acid mutation in the PDZ domain of ephrin B1 in mice has been shown to cause skeletal defects (13), in aggregate indicate that ephrin B1-mediated reverse signaling is critically important in regulating osteoblast differentiation. Besides the activation of ephrin B1 reverse signaling, the role and molecular pathways of EphB2 receptor in bone cells are unknown. In mouse small intestine and colon, EphB2 signaling directs stem cell migration, promotes cell-cycle reentry of progenitor cells and stimulates cell proliferation (25). Whether EphB2 can also modulate mesenchymal stem cell adhesion, migration, proliferation and/or differentiation in bone *in vivo* remains to be established. Therefore, future studies involving generation of conditional knock-in mice in which WT copy of ephrin B1 is replaced by truncated or mutated ephrin B1 incapable of binding PDZ domain proteins and/or WT copy of EphB2 receptor is replaced by intracellular domains-truncated EphB2 that can bind to ephrin B1 but

does not initiate forward signaling are necessary to convincingly demonstrate the relative contribution of ephrin B1 reverse and forward signaling in regulating bone formation.

In terms of the molecular pathway by which ephrin B1-mediated reverse signaling could regulate osteoblasts, investigations from endothelial cells and *Xenopus* oocytes have shown that ephrin B1 interaction with its receptors can induce a rapid co-clustering of ephrin B1 and Src family kinases leading to rapid phosphorylation of the tyrosine sites at the C terminus (6, 39) and subsequent recruitment of PDZ adaptor proteins (9). However, it is currently unknown what downstream signaling molecules bind to the phosphorylated tails of ephrin B1 in bone cells. In our study, we have demonstrated that ephrin B1 interacts with PTPN13 and TAZ via NHEFR1 in BMS cells. The activation of ephrin B1 reverse signaling via exogenous addition of soluble EphB2-Fc receptor resulted in significant increase in TAZ dephosphorylation and nuclear translocation in BMS cells as well as in C3H10T1/2 cells that over-express GFP-TAZ and ephrin B1. We have also shown that disruption of TAZ expression using specific lentivirus shRNA resulted in significant blockade of ephrin B1 reverse signaling mediated increases in osterix in BMS cells. Our data provide, for the first time, experimental proof that TAZ and NHERF1 are important downstream players in ephrin B1 reverse signaling.

While our in vitro studies and published data on the skeletal phenotypes of mice lacking TAZ and NHERF1 are consistent with our proposed model that an interaction between ephrin B1, NHERF1 and TAZ is involved in regulating osteoblast differentiation, it remains to be determined whether additional pathways are involved in mediating ephrin B1 effects on bone. In this regard, recent studies have shown that TAZ can also promote tumor cell migration, cell proliferation, epithelial-mesenchymal transition and E3 ligase-mediated protein degradation (7, 31, 47). Thus, TAZ may have other functions in bone besides regulating expression of genes related to the osteoblast differentiation pathway. In addition, NHERF1 functions to control renal phosphate transport (44). Therefore, the relative contributions of NHERF1 pathway in bone cells via regulating ephrin B1 signaling versus kidney cells via regulation of phosphate transport

to the skeletal phenotype in NHERF1 KO mice remains to be determined. Furthermore, the reduced severity of skeletal phenotype in the NHERF1 or TAZ KO mice as compared to ephrin B1 osteoblast-specific conditional KO mice suggests potential involvement of other signaling pathways besides the TAZ-mediated signaling in mediating ephrin B1 effects on bone formation *in vivo*.

In conclusion, we have demonstrated that targeted deletion of ephrin B1 in osteoblasts results in severe calvarial defects, decreased bone size, BMD and trabecular bone. The impairment of osteoblast differentiation and bone formation in the ephrin B1 conditional KO mice appears to be due to reduced expression of the osterix gene. Activation of ephrin B1 reverse signaling upon interaction with its receptors stimulates TAZ dephosphorylation, nuclear trafficking, transactivation and TAZ target gene transcription. Therefore, our findings provide a novel molecular pathway by which ephrin B1 regulates bone formation.

Acknowledgements:

This work was supported by Assistance Award No. DAMD17-03-2-0021 provided by the U.S. Army Medical Research Acquisition Activity, 820 Chandler Street, Fort Detrick MD 21702-5014 and VA Merit Review Award provided by the Office of Research and Development, Medical Research Service, Department of Veterans Affairs. The information contained in this publication does not necessarily reflect the position or the policy of the Government, and no official endorsement should be inferred. All work was performed at facilities provided by the Jerry L. Pettis Memorial VA Medical Center in Loma Linda, CA. 92357

We would like to thank Catrina M. Alarcon and Anil Kapoor for their technical assistance. We are also grateful to Dr. Philippe Soriano at the Mount Sinai School of Medicine, Dr. Koichi Matsuo at the Keio University, Dr. Cai Bin Cui at the University of North Carolina, Dr. Bert Vogelstein at Howard Hughes Medical Institute at Johns Hopkins, and Drs. Michael B. Yaffe and Mary Q. Stewart at the Massachusetts Institute of Technology for providing reagents.

References

1. **Adams, R. H., G. A. Wilkinson, C. Weiss, F. Diella, N. W. Gale, U. Deutsch, W. Risau, and R. Klein.** 1999. Roles of ephrinB ligands and EphB receptors in cardiovascular development: demarcation of arterial/venous domains, vascular morphogenesis, and sprouting angiogenesis. Genes Dev **13:**295-306.
2. **Beamer, W. G., L. R. Donahue, C. J. Rosen, and D. J. Baylink.** 1996. Genetic variability in adult bone density among inbred strains of mice. Bone **18:**397-403.
3. **Beck, L., A. C. Karaplis, N. Amizuka, A. S. Hewson, H. Ozawa, and H. S. Tenenhouse.** 1998. Targeted inactivation of Npt2 in mice leads to severe renal phosphate wasting, hypercalciuria, and skeletal abnormalities. Proc Natl Acad Sci U S A **95:**5372-7.
4. **Beckmann, M. P., D. P. Cerretti, P. Baum, T. Vanden Bos, L. James, T. Farrah, C. Kozlosky, T. Hollingsworth, H. Shilling, E. Maraskovsky, and et al.** 1994. Molecular characterization of a family of ligands for eph-related tyrosine kinase receptors. Embo J **13:**3757-62.
5. **Bong, Y. S., H. S. Lee, L. Carim-Todd, K. Mood, T. G. Nishanian, L. Tessarollo, and I. O. Daar.** 2007. ephrinB1 signals from the cell surface to the nucleus by recruitment of STAT3. Proc Natl Acad Sci U S A **104:**17305-10.
6. **Bong, Y. S., Y. H. Park, H. S. Lee, K. Mood, A. Ishimura, and I. O. Daar.** 2004. Tyr-298 in ephrinB1 is critical for an interaction with the Grb4 adaptor protein. Biochem J **377:**499-507.
7. **Chan, S. W., C. J. Lim, K. Guo, C. P. Ng, I. Lee, W. Hunziker, Q. Zeng, and W. Hong.** 2008. A role for TAZ in migration, invasion, and tumorigenesis of breast cancer cells. Cancer Res **68:**2592-8.

8. **Compagni, A., M. Logan, R. Klein, and R. H. Adams.** 2003. Control of skeletal patterning by ephrinB1-EphB interactions. Dev Cell **5:**217-30.
9. **Cowan, C. A., and M. Henkemeyer.** 2001. The SH2/SH3 adaptor Grb4 transduces B-ephrin reverse signals. Nature **413:**174-9.
10. **Cui, C. B., L. F. Cooper, X. Yang, G. Karsenty, and I. Aukhil.** 2003. Transcriptional coactivation of bone-specific transcription factor Cbfa1 by TAZ. Mol Cell Biol **23:**1004-13.
11. **Davis, S., N. W. Gale, T. H. Aldrich, P. C. Maisonpierre, V. Lhotak, T. Pawson, M. Goldfarb, and G. D. Yancopoulos.** 1994. Ligands for EPH-related receptor tyrosine kinases that require membrane attachment or clustering for activity. Science **266:**816-9.
12. **Davy, A., J. Aubin, and P. Soriano.** 2004. Ephrin-B1 forward and reverse signaling are required during mouse development. Genes Dev **18:**572-83.
13. **Davy, A., J. O. Bush, and P. Soriano.** 2006. Inhibition of gap junction communication at ectopic Eph/ephrin boundaries underlies craniofrontonasal syndrome. PLoS Biol **4:**e315.
14. **Dottori, M., L. Hartley, M. Galea, G. Paxinos, M. Polizzotto, T. Kilpatrick, P. F. Bartlett, M. Murphy, F. Kontgen, and A. W. Boyd.** 1998. EphA4 (Sek1) receptor tyrosine kinase is required for the development of the corticospinal tract. Proc Natl Acad Sci U S A **95:**13248-53.
15. **Dravis, C., N. Yokoyama, M. J. Chumley, C. A. Cowan, R. E. Silvany, J. Shay, L. A. Baker, and M. Henkemeyer.** 2004. Bidirectional signaling mediated by ephrin-B2 and EphB2 controls urorectal development. Dev Biol **271:**272-90.

16. **Engin, F., Z. Yao, T. Yang, G. Zhou, T. Bertin, M. M. Jiang, Y. Chen, L. Wang, H. Zheng, R. E. Sutton, B. F. Boyce, and B. Lee.** 2008. Dimorphic effects of Notch signaling in bone homeostasis. Nat Med **14:**299-305.

17. **Florin, L., H. Alter, H. J. Grone, A. Szabowski, G. Schutz, and P. Angel.** 2004. Cre recombinase-mediated gene targeting of mesenchymal cells. Genesis **38:**139-44.

18. **Gerety, S. S., H. U. Wang, Z. F. Chen, and D. J. Anderson.** 1999. Symmetrical mutant phenotypes of the receptor EphB4 and its specific transmembrane ligand ephrin-B2 in cardiovascular development. Mol Cell **4:**403-14.

19. **Glaser, D. L., and F. S. Kaplan.** 1997. Osteoporosis. Definition and clinical presentation. Spine **22:**12S-16S.

20. **Govoni, K. E., J. E. Wergedal, R. Chadwick, A. Srivastava, and S. Mohan.** 2008. Pre-pubertal OVX increases IGF-I expression and bone accretion in C57BL/6J mice. Am J Physiol Endocrinol Metab **295:**E1172-80.

21. **Govoni, K. E., J. E. Wergedal, L. Florin, P. Angel, D. J. Baylink, and S. Mohan.** 2007. Conditional deletion of IGF-I in collagen type 1{alpha}2 (Col1{alpha}2) expressing cells results in postnatal lethality and a dramatic reduction in bone accretion. Endocrinology **148:**5706-15.

22. **Gubbay, J., J. Collignon, P. Koopman, B. Capel, A. Economou, A. Munsterberg, N. Vivian, P. Goodfellow, and R. Lovell-Badge.** 1990. A gene mapping to the sex-determining region of the mouse Y chromosome is a member of a novel family of embryonically expressed genes. Nature **346:**245-50.

23. **Henkemeyer, M., D. Orioli, J. T. Henderson, T. M. Saxton, J. Roder, T. Pawson, and R. Klein.** 1996. Nuk controls pathfinding of commissural axons in the mammalian central nervous system. Cell **86:**35-46.

24. **Hirai, A., M. Tada, K. Furuuchi, S. Ishikawa, K. Makiyama, J. Hamada, F. Okada, I. Kobayashi, H. Fukuda, and T. Moriuchi.** 2004. Expression of AIE-75 PDZ-domain protein induces G2/M cell cycle arrest in human colorectal adenocarcinoma SW480 cells. Cancer Lett **211:**209-18.

25. **Holmberg, J., M. Genander, M. M. Halford, C. Anneren, M. Sondell, M. J. Chumley, R. E. Silvany, M. Henkemeyer, and J. Frisen.** 2006. EphB receptors coordinate migration and proliferation in the intestinal stem cell niche. Cell **125:**1151-63.

26. **Hong, J. H., E. S. Hwang, M. T. McManus, A. Amsterdam, Y. Tian, R. Kalmukova, E. Mueller, T. Benjamin, B. M. Spiegelman, P. A. Sharp, N. Hopkins, and M. B. Yaffe.** 2005. TAZ, a transcriptional modulator of mesenchymal stem cell differentiation. Science **309:**1074-8.

27. **Hong, J. H., and M. B. Yaffe.** 2006. TAZ: a beta-catenin-like molecule that regulates mesenchymal stem cell differentiation. Cell Cycle **5:**176-9.

28. **Jensen, P. L.** 2000. Eph receptors and ephrins. Stem Cells **18:**63-4.

29. **Kanai, F., P. A. Marignani, D. Sarbassova, R. Yagi, R. A. Hall, M. Donowitz, A. Hisaminato, T. Fujiwara, Y. Ito, L. C. Cantley, and M. B. Yaffe.** 2000. TAZ: a novel transcriptional co-activator regulated by interactions with 14-3-3 and PDZ domain proteins. Embo J **19:**6778-91.

30. **Lee, H. S., T. G. Nishanian, K. Mood, Y. S. Bong, and I. O. Daar.** 2008. EphrinB1 controls cell-cell junctions through the Par polarity complex. Nat Cell Biol **10:**979-86.

31. **Lei, Q. Y., H. Zhang, B. Zhao, Z. Y. Zha, F. Bai, X. H. Pei, S. Zhao, Y. Xiong, and K. L. Guan.** 2008. TAZ promotes cell proliferation and epithelial-mesenchymal transition and is inhibited by the hippo pathway. Mol Cell Biol **28:**2426-36.

32. **Lin, D., G. D. Gish, Z. Songyang, and T. Pawson.** 1999. The carboxyl terminus of B class ephrins constitutes a PDZ domain binding motif. J Biol Chem **274:**3726-33.

33. **Lu, Q., E. E. Sun, R. S. Klein, and J. G. Flanagan.** 2001. Ephrin-B reverse signaling is mediated by a novel PDZ-RGS protein and selectively inhibits G protein-coupled chemoattraction. Cell **105:**69-79.

34. **Makinen, T., R. H. Adams, J. Bailey, Q. Lu, A. Ziemiecki, K. Alitalo, R. Klein, and G. A. Wilkinson.** 2005. PDZ interaction site in ephrinB2 is required for the remodeling of lymphatic vasculature. Genes Dev **19:**397-410.

35. **Marquardt, T., R. Shirasaki, S. Ghosh, S. E. Andrews, N. Carter, T. Hunter, and S. L. Pfaff.** 2005. Coexpressed EphA receptors and ephrin-A ligands mediate opposing actions on growth cone navigation from distinct membrane domains. Cell **121:**127-39.

36. **McLeod, M. J.** 1980. Differential staining of cartilage and bone in whole mouse fetuses by alcian blue and alizarin red S. Teratology **22:**299-301.

37. **Morita, S., T. Kojima, and T. Kitamura.** 2000. Plat-E: an efficient and stable system for transient packaging of retroviruses. Gene Ther **7:**1063-6.

38. **Orioli, D., M. Henkemeyer, G. Lemke, R. Klein, and T. Pawson.** 1996. Sek4 and Nuk receptors cooperate in guidance of commissural axons and in palate formation. Embo J **15:**6035-49.

39. **Palmer, A., M. Zimmer, K. S. Erdmann, V. Eulenburg, A. Porthin, R. Heumann, U. Deutsch, and R. Klein.** 2002. EphrinB phosphorylation and reverse signaling: regulation by Src kinases and PTP-BL phosphatase. Mol Cell **9:**725-37.

40. **Parfitt, A. M., M. K. Drezner, F. H. Glorieux, J. A. Kanis, H. Malluche, P. J. Meunier, S. M. Ott, and R. R. Recker.** 1987. Bone histomorphometry: standardization of nomenclature, symbols, and units. Report of the ASBMR Histomorphometry Nomenclature Committee. J Bone Miner Res **2:**595-610.

41. **Qin, X., J. E. Wergedal, M. Rehage, K. Tran, J. Newton, P. Lam, D. J. Baylink, and S. Mohan.** 2006. Pregnancy-associated plasma protein-A increases osteoblast proliferation in vitro and bone formation in vivo. Endocrinology **147:**5653-61.

42. **Rubinson, D. A., C. P. Dillon, A. V. Kwiatkowski, C. Sievers, L. Yang, J. Kopinja, D. L. Rooney, M. Zhang, M. M. Ihrig, M. T. McManus, F. B. Gertler, M. L. Scott, and L. Van Parijs.** 2003. A lentivirus-based system to functionally silence genes in primary mammalian cells, stem cells and transgenic mice by RNA interference. Nat Genet **33:**401-6.

43. **Schroeder, T. M., A. K. Nair, R. Staggs, A. F. Lamblin, and J. J. Westendorf.** 2007. Gene profile analysis of osteoblast genes differentially regulated by histone deacetylase inhibitors. BMC Genomics **8:**362.

44. **Shenolikar, S., J. W. Voltz, C. M. Minkoff, J. B. Wade, and E. J. Weinman.** 2002. Targeted disruption of the mouse NHERF-1 gene promotes internalization of proximal tubule sodium-phosphate cotransporter type IIa and renal phosphate wasting. Proc Natl Acad Sci U S A **99:**11470-5.

45. **Songyang, Z., A. S. Fanning, C. Fu, J. Xu, S. M. Marfatia, A. H. Chishti, A. Crompton, A. C. Chan, J. M. Anderson, and L. C. Cantley.** 1997. Recognition of unique carboxyl-terminal motifs by distinct PDZ domains. Science **275:**73-7.

46. **Srivastava, A. K., S. Bhattacharyya, G. Castillo, N. Miyakoshi, S. Mohan, and D. J. Baylink.** 2000. Development and evaluation of C-telopeptide enzyme-linked immunoassay for measurement of bone resorption in mouse serum. Bone **27:**529-33.

47. **Tian, Y., R. Kolb, J. H. Hong, J. Carroll, D. Li, J. You, R. Bronson, M. B. Yaffe, J. Zhou, and T. Benjamin.** 2007. TAZ promotes PC2 degradation through a SCFbeta-Trcp E3 ligase complex. Mol Cell Biol **27:**6383-95.

48. **Torres, R., B. L. Firestein, H. Dong, J. Staudinger, E. N. Olson, R. L. Huganir, D. S. Bredt, N. W. Gale, and G. D. Yancopoulos.** 1998. PDZ proteins bind, cluster, and synaptically colocalize with Eph receptors and their ephrin ligands. Neuron **21:**1453-63.

49. **Twigg, S. R., R. Kan, C. Babbs, E. G. Bochukova, S. P. Robertson, S. A. Wall, G. M. Morriss-Kay, and A. O. Wilkie.** 2004. Mutations of ephrin-B1 (EFNB1), a marker of tissue boundary formation, cause craniofrontonasal syndrome. Proc Natl Acad Sci U S A **101:**8652-7.

50. **Twigg, S. R., K. Matsumoto, A. M. Kidd, A. Goriely, I. B. Taylor, R. B. Fisher, A. J. Hoogeboom, I. M. Mathijssen, M. T. Lourenco, J. E. Morton, E. Sweeney, L. C. Wilson, H. G. Brunner, J. B. Mulliken, S. A. Wall, and A. O. Wilkie.** 2006. The origin of EFNB1 mutations in craniofrontonasal syndrome: frequent somatic mosaicism and explanation of the paucity of carrier males. Am J Hum Genet **78:**999-1010.

51. **Williams, S. E., F. Mann, L. Erskine, T. Sakurai, S. Wei, D. J. Rossi, N. W. Gale, C. E. Holt, C. A. Mason, and M. Henkemeyer.** 2003. Ephrin-B2 and EphB1 mediate retinal axon divergence at the optic chiasm. Neuron **39:**919-35.

52. **Wong, G. L., and D. V. Cohn.** 1975. Target cells in bone for parathormone and calcitonin are different: enrichment for each cell type by sequential digestion of mouse calvaria and selective adhesion to polymeric surfaces. Proc Natl Acad Sci U S A **72:**3167-71.

53. **Xing, W., D. Baylink, C. Kesavan, Y. Hu, S. Kapoor, R. B. Chadwick, and S. Mohan.** 2005. Global gene expression analysis in the bones reveals involvement of several novel genes and pathways in mediating an anabolic response of mechanical loading in mice. J Cell Biochem **96:**1049-60.

54. **Xing, W., D. Baylink, C. Kesavan, and S. Mohan.** 2004. HSV-1 amplicon-mediated transfer of 128-kb BMP-2 genomic locus stimulates osteoblast differentiation in vitro. Biochem Biophys Res Commun **319:**781-6.

55. **Xing, W., A. Singgih, A. Kapoor, C. M. Alarcon, D. J. Baylink, and S. Mohan.** 2007. Nuclear factor-E2-related factor-1 mediates ascorbic acid induction of osterix expression via interaction with antioxidant-responsive element in bone cells. J Biol Chem **282:**22052-61.

56. **Yu, G., H. Luo, Y. Wu, and J. Wu.** 2004. EphrinB1 is essential in T-cell-T-cell co-operation during T-cell activation. J Biol Chem **279:**55531-9.

57. **Zhao, C., N. Irie, Y. Takada, K. Shimoda, T. Miyamoto, T. Nishiwaki, T. Suda, and K. Matsuo.** 2006. Bidirectional ephrinB2-EphB4 signaling controls bone homeostasis. Cell Metab **4:**111-21.

Legends

Figure 1. Ephrin B1 deficiency in osteoblasts caused skull defects and reduced body size. **(A):** Breeding scheme for generation of ephrin B1 (efnb1) conditional KO and WT mice. **(B):** Loss of ephrin B1 expression in osteoblasts from ephrin B1 conditional KO mice measured by Western blot. **(C)** Female embryos at E19.5, arrowhead indicates the exencephaly. **(D)** Alizarin red and alcian blue staining of the skulls of the same embryos as (C), arrowheads indicate skull defects. **(E)** Alizarin red and alcian blue staining of the same embryo skeletons as (C), arrowheads indicate calvarial defects**.** **(F)** Body size of 3 week-old WT and KO mice. **(G)** Body length of WT and KO mice at 3 and 8 weeks of age (N=14).

Figure 2. Ephrin B1 deficiency in osteoblasts caused reduced bone size and peak bone BMD. **(A)** Femurs of WT and KO mice at 8 weeks of age. **(B)** Femur length of WT and KO mice at 8 weeks of age (N=14). **(C)** Percentage of total body BMC, BMD and bone area of KO mice as compared with the gender-matched WT littermates at 3 and 8 weeks of age measured by DEXA (N=14). **(D)** μ-CT images of cross section, periosteal circumference (PC) and endosteal circuemference (EC) of the femurs at mid diaphysis from 8 weeks old female mice. **(E-G)** Cortical bone volume (BV), total tissue volume (TV) and BV/TV of the femurs isolated from 8 weeks old female mice measured by μCT. Asterisks indicate a significant difference in KO mice as compared with WT mice (N=6, $P < 0.05$).

Figure 3. Reduced trabecular bone volume, bone formation rate (BFR) and mineral apposition rate (MAR) in ephrin B1 KO mice. **(A)** Three-dimensional μ-CT images of distal femurs isolated from 8 week old females. **(B)** Two-dimensional μ-CT images of trabecular bone of distal femurs. **(C)** Trabecular numbers (TN) measured by μ-CT at distal femurs of ephrin B1 KO and WT females (N=6)**.** **(D)** Trabecular bone volume/total tissue volume (BV/TV) (N=6). **(F)** Images of calcein double labeling of the femurs from 3-week old WT and KO mice. **(G)** BFR (N=8). **(H)**

MAR (N=8). Asterisks indicate a significant difference in KO mice as compared with WT mice ($P < 0.05$).

Figure 4. Lack of ephrin B1 expression in osteoblastic lineage cells does not affect bone resorption. **(A-B)** TRAP staining for periosteal and endosteal bones examined at the mid diaphysis of femur of 3 week old mice, respectively (N=8). **(C)** Serum levels of C-telopeptide (C-TELO) of 3 week old mice (N=12). **(D)** Expression of ephrinB1 by the Western blot using cell lysates from osteoclast precursors from 3 week old KO and WT mice.

Figure 5. Interaction of ephrin B1 and EphB2 by cell-cell contact mediates osteoblast differentiation**. (A)** Ephrin B1 expression in BMS cells (BMS) measured by Western blot. +C: Positive control of cellular lysate from C3H10T1/2 cells over expressing ephrin B1. **(B)** Trace amount of ephrin B2 expression in BMS cells. +C: positive control of cellular lysate from C3H10T1/2 cells over expressing ephrin B2. **(C)** EphB2 expression in BMS cells. +C: positive control of cellular lysate from C3H10T1/2 cells over expressing EphB2. **(D)** EphB4 was not detectable in BMS cells. +C: positive control of recombinant EphB4 protein (5 and 10 ng). **(E)**: Images of nodule formation from BMS cells of ephrin B1 KO and WT mice, stained by Alizarin red staining. **(F)**: Quantitative mineralization area measured by OsteoMeasure system. **(G)** Activation of ephrin B1 stimulates osteoblast differentiation. BMS cells from WT and ephrin B1 conditional KO mice were stimulated with 2 μg/ml of EphB2-Fc in a differentiation medium for 6 days, followed by ALP staining and ALP activity assay. ALP activity values are Mean ±SD and expressed as % of FC control. Asterisk indicates a significant difference vs FC control (N=6, $P < 0.01$).

Figure 6. Ephrin B1 reverse signaling regulates osterix expression. **(A)** Expressions of ALP, osterix, Runx2, MSX1, ephrin B1 and EphB2 in bones from 3 week old mice, measured by RT

real-time-PCR. Values are means ± S.D from 6 replicates. Asterisks indicate a significant difference in KO mice compared with WT mice ($P < 0.01$). **(B)** Activation of ephrin B1 reverse signaling stimulates osterix expression in BMS cells. BMS cells from WT and KO mice were treated with clustered EphB2-FC or control FC in a differentiation medium. After 72 hours treatment, cellular protein was extracted for Western blotting. **(C)** The intensity of Western blot signals of osterix expression was quantitated by ImageQuant, normalized to the signals of β-actin, and expressed as fold change over the intensity of WT control.

Figure 7. Activation of ephrin B1 recruits PTPN13, NHERF1 and TAZ to the phosphorylated ephrin B1, and stimulates TAZ nuclear translocation. **(A)** Interaction of ephrin B1 with TAZ, NHERF1 and PTPN13 in BMS cells by immunoprecipitated. **(B)** Dynamic protein complex formation of ephrin B1, NHERF1 and PTPN13 in C3H10T1/2 cells over expressing ephrin B1 by immunoprecipitation **(C)** Time-dependent ephrin B phosphorylation and TAZ dephosphorylation in C3H10T1/2 cells over expressing ephrin B1 and TAZ by Western blot. **(D)** Nuclear trafficking of TAZ. C3H10T1/2 cells were cotransfected with pEGFP-N-TAZ and pcDNA-ephrinB1 (1 & 2); pEGFP-TAZ alone (3 & 4); pEGFP-TAZ and pcDNA-ephrinB1 (5 & 6). Twenty-four hours later, cells were treated with clustered control Fc (1, 2 & 3) or EphB2-Fc (4, 5 & 6) for 4 hours, followed by examination under fluorescent microscope. Arrows indicate nuclear localized TAZ. **(E)** Endogenous TAZ nuclear translocation in BMS cells by Western blot. BMS cells from WT and ephrin B1 KO mice were treated with clustered EphB2-Fc for 4 hours.

Figure 8. Knockdown of TAZ and NHERF1 expression decreases ephrin B1 reverse signaling-mediated osterix expression. BMS cells were infected with Lentivirus shRNA, and treated with clustered EphB2 for 3 days. (A) TAZ and NHERF1 expression analyzed by Western blot. (B) TAZ and NHERF1 expression quantified by RT real-time PCR. (C) Osterix expression

quantified by RT real-time PCR. Asterisks indicate a significant difference in KO mice as compared with WT mice (N=3, $P < 0.01$).

Sca-1$^+$ Hematopoietic Cell–based Gene Therapy with a Modified FGF-2 Increased Endosteal/Trabecular Bone Formation in Mice

Susan L Hall[1,2], Kin-Hing William Lau[1–3], Shin-Tai Chen[1–3], Jon E Wergedal[1–3], Apurva Srivastava[1,2], Henry Klamut[1,2], Matilda H-C Sheng[1,2], Daila S Gridley[4], Subburaman Mohan[1–3] and David J Baylink[2,3]

[1]Musculoskeletal Disease Center, Jerry L. Pettis Memorial V.A. Medical Center, Loma Linda, California, USA; [2]Department of Medicine, Loma Linda University, Loma Linda, California, USA; [3]Department of Biochemistry, Loma Linda University, Loma Linda, California, USA; [4]Department of Radiation Medicine, Radiobiology Program, Loma Linda University, Loma Linda, California, USA

This study assessed the feasibility of using an *ex vivo* stem cell antigen-1–positive (Sca-1$^+$) cell–based systemic fibroblast growth factor-2 (FGF-2) gene therapy to promote endosteal bone formation. Sca-1$^+$ cells were used because of their ability to home to, and engraft into, the bone marrow cavity. The human FGF-2 gene was modified to increase protein secretion and stability by adding the bone morphogeneic protein (BMP)-2/4 hybrid signal sequence and by mutating two key cysteines. Retro-orbital injection of Sca-1$^+$ cells transduced with a Moloney leukemia virus (MLV)–based vector expressing the modified FGF-2 gene into sub-lethally irradiated W_{41}/W_{41} recipient mice resulted in long-term engraftment, more than 100-fold elevation in serum FGF-2 level, increased serum bone-formation markers, and massive endosteal bone formation. In recipient mice showing very high serum FGF-2 levels (>2,000 pg/ml), this enhanced endosteal bone formation was so robust that the marrow space was filled with bony tissues and insufficient calcium was available for the mineralization of all the newly formed bone, which led to secondary hyperparathyroidism and osteomalacia. These adverse effects appeared to be dose related. In conclusion, this study provided compelling test-of-principle evidence for the feasibility of using an Sca-1$^+$ cell–based *ex vivo* systemic FGF-2 gene therapy strategy to promote endosteal bone formation.

Received 31 January 2007; accepted 24 May 2007; published online 24 July 2007. doi:10.1038/sj.mt.6300258

INTRODUCTION

Osteoporosis is characterized by fragile bones, resulting primarily from insufficient bone formation to compensate for increases in bone resorption. Although the current therapy modalities for osteoporosis, which include several anti-resorptive agents and one anabolic agent, have each demonstrated clinical efficacy, they may be inadequate for patients with severe bone loss, who are at the highest risk for fracture. These individuals require a therapy that can provide sufficient amounts of new bone in a relatively short time to increase bone strength rapidly and prevent fractures. Present therapies, including the anabolic parathyroid hormone (PTH) therapy, have a relatively slow rate of acquisition of bone, requiring months to years to achieve clinically significant changes.

Basic fibroblast growth factor-2 (FGF-2) shows remarkable promise as an agent that could rapidly enhance bone formation through its stimulatory effects on proliferation[1–3] and survival[4] of osteoprogenitor cells. Systemic administration of recombinant FGF-2 protein increases bone formation in vertebrae and long bones[5–15] and promotes fracture repair.[16] FGF-2 stimulates primarily trabecular bone formation on the endosteum with little effect on periosteal bone formation.[5] It is also able to initiate the growth of new trabeculae[9,11] and increase trabecular mass and interconnectivity.[11,13] Disruption of the *FGF-2* in mice reduced bone formation and bone mass[17] and blunted the anabolic effect of PTH.[18]

The clinical utility of FGF-2 and other anabolic bone growth factors is restricted by issues involving the delivery of the therapeutic protein and non-skeletal side effects. Protein therapy has limited clinical application because large, often supra-physiological, quantities of the protein are required to achieve therapeutic effect. An alternative approach is to deliver the therapeutic protein locally to the endosteal bone surface via gene therapy. We have previously evaluated the feasibility of intramedullary injection of marrow stromal cells transduced with a Moloney leukemia virus (MLV)–based vector expressing a bone morphogenic protein-4 (*BMP-4*) gene to promote endosteal bone formation in a murine *ex vivo* skeletal gene therapy model.[19] Although this study indicated the feasibility of using *ex vivo* gene therapy approaches to stimulate endosteal bone formation, the amount of endosteal bone formed was small, likely because the transplanted *BMP-4* expressing marrow stromal cells did not stay in the bone marrow (BM) space.

Hematopoietic stem cells (HSCs) innately home to the BM cavity[20] and localize at the endosteal surface.[21,22] There is an intimate relationship between HSCs and osteoblastic bone-forming

Correspondence: *K.-H. William Lau, Musculoskeletal Disease Center (151), Jerry L. Pettis Memorial VA Medical Center, 11201 Benton Street, Loma Linda, California 92357, USA. E-mail: William.Lau@med.va.gov*

cells within the HSC niche.[23,24] Gene transfer into HSCs can be effectively mediated with retroviral vectors without affecting their multilineage reconstitution capacity in myeloablated recipient animals.[25] Thus, HSCs could be an alternative cell vehicle to deliver the growth factor protein as a means of improving the maintenance of donor cells at the endosteal bone surface. We recently showed that intravenous injection of a retroviral vector–transduced stem cell antigen-1–positive (Sca-1$^+$)–enriched cell population into sub-lethally irradiated, myelo-suppressed W_{41}/W_{41} recipient mice yielded consistently high levels of long-term engraftment.[26] Thus, this study sought to use this transplantation model to test the feasibility of using an *ex vivo* Sca-1$^+$ cell–based systemic *FGF-2* gene therapy strategy to promote endosteal bone formation.

Because the possibility of using a hematopoietic progenitor cell–based *ex vivo* systemic gene therapy to promote bone formation has never been tested, our primary objective was to demonstrate feasibility rather than to assess clinical efficacy. Thus, to minimize the possibility of insufficient FGF-2 expression for an effect, our experimental design included the use of an expression system that would result in maximal FGF-2 production in the engrafted Sca-1$^+$ cells. *FGF-2* does not have a classical secretion signal sequence and is secreted by a highly inefficient, energy-dependent, non–endoplasmic reticulum/Golgi pathway.[27] Therefore, we used a modified *FGF-2* in an MLV-based vector (pY-BMPFGFC2SC3N) for this study. Previously, we showed that addition of the BMP-2/4 hybrid secretion signal to the 5′ end of the human *FGF-2* and mutations of cysteine-70 to serine (C2S) and cysteine-88 to asparagine (C3N) led to a marked and consistent increase in secretion of functional FGF-2 protein in transduced mammalian cells.[28] Because, in the present study, this modified *FGF-2* vector yielded very high levels of FGF-2 protein in the circulation, we were able to evaluate the anabolic bone-stimulating capability as well as the adverse effects of high FGF-2 expression in recipient mice.

RESULTS

Transduction of murine Sca-1$^+$ cells with MLV-based vectors

The transduction efficiency of murine Sca-1$^+$ cells, assessed by measuring the percentage of green fluorescent protein (GFP)–expressing cells 48 hours after transduction with an MLV vector expressing the *GFP* marker gene (pY-GFP), was consistently greater than 50%. We compared the amount of FGF-2 protein secreted into conditioned medium by Sca-1$^+$ cells 72 hours after transduction with the MLV-based vector expressing the unmodified human *FGF-2* (pY-FGF), the modified *FGF-2* (pY-BMPFGFC2SC3N), or the *GFP* reporter gene (pY-GFP). The average amount of FGF-2 secreted by the pY-GFP Sca-1$^+$ cells was scarcely detectable (~2 ng/10^6 cells/24 hours, the assay detection limit) and that of pY-FGF-transduced cells was very low (~18 ng/10^6 cells/24 hours). The amount secreted by pY-BMPFGFC2SC3N-transduced Sca-1$^+$ cells was more than 320 ng/10^6 cells/24 hours, which was more than 16-fold greater than the amount secreted by the pY-FGF-transduced cells, confirming that the modifications increased FGF-2 protein secretion.

Retro-orbital delivery of MLV-transduced Sca-1$^+$ cells into sub-lethally irradiated W_{41}/W_{41} recipient mice

W_{41}/W_{41} mice are hematopoietic deficient owing to mutations of the W locus encoding the *c-kit* receptor gene.[29] The advantage of this genetically myelo-suppressed recipient mouse model is avoidance of irradiation preconditioning,[30] but the disadvantage is that lower levels of engraftment are achieved compared with preconditioned mice. However, the combination of W_{41}/W_{41} recipient mice and a sub-lethal dose of radiation (5 Gy) produced consistent, high-level, and long-term engraftment with minimal morbidity and mortality.[26] To test the feasibility of using Sca-1$^+$-enriched cells to deliver the modified *FGF-2* gene to the BM cavity, pY-BMPFGFC2SC3N-transduced Sca-1$^+$ cells or pY-GFP-transduced cells were each transplanted intravenously into eight sub-lethally irradiated W_{41}/W_{41} mice. At 10 and 12 weeks after transplantation, the percentage of GFP-expressing cells was determined in the peripheral blood (PB) and BM by fluorescence-activated cell sorting analysis. The percentage of GFP-expressing donor cells in the mononuclear blood cells of recipient mice transplanted with pY-GFP-transduced cells was 35.5 ± 4.3% and 34.1 ± 4.1% at weeks 10 and 12, respectively. As expected, the percentage of GFP$^+$ cells in the BM of the pY-GFP recipient mice at week 12 was one-third to one-half lower than that in PB (11.6 ± 2.4%). Thus, as reported previously,[31] MLV transduction of Sca-1$^+$ cells does not limit engraftment. Mice receiving the modified *FGF-2* vector–transduced Sca-1$^+$ cells showed only background levels of green fluorescence in PB cells (0.40 ± 0.24% at week 10 and 0.32 ± 0.15% at week 12) and BM cells (0.44 ± 0.11% at week 12). The serum FGF-2 level in each mouse was measured to confirm engraftment and FGF-2 expression (**Table 1**). The mean serum FGF-2 level in the pY-GFP-transplanted control mice was 35.6 pg/ml, which was not different from the level in untreated mice (data not shown). The average serum FGF-2 level in mice that received pY-BMPFGFC2SC3N-transduced Sca-1$^+$ cells was approximately 100-fold higher than that in the pY-GFP control group, but the serum level of individual recipients was highly variable (ranging from 77 to 6,400 pg/ml) with a within-group coefficient of variation of 0.98. Despite this large within-group variation, the increase in serum FGF-2 level was highly significant ($P < 0.02$).

To exclude FGF-2-related variable engraftment as the cause of the large variation in *FGF-2* transgene expression, we transplanted mice using donor cells from TgN *β*-actin–enhanced *GFP* (TgN-GFP) mice, which constitutively express the enhanced *GFP* marker gene via the chicken *β-actin* promoter. Recipient W_{41}/W_{41} mice were transplanted with pY-BMPFGFC2SC3N-transduced ($N = 14$) or *β*-galactosidase (*β-gal*) gene–transduced (control, $N = 12$) Sca-1$^+$ cells from the TgN-GFP donor mice. Mice were killed at 2, 4, and 6 weeks after transplantation, and serum FGF-2 levels and chimerism (percentage of GFP-positive cells) in the BM and PB were evaluated. As in previous experiments, serum FGF-2 levels in the *FGF-2*-transplanted group were highly variable (ranging from 65 to 5,621 pg/ml). This wide variation did not appear to be related to effects of FGF-2 on engraftment levels, as there were no significant differences in chimerism level in either the PB cells or BM cells between the two groups (**Figure 1**).

Table 1 Serum fibroblast growth factor-2 (FGF-2), alkaline phosphatase (ALP), osteocalcin, and tibial ALP levels in recipient mice 10 or 12 weeks after transplantation with stem cell antigen-1–positive (Sca-1$^+$) cells transduced with the green fluorescent protein (GFP) vector (pY-GFP) or the modified FGF-2 vector (pY-BMPFGFC2SC3N)[a]

Treatment group	Serum FGF-2[b] (pg/ml)	Serum ALP (mU/ml)	Serum osteocalcin (ng/ml)	Tibial ALP (mU/mg extract protein)
GFP group (pY-GFP) (n = 8)	35.6 ± 2.1 (28–43)	177.8 ± 8.6 (145–212)	8.05 ± 0.18 (4.2–12.8)	0.433 ± 0.129 (0.006–0.307)
FGF-2 group (pY-BMPFGFC2SC3N) (n = 7)	2,503 ± 929.4* (77–6,400)	272 ± 37.3* (166–389)	9.91 ± 2.67 (3.5–24.8)	3.521 ± 0.846* (0.451–13.128)

[a]Three of the eight pY-BMPFGFC2SC3N-transplanted recipient mice were noticeably ill and were killed at week 10. The remainder of the mice were killed at week 12.
[b]Most of the pY-BMPFGFC2SC3N-transplanted recipient mice had serum FGF-2 levels higher than the upper limit of the enzyme-linked immunosorbent assay (>640 pg/ml). The reported values for these mice were extrapolated from the standard curve.
*P < 0.05, two-tailed Student's t-test, unequal variances.
Figures are mean ± SEM range.

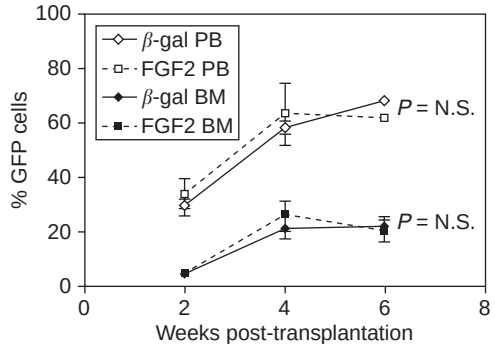

Figure 1 Effect of fibroblast growth factor-2 (FGF-2) transgene expression on early engraftment efficiency. Donor stem cell antigen-1–positive (Sca-1$^+$) cells harvested from green fluorescent protein (GFP)–expressing TgN-GFP transgenic mice were transduced with pY-BMPFGFC2SC3N vector (FGF-2 group) or pY-β-galactosidase (β-gal group) and transplanted into W_{41}/W_{41} recipient mice. Engraftment in peripheral blood (PB) cells or in bone marrow (BM) cells was determined by measuring the percentage of GFP-expressing cells 2, 4, or 6 weeks after transplantation. N.S. = no significant difference. Mean ± SEM.

To evaluate the time course of *FGF-2* transgene expression, the pY-BMPFGFC2SC3N- and pY-GFP-transduced Sca-1$^+$ cells were each transplanted into eight recipient mice, and serum FGF-2 levels at 8, 10, 12, and 14 weeks after transplantation were measured (**Figure 2a**). With the exception of the 14-week time point, the serum FGF-2 level of the FGF-2 group was significantly higher than that of the GFP controls. At 14 weeks, there was an apparent decline in serum FGF-2 level, which may represent transcriptional gene silencing, commonly observed in gene transfer mediated by MLV vectors.[32]

Transplantation of modified *FGF-2*-expressing Sca-1$^+$ cells induced endosteal bone formation

Table 1 also shows that mice that received the pY-BMPFGFC-2SC3N-transduced Sca-1$^+$ cells showed increases in biochemical bone-formation markers at 10–12 weeks after transplantation. Serum alkaline phosphatase (ALP) activity was significantly (P < 0.05) increased in the FGF-2 group compared with controls. The serum osteocalcin level in the FGF-2 group was also higher than in the GFP group, albeit this increase did not reach a statistically significant level, presumably owing to the large within-group variation and small group size. The FGF-2 group had an eightfold increase (P < 0.02) in tibial ALP activity (normalized to protein content) compared with the GFP group. The serum FGF-2 level of the FGF-2 group correlated positively (r = 0.74, P < 0.002) with the tibial ALP activity (**Figure 2b**), suggesting that increases in FGF-2 expression results in increased bone formation.

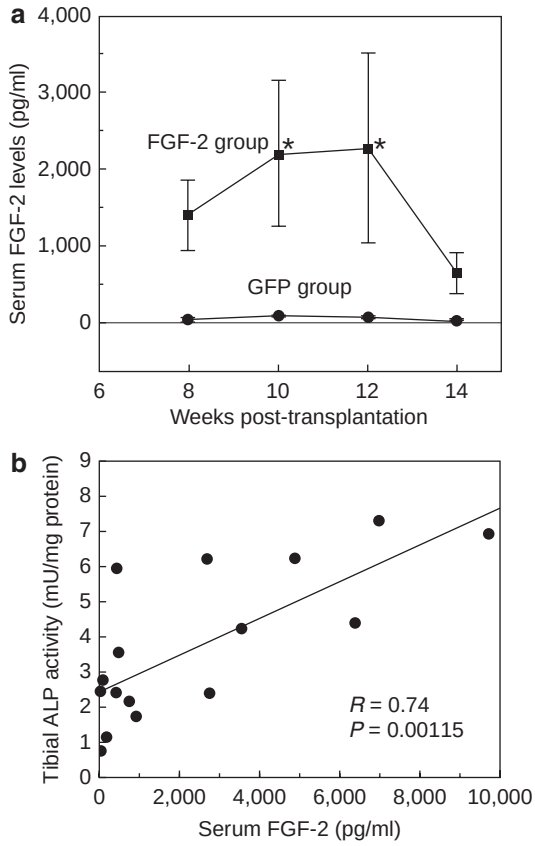

Figure 2 Serum fibroblast growth factor-2 (FGF-2) levels over time in recipient mice and scatter plot between recipient serum FGF-2 levels and tibial extract alkaline phosphatase (ALP) activity. (**a**) Serum FGF-2 levels at 8, 10, 12, and 14 weeks after transplantation, as measured by enzyme-linked immunosorbent assay. Mean ± SEM (n = 8 each). The FGF-2 group represents mice transplanted with pY-BMPFGFC2SC3N-transduced stem cell antigen-1–positive (Sca-1$^+$) cells, and the green fluorescent protein (GFP) group represents mice transplanted with pY-GFP-transduced cells. *P < 0.05 compared with the GFP group. (**b**) Correlation between serum FGF-2 levels and tibial extract ALP activity (normalized to bone protein content) in recipient mice transplanted with Sca-1$^+$ cells transduced with the modified *FGF-2* vector (pY-BMPFGFC2SC3N) at 10 or 12 weeks after transplantation.

Table 2 shows the peripheral quantitative computed tomography (pQCT) bone mineral density (BMD) and bone mass parameters of recipient mice. At 10–14 weeks after transplantation, there was a significant increase in total volumetric BMD (vBMD) (14%) and trabecular vBMD (250%), but not cortical vBMD, in the FGF-2 group compared with the GFP group. The small (4%) decrease in endosteal circumference in the FGF-2 group compared with controls is consistent with an increase in endosteal bone formation. The FGF-2 group also showed a significant decrease (13%) in cortical thickness and a smaller (8%) periosteal circumference, suggesting that although transplantation of the modified *FGF-2*-expressing cells caused an increase in endosteal trabecular bone formation, it might also have caused bone loss at cortical and/or periosteal sites. Linear regression analysis between the serum FGF-2 level and pQCT parameters revealed positive correlations between serum FGF-2 and total vBMD ($r = 0.37$, $P < 0.05$) and trabecular vBMD ($r = 0.54$, $P < 0.002$). Conversely, serum FGF-2 correlated inversely with cortical thickness ($r = -0.51$, $P < 0.005$), periosteal circumference ($r = -0.62$, $P < 0.0004$), and endosteal circumference ($r = -0.47$, $P < 0.01$), suggesting that the changes in these parameters were related to serum FGF-2 level.

Table 2 Effects of transplantation of stem cell antigen-1–positive (Sca-1$^+$) cells transduced with the green fluorescent protein (GFP) vector (pY-GFP) or the modified fibroblast growth factor-2 (FGF-2) vector (pY-BMPFGFC2SC3N) on the cross-sectional and volumetric bone parameters of the femurs of recipient mice at week 14 after transplantation

Bone parameters	GFP (pY-GFP) group	FGF-2 (pY-BMPFGFC2SC3N) group
Total vBMD (mg/cm^3)	741.0 ± 11.7	847.0 ± 68.9*
Trabecular vBMD (mg/cm^3)	229.0 ± 11.7	573.0 ± 113.1**
Cortical vBMD (mg/cm^3)	1,099.0 ± 18.4	1,115.0 ± 49.9
Endosteal circumference (mm)	3.36 ± 0.08	3.22 ± 0.09
Cortical thickness (mm)	0.292 ± 0.007	0.254 ± 0.021*
Periosteal circumference (mm)	5.20 ± 0.09	4.80 ± 0.17***

Abbreviations: vBMD, volumetric bone mineral density.
*$P < 0.05$, **$P < 0.001$, ***$P < 0.01$, and two-tailed Student's *t*-test, unequal variances.
Figures are mean ± SEM; $n = 15$ per group, for a total of 30 mice.

Table 3 Effects of transplantation of stem cell antigen-1–positive (Sca-1$^+$) cells transduced with the green fluorescent protein (GFP) vector (pY-GFP) or the modified fibroblast growth factor-2 (FGF-2) vector (pY-BMPFGFC2SC3N) on the weight of major internal organs of recipient mice at 14 weeks after transplantation

Internal organ	GFP (pY-GFP) group Mean weight (g) ($n = 7$)	FGF-2 (pY-BMPFGFC2SC3N) group Mean weight (g) ($n = 8$)
Heart	0.138 ± 0.008	0.133 ± 0.011
Kidneys (average)	0.165 ± 0.005	0.169 ± 0.006
Spleen	0.082 ± 0.007	0.370 ± 0.057**
Liver	1.203 ± 0.112	1.495 ± 0.053*
Lung	0.367 ± 0.021	0.364 ± 0.040
Intestine/stomach	2.996 ± 0.104	3.221 ± 0.212

*$P < 0.05$ and **$P < 0.0001$ compared to the pY-GFP group, two-tailed Student's *t*-test, equal variance.
Figures are mean ± SEM.

Effects of *FGF-2*-expressing Sca-1$^+$ cell transplantation on major organs of recipient mice

The weight of major organs at the time the mice were killed (week 14) was measured to evaluate whether the high serum FGF-2 level would adversely affect the general health of the mice (Table 3). There was no significant difference in the weight of the hearts, kidneys, lungs, and intestines/stomachs of mice between the FGF-2 group and the control group. However, the weights of the spleens and livers were significantly increased, indicating organ enlargement. The increase in liver weight was modest (24%), but spleen weight increased 4.5-fold in the FGF-2 group. Gross examination of other vital organs did not reveal obvious abnormalities.

Histological analysis of paraffin-embedded organs (heart, lungs, liver, spleen, and kidneys) was also performed. No obvious differences in the microscopic structures of the hearts, lungs, and livers were observed between FGF-2-transplanted and control mice. A close examination of the spleens of FGF-2 recipient mice, however, did show an increase in diffuse lymphatic tissue compared with spleens of control mice (data not shown).

Effects of transplantation of *FGF-2*-expressing Sca-1$^+$ cells on bone histomorphometry

Gross examination during dissection of the long bones of recipient mice with very high serum FGF-2 levels (>4,000 pg/ml) revealed an unusual gross appearance (Figure 3a). Instead of the characteristic maroon color of long bones (representing red marrow), the femurs of mice with high serum FGF-2 levels were white, suggesting a loss of BM within the marrow cavity. The lack of BM may explain why mice transplanted with the modified FGF-2-expressing Sca-1$^+$ cells showed enlarged spleens and livers. Since the spleen and liver are extramedullary sites for hematopoiesis, we presume the organ enlargement was due to extramedullary hematopoiesis as a result of reduced marrow space.

To examine changes in the marrow cavity further, one femur of each mouse was demineralized and embedded in paraffin, and serial longitudinal sections were stained for collagen with Mallory's stain. Three histological profiles emerged that correlated with serum FGF-2 levels. Photomicrographs of sections of the diaphyseal portions of femurs from three representative mice with low (left panel), intermediate (middle panel), and high (right panel) serum FGF-2 levels are shown in Figure 3b. In sections from mice with high serum FGF-2 levels of more than 1,000 pg/ml ($n = 6$), most of the marrow cavity was filled with collagen-positive (dark blue) osteoid-like material. Increases (but to a lesser degree) in the amount of collagen-positive matrix were observed in sections from recipient mice with intermediate serum FGF-2 levels (>100 pg/ml and <1,000 pg/ml) compared with sections from control mice with low serum FGF-2 levels (<100 pg/ml). The strong blue staining for type I collagen fibers confirmed that the tissues observed within the marrow cavity

were bony tissues. The pattern observed in hematoxylin-and-eosin-stained sections of the femurs were consistent with a classical lamellar pattern (data not shown), suggesting the formation of apparently normal lamellar bone.

Quantitative static bone histomorphometry measurements were performed on the distal femoral diaphyses of 10 randomly selected recipient mice (**Table 4**). The percentage cancellous bone area, trabecular thickness, and number were significantly increased (53-fold, 2-fold, and 18-fold, respectively), indicating a massive effect on trabecular bone formation. Additional support of this conclusion was an approximately 73-fold decrease in the trabecular separation. The large variation observed in trabecular separation in the GFP-transplanted mice was due to the paucity of trabeculae in this region in normal murine bone.

To examine mineralization patterns of the endosteal bone surface in the recipient mice, the contralateral, non-demineralized femur of each mouse was embedded in methylmethacrylate, and longitudinal serial sections were stained with Goldner's trichrome. Normal mineralization patterns were observed in the femurs of mice expressing *FGF-2* at levels similar to the levels in control mice (data not shown) and in the femurs of mice with intermediate levels of *FGF-2* expression. For example, in a representative photomicrograph of femur marrow cavity of a mouse transplanted with *FGF-2*-expressing cells that had an intermediate serum level of *FGF-2* (191 pg/ml, left panel of **Figure 3c**), a modest layer of newly laid unmineralized osteoid matrix (red-stained tissue) can be observed on the endosteal surface of the mineralized trabecular spicule (blue/green-stained tissue). In contrast, large areas of unmineralized bone were observed on the endosteal surface of femurs of mice with excessive levels of FGF-2, as shown in the photomicrograph of a representative mouse with high serum FGF-2 (6,400 pg/ml, right panel of **Figure 3c**). This pattern of incomplete bone mineralization is characteristic of conditions of rapid bone formation that result in calcium deficiency and osteomalacia, suggesting that the bone formation in these mice was so robust that normal serum calcium levels were insufficient to mineralize the newly formed bone.

Secondary hyperparathyroidism in mice with high serum FGF-2 and excessive endosteal bone formation

Mice with high serum FGF-2 and excessive endosteal bone formation developed secondary hyperparathyroidism. Secondary hyperparathyroidism is a well-known consequence of calcium insufficiency. Thus, we measured serum PTH levels, as a surrogate index of calcium insufficiency, in each of the 30 recipient mice (15 GFP-treated and 15 FGF-2-treated mice) from the pooled experiments included in the pQCT data analysis (**Table 2**). Twelve of the GFP-treated control mice and two mice from the FGF-2 group had serum PTH levels below the sensitivity of the enzyme-linked immunosorbent assay (<3 pg/ml) and serum FGF-2 levels below 114 pg/ml, and thus these mice were excluded from the analysis. Linear regression performed on the remaining 16 serum

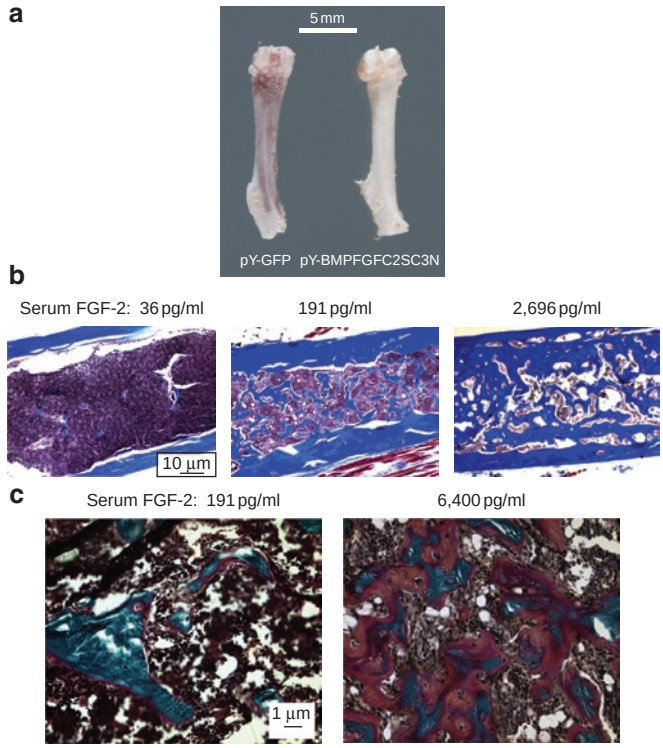

Figure 3 Gross and histological analysis of representative femurs of recipient mice. (**a**) Gross anatomy of femurs from representative mice transplanted with green fluorescent protein (GFP)–transduced stem cell antigen-1–positive (Sca-1$^+$) cells (left) or modified fibroblast growth factor-2 (*FGF-2*)–transduced Sca-1$^+$ cells and showing high (>4,000 pg/ml) serum FGF-2 level (right) at 10 weeks after transplantation. (**b**) Histological sections stained with Mallory's dye for collagen of demineralized femurs from three representative recipient mice expressing different levels of serum FGF-2. Blue-stained material represents tissue positive for type I collagen. Left panel: control (serum FGF-2 = 36 pg/ml); middle panel: a recipient mouse expressing intermediate serum FGF-2 levels (191 pg/ml); right panel: a recipient mouse expressing high serum FGF-2 levels (2,696 pg/ml). (**c**) Histological sections of non-demineralized femurs stained with Goldner's trichrome. Bluish-green material represents mineralized bony tissue and red material represents newly laid, unmineralized osteoid. Left panel: a recipient mouse expressing intermediate serum FGF-2 levels (191 pg/ml); right panel: a recipient mouse expressing high serum FGF-2 levels (6,400 pg/ml).

Table 4 Bone histomorphometric analysis of distal femoral diaphyses of recipient mice transplanted with stem cell antigen-1–positive (Sca-1$^+$) cells transduced with the green fluorescent protein (GFP) vector (pY-GFP) or the modified fibroblast growth factor-2 (FGF-2) vector (pY-BMPFGFC2SC3N) at weeks 10–12 after transplantation

Treatment group	Cancellous bone area (%)[a]	Tb.Th (μm)	Tb.N (#/mm)	Tb.Sp (μm)
pY-GFP group	0.40 ± 0.22	14.9 ± 1.51	0.40 ± 0.25	9,237 ± 3,269
pY-BMPFGFC2SC3N group	21.4 ± 3.90*	30.4 ± 3.31*	7.10 ± 1.06**	127.0 ± 30.1***

Abbreviations: Tb.Th, trabecular thickness; Tb.N, trabecular number; Tb.Sp, trabecular separation.
[a]Cancellous bone area was measured as cancellous bone area as a percentage tissue area.
*P < 0.005, **P < 0.001, ***P < 0.05, two-tailed Student's t-test, unequal variances.
Figures are mean ± SEM; n = 5 per group, for a total of 10 mice.

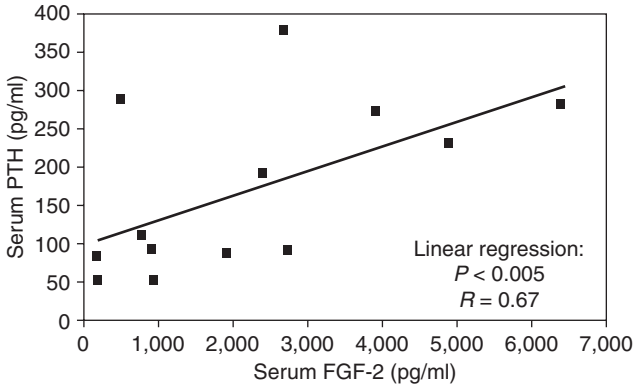

Figure 4 Scatter plot between recipient serum fibroblast growth factor-2 (FGF-2) levels and serum parathyroid hormone (PTH) levels. Correlation between serum FGF-2 levels and serum PTH levels in mice transplanted with stem cell antigen-1–positive (Sca-1$^+$) cells transduced with either green fluorescent protein–transduced Sca-1$^+$ cells or modified FGF-2-transduced Sca-1$^+$ cells at 14 weeks after transplantation.

samples showed that serum PTH was correlated positively and strongly with serum FGF-2 (**Figure 4**). In addition, total serum calcium of a subset of recipient mice was measured. Serum calcium levels in the FGF-2 group ($N = 6$) were significantly lower than those in the GFP controls ($N = 8$) (9.8 ± 0.75 versus 10.7 ± 0.6, respectively, $P < 0.04$). These data suggest that, in addition to the robust *de novo* endosteal bone formation, high *FGF-2* expression causes hypocalcemia, hyperparathyroidism, and osteomalacia.

DISCUSSION

In this article, we show that intravenous transplantation of Sca-1$^+$ cells transduced with an MLV-based vector expressing a modified *FGF-2* gene into sub-lethally irradiated W_{41}/W_{41} recipient mice led to long-term engraftment of *FGF-2*-expressing cells in the BM cavity. Thus, the use of Sca-1$^+$ cells as vehicle cells overcame an important limitation of previous strategies—the inability of transduced vehicle cells to stay in the marrow cavity[19]—and represents a significant breakthrough in terms of the development of an *ex vivo* systemic gene therapy for osteoporosis. More important, this study demonstrates that intravenous transplantation of Sca-1$^+$ cells expressing a bone growth factor gene (the modified *FGF-2* gene) produced large increases in trabecular BMD and *de novo* bone formation at endosteal surfaces. These findings not only are consistent with the previous suggestion that FGF-2 preferentially stimulates trabecular bone formation on the endosteum[5–11] but also clearly demonstrate the feasibility of using our *ex vivo* progenitor cell–based gene therapy strategy to promote endosteal/trabecular bone formation. This HSC-based strategy is very attractive because it is minimally invasive and is applicable for generalized osteoporosis, as it would enhance trabecular bone formation at the endosteum throughout the skeleton.

Among the most exciting findings of this study is that intravenous injection of the *FGF-2*-transduced Sca-1$^+$ cells that resulted in high serum FGF-2 levels not only promoted endosteal/trabecular bone formation but in fact led to massive *de novo* bone formation that almost completely filled up the marrow cavity. This indicates that our Sca-1$^+$ cell–based gene therapy strategy has a very high bone-formation capacity. To our knowledge, the magnitude of osteogenic response demonstrated with our model is quite novel. This is important, as current cell, gene, or protein therapies to increase endosteal bone formation have relatively low bone-formation capacity. Therefore, the high capacity of our gene therapy could overcome an important deficiency in the field of osteoporosis treatment: the inability to produce sufficient amounts of bone within a realistic timeframe.

The mechanism for the surprisingly high bone-formation capacity with our *ex vivo FGF-2* gene therapy is not clear. In this regard, *FGF-2* has been shown to promote osteoprogenitor cell proliferation,[1–3] survival,[4] and maintenance of osteogenic potential.[1,3] Thus, one mechanism that may in part be responsible could be the ability of FGF-2 to augment the osteoprogenitor cell pool, which could then increase the number of bone-forming cells. In addition, FGF-2 is a potent stimulator of angiogenesis,[33,34] a process essential for bone formation. Therefore, it is possible that the unique combined ability of FGF-2 to increase the osteoprogenitor cell pool and enhance angiogenesis may be responsible for the effect of this gene therapy. The *FGF-2* gene used in this study was modified to increase its secretion and stability. Although the modified FGF-2 protein could be glycosylated as two of its four cysteines were mutated to glycosylatable amino acids (serine and asparagine), we have shown that these modifications did not significantly alter the ability of the FGF-2 molecule to bind heparin, to stimulate fibroblast proliferation, or to activate the Erk1/2 signaling pathway.[28] Thus, we tentatively conclude that the high bone-formation capacity of this therapy is unrelated to the modification of the gene. Additional work is needed to determine the mechanism for the surprisingly large bone-formation capacity of our systemic *ex vivo* Sca-1$^+$ cell-based *FGF-2* gene therapy strategy.

Previous studies,[5–15] particularly those of Wronski *et al.* and Mayahara *et al.*, have shown that direct administration of recombinant FGF-2 protein yielded significant increases in endosteal/trabecular bone formation. However, direct comparison of the efficacy of the FGF-2 protein therapy approach and that of our Sca-1$^+$ cell–based *FGF-2* gene therapy strategy is difficult owing to differences in animal models, experimental design, and treatment duration. Nevertheless, the endosteal/trabecular bone formation produced by our systemic gene therapy was significantly greater than that achieved by protein therapy. Specifically, we observed a 52-fold increase in the percentage of cancellous bone area, whereas a 4.5-fold increase was reported by Nagai *et al.*[8] in mice intravenously injected with 0.1 mg/kg/day of FGF-2 protein. Similarly, the increases in trabecular bone parameters in rats treated for 60 days with FGF-2 protein[13] were smaller than that those observed in our study. The circulating levels of FGF-2 in previous protein therapy studies were not reported. However, by extrapolation from the reported amounts of FGF-2 protein administered, the average blood volumes in rodents, and the assumption that the FGF-2 protein is systemically distributed without rapid clearance, the circulating levels of FGF-2 in the protein therapy studies were estimated to be at least 100- to 1,000-fold higher than the serum FGF-2 levels of our FGF-2-treated mice. Although the duration of previous protein therapy was shorter than the duration of this study, the difference

in treatment duration cannot account for the large difference in bone formation between the protein therapy and our *ex vivo* systemic gene therapy. This raises the interesting possibility that the Sca-1$^+$ cell–based systemic gene therapy is more effective than protein therapy in delivering the therapeutic protein (FGF-2) to the endosteal surface and thus more effective in terms of stimulating endosteal/trabecular bone formation.

Although our strategy represents an exciting innovation, numerous additional studies and modifications will be required before human application is attempted. For example, of high priority is the use of mechanical testing to establish whether this therapy strengthens the skeleton. The robust bone formation induced by the FGF-2 gene therapy might actually weaken the overall bone structure, leading to reduction of bone strength. However, before this can be assessed appropriately, it is necessary to eliminate the observed hypocalcemia, secondary hyperparathyroidism, and osteomalacia, which presumably develop in response to the large and rapid increase in bone formation. In our study, mice with serum FGF-2 levels greater than 200 pg/ml developed hyperparathyroidism, and mice with serum FGF-2 levels greater than 1,000 pg/ml had hyperparathyroidism and osteomalacia. A consequence to secondary hyperparathyroidism is an increase in cortical bone resorption. The inverse correlation between cortical thickness, periosteal circumference in femurs, and serum FGF-2 levels was consistent with an increase in resorption at cortical bone, particularly at the periosteum. In terms of bone strength, a loss of cortical bone mass or structure could negate any benefit gained from an increase in trabecular bone formation. There is a precedent whereby large, rapid increases in bone formation, as seen in fluoride-treated patients, result in secondary hyperparathyroidism and osteomalacia[35,36] and whereby the secondary hyperparathyroidism in fluoride-treated patients also led to increased bone resorption and significant bone loss at peripheral cortical sites.[36,37] The correlation between serum FGF-2 levels and both the degree of bone mineralization and serum PTH levels observed in this study are consistent with this speculation. An additional concern regarding the enormous *de novo* bone formation in the marrow cavity was a drastic loss of marrow space in mice with high serum FGF-2 levels. Extramedullary hematopoiesis within the spleen and, to a lesser extent, the liver apparently increased to compensate for the decreased medullary hematopoiesis, as evidenced by organ enlargement. These serious adverse events were seen primarily in recipient mice with the highest serum levels of FGF-2, suggesting that they may be dose related. We believe that these effects could be reduced or avoided by lowering the therapeutic dose, which could be achieved by lowering the number of FGF-2-expressing cells transplanted, lowering the transduction level of the donor cells by reducing viral titers, and/or controlling transgene expression with a regulatable promoter. We should emphasize that the experimental intent of this study was to address the feasibility of using an HSC-based *ex vivo* gene therapy to promote endosteal/trabecular bone formation by maximizing *FGF-2* transgene expression. The fact that this approach resulted in robust bone formation clearly demonstrates feasibility but also emphatically underscores the potent capacity of this therapy to increase endosteal/trabecular bone formation.

Another important safety concern to be addressed before clinical application of our approach is the potential for attendant malignant transformation that may occur with regenerative therapies involving a high level of cell proliferation. Indeed, osteosarcoma occurred in rats treated with high doses of PTH(1–34) for relatively long periods; however, this complication has not been observed in humans treated at therapeutic doses with this agent. Nevertheless, the short- and long-term effects of elevated serum FGF-2 on skeletal and non-skeletal tissues will need to be determined before clinical use.

Finally, two additional issues limit the therapeutic potential of our strategy: (i) the wide variation in transgene expression (2- to 200-fold of normal serum FGF-2) and (ii) the requirement for cytotoxic preconditioning before marrow transplantation. The magnitude of variation we observed is similar to that reported by others using retroviral vectors for the transduction of hematopoietic progenitor cells.[38,39] Although the precise mechanisms contributing to this variation are poorly understood, it may be the result of a combination of various factors, including, but not limited to, gene integration events, clonal selection, and engraftment kinetics. In addition, morbidity and mortality risks associated with contemporary preconditioning regimens cast doubt on the therapeutic utility of our strategy. These issues must be satisfactorily resolved. However, in light of the current enthusiasm for stem cell and molecular therapies, we anticipate that relevant technological advances will occur in methods to minimize variation in transgene expression and in transplantation protocols involving minimal preconditioning. Considering the enormous osteogenic skeletal response observed with our strategy, such follow-up studies seem well justified.

In summary, we have clearly demonstrated the feasibility of using our systemic *ex vivo* gene transfer system to deliver a bone growth factor gene (the modified *FGF-2*) to promote massive endosteal/trabecular bone formation in mice. Our system is the only gene transfer approach reported thus far that can produce substantial endosteal/trabecular bone formation within a relatively short treatment time. Although serious side effects occurred with this therapeutic strategy, these side effects appeared to be dose related. Much work is required to optimize the logistics and safety profile of this therapy, but these results provide compelling test-of-principle evidence that Sca-1$^+$ cells are an effective target cell population and that FGF-2 is an effective bone growth factor gene for use in an *ex vivo* systemic gene therapy strategy to promote endosteal/trabecular bone formation.

MATERIALS AND METHODS

Animals. Wild-type C57BL/6J and TgN β-actin-enhanced GFP (TgN-GFP) transgenic mice were purchased from The Jackson Laboratories (Bar Harbor, ME). The C57BL/6J-W_{41}/W_{41} strain (W_{41}/W_{41}) was graciously provided by Dr. Jane Barker of the St. Louis University School of Medicine (St. Louis, MO). All animals were housed and maintained within the Veterinary Medical Unit of the Jerry Pettis VA Medical Center. All procedures were performed under humane conditions and approved by two Institutional Animal Care and Use Committees (Jerry Pettis VA Medical Center and Loma Linda University).

BM Sca-1$^+$ cell population isolation. Full details of cell harvest and isolation methods are described elsewhere.[26] In brief, whole BM cells were

harvested from C57BL/6J or TgN-GFP mice by flushing tibiae and femurs with phosphate-buffered saline plus 0.5% bovine serum albumin (Sigma-Aldrich, St. Louis, MO) using a needle and syringe. Erythrocytes were removed by osmotic lysis and the remaining mononuclear cell preparation was enriched for Sca-1^+ cells using immunomagnetic sorting.

MLV-based modified human FGF-2 expression vector construction. The construction of the MLV-based vectors expressing the enhanced *GFP* marker (pY-GFP) and modified human *FGF-2* gene (pY-BMPFGFC2S/C3N) has been described in detail elsewhere.[26,28]

Transduction of Sca-1^+ cells with MLV-based vectors. Sca-1^+ cells were plated in 6-well plates (Becton Dickinson, Franklin Lakes, NJ) coated with retronectin (Takara, Otsu, Shiga, Japan) at a density of 4×10^6 cells/well in Iscove's modified Dulbecco's medium (Invitrogen, Grand Island, NY) containing 20% fetal bovine serum (BioWhitaker, Walkersville, MD), 50 ng/ml of human flt-3L, 50 ng/ml of murine stem cell factor, 50 ng/ml of interleukin-6, 10 ng/ml of murine interleukin-3, 0.1 ng/ml murine interleukin-1α (all from Peprotech, Rocky Hills, NJ), 100 µmol/l of deoxyribonucleotide triphosphate (Roche Diagnostics, Indianapolis, ID), as described previously.[26] After overnight incubation, 40 µl of concentrated viral stock (5×10^5 transforming units/µl) was applied to the cells. The medium was removed 8 hours later, and the transduction was repeated. Cell yields were measured by manual count of viable cells as determined by trypan dye exclusion, and transduced cells were transplanted into recipient mice 12–24 hours after transduction. Transduction efficiency was assessed by measurement of either the percentage of GFP cells as determined by fluorescence-activated cell sorting analysis (pY-GFP-transduced cells) or FGF-2 levels in the conditioned medium of pY-BMPFGFC2S/C3N-transduced cells as determined by enzyme-linked immunosorbent assay (R&D Systems, Minneapolis, MN).

Transplantation. Two weeks before and two weeks after irradiation, recipient mice were provided sterile food and autoclaved, acidified water (pH 2.0–2.5) containing 50 mg/l neomycin sulfate (Sigma-Aldrich, St. Louis, MO) and 13 mg/l polymixin B sulfate (Sigma-Aldrich, St. Louis, MO). Mice were preconditioned by total body irradiation from a ^{60}Co source delivering a single dose of 5 Gy (80 cGy/minute). Transduced donor Sca-1^+ cells (500,000 Sca-1^+ cells in 30 µl sterile saline) were transplanted into anesthetized W_{41}/ W_{41} recipient mice 4 hours after irradiation via retro-orbital injection. Engraftment was assessed as the percentage of GFP-expressing cells as determined by analysis of mononuclear cells in recipient PB or BM with a FACSCalibur System (BD Biosciences, San Jose, CA).

Serum and bone extract analysis. Serum FGF-2 protein levels of recipient mice were determined by enzyme-linked immunosorbent assay (R&D Systems, Minneapolis, MN). Serum ALP and calcium were measured using an Hitachi 912 Clinical Chemistry analyzer (Stratec SA Plus, White Plains, NY). Serum PTH was measured by enzyme-linked immunosorbent assay (PTH Immunoassay Kit, ALPCO, Salem, NH). Bone extract ALP activity was assayed by a colorimetric assay as described previously.[40]

pQCT measurements. Femurs were formalin fixed and stored in phosphate-buffered saline containing 0.5% sodium azide. Cross-sectional and volumetric bone parameters (total, trabecular, and cortical vBMD, cortical thickness, and periosteal and endosteal circumferences) were measured using an XCT 960M with XCT software version 5.40 (Roche Diagnostics, Basel, Switzerland) in a multi-specimen holder designed for the XCT 960M as previously described.[41] Total, cortical, and trabecular vBMD values were calculated by dividing the total, cortical, and trabecular mineral content by the total, cortical, and trabecular bone volume, respectively, and expressed as milligrams per cubic centimeter.

Bone tissue histology and quantitative histomorphometry. After pQCT measurements, left femurs were decalcified in 14% EDTA (Sigma-Aldrich, St. Louis, MO) for 2 weeks at 4 °C, dehydrated in ethanol, infiltrated, and embedded in paraffin wax. Longitudinal serial sections (5 µm in thickness) were stained with hematoxylin and eosin and Mallory's trichrome for detection of collagen. Quantitative static bone histomorphometry measurements were performed on hematoxylin-and-eosin-stained sections of distal femoral diaphyses of 10 randomly selected recipient mice. Percentage cancellous bone area was calculated by dividing total area by total tissue area. Right femurs were embedded into methylmethacrylate and serial sections (5 µm in thickness) were stained with Goldner's trichrome stain for assessment of bone mineralization as previously described.[42]

Statistical analysis. Comparisons of differences were performed using two-tailed, two-sample independent *t*-tests and linear regression. Results were considered significant when $P < 0.05$. All data are reported as mean ± SEM.

ACKNOWLEDGMENTS

This work was supported in part by a special appropriation to the Jerry L. Pettis Memorial VA Medical Center—Musculoskeletal Disease Center. All work, except the irradiation procedure, was performed in facilities provided by the Department of Veterans Affairs. The authors acknowledge the excellent technical assistance from Joshua Fell, Cynthia Dixon, Nancy Lowen, Carolyn Hargrave, Jann Smallwood, Aurora Petril, and Mahinta Kadiel (all of the Musculoskeletal Disease Center of the Jerry L. Pettis Memorial VA Medical center), and Erban Bayeta (of the Department of Radiation Medicine, Loma Linda University).

REFERENCES

1. Martin, I, Muraglia, A, Campanile, G, Cancedda, R and Quarto, R (1997). Fibroblast growth factor-2 supports *ex vivo* expansion and maintenance of osteogenic precursors from human bone marrow. *Endocrinology* **138**: 4456–4462.
2. Walsh, S, Jefferiss, C, Stewart, K, Jordan, GR, Screen, J and Beresford, JN (2000). Expression of the developmental markers STRO-1 and alkaline phosphatase in cultures of human marrow stromal cells: regulation by fibroblast growth factor (FGF)-2 and relationship to the expression of FGF receptors 1-4. *Bone* **27**: 185–195.
3. Baddoo, M, Hill, K, Wilkinson, R, Gaupp, D, Hughes, C, Kopen, GC *et al.* (2003). Characterization of mesenchymal stem cells isolated from murine bone marrow by negative selection. *J Cell Biochem* **89**: 1235–1249.
4. Bianchi, G, Banfi, A, Mastrogiacomo, M, Notaro, R, Luzzatto, L, Cancedda, R *et al.* (2003). *Ex vivo* enrichment of mesenchymal cell progenitors by fibroblast growth factor 2. *Exp Cell Res* **287**: 98–105.
5. Mayahara, H, Ito, T, Nagai, H, Miyajima, H, Tsukuda, R, Taketomi, S *et al.* (1993). *In vivo* stimulation of endosteal bone formation by basic fibroblast growth factor in rats. *Growth Factors* **9**: 73–80.
6. Nagai, H, Tsukuda, R and Mayahara, H (1995). Effects of basic fibroblast growth factor (bFGF) on bone formation in growing rats. *Bone* **16**: 367–373.
7. Nakamura, T, Hanada, K, Tamura, M, Shibanushi, T, Nigi, H, Tagawa, M *et al.* (1995). Stimulation of endosteal bone formation by systemic injections of recombinant basic fibroblast growth factor in rats. *Endocrinology* **136**: 1276–1284.
8. Nagai, H, Tsukuda, R, Yamasaki, H and Mayahara, H (1999). Systemic injection of FGF-2 stimulates endocortical bone modelling in SAMP6, a murine model of low turnover osteopenia. *J Vet Med Sci* **61**: 869–875.
9. Liang, H, Pun, S and Wronski, TJ (1999). Bone anabolic effects of basic fibroblast growth factor in ovariectomized rats. *Endocrinology* **140**: 5780–5788.
10. Iwaniec, UT, Mosekilde, L, Mitova-Caneva, NG, Thomsen, JS and Wronski, TJ (2002). Sequential treatment with basic fibroblast growth factor and PTH is more efficacious than treatment with PTH alone for increasing vertebral bone mass and strength in osteopenic ovariectomized rats. *Endocrinology* **143**: 2515–2526.
11. Lane, NE, Kumer, J, Yao, W, Breunig, T, Wronski, T, Modin, G *et al.* (2003). Basic fibroblast growth factor forms new trabeculae that physically connect with pre-existing trabeculae, and this new bone is maintained with an anti-resorptive agent and enhanced with an anabolic agent in an osteopenic rat model. *Osteoporos Int* **14**: 374–382.
12. Iwaniec, UT, Magee, KA, Mitova-Caneva, NG and Wronski, TJ (2003). Bone anabolic effects of subcutaneous treatment with basic fibroblast growth factor alone and in combination with estrogen in osteopenic ovariectomized rats. *Bone* **33**: 380–386.
13. Lane, NE, Yao, W, Kinney, JH, Modin, G, Balooch, M and Wronski, TJ (2003). Both hPTH(1-34) and bFGF increase trabecular bone mass in osteopenic rats but they have different effects on trabecular bone architecture. *J Bone Miner Res* **18**: 2105–2115.
14. Power, RA, Iwaniec, UT and Wronski, TJ (2002). Changes in gene expression associated with the bone anabolic effects of basic fibroblast growth factor in aged ovariectomized rats. *Bone* **31**: 143–148.
15. Yao, W, Hadi, T, Jiang, Y, Lotz, J, Wronski, TJ and Lane, NE (2005). Basic fibroblast growth factor improves trabecular bone connectivity and bone strength in the lumbar vertebral body of osteopenic rats. *Osteoporos Int* **16**: 1939–1947.

16. Kawaguchi, H, Nakamura, K, Tabata, Y, Ikada, Y, Aoyama, I, Anzai, J *et al.* (2001). Acceleration of fracture healing in nonhuman primates by fibroblast growth factor-2. *J Clin Endocrinol Metab* **86**: 875–880.
17. Montero, A, Okada, Y, Tomita, M, Ito, M, Tsurukami, H, Nakamura, T *et al.* (2000). Disruption of the fibroblast growth factor-2 gene results in decreased bone mass and bone formation. *J Clin Invest* **105**: 1085–1093.
18. Hurley, MM, Okada, Y, Xiao, L, Tanaka, Y, Ito, M, Okimoto, N *et al.* (2006). Impaired bone anabolic response to parathyroid hormone in $Fgf2^{-/-}$ and $Fgf2^{+/-}$ mice. *Biochem Biophys Res Commun* **341**: 989–994.
19. Zhang, XS, Linkhart, TA, Chen, ST, Peng, H, Wergedal, JE, Guttierez, GG *et al.* (2004). Local *ex vivo* gene therapy with bone marrow stromal cells expressing human BMP4 promotes endosteal bone formation in mice. *J Gene Med* **6**: 4–15.
20. Spangrude, GJ, Smith, L, Uchida, N, Ikuta, K, Heimfeld, S, Friedman, J *et al.* (1991). Mouse hematopoietic stem cells. *Blood* **78**: 1395–1402.
21. Nilsson, SK, Dooner, MS, Tiarks, CY, Weier, HU and Quesenberry, PJ (1997). Potential and distribution of transplanted hematopoietic stem cells in a nonablated mouse model. *Blood* **89**: 4013–4020.
22. Askenasy, N, Zorina, T, Farkas, DL and Shalit, I (2002). Transplanted hematopoietic cells seed in clusters in recipient bone marrow *in vivo*. *Stem Cells* **20**: 301–310.
23. Zhang, J, Niu, C, Ye, L, Huang, H, He, X, Tong, WG *et al.* (2003). Identification of the haematopoietic stem cell niche and control of the niche size. *Nature* **425**: 836–841.
24. Calvi, LM, Adams, GB, Weibrecht, KW, Weber, JM, Olson, DP, Knight, MC *et al.* (2003). Osteoblastic cells regulate the haematopoietic stem cell niche. *Nature* **425**: 841–846.
25. Deola, S, Scaramuzza, S, Birolo, RS, Carballido-Perrig, N, Ficara, F, Mocchetti, C *et al.* (2004). Mobilized blood $CD34^+$ cells transduced and selected with a clinically applicable protocol reconstitute lymphopoiesis in SCID-Hu mice. *Hum Gene Ther* **15**: 305–311.
26. Hall, S, Lau, K-HW, Chen, ST, Felt, JC, Gridley, DS, Yee, KJ *et al.* (2007). An improved mouse Sca-1^+ cell-based bone marrow transplantation model for use in gene- and cell-based therapeutic studies. *Acta Haematol* **117**: 24–33.
27. Florkiewicz, RZ, Majack, RA, Buechler, RD and Florkiewicz, E (1995). Quantitative export of FGF-2 occurs through an alternative, energy-dependent, non-ER/Golgi pathway. *J Cell Physiol* **162**: 388–399.
28. Chen, ST, Gysin, R, Kapur, S, Baylink, DJ and Lau, K-HW (2007). Modifications of the fibroblast growth factor-2 gene led to a marked enhancement in secretion and stability of the recombinant fibroblast growth factor-2 protein. *J Cell Biochem* **100**: 1493–1508.
29. Geissler, EN and Russell, ES (1983). Analysis of the hematopoietic effects of new dominant spotting (W) mutations of the mouse. I. Influence upon hematopoietic stem cells. *Exp Hematol* **11**: 452–460.
30. Soper, BW, Duffy, TM, Vogler, CA and Barker, JE (1999). A genetically myeloablated MPS VII model detects the expansion and curative properties of as few as 100 enriched murine stem cells. *Exp Hematol* **27**: 1691–1704.
31. Kang, E, Giri, N, Wu, T, Sellers, S, Kirby, M, Hanazono, Y *et al.* (2001). *In vivo* persistence of retrovirally transduced murine long-term repopulating cells is not limited by expression of foreign gene products in the fully or minimally myeloablated setting. *Hum Gene Ther* **12**: 1663–1672.
32. Svoboda, J, Hejnar, J, Geryk, J, Elleder, D and Vernerova, Z (2000). Retroviruses in foreign species and the problem of provirus silencing. *Gene* **261**: 181–188.
33. Ruel, M and Sellke, FW (2003). Angiogenic protein therapy. *Semin Thorac Cardiovasc Surg* **15**: 222–235.
34. Presta, M, Dell'Era, P, Mitola, S, Moroni, E, Ronca, R and Rusnati, M (2005). Fibroblast growth factor/fibroblast growth factor receptor system in angiogenesis. *Cytokine Growth Factor Rev* **16**: 159–178.
35. Lundy, MW, Stauffer, M, Wergedal, JE, Baylink, DJ, Featherstone, JD, Hodgson, SF *et al.* (1995). Histomorphometric analysis of iliac crest bone biopsies in placebo-treated versus fluoride-treated subjects. *Osteoporos Int* **5**: 115–129.
36. Dure-Smith, BA, Farley, SM, Linkhart, SG, Farley, JR and Baylink, DJ (1996). Calcium deficiency in fluoride-treated osteoporotic patients despite calcium supplementation. *J Clin Endocrinol Metab* **81**: 269–275.
37. Duursma, SA, Glerum, JH, van Dijk, A, Bosch, R, Kerkhoff, H, van Putten, J *et al.* (1987). Responders and non-responders after fluoride therapy in osteoporosis. *Bone* **8**: 131–136.
38. Kaneko, S, Onodera, M, Fujiki, Y, Nagasawa, T and Nakauchi, H (2001). Simplified retroviral vector gcsap with murine stem cell virus long terminal repeat allows high and continued expression of enhanced green fluorescent protein by human hematopoietic progenitors engrafted in nonobese diabetic/severe combined immunodeficient mice. *Hum Gene Ther* **12**: 35–44.
39. Mostoslavsky, G, Kotton, DN, Fabian, AJ, Gray, JT, Lee, JS and Mulligan, RC (2005). Efficiency of transduction of highly purified murine hematopoietic stem cells by lentiviral and oncoretroviral vectors under conditions of minimal *in vitro* manipulation. *Mol Ther* **11**: 932–940.
40. Farley, JR, Hall, SL, Herring, S and Tarbaux, NM (1992). Two biochemical indices of mouse bone formation are increased, *in vivo*, in response to calcitonin. *Calcif Tissue Int* **50**: 67–73.
41. Wergedal, JE, Ackert-Bicknell, CL, Tsaih, S-W, Sheng, MH-C, Mohan, S, Beamer, WG *et al.* (2006). Femur mechanical properties in the F_2 progeny of an NZB/B1NJ x RF/J cross are regulated predominantly by genetic loci that regulate bone geometry. *J Bone Miner Res* **21**: 1256–1266.
42. Sheng, MH-C, Baylink, DJ, Beamer, WG, Donahue, LR, Lau, K-HW and Wergedal, JE (2002). Regulation of bone volume is different in the metaphyses of the femur and vertebra of C3H/HeJ and C57BL/6J mice. *Bone* **30**: 486–491.

Original Paper

Acta Hæmatologica

Acta Haematol 2007;117:24–33
DOI: 10.1159/000096785

Received: November 30, 2005
Accepted after revision: April 11, 2006
Published online: November 8, 2006

An Improved Mouse Sca-1+ Cell-Based Bone Marrow Transplantation Model for Use in Gene- and Cell-Based Therapeutic Studies

Susan L. Hall[a, b] K.-H. William Lau[a, b] Shin-Tai Chen[a, b] Joshua C. Felt[a]
Daila S. Gridley[c] Jiing-Kuan Yee[d] David J. Baylink[a, b]

[a]Musculoskeletal Disease Center, Jerry L. Pettis Memorial VA Medical Center, Departments of [b]Medicine and Biochemistry and [c]Radiation Medicine, Radiobiology Program, Loma Linda University, Loma Linda, Calif., and [d]City of Hope, Duarte, Calif., USA

Key Words
Bone marrow transplantation · Cell therapy · Engraftment · Gene therapy · Hematopoietic progenitor cells

Abstract
This study sought to develop a murine bone marrow transplantation strategy that would yield consistently high levels of long-term engraftment without significant morbidity and mortality. Hematopoietic stem cell (HSC)-enriched Sca-1+ cells were used for transplantation because of their propensity of homing to bone marrow. Green fluorescent protein (GFP)-expressing transgenic mice were used as donors. Murine Sca-1+ cells were enriched 13-fold from whole bone marrow with immunomagnetic column chromatography. Retroorbital injections yielded highly reproducible and higher levels of engraftment compared with tail vein injections. The combination of W^{41}/W^{41} recipient mice and sublethal irradiation preconditioning produced long-term engraftment with minimal morbidity and mortality. A 24-hour delay between the sublethal irradiation and transplantation did not affect the efficiency and level of engraftment, but provided flexibility with respect to the timing of transplantation. Based on these findings, a mouse Sca-1+ cell-based strategy, involving the retroorbital injection of Sca-1+ cells into sublethally irradiated, myelosuppressed W^{41}/W^{41} recipient mice within 24 h after irradiation, was developed. Transplantation of lentiviral vector-transduced wild-type Sca-1+ cells expressing GFP by this strategy led to consistently high levels of long-term engraftment. In summary, this murine Sca-1+ cell-based strategy could be used in studies of HSC-based gene or cell therapies.

Introduction

Gene and cell therapies via bone marrow transplantation (BMT) represent an exciting research area for potential treatments of numerous medical conditions, such as hereditary immunodeficiencies [1], hemoglobinopathies [2], cancers [3] and skeletal disorders [4]. Prior to clinical trials of these applications in humans, appropriate animal models are vital for studies providing proof-of-principal evaluation, assessment of therapeutic efficacy and safety monitoring. Accordingly, a number of BMT animal models have been developed for use in gene therapy. The most widely studied animal model of BMT for gene therapy is the murine hematopoietic stem cell (HSC) transplantation model.

KARGER

Fax +41 61 306 12 34
E-Mail karger@karger.ch
www.karger.com

0001–5792/07/1171–0024$23.50/0

Accessible online at:
www.karger.com/aha

K.-H. William Lau, PhD
Musculoskeletal Disease Center (151), Jerry L. Pettis Memorial VA Medical Center
11201 Benton Street, Loma Linda, CA 92357 (USA)
Tel. +1 909 825 7084, ext. 2836, Fax +1 909 796 1680
E-Mail William.Lau@med.va.gov

Long-term engraftment of donor cells is essential for the success of BMT-based gene therapy approaches. BMT engraftment is affected by a number of variables, such as recipient preconditioning, HSC numbers and purity, route of delivery of donor cells, and ancillary treatment of HSCs. Accordingly, there have been a number of variations in the strategy of this model designed to enhance engraftment. Each variation in strategy has its own advantages and disadvantages. For example, engraftment has been demonstrated in nonmyeloablated recipients in some studies [5–7]. The advantage of this strategy is that it caused low morbidity and mortality in the recipients, whereas it is a major disadvantage that it requires large cell doses [8] and/or infusions over several days [7, 9]. On the other hand, successful engraftment with cell numbers as low as a single HSC has been documented in myeloablated recipients [10–12], but this strategy exposes recipients to lethal doses of irradiation (leading to significant host morbidity and mortality) and requires stringent maintenance of aseptic conditions (to minimize the infection associated with myeloablation). Mild or sublethal irradiation falls between these two extremes and yields engraftment with transplantation of intermediate numbers of cells and reduced morbidity and mortality [13–16]. However, engraftment under these conditions can be highly inconsistent. An alternative approach to myeloablation is to use genetically myelosuppressed recipient mice. Accordingly, murine strains resulting from deletions or mutations in the W locus encoding the c-kit gene [17, 18] are hematopoietic deficient [19, 20]. The use of W^{41}/W^{41} recipient mice has shown enhanced engraftment [21, 22]. The advantage of the w^{-}/w^{-} recipient mice is the avoidance of irradiation, with the disadvantage of lower levels of engraftment than those in preconditioned mice. Other studies dealt with other variables, such as the use of selective HSC cell subpopulation for the transplantation, the selection of appropriate donor and recipient mouse inbred strains, the timing of transplantation after preconditioning, and/or the mode of donor HSC delivery to recipients. Inasmuch as the results of many HSC transplantation strategies are encouraging, further improvements are warranted.

The objective of this study was to develop an improved murine HSC-based transplantation strategy that would lead to a consistent and high level of long-term engraftment by combining several approaches. This strategy should allow us to take advantage of various desirable aspects of the selected strategies and, at the same time, to minimize their limitations. Our approach was to use HSC-enriched Sca-1+ cells for transplantation because of their propensity of homing to bone [23]. We used Sca-1+ cells, isolated from green fluorescent protein (GFP)-expressing transgenic mice, as donor cells to distinguish cells of donor from those of host origin. Enrichment for HSCs using only one cell marker has the advantages of relative ease and lower cost of donor cell preparation. We then compared the effects of two methods of cell delivery (retroorbital vs. tail vein injection) on engraftment efficiency, the chimeric level and engraftment consistency. We next evaluated whether the combined use of sublethal irradiation and W^{41}/W^{41} recipient mice would improve engraftment and reduce morbidity. Finally, to provide flexibility in the procedure with respect to the timing of transplantation, we also assessed whether a 24-hour delay in HSC transplantation after sublethal irradiation would affect engraftment. On the basis of the results of these experiments, we have developed an improved murine HSC-based transplantation strategy that leads to consistent (in every injected mouse), robust, long-term engraftment with reduced morbidity and/or mortality. With this strategy, we demonstrated that sublethally irradiated W^{41}/W^{41} recipient mice injected with Sca-1+ cells transduced with a lentiviral vector showed long-term engraftment and GFP transgene expression in every recipient mouse.

Materials and Methods

Animals

The TgN β-actin-EGFP (TgN-GFP) donor mice and the wild-type C57BL/6J mouse strain were purchased from Jackson Laboratory (Bar Harbor, Me., USA). The C57BL/6J-W^{41}/W^{41} strain was provided as a generous gift by Dr. Jane Barker, Department of Physiology, St. Louis University School of Medicine, St. Louis, Mo., USA. All animals were housed and maintained within the Veterinary Medical Unit of the Jerry L. Pettis Memorial VA Medical Center. All procedures were performed under humane conditions and were approved by two Institutional Animal Care and Use Committees (the Jerry L. Pettis Memorial VA Medical Center and the Loma Linda University).

Sca-1+ Cell Enrichment

Whole bone marrow (WBM) cells were harvested from TgN-GFP mice by flushing tibiae and femurs with phosphate-buffered saline using a 26-gauge needle and syringe. Erythrocytes were removed by osmotic lysis using a solution of 155 mM NH_4Cl, 10 mM $KHCO_3$ and 110 μM Na_2 EDTA, followed by rinsing with phosphate-buffered saline. The cell preparation was then incubated with magnetic microbeads conjugated with antibody specific to Sca-1 and applied twice to an automated magnetic separation column (AutoMacs™) according to the manufacturer's instructions (Miltenyi Biotec, Inc., Auburn, Calif., USA). Cell yields of aliquots of the WBM, erythrocyte-lyzed and Sca-1+ cell-en-

Table 1. Cell yield, recovery and enrichment of Sca-1+ and/or GFP+ cells during the Sca-1+ cell enrichment process

	Number of cells per donor mouse, $\times 10^6$	Recovery %	Sca-1+ GFP+ cells, %	Sca-1+ GFP– cells, %	Total Sca-1+ cells, %	Fold enrichment of Sca-1+ cells
WBM	116.0 ± 15.5	100	4.7 ± 0.5	1.2 ± 0.4	5.8 ± 0.7	1
Erythrocyte-lyzed cell subpopulation	43.9 ± 8.5	37.8	8.0 ± 1.7	2.8 ± 0.8	10.7 ± 0.9	2
Sca-1+ enriched cell subpopulation	3.0 ± 0.7	2.6	57.7 ± 9.9	16.6 ± 5.1	74.3 ± 5.3	13

Results are shown as mean ± SD for 4 replicate experiments.

riched preparations were measured by manual cell count of viable cells as determined by trypan blue dye exclusion. Recovery was calculated by dividing the number of cells counted after the lysis of erythrocytes and Sca-1+ enrichment steps by the number of WBM cells harvested. To assess enrichment efficiency, aliquots of each cell preparation were incubated with either phycoerythrin (PE)-conjugated Sca-1-specific or PE-conjugated rat isotype control antibody (Pharmingen, San Diego, Calif., USA) and analyzed for Sca-1 and/or GFP expression with a FACSCalibur System (BD Biosciences, San Jose, Calif., USA). The percentage of Sca-1+ cells was calculated by subtracting the value obtained with the PE-conjugated rat isotype control antibody from that obtained with the PE-conjugated Sca-1-specific antibody.

Transplantation

Two weeks before and 2 weeks after the irradiation procedure, recipient mice were provided sterile food and autoclaved, acidified water (pH 2.0–2.5) containing 50 mg/l neomycin SO_4 and 13 mg/l polymyxin B SO_4. Recipient mice were preconditioned by total body irradiation using a ^{60}Co source delivering a single radiation dose of 500 cGy at a rate of 80 cGy per minute. For nonirradiated controls, sham irradiations were performed in parallel. Unless otherwise stated, Sca-1+ cells were transplanted into recipients 4 h after the irradiation via lateral tail vein or retroorbital injection in a volume of 30 μl sterile normal saline solution. For the tail vein injection approach, 30 W^{41}/W^{41} recipient mice were transplanted via the tail vein injection method with 400,000 Sca-1+ cells harvested from TgN-GFP donor mice. For the retroorbital injection method, an aliquot of 400,000 Sca-1+ cells of the same donor cell preparation was injected into each of the 6 W^{41}/W^{41} recipient mice via the retroorbital plexus. Based on previous experience, more mice were put on the tail vein injection arm because we anticipated that the technically more difficult tail vein injection would produce a much larger variation in engraftment than retroorbital injection.

Analysis of Engraftment

Peripheral blood was collected via the lateral tail vein. Erythrocytes were lyzed and FACS analysis was performed for GFP-expressing donor cells.

Lentiviral Vector Production and Preparation of Enhanced GFP Expression Lentiviral Vector-Transduced Sca-1+ Cells for Transplantation

A third-generation lentiviral vector containing the enhanced GFP (eGFP) gene (driven by a CMV promoter) was produced by cotransfection of 293T cells with the four-plasmid system as described previously [24]. The harvested vectors were concentrated by ultracentrifugation and titered by endpoint dilution as described [24]. Sca-1+ cells were plated in 6-well retronectin-coated plates at a density of 4×10^6 cells/well in IMDM media containing 20% fetal bovine serum, 50 ng/ml of human Flt-3L, murine stem cell factor, IL-6, murine IL-3, murine IL-1α and 100 μM of dNTP as described previously [25]. After an overnight incubation, 40 μl of concentrated viral stock (5×10^5 tfu/μl) was applied to the cells. The medium was then removed 8 h later, and the transduction was repeated once. The transduced cells were transplanted into recipient mice 12–24 h after transduction.

Statistical Analysis

Comparison of differences between two variables was performed using the two-tailed, two-sample with equal variances, independent t test. Comparison of multiple groups was performed with one-way ANOVA. Results were considered significant when $p < 0.05$. All data are reported as mean ± standard deviation (SD).

Results

Enrichment for Sca-1+ Cells

Table 1 shows the FACS analysis representative of a WBM cell population and its corresponding enriched Sca-1+ cell population. Although WBM cells were isolated from the GFP transgenic mice, only approximately 80% of the Sca-1+ cells in this cell population expressed GFP (GFP+). Thus, we determined the relative percentage of the Sca-1+ cells that were GFP+ versus those that were GFP– during the enrichment process. Table 1 summarizes the cell yield per donor mouse, recovery, percent of Sca-1+ cells (GFP+, GFP– and total fractions), and fold of enrichment at each isolation step of 4 independent experiments. The overall enrichment of Sca-1+ cells by this procedure was about 13-fold. After the enrichment, approximately 80% of the Sca-1+ cells remained GFP+, indicating that this enrichment method does not discriminate GFP+ Sca-1+ cells from GFP– Sca-1+ cells.

Retroorbital Injection versus Tail Vein Injection

Tail vein injection and retroorbital injection are two frequently used routes for delivering cells or test compounds into the circulation of recipient rodents. Accordingly, we compared the engraftment efficiency and the chimera levels between the retroorbital injection method and the tail vein injection study at 8, 24, 32, 36 and 40 weeks after transplant and assessed for engraftment (fig. 1). At each time point, all mice (6 of 6) in the retroorbitally injected group demonstrated significant engraftment, whereas only 11 out of 30 (37%) of the tail vein-injected mice showed evidence of engraftment. When engraftment in those 11 tail vein-injected mice was compared with that in the retroorbitally injected mice (i.e. excluding the 19 nonengrafted tail vein-injected mice), the retroorbital group showed a higher (72–82%) chimeric level than the tail vein group (56–66%) at each time point, although the differences did not reach a statistically significant level (fig. 1). The variation of the engraftment in the tail vein-injected group was also significantly larger than that in the retroorbital group in that the coefficient of variation in the tail vein group compared with the retroorbital group was 3- to 4-fold larger (table 2). The retroorbital injection method is relatively safe to the host, as none of the mice (over 200 throughout the study) injected by retroorbital injection suffered adverse effects to their eyes, and, in most experiments, no animal was lost due to anesthesia or any other complication. Although the mice in the tail vein-injected group were not anesthetized, we believe that the observed difference in engraftment was due to differences in the technical method of delivering the cells, rather than any biological effect due to the anesthesia.

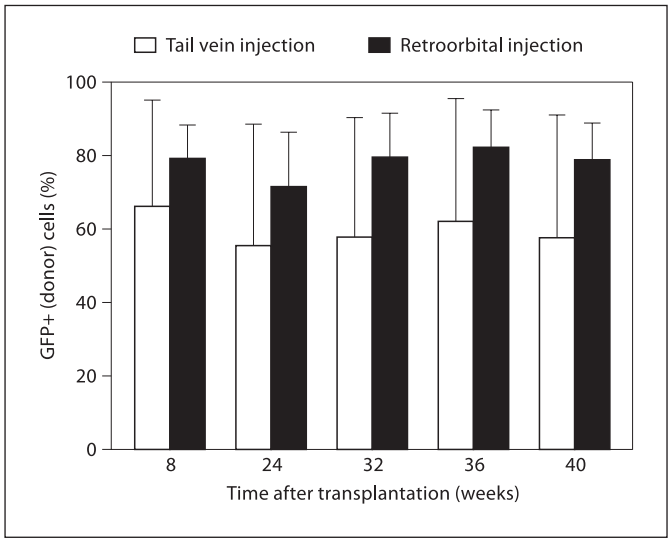

Fig. 1. Comparison of the engraftment efficiency between the tail vein injection route and the retroorbital injection route of transplantation. The engraftment efficiency was assessed by measuring the mean percentage of eGFP-positive cells in host mice peripheral blood over time. Mice were transplanted with 400,000 Sca-1+ cells from eGFP transgenic donor mice through either the tail vein injection route or the retroorbital injection route. At indicated time points, peripheral blood was collected and assayed for the percentage of eGFP cells by flow cytometry. The coefficients of variation of the engraftment between the two test groups are shown in table 2.

Table 2. Comparison of coefficients of variation of the engraftment between the tail vein-injected group and the retroorbitally injected group

	Coefficient of variation, weeks				
	8	24	33	37	40
Tail vein-injected group	0.44	0.59	0.56	0.54	0.53
Retroorbitally injected group	0.11	0.20	0.14	0.12	0.14

Coefficients of variation were calculated from data presented in figure 1, as SD divided by the mean for each time point.

Effect of Preconditioning on Engraftment Levels

We next evaluated the combined effects of preconditioning and the use of W^{41}/W^{41} recipient mice on engraftment at 4, 12 and 16 weeks by comparing engraftment efficiencies in 4 recipient models (n = 6 per group): (1) nonirradiated C57BL/6J wild-type mice, (2) nonirradiated W^{41}/W^{41} mice, (3) sublethally (500 cGy) irradiated C57BL/6J wild-type mice, and (4) sublethally irradiated W^{41}/W^{41} mice. The results are shown in figure 2. At all 3 time points, analysis by one-way ANOVA revealed statistically significant differences between the 4 recipient models ($p < 0.01$ in all comparisons except at the 12-week comparisons of wild-type vs. W^{41}/W^{41} mice; $p < 0.05$). The engraftment in nonirradiated wild-type recipients was negligible (0.54 ± 0.18, 0.24 ± 0.24 and 0.06 ± 0.06% for 4, 12 and 16 weeks, respectively). Nonirradiated W^{41}/W^{41} hosts had significantly increased engraftment (7.0 ± 5.7, 25.8 ± 22.6 and 22.7 ± 13.7%, respectively). Radiation preconditioning of wild-type mice markedly improved engraftment at each time point (49.2 ± 6.0, 57.2 ± 7.8 and 54.0 ± 7.2%, respectively). The highest level of chimerism was observed in the W^{41}/W^{41} recipients receiving the sublethal irradiation (73.1± 5.1,

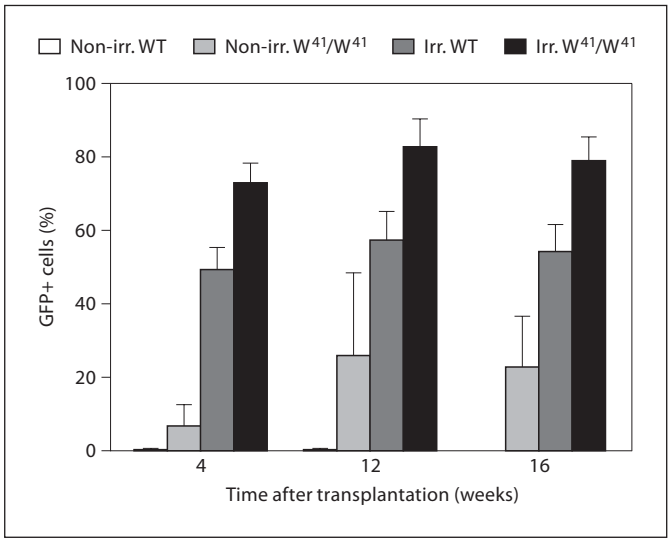

Fig. 2. Comparison of the engraftment efficiency in wild-type C57BL/6J or W^{41}/W^{41} recipient mice with or without sublethal irradiation. Engraftment was determined by measuring the mean percentage of eGFP-positive cells in peripheral blood over time. Five hundred thousand Sca-1+ cells from eGFP transgenic donor mice were transplanted into nonirradiated wild-type (non-irr. WT), nonirradiated W^{41}/W^{41} (non-irr. W^{41}/W^{41}), irradiated wild-type (irr. WT) or irradiated W^{41}/W^{41} (irr. W^{41}/W^{41}) recipient mice. At indicated time points, peripheral blood was collected and assayed for the percentage of GFP cells by flow cytometry.

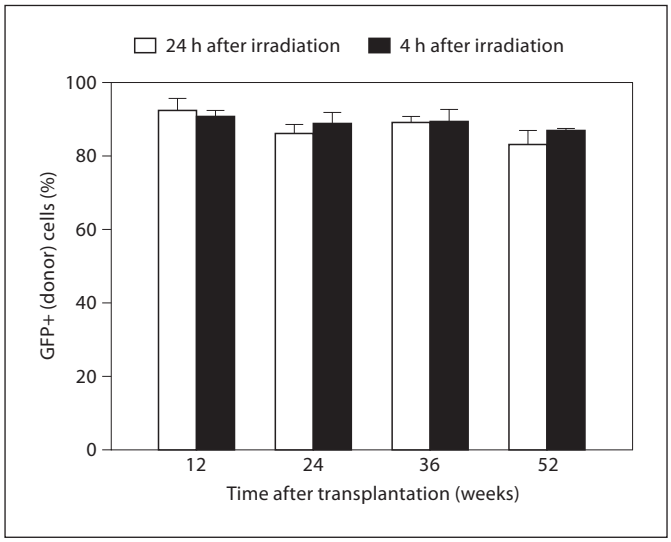

Fig. 3. The mean percentage of GFP-positive cells in peripheral blood of recipient mice preconditioned by sublethal irradiation either 4 or 24 h prior to TgN-eGFP donor Sca-1+ cell transplantation. Six W^{41}/W^{41} recipient mice were subjected to a single 500 cGy dose of irradiation. Another 6 W^{41}/W^{41} recipient mice received the same dose of radiation 24 h later. Four hours later, both groups were injected with 2×10^6 Sca-1+ enriched cells via the retroorbital vein. At 12, 24, 36 and 52 weeks after transplantation, peripheral blood was assayed for the percentage of GFP cells by flow cytometry. All 12 mice were engrafted successfully.

82.6 ± 7.3 and 78.9 ± 6.0%, respectively), indicating that the combination of preconditioning and the use of genetically myelosuppressed recipient mice produced at least an additive enhancement in engraftment. The enhanced engraftment produced by the combination persisted for as long as 1 year without significant reduction in chimera levels (data not shown).

Effect of Delay of Injection on Long-Term Reconstitution

We next tested whether a 24-hour delay of the initiation of HSC transplantation after the sublethal irradiation would affect long-term engraftment. As seen in figure 3, there was no significant difference in the engraftment level between mice transplanted 4 versus 24 h after irradiation at any time point. Furthermore, engraftment was relatively high and persisted up to 52 weeks (experimental endpoint). These findings indicate that a 24-hour delay between sublethal irradiation and transplantation through retroorbital injection did not affect the efficiency and level of short- or long-term engraftment.

Evidence for Engraftment of Self-Renewing Stem Cells

To ensure that engraftment of self-renewing stem cells had indeed occurred in the transplanted mice, erythrocyte-lyzed BM cells (5.75×10^6 cells in 30 μl) of several primary recipient mice with relatively high engraftment levels (70% GFP+ cells in peripheral blood) as well as those of nonengrafted primary recipient mice (<1% GFP+ cells in peripheral blood) were each transplanted into 2 secondary sublethally irradiated W^{41}/W^{41} recipient mice 25 weeks after the primary transplantation. The secondary recipient mice were then analyzed for chimerism at 36 weeks after transplantation. We found that secondary recipient mice receiving BM cells from the engrafted primary mice showed significant levels of GFP+ cells in peripheral blood, ranging from 9 to 47%. Conversely, those secondary recipient mice receiving BM cells from the nonengrafted primary mice had no (0–0.02%) measurable level of GFP+ cells in peripheral blood. These findings indicate that engraftment of self-renewing stem cells indeed occurred in recipient mice with our strategy.

Table 3. Engraftment of multilineage hematopoietic cells in recipient mice transplanted with GFP-expressing Sca-1+ cells from TgN-GFP mice

Hematopoietic cell lineage	Total cells, from both donor (PE+ and GFP+ cells) and recipient host (PE+ and GFP– cells) origin, %	Total cells from recipient host origin (PE+ and GFP– cells), %	Total cells from donor origin (PE+ and GFP+ cells), %	p value[1] (recipient host origin vs. donor origin)
T lymphocytes	19.4 ± 5.8	14.7 ± 3.0	11.8 ± 4.4	NS
Mac/Mono/Gr	32.2 ± 25.7	6.9 ± 3.5	22.9 ± 5.8	<0.001
B lymphocytes	21.4 ± 6.7	11.6 ± 5.2	22.9 ± 7.2	<0.01
Erythroid	4.8 ± 3.8	undetectable	5.4 ± 2.8	<0.001

Results are shown as mean ± SD. For this analysis, W^{41}/W^{41} mice were transplanted with GFP-expressing Sca-1 cells isolated from TgN-GFP mice. Five months after transplantation, erythrocyte-lyzed BM cells from recipient mice were incubated with PE-conjugated antibodies specific to various hematopoietic lineages: (1) for T lymphocytes, a mixture of CD3-, CD4e- and CD8a-specific antibodies was used; (2) for monocytes/macrophages/neutrophils (Mac/Mono/Gr) lineage, a mixture of Mac-1- and Gr-1-specific antibodies was used; (3) for B lymphocytes, a B220-specific antibody was used; (4) for erythroid lineage cells, a Ter-119-specific antibody was used. The percentage of each hematopoietic cell lineage in peripheral cells was determined with a FACSCalibur System. Cells positive for PE but negative for GFP were considered of recipient host origin, while cells positive for PE and positive for GFP were considered of donor origin.

[1] p values were determined by independent two-tailed t test.

Evidence of Multilineage Hematopoietic Cell Repopulation in Recipient Mice

To assess the pluripotent ability of the engrafted Sca-1+ donor cells to produce multilineage hematopoietic cells, we measured, by FACS, the percentage of four hematopoietic lineages (T lymphocytes, B lymphocytes, neutrophils/granulocytes/monocytes and erythroid) in the peripheral blood of recipient mice transplanted with GFP-expressing Sca-1+ cells from TgN-GFP mice. Table 3 shows the mean ± SD for each cell lineage type in mice transplanted with Sca-1+ cells 5 months after transplantation. Cells that were PE+ and GFP+ were of donor origin, while cells that were PE+ but GFP– were considered of recipient host origin. No significant difference in contribution of T-lymphocyte lineage was observed between host (14.7%) and donor (11.8%) origin. In contrast, donor cells contributed a larger percentage than host cells to the macrophage-monocyte-neutrophil lineage (22.9 vs. 6.9%; $p < 0.001$) and B lymphocytes (22.9 vs. 6.9%; $p < 0.01$). The erythroid hematopoietic compartment was made up exclusively of cells of donor origin. These results are comparable with the relative distribution of cells of hematopoietic lineage in peripheral blood of control mice reported by Morel et al. [26]. Thus, the results indicate that our Sca-1+ cell transplantation strategy could lead to multilineage hematopoietic cell engraftment.

Engraftment Efficiency of Genetically Altered Sca-1+ Cells

Because our ultimate objective was to utilize this HSC transplantation strategy to develop an ex vivo gene therapy protocol, we needed to ensure that ex vivo modification of Sca-1+ cells with viral transduction would not affect engraftment efficiency or levels. To address this issue, Sca-1+ cells of C57BL/6J wild-type mice were transduced with a lentiviral vector expressing GFP. Forty-eight hours after transduction, cells were stained with propidium iodide for assessment of cell viability and GFP expression. The viral transduction caused significant cell death (81%), because a relatively high multiplicity of infection (approximately 15) of viral vector was used. The GFP expression level of the transduced Sca-1+ cells was analyzed with FACS 2 and 5 days after transduction, which showed that approximately half of the transduced cells (51% at 2 days and 49% at 5 days after transduction) expressed the GFP transgene, indicating an approximately 50% transduction efficiency (fig. 4a).

An aliquot of 500,000 cells of the transduced cell preparation was injected into 12 sublethally irradiated W^{41}/W^{41} recipient mice 48 h after transduction. At 9 weeks after transplant, peripheral blood was collected from recipient mice for the percentage of GFP+ cells by FACS analysis for GFP+ mononuclear blood samples, which showed >80% GFP+ cells. Figure 4b shows the FACS

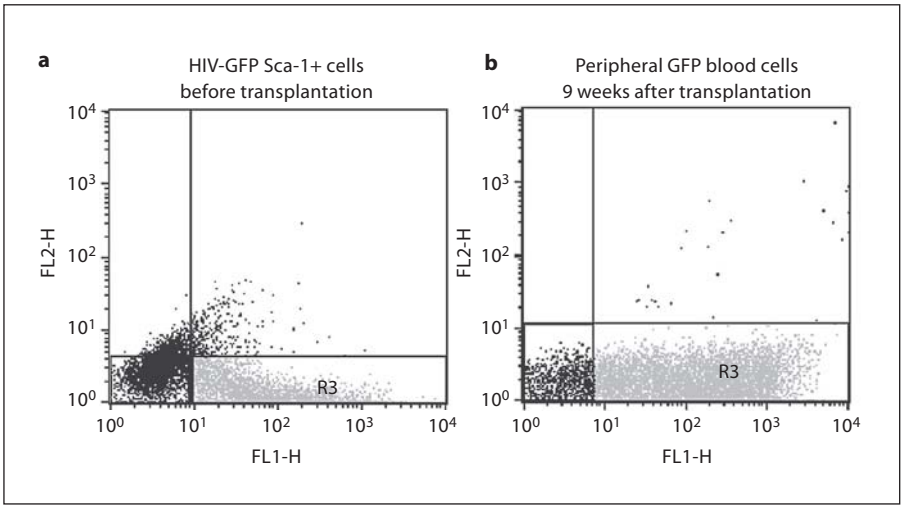

Fig. 4. Percentage of GFP-expressing donor cells in C57BL/6J Sca-1+ cells transduced with an HIV-based vector expressing the GFP marker gene 5 days after transduction (**a**) and in peripheral blood of a representative recipient mouse 9 weeks after transplantation (**b**). The percentage of GFP+ cells was analyzed by FACS.

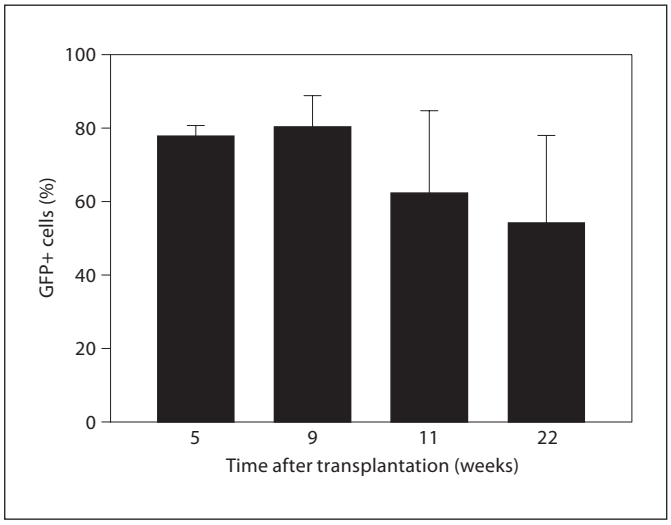

Fig. 5. The mean percentage of eGFP-positive cells in peripheral blood of host mice transplanted with Sca-1+ cells transduced with an HIV-based viral vector expressing the eGFP marker gene at 5, 9, 11 and 22 weeks after transplantation.

analysis of a representative recipient mouse. Figure 5 shows a 50–60% long-term engraftment level in each of the recipient mice. It also reveals a time-dependent, small decline in the percentage of GFP-expressing cells at 5, 9, 11 and 22 weeks after transplant. The reason for this small gradual decline is unknown. The Sca-1+ enriched cell subpopulation is a heterogeneous population of both hematopoietic progenitor cells and HSCs. It is possible that the engrafted GFP+ hematopoietic progenitor cells gradually differentiated and eventually lost their engraftment ability. This gradual decline may reflect the time-dependent loss of GFP expressing hematopoietic progenitor cells. Alternatively, this could suggest a gradual increase in silencing of GFP expression.

Discussion

In this study, we have developed a murine Sca-1+ cell-based BMT strategy, involving the injection of the Sca-1+ cell-enriched HSC subpopulation into sublethally irradiated, genetically myelosuppressed W^{41}/W^{41} recipient mice through retroorbital vein postirradiation. This strategy provided consistent (in every recipient mouse), long-term engraftment of high chimera levels with only a few hundred thousands of Sca-1+ donor cells, yet caused minimal host morbidity and mortality. Accordingly, the engraftment efficiency (estimated by measuring the relative percentage of GFP-expressing Sca-1+ donor cells in the peripheral blood of recipients by FACS) in the 264 recipient mice transplanted with GFP-expressing Sca-1+ cells in our laboratory during the past 2 years was 75.6 $\pm$ 23.9% (the low and high 95% confidence interval for the probability being 36.3 and 114.9%, respectively). Since approximately 80% of the Sca-1+ cells of the TgN-GFP transgenic mice are GFP+, the actual chimera level could be significantly greater, possibly even approaching full (100% chimera) engraftment. In addition, of the 264 mice receiving the transplantation, 253 (96%) survived the procedure with no obvious ill effects. The 95% confidence interval for the probability was 0.93 and 0.98, respectively. However, we should note that in most of our

experiments, we did not lose any animals. The majority of mice lost during the past 2 years was from two large experiments (n = 45 and n = 50, respectively). The decrease in animal survival in these experiments was primarily due to overdose of anesthesia, likely as a result of staff fatigue. We are unable to directly compare the engraftment and murine loss rate of our strategy with those of published strategies, because information regarding the murine loss rate (with confidence limits) in other published engraftment strategies has not been regularly reported. Nevertheless, we strongly believe that our strategy leads to high levels and consistent engraftment with very low host morbidity and mortality. Most importantly, injections of Sca-1+ cells derived from wild-type C57BL/6J mice transduced with a lentiviral vector expressing the GFP reporter gene yielded highly consistent and high levels (50–60%) of long-term engraftment, suggesting that our strategy could be used in studies of gene or cell-based therapies.

Several noteworthy features of our strategy may be responsible for our success in getting consistent, high levels of chimera with minimal host morbidity and mortality. First, commonly used WBM-based transplantation protocols require several millions of WBM cells to achieve appreciable engraftment [27]. Intravenous injections of a large number of cells are technically difficult. The large cell dose requirement also makes this strategy less desirable for gene therapy because it necessitates high viral titers and/or high multiplicities of infection for adequate levels of gene transfer. Our strategy uses Sca-1+ cells as donor cells. Sca-1, a phosphatidylinositol-linked cell surface glycoprotein, is a cell surface marker of primitive HSCs [28, 29], which have shown to home to and engraft in bone after intravenous injection [11, 28]. Thus, a much lower number of Sca-1+ donor cells were needed for successful engraftment compared with the WBM cell-based transplantation strategy. Moreover, HSC-enriched cell preparations have been shown to provide both short-term radioprotection [30, 31] and long-term, multilineage reconstitution [10, 30, 31] in lethally irradiated mice. Although extra technical steps are needed for the isolation of the Sca-1+ enriched subpopulation, recent advances in the fluorescent-assisted cell sorting technology and/or immunomagnetic assisted cell isolation methods make the isolation of Sca-1+ enriched cell subpopulations relatively cost-effective and a routine procedure.

Second, our strategy used myelosuppressed W^{41}/W^{41} recipient mice as well as sublethal irradiation to maximize engraftment and, at the same time, to minimize side effects due to irradiation preconditioning [21]. This design was based on previous observations that (1) sublethal irradiation produced a dose-dependent enhancement in engraftment [13], and (2) that the use of W^{41}/W^{41} recipient mice markedly enhanced engraftment levels [21, 22, 32]. Because the mechanism leading to myelosuppression by irradiation is different from that in W^{41}/W^{41} mice, we surmised that it might be possible to use low doses of irradiation in W^{41}/W^{41} recipient mice to reduce host mortality and morbidity due to high dosage of radiation without significant reduction in engraftment. Our findings that a sublethal radiation dose in W^{41}/W^{41} recipient mice produced an additive enhancing effect on long-term engraftment with relatively low host mortality and morbidity confirmed this premise. To provide flexibility in the procedure with respect to the timing of HSC transplantation, we also included an up to 24-hour delay between the time of transplantation and the time of irradiation. This delay is feasible because, under our experimental conditions, there were no significant differences in engraftment with a 4- or 24-hour delay between irradiation and transplantation. Although a single irradiation dose of 500 cGy was used in this study – because previous studies indicated that this dose was the minimal radiation dose that would provide sufficient myelosuppression for high levels of engraftment in the C57BL/6J allogenic model [33] – the optimal radiation dosage for our strategy remains to be determined.

The third noteworthy aspect of our strategy is the retroorbital delivery of donor cells. Retroorbital delivery of donor cells in mice is less technically demanding and the results are less variable than in the tail vein injection approach, which is the most commonly used and convenient route of cell delivery for murine BMT models. Previous direct comparison between tail vein injection and retroorbital injection showed no differences in organ distribution or blood concentration of injected material [34], suggesting that retroorbital injection could be a reliable delivery method of donor cells. In our study, retroorbital injection resulted in greatly enhanced engraftment success (from 37 to 100%), higher engraftment levels, and a significant reduction in variation compared with the tail vein method. The retroorbital injection method also led to engraftment in every injected mouse and a 3- to 4-fold reduction in intra-assay variations compared with the tail vein method. Since the power of an experiment is directly proportional to sample size and magnitude of the difference to be detected and inversely proportional to the inherent variability of the observations [35], the reduction in intra-assay variability with our strategy generates an increase in experimental power and the ability to

detect small differences and/or decreased sample size required.

The use of GFP transgenic mouse Sca-1+ cells as donor cells affords a convenient and reliable means to distinguish cells of donor from host origin and as such facilitates assessments of engraftment. This approach is feasible because both the TgN-GFP transgenic mice and the W^{41}/W^{41} recipient mice are of C57BL/6J background. The C57BL/6J mouse strain offers several additional attractive features. First, this mouse strain is widely used in animal research, and a large body of genetic and biological information about this mouse strain is known. Second, numerous transgenic, knockout or mutant variations have been developed on this strain background and will be available for use in assessment of the functional role of the test gene with our strategy. Third, since it has been demonstrated that up to 99% of cells with marrow reconstituting ability are contained within the Sca-1+ subset in C57BL/6J mice [36], the harvest of Sca-1+ cells from this mouse strain and its varieties would provide cell preparations with relatively high repopulating potential.

In summary, we have successfully developed an improved murine BMT strategy that had allowed consistent, persistent and robust engraftment. Although several aspects of our strategy have each individually been used by others, our approach, to our knowledge, is the first attempt to combine all of the various strategies in a single strategy. Our results are promising and indicate that our improved Sca-1+ cell-based BMT strategy could be used in studies of HSC-based gene or cell therapies.

Acknowledgments

This work was supported in part by a special appropriation to the Jerry L. Pettis Memorial VA Medical Center – Musculoskeletal Disease Center. All work, except the irradiation procedure, was performed in facilities provided by the Department of Veterans Affairs. The animal irradiation procedure was performed within the Department of Radiation Medicine at Loma Linda University.

References

1 Buckley RH: Molecular defects in human severe combined immunodeficiency and approaches to immune reconstitution. Annu Rev Immunol 2004;22:625–655.
2 Puthenveetil G, Malik P: Gene therapy for hemoglobinopathies: are we there yet? Curr Hematol Rep 2004;3:298–305.
3 Fuchs EJ, Whartenby KA: Hematopoietic stem cell transplant as a platform for tumor immunotherapy. Curr Opin Mol Ther 2004;6:48–53.
4 Klamut HJ, Chen ST, Lau KHW, Baylink DJ: Progress toward skeletal gene therapy. Crit Rev Eukaryot Gene Expr 2004;14:89–136.
5 Micklem HS, Clarke CM, Evans EP, Ford CE: Fate of chromosome-marked mouse bone marrow cells transfused into normal syngeneic recipients. Transplantation 1968;6:299–302.
6 Saxe DF, Boggs SS, Boggs DR: Transplantation of chromosomally marked syngeneic marrow cells into mice not subjected to hematopoietic stem cell depletion. Exp Hematol 1984;12:277–283.
7 Stewart FM, Crittenden RB, Lowry PA, Pearson-White S, Quesenberry PJ: Long-term engraftment of normal and post-5-fluorouracil murine marrow into normal nonmyeloablated mice. Blood 1993;81:2566–2571.
8 Ramshaw HS, Crittenden RB, Dooner M, Peters SO, Rao SS, Quesenberry PJ: High levels of engraftment with a single infusion of bone marrow cells into normal unprepared mice. Biol Blood Marrow Transplant 1995;1:74–80.
9 Brecher G, Ansell JD, Micklem HS, Tjio JH, Cronkite EP: Special proliferative sites are not needed for seeding and proliferation of transfused bone marrow cells in normal syngeneic mice. Proc Natl Acad Sci USA 1982;79:5085–5087.
10 Osawa M, Hanada K, Hamada H, Nakauchi H: Long-term lymphohematopoietic reconstitution by a single CD34-low/negative hematopoietic stem cell. Science 1996;273:242–245.
11 Krause DS, Theise ND, Collector MI, Henegariu O, Hwang S, Gardner R, Neutzel S, Sharkis SJ: Multi-organ, multi-lineage engraftment by a single bone marrow-derived stem cell. Cell 2001;105:369–377.
12 Matsuzaki Y, Kinjo K, Mulligan RC, Okano H: Unexpectedly efficient homing capacity of purified murine hematopoietic stem cells. Immunity 2004;20:87–93.
13 Mardiney M 3rd, Malech HL: Enhanced engraftment of hematopoietic progenitor cells in mice treated with granulocyte colony-stimulating factor before low-dose irradiation: implications for gene therapy. Blood 1996;87:4049–4056.
14 Stewart FM, Zhong S, Wuu J, Hsieh C, Nilsson SK, Quesenberry PJ: Lymphohematopoietic engraftment in minimally myeloablated hosts. Blood 1998;91:3681–3687.
15 James RI, Warlick CA, Diers MD, Gunther R, McIvor RS: Mild preconditioning and low-level engraftment confer methotrexate resistance in mice transplanted with marrow expressing drug-resistant dihydrofolate reductase activity. Blood 2000;96:1334–1341.
16 Tomita Y, Sachs DH, Sykes M: Myelosuppressive conditioning is required to achieve engraftment of pluripotent stem cells contained in moderate doses of syngeneic bone marrow. Blood 1994;83:939–948.
17 Nocka K, Tan JC, Chiu E, Chu TY, Ray P, Traktman P, Besmer P: Molecular bases of dominant negative and loss of function mutations at the murine c-kit/white spotting locus: W37, Wv, W41 and W. EMBO J 1990;9:1805–1813.
18 Reith AD, Rottapel R, Giddens E, Brady C, Forrester L, Bernstein A: W mutant mice with mild or severe developmental defects contain distinct point mutations in the kinase domain of the c-kit receptor. Genes Dev 1990;4:390–400.

19 Geissler EN, McFarland EC, Russell ES: Analysis of pleiotropism at the dominant white-spotting (W) locus of the house mouse: a description of ten new W alleles. Genetics 1981;97:337–361.
20 Geissler EN, Russell ES: Analysis of the hematopoietic effects of new dominant spotting (W) mutations of the mouse. 1. Influence upon hematopoietic stem cells. Exp Hematol 1983;11:452–460.
21 Trevisan M, Yan XQ, Iscove NN: Cycle initiation and colony formation in culture by murine marrow cells with long-term reconstituting potential in vivo. Blood 1996;88: 4149–4158.
22 Soper BW, Duffy TM, Vogler CA, Barker JE: A genetically myeloablated MPS VII model detects the expansion and curative properties of as few as 100 enriched murine stem cells. Exp Hematol 1999;27:1691–1704.
23 Plett PA, Frankovitz SM, Orschell CM: Distribution of marrow repopulating cells between bone marrow and spleen early after transplantation. Blood 2003;102:2285–2291.
24 Yam PY, Li S, Wu J, Hu J, Zaia JA, Yee JK: Design of HIV vectors for efficient gene delivery into human hematopoietic cells. Mol Ther 2002;5:479–484.
25 Hanawa H, Kelly PF, Nathwani AC, Persons DA, Vandergriff JA, Hargrove P, Vanin EF, Nienhuis AW: Comparison of various envelope proteins for their ability to pseudotype lentiviral vectors and transduce primitive hematopoietic cells from human blood. Mol Ther 2002;5:242–251.
26 Morel F, Salimi S, Markovits J, Austin T, Plavec I: Hematologic recovery in mice transplanted with bone marrow stem cells expressing anti-human immunodeficiency virus genes. Hum Gene Ther 1999;10:2779–2787.
27 Micklem HS, Lennon JE, Ansell JD, Gray RA: Numbers and dispersion of repopulating hematopoietic cell clones in radiation chimeras as functions of injected dose. Exp Hematol 1987;15:251–257.
28 Spangrude GJ, Heimfeld S, Weissman IL: Purification and characterization of mouse hematopoietic stem cells. Science 1988;241: 58–62.
29 Uchida N, Jerabek L, Weissman IL: Searching for hematopoietic stem cells. 2. The heterogeneity of Thy-1.1(lo)Lin(–/lo)Sca-1+ mouse hematopoietic stem cells separated by counterflow centrifugal elutriation. Exp Hematol 1996;24:649–659.
30 Zhao Y, Lin Y, Zhan Y, Yang G, Louie J, Harrison DE, Anderson WF: Murine hematopoietic stem cell characterization and its regulation in BM transplantation. Blood 2000; 96:3016–3022.
31 Okada S, Nakauchi H, Nagayoshi K, Nishikawa S, Miura Y, Suda T: In vivo and in vitro stem cell function of c-kit- and Sca-1-positive murine hematopoietic cells. Blood 1992; 80:3044–3050.
32 Blazar BR, Taylor PA, Vallera DA: Adult bone marrow-derived pluripotent hematopoietic stem cells are engraftable when transferred in utero into moderately anemic fetal recipients. Blood 1995;85:833–841.
33 Down JD, Tarbell NJ, Thames HD, Mauch PM: Syngeneic and allogeneic bone marrow engraftment after total body irradiation: dependence on dose, dose rate, and fractionation. Blood 1991;77:661–669.
34 Price JE, Barth RF, Johnson CW, Staubus AE: Injection of cells and monoclonal antibodies into mice: comparison of tail vein and retroorbital routes. Proc Soc Exp Biol Med 1984;177:347–353.
35 Samuals M: Statistics for the Life Sciences. San Francisco, Dellen Publishing Company, 1989.
36 Spangrude GJ, Brooks DM: Mouse strain variability in the expression of the hematopoietic stem cell antigen Ly-6A/E by bone marrow cells. Blood 1993;82:3327–3332.

THE JOURNAL OF GENE MEDICINE
J Gene Med 2009; **11**: 877–888.
Published online 23 July 2009 in Wiley InterScience (www.interscience.wiley.com) **DOI:** 10.1002/jgm.1369

RESEARCH ARTICLE

Stem cell antigen-1$^+$ cell-based bone morphogenetic protein-4 gene transfer strategy in mice failed to promote endosteal bone formation

Susan L. Hall[1,2]*
Shin-Tai Chen[1,3]
Reinhard Gysin[1,2]
Daila S. Gridley[4]
Subburaman Mohan[1,2,3,5]
K.-H. William Lau[1,2,3]

[1]*Musculoskeletal Disease Center, Jerry L. Pettis Memorial VA Medical Center, Loma Linda, CA, USA*

[2]*Department of Medicine, Loma Linda University School of Medicine, Loma Linda, CA, USA*

[3]*Department of Biochemistry, Loma Linda University School of Medicine, Loma Linda, CA, USA*

[4]*Department of Radiation Medicine, Radiation Research Laboratories, Loma Linda University School of Medicine, Loma Linda, CA, USA*

[5]*Department of Physiology, Loma Linda University School of Medicine, Loma Linda, CA, USA*

*Correspondence to: Susan L. Hall, Musculoskeletal Disease Center (151), Jerry L. Pettis Memorial VA Medical Center, 11201 Benton Street, Loma Linda, California 92357, USA. E-mail: susan.hall1@va.gov

Received: 21 January 2009
Revised: 13 May 2009
Accepted: 1 June 2009

Abstract

Background This study assessed whether a Sca-1$^+$ cell-based *ex vivo* gene transfer strategy, which has been shown to promote robust endosteal bone formation with a modified fibroblast growth factor-2 (FGF2) gene, can be extended to use with bone morphogenetic protein (BMP)2/4 hybrid gene.

Methods Sublethally irradiated recipient mice were transplanted with lentiviral (LV)-BMP2/4-transduced Sca-1$^+$ cells. Bone parameters were monitored by pQCT and μCT. Gene expression was assessed by the real-time reverse transcriptase-polymerase chain reaction.

Results Recipient mice of LV-BMP2/4-transduced Sca-1$^+$ cells yielded high engraftment and increased BMP4 mRNA levels in marrow cells; but exhibited only insignificant increases in serum and bone alkaline phosphatase activity compared to control mice. pQCT and μCT analyses of femurs showed that, with the exception of small changes in trabecular bone mineral density and cortical bone mineral content in LV-BMP2/4 mice, there were no differences in measured bone parameters between mice of the LV-BMP2/4 group and controls. The lack of large endosteal bone formation effects with the BMP4 strategy could not be attributed to ineffective engraftment or expansion of BMP4-expressing Sca-1$^+$ cells, an inability of the transduced cells to secrete active BMP4 proteins, or to use of the LV-based vector.

Conclusions Sca-1$^+$ cell-based BMP4 *ex vivo* strategy did not promote robust endosteal bone formation, raising the possibility of intrinsic differences between FGF2- and BMP4-based strategies in their ability to promote endosteal bone formation. It emphasizes the importance of choosing an appropriate bone growth factor gene for delivery by this Sca-1$^+$ cell-based *ex vivo* systemic gene transfer strategy to promote bone formation. Copyright © 2009 John Wiley & Sons, Ltd.

Keywords bone morphogenetic protein 4; endosteal bone formation; *ex vivo*; gene therapy; hematopoietic stem cells; mice; Sca-1$^+$ cell

Introduction

Osteoporosis is a debilitating disease characterized by a significant loss of bone mass, which leads to the deterioration of the mechanical integrity of the skeleton and increases the risk of nontraumatic fracture [1]. Currently, there are several effective small molecule anti-resorptive therapies for osteoporosis.

Although these anti-resorptive therapies produce modest gains in bone mass (3–5% per year) and significant reduction in fracture risk [2], they have a low bone formation capacity and may not be able to produce sufficient increases in the amounts of bony tissues to improve mechanical integrity within a reasonable time frame, especially in patients with severe osteoporosis. A daily injection-based osteogenic therapy, teriparatide [recombinant parathyroid hormone (PTH)], which yields higher rates of bone formation, has recently been approved by the Food and Drug Administrattion (FDA) for osteoporosis [3,4], but its superiority in fracture prevention compared to anti-resorptive therapies has not been established [5]. Teriparatide therapy is also limited by patient compliance with daily injections. In addition, the drastic reduction in clinical efficacy after 2 years of teriparatide therapy [6] and the development of malignant osteosarcoma in rats treated with PTH after 18 months [7] have led to FDA recommendations to restrict its use in humans to 2 years. Thus, there is still a great need for an anabolic therapy with large bone formation capacity for patients with severe osteoporosis.

Our laboratory has been interested in the development of a systemic gene transfer-based strategy to promote bone formation for the treatment of severe osteoporosis and related bone thinning diseases. Accordingly, we have previously developed an improved hematopoietic stem cell (HSC)-based *ex vivo* gene transfer strategy capable of delivering a bone growth factor gene directly to the bone marrow (BM) cavity [8]. This strategy takes advantage of the propensity of HSC-containing stem cell antigen-1 positive (Sca-1^+) cells to home and engraft in the bone marrow cavity [9], and uses genetically engineered Sca-1^+ cells expressing a bone growth factor gene to promote endosteal bone formation. The feasibility of this strategy has been established by a recent study [10] in which we showed that transplantation of Sca-1^+ cells transduced with a Moloney leukemia virus (MLV)-based vector expressing a modified human fibroblast growth factor 2 (FGF2) gene into sublethally irradiated c-kit-deficient recipient mice led to marked increases in serum FGF2 levels and endosteal/trabecular bone formation. This feasibility study also confirmed the immense bone formation capacity of this gene transfer-based strategy because the increased endosteal bone formation in those recipient mice that had very high serum FGF2 levels was so vigorous that the entire bone marrow space was almost completely filled with newly formed bone 10 weeks post-transplantation [10]. The newly formed bone was of lamellar nature, suggesting normal bone formation. Accordingly, these results indicate that our HSC-based *ex vivo* systemic gene therapy strategy has the potential to be developed into an effective means to promote rapid endosteal bone formation and could be an attractive therapeutic alternative to the current small molecule-based therapies to treat patients with severe osteoporosis.

Although our previous studies have indicated great potential for this HSC-based *ex vivo* gene transfer model to be developed into an effective systemic strategy to treat severe osteoporosis, one of the key questions is whether this strategy can be expanded to other bone growth factor genes. This question needs to be addressed because it is highly relevant to the flexibility and overall utility of this strategy as an osteogenic therapy. Accordingly, the present study sought to determine whether the robust endosteal bone formation previously reported for the Sca-1^+ cell-based FGF2 *ex vivo* gene transfer strategy [10] could also be attained by the same Sca-1^+ cell-based strategy delivering an alternative osteogenic gene. We chose the bone morphogenetic protein (BMP)4 gene as the transgene for this study because BMPs belong to a multigene family of osteoinductive growth factors that are potent stimulators of differentiation of osteoblasts and chondroblasts [11] and also promote fracture repair [12,13] and bone regeneration [14]. In the present study, we transplanted c-kit-deficient recipient mice (W^{41}/ W^{41} strain) with Sca-1^+ donor cells transduced with retroviral vectors expressing either the β-galactosidase (β-gal) control gene or a BMP2/4 hybrid gene (in which the large portion of the BMP4 signal sequence was replaced with the complete BMP2 signal sequence to enhance secretion of mature BMP4 protein [15]). The W^{41}/ W^{41} mouse strain has a point mutation in the c-kit gene [16] which results in a deficiency in HSC number [17]. This strain was used as transplantation recipients because efficient engraftment is achieved without toxic preconditioning [18]. We then assessed engraftment efficiency, BMP4 transgene expression and endosteal bone formation [evaluated by pQCT, μCT, and serum and bone alkaline phosphatase (AP) activity]. In some experiments, recipient mice receiving Sca-1^+ cells transduced with an MLV-based vector expressing the modified human FGF2 transgene [10,19] were included for comparison.

Materials and methods

Animals

Trans Golgi network β-actin-enhanced green flourescent protein (TgN-GFP) transgenic (C57BL/6J background) and C57BL/6J wild-type mice were purchased from Jackson Laboratories (Bar Harbor, ME, USA). The W^{41}/ W^{41} strain of mice (C57BL/6J background) was graciously provided by Dr Jane Barker of the St. Louis University School of Medicine (St. Louis, MO, USA). Animals were housed within the Veterinary Medical Unit of the Jerry Pettis VA Medical Center. All animal procedures were approved by two Institutional Animal Care and Use Committees (Jerry Pettis Memorial VA Medical Center and Loma Linda University).

BM Sca-1^+ cell population isolation

The procedures for isolating Sca-1^+ cell-enriched populations from donor mice are described elsewhere [8].

DOI: 10.1002/jgm

Briefly, whole BM cells were harvested from TgN-GFP mice by flushing tibiae and femurs with phosphate-buffered saline containing 0.5% bovine serum albumin (Sigma-Aldrich, St, Louis, MO, USA). Erythrocytes were removed by osmotic lysis and the remaining mononuclear cell preparation was enriched for Sca-1$^+$ cells by immunomagnetic sorting using anti-Sca-1$^+$ microbeads (Miltenyi Biotech, Inc., Auburn, CA, USA).

MLV-based modified vectors

The MLV-based vectors expressing the enhanced GFP marker gene (MLV-GFP), a modified human FGF2 gene (MLV-FGF2) or a modified BMP2/4 gene (MLV-BMP2/4) were constructed as previously described [15,19]. In the human BMP4 transgene, the majority of native BMP4 signal peptide was replaced with the BMP2 signal peptide to enhance protein secretion (previously designated as pY-BMP2/4 [15]). The human FGF2 transgene was modified by adding the BMP2/4 secretion signal and by mutating two cysteines (i.e. Cys70 and Cys88) to serine and aspartic acid, respectively (previously designated as pY-BMPFGFC2S/C3N [19]).

LV-based modified vectors

Third-generation lentiviral vectors containing either the β-gal gene, GFP gene or BMP2/4 modified gene were produced by cotransfection of 293T cells with the four-plasmid system as previously described [8,20].

Viral transduction of Sca-1$^+$ cells

Sca-1$^+$ cells were plated in retronectin-coated plates (Takara, Otsu, Shiga, Japan) at a density of 4×10^6 cells/well in Iscove's modified Dulbecco's medium (Invitrogen, Grand Island, NY, USA) containing 20% fetal bovine serum (BioWhitaker, Walkersville, MD, USA), 50 ng/ml human flt-3L, 50 ng/ml murine stem cell factor, 50 ng/ml interleukin (IL)-6, 10 ng/ml murine IL-3, 0.1 ng/ml murine IL-1α (all from PeproTech, Rocky Hills, NJ, USA), 100 µmol/l dNTPs (Roche Diagnostics, Indianapolis, ID, USA), as described previously [8]. After overnight incubation, 40 µl of the respective concentrated viral stock [5×10^5 transforming units/μl] was applied to the cells. The medium was removed 8 h later, and the transduction was repeated once. Cells were transplanted into recipient mice 12–20 h after transduction.

Transplantation

The Sca-1$^+$ transplantation procedure was carried out as described previously [8]. Briefly, W^{41}/ W^{41} recipient mice were preconditioned by total body irradiation, and donor Sca-1$^+$ cells (350 000–500 000 cells) were transplanted into anaesthetized mice 4 h after irradiation via retro-orbital injection. Previous studies indicated that delivery via retro-orbital plexus results in higher donor cell engraftment and reduced variation compared to tail vein injection [8]. Engraftment was assessed at the indicated time points as the percentage of GFP-expressing mononuclear cells in the peripheral blood of recipient mice by analysis with a FACSCalibur System (BD Biosciences, San Jose, CA, USA).

Quantitative real-time polymerase chain reaction (PCR) and reverse transcriptase (RT)- PCR

Total DNA was isolated from cells using the Qiagen QIAamp DNA Blood Mini Kit (Qiagen, Valencia, CA, USA). Total RNA was isolated from cells, contaminating DNA was removed using the Qiagen RNeasy Mini kit and cDNA was synthesized with the Superscript II RT first strand synthesis system (Invitrogen, Carlsbad, CA, USA), 250 ng random hexamer primers and 160 ng total RNA in a 20-µl volume. Real-time PCR reactions were performed with 2 µl DNA or cDNA, 10 pmol of each primer set, and HotStarTaq DNA Polymerase using a QuantiTect SYBR Green PCR Kit (Qiagen) in an Opticon DNA Engine (MJ Research/Bio-Rad, Hercules, CA, USA). Primer sets used to create amplicons specific for coding sequences of the human transgenes were: FGF2 (accession no. NM_002 006.2) [forward (position 511): 5′-GGC TTC TTC CTG CGC ATC CA-3′, reverse (position 833) 5′-GCT TTC TGC CCA GGT CCT GT-3′] and BMP2/4 (accession no. NM_001 200.2) (BMP2) [forward (position 598) 5′-AAT GCA AGC AGG TGG GAA AGT-3′] (accession no. NM_130 851.2) (BMP4) [reverse (position 953) 5′-CTG AAG TCC ACA TAG AGC GAG-3′]. To normalize the data, a primer set specific to mouse peptidylproplyl isomerase A (Ppia) (accession no. NM_008 907.1), a housekeeping gene, [forward (position 314) 5′-GCA TAC AGG TCC TGG CAT CT-3′, reverse (position 501) 5′-TGC TGG TCT TGC CAT TC-3′] was used. DNA and mRNA abundances were quantified as the critical cycle threshold (ΔC_T) method: C_T of the gene-of-interest – C_T of Ppia, based on the assumption that cell Ppia DNA and mRNA levels are constant and RT and PCR reaction efficiencies are constant. Results were shown as the mean ± SEM of duplicates, with the difference in one cycle representing a two-fold difference in relative mRNA abundance. Fold changes in mRNA levels were calculated by the $2^{-\Delta\Delta}C_T$ method [21].

To compare relative transgene expression levels in the bone marrow cells of recipient mice transplanted with FGF2-expressing Sca-1$^+$ cells with those of recipient mice receiving BMP4-expressing cells, a standard curve method was used to determine the number of mRNA copies of respective transgene [22] to avoid the confounding issue of potential variations in priming efficiencies of different primer sets. A standard curve for the human FGF2, human BMP2/4 and murine Ppia cDNA was constructed by plotting respective C_T values against known amounts

DOI: 10.1002/jgm

of the human FGF2, human BMP2/4 or murine Ppia cDNA plasmid standards. The relative transgene expression was determined from each respective standard curve and converted to number of mRNA molecules using the formula: number of molecules = pg nucleic acid × Avogadro's number/plasmid molecular weight. Data are presented normalized to the number of mRNA molecules of the housekeeping gene Ppia and expressed as number of transgene mRNA molecules per 1×10^6 molecules of Ppia mRNA.

Serum and bone extract AP analysis

Serum AP activity was measured using a Hitachi 912 Clinical Chemistry analyser (Stratec SA Plus, White Plains, NY, USA). Proteins from tibiae of recipient mice were extracted in 500 ml of 0.05% TRITON X-100 and bone extract AP activity was assayed by a colorimetric assay as described previously [23] and normalized against cellular protein level determined by the Pierce BCA assay (Thermo Scientific, Waltham, MA, USA).

pQCT measurements

Cross-sectional and volumetric bone parameters (total, trabecular, and cortical vBMD, bone mineral content (BMC), bone volume (BV) cortical thickness, and periosteal and endosteal circumferences) were measured using an XCT 960M with XCT software, version 5.40 (Roche Diagnostics, Basel, Switzerland) as previously described [10,24].

μCT measurements

The trabecular bone architecture of the distal femoral metaphysic region of recipient mice was assessed using high resolution μCT (10 µm voxel size) (VivaCT40, Scanco Medical AG, Switzerland). A threshold of 200 was used and 200 (10.5 µm) transverse CT slices were performed in the region 360 µm proximal to the growth plate and extending an additional 2100 µm proximally. Parameters measured were bone volume fraction (BV/total volume, %), trabecular thickness, trabecular number, trabecular separation, connectivity density and structure model index.

Western immunoblot analysis

Protein was extracted from 500 000 Sca-1^+ cells transduced with LV-based vectors containing the enhanced GFP or BMP2/4 hybrid gene, 48 h post transduction. Lysate proteins were fractionated on a 12% polyacrylamide-sodium dodecyl sulfate gel and transblotted onto a 0.2-µm polyvinylidene fluoride membrane (Bio-Rad). The membrane was blocked with 1% skim milk, and blotted with 1 µg/ml monoclonal anti-human BMP4 antibody (R&D Systems, St Paul, MN, USA) and with 1 : 1000-diluted horseradish peroxidase (HRP)-labeled goat anti-mouse immunoglobulin G (Pierce, Rockford, IL, USA). The BMP4 protein band was then visualized with the SuperSignal West Pico Chemiluminescent Substrate kit (Pierce).

BMP4 bioactivity assay

The biological activity of secreted recombinant BMP4 was assessed by measuring the ability of conditioned media (CM) from cell cultures of LV-BMP2/4-transduced Sca-1^+ cells to stimulate AP activity in murine C2C12 myoblastic cells, using a protocol [15] adapted for Sca-1^+ cells. Briefly, Sca-1^+ cells were transduced with either the LV-BMP2/4 or LV-GFP vector as described above. After 4 days, an aliquot (100 µl) of serially diluted CM samples in triplicate were applied to C2C12 cells, which had been seeded 48 h previously at a density of 250 cells/mm^2. After 72 h, cell extracts were prepared in 0.05% Triton X-100. The AP enzymatic activity in the C2C12 cell extracts was determined by measuring production of *p*-nitrophenolate from *p*-nitrophenylphosphate using the Sigma Diagnostics AP kit (Sigma-Aldrich). The ability of known amounts of recombinant human BMP4 protein (i.e. 10, 50 and 100 ng/ml) to stimulate AP activity in C2C12 cells after 24 h was also determined in a parallel experiment for comparison.

Statistical analysis

Comparison of differences between two variables was performed using the two-tailed, two-sample with equal variances independent *t*-test. Comparison of multiple groups was performed with one-way analysis of variance (ANOVA) or two-way ANOVA with Tukey's HSD post-hoc testing as appropriate. Because normal distribution of measurements of C_T and ΔC_T in real time PCR and RT-PCR experiments could not be assumed, significance was confirmed by the Mann–Whitney nonparametric test. $p < 0.05$ was considered statistically significant. All data are reported as the mean ± SEM.

Results

Transplantation of LV-BMP2/4-transduced Sca-1^+ cells into sublethally irradiated W^{41}/W^{41} recipient mice

To evaluate whether the Sca-1^+ cell-based systemic BMP4 *ex vivo* gene transfer strategy is effective in promoting endosteal bone formation in recipient mice, we transplanted Sca-1^+ donor cells (350 000 cells per mouse) from TgN-GFP mice that were transduced with an LV-based vector expressing either the BMP2/4 gene or β-gal control gene into two groups of eight

DOI: 10.1002/jgm

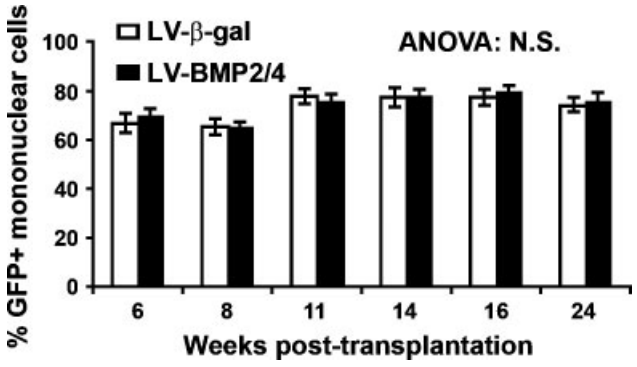

Figure 1. Engraftment of Sca-1$^+$ cells transduced with LV-based vectors in W^{41}/W^{41} recipient mice preconditioned by sublethal irradiation. Engraftment was reflected by the percentage of GFP-positive mononuclear cells in peripheral blood at the indicated time points post-transplantation. The results are shown as the mean ± SEM with $n = 6$ for LV-β-gal group and $n = 7$ for LV-BMP2/4 group. Analysis by two-factor ANOVA revealed no significant differences (NS; $p > 0.05$) between the two treatment groups at any of the test time points

recipient mice. The TgN-GFP strain was used as the source of donor cells to allow for quantification of engraftment after transplantation, whereas the W^{41}/W^{41} strain was used as recipients to achieve high engraftment efficiency with reduced irradiation preconditioning [8]. LV-based vectors were used in the present study because these vectors are considered to be more effective in transducing HSCs than MLV-based vectors [25]. Peripheral blood was obtained through retro-orbital vein under anesthesia at 6, 8, 11, 14, 16 and 24 weeks post-transplantation from each recipient mouse, and engraftment was determined by measuring the percentage of GFP-expressing mononuclear cells. One recipient mouse of the LV-β-gal group died from anesthesia during transplantation and one mouse from each group showed low engraftment levels (<45% chimerism), presumably as a result of technical variation associated with the retro-orbital injection, and were excluded from the study. The Sca-1$^+$ cell-based transplantation strategy yielded high levels (70–80%) of chimerism, and the expression of the human BMP4 transgene did not significantly affect engraftment (Figure 1). Furthermore, the level of chimerism in mice receiving Sca-1$^+$ cells transduced with LV-based vectors was similar to that in mice transplanted with MLV vector-transduced Sca-1$^+$ cells and those with untransduced Sca-1$^+$ cells [8,10], indicating that transduction with LV-based vectors or BMP4 overexpression does not adversely affect the engraftment of Sca-1$^+$ cells.

To confirm effective engraftment and expansion of BMP4-expressing Sca-1$^+$ cells in the recipient mice, we measured the incorporation of the BMP2/4 DNA plasmid into the genome of the recipients' peripheral blood cells (at 8 weeks post-transplantation) and BM cells (at 26 weeks post-transplantation) using real-time PCR. The results from these studies using a primer set specific for the human BMP4 gene are reported in Table 1 as ΔC_T (C_T of human BMP4 – C_T of murine Ppia). The ΔC_T of the human BMP4 gene in the DNA of peripheral blood cells at 8 weeks and the DNA of BM cells at 26 weeks of mice transplanted with the LV-BMP2/4-transduced Sca-1$^+$ cells were each significantly less than that of corresponding cells of recipient mice of LV-β-gal-transduced Sca-1$^+$ cells. These reductions in ΔC_T correspond to approximately 400-fold and 900-fold increases, respectively, in the BMP4 DNA content in peripheral blood cells and BM cells of recipient mice of the LV-BMP2/4 group compared to the levels observed in controls (i.e. background noise as a result of inter-species cross reactivity). To confirm an increase in BMP2/4 gene expression, we also measured the relative BMP4 mRNA levels in BM cells 26 weeks post-transplantation by real-time RT-PCR. The recipient mice of LV-BMP2/4-transduced Sca-1$^+$ cells had an approximately 1900-fold increase in the BMP4 mRNA level compared to control recipient mice of the LV-β-gal-transduced cells (Table 2). The presence of high levels of human BMP4 DNA and mRNA in the bone marrow of the recipient mice 6 months after transplantation indicate that: (i) Sca-1$^+$ cells were successfully transduced with the LV-BMP2/4 vector; (ii) after intravenous injection, the transduced cells established long-term engraftment in the bone marrow cavity of the recipient animals; and (iii) BMP2/4 transgene expression by the engrafted cells persisted for at least 6 months after transplantation.

Table 1. Determination of the relative gene copies of human BMP4 DNA in peripheral blood cells and bone marrow cells of recipient mice by real-time PCR

Group	C_T for BMP4 DNA	C_T for Ppia DNA	ΔC_T	Fold differences versus LV-β-gal group*	Mann–Whitney nonparametric test
Peripheral blood cells at 8 weeks					
LV-β-gal	34.08 ± 0.72**	19.25 ± 0.17	14.83 ± 0.84	–	–
LV-BMP2/4	25.55 ± 0.32	19.41 ± 0.13	6.14 ± 0.35	413-fold	$P < 0.004$
Bone marrow cells at 26 weeks					
LV-β-gal	33.89 ± 0.40**	17.67 ± 0.12	16.22 ± 0.43	–	–
LV-BMP2/4	24.69 ± 0.42	18.24 ± 0.13	6.42 ± 0.36	871-fold	$P < 0.004$

The results are reported as C_T and ΔC_T (mean ± SEM, with $n = 6$ for the LV-β-gal group and $n = 7$ for the LV-BMP2/4 group). *Fold differences compared to the LV-β-gal group were calculated by the $2^{-\Delta\Delta C_T}$ method [21]. **C_T > 30 cycles represent the basal 'noise' value of our RT-PCR analysis and the levels may be considered as insignificant.

DOI: 10.1002/jgm

Table 2. Determination of the relative human BMP4 mRNA levels in bone marrow cells of recipient mice at 26 weeks post-transplantation by real-time RT-PCR

Group	BMP4 mRNA (C_T)	Ppia mRNA (C_T)	ΔC_T	Fold differences versus LV-β-gal group*	Mann–Whitney nonparametric test
LV-β-gal	33.91 ± 0.16**	21.86 ± 0.19	12.05 ± 0.29	–	–
LV-BMP2/4	23.16 ± 1.16	21.98 ± 0.33	1.18 ± 1.22	1,874-fold	$P < 0.004$

The results are reported as C_T and ΔC_T (mean $\pm$ SEM, with $n = 6$ for the LV-β-gal group and $n = 7$ for the LV-BMP2/4 group). *Fold differences compared to the LV-β-gal group was calculated by the $2^{-\Delta\Delta C_T}$ method [21]. **$C_T > 30$ cycles represent the basal 'noise' value of our RT-PCR analysis and the levels may be considered as insignificant.

Effects of Sca-1$^+$ cell-based LV-BMP2/4 *ex vivo* gene transfer strategy on endosteal bone formation

To assess bone effects of the Sca-1$^+$ cell-based LV-BMP2/4 gene transfer strategy, all recipient mice were euthanized 26 weeks post-transplantation. Blood samples were collected for measurement of serum AP (a marker of bone formation) and tibias were removed for evaluation of bone AP activity. Figure 2 shows that, although both serum and tibial AP activity of the recipient mice of the LV-BMP2/4 group were slightly higher (approximately 10% and 20%, respectively) than those of the recipient mice of the LV-β-gal group, these increases were not statistically significant. These findings suggest that bone formation was only minimally enhanced by the transplantation of Sca-1$^+$ cells overexpressing BMP4.

pQCT analyses of BMD and bone size parameters of femurs revealed that, with the exception of a significant 17% increase ($p < 0.020$) in trabecular BMD, the total and cortical BMD, cortical thickness, periosteal circumference and endosteal circumference of the femurs of recipient mice of LV-BMP2/4-transduced Sca-1$^+$ cells were not significantly different from the femurs of control mice. Total, trabecular and cortical BMC in receipient mice of LV-BMP2/4-transduced Sca-1$^+$ cells were also not increased (Table 3). The lack of a large increase in cortical thickness and/or the absence of a significant reduction in endosteal circumference by the transplantation of LV-BMP2/4-transduced Sca-1$^+$ cells do not support a substantial increase in endosteal bone formation. Three-dimensional analyses of bone parameters of these same femurs by μCT (Table 4) also showed no significant differences in any of the measured μCT parameters between the LV-BMP2/4 and the LV-β-gal groups of recipient mice. Thus, the Sca-1$^+$ cell-based systemic BMP4 gene therapy strategy, unlike the FGF2-based strategy [10], did not result in extensive endosteal bone formation in recipient mice.

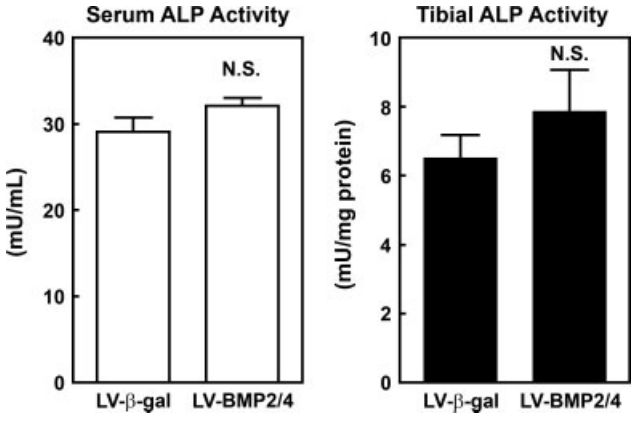

Figure 2. Serum and tibial AP activity in recipient mice transplanted with LV-BMP2/4- or LV-β-gal-transduced Sca-1$^+$ cells 26 weeks post-transplantation. Serum AP activity (left panel) and AP activity in tibial extract (right panel) of six recipient W^{41}/W^{41} mice transplanted with LV-β-gal-transduced Sca-1$^+$ cells and seven recipient W^{41}/W^{41} mice transplanted with LV-BMP2/4-transduced Sca-1$^+$ cells after 26 weeks were assayed. The results are shown as the mean ± SEM. Serum AP activity is shown as mU/ml; whereas tibial AP activity is reported as mU/mg cellular protein. A two-tailed Student's *t*-test revealed no significant differences (NS) between the two groups in serum AP activity or in tibial AP activity

Effects of Sca-1$^+$ cell-based MLV-BMP2/4 gene transfer strategy on endosteal bone formation

Our previous study with the FGF2-based strategy employed MLV-based vectors [10]. Therefore, to rule out the remote possibility that the lack of a sizable enhancing effect of the LV-BMP2/4-based strategy on bone formation was a result of the use of LV-based vectors, we next performed a study to compare the effects of the MLV-BMP2/4-based strategy with those of the MLV-FGF2-based strategy. In this study, approximately 500 000 Sca-1$^+$ cells from wild-type C57BL/6J donor mice, transduced with either the MLV-BMP2/4, MLV-FGF2 or MLV-GFP vector, were transplanted intravenously into three groups ($n = 8$ per group) of recipient mice. Effective engraftment of the transduced cells was confirmed by the finding of high chimerism of GFP-expressing cells in the peripheral blood of recipient mice transplanted with MLV-GFP-transduced cells (data not shown). At 16 weeks post-transplantation, all recipient mice were euthanized for serum and tibial AP activity as well as pQCT measurements. Average tibial AP activity in the bones of mice transplanted with MLV-BMP2/4-transduced cells was increased compared to mice in the MLV-GFP control group; however, this increase was not statistically significant (2.57 ± 0.20 versus 2.22 ± 0.20, $p =$ N.S.). By contrast, mice that received MLV-FGF2-transduced cells showed a 73% increase in tibial AP activity compared

DOI: 10.1002/jgm

Table 3. pQCT measurements of BMD and bone size parameters of recipient mice transplanted with LV-BMP2/4-transduced Sca-1$^+$ cells compared to those of recipient mice transplanted with LV-β-gal-transduced Sca-1$^+$ cells 26 weeks post-transplantation (mean ± SEM)

	Total BMD (mg/mm^3)	Total BMC (mg)	Trabecular BMD (mg/mm^3)	Trabecular BMC (mg)	Cortical BMD (mg/mm^3)	Cortical BMC (mg)	Cortical thickness (mm)	Periosteal circumference (mm)	Endosteal circumference (mm)
LV-β-gal ($n = 6$)	0.770 ± 0.013	31.83 ± 0.81	0.266 ± 0.011	4.02 ± 0.20	1.106 ± 0.012	26.68 ± 0.78	0.328 ± 0.007	5.674 ± 0.081	3.612 ± 0.103
LV-BMP2/4 ($n = 7$)	0.790 ± 0.014	29.61 ± 0.68	0.312 ± 0.013	4.13 ± 0.24	1.094 ± 0.022	24.41 ± 0.71	0.322 ± 0.006	5.476 ± 0.075	3.454 ± 0.089
p^*	NS	NS	0.020	NS	NS	0.05	NS	NS	NS

*Statistical significance was determined by two-tailed Student's t-test. NS, not significant (i.e. $p > 0.05$).

to controls (3.84 ± 0.72 versus 2.22 ± 0.20, $p < 0.05$). There were no significant differences in serum AP activity among the three groups of recipient mice (data not shown). Consistent with previous findings [10], Figure 3 shows that the average trabecular BMD of femurs of recipient mice transplanted with cells expressing FGF2 was significantly increased (2.2-fold) over that of control mice (556 ± 114 versus 249 ± 9 mg/mm^3, respectively, $p < 0.002$). Conversely, mice transplanted with Sca-1$^+$ cells transduced with MLV-BMP2/4 showed only a modest but not statistically significant increase (by approximately 8%) in the average trabecular BMD compared to the GFP control recipient mice (270 ± 15 versus 249 ± 9 mg/mm^3, respectively, $p =$ not significant). Similar to what we observed in the LV-based BMP2/4 study (Table 3), there were also no significant differences in pQCT parameters between the femurs of recipient mice of the MLV-BMP2/4 group and those of the MLV-GFP control group (data not shown). Thus, the lack of an enhancing effect of the Sca-1$^+$ cell-based BMP2/4 strategy on endosteal bone formation was not a result of the use of LV-based vectors to transduce donor Sca-1$^+$ cells.

BMP4 transgene expression in recipient mice transplanted with MLV-BMP2/4-transduced Sca-1$^+$ cells

To test whether the lack of a large enhancing effect on endosteal bone formation with the Sca-1$^+$ cell-based BMP4 *ex vivo* gene transfer strategy was a result of reduced engraftment (and/or expansion) of MLV-BMP4-expressing Sca-1$^+$ cells in recipient mice compared to those of FGF2-expressing Sca-1$^+$ cells, we measured the relative levels of human BMP4 and human FGF2 mRNA in BM cell extracts of recipient mice transplanted with MLV-BMP2/4- and MLV-FGF2-transduced Sca-1$^+$ cells, respectively, 16 weeks post-transplantation by real-time RT-PCR. To correct for potential differences in priming efficiencies of the respective primers, the results are shown as the number of molecules of transgene mRNA per million molecules of mRNA of a housekeeping gene (Ppia mRNA) (Table 5). As in previous studies [10], large variations in transgene expression were observed with each of the transplantation groups, particularly the MLV-FGF2 group. In spite of the large intra-group variation, FGF-2 mRNA levels were significantly increased in mice transplanted with FGF-2-transduced cells compared to mice transplanted with MLV-GFP-transduced cells and those with MLV-BMP2/4-transduced cells (approximately 2500-fold and 1600-fold, respectively). The BMP4 mRNA levels were also significantly increased (approximately 4000-fold and 1000-fold, respectively) in BM cells of recipient mice transplanted with MLV-BMP2/4-transduced Sca-1$^+$ cells compared to those of mice in the MLV-GFP group and those in the MLV-FGF2 group. These findings indicate that the relative level of engraftment and/or expansion of BMP4-expressing cells in BM of MLV-BMP4 recipient mice were not reduced compared to that

DOI: 10.1002/jgm

Table 4. μCT measurements of femurs of recipient mice transplanted with LV-BMP2/4-transduced Sca-1$^+$ cells compared to those of recipient mice transplanted with LV-β-gal-transduced Sca-1$^+$ cells 26 weeks post-transplantation (mean ± SEM)

Group	TV (mm^3)	BV (mm^3)	% BV/TV	Conn-Dens. (mm^3)	TRI-SMI (unit)	DT-Tb.N	DT-Tb.Th (mm)	DT-Tb.Sp (mm)
LV-β-gal ($n = 6$)	2.93 ± 0.09	0.212 ± 0.010	7.24 ± 0.35	58.1 ± 7.3	2.82 ± 0.07	3.48 ± 0.09	0.046 ± 0.001	0.28 ± 0.01
LV-BMP2/4 ($n = 7$)	2.86 ± 0.08	0.182 ± 0.020	6.38 ± 0.63	48.6 ± 6.7	2.85 ± 0.10	3.25 ± 0.10	0.046 ± 0.001	0.31 ± 0.01
p^{**}	NS	NS	NS	NS	NS	NS	NS	NS

TV, total volume; BV, bone voume; % BV/TV, relative bone volume percentage; Conn-Dens, connectivity density normalized by TV; TRI-SMI, structural model (0 for parallel plates, 3 for cylindrical rods); DT-Tb.N, trabecular number; DT-Tb.Th, trabecular thickness; DT-Tb.Sp, trabecular separation. **Statistical significance was determined by two-tailed Student's *t*-test. NS, not significant (i.e. $p > 0.05$).

of FGF2-expressing cells in the MLV-FGF2 group and in fact were approximately two-fold greater (Table 5). Thus, the lack of significant effects on endosteal bone formation observed in mice transplanted with MLV-BMP2/4-transduced cells was unlikely to be a result of poor engraftment and/or expansion of BMP4-expressing cells.

Relative amounts and biological activity of BMP4 protein secreted by retroviral transduced Sca-1$^+$ cells

To determine that the lack of a robust enhancing effect on endosteal bone formation in recipient mice of BMP4-expressing Sca-1$^+$ cells was not a result of ineffective production and/or secretion of mature, functionally active BMP4 protein by the BMP2/4-expressing Sca-1$^+$ cells, we measured the amounts of mature BMP4 protein produced by LV-BMP2/4-transduced Sca-1$^+$ cells by western immunoblot analysis. Cell lysates of LV-BM2/4-transduced, but not LV-GFP-transduced, Sca-1$^+$ cells contained substantial amounts (approximately 5 ng/500 000 cells) of a single immunoreactive protein band recognized by the anti-BMP4 antibody that has a molecular size similar to that of the recombinant BMP4 protein standard (Figure 4A). Next, to determine whether the BMP4 protein secreted from LV-BMP2/4-transduced Sca-1$^+$ cells was functionally active, we assayed the biological activity of the BMP4 protein in the CM using the mouse C2C12 myoblastic cell-based bioassay. This bioassay is frequently used to determine the biological activity of BMPs and is based on the principal that primitive C2C12 myoblastic cells are induced by BMPs to differentiate along the osteogenic linage as evidenced by production of AP [26–28]. As shown in Figure 4B, the CM from the cultures of Sca-1$^+$ cells transduced with the LV-BMP2/4 vector, in contrast to the CM of LV-GFP-transduced cells, showed a dose-dependent stimulation of cellular AP activity in the C2C12 cells. The stimulation of AP activity in the same C2C12 cells by the known amounts of recombinant BMP4 protein after 48 h was also determined in a parallel experiment. It was found that 10, 50 and 100 ng/ml of BMP4, respectively, increased the AP activity of C2C12 cells to 150%, 222% and 394% of the vehicle-treated control ($p < 0.001$, ANOVA). Therefore, the greater than 20-fold increase in AP activity by the undiluted CM indicated that the amounts of biologically active BMP4 in the CM was much greater than 100 ng/ml. These findings suggest that Sca-1$^+$ cells transduced with a retroviral vector expressing BMP2/4 were capable of producing and secreting substantial amounts of biologically active BMP4 protein.

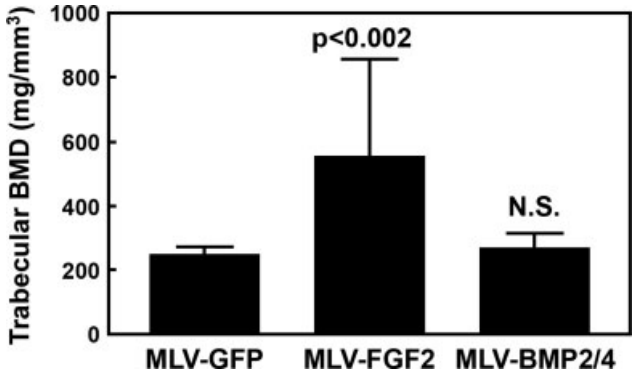

Figure 3. Total trabecular BMD in recipient mice transplanted with MLV-BMP2/4, MLV-FGF2- or MLV-GFP-transduced Sca-1$^+$ cells at 16 weeks post-transplantation. Trabecular BMD was measured by pQCT. Each test group contained eight mice. One-way ANOVA showed no significant difference (NS) between the MLV-BMP2/4 group and the MLV-GFP control group, but a highly significant difference ($p < 0.002$) between the MLV-FGF2 group and the MLV-GFP control group

Discussion

In previous studies, direct injection of bone marrow stromal cells transduced with the MLV-based BMP2/4 vector into the femoral marrow cavity of recipient mice induced new bone formation along the endosteal surface [29]. However, this effect was small, presumably because donor cells (and therefore transgene expression) were not maintained in the marrow cavity for more than 14 days after injection. In the present study, we have demonstrated that transplantation of Sca-1$^+$ cells transduced with LV-BMP2/4 in W^{41}/W^{41} recipient mice yielded high, long-term engraftment of donor cells in the bone marrow cavity of the recipient mice. Furthermore, engraftment kinetics of the LV-BMP2/4 donor cells were similar to those of the LV-β-gal donor cells and, at 26 weeks post-transplantation, mice engrafted with the LV-BMP2/4-transduced cells had an approximately 900-fold increase in the relative BMP4 gene content in the

DOI: 10.1002/jgm

Table 5. Relative mRNA levels of the human FGF-2 and human BMP4 transgenes in bone marrow extracts of recipient mice transplanted with MLV-GFP-, MLV-FGF2- or MLV-BMP2/4-transduced Sca-1$^+$ cells 16 weeks post-transplantation (mean ± SEM)

Group	Relative FGF2 mRNA level (FGF2 mRNA molecules/million Ppia mRNA molecules)*	Relative BMP4 mRNA level (BMP4 mRNA molecules/million Ppia mRNA molecules)**
MLV-GFP ($n = 8$)	0.76 ± 0.5	1.14 ± 0.23
MLV-FGF2 ($n = 8$)	$1893 \pm 371^{\dagger}$	4.93 ± 2.67
MLV-BMP2/4 ($n = 8$)	1.16 ± 0.65	$5002 \pm 2.432^{\ddagger}$

*FGF2 mRNA levels were determined by real-time RT-PCR, using the standard curve method [19] with FGF2 cDNA to construct a standard curve, and the results were shown as molecules of FGF2 mRNA per million molecules of the housekeeping gene (Ppia) mRNA; **BMP4 mRNA levels were determined by real-time RT-PCR, using the standard curve method [19] with BMP4 cDNA to construct a standard curve, and the results are shown as molecules of BMP4 mRNA per million molecules of the housekeeping gene (Ppia) mRNA. †One-way ANOVA analysis: $p < 0.005$ compared to GFP and BMP2/4 groups. ‡One-way ANOVA analysis: $p < 0.008$ compared to GFP and FGF2 groups.

genome of BM cells and an approximately 1900-fold increase in the relative levels of BMP4 mRNA compared to control mice. Yet, in spite of the successful engraftment and long duration of significant transgene expression by the donor cells, transplantation of BMP4-expressing Sca-1$^+$ cells did not lead to large increases in endosteal bone formation. Accordingly, although we observed insignificant increases in serum and bone AP activity, and a small but significant increase in the trabecular BMD in recipient mice of LV-BMP2/4-transduced Sca-1$^+$ cells compared to control mice, there were no significant differences in any of the other pQCT or μCT measurements of bone mass, density or size between the two groups. Thus, even if the Sca-1$^+$ cell-based BMP4 *ex vivo* gene transfer strategy had osteogenic effects on endosteal bone formation, these effects were marginal. Consequently, unlike the FGF-2-based strategy [10], the Sca-1$^+$ cell-based BMP4 *ex vivo* gene transfer strategy was ineffective in promoting endosteal bone formation in recipient mice.

The lack of a large bone formation effect with the BMP4-based strategy is interesting; but it is also somewhat surprising, given that: (i) in the rat fracture model, intramedullary delivery of MLV-BMP2/4 vector to the femur was shown to significantly enhance bone formation at the fracture site [30] and (ii) there is recent evidence that HSC-derived BMP2 and BMP6 have regulatory roles in the HSC-mediated induction of mesenchymal stromal cells into osteoblasts within the HSC niche at the endosteum in response to stresses [31]. The mechanistic reason(s) for the apparent lack of a robust endosteal bone formation response in recipient mice of BMP4-expressing Sca-1$^+$ cells is unclear. It did not appear to be a result of the use of LV-based rather than MLV-based vectors to transduce the cells because transplantation of MLV-BMP2/4-transduced Sca-1$^+$ cells into recipient mice also did not yield significant endosteal bone formation. The lack of extensive endosteal bone formation was also not likely to be a result of inefficient BMP4 expression by engrafted transduced cells compared to FGF2 expression by engrafted FGF2-expressing Sca-1$^+$ cells. Based on the 97% homology observed between amino acid sequences of the human and murine BMP proteins [32], it is also unlikely that the lack of effect was a result of inter-species protein differences. Furthermore, the fact that the CM of LV-BMP2/4-transduced Sca-1$^+$ cells was able to induce transdifferentiation of murine C2C12 cells into osteoblastic cells indicates that the secreted BMP4 protein was biologically active. This would imply that the lack of a robust endosteal bone formation effect *in vivo* was not a result of the inability of the engrafted Sca-1$^+$ cells to secrete functionally active protein. Consequently, these observations, when taken together, lead to our tentative conclusion that there are significant intrinsic differences between the Sca-1$^+$ cell-based BMP4 *ex vivo* gene transfer strategy and the FGF2 strategy that led to the observed differences in their ability to promote endosteal bone formation in recipient mice under our experimental conditions.

Although the potential intrinsic differences between the BMP4 strategy and the FGF2 strategy are not clear, there are at least two well known disparities between FGF2-mediated bone formation and BMP4-induced bone formation that might, in part, contribute to the observed differential effects. First, FGF2 appears to be a relatively more potent stimulator of bone formation than BMP4 *in vivo* and *in vitro*. Effective *in vitro* dosages of FGF2 to stimulate osteoblast proliferation and bone formation are relatively low and in pM levels, whereas effective *in vitro* dosages of BMP4 to promote bone formation are two- to three-orders of magnitude greater and are frequently in nM levels [33]. Similarly, significantly lower amounts of FGF2 protein (i.e. in the range of μg/kg) compared to amounts of BMP4 protein (i.e. in the range of mg/kg) were required to elicit osteogenic responses in animal models [34,35]. Therefore, it is conceivable that although the engrafted Sca-1$^+$ cells expressed and secreted substantial amounts of functionally active BMP4 and FGF2, respectively, the amounts of BMP4 protein (contrary to the FGF2 protein) secreted by the engrafted Sca-1$^+$ cells in the bone marrow cavity of recipient mice might be insufficient to promote significant increases in endosteal bone formation. A quantitative comparison between circulating BMP4 and FGF2 levels in respective recipient mice would allow for better assessment of this possibility. However, although an enzyme-linked immunosorbent assay for BMP-4 is commercially available, the assay has not been validated for measurement of circulating BMP4 proteins without artifacts resulting from binding proteins. Therefore,

DOI: 10.1002/jgm

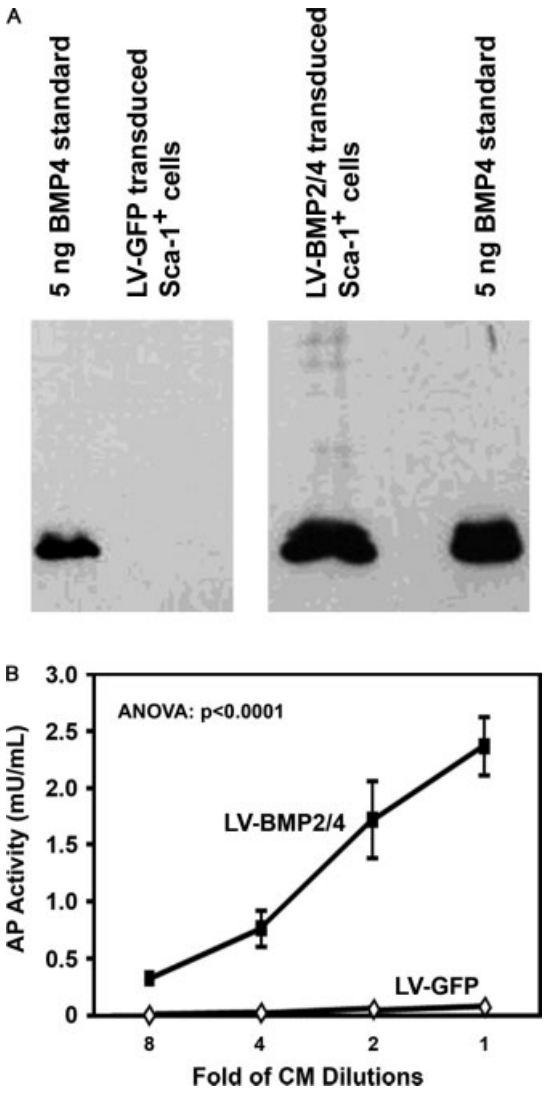

Figure 4. Western immunoblot analysis (A) and biological activity (B) for BMP4 protein produced by Sca-1$^+$ cells transduced with the LV-BMP2/4 vector or the LV-GFP control vector. Sca-1$^+$ cells were transduced with an LV-based vector expressing either the GFP control gene or the BMP2/4 gene *in vitro*. Cell extracts of the transduced cells were collected 48 h after the transduction, and the cellular content of BMP4 protein was measured by western immunoblots using a primary anti-BMP-4: monoclonal antibody and a secondary anti-mouse immunoglobulin G-HRP antibody (A). Recombinant human BMP4 protein standard (5 ng) was included in the western blots for comparison. CM from cell cultures of Sca-1$^+$ cells transduced with either the LV-BMP2/4 vector or LV-GFP control vector was collected and the respective serially diluted CM was added to six replicate wells of C2C12 myogenic cells. The cellular AP activity in each C2C12 cell culture was measured 72 h later (B) and the results are shown as the mean ± SEM. Statistical significance of the difference between the LV-BMP2/4 group and the LV-GFP control group was assessed by ANOVA

because of the difficulty of accurately assessing *in vivo* circulating BMP4 levels in the mouse model, we did not measure and/or compare the amounts of BMP4 protein versus FGF2 protein in the circulation or bone marrow cavity of respective recipient mice in the present study. However, our previous study with recipient mice of MLV-FGF2-induced Sca-1$^+$ cells [10] revealed that the serum FGF2 levels of the recipient mice were in the range of 1–6 ng/ml, with most of the mice exhibiting serum FGF2 levels of less than 1 ng/ml. These levels corresponded to less than 1 nM. There was approximately two-fold more BMP4 mRNA molecules than FGF2 mRNA molecules in the BM cells of the respective recipient mice. Assuming the translation efficiency of BMP4 and FGF2 mRNAs are similar, we would expect approximately twice as much BMP4 protein than FGF2 protein in the circulation and perhaps also in bone marrow cavity of respective recipient mice. This would suggest that the circulating BMP4 protein levels in recipient mice would be no more than 2 nM, which would be below the levels needed for inducing an osteogenic response *in vitro* [33]. Although this is an interesting possibility, additional work is needed to confirm that the engrafted transduced Sca-1$^+$ cells were indeed unable to produce sufficient amounts of BMP4 within the marrow niche to promote robust endosteal bone formation in recipient mice.

Another established difference between BMP4-induced bone formation and FGF2-mediated bone formation is that, in addition to its ability to stimulate the proliferation [36], survival [37] and osteogenic potential [38] of osteoprogenitors, FGF2 is also a well known potent stimulator of angiogenesis [39]. Angiogenesis has been demonstrated to play an essential role in bone regeneration and fracture repair [40], and suppression of angiogenesis with an inhibitor drastically impaired trabecular bone formation in a rabbit metaphysis implant model, implicating an important role of angiogenesis in trabecular bone formation [41]. Although BMPs, including BMP4, have been shown to induce vascular endothelial growth factor (VEGF) (an established stimulator of angiogenesis) expression in osteoblastic cells, *in vitro* [42], it is widely thought that BMP-mediated bone formation occurs primarily through stimulation of osteoblastic differentiation [43]. Thus, there is a possibility that, although the BMP4 protein produced by the engrafted Sca-1$^+$ cells is capable of promoting endosteal bone formation, massive increases in trabecular bone formation on the endosteum by the *ex vivo* gene transfer strategy may also require large increases in angiogenesis, which may be lacking in the BMP4 strategy. Consistent with this speculation, VEGF has been reported to have synergistic enhancing effects of BMP4-mediated bone formation [44]. This is a very interesting possibility, which will be addressed in our future studies aiming to determine whether the Sca-1$^+$ cell based *ex vivo* gene transfer strategy to express both BMP4 and VEGF in combination would have a more vigorous endosteal bone formation effect than the strategy with each single growth factor alone.

There are also other alternative possibilities that might provide potential mechanistic explanations for the lack of an endosteal bone formation response to the Sca-1$^+$ cell-based BMP4 *ex vivo* gene transfer strategy. In this regard, the cells that contribute to endosteal bone formation, although poorly defined, are generally assumed to be

DOI: 10.1002/jgm

stromal cells of the osteoblastic lineage, which are distinct from cells of the HSC lineage. There is a possibility that FGF2 and BMP4 each may act on different target cell types. Accordingly, FGF2 produced by the engrafted Sca-1$^+$ HSCs may act in a paracrine manner to stimulate various cell types, eventually leading to substantial recruitment, proliferation and osteogenic differentiation of stromal cells to yield massive endosteal bone formation. By contrast, the Sca-1$^+$ HSC-derived BMP4 may act on nearby stromal cells primarily to promote osteogenic differentiation, without enhancing recruitment and/or expansion of the stromal cell population, resulting in an insignificant increase in endosteal bone formation in the recipient mice. Alternatively, the optimal bone forming effects of BMP4 but not FGF2 at the endosteum may require some sort of injury or immunological challenge. Analogous to the heterotrophic bone formation observed in patients with fibrodysplasia ossificans progressive (a rare genetic disease with a constitutive BMP receptor), which occurs after physical trauma, surgery, viral illness or myositis [45], it is possible that optimal endosteal bone formation responses in BMP4-expressing Sca-1$^+$ recipient mice may also require skeletal challenges, such as fracture or infection. These interesting possibilities will be investigated in our future studies.

In summary, we have shown that, although the Sca-1$^+$ cell-based FGF2 *ex vivo* gene transfer strategy yielded robust endosteal bone formation in recipient mice, the same strategy delivering a BMP4 gene failed to produce significant amounts of endosteal bone formation. Although the exact mechanistic reasons for the lack of a sizable endosteal bone formation response are not yet determined, the present study clearly demonstrates that the appropriate choice of the bone growth factor gene to be delivered by this Sca-1$^+$ cell-based gene transfer strategy is a very important consideration.

Acknowledgements

This work was supported in part by a special appropriation to the Jerry L. Pettis Memorial VA Medical Center–Musculoskeletal Disease Center. All work, except the irradiation procedure, was performed in facilities provided by the Department of Veterans Affairs. The authors acknowledge the excellent technical assistance from Joshua Felt, Cynthia Dixon, Jann Smallwood, Mahita Kadmiel and Anil Kapoor (all from the Musculoskeletal Disease Center of the Jerry L. Pettis Memorial VA Medical Center), and Erban Bayeta (of the Department of Radiation Medicine, Loma Linda University).

References

1. Bouxsein ML. Biomechanics of age-related fractures. In *Osteoporosis*, 2nd edn, Marcus R, Feldman D, Kelsey J (eds), Vol. 1. Academic Press: San Diego, CA, 2001; 509–531.
2. Iwamoto J, Takeda T, Sato Y. Efficacy and safety of alendronate and risedronate for postmenopausal osteoporosis. *Curr Med Res Opin* 2006; **22**: 919–928.
3. Saag KG, Shane E, Boonen S, *et al*. Teriparatide or alendronate in glucocorticoid-induced osteoporosis. *N Engl J Med* 2007; **357**: 2028–2039.
4. Neer RM, Arnaud CD, Zanchetta JR, *et al*. Effect of parathyroid hormone (1–34) on fractures and bone mineral density in postmenopausal women with osteoporosis. *N Engl J Med* 2001; **344**: 1434–1441.
5. MacLean C, Newberry S, Maglione M, *et al*. Systematic review: comparative effectiveness of treatments to prevent fractures in men and women with low bone density or osteoporosis. *Ann Intern Med* 2008; **148**: 197–213.
6. Cosman F. Anabolic therapy for osteoporosis: parathyroid hormone. *Curr Osteoporos Rep* 2005; **3**: 143–149.
7. Vahle JL, Sato M, Long GG, *et al*. Skeletal changes in rats given daily subcutaneous injections of recombinant human parathyroid hormone (1–34) for two years and relevance to human safety. *Toxicol Pathol* 2008; **30**: 312–321.
8. Hall SL, Lau K-HW, Chen S-T, *et al*. An improved mouse Sca-1$^+$ cell-based bone marrow transplantation model for use in gene- and cell-based therapeutic studies. *Acta Haematol* 2007; **117**: 24–33.
9. Spangrude GI, Brooks DM, Tumas DB. Long-term repopulation of irradiated mice with limiting numbers of purified hematopoietic stem cells: in vivo expansion of stem cell phenotype but not function. *Blood* 1995; **85**: 1006–1016.
10. Hall SL, Lau K-HW, Chen S-T, *et al*. Sca-1$^+$ hematopoietic cell-based gene therapy with a modified FGF-2 gene increased endosteal/trabecular bone formation in mice. *Mol Therapy* 2007; **15**: 1881–1889.
11. Ryoo HM, Lee MH, Kim YJ. Critical molecular switches involved in BMP-2-induced osteogenic differentiation of mesenchymal cells. *Gene* 2006; **366**: 51–57.
12. Einhorn TA, Majeska RJ, Mohaideen A, *et al*. A single percutaneous injection of recombinant human bone morphogenetic protein-2 accelerates fractures fracture repair. *J Bone Joint Surg Am* 2003; **85**: 1425–1435.
13. Rundle CH, Miyakoshi N, Kasukawa Y, *et al*. In vivo bone formation in fracture repair by direct retroviral-based gene therapy with BMP-4. *Bone* 2003; **32**: 591–601.
14. Gysin R, Wergedal JE, Sheng MH-C, *et al*. Ex vivo gene therapy with stromal cells transduced with a retroviral vector containing the BMP4 gene completely heals critical size calvarial defect in rats. *Gene Therapy* 2002; **9**: 991–999.
15. Peng H, Chen S-T, Wergedal JE, *et al*. Development of an MFG-based retroviral vector system for high secretion of functionally active human BMP-4. *Mol Therapy* 2001; **4**: 95–104.
16. Reith AD, Rottapel R, Giddens E, *et al*. W mutant mice with mild or severe developmental defects contain distinct point mutations in the kinase domain of the c-kit receptor. *Genes Dev* 1990; **4**: 390–400.
17. Geissler EN, Russell ES. Analysis of the hematopoietic effects of new dominant spotting (W) mutations of the mouse. 1. Influence upon hematopoietic stem cells. *Exp Hematol* 1983; **11**: 452–460.
18. Soper BW, Duffy TM, *et al*. A genetically myeloablated MPS VII model detects the expansion and curative properties of as few as 100 enriched murine stem cells. *Exp Hematol* 1999; **27**: 1691–704.
19. Chen S-T, Gysin R, Kapur S, Baylink DJ, Lau K-HW. Modifications of the fibroblast growth factor-2 gene led to a marked enhancement in secretion and stability of the recombinant fibroblast growth factor-2 protein. *J Cell Biochem* 2007; **100**: 1493–1508.
20. Yam PY, Li S, Wu J, *et al*. Design of LV vectors for efficient gene delivery into human hematopoietic cells. *Mol Therapy* 2002; **5**: 479–484.
21. Livak KJ, Schmittgen TD. Analysis of relative gene expression data using real-time quantitative PCR and the $2^{-\Delta\Delta C}{}_T$ method. *Methods* 2001; **25**: 402–408.
22. Rundle CH, Strong DD, Chen S-T, *et al*. Retroviral-based gene therapy with cyclooxygenase-2 promotes the union of bony callus tissues and accelerates fracture healing in the rat. *J Gene Med* 2008; **10**: 229–241.
23. Farley JR, Hall SL, Herring S, Tarbaux NM. Two biochemical indices of mouse bone formation are increased, *in vivo*, in response to calcitonin. *Calcif Tissue Int* 1992; **50**: 67–73.
24. Wergedal JE, Ackert-Bicknell CL, Tsaih S-W, *et al*. Femur mechanical properties in the F2 progeny of an NZB/B1NJ × RF/J cross are regulated predominantly by genetic loci that regulate bone geometry. *J Bone Miner Res* 2006; **21**: 1256–1266.
25. Bai Y, Soda Y, Izawa K, *et al*. Effective transduction and stable transgene expression in human blood cells by a third-generation lentivial vector. *Gene Therapy* 2003; **10**: 1446–1457.

26. Franceschi RT, Wang D, Krebsbach PH, Rutherford RB. Gene therapy for bone formation: in vitro and in vivo osteogenic activity of an adenovirus expressing BMP7. *J Cell Biochem* 2000; **78**: 476–486.
27. Nishimura R, Kato Y, Chen D, *et al*. Smad5 and DPC4 are key molecules in mediating BMP-2-induced osteoblastic differentiation of the pluripotent mesenchymal precursor cell line C2C12. *J Biol Chem* 1998; **273**: 1872–1879.
28. Katagiri T, Yamaguchi A, Komaki M, *et al*. Bone morphogenetic protein-2 converts the differentiation pathway of C2C12 myoblasts into the osteoblast lineage. *J Cell Biol* 1994; **127**: 1755–1766.
29. Zhang XS, Linkhart TA, Chen S-T, *et al*. Local ex vivo gene therapy with bone marrow stromal cells expressing human BMP4 promotes endosteal bone formation in mice. *J Gene Med* 2004; **6**: 4–15.
30. Rundle CH, Chen S-T, Porte R, Wergedal JE, Lau K-HW. Retroviral-based BMP-4 in vivo gene transfer strategy with intramedullary viral delivery optimizes transgene expression in rat femur fractures. *Open Tissue Eng Regener Med J* 2008; **1**: 14–22.
31. Jung Y, Song J, Shiozawa Y, *et al*. Hematopoietic stem cells regulate mesenchymal stromal cell induction into osteoblasts thereby participating in the formation of the stem cell niche. *Stem Cells* 2008; **26**: 2042–2051.
32. Katoh Y, Katoh M. Comparative genomics on BMP4 othrologs. *Int J Oncol* 2005; **27**: 581–585.
33. Varkey M, Kucharski C, Hague T, Sebald W, Uludağ H. In vitro osteogenic response of rat bone marrow cells to bFGF and BMP-2 treatments. *Clin Orthop Relat Res* 2006; **443**: 113–123.
34. Varkey M, Kucharski C, Doschak MR, *et al*. Osteogenic response of bone marrow stromal cells from normal and ovariectomized rats treated with a low dose of basic fibroblast growth factor. *Tissue Eng* 2007; **13**: 809–817.
35. Herford AS, Boyne PJ. Reconstruction of mandibular continuity defects with bone morphogenetic protein-2 (rhBMP-2). *J Oral Maxillofac Surg* 2008; **66**: 616–624.
36. Benavente CA, Sierralta WD, Conget PA, Minguell JJ. Subcellular distribution and mitogenic effect of basic fibroblast growth factor in mesenchymal uncommitted stem cells. *Growth Factors* 2003; **21**: 87–94.
37. Bianchi G, Banfi A, Mastrgiacomo M, *et al*. Ex vivo enrichment of mesenchymal cell progenitors by fibroblast growth factor 2. *Exp Cell Res* 2003; **287**: 98–105.
38. Baddoo M, Hill K, Wilkinson R, *et al*. Characterization of mesenchymal stem cells isolated from murine bone marrow by negative selection. *J Cell Biochem* 2003; **89**: 1235–1249.
39. Presta M, Dell'Era P, Mitola S, *et al*. Fibroblast growth factor/fibroblast growth factor receptor system in angiogenesis. *Cytokine Growth Factor Rev* 2005; **16**: 159–178.
40. Carvalho RS, Einhorn TA, Lehmann W, *et al*. The role of angiogenesis in a murine tibial model of distraction osteogenesis. *Bone* 2004; **34**: 849–861.
41. Mair B, Fuerst G, Kubitzky P, *et al*. The anti-angiogenic substance TNP-470 impairs peri-implant bone formation: a pilot study in the rabbit metaphysis model. *Clin Oral Implants Res* 2007; **18**: 370–375.
42. Deckers MM, van Bezooijen RL, van der Horst G, *et al*. Bone morphogenetic proteins stimulate angiogenesis through osteoblast-derived vascular endothelial growth factor A. *Endocrinology* 2002; **143**: 1545–1553.
43. Yamaguchi A, Komori T, Suda T. Regulation of osteoblast differentiation mediated by bone morphogenetic proteins, hedgehogs, and Cbfa1. *Endocr Rev* 2000; **21**: 393–411.
44. Peng H, Wright V, Usas A, *et al*. Synergistic enhancement of bone formation and healing by stem cell-expressed VEGF and bone morphogenetic protein-4. *J Clin Invest* 2002; **110**: 751–759.
45. Shore EM, Kaplan FS. Insights from a rare genetic disorder of extra-skeletal bone formation, fibrodysplasia ossificans progressiva (FOP). *Bone* 2008; **43**: 427–433.

DOI: 10.1002/jgm

Calcif Tissue Int
DOI 10.1007/s00223-009-9282-2

Marrow Stromal Cell-Based Cyclooxygenase 2 Ex Vivo Gene-Transfer Strategy Surprisingly Lacks Bone-Regeneration Effects and Suppresses the Bone-Regeneration Action of Bone Morphogenetic Protein 4 in a Mouse Critical-Sized Calvarial Defect Model

K.-H. William Lau · Reinhard Gysin · Shin-Tai Chen · Jon E. Wergedal · David J. Baylink · Subburaman Mohan

Received: 3 June 2009 / Accepted: 2 August 2009

Abstract This study evaluated whether the murine leukemia virus (MLV)–based cyclooxygenase-2 (Cox-2) ex vivo gene-transfer strategy promotes healing of calvarial defects and/or synergistically enhances bone morphogenetic protein (BMP) 4–mediated bone regeneration. Gelatin scaffolds impregnated with mouse marrow stromal cells (MSCs) transduced with MLV-expressing BMP4, Cox-2, or a control gene were implanted into mouse calvarial defects. Bone regeneration was assessed by X-ray, dual-energy X-ray absorptiometry, and histology. In vitro, Cox-2 or prostanglandin E_2 enhanced synergistically the osteoblastic differentiation action of BMP4 in mouse MSCs. In vivo, implantation of BMP4-expressing MSCs yielded massive bone regeneration in calvarial defects after 2 weeks, but the Cox-2 strategy surprisingly did not promote bone regeneration even after 4 weeks. Staining for alkaline phosphatase (ALP)–expressing osteoblasts was strong throughout the defect of animals receiving BMP2/4-expressing cells, but defects receiving Cox-2-expressing cells displayed weak ALP staining along the edge of original intact bone, indicating that the Cox-2 strategy lacked bone-regeneration effects. The Cox-2 strategy not only lacked bone-regeneration effects but also suppressed the BMP4-induced bone regeneration. In vitro coculture of Cox-2-expressing MSCs with BMP4-expressing MSCs in gelatin scaffolds reduced BMP4 mRNA transcript levels, suggesting that Cox-2 may promote *BMP4* gene silencing in BMP4-expressing cells, which may play a role in the suppressive action of Cox-2 on BMP4-mediated bone formation. In summary, the Cox-2 ex vivo gene-transfer strategy not only lacks bone-regeneration effects but also suppresses the bone-regeneration action of BMP4 in healing of calvarial defects.

Keywords Bone morphogenetic protein 4 · Cyclooxygenase 2 · Marrow stromal cell · Calvarial defect · Bone regeneration · Gene therapy · Ex vivo · Mice

K.-H. W. Lau (✉) · R. Gysin · S.-T. Chen · J. E. Wergedal · S. Mohan
Musculoskeletal Disease Center (151), Jerry L. Pettis Memorial VA Medical Center, 11201 Benton Street, Loma Linda, CA 92357, USA
e-mail: William.Lau@med.va.gov

K.-H. W. Lau · R. Gysin · S.-T. Chen · J. E. Wergedal · D. J. Baylink · S. Mohan
Department of Medicine, Loma Linda University School of Medicine, Loma Linda, CA 92350, USA

K.-H. W. Lau · S.-T. Chen · J. E. Wergedal · S. Mohan
Department of Biochemistry, Loma Linda University School of Medicine, Loma Linda, CA 92350, USA

S. Mohan
Department of Physiology, Loma Linda University School of Medicine, Loma Linda, CA 92350, USA

Localized skeletal lesions and defects, including all types of complex or nonunion fractures, aseptic necrosis, and all types of bony defects, are considerable causes of human suffering and economic loss [1]. Current therapeutic strategies include autologous and allogenic bone grafts, use of osteoconductive structures or scaffolds, and local implantation of osteogenic growth factors [2]. While these strategies, particularly osteogenic protein therapies, are reasonably successful at promoting fracture healing and

Journal : Large 223 | Dispatch : 31-8-2009 | Pages : 12
Article No. : 9282 | ☐ LE | ☐ TYPESET
MS Code : CTI-09-0131 | ☑ CP | ☑ DISK

bone regeneration [3–8], their osteogenic effects are not optimal, particularly for the aging population with a diminishing capacity for bone regeneration and repair. Osteogenic protein therapies also often require very high dosages and multiple applications (or sustained-release strategies) for optimal effect [9–11]. Accordingly, there is still a critical need for more effective therapeutic strategies that impact positively on fracture healing and bone regeneration.

Gene transfer–based molecular therapy that introduces an osteogenic gene directly to the site of skeletal defect is an attractive alternative to protein therapies. It provides an effective means for a sustained and/or regulated as well as targeted expression of the osteogenic factor at the skeletal defect site to promote bone repair and regeneration [12]. Gene transfer–based therapies [12–21] expressing a single osteogenic growth factor gene, particularly a bone morphogenetic protein (BMP), have shown promising results in a number of animal models of bone fracture and regeneration. However, bone repair and regeneration are highly complex and involve multiple cellular processes that entail different types of growth factors [22]. Thus, while the effects of BMP-based single-factor gene-transfer strategies on fracture healing and bone regeneration have been impressive, due to their unique ability to initiate signaling events that promote the commitment of mesenchymal stem cells to the osteoblastic lineage [23] and to induce ectopic bone formation [24], these strategies may require additional growth factors that impact positively on other aspects of bone regeneration, such as angiogenesis and remodeling, to achieve optimal bone-regeneration effects. It has been shown that, with a muscle-derived stem cell–based ex vivo gene transfer approach, the combination of a BMP4 and VEGF (which is an angiogenic growth factor) strategy yielded synergistic enhancement in bone healing compared to a BMP4 strategy alone [25, 26].

The objectives of this study were twofold. First, we evaluated whether the murine leukemia virus (MLV)–based ex vivo gene-transfer strategy delivering a cyclooxygenase-2 (*Cox-2*) gene would be as effective as the BMP4 strategy in promoting bone regeneration of critical-sized calvarial defects in the mouse. The *Cox-2* gene was chosen for testing because it has been shown to be essential for fracture repair [27, 28] and the MLV-based *Cox-2* gene-transfer strategy accelerated bridging of the fracture gap in a rat femoral fracture model [20]. Cox-2 and its bioactive product, PGE_2, promoted bone remodeling [29] and angiogenesis [30], both processes being critical for optimal bone repair and regeneration [31]. The mouse critical-sized calvarial defect model was used because (1) the healing of this bony defect does not occur spontaneously over an extended period of healing time and (2) the MLV-BMP2/4-based ex vivo gene-transfer strategy induced complete healing of critical-sized calvarial defects in the rat within 3–4 weeks [19]. Second, we assessed if the combination ex vivo gene transfer–based strategy delivering both the *Cox-2* gene and the *BMP2/4* hybrid gene would be more effective at promoting healing of critical-sized calvarial defects compared to the same strategy delivering the *BMP2/4* hybrid gene alone, which has been shown to promote fracture repair in the rat [18] and the mouse [32] as well as to enhance bone regeneration of calvarial defects in the rat [19]. Marrow stromal cells (MSCs) were selected as the ex vivo cell vehicle because they contain osteoprogenitors and the rat MSC-based MLV-BMP2/4 ex vivo gene-transfer strategy promoted healing of critical-sized calvarial defects in the rat [19].

Materials and Methods

MLV-Based Viral Vectors

MLV-based vectors expressing a human *BMP2/4* hybrid gene, a human *Cox-2* gene, or a reporter control gene (*β-gal*actosidase [*β-gal*] or green fluorescent protein [GFP]) were constructed and produced as described previously [18–20, 33]. In the *BMP2/4* hybrid gene, the native signaling peptide sequence of *BMP4* was replaced with that of *BMP2* to enhance secretion of mature and functionally active BMP4 protein by the transduced cells [33].

Preparation and Culture of Mouse MSCs

MSCs were isolated from long bones of C57BL/6J mice of 7–8 weeks of age (obtained from Jackson Laboratories, Bar Harbor, ME). Briefly, femora and tibiae were dissected, and bone marrow cells were collected by flushing the cavity with the alpha-modification of Eagle's medium (αMEM; GIBCO BRL Life Technologies, Rockville, MD). Isolated cells were cultured in αMEM supplemented with 15% fetal bovine serum (FBS, GIBCO BRL Life Technologies) at 37°C for 2 days. Nonadherent cells were discarded, and adherent MSCs were cultured in αMEM with 15% FBS until confluent. Under these conditions, murine MSCs could be cultured for 8–12 weekly passages without a significant loss of proliferative capacity. Cells from the first passage of multiple preparations were pooled and kept frozen in liquid nitrogen until use.

MLV-Transduction of Murine MSCs

Primary murine BMCs were transduced with the MLV-based vectors expressing *BMP2/4*, *Cox-2*, or a reporter gene (*β-gal* or GFP) using an established protocol [18–20, 33]. Briefly, MSCs were plated in six-well dishes, grown to

Journal : Large 223 Dispatch : 31-8-2009 Pages : 12
Article No. : 9282 LE TYPESET
MS Code : CTI-09-0131 CP DISK

50–70% confluence, and transduced three times (for 12 hours each) with the respective MLV vector at a concentration corresponding to 10–20 transforming units/cell in αMEM, 15% FBS, and 8 μg/mL of polybrene over a span of 36 hours. After the transduction, the virus-containing medium was replaced with fresh αMEM supplemented with 15% FBS. Transduced MSCs were expanded for three to six weekly passages prior to use.

Calvarial Defect Surgery

All animal protocols were approved by the Institutional Animal Care and Use Committee of the Jerry Pettis Memorial VA Medical Center. Male C57BL/6J mice, 7–8 weeks of age, were maintained in the Veterinary Medical Unit of the Jerry Pettis VA Medical Center for 7–14 days prior to surgery. Mice were anesthetized by intraperitoneal injection of ketamine and xylazine. The surgical site at the top of the skull was prepared by shaving and cleaning with disinfectant. A 3-cm incision was made over the calvariae and the skin held open by retractors. The periosteum was pushed to the side bilaterally, and a 5-mm diameter critical-sized defect in the calvariae was created with a diamond-based dental burr. The calvarial disk was removed by severing the remaining connections with a blunt surgical probe. Careful handling of the instrument was required to avoid damaging the dura mater, which could cause excessive blood loss and death of the animal.

For implantation of MSCs, gelatin-based sponges (Gelfoam; Pharmacia and Upjohn, Kalamazoo, MI) were cut to the size of the defect and placed in six-well plates. The indicated number of transduced murine MSCs (in a volume of 200 μL) was added slowly onto the Gelfoam disk and left to settle for 15 minutes. After 1 hour of incubation at 37°C, 5 mL of αMEM supplemented with 15% FCS was added and the cells were allowed to attach to the Gelfoam matrix overnight. The MSC-impregnated Gelfoam disk was inserted into each defect to completely fill in the hole. The skin was then closed using 4-0 silk sutures. The animals were monitored closely until they fully recovered from the anesthesia.

X-Ray Imaging (Faxitron) and Densitometry (PIXImus)

At the end point of each experiment, mice were killed and the calvariae dissected out for analysis. Bone regeneration was assessed with soft X-ray using an MX20 X-ray specimen radiography system (Faxitron X-ray, Wheeling, IL). Bone mineral density (BMD) was measured by dual-energy X-ray absorptiometry (DEXA) using a PIXImus soft-X-ray densitometer (Lunar, Madison, WI) and the analysis software (version 1.45) provided by the manufacturer. A rectangular area encompassing the defect was defined as the total area of measurement. The 5-mm circular defect area was determined, and the peripheral area outside the defect (containing the original intact bone) was also determined for comparison.

Quantitative Real-Time Reverse Transcriptase-Polymerase Chain Reaction

Total RNA was isolated from the test cells, and the contaminating DNA was removed by DNAse treatment using the RNeasy Mini kit (Qiagen, Valencia, CA). Complementary DNA (cDNA) was synthesized using the Superscript II RT first-strand synthesis system (Invitrogen, Carlsbad, CA) with 250 ng of random hexamer primers and 160 ng of total RNA in a 20-μL volume. Real-time PCRs were performed with 2 μL of cDNA, 10 pmoles of each primer set, and HotStarTaq DNA Polymerase using a QuantiTect SYBR Green PCR Kit (Qiagen) in an Opticon DNA Engine (MJ Research/Bio-Rad, Hercules, CA). The primer set for human *BMP4* was as follows: 5′-AAT GCA AGC AGG TGG GAA AGT-3′ (forward) and 5′-CTG AAG TCC ACA TAG AGC GAG-3′ (reverse). PCR amplification conditions were 95°C for 15 minutes, 30 cycles with 95°C 30 seconds, annealing at 56.4–57.2°C for 30 seconds, and extension at 72°C for 30 seconds. Expression of BMP4 was calculated relative to glyceraldehyde 3-phosphate dehydrogenase (GAPDH), which was determined with the following primer set: 5′-AAG ATG GTG AAG GTC GGT GT-3′ (forward) and 5′-GCA TGG ACT GTG GTC ATG AG-3′ (reverse). The mRNA abundance was quantified by the cycle threshold, ΔC_T, method [34] against standard curves constructed with known amounts of cDNA of the respective target gene.

Western Immunoblot Analysis

Cellular protein was extracted from transduced MSCs 7 days after the viral transduction with sodium dodecyl sulfate-polyacrylamide gel electrophoresis (SDS-PAGE) sample buffer. The lysate proteins were fractionated on 12% SDS-PAGE gels and transblotted onto a 0.2-μm PVDF membrane (Bio-Rad, Hercules, CA). The membrane was blocked with 1% skim milk and incubated with 1 μg/mL monoclonal anti-human BMP4 antibody or a polyclonal anti-human Cox-2 antibody (R&D Systems, St. Paul, MN), washed, and incubated with a horseradish peroxidase–labeled goat anti-mouse IgG (Pierce, Rockford, IL). The respective BMP4 and Cox-2 protein bands were visualized with chemiluminescence (SuperSignal West Pico Chemiluminescent Substrate, Pierce). Mature recombinant human BMP-4 protein is a homodimeric protein consisting of two 116–amino acid chains; the predicted molecular weight of each monomer is 13 kDa, but the apparent molecular weight

Journal : Large 223 | Dispatch : 31-8-2009 | Pages : 12
Article No. : 9282 | LE | TYPESET
MS Code : CTI-09-0131 | CP | DISK

of the monomer (determined by SDS-PAGE under reducing conditions) is ~24 kDa due to extensive glycosylation. Mature recombinant human Cox-2 protein exists as a non-glycosylated monomer with an apparent molecular weight of ~72 kDa. Thus, the relative amounts of cellular mature BMP4 and Cox-2 proteins, respectively, were estimated by comparing the relative density (determined by laser densitometry) of the 24-kDa and 72-kDa protein bands to that of known amounts of recombinant BMP4 and Cox-2 proteins on the same blot. Results are shown as the amount of respective protein per 1×10^6 cells.

Alkaline Phosphatase Assay

Primary MSCs were treated with the indicated effectors for 3 or 7 days. Cell extracts were prepared by extracting each treated cell culture with 0.1% Triton X-100, and alkaline phosphatase (ALP) activity was assayed by a colorimetric assay as described previously [35].

Statistical Analysis

Statistical significance of the difference between two variables was determined with the two-tailed, two-sample with equal variances independent Student's *t*-test. Results were considered significant when $P < 0.05$. All data are reported as mean ± standard deviation (SD).

Results

Effective Transduction of Murine MSCs by MLV-Based Vectors and Transgene Expression

Untransduced MSCs did not express β-gal or GFP (Fig. 1a, left panel). In contrast, >90% of the MLV-β-gal-transduced MSCs showed strong β-gal activity (middle panel) and >90% of the MLV-eGFP-transduced MSCs showed strong GFP levels (right panel) 14 days after transduction, confirming that primary murine MSCs can be effectively transduced with the MLV vectors. To ascertain that murine MSCs transduced with the MLV-BMP2/4 or MLV-Cox-2 vector expressed substantial amounts of mature BMP4 and Cox-2 proteins, respectively, the relative cellular levels of mature human BMP4 or Cox-2 in respective transduced MSC populations were measured by Western immunoblot assays 7 days posttransduction (Fig. 1b, c). Untransduced cells did not express detectable levels of human BMP4 or Cox-2 protein (data not shown), but cell extracts of MSCs transduced with MLV-BMP2/4 or MLV-Cox-2 contained substantial amounts of mature human BMP4 protein or

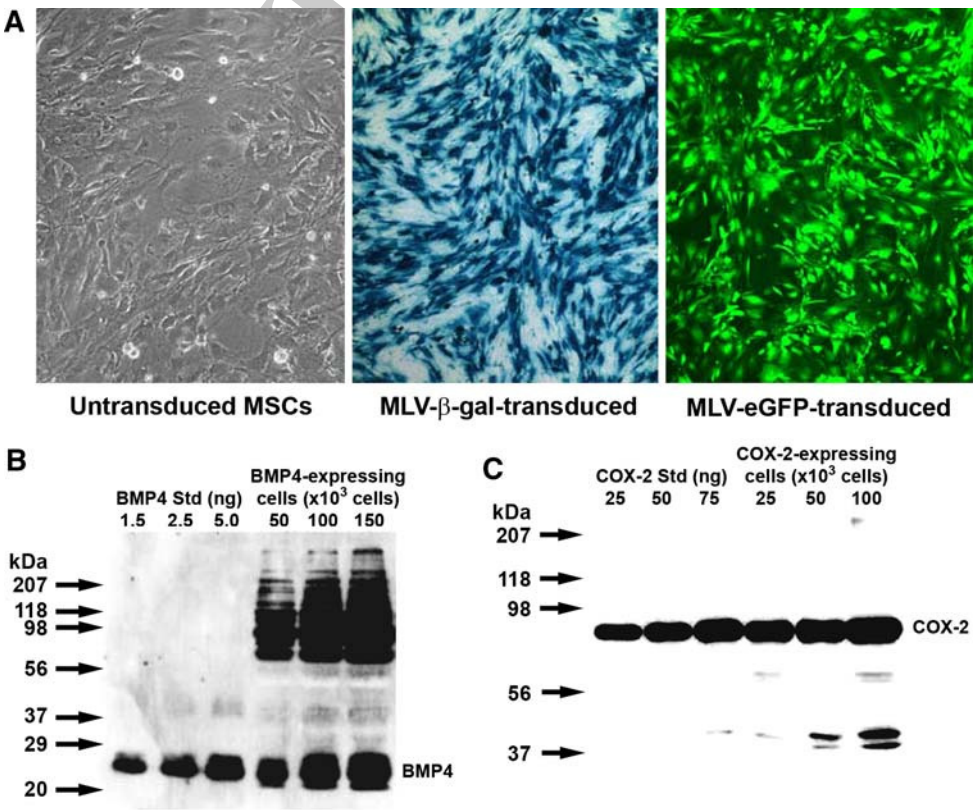

Fig. 1 Transgene expression in primary mouse MSCs transduced with MLV-based vectors. **a** Photomicrographs of confluent cultures of untransduced primary mouse MSCs (*left*), MSCs transduced with the MLV-β-gal vector stained with X-gal in which β-gal-expressing cells stained blue (*middle*), and MSCs transduced with the MLV-eGFP vector under a fluorescent microscope (*right*). **b**, **c** Western blots for expression of cellular human BMP4 protein (**b**) and human Cox-2 protein (**c**) in, respectively, MLV-BMP2/4-transduced and MLV-Cox-2-transduced primary MSCs at 7 days posttransduction

Journal : Large 223 | Dispatch : 31-8-2009 | Pages : 12
Article No. : 9282 | LE | TYPESET
MS Code : CTI-09-0131 | CP | DISK

Cox-2 protein, respectively. The amounts of mature human BMP4 protein in MLV-BMP2/4-transduced MSCs were estimated to be between 100 and 200 ng/10^6 cells, and the amounts of mature Cox-2 protein in MLV-Cox-2-transduced cells were between 1,500 and 3,000 ng/10^6 cells. Unlike Cox-2, which is an intracellular protein, BMP4 is a secretory protein. Although we did not measure the amounts of mature human BMP4 protein secreted by the transduced cells in this experiment, we have previously shown that rat MSCs transduced with the same MLV-BMP2/4 construct secreted up to 1 μg/10^6 cells/24 hours [33]. Because the transduction efficiency of this MLV vector and the relative biosynthesis rate of mature BMP4 were very similar between rat MSCs and mouse MSCs (data not shown), the MLV-BMP2/4-transduced mouse MSCs would most likely also secrete similar high levels of mature human BMP4 protein.

Synergistic Stimulatory Interaction Between Cox-2 (and PGE_2) and BMP4 on Osteoblastic Differentiation of Mouse MSCs In Vitro

To test our assumption that Cox-2 (or PGE_2) would produce synergistic interaction with BMP4 on osteoblastic differentiation of MSCs in vitro, we treated mouse MSCs with 200 ng/mL recombinant BMP4 protein, 10 μM PGE_2, or both. To monitor osteoblastic differentiation, we measured cellular ALP activity (a well-accepted marker of osteoblast differentiation [36]) in extracts of treated MSCs after 3 and 7 days. Figure 2a shows that treatment with BMP4 alone for 7 days led to an approximately eightfold increase in ALP activity and treatment with PGE_2 alone for 7 days yielded an approximately twofold increase. The combination treatment with PGE_2 and BMP4 yielded a significantly larger increase ($P < 0.05$, ANOVA) compared to BMP-4 or PGE_2 alone. The same results were also seen after 3 days of treatment (data not shown). These results were highly reproducible and obtained in two repeat experiments.

To test if Cox-2 would also act synergistically with BMP4 on osteoblastic differentiation of MSCs in vitro, we assessed the effects of coculture of Cox-2-expressing MSCs with BMP4-expressing cells on cellular ALP activity compared to that in the BMP4 or Cox-2 alone group at three different cell densities (i.e., 50,000, 25,000, or 10,000 cells of each transduced cell type) of BMP4- and Cox-2-expressing MSCs (each in 1:1 ratio). As expected, BMP4-expressing cells showed significant increases in ALP activity after 7 days in culture compared to GFP-expressing control cells, and the extent of the increase was proportional to the number of BMP4-expressing cells plated (Fig. 2b). When Cox-2-expressing cells were cocultured with BMP4-expressing cells, the increase in ALP activity was significantly ($P < 0.05$, ANOVA) greater than that in BMP4-expressing cells alone, suggesting a synergistic stimulation by Cox-2-expressing cells. The synergistic interaction was seen in all test cell densities and was observed after 3 days (data not shown).

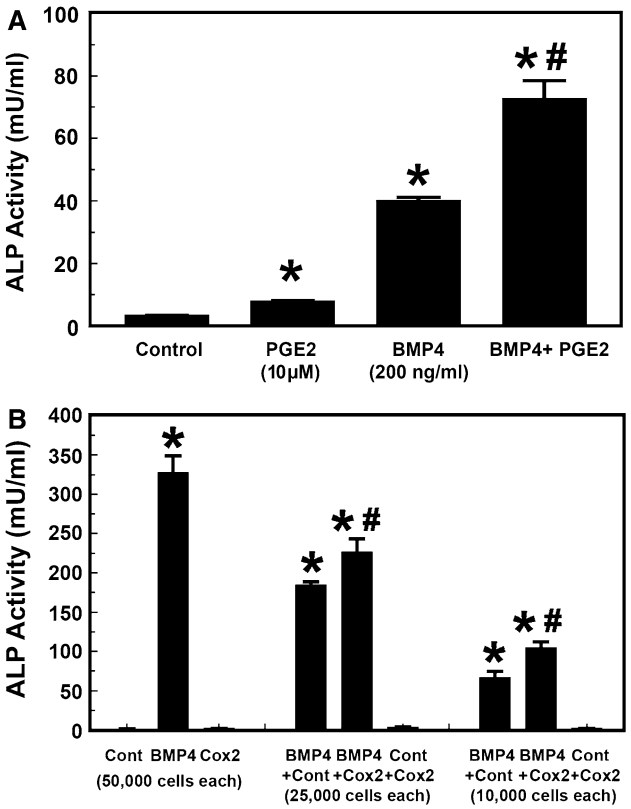

Fig. 2 Synergistic stimulation of ALP expression in primary mouse MSCs by PGE_2 (**a**) or Cox-2 expression (**b**) and BMP4 in vitro. **a** Primary mouse MSCs were treated with PGE_2 (10 μM), recombinant human BMP4 (200 ng/mL), each alone or in combination, as described in "Materials and Methods." ALP activity in each extract is shown as mean ± SD. * $P < 0.05$ compared to the vehicle control and # $P < 0.05$ compared to BMP4 alone. ANOVA indicates a significant ($P < 0.05$) interaction between PGE_2 and BMP4 treatment. **b** Cellular ALP activity in 7-day cultures with various numbers (i.e., 50,000, 25,000, or 10,000) of BMP4-expressing mouse MSCs, Cox-2-expressing MSCs, or GFP-expressing control MSCs is shown as mean ± SD (n = 6/group). * $P < 0.05$ compared to GFP-expressing control cells and # $P < 0.05$ compared to each corresponding BMP4-expressing cell group. ANOVA indicates a significant ($P < 0.05$) interaction between Cox-2 and BMP4 treatment

Bone-Regeneration Effects of MSC-Based Ex Vivo MLV-BMP2/4 and MLV-Cox-2 Gene-Transfer Strategies, Alone or in Combination, in the Mouse Critical-Sized Calvarial Defect Model

We next determined the relative potency of the MLV-BMP2/4- and MLV-Cox-2-based ex vivo gene-transfer strategies, alone and in combination, in promoting healing of critical-sized calvarial defects in syngeneic C57BL/6J

Journal : Large 223 | Dispatch : 31-8-2009 | Pages : 12
Article No. : 9282 | LE | TYPESET
MS Code : CTI-09-0131 | CP | DISK

mice. In this experiment, a Gelfoam scaffold disk impregnated with a total of 1×10^6 mouse MSCs transduced with the MLV-BMP2/4, MLV-Cox-2, or MLV-β-gal control vector was implanted into the critical-sized defect of groups of five mice each. To evaluate the bone-regeneration effect of the BMP2/4 and Cox-2 combination strategy, an additional group of five mice was implanted with Gelfoam scaffold disks, impregnated with 8×10^5 MLV-BMP2/4-transduced MSCs and 2×10^5 MLV-Cox-2-transduced MSCs. Assessment of bone regeneration over the defect by soft X-ray at 2 weeks (Fig. 3a) revealed that calvarial defects implanted with MSCs expressing BMP4 with or without Cox-2 were completely healed. The bone-regeneration ability of BMP4 was so potent that the regenerated bone overfilled the defect as the thickness of the regenerated bone exceeded that of the surrounding original intact bone (Fig. 3b). In contrast, no X-ray evidence for bone formation was seen in defects implanted with Cox-2-expressing cells (Fig. 3a). The Cox-2-treated and control defects were filled mostly with soft tissues (data not shown).

Histological staining for ALP-expressing osteoblastic cells within the defects after 2 weeks of healing was strong throughout the defect of animals receiving BMP2/4-expressing cells (Fig. 4, top panel). Defects of the Cox-2 alone group (bottom panel) and the β-gal control group (data not shown) displayed only weak ALP staining along the original intact bone and at the edge of the defects. These findings are consistent with the lack of de novo bone formation in defects implanted with Cox-2-expressing MSCs.

Previous experiments utilizing *Cox-2* as the therapeutic gene in a rat femur fracture model have shown that significant *Cox-2*-mediated increases in bone formation did not occur until 14–21 days posttreatment [20]. To evaluate if the *Cox-2*-mediated calvarial healing is also delayed, we extended the healing time to 4 weeks in a repeat experiment. Figure 3c shows that the areal BMD over the defect area of mice implanted with BMP4 cells alone reached 159 $\pm$ 57% of the areal BMD of surrounding intact bone (i.e., 40.1 $\pm$ 7.5 vs. 25.3 $\pm$ 1.2 mg/cm^2, $P < 0.01$). No significant bone regeneration occurred in defects receiving only

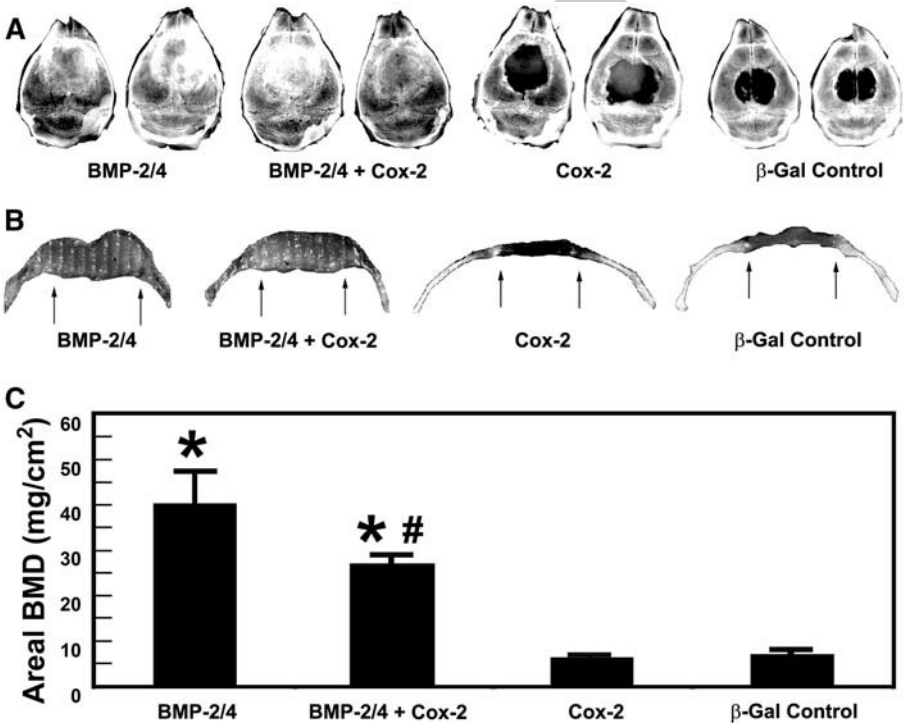

Fig. 3 Comparison of bone-regeneration effects of the BMP4 ex vivo gene-transfer strategy and the Cox-2 ex vivo gene-transfer strategy, each alone or in combination, in the mouse critical-sized calvarial defect model. **a** Digital soft X-ray image of healing calvariae of two representative mice per group after 2 weeks of healing. Each defect was implanted with a Gelfoam implant containing a total of 1×10^6 MSCs: BMP-2/4 group received 1×10^6 MLV-BMP2/4-transduced MSCs, BMP-2/4 + Cox-2 group received 8×10^5 MLV-BMP2/4-transduced MSCs along with 2×10^5 MLV-Cox-2-transduced MSCs, Cox-2 group received 2×10^5 MLV-Cox-2-transduced MSCs and 8×10^5 MLV-β-gal-transduced control cells, and control group received 1×10^6 MLV-β-gal-transduced control MSCs only. **b** Cross-sectional images of calvarial defect of a representative mouse of each treatment group after 4 weeks of healing. Old lamellar bone was stained with Goldner's stain. *Arrows* mark the edges of the 5-mm defects. **c** Areal BMD (by PIXImus DEXA) over the healing calvarial defects after 4 weeks of healing. Results are shown as mean $\pm$ SD from four mice per treatment group. * $P < 0.05$ compared to control group and $^{\#}$ $P < 0.05$ compared to BMP-2/4 alone group

Journal : Large 223 | Dispatch : 31-8-2009 | Pages : 12
Article No. : 9282 | LE | TYPESET
MS Code : CTI-09-0131 | CP | DISK

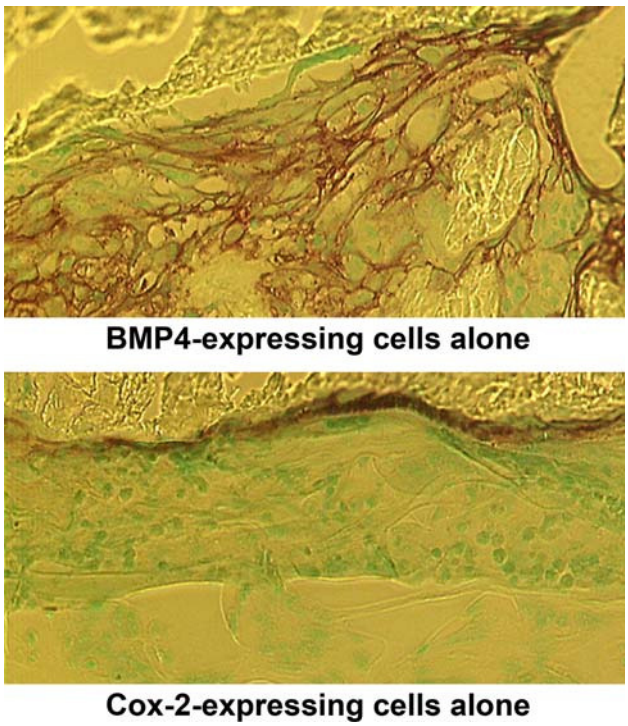

Fig. 4 Histology of calvarial defect area after 2 weeks of healing. *Top panel* A representative section of the healing defect treated with BMP4-expressing MSCs after 2 weeks. Strong ALP activity (stained in *reddish brown*) was found throughout the defect. *Bottom panel* A representative section of the healing defect treated with Cox-2-expressing cells after 2 weeks. Only weak ALP staining was found along the original intact bone and at the edge of the defects

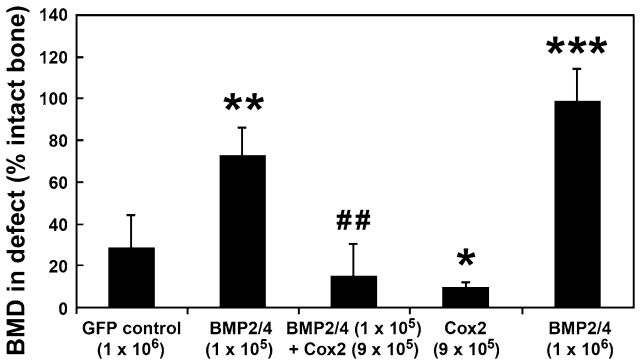

Fig. 5 Bone regeneration in mouse critical-sized calvarial defects after 4 weeks with BMP-4 and Cox-2 ex vivo gene-transfer strategy, each alone or in combination. Mouse critical-sized calvarial defects were implanted with Gelfoam impregnated with 1×10^6 GFP-expressing primary mouse MSCs alone (control cells), 1×10^5 BMP4-expressing cells plus 9×10^5 GFP control cells (BMP4 cells), 9×10^5 Cox-2 expressing cells plus 1×10^5 BMP expressing cells (BMP4 + Cox-2 cells), or 9×10^5 Cox-2 expressing cells plus 1×10^5 GFP expressing control cells (Cox-2 cells). Areal BMD was determined as described in "Materials and Methods" after 4 weeks. Results are shown as relative percentage of the surrounding original intact bone. Values are shown as average ± SD from four animals per test group. * $P < 0.05$ and ** $P < 0.01$ compared with control group, ## $P < 0.01$ compared with BMP4 group

Cox-2-expressing cells even after 4 weeks as the areal BMD within the defect of the Cox-2 alone group was not different significantly from that of the β-gal-negative control group (i.e., 6.5 ± 0.5 vs. 7.4 ± 0.9 mg/cm^2, P = nonsignificant). Implants with the combination of BMP4- and Cox-2-expressing cells resulted in slightly but significantly lower areal BMD (i.e., 27.0 ± 2.3 vs. 25.3 ± 1.2 mg/cm^2, $P < 0.05$) than that with BMP-4-expressing cells alone, suggesting that the Cox-2 strategy might have even suppressed the bone-regeneration action of BMP4 in this calvarial defect model.

The total number of BMP4-expressing cells in the absence of Cox-2-expressing cells in this particular experiment was 20% more than that in the BMP4 and Cox-2 combination group (1×10^6 vs. 8×10^5 cells). Thus, to rule the possibility that the reduced bone-regeneration effects could have been due to the 20% fewer BMP4-expressing cells in the combination group, we repeated the experiment with two modifications: (1) the number of BMP4-expressing MSCs in Gelfoam scaffolds was kept at 1×10^5 cells per implant and (2) the number of Cox-2-expressing cells was increased to 9×10^5 cells per implant to enhance the chance of detecting suppressive effects of the Cox-2 strategy. Appropriate numbers of GFP-expressing control MSCs were added to each Gelfoam implant to maintain the number of total MSCs in the scaffold at 1×10^6. There were five test groups with four mice each: (1) negative control group, which received an implant containing 1×10^6 GFP-expressing MSCs; (2) BMP4 alone group, which received 1×10^5 BMP4-expressing MSCs and 9×10^5 GFP-expressing control cells; (3) BMP4–Cox-2 combination group, which received 1×10^5 BMP4-expressing MSCs and 9×10^5 Cox-2-expressing cells; (4) Cox-2 alone group, which received 9×10^5 Cox-2-expressing cells and 1×10^5 GFP-expressing control cells; and (5) a positive control group, which received 1×10^6 BMP-4-expressing cells. Figure 5 shows that defects treated with this dosage of BMP4-expressing cells alone significantly increased areal BMD over the defect area to ~70% of that of surrounding original calvarial bone. Defects receiving Cox-2-expressing cells alone not only did not increase but slightly reduced the areal BMD over the defect area compared to control defects that received only GFP-expressing cells. The most striking observation was the complete suppression of the bone-regeneration response to the BMP4-expressing cells when they were combined with a ninefold excess of Cox-2-expressing cells. This experiment was repeated three times with different ratios of BMP4-expressing cells to Cox-2-expressing cells (i.e., 1:1, 1:3, and 1:9), and each yielded significant suppressive effects of the Cox-2 strategy on the bone-

Journal : Large 223 | Dispatch : 31-8-2009 | Pages : 12
Article No. : 9282 | LE | TYPESET
MS Code : CTI-09-0131 | CP | DISK

regeneration action of BMP4 in healing of the critical-sized calvarial defects.

Effects of Cox-2 on BMP4 Transgene Expression in MSCs Transduced with MLV-BMP2/4 Vector In Vitro

To test if the suppressive action of the Cox-2 strategy on the bone-regeneration effect of the BMP4 strategy was in part mediated by Cox-2-dependent inhibition of BMP4 expression in Gelfoam scaffolds, we measured the relative levels of human BMP4 mRNA transcript in Gelfoam impregnated with 1×10^5 BMP-4 expressing MSCs in the absence or presence of low (1×10^5 cells/scaffold) and high (9×10^5 cells/scaffold) numbers of Cox-2-expressing MSCs after incubation in culture medium for 1 day or 4 days in vitro. To ensure that there were sufficient numbers of cells to cover the entire scaffold that would yield more optimal recovery of total RNA isolation, the total number of transduced MSCs in each scaffold was increased to 2×10^6 by supplementing them with GFP-expressing MSCs. The relative level of human BMP4 mRNA was normalized against mouse GAPDH mRNA transcript to adjust for variations in the cell number. There was a time-dependent decrease in the human BMP4 mRNA transcript, normalized against the endogenous mouse GAPDH mRNA transcript level in Gelfoam scaffolds (Fig. 6). Because there were no significant time-dependent changes in GAPDH mRNA levels (data not shown), the reduction of BMP4 mRNA transcript may be due to gene silencing of the human *BMP4* transgene in the transduced MSCs, which is not unexpected because time-dependent silencing of the transgene expression is known to occur with MLV-based vectors [37]. However, the time-dependent decrease in the human BMP4 mRNA transcript was significantly enhanced ($P < 0.05$, ANOVA) by the presence of Cox-2-expressing MSCs (Fig. 6). Again, because the presence of Cox-2-expressing MSCs also did not alter the GAPDH mRNA level, it appears that Cox-2-overexpressing cells further augmented the silencing of *BMP4* transgene expression in MLV-BMP4-transduced MSCs.

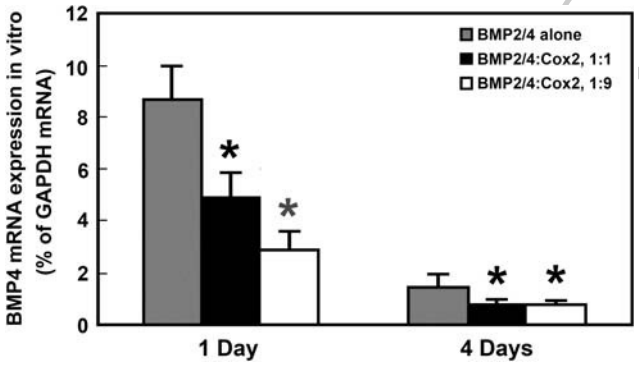

Fig. 6 Effects of Cox-2 expression on *BMP4* transgene expression in MLV-BMP2/4-transduced mouse MSCs in vitro. Gelfoam disks (5 × 10 mm) were impregnated with 2×10^5 BMP4-expressing MSCs in combination with Cox-2-expressing MSCs (or GFP-expressing cells) in 1:1 or 1:9 ratio. The total number of transduced cells in each Gelfoam scaffold was 2×10^6. After 1 or 4 days in culture, the disks were washed briefly with PBS and cut in half, and the total RNA was isolated and reverse-transcribed to cDNA. Relative levels of human *BMP4* transgene transcript were determined by real-time RT-PCR assay using a primer set specific for human BMP4. The relative human BMP4 transcript levels (as percentage of endogenous GAPDH transcript level) are shown as average ± SD from three scaffolds per group. Each was done in triplicate. * $P < 0.05$ compared to BMP2/4 alone

Discussion

Two key findings of this study are surprising and very intriguing. First, despite the large body of in vitro and in vivo evidence that Cox-2 and its biological product, PGE_2, are potent osteogenic factors [29, 38], there is a complete lack of X-ray, densitometric, and/or histological evidence for an osteogenic response to the MSC-based Cox-2 ex vivo gene-transfer strategy in the healing of the mouse critical-sized calvarial defect in this study. The apparent lack of bone-regeneration response to the MSC-based Cox-2 ex vivo gene-transfer strategy was not due to inefficient retroviral transduction of primary mouse MSCs since the transduction efficiency of our MLV vectors in these cells was ~90%. In vitro characterization of the MLV-Cox-2-transduced MSCs revealed that the transduced MSCs produced up to 3,000 ng of mature human Cox-2 protein per million cells per 24 hours. This amount of human Cox-2 protein was similar to that of mature human BMP4 protein produced and secreted by MLV-BMP2/4-transduced MSCs [33], which induced massive bone formation when implanted in the mouse calvarial defect model in this study. Thus, the lack of bone-regeneration response to the Cox-2 strategy was probably not due to ineffective Cox-2 production by the transduced MSCs. Similarly, the lack of bone-regeneration response was also not due to production of inactive Cox-2 protein since our previous studies have demonstrated that the human Cox-2 protein produced by rat MSCs with our MLV-based vectors was able to induce PGE_2 biosynthesis, promote osteoblastic differentiation of MSCs in vitro, and enhance fracture healing in vivo [20].

The mechanism(s) responsible for the surprising lack of bone-regeneration response to the ex vivo Cox-2 strategy is unclear. There are several potential mechanistic explanations. First, most of the past studies that demonstrated bone-regeneration effects of Cox-2 and PGE_2 were performed with long bones [20, 27, 28, 38, 39], which utilize both endochondral and intramembranous bone formation for bone regeneration and repair [22]. In contrast, the

Journal : Large 223 Dispatch : 31-8-2009 Pages : 12
Article No. : 9282 LE TYPESET
MS Code : CTI-09-0131 CP DISK

healing of calvarial defects involves only intramembranous bone formation [40]. Thus, it may be possible that Cox-2 (and/or PGE_2) stimulates only endochondral, but not intramembranous, bone formation. However, we do not favor this possibility since mice deficient in Cox-2 expression exhibited impaired intramembranous as well as endochondral bone formation [28].

The second possibility relates to the fact that the Cox-2-expressing cells were placed at the center of the Gelfoam disk, which was then inserted into a relatively large (5 mm, i.d.) calvarial defect. Accordingly, the Cox-2-expressing cells were located some distance away from the edge of the defect, where bone regeneration would take place. Cox-2 is an intracellular enzyme, and its anabolic actions are mediated primarily by PGE_2. It is presumed that the secreted PGE_2 will permeate toward the edge of the defect to promote bone regeneration. For a significant bone-regeneration response, the impregnated Cox-2-expressing MSCs within the Gelfoam scaffold must be able to produce sufficient amounts of PGE_2 that would permeate to the edge of the healing defect. However, our recent findings indicate that MLV-Cox-2-transduced rat MSCs produced several-fold less PGE_2 than MLV-Cox-2-transduced rat osteoblasts in vitro [20], raising the possibility that MSCs may have significantly lower capacity for PGE_2 production compared with osteoblasts. Thus, it is possible that the MLV-Cox-2-transduced mouse MSCs may not produce sufficient PGE_2 gradient needed to elicit a bone-regeneration response in this calvarial defect model. Quantitative analysis of the concentration gradient of PGE_2 within the healing defect would provide helpful clues about the validity of this possibility. However, we did not measure the PGE_2 production within the Gelfoam scaffold in this study because reliable determinations of the PGE_2 gradient within Gelfoam scaffolds are technically difficult. On the other hand, our finding that increasing the dosage of Cox-2-expressing cells from 1 x 10^5 to 9 $\times$ 10^5 per scaffold not only did not enhance but even suppressed the basal bone-formation response compared to the GFP-expressing control MSCs would argue against this possibility.

Recent evidence has suggested that Cox-2 has a suppressing effect on the proliferation of osteoblasts [41]. Thus, the third possibility is that the lack of bone-regeneration response of the Cox-2 strategy is due in part to the suppressive effect of Cox-2 on the proliferation of osteoblastic cells at the defect site. However, although we did not measure the effects of Cox-2 expression on the proliferation of murine MSCs, we did not note large differences in the cell population doubling time between the MLV-Cox-2-transduced MSCs and the MLV-β-gal-transduced control MSCs as well as the untransduced murine MSCs. On the other hand, we cannot completely dismiss this interesting possibility.

A recent study showed that MSCs and calvarial osteoblasts of Cox-2-deficient mice exhibited an enhanced response to PTH-induced osteoblast differentiation and bone nodule mineralization in vitro and that the Cox-2-specific inhibitor NS-398 also synergistically enhanced the osteogenic effects of PTH in MSCs and calvarial osteoblasts of wild-type mice [42]. This suggests that Cox-2 may have potential suppressive effects on the osteogenic action of PTH in vivo. Although the mechanism by which Cox-2 suppresses the osteogenic action of PTH has not been defined, it is suggested that Cox-2 and/or PGE_2 reduce the osteogenic action of PTH by either inhibiting the suppressive action of PTH on the expression of sclerostin, a key inhibitor of Wnt signaling [43], or directly increasing the expression of sclerostin in osteoblastic cells [42]. The potential inhibitory effect of Cox-2 (and/or PGE_2) on the osteogenic action of PTH could be pertinent to the potential mechanism for the lack of bone-regeneration response in intramembranous bone formation to the Cox-2 ex vivo gene-transfer strategy since PTHrp (and perhaps PTH) has been reported to be required for normal intramembranous bone development [44]. Unfortunately, our original experimental design did not include measurements of the expression levels of sclerostin in the healing defects. The concept that Cox-2 could have suppressive effects on the osteogenic actions of other bone growth factors through regulation of secretion of sclerostin is very interesting and will be pursued in our future studies.

The second and more puzzling observation of this study is that the Cox-2 ex vivo gene-transfer strategy when used in combination with the BMP2/4 strategy not only did not synergistically enhance but actually suppressed the bone-regeneration action of the BMP4 strategy in this critical-sized calvarial defect model. The suppressive action of Cox-2-expressing cells on BMP4-mediated bone regeneration appeared to be dose-dependent as the inhibition was greater in the presence of more Cox-2-expressing cells (i.e., 9:1 ratio of Cox-2-expressing cells to BMP4-expressing cells; Fig. 5) than in the presence of fewer Cox-2-expressing MSCs (i.e., 1:4 ratio of Cox-2-expressing cells to BMP4-expressing cells; Fig. 3), suggesting that the suppressive effects were mediated through Cox-2 expression in the transduced cells.

The mechanism(s) contributing to the suppressive effects of Cox-2 expression on the bone-regeneration actions of the nearby BMP4-expressing MSCs in healing critical-sized calvarial defects in vivo can only be speculated. In this regard, the recent findings that Cox-2 and/or PGE_2 suppress the osteogenic action of PTH through an increase in expression of sclerostin [42] and that sclerostin is a potent inhibitor of the osteogenic actions of BMPs [45] raise the interesting possibility that the increased sclerostin expression in osteoblastic MSCs mediated by the Cox-2 ex

Journal : Large 223 Dispatch : 31-8-2009 Pages : 12
Article No. : 9282 LE TYPESET
MS Code : CTI-09-0131 CP DISK

vivo gene-transfer strategy may suppress the bone-regeneration action of the BMP4 strategy. On the other hand, our in vivo studies have clearly demonstrated that Cox-2 and/or PGE_2 not only did not suppress but synergistically enhanced the BMP4-induced osteoblastic differentiation of the transduced MSCs do not support a direct inhibitory effect of Cox-2 and/or PGE_2 on the osteogenic actions of BMP4. However, our in vitro findings did not preclude the possibility that the in vivo inhibitory effects of Cox-2 and/or PGE_2 may be mediated through indirect actions of Cox-2 and/or PGE_2 on the expression of inhibitory proteins, such as sclerostin, in other cell types, such as osteocytes. In addition, although it is generally assumed that the biological actions of Cox-2 are mediated primarily through PGE_2, Cox-2 also produces other eicosanoids, including other prostaglandins, prostacyclin, leukotrienes, and thromboxanes. There is also the remote possibility that the suppressive action of Cox-2 on BMP4-induced bone regeneration may be mediated through these eicosanoids. However, one of the key in vitro findings in this study raises yet another potential mechanism. Accordingly, coculturing of Cox-2-expressing MSCs with BMP4-expressing MSCs in Gelfoam scaffolds in vitro was found to significantly reduce the total BMP4 mRNA transcript level. This observation can be interpreted as that coculturing of BMP4-expressing cells with Cox-2-expressing cells in the context of Gelfoams could lead to gene silencing of the *BMP4* transgene expression in BMP4-expressing cells. Alternatively, it may also be interpreted as that the presence of Cox-2-expressing cells somehow induced death (apoptosis) of BMP4-expressing cells. While our experimental design did not allow us to distinguish the two alternative interpretations, our data that coculture of BMP4-expressing cells and Cox-2-expressing cells in the Gelfoam matrix did not yield a similar decrease in the mRNA transcript level of the housekeeping gene, *GAPDH*, are consistent with a mechanism that involves Cox-2-dependent silencing of *BMP4* gene expression. In this regard, transcription from retrovirus long terminal repeats (LTRs) is known to be silenced in stem cells [37, 46]. Both methylase-dependent and -independent mechanisms have been shown to be involved in silencing of the LTR promoter [47]. Future studies are needed to identify if Cox-2-induced silencing of the LTR promoter occurs in vivo and contributes to reduced BMP4 expression and suppression of bone formation at the calvarial defect site.

There may be potential regulatory effects of PGE_2 on bone cell production of BMPs as it has been reported that PGE_2 treatments increased bone formation and BMP7 mRNA and protein levels in vivo and in vitro, but the effects of PGE_2 on the increases in BMP7 mRNA and protein levels were mediated through posttranscriptional mechanisms [48]. Thus, we cannot completely dismiss the remote possibility that PGE_2 produced by Cox-2-expressing MSCs, while enhancing BMP7 mRNA stability, may decrease the stability of BMP4 mRNA through posttranscriptional mechanisms. This possibility, if confirmed, would provide an alternative mechanism that could explain the significant reduction in the total BMP4 mRNA transcript level, when BMP4-expressing MSCs were cocultured with Cox-2-expressing MSCs. However, the issue of whether PGE_2 produced by Cox-2-transduced cells would have any effect on BMP4 mRNA stability remains to be determined.

In summary, this study discloses two surprising discoveries of the MLV-based Cox-2 ex vivo gene-transfer strategy in that it not only completely lacks bone-regeneration effects but also markedly suppresses the bone-regeneration action of the BMP4 ex vivo gene-transfer strategy in healing of mouse calvarial defects in a dose-dependent manner. Our in vitro studies have suggested several possible explanations for the lack of an osteogenic action of the Cox-2 strategy and the suppressive effects of the Cox-2 strategy on the BMP4-induced bone formation at the calvarial defect, but more sophisticated studies will be needed to definitively define the mechanisms.

Acknowledgements This work was supported by a special appropriation to the Jerry L. Pettis Memorial VA Medical Center, Musculoskeletal Disease Center, and by an Assistance Award from the United States Army (DAMD-17-03-2-0021). The United States Army Medical Research Acquisition Activity (820 Chandler Street, Fort Detrick, MD 21702-5014) is the awarding and administering acquisition office. The information contained in this publication does not necessarily reflect the position or policy of the government, and no official endorsement should be inferred. All work was performed in facilities provided by the Department of Veterans Affairs.

References

1. Braithwaite RS, Col NF, Wong JB (2003) Estimating hip fracture morbidity, mortality and costs. J Am Geriatr Soc 51:364–370
2. Schmidmaier G, Schwabe P, Strobel C, Wildemann B (2008) Carrier systems and application of growth factors in orthopaedics. Injury 39(Suppl 2):S37–S43
3. Lieberman JR, Daluiski A, Einhorn TA (2002) The role of growth factors in the repair of bone. Biology and clinical applications. J Bone Joint Surg Am 84:1032–1044
4. Simpson AH, Mills L, Noble B (2006) The role of growth factors and related agents in accelerating fracture healing. J Bone Joint Surg Br 88:701–705
5. Kanakaris NK, Giannoudis PV (2008) Clinical applications of bone morphogenetic proteins: current evidence. J Surg Orthop Adv 17:133–146
6. Barnes GL, Kakar S, Vora S, Morgan EF, Gerstenfeld LC, Einhorn TA (2008) Stimulation of fracture-healing with systemic intermittent parathyroid hormone treatment. J Bone Joint Surg Am 90(Suppl 1):120–127
7. Dereka XE, Markopoulou CE, Vrotsos IA (2006) Role of growth factors on periodontal repair. Growth Factors 24:260–267
8. Sanchez M, Anitua E, Cugat R, Azofra J, Seijas R, Andia I (2009) Nonunions treated with autologous preparation rich in growth factors. J Orthop Trauma 23:52–59

Journal : Large 223 | Dispatch : 31-8-2009 | Pages : 12
Article No. : 9282 | LE | TYPESET
MS Code : CTI-09-0131 | CP | DISK

9. Luginbuehl V, Meinel L, Merkle HP, Gander B (2004) Localized delivery of growth factors for bone repair. Eur J Pharm Biopharm 58:197–208
10. Jones CB, Sabatino CT, Badura JM, Sietsema DL, Marotta JS (2008) Improved healing efficacy in canine ulnar segmental defects with increasing recombinant human bone morphogenetic protein-2/allograft ratios. J Orthop Trauma 22:550–559
11. Hafeman AE, Li B, Yoshii T, Zienkiewicz K, Davidson JM, Guelcher SA (2008) Injectable biodegradable polyurethane scaffolds with release of platelet-derived growth factor for tissue repair and regeneration. Pharm Res 5:2387–2399
12. Klamut HJ, Chen S-T, Lau K-HW, Baylink DJ (2004) Progress toward skeletal gene therapy. Crit Rev Eukaryotic Gene Exp 14:89–136
13. Shen FH, Visger JM, Balian G, Hurwitz SR, Diduch DR (2002) Systemically administered mesenchymal stromal cells transduced with insulin-like growth factor-I localize to a fracture site and potentiate healing. J Orthop Trauma 16:651–659
14. Franceschi RT, Wang D, Krebsbach PH, Rutherford RB (2000) Gene therapy for bone formation: in vitro and in vivo osteogenic activity of an adenovirus expressing BMP7. J Cell Biochem 78:476–486
15. Betz OB, Betz VM, Nazarian A, Egermann M, Gerstenfeld LC, Einhorn TA, Vrahas MS, Bouxsein ML, Evans CH (2007) Delayed administration of adenoviral BMP-2 vector improves the formation of bone in osseous defects. Gene Ther 14:1039–1044
16. Tarkka T, Sipola A, Jämsä T, Soin Y, Ylä-Herttuala S, Tuukkanen J, Hautala T (2003) Adenoviral VEGF-A gene transfer induces angiogenesis and promotes bone formation in healing osseous tissues. J Gene Med 5:560–566
17. Shen HC, Peng H, Usas A, Gearhart B, Fu FH, Huard J (2004) Structural and functional healing of critical-size segmental bone defects by transduced muscle-derived cells expressing BMP4. J Gene Med 6:984–991
18. Rundle CH, Miyakoshi N, Kasukawa Y, Chen S-T, Sheng MH-C, Wergedal JE, Lau K-HW, Baylink DJ (2003) In vivo bone formation in fracture repair by direct retroviral-based gene therapy with BMP-4. Bone 32:591–601
19. Gysin R, Wergedal JE, Sheng MH-C, Kasukawa Y, Miyakoshi N, Chen S-T, Peng H, Lau K-HW, Mohan S, Baylink DJ (2002) Ex vivo gene therapy with stromal cells transduced with a retroviral vector containing the BMP4 gene completely heals critical size calvarial defect in rats. Gene Ther 9:991–999
20. Rundle CH, Strong DD, Chen S-T, Linkhart TA, Sheng M-HC, Wergedal JE, Lau K-HW, Baylink DJ (2008) Retroviral-based gene therapy with cyclooxygenase-2 promotes the union of bony callus tissues and accelerates fracture healing in the rat. J Gene Med 10:229–241
21. Zhang XS, Linkhart TA, Chen S-T, Peng H, Wergedal JE, Guttierez GG, Sheng MH-C, Lau K-HW, Baylink DJ (2004) Local ex vivo gene therapy with bone marrow stromal cells expressing human BMP4 promotes endosteal bone formation in mice. J Gene Med 6:4–15
22. Bolander ME (1992) Regulation of fracture repair by growth factors. Proc Soc Exp Biol Med 200:165–170
23. Abe E, Yamamoto M, Taguchi Y, Lecka-Czernik B, O'Brien CA, Economides AN, Stahl N, Jilka RL, Manolagas SC (2000) Essential requirement of BMPs-2/4 for both osteoblast and osteoclast formation in murine bone marrow cultures from adult mice: antagonism by noggin. J Bone Miner Res 15:663–673
24. Wozney JM, Rosen V (1998) Bone morphogenetic protein and bone morphogenetic protein gene family in bone formation and repair. Clin Orthop 346:26–37
25. Peng H, Wright V, Usas A, Gearhart B, Shen HC, Cummins J, Huard J (2002) Synergistic enhancement of bone formation and healing by stem cell-expressed VEGF and bone morphogenetic protein-4. J Clin Invest 110:751–759
26. Peng H, Usas A, Olshanski A, Ho AM, Gearhart B, Cooper GM, Huard J (2005) VEGF improves, whereas sFlt1 inhibits, BMP2-induced bone formation and bone healing through modulation of angiogenesis. J Bone Miner Res 20:2017–2027
27. Simon AM, Manigrasso MB, O'Connor JP (2002) Cyclo-oxygenase 2 function is essential for bone fracture healing. J Bone Miner Res 17:963–976
28. Zhang X, Schwarz EM, Young DA, Puzas JE, Rosier RN, O'Keefe RJ (2002) Cyclooxygenase-2 regulates mesenchymal cell differentiation into the osteoblast lineage and is critically involved in bone repair. J Clin Invest 109:1405–1415
29. Kawaguchi H, Pilbeam CC, Harrison JR, Raisz LG (1995) The role of prostaglandins in the regulation of bone metabolism. Clin Orthop 313:36–46
30. Klenke FM, Gebhard MM, Ewerbecj V, Abdollahi A, Huber PE, Sckell A (2006) The selective Cox-2 inhibitor celecoxib suppresses angiogenesis and growth of secondary bone tumors: an intravital microscopy study in mice. BMC Cancer 6:9
31. Carvalho RS, Einhorn TA, Lehmann W, Edgar C, Al-Yamani A, Apazidis A, Pacicca D, Clemens TL, Gerstenfeld LC (2004) The role of angiogenesis in a murine tibial model of distraction osteogenesis. Bone 34:849–861
32. Rundle CH, Chen S-T, Porte R, Wergedal JE, Lau K-HW (2008) Retroviral-based BMP-4 in vivo gene transfer strategy with intramedullary viral delivery optimizes transgene expression in rat femur fractures. Open Tiss Eng Regen Med J 1:14–22
33. Peng H, Chen S-T, Wergedal JE, Polo JM, Yee J-K, Lau K-HW, Baylink DJ (2001) Development of an MFG-based retroviral vector system for high secretion of functionally active human BMP-4. Mol Ther 4:95–104
34. Livak KJ, Schmittgen TD (2001) Analysis of relative gene expression data using real-time quantitative PCR and the $2^{-\Delta\Delta C}_{T}$ method. Methods 25:402–408
35. Farley JR, Hall SL, Herring S, Tarbaux NM (1992) Two biochemical indices of mouse bone formation are increased, in vivo, in response to calcitonin. Calcif Tissue Int 50:67–73
36. Farley JR, Baylink DJ (1986) Skeletal alkaline phosphatase activity as a bone formation index in vitro. Metabolism 35:563–571
37. Gram GJ, Nielsen SD, Hansen JE (1998) Spontaneous silencing of humanized green fluorescent protein (hGFP) gene expression from a retroviral vector by DNA methylation. J Hematother 7:333–341
38. Keila S, Kelner A, Weinreb M (2001) Systemic prostaglandin E_2 increases cancellous bone formation and mass in aging rats and stimulates their bone marrow osteogenic capacity in vivo and in vitro. J Endocrinol 168:131–139
39. Keller J (1996) Effects of indomethacin and local prostaglandin E_2 on fracture healing in rabbits. Dan Med Bull 43:317–329
40. Komuro Y, Akizuki T, Kurakata M, Ohmori K (1999) Histological examination of regenerated bone through craniofacial bone distraction in clinical studies. J Craniofac Surg 10:308–311
41. Xu Z, Choudhary S, Voznesensky O, Mehrotra M, Woodard M, Hansen M, Herschman H, Pilbeam C (2006) Overexpression of Cox-2 in human osteosarcoma cells decreases proliferation and increases apoptosis. Cancer Res 66:6657–6664
42. Choudhary S, Huang H, Raisz L, Philbeam C (2008) Anabolic effects of PTH in cyclooxygenase-2 knockout osteoblasts in vitro. Biochem Biophys Res Commun 372:536–541
43. Li X, Zhang Y, Kang H, Liu W, Liu P, Zhang J, Harris SE, Wu D (2005) Sclerostin binds to LRP5/6 and antagonizes canonical Wnt signaling. J Biol Chem 280:19883–19887
44. Suda N, Baba O, Udagawa N, Terashima T, Kitahara Y, Takano Y, Kuroda T, Senior PV, Beck F, Hammond VE (2001)

Journal : Large 223 | Dispatch : 31-8-2009 | Pages : 12
Article No. : 9282 | ☐ LE | ☐ TYPESET
MS Code : CTI-09-0131 | ☑ CP | ☑ DISK

Parathyroid hormone–related protein is required for normal intramembranous bone development. J Bone Miner Res 16: 2182–2191

45. ten Dijke P, Krause C, de Gorter DJ, Löwik CW, van Bezooijen RL (2008) Osteocyte-derived sclerostin inhibits bone formation: its role in bone morphogenetic protein and Wnt signaling. J Bone Joint Surg Am 90(Suppl 1):31–35
46. Swindle CS, Kim HG, Klug CA (2004) Mutation of CpGs in the murine stem cell virus retrovial vector long terminal repeat represses silencing in embryonic stem cells. J Biol Chem 279: 34–41
47. Pannell D, Ellis J (2001) Silencing of gene expression: implications for design of retrovirus vectors. Rev Med Virol 11:205–217
48. Paralkar VM, Grasser WA, Mansolf AL, Baumann AP, Own TA, Smock SL, Martinovic S, Borovecki F, Vukicevic S, Ke HZ, Thompson DD (2002) Regulation of BMP-7 expression by retinoic acid and prostaglandin E_2. J Cell Physiol 190:207–217

Journal : **Large 223** Dispatch : **31-8-2009** Pages : **12**
Article No. : **9282** ☐ LE ☐ TYPESET
MS Code : **CTI-09-0131** ☑ CP ☑ DISK